HARMO21

PROCEEDINGS

27-30 September, Aveiro, Portugal
University of Aveiro

http://harmo21.web.ua.pt

universidade de aveiro

HARMO 21

21st International Conference on Harmonisation within Atmospheric Dispersion Modelling for Regulatory Purposes
27-30 September 2022 | Aveiro, Portugal

PROCEEDINGS

Edited by
Silvia Trini-Castelli
Ana Isabel Miranda
Bruno Augusto
Joana Ferreira

AVEIRO, 2022

History of the Harmonisation Workshop/Conference:
1st Harmo workshop, Risø National Laboratory, Denmark, 1992
2nd Harmo workshop, Manno, Switzerland1993
3rd Harmo workshop, Mol, Belgium, 1994
4th Harmo workshop, Oostende, Belgium, 1996
5th Harmo conference, Rodos, Greece, 1998
6th Harmo conference, Rouen, France, 1999
7th Harmo conference, Belgirate, Italy, 2001
8th Harmo conference, Sofia, Bulgaria, 2002
9th Harmo conference, Garmisch-Partenkirchen, Germany, 2004
10th Harmo conference, Crete, Greece, 2005
11th Harmo conference, Cambridge, UK, 2007
12th Harmo conference, Cavtat, Croatia, 2008
13th Harmo conference, Paris, France, 2010
14th Harmo conference, Kos, Greece, 2011
15th Harmo conference, Madrid, Spain, 2013
16th Harmo conference, Varna, Bulgaria, 2014
17th Harmo conference, Budapest, Hundary, 2016
18th Harmo conference, Bologna, Italia, 2017
19th Harmo conference, Bruges, Belgium, 2019
20th Harmo conference, Tartu, Estonia, 2021

The scientific focus of Harmo 21 is on the following topics:
• Model evaluation and quality assurance – model validation, model intercomparisons, model uncertainties and model sensitivities
• Environmental impact assessment: Air pollution management and decision support systems
• Use of modelling in support of EU air quality directives, including FAIRMODE
• Parametrization of physical processes in mesoscale meteorology relevant for air quality modelling
• Urban scale and street canyon modelling: Meteorology and air quality
• Use of modelling in health and exposure assessments • Inverse dispersion modelling and source identification
• Modelling air dispersion and exposure to accidental releases
• Mathematical problems in air quality modelling
• Highlights of past work. Session devoted to reviews and to prominent scientists and ‘golden papers’ of the past, which have still relevance and should not be forgotten
• Nature-based Solutions

Steering Committee:
Prof. J. Bartzis, University of West Macedonia, Greece
Prof. E. Batchvarova, CAWRI-BAS, Sofia, Bulgaria
Prof. C. Borrego, University of Aveiro, Portugal
Prof. L. Bozó, HMS, Budapest, Hungary
Dr. B. Carissimo, EdF R&D, Chatou, France
Dr. D. Carruthers, CERC, Cambridge, UK
Prof. S. Di Sabatino, Bologna University, Italy
Prof. M. Ketzel, Aarhus University, Denmark
Dr. F. Martin, Ciemat, Spain
Prof. C. Mensink, VITO, Mol, Belgium
Prof. N. Moussiopoulos, Univ. Of Thessaloniki, Greece
Dr. H. Olesen, Aarhus University, Denmark
Dr. P. Suppan, KIT/IMK-IFU, Garmisch-Partenkirchen, Germany
Dr. P. Thunis, JRC, Ispra, Italy
Dr. S. Trini Castelli, CNR-ISAC, Italy (Chair)

Scientific Committee:
Dr. A. Albergel, Aria Technologies, France
Dr. P. Armand, CEA, France
Prof. J. Bartzis, University of West Macedonia, Greece
Prof. E. Batchvarova, CAWRI-BAS, Sofia, Bulgaria
Prof. C. Borrego, University of Aveiro, Portugal
Prof. L. Bozó, HMS, Budapest, Hungary
Dr. B. Carissimo, EdF R&D, Chatou, France
Dr. D. Carruthers, CERC, Cambridge, UK
Dr. C. Cuvelier, ex. JRC, Ispra, Italy
Prof. S. Di Sabatino, Bologna University, Italy
Dr. Z. Ferenczi, HMS, Budapest, Hungary
Dr. C. Gama, University of Aveiro, Portugal
Dr. D. Hertwig, University of Reading, UK
Dr. A. Jeričević, CCAA, Croatia
Prof. M. Kaasik, University of Tartu, Estonia
Prof. M. Ketzel, Aarhus University, Denmark
Prof. B. Leitl, Met. Inst., Univ. Hamburg, Germany
Dr. F. Martin, CIEMAT, Spain
Prof. C. Mensink, VITO, Mol, Belgium
Prof. A.I. Miranda, University of Aveiro, Portugal
Prof. N. Moussiopoulos, Univ. Of Thessaloniki, Greece
Dr. V. Rodrigues, University of Aveiro, Portugal
Prof. R. San Jose, Technical Univ. of Madrid, Spain
Dr. P. Suppan, KIT/IMK-IFU, Garmisch-Partenkirchen, Germany
Prof. D. Syrakov, NIMH, Sofia, Bulgaria

Dr. D. Thomson, The Met Office, Exeter, UK
Dr. P. Thunis, JRC, Ispra, Italy
Dr. S. Trini Castelli, CNR-ISAC, Italy

Local Organizing Committee:
Ana Isabel Miranda (chair)
Alexandra Monteiro
Joana Ferreira
Bruno Augusto
Carla Gama
Vera Rodrigues

CONTENTS

21th International Conference on
Harmonisation within Atmospheric Dispersion Modelling
for Regulatory Purposes
27-30 September 2022, Aveiro, Portugal

TOPIC 1:

MODEL EVALUATION AND QUALITY ASSURANCE – MODEL VALIDATION, MODEL INTERCOMPARISONS, MODEL UNCERTAINTIES AND MODEL SENSITIVITIES

21st International Conference on
Harmonization within Atmospheric Dispersion Modelling for Regulatory Purposes
27-30 September 2022, Aveiro, Portugal

IMPROVEMENT AND VALIDATION OF THE ACEW POLLUTION STATISTICAL MODEL OVER THE AIX-MARSEILLE METROPOLIS

Daniel Loeb[1], Léo Bargain[2], Maxime Nibart[3]
[1]ARIA Technologies, Boulogne-Billancourt, France
[2]Université Paris-Saclay, Orsay, France
[3]ARIA Technologies, Boulogne-Billancourt, France

Abstract: *ACEW (AirCityEveryWhere) is a tool developed by ARIA Technologies that calculates and provides emission inventories for any location on earth. To do so, ACEW extrapolates pollutant emissions from traffic data and uses machine learning in order to make AADT (Average Annual Daily Traffic) estimations for each segment of the road covering the zone of interest. This requires a thorough investigation in order to determine which road characteristics can be used to make reliable traffic predictions. In this study, it is demonstrated that some features can be overlooked by a machine learning model and additionally that features overly specific to the chosen location can lead to an overfit. Furthermore, the use of the machine learning algorithm called Random Forest proved to be useful for traffic estimation over the Aix-Marseille metropolis since its wide range of hyperparameters and their optimization resulted in significantly improved ACEW estimations of AADT and better potential generalization of the ACEW method to other geographical areas.*

Key words: *machine learning*, *AADT*, *random forest, hyperparameters*

INTRODUCTION

The quality of the air we breathe can be highly deteriorated by road traffic. Indeed, vehicles are a source of numerous chemical compounds and particles, like CO and particulate matter (PM) that are harmful to our health. For example, it is estimated that PM pollution was responsible for over 300,000 premature deaths in the EU in 2019.

Concerned about this public health issue, the Aix-Marseille metropolis launched the DIAMS project with the intent of raising the awareness of the public about the topic of air quality. To do so, the Aix-Marseille metropolis collaborates with several partners, including ARIA Technologies in order to model dispersion of air pollutants over the metropolis. Part of simulating this dispersion relies on the calculation of emission inventories. These inventories can be extrapolated from traffic volumes, which may or may not be available over the entirety of the road network of the study location. In order to compensate for potential missing or unavailable data in traffic volume datasets, Aria Technologies developed ACEW, a tool that provides emission inventories using AADT data for any chosen location on earth. While the geographical data processing algorithms of this tool have been tested, the machine learning model it depends on to make traffic estimations has begun to be examined, validated and further improved.

MATERIALS AND METHODS

Data: The data used in order to train and test the model is provided by the Aix-Marseille metropolis.

Algorithm: The python module RandomForestRegressor was employed in order to use the Random Forest algorithm. The random forest algorithm is considered to be a robust one, resistant to overfit and capable of very good performance (Schonlau and Zou, 2020).

Performance indicators: Three indicators were chosen to quantify the quality of AADT estimations: RMSE (Root Mean Squared Error), MAPE (Mean Absolute Percentage Error) and R^2 (Coefficient of determination). The RMSE represents the average difference between the observed and simulated AADT values. The MAPE represents the average difference between the observed and simulated AADT values as a percentage of the observed value. The R^2 represents the proportion of the variance in the outcome variable that is explained by the predictions. We hope to see to observe minimal MAPE and RMSE indicators and maximal R^2 values when evaluating model performance.

Optimization of hyperparameters: The python module RandomSearchCV was used in order to choose one of the best possible combinations of hyperparameters, which is important in order to avoid overfitting and underperforming. There is no clearly defined way to optimize hyperparameters, rather needing to define a range of values for each hyperparameter, from which calculus decides which one of the randomly picked combinations is the best. In order to spare calculus time, this module was chosen over GridSearchCV that considers all combinations. Moreover, RandomForestRegressor has over ten hyperparameters but only six of them were analyzed. The chosen hyperparameters and explored values are presented in table 1.

Table 1. Random Forest hyperparameters to optimize

Hyperparameter	Description	Explored values
n_estimator	number of trees in the forest	200,400,600,800,1000
max_features	number of features to consider when looking for the best split	Auto, Sqrt
max_depth	maximum number of nodes in a branch	5, 10, 15
min_samples_split	minimum number of samples to split	2, 4, 6, 8, 10
min_samples_leaf	minimum number of samples for a leaf	5, 10, 15
bootstrap	whether bootstrap samples are used when building trees	True, False

It was chosen that 100 of the 900 combinations would be tested, reducing the calculus time from over twenty days to a few hours. The indicator for selecting the best combination was chosen to be R^2.

Validation: The python module cross_validate was used in order assess the model's performance, the chosen method was a 10-fold cross validation. This method consists of randomly splitting the dataset into ten subsets, then using nine of them to train the algorithm while the remaining one allows us to test the model. There are ten iterations, so that every one of the ten subsets is alternatively used as the testing dataset. If the performances are similar no matter the training and testing datasets, we can conclude that the algorithm is well configured. For all indicators, the maximum, minimum and mean of the ten iterations are presented, the maximum and minimum showing the performance variability and the mean allowing easy comparisons between experiments.

RESULTS AND DISCUSSION

Firstly, we investigated whether every explanatory variable at our disposal was useful to the model. These variables are presented in table 2.

Table 2. Explanatory variables at our disposal

Variable	Description
xcoord	Horizontal coordinate of the center of the road (EPSG:4326)
ycoord	Vertical coordinate of the center of the road (EPSG:4326)
urbain	Road in an urban area or not
dens_1	Density of population in a 1 km² area around the center of the road
importance	Type of the road
roadwidth	Width of the road
lanes	Number of lanes of the road
maxweight	Maximum weight allowed on the road
maxheight	Maximum height allowed on the road
maxspeed	Maximum speed allowed on the road
oneway	One-way road or not

All these variables except two characterize the roads, while AADT prediction models commonly use socioeconomic attributes (Sfyridis and Agnolucci, 2020), which is difficult to implement in our case because ACEW collects information from OpenStreetMap. Thereby performance is likely to be limited without further data processing.

The *xcoord* and *ycoord* variables were initially and qualitatively thought to be good explanatory variables, allowing the model to approximately locate a road before it estimates its AADT. However, we did hypothesize that these variables could lead to an overfit. Indeed, each value couple (*xcoord* ; *ycoord*) locates one and only one road, which means that these two variables are adequate for the model to estimate the AADT of every road pre-contained in its training dataset. In order to estimate the impact of these variables on the model, we compared the model's performances on training and testing datasets with and without them, the algorithm was a Random Forest with default hyperparameter values. The results of the experiment are presented in Table 3 and Table 4.

Table 3. Performances on testing and training datasets with *xcoord* and *ycoord* among explanatory variables

R^2 test	R^2 train	RMSE test	RMSE train	MAPE test	MAPE train
Max: 0.102	Max: 0.917	Max: 6258	Max: 1460	Max: 287%	Max: 38.4%
Min: -0.572	Min: 0.913	Min: 2907	Min: 1348	Min: 124%	Min: 34.1%
Mean: -0.073	Mean: 0.914	Mean: 4718	Mean: 1410	Mean: 205%	Mean: 36.4%

Table 4. Performances on testing and training datasets without *xcoord* and *ycoord* among explanatory variables

R^2 test	R^2 train	RMSE test	RMSE train	MAPE test	MAPE train
Max: 0.112	Max: 0.452	Max: 6374	Max: 3741	Max: 186%	Max: 118%
Min: -0.103	Min: 0.432	Min: 2908	Min: 3420	Min: 112%	Min: 104%
Mean: -0.041	Mean: 0.439	Mean: 4520	Mean: 3601	Mean: 152%	Mean: 112%

It appears that when we use *xcoord* and *ycoord* as explanatory variables, the performances are high on the training dataset, but far lower on the testing dataset, indicating a clear overfit. We also observed that there is still an overfit when removing these two variables, but the performance difference between training and testing datasets decreases significantly, showing that the *xcoord* and *ycoord* variables are a source of overfit. Moreover, it appears that the model performs better on the testing dataset without the two variables, which is a consequence of a smaller overfit. The conclusion of this experiment is that we need to remove the *xcoord* and *ycoord* variables, which will be the case for all the following experiments.

Another line of questioning was whether the gain in performance provided by the variables *roadwidth*, *lanes*, *maxheight*, *maxweight* and *maxspeed* was considerable, since their values are often inaccessible. The experiment consisted of testing the model without these five variables, the algorithm was a Random Forest with default hyperparameters values. The results are presented in Table 5.

Table 5. Performances on testing and training datasets after removing the five explanatory variables

R^2 test	R^2 train	RMSE test	RMSE train	MAPE test	MAPE train
Max: 0.084	Max: 0.377	Max: 6622	Max: 3982	Max: 188%	Max: 127%
Min: -0.038	Min: 0.357	Min: 2787	Min: 3634	Min: 105%	Min: 112%
Mean: -0.021	Mean: 0.364	Mean: 4586	Mean: 3833	Mean: 147%	Mean: 120%

By comparing Table 4 and Table 5, we can conclude that these 5 variables should be removed, since they do not result in an improved model performance on the testing dataset while unnecessarily increasing the model's complexity. Finally, out of all the variables initially at our disposal, only four are considered exploitable, significantly simplifying the model and reducing the risk of overfitting.

It can be observed that in all of the previous experiments, the model's performance was clearly superior when applied to the training dataset rather than on the testing dataset. We hypothesized that this was caused by the default values of the RandomForest hyperparameters, since their role is to control the algorithm's

training. For this reason, we worked on finding a better combination of values for the hyperparameters, which led to the modifications presented in Table 6 and to the results presented in Table 7.

Table 6. Optimization of hyperparameters

Hyperparameter	Default value	New value
n_estimator	100	600
max_features	1	Sqrt (= 2)
max_depth	None : nodes expand until all leaves are pure or until all leaves contain less than min_samples_split samples	5
min_samples_split	2	4
min_samples_leaf	1	10
boostrap	True	True

Table 7. Performances on testing and training datasets after optimizing hyperparameters

R^2 test	R^2 train	RMSE test	RMSE train	MAPE test	MAPE train
Max: 0.249	Max: 0.258	Max: 5739	Max: 4312	Max: 199%	Max: 142%
Min: 0.178	Min: 0.248	Min: 2433	Min: 3958	Min: 107%	Min: 126%
Mean: 0.229	Mean: 0.252	Mean: 4079	Mean: 4157	Mean: 135%	Mean: 134%

Two main observations were made comparing Table 5 and Table 7. Firstly, we can see that the model's performance greatly increased on the testing dataset, with R^2 going from around 0 to 0.229 on average. Secondly, performances on training and testing datasets have become similar, indicating that there is no longer a clear overfit. While the predictions have improved, performance might be further enhanced by taking the time to find one of the very best combinations of hyperparameters.

To summarize, figures 1, 2 and 3 show the model's improvement in generalization and in AADT estimations on testing datasets.

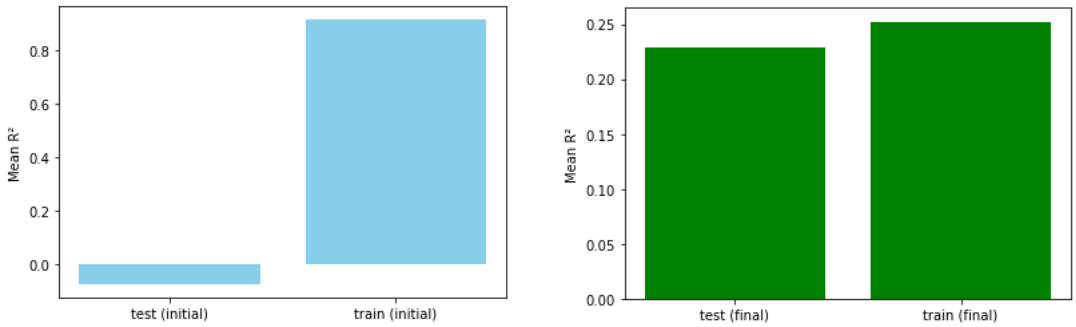

Figure 1. *Global evolution of the R^2 indicator on testing and training datasets*

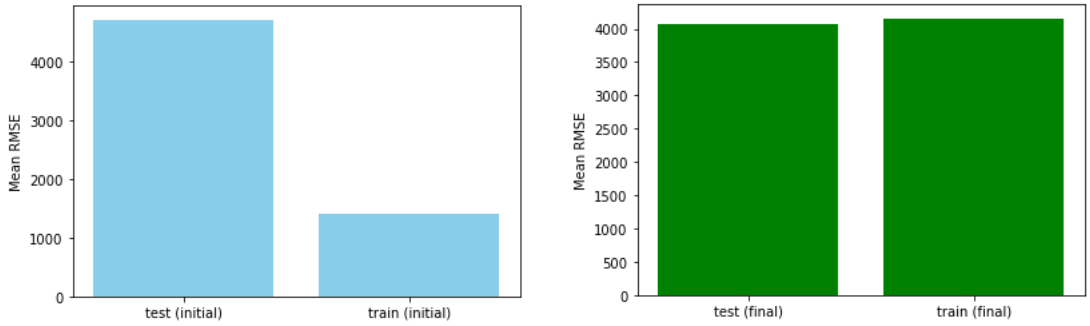

Figure 2. *Global evolution of the RMSE indicator on testing and training datasets*

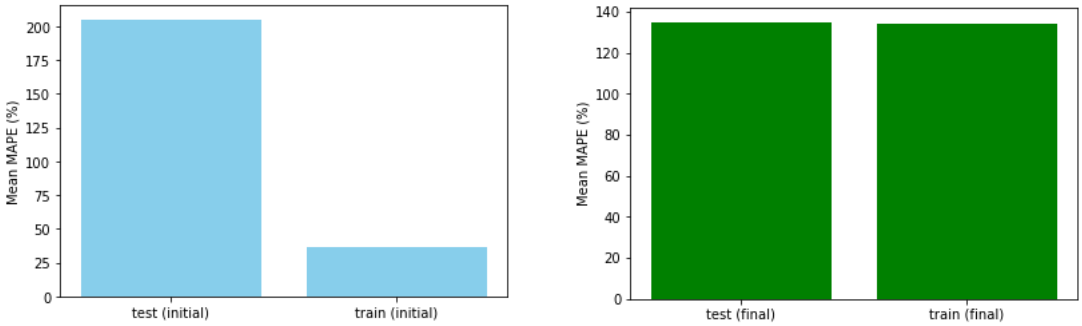

Figure 3. *Global evolution of the MAPE indicator on training and testing datasets*

CONCLUSIONS

The purpose of this study was to make the best possible AADT estimations over the Aix-Marseille metropolis using ACEW. To do so, we examined the use of geographic coordinates as explanatory variables of AADT, as well as the use of variables with incomplete values. We also analyzed the role of hyperparameters on overfitting and performance of the Random Forest method.

Our work showed that using geographic coordinates as explanatory variables led to poor AADT estimations because it allowed the model to make decisions overly specific to its training dataset, allowing us to recreate the dataset closely, but not to apply the model to other locations. It was also demonstrated that many explanatory variables at our disposal did not provide a gain in performance because of extensively incomplete values. Finally, it was revealed that optimized hyperparameter values are key for avoiding overfitting and ensuring satisfactory performance of the statistical model.

REFERENCES

M.Schonlau and R.Yuyan Zou, 2020 : The random forest algorithm for statistical learning. *The Stata Journal*, **20**, 3-29.

A.Sfyridis and P.Agnolucci, 2020 : Annual average daily traffic estimation in England and Wales : An application of clustering and regression modeling. *Journal of Transport Geography*, **83**.

21st International Conference on
Harmonisation within Atmospheric Dispersion Modelling for Regulatory Purposes
27-30 September 2022, Aveiro, Portugal

NEAR-RANGE GAUSSIAN PLUME MODELLING FOR GAMMA DOSE RATE RECONSTRUCTION

Jens Peter Frankemölle[1,2], Johan Camps[1], Pieter De Meutter[1] and Johan Meyers[2]

[1]SCK CEN, Belgian Nuclear Research Centre, Boeretang 200, BE-2400 Mol, Belgium
[2]KU Leuven, Dept. Mechanical Engineering, Celestijnenlaan 300, BE-3000 Leuven, Belgium

Abstract: In the context of nuclear facilities, atmospheric dispersion modelling is often used for emergency planning and during accidents. Gamma dose rate stations, that are installed in the vicinity of many nuclear facilities as part of an early warning network, are often the first source of information when radioactivity is released to the atmosphere. Moreover, at some installations these stations are also able to pick up emissions during routine operation. In this work, we perform near-range atmospheric transport and dispersion simulations at three nuclear installations (of which two were operating normally and one during an incident) under varying meteorological conditions. The purpose of this modelling is to check consistency between the various components of several unexplored datasets. Source terms are estimated based on stack monitoring and/or calculations, and meteorological data were obtained on-site. A Gaussian plume model is used for the dispersion calculations, and gamma dose rates are calculated through volumetric integration over the full cloud and all different photon energies rather than using dose coefficients. Modelling results are subsequently compared with gamma dose rates that were observed using both fixed and mobile measurement stations. Largely consistent results were obtained between observed dose rates and modelling results.

KEY WORDS: **NEAR-RANGE, ATMOSPHERIC DISPERSION, GAUSSIAN PLUME, GAMMA DOSE RATE, RADIONUCLIDES**

INTRODUCTION

In this study, we performed calculations for the near-range atmospheric dispersion of several types of gamma-emitting radionuclides at different facilities in Belgium. Such calculations are of critical importance to determine the impact of radiological contamination in the event of a radiological or nuclear emergency but also in preparing for such emergencies. Using concentration fields obtained by a Gaussian plume model (Bultynck and Malet, 1972), we calculated ambient dose equivalent rates (Healy and Baker, 1968) and compared those to real measurements from TELERAD stations (Sonck et al, 2008). The aim is to check the consistency between meteorological and source term data on the one hand and ambient dose equivalent rates on the other. To this end, we present three case studies. For case I, we reproduced results from a 2017 campaign at the National Institute for Radioelements (IRE) in Fleurus (Camps et al, 2019). For case II, we simulated the 2019 anomalous release of Se-75 from the Belgian Reactor 2 (BR2) at SCK CEN in Mol (De Meutter and Hoffman, 2020). For case III, we simulated the continuous release of Ar-41 over the course of a day's routine operation of the Belgian Reactor 1 (BR1) at SCK CEN (Bijloos et al, 2020).

MODEL

In this study, we used a Gaussian plume model (GPM) including ground surface reflection and a dispersion parametrisation that was specifically developed for the SCK CEN site in Mol (Bultynck and Malet, 1972), which is characterised by its flat terrain and many trees. The horizontal and vertical dispersion coefficients are a function of the atmospheric stability and the downwind distance. Moreover, they are multiplied by a correction factor to account for variations in the meteorological sampling periods

(Beychock, 1994). The model further accounts for plume rise (Briggs, 1971) and dispersion is constrained to the height of the mixing length of the boundary layer, which also depends on the atmospheric stability (Kretzschmar, Mertens and Vanderborght, 1984). In a given time window, the meteorological conditions enter through the wind speed and direction, the ambient temperature and the atmospheric stability class. Meanwhile, the source is defined by a radiological emission rate (Bq s^{-1}), the emission height and the total gas outflow and temperature out of the stack. Plume profiles are calculated for consecutive time windows and then projected onto a three-dimensional domain in the correct wind direction.

This spatially resolved concentration field $\chi(\boldsymbol{r}')$ can be used to calculate the ambient dose equivalent rate at a detector in location $\boldsymbol{r}$. However, a single radionuclide can have many different decay pathways and all of these need to be taken into account separately. For example, Se-75 emits 21 γ-rays with different energies E_γ and intensities I_γ. We describe the ambient dose equivalent rate as (Healy and Baker, 1968)

$$\frac{\partial}{\partial t}H^*(10,\boldsymbol{r}) = \sum_\gamma C_\gamma I_\gamma \left[\frac{\mu_{\text{en}} K E_\gamma}{4\pi\rho}\iiint \frac{B(\mu r)\exp[-\mu r]}{r^2}\chi(\boldsymbol{r}')\mathrm{d}\boldsymbol{r}'\right] \quad (1)$$

where $[\ldots]$ is the dose rate integral over all point sources $\chi(\boldsymbol{r}')\mathrm{d}\boldsymbol{r}'$ that form the plume. Here, $r = \|\boldsymbol{r}' - \boldsymbol{r}\|$ is the source–detector distance. The mass attenuation coefficients μ/ρ and mass energy absorption coefficients μ_{en}/ρ (with ρ the air density) depend on E_γ (Martin, 2013) as does the build-up factor $B(\mu r)$ (Trubey et al, 1991). $K = 1.6 \times 10^{-13}$ is a proportionality constant. The factors C_γ are γ-dependent conversion factors (ICRP, 1996) to go from Gy s^{-1} to Sv s^{-1}. Taking $\sum C_\gamma I_\gamma [\ldots]_\gamma$ finally yields the total ambient dose equivalent rate in a point $\boldsymbol{r}$ due to a radionuclide concentration field $\chi(\boldsymbol{r}')$. The Python source code – Atmospheric Dispersion and Dose Equivalent Rates (ADDER) – has been made publicly available at *https://gitlab.com/jpfr95/adder*.

CASE I: routine release at ire in 2017

A three-day measurement campaign was conducted at the National Institute for Radioelements (IRE) on 12, 13 and 15 September 2017. The object of that campaign was to measure a plume consisting of Xe-133, Xe-133m, Xe-135 and Xe-135m that is routinely emitted at IRE (Camps et al, 2019). On-site wind data were available each ten minutes at a height of 30 m, the same as the stack height. To determine the atmospheric stability, data from a meteorological mast in Mol were used. Source term data were available each fifteen minutes for all four separate isotopes. Finally, dose rates were available from eight TELERAD stations (Sonck et al, 2008). Three of these were fixed while five others could be moved around (Figure 1).

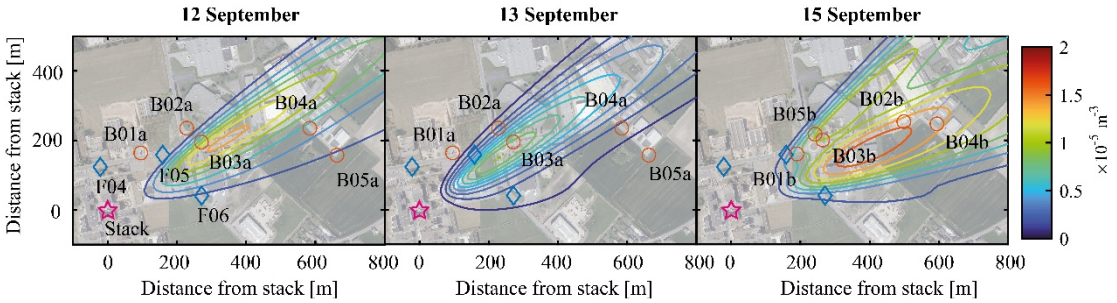

Figure 1. Average concentration profiles for a unit release superimposed on an aerial photograph of the IRE site in Fleurus dated 2018 (*https://geoportail.wallonie.be*). Also plotted are the locations of the stack (pink stars), the fixed TELERAD stations (blue diamonds) and the mobile TELERAD stations (red circles).

Simulations were performed on a 2.4-km-by-2.4-km-by-0.2-km grid with a 10-meter spacing in all dimensions. Briggs' buoyant plume rise formula was switched off while the stack height was artificially increased to 35 m to account for momentum plume rise, which is not included in the model. The GPM

was used to simulate unit releases because the isotope ratios varied over time. The time-averaged results are shown in Figure 1. Contributions to the dose rate were then separately calculated for each of the isotopes in each of the detectors at each point in time. The total simulated dose rates are shown in Figure 2 and compared to TELERAD measurements. Limited data were available to cleanly subtract the background radiation level, so the assumption was made that the first timestamp of a detector in the morning was indicative of the background. Overall, the match between GPM and TELERAD is good, but results are better for 12 and 13 September than for 15 September. This might be related to the combination of a more variable wind (as evidenced by Figure 1) and a much lower average wind speed. The wind speed averaged 6.1 m s^{-1} on 12 September and 10.3 m s^{-1} on 13 September, while it was only 2.9 m s^{-1} on 15 September.

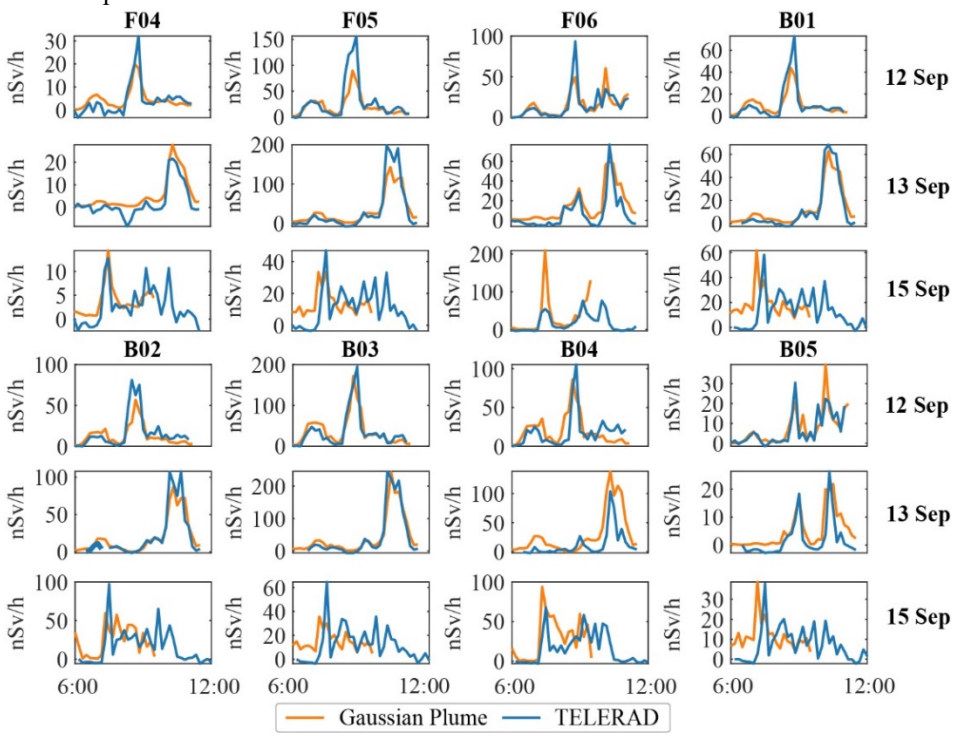

Figure 2. Results of GPM compared to TELERAD data for the IRE case. F04–F06 are fixed stations while B01–B05 are mobile stations. The background radiation is subtracted from the TELERAD signals (see text).

Case II: anomalous release at br2 in 2019

A small but measurable puff of radioactive Se-75 was released to the atmosphere during an incident in one of the hot cells at the Belgian Reactor 2 (BR2) of the Belgian Nuclear Research Centre (SCK CEN) in Mol on 15 May 2019 (De Meutter and Hoffman, 2020). This release was picked up by three TELERAD stations downwind of the BR2 stack (Figure 3). However, the release was so small that the increase in dose rate was only slightly bigger than the fluctuations in the radiation background (Figure 4). On-site wind data were available at a height of 69 m each ten minutes. Additionally, measurements of the ambient temperature at 8 m and 114 m were available each ten minutes to determine the stability class and account for plume rise. There was an ENE wind averaging 6.3 m s^{-1} and a slightly unstable atmosphere of class four. Additionally, the integrated source term of the puff was available. Under the assumption of a constant release for half an hour between 15:10–15:40 CEST (UTC+2), this allowed for the formulation of an emission rate. The BR2 stack has a height of 60 m, a gas outflow of 41.7 m^3 s^{-1} and an (assumed) gas temperature of 15°C.

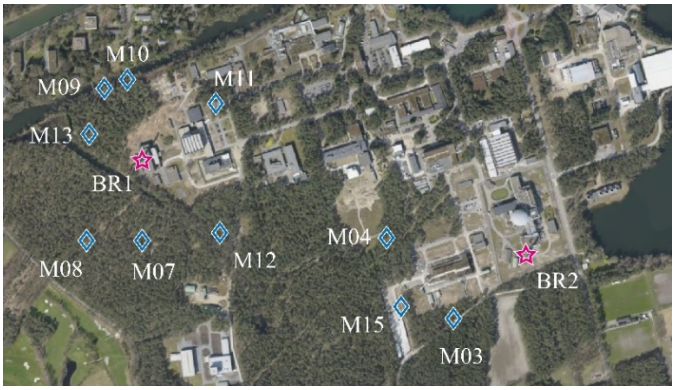

Figure 3. Aerial photograph of the SCK CEN site in Mol dated 2013–2015 (*https://www.geopunt.be/*). Locations of the BR1 and BR2 stacks (purple stars) along with several TELERAD stations (blue diamonds) are indicated.

A manuscript (Frankemölle et al, 2022) is under preparation that will cover the near-range dispersion of this anomalous release more fully in the future including deposition and concentration measurements. Here, we focus on the three TELERAD detectors. Since these detectors are close to the BR2, the release was simulated on a small grid of only 500-m-by-500-m-by-200-m with a 10-meter spacing in all dimensions. Plume rise was enabled. Simulations results are shown in Figure 4 together with TELERAD data. Based on the available meteorological and source term data, the GPM matches the TELERAD data quite well.

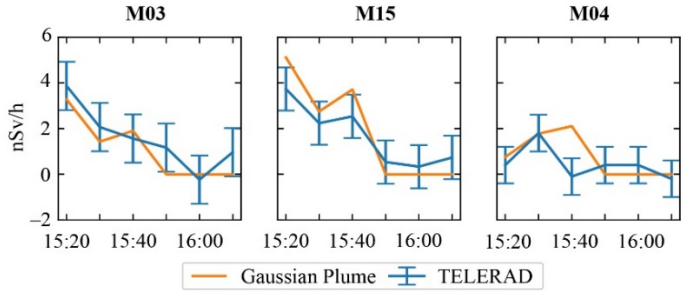

Figure 4. Results of GPM versus TELERAD measurements for the BR2 case. The mean background radiation is calculated based on the period 12:00–15:00. Error bars denote the 95% confidence intervals of that mean background.

Case III: routine release at br1 in 2019

The Belgian Reactor 1 (BR1) at SCK CEN in Mol is an air-cooled reactor that emits Ar-41 during routine operation. Seven TELERAD stations that surround the reactor (Figure 3) routinely pick up increased dose rates during operation (Bijloos et al, 2020). The same meteorological data were available here as in case II and the BR1 stack is also 60 m high. Plume rise is neglected. As the source term, we used ten-minute averaged data from an uncalibrated detector in the BR1 stack that monitors the relative release rate of Ar-41 and we scaled it so that its mean release rate during stable operation amounted to 57 GBq h^{-1} (Bijloos et al, 2020) initially. The release was simulated on an 500-m-by-500-m-by-200-m grid with a 10-meter grid spacing in all dimensions. Results are shown in Figure 5.

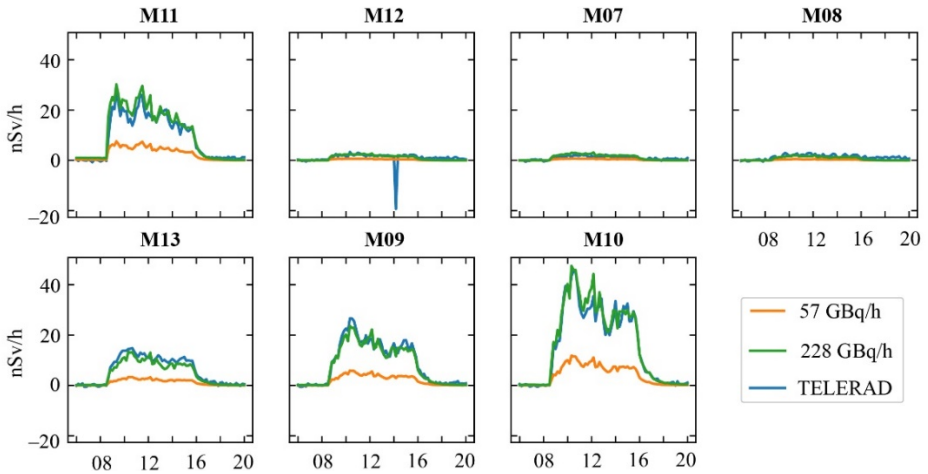

Figure 5. Simulations of the ambient dose equivalent rates in seven TELERAD stations around the BR1 compared to actual measurements. Two source term estimates, 57 GBq h^{-1} and 228 GBq h^{-1}, were compared.

We find that using a source term of 57 GBq h^{-1} leads to around a factor of 4 underestimation of the ambient dose equivalent rates at all TELERAD stations. This is in line with Bijloos et al (2020), who found a factor of 3.5 to 4 underestimation using various dispersion models for the BR1. They found that an alternative estimate for the BR1 source term of 150 GBq h^{-1} (Rojas-Palma et al, 2004) yielded better results that were, however, still off by a factor of 1.2 to 1.5. Motivated by our and their findings, we also tested a fourfold increased source term of 228 GBq h^{-1}. In this case, we observe that the data match very well.

DISCUSSION AND CONCLUSION

In this study, we set out to confirm the consistency between meteorological and source term data on the one hand and measurements of ambient dose equivalent rates by TELERAD stations on the other using a Gaussian plume model (GPM). Routine and anomalous releases from three different nuclear facilities were analysed. Largely consistent results were obtained for IRE and BR2. For BR1, consistent results could only be obtained with a four times larger source term than the current accepted value. That results for IRE and BR2 – more complex situations with multiple emission lines and/or very small detections – should yield considerably better results begs the question whether the values quoted (Bijloos et al, 2020; Rojas-Palma et al, 2004) adequately describe the true source term. This was previously pointed out by Bijloos et al (2020). Overall, GPM seems well-suited to simulating ambient dose equivalent rates. Envisaged next steps are to combine GPM with Bayesian inference or data assimilation approaches to yield even closer matches. In the future, GPM might even be used estimate the source term of the BR1 directly from TELERAD data.

ACKNOWLEDGEMENTS

The authors would like to thank François Menneson from FANC-AFCN for providing access to the TELERAD data.

REFERENCES

Beychock, M. R., 1994: Fundamentals of stack gas dispersion, 3rd Edition, M.R. Beychock, Irvine.

Briggs, G. A., 1971: Some recent analyses of plume rise observations – des analyses recentes des observations de panache montante in Englund, H. M. and W. T. Beery (eds.): Proceedings of the Second International Clean Air Congress, Academic Press, New York, 1029-1032.

Bijloos, G., J. Camps, L. Tubex and J. Meyers, 2020: Parametrization of homogeneous forested areas and effect on simulated dose rates near a nuclear research reactor. Journal of Environmental Radioactivity, ***225****, 106445.*

Bultynck, H. and L. M. Malet, 1972: Evaluation of atmospheric dilution factors for effluents diffused from an elevated continuous point source. Tellus*,* ***24****, 455-477.*

Camps, J., C. Gueibe, J. Rutten, T. Vidmar, F. Menneson, A. Delcloo and B. Deconninck, 2019: Source term estimation of xenon releases from medical isotope production: a test case for near-range atmospheric dispersion modelling. 5th NERIS Workshop, Roskilde, Denmark, 3–5 April 2019.

De Meutter, P. And I. Hoffman, 2020: Bayesian source reconstruction of an anomalous Selenium-75 release at a nuclear research institute. Journal of Environmental Radioactivity, ***218****, 106225.*

Frankemölle, J. P. K. W., J. Camps, P. De Meutter, P. Antoine, A. W. Delcloo, F. Vermeersch and J. Meyers, 2022: Near-range atmospheric dispersion of an anomalous selenium-75 emission. Manuscript under preparation.

Healy, J. W. and R. E. Baker, 1968: Radioactive cloud-dose calculations in Slade, D. H. (ed.): Meteorology and atomic energy, 301-377.

ICRP, 1996: Conversion Coefficients for use in Radiological Protection against External Radiation, ICRP Publication 74, Annals of the ICRP, ***26****.*

Kretzschmar, J.G., I. Mertens and B. Vanderborght, 1984: Sensitivity, applicability and validation of bi-gaussian off- and on-line models for the evaluation of the consequences of accidental releases in nuclear facilities: final report contract no. SR-028-B, Commision of the European Communities, Luxemburg.

Martin, J. E., 2013: Physics for Radiation Protection, Wiley, Weinheim.

Rojas-Palma, C., H. K. Aage, P. Astrup, K. Bargholz, M. Drews, H. E. Jørgensen, U. Korsbech, B. Lauritzen, T. Mikkelsen, S. Thykier-Nielsen and R. Van Ammel, 2004: Experimental evaluation of gamma fluence-rate predictions from argon-41 releases to the atmosphere over a nuclear research reactor site. Radiation Protection Dosimetry, ***108****, 161-168.*

Sonck, M., M. Desmedt, J. Claes and L. Sombré, 2008: TELERAD: the Radiological Surveillance Network and Early Warning System in Belgium. International congress of the International Radiation Protection Associations (IRPA): Strengthening radiation protection worldwide, Buenos Aires, Argentina, 19–24 October 2008.

Trubey, D. K., C. M. Eisenhauer, A. Foderaro, D. V. Gopinath, Y. Harima, J. H. Hubbell, K. Shure and S. Su., 1991: Gamma-ray attenuation coefficients and buildup factors for engineering materials, American National Standard ANSI/ANS-6.4.3-1991, American Nuclear Society, La Grange Park.

21st International Conference on
Harmonisation within Atmospheric Dispersion Modelling for Regulatory Purposes
27-30 September 2022, Aveiro, Portugal

ASSESSMENT OF THE IMPACT OF THE RESIDENTIAL HEATING EMISSIONS ON CONCENTRATIONS BY LOCAL AND REGIONAL AIR-QUALITY MODELS

Dušan Štefánik[1], Jana Krajčovičová[1], Juraj Beňo[1] and Katarína Belohorcová[2]

[1] Slovak Hydrometeorological Institute, Jeséniova 17, 833 15, Bratislava, Slovakia
[2] Ministry of Environment of the Slovak Republic, Námestie Ľ. Štúra 1, 812 35 Bratislava, Slovakia

Abstract: Comparison of three models differing in resolution and mathematical formulation - CALPUFF Lagrangian puff model, CMAQ Eulerian chemical transport model and IFDM Gaussian dispersion model - is presented. Modelling results for $PM_{2.5}$ concentrations coming from residential heating emissions over a selected local domain in Slovakia are compared and the differences as well as the usability of the models for local source apportionment is discussed.

Key words: *residential heating, $PM_{2.5}$, chemical-transport model, Lagrangian puff model, Gaussian dispersion model*

INTRODUCTION

Residential heating is the main contributor to the adverse air quality during winter periods in many regions in Central and Eastern Europe. In Slovakia, there are many villages and small towns without connections to central heating systems or natural gas distribution. Therefore, the local heating using solid fuel (mainly wood) is mostly used there. Moreover, the increasing energy prices also contribute to households leaning towards cheaper solid fuel. The consequence of this development is that the annual concentration limits for benzo(a)pyrene and $PM_{2.5}$, and the number of daily PM_{10} exceedances continue to occur at many air quality monitoring stations situated near residential areas. Since the number of air quality monitoring sites is rather limited, there is a need for reliable modelling outputs not only to assess the concentrations at locations without monitoring stations, but also to carry on the source apportionment at monitoring sites. In this paper, we attempt to compare the modelling results for $PM_{2.5}$ concentrations of several models differing in resolution and mathematical formulation: CALPUFF Lagrangian puff model, CMAQ Eulerian chemical transport model and IFDM Gaussian dispersion model. The local modelling domain includes the town of Jelšava, which according to the measurements is one of the locations with the worst air-quality due to PM in Slovakia, as well as the whole mountain valley NW of Jelšava with the town of Revúca and several smaller villages with solid fuel heating. The simulations are only performed for the residential heating emissions. The results are demonstrated using $PM_{2.5}$ as it represents almost all of PM_{10} emissions from residential heating.

SIMULATION DOMAIN AND EMISSIONS

Simulations were performed for the whole month of January 2021 for the domain of Jelšava, which is a mountain valley with adverse dispersion conditions especially in winter time. The size of the domain is roughly 13 km x 10 km.

The emissions from residential heating were computed using emission model REM_v2 (Krajcovicova et. al, 2020). PM emission totals in January 2021 for the whole domain are as follows: PM_{10} = 13.1 t and $PM_{2.5}$=12.8 t. 47 % of $PM_{2.5}$ emissions represents organic carbon and 10% black carbon. Figure 1 shows the simulation domain with residential heating emissions resolution of 50 m for CALPUFF and IFDM and 2 km for CMAQ. The diurnal and monthly emission profiles used in CMAQ and CALPUFF simulations are displayed in Fig. 2. The diurnal profile is adopted from CAMS methodology (Guevara et al., 2021) and the monthly profile is based on mean daily temperatures measured at meteorological station in Revúca. The

emission rate at each hour is calculated as annual emission total multiplied by diurnal and monthly profile values from Fig. 2 divided by 8760. Constant emission profile was used for IFDM simulation.

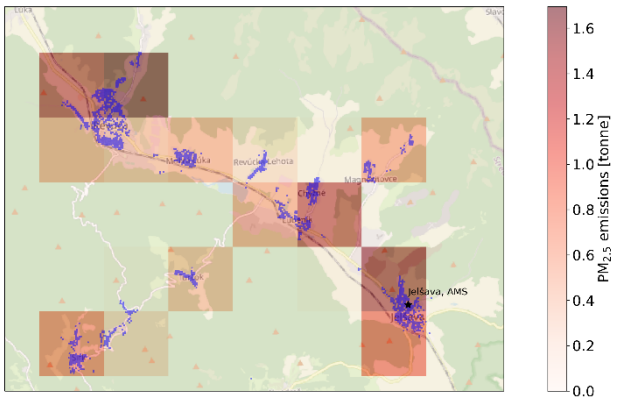

Figure 1. Red squares: $PM_{2.5}$ emissions for January in CMAQ model. Blue raster: distribution of $PM_{2.5}$ emissions to the IFDM and CALPUFF models (the emission flux is not shown).

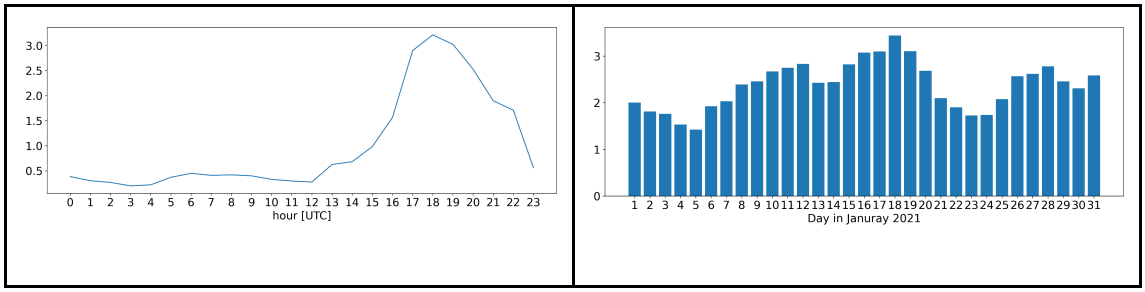

Figure 2. Emissions profiles for residential heating: diurnal (left) and monthly (right) used in CALPUFF and CMAQ calculations.

MODELS

ALADIN forecasting model (Termonia et. al., 2018, Derkova et. al., 2017) meteorological data output with the resolution of 4.5 km was used as input to IFDM and CALPUFF. For the CMAQ model a complex set of meteorological 2D and 3D parameters from model Aladin with 2 km resolution were used.

CALPUFF

CALPUFF (Scire et al, 2000a) version 7.2.1 was used to model concentrations of $PM_{2.5}$. CALPUFF is a Lagrangian puff model which is capable of treating complex terrain, low wind and calm situations which frequently occur in the mountain valleys. CALMET (Scire et al, 2000b) version 6.5.0 meteorological fields was used to process ALADIN meteorological inputs to high resolution grid. CALMET is a diagnostic meteorological model for computation of high resolution terrain-following winds and micrometeorological parameters necessary as inputs for CALPUFF model. The emissions were represented as volume sources corresponding to the emission squares of 50m.

CMAQ

The Community Multiscale Air Quality (CMAQ) model is a third-generation Eulerian mathematical air quality model (Byun and Schere, 2006). It can be used on various spatial scales from local to hemispheric and for corresponding time scales. It simulates ozone, particulate matter (PM), toxic airborne pollutants,

visibility, and acidic and nutrient pollutant species throughout the troposphere. In the simulation, the CMAQ meteorological inputs are taken from the model Aladin, corresponding to the model resolution of 2 km. Boundary conditions are zero except for the ozone. The CMAQ model version 5.3.3 was used (US EPA, 2021). The residential heating emissions are represented as area sources with 2 km resolution.

IFDM

IFDM (Immission Frequency Distribution Model) is a bi-Gaussian dispersion model developed by VITO to calculate the local dispersion of pollutants in the atmosphere based on meteorological data such as wind speed, wind direction and temperature (Lefebvre et al., 2011a, 2011b). It does not explicitly include the influence of the terrain and is unable to capture calm wind periods. However, as the meteorology for a particular source is always taken from the nearest Aladin gridpoint, a terrain influence is indirectly included through the wind speed and direction from the meteorological model. Emissions gridded in the 50 m squares were represented as point sources at the centres of grid cells. Results were interpolated into the regular grid with 10 m resolution.

Model	**CALPUFF**	**IFDM**	**CMAQ**
Type	Lagrangian puff	Gaussian	Eulerian CTM
Horizontal (terrain) resolution	250 m	no terrain included	2 km
Model output resolution	250 m	10 m	2 km
Number of vertical layers	11	NA	19
Top layer height	3 000 m	NA	17 000 m

Table 1. Selected parameters of the models.

RESULTS

Mean monthly concentrations in January

Mean $PM_{2.5}$ concentrations for the whole simulation period resulting from CALPUFF and IFDM models are shown in Fig. 3. These local models provide outputs at high resolution. On the other hand, CMAQ, being a CTM model, requires a lot of computer resources and therefore its typical resolutions are several km. Fig. 4 shows mean $PM_{2.5}$ concentrations computed by CMAQ, together with the downgraded results from CALPUFF and IFDM models. We can see that the CMAQ concentrations are rather low in comparison with other models even if those are downgraded to the 2 km resolution corresponding to CMAQ, while CALPUFF model gives the highest concentrations of all. Domain-wide statistics are as follows: CALPUFF vs. CMAQ: BIAS = 8.2 , RMSE = 9.0, r =0.77; IFDM vs. CMAQ: BIAS = 0.27, RMSE = 1.0, r =0.90; IFDM vs. CALPUFF: BIAS = -7.7 , RMSE = 8.3, r =0.80. The statistics show the closest similarity between the IFDM and CMAQ model results. Comparing these two models, CMAQ gives lower concentrations for all grid cells but those with small emissions and bad dispersion conditions caused by the terrain.

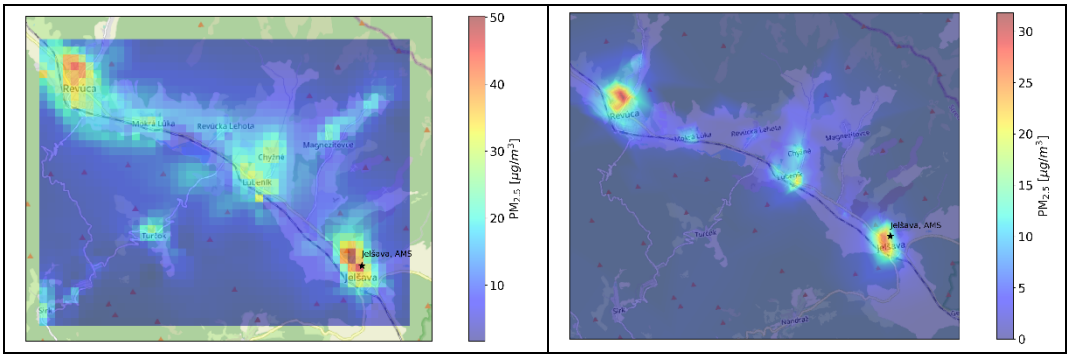

Figure 3. Mean $PM_{2.5}$ concentrations from residential heating in January 2021 calculated by a) CALPUFF model (left panel); b) IFDM model (right panel)

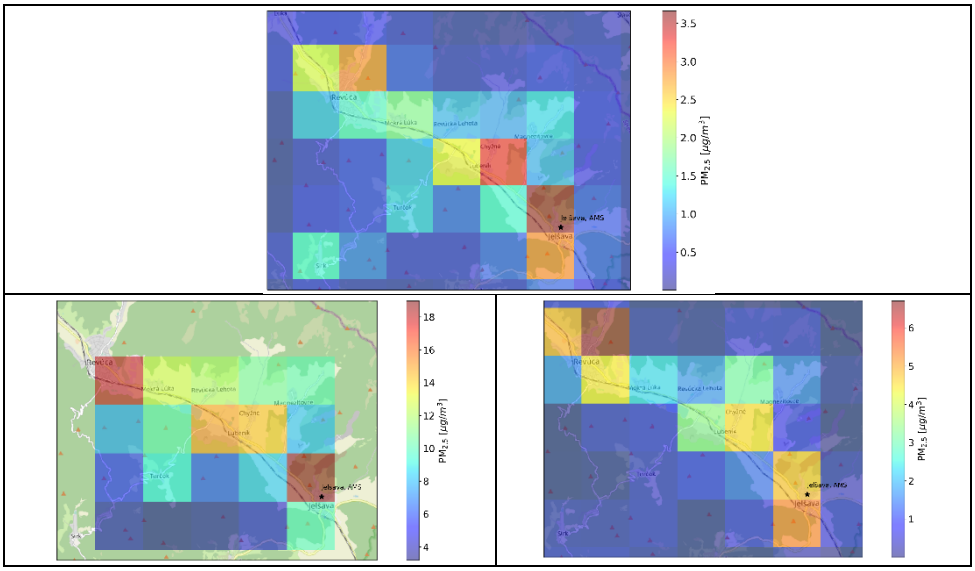

Figure 4. Mean $PM_{2.5}$ concentrations from residential heating in January calculated by CMAQ model (top).$PM_{2.5}$ concentrations resampled to the CMAQ resolution: a) CALPUFF model (bottom left); b) IFDM model (bottom right)

Concentrations at the monitoring station

The predicted hourly $PM_{2.5}$ concentrations at the monitoring station location in Jelšava, together with the measured values are presented in Fig. 5. CMAQ model underestimates the concentrations since the 2 km resolution is not capable of seeing this hot-spot. On the other hand, CALPUFF and to a certain degree IFDM give values for some hours which highly exceed measured concentrations. Therefore, in case of CALPUFF simulations we experimented with different diurnal profiles. It turned out that the unrealistic high peaks decreased when constant diurnal profile was used (Fig. 6) and monthly mean domain maximum also decreased by ~15%. .

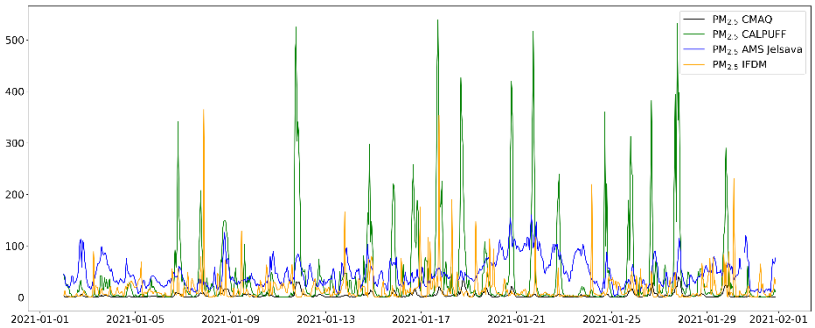

Figure 5. Hourly $PM_{2.5}$ concentrations at Jelšava monitoring station – models and measurements.

CONCLUSIONS

The simulations demonstrated the expected result that the resolution of the model is crucial to obtain realistic concentration values in hot-spots, especially in complex mountainous locations. Besides this, we learned that the diurnal emission profile is also very important, especially in case of CALPUFF model using high resolution terrain-adjusted meterology. After downgrading two local models to the 2 km resolution, seemingly comparable concentrations were obtained using CMAQ and IFDM models, while CALPUFF seemed to overestimate especially when CAMS emission profile was used. This can not be interpreted in the way that IFDM and CMAQ results are better than CALPUFF, as their higher correlation may be accidental (they use completely different diurnal emission profiles - completely constant versus CAMS profile with high amplitude). Further simulations and more insight into the differences in the meteorological

fields in relation to the modeling results is necessary, as well as to the impact of the diurnal emission profiles, especially in case of IFDM and CALPUFF models As it seems that local models are sensitive to diurnal emission profiles, it is also necessary to develop emission profiles for residential heating which would be as close to reality as possible.

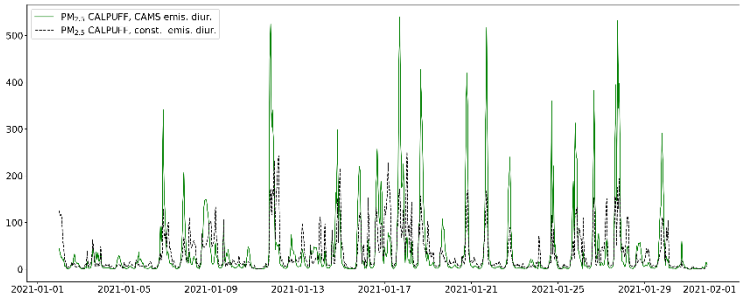

Figure 6. Calpuff hourly $PM_{2.5}$ concentrations with constant and CAMS diurnal emission profiles at Jelšava monitoring station.

REFERENCES

Derková et. al., 2017: Recent improvements in the ALADIN/SHMU operational system. *Meteorological Journal,* Vol.**20**, No. 2, pp 45-52.

Byun, D., Schere, K., 2006. Review of the governing equations, computational algorithms, and other components of the Model-3 Community Multiscale Air Quality (CMAQ) *Modeling System. Appl. Mech. Rev.* **59** (2), 51–77. https://doi.org/10.1115/1.2128636.

Guevara, Marc Jorba, Oriol Tena Medina, Carles Denier van der Gon, Hugo Kuenen, Jeroen Elguindi, Nellie Darras, Sabine Granier, Claire Pérez García-Pando, Carlos. (2021). Copernicus Atmosphere Monitoring Service TEMPOral profiles (CAMS-TEMPO): global and European emission temporal profile maps for atmospheric chemistry modelling. *Earth System Science Data*. **13**. 367-404. 10.5194/essd-13-367-2021

Lefebvre, W., Fierens, F., Trimpeneers, E., Janssen, S., Van de Vel, K., Deutsch, F., Viaene, P., Vankerkom, J., Dumont, G., Vanpoucke, C., Mensink, C., Peelaerts, W., Vliegen, J., 2011a. Modeling the effects of a speed limit reduction on traffic-related elemental carbon (EC) concentrations and population exposure to EC. Atmospheric Environment 45, 197e207. http://dx.doi.org/10.1016/j.atmosenv.2010.09.026.

Lefebvre, W., Vercauteren, J., Schrooten, L., Janssen, S., Degraeuwe, B., Maenhaut, W., de Vlieger, I., Vankerkom, J., Cosemans, G., Mensink, C., Veldeman, N., Deutsch, F., Van Looy, S., Peelaerts, W., Lefebre, F., 2011b. Validation of the MIMOSA-AURORA-IFDM model chain for policy support: modeling concentrations of elemental carbon in Flanders. Atmospheric Environment 45/37, 6705e6713. http://dx.doi.org/10.1016/j.atmosenv.2011.08.033.

Scire J.S., Robe F.R., Fernau M.E., Yamartino R.J., 2000b: A User's Guide for the CALMET Meteorological Model, Earth Tech, Inc., Concord, MA

Scire, J.S., Strimaitis, D.G. and Yamartino, R.J., 2000a: A User's Guide for the CALPUFF Dispersion Model, Earth Tech, Inc., Concord, MA.

United States Environmental Protection Agency. (2020). CMAQ (Version 5.3.2) [Software]. Available from https://doi.org/10.5281/zenodo.4081737

Termonia et.al., 2018: The ALADIN System and its Canonical Model Configurations AROME CY41T1 and ALARO CY40T1. *Geosci. Model Dev*., Vol. **11**, pp 257-281.

21st International Conference on
Harmonisation within Atmospheric Dispersion Modelling for Regulatory Purposes
27-30 September 2022, Aveiro, Portugal

DEFRA 2021 AIR QUALITY MODEL INTER-COMPARISON EXERCISE

David Carruthers[1], Jenny Stocker[1], Amy Stidworthy[1], Christina Hood[1], Rose Jackson[1], George McCosh[1], Stephen Smith[1], Daniel Connolly[1], Shyn Tong[2], Alison Davies[2], Sean Beevers[3], Nutthida Kitwiroon[3], Nosha Assareh[3], Vivien Bright[4], Lucy Neal[4], Paul Agnew[4], John Stedman[5], Beth Conlan[5], Massimo Vieno[6], Eiko Nemitz[6], Stefan Reis[6]

[1]CERC, 3 King's Parade, Cambridge, CB2 1SJ, UK
[2]Department for Environment, Food & Rural Affairs, Seacole Building, 2 Marsham Street, London, SW1P 4DF, UK
[3]Environmental Research Group, School of Public Health, Michael Uren Biomedical Engineering Hub, White City Campus, Wood Lane, London, W12 0BZ, UK
[4]Met Office, FitzRoy Road, Exeter, EX1 3PB, UK
[5]Ricardo, The Gemini Building, Fermi Avenue, Harwell, Didcot OX11 0QR, UK
[6]Centre for Ecology and Hydrology, Edinburgh, EH26 0QB, UK

Abstract: The UK takes a combined measurement and modelling approach to reporting associated with the Air Quality Standards Regulations (AQSR, previously the EU Air Quality Directive) pollutant metrics, with modelling currently being performed on behalf of the UK Department for Environment, Food & Rural Affairs (Defra) by Ricardo using the Pollution Climate Mapping (PCM) system. The primary purpose of the Defra 2021 Air Quality Model Inter-Comparison Exercise was to assess the capabilities of four air quality modelling systems in terms of their suitability for AQSR reporting, specifically: PCM; the CMAQ-Urban model driven by WRF meteorology (Environmental Research Group at Imperial College, London); the Air Quality model within the UK Met Office's Unified Model (AQUM-SPPO); and a WRF – EMEP application for the UK (UK Centre for Ecology and Hydrology). This paper provides a project overview and presents key conclusions. All models were configured to calculate pollutant concentrations for 2018 at over 400 monitor locations, gridded concentrations at the models' highest resolution over all of the UK, and, for three of the four models, near-road concentrations associated with the major road network. A wide range of metrics were calculated to assess model performance using NO_x, NO_2, O_3, $PM_{2.5}$ and PM_{10} measurement datasets. In addition to visual comparison of air quality maps, derived statistics such as areas in exceedance were calculated separately for 28 agglomeration and 15 non-agglomeration zones. A documented assessment of the models' formulations, configurations and inputs led to an informed model inter-comparison. Meteorological model performance has been evaluated at seven sites over the UK (wind speed, direction and temperature), and the relationship between modelled wind and pollutant concentrations has been investigated. Technical diagnostics have been used to assess how well the models account for NO_x chemistry, in addition to the models' ability to represent coarse and fine particulate concentrations. Conclusions of the study include: a quantitative inter-comparison of zonal exceedances, which are very similar for O_3 metrics but differ between models for NO_2 and particulates; and a qualitative discussion of the models' strengths and weaknesses in relation to AQSR reporting.

Key words: *Air quality, dispersion, inter-comparison, model, air quality directive, Defra, UK, AQSR*

INTRODUCTION

Four groups which run air quality (AQ) modelling systems with the potential to provide outputs suitable for assessing compliance with the Air Quality Standards Regulations (AQSR, 2010, previously the EU Air Quality Directive, AQD, 2008) were invited to participate in the Defra 2021 Air Quality Model Inter-Comparison Exercise (MIE). The Environmental Research Group at Imperial College London (ERG-ICL) used their CMAQ-Urban model (Beevers *et al.*, 2012), with WRF (Skamarock *et al.*, 2019) meteorological data; the Met Office (MO) ran their Air Quality Unified Model (AQUM-SPPO, Neal *et al.*, 2014); Ricardo supplied the Pollution Climate Mapping system (PCM, Brookes *et al.*, 2020); and the UK Centre for Ecology and Hydrology (UKCEH) ran EMEP (Simpson *et al.* 2012, Vieno *et al.*, 2016), also using WRF. The MIE comprised four tasks. The first task involved a mainly qualitative review and assessment of the

models' formulations, configurations and inputs. The second task was an inter-comparison of AQSR pollutant metrics and maps. The third task involved a comprehensive evaluation of model performance relative to measured air pollutant concentrations. Modelled urban air quality was assessed in the final task, with a focus on two conurbations, Greater London and Greater Manchester.

This article provides a study overview: key aspects of the models' differing formulations and configurations are discussed; some examples from the extensive model evaluation exercise are presented followed by results relating to the application of each model to compliance reporting; and outcomes are summarised.

MODELS' FORMULATION AND CONFIGURATION

ERG-ICL, MO and UKCEH run regional meteorological and chemical transport models that predict pollutant concentrations at hourly resolution whereas Ricardo's modelling system calculates annual average concentration values. Three of the four models (CMAQ-Urban, AQUM-SPPO and PCM) calculate concentrations at roadside as well as regionally. CMAQ-Urban generates modelled concentrations that vary continuously between regional and local scales, up to 20 m grid resolution. MO and Ricardo generate separate gridded (resolutions ~12 km and 1 km respectively) and roadside datasets. EMEP's spatial resolution for this study was 1 km. MO and Ricardo apply post-processing calibration; the methods used differ, as do the measurement datasets used for the calibration. ERG-ICL and UKCEH do not apply any post-processing calibration, but use measurement datasets to refine model boundary conditions (O_3); refinement of model boundary conditions for O_3 using measurements is also carried out by the MO. Local modelling approaches differ significantly between groups. ERG-ICL use a near-road dispersion kernel based on ADMS-Roads version 5.0 (CERC, 2022), and a simple NO_X chemistry scheme; local modelling effects are included up to 225 m from each road source modelled, and account is taken of the influence of street canyons on dispersion. MO use a post-processing bias correction approach to estimate roadside concentrations; some regional variation of roadside increments is modelled, but no account is taken of specific road link features in terms of emissions or geometry such as carriageway widths or canyon properties. Ricardo uses near-source dispersion kernels derived from ADMS-Roads version 4.1 for roads, and from ADMS versions 3 and 5.2 for point sources, with an oxidant partitioning model for NO_X chemistry. In the form used by UKCEH in this MIE, EMEP does not conduct sub-grid scale modelling.

A range of land use and surface property values used as input to the hourly resolution meteorological models have been inter-compared at 15 sites throughout the UK, representing a variety of environments. The land use categories used by the different models are consistent for regional models using the same input data at relatively similar resolution (WRF at 2 and 1 km by ERG-ICL and UKCEH respectively). Input surface roughness lengths for meteorological modelling are broadly similar across all models although roughness lengths used by ERG-ICL are generally higher in urban areas than for the other models, and have more seasonal variation. WRF is also used in PCM but at much lower (50 km) resolution, and there are other configurations differences. Modelled meteorological parameters were evaluated using measurements from seven of the 15 sites used in the land use / surface roughness inter-comparison (Figure 1). FAIRMODE meteorological parameter benchmarks indicate that the MO meteorological model performs best, satisfying the benchmark criteria for all parameters evaluated (wind speed, wind direction and temperature). All other models demonstrate a slight negative bias for temperature, and ERG-ICL also underpredicts wind speed. There is broad consistency in terms of the anthropogenic emissions inputs used by the modelling teams, specifically data from the National Atmospheric Emissions Inventory (NAEI, 2020) for the UK and EMEP for Europe. ERG-ICL adjust their emissions from light duty vehicles using bottom-up calculations with emission factors derived from remote sensing data, resulting in total emission

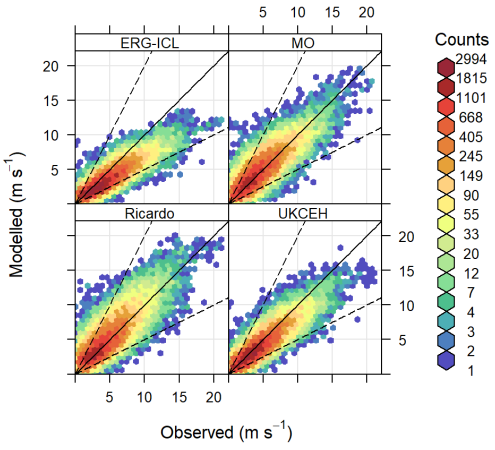

Figure 1. Frequency scatter plot of hourly modelled and observed wind speed data at 10 m above ground across seven meteorological evaluation sites; colours indicating the density of data points in each region of the graph.

increases of 5%, 30% and 150% for NO_X, $PM_{2.5}$ and PM_{10} respectively when compared to the base NAEI. The assumptions relating to the proportion of traffic NO_X emitted as primary NO_2 varies greatly between modelling groups. MO use the lowest value, assuming that all NO_X is emitted as NO, and ERG-ICL assume the highest proportion, with values ranging from 0.16 to 0.30. Non-road traffic primary NO_2 emissions assumptions also vary, with proportions ranging from 0 to 0.14.

Model evaluation at AIR POLLUTION monitoring sites

Model predictions of core AQSR pollutants NO_X, NO_2, O_3, PM_{10} and $PM_{2.5}$ have been compared with hourly measurements from 415 UK monitoring sites for 2018. Models have been evaluated separately at background (including rural, suburban and urban background), roadside and industrial sites, with comparisons on three timescales: annual, hourly and, where relevant, the AQSR short-term averaging periods. PCM calculates only annual metrics, so hourly and AQSR short-term limit assessments exclude PCM. The CERC Model Evaluation Toolkit (2021), which uses tools from the openair package (Carslaw and Ropkins, 2012), was used to produce a comprehensive set of statistics and graphs to quantitatively assess each model's performance in relation to observations; the statistics include the mean, root mean square error (RMSE), normalized mean bias (NMB) and normalized mean square standard deviation (NMSD) for both the annual and hourly data. The number of short-term AQSR limit exceedances has been calculated. FAIRMODE metrics, which allow for measurement uncertainty, have also been calculated.

As an example, Table 1 presents a selection of statistics associated with evaluation of annual average NO_2. There is good overall agreement between modelled concentrations and observations for CMAQ-Urban and PCM; EMEP underestimates NO_2 at background sites. AQUM-SPPO has good agreement overall, but further categorisation of the statistics (not presented) indicates overestimation at rural sites. AQUM-SPPO and EMEP underestimate variability, whereas CMAQ-Urban overestimates variability. With regard to the FAIRMODE metric $MQI_{annual\ 90}$, both AQUM-SPPO and PCM achieve the annual threshold criteria (less than 1 for an acceptable model) at background sites; none of the models achieve this criteria at roadside. PCM gives the best prediction in terms of the number of sites exceeding the AQSR annual mean limit value (40 µg/m³), although CMAQ-Urban also demonstrates good performance for this metric at roadside sites.

Table 1. Model evaluation statistics for annual mean NO_2 (µg/m³) at background and roadside sites; best result per statistic per site type in bold; last column shows number of sites exceeding the annual limit value (40 µg/m³).

Site type	Modelling group	Model	Mean	RMSE	NMB	NMSD	$MQI_{annual\ 90}$	Sites exc. annual limit
Background		**Observed**	19.8					1
	ERG-ICL	CMAQ-Urban	21.6	5.8	0.09	0.32	1.06	11
	MO	AQUM-SPPO	18.3	6.0	-0.08	-0.46	0.96	0
	Ricardo	PCM	**18.5**	**4.7**	**-0.07**	**0.04**	**0.73**	**3**
	UKCEH	EMEP	15.0	6.9	-0.25	-0.18	1.10	0
Roadside		**Observed**	36.6					51
	ERG-ICL	CMAQ-Urban	38.8	13.1	**0.06**	0.36	1.43	56
	MO	AQUM-SPPO	33.0	12.4	-0.10	-0.67	1.45	22
	Ricardo	PCM	**34.6**	**9.6**	**-0.06**	**-0.20**	**1.27**	**47**
	UKCEH	EMEP	14.9	24.3	-0.59	-0.57	2.70	0

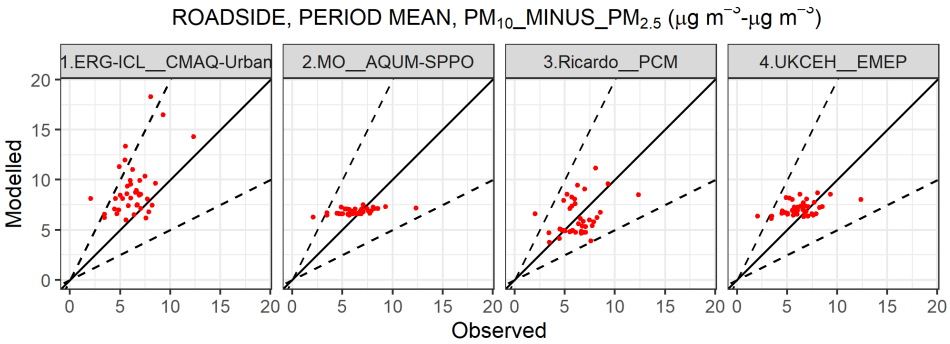

Figure 2. Modelled versus observed annual mean coarse particulate levels (PM_{10} – $PM_{2.5}$, µg/m³) at 40 roadside sites.

In the case of $PM_{2.5}$ and PM_{10} (not shown), all models show good overall agreement between modelled concentrations and observations for annual means, and all pass the corresponding FAIRMODE threshold criteria at both background and roadside sites apart from CMAQ-Urban at roadside sites. This likely relates to CMAQ-Urban's tendency to overestimate coarse particulate traffic emissions, demonstrated by the annual mean evaluation, Figure 2**Error! Reference source not found.** which highlights the need for consideration of a range of metrics when undertaking an evaluation study; for instance, calibration ensures that AQUM-SPPO predicts the correct mean coarse component, but model variability is significantly lower than observed.

COMPLIANCE MAPPING AND STATISTICS

Only annual metrics have been considered in the compliance reporting metric assessment, to allow direct comparison with PCM outputs. The compliance reporting calculation methodology follows that used by Ricardo in their AQSR reporting work for Defra. Pollutant concentration metrics have been derived for 28 agglomeration (urban) zones and 15 non-agglomeration (rural) zones. Separate calculations have been performed using gridded and roadside datasets. Zonal exceedances are calculated as the maximum concentrations over gridded and road datasets. PCM and MO calculate only one 'roadside' concentration associated with each of the 8586 UK urban road 'sections' modelled in the study. ERG-ICL's roadside concentrations have been calculated as an average over pavements, defined as a 2.5 m wide buffer on either side of the full modelled road network. The ERG-ICL CMAQ-Urban grid is fine resolution (20 m) for all pollutants excluding O_3, which is 2km resolution.

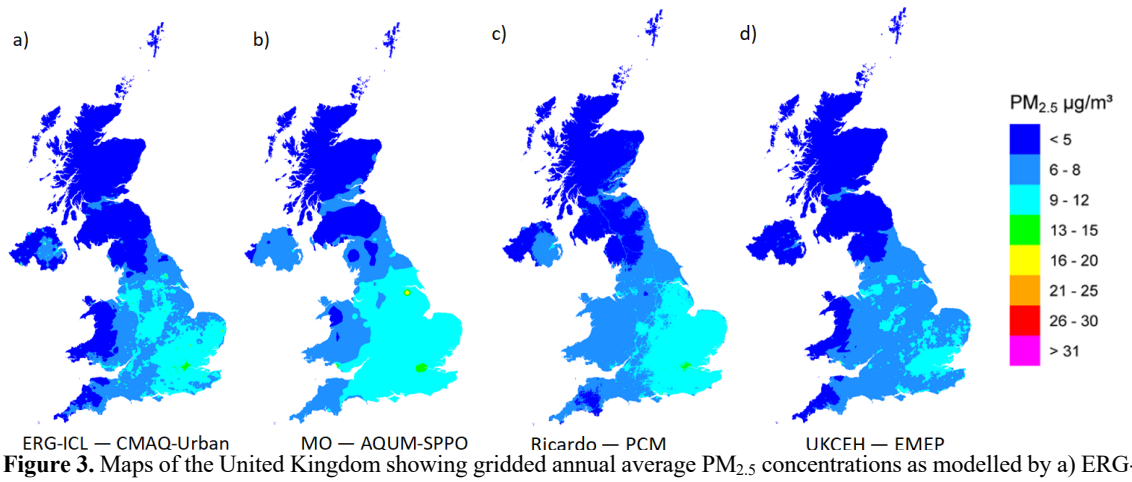

Figure 3. Maps of the United Kingdom showing gridded annual average $PM_{2.5}$ concentrations as modelled by a) ERG-ICL (CMAQ-Urban) b) MO (AQUM-SPPO) c) Ricardo (PCM) and d) UKCEH (EMEP). Note: grid resolutions differ for each modelling group.

Gridded concentrations of NO_2, $PM_{2.5}$, PM_{10} and O_3 have been mapped using colour scales corresponding to AQSR limit, target and long-term objective values. Example $PM_{2.5}$ air pollution maps are shown in Figure 3. All models show a similar spatial distribution of $PM_{2.5}$ for the lower concentration ranges (less than 10 µg/m³). However, map details differ between models in terms of peak concentrations, partly due to the differing approaches taken to modelling non-traffic sources such as industry and calcium rich dust. CMAQ-Urban predicts exceedances of the annual average limit value (25 µg/m³) in approximately 50% of zones, which is likely to be an overestimate due to the assumed release height of some non-road sources and road carriageways not being excluded from the exceedance calculations. None of the other models predict exceedances of this limit value. Table 2 summarises outcomes of the compliance reporting calculations using the four models. For NO_2, roadside exceedances are broadly consistent between CMAQ-Urban and PCM; gridded exceedances of NO_2 include road carriageways so are not entirely consistent with the AQSR for CMAQ-Urban. AQUM-SPPO and EMEP predict few or zero exceedances of the NO_2 limit value. Zonal exceedances relating to both O_3 metrics are consistent across all models, with models predicting few, or no, zonal exceedances of the target values, but with exceedances of the long-term objectives in most zones.

Table 2. Overall modelled exceedances (combined gridded and roadside) over the defined 43 zones. Note: there are instances of overlap between gridded and roadside zonal exceedances. Limit Value = LV, Target Value = TV, Long-Term Objective = LTO; *Grid exceedances include road carriageways; **CMAQ only for O_3.

Pollutant	Time period	Threshold	Grid / road	ERG-ICL CMAQ-Urban*	MO AQUM-SPPO	Ricardo PCM	UKCEH EMEP
NO_2	Annual	40 µg/m³ (LV)	Grid	42*	0	1	0
			Road	32	2	34	0
			Total	**42***	**2**	**34**	**0**
O_3	No. of days 8-hour rolling mean > 120 µg/m³	25 days (TV)	Grid	1	1	0	0
		1 day (LTO)		42	43	43	43
	Seasonal (May to July) – AOT40	18000 µg/m³.h (TV)		0	1	0	4
		6000 µg/m³.h (LTO)		40	40	38	43
$PM_{2.5}$	Annual	25 µg/m³ (LV)	Grid	18	0	0	0
			Road	1	0	0	0
			Total	**18**	**0**	**0**	**0**
PM_{10}	Annual	40 µg/m³ (LV)	Grid	38	0	0	0
			Road	3	0	0	0
			Total	**38**	**0**	**0**	**0**

DISCUSSION

The MIE has identified the four models' strengths and weaknesses, and conclusions have been drawn in relation to the models' suitability for AQSR reporting purposes. This study was comprehensive, but only a small subset of results is presented in this article.

Acknowledgements

This work undertaken under a Memorandum of Agreement formed between Defra, CERC, Imperial College London, the UK Met Office, Ricardo and the UK Centre for Ecology and Hydrology.

REFERENCES

AQD, 2008: Directive 2008/50/EC of the European Parliament and of the Council of 21 May 2008 on ambient air quality and cleaner air for Europe. Official Journal of the European Union, 152, 1–44.

AQSR, 2010: UK Statutory Instruments 2010 No. 1001 The Air Quality Standards Regulations 2010.

Beevers, S. D., Kitwiroon, N., Williams, M. L., & Carslaw, D. C., 2012: One way coupling of CMAQ and a road source dispersion model for fine scale air pollution predictions. *Atmos. Env.*, **59**, 47–58.

Skamarock, W. C. et al., 2019: A Description of the Advanced Research WRF Model Version 4 (No. NCAR/TN-556+STR).

Neal, L. S., Agnew, P., Mosely, S., Ordóñez, C., Savage, N. H., Tilbee, M., 2014: Application of a statistical post-processing technique to a gridded, operational air quality forecast. *Atmos. Env.*, **98**, 385-393.

Brookes D, Stedman J, Kent A, Whiting S, Rose R, Williams C., Pugsley, K., 2020: Technical report on UK supplementary assessment under The Air Quality Directive (2008/50/EC), The Air Quality Framework Directive (96/62/EC) and Fourth Daughter Directive (2004/107/EC) for 2018. Ricardo report reference ED12633 - Issue Number 1. Ricardo Energy & Environment/R/3470.

Simpson, D. *et al.*, 2012: The EMEP MSC-W chemical transport model – technical description. *Atmos. Chem. and Phys.*, **12**, 7825-7865.

Vieno, M., Heal, M.R., Williams, M.L., Carnell, E.J., Nemitz, E., Stedman, J.R. and Reis, S., 2016: The sensitivities of emissions reductions for the mitigation of UK PM 2.5. *Atmos. Chem. and Phys.*, **16(1)**, 265-276.

CERC, 2022: ADMS Technical Specifications, available online at https://www.cerc.co.uk/TechSpec (accessed April 2022)

NAEI, 2020: 13 Richmond B, Misra A, Broomfield M, Brown P, Karagianni E, Murrells T, Pang Y, Passant N, Pearson B, Stewart R, Thistlethwaite G, Wakeling D, Walker C, Wiltshire J, Hobson M, Gibbs M, Misselbrook T, Dragosits U, Tomlinson S (2020). UK Informative Inventory Report (1990 to 2018). National Atmospheric Emissions Inventory, Ricardo Energy & Environment.

Model Evaluation Toolkit (version 5.1), 2021: https://www.cerc.co.uk/ModelEvaluationToolkit

Carslaw, D. C. and Ropkins, K., 2012: openair --- an R package for air quality data analysis. *Env. Mod. & Soft*. **Volume 27-28**, 52-61.

21st International Conference on
Harmonisation within Atmospheric Dispersion Modelling for Regulatory Purposes
27-30 September 2022, Aveiro, Portugal

NUMERICAL MODELLING OF POLLUTANT DISPERSION OVER AN IDEALIZED URBAN AREA USING DIFFERENT ALGEBRAIC CLOSURE MODELS

Boulos Alam[1], Rayan Nkenfack [1], Amir Ali Feiz[1], Pierre Ngae[1], Pramod Kumar[2] and Amer Chpoun[1]

[1]Université Paris-Saclay, Univ Evry, LMEE, 91020, Evry, France
[2]Université Paris-Saclay, CNRS, CEA, UVSQ, Laboratoire des sciences du climat et de l'environnement, 91191, Gif-sur-Yvette, France

Abstract: In this study, we evaluate the performance of different turbulence models for velocity-scalar correlations implemented in the CFD code Code_Saturne®. The evaluation is done with observations from a test case of the Mock Urban Setting Test (MUST) campaign in an urban-like environment and slightly stable atmospheric conditions. The results show that the k-ε model associated with an algebraic SGDH model predicts 75% of the concentrations within a factor of two of the observations. The performance of the k-ε model is compared to that of the R_{ij}-ε model when used with the algebraic SGDH, GGDH models and with the scalar flux transport equation DFM. The DFM model shows promise in predicting maximum concentrations under slightly stable atmospheric conditions, despite its relatively high computational cost. This model predicts 69% of the concentrations within a factor of two of the observations, and is therefore more efficient than the SGDH and GGDH models.

Key words: *CFD modelling, MUST experiment, algebraic models, scalar turbulent fluxes , stable conditions.*

INTRODUCTION

The dispersion of gaseous pollutants in an urban area is characterized by complex turbulence features, such as flow detachment and high shear zones. In addition to this dynamic turbulence, thermal turbulence in the atmospheric boundary layer (ABL) tends to dampen the turbulent fluctuations resulting from flow shear under stable or very stable stratification conditions, thus reducing the dispersion of pollutants. The complexity of the physical phenomena involved in these conditions leads to a strong anisotropy of the ABL, which limits the capacity of standard isotropic models to correctly predict the dispersion field. Computational fluid dynamics (CFD) models are one of the most promising tools to describe the dispersion of pollutants in the near field of buildings. Reynolds averaged Navier-Stokes (RANS) models are the most commonly used CFD techniques to study turbulent pollutant transport, where the scalar transport equation is often solved using the Simple Gradient Diffusion Hypothesis (SGDH) for turbulent scalar flows. The objective of this work is to perform a comprehensive validation study of different anisotropic turbulence models for flow and scalar fields. The simulations are evaluated using the results of the Mock Urban Setting Test *MUST* (Biltoft, 2001) (Yee and Biltoft, 2004), which is a near full-scale experiment involving the release of a neutral gas from a point source within an array of rectangular shipping containers. A single trial of the experiment is chosen to simulate flow and dispersion patterns near the source and at larger distances, in weakly atmospheric stable conditions. The numerical simulations are performed with the three-dimensional (3D) CFD model *Code_Saturne®*. The standard k–ε model (Launder and Spalding, 1983) and a Reynolds Stress Transport closure, R_{ij}-ε LRR (Launder et al., 1975) are employed and compared to predict the flow field, while the SGDH is initially adopted to relate the scalar flux to mean gradients of the concentration field. An additional analysis of algebraic closures for turbulent scalar fluxes based on the differential flux model (DFM) (Dehoux, 2012) and generalized gradient diffusion hypothesis (GGDH) (Daly and Harlow, 1970) is also presented and the results are compared to the prediction given by the SGDH model. The capabilities and limitations of the tested models for both wind flow and concentration fields are evaluated rigorously using multiple validation metrics.

Description of Trial #2692157 of the MUST campaign

This trial was performed under weakly stable atmospheric conditions, with a moderate wind amplitude (2.1 < U < 5 m/s). It is of stability class F according to the Pasquill classification (Pasquill, 1972) (100 < L < 200). The source is located at a height of 2.7 meters, thus above the containers which are 2.54 meters high. Polypropylene (C_3H_6) gas is released in the southeast corner of the container grid with a flow rate of 225 litres/min for a duration of 15 min. The concentration field is measured by 48 PIDs (Photoionization Detectors) placed at 1.6 meters from the ground and arranged horizontally along 4 rows and vertically along a 32 m high mast placed in the center of the canopy. The characteristics of this trial are summarized in Table 1.

Table 3. Summary table of the characteristics of the trial #2692157: U is the mean wind speed, α is the wind direction measured from the north, k is the turbulent kinetic energy, Q is the pollutant flowrate, z_s is the release height, u_* is the friction velocity, L is the Obukhov length and ε is the dissipation rate.

U (ms^{-1})	α (deg)	k (m^2s^{-2})	Q ($Lmin^{-1}$)	z_s (m)	u_* (ms^{-1})	L (m)	ε (m^2s^{-3})
2.98	43	0.505	225	2.7	0.39	130	0.042

Numerical setup

In order to reproduce the configuration of the experimental field as faithfully as possible, the geometry is first drawn using the CAD software *Salome*. The dimensions of the computational domain are 240 m in length and width and 50 m in height. A two-dimensional (2D) mesh algorithm is used to generate an unstructured mesh in the ground plane, with finer meshes near the obstacles. Subsequently, this 2D planar mesh is extruded in the vertical direction with an growth factor so as to have a mesh height of 0.25 m near the ground and 5.5 m at the top of the domain. The total number of cells in the domain is 1210582. Figure 1 shows a three-dimensional (3D) representation of the mesh of the computational domain. The mesh is chosen after a sensitivity study performed on three grid sizes on trial #2692157. The simulations are performed in steady-state mode to solve the wind field and the dispersion of passive scalar in the domain. Two simulations have been implemented: the first simulation is used to compute the dynamic fields, i.e. only the wind flow, whereas, the second simulation is used to calculate the dispersion of the pollutants, within this pre-calculated stationnary wind field. To ensure convergence of the results, the accuracy of the solver is set to 10^{-4} for all calculated variables. The numerical scheme for each variable (convection scheme) is automatically defined by the solver. The SIMPLE (Semi-Implicit Method for Pressure-Linked Equations) algorithm is used for the pressure-velocity coupling with a reduction of the relaxation coefficient. At the inlet of the domain, a Dirichlet-type condition is applied using analytical profiles for velocity, temperature and turbulent variables. At the exit of the domain, a Neumann-type condition is applied, except for pressure. For the ground and the containers, a non-slip boundary condition is imposed with a roughness of 0.04 meters. The side faces will automatically behave as the inlet or outlet face of the flow depending on the direction of the wind. The k-ε turbulence model is used with the SGDH approach. In addition, the R_{ij}-ε model is applied with the SGDH and GGDH approaches as well as with the DFM model. The profile of Businger et al. (1971) is applied with the k-ε and R_{ij}-ε models (both with SGDH). The profiles of Pena et al. (2009) and Gryning et al. (2007) are applied with the R_{ij}-ε model (with GGDH and DFM, respectively). As for the turbulent variables, they are calculated from the profiles of Gorlé et al. (2009) for the k-ε and R_{ij}-ε models (both with SGDH), and from the profiles of Kerschgens et al. (2000) for the R_{ij}-ε (with GGDH and DFM). In what follows, the analysis of the simulation results will be based only on the turbulence models used in each simulation.

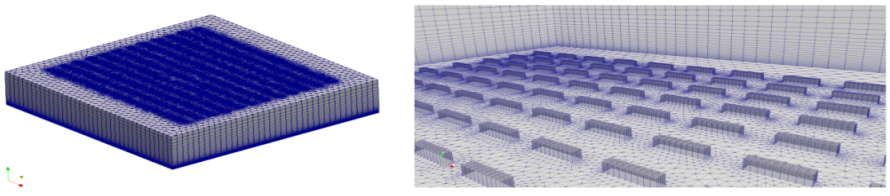

(a) (b)

Figure 4. Representation of the 3-D mesh of the MUST computational domain: (a) External view; (b) Internal view

Results and discussion

Figure 2 shows the predicted mean concentration field at a height of 1.6 meters above ground with the k-ε and R_{ij}-ε models. Note that the plume is much larger and extends over the entire grid when using the k-ε model. This can be explained by the fact that the k-ε model predicts an overproduction of turbulence which increases the turbulent transport flux and thus leads to more lateral diffusion of the pollutant over the extent of the grid. We can also note that the directional line of the plume does not coincide with the wind direction (43 deg from the north). This is due to the presence of a channeling effect imposed by the containers on the plume, making it deviate from the wind direction. This phenomenon of plume deflection was also observed by Milliez and Carissimo (2007), Kumar et al. (2015) and Bahlali et al. (2018a).

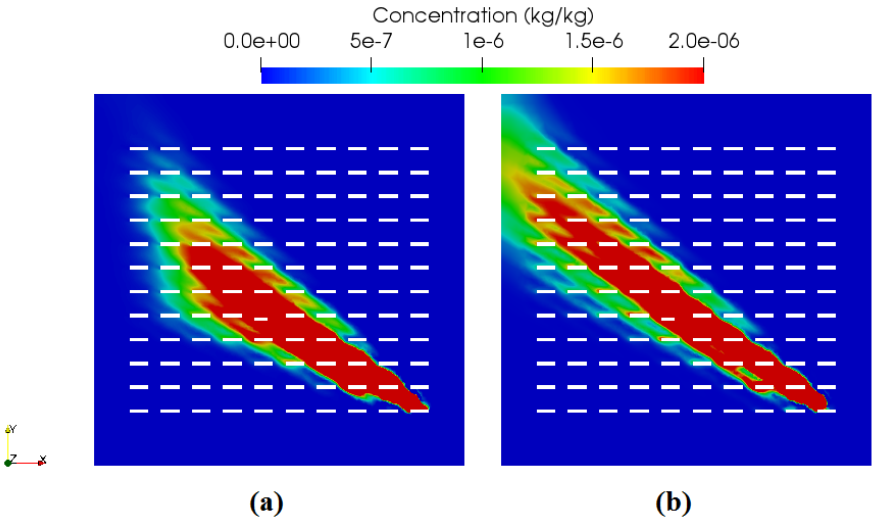

Figure 5. Average pollutant concentration field (kg/kg) near the ground, with models (a) k-ε and (b) R_{ij}-ε (with SGDH) for trial #2692157

Figure 3 shows the comparison between observed and predicted concentrations at receptor locations using different turbulence models. We observe one main peak followed by four secondary peaks. The concentration peaks are recorded by the receptors located in the wind direction. We also note that the concentration intensity at the main peak (7 ppmv) is about twice as high as the main peak observed in trial #2681829 with neutral stability condition (3.5 ppmv, not shown here). This increase in concentration is primarily due to the atmospheric conditions of the experiment. Because trial #2692157 was conducted under moderately stable atmospheric conditions, turbulence generation is attenuated by the thermal stratification of the ABL, resulting in reduced turbulent transport of the pollutant; therefore, concentrations are locally higher. We also observe in this case a good correspondence between the numerical results and the measurements concerning the position of the peaks. As for the magnitude of the highest peak, all the models used overestimate it, except for the R_{ij}-ε (with GGDH) model which is the only one to predict the maximum concentration measured by the third sensor. However, moving away from the source, this same model seems to underestimate the concentration the most among the other models. In general, the predictions obtained by all models are almost close to the experimental measurements when moving away from the source. Furthermore, no model is able to correctly reproduce the vertical concentration profile (profile corresponding to receptors 41 to 48). The results of the statistical study to evaluate the accuracy of each model are presented in Table 2. A model is considered perfect if: NMSE = FB = 0 and COR = FAC2 = MG = VG = 1 (Chang and Hanna, 2004). A model is considered sufficiently efficient if it provides the following results (Chang and Hanna, 2004): $-0.3 < FB < 0.3$, $0.7 < MG < 1.3$, $NMSE < 4$, $VG < 1.6$ et $FAC2 \geq 0.5$. All FB values are positive, indicating that all models on average tend to under-predict concentration, with the k-ε model being the least under-predicting model. Examination of the MG values in Table 2 shows that no model manages to meet the acceptance criterion, with the k-ε model being the closest to the tolerable range. The same is true for the VG values. As for the NMSE values, they are all within the accepted range. Therefore, all models perform well for linear measures (FB and NMSE), but

appear to have a systematic bias at low concentrations based on values for logarithmic measures (MG and VG). All models succeed in having more than 50% of the concentration within a factor-of-two (FAC2) of the observations. The k-ε model is the best performing with 75% of the predictions within a factor-of-two of the observations. As for the R_{ij}-ε model, it performs significantly less well with about 63%, 60% and 69% with SGDH, GGDH and DFM models, respectively. Finally, good one-to-one correlations can be observed for all models through the high values of the correlation coefficient, the highest of which is for the R_{ij}-ε (with GGDH and DFM) models (COR = 0.92). Comparing the k-ε and R_{ij}-ε models, we see that the latter, known as anisotropic, does not necessarily improve predictions over the former, regardless of the scalar turbulent flux model with which it is associated. However, a study done by Bahlali et al. (2018a) shows that the use of the R_{ij}-ε model provides a more physical representation of the influence of obstacles on the concentration profiles. All three models for velocity-scalar correlation (SGDH, GGDH, and DFM), employed with the R_{ij}-ε model, score three on the statistical evaluation and thus can all be retained. Using the GGDH assumption that solves the Reynolds stress tensor does not improve predictions over the isotropic SGDH model (lower FAC2 and more under-prediction). The GGDH model causes numerical oscillations when applied to a flow with thermal stratification. The DFM model, on the other hand, is more adequate for stratified atmospheric flows and performs better than the GGDH model (less under-prediction and higher FAC2). This is probably due to the presence of a gravity term with scalar variance in the transport equation for turbulent scalar fluxes.

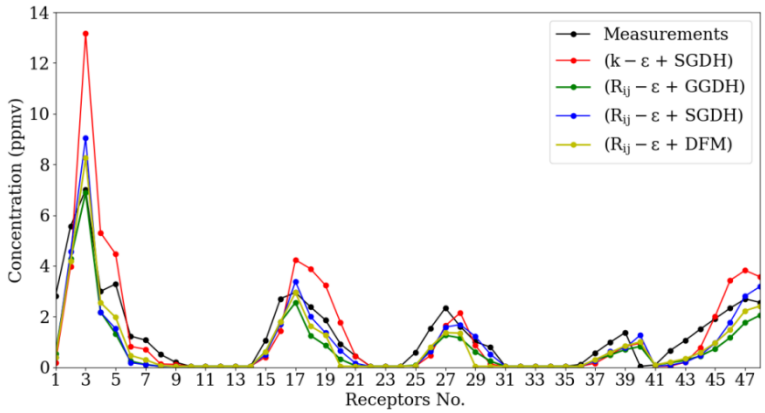

Figure 6. Comparison between the measured and predicted concentration profile on all PID sensors for trial #2692157

Table 2. Statistical performance measures evaluated for trial #2692157: Fractional Bias (FB), Geometric Mean Bias (MG), Normalized Mean Square Error (NMSE), Geometric Variance (VG), Factor of Two (FAC2), Correlation Coefficient (COR)

	FB	**MG**	**NMSE**	**VG**	**FAC2(%)**	**COR**
k-ε + SGDH	0.13	1.39	0.37	2.23	75	0.91
R_{ij}-ε + SGDH	0.27	1.66	0.45	3.3	62.5	0.90
R_{ij}-ε + GGDH	0.5	1.81	0.59	2.98	60.4	0.92
R_{ij}-ε + DFM	0.37	1.86	0.45	4.47	68.8	0.92

Conclusion and perspectives

This study presents 3D CFD simulations of the dispersion of a pollutant under weakly stable conditions. The CFD model Code_Saturne® is evaluated with concentration measurements obtained from a MUST experiment trial in a complex urban field. Simulations are performed using two turbulence models, k-ε and R_{ij}-ε LRR, and scalar turbulent fluxes are evaluated using SGDH, GGDH and the differential transport equation (DFM). Qualitative and quantitative analysis shows that the performance of the models is reasonably acceptable in terms of capturing the multiple concentration peaks and the hourly average concentration distribution. All models show an overall under-prediction of the mean concentration. The

comparison between the k-ε and R_{ij}-ε models shows that the former generates an overproduction of turbulence near the ground, inducing a much larger plume laterally. The isotropic model predicts nearly 75% of the concentration values within a factor of two, while offering a better compromise between accuracy and computation time, and is therefore perfect for impact studies. Using the differential transport equation to solve for scalar turbulent flows improves predictions with nearly 69% of concentration values within a factor of two of the observations. It also provides better correlation with experimental measurements, compared to algebraic models such as SGDH and GGDH. Regardless of its computational cost, this model proves to be very adequate to study atmospheric dispersion in complex terrain with low stability conditions. Further studies have also been conducted on the different algebraic models and the scalar transport equation to further evaluate their performance, especially under very stable atmospheric conditions. It would also be necessary to adjust the various constants implemented in the formulation of these models so that they better fit the dispersion problem.

REFERENCES

Bahlali, M.L., Dupont, E. and Carissimo, B., 2019. Atmospheric dispersion using a Lagrangian stochastic approach: Application to an idealized urban area under neutral and stable meteorological conditions. *Journal of Wind Engineering and Industrial Aerodynamics*, *193*, p.103976.

Biltoft, C.A., 2001. Customer report for mock urban setting test. *DPG Document*, (8-CO), pp.160-000.

Businger, J.A., Wyngaard, J.C., Izumi, Y. and Bradley, E.F., 1971. Flux-profile relationships in the atmospheric surface layer. *Journal of the atmospheric Sciences*, *28*(2), pp.181-189.

Chang, J.C. and Hanna, S.R., 2004. Air quality model performance evaluation. *Meteorology and Atmospheric Physics*, *87*(1), pp.167-196.

Daly, B.J. and Harlow, F.H., 1970. Transport equations in turbulence. *The physics of fluids*, *13*(11), pp.2634-2649.

Dehoux, F., 2012. *Modélisation statistique des écoulements turbulents en convection forcée, mixte et naturelle* (Doctoral dissertation, Poitiers).

Gorlé, C.V., Van Beeck, J.P.A.J., Rambaud, P. and Van Tendeloo, G., 2009. CFD modelling of small particle dispersion: the influence of the turbulence kinetic energy in the atmospheric boundary layer. *Atmospheric environment*, *43*(3), pp.673-681

Gryning, S.E., Batchvarova, E., Brümmer, B., Jørgensen, H. and Larsen, S., 2007. On the extension of the wind profile over homogeneous terrain beyond the surface boundary layer. *Boundary-layer meteorology*, *124*(2), pp.251-268.

Kerschgens, M.J., Nölle, C. and Martens, R., 2000. Comments on turbulence parameters for the calculation of dispersion in the atmospheric boundary layer. *Meteorologische Zeitschrift*, pp.155-163.

Kumar, P., Feiz, A.A., Ngae, P., Singh, S.K. and Issartel, J.P., 2015. CFD simulation of short-range plume dispersion from a point release in an urban like environment. *Atmospheric Environment*, *122*, pp.645-656.

Launder, B.E., Reece, G.J. and Rodi, W., 1975. Progress in the development of a Reynolds-stress turbulence closure. *Journal of fluid mechanics*, *68*(3), pp.537-566.

Launder, B.E. and Spalding, D.B., 1983. The numerical computation of turbulent flows. In *Numerical prediction of flow, heat transfer, turbulence and combustion* (pp. 96-116). Pergamon.

Milliez, M. and Carissimo, B., 2007. Numerical simulations of pollutant dispersion in an idealized urban area, for different meteorological conditions. *Boundary-Layer Meteorology*, *122*(2), pp.321-342.

Pasquill, F., 1972. Some aspects of boundary layer description. *Quarterly Journal of the Royal Meteorological Society*, *98*(417), pp.469-494.

Pena, A., Gryning, S.E., Hasager, C.B. and Courtney, M., 2009. Extending the wind profile much higher than the surface layer. *EWEC Marseille*.

Yee, E. and Biltoft, C.A., 2004. Concentration fluctuation measurements in a plume dispersing through a regular array of obstacles. *Boundary-Layer Meteorology*, *111*(3), pp.363-415.

21st International Conference on
Harmonisation within Atmospheric Dispersion Modelling for Regulatory Purposes
27-30 September 2022, Aveiro, Portugal

$PM_{2.5}$ PREDICTIONS FOR URBAN MONITORING SITES IN BUDAPEST USING STATISTICAL FUSION OF CAMS AIR QUALITY MODELS

Adrienn Varga-Balogh [1], Ádám Leelőssy [1] and Róbert Mészáros [1]

[1] Eötvös Loránd University, Institute of Geography and Earth Sciences, Department of Meteorology, Pázmány Péter sétány 1/A, 1117 Budapest, Hungary

Abstract: For urban monitoring sites, air quality forecasting with atmospheric chemistry transport models have limitations due to the complexity of air pollution sources in cities. In the winter, communal heating is the main source of air pollutants in Hungary. Winter stagnation events with low wind speed can increase concentrations and cause the deviation of air quality guidelines within the city.
For Budapest, the capital of Hungary, a time-dependent downscaling method was used to predict the daily mean of $PM_{2.5}$ concentration for the heating seasons in 2018–2021. Nine individual models of the Copernicus Atmosphere Monitoring Service (CAMS) were compared to six urban measurement points' $PM_{2.5}$ data in Budapest. Downscaled predictions were produced by the linear combination of the CAMS models using spatially constant and time-dependent weights fit on the previous 10-days long period. The last 10-day bias was also corrected in the models.
Downscaling generally reduced the root mean square error (RMSE) for the heating season, especially for the smog episodes, as the method reduced the high underestimation of $PM_{2.5}$ in contaminated periods. Predictions from the model fusion were more efficient in smog episodes and had similar overall efficiency to the bias-corrected ensemble. The fusion of the CAMS models leads to a more accurate forecast of wintertime $PM_{2.5}$ peaks in urban monitoring sites of Budapest than using any of the individual models.

Key words: *PM2.5; CAMS; Budapest; air quality; data fusion*

INTRODUCTION

Most cities have been facing polluted air conditions. In the case of Budapest, the capital city of Hungary, especially winter stagnation events can cause heavily polluted episodes due to residential heating.

The $PM_{2.5}$ forecasts of the Copernicus Atmosphere Monitoring Service (CAMS) models were used. CAMS includes the air quality forecast of several models developed independently: CHIMERE, EMEP, LOTOS-EUROS, MATCH, MOCAGE, SILAM, EURAD-IM, DEHM (from 2019), GEM-AQ (from 2019), and the multi-model ENSEMBLE forecast as the median of the individual values.
Air quality data is available from the Hungarian Air Quality Network, which has six stations measuring $PM_{2.5}$ in Budapest and providing hourly $PM_{2.5}$ measurements.

methods

A time-dependent linear combination for CAMS models were presented by Sofiev et al. (2017). The data of $PM_{2.5}$ monitoring sites of Budapest were used to fit the linear combination on a 10-day training period. The forecasted concentrations by the fusion model $\left(c_{fusion}(x,t)\right)$ at location x and time t:

$$c_{fusion}(x,t) = w_{0,t} + \sum_{i=1}^{M} w_{i,t} c_{i,x,t} \,, \tag{1}$$

where the prediction $\left(c_{i,x,t}\right)$ was the uncorrected/bias-corrected $PM_{2.5}$ forecast of the i^{th} model for a measurement station from the nearest gridpoint. *M* is the number of models used, seven in the winters of

2018–2019, nine afterwards (in the winters of 2019–2020, 2020–2021 and 2021–2022). In June 2022, two extra models were added. The weights (w_t) were fit for each day on the previous 10-day training period by minimizing the J_t cost function for all available sites.

$$J_t = \sqrt{\frac{1}{X \cdot T} \sum_{x=1}^{X} \sum_{\tau=T-d}^{t-d} \left(c_{fusion}(x,t) - c_{obs}(x,t) \right)^2} + R. \quad (2)$$

The weights are variant in time for each model, and spatially consistent. The regularization term *R* minimizes the differences in weights between the consecutive timesteps and among models:

$$R = \alpha \sum_{i=1}^{M} \left(w(i,t) - \frac{1}{M} \right)^2 + \beta \sum_{i=1}^{M} \left(w(i,t) - w(i,t-1) \right)^2. \quad (3)$$

The model bias was calculated on a rolling 10-day period, then added to the next days' forecast. This way, a bias-corrected dataset was created. For the heating seasons, the optimized fusion forecasts were produced from both the CAMS model forecasts and the bias-corrected model-forecasts.

The performance of the models was measured in terms of mean absolute error (bias), root mean square error (RMSE), Pearson correlation (r) and accuracy of EAQI (European Air Quality Index) categories.

results

For the heating seasons (defined between 15 October – 15 April), in the winters of 2018, 2019, 2020 and 2021 the $PM_{2.5}$ levels and forecasts were investigated. The analysis of the 2018–2019 period was described in detail in Varga-Balogh et. al. (2020).

In Fig. 1., the time series of the forecasts is presented for the last three winter periods. The CAMS ENSEMBLE and fusion model is shown with the $PM_{2.5}$ values measured at Kőrakás park measurement station. Results from the bias-corrected models are added with dotted lines. In Hungary, stagnation events can occur often in the winters, when persistent anticyclonic conditions with low windspeeds and weak mixing in the lower troposphere lead to poor air quality situations. Each winter showed different weather conditions. In January 2020, a longer period appeared with high concentrations of $PM_{2.5}$, while the last winter was different: only short periods were above the WHO guideline (25 μg m^{-1}) concentration. A general overestimation was observable by the CAMS ENSEMBLE.

The errors of the bias-corrected CAMS ENSEMBLE is a consequence of the 10-day bias-correction period. When the uncorrected model had given relatively strong underestimation for the previous days, the correction shifted the forecast to overestimation especially in cases of longer periods with high $PM_{2.5}$ concentrations followed by a relatively clear period. (E.g.: the end of the heating season in 2020, end of December 2019.)

The errors of the fusion model can also be attributed to the 10-day training period. In winter stagnation episodes (anticyclonic conditions), high concentrations of $PM_{2.5}$ is followed by a cold front with high windspeed and rapid cleansing in air pollution. The rapid improvement of air pollution is not caught by the fusion model. (End of January 2020.)

The forecast for the heating season of 2021–2022 led to errors both in cases of ENSEMBLE and fusion models due to the high variability of air pollution.

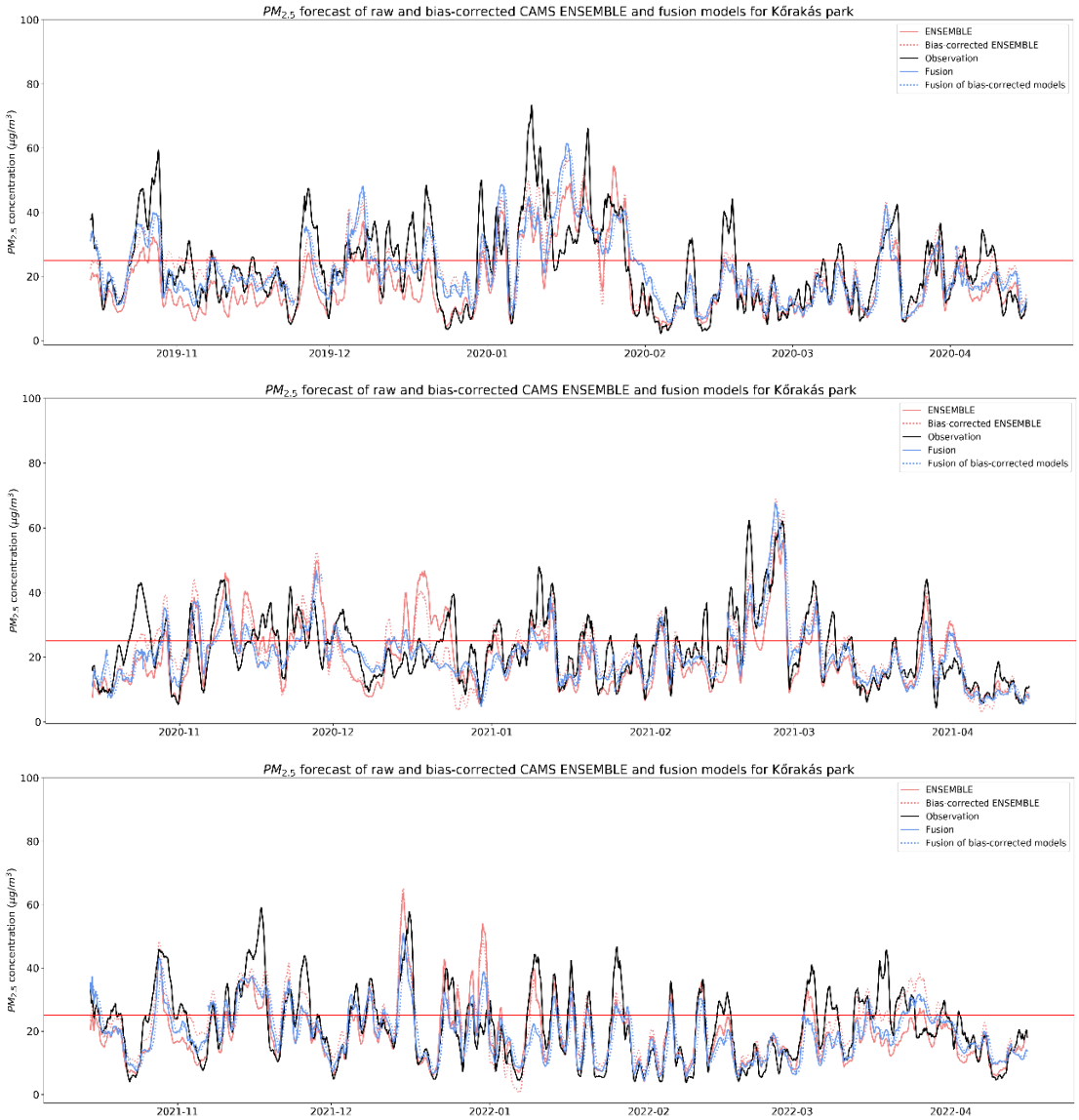

Figure 7. Time series of $PM_{2.5}$ measurements at Kőrakás park measurement station with black line (24h moving average), uncorrected (red) and bias-corrected (dotted red) CAMS ENSEMBLE, and the optimized fusion model of uncorrected (blue) and bias-corrected models (dotted blue) for the heating seasons of 2019–2020, 2020–2021 and 2021–2022

In terms of bias, RMSE, Pearson correlation (r), the CAMS ENSEMBLE performed nearly as the fusion models. The bias-correction improved the forecasts of the individual models as well as the performance of CAMS ENSEMBLE, however in some cases, the fusion of uncorrected models performed better than the fusion of bias-corrected models. The validation statistics for the heating season of 2021–2022 is presented in Figure 2.

The time series of the model-weight was also investigated (Figure 3). Although in the winter of 2018–2019, the high air pollution levels well-correlated with the high weights of the SILAM model (Varga-Balogh et. al., 2020), in the rapidly changing air quality of the 2021–2022 heating season (no stagnation event occurred), the SILAM model was overperformed by the others.

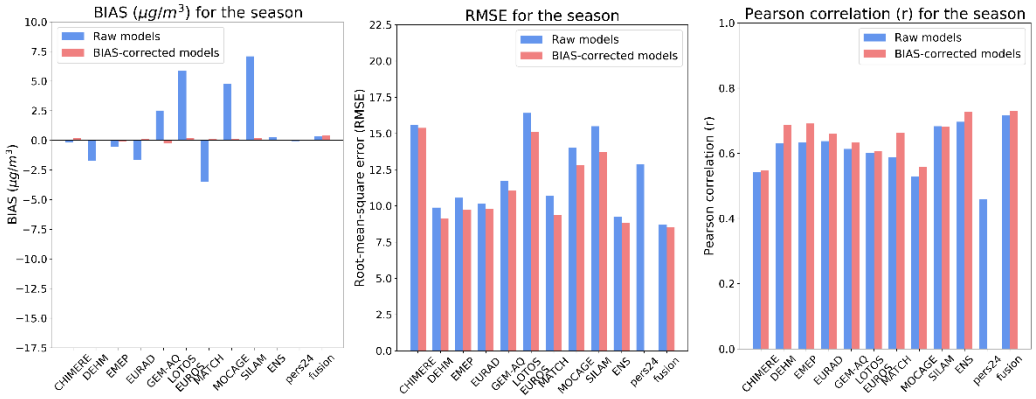

Figure 2. Validation for the heating season of 2021–2022. Bias, RMSE and Pearson correlation is presented for the uncorrected (blue) and bias-corrected (red columns) CAMS, CAMS ENSEMBLE, 24-h persistence, and fusion models.

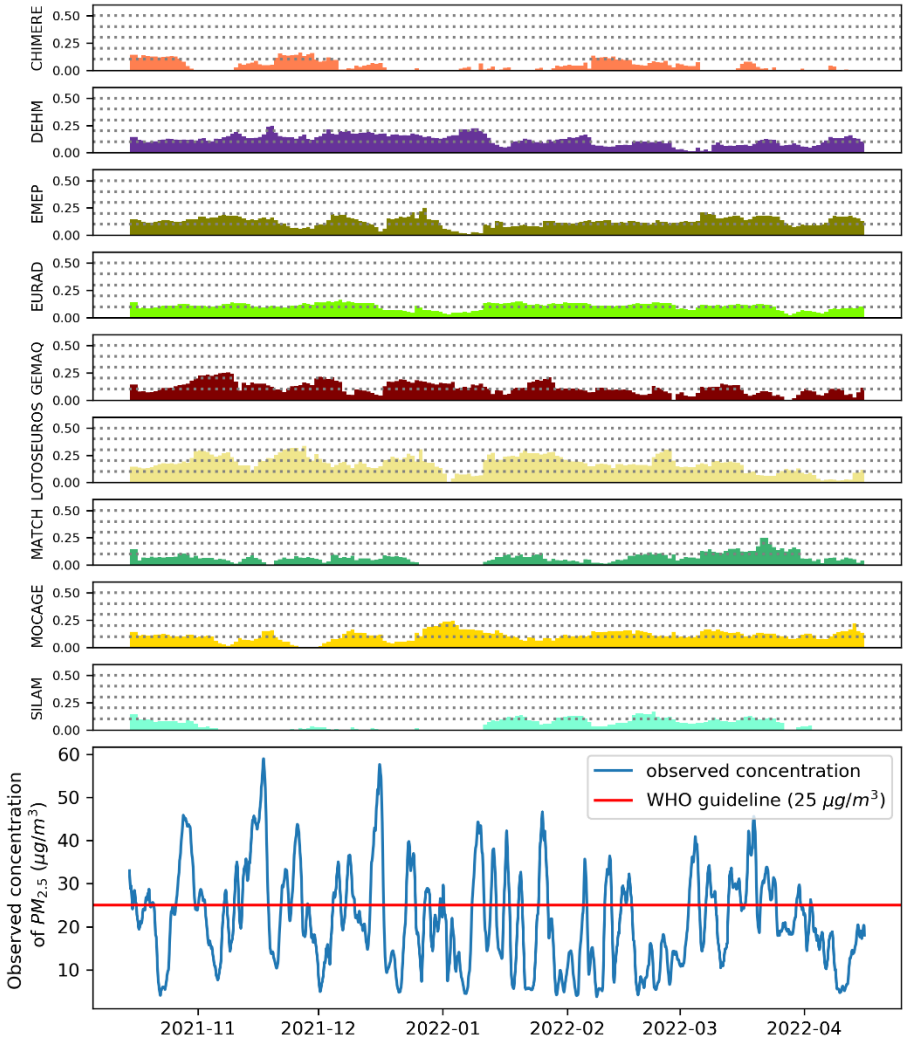

Figure 3. Time series of the applied model-weights and observed concentrations of $PM_{2.5}$ at Kőrakás park measurement station in the heating season of 2021–2022.

conclusions

The CAMS $PM_{2.5}$ forecasts were compared to air quality measurement stations of Budapest for four heating seasons. Furthermore, bias was corrected on the previous 10-day data, and also a 10-day training period was applied for an optimization to produce a linear combination of the model forecasts. The CAMS ENSEMBLE was better than individual models in terms of bias, RMSE and Pearson correlation (r). Bias-corrected models mostly performed better than the uncorrected models in $PM_{2.5}$ forecasts, especially ENSEMBLE forecast improved for all winters with bias-correction.

Fusion model performs nearly as ENSEMBLE forecast, however in winter stagnation events, it performs better than CAMS and CAMS ENSEMBLE models.

The time series of the weights were examined to see which model performed best. Model weights were found to be strongly weather-dependent and variable among winters with many and no stagnation events.

funding

This work was supported by the National Research, Development and Innovation Office of Hungary (grant No. 128805 and 128818). The research was funded by the National Multidisciplinary Laboratory for Climate Change, RRF-2.3.1-21-2021 project.

REFERENCES

Sofiev, M., Ritenberga, O., Albertini, R., Arteta, J., Belmonte, J., Bernstein, C.G., Bonini, M., Celenk, S., Damialis, A., Douros, J., et al., 2017: Multi-model ensemble simulations of olive pollen distribution in Europe in 2014: Current status and outlook. *Atmos. Chem. Phys*., **17**, 12341–12360.

Varga-Balogh, A., Leelőssy, Á., Lagzi, I., Mészáros, R., 2020: Time-Dependent Downscaling of PM2.5 Predictions from CAMS Air Quality Models to Urban Monitoring Sites in Budapest. *Atmosphere*, **11**, 669.

21st International Conference on
Harmonisation within Atmospheric Dispersion Modelling for Regulatory Purposes
27-30 September 2022, Aveiro, Portugal

COMPARISON OF SOURCE APPORTIONMENT METHODS TO ATTRIBUTE SUMMER TROPOSPHERIC O_3 AND NO_2 LEVELS IN MADRID (SPAIN)

Rafael Borge[1], David de la Paz[1]

[1] Universidad Politécnica de Madrid (UPM). Department of Chemical and Environmental Engineering, ETSII-UPM – Calle José Gutiérrez Abascal 2, 28006, Madrid, Spain

Abstract:
Tropospheric ozone (O_3) is a secondary pollutant formed in the atmosphere through complex chemical reactions that involve a number or precursors, mainly volatile organic compounds (VOC) and nitrogen oxides (NO_X). Atmospheric photochemistry is also affected by meteorological conditions, including temperature and solar radiation, so O_3 concentration typically peaks up in summer. Recent emission abatement measures targeted to comply with NO_2 air quality standards have increased the oxidant (e.g. O_3) levels of many urban atmospheres in Europe (e.g., Madrid, Spain among others). Source apportionment studies may help to understand the reasons for such phenomena and to identify air pollution controls to reduce both NO_2 and O_3 around the main urban areas. The most traditional way to examine an air pollution control option is the single perturbation or brute force method using chemical-transport models. The contribution of a particular source is derived from the comparison of two model simulations; one simulation with a complete emission inventory and other simulation in which the source of interest is removed. This approach, however has some limitations, especially for chemical species governed by non-linear dynamics. In this contribution, we compare the results of this approach to that of a mass-transfer method that tags the emission of the sectors of interest and track them through the chemical reaction and transport processes in a representative summer month in the Madrid Region. Here, we compare two implementations of the CMAQ (Community Multiscale Air Quality) ISAM (Integrated Source Apportionment Method), corresponding to versions 5.0.2 and 5.3.2. The attribution in the first approach relies on a previous assessment of NO_X/VOC ambient concentration ratio to identify the sensitivity to O_3 precursors at each temporal step and consequently make the apportionment to the source of that particular precursor. The second approach, proportionally attributes the pollutant tracked to each of the reactants, regardless of sensitivity considerations. This provides a more realistic view but has a more complex interpretation. For instance, we found that the attribution to boundary conditions changes considerably, especially for NO_2, partly due to the influence of external O_3 contributions to our modeling domain.

Key words: *Air Quality, Source Apportionment, Modelling, Emission sources*

INTRODUCTION

Air pollution is one of the main environmental concerns and a major threat to public health. According to the World Health Organization (WHO, 2021), 4.2 million premature deaths were related to ambient (outdoor) air pollution worldwide in 2016. The burden of disease can be attributed mainly to fine particulate matter ($PM_{2.5}$), nitrogen dioxide (NO_2) and tropospheric ozone (O_3) and disproportionally low- and middle-income countries. But even in developed regions such as Europe that have taken action to curb emissions, air quality issues remain (EEA, 2021). For instance, air standards (according to Directive 2008/50/EC) are often exceeded in some Spanish cities, such as Madrid. Air pollution levels are generally declining in this city. In 2021 only one air quality monitoring station (AQMS) reported an annual NO_2 concentration mean above 40 $\mu g/m^3$, in contrast with 7 AQMS exceeding the NO_2 annual limit value in 2018. The trends for O_3 are not so clear. The target value for the protection of human health (maximum daily eight-hour mean below 120 40 $\mu g/m^3$) was exceeded by 6 and 5 AQMS in 2018 and 2021, respectively. $PM_{2.5}$ ambient concentration levels are in compliance with legal standards for all AQMS. Despite general positive trends, meeting EU standards for all pollutants pose a significant challenge. NO_x and $PM_{2,5}$ emissions levels were reduced up to 50% and 15% respectively during COVID-19 restrictions in 2020 in Spain (Guevara et al., 2021). Even though, that was insufficient to meet the NO_2 annual limit in some traffic hot-spots. That illustrates the difficulty of eventually reach the WHO guidelines (WHO, 2021) and supports the need to design and implement further emission abatement strategies. As a first step, that requires identifying the sources responsible for current ambient concentration levels, especially for secondary photochemical

pollutants. This study applies different methods to understand the source contribution to NO_2 and O_3 levels in Madrid for a summer month.

Materials and methods

We used 3 nested modeling domains with an innermost domain covering Madrid and surroundings with 136 km in the east-west direction and 144 km in the north-south direction, with 1 km^2 spatial resolution (Figure 1a). They all have a 35-level vertical structure covering the whole Tropossfere with 18 layers within the first kilometer.

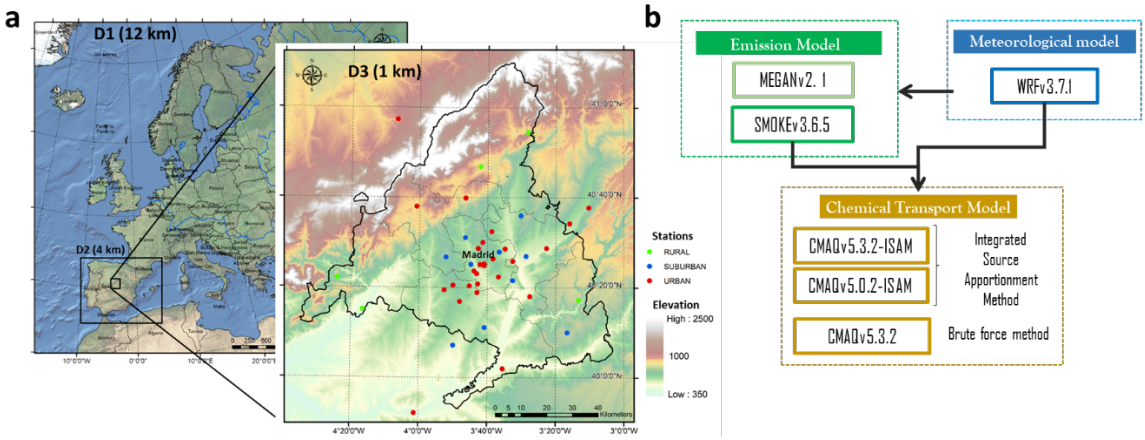

Figure 8. Nested modeling setup and detailed of the innermost 1 km^2-resolution domain over Madrid (a). Basic flowchart of the modeling system used in this study (b).

The first component of the state-of-the-science modeling system used in this study (Figure 1b) is the WRFv3.7.1 (Weather Research and Forecasting) meteorological model Skamarock and Klemp, 2008). Physical options and parameterizations are based on previous studies on this area (Borge et al., 2008a; de la Paz et al., 2016). Antrhopogenic emissions are processed through the SMOKEv3.6.5 (Sparse Matrix Operator Kernel System) US EPA model (Baek and Seppanen, 2018), adapted to the Iberian Peninsula (Borge et al., 2014; Borge et al., 2008b). Biogenic emissions were generated by MEGAN v2.1 (Model Emissions Gases and Aerosols from Nature) (Guenther et al., 2012). Finaly, we used two different versions of the CMAQ (Community Multiscale Air Quality) chemical-transport model (Byun and Schere, 2006) that implement alternative versions of ISAM (Integrated Source Apportionment Method) (Kwok et al., 2015). While both share the conceptual basis and can be classificed as a tagging mehtod (Thunis et al., 2019), CMAQv5.0.2-ISAM attributes the formation of a secondary pollutant to the sector the limitting reactive is emmited from. In contrast, CMAQv5.3.2-ISAM tracks the contribution of all the precursors and proportionally attributes the products to the corresponding sources. We compare these two alternatives with the classical single-perturbation method (SPM) or ”zero-out” approach, where emissions from each sector are removed one at a time, using CMAQv5.3.2. In all experiments, we used the Carbon Bond 5 (CB05) chemical mechanism with updated toluene and chlorine chemistry (CB05TUCL) (Sarwar et al., 2012; Whitten et al., 2010) and the aerosol module AERO6 (Appel et al., 2013). Dynamic chemical boundary conditions are provided by the Hemispheric CMAQ (Mathur et al., 2017).

We study the source apportionment of NO_2 and O_3 for typical summer conditons (high solar radiation and temperatures that favour the production of the later). The reference period, July 2016, was used in previous studies to characterize O_3 formation in this region (Querol, 2018).

As for the tagged sectors, we tracked all the SNAP (Selected Nomenclature for Air Pollution gropus. As shown in Figure 2, we merged all industrial activities and power generation (SNAP 01 to SNAP 03) due to their limmited presence in this modeling domain. According to our inventory, road traffic (SNAP 07) and solvent use (SNAP 06) are the main source of NO_X and VOC emissions, with a total share of 65% and 49%, respectively.

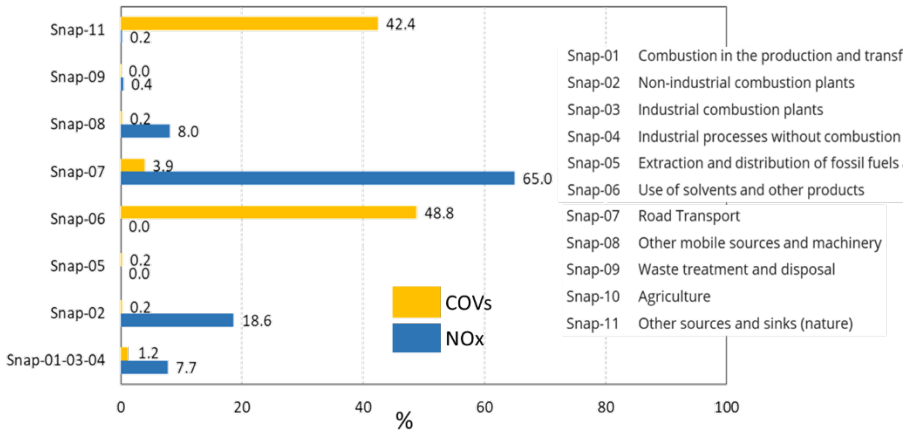

Figure 2. NO_X and VOC emissions of tagged sectors for the source apportionment analysis

RESULTS

The differences on the atrribution of average monthly NO_2 ambient concentration levels can be illustrated by analyzing the resutls for the SNAP 07 sector (Figure 3), the main source of this pollutant according to the three methods compared. As an average over the region, the SPM or "brute force method" (Figure 3a) attributes 67% of NO_2 tho road traffic. This is in agreement with the outcomes from CMAQ-ISAM v5.0.2 (Figure 3c) (63%), but the latest ISAM version (CMAQv5.3.2, Figure 3b) apportions only 32% of NO_2 to this sector. Oppositely, boundary conditions are given a much larger attribution due to the influence of O_3 transported into the modeling domain.

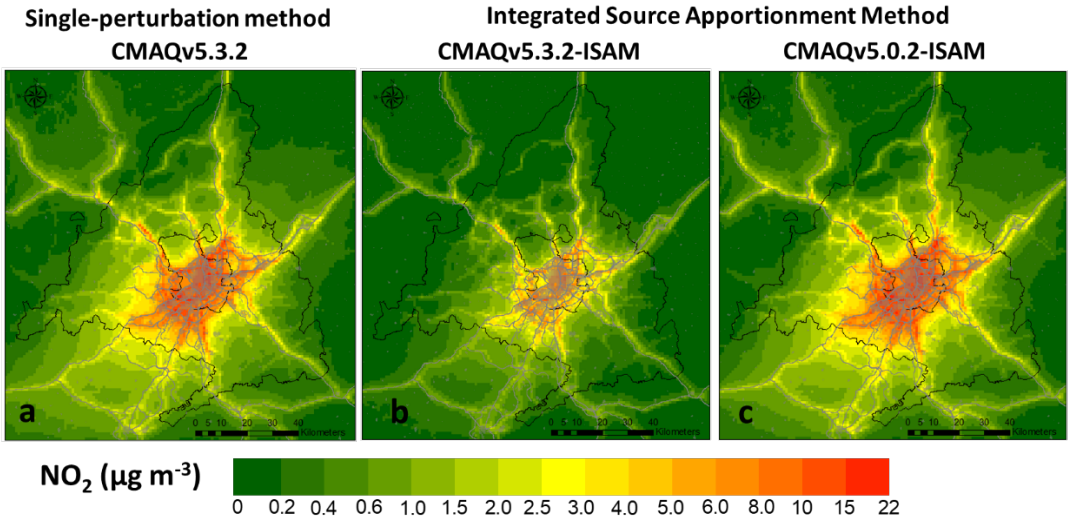

Figure 3. Average NO_2 concentration in the Madrid region (July 2016) attributed to road traffic (SNAP 07)

The differences on the atrribution of average monthly NO_2 ambient concentration levels can be illustrated by analyzing the resutls for the SNAP 07 sector (Figure 3), the main source of this pollutant according to the three methods compared. As an average over the region, the SPM or "brute force method" (Figure 3a) attributes 67% of NO_2 tho road traffic. This is in agreement with the outcomes from CMAQ-ISAM v5.0.2 (Figure 3c) (63%), but the latest ISAM version (CMAQv5.3.2, Figure 3b) apportions only 32% of NO_2 to this sector. Oppositely, boundary conditions are given a much larger attribution due to the influence of O_3 transported into the modeling domain.

The results for O_3, a purely secondary pollutant, are illustrated in Figure 4. The base model run (that including emissions from all sectors) yields lower average O_3 concentrations in the city center than that

where emissions from road traffic have been removed. Therefore, we obtained a negative attribution of O_3 (up to -9 µg m^{-3}) in areas dominated by traffic emissions (downtown Madrid and the main roads), as clearly shown in Figure 4a. This is mainly due to reduced O_3 consumption through NOx titration. Oppositely, ISAM only accounts for O_3 formation, i.e. it explains current levels and thus, no negative contributions are attributed. The latest ISAM version (Figure 4b) yields higher O_3 apportionments to road traffic (up to 9 µg m^{-3}; around 4%) than CMAQ-ISAM v5.0.2 (up to 4 µg m^{-3}; around 2%). In both cases, O_3 is strongly dominated by boundary conditions (de la Paz et al., 2012). Of note, determining that contribution would require additional model runs with perturbed BC in the SPM (Borge et al., 2014).

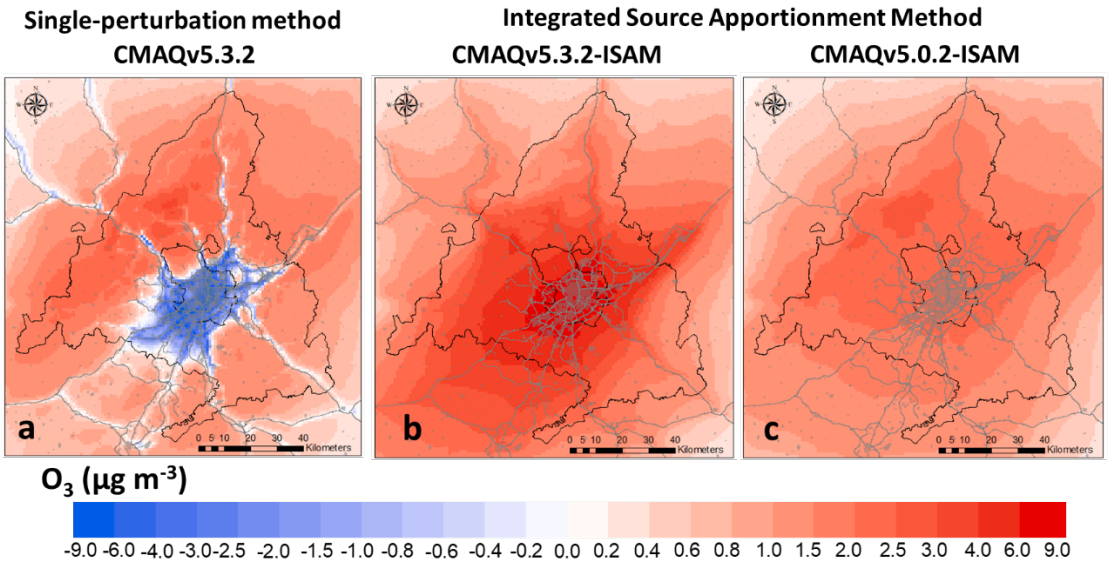

Figure 4. Average O_3 concentration in the Madrid region (July 2016) attributed to road traffic (SNAP 07)

cONCLUSIONS

Despite significant opperational differences, not analyzed in this contribution, this work illustrates that the results of different NO_2 and O_3 source apportionment methods for may substantially differ. The key to interpret them and inform potential abatement measures is to understand that the information convey not directly comparable. The SPM is a sensitivity analysis that shows what would happen if the emissions from a given sector would be removed. While this may have limited interest for the design of specific plans and measures, it informs of the relative importance of diffrent sectors and provides an idea of the maximum abatement potential for each of them. Oppositelly, ISAM provides a detailed view of the current contributions of emitting sectors to ambient concentration levels. CMAQ-ISAM v5.0.2 apportions secondary pollutants to direct primary precursors while CMAQ-ISAM v5.3.2 proportionally attributes the pollutant tracked to each of the reactants, allowing to apportion a secondary pollutant to sectors where precursors are not emitted. This provides a more realistic view but has a more complex interpretation. For instance, we found that the attribution to boundary conditions changes considerably, especially for NO_2, partly due to the influence of external O_3 contributions to our modeling domain. We think all methods may assist the planning process by helping at the identification of target sectors but they should be accompained by the simulation of specific scenarios to anticipate the potential outcome of a given intervention.

REFERENCES

Appel K, Pouliot G, Simon H, Sarwar G, Pye H, Napelenok S, et al. Evaluation of dust and trace metal estimates from the Community Multiscale Air Quality (CMAQ) model version 5.0. Geoscientific Model Development 2013; 6: 883-899.

Baek BH, Seppanen C. Sparse Matrix Operator Kernel Emissions (SMOKE) Modeling System (Version SMOKE User's Documentation), 2018.

Borge R, Lumbreras J, Pérez J, de la Paz D, Vedrenne M, de Andrés JM, et al. Emission inventories and modeling requirements for the development of air quality plans. Application to Madrid (Spain). Science of the Total Environment 2014; 466-467: 809-819.

Borge, R., Alexandrov, V., del Vas, J.J., Lumbreras, J., Rodríguez, M.E., 2008a. A comprehensive sensitivity analysis of the WRF model for air quality applications over the Iberian Peninsula. Atmospheric Environment 42, 8560–8574.

Borge, R.; Lumbreras, J. and Rodríguez, M.E., 2008b. Development of a high-resolution emission inventory for Spain using the smoke modelling system: A case study for the years 2000 and 2010. Environmental Modelling & Software 23, 1026-1044.

Byun D, Schere KL. Review of the governing equations, computational algorithms, and other components of the Models-3 Community Multiscale Air Quality (CMAQ) modeling system. Applied Mechanics Reviews 2006; 59: 51-77

de la Paz D, Borge R, Martilli A. Assessment of a high resolution annual WRF-BEP/CMAQ simulation for the urban area of Madrid (Spain). Atmospheric Environment 2016; 144: 282-296.

de la Paz, D., Borge, R., Pérez, J., de Andrés, J.M., 2020. Contributions to summer ground-level O_3 in the Madrid region. 12th International Conference on Air Quality - Science and Application 9-13 March 2020, Thessaloniki (Greece). Proceedings of Abstracts p. 153. ISBN: 978-1-5272-5829-7.

European Environmental Agency (EEA), 2021. Air quality in Europe 2021. Report no. 15/2021. ISBN 978-92-9480-403-7 - ISSN 1977-8449 - doi: 10.2800/549289. https://www.eea.europa.eu//publications/air-quality-in-europe-2021

Guevara, M., Jorba, O., Soret, A., Petetin, H., Bowdalo, D., Serradell, K., Tena, C., Denier van der Gon, H., Kuenen, J., Peuch, V.-H., and Pérez García-Pando, C.: Time-resolved emission reductions for atmospheric chemistry modelling in Europe during the COVID-19 lockdowns, Atmos. Chem. Phys., 21, 773–797, https://doi.org/10.5194/acp-21-773-2021, 2021.

Guenther AB, Jiang X, Heald CL, Sakulyanontvittaya T, Duhl T, Emmons LK, et al. The Model of Emissions of Gases and Aerosols from Nature version 2.1 (MEGAN2.1): an extended and updated framework for modeling biogenic emissions. Geosci. Model Dev. 2012; 5: 1471-1492.

Kwok, R.H.F, Baker, K.R., Napelenok, S.L., & Tonnesen, G.S., 2015. Photochemical grid model implementation of VOC, NOx, and O_3 source apportionment. Geosci. Model Dev., 8, 99-114.

Mathur, R., Xing, J., Gilliam, R., Sarwar, G., Hogrefe, C., Pleim, J., Pouliot, G., Roselle, S., Spero, T. L., Wong, D. C., and Young, J., 2017. Extending the Community Multiscale Air Quality (CMAQ) modeling system to hemispheric scales: overview of process considerations and initial applications. Atmospheric Chemistry and Physics 17, 12449-12474.

Querol, X., Alastuey, A., Gangoiti, G., Perez, N., Lee, H. K., Eun, H. R., ... & Ahn, K. H. (2018). Phenomenology of summer ozone episodes over the Madrid Metropolitan Area, central Spain. Atmospheric Chemistry and Physics, 18(9), 6511-6533.

Sarwar G, Simon H, Bhave P, Yarwood G. Examining the impact of heterogeneous nitryl chloride production on air quality across the United States. Atmospheric Chemistry and Physics 2012; 12: 6455-6473.

Skamarock WC, Klemp JB. A time-split nonhydrostatic atmospheric model for weather research and forecasting applications. Journal of Computational Physics 2008; 227: 3465-3485.

Thunis, P., Clappier, A., Tarrason, L., Cuvelier, C., Monteiro, A., Pisoni, E., Wesseling, J., Belis, C.A., Pirovano, G., Janssen, S., Guerreiro, C., Peduzzi, E., 2019. Source apportionment to support air quality planning: Strengths and weaknesses of existing approaches. Environment International 130, 104825.

Whitten GZ, Heo G, Kimura Y, McDonald-Buller E, Allen DT, Carter WP, et al. A new condensed toluene mechanism for Carbon Bond: CB05-TU. Atmospheric Environment 2010; 44: 5346-5355.

World Health Organization. (2021). WHO global air quality guidelines: particulate matter ($PM_{2.5}$ and PM_{10}), ozone, nitrogen dioxide, sulfur dioxide and carbon monoxide. World Health Organization. https://apps.who.int/iris/handle/10665/345329.

21st International Conference on
Harmonisation within Atmospheric Dispersion Modelling for Regulatory Purposes
27-30 September 2022, Aveiro, Portugal

SMOKE PLUME FROM FIRE LAGRANGIAN SIMULATION: DEPENDENCE ON DRAG COEFFICIENT AND RESOLUTION

Bianca Tenti[1,2], Enrico Ferrero[1,3]

[1]Università del Piemonte Orientale, Vercelli, Italy
[2]Università di Torino, Torino, Italy
[3]ISAC-CNR, Torino, Italy

ABSTRACT: ***IN THIS WORK A NUMERICAL SIMULATION OF THE PLUME DISPERSED FROM A FIRE IS PERFORMED USING THE LAGRANGIAN STOCHASTIC PARTICLE MODEL SPRAYWEB AND THE RESULTS ARE COMPARED TO A FIELD EXPERIMENT, CARRIED OUT IN AUGUST 2013 IN IDAHO (USA). THE PLUME RISE SCHEME USED IS NOT BASED ON AN ANALYTICAL MODEL AND THE ONLY TWO ASSUMPTIONS REQUIRED ARE THE DRAG COEFFICIENT (CD) VALUE AND THE CELL SIZE. HERE WE WANT TO ASSESS THE DEPENDENCE OF THE MODEL ON THE VALUES CHOSEN FOR THESE TWO PARAMETERS.***

Key words: *Plume rise, dispersion model, drag coefficient*

INTRODUCTION

Correct modeling of the plume rise is fundamental for a proper description of pollutants dispersion, especially for highly buoyant wildfire plumes. In this work, a numerical simulation of the plume dispersed from a fire is performed applying the recent plume rise scheme suggested by Alessandrini et al. (2013) introduced in the Lagrangian stochastic particle model SPRAYWEB (Tinarelli et al., 2000, Alessandrini and Ferrero, 2009, Ferrero et al., 2022) and the results are compared to ground-based mobile elastic scanning lidar measurements of the maximum height of a plume coming from a prescribed 66 ha burn ignited during a field experiment, carried out in August 2013 in Idaho (USA) (Kovalev et al., 2014, Zhou et al., 2018). According to the algorithm, the plume is split into many cubic grid cells and at each time step the temperature and the momentum difference between the plume and background atmosphere is computed for each cell. One of the greatest advantages of this plume rise scheme is that it is not based on an analytical model and the only two assumptions required are the drag coefficient value and the cell size. With the aim of finding a general expression for the drag coefficient and a rule for the choice of the grid cells dimension, we assess the dependence of the model on the values chosen for these two parameters. So far, given the lack of a generally accepted value in the literature, the drag coefficient proposed by Ooms (1972) was adopted. However, different C_D expressions can be found in the literature; some of them are here tested comparing model results with experimental datasets.
Furthermore, to improve the results, we also perform some tests to estimate the optimal source-to-cell size ratio for the horizontal grid. The results are presented in terms of the comparison of the maximum plume height trend predicted by the model and the observations. An evaluation of the best model for C_D is shown through the Taylor diagram.

THE PLUME RISE SCHEME AND DRAG COEFFICIENT MODELS

The plume rise scheme suggested by Alessandrini et al. (2013) is based on the Lagrangian description of the plume evolution in terms of particle trajectories, while the temperature and momentum differences, which are responsible for the plume buoyancy, are calculated on a fixed grid. At each time step $\Delta t=t_1-t_0$ temperature and momentum differences (ΔT and w_c respectively) between each grid cubic cell and the surrounding environment are computed using the following equations:

$$\Delta T(t_1) = \Delta T(t_0) + \Gamma(z_c) w_c(t_0) \Delta t + 0.0098 w_c(t_0) \Delta t, \quad (1)$$

$$w_c(t_1) = w_c(t_0) + \frac{\Delta T_c(t_1)}{\Delta T_c + T_a(z_c)} g \Delta t + \frac{0.5 C_D S w_c^2(t_0) \rho_a}{\rho_p V_c} \Delta t, \quad (2)$$

where z_c is the cell height, T_a the ambient temperature, g the gravity, C_D the drag coefficient, S and V_c the cell section and volume, ρ_a and ρ_p the ambient and plume density.
Four drag coefficient expressions which depend on the Reynolds number of the cells (Re_c) are tested comparing the model results with respect to observations.
For each cell the correspondent Reynolds number is calculated as follows:

$$Re_c = \varphi \frac{|U_c|}{\nu}, \quad (3)$$

where φ is the equivalent cell diameter, V_c is the cell vertical velocity and ν is the kinematic viscosity of air.

Table 4. Drag coefficient expressions.

AUTHOR	*C_D EXPRESSION*	
TURTON AND LEVENSPIEL (1986)	$C_D = \frac{24}{Re_c}(1 + 0.173 Re_c^{0.657}) + \frac{0.413}{1+16300 Re_c^{-1.09}}, \ if\ Re_c < 2 \times 10^5$	*(4)*
BROWN AND LAWLER (2003)	$C_D = \frac{24}{Re_c}(1 + 0.15 Re_c^{0.681}) + \frac{0.407}{1+8710 Re_c^{-1}}, \quad if\ Re_c < 2 \times 10^5$	*(5)*
CHENG (2009)	$C_D = \frac{24}{Re_c}(1 + 0.27 Re_c)^{0.43} + 0.47(1 - exp\ (-0.04 Re_c^{0.38}))$	*(6)*
MIKHAILOV AND SILVA FREIRE (2013)	$C_D = \frac{777\left(\left(\frac{669806}{875}\right)+\left(\frac{114976}{1155}\right)Re_c+\left(\frac{707}{1380}\right)Re_c^2\right)}{646 Re_c\left(\left(\frac{32869}{952}\right)+\left(\frac{924}{643}\right)Re_c+\left(\frac{1}{385718}\right)Re_c^2\right)}$	*(7)*

The first three expressions presented in Table 1 are similar, as a sort of Stokes' law extended for higher Reynolds numbers, but with different constants derived by fitting experimental data. The latter is derived from the Shanks transformation of Goldstein series (Goldstein, 1929, Shanks, 1955) improved by fitting its coefficients directly to experimental data. These four expressions are implemented within the plume rise scheme. As meteorological input we use the WRF simulation provided by Ferrero et al. (2019), with turbulence field reconstructed by WSI (WRF-SPRAYWEB Interface). The dispersion is simulated by the Langrangian Stochastic model SPRAYWEB and the results are compared to measurements taken during the field experiment organized by the US Environmental Protection Agency (EPA) over complex terrain in Idaho with a ground-based mobile elastic scanning lidar (Kovalev et al., 2014, Zhou et al., 2018).

RESULTS

Figure 1 shows the maximum height of the plume as a function of time predicted by the model compared with the observations. In order to estimate the maximum plume height we consider two vertical standard deviation of the plume distribution above the mean particles height.
Data are smoothed using a moving-average smoothing function; the different colors indicate results obtained using different expressions for the drag coefficient and lidar observations of maximum plume height are also reported (black circles).
Almost all the models well reproduce lidar measurements in the second phase of the simulation, except for the Mikhailov and Silva Freire (2013) one. As for the initial phase of the event, observations are probably not very reliable since the values measured by the lidar are higher than the ones taken during the stability phase of the plume. The discrepancies between the observations and the model results could be due to a very fluctuating behavior of the plume in the initial phase which causes the lidar to measure very high values.

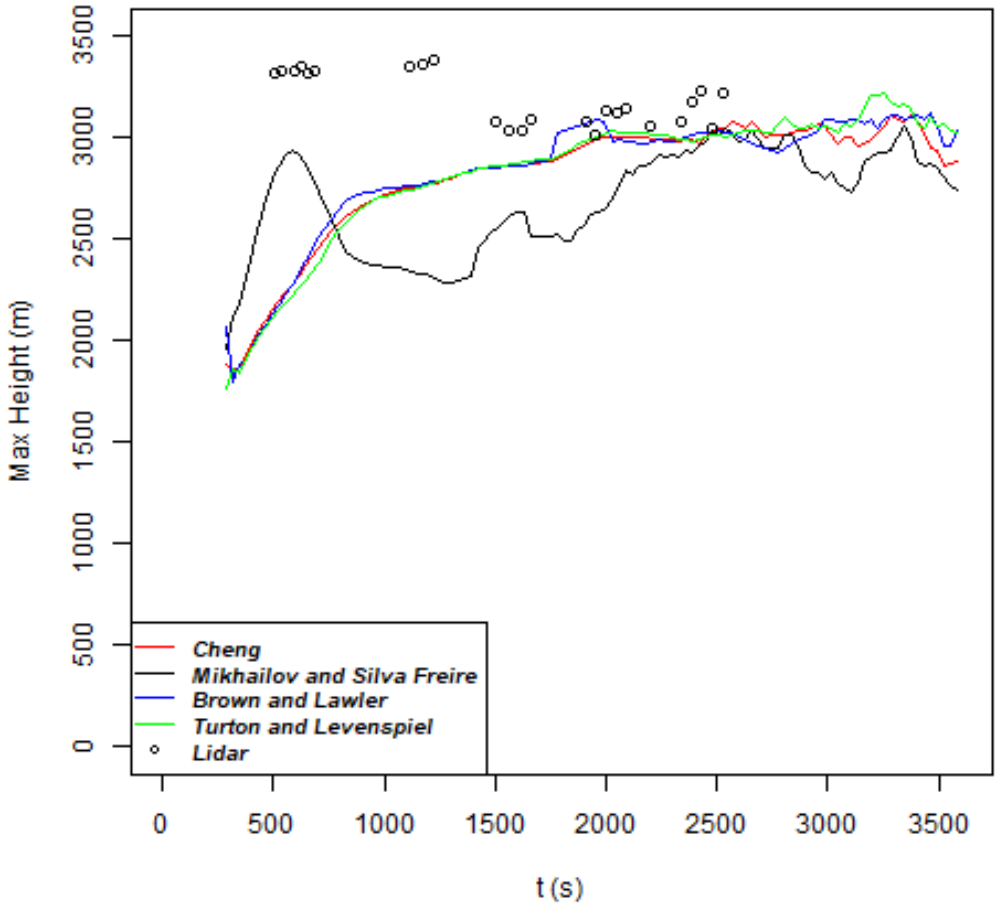

Figure 9. Plume maximum height as a function of time

Given the possible low reliability of the data observed during the first phase of the fire, the Taylor diagram presented in Figure 2 is created considering only the stability phase of the plume. In general, this analysis shows that there are differences between the four models which are hardly visible by observing Figure 1. Turton and Levenspiel (1986) model shows a very low correlation, while the correlation of the other models is around 0.4-0.5. As expected Mikhailov and Silva Freire (2013) expression for drag coefficient gives the highest root mean squared error. The two most faithful models are those of Cheng (2009) and Brown and Lawler (2003).

As for the horizontal resolution of the plume rise scheme, we performed some simulations varying the dimension of the grid cells, and we found that there is no particular dependence of the results on it.

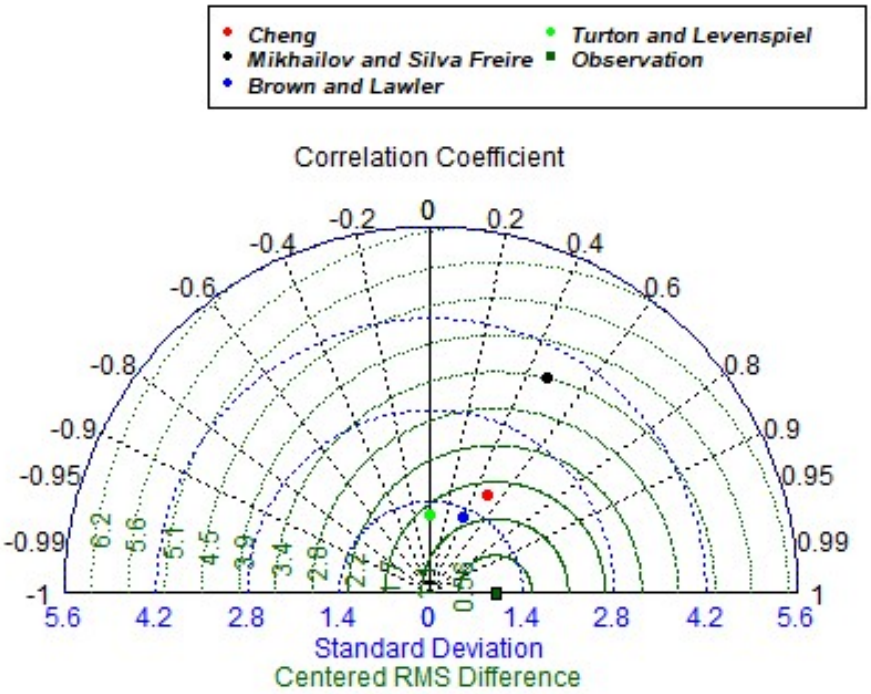

Figure 10. Taylor diagram for the four drag coefficient expressions

CONCLUSIONS

In this work we studied the dependence of the plume rise scheme embedded in the Langrangian Stochastic model SPRAYWEB on the drag coefficient and on the horizontal resolution. We tested 4 different expressions of the drag coefficient depending on the Reynolds number found in the literature, three of which are derived from Stokes' law and one from the Shanks transformation of Goldstein series (Goldstein, 1929, Shanks, 1955). Generally speaking, from the results it is evident that for this type of application the models deriving from the Stokes law have a better performance. In particular, the models of Cheng (2009) and Brown and Lawler (2003) give results that better agree with the observations. The model of Brown and Lawler (2003) can only be applied in case of Reynolds numbers less than 2×10^5, while the one of Cheng (2009) has no restrictions and this makes it the best choice for our purposes. Regarding the horizontal resolution we did not find a strong dependence of the results in case of small prescribed fires. As future work we want to test the same drag coefficient expressions on other case studies to confirm what emerged in this study.

REFERENCES

Alessandrini, S. and E. Ferrero, 2009: A hybrid lagrangian-eulerian particle model for reacting pollutant dispersion in non-homogeneous non-isotropic turbulence. *Physica A*, 388 (8), 1375– 1387.

Alessandrini, S., Ferrero, E., and Anfossi, D., 2013: A new Lagrangian method for modelling the buoyant plume rise. *Atmospheric environment*, 77, 239-249.

Brown, P. P., and Lawler, D. F., 2003: Sphere drag and settling velocity revisited. *Journal of environmental engineering*, 129(3), 222-231.

Cheng, N. S., 2009: Comparison of formulas for drag coefficient and settling velocity of spherical particles. *Powder Technology*, 189(3), 395-398.

Ferrero, E., Alessandrini, S., Anderson, B., Tomasi, E., Jimenez, P., and Meech, S., 2019: Lagrangian simulation of smoke plume from fire and validation using ground-based lidar and aircraft measurements. *Atmospheric Environment*, 213, 659-674.

Ferrero, E., Alessandrini, S., Meech, S., and Rozoff, C., 2022: A 3D Lagrangian stochastic particle model for the concentration variance dispersion. *Bull. of Atmos. Sci.& Technol.* **3,** 2.

Goldstein, S., 1929: The steady flow of viscous fluid past a fixed spherical obstacle at small Reynolds numbers. *Proceedings of the Royal Society of London*, 123(791), 225-235.

Kovalev, V., Urbanski, S., Petkov, A., Scalise, A., Wold, C., and Hao, W. M., 2014: Validation of smoke plume rise models using ground-based Lidar. In *Remote Sensing for Agriculture, Ecosystems, and Hydrology XVI* (Vol. 9239, pp. 478-486). SPIE.

Mikhailov, M. D. and Freire, A. S., 2013: The drag coefficient of a sphere: An approximation using Shanks transform. *Powder technology*, 237, 432-435.

Shanks, D., 1955: Non-linear transformations of divergent and slowly convergent sequences. *Journal of Mathematics and Physics*, 34(1-4), 1-42.

Tinarelli, G., Anfossi, D., Trini Castelli, S., Bider, M., Ferrero, E., 2000: A New High Performance Version of the Lagrangian Particle Dispersion Model Spray, Some Case Studies. *Springer US*, Boston, MA, pp. 499–507.

Turton, R. and Levenspiel, O., 1986: A short note on the drag correlation for spheres. *Powder technology*, 47(1), 83-86.

Zhou, L., Baker, K. R., Napelenok, S. L., Pouliot, G., Elleman, R., O'Neill, S. M., Urbanski, S. P., and Wong, D. C., 2018: Modeling crop residue burning experiments to evaluate smoke emissions and plume transport. *Science of The Total Environment*, 627, 523-533.

21st International Conference on
Harmonisation within Atmospheric Dispersion Modelling for Regulatory Purposes
27-30 September 2022, Aveiro, Portugal

PHAST MODELLING OF THE DESERT TORTOISE AND FLADIS AMMONIA TRIALS FOR THE JACK RABBIT III MODEL INTER-COMPARISON EXERCISE

Alison McGillivray[1], Mike Harper[2], Frank Hart[2], Stephen Puttick[3], Adeel Ibrahim[3], Laurent Verdier[4], Simon Gant[1], Rory Hetherington[1] and Harvey Tucker[5]

[1] Health and Safety Executive (HSE), Buxton, Derbyshire, UK
[2] DNV, Stockport, Greater Manchester, UK
[3] Syngenta, Huddersfield, Yorkshire, UK
[4] DGA Maîtrise NRBC, Vert le Petit, France
[5] Health and Safety Executive (HSE), Bootle, Merseyside, UK

Abstract:
As part of the Jack Rabbit III (JRIII) project, an international model inter-comparison exercise has been conducted where a number of dispersion modelling groups have simulated the Desert Tortoise and FLADIS ammonia trials. The objective of this work has been to understand the strengths and weaknesses of models that may be used to design the forthcoming JRIII ammonia experiments. This paper presents the dispersion modelling undertaken by four organisations: the UK's Health and Safety Executive (HSE), DNV, Syngenta and DGA Maîtrise NRBC (DGA), who all used the DNV Phast dispersion model. Although HSE do not use Phast for regulatory purposes, the organisation recognises that Phast and other integral models are widely used by industry and that it is good practice to keep abreast of current science and to participate in exercises such as this. The initial results produced by each group were based on the same experimental input data, but the methods used to derive the dispersion results were all developed independently. The results show that, overall, the predictions were in good agreement with measured concentrations in the Desert Tortoise trials and were in mixed agreement when compared to the FLADIS trial data. Results from the different organisations were within a factor of two of each other for the Desert Tortoise trials and a factor of four for all the FLADIS trials. The main cause of discrepancy in the results for the FLADIS trials was the specification of exit pressures and temperatures that resulted in vapour source conditions being used in some Phast runs and saturated liquid source conditions in others. Suggestions are given on the modelling approach that should be used when using Phast to simulate the future JRIII pressure-liquefied ammonia release trials.

Keywords: *Jack Rabbit III, Desert Tortoise, FLADIS, ammonia, dispersion modelling, Phast*

INTRODUCTION

Part of the strategy for reducing the effects from climate change is based on a shift from fossil fuels towards renewable energy and alternative energy sources. Recently, the focus has been on hydrogen-based infrastructure but the use of green (zero-carbon) ammonia can also contribute towards meeting climate targets. The adoption of ammonia as a clean fuel subsequently means that more ammonia will be present throughout the distribution network and that accidents may become more frequent. Understanding the ways in which ammonia infrastructure can fail and the corresponding consequences is important to ensure safe usage.

An effective way of understanding the consequences (and associated risks) with chemical storage and transport is through experiment. A series of large-scale experiments involving the release of anhydrous ammonia are currently being planned, known as the Jack Rabbit III (JRIII) trials. An international modelling comparison exercise has been completed prior to the experiments taking place. The aim of this exercise was to identify any modelling knowledge gaps and to understand the effect of using different approaches for modelling releases of ammonia. Previous experiments were used as a benchmark; source term data for three Desert Tortoise (DT) (Goldwire *et al*., 1985) and three FLADIS (FL) (Nielsen and Ott, 1996) trials were supplied to ensure that each organisation began their analysis with the same input data for their model of choice. This way, any differences in the results would reflect the characteristics of the type of model used, the method employed and the assumptions that were applied. Another aim of this work was to determine the most appropriate method for modelling ammonia releases. Any new knowledge gained

from this exercise will inform the setup of the future JRIII experimental work. Four organisations used DNV's Phast model to perform the analysis: the UK's Health and Safety Executive (HSE), DNV, Syngenta and DGA Maîtrise NRBC (DGA). This paper examines the modelling approaches taken by the four groups and focuses on the results for the DT1 and FL09 trials. Modelling results for all six trials will be given in the conference presentation.

PHAST MODELLING APPROACHES

Table 1 summarises the input conditions that were provided to the participants involved in the JRIII modelling exercise. HSE used all the data in Table 1 and assumed a leak in a pressurised vessel using version 8.4 of Phast to represent the DT1 and FL09 releases. The mass flow rate predicted by Phast differed slightly from the value given in Table 1. Therefore, a user-defined source was created based on the results of the source term generated by Phast but with the release duration and mass flow rate edited to match the values given in Table 1. Phast was then run with the user-defined source. For DT1, concentrations were output at a height of 1 m, which matched the height of the lowest sensors in the Desert Tortoise experiments. For FLADIS, the sensors were at different heights on the three measurement arcs in the experiments. Three spot values at different heights (matching the sensor heights in the experiments) were therefore output from Phast for FL09.

Table 5. Supplied orifice input data for Desert Tortoise trial 1 (DT1) and FLADIS trial 9 (FL09)

Input	DT1	FL09
Orifice diameter (m)	0.081	0.0063
Release height (m)	0.79	1.5
Exit temperature (°C)	21.5	13.7
Exit pressure (barg)	9.22	5.91
Release rate (kg/s)	80	0.4
Release duration (s)	126	900
Site average wind speed (m/s)	7.42	6.1
at reference height (m)	2	10
Surface roughness (m)	0.003	0.04
Pasquill stability class	D	D
Ambient air temperature (°C)	28.8	15.5
Ambient air pressure (bar)	0.909	1.02
Relative humidity (%)	13.2	86
Averaging time for mean values (s)	80	600

DNV used the latest version of Phast (v8.61) and modelled the Desert Tortoise and FLADIS trials using user-defined sources rather than the software's in-built source models. The post-expansion liquid fraction and velocity source conditions were taken from the SMEDIS database (Carissimo *et al*., 2001). The droplet diameter was calculated by setting up separate leak scenarios in Phast using the default isentropic atmospheric expansion model and the modified CCPS droplet correlation. The resulting predicted droplet diameter was then used as an input to the user-defined source for the Phast runs. The modified CCPS correlation has previously been shown to provide predictions in good agreement against experimental rainout data (see, for example, Witlox *et al.,* 2007).

Syngenta modelled the Desert Tortoise and FLADIS trials using the leak in a pressure vessel model in Phast Version 8.61. The orifice diameter for FL09 (0.0063 m) resulted in a release rate of 0.03 kg/s, which is an order of magnitude lower than the measured release rate. Therefore, Syngenta increased the orifice diameter from 0.0063 m to 0.022 m to obtain the required release rate of 0.4 kg/s.

DGA used Phast version 8.61 and assumed that the ammonia was stored in a pressure vessel using the temperature/bubble point option at ambient temperature which defaulted to a vapour release. The fixed-duration release option was chosen to match the specified release rate in Table 1. This option does not require the input of the orifice diameter, the exit temperature or the exit pressure. The final velocity, liquid fraction and droplet parameters were all calculated by Phast.

Table 2 shows the intermediate data used by each organisation, i.e., the condition of the jet at the point where it has expanded to reach atmospheric pressure. HSE, Syngenta and DGA used Phast to calculate the final post-expansion velocity, liquid fraction and droplet diameter while DNV used the SMEDIS database.

Table 2. Final data after atmospheric expansion for the DT1 and FL09 trials

	Desert Tortoise DT1				FLADIS FL09			
	HSE	**DNV**	**Syngenta**	**DGA**	**HSE**	**DNV**	**Syngenta**	**DGA**
Core averaging time (s)	80	80	80	18.75	600	600	600	18.75
Final velocity (m/s)	246	90.3	246	663	617	65.2	617	624
Liquid fraction	0.825	0.82	0.83	0.09	0.082	0.84	0.08	0.09
Droplet diameter (μm)	83.7	107	83.7	0.94	0.91	144	0.9	0.9

For DT1, the HSE, DNV and Syngenta source conditions given in Table 2 were broadly similar, with a post-expansion liquid fraction of around 82% and a relatively large droplet size of around 80 – 110 μm. HSE used a higher final velocity than DNV (246 m/s versus 90 m/s), which HSE calculated using the default Phast isentropic expansion model. The DGA source conditions were quite different for DT1, with a liquid fraction of just 9%, a small droplet size of < 1 μm and a high velocity of 663 m/s. The DGA conditions are indicative of a vapour-phase release, although the experimental trials recorded a liquid release (see Figure 1).

For FL09, HSE, Syngenta and DGA all used much higher final velocities (> 600 m/s), lower liquid fractions (< 10%) and smaller droplet diameters (< 1 μm) as compared to the conditions used by DNV. The cause of this significant difference in source conditions was related to the exit pressure and temperature, specified in Table 1. Figure 1 plots these exit pressures and temperatures on the phase diagram. This shows that the Desert Tortoise conditions sit within the liquid region but the FLADIS conditions fall close to the saturation line. FL16 sits just on the liquid side but FL09 and FL24 fall into the vapour phase, according to the DIPPR saturation curve (which is used by Phast). The NIST saturation vapour pressure curve is included for comparison purposes and falls slightly below the DIPPR curve. All six experimental trials were saturated liquid releases with a liquid fraction at the orifice close to 100% liquid. The fact that the FL09 and FL24 points fall below the DIPPR saturation curve may be due to non-equilibrium effects or the pressures and temperatures being recorded at slightly different locations in the orifice. The consequence of using these exit pressures and temperatures to setup the Phast source conditions is that trials FL09 and FL24 were modelled as vapour releases by HSE, Syngenta and DGA. By using the SMEDIS source conditions, DNV used more appropriate source conditions for representing a saturated liquid release.

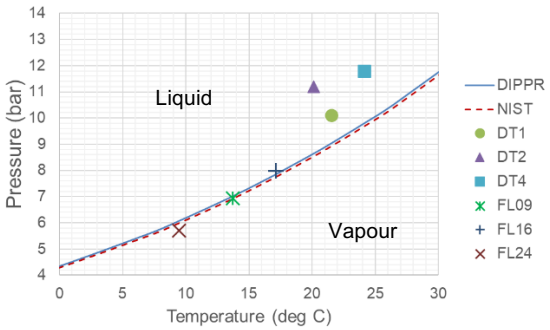

Figure 1. Pressure –temperature phase diagram for ammonia. The markers show the phase at the exit conditions for the Desert Tortoise and FLADIS trials.

The core averaging time is a user-defined input which is often left at the default value of 18.75 s. HSE, DNV and Syngenta changed the core averaging time to match the averaging time for mean values which was provided at the start of the exercise (see Table 1) while DGA kept the default value. DNV recommends setting the core averaging time in Phast to the same value as the averaging time of interest.

RESULTS

Figure 2 shows the results obtained by each organisation for DT1 (left) and FL09 (right). For DT1, HSE, Syngenta and DNV produced predicted concentrations at a height of 1 m, while DGA produced spot values at the two sensor locations. Despite the use of four different methods, there was good agreement between the results obtained for the DT1 trial, and it appears that the results were largely insensitive to the inputs that were varied. When compared to the experimental data (grey diamonds), all of the predictions performed

well, but most tended to overpredict the concentration at the first sensor position at 100 m from the release point. The dip at approximately 50 m in DNV's result corresponds to the point where the droplets touched down and there was rainout (concentrations output from Phast include both vapour and liquid components). The droplet trajectories in Phast are based on a single Sauter mean diameter, and they generally track slightly lower than the plume centreline. The far-field DNV concentrations were lower, due to the attenuated mass caused by rainout, which led to an earlier transition from dense to passive dispersion. Although not shown here, there was good overall agreement for the DT2 and DT4 trials, with DT2 showing the closest match out of the three.

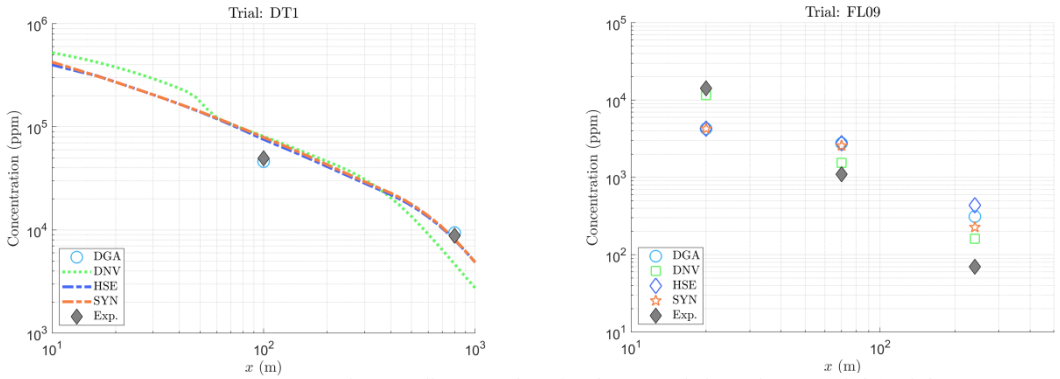

Figure 2. Concentration vs. distance plots for the DT1 (left) and FL09 (right) trials.

For the FL09 trial, the comparison between predictions and measurements did not show as good agreement as for the DT1 trial. Results for the FL16 and FL24 trials show similar patterns. All of the Phast results underpredicted the measurements in the near-field and overpredicted in the far-field. In the near-field, HSE, Syngenta and DGA obtained similar results, but the DNV predictions were in best agreement with the experimental data. Across all of the FLADIS trials, the model predictions from the different groups varied by up to a factor of four. The maximum over-prediction of measured concentrations was up to a factor of ten. However, this was largely due to the choice of vapour source conditions. The DNV predictions, using appropriate source conditions for a saturated liquid release, were in closer agreement with the measurements with more than half the predictions within a factor of two of the measurements.

Once the analysis presented above was complete, the Phast modellers met to examine the results and compare modelling approaches. From these discussions, the issues relating to modelling vapour phase releases rather than liquid phase releases were identified. HSE, Syngenta and DGA revised their inputs to see how modelling the release as a liquid would affect their results. The simplest way to do this in Phast is to select one of the bubble point options which sets the conditions to saturation. The user then changes the phase to liquid on the "material tab" in the Phast user interface. HSE selected the "temperature/bubble point" option which kept the temperature at 13.7 °C but changed the pressure to 5.94 barg which, although similar to the original input conditions in Table 1 (5.91 barg) meant the correct liquid phase could be selected. When the studies were re-run with the liquid phase selected, the final velocity did not reduce as much as expected. HSE generated a final velocity of 202 m/s (droplet size: 112 µm and liquid fraction: 0.85) which is still significantly higher than DNV's velocity of 65.2 m/s.

During the analysis it became apparent that this high velocity was due to the choice of the atmospheric expansion model. The default option (used by HSE, Syngenta and DGA) selects "conservation of momentum" if rainout is not possible, or typically (for two-phase releases) the "isentropic" expansion method. This latter choice is the default because the CCPS droplet correlation in Phast was derived using an isentropic assumption. However, it does result in artificially high final velocities. Changing the atmospheric expansion method from the default to "conservation of momentum" produces a more realistic and lower final velocity (Witlox and Bowen, 2002; Witlox *et al*., 2014). Using a liquid release and the "conservation of momentum" option, HSE produced a final velocity of 49.4 m/s (droplet size: 142 µm and liquid fraction: 0.84). If the four organisations had simulated a liquid release using the "conservation of

momentum" option, then the agreement between the predictions and against the experimental data would have been much closer.

Three groups used Phast version 8.61 while HSE used version 8.4. A number of changes were made to several Phast dispersion sub-models between these two versions, but these had limited impact on the scenarios modelled here. It is recommended to use the most up to date version of Phast, where possible.

Differences between model predictions and measurements can arise from uncertainty or variability in the experiments. For example, there was standing water on the test site in trials DT1 and DT2, which may have affected the humidity and/or atmospheric stability. Several of the modelling teams performed sensitivity studies to examine the potential impact of these uncertainties. Details are provided in the presentation accompanying this extended abstract at the Harmo conference.

SUGGESTIONS FOR FUTURE PHAST MODELLING OF PRESSURE-LIQUEFIED RELEASES

Improved predictions for pressure-liquefied releases can be obtained using non-default options in Phast. The following recommendations are given for Phast users when simulating pressure-liquefied releases, in addition to the usual Phast recommended practices:

1. Check the specified orifice exit pressures and temperatures on a phase diagram to confirm that the conditions input to Phast produce the expected phase of the ammonia released in the experiments (i.e., liquid or vapour). Also, check the predicted liquid fraction in the Phast results.
2. Set the core averaging time to be the same as the specified averaging time.
3. For cases with rainout, find the initial post-expansion ammonia droplet diameter by running a simulation using the default isentropic expansion model and the CCPS droplet size correlation.
4. Re-run the same Phast case using the conservation of momentum atmospheric expansion model, which gives a more representative post-expansion source velocity.
5. Produce a user-defined source from Step 4 and change the droplet size to that found from Step 3, and then run Phast. This approach will use the best estimate for the release velocity and droplet size.

CONCLUSIONS

Four modelling groups (HSE, DNV, Syngenta and DGA) produced results using Phast for the JRIII modelling exercise on Desert Tortoise and FLADIS. Each group took a slightly different modelling approach. Predictions were generally in mixed agreement with the measurements; there were differences between the Phast predictions of up to a factor of two for Desert Tortoise and a factor of four for the three FLADIS trials as a whole. The causes of these discrepancies were investigated and the exercise provided valuable learning lessons for all the organisations involved in this work.

REFERENCES

Carissimo, B., S.F. Jagger, N.C. Daish, A. Halford, S. Selmoer-Olsen, K. Riikonen, J.M. Perroux, J. Wurtz, J.G. Bartzis, N.J. Duijm, K. Ham, M. Schatzmann and R. Hall, 2001: The SMEDIS database and validation exercise. International Journal of Environment and Pollution. 16 (1-6), p614-629.

Goldwire, H.C. Jr, T.G. McRae, C.W. Johnson, D.L. Hipple, R.P. Koopman, J.W. McClure, L.K. Morris and R.T. Cederwall, 1983: Desert Tortoise series data report 1983 Pressurized ammonia spills. LLNL report UCID-20562. https://www.osti.gov/biblio/6393901, last accessed July 2022.

Nielsen M. and S. Ott, 1996: FLADIS field experiments: final report, Risø-R-898(EN), Risø National Laboratory, Roskilde, Denmark, July 1996.

Witlox, H.W.M. and P. Bowen, 2002: Flashing liquid jets and two-phase dispersion, A review. Health and Safety Executive (HSE) Contract Research Report 403/2002. https://www.hse.gov.uk/research/crr_htm/crr02403.htm, last accessed July 2022.

Witlox, H.W.M., M. Harper, A. Oke and J. Stene, 2014: Phast validation of discharge and atmospheric dispersion for pressurised carbon dioxide releases, Journal of Loss Prevention in the Process Industries 30, p243-255. http://dx.doi.org/10.1016/j.jlp.2013.10.006, last accessed July 2022.

Witlox, H., Harper, M., Bowen, P. and Cleary, V., 2007: Flashing liquid jets and two-phase droplet dispersion II. Comparison and validation of droplet size and rainout formulations, Journal of Hazardous Materials 142, p797-809. doi:10.1016/j.jhazmat.2006.06.126 | Elsevier Enhanced Reader, last accessed July 2022.

ACKNOWLEDGEMENT The contributions to this publication by HSE staff were funded by HSE. Its contents, including any opinions and/or conclusions expressed, are those of the authors alone and do not necessarily reflect HSE policy.

21st International Conference on
Harmonisation within Atmospheric Dispersion Modelling for Regulatory Purposes
27-30 September 2022, Aveiro, Portugal

VALIDATION OF A LAGRANGIAN DISPERSION MODEL WITH SPECTRAL IMAGING.

Tristan Carion[1], Andy Delcloo[2] and Bart Janssens[1]

[1]Royal Military Academy, Brussels, Belgium
[2]Royal Meteorological Institute of Belgium, Ukkel, Belgium

Abstract: A toolbox for assessing the impact of CBRN-type incidents is currently being developed by the Royal Military Academy of Belgium and is hosted on the European Weather Cloud system. The toolbox is designed to provide ensemble dispersion modelling capabilities for any worldwide release, benefiting from real-time access to the latest global ensemble forecasts from the Integrated Forecasting System from ECMWF. One of the dispersion models that the toolbox offers is the FLEXPART Lagrangian dispersion and transport model. The present study compares the dispersion results obtained with FLEXPART coupled to ECMWF meteorological fields to multiple chemicals released at various concentrations in a data collection campaign conducted in Suffield, Canada in 2014. This campaign aims to understand the phenomenology of hyperspectral imaging when applied to CBRN-type releases by collecting extensive airborne and ground-based hyperspectral and complementary sensors data during multiple controlled releases of gasses near the ground. In conjunction with measurements of ground concentrations, these images can be used to determine the spatial distribution of released gas concentrations for statistical evaluation of the results of the FLEXPART simulation. This statistical evaluation can provide some insight into the level of confidence we can have in the tool when it is used for similar non-controlled situations. An evaluation of the model setup will be shown.

Keywords: *CBRN, validation, Lagrangian dispersion model.*

INTRODUCTION

The impact assessment and the risk mitigation after the – intentional or inadvertent – release of a CBRN (Chemical, Biological, Radiological and Nuclear) agent can benefit from concentration predictions obtained with atmospheric dispersion models. Therefore, the Royal Military Academy of Belgium is developing a web-based framework to run multiple dispersion models using input meteorological data from ECMWF forecasts or reanalyses. The backend of the framework runs with Julia, a modern technical computing language that provides, amongst other things, performance, composability and clearness. Therefore, the models had to be written or interfaced in Julia. For example, Flexpart.jl, a wrapper around the FLEXPART Lagrangian dispersion model, was developed. It provides a simple way of installing, parameterising, running and post-processing FLEXPART.

To assess the ability of FLEXPART to predict the concentration distribution in the case of CBRN releases, a comparative analysis of the dispersion model results can be made with the data collected during the so-called Pronghorn campaign. This campaign, conducted in Suffield, Canada in August 2014, consisted of several experimental scenarios simulating the release of CBRN agents. Airborne longwave hyperspectral and ground-based sensors were deployed to study their ability to detect several types of CBRN threats (chemical spills, gas and aerosol releases…).

General description of the experiments

The Pronghorn campaign was a collaboration of multiple NATO nations, driven by an interest in collecting and exploiting thermal hyperspectral measurements. It occurred near Suffield, Canada, in open, flat terrain, mostly under summer conditions. Various experimental sites were set up to study the phenomenology of hyperspectral imaging in different cases (e.g. hyperspectral change detection, detection of chemical spills, indirect illumination effects). Airborne imaging sensors sampled imagery of the experimental scenes, supported by an array of ground-based sensors for calibration and ground-truthing. Figure 1 shows an aerial view of the experimental setup along with the flight lines, which ranged in altitude from 500m to 3000m above ground.

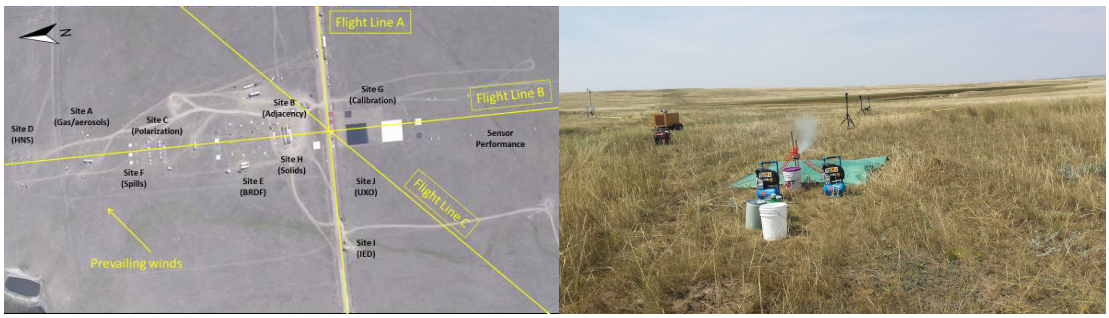

Figure 1. Experimental setup. Left: Aerial view of the Pronghorn trial site at CFB Suffield showing the location of each experiment with overlaid flight lines. Right: Plume generator with ground-based sensors.

Site A experiments setup

Site A hosted the experiences involving pressurised liquid and gas releases, simulating two scenarios. The first one is the impact of a missile loaded with a Chemical Warfare Agent (CWA) that spreads into the atmosphere as an aerosol. The second one consisted of a tank with pressurised liquid getting damaged due to an unforeseen reason. The chemical product then leaks in a gaseous state. Both scenarios were simulated using a plume generator containing various chemicals (see Figure 1). For some releases, 2 or 3 ground-based sensors were located a few meters downwind (typically at 15, 30 and 45m). A meteorological station recorded the surface atmospheric conditions with a time interval of one minute, and weather balloon sounders measured the wind, the temperature, the relative humidity and the pressure from an altitude of 700m to 10,000m.

Releases scale

For the first scenario, the aerosol releases lasted a few hours, for a total quantity of 1kg to 50kg of the chemical species. The gas releases for the second scenario were shorter in time but with high emission rates, as depicted in Figure 2.

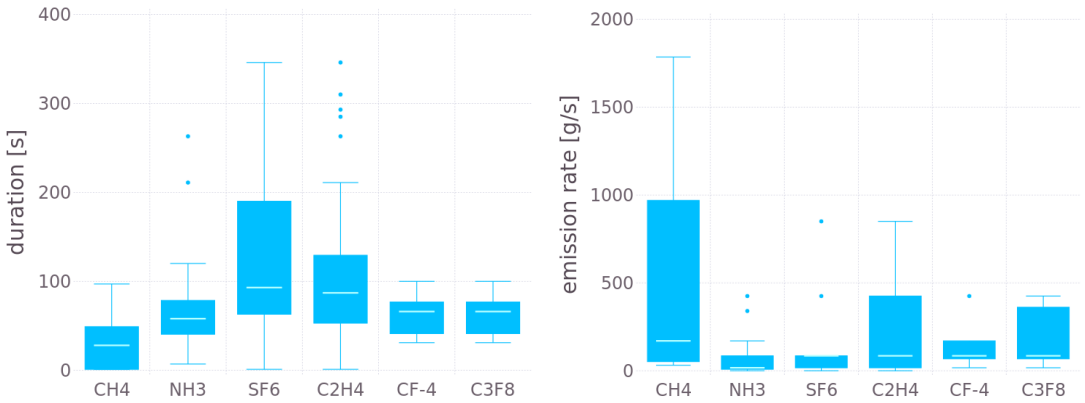

Figure 2. Boxplots of the duration and emission rate of most of the gas releases. Left: duration. Right: emission rate

CONCLUSION

The web-based dispersion modelling framework in current development will help decision-makers to assess the impact of CBRN-type release hazards. The models, implemented or interfaced in the modern scientific computing language Julia, need to be validated against such types of incidents. The Pronghorn campaign, which we briefly described here, collected a large dataset of hyperspectral images and ground-based sensor data that, to our knowledge, was not yet used for atmospheric model validation. Firstly, the hyperspectral images showing the spatial extent of the plume will be compared to the spatial extent given by the simulations. Secondly, the coupling of the spectral data with the ground-based sensor measurements will allow one to estimate the spatial distribution of the concentration, which can also be compared with the simulated concentrations. This analysis will provide an evaluation of the ability of the models, run with ECMWF forecasts, to predict the local plume dispersion after short-scale CBRN-type incidents.

21st International Conference on
Harmonisation within Atmospheric Dispersion Modelling for Regulatory Purposes
27-30 September 2022, Aveiro, Portugal

SUMMARY OF RESULTS FROM THE JACK RABBIT III INTERNATIONAL MODEL INTER-COMPARISON EXERCISE ON DESERT TORTOISE AND FLADIS

Simon Gant[1], Joseph Chang[2], Sun McMasters[3], Ray Jablonski[3], Helen Mearns[3], Shannon Fox[3], Ron Meris[4], Scott Bradley[4], Sean Miner[4], Matthew King[4], Steven Hanna[5], Thomas Mazzola[6], Tom Spicer[7], Rory Hetherington[1], Alison McGillivray[1], Adrian Kelsey[1], Harvey Tucker[1], Graham Tickle[8], Oscar Björnham[9], Bertrand Carissimo[10], Luciano Fabbri[11], Maureen Wood[11], Karim Habib[12], Mike Harper[13], Frank Hart[13]Thomas Vik[14], Anders Helgeland[14], Joel Howard[15], Veronica Bowman[15], Daniel Silk[15], Lorenzo Mauri[16], Shona Mackie[16], Andreas Mack[16], Jean-Marc Lacome[17], Stephen Puttick[18], Adeel Ibrahim[18], Derek Miller[19], Seshu Dharmavaram[19], Amy Shen[19], Alyssa Cunningham[20], Desiree Beverley[20], Matthew O'Neal[20], Laurent Verdier[21], Stéphane Burkhart[21], Chris Dixon[22]

[1] Health and Safety Executive (HSE), Buxton, Derbyshire and Bootle, Merseyside, UK
[2] RAND Corporation, Arlington, Virginia, USA
[3] Chemical Security Analysis Center (CSAC), Science and Technology Directorate (S&T), Department of Homeland Security (DHS), Aberdeen Proving Ground, Maryland, USA
[4] Defense Threat Reduction Agency (DTRA), Fort Belvoir, Virginia, USA
[5] Hanna Consultants, Inc., Kennebunkport, Maine, USA
[6] Systems Planning and Analysis, Inc. (SPA), Alexandria, Virginia, USA
[7] University of Arkansas, Fayetteville, Arkansas, USA
[8] GT Science and Software, Waverton, Cheshire, UK
[9] Swedish Defence Research Agency (FOI), Umeå, Sweden
[10] EDF/Ecole des Ponts, Paris, France
[11] European Joint Research Centre (JRC), Ispra, Italy
[12] Bundesanstalt für Materialforschung und -prüfung (BAM), Berlin, Germany
[13] DNV, Stockport, UK
[14] Norwegian Defence Research Establishment (FFI), Kjeller, Norway
[15] Defence Science and Technology Laboratory (DSTL), Porton Down, UK
[16] Gexcon, Bergen, Norway and Driebergen-Rijsenburg, Netherlands
[17] Institut National de l'Environnement Industriel et des Risques (INERIS), Verneuil-en-Halatte, France
[18] Syngenta, Huddersfield, Yorkshire, UK
[19] Air Products, Allentown, Pennsylvania, USA
[20] Naval Surface Warfare Center (NSWC), Indian Head, Maryland, USA
[21] Direction Générale de l'Armement (DGA), Paris, France
[22] Shell, York Road, London, UK

Abstract: A series of new experiments involving large-scale releases of anhydrous ammonia are currently being planned for 2024 and 2025, known as the Jack Rabbit III trials (JRIII). The aim of the project is to address gaps in modelling methodologies and emergency response procedures. To support the project, an international model inter-comparison exercise was initiated in 2021 to evaluate the performance of atmospheric dispersion models using data from the Desert Tortoise and FLADIS trials. The objective of the collaborative modelling exercise was to understand the capabilities and limitations of models that could be used to design the new JRIII trials (e.g., suitable sensor placement). Dispersion modelling teams from around the world were invited to participate on a voluntary basis. The exercise followed a similar successful model inter-comparison exercise conducted in 2019-20 on the Jack Rabbit II chlorine dispersion dataset. The coordinators of the JRIII inter-comparison exercise provided a set of model inputs for the participants to use and requested model predictions to be provided to them in a standardized format. Twenty independent modelling teams from North America and Europe provided results using a range of different models (i.e., empirically-based nomograms, integral, Gaussian puff, and computational fluid dynamics models). The agreement between model predictions and measurements varied considerably between different models. Given appropriate inputs, most models generally predicted concentrations that agreed well with the data. Useful insights were gained through discussions between participants involved in the exercise.

Key words: *Jack Rabbit III, Desert Tortoise, FLADIS, anhydrous ammonia, two-phase jets, dispersion*

INTRODUCTION

The worldwide use of ammonia as an agricultural fertilizer, chemical feedstock and refrigerant has been growing in recent years and is forecast to increase significantly in the coming decades with the use of ammonia as a renewable energy vector. It is important to ensure the safety and security of this ammonia infrastructure, which requires an understanding of the potential consequences of ammonia releases. Atmospheric dispersion models and their source term models are critical to that effort. These models must be verified, validated and properly tested, before being used for emergency response, regulatory risk assessments and incident investigation. Ammonia is both acutely toxic and flammable. Its 10-minute Acute Exposure Guideline Levels are 2,700 ppm for life threatening effects or death (AEGL-3) and 220 ppm for irreversible effects and/or impaired escape (AEGL-2). Its lower and upper flammability limits are 16% and 27% by volume, respectively.

To improve our understanding of potential ammonia risks and address critical knowledge gaps (Hanna *et al*., 2021), CSAC and DTRA are currently planning a series of large-scale anhydrous ammonia release experiments, known as the Jack Rabbit III trials (JRIII). To support the JRIII project, an initial collaborative modelling exercise was launched in 2021 to understand the strengths and weaknesses of atmospheric dispersion models using existing data for ammonia releases from previous experiments. The aim was to assess the accuracy of models that may be used to design the JRIII trials (e.g., for sensor placement). A secondary goal was to run model sensitivity tests to identify important parameters that may need to be carefully controlled or measured in the JRIII trials. Modelling experts from defence agencies, government laboratories, industry and consultancies in North America and Europe were invited to participate on a voluntary basis. Each group was asked to provide dispersion model predictions for six previous field-scale ammonia release experiments. The exercise was not a competition but a collaborative effort, with the ultimate goal of improving toxic industrial chemical modelling tools.

Description of Modelling Exercise and Experimental Datasets

The six previous field trials selected for the modelling exercise were taken from the Desert Tortoise and FLADIS experiments (Goldwire et al., 1985; Nielsen and Ott, 1996). Data for these trials was primarily sourced from the SMEDIS dataset (Carissimo *et al*. 2001). All inputs were carefully checked and cross-referenced against the original data reports and other literature. In some cases, minor adjustments were made to the SMEDIS values. Modellers were provided with a full description of the trials, including a summary of model inputs (Table 1) and suggestions for sensitivity tests that could be run to examine uncertainties. The modellers were requested to submit the results to the coordinators of the exercise (Joe Chang and Simon Gant) in a standardized format, to facilitate cross-plotting of the results.

The Desert Tortoise trials took place in 1983 at the Nevada Test Site, Nevada, USA. To date, they are the largest-scale atmospheric dispersion experiments conducted on pressure-liquefied ammonia. They involved releases of between 10 and 41 metric tonnes of ammonia, release rates of between 81 kg/s and 133 kg/s and gas concentrations measured downwind primarily at distances of 100 m and 800 m. Releases were directed horizontally from a height of 0.79 m across flat, open terrain. The test series consisted of four trials. Three of these were selected for the JRIII exercise (trials DT1, DT2 and DT4). In trials DT1 and DT2, there was some standing water present at the test site due to rainfall on the preceding days. This had evaporated by the time that trial DT4 was conducted. Some liquid ammonia in the two-phase jets rained-out on the ground in all of the trials and formed an evaporating pool. There are different accounts in the literature for the rain-out fraction, which vary between 5% and 36% of the total mass of ammonia released. One of the challenges in assessing the precise amount of rainout was the presence of standing water in the early trials.

The FLADIS trials took place in Landskrona, Sweden, in 1993-1994. They were much smaller in scale than Desert Tortoise, with pressure-liquefied ammonia discharge rates of between 0.25 kg/s and 0.55 kg/s. There were 27 trials in the test series and three were selected for the JRIII modelling exercise (trials FLADIS9, FLADIS16 and FLADIS24). These three trials all involved releases directed horizontally from a height of 1.5 m, with no rainout of liquid ammonia on the ground (due to the release height and the scale of the release). Concentrations were measured at distances of approximately 20 m, 70 m and 240 m. The ambient humidity in the FLADIS trials was higher and more representative of a damp European climate than the arid high-altitude Nevada Test Site used for the Desert Tortoise trials.

Table 6. Model input conditions for the Desert Tortoise and FLADIS trials

		DT1	DT2	DT4	FLADIS9	FLADIS16	FLADIS24
Orifice diameter	m	0.081	0.0945	0.0945	0.0063	0.004	0.0063
Release height	m	0.79	0.79	0.79	1.5	1.5	1.5
Exit temperature	°C	21.5	20.1	24.1	13.7	17.1	9.45
Exit pressure	bara	10.1	11.2	11.8	6.93	7.98	5.70
	barg	9.22	10.3	10.9	5.91	6.96	4.69
Release rate	kg/s	80.0	117	108	0.40	0.27	0.46
Release duration	s	126	255	381	900	1200[g]	600
Rainout mass fraction	%	5	5	5	0	0	0
Site average wind speed	m/s	7.42	5.76	4.51	6.1	4.4	4.9
at reference height	m	2	2	2	10	10	10
Friction velocity	m/s	0.442	0.339	0.286	0.44	0.41	0.405
Surface roughness	m	0.003	0.003	0.003	0.04	0.04	0.04
Monin-Obukhov length	m	92.7	94.7	45.2	348	138	-77
Pasquill stability class	-	D	D	D-E	D	D-E	C-D
Ambient temperature	°C	28.8	30.4	32.4	15.5	16.5	17.5
at reference height	m	0.82	0.82	0.82	1.5	1.5	1.5
Ambient pressure	bar	0.909	0.910	0.903	1.020	1.020	1.013
Relative humidity	%	13.2	17.5	21.3	86	62	53.6
Averaging time for mean values	s	80	160	300	600	600	400
Approx. coordinates of release point		36°48'05.8" N 115°57'35.7" W			55°51'37.0" N 12°50'34.8 E		
		36.801607, -115.959929			55.860278, 12.843000		
Date of release		24/8/83	29/8/83	6/9/83	7/8/93	13/8/93	30/8/94
Start time (local)	h:m	16:37	11:20	15:37	14:39	19:51	16:06

In both the Desert Tortoise and FLADIS trials, a nitrogen padding system was used to force liquid ammonia from the storage vessel(s) through pipework to the release orifice. This meant that for all of the selected trials, the ammonia liquid mass fraction at the orifice was effectively 100%. Some of the models used by participants in the modelling exercise could not directly simulate the resulting two-phase jets and required vapour-only source conditions. A set of equivalent vapour-only conditions were provided to the modelling exercise participants, using the methodology adopted in the SMEDIS project (i.e., assuming conservation of mass, momentum and enthalpy). Some modellers chose to use these conditions, whilst others used their own preferred methods of calculating vapour-only source conditions.

The list of participants in the exercise and details of the models used are summarized in Table 2. They included 3 sets of results from empirically-based nomograms and/or Gaussian plume models, 11 sets of integral model predictions, 6 sets of Gaussian puff or Lagrangian models and 4 sets of CFD results. Some models were run for only selected Desert Tortoise or FLADIS trials, rather than all six trials.

Results

Predicted maximum arc-wise concentrations are compared to measured values for trials DT1 and FLADIS9 in Figure 1 (enlarged versions of these graphs will be made available in the slides presented at the conference). A similar degree of spread in results was observed between the three Desert Tortoise trials and the three FLADIS trials. The range in predictions spanned roughly between one and two orders of magnitude about the measurements with a tendency for models to over-predict at 100 m and under-predict at 800 m in the Desert Tortoise trials, and with less spatial bias in the FLADIS trials.

#	Organisation	Model	Model Type				Desert Tortoise			FLADIS		
			A	B	C	D	1	2	4	9	16	24
1	Air Products, USA	VentJet										
2	BAM, Germany	AUSTAL										
3		VDI										
4	DGA, France	PHAST v8.6										
5		Code-Saturne v6.0										
6	DNV, UK	PHAST v8.61										
7	DSTL, UK	HPAC v6.5										
8	DTRA, ABQ, USA	HPAC v6.7										
9	DTRA, Fort Belvoir, USA	HPAC										
10	EDF/Ecole des Ponts, France	Code-Saturne v7.0										
11		Crunch v3.1										
12	FFI, Norway	ARGOS v9.10										
13	FOI, Sweden	PUMA										
14	Gexcon, Netherlands	EFFECTS v11.4										
15	Gexcon, Norway	FLACS										
16	GT Science & Software	DRIFT v3.7.19										
17	Hanna Consultants, USA	Britter & McQuaid WB										
18		Gaussian plume model										
19	HSE, UK	DRIFT v3.7.12										
20		PHAST v8.4										
21	INERIS, France	FDS v6.7										
22	JRC, Italy	ADAM v3.0										
23	NSWC, USA	RAILCAR-ALOHA										
24	Shell, UK	FRED 2022										
25	Syngenta, UK	PHAST v8.61										

Model Type: A = Empirically-based nomograms/Gaussian plume model; B = Integral model; C = Gaussian puff/Lagrangian model; D = CFD. Shading in the right six columns indicates model was run for that trial.

Significant differences between HPAC results from different groups arose from differences in modelling approach. One group adopted the same methodology commonly applied to requests for Reachback support under operational settings, i.e., using only limited information from Table 1 and making conservative choices of hole sizes, weather conditions etc. Another HPAC group instead used a more complete set of inputs from Table 1. The results from empirically-based nomograms, Gaussian plume and integral models generally showed less scatter about the measurements compared to that shown by Gaussian puff or Lagrangian models (Figure 2). Four independent groups used the PHAST integral model and each group took a slightly different modelling approach, which resulted in minor differences in predicted concentrations. The four CFD models all gave quite similar results (mostly, within a factor of two of each other), despite them each using quite different modelling approaches (e.g., LES versus RANS).

Sensitivity tests were undertaken by some of the modelling groups (results not shown here), which provided useful information. For example, HPAC results were found to be sensitive to both the assumed liquid fraction and atmospheric stability. EFFECTS results were relatively insensitive to rainout and surface roughness. FLACS results showed some sensitivity to the way in which equivalent vapour-only source conditions were derived and how they were implemented in the CFD code (both the shape of the vapour-only source window and the source velocity profile).

Further results, including plume widths and statistical performance measures are provided in the accompanying presentation at the Harmo-21 conference.

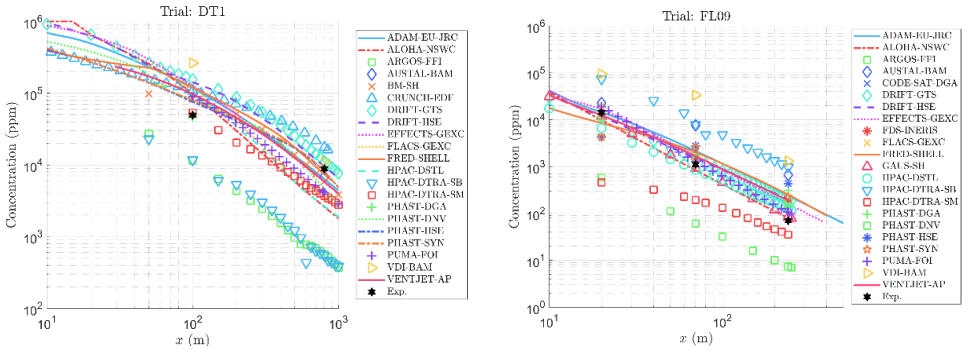

Figure 11. Maximum arc-wise concentrations for trials DT1 and FLADIS9 (all models)

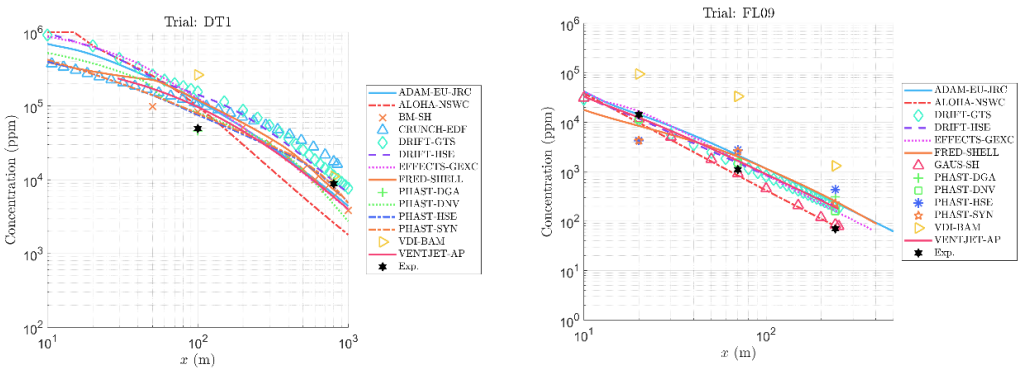

Figure 2. Maximum arc-wise concentrations for trials DT1 and FLADIS9 for empirically-based nomograms, Gaussian plume and integral models only

Conclusions

A model inter-comparison exercise has been undertaken using data from the Desert Tortoise and FLADIS ammonia trials. A total of 25 sets of model predictions were provided by 20 independent groups. The agreement between model predictions and measurements varied considerably between different models. Given appropriate inputs, most models generally predicted concentrations that agreed well with the data. Useful insights were gained through discussions between participants involved in the exercise into the choice of modelling approach – especially, in cases where different groups used the same model. The modelling exercise and analysis of the Desert Tortoise and FLADIS data provided useful insights into the design of the future JRIII trials. For example, analysis of the Desert Tortoise trials highlighted the need for a greater number of concentration sensors in the far-field than were present in the Desert Tortoise trials to measure the full extent of the hazardous cloud. A future collaborative JRIII modelling exercise may be undertaken to examine a previous large-scale ammonia incident.

REFERENCES

Carissimo B., S.F. Jagger, N.C. Daish, A. Halford, S. Selmoer-Olsen, K. Riikonen, J.M. Perroux, J. Wurtz, J.G. Bartzis, N.J. Duijm, K. Ham, M. Schatzmann and R. Hall, 2001: The SMEDIS database and validation exercise. International Journal of Environment and Pollution. 16 (1-6), p614-629.

Goldwire H.C. Jr, T.G. McRae, C.W. Johnson, D.L. Hipple, R.P. Koopman, J.W. McClure, L.K. Morris and R.T. Cederwall, 1983: Desert Tortoise series data report 1983 Pressurized ammonia spills. Lawrence Livermore National Laboratory report UCID-20562. https://www.osti.gov/biblio/6393901

Hanna, S., T. Mazzola, J. Chang, T. Spicer, S. Gant and R. Batt, 2021: Gaps in toxic industrial chemical model systems: Improvements and changes over past 10 years, Process Safety Progress, e12289, 16 pp., http://dx.doi.org/10.1002/prs.12289

Nielsen M. and S. Ott, 1996: FLADIS field experiments: final report, Risø-R-898(EN), Risø National Laboratory, Roskilde, Denmark, July 1

ACKNOWLEDGEMENT The contributions to this publication by HSE staff were funded by HSE. Its contents, including any opinions and/or conclusions expressed, are those of the authors alone and do not necessarily reflect HSE policy.

21st International Conference on
Harmonisation within Atmospheric Dispersion Modelling for Regulatory Purposes
27-30 September 2022, Aveiro, Portugal

DISPERSION OF RADIONUCLIDES IN A URBAN ENVIRONMENT (DIFLU): COMPARISON OF NUMERICAL RESULTS WITH EXPERIMENTAL MEASUREMENTS

Liying Chen[1], Malo Le Guellec[1], Amita Tripathi[1], Sophie Vecchiola[2], Anne Mathieu[2], Philippe Laguionie[2], Olivier Connan[2], Denis Maro[2], Luc Solier[2], Irène Korsakissok[2]

[1]Fluidyn, 84 rue Charles Michels Bât.IRIS Hall B, 93200, Saint-Denis, France
[2]Department of healthcare and Environmental Science, French institute for radiation protection and nuclear safety, France

Abstract: The DIFLU project (DIspersion of FLuor 18 in an Urban environment) has been initiated by IRSN alongside with FLUIDYN France and Ecole Centrale Lyon to assess the performance of numerical simulation in the evaluation of the impact of radionuclide dispersion in urban areas.
The project is specifically aimed at the release in atmosphere of fluorine 18 used in medical imaging by cyclotrons located in hospital premices, so near housing, offices and health care centers. Such impact assessments have been performed in the past with Gaussian or 2D modelling, which cannot take into account the specificities of the release environment, such as obstacles and buildings, which are expected to have a strong influence in the nearfield. Therefore, the DIFLU project aimed at comparing the results of experimental campaigns with results from 3D-CFD (Computational Fluid Dynamics) models, among them fluidyn-PANACHE.
In 2019, the cyclotron located in Beuvry (North of France) was used to carry out two atmospheric tracing experiments using helium as a tracer gas, emitted from a chimney above the cyclotron. The first campaign results have been presented before. The results of the comparisons between the experimental data and the numerical results for the second campaign are presented here. The comparison is carried out both for the flow behaviour (local wind velocities) and for the tracer behaviour (concentrations).
The statistical evaluation results show the CFD model Fluidyn-PANACHE is capable of simulating the Fluor 18 dispersion in urban environment.

Key words**:** *atmospheric pollution dispersion, CFD model evaluation, Fluidyn-PANACHE, radionuclide dispersion*

Introduction

Radionuclide impact assessment within urban environment in near-field (<3km) is more and more predicted with CFD dynamic codes. A CFD model solves the Navier–Stokes equations using a small grid size (of the order 1m or even less) (Hanna et al., 2004). Compared with simple Gaussian dispersion model or other analytical approximations, the CFD model efficiently predicts the obstacles influence on wind patterns and cloud shapes (Kumar& al., 2015).
Nevertheless, the CFD model evaluation against experimental datasets is one important point to estimate its capability to provide reliable and valuable information in emergency planning or chronic impact assessment (Hanna & al., 2004; Riddle & al., 2004).
To meet this objective, DIFLU (DIspersion of FLUorine) project has been initiated in order to provide a database of observations (concentrations, wind velocities) in the near field (<200m) of a release for model validation.

The current paper concerns the Fluidyn-PANACHE CFD model evaluation. PANACHE uses physical models and deterministic solutions that are adapted to any kind of release scenarios, complex environments and pollutant characteristics. To demonstrate the PANACHE model's capabilities with regard of dispersion in urban environment in the framework of DIFLU project, numerical results have been compared with experimental datasets.

Description of the DIFLU experiments

DATASETS OF MEASUREMENTS

DIFLU project aims to study near field dispersion of a gas emitted in an urban or industrial environment. Two campaigns were carried out in october and december 2019 at the Beuvry hospital site (northen France). For the December campaign, a total of 10 helium releases and 200 atmospheric concentration measurements were made at distances up to 560 m from the release point.

Helium releases were most of the time located in the hydraulic vein of the stack oriented with an angle of -45° to the horizontal on the roof of the cyclotron at 10 m high. The total flow rate was 7200 ± 100 m^3/h and the emission flow velocity were 6 m/s.

WEATHER DATABASE

For the December campaign, a wind LIDAR was deployed for wind speed and direction from 40 to 290 m height (Table 1), as well as four anemometers (between 3.6 and 11 m height) for the measurement of wind characteristics and turbulent parameters.

Table 7. Weather data recorded by the LIDAR at z=40 m

Experience	Wind speed		Wind direction	
	$\bar{u}$ (m/s)	σ_U (m/s)	$\overline{Th}$ (°)	σ_{Th} (°)
2-1	6.0	0.6	173.5	6.0
2-2	7.6	1.1	172.2	6.6
2-3	7.7	1.1	174.3	5.5
2-4	2.5	0.4	212.0	4.4
2-5	3.3	0.5	191.8	4.8
2-6	3.5	0.3	203.6	7.1
2-7	4.1	0.5	187.0	5.6
2-8	3.8	0.6	166.8	5.5
2-9	5.5	0.6	168.6	5.0
2-10	8.9	1.7	160.6	7.7

The wind direction ranges from 160 ° to 212° and the standard deviation goes from 4.8° to 7.7°. The wind speed ranges from 2.5 m/s to 8.9 m/s. Four experiences get a wind speed at 40 m lower than 4 m/s. The standard deviation of the wind speed represents from 9% to 19% of the average speed.

The weather data recorded by the LIDAR have been used to defined the boundary conditions of the computational domain. The windfield results have been compared at the four anemometers locations for 40 couples wind direction/wind speed extracted from the weather database.

Description of the CFD model

Fluidyn-PANACHE is a 3D diagnostic model for atmospheric dispersion modelling over complex terrain with topography and obstacles.

GOVERNING EQUATIONS

The Fluidyn-PANACHE model solves the Navier-Stokes equations along with the equations describing conservation of species concentration, mass, and energy for a mixture of ideal gases.

Fluidyn-PANACHE solves the Reynolds averaged forms of these equations for turbulent flow. The Reynolds stresses are modeled using the linear eddy viscosity model (LEVM) (Ferziger and Peric, 2002). Ideal gas law is used for the thermodynamic model of mixture of gases. Air is modeled as moist air with effective properties of the mixture of dry air and water vapor.

TURBULENCE MODEL

The Fluidyn-PANACHE model uses modified standard k-ε turbulence model to solve the turbulence structure within the domain. The implementation of this model is derived from the standard high-*Re* form

with corrections for buoyancy and compressibility (Hanjalic, 2005). It solves the transport equations for turbulent kinetic energy, *k* and its dissipation rate, ε.

BOUNDARY CONDITIONS

Boundary conditions are required on the main domain boundary, the ground, and on obstacles. The top boundary is treated as an outflow boundary. The lateral boundaries of the domain are treated as inflow and outflow boundaries based on the direction of the wind with respect to the domain boundary.

WIND PROFILE

A log-law profile based on Monin–Obukhov (M–O) similarity theory is used to parameterize the inflow boundary condition. The reference velocity and direction of the wind profile was mesured at 40 m during the campaign.

TURBULENCE PROFILE

The turbulence profile selected for this study is a semi-empirical model based on similarity theory and measurements (Han & al., 2000).

Statistical performance measures (SPM)

The evaluation dataset contains pairs of Cp (predicted concentration) and Co (observed concentration), which represent averages over the same averaging time. In the frame of DIFLU, the sampling time ranges from 8 to 10 min beside the case.

Before calculating various statistical performance measures, it is also recommended that exploratory data analysis be performed by simply tracing scatter plot or quantile-quantile plot.

Then, quantitative evaluation of the performance of atmospheric dispersion models requires the definition of appropriate statistical performance measures (SPM) which compare model predictions with measurements. The decision criteria comprise a combination of elements drawn from scientific assessment, the verification process, and the extent to which quantitative values of the SPM output from the validation exercise are also met. Chang et Hanna (2004) propose the following modified quantitative assessment criteria to be met by a model:

- Fractional Bias (FB) with -0.3<FB<0.3;
- Normalized Mean Square Error (NMSE) with NMSE<4;
- Fraction of predictions within a factor 2 of observations (FAC2) with FAC2> 50%.

In addition to these standard criteria, the Fraction of predictions within a factor 5 of observations (FAC5) has been calculated

It is important for environmental applications like radionuclide impact to evaluate model predictions at specific locations such as densely-populated neighborhoods. That is why, to meet the objective of DIFLU project and unlike the mostly comparisons made for Gaussian models, the performance of the CFD model is not conducted only for the maximum concentration on a sampling line but point to point. Pairing in space is clearly most stringent.

Results and discussions

WINDFIELD MODEL VALIDATION

The comparison of the simulation results (Wind speed, Wind direction and Turbulent Kinetic Energy (TKE)) with the experimental data at the 4 anemometers positions is presented on the figures below.

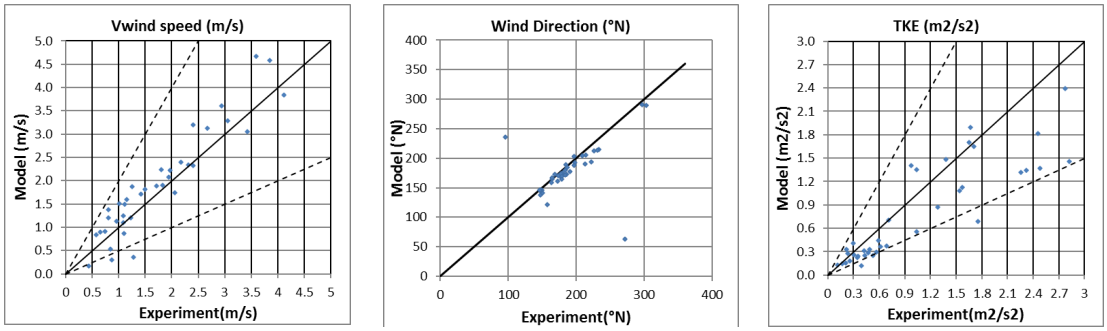

Figure 12: Scatter plots of the model/experiment comparison for wind speed, wind direction and TKE

The comparison shows a very good agreement with experimental results. The TKE is slightly under-predicted by the model.

The statistical performance measures for the wind speed are FB=0.04, NMSE=0.04, FAC2=94%

Dispersion model validation

For regulatory applications of IRSN, sites with routine emissions, the primary objective is how well a model simulates the long-term averaged concentration anywhere on the sampling network. That is why, the dispersion modelling considers averaged wind conditions (speed and direction) over each experiment even if weather measurements are available at higher frequency. No modification or tuning have been done to improve the modelling results because it is not the objective of DIFLU project. The CFD model has been used similarly as for an impact study.

The helium concentrations from the modelling tool are compared with experimental values for each point and the SPM criteria are then computed.

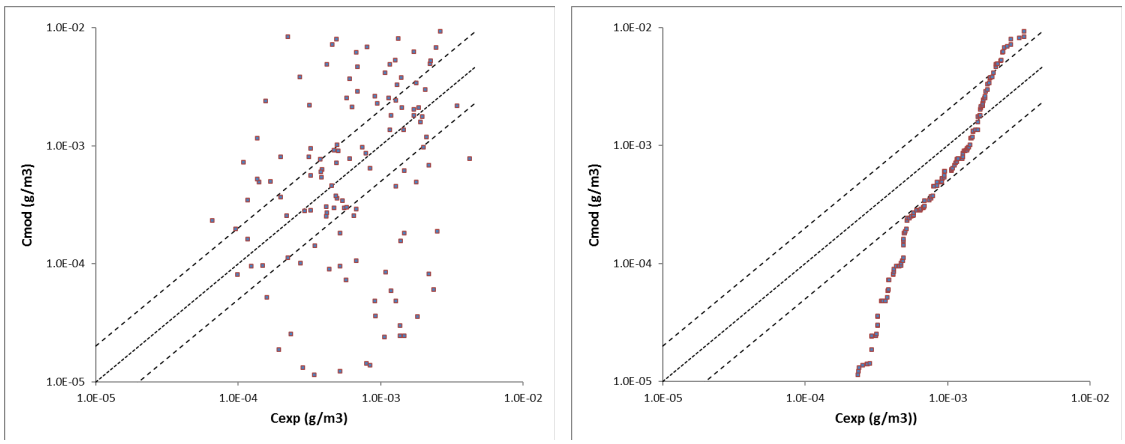

Figure 13: (a) Scatter plot and (b)Q-Q plot of predicted versus observed concentration

The scatter plot shows that 34% of the pairs are in the range of the FAC2. The Quantile Quantile-plot shows the tendency of the modelling tool to underestimate low concentration and overestimate high concentration. This could be explained by the averaged wind direction and the parameters of the turbulence model.

The results indicate inhomogeneity between the experiments. The case 2-02 and 2-03 give the best performance. The case 2-01 gives the worst comparison. It seems that the averaged wind direction for the modeling make the plume miss the sensors. The comparison could be improved by considering the wind direction fluctuations at the boundary conditions.

Table 8. SPM criteria the datasets[1]

	FB	NMSE	FAC2	FAC5
2-01	1.39	6.64	5%	5%
2-02	0.23	0.73	64%	86%
2-03	-0.09	0.76	37%	79%
2-04	-0.86	7.82	18%	29%
2-05	-0.55	3.10	24%	43%
2-06	-1.04	4.04	24%	79%
2-07	-0.31	5.89	16%	37%
2-08	0.46	4.96	29%	61%
2-10	1.00	1.87	29%	54%

The statistical performance measures for the overall experiments are FB=0.37, NMSE=3.81, FAC2=34%, FAC5=65%.

Conclusion

The present paper shows the performance of a 3D-CFD modelling tool (fluidyn-PANACHE) in the frame of DIFLU project dedicated to the evaluation of the impact of radionuclide dispersion in urban areas. The comparison consists in paired concentrations (observed vs modelled) in space and not maximum arc-wise concentrations.

For the second campaign, the CFD model used in a standard way has shown acceptable performance for the objectives of the DIFLU project. Some cases could be improved by considering wind direction fluctuations or tuning turbulence parameters.

References

Ferziger, J.H. and M. Perić, 2002: Computational Methods for Fluid Dynamics, Springer.

Han, J., S.P. Arya, S. Shen and Y-L Lin, 2000: An Estimation of Turbulent Kinetic Energy and Energy Dissipation Rate Based on Atmospheric Boundary Layer Similarity Theory, NASA/CR-2000-210298.

Hanjalic, K., 2005: Turbulence And Transport Phenomena: Modelling and Simulation, Turbulence Modeling and Simulation (TMS) Workshop, Technische Universität Darmstadt.

Kumar, P.,Feiz, A-A, Ngae, P., Singh, S.K. and Issartel, J.P., 2015: CFD simulation of short-range plume dispersion from a point release in an urban like environment. *Atmospheric Environment*, 122, 645-656.

[1] The case 2-09 is not presented because measured concentrations show unphysical constant concentration at all the sensors.

21st International Conference on
Harmonisation within Atmospheric Dispersion Modelling for Regulatory Purposes
27-30 September 2022, Aveiro, Portugal

DRIFT MODELLING OF THE DESERT TORTOISE AND FLADIS AMMONIA TRIALS FOR THE JACK RABBIT III MODEL INTER-COMPARISON EXERCISE

Rory Hetherington[1], Graham Tickle[2], Veronica Bowman[3], Daniel Silk[3], Simon Gant[1], Adrian Kelsey[1], Alison McGillivray[1], and Harvey Tucker[4].

[1] Health and Safety Executive (HSE), Buxton, UK
[2] GT Science and Software, Waverton, Cheshire, UK
[3] Defence Science and Technology Laboratory (DSTL), Porton Down, UK
[4] Health and Safety Executive (HSE), Bootle, UK

Abstract:
As part of the Jack Rabbit III (JRIII) project, a Modelers Working Group (MWG) has been coordinating an international model inter-comparison exercise using data from six pressure-liquefied ammonia release experiments from the Desert Tortoise (1983) and FLADIS (1993-4) trials. The aim of the collaborative modelling exercise has been to understand the capabilities and limitations of models that could be used to design the new JRIII trials (e.g., to design suitable sensor placement). This paper focuses on DRIFT integral model results that have been produced for the exercise. The coordinators of the modelling exercise provided participants with baseline input parameters, plus suggestions of possible sensitivity tests based on analysis of uncertainties in the Desert Tortoise and FLADIS trials. These included ranges of values for the rainout fraction, wind speed, Monin-Obukhov length, and relative humidity. To investigate the impact of these uncertainties, HSE used a Gaussian process emulator to perform a global sensitivity analysis on DRIFT. Results are presented here to show how the variable model inputs affect the predicted concentrations at different downwind distances in the dispersing plume. The baseline set of DRIFT predictions are shown to be in good agreement with the experimental data, with over half of the centreline concentrations within a factor of two of the measurements. One trial from the Desert Tortoise experimental programme was selected for sensitivity analysis. Sensitivity analysis shows that the predicted concentrations are strongly affected by the wind speed and atmospheric stability. The rainout fraction has a modest effect and its importance gradually diminishes with distance downwind. Relative humidity is shown to have very little influence, despite the fact that DRIFT takes into account reactions between ammonia and atmospheric water vapour. The exercise provides insight into the predictive capabilities of DRIFT for simulating pressure-liquefied ammonia releases.

Key words: *Jack Rabbit III, dispersion modelling, Gaussian process emulator, sensitivity analysis, ammonia.*

INTRODUCTION

As part of the Jack Rabbit III (JRIII) project, a Modelers Working Group (MWG) have been coordinating an international model inter-comparison exercise using data from six previous pressure-liquefied ammonia release experiments. These six experiments were taken from the Desert Tortoise (1983) and FLADIS (1993-4) trials (Goldwire *et al*., 1985; Nielsen *et al*., 1994). Coordinators of the modelling exercise provided participants with a set of baseline input parameters for the six trials. Also included were suggestions of sensitivity tests that could be investigated, based on analysis of uncertainties in the experiments. These included ranges of values for four model inputs: liquid rainout, wind speed, Monin-Obukhov length, and relative humidity. The aim of the exercise was to assess the performance of dispersion models and to investigate their sensitivity to variability in certain model input parameters.

This paper focuses on the DRIFT integral model results that have been produced for the exercise. In addition to simulating the base case for validation against experimental results, a total of 150 other simulations were run to construct a Gaussian process emulator and perform a global sensitivity analysis. Instead of varying one parameter at a time and fixing all other model inputs, each of these 150 simulations varied all four input parameters simultaneously. The emulator was then used to identify model inputs that had a significant influence on the downwind dispersion behaviour. Results are presented here to show how the variable

model inputs influenced the predicted concentrations at different downwind distances in the dispersing plume.

METHODOLOGY

Desert Tortoise and FLADIS

Table 1 presents conditions for the selected Desert Tortoise and FLADIS trials, which were mostly taken from the SMEDIS database (Carissimo *et al*., 2001). The table here only includes inputs required by DRIFT, but MWG participants were provided with more information as some dispersion models require different inputs. All six trials involved horizontal releases of pressure-liquefied ammonia, and for the purpose of this study 100% liquid has been assumed at the exit nozzle which is consistent with the normal assumption for a padded release, but does not account for flashing that may have been induced by pressure losses, e.g. due to the presence of a knee-bend immediately upstream of the exit orifice in Desert Tortoise. There was a considerable difference in the amount of ammonia released between Desert Tortoise and FLADIS, with the former trials involving release rates of 80 to 117 kg s^{-1}, whilst FLADIS involved release rates of only 0.3 to 0.5 kg s^{-1}. The atmospheric weather conditions were also quite different. The Desert Tortoise trials were conducted in the Nevada desert on a lake bed, which was normally dry, although rain on previous days meant that surface water was present in trials DT1 and DT2. The FLADIS trials were conducted in Sweden, close to the Öresund strait, at a test site with some vegetation (10 - 30 cm high grass). The influence of test site location is evident in Table 1; the FLADIS trials had a larger aerodynamic surface roughness and increased humidity. Additionally, buildings upwind of the FLADIS release were reported to contribute to the atmospheric turbulence. There was no rain-out of liquid ammonia in the FLADIS tests, compared to 5% estimated rainout in the Desert Tortoise trials.

Table 1 Model input conditions for the Desert Tortoise and FLADIS trials.

	DT1	**DT2**	**DT4**	**FL09**	**FL16**	**FL24**
Orifice diameter (m)	0.081	0.0945	0.0945	0.0063	0.004	0.0063
Release height (m)	0.79	0.79	0.79	1.5	1.5	1.5
Exit temperature (K)	294.65	293.25	297.25	286.85	290.25	282.6
Exit pressure (bara)	10.1	11.2	11.8	6.93	7.98	5.70
Release rate (kg s^{-1})	80.0	117.0	108.0	0.40	0.27	0.46
Release duration (s)	126	255	381	900	1200	600
Rainout mass fraction (%)	5	5	5	0	0	0
Wind speed (m s^{-1})	7.42	5.76	4.51	6.1	4.4	4.9
at reference height (m)	2	2	2	10	10	10
Friction velocity (m s^{-1})	0.442	0.339	0.286	0.44	0.41	0.405
Surface roughness (m)	0.003	0.003	0.003	0.04	0.04	0.04
Monin-Obukhov length (m)	92.7	94.7	45.2	348	138	-77
Ambient temperature (K)	301.95	303.55	305.55	288.65	289.65	290.65
at reference height (m)	0.82	0.82	0.82	1.5	1.5	1.5
Ambient pressure (bara)	0.909	0.909	0.903	1.02	1.02	1.013
Relative humidity (%)	13.2	17.5	21.3	86	62	53.6
Averaging time (s)	80	160	300	600	600	400

DRIFT

The Desert Tortoise and FLADIS experiments were modelled using DRIFT version 3.7.19. DRIFT (Dispersion of Releases Involving Flammables or Toxics) is a gas dispersion model, originally developed by the UK Atomic Energy Authority (UKAEA), and subsequently maintained by ESR Technology, with the support of the UK Health and Safety Executive (HSE). DRIFT is used within HSE to model atmospheric dispersion of toxic and flammable substances for the purpose of providing public safety advice on

hazardous substance consent applications and land-use planning. Model evaluation of DRIFT has been undertaken for a variety of release scenarios (Cruse *et al*. 2016, Coldrick and Webber, 2017). A mathematical description of DRIFT can be found in the report by Tickle and Carlisle (2008). DRIFT was also used previously to model the Jack Rabbit II chlorine trials (Gant *et al*., 2021).

The Desert Tortoise and FLADIS ammonia jet releases were modelled using the two-phase jet model in DRIFT. The model accounts for condensation of water vapour from the air in the cold jet, reactions between ammonia and water, and evaporation of aerosol droplets that contain a fraction of liquid water and ammonia. The baseline set of simulations used a rainout fraction of 5% for Desert Tortoise, and 0% for FLADIS. Rainout was modelled as deposition of liquid ammonia onto the ground at the source, with the deposited ammonia effectively removed from the simulation (i.e., pool evaporation was not modelled). Atmospheric conditions in DRIFT were specified using the inverse Monin-Obukhov length, friction velocity, and roughness length.

Validation against experimental results

Figure 14 shows the predicted plume centreline (arc-max) concentrations and cloud widths from the six trials against experimental data. Overall, DRIFT was in good agreement with the data, with more than half of the predicted concentrations within a factor of two of the measured values. There was a slight over-prediction in concentration for all three DT trials at the first sensor arc at 100 m but closer agreement to the experimental data at the second sensor arc at 800 m. DRIFT slightly under-predicted concentrations in the FLADIS trials 16 and 24 near the orifice at 20 m and slightly over-predicted them in the far-field at 240 m in the FL09 trial. Predicted cloud widths were in good agreement with the experimental data. The cloud width was taken here to be the distance from the centreline to the point at which concentration dropped to $C_{cl}/\sqrt{e}$, where C_{cl} is the centreline concentration. The results confirmed that DRIFT is capable of modelling horizontal two-phase ammonia jet releases at different scales.

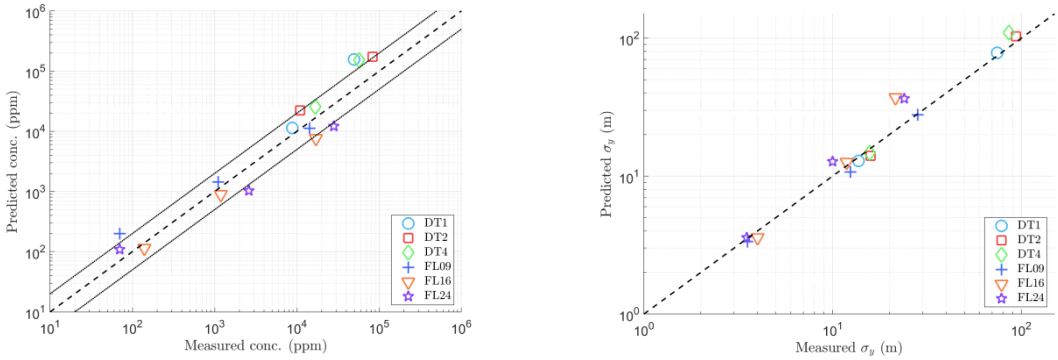

Figure 14 Left: predicted versus measured arc-max concentration for six Desert Tortoise and FLADIS trials. A dashed line indicates where predicted (DRIFT) and measured (experiment) concentration are equal. A solid line above and below indicates the range where measured concentration is a factor of 1/2 and 2 of predicted concentration, respectively. Right: predicted versus measured cloud width σ_y.

SENSITIVITY ANALYSIS OF DT1

DT1 was selected for further analysis, due to the potential similarities between this trial and future JRIII ammonia releases. Four model input parameters were selected for sensitivity analysis: rainout mass fraction, site average wind speed, Monin-Obukhov length, and relative humidity. There were uncertainties associated with these four model inputs in the DT1 trial, due to measurement issues, changing meteorological conditions and the presence of standing water on the test site. Table 2 presents the sensitivity parameters used in the current study. There were different estimates in the literature for the rain-out fraction, which varied between 5% and 36% of the total mass of ammonia released. For the purposes of this study, the baseline value was set at 5% and a range of 0% to 40% was used in the sensitivity analysis. Due to uncertainties arising from the presence of standing water, the relative humidity was varied from 5% to 60% and the atmospheric stability was varied from neutral to slightly unstable conditions, as indicated by the inverse Monin-Obukhov length varying between 0.01 m^{-1} and -0.07 m^{-1}. The measured wind speed of 7.4 m s^{-1} in the DT1 trial was high compared to wind speeds commonly used in regulatory risk assessments

(and observed in previous field trials such as Jack Rabbit II). A wide range for one model input can cause it to dominate the results of a sensitivity analysis. Due to these considerations, a range of lower wind speeds between 2 to 6 m s^{-1} were used in the sensitivity analysis. A maximin Latin Hypercube design was used to generate a uniform distribution of parameter values between the minimum and maximum values.

A total of 150 DRIFT simulations were run for DT1 and centreline concentrations were output in the downwind direction at a fixed height of 1 m. Figure 15 plots the predicted concentrations from all 150 DRIFT runs, in addition to the baseline results and experimental data. The spread in predicted concentrations generally increased with distance downwind. At 100 m, all of the predicted concentrations were higher than the measurements (by approximately a factor of 1.5 to 2.5). Further downwind at 800 m, the baseline concentration was in close agreement with the measured concentration, and the 150 runs gave concentrations that spanned roughly half an order-of-magnitude above and below the baseline value. The marked increase in spread of predicted concentrations at a distance of around 50 m coincided with the point where the cloud centreline reached ground level, and the cloud transitioned from a free-jet into a wall-jet, with the cloud spreading along the ground.

Table 2 Model input parameters and assumed range.

Parameter	Min	Max	Base Case
Rainout mass fraction (%)	0	40	5
Site average wind speed (m s^{-1})	2	6	7.4
Inverse M-O length[a], $1/L_a$ (m^{-1})	-0.07	0.01	0.011
Relative humidity (%)	5	60	13.2

[a] The inverse length was used instead of the Monin-Obukhov length L_a to avoid singularities under neutral stability conditions when $1/L_a = 0$.

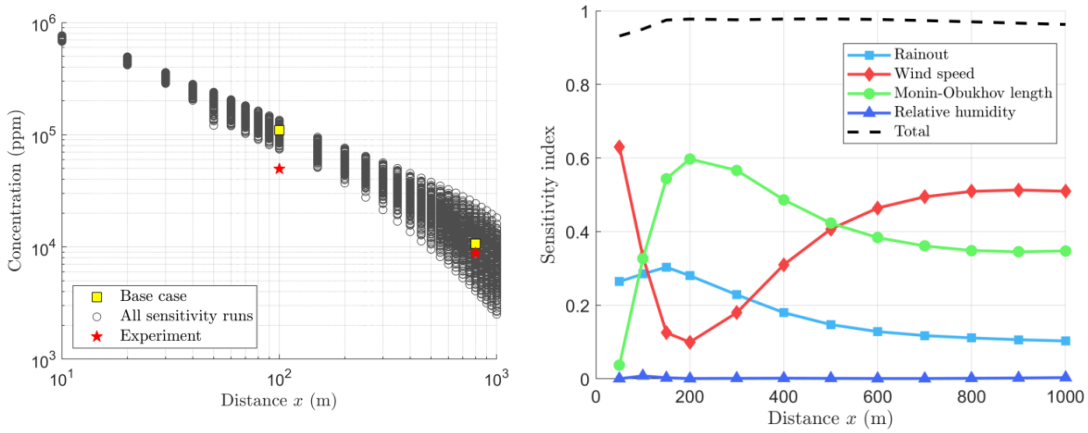

Figure 15 Left: Centreline concentrations at 1 m height for DT1 from DRIFT baseline case and 150 DRIFT sensitivity tests and experimental data. Right: Sensitivity index (i.e., main effect) from GEM analysis of DRIFT runs.

Gaussian Emulation Machine (GEM)

Statistical analysis of DRIFT results was undertaken using the Gaussian Emulation Machine (GEM), v1.1 (Kennedy, 2022). GEM determines which model inputs affected the selected output in terms of the sensitivity index (main effect), i.e., the fraction of total output variance that was due to varying that input. GEM also outputs the total effect for each input, which includes all the interactions between that parameter and other inputs. However, interactions between the four model inputs were found to be negligible (as indicated by the Total line in Figure 2) and they are therefore not discussed further here. The sensitivity index for each variable is plotted as a function of downwind position in Figure 2 (right-hand side). Sensitivity indices are normalised with the total variance and the left-hand plot shows that this total variance increased with distance downwind. It is clear from the right-hand graph that varying the relative humidity between 5% and 60% RH had little influence on the predicted centreline concentrations, compared to varying the other model input parameters. The effect of varying the rainout fraction, wind speed, and Monin-Obukhov changed rapidly within the first 200 m from the source. Overall, the two main dominant

inputs were the wind speed and atmospheric stability. The rainout fraction had a more modest effect, and its importance gradually diminished with distance downwind. Figure 2 demonstrates the usefulness of assessing model sensitivity at various downwind distances.

CONCLUSIONS

The DRIFT integral model was used to simulate six trials from the Desert Tortoise (1983) and FLADIS (1993-1994) ammonia field experiments. Good agreement was obtained between predicted centreline concentrations and measured values, with more than half of the DRIFT predicted centreline concentrations within a factor of two of the measurements. A sensitivity analysis was also undertaken on the Desert Tortoise trial DT1, which is expected to be of similar scale and conditions to future JRIII trials. A Gaussian process emulator has been fitted to 150 DRIFT simulations. Four model input parameters were varied and their effect on the predicted centreline concentration was investigated. The range of predicted plume centreline concentrations from the 150 DRIFT runs at the first sensor arc at 100 m were all higher than the experimental measurement. On the second sensor arc at 800 m, the 150 DRIFT runs spanned roughly half an order-of-magnitude above and below the measured centreline concentration. The relative importance of model inputs, such as the wind speed, was shown to vary significantly as a function of downwind position. Unsurprisingly, the two main dominant input parameters were the wind speed and atmospheric stability. The rainout fraction had a modest effect. Varying the relative humidity between 5% and 60% RH had very little influence on the predicted centreline concentrations. The exercise was useful in understanding the predictive capabilities of DRIFT and its sensitivity to four uncertain input parameters. This information will be useful when DRIFT is used to help setup the future JRIII ammonia trials, e.g., to help position sensor arrays.

REFERENCES

Carissimo B., S.F. Jagger, N.C. Daish, A. Halford, S. Selmoer-Olsen, K. Riikonen, J.M. Perroux, J. Wurtz, J.G. Bartzis, N.J. Duijm, K. Ham, M. Schatzmann and R. Hall, 2001: The SMEDIS database and validation exercise. International Journal of Environment and Pollution. 16 (1-6), p614-629.

Coldrick, S. and D. Webber, 2017: Evaluation of the DRIFT gas dispersion model version 3.6.4. *HSE Research Report RR1100.* https://www.hse.gov.uk/research/rrhtm/rr1100.htm (accessed 30 June 2022).

Cruse, H., McGillivray, A., Chaplin, Z., Coldrick, S., Tickle, G., Tucker, H. and Macbeth, R., 2016. Gas dispersion modelling using the DRIFT 3 model to assess toxic and flammable chemical major hazards. In IChemE Hazards 26 Conference. https://www.icheme.org/media/11764/hazards-26-paper-27-gas-and-vapour-dispersion-modelling-using-the-drift-3-model-to-assess-the-safety-from-toxic-and-flammable-chemical-major-hazards.pdf (accessed 30 June 2022).

Gant, S.E., Kelsey, A., McNally, K., Witlox, H.W.M. and Bilio, M., 2013. Methodology for global sensitivity analysis of consequence models. Journal of Loss Prevention in the Process Industries, 26(4), pp.792-802. https://doi.org/10.1016/j.jlp.2013.02.009 (accessed 30 June 2022).

Gant, S., Tickle, G., Kelsey, A. and Tucker, H., 2021. DRIFT dispersion model predictions for the Jack Rabbit II model inter-comparison exercise. Atmospheric Environment, 244, p.117717. https://doi.org/10.1016/j.atmosenv.2020.117717 (accessed 30 June 2022)

Goldwire Jr, H.C., McRae, T.G., Johnson, G.W., Hipple, D.L., Koopman, R.P., McClure, J.W., Morris, L.K. and Cederwall, R.T., 1985. Desert Tortoise series data report: 1983 pressurized ammonia spills (No. UCID-20562). Lawrence Livermore National Lab., CA (USA). https://www.osti.gov/biblio/6393901 (accessed 30 June 2022)

Kennedy M. C., 2022. Software: Gaussian emulation machine for sensitivity analysis. https://www.tonyohagan.co.uk/academic/GEM/ (accessed 23 May 2022).

Nielsen, M., Bengtsson, R., Jones, C., Nyren, K., Ott, S. and Ride, D., 1994. Design of the FLADIS field experiments with dispersion of liquefied ammonia.

Tickle, G. and J. Carlisle, 2008: Extension of the dense gas dispersion model DRIFT to include buoyant lift-off and buoyant rise. *HSE Research Report RR629.* https://www.hse.gov.uk/research/rrhtm/rr629.htm (accessed 30 June 2022).

ACKNOWLEDGEMENT The contributions to this publication by HSE staff were funded by HSE. Its contents, including any opinions and/or conclusions expressed, are those of the authors alone and do not necessarily reflect HSE policy.

21st International Conference on
Harmonisation within Atmospheric Dispersion Modelling for Regulatory Purposes
27-30 September 2022, Aveiro, Portugal

SO_2 AND NO_X PEAK CONCENTRATIONS, VERTICAL PROFILES AND MODEL-IDENTIFIED ORIGINS FROM DISTANT SOURCES

Raido Kiss[1], Marko Kaasik[1], Terje Tammekivi[1] and Steffen M. Noe[2]

[1]Institute of Physics, University of Tartu, Tartu, Estonia
[2]Institute of Forestry and Rural Engineering, Estonian University of Life Sciences, Tartu, Estonia

Abstract: Atmospheric chemistry-transport models struggle to predict correct concentrations of the modelled pollutant during ground-based temperature inversions. The aim of this study was to evaluate the performance of SILAM model during such inversions. For evaluation, emissions from known tall stack sources of SO_2 and NO_x were applied; modelled concentrations were compared with mast measurements up to 110 m above surface. In inversion conditions the concentrations related to those elevated point sources were found remarkably higher at higher levels. Results show that in half of the inversion cases SILAM diagnoses the temperature inversion well and in almost all of the latter cases, SILAM predicts the vertical profile of modelled pollutant concentration correctly. In general, SILAM tends to underestimate the inversion strength and near-surface concentrations. The reasons may be, respectively, related to the parametrization of the surface layer and the underestimation of vertical dispersion. In modelled concentrations the usual duration of peaks was shorter than measured. The reason may be underestimation of horizontal dispersion.

Key words: *atmospheric chemistry-transport model; near-surface temperature inversion; model validation*

INTRODUCTION

This practical research grew out of model experiments with the atmospheric chemistry-transport model SILAM (Sofiev et al, 2015). While modelling the dispersion of SO_2 from tall (70-250 m) stacks in North-Eastern Estonia, SILAM showed plumes of higher SO_2 concentration passing over rural monitoring stations far away from the stacks. In these ground-based stations, however, every modelled plume did not bring about a noticeable increase (”peak”) of SO_2 concentration. Assuming that the plume trajectories, driven by HIRLAM short-term forecast, are rather reliable, we hypothesized that thermal inversions formed during such episodes might prevent fast penetration of admixtures from higher above to the surface layer. It is known that atmospheric models are in general less reliable in thermal inversion.

To check our hypothesis, this research was made using a five-year period of SO_2, NO_x and temperature measurements from a rural 130 m tall mast, located 110-150 km from the pollution sources. The mast measurements of vertical profiles of both potential temperature and pollutant concentration were used. This research focuses on cases, when remarkably high (up to 20 times the background level) short-term concentrations (”peaks”, duration up to 12 hours) of SO_2 and/or NO_x occur in a rural area, with specific concentration vertical profile in planetary boundary layer: the concentration above is higher than at lower levels. Such a profile indicates either origin from an elevated point source or possibly ascending air mass at some point on the advection path of these trace gases. The aim of this study was to evaluate the performance of SILAM in modelling SO_2 and NO_x concentrations during these cases of ground-based thermal inversion.

methods

The concentration and temperature profiles measured during 2016 – 2020 in a 110 m tall mast at rural (forested) SMEAR Estonia site (Järvselja, Estonia) were used to specify the cases (location: see Figure 1). In total about 20 cases meeting the main criterion (concentration increasing with height) were selected. It appears that all these events have a pronounced temperature inversion between all or some of the 5 mast measurement heights (30, 50, 70, 90 and 110 m), which obviously prevents fast penetration of admixtures from higher above to the surface layer. Both wintertime steady inversions and summer night-time inversions contribute to these events. To confirm the inversion condition at Järvselja was not a fluke,

temperatures measured in 24-meter masts at Aseri, Uulu and Külitse, Estonia (locations: see Figure 1), were used to see the extent of inversions.

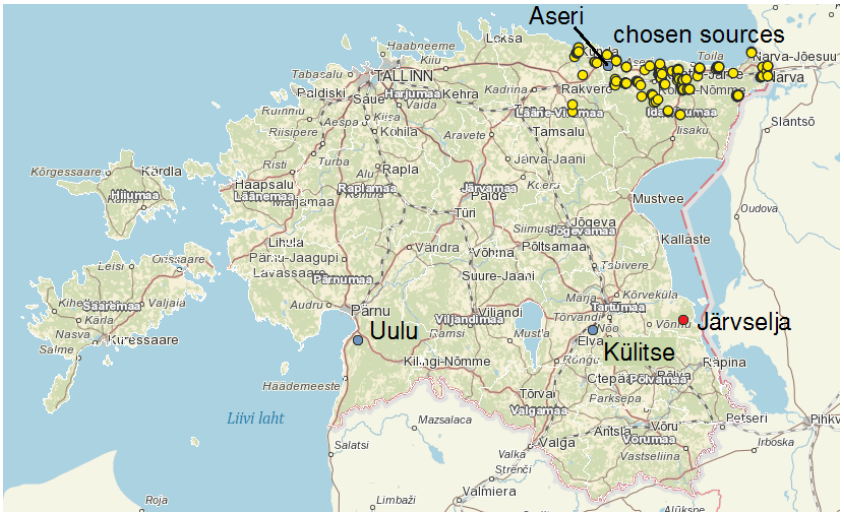

Figure 16. All data sources used in this research: Järvselja mast marked in red, lower masts in blue and initially chosen industrial pollution sources (stacks) in yellow. In the calculations only sources with emission more than 1 g s^{-1} were used.

The biggest known sources of SO_2 and NO_x in Estonia are tall stacks of thermal power plants and chemical industries in North-Eastern Estonia, about 110 – 150 km away from the measurement site. To initially (vaguely) confirm that measured concentration peaks (present during selected 20 cases) originate from these stacks, NOAA HYSPLIT model (Stein et al, 2015) was used for backward air mass trajectory tracing. If HYSPLIT showed the air mass trajectories going over North-Eastern Estonia, more detailed studies were done in the domain covering Estonia using SILAM model at resolution of 0.025°of latitude and 0.05°of longitude, which is about 2.8 km. Firstly, the model was run in inverse (adjoint, receptor-oriented) mode to more accurately confirm that the measured peaks originated from this industrial area, not from other (more distant) sources. SO_2 concentrations measured at 110 m mast height were used as model input, as on this height, usually the highest concentrations were measured. The output, sensitivity distribution in time, was visualized with the OpenGrADS software. To see if outputs differ, a sensitivity study was conducted: same adjoint runs were made with sensitivity source (measured concentration) emitted from a column at heights 0-50 m. For all SILAM runs, the necessary weather data originated from the HIRLAM NWP model (Estonian Weather Service).

After thoroughly confirming the origin of the concentration peaks to be North-Eastern Estonia, SILAM was run in the direct (forward, source-oriented) mode. For that, NO_x and SO_2 emission data for the industrial stacks (tons per year) was known. As the daily, weekly and monthly variation of the emissions was unknown, it had to be estimated taking into account the type of the source (chemical industry or power plant). Using the emission data (now in g s^{-1}), dispersion of the pollutants was calculated. Only sources emitting more than 1 g s^{-1} were used in the run, in total 20-30 sources were used (Figure 1). Modelled time series and vertical profiles of concentration and (potential) temperature were compared with data measured at the Järvselja mast location.

Regarding the time series, measured and modelled average concentration at peak maximum were compared, as well as peak duration. Using all peak maxima, fraction in factor two index (FA2) was calculated for both SO_2 and NO_x. Furthermore, modelled and measured inversion strengths (in this study, temperature difference between 30 m and 70 m mast height) at peak maximum were compared. Vertical profiles of potential temperature and pollutant concentration (taken from peak maxima) were compared qualitatively. It was considered that SILAM modelled the profiles well, if the shape of profiles was visibly similar.

results

From the 20 selected inversion cases, HYSPLIT showed the contribution of North-East Estonian industrial stacks for 12 cases, all confirmed by SILAM adjoint runs. Other events are likely induced by more distant sources outside of the country. Due to other limitations, it was possible to completely study 6 cases, containing in total 17 pollutant concentration peaks. During almost all of these cases, lower masts (Aseri, Uulu, Külitse) showed inversions as well (temperature difference between 22 m and 8 m mast heights 0.2...4.5 °C), which means the inversions were extensive, possibly ranging all over continental Estonia.

The sensitivity study showed sensitivity distributions similar to the adjoint run most of the time. However, five modelled cases out of seven still showed some level of difference for at least two hours at a time. The difference was sensitivity distribution converging closer to the monitoring station in the sensitivity study. The distribution was lower further away (Figure 2). These differences were too small to prevent the North-Eastern Estonian sources to contribute to a particular peak.

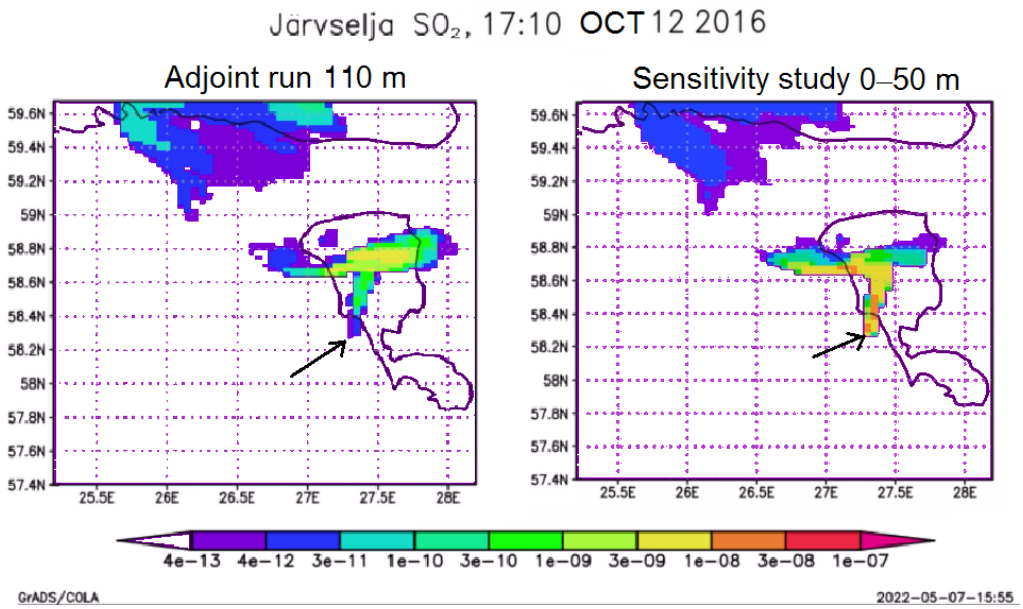

Figure 17. Comparison between an adjoint run at 110 m and sensitivity study at 0-50 m for an SO_2 peak. The sensitivity study shows higher sensitivity distribution close to Järvselja (marked with an arrow) and lower distribution further away. The colour scale is in arbitrary, non-normalized units.

After direct (source-oriented) runs were made, comparison of time series at mast location showed that, on average, SILAM-modelled peaks lasted three hours less than measured peaks. The fraction in factor two (FA2) results for SO_2 and NO_x were, respectively 5/9 and 1/8, which means that (e.g. for SO_2) the average modelled concentration at peak maximum did not differ more than two times from the measured value (5 cases out of 9). SILAM predicts the peak values better during a weaker inversion (measured temperature difference between 30 and 70 m less than 1 °C). Inversion strength at concentration peak maximum was up to 3.1 °C underestimated by SILAM. Potential temperature profiles were properly reproduced by SILAM in four cases out of eight. If temperature profile was reproduced, three times out of four the concentration profile fitted as well. In total, 3/9 and 5/8 concentration profiles for respectively SO_2 and NO_x were reproduced. For detailed results see Table 1. Examples of vertical profiles are given on Figure 3.

Table 9. A concise table of most important results.

Event	Measured inversion strength 30-70 m (°C)	Modelled inversion strength 30-70 m (°C)	Inversion strength underestimated (°C)	Potential temperature profile correct?	Concentration profile correct?		Peak estimated by SILAM	
					SO_2	NO_x	SO_2	NO_x
13.10.2016 1	gaps in data	2.1	-	-	no	yes	under	under
13.10.2016 2	gaps in data	0.8	-	-	yes	no	under	under
13.10.2016 3	gaps in data	-0.2	-	-	no	yes	under	under
16.05.2017	3.4	0.4	3.1	no	no	no	under	under
24.07.2017	1.5	-0.1	1.6	yes	no	no	well	over
27.08.2017	2.9	1.6	1.3	yes	yes	yes	well	over
04.03.2018 1	0.4	-0.4	0.8	yes	-	yes	-	under
04.03.2018 2	0.3	-0.4	0.7	no	no	-	well	-
04.03.2018 3	0.7	-0.2	0.9	yes	yes	-	well	-
24.01.2019	0.3	-0.3	0.6	no	no	yes	well	well
						FA2:	5/9	1/8

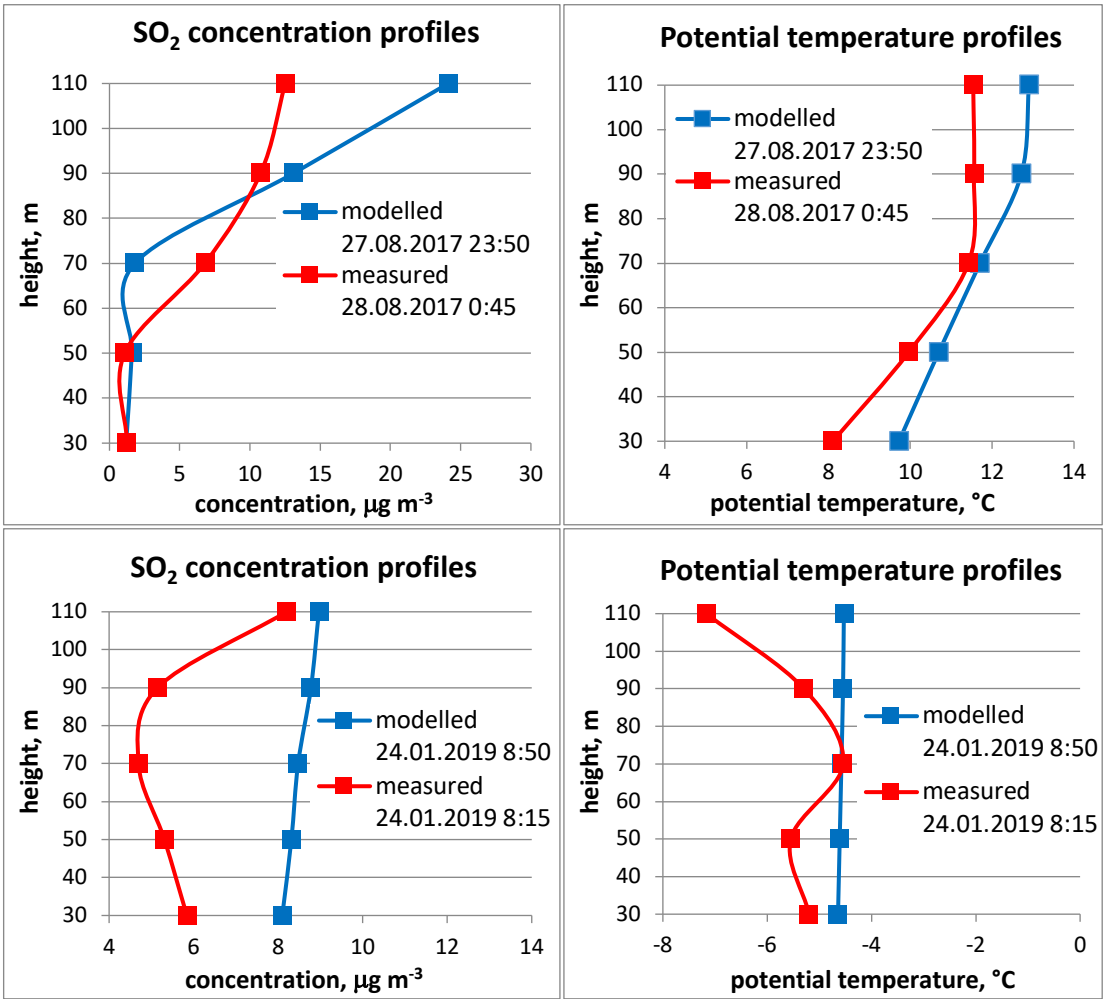

Figure 18. Examples of SO_2 concentration and potential temperature vertical profile for two events. Upper ones were deemed well-assessed, lower ones poorly assessed by SILAM.

discussion

The sensitivity study shows all the pollution originating roughly from the same area for both 110 m and 0-50 m height. At the same time, sensitivity study does not reflect all the details in reality. Forest canopy reaches up to a height of 30 meters at Järvselja, but SILAM does not consider the in-canopy processes.

Most of modelled concentration peaks (averages of concentrations at peak maximum) are seen to be underestimated. This may mean underestimation of pollutant vertical dispersion in the model. SILAM usually showed highest pollutant concentration above the mast (110-600 m). If pollutant dispersion is underestimated in the model, the resulting peak concentrations are underestimated. However, as variation of emissions in time had to be estimated (having only yearly emissions available), a notable amount of uncertainty was introduced.

Modelled durations of peaks were shorter than measured. One explanation is that horizontal dispersion of pollutant is underestimated, too. If pollutants dispersed horizontally more, the plume would take a longer time to pass over the monitoring station in the model, resulting in a longer duration of the peak.

SILAM in most of the cases underestimates the strength of inversion. Inaccuracies are understandable, as maximum three layers in HIRLAM meteorological fields cover five measurement heights in the mast. If these data points are poorly represented by HIRLAM, it is likely that SILAM assesses the inversion condition poorly as well. In addition, tree canopies can affect the air mass on lower levels. To pinpoint the cause of inversion strength underestimation, it is necessary to look into the parametrization of the surface layer in SILAM.

CONCLUSIONS

The aim of this study was to evaluate the performance of atmospheric chemistry-transport model SILAM during specific conditions of PBL thermal inversion using peak concentrations originating from distant elevated sources. Based on the fraction of factor two (FA2) index, SILAM assesses average peak concentrations fairly less than half of the time. SO_2 peaks are assessed better than NO_x. Most of the time, average peak concentrations are underestimated, which may mean underestimation of pollutant vertical distribution. However, uncertainty originating from emission data is considerable. The horizontal dispersion of the pollutant may be underestimated as well, as modelled peaks are shorter in duration. SILAM tends to underestimate inversion strength (at least at heights 30-70 m). To understand the reasons, it is necessary to look into the parametrization of the surface layer in SILAM.

Acknowledgements

This research was funded by EU structural and investment funds, project No. 2014-2020.4.01.21-0363 and Estonian Ministry of Education and Science, research grant PRG714 and. The measurements at Tahkuse station are supported by the Estonian Environment Agency contract LLTFY18213 contributing to the fulfilment of the National Environmental Monitoring Program. SMEAR Estonia measurements and data provision are supported by the Estonian Ministry of Sciences projects (grant nos. P180021, P180274, P200196) and by the Estonian Research Infrastructures Roadmap Project “Estonian Environmental Observatory” (3.2.0304.11-0395). We thank Erik Teinemaa from Estonian Environmental Research Centre for kind assistance.

REFERENCES

Sofiev, M, J. Vira, R. Kouznetsov, M. Prank, J. Soares, E. Genikhovich, 2015: Construction of an Eulerian atmospheric dispersion model based on the advection algorithm of M. Galperin: dynamic cores v. 4 and 5 of SILAM v. 5.5. *Geoscientific Model Development Discussions*, **8(3)**, 2905-2947.

Stein, A.F, R.R. Draxler, G.D. Rolph, B.J.B. Stunder, M.D. Cohen, F. Ngan, 2015: NOAA’s HYSPLIT Atmospheric Transport and Dispersion Modeling System. *Bulletin of the American Meteorological Society*, **96(12)**, 2059-2077.

21st International Conference on
Harmonisation within Atmospheric Dispersion Modelling for Regulatory Purposes
27-30 September 2022, Aveiro, Portugal

SENSITIVITY ANALYSIS OF MICROSCALE POLLUTANT DISPERSION LARGE-EDDY SIMULATIONS TOWARDS OBSERVATION NETWORK DESIGN

Eliott Lumet[1,2], Mélanie C. Rochoux[1], Simon Lacroix[2], Thomas Jaravel[1] and Olivier Vermorel[3]

[1]CECI, Université de Toulouse, CNRS, CERFACS, Toulouse, France
[2]LAAS-CNRS, Toulouse, France
[3]CERFACS, Toulouse, France

Abstract: We present a detailed study of the influence of the atmospheric boundary-layer variability on large-eddy simulation (LES) model predictions in the context of microscale pollutant dispersion in urban-like environments. For this purpose, we have developed a new approach to model inflow boundary conditions and their related uncertainties that are essential to represent how the large atmospheric scales influence the microscale flow features in a complex urban geometry. In a preliminary step, we have considered uncertainties in the inflow mean wind direction and in the friction velocity of the mean wind velocity logarithmic profile. We have then built a perturbed-physics ensemble of tracer concentration fields by integration of the LES model in a multi-query framework. In this study, the ensemble of LES fields is obtained for the Mock Urban Setting Test (MUST) field-scale experiment and it is used to carry out a global sensitivity analysis, i.e. to quantify the LES model spatial dependencies to the mean wind direction and the friction velocity.

KEY WORDS: **MICROSCALE DISPERSION, MUST, LARGE-EDDY SIMULATION, INFLOW BOUNDARY CONDITIONS, SENSITIVITY ANALYSIS**

INTRODUCTION

Large-eddy simulations (LES) are a promising approach to simulate microscale meteorology and pollutant dispersion in complex urban environments, since they can accurately capture highly unsteady and complex flow topologies typically found in the wake of buildings, and thereby track the spatiotemporal variability of pollutant concentration in urban canopies. This is of primary importance to capture the peak pollutant concentrations for instance (Philips et al. 2013). However, to correctly predict microscale pollutant dispersion in complex geometry, LES models have to account for the variability of the atmospheric boundary-layer and in particular for the complex interactions with the turbulence mesoscales (Nagel et al. 2022). For this purpose, boundary conditions models can be used, but their parameters are highly uncertain and it is therefore advised to adopt a probabilistic representation of the boundary conditions to reflect their uncertainties (Dauxois et al. 2021). In this context, we aim at applying data assimilation methods to LES dispersion models, i.e. at solving an inverse problem that combines LES model predictions with in situ measurements to infer more accurate inflow boundary conditions (Defforge et al. 2021). It is therefore of primary importance to identify where to place sensors to extract the most informative data and thus have a well-posed data assimilation problem (Peng et al 2014). To design the observation network, a preliminary step consists in carrying out a sensitivity analysis to spot which areas are subject to high uncertainties in the LES predictions, and thereby determine in which areas potential sensors could be used to reconstruct information on the uncertain inflow boundary condition. In this study, this approach has been applied to one near-neutral trial of the Mock Urban Setting Test (MUST) experiment, which is a good validation case for the LES simulations (Yee and Biltoft, 2004) and which is used here to provide a proof of concept of the proposed sensitivity analysis approach.

The must (mock urban setting test) case

THE EXPERIMENT

MUST is a field-scale experiment performed in September 2001 in Utah, USA, to provide extensive measurements of pollutant dispersion within an urban-like canopy for model development and validation purpose (Yee and Biltoft, 2004). The simplified urban canopy is represented by an array of 120 regularly-spaced shipping containers disposed over a flat and homogeneous terrain. Each container measures 12.2 m long, 2.42 m wide and 2.54 m high. A series of trials was performed for which a non-reactive gas, propylene, was released under different atmospheric conditions during 15 minutes. For this study, we simulate the trial 2681829 corresponding to near-neutral atmospheric conditions since it has been extensively studied in the literature (it is of particular interest to study the container impact on the incident flow within the container array) and is therefore a relevant validation test case for our modeling approach.

The large-eddy simulation solver and related modeling choices

To reproduce the MUST case, we design and run obstacle-resolved LES to predict the temporal evolution of the flow and the propylene transport across the container array. For this purpose, we use the AVBP solver developed by CERFACS (*https://www.cerfacs.fr/avbp7x*) which solves the filtered compressible Navier-Stokes equations on unstructured meshes using a finite volume discretization and the second-order in time and space Lax-Wendroff scheme. Since the Mach number of atmospheric boundary-layer flows is very low, an artificial compressibility approach, also known as pressure gradient scaling, is used to artificially increase the time-step and thereby reduce the computational time.

The computational domain is a square box of size $L \times l \times h = 420\ \text{m} \times 420\ \text{m} \times 50\ \text{m}$ (Fig. 1). It is discretized based on an unstructured tetrahedral mesh of $14{,}7 \times 10^6$ cells, with refinement in area of interest and towards walls, down to 30 cm resolution at the obstacles level. To efficiently handle changes in the mean inflow direction, the computational domain is separated in two subdomains (Fig. 1): the peripheric domain D2 that is turned to align with the mean inflow direction, and the inner domain D1 that is fixed. We solve the Navier-Stokes equations on all subdomains using the coupling library CWIPI. This is useful to avoid generating a new mesh for each new set of input parameters and facilitate the generation of a large ensemble of LES runs.

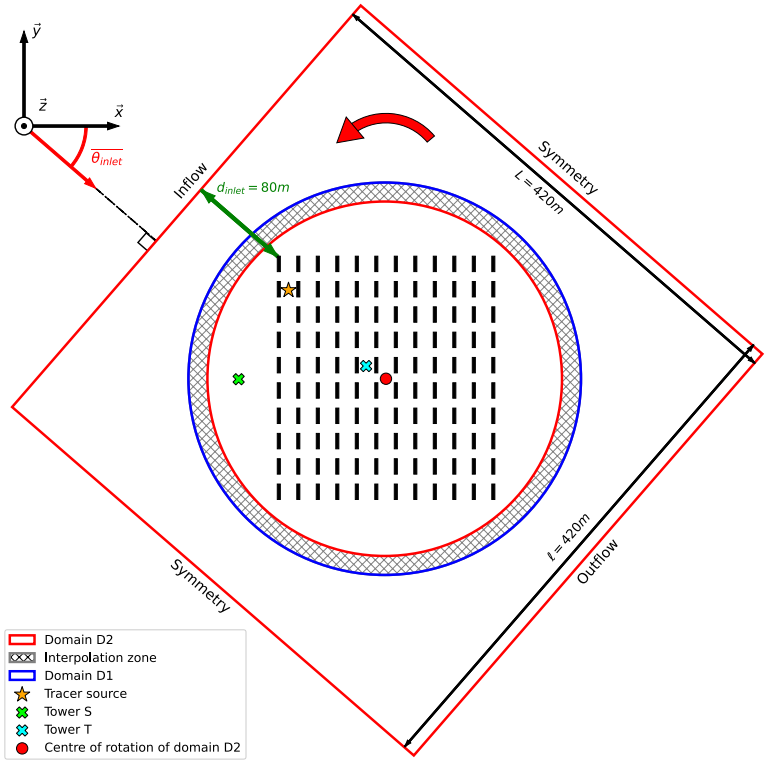

Figure 19. Schematic of the simulation subdomains D1 and D2 for the simulated MUST trial using LES: the fixed inner domain is in blue, the rotating peripheric domain D2 is in red, and the overlap area between D1 and D2 is hatched. Lateral boundary conditions are indicated. The orange star represents the emission source location. The cross symbols represent the towers at which observations were acquired during the trial: the upstream tower S is indicated in green, while the inner tower T is indicated in blue.

A mean wind log-law vertical profile (Eq. 1) is imposed at the inlet based on the Monin-Obukhov similarity theory in neutral atmospheric conditions:

$$\overline{U(z)} = \frac{u_*}{\kappa} \ln\left(\frac{z+z_0}{z_0}\right). \quad (1)$$

This profile was fitted with the experimental data obtained at Tower S (Fig. 1), which is located upstream of the container array. Wind fluctuations are added to the mean inlet wind profile using the Kraichnan synthetic injection method following the Passot-Pouquet turbulence spectrum (Daviller et al. 2019). In this study, we impose a prescribed mean vertical profile of the Reynolds tensor obtained from a free-field precursor simulation of the atmospheric boundary-layer. This novel approach provides a way to have inhomogeneous anisotropic inflow boundary conditions and only requires to know the friction velocity u_*, the ground rugosity z_0 and the mean wind direction $\overline{\theta_{inlet}}$ to parametrize inflow turbulence. In complement to the inlet, wall laws with adapted roughness are used for the ground and the buildings, outflow boundary conditions are used for the outlet and top boundaries, while symmetry is imposed on the domain sides (Fig. 1). Propylene is released as a passive gas tracer from a continuous and constant point source emission.

GLOBAL Sensitivity Analysis framework

The key idea of global sensitivity analysis in this context is to quantify how uncertainties in each input parameter influence the variance of a given quantity of interest in the LES model. This is useful to spot the most influential parameters on the LES model response across the computational domain. A preliminary One-At-a-Time (OAT) sensitivity analysis showed that perturbations of the ground roughness length z_0 and of the inflow turbulent kinetic energy parameter do not significantly impact the simulated mean fields of interest comparatively with the atmospheric boundary-layer intrinsic variability. We also

assume that the emission source parameters, position and intensity, are known. The sensitivity analysis is therefore restricted to the two inflow parameters that have the strongest impact on the LES predictions: the friction velocity u_* that drives the mean inflow profile (Eq. 1), and the mean inlet wind direction $\overline{\theta_{inlet}}$.

Parameter space sampling

The range of variation of the two uncertain parameters is defined from a climatology obtained in the vicinity of the MUST area. Wind statistics were computed based on 12 days of meteorological measurements from the station SAMS #08 located 1600 m southeast of the obstacles (Yee and Biltoft, 2004). According to these statistics, most of the wind velocity magnitude measurements at 10-m AGL are between 0 and 12 m s^{-1}. To avoid complications with very low wind speed, we limit the range to [1; 12 m.s^{-1}]. We can also note that no wind direction prevails. Since it is a preliminary study and to reduce the computational cost associated with the parameter space sampling, we limit the wind angle to a variation of $\pm 30°$ from the North direction. The mean wind angle of $-40.95°$ recorded at the upstream Tower S (Fig. 1) is included in this interval $[-60°, 0°]$ expressed in the MUST frame of reference.
Once the range of variation of the parameters is defined, the next step is to choose for which values of the parameters the LES model is run to generate the ensemble. Since the LES model is very computationally expensive, it is not possible to have a very large sample (our budget is limited to 100 runs) but still we need to have a good coverage of the uncertain space to capture well the LES model response. We therefore use the Halton's low-discrepancy sequence to homogeneously sample the input parameter space (Fig. 2).

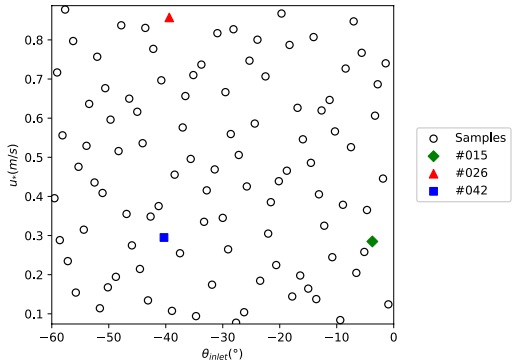

Figure 20. Parameter space sampling obtained with the Halton's low-discrepancy sequence with the inlet wind direction in the *x*-axis and the friction velocity in the *y*-axis: each point is a pair of parameters for which a LES is run.

The LES model is then integrated for each sample parameters of the Halton's sequence. It simulates unsteady flow and tracer concentration fields across the domain from which time-averaged statistics can be derived. For validation, we compare LES averages over a 200-s time period after a spin-up with experimental data acquired over the [300 s; 500 s] time period of the trial 2681829 following recommendations by Yee and Biltoft (2004). Note that the spin-up duration is scaled by the friction velocity because when the wind speed is slow, the plume takes longer to establish. The Reynolds tensor profile prescribed for the turbulence injection is also scaled by u_* and rotated to align with $\overline{\theta_{inlet}}$.

Sobol' sensitivity indices

To study the sensitivities of our LES model to the mean inlet wind direction and friction velocity, we estimate the first-order Sobol indices S_i using the Monte Carlo method from Saltelli (2002). These indices give the share of total model variance, for one field Y, explained by each input parameter X_i (Eq. 2):

$$S_i = \frac{\mathbb{V}(\mathbb{E}(Y|X_i)}{\mathbb{V}(Y)}. \quad (2)$$

These indices vary between 0 and 1, 1 meaning that 100% of the LES model variance is due to the standalone *i*th parameter. This analysis is performed for each node of a specific analysis grid defined as a 1-m resolution horizontal cut of the D1 domain at a height of 1.6 m. To limit the cost of the Saltelli

method, we use a Radial Basis Function (RBF) to interpolate the LES model predictions between the samples from the Halton's sequence. The RBF model was validated and its hyperparameters (kernel model, number of neighbors, etc) were optimized by splitting the Halton's sequence sample into a training set (80 members) and a validation set (20 members), leading to a mean absolute error of 0.189 ppm. Tests showed that a Saltelli's sequence of 2048 samples was enough to have converged estimated Sobol' indices.

REsults

The effect of the input parameter perturbations on the plume shape is highlighted by comparing the 1 ppm-isolines of the (time-averaged) mean tracer concentration fields obtained for three ensemble members of the Halton's sequence (Fig. 3); these members are representative of the variety of the LES model response in this study. As expected, when the friction velocity increases, the plume is shorter, while the plume centerline remains the same. The wind inlet direction has more impact since it deflects the plume centerline and can significantly change the flow-obstacle interactions.

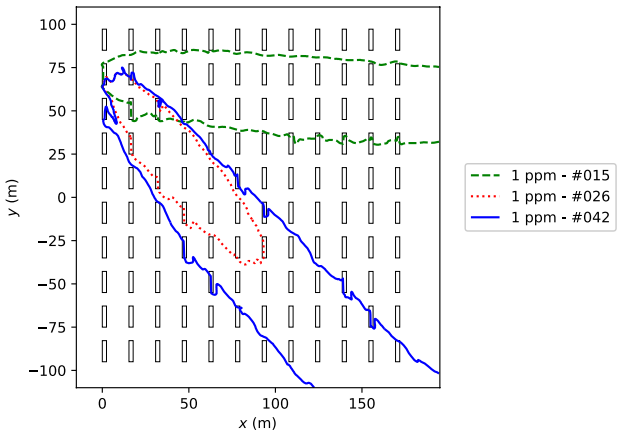

Figure 21. Comparison of the 1 ppm-isoline at $z = 1.6$ m predicted by the LES simulations corresponding to the Halton sample #015 in green, #026 in red, and #042 in blue. The corresponding input parameters are shown in Fig. 2.

The first-order Sobol indices (Eq. 2) are estimated for the horizontal cut at $z = 1.6$ m of the mean tracer concentration field. We thereby obtain 2-D maps of Sobol' indices (Fig. 4), which demonstrate that there are spatially organized patterns of concentration dependency to the inflow boundary conditions parameters in our LES model. The sides of the ensemble-averaged plume centerline are mainly dependent on the inflow wind direction (the yellow-to-orange areas on the left panel of Fig. 4) as these regions are crossed by the plume only for some extreme wind direction values. On the contrary, the concentration in the near source region appears to be mainly driven by the wind velocity (the yellow-to-orange areas on the right panel of Fig. 4). There is also a region where both wind velocity and wind direction have a more equal contribution to the tracer concentration (the pink-to-purple areas in Fig. 4); this is related to the plume size associated with the ensemble mean. These sensitivity maps are clearly useful from an experimental design perspective, as they tell us where the sensors would be able to catch perturbations information on the wind boundary conditions in a data assimilation framework.

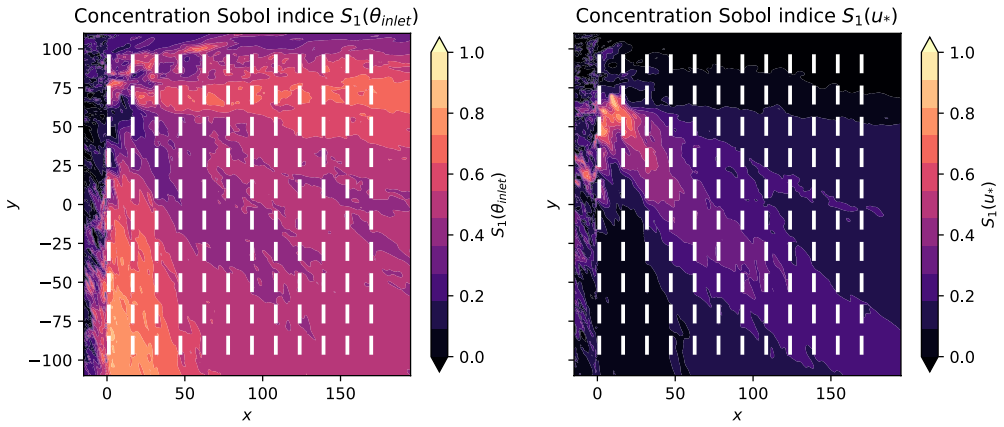

Figure 22. First-order Sobol indices of the mean concentration field at $z = 1.6$ m with respect to the mean inlet wind direction (left) and to the prescribed friction velocity (right).

Conclusion

To investigate the LES model sensitivities to the wind boundary conditions in the context of microscale dispersion, we designed and built a perturbed-physics ensemble of LES for a near-neutral trial of the MUST field campaign. From a modeling viewpoint, a particular focus has been on the development of inflow boundary conditions representative of atmospheric boundary-layer turbulence using a synthetic injection method combined with free-field precursor simulation to impose anisotropic vertical wind profiles at the boundary conditions. From a stochastic viewpoint, the LES model response (i.e. the relationship between the 2-D mean tracer concentration field at the human level and the wind direction and friction velocity) was studied using Sobol' indices. This allows to identify which regions of the microscale domain are the most sensitive to the wind direction and/or to the friction velocity. Future work includes replacing the RBF simple interpolation by a more robust metamodel based on machine learning to increase representativeness of the sensitivity analysis. This will pave the way towards designing a data assimilation framework to estimate the uncertain inflow parameters by aggregating surrogate model predictions with in-situ measurements. To go further, we will investigate how we can use the spatial distribution of the LES model sensitivities to provide guidelines to optimize the sensors' locations so as to improve data assimilation performance.

REFERENCES

Dauxois, T. and T. Peacock, et al. *2021: Confronting grand challenges in environmental fluid mechanics.* Physical review fluids, ***6(2)**, 020501.*

Daviller, G., G. Oztarlik, and T. Poinsot, 2019: A generalized non-reflecting inlet boundary condition for steady and forced compressible flows with injection of vortical and acoustic waves. Computers & Fluids, ***190**, 503-513.*

Defforge, C. L., B. Carissimo, M. Bocquet, R. Bresson and P. Armand, 2021: Improving numerical dispersion modelling in built environments with data assimilation using the iterative ensemble kalman smoother. Boundary-Layer Meteorology, ***179(2)**, 209-240.*

Nagel, T., R. Schoetter, V. Masson, C. Lac, and B. Carissimo, 2022: Numerical Analysis of the Atmospheric Boundary-Layer Turbulence Influence on Microscale Transport of Pollutant in an Idealized Urban Environment. Boundary-Layer Meteorology, ***184(1)**, 113-141.*

Peng, L., D. Lipinski and K. Mohseni, 2014: Dynamic data driven application system for plume estimation using UAVs. Journal of Intelligent & Robotic Systems, ***74(1)**, 421-436.*

Philips, D. A., R. Rossi, and G. Iaccarino, 2013: Large-eddy simulation of passive scalar dispersion in an urban-like canopy. Journal of Fluid Mechanics, ***723**, 404-428.*

Saltelli, A., 2002: Sensitivity analysis for importance assessment. Risk analysis, ***22(3)**, 579-590.*

Yee, E., C. A. Biltoft, 2004: Concentration fluctuation measurements in a plume dispersing through a regular array of obstacles. Boundary-Layer Meteorology, ***111(3)****, 363-415.*

21st International Conference on
Harmonisation within Atmospheric Dispersion Modelling for Regulatory Purposes
27-30 September 2022, Aveiro, Portugal

SOURCE APPORTIONMENT ANALYSIS IN PM AND O_3 CONCENTRATIONS DURING COVID-19 LOCKDOWN PERIOD IN MADRID (SPAIN)

Roberto San José and Juan L. Pérez-Camanyo

Environmental Software and Modelling Group, Computer Science School, Technical University of Madrid (UPM), Madrid, Spain.

Abstract: In a first analysis of the impacts of the reduction of anthropogenic emissions during COVID-19 lockdown over Madrid (Spain) area, we found an important NOx level reduction but the O_3 and PM concentrations were increased. In this work the causes of the increments are studied using Source Apportionment Technology (SAT) included in the Comprehensive Air Quality Model with Extensions (CAMx) model. CAMx is driven by the Weather Research and Forecasting model (WRF). Two simulations are run: one simulation considers the emission reductions during the lockdown (COVID simulation) and a second simulation," business as usual" (BAU simulation) with an emissions scenario without restrictions. Source apportionment techniques are used to identify and quantify the contributions from main pollution sources with the purpose to provide understanding on what measures should be taken to address them and this work shows the potential of these technique. SAT was used to estimate the contributions of multiple sources, and pollutant types (NOx and VOC) to ozone and particle formation in a single model run. Differences in SAT results under baseline (BAU) and COVID scenarios are used to quantify the contributions of O_3 and PM2.5 reductions associated with emissions reduction in individual sectors due to the lowered human activities with a high spatial resolution (1 km). Road transport is the main emission source reduced by the lockdown and reduction in NOx emissions (59%) is higher that VOC reduction (14%). This study helps to elucidate the complex and nonlinear response of O_3 and PM concentrations after a reduction of emissions mainly from the transport sector, during the COVID-19 lockdown period, that must be taken into account in the control strategies to mitigate haze pollution. The results show that despite extreme reductions in primary emissions, current air pollution cannot be fully tackled. Further consideration needs to be given to the reorganisation of energy and industrial strategy together with trans-regional joint monitoring for a comprehensive long-term air pollution plan. Source apportionment studies can support of authorities responsible to develop air quality plans.

Key words: *Source Apportionment, COVID-19, lockdown, CAMx, WRF/Chem*

INTRODUCTION

The decrease in economic activities during COVID-19 lockdown has led to the reduction of anthropogenic emissions. This situation offers us an unprecedented opportunity to test the performance of our numerical modelling tools. The lockdown has made possible to quantify the decreases and increases of the air pollution concentrations after a drastic emissions reduction. This has allowed us to evaluate the efficiency of reducing emissions to the atmosphere in the air pollution concentrations. The results of these experiments will help to develop well-balanced emission reduction strategies to improve the Madrid air quality. Understanding how air quality responds to the emission reductions during COVID-19 pandemic will provide important insight into the future development of emissions control strategies. In this situation to understand the air pollution concentrations attributed to both source regions and emission categories, source apportionment of PM and O_3 is applied. Also, brute force method was applied to quantify the impacts of emission reduction in the concentrations.

MATERIAL AND METHODS

The following sections gives a short description of the designs air quality simulations, periods, domains and models.

SIMULATIONS

The impact of COVID lockdown on Madrid (Spain) air quality is estimated by running two simulations, one simulation considers the emission reductions during the lockdown (COVID simulation) and a second simulation," business as usual" (BAU simulation) with an emissions scenario without restrictions. Meteorology-air quality modeling was performed for February, 1, 2020 to April, 12, 2020 with two days spin up period. On March, 8, 2020, the first emission reductions were observed. On March, 15, 2020, the national lockdown was effective. On March, 28, 2020, the Spanish government banned all non-essential activity. On April, 13, 2020, workers in some non-essential sectors, such as construction and industry, who could not work remotely were allowed to return to work. Based on this date we have split the simulation time period in two symmetric periods with 36 days each one, the first one 01/February – 07/March called as pre-lockdown period and 08/March-12/April called lockdown period.

MODELS

We use the Weather Research and Forecasting model (WRF) with Chemistry (WRF/Chem) model (Grell et al., 2005) and the CAMx with its extension SAT (Source Apportionment) to study the impact of the COVID-19 lockdown measures on air quality in Madrid city. The models were applied over three computational domains, one covering all Iberian Peninsula with a spatial resolution of 25 km, a second nested domain covering Madrid Community with 5 km of spatial resolution and finally the last nested domain with 1 km of spatial resolution over Madrid city. All domain with 35 vertical levels. The WRF/Chem simulation also produce meteorological fields to drive the CAMx simulation.

The chemical initial and boundary conditions were extracted from the output (WACCM 0.9º x 0.-125º) of the Whole Atmosphere Community Climate Model (Marsh et al., 2013). WRF is driven by initial and boundary conditions provided every 6 h by the Global Forecast System (GFS) produced by the European National Centers for Environmental Prediction (NCEP), NCEP GDAS Final Analysis 0.25º (ds083.3)
We obtain anthropogenic emissions in Europe without the influence of COVID-19 lockdown measures (BAU) from the CAMS-REG-AP (Granier et al., 2019) European emission inventory (v4.2_ry 2019) with a 0.05º by 0.1º spatial resolution, processed by the EMIMO (UPM) tool to produce WRF/Chem and CAMx ready emissions (CMBZ-MOSAIC and CB06-CF). To evaluate the effect of the COVID-19 response actions, we conducted another simulation (COVID) in which the anthropogenic emission inventory after March 8 is adjusted to account for the emission changes due to the COVID-19 lockdown. Emissions reductions estimations during the lockdown were published in a recent article (Guevara et al., 2021). Here, we have specific daily reduction rates for the following emission activities: public power, industry, road transport and aviation for each European country.

RESULTS

In the next section results of the simulations are presented. First the evaluation of the simulation and in the next section impacts of lockdown reduction and source appointment analysis.

EVALUATION

We have compared the hourly simulated concentrations with observational hourly data from the Madrid municipality and regional air quality observation networks with 48 monitoring station to analyze the WRF/Chem simulations performance. To have a representative and unique value, statistical performance indicators are calculated using the average values of the 48 monitoring stations and the corresponding model values for the COVID simulation. Results are presented in Table 1 for Normalized Mean Bias (NMB); Root Mean Square Error (RMSE) and Pearson's temporal correlation (R^2).

In general, the performance results of both models show that the simulations capture the magnitude and temporal evolution of the four key air pollutants reasonably well, with the statistical indicators within the expected ranges. Good results have been obtained for NO_2 and O_3 with a small overestimation of NO_2 and underestimation of O_3 in the WRF/Chem simulation. For particulate matter the WRF-CAMx simulation obtains poorer R^2 results and a small underestimation below 20%. The best performance corresponds to the lockdown period. Simulated results for the lockdown period, using the adjusted emission inventory agree better with surface observations than the pre-lockdown period, where the BAU emission inventory is

applied. NMB numbers and correlation coefficient is found to be better than in the pre-lockdown period. The improvement in model performance in the lockdown period demonstrate the good accuracy of the emission restriction estimated in Guevara et al., 2020. This air quality simulation is somehow a validation approach of the emission reductions proposed by Guevara et al., 2021.

Table 10. Performance evaluation of WRF/Chem and WRF-CAMx for pre-lockdown and lockdown periods

		NMB (%)		RMSE (µg/m3)		R^2 [0,1]	
	Model	**Pre-lockdown**	**Lock-down**	**Pre-lockdown**	**Lock-down**	**Pre-lockdown**	**Lock-down**
NO_2	WRF/Chem	18	9	14	9	0.67	0.72
	WRF-CAMx	15	-5	19	10	0.57	0.76
O_3	WRF/Chem	-14	-2	15	13	0.75	0.78
	WRF-CAMx	3	7	15	13	0.74	0.76
PM10	WRF/Chem	18	-18	14	20	0.67	0.46
	WRF-CAMx	-18	-11	20	9	0.46	0.67
PM2.5	WRF/Chem	27	24	11	6	0.53	0.57
	WRF-CAMx	-16	-14	9	5	0.48	0.55

IMPACTS

The proposed approach compares two simulations: COVID simulation which tries to reproduce the observed data in the monitoring stations with emission reductions respect to the BAU simulation (no lockdown restriction) with the two simulation tools WRF/Chem and WRF-CAMx. Figure 1 presents the impacts (differences between COVID and BAU simulations) of lockdown measures on the NO_2 time average concentrations for the period March 08 to April 12.

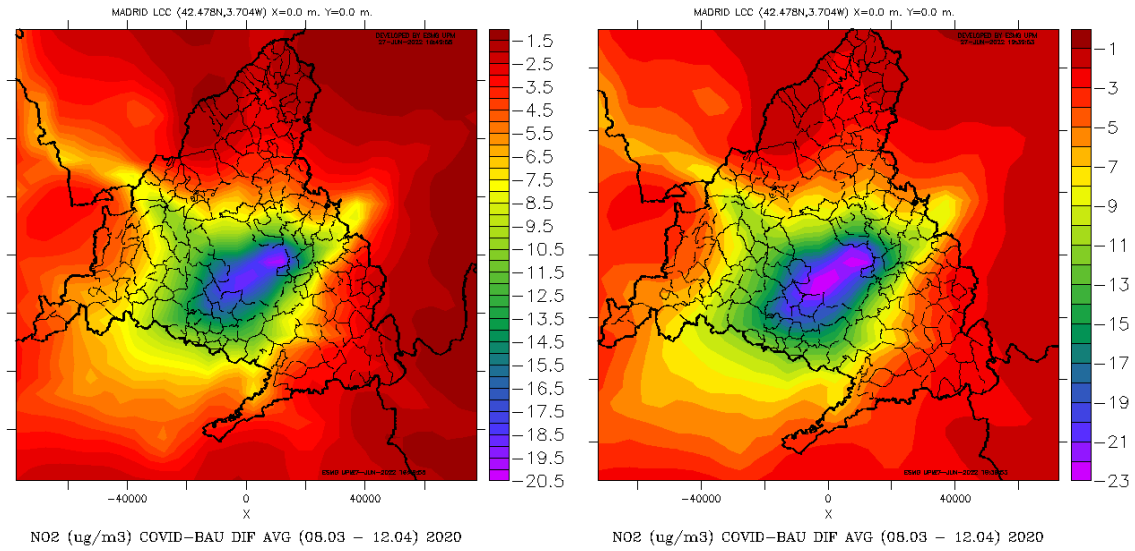

Figure 23. Map of differences (COVID-19BAU) of average surface concentrations (µg m−3) for the period March, 08 to April, 12 for ozone with the WRF/Chem (left) and WRF-CAMx (right).

Figure 1 shows how the impacts on NO_2 concentrations from emission reductions due to lock-down are spatially distributed in a similar way in both models. The largest reduction is seen in the city of Madrid due to the decrease in traffic emissions, in the area of the city of Madrid it is observed that the decreases are a little higher in the WRF-CAMx simulation (-23%) compared to the WRF/Chem (-20%). These decreases in NO_2 concentrations caused increases in O_3 concentrations that are not shown but will be analysed with the source apportionment in the next section.

SOURCE APPOINTMENT

We have applied the technique the Source apportionment (SAT) to estimates the contributions from 4 source areas: North-West (Z1), North-East (Z2), South-West (Z3) and South-East (Z4) quadrants of the computational domain, and 12 emissions categories: Public power (S1), Industry(S2), Other Stationary combustions (S3), Fugitives (S4), Solvents (S5), Road transport (S6), Shipping (S7), Aviation (S8), Off road (S9), Waste (S10), Agricultural livestock (S11) and Other agricultural (S12). The SAT also allows to know the contribution of the boundary conditions. In case of O_3 the SAT methodology also estimates the fractions of ozone formed under VOC- or NOX-limited conditions. In Madrid O_3 formation is dominated by VOC limited conditions it is when the rate of OH production is less than the rate of production of NOx, ozone production is VOC-limited. Here, ozone is most effectively reduced by lowering VOCs in case of NOx reductions, there will be O_3 increments. Figure 2 shows the contribution (%) of the analysed elements with the SAT technology.

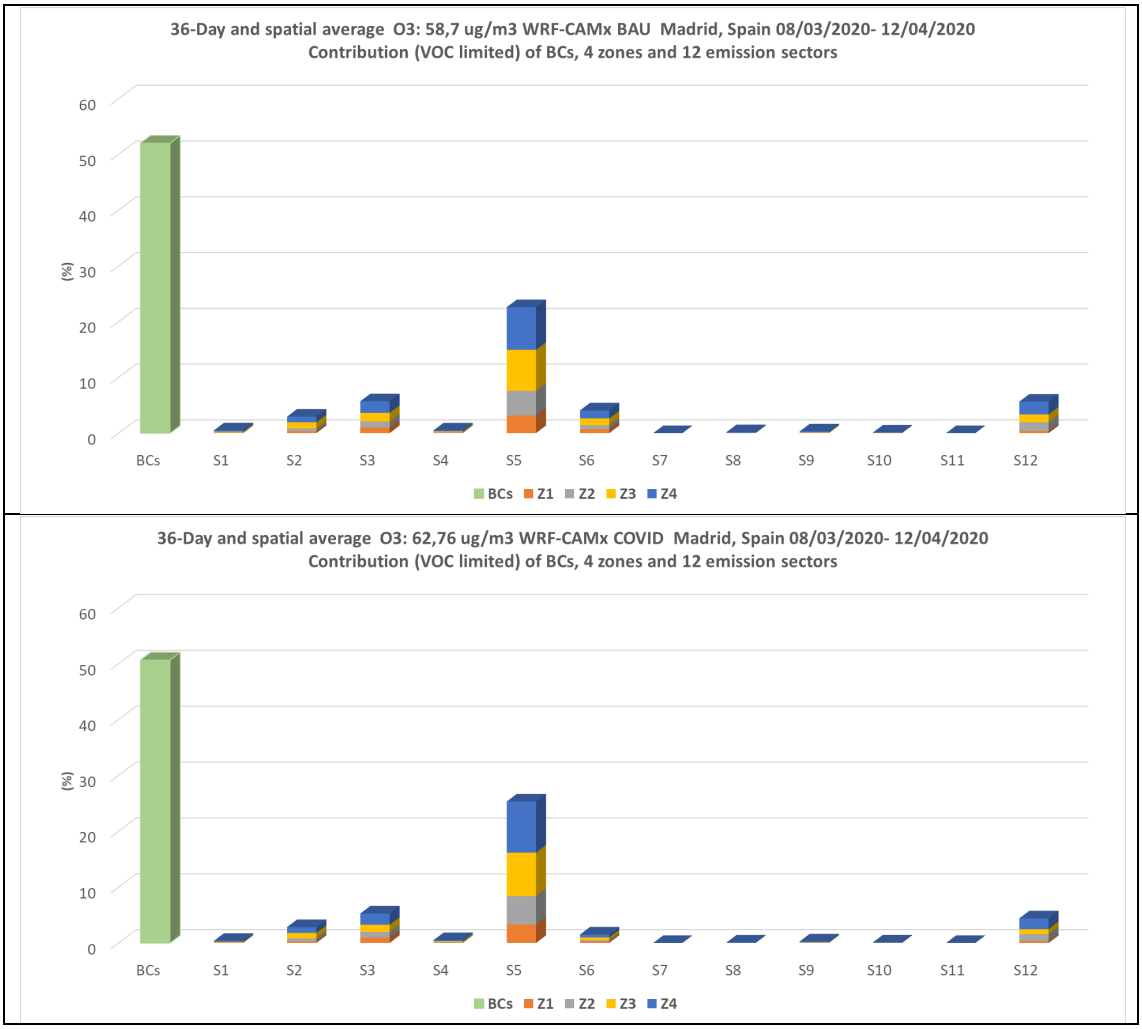

Figure 2. Contribution of the boundary conditions, four zones and twelve emission sources to O_3 average concentration under VOC limited conditions in the simulation BAU (upper) and COVID (lower)

In Figure 2 we can see that 50% of the O_3 comes from the boundary conditions. Solvent use is the main emission source and the contribution is larger in the south of the Madrid region (zone 3 and 4). During

the lockdown period (COVID simulation) there is a reduction of the contribution of road transport (S6), but increase the contribution of solvents (S5) under VOC limited conditions.

CONCLUSIONS

Using the COVID-19 as an unprecedented experiment with substantial emission reductions from multiple sectors (in particular the transport sector), This study helps to elucidate the complex and nonlinear response of chemical composition of the air pollution. The impact of COVID lockdown on Madrid Community (Spain) air quality is estimated by running two simulations, one simulation considers the emission reductions during the lockdown (COVID simulation) and a second simulation, "business as usual" (BAU simulation) with an emissions scenario without restrictions with two air quality models: WRF/Chem and WRF-CAMx Simulated results for the lockdown period, using the adjusted emission inventory agree better with surface observations than the pre-lockdown period, where the BAU emission inventory is applied.

In general, the performance results show that the simulations capture the magnitude and temporal evolution of the four key air pollutants reasonably well, with the statistical indicators within the expected ranges. WRF/Chem underestimates O_3 concentrations (-14%) and WRF-CAMx gets better results (+3%) with a small overestimation. WRF/Chem overestimates PM concentrations and WRF-CAMx underestimates them. WRF/Chem gets better correlation coefficients than WRF-CAMx.

The reduction of emissions mainly from the transport sector, during the COVID-19 lockdown period in all Spain, has produced significant changes in the air quality in the Madrid city in term of reduction of NO_2 concentrations (high reduction), PM10 and PM2.5 concentrations (moderate reduction) and increase in O_3 concentrations (secondary pollutant). The spatial distribution of the impacts of the lockdown are similar in WRF/Chem and WRF-CAMx. WRF-CAMx produces higher impacts than WRF/Chem. BAU-COVID results reflect an important reduction in NOx concentrations and important ozone increases. These increases are higher in WRF/Chem than in WRF-CAMx. Boundary conditions are the main source of the air pollution concentration (40-50%). The O_3 formation is dominated by VOC limited situation. This produces increases of O_3 during the lockdown period (NOx reduction).

The lesson from the COVID-19 lockdown showed that improvement in air quality requires the reduction in NOx emissions accompanied by a well-balanced reduction in VOC emissions to avoid the side effect on urban O_3 pollution. The results evidence that emission mitigation strategies have to be a coordinated and balanced strategy for controlling multiple pollutants and the possible strategies can be simulated before its implementations with air quality modelling tools as used in this experiment.

REFERENCES

Granier, C.; Darras, S.; Denier van der Gon, H.; Doubalova, J.; Elguindi, N.; Galle, B. et al. (2019): The Copernicus Atmosphere Monitoring Service global and regional emissions (April 2019 version). Available online at https://atmosphere.copernicus.eu/sites/default/files/2019-06/cams_emissions_general_document_apr2019_v7.pdf, checked on 2/6/2020.

Grell, G., Peckham, S., Schmitz, R., McKeen, S., Frost, G., Skamarock, W. and Eder, B., 2005. Fully coupled "online" chemistry within the WRF model. Atmospheric Environment, 39(37), pp.6957-6975.

Guevara, M., Jorba, O., Soret, A., Petetin, H., Bowdalo, D., Serradell, K., Tena, C., Denier van der Gon, H., Kuenen, J., Peuch, V. and Pérez García-Pando, C., 2021. Time-resolved emission reductions for atmospheric chemistry modelling in Europe during the COVID-19 lockdowns. Atmospheric Chemistry and Physics, 21(2), pp.773-797.

Marsh, D., Mills, M., Kinnison, D., Lamarque, J., Calvo, N. and Polvani, L., 2013. Climate Change from 1850 to 2005 Simulated in CESM1(WACCM). Journal of Climate, 26(19), pp.7372-7391.

ACKNOWLEDGEMENTS

The UPM authors thankfully acknowledge the computer resources, technical expertise and assistance provided by the Centro de Supercomputación y Visualización de Madrid (CESVIMA).

21st International Conference on
Harmonisation within Atmospheric Dispersion Modelling for Regulatory Purposes
27-30 September 2022, Aveiro, Portugal

RECENT DEVELOPMENTS IN HIGH-RESOLUTION WIND FIELD MODELLING IN COMPLEX TERRAIN FOR DISPERSION SIMULATIONS USING GRAMM-SCI

Dietmar Oettl

Regional Government of Styria, Austria

Abstract: The rather complex terrain in Austria requires that wind fields with sub-kilometer resolutions be generated prior to any kind of dispersion modelling. Proper modelling of highly-resolved flows in alpine regions is still a matter of research and no harmonized methodology is available at the moment. In order to harmonize the meteorological input for dispersion modelling at the regional level, authorities in Austria aim at providing so-called wind-field libraries for a certain reference year for all stakeholders involved in air-quality assessments. The region of Styria was the first one, who established a library using the prognostic, non-hydrostatic mesoscale model GRAMM with a horizontal resolution of 300 m in 2015. Over the years attempts have been made for improving the quality of the wind fields. One of the most challenging issues is the interaction between synoptic-scale flows and local thermally-driven winds. In this work the newly developed mesoscale model GRAMM-SCI is presented, which is driven by ERA5 reanalysis data. Especially, novel nudging techniques allow for nesting and downscaling wind fields with a horizontal resolution of 100 – 200 m. Moreover, a methodology called 'match-to-observation' will be presented, which greatly improves the final quality of wind fields. For the first time, a wind-field library for the reference year 2017 has been generated for Styria with this new approach.

Key words: *GRAMM-SCI, wind-field simulations, complex terrain, ERA5.*

INTRODUCTION

Dispersion modelling in complex terrain is challenging for several reasons but most notably due to the influence of the topography on the local flow field. In particular, the interaction between local thermally-driven winds and synoptic-scale flows influence the dispersion of air-borne substances. Prognostic non-hydrostatic wind-field models are nowadays widely used for providing flow fields for local-scale dispersion models. In Austria, the Graz Mesoscale Modell GRAMM (Oettl, 2020a) has become an important tool for local authorities for generating so-called wind-field libraries, which are subsequently used as input to the Lagrangian Particle Model GRAL (Oettl, 2020b). Up to now, these wind-field libraries were based on a methodology, which did not allow for a proper initialization of GRAMM using large-scale meteorological fields. Since 2019 the GRAMM model has been further developed by the Air Quality Control unit of Styria, Austria, in order to make use of ERA5 reanalysis data (Copernicus Climate Change Service, 2017) for initialization and for prescribing transient boundary conditions. Model description and evaluation studies in alpine regions have already been published by Oettl (2020c), Oettl and Veratti (2021), Oettl (2021), and Oettl and Bergamin (2022). A brief overview about the most important developments will be presented in the next chapter.

Methodology

BRIEF DESCRIPTION OF GRAMM-SCI

In the presence of forests a drag law has been introduced in the conservation equation for the wind components according to

$$-c_D \cdot n \cdot LAD \cdot |U| \cdot u_i, \tag{1}$$

where c_D is an empirical drag-coefficient (0.15n²), n is the dimensionless vegetation coverage, LAD the leave-area density [m²/m³], u_i the wind-speed component [m/s], and U the total wind speed [m/s]. The heights of trees are assumed to be 10 m for agro-forests, and 20 m for all other types. Currently, fixed values for the leave area densities are applied: 0.1 m²/m³ for deciduous and agro-forests, and 0.15 m²/m³ for

coniferous forests. It should be noted that Wagner et al. (2019) and Leukauf et al. (2019) utilized the same approach for the WRF model. Furthermore, as pointed out by Stuenzi et al. (2021) forests have a large impact on radiative and turbulent heat fluxes. One of the main sources for increased surface temperatures within the forest canopy during the night is the so-called below-canopy longwave enhancement. This effect has been accounted for in GRAMM-SCI in a simplified way by reducing the emissivities ε of forested areas.

A new 1.5-order turbulence closure solving the prognostic equation for the turbulent kinetic energy k has been introduced in the current model version using a diagnostic formula for the dissipation rate of the turbulent kinetic energy. The required length scale is hereby calculated according to the proposal of Bougeault and Lacarrère (1989). The original terrain-following grid of GRAMM has been replaced by a hybrid grid using terrain-following coordinates up to the highest elevation within the model domain. Above this height the model levels have exactly the same height above sea level. In this way, strong vertical temperature gradients, i.e. in the transition zone between the troposphere and stratosphere, are captured better improving the representation of large-scale thermal-pressure fields. In the nested model runs, meteorological fields of GRAMM-SCI are nudged towards the corresponding fields of the previous model run using the following equation:

$$\varphi_{Nest} = \varphi_{Nest} - \alpha(\varphi_{Nest} - \varphi_0)dt \quad (2)$$

$$\alpha = e^{-\gamma(z)} \quad (3)$$

φ_{Nest} is any quantity of the nested model run and φ_0 is the corresponding quantity of the model run used for nesting. The variable $\gamma(z)$ not only is height dependent, but takes different values depending on the considered quantity but also on the nesting methodology. In the first model run, where GRAMM-SCI is driven by ERA5 data, $\gamma(z)$ is different than in the second model run, where GRAMM-SCI is nested within GRAMM-SCI. In the last model run, a so-called final downscaling technique is applied, where GRAMM-SCI fields are interpolated on a grid with a very high spatial resolution on an hourly basis. The main idea of the whole nesting methodology derives from the fact that large-scale pressure gradients acting outside of small modelling domains cannot be captured anymore. Therefore, model forcing via lateral boundaries and tentatively nudging techniques are required. Numerous test runs for different areas indicated that the usage of a nudging technique improves results compared when forcing is invoked exclusively at the lateral boundaries. It should be stressed that within the boundary layer a maximum degree of freedom remains in the model equations (i.e. $\alpha \sim 0$) such that local winds can develop. For a detailed description of the entire GRAMM-SCI model the reader is referred to Oettl (2022).

MODEL SETUP

Three nested modelling domains have been used (**Figure 24**). In the largest domain, where GRAMM-SCI has been driven directly by ERA5 reanalysis data, a horizontal grid resolution of 1 km has been defined. ERA5 data based on 6-hour intervals were utilized and boundary conditions have been updated every 3 hours accordingly. 26 layers were defined in the vertical direction and the first grid point 5 m above the surface. The model top was set at 18 km, and the first domain covers an area of 350 x 250 km². In addition, three nested model domains have been defined with a horizontal grid resolution of 400 m, 25 vertical layers with the model top at 15 km. Eventually, 23 subdomains with a horizontal grid resolution of 200 m have been set up, where a downscaling technique has been applied.

In order to establish the wind-field library for the reference year 2017, the time-series for the months January, March, May, July, August, October and December 2017 have been computed, which took about 5 months computation time utilizing two workstations with 16 cores each. In a second step, these hourly stored meteorological fields have been used as input for the so-called match-to-observation algorithm (e.g. Berchet et al., 2017). Hereby, the best-fitting wind field and corresponding stability-class field (derived from the computed meteorological fields of GRAMM-SCI) for each hour of the year is selected based on all available meteorological observations within the modelling domain. The number of stations varyies greatly among the 23 subdomains between only 2 in an alpine area and up to 17 stations in the greater area of Graz. Naturally, with increasing number of available observations it becomes more difficult to select a simulated flow field that would fit perfectly to all observations. Horizontal meandering of atmospheric

flows in low-wind speed conditions, which are extremly frequent in Styria, is one reason, why it is impossible to compute flow fields in perfect agreement with observed wind speeds and –directions at a multitude of monitoring stations at a particular hour of the year (e.g. Marth, 2019).

The final results, which cover the entire year 2017 - even though not the whole year has been simulated initially - will be presented in the next chapter.

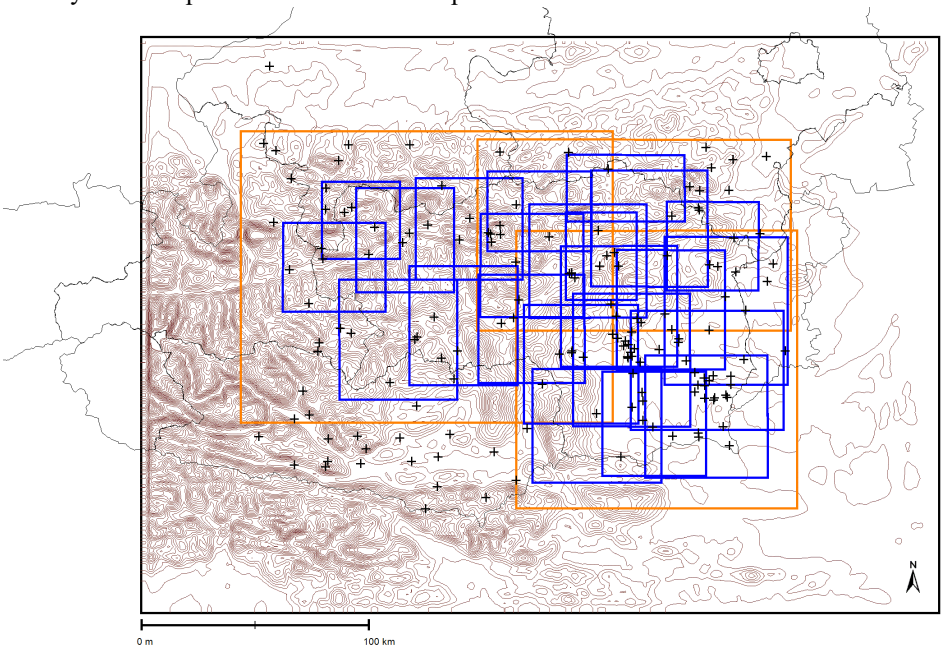

Figure 24. Model domain (black), nested model runs (orange), and downscaling domains (blue). Meteorological observation sites are indicated by crosses

Results

Figure 25 depicts the mean hourly bias of wind speed and –direction averaged according to topographical characteristics of the monitoring sites. The largest bias of 3.4 ms^{-1} is found for monitoring stations at mountain sites due to the high absolute wind speeds usually observed at high altitudes, while the lowest wind speed biases (~0.5 m/s) are evident in basins and valleys characterised by low wind speeds. The differences in wind direction biases is smaller than for wind speed and varies only between 30 and 45 degrees, which is remarkable when considering the uncertainties in modelled wind directions associated with the unpredictable behaviour of horizontal flow meandering in low wind-speed conditions. The bias regarding the annual mean wind speed averaged over all available stations (in total 100) is less than 0.2 ms^{-1}. Even at the mountain sites the bias does not exceed 0.3 ms^{-1}, which would make the wind-field library probably suitable for the assessment of wind-energy potentials, too.

Figure 26 to **Figure 29** illustrate a few examples of observed and modelled wind-direction frequencies. The colours indicate the frequency of certain wind speeds for each sector. Generally, very good results have been obtained with this respect for stations used for the match-to-observation algorithm. Nevertheless, a comparison with observations at monitoring sites not used for the match-to-observation algorithm (because these observations have been made in a different year than 2017) indicate also a satisfying performance of the modelling technique. A presentation of the evaluation at such sites is not possible here due to the page limitation. A comparison between the results presented in **Figure 26** and **Figure 28** is interesting, due to the fact that these monitoring sites are situated only 9 km apart. While the valley station is located at a height of 207 m above sea level, the hill station is at 415 m on top of a small hill. Though the vertical distance between the two sites is just about 200 m, a completely different wind regime is clearly visible. While westerly winds dominate at the valley station, caused by the valley of the river Mur, northerly and southerly winds are characteristic for the hill station indicating that large-scale pressure gradients already influence the station. Furthermore, the mean annual wind speeds are quite different. Notably, GRAMM-SCI is able to simulate such distinctive features.

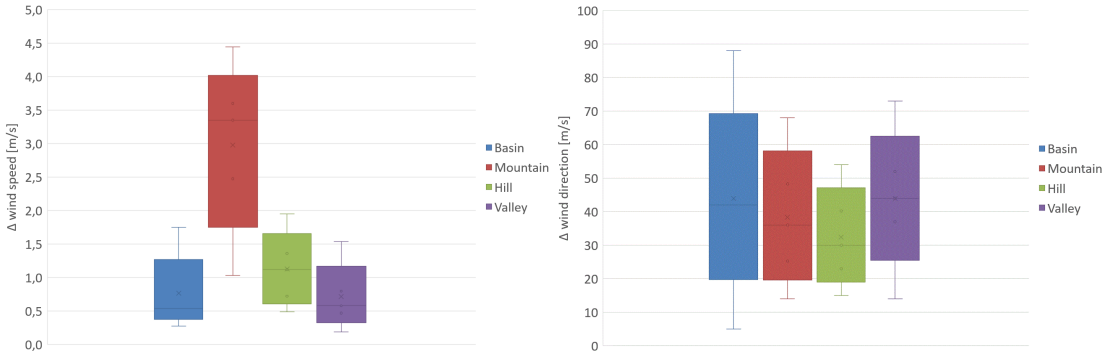

Figure 25. Hourly bias in wind speed and –direction averaged over the entire year and seperated according to the topographical characteristics of the monitoring stations used for the evaluation

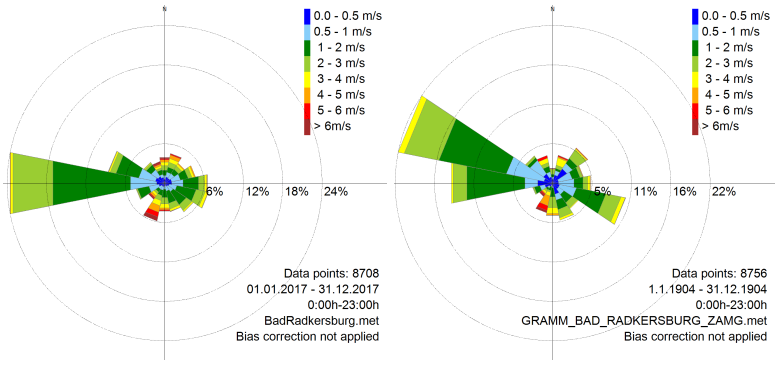

Figure 26. Comparison of observed (left) and modelled (right) wind-direction frequencies for a valley station

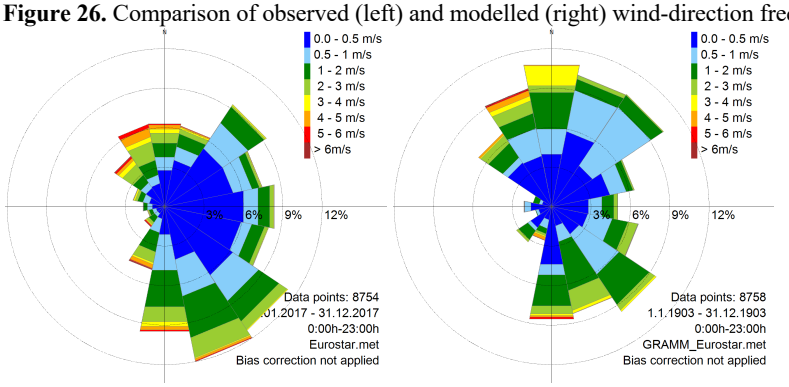

Figure 27. Comparison of observed (left) and modelled (right) wind-direction frequencies for a basin station

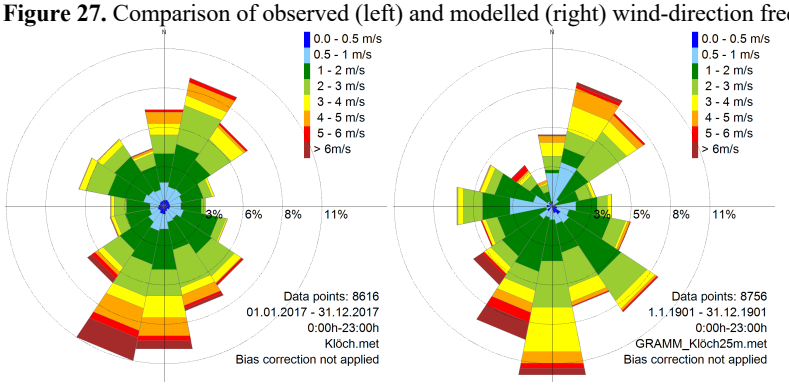

Figure 28. Comparison of observed (left) and modelled (right) wind-direction frequencies for a hill station

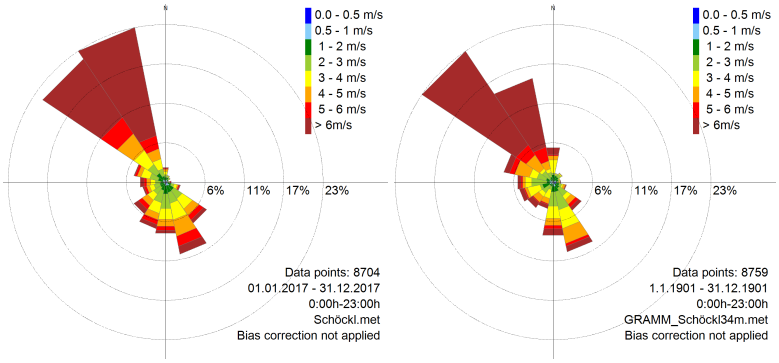

Figure 29. Comparison of observed (left) and modelled (right) wind-direction frequencies for a mountain station

REFERENCES

Berchet, A., K. Zink, C. Müller, D. Oettl, J. Brunner, L. Emmenegger, and D. Brunner, 2017: A cost-effective method for simulation city-wide air flow and pollutant dispersion at building resolving scale. *Atmos Environ*, **158**, 181-196

Bougeault, P., and P. Lacarrère, 1989: Parameterization of Orography-Induced Turbulence in a Mesobeta-Scale Model. *Mon. Wea. Rev.*, **117**, 1872-1890

Copernicus Climate Change Service (C3S), 2017: ERA5: Fifth generation of ECMWF atmospheric reanalyses of the global climate. Copernicus Climate Change Service Climate Data Store (CDS), date of access: *18 Mar 20*. https://cds.climate.copernicus.eu/cdsapp#!/home

Mahrt, L., 2019: Microfronts in the nocturnal boundary layer. *Q. J. Roy. Meteor. Soc.*, **145** (719), 546-562

Oettl, D., 2020a: Documentation of the prognostic mesoscale Model GRAMM Vs. 20.1. Amt d. Stmk. Landesregierung, Graz, 125 pp (http://lampz.tugraz.at/~gral/)

Oettl, D., 2020b: Documentation of the Lagrangian Particle Model GRAL Vs. 20.1. Amt d. Stmk. Landesregierung, Graz, 208 pp (http://lampz.tugraz.at/~gral/)

Oettl, D., 2020c: Evaluierung des nichthydrostatischen mesoskaligen Modells GRAMM-SCI anhand der VDI Richtlinie 3783 Blatt 7. *Gefahrstoffe – Reinhaltung der Luft*, **80**, 318-324

Oettl, D., and G. Veratti, 2021: A comparative study of mesoscale flow-field modelling in an Eastern Alpine region using WRF and GRAMM-SCI. *Atmos Res*, **249**, 105288

Oettl, D., 2021b: Development of the mesoscale model GRAMM-SCI: Evaluation of simulated highly-resolved flow fields in an Alpine and Pre-Alpine region. *Atmos*, **12**, 298, doi: 10.3390/atmos12030298

Oettl, D., and L. Bergamin, 2022: Windfeldsimulationen mit GRAMM-SCI in herausfordernden topographischen Verhältnissen in der Schweiz. *Gefahrstoffe – Reinhaltung der Luft*, (in print)

Oettl, D., 2022: Documentation of the prognostic mesoscale Model GRAMM-SCI Vs. 22.6. Amt d. Stmk. Landesregierung, Graz, 125 pp (https://www.researchgate.net/publication/348620821_Documentation_of_the_prognostic_mesoscale_model_GRAMM-SCI_Graz_Mesoscale_Model_-Scientific)

Stuenzi, S.M., J. Boike, W. Cable, U. Herzschuh, St. Kruse, L.A. Pestryakova, Th. Schneider von Deimling, S. Westermann, E.S. Zakharov, and M. Langer, 2021: Variability of the surface energy balance in permafrost-underlain boreal forest. *Biogeosciences*, **18**, 343-365

s21st International Conference on
Harmonisation within Atmospheric Dispersion Modelling for Regulatory Purposes
27-30 September 2022, Aveiro, Portugal

CALIBRATING MULTI-MODEL ENSEMBLE PREDICTIONS FROM THE JACK RABBIT III INTERNATIONAL MODEL INTER-COMPARISON EXERCISE

Daniel Silk[1], Stephanie Schaap[1], Veronica Bowman[1], Joel Howard[1],Simon Gant[2], Rory Hetherington[2], Adrian Kelsey[2] and Graham Tickle[3]

[1]Dstl, UK
[2]UK Health and Safety Executive
[3]GT Science and Software, UK

Abstract: Structural uncertainty describes the discrepancy between a model and reality. This discrepancy can arise for various reasons, including computational/observational limitations, model simplification, and genuine uncertainty about reality. Without careful analysis, structural uncertainty will propagate as unquantified errors in downstream analysis and decision making. The Jack Rabbit III (JRIII) International Model Inter-Comparison Exercise (IMICE), which aims to inform the future JRIII trial design for large-scale releases of anhydrous ammonia, presents an opportunity to study the structural uncertainty in dispersion modelling. By considering the multiple dispersion models within IMICE as an ensemble, the uncertainty can be quantified and its impact can potentially be minimized. Here we investigate the performance of low-burden ensemble methods, such as Ensemble Model Output Statistics (EMOS), for calibration of multi-model ensemble predictions of centerline concentrations. Furthermore, we explore how multi-model ensembles can be used to guide the experimental design of trials (e.g., the placement of sensors), where the objective is to inform the weights of a model combination, or predictions under other untestable conditions.

Key words: *Jack Rabbit III; dispersion modelling; model combination; uncertainty quantification; trial design*

INTRODUCTION

Structural uncertainty in models is an often overlooked source of error that can propagate to downstream analysis and decision making. If the ensemble includes a sufficiently high-fidelity description of reality, structural uncertainty can be addressed using Bayesian model selection/averaging (Madigan, et al., 1996) (Raftery, 1997). When all models are misspecified to some degree, model selection/averaging tends to over-fit the available data by designating all posterior support to a single model, which can result in inflated confidence in subsequent predictions and analysis (Minka, 2000). In this latter case, Bayesian model combination (Monteith, Carroll, Seppi, & Martinez, 2011) or Bayesian model stacking, ideally using leave-one-out predictions, have been shown to avoid these pitfalls (Yao, Vehtari, Simpson, & Gelman, 2018). However, within the atmospheric dispersion setting, these approaches can require a prohibitive number of model runs. In some instances, the available computational budget may only stretch to a handful, or even a single model run – considerably less than the thousands of runs required to fully explore a high dimensional and complex Bayesian posterior distribution.

This remainder of the abstract considers two scenarios: Firstly, we explore how the effects of structural uncertainty can be quantified and minimized when only point estimates are available from the individual dispersion models. Secondly, we consider a scenario where an expanded computational budget is available to build statistical emulators of the dispersion models. Within this latter context, the full Bayesian toolset

is available, which we use to examine how multi-model ensembles might be harnessed to guide the experimental design of future chemical release trials.

LOW-BURDEN CALIBRATION OF MULTI-MODEL ENSEMBLES

The ability of multi-model ensemble methods to improve predictive power has long been recognized in weather forecasting (Gneiting, et al., 2005) and climate science (Semenov, 2010), and recently has been applied to combine COVID-19 projections (Silk, et al., 2022) (Maishman, et al., 2022). We explore the utility of low-burden multi-model ensemble methods that only require single runs of the individual models for training and prediction. The methods are assessed against observational data from three releases from the FLADIS trials (Nielsen & Ott, 1996), and three releases from the Desert Tortoise trials (Goldwire, 1985), and uses centerline concentration predictions generated by 15 models from the JRIII IMICE. Following (Gneiting, 2005), ensemble predictions are constructed using Ensemble Model Output Statistics (EMOS) which employ regression models with individual model predictions as covariates. The predictions are robustly calibrated by optimizing the regression coefficients with respect to a strictly proper scoring rule (Gneiting & Raftery, 2007) – specifically, the Continuous Ranked Probability Score (CRPS) which is negatively oriented (i.e., lower values correspond to better calibrated predictions). Mathematically, centerline concentration observations, $z(x)$, derived from sensor arrays for each release of each trial are modelled as

$$\hat{z}(x) = a + \sum_{m=1}^{M} b_m y_m(x) + \epsilon, \tag{1}$$

where x includes all the specific trial release conditions (e.g., weather and terrain) and measurement parameters (e.g., distance from source) in sufficient detail so that simulations, $y_m(x)$ can be obtained from the individual models $f_m(x)$. The error term, ϵ, is assumed Gaussian, identically and independently distributed across releases, and with zero-mean and variance modelled as $c + dS^2$, where S is the ensemble standard deviation, and c and d are additional parameters to be optimized with respect to the CRPS. Performance was evaluated within a leave-one-release-out strategy; data from each release was used in turn as the out-of-sample test data, for an ensemble trained on a different set of releases.

The results of applying EMOS to the trials data (illustrated in Figure 30) generally resulted in tight prediction intervals relative to the spread of the individual models, and outperformed the simple mean in most cases. Improved predictive performance was obtained when training and testing was performed within trials, rather than across trials. Table 11. quantifies the utility of the ensemble methods by comparing the CRPS and 95% prediction Interval score (Gneiting & Raftery, 2007) for the EMOS predictions, with those of the ensemble mean and empirical 95% interval, for the full set of six releases. The EMOS method is found to provide better predictions for all but one release.

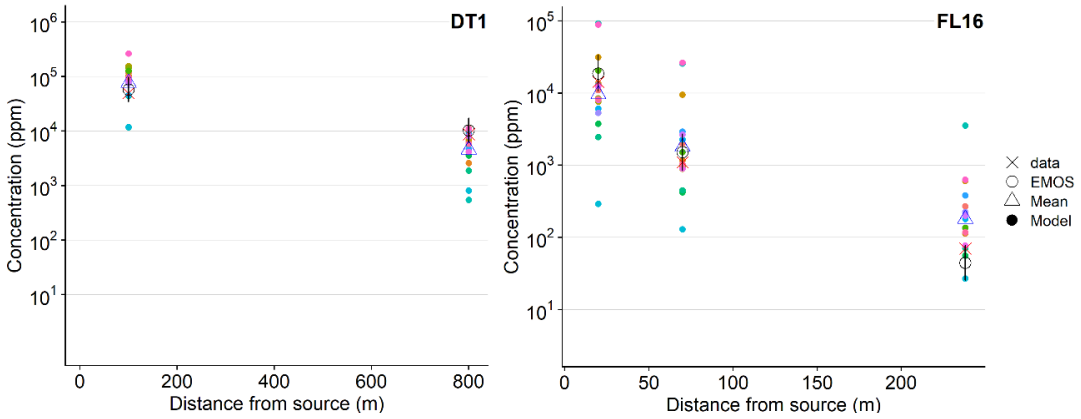

Figure 30. Predictions for centreline concentrations for Desert Tortoise release 1 (left), and FLADIS release 16 (right) from the individual models, EMOS ensemble prediction, and the mean of the individual model predictions. Vertical lines indicate the EMOS 95% prediction interval. The cross show the obervational data.

Table 11. Average *improvement* in CRPS for the EMOS predictive distribution over the empirical ensemble distribution. 95% prediction intervals. Negative values indicate that the EMOS method performs worse. The improvement in the Interval score for the corresponding 95% predictions intervals is also shown.

Release	CRPS Improvement	95% Prediction Interval Score
DT 1	0.071	0.099
DT 2	0.022	0.001
DT 4	0.152	0.221
FLADIS 9	0.120	0.190
FLADIS 16	0.119	0.133
FLADIS 24	-0.079	-0.155

ENSEMBLE GUIDED EXPERIMENTAL DESIGN

A common approach to managing the computational expense of intensive computer code such as dispersion models is to build emulators – statistical meta-models that are cheap to run and may be constructed from a small number of simulations from the original model (Bowman, 2016) (Jackson, 2019). Once built, the emulator can replace (or support) the original model, and the full statistical machinery can be utilized (e.g. (Kennedy, 2001) (Le Gratiet, Marelli, & Sudret, 2017) (Wilkinson, 2014)), whilst accounting for the additional *code uncertainty* arising from their use. The approach is illustrated within a Bayesian Model Combination framework (Monteith, Carroll, Seppi, & Martinez, 2011). Using ideas from information theory, it is shown how a combination of dispersion models, each represented by a Gaussian Process (GP) emulator (Rasmussen, 2003), can be used to guide the design of chemical release trials, in order to maximize the expected information content of the generated sensor data.

The model combination is written as the linear sum

$$z(x,\theta) = \sum_{m=1}^{M} w_m \, g_m(x,\theta) + \epsilon, \tag{2}$$

where

$$w \sim Dir(\alpha); \quad g_m \sim GP[\mu_m(x,\theta), \Sigma_m(x,\theta)]; \quad \epsilon \sim N(0,\sigma^2).$$

Here, the emulators g_m are the result of Bayesian updates of GP priors using training simulations $Y_m = \left(y_{m,1}, y_{m,2}, \dots, y_{m,N}\right)^T$ of the models, f_m, for designs of inputs $\Theta_m = \left(\theta_{m,1}, \theta_{m,2}, \dots, \theta_{m,N}\right)^T$, $X_m = \left(x_{m,1}, x_{m,2}, \dots, x_{m,N}\right)^T$. Prior knowledge about the model weights $w = (w_1, \dots, w_M)$ is represented by a Dirichlet distribution with hyper-parameter α. The variable x represents the experimental control parameters (e.g., sensor locations), and $\theta \sim p(\theta)$ describes the variability in the environmental conditions of the future trials (e.g., weather conditions). The amount of information contained in a future observation, z, about a variable of interest, ϕ, can be quantified using the *mutual information*, which is defined by

$$I_x(z,\phi) = H(\phi) - \int H(\phi|z)p(z)dz\,, \tag{3}$$

where $H(\cdot)$ denotes the Shannon entropy which provides a formal measure of the uncertainty in a probability distribution, i.e.,

$$H(\phi) = -\int p(\phi)\log[p(\phi)]d\phi\,, \quad H(\phi|z) = -\int p(\phi|z)\log[p(\phi|z)]d\phi \tag{4}$$

Note that the dependence of z on x and θ is suppressed for clarity of notation. A Bayesian experimental design protocol seeks the experiment with parameters x that maximizes the mutual information $I_x(z,\phi)$ (Liepe, Filippi, Komorowski, & Stumpf, 2013). Below, this approach is applied to the objective of

identifying the most informative trial design for learning about the weights of the model combination defined in equation (2). Applying the reasoning in (Liepe, Filippi, Komorowski, & Stumpf, 2013), we set $\phi = w = (w_1, \ldots w_m)$ and derive a Monte Carlo estimate for the mutual information between the data arising from trial parameters, x, and the weights of the model combination:

$$I_x(z,w) = \frac{1}{N_1}\sum_{i=1}^{N_1}\left[log\left(\frac{1}{N_3}\sum_{k=1}^{N_3} p\left(z^{(i)}\middle|w^{(i)},\theta^{(k)}\right)\right) - log\left(\frac{1}{N_2}\sum_{j=N_1+1}^{N_2} p\left(z^{(i)}\middle|w^{(j)}\theta^{(j)}\right)\right)\right], \qquad (5)$$

where $\left\{w^{(i)},\theta^{(i)}\right\} \sim p(z,w,\theta) = p(z|w,\theta)p(w)p(\theta)$, $z^{(i)}$ is simulated using equation (2), and $\left\{w^{(j)},\theta^{(j)}\right\}_{j=1,\ldots,N_2}$ and $\left\{\theta^{(k)}\right\}_{k=1,\ldots,N_3}$ are additional Monte Carlo samples drawn from the independent prior distributions, $p(w)$ and $p(\theta)$.

Note that a similar expression can, for example, be derived for the mutual information between $z(x,\theta)$ and the outcome of an unobserved, and perhaps untestable release, $z(x',\theta')$. This would potentially allow a trial to be optimally designed to inform modelling predictions for a specific set of untestable chemical release scenarios of interest. Importantly, from equation (2), $z^{(i)}$ and the conditional probabilities in equation (5) can be rapidly simulated from known sums of conditionally independent normal distributions, e.g.

$$p\left(z^{(i)}\middle|w^{(i)},\theta^{(k)}\right) \sim N\left(\sum_{m=1}^{M} w_m^{(i)}\mu_m(x,\theta^{(k)}), \sum_{m=1}^{M} {w_m^{(i)}}^2\,\Sigma_m(x,\theta^{(k)}) + \sigma^2\right). \qquad (6)$$

The model guided experimental design approach is illustrated below using an emulator of the DRIFT model (using a Gaussian Process with Kronecker product covariance decomposition between x and θ), and sets of toy emulators derived from the DRIFT emulator using non-linear transformations of the input-output space. Together, these emulators represent mock multi-model ensembles that provide ensemble predictions of the centerline concentrations for different potential trial designs.

Figure 31 quantifies the expected amount of information contained within future centerline concentration observations and the model combination weights, for different placements of two sensor arcs. These results and other simulation studies (not shown) demonstrate how *a priori,* informative sensor placements are dependent upon the model ensemble, prior beliefs about the environmental conditions, and the code uncertainty arising from a limited budget of model runs.

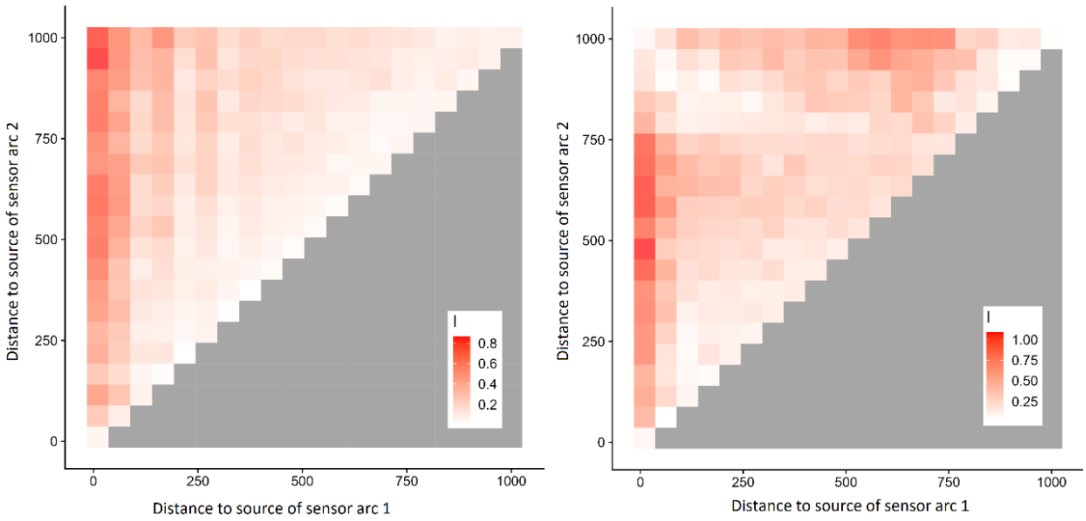

Figure 31. Heatmaps of the expected mutual information (I) between potential observations of the centreline

concentration from two sensor arcs and model combination weights for two different ensembles of five mock dispersion models each.

CONCLUSIONS

Structural uncertainty in models is an often overlooked source of error that can propagate to downstream analysis and decision making. Initial results reported here with the limited available data suggest the utility of low-burden ensemble methods for quantifying and minimizing this uncertainty, whilst improving predictive power. Further effort is required to understand how best to pool information between trials, in order to improve predictive performance across different trial designs.

An important motivation for undertaking the current work is to explore how multi-model ensembles could potentially be used to inform the design of the future JRIII experiments. This study has demonstrated how an emulator-powered Bayesian information theoretic framework can allow the expected information content of different trial designs to be evaluated with respect to structural and other sources of uncertainty.

REFERENCES

Bowman, V. E, 2016: Emulation of multivariate simulators using thin-plate splines with application to atmospheric dispersion. *SIAM/ASA Journal on Uncertainty Quantification*.

Gneiting, T, 2005: Calibrated probabilistic forecasting using ensemble model output statistics and minimum CRPS estimation. Monthly Weather Review.

Gneiting, T., & Raftery, A. E, 2007: Strictly proper scoring rules, prediction, and estimation. Journal of the American statistical Association.

Goldwire, H. E, 1985: Desert Tortoise Series Data Report 1983 Pressurized Ammonia Spills. Lawrence Livermore National Laboratory.

Hetherington, R., et. al, 2022: DRIFT modelling of the Desert Tortoise and FLADIS ammonia trials for the Jack Rabbit III model inter-comparison exercise. In Preparation.

Jackson, S. E, 2019: Bayes Linear Emulation of Simulator Networks. 10.48550/ARXIV.1910.08003.

Kennedy, M. C, 2001: Bayesian calibration of computer models. Journal of the Royal Statistical Society: Series B

Le Gratiet, L., Marelli, S., & Sudret, B, 2017: Metamodel-based sensitivity analysis: polynomial chaos expansions and Gaussian processes. Handbook of uncertainty quantification.

Liepe, J., Filippi, S., Komorowski, M., & Stumpf, M. P, 2013: Maximizing the information content of experiments in systems biology. PLoS computational biology.

Madigan, D., Raftery, A. E., Volinsky, C., & Hoeting, J, 1996: Bayesian model averaging. Proceedings of the AAAI Workshop on Integrating Multiple Learned Models, Portland, OR.

Minka, T. P, 2000: Bayesian model averaging is not model combination. Available electronically at http://www. stat. cmu. edu/minka/papers/bma. html.

Monteith, K., Carroll, J. L., Seppi, K., & Martinez, T, 2011: Turning Bayesian model averaging into Bayesian model combination. The 2011 International Joint Conference on Neural Networks.

Nielsen, M., & Ott, S, 1996: Fladis field experiments. Final report.

Raftery, A. E, 1997: Bayesian model averaging for linear regression models. Journal of the American Statistical Association.

Rasmussen, C. E, 2003: Gaussian processes in machine learning. I Summer school on machine learning. Springer.

Semenov, M. A, 2010: Use of multi-model ensembles from global climate models for assessment of climate change impacts. Climate research.

Silk, D. S., Bowman, V. E., Semochkina, D., Dalrymple, U., & Woods, D. C, 2022: Uncertainty quantification for epidemiological forecasts of COVID-19 through combinations of model predictions. Statistical Methods in Medical Research.

Maishman, T., et. al, 2022: Statistical methods used to combine the effective reproduction number, R(t), and other related measures of COVID-19 in the UK. Statistical Methods in Medical Research.

Wilkinson, R, 2014: Accelerating ABC methods using Gaussian processes. Artificial Intelligence and Statistics.

Yao, Y., Vehtari, A., Simpson, D., & Gelman, A, 2018: Using stacking to average Bayesian predictive distributions. Bayesian Analysis.

21st International Conference on
Harmonisation within Atmospheric Dispersion Modelling for Regulatory Purposes
27-30 September 2022, Aveiro, Portugal

INNOVATIVE PROBABILISTIC MODELLING OF RISK ZONES IN THE EVENT OF ACCIDENTAL ATMOSPHERIC RELEASES

Maéva Caillat[1], Valentin Pibernus[1], Sylvain Girard[1], Patrick Armand[2] and Christophe Duchenne[2]

[1]PHIMECA Engineering, F-75012 Paris, France
[2]CEA, DAM, DIF, F-91297 Arpajon, France

Abstract: 3D models present very promising prospects for simulating the local-scale and high-resolution distribution of releases which are potentially dangerous for human health and the environment. To encourage the taking into account of their results by the rescue teams and their authorities, it is today very desirable that the concentration or dose maps produced by the 3D models also provide information on the uncertainties associated with them. To do so, we developed a methodology to accurately estimate the probability of exceeding a concentration threshold in the event of accidental or malevolent releases into the atmosphere. This methodology assesses uncertainty with confidence or credible intervals using alternatively the frequentist approach and a novel Bayesian approach based on spatial Gaussian processes able to lower the limit of significance of the probability estimation. The Bayesian approach was validated on synthetic data, then used in the frame of a real situation inspired by the Lubrizol accident in January 2013 in Rouen (France). We show that the Bayesian model gives more accurate and narrower than the classical confidence intervals, and is able to lower the significance limit of the estimate, thus to draw decision maps which are of real help in view of decision-making.

Key words: *Atmospheric dispersion, danger zones, uncertainty estimation, probabilistic approach.*

INTRODUCTION

At the local scale, the flow and dispersion in the atmosphere are strongly influenced not only by the synoptic meteorological situation, but also by the details of topography and land-use and the presence of buildings, if any. Thus, 3D models are well suited for the assessment of chemical or radiological releases into the air that may have consequences on human health and the environment. These models are more and more used both for regulatory purposes and emergency preparedness and response. Decision-makers, like operators of industrial facilities, civil security officials or public authorities, would be ready to exploit these models provided they are embedded in operational decision-support systems. Moreover, the scientific community and, increasingly, the users are well aware of the uncertainties on the input data of the models, the models themselves and the representativeness of their results. It is therefore highly desirable that part of the research on atmospheric dispersion be oriented towards taking uncertainties into account.

In this short paper, we take an interest in a case study inspired by the industrial accident that occurred in January 2013, at the Lubrizol chemical plant located in Rouen (France). Operational mistakes and system failures in the plant resulted in extended releases of hydrogen sulfide and mercaptan, both of which are foul-smelling when they exceed a specified concentration. The features of the incident are very complex in several respects, namely the terrain characterized by a rugged topography and alternating industrialized, urban and natural areas, the long-lasting and variable kinetics of the releases combined with the highly fluctuating meteorological conditions during and after the releases.

We simulated the dispersion of pollutants in the atmosphere using a modeling system whose input data, notably meteorological or related to the source term, are extremely uncertain. While epistemic uncertainties are not the only ones, taking them into account in a probabilistic framework is absolutely required for reliable decision-making (Girard *et al.*, 2020). In this study, our objective was to estimate the probability of exceeding a concentration threshold that might represent a certain level of danger in the context of atmospheric dispersion. We took a step-by-step approach. We estimated the area where the concentration threshold was exceedeed by a unique deterministic simulation. Then, we performed several simulations and evaluated point by point the probability of exceedance of the concentration threshold. Then, we tried to estimate the confidence and credible intervals associated to a given probability of exceedance. While this

approach succeeds in accounting for the uncertainties, it highlights the limit of significance. Eventually, to lower this limit, we used a credible interval with a conditional spatial independence criterion.

In the short paper, we present the PMSS simulations carried out to create the Lubrizol accident data set, the deterministic map of the area where a given concentration threshold is exceeded, the probabilistic decision map of the same area and the confidence intervals, our Bayesian approach exploiting the spatial correlation of the concentrations, and finally, the results of this approach, which are commented on.

PMSS FLOW AND DISPERSION SIMULATIONS

The simulations were performed with Parallel-Micro-SWIFT-SPRAY (PMSS). Originally, Micro-SWIFT-SPRAY (MSS) (Tinarelli *et al.* ,2013) was developed to provide a simplified but rigorous CFD solution in a limited amount of time of the flow and dispersion in built-up environments. MSS combined the high resolution local scale versions of SWIFT and SPRAY models. SWIFT is a 3D diagnostic mass-consistent model using a terrain-following vertical coordinate. Large-scale meteorological data, local meteorological measurements, and analytical results of formulae in building-modified flow areas, if any, are interpolated and adjusted to generate 3D wind fields. Turbulent flow parameters are also computed by SWIFT to be used by SPRAY. SPRAY is a Lagrangian particle dispersion model able to take into account the presence of obstacles. The dispersion of the release is simulated by following the trajectories of a large number of numerical particles. Trajectories are obtained by integrating in time the particle velocity, which is the sum of a transport component defined by the local averaged wind, generally provided by SWIFT and a stochastic component, representing the dispersion due to atmospheric turbulence.

SWIFT and SPRAY handle complex terrains and changing meteorological conditions, as well as specific release features, such as heavy or light gases. Recently, SWIFT and SPRAY were parallelized across time, space and numerical particles, resulting in the PMSS system (Oldrini *et al.*, 2017). The parallelism was shown to be very efficient, both on a multi-core laptop and on clusters of several hundreds of cores in a high-performance computing center (Oldrini *et al.*, 2019) (Armand *et al.*, 2021). PMSS was systematically validated against experimental wind tunnel and field campaigns for short and extended releases (Trini Castelli *et al.*, 2018). In all configurations, the PMSS results complied with the statistical acceptance criteria defined by Hanna and Chang (2012) used for validating dispersion models in built-up environments.

DETERMINISTIC DECISION MAP

We simulated chemical concentrations in the air generated by the accident that happened on January 2013 at the Lubrizol chemical plant in Rouen (France). Hydrogen sulfide and mercaptan were released from the plant stacks throughout the accident. Consequently, thousands of people smelled the chemicals, some of them suffering from nausea and headaches. In our study, we considered the 35-kilometer wide square area centered on the incident site. The simulation covered a 35-hour period, so that all hazardous materials were either deposited or left the simulation domain by the end of the period. The input meteorological data were obtained from the community weather reconstruction and forecast meso-scale modelling system WRF (Skamarock *et al.*, 2005). The source term was adapted from data established by Ismert and Durif (2014). Our objective was to predict whether an arbitrary concentration threshold was exceeded on the studied area over the whole period. We chose a threshold value, namely 2 $\mu g.cm^{-3}$, to create a fictitious restricted area where the population and first responders could be at risk. **Figure 1** shows the results of the deterministic simulation. Even if this model enables us to make some predictions on the concentrations, it does not take account of uncertainty. Yet, the inputs are substantially uncertain, and the results are too.

PROBABILISTIC DECISION MAP AND CONFIDENCE INTERVALS

Next, we accounted for uncertainty in the input parameters and carried out 100 simulations using PMSS with different sets of the wind speed, wind direction, rain intensity, and release rate of the chemical. The small sample size is representative of an emergency, for which results must be given as quickly as possible, while each simulation requires up to one hour and are run in parallel on suitable computing resources.

Let $Y(s,t)$ be the term of propagation of uncertainty, *i.e.* the chemical concentration at a given point s and time t. In the study, we focus on the maximum temporal concentration at each location throughout the simulation $Y(s) = \sup_{t\in[t_0,t_{\text{simu}}]} Y(s,t)$. Let $X(s,t)$ be the random vector of uncertainties, which can contain any kind of information, such as the spatial coordinates or distance to the source term or variables like wind speed, wind direction, rain intensity or release rate. Denoting the atmospheric dispersion model by f, we wish to assess the distribution of $Y(s,t) = f\big(X(s,t)\big)$. Let $\zeta \in \mathbb{R}^+$ be a concentration threshold and $Z(s) = I_{\{Y(s)>\zeta\}}$ a variable worth 1 if the concentration exceeds the concentration threshold at a s and 0 otherwise. $p_X(s) = \Pr(Y(s) > \zeta)$ represents the probability that the concentration at s is higher than the concentration threshold. Z follows a Bernoulli distribution of parameter p_X: $Z \sim \mathcal{B}(p)$. Let $p_{lim} \in \mathbb{R}^+$ be the threshold of the probability of exceeding a concentration. We focus on the event $\{p_X(s) > p_{lim}\}$ to make decision.

Let's now consider independent and identically distributed random variables $Z_i(s)\ \{i = 0 \dots n\}$ that follow a Bernoulli distribution of parameter $p_X(s)$. Let $S_n(s) = \sum_{i=1}^{n} Z_i\,(s) \sim \mathcal{B}\big(n, p_X(s)\big)$ be the number of times the concentration at s exceeds the threshold or the binomial distribution with parameters n and $p_X(s)$. In a previous work (Girard *et al.*, 2020), we estimated $p_X(s)$ with the sample mean estimator $\hat{P}_n(s) = S_n/n$. **Figure 2** shows the estimated probabilities of exceeding the chosen threshold concentration of 2 µg.cm^{-3}. Colors indicate the probability from 0 (yellow) to 1 (black).

Unfortunately, a decision based on a point estimator does not inform us about the estimation uncertainty, contrary to credible and confidence intervals (*N.B.* credible intervals account for an actual observed sample, here dispersion simulations, which is not the case for confidence intervals). These intervals set limits to $p_X(s)$ thanks to two estimators, the lower and upper bounds of the interval $L_X(S_n(s),\alpha)$ and $U_X(S_n(s),\alpha)$. Let $I_X(n,s,\alpha)$ be a confidence or credible interval which contains $p_X(s)$ with a confidence level of $1-\alpha$, with α the risk accepted to be as low as possible. The actual coverage probability at a fixed value of p_X is an estimate of the probability that the interval actually contains p_X. A conservative interval has its actual coverage probability greater or equal to the nominal confidence level $1-\alpha$. Conversely, a mean correct interval has a mean coverage probability of at least $1-\alpha$, but its actual coverage probability is lower for extreme values of p_X, close to 0 or 1. In this study, we focused on mean correct intervals, as they are narrower than conservative ones. For $n \geq 40$, Brown *et al.* (2001) recommend the adjusted Wald interval, also called Add 4 (Agresti and Coull, 1998). A confidence or credible interval is divided into three zones, each one with a different decision-making. **Figure 3** shows examples of these maps:

- In the red area where the lower bound of the interval is greater than p_{lim}, there is strong evidence that we exceed the critical level at location s.
- In the white area where the upper bound of the interval is lower than p_{lim}, there is strong evidence that we are below the critical level at location s.
- In the grey area where p_{lim} is enclosed by the interval bounds, it is not easy to compare p_X and p_{lim} and the result is non significant.

The left and right decision maps on **Figure 3** are computed with the same data and parameters, except for the probability threshold p_{lim}. It illustrates the loss of significativity phenomenon: when p_{lim} goes under a certain value (dependent on sample size and confidence level), the map becomes useless to the decider!

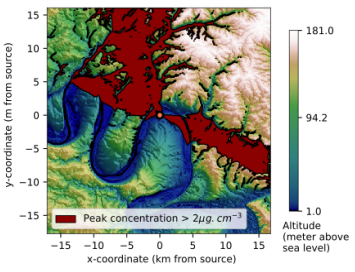

Figure 1. Concentration map of the chemical with a given concentration threshold.

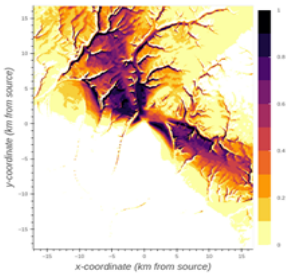

Figure 2. Probability of exceeding the concentration threshold with the sample mean.

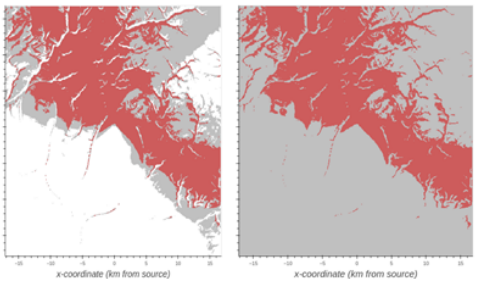

Figure 3. Decision maps accounting for credible intervals computed with the same parameters, except for the probability threshold p_{lim} going from 5% (left) to 4% (right).

INTRODUCING SPATIAL CORRELATION IN THE BAYESIAN APPROACH

In the previous model, the n-sample $Z_1(s),\dots,Z_n(s)$ of $Z(s)$ was supposed to be independent for every location $s \in \mathbb{R}^2$ and the spatial structure of the data was ignored. However, any geostatistical data have a continuously varying response in space. Therefore, the information in location s may help improving the estimations in nearby points $s+h$. From now on, let's consider Bayesian statistics, where the parameter p_X becomes the random variable P_X, and the hierarchical model inspired from Diggle and Ribeiro (2007):

$$S_n(s) \mid P_X(s) = \sum_{i=1}^{n} Z_i(s) \mid P_X(s) \sim \mathcal{B}\big(n, p_X(s)\big) \quad (1)$$

$$logit\big(P_X(s)\big) \mid \beta, \tau, \lambda \sim \text{GaussianProcess}\left(X^T(s)\,\beta, \gamma(h) = \tau\, exp\left(-\frac{\|h\|}{\lambda}\right)\right) \quad (2)$$

with $X(s)$ the design matrix, β a mean parameter, τ a variance parameter, and λ a scale parameter. Equation (1) assumes the conditional independence of $S_n(s)$ which is the number of times the concentration threshold is exceeded at location s. A spatial Gaussian process $\{SGP(s): s \in \mathbb{R}^2\}$ is a stochastic process of which the joint distribution $SGP = \{SGP(s_1) \dots SGP(s_K)\}$ is multivariate normal for every set of positions $\{s_1 \dots s_K\}$ with $s_j \in \mathbb{R}^2$. Any such process is completely defined by its mean function $\mu(s) = \mathbb{E}[SGP(s)]$, and its covariance function $\gamma(s,s') = \text{cov}\big(SGP(s), SGP(s')\big)$.

For a set of positions $\{s_1 \dots s_K\}$, let's define the isotropic spatial Gaussian process SGP_X as this:

$$SGP_X = \{SGP_X(s_1) \dots SGP_X(s_K)\} = \big\{logit\big(P_X(s_1)\big) \dots logit\big(P_X(s_K)\big)\big\} \sim \mathcal{N}_K(\mu, \Sigma) \quad (3)$$

with the K-dimensional mean vector $\mu = \Big(\mu\big(s_j\big)\Big)_{j=1}^{K} = \big(X^T(s_j)\beta\big)_{j=1}^{K} = X^T\beta$,

and the KxK-dimensional matrix Σ such that $\Sigma_{ij} = \gamma\big(s_i, s_j\big) = \tau exp\left(-\frac{\|s_i - s_j\|}{\lambda}\right)$.

The covariance function $\gamma: \mathbb{R}^2 \times \mathbb{R}^2 \to [0, \tau]$ is negligible with respect to τ at a distance of more than 3λ.
The design matrix is $X(s) = [1 \quad X^{(1)}(s) \quad X^{(2)}(s) \quad X^{(3)}(s)]^T$ with the explanatory variables being $X^{(1)}(s)$ the y-coordinate, $X^{(2)}(s)$ the x-coordinate, and $X^{(3)}(s)$ the distance to the source term.

Prior distributions encode our initial knowledge about the parameters of the model. As the parameters $(\beta_i)_{i \in [\![1,4]\!]}$ can take any value in $\mathbb{R}$, we choose a normal distribution *a priori*: $\forall i \in [\![1,4]\!]\ \beta_i \sim \mathcal{N}\big(\mu_{\beta_i}, \sigma^2_{\beta_i}\big)$. As the parameter τ is the variance of $SGP_X(s)$ for any location, we choose an inverse gamma distribution because it is defined on $\mathbb{R}^+$ and induces conjugate distributions: $\tau \sim \text{InvGamma}(\delta_\tau, \phi_\tau)$. As the parameter λ must be strictly positive, we choose a gamma distribution a priori: $\lambda \sim \Gamma(k_\lambda, \theta_\lambda)$.

To build the posterior distribution of $\{P\big(s_j\big): j \in [\![1,K]\!]\}$ from n observations of $Z\big(s_j\big)$, we use Monte Carlo Markov chains whose stationary distribution corresponds to the posterior distribution in Bayesian statistics. Except for τ which is an inverse gamma distribution, the posterior distributions of β_i, λ and $SGP_X\big(s_j\big)$ are constructed using the Metropolis-Hastings algorithm within a Gibbs sampler (Geman and Geman, 1984). Finally, we built a Markov chain for β, τ, λ and $SGP_X\big(s_j\big)$, that is to say a chain of dimension *lenbeta* (the dimension of β) + 2 + K (the number of points of the map).

RESULTS OF THE BAYESIAN APPROACH AND DISCUSSION

Application and validation of the spatial Gaussian process

First, the method was tested on simulated data to ensure the existence of the parameters β^{true}, τ^{true} and λ^{true}, which we tried to retrieve. We generated a simulation SGP_X^{simu} of the spatial Gaussian process $SGP_X \sim \mathcal{N}\big(X^T\beta^{true}, \Sigma(\tau^{true}, \lambda^{true})\big)$. SGP_X is a vector of dimension K, which we can represent as an exceedance probability map of dimension $\sqrt{K} \times \sqrt{K}$ by applying to it the expit function which sends $\mathbb{R}$ to [0,1]. Thus, we used this realization to simulate $S_n^{\text{simu}}(s) \sim \mathcal{B}(n, P_X^{\text{simu}}(s) = expit\left(SGP_X^{\text{simu}}(s)\right)$.

We assigned fictive values to the parameters ($\beta^{true} = [-8, 0.2, 0.2, -0.3]$, $\tau^{true} = 1$, $\lambda^{true} = 1$, and $n = 100$) to assess the model and considered uninformative or low-informative prior distributions as follows:

$\forall i \in [\![1,4]\!]\ \beta_i \sim \mathcal{N}\big(\mu_{\beta_i} = 0, \sigma^2_{\beta_i} = 100\big)$, $\tau \sim \text{InvGamma}(\delta_\tau = 1, \phi_\tau = 1)$, and $\lambda \sim \Gamma(k_\lambda = 2, \theta_\lambda = 0.5)$

Figure 4 shows a realization of this process used as the target for the probability estimation algorithm.

In the next step, β_i were randomly initialized between -1 and 1. We arbitrarily initialized τ at 1 because it is the order of magnitude of the parameters that interest us: $\tau \leq 0.1$ is almost trivial and $\tau \geq 10$ renders very unstructured, white noise type maps. We also arbitrarily initialized λ at 1 so that it adapts to the size of the map. Expert knowledge could allow a better initialization on real data. Since we suspect that the true value of S is around the sample mean, we initiliazed $SGP_X(s_j)$ at its sample mean. We fixed the variances of the proposal kernels to have an acceptance rate close to 0.234.

Markov chains (not presented in this short paper) of the MCMC algorithm were output for 10,000 iterations, removing the first 2,000 terms, notably the burning period, as well as one term out of two to reduce the temporal dependence of the chain. The MCMC algorithm has good mixing properties, since the output Markov chains look like a Gaussian noise. All the chains are centered on their true parameters: $\beta_{mean} = [-7.95, 0.20, 0.21, -0.31]$, $\tau_{mean} = 1.06$, and $\lambda_{mean} = 1.03$. As expected, τ and λ are highly correlated.

Performances of the Bayesian method

While the Bayesian approach slightly improves point estimation, its main interest lies in interval estimation. To compare the Bayesian and Add 4 intervals, we generated 1,000 maps of size 10 x 10, thus a total of 100,000 different locations and we drew $n = 100$ realizations of $\mathcal{B}(P(s))$. From this sample, we estimated the uncertainty on $P_X(s)$ by building Bayesian and Add 4 credible intervals for each location. We could then compute the average coverage probability by assessing how many intervals contained the actual value $P_X(s)$ among the 100,000 different locations. **Table 1** compares the performances of the Bayesian and Add 4 intervals, computed with the test case illustrated in **Figure 4**. With smaller average coverage probability, Bayesian intervals are slightly less conservative, but they achieve significantly smaller expected widths (20% on average) than those computed with the Add 4 method, which make them an attractive choice.

Table 1. Average coverage probability and expected width of the Bayesian and the Add 4 intervals.

Interval	Average coverage probability	Expected width
Bayesian at 95%	94.3% ± (8.2% x 10^{-2})	(1.29 x 10^{-1}) ± (5.9 x 10^{-4})
Bayesian at 99%	98.3% ± (4.4% x 10^{-2})	(1.64 x 10^{-1}) ± (7.5 x 10^{-4})
Add 4 at 95%	95.6% ± (6.6% x 10^{-2})	(1.55 x 10^{-1}) ± (5.0 x 10^{-4})
Add 4 at 99%	99.2% ± (2.9% x 10^{-2})	(2.04 x 10^{-1}) ± (6.6 x 10^{-4})

Bayesian intervals as part of a decision making process

Bayesian intervals bring two improvements when drawing decision maps as those on **Figure 3**:

- It reduces the width of the gray zone of a significant amount.
- It counteracts the loss of significativity by preventing the grey zone to spread when considering small probability threshold or small risk, what is the main interest of our Bayesian estimator.

Figure 5 shows the decision maps drawn with the Add 4 confidence interval and our Bayesian hierarchical model for the Lubrizol data set. It illustrates the capacity of the Bayesian estimator to be robust against loss of significativity and produce a map that, unlike the Add 4 interval, is actually usable by decision-makers.

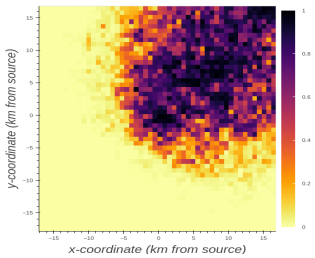

Figure 4. Target probability map generated for testing the Bayesian algorithm.

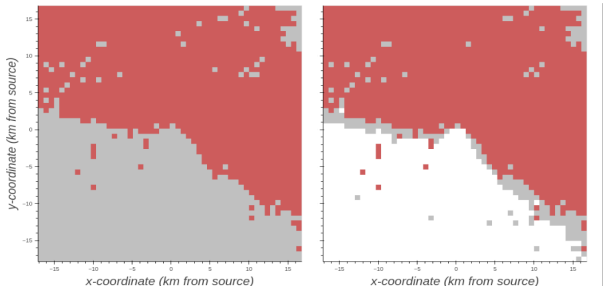

Figure 5. Decision maps obtained with the Add4 interval (left) and the Bayesian estimators (right).

Computational times

Computational times on an Intel Core i7-10810U processor with a speed between 1.1 GHz and 4.9 GHz are given in **Table 2** for different numbers of locations *K* and 10,000 MCMC iterations. The MCMC algorithm is very time-consuming and the main limitation in the implementation of the Bayesian hierarchical model in comparison with the Add 4 method.

Table 2. Computational time depending on the number of locations K and for $N_{chain} = 10,000$ iterations.

Number of locations	MCMC computation time	Add 4 computation time
25	9 s	0.01 s
900	28 min 7 s	0.11 s
2,500	12 h 48 min 1 s	0.22 s

CONCLUSION

In this short paper, we compare two different strategies for building decision maps from interval estimation of the probability of exceeding a concentration threshold: the classical frequentist approach and a novel Bayesian approach. This is a step forward decision maps built-up from point estimation of the exceedance probabilities presented in Girard *et al.* (2020). The Bayesian approach is extensively tested with synthetic data and applied to a case study inspired by the Lubrizol accident in January 2013 in Rouen (France).

While confidence or credible intervals are associated with a controllable nominal risk and extremely useful to construct decision maps, they have a limit of significance. Indeed, when the sample size, the accepted risk and/or the probability threshold become small, the decision map may be of no use to make decisions. To solve this problem, we implemented a Bayesian hierarchical model based on spatial Gaussian processes to encode the spatial dependence of the probabilities of exceeding a concentration threshold between nearby points in the probabilistic model. We showed on simulated data that the Bayesian model was more accurate and narrower than the Add 4 confidence intervals, and able to lower the significance limit of the estimate, thus to draw informative decision maps when Add 4 was of no help for this. However, the computational time of the Bayesian model was much longer than Add 4, especially for a large number of points on maps.

To the best of our knowledge, this is the first time that a scientifically reliable method has the potential to provide information in emergency involving atmospheric releases on the confidence level of concentration maps. In the future, we plan to reduce the computational time of the Bayesian model by running iterations of the MCMC algorithm simultaneously and making points absolutely independent after a certain distance. We also plan to transform our decision method into an interactive and user-friendly tool that could help better grasp the concept of estimation uncertainty on decision maps.

REFERENCES

Agresti, A. and B.A. Coull, 1998: Approximate is better than "exact" for interval estimation of binomial proportions. The American Statistician, 52 (2), 119–126.

Armand, P., O. Oldrini, C. Duchenne and S. Perdriel, 2021: Topical 3D modelling and simulation of air dispersion hazards as a new paradigm to support emergency preparedness and response. Environmental Modelling & Software, 143, 105–129.

Brown, T.T., L.D.Cai and A. Das Gupta, 2001: Interval estimation for a binomial proportion. Statistical Science, 16 (2), 101–117.

Geman, S. and D. Geman, 1984: Stochastic relaxation, Gibbs distributions, and the Bayesian restoration of images. IEEE PAMI-6.

Girard, S., P. Armand, C. Duchenne and T. Yalamas, 2020: Stochastic perturbations and dimension reduction for modelling uncertainty of atmospheric dispersion simulations. *Atmospheric Environment*, 117313.

Hanna, S. and J. Chang, 2012: Acceptance criteria for urban dispersion model evaluation. Meteorology and Atmospheric Physics, 116, 133–146.

Ismert, M. and M. Durif. 2014: Accident de Lubrizol du 21 janvier 2013. Couplage entre dispersion du nuage odorant et plaintes et appréciation des risques sanitaires associés. Rapport INERIS-DRC-13-137709-03375 B.

Oldrini, O., P. Armand, C. Duchenne and S. Perdriel., 2019: Parallelization performances of PMSS flow and dispersion modelling system over a huge urban area. *Atmosphere*, 10 (7), 404–420.

Oldrini, O., P. Armand, C. Duchenne, C. Olry, J. Moussafir and G. Tinarelli, 2017: Description and preliminary validation of the PMSS fast response parallel atmospheric flow and dispersion solver in complex built-up areas. *Environmental Fluid Mechanics*, 17 (5), 997–1014.

Tinarelli, G., L. Mortarini, S. Trini Castelli, G. Carlino, J. Moussafir, C. Olry, P. Armand and D. Anfossi, 2013: Description and preliminary validation of the PMSS fast response parallel atmospheric flow and dispersion Solver in complex built-up areas, American Geophysical Union (AGU), No. 200 (A), 311–327.

Skamarock, W.C., J.B. Klemp, J. Dudhia, D.O. Gill, D.M. Barker, W. Wang and J.G. Powers, 2005: A description of the advanced research WRF version 2. National Center For Atmospheric Research, Boulder (CO), USA.

Trini Castelli, S., P. Armand, G. Tinarelli, C. Duchenne and M. Nibart, 2018: Validation of a Lagrangian particle dispersion model with wind tunnel and field experiments in urban environment. Atmospheric Environment, 193, 273–289.

21st International Conference on
Harmonisation within Atmospheric Dispersion Modelling for Regulatory Purposes
27-30 September 2022, Aveiro, Portugal

NEW INSIGHT ON 3D MODELLING OF THE DISPERSION OF GASES RELEASED FROM AN INDUSTRIAL FACILITY IN A COMPLEX ENVIRONMENT

Patrick Armand[1] and Christophe Duchenne[1]

[1]CEA, DAM, DIF, F-91297 Arpajon, France

Abstract: Routine operation of industrial plants as possible accidents that cannot be ruled out result in releases of gases or particles into the air. The accurate simulation of the space and time distribution of these emissions is crucial to assess their harmlessness to health and the compliance with the environmental regulation in normal conditions and to estimate any potential health impact in adverse conditions. Most of the industrial sites encompass built-up areas and are located in complex environments characterized by a rugged terrain and a heterogeneous land use. As the Gaussian-type models are definitely not adapted to these configurations, this paper dedicates to exemplifying the use of a 3D modelling system in the case of authorized gaseous releases from the plants of a research center. The main steps of the study consist in creating the 3D numerical mock-up of the site under consideration and perfoming twin experiments of the hourly flow and dispersion for the whole year 2018. The wind and concentration fields are strongly influenced by the topography and land use over the whole terrain and, locally, by the buildings. The comparison between the simulated concentrations and measurements at some monitoring points highligths some discrepancies for which explanations are provided. While our results need further analysis, they illustrate the interest of 3D modelling in the field of impact assessment.

Key words: *3D multi-scale modelling, atmospheric flow and dispersion, impact assessment.*

INTRODUCTION

Most industrial facilities release gaseous or particulate, chemical or radioactive materials in the atmosphere. Authorized and controlled emissions must obviously be totally harmless for the population and their impact on the environment must be as limited as possible and comply with the regulation. Furthermore, the health consequences of potential accidental emissions must be assessed in advance in order to anticipate adapted counter-measures. Whatever the type of release, the facility operators should know and be able to determine the space and time distribution of the materials, which their plants are likely to release in the atmosphere.

Even today, Gaussian models are extensively used to assess the impact of atmospheric releases on health and the environment, at least for regulatory purpose. Yet, the assumptions underlying these models, namely a flat unobstructed terrain and a uniform wind field are far from being verified on real sites and in real life. While some Gaussian models were upgraded to take account of isolated buildings or specific configurations like street canyons, they cannot encompass the complexity and diversity of most industrial sites. Above all, simplistic models may be inappropriate for the proper and rigorous impact assessment of industrial plants, one major conclusion of the COST Action ES 1006 (Armand *et al.*, 2015; Baumann Stanzer *et al.*, 2015).

Conversely, the 3D models provide realistic results, thus a better insight into the consequences of normal or accidental atmospheric releases (Armand and Duchenne, 2019a, 2019b; Armand et al., 2021). While not restrained by oversimplifying hypotheses, these models benefit from thorough development and validation, and from increasingly affordable powerful computational resources. In this context, we have engaged for more than ten years in the development of a generic and flexible high resolution modelling system capable of downscaling weather forecast from meso-scale to local scale and simulating the transport, dispersion and deposition of gases or particles released into the air in routine operation or in the event of an accident.

Local scale simulations are carried out with PMSS, which is the parallel version of Micro-SWIFT-SPRAY, developed as a quick solution of the 3D flow and dispersion in built-up environments. PMSS combines the Micro-SWIFT mass-consistent diagnostic flow model and Micro-SPRAY Lagrangian particle dispersion model (Tinarelli et al., 2013). The major features of PMSS are to deal with nested domains and to explicitly account for the effects of the obstacles on the flow and dispersion. The parallelization of PMSS has proven to be efficient in very large and highly resolved computational domains (Oldrini, Armand *et al.*, 2017, 2019, 2021a, 2021b). A great attention has been paid to PMSS validation against numerous experimental trials in wind tunnel and at full scale (Trini Castelli et al., 2016, 2018; Oldrini and Armand, 2019).

This short paper is the continuation of two previous papers (Armand and Duchenne, 2021a and 2021b) that present the application of our modelling system to evaluate the incidence of routine operation conditions at a research center. In the absence of total containment, some facilities release authorized amounts of gases into the atmosphere. The site under consideration has complex features. Indeed, it has a quite large number of buildings and it is located on a plateau surrounded by a rugged terrain. Our 3D modelling system is used to simulate the flow and the distribution of the gases for the whole 2018 year in order to eventually check that the activities of the center do not have any consequences on health and the environment.

In the paper, we first present the flow results interpreted according to the characteristics of the environment such as the hilly terrain and presence of forested areas. Then, we comment on the dispersion results, which show a variably satisfactory agreement between the calculated and measured concentrations at the different monitoring points. As a conclusion, tentative explanations of the discrepancies between computations and measurements are proposed. Details abut the meteorological characterization of the site and the dispersion computations can also be found in our previous papers (Armand and Duchenne, 2021a and 2021b).

METEOROLOGICAL DATA AND FLOW SIMULATIONS

Meteorological study

First, we carried out a meteorological study with the available data for the year 2018 chosen as an example. On one hand, **Figure 1** shows the wind rose built using the data of the meteorological mast set up on the center measuring the wind speed and direction at 10 m and the air temperature at 2 m above the ground. On the other hand, AROME hourly data projected on a regular mesh with a resolution of 0.025° (*i.e.* 2.7 km x 1.9 km in the SN and WE directions) were compiled to establish wind roses in 5 velocity and 36 direction classes (like for the wind rose of the mast). **Figure 2** shows that the AROME wind roses at the 45 points of the AROME grid over the simulation domain of 13 km x 14 km centered on the site. While the area under consideration is quite small, AROME wind roses present disparities due to orographic and land use effects. Furthermore, AROME data extracted at the coordinates of the mast are very close to the wind data measured on the mast. Thus, we decided to use AROME as input data of Micro-SWIFT flow model in PMSS.

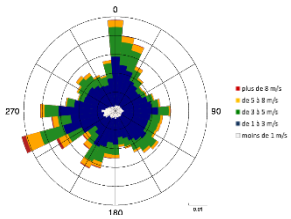

Figure 1. Wind rose in 2018 at a height of 10 m built from data measured on the meteorological mast.

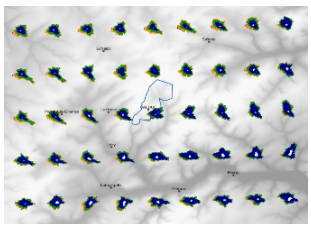

Figure 2. Wind roses in 2018 at a height of 10 m built from AROME data (Météo France).

Micro-scale meteorological simulations

The resolution of meso-scale flow data may be insufficient to account for narrow valleys around the site with a width of 1 km or less and is not suitable for simulations around and in-between buildings. Therefore, AROME hourly data (wind, temperature…) were downscaled for the whole year 2018 using PMSS.

Figure 3 and **Table 1** give features of PMSS computational domains. The largest domain has a resolution of 20 m and is divided into nine tiles so that the memory capacity of the computer nodes is not exceeded. Six local domains have a resolution of 2 m and cover the upper part and the lower part of the center, as well as four villages surrounding the center where atmospheric sampling devices are installed and in operation.

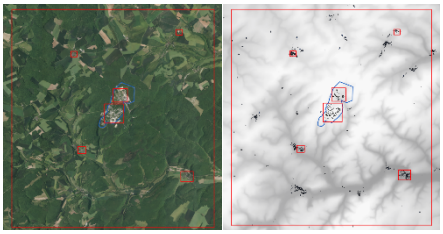

Figure 3. View of the PMSS nested simulation domains.

Table 1. Features of PMSS computational grids.

Domain	Resolution (in m)	Dimensions (in km x km)	Number of nodes	Division into tiles
Large one	20	12.98 x 13.98	650 x 700	Yes (9 tiles)
Center upper	2	1.24 x 1.22	621 x 611	Yes (4 tiles)
Center lower	2	0.92 x 0.86	461 x 431	No
Village L	2	0.50 x 0.45	251 x 226	No
Village M	2	0.80 x 0.65	401 x 326	No
Village E	2	0.40 x 0.35	201 x 176	No
Village S	2	0.40 x 0.35	201 x 176	No

Results of micro-scale flow calculations

Figure 4 shows the wind field over the large domain at a height of 10 m on 1 Nov. 2018 at 9:00. **Figure 5** shows the wind field over the upper part of the center at a height 2 m (same timeframe). While the buildings influence the wind speed and direction, their wakes interact only weakly as they are distant from each other. **Figure 6** shows the wind field over village E domain at a height of 2 m (same timeframe). Old construction houses, close to each other, lead to a complex pattern with wakes interacting inside the streets of the village.

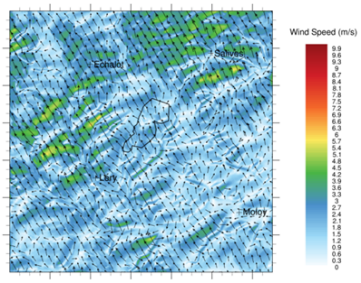

Figure 4. Wind field at 10 m on the regional domain on 1 Nov. 2018 at 9:00.

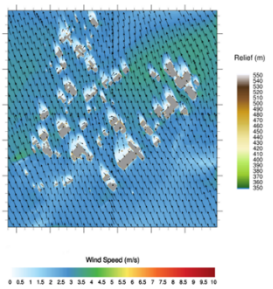

Figure 5. Wind field at 2 m on the upper part of the center on 1 Nov.2018 at 9:00.

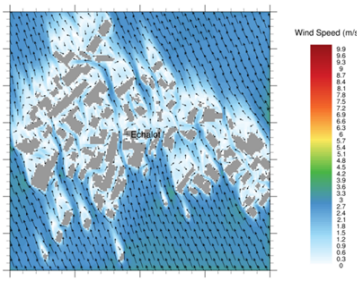

Figure 6. Wind field at 2 m on the village E domain on 1 Nov. 2018 at 9:00.

DISPERSION SIMULATIONS

Micro-SPRAY simulations were carried out in order to evaluate the spatio-temporal repartition of the gases emitted through the stacks of some facilities of the research center. Of course, these releases are authorized and strictly controlled. Depending on the plants, the releases are unequal in amplitude and time distribution, both daily and seasonally, in particular due to different activities performed. High frequency measurements show that the actual timing of the releases is complex and has both a background and a number of peaks.

In total, eight emission sources were represented by numerical particle numbers proportional to the releases, corresponding to several hundred billion particles for the whole of 2018. The dispersion computations were linked in chronological order (*i.e.* the particle plume at the end of a calculation initiates the following one). The dry deposition on the ground and washing by the rain of the gaseous emissions were taken into account. Finally, atmospheric concentrations were averaged and stored on an hourly basis throughout 2018.

Dispersion simulations were performed without the buildings in the 20 m resolution domain, and with the buildings considering the 20 m domain and the 6 domains of 2 m resolution divided (*cf.* **Table 1**). Buildings were accounted for in the villages where sampling stations are set up in order to study their possible effect on the concentration measurements. Air intake on the roof of the sampling stations is located at the height of 3 m, at which the concentrations results are shown.

Distribution of the releases without accounting for the built-up environment

Figure 7 shows the spatial distribution of the atmospheric concentration on 1 Nov. 2018 averaged between 8:00 and 9:00 and between 18:00 and 19:00 at a height of 3 m above the ground, following the releases of all facilities. The plumes are relatively straight, even when the wind is blowing at low speed around 19:00. The influence of the relief is visible in the valleys perpendicular to the axes of progression of the plumes. The low ground concentrations indicate that the plume passes over the valley without descending the slopes. **Figure 8** shows the annual average concentration computed for all releases for the year 2018. The maximum concentration is within the center. Outside, the concentration is very low everywhere. It appears clearly that the repartition near the ground is influenced by the relief and land use. The concentrations evaluated inside the valleys, even the small ones, are much lower than the concentrations on the neighboring plateaus.

Distribution of the releases accounting for the built-up environment

Figure 9 shows the spatial distribution of the atmospheric concentration on 1 Nov. 2018 averaged between 8:00 and 9:00 and between 18:00 and 19:00, near the ground. The plumes are similar to those in **Figure 7**. Thus, the buildings' influence on the repartition of the releases is not significant outside of the center limits. **Figure 10** shows the average concentration field on the village S domain on 1 Nov. 2018 between 18:00 and 19:00. Despite a pixilation effect inherent to the Lagrangian dispersion model and the cells of different volumes in the nested domains, low concentrations are observed in the wakes of the buildings. Consistently, the wakes extend downstream from the 2 m resolution domain into the 20 m resolution domain.

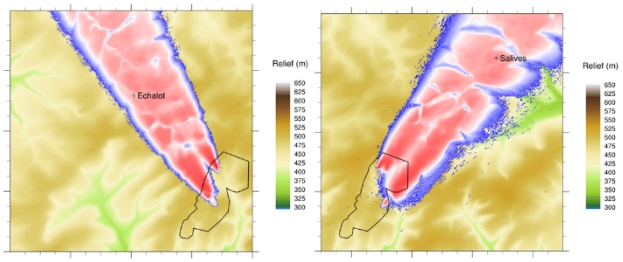

Figure 7. Concentration fields at 3 m on 1 Nov. 2018 at 9:00 and 19:00, following the releases from all the installations (without the buildings).

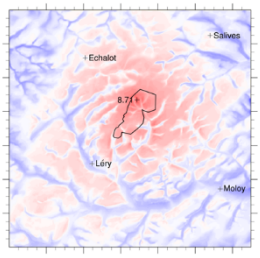

Figure 8. Annual average concentration at 3 m for the releases of the year 2018.

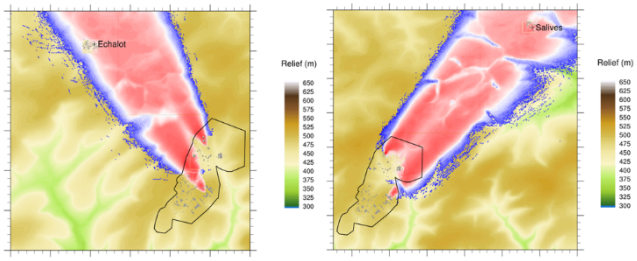

Figure 9. Concentration fields at a 3 m on 1 Nov. 2018 at 9:00 and 19:00, following the releases from all the installations (buildings accounted for).

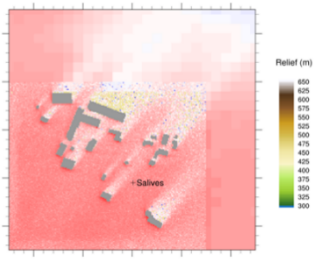

Figure 10. Zoom on the village S of the concentration on 1 Nov. 2018 at 19:00.

Vertical cross sections of plumes

Figure 11 and **Figure 12** show vertical sections of the turbulent kinetic energy on the left and concentration on the right simulated by PMSS. The thin black line is the mixing height estimated by the AROME model. The former figure corresponds to the stable meteorological situation on 4 Nov. 2018 at 18:00. The released gas is distributed relatively evenly in a layer less than 200 meters high, between the ground and the mixing height. The concentration decreases, then increases from east to west. This is because the followed plume has its axis not exactly in the section plane and merges with other plumes in the western part of the section. The latter figure corresponds to a slightly unstable meteorological situation on 11 May 2018 at 9:00. After one kilometer, the released gas mixes efficiently over the height of around 600 meters of the mixing layer. These situations exemplify that the plume vertical diffusion is consistent with the atmospheric stability.

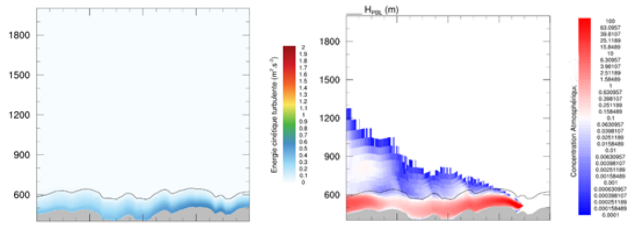

Figure 11. West-east vertical sections of the turbulent kinetic energy and concentration fields on 4 Nov. 2018 at 18:00.

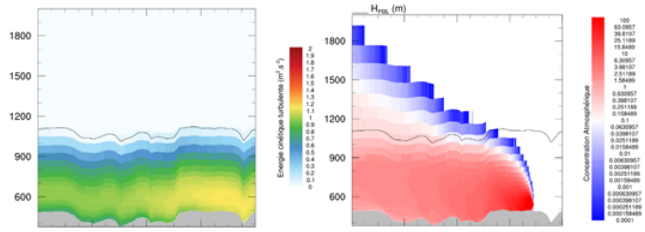

Figure 12. West-east vertical sections of the turbulent kinetic energy and concentration fields on 11 May 2018 at 09:00.

Comparison of the computations to environmental measurements

Villages around the center are equipped with continuous sampling stations providing weekly measurements of the local atmospheric volume concentrations. These measurements as the concentrations computed over the same time intervals show a strong spatial variability even by averaging the concentrations over a week.

Figure 13 shows, by way of example, the time series of the weekly concentration measured at the village S station (blue curve) and computed by Micro-SPRAY (red and green curves) at the same coordinates and at 3 m above the ground. The shaded areas indicate the uncertainty associated with the measurement. When the measurement is below the detection limit (DL), the shaded area extends from 0 to the value of the DL. Measurements below the LD are associated with zero or very low calculated concentrations. In the case of measurements above the LD, the simulated activities are most often outside the confidence interval. When comparing the numerical results with the measurements, it can be observed that the dynamics of the signal

is globally correct but the simulated concentrations are noticeably lower than the measured concentrations. This is visible in the same way at the other three sampling stations.

Such discrepancies between calculations and measurements are unusual in the implementation of PMSS, which has given very satisfactory results in many validation test cases and respects the criteria of Hanna and Chang (2012). In order to check our results, an alternative series of hourly dispersion simulations (green curve) in the period between May and December 2018 was run changing some modelling options. While the characteristics of the atmosphere and turbulence were evaluated directly by Micro-SWIFT in the first computations (red curve), we estimated them from the AROME data in the second series of computations (green curve). The Monin-Obukhov length as the standard deviations of the fluctuating velocities and the Lagrangian time scales were computed in an external module using AROME turbulent kinetic energy data. Then, these fields were interpolated by Micro-SWIFT before being input to Micro-SPRAY. As a result, the concentrations are comparable whether they are computed by Micro-SWIFT or derived from AROME.

Figure 14 shows the time series of the weekly concentration measured at the village S station (blue curve) and computed by Micro-SPRAY (red curve) over the last eight months of the year 2018. In addition, Micro-SPRAY results are given in the 26 adjacent grid cells around the coordinates of the station. While there is a low horizontal variability, the concentrations generally increases with the elevation, up to a factor of two, or decreases at some times. However, the numerical results remain lower than the measurements.

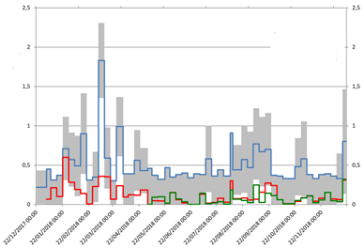

Figure 13. Comparison of measurements at village S with the concentrations calculated by Micro-SPRAY in two different ways.

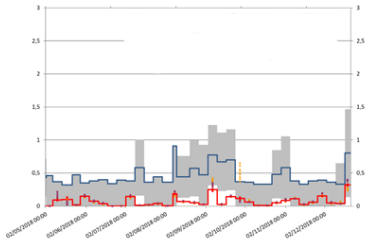

Figure 14. Comparison of measurements at village S with the concentrations calculated by Micro-SPRAY at 26 grid points around the measurement point.

While the previous figure shows the concentration variations in the limited vicinity of a measuring station, **Figure 15** and **Figure 16** illustrate the concentration sensitivity to the location in the simulation domain. More precisely, these figures present the zones (in blue) where the average simulated concentrations at a height of 3 m are greater than the measurement on the station and for the weekly period under consideration (taking account of the measurement uncertainty). While the concentrations evaluated by Micro-SPRAY are lower than the measured ones at the position of the station, they are comparable to the measurements at a distance of only 200 m in the chosen cases where the sampling stations are located at the bottom of valleys.

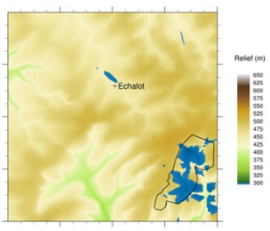

Figure 15. Zones in blue where the average simulated concentration between 3 and 10 Sept. 2018 is greater than the measured concentration at village E.

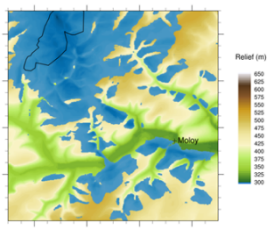

Figure 16. Zones in blue where the average simulated concentration between 4 and 11 June 2018 is greater than the measured concentration at village M.

CONCLUSIONS

This short paper sums up the 3D simulations of the airflow and dispersion of gases emitted by the facilities at a research center comprising several buildings and located on a rugged terrain. Computations are carried out on an hourly basis throughout 2018 using a 3D digital mock-up and PMSS modelling system, explicitly accounting for the topography, the land use and the buildings on the site and in neighboring villages where environmental monitoring stations are set up. There is a principal simulation domain whose dimensions are 13 x 14 km and resolution is 20 m 2 m with nested domains of resolution 2 m encompassing the buildings.

PMSS flow and dispersion simulations bring out several interesting points, some of which are listed here:

- Wind roses derived from AROME or Micro-SWIFT meteorological data turn out to be different even for adjacent grid points due to the contrasted relief, land use, and presence of built up areas.
- AROME or Micro-SWIFT results compare very well with the wind measurements at the mast.
- Hourly as average annual concentrations computed with Micro-SPRAY reveal orographic effects on the large domain and, more locally, areas in the buildings' wakes sheltered from the plumes.
- Turbulent fields input to Micro-SPRAY were either evaluated by Micro-SWIFT or inferred from the AROME data. Whatever the model, the concentrations simulated over weekly periods at the monitoring stations tend to underestimate the measurements. Nowadays, the preferred explanation is related to the source terms, which are known on average over one week, whereas high-resolution measurements show peaks of one hour or less up to 100 times higher than the background releases. Thus, detections above the DL are rare events combining enough high amplitude emissions from one or several sources synchronized with meteorological conditions heading the releases to the measurement stations. We also showed that the concentration field has strong gradients due to the narrow plumes above the uneven terrain. It is thus likely that simulated plumes will miss stations.
- Notwithstanding future work aimed at solving the above-mentioned discrepancies, the hourly, as the annual concentrations are very low, which demonstrates a weak marking of the environment.

Eventually, the 3D simulations reveal the significant influence of the relief, land use and buildings on the flow and dispersion of releases into the atmosphere. Therefore, 3D models should be leveraged in order to more realistically and reliably evaluate the space and time repartition of gases or particles emitted in the air and more safely and convincingly assess their impact on health and the environment.

REFERENCES

Armand, P. et al., 2015: Best Practice Guidelines for the use of Atmospheric Dispersion Models in Emergency Response Tools at local-scale in case of hazmat releases into the air. COST Action ES1006.

Armand, P. and C. Duchenne, 2021b: 3D multi-scale weather and dispersion models applied to assess the impact of industrial plants on human health and the environment. Proc. 38th Int. Technical Meeting on Air Pollution Modelling and its Application, ITM 2021, Barcelone, Spain, 18-22 Oct. 2021.

Armand, P. and C. Duchenne, 2021a: A new methodology based on 3D multi-scale modelling to assess the impact on health and the environment of industrial facilities. Proc. 20th Int. Conf. on Harmonisation within Atmospheric Dispersion Modelling for Regulatory Purposes, Tartu, Estonia, 14-18 June 2021.

Armand, P. and C. Duchenne, 2019b: Urgency management of adverse atmospheric releases with a forefront multi-scale high resolution modelling and decision-support system. Proc. 37th Int. Technical Meeting on Air Pollution Modelling and its Application, Hamburg, Germany, 23-27 Sept. 2019.

Armand, P. and C. Duchenne, 2019a: A multi-scale modelling system operable in case of an emergency. Application to a fictitious attack against a critical infrastructure. Proc. 19th Int. Conf. on Harmonisation within Atmospheric Dispersion Modelling for Regulatory Purposes, Bruges, Belgium, 3-6 June 2019.

Armand, P., O. Oldrini, C. Duchenne and S. Perdriel, 2021: Topical 3D modelling and simulation of air dispersion hazards as a new paradigm to support emergency preparedness and response. *Env. Mod. & Soft.*, 143, 105129.

Baumann Stanzer, K. et al., 2015: Model evaluation case studies: Approach and results. COST Action ES1006.

Hanna, S. and J. Chang, 2012: Acceptance criteria for urban dispersion model evaluation. Meteorology and Atmospheric Physics, 116, 133–146.

Oldrini, O. and P. Armand, 2019: Validation and sensitivity study of the PMSS modelling system for puff releases in the Joint Urban 2003 field experiment. *Bound-Layer Meteorol*., 171 (3), 513-535.

Oldrini, O., P. Armand, C. Duchenne, C. Olry and G. Tinarelli, 2017: Description and preliminary validation of the PMSS fast response parallel atmospheric flow and dispersion solver in complex built-up areas. *Env. Fluid Mech.*, 17 (3), 1-18.

Oldrini, O., P. Armand, C. Duchenne and S. Perdriel, 2019: Parallelization performances of PMSS flow and dispersion modelling system over a huge urban area. *Atmosphere* 10 (7), 404.

Oldrini, O., P. Armand, C. Duchenne, S. Perdriel and M. Nibart, 2021a: Accelerated time and high-resolution 3D modeling of the flow and dispersion of noxious substances over a gigantic urban area – The EMERGENCIES project. *Atmosphere*, 12 (5), 640.

Oldrini, O., S. Perdriel, P. Armand and C. Duchenne, 2021b: High speed visualization of very large high-resolution simulations for air hazard transport and dispersion. *Atmosphere*, 12 (7), 920.

Tinarelli, G. et al., 2013: Review and validation of Micro-Spray, a Lagrangian particle model of turbulent dispersion. In Lagrangian Modelling of the Atmosphere, Geophysical Monograph, Vol. 200, 311-327.

Trini Castelli S. et al., 2016: Evaluation of local-scale models for accidental releases in built environments – Results of the modelling exercises in COST Action ES1006. In Air Pollution Modeling and its Application XXIV, Springer International Publishing Switzerland, 497-502.

Trini Castelli, S., P. Armand, G. Tinarelli, C. Duchenne and M. Nibart, 2018: Validation of a Lagrangian particle dispersion model with wind tunnel and field experiments in urban environment. *Atmos. Env.*, 193, 273-289.

21st International Conference on
Harmonisation within Atmospheric Dispersion Modelling for Regulatory Purposes
27-30 September 2022, Aveiro, Portugal

ANALYSIS OF THE INFLUENCE OF GEOMETRIC AND VENTILATION FACTORS ON INDOOR POLLUTANT DISPERSION: A NUMERICAL STUDY

Agnese Pini[1], Tommaso Vigilante[1], Livia Grandoni[1], Giovanni Leuzzi[1], Armando Pelliccioni[2], Paolo Monti[1]

[1]DICEA, University of Rome "La Sapienza", Rome, Italy
[2]INAIL-DIMEILA, Monteporzio Catone, Rome, Italy

Abstract: Particle material (PM) concentration fields obtained using Computational Fluid Dynamics (CFD) concerning a series of ideal cases regarding parallelepiped rooms of different sizes and inlet velocities at the openings have been analysed, with the aim of delineating the role played by natural ventilation and room geometry on indoor dispersion. The numerical results have been compared with the concentrations obtained using a Box Model based on the mass balance. The results show a reasonably good agreement between the emptying times of the rooms calculated by the CFD and the Box Model, particularly when the room is square shaped. It was also found that the emptying time assumes an almost constant value once normalized with the inlet velocity and room diagonal. Since these are known values, it is possible to infer the emptying time avoiding the use of highly time-consuming numerical simulations.

Key words: *Box model; CFD; DPM; Indoor; Particle dispersion modelling.*

INTRODUCTION

Air quality is one of the fundamental aspects for the well-being and comfort of people both indoors and outdoors. For this reason, studies aiming at improving air quality has become one of the main topics covered by the scientific community (Kalimeri et al. 2019; Pelliccioni et al. 2020). The event that has affected our society in the last two years (e.g., Campanelli et al. 2021) has increased the hours that the population spends in confined environments. In fact, in several countries people, on average, spend approximately 90% of their time indoors, where the concentrations of some pollutants are often 2–5 times higher than typical outdoor concentrations (U.S. EPA 2021). For this reason, studies of indoor pollutant dispersion have become crucial to ensure a healthy life for people.

The objective of this paper is to investigate particle material (PM) dispersion indoors using Computational Fluid Dynamics (CFD), which has proved to be useful in the analysis of indoor PM dispersion and indoor-outdoor interaction (e.g., Blocken 2015). The simulations were carried out by examining ideal cases consisting of parallelepiped rooms of different sizes and injection characteristics of PM from an opening. The PM concentration is obtained via the mixed Eulerian-Lagrangian method, i.e., the dispersed phase is calculated by determining the trajectories of the particles dispersed in the continuous phase (Lagrangian description). Particular attention is payed to the filling and emptying phases of the room and the way in which these depend on the room size and boundary conditions. With regard to the emptying phase, the CFD results will be compared to those obtained by means of a simple Box Model based on the mass balance.

CFD SIMULATIONS: COMPUTATIONAL DOMAINS AND SETTINGS

Four different parallelepiped rooms were considered in the analysis. For each geometry the rooms were set up with a different number of windows but only one of these, always in the same position, was considered as open. In particular, the rooms have two openings placed on the two opposite walls (Figure 1): a window, which represents the inlet, of size 1.4x1.4 m^2, positioned one meter from the right sidewall; a door, which represents the outlet, of area 1x2 m^2, located one meter from the left sidewall. The CFD model ANSYS Fluent 18.2 (ANSYS, 2011), was employed to simulate the airflow and evaluate PM dispersion for the four geometrical configurations and different boundary conditions. GAMBIT 2.4.6 was used to build the

(structured) meshes (cell width 7.5 cm). The main characteristics of the four geometries, hereinafter C1, C2, C3 and C4, are listed in Figure 1. Grid independence analysis (not shown) allows us to affirm that all four grids provide nearly grid-independent results.

Case C1	
Area	16 m^2
Height	3.5 m
Volume	56 m^3
Cell number	132023
Cell size	0.075 m
Node number	139968

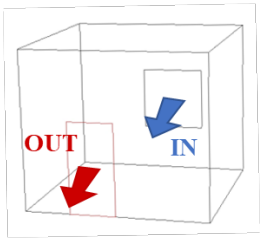

Case C2	
Area	32 m^2
Height	3.5 m
Volume	112 m^3
Cell number	266537
Cell size	0.075 m
Node number	279936

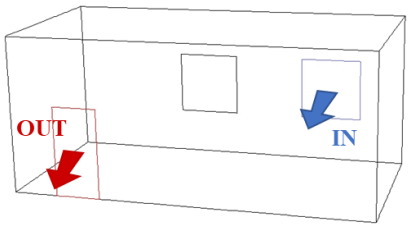

Case C3	
Area	48 m^2
Height	3.5 m
Volume	168 m^3
Cell number	398560
Cell size	0.075 m
Node number	417312

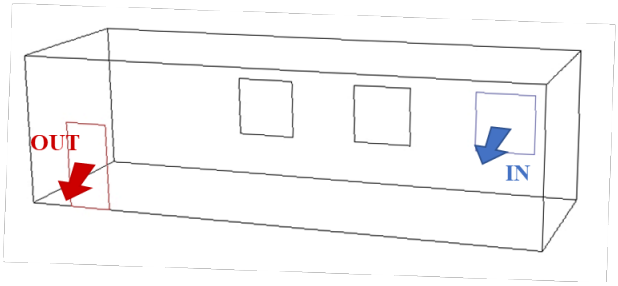

Case C4	
Area	64 m^2
Height	3.5 m
Volume	224 m^3
Cell number	530583
Cell size	0.075 m
Node number	554688

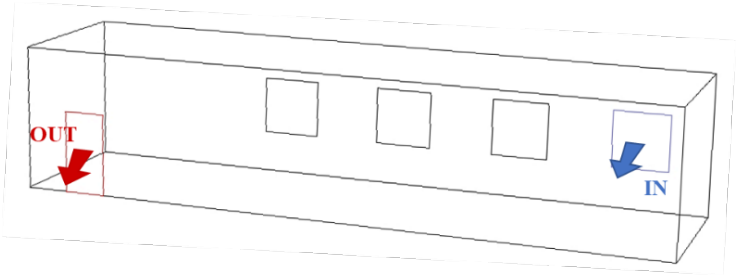

Figure 32. Main characteristics of the four rooms considered in the analysis.

The RANS equations, along with the re-normalization group (RNG) k-ε model (e.g., Xu and Wang 2017) were employed to predict the average velocity field inside the room. Here, k is turbulence kinetic energy and ε its dissipation rate. Besides, the Fluent Discrete Phase Model (DPM) was used to simulate injection and diffusion of the PM. The DPM simulates the continuous and the discrete phases by means of the Eulerian and the Lagrangian approach, respectively. The interaction between the two phases is taken into account by the DPM coupling the solution along with an unsteady particle tracking (time step 1 s). The residual values used to control the solution convergence have been set equal to 10^{-6} for continuity, the three velocity components, k and ε. For each geometry, the simulations were carried out in steady conditions for four values of the inlet velocity (U_{IN}=0.3, 0.5, 0.7 and 0.9 m s^{-1}) normal to the window for a total of 16 runs. A PM 1 μm in diameter and 1650 kg m^{-3} in density has been considered for the analysis. The particle

velocity at the inlet has been assumed evenly distributed and equal to that of air. A constant PM flow rate of 10^{-8} kg s^{-1} has been considered.
For all the 16 runs, after the stationary condition for the velocity field has been obtained, the PM is injected from the window (filling phase). Once a steady condition for the PM concentration has been reached, clean air is again blown through the window (emptying phase).

RESULTS AND DISCUSSION

By way of example, Figure 2 shows the velocity magnitude simulated at z=1.75 m above the floor level for the four geometries with U_{IN}=0.3 m s^{-1}. It can be noted that, except in case C1, an area with very low velocity occurs at the right of the entering flow. The size of the low-velocity area increases passing from the smallest to the largest room. In fact, while for C1 the air after entering the window continues to flow nearly straight towards the door, in the other cases the air hits the opposite wall and then flows parallel to it before exiting the door, giving rise to a low-velocity area near the wall opposite the door. Similar considerations can be drawn from the analysis of the velocity fields obtained using the other three U_{IN}.

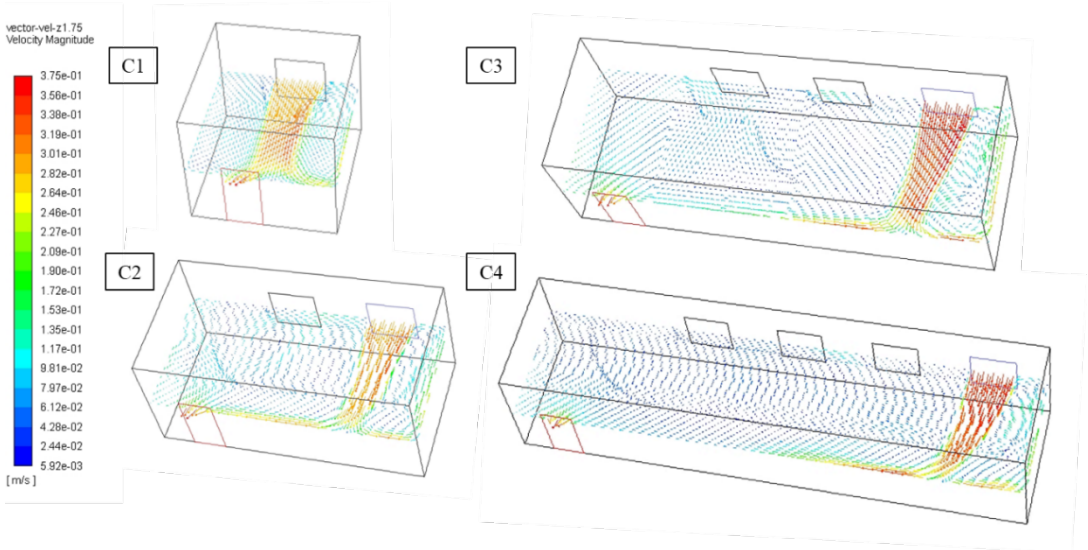

Figure 2. Velocity magnitude simulated at 1.75 m above the floor level for the four geometries (U_{IN}=0.3 ms^{-1}).

Figure 3a shows the time histories of PM concentration – spatially averaged in the room – simulated for case C1 for the four U_{IN}. The PM injection at the window starts after the flow field has reached the steady condition (t=0) and lasts 1800 s (filling phase), an interval long enough for the concentration field to reach the steady state condition in all the investigated cases. Then, clean air enters again from the window (emptying phase) for 1800 s.

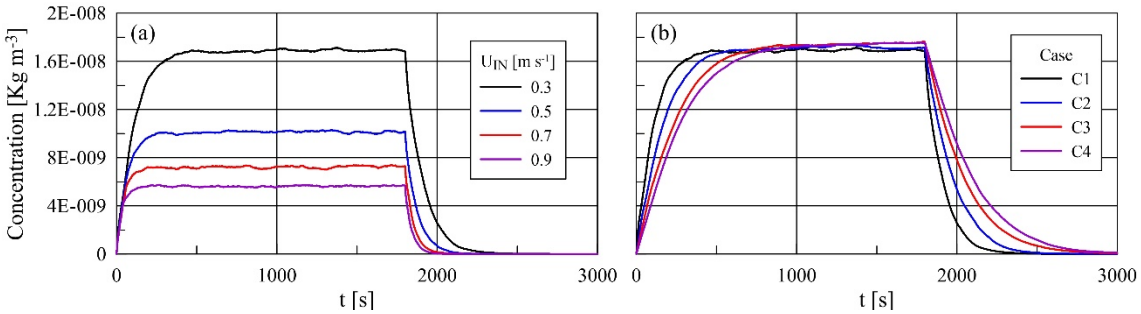

Figure 3. (a) Time histories of the average PM concentration for case C1 as a function of the inlet velocity U_{IN}. (b) Time histories of the average concentration for U_{IN}=0.3 ms^{-1} for the four study cases.

As expected, the average concentration decreases as velocity increases and so does the time (T_F) needed to reach the steady condition for the concentration during the filling phase. The same applies during the emptying phase, i.e., the higher the inlet velocity the shorter the emptying time (T_E).
Figure 3b depicts the time histories of the average PM concentrations calculated for the four geometries when U_{IN}=0.3 m s^{-1}. It is apparent that the larger the room the longer T_E and T_F. Figure 4 depicts filling and emptying times calculated for the 16 runs. It is possible to summarize what was observed above: U_{IN} being equal, T_E and T_F increase as the size of the room increases; on the other hand, area of the room being equal, T_E and T_F decrease as U_{IN} increases.

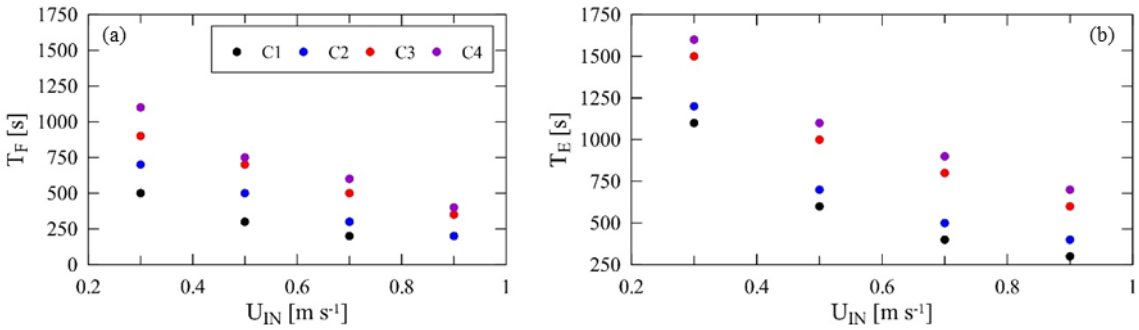

Figure 4. Filling time (a) and emptying time (b) as a function of the inlet velocity and room geometry.

Let us now consider the Box Model. Most of them assume that the pollutant concentration is homogeneous within the control volume considered for the analysis and that the pollutant mixes instantaneously. Hence, it is possible to calculate the pollutant concentration based on the mass balance, considering both natural ventilation and infiltration phenomena. With the view to simplify the model, particle sedimentation can be neglected, as the particle size is small; furthermore, source terms and resuspension can be also assumed negligible. Under these hypotheses, the mass balance can be written as (e.g., Pini et al. 2020):

$$\frac{dC_{IN}}{dt} = a(PC_W - C_{IN}) \quad (1)$$

Here, a is the air exchange rate, defined as the number of air changes in the room per unit of time (determined as the ratio between the inlet flow rate, Q_{IN}= U_{IN}·(window area), and the room volume, V), P is the infiltration factor (P=1 for open window), C_W and C_{IN} are the inlet and the indoor concentration, respectively. In discrete form:

$$C_{IN}^{(i+1)} = C_{IN}^{(i)} + a^{(i)}\left(C_W^{(i)} - C_{IN}^{(i)}\right)\Delta t \quad (2)$$

where i is the iteration step and Δt the time interval. The quantity $\Delta = (T_E|_{BM} - T_E|_{CFD})/T_E|_{BM} \cdot 100$ [%] calculated for the 16 simulations is depicted in Figure 5. Here $T_E|_{BM}$ and $T_E|_{CFD}$ are the emptying time calculated with the Box Model and the CFD respectively. In order to avoid uncertainties in T_E determination, in what follows T_E is assumed as the time needed to reach 10% of the room concentration at the steady state. Assuming that Fluent provides more correct results than the Box Model (we may only speculate that since no experimental data to validate the models are available), the Box Model works reasonably good for regular geometries, in which the hypothesis of uniform concentration is more reasonable. In fact, for C1 and C2 the differences between the emptying times calculated by the Box Model and the CFD are negligible irrespective of the inlet velocity (Δ<2%). On the contrary, when the geometries are far to be cubic, i.e., C3 and C4, the hypothesis of uniform concentration appears too far from reality, and therefore the deviations from the results obtained with the CFD are greater. However, the differences between the two models remain well below 10%, which is an acceptable threshold given the simplifying hypothesis adopted in equation 1.

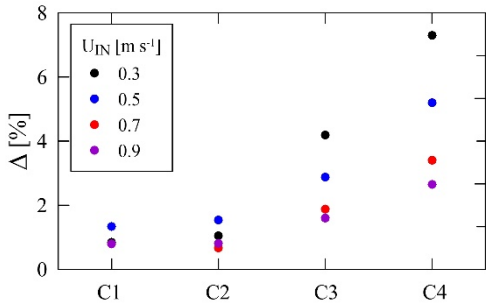

Figure 5. Percentage difference $\Delta = (T_E|_{BM} - T_E|_{CFD})/T_E|_{BM} \cdot 100$ for the 16 simulations.

Finally, an attempt was made to normalize the emptying time. Three different time scales, T_s, were taken into consideration, i.e., V/Q_{IN}, D/U_{IN} and k/ε, (where V and D are, respectively, volume and diagonal of the room), from which it is possible to calculate the ratio $\alpha = T_E/T_S$. It is important to observe how the first two scales can be determined *a priori* as they depend on room geometry and boundary conditions (known quantities). Conversely, $T_S=k/\varepsilon$ can only be calculated starting from CFD simulations, thus being less applicable than the first two. The values of α were analyzed considering all the three time scales for all the geometries considered as the percentage of emptying varied. Among the three time scales, $T_S=D/U_{IN}$ seems to be the best choice (lower fluctuation of α) for all the 16 simulations. The values of α obtained for the 16 simulations are listed in Table 1.

	U_{IN}=0.3 m s^{-1}	U_{IN}=0.5 m s^{-1}	U_{IN}=0.7 m s^{-1}	U_{IN}=0.9 m s^{-1}	$\bar{\alpha}$
C1	12.9	13.1	14.4	15.1	**13.9**
C2	12.4	11.9	13.1	12.2	**12.4**
C3	12.1	11.9	12.3	12.1	**12.1**
C4	11.1	10.7	11.3	11.4	**11.1**

Table 1. Values of $\alpha = T_E/T_S = T_E U_{IN}/D$ for the 16 simulations. The last column lists α averaged over the four room geometries.

By averaging over all the 16 simulations, a value of α close to 12.4 is obtained.

In conclusion, two interesting features were found in this work: (a) For the type of room geometry considered in the analysis, the PM concentration simulated analytically by a simple Box Model are comparable to those simulated by a CFD model; (b) when the window-door distance is similar to the room diagonal, it is possible to determine the emptying time without the need to conduct computationally expensive numerical simulations

REFERENCES

ANSYS. (2011). ANSYS FLUENT User's Guide – Release 14.0. ANSYS. Canonsburg, PA.

Blocken, B., 2015: Computational Fluid Dynamics for urban physics: Importance, scales, possibilities, limitations and ten tips and tricks towards accurate and reliable simulations. *Build. Environ.,* **91**, 219-245.

Chen, C. and B. Zhao, 2011: Review of relationship between indoor and outdoor particles: I/O ratio, infiltration factor and penetration factor. *Atmos. Environ.*, **45**, 275-288.

Chen, C., B. Zhao, W. Zhou, X. Jiang, and Z. Tan, 2012: A methodology for predicting particle penetration factor through cracks of windows and doors for actual engineering application. *Build. Environ.,* **47**, 339-348.

Campanelli, M, et al. (2021) A wide-ranging investigation of the COVID-19 lockdown effects on the atmospheric composition in various Italian urban sites (AER – LOCUS). *Urban Climate*, **39**, 100954. https://doi.org/10.1016/j.uclim.2021.100954.

Iannarelli, A.M., Di Bernardino, A., Casadio, S., Bassani, C., Cacciani, M., Campanelli, M,, Casasanta, G., Cadau, E., Diemoz, H., Mevi, G., Siani, A.M., Cardaci, M. (2022) The Boundary Layer Air

Quality-Analysis Using Network of Instruments (BAQUNIN) Supersite for Atmospheric Research and Satellite Validation over Rome Area. *Bull. Am. Meteorol. Soc.*, **103**, E599-E618.
Kalimeri, K.K., J.G. Bartzis, I.A. Sakellaris, E. de Oliveira Fernandes (2019) Investigation of the PM2.5, NO2 and O3 I/O ratios for office and school microenvironments. *Environ. Res.*, **179**, 108791.
Pelliccioni A., et al. (2020) Integrated evaluation of indoor particulate exposure: The Viepi project. *Sustainability*, **12**, 9758.
Pini, A., et. al. (2020) A Simplified Analytical Model of Ultrafine Particle Concentration within an Indoor Environment." *IOP Conference Series: Earth and Environmental Science* 489 (1).
Xu, G. and J. Wang, 2017: CFD modeling of particle dispersion and deposition coupled with particle dynamical models in a ventilated room. *Atmos. Environ.*, **166**, 300-314.
U.S. Environmental Protection Agency (2021) Indoor air quality: What are the trends in indoor air quality and their effects on human health? https://www.epa.gov/report-environment/indoor-air-quality (accessed 4th July 2022).

21st International Conference on
Harmonisation within Atmospheric Dispersion Modelling for Regulatory Purposes
27-30 September 2022, Aveiro, Portugal

TREATMENT OF THE NEAR GROUND EFFECT IN LAGRANGIAN STOCHASTIC METHODS APPLIED TO A 2-D POINT SOURCE DISPERSION AFTER AN ISOLATED OBSTACLE IN A NEUTRAL FLOW.

Guilhem Balvet, Martin Ferrand, Yelva Roustan, Jean-Pierre Minier, Christophe Henry, Inria Sophia Antipolis

SHORT ABSTRACT

Abstract title: Treatment of the near ground effect in Lagrangian stochastic methods applied to a 2-D point source dispersion after an isolated obstacle in a neutral flow.

Name and Affiliation of the First Author: Guilhem Balvet, CEREA, École des Ponts, EDF R&D, Ile de France, France

Email of first author: guilhem.balvet@edf.fr

Names and Affiliations of the Co-authors: Martin Ferrand, Yelva Roustan, Jean-Pierre Minier, CEREA, École des Ponts, EDF R&D, Ile de France, France Christophe Henry, Inria Sophia Antipolis - Méditerranée, Valbonne, France

Abstract text *(maximum 350 words.)*

Lagrangian stochastic methods tend to be increasingly used in atmospheric flows since they treat without spurious numerical diffusion transport as well as local source terms of any kind, which is of interest for reactive and poly-dispersed flows. In practice, hybrid moments/probability density function (PDF) methods, in which particles are transported using free-of-statistical-noise moments of a carrier flow (pre-)computed with a moments approach, is particularly attractive. However, in such formulation the influence of the wall-function boundary conditions has not always been thoroughly checked. These boundary conditions were developed by Dreeben and Pope (1997) and Minier and Pozorsky (1999) but analyzed only for stand-alone PDF approaches. Furthermore, using high Reynolds methods, in the vicinity of the wall both the mean velocity gradient and the dissipation rate diverge. This yields to a great inhomogeneity within the first cell near the wall which can yield to numerical discrepancies. The interpolation of the free-of-statistical-noise moments at the position of the particles is then a key point to put forward.

These issues are addressed here using a Rotta/simplified Langevin model. The effect of both the boundary conditions and the interpolation will be validated on a case of point source dispersion of pollutant after an obstacle in a neutral flow as proposed by Gamel (2015). First, the moments for the whole flow in all the domain are computed using the moment model. Second, to limit the computation cost, only the flow issued from the point source is simulated in the PDF methods using a Monte-Carlo approach. A great number of particles are injected at the point source location and is transported through the resolution of stochastic differential equations. The statistics obtained on this set of particles will then be conditioned by their original location. Thus, the corresponding velocity differ from the mean values measured for the whole flow. However,

the concentration being injected only in this point, its evolution can be properly treated by such an approach; the mean and variance of the concentration, but also the turbulent flux can be extracted for this kind of simulation. These moments are compared with Gamel experimental results.

21st International Conference on
Harmonisation within Atmospheric Dispersion Modelling for Regulatory Purposes
27-30 September 2022, Aveiro, Portugal

EURODELTA-CARB EXERCISE: INTERCOMPARISON OF MODELLED ESTIMATES OF BENZO(A)PYRENE (BAP) IN EUROPE

Alexey Gusev, Emese Homolya, Krisztina Lázár, Anita Tóth

SHORT ABSTRACT

Abstract title: EURODELTA-Carb exercise: Intercomparison of modelled estimates of benzo(a)pyrene (BaP) in Europe

Name and Affiliation of the First Author: Alexey Gusev; Meteorological Synthesizing Centre East (MSC-E), Moscow, Russia

Email of first author: alexey.gusev@msceast.org

Names and Affiliations of the Co-authors:

Marta G. Vivanco, Mark R. Theobald, Juan Luis Garrido, Victoria Gil; Atmospheric Modelling Unit, CIEMAT, Av. Complutense, 40, 28040 Madrid, Spain

Florian Couvidat , Augustin Colette; INERIS, National Institute for Industrial Environment and Risks, Parc Technologique ALATA, 60550, Verneuil-en-Halatte, France

Mario Adani, Ilaria D'Elia, Mihaela Mircea; ENEA, Italian National Agency for New Technologies, Energy and Sustainable Economic Development Via Martiri di Monte Sole 4, 40129 Bologna, Italy

Abstract text *(maximum 350 words.)*

Concentrations of benzo(a)pyrene (BaP) are routinely measured throughout Europe as a marker of the carcinogenic risk of polycyclic aromatic hydrocarbons (PAHs). Due to the low density of measurement locations in many countries, estimates of the spatial distribution of BaP concentrations rely heavily on modelling estimates. In this study, we compare the temporal and spatial distributions of BaP concentrations simulated in Europe during the period December 2017 to December 2018 by three chemistry transport models (CHIMERE, GLEMOS, MINNI). Modelling results are evaluated with the observed concentrations from the EMEP monitoring network. The three models all used the same BaP EMEP emission data, whilst the other input data (meteorology, temporal emission profiles, land use, etc.) varied from model to model. Although the results show a large variation between the model outputs, both spatial and temporal, similar characteristics in the results (e.g. areas where all models under- or

overestimate concentrations), provide an indication of uncertainties in the emission data and/or the observed values.

21st International Conference on
Harmonisation within Atmospheric Dispersion Modelling for Regulatory Purposes
27-30 September 2022, Aveiro, Portugal

EVALUATION OF MODELLED SOURCE ATTRIBUTIONS WITH OBSERVATIONAL BASED SOURCE ATTRIBUTION

Renske Timmermans, M. Schaap, R. Kranenburg, Pinxteren, Augustin Colette, Stephen Matthew Platt

SHORT ABSTRACT

Abstract title: Evaluation of modelled source attributions with observational based source attribution

Name and Affiliation of the First Author: Renske Timmermans (TNO)

Email of first author: renske.timmermans@tno.nl

Names and Affiliations of the Co-authors: M. Schaap (TNO), R. Kranenburg (TNO), D. v. Pinxteren (TROPOS), Augustin Colette (INERIS), Stephen Matthew Platt (NILU)

Abstract text *(maximum 350 words.)*

Outdoor air pollution was estimated by the World Health Organization to be responsible for 4.2 million premature deaths in 2016, with largest health impacts associated to particulate matter (PM) exposure induced respiratory and cardiovascular diseases and cancer. Improving the air quality will bring major health benefits. However, air pollution is a complex, multi-faceted problem which can only be understood and cost-effectively tackled if authorities have accurate information on its origin. The quantification of main contributing sectors as well as natural contributions discriminating between local and transboundary sources is of particular interest.

One way to provide information on the main contributing sectors or regions to air pollution is the use of a chemistry transport model with a tagging method, as is done within our LOTOS-EUROS model. To evaluate the performance of our model we compare our modelled concentrations with observations. However to evaluate the derived source contributions we need other types of information. We will present results from comparisons of our tagging results with observational based source attribution and concentrations from tracers representative for specific sources. This includes results from a study in Eastern Germany, and a comparison study from the EURODELTA-CARB exercise on residential wood combustion. In both these studies the observational based method involves the application positive matrix factorisation (PMF) to the observational dataset.
We will highlight the challenges for such comparisons, such as the assurance of comparability between modelled and empirical source contributions. We will

furthermore illustrate the usefulness of such comparisons for assessing the quality of the modelled source attribution but also for verification of emissions used in the model.

21st International Conference on
Harmonisation within Atmospheric Dispersion Modelling for Regulatory Purposes
27-30 September 2022, Aveiro, Portugal

THE FAIRMODE CT9 PLATFORM: ASSESSING SENSITIVITY OF MODEL RESPONSES TO EMISSION CHANGES TOWARDS EFFECTIVE EMISSION REDUCTION STRATEGIES

Bertrand Bessagnet, Kees Cuvelier, Enrico Pisoni, Philippe Thunis, Alexander de Meij, Alexandra Monteiro, Angelos Violaris, Jonilda Kushta, Bruce R. Denby, Qing Mu, Eivind G. Wærsted, Marta García Vivanco, Mark R. Theobald, Victoria Gil, Ranjeet S Sokhi, Kester Momoh, Ummugulsum Alyuz, Rajasree VPM, Saurabh Kumar, Elissavet Bossioli, Georgia Methymaki, Darijo Brzoja, Velimir Milić, Arineh Cholakian, Romain Pennel, Sylvain Mailler, Laurent Menut, Gino Briganti, Mihaela Mircea, Claudia Flandorfer, Kathrin Baumann-Stanzer, Virginie Hutsemékers, Elke Trimpeneers

SHORT ABSTRACT

The FAIRMODE CT9 platform: assessing sensitivity of model responses to emission changes towards effective emission reduction strategies

Bertrand Bessagnet; European Commission, Joint Research Centre (JRC), Ispra, Italy bertrand.bessagnet@ec.europa.eu
Kees Cuvelier, Enrico Pisoni, Philippe Thunis; European Commission, Joint Research Centre (JRC), Ispra, Italy*

Alexander de Meij; MetClim, Varese, Italy

Alexandra Monteiro; CESAM, Department of Environment and Planning, University of Aveiro, 3810-193, Aveiro, Portugal

Angelos Violaris, Jonilda Kushta; The Cyprus Institute, Climate and Atmosphere Research Center, 20 Konstantinou Kavafi Street, 2121 Nicosia, Cyprus

Bruce R. Denby, Qing Mu, Eivind G. Wærsted; Norwegian Meteorological Institute, Henrik Mohns plass 1, 0313 Oslo, Norway

Marta García Vivanco, Mark R. Theobald, Victoria Gil; Atmospheric Modelling Unit. Environment Department, CIEMAT - Avda. Complutense, 40, 28040 Madrid, Spain

Ranjeet S Sokhi, Kester Momoh, Ummugulsum Alyuz, Rajasree VPM, Saurabh Kumar; Centre for Climate Change Research (C3R) and Centre for Atmospheric and Climate Physics (CACP), Department of Physics, Astronomy and Mathematics, University of Hertfordshire; College Lane, Hatfield, AL10 9AB, United Kingdom

Elissavet Bossioli, Georgia Methymaki; Department of Physics, Sector of Environmental Physics & Meteorology, National and Kapodistrian University of Athens, Athens, Greece

Darijo Brzoja, Velimir Milić; Croatian Meteorological and Hydrological Service, Ravnice 48, 10000 Zagreb, Croatia

Arineh Cholakian, Romain Pennel, Sylvain Mailler, Laurent Menut; Laboratoire de Météorologie Dynamique (LMD), Ecole Polytechnique, IPSL Research University, Ecole Normale Supérieure, Université Paris-Saclay, Sorbonne Universités, UPMC Univ Paris 06, CNRS, Route de Saclay, 91128 Palaiseau, France

Gino Briganti, Mihaela Mircea; ENEA – National Agency for New Technologies, Energy and Sustainable Economic Development, Bologna, Italy

Claudia Flandorfer, Kathrin Baumann-Stanzer; Zentralanstalt für Meteorologie und Geodynamik (ZAMG), Hohe Warte 38, 1190 Vienna, Austria

Virginie Hutsemékers, Elke Trimpeneers; Belgian Interregional Environment Agency, Rue Gaucheret 92-94, 1030 Brussel, Belgium

**Retired with Active Senior agreement*

Abstract

Air quality models are essential tools for the assessment and prediction of the distribution of pollutant concentrations in the atmosphere. The Forum for Air Quality Modelling (FAIRMODE) in Europe was launched in 2007 to bring together air quality modellers and users in order to promote and support the harmonized use of models by EU Member States, with emphasis on applications under the European Air Quality Directive. In this directive, the use of modelling tools is recommended, in particular to evaluate air quality plans to curb air pollution.

In the framework of FAIRMODE and, in particular, in its Cross Cutting Task 9 (CT9), the set-up of a dedicated intercomparison exercise has been decided. The goal is to evaluate the robustness of air quality models when studying projections and to address the issue of the sensitivity of model responses to emission changes, in particular to identify, investigate and possibly reduce model discrepancies. This will allow for robust support to model users and developers, and, consequently, policy makers.

The goal of this presentation is three-fold: (i) presenting the FAIRMODE CT9 platform and the set of models involved, (ii) introducing the benchmark tool used to evaluate model differences, and (iii) providing a first evaluation of model responses to emission changes through the use of adequate statistical indicators.

21st International Conference on
Harmonisation within Atmospheric Dispersion Modelling for Regulatory Purposes
27-30 September 2022, Aveiro, Portugal

SPATIAL MODEL FOR DAILY AIR QUALITY HIGH RESOLUTION ESTIMATION

H21-137

Morgan Jacquinot[1], Romain Derain[1], Alexandre Armengaud[1], Sonia Oppo[1]
[1]AtmoSud, Air Quality Observatory in South Region, France, www.atmosud.org
Contact: morgan.jacquinot@atmosud.org

INTRODUCTION

AZUR is a modelling platform that creates daily high-resolution concentration cartographies for pollutants like PM10, PM2.5 and NO_2 on millions grid cells in short time computing compared to deterministic model. It produces cartography until day+2 at 25m of resolution, considering the punctual measurements and forecasts. The input data of this platform are:

- annual concentration maps coming from ADMS-Urban model mix with geostatistical method (Seaton et al. 2022).

- punctual measurement and forecast simulated by the Eurlerian Chemistry Transport model CHIMERE (Menut et al., 2021).

This work examines the relationships between daily and annual nitrogen dioxide values in order to provide a statistical model capable of fine-scale estimation of daily concentrations over large areas. The reduced computation time allows the provision of daily maps used by the French air quality observatories.
In this study we worked on all 22 nitrogen dioxide measurement stations of the PACA region. The park is characterized by 6 stations under traffic influence and 16 rural, urban, and peri-urban background stations. The daily value of interest for nitrogen dioxide is the daily hourly maximum. In addition, we have annual averages estimated on a regular grid covering the whole PACA region. They are produced with the ADMS Urban model associated with a post processing by kriging. Annual spatial variations are provided by the large number of temporary campaigns carried out using passive tubes in addition to the 22 fixed stations of the park.
The relationships between daily and annual values are studied (Gressent et al., 2020). We perform an analysis of the pairs of measuring stations for which we calculate the ratio of their daily and annual values respectively. From these results we highlight that this relationship depends on the range of values of the daily measurements considered. This range of values is represented by the rank of the daily measurements when they are seen as percentiles of their annual distribution.
Fine scale daily maps are usually computed from dispersion models involving multiple parameters related in particular to emissions which require regular updating and high computation time. The aim of this work is to provide a simpler model, easily adaptable to other regions and capable of estimating nitrogen dioxide concentrations with a good approximation.

RELATIONSHIP BETWEEN ANNUAL AVERAGE AND HOURLY MAXIMUM

In this part we study the relations between the annual means and the daily values in nitrogen dioxide on the whole of the couples of stations of measurements of the PACA region. These relations depend on the rank p of the daily values.

Let us consider an annual history of the daily values of a station of measurement of nitrogen dioxide. For all the pairs of stations s_i.and $s_{i'}$ and for a fixed rank p, we calculate the ratio of their daily deciles q_p :

$$\frac{q_p(s_{i'})}{q_p(s_i)}$$

As well as the ratio of their annual average y:

$$\frac{y(s_{i'})}{y(s_i)}$$

Figure. 1 : Relationship between the ratios of the annual means and the ratios of daily deciles of rank 80, in red a spline function fit.

Figure 1 shows that for the daily deciles q_{80} their ratios are lower than the ratios of the means, indeed the curve of adjustment is under the bisector represented in dotted line. By calculating these ratios for several deciles, we can observe how these relationships vary (Figure 2).

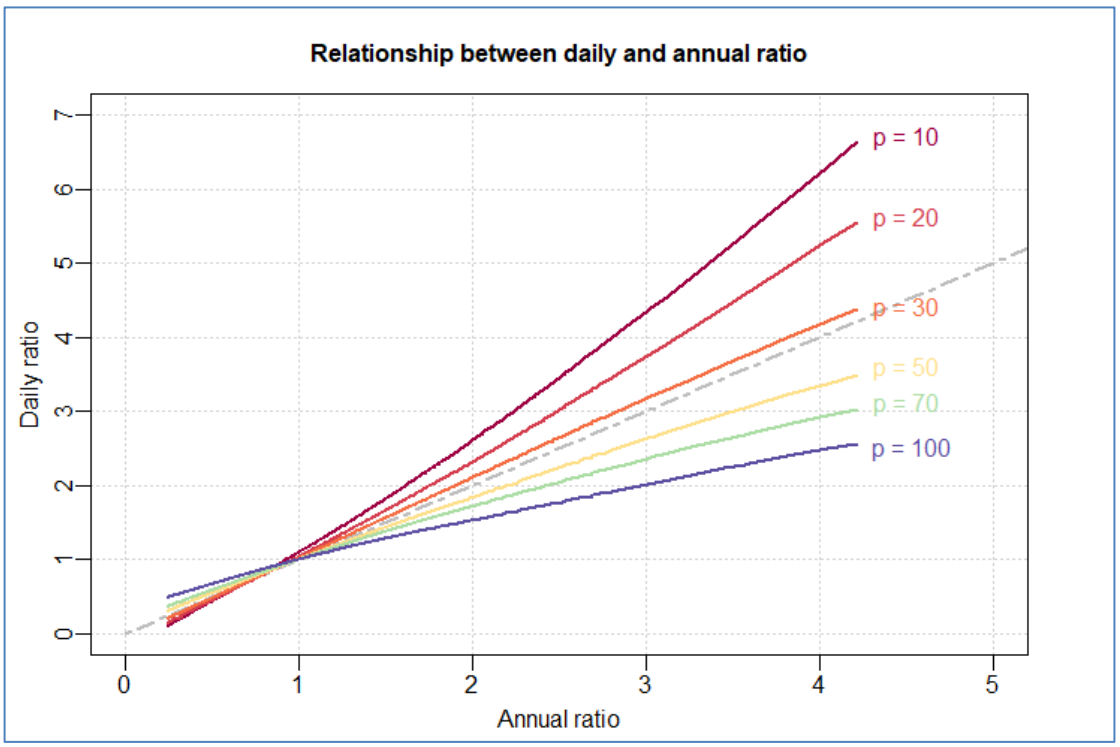

Figure 2 : Relationship between the ratios of annual averages and daily deciles for 6 deciles, represented by their spline fit.

The representation of these relationships for different daily deciles (Figure 2) shows that they evolve as follows:

- - For the deciles of low rank ($q_{\{10, 10, 30\}}$) the daily ratios are higher than the annual ratios
- - For the deciles of higher rank ($q_{\{50, 70, 100\}}$) the daily ratios are lower than the annual ratios.

Consider a pair of stations with an annual ratio of 4 (Figure 2). On days with high NO_2 levels in the air, the daily ratio is equal to 2.5 (q_{100} curve). On days with low NO_2 levels, the daily ratio is equal to 6.5 (q_{10} curve). In general, when NO_2 levels increase, the daily ratios decrease. For two measuring stations the ratio of their daily deciles, therefore, depends on the ratio of their annual averages as well as the rank p. The following relationship can be written:

$$\frac{q_p(s_{i'})}{q_p(s_i)} = f\left(\frac{y(s_{i'})}{y(s_i)}, p\right) \quad (1)$$

We suggest for this function f a polynomial of degree n. Equation (1) then becomes:

$$\frac{q_p(s_{i'})}{q_p(s_i)} = \sum_{j+k<n} \beta_{j,k} \left(\frac{y(s_{i'})}{y(s_i)}\right)^j p^k \quad (2)$$

With $\beta_{j,k}$ coefficients and $p \in [0,100]$.

USING THE MODEL

Let s_0 be a point of the mesh. We have an evaluation of its annual value $y(s_0)$. The daily value at point s_0 is the unknown to be determined. We note $\hat{q}_{s_i}(s_0)$ the estimate of this value made from the station s_i. Equation (2) then becomes:

$$\hat{q}_{s_i}(s_0) = q_p(s_i) \sum_{j+k<n} \beta_{j,k} \left(\frac{y(s_0)}{y(s_i)}\right)^j p^k \quad (3)$$

This formulation assumes that if the day value measured at the station is the p^{th} percentile in the annual daily value distribution then the estimated day value at the grid point corresponds to the percentile of the same rank. This assumption is verified when the point s_0 is in the area of representativeness of the station s_i.This translates into the fact that the station's area of representativeness must be homogeneous in terms of weather and emission variations.

Note that the average emissions need not be identical at the grid point and at the station due to the presence of the term $\frac{y(s_0)}{y(s_i)}$ in the equation (3) which allows for spatial variations in the annual average pollution level.

A mesh point may be in the representativeness area of several neighboring measurement sites, or it may be on the border of several areas without belonging entirely to one of them. Therefore, for a given mesh point, each station s_i whose area of representativeness contains s_0 produces an estimate $\hat{q}_{s_i}(s_0)$. The overall estimate at s_0, denoted $\hat{z}(s_0)$, given by equation (4), is the inverse distance-weighted average of the estimates $\hat{q}_{s_i}(s_0)$.

$$\hat{z}(s_0) = \sum_{s_i \in E_{s_0}} \lambda_i \hat{q}_{s_i}(s_0) \quad with \sum_{s_i \in E_{s_0}} \lambda_i = 1 \quad (4)$$

With :

- E_{s_0}: set of stations whose area of representativeness contains the mesh point s_0,
- λ_i: weights depending on the distance of s_i to s_0,

The weights λ_i are calculated from the inverse square distance of the stations s_i at the mesh point s_0.

RESULTS

In order to evaluate the performance of the model, we calculate cross-validation estimates for the pollutants NO_2 and PM10 over the year 2019. The objective variables are the daily hourly maximum for NO_2, and the daily average for PM10.

The annual values used correspond to the year 2018, the ranks are calculated from the distribution of day values from 2016 to 2018.

In order to compare the results obtained with the suggested method, we perform a kriging with external drift using the annual mean, in global neighborhood on the same set of stations. The adjustment of the daily variogram is done automatically with a zero-nugget effect.

Tables 1 and 2 present the results of the leave-one-out-cross-validation by group of stations, on the one hand the background sites, on the other hand the sites under the influence of road traffic. For NO_2, for the background sites, the suggested method has an advantage of 4.7 % with an RMSE of 15.79 against 15.04. For the sites under traffic influence, the kriging method is better by 9.87 % with an RMSE of 17.41 against 19.12. Concerning PM10, the difference is null for the background sites and 19.93 % for the traffic sites, in favor of the proposed method.

	RMSE Proposed Method	RMSE Krigeage	Δ RMSE %	Correlation (R) Proposed method	Correlation (R) Krigeage

Background stations	15.04	15.79	4.76%	0.81	0.79
Traffic stations	19.12	17.41	-9.87%	0.78	0.79

Table 1 : NO_2 scores of the two methods by leave-one-out-cross-validation for all stations in the fleet.

	RMSE Proposed Method	**RMSE Krigeage**	**Δ RMSE %**	**Correlation (R) Proposed method**	**Correlation (R) Krigeage**
Background stations	4.61	4.62	0.09%	0.85	0.84
Traffic stations	6.24	7.79	19.93%	0.85	0.76

Table 2 : PM10 scores of the two methods by leave-one-out-cross-validation for all stations in the fleet.

CONCLUSION

We have suggested a statistical method of spatial estimation for ambient air quality. It allows to build daily maps for different pollutants from an annual map and a network of measurement stations. The scores obtained are close to those of a kriging with external drift for the background stations, with more marked differences for the sites under the influence of road traffic.

The inverse distance interpolation implies a fixed representativeness from one day to another. This leads us to consider an improvement of the model for the calculation of the weights. The calculation of a variogram on the rank of daily values could replace the inverse distance proposed by equation (4). This would imply variable range on a daily basis as in the case of kriging.

The presented method can be easily adapted for forecast mapping by replacing the daily value measured at the stations by the forecasted value. The calculation of the rank is then made from this forecasted value within the distribution of the measured daily values. Finally, the model can also be adapted for PM10 and PM2.5 and even for ozone if the domain has a well defined annual spatial structure.

REFERENCES

- Gressent A., L. Malherbe, A. Colette , H. Rollin, R. Scimiab: Data fusion for air quality mapping using low-cost sensor observations, Environment International Volume 143, October 2020, 105965.

- Seaton M, O'Neill J, Bien B, Hood C, Jackson M, Jackson R, Johnson K, Oades M, Stidworthy A, Stocker J and Carruthers D,2022: A Multi-model Air Quality System for Health Research: Road model development and evaluation. Environmental Modelling and Software, DOI: 10.1016/j.envsoft.2022.105455.

- Menut L., B. Bessagnet, R.Briant, A.Cholakian, F.Couvidat, S.Mailler, R.Pennel, G.Siour, P.Tuccella, S.Turquety, and M.Valari, The CHIMERE v2020r1 online chemistry-transport model, Geoscientific Model Development, 14, 6781-6811, 2021.

21st International Conference on
Harmonisation within Atmospheric Dispersion Modelling for Regulatory Purposes
27-30 September 2022, Aveiro, Portugal

SPATIAL MODEL FOR DAILY AIR QUALITY HIGH RESOLUTION ESTIMATION

H21-137

Morgan Jacquinot[1], Romain Derain[1], Alexandre Armengaud[1], Sonia Oppo[1]
[1]AtmoSud, Air Quality Observatory in South Region, France, www.atmosud.org
Contact: morgan.jacquinot@atmosud.org

21st International Conference on
Harmonisation within Atmospheric Dispersion Modelling for Regulatory Purposes
27-30 September 2022, Aveiro, Portugal

EFFECT OF THE UNCERTAINTY IN METEOROLOGY ON AIR QUALITY MODEL PREDICTIONS

Zita Ferenczi, Emese Homolya, Krisztina Lázár, and Anita Tóth

SHORT ABSTRACT

Abstract title: Effect of the uncertainty in meteorology on air quality model predictions
Name and Affiliation of the First Author: Zita Ferenczi, Hungarian Meteorological Service *Email of first author*: ferenczi.z@met.hu
Names and Affiliations of the Co-authors: Emese Homolya, Krisztina Lázár, and Anita Tóth

Abstract text

An operational air quality forecasting model system has been developed and provides daily forecasts of ozone, nitrogen oxides, and particulate matter for the area of Hungary and three big cites of the country (Budapest, Miskolc, and Pécs). The core of the model system is the CHIMERE off-line chemical transport model. The AROME numerical
weather prediction model provides the gridded meteorological inputs for the chemical model calculations. It is essential to have a quantitative understanding of the uncertainty in model output arising from uncertainties in the input meteorological fields. The main aim of this research is to probe the response of an air quality model to its uncertain meteorological inputs. Ensembles are one method to explore how uncertainty in meteorology affects air pollution concentrations. During the past decades, meteorological ensemble modeling has received extensive research and operational interest because of its ability to better characterize forecast uncertainty. One such ensemble forecast system is the one of the AROME model, which has an 11-member ensemble where each member is perturbed by initial and lateral boundary conditions. In this work we focus on wintertime particulate matter concentrations, since this pollutant is extremely sensitive to near-surface mixing processes. Selecting a number of extreme air pollution situations we will show what the impact of the meteorological uncertainty is on the simulated concentration fields using AROME ensemble members.

21st International Conference on
Harmonisation within Atmospheric Dispersion Modelling for Regulatory Purposes
27-30 September 2022, Aveiro, Portugal

RECENT DEVELOPMENTS IN HIGH-RESOLUTION WIND FIELD MODELLING IN COMPLEX TERRAIN FOR DISPERSION SIMULATIONS USING GRAMM-SCI

Dietmar Öttl

SHORT ABSTRACT

Abstract title: Recent developments in high-resolution wind field modelling in complex terrain for dispersion simulations using GRAMM-SCI

Name and Affiliation of the First Author: Dietmar Oettl, Regional Government of Styria, Austria

Email of first author: Dietmar.oettl@stmk.gv.at

Names and Affiliations of the Co-authors:

Abstract text *(maximum 350 words.)*

The rather complex terrain in Austria requires that wind fields with sub-kilometer resolutions be generated prior to any kind of dispersion modelling. Proper modelling of highly-resolved flows in alpine regions is still a matter of research and no harmonized methodology is available at the moment. In order to harmonize the meteorological input for dispersion modelling at the regional level, authorities in Austria aim at providing so-called wind-field libraries for a certain reference year for all stakeholders involved in air-quality assessments. The region of Styria was the first one, who established a library using the prognostic, non-hydrostatic mesoscale model GRAMM with a horizontal resolution of 300 m in 2015. Over the years attempts have been made for improving the quality of the wind fields. One of the most challenging issues is the interaction between synoptic-scale flows and local thermally-driven winds. In this work the newly developed mesoscale model GRAMM-SCI is presented, which is driven by ERA5 reanalysis data. Especially, novel nudging techniques allow for nesting and downscaling wind fields with a horizontal resolution of 100 – 200 m. Moreover, a methodology called ‘match-to-observation’ will be presented, which greatly improves the final quality of wind fields. For the first time, a wind-field library for the reference year 2017 has been generated for Styria with this new approach. The quality of the surface wind fields are evaluated by comparison with a large number of observations and the existing wind-field library.

21st International Conference on
Harmonisation within Atmospheric Dispersion Modelling for Regulatory Purposes
27-30 September 2022, Aveiro, Portugal

THE ASPECTS OF NUMERICAL SIMULATIONS ON DESERT DUST OUTBREAKS OVER THE ADRIATIC SEA; INFLUENCE OF ASIAN AND AFRICAN DESERTS

Boris Mifka, Maja Telišman Prtenjak, Ivna Kavre Piltaver, Darko Mekterović, Josipa Kuzmić , Marijan Marcijuš, Irena Ciglenečki

SHORT ABSTRACT

Abstract title: **The aspects of numerical simulations on desert dust outbreaks over the Adriatic Sea; influence of Asian and African deserts**

Name and Affiliation of the First Author: Boris Mifka[1] ([1]Department of Physics, University of Rijeka, Radmile Matejčić 2, 51000 Rijeka, Croatia)

Email of first author: boris.mifka@phy.uniri.hr

Names and Affiliations of the Co-authors: Maja Telišman Prtenjak[2], Ivna Kavre Piltaver[1,3], Darko Mekterović[1], Josipa Kuzmić[4], Marijan Marcijuš[5], Irena Ciglenečki[6]

[2]Department of Geophysics, Faculty of Science, University of Zagreb, Horvatovac 95, 10000 Zagreb, Croatia
[3]University of Rijeka, Centre for Micro- and Nanosciences and Technologies, Radmile Matejčić 2, 51000 Rijeka, Croatia
[4]Croatian Meteorological and Hydrological Service, Ravnice 48, 10000, Zagreb, Croatia
[5]Division of Materials Chemistry, Ruđer Bošković Institute, Bijenička cesta 54, 10000 Zagreb, Croatia
[6]Laboratory for Physical Oceanography and Chemistry of Aquatic Systems, Division for Marine and Environmental Research, Ruđer Bošković Institute, Bijenička cesta 54, 10000 Zagreb, Croatia

Abstract text *(maximum 350 words.)*

Airborne mineral dust is one of the most important factors in air quality and climate change. While the Saharan dust related transport towards European countries is well investigated and documented, there is less research of the advection from Asian deserts. Here, we provide the simulations of the two dust outbreaks in Croatia; one of 'typical' Saharan origin and other with sources toward the east (i.e., the Caspian Sea). In both cases, the WRF-Chem model was applied to simulate the dust emission, transport and deposition.

In the first case, the increase of PM_{10} hourly values was observed over the Adriatic coast in September 2015. Although the model does not capture the convective processes detected by the NASCube methode, it exhibits a good agreement with AOD observed at AERONET stations in the Mediterranean and with PM_{10} at air quality stations in Adriatic. The main mechanism was found to be a NLLJ morning breakdown over sources in Algeria and Tunisia.

In the second case, the untypically extreme dust outbreak was observed over the Balkan region from 27 to 30 March 2020. The anticyclone north of Croatia and cyclone over Anatolia formed a strong pressure gradient driving a transport from desert sources

east to the Caspian Sea. However, the PM_{10} chemical and morphological (SEM analyses) composition at the site in the northern Adriatic indicate mainly the presence of the Saharan dust. Preceding the Asian dust advection, the presence of Saharan dust transport towards Balkan driven by Sharav cyclone was observed. The model shows high correlation with PM_{10} hourly values from regional air quality stations but it underestimates the observations. Modelling results indicate the transport from Asia was below ~2 km, while the Saharan was up to ~8 km amsl. The mixing of the Asian and Saharan dust plume over Balkan was favoured by subsidence due to

anticyclonic high pressure conditions, and it is the most plausible explanation for the observed PMs chemical and morphological results.

Financial support of Croatian Science Foundation project MARRES, IP-2018-01-1717, is highly acknowledged.

21st International Conference on
Harmonisation within Atmospheric Dispersion Modelling for Regulatory Purposes
27-30 September 2022, Aveiro, Portugal

Measurement-model fusion techniques to quantify nitrogen deposition in the Netherlands

Roy Wichink Kruit - National institute for Public Health and the Environment (RIVM, the Netherlands)

Roy.wichink.kruit@rivm.nl

Addo van Pul - National institute for Public Health and the Environment (RIVM, the Netherlands)

Koen Siteur - National institute for Public Health and the Environment (RIVM, the Netherlands)

Abstract

The atmospheric deposition of nitrogen is an important cause for the loss of biodiversity. Nitrogen deposition predominantly consists of four major components: wet and dry deposition of NO_y and NH_x. Measurements are the most direct way to quantify these components. However, accurate measurements of the dry deposition components are scarce, and the number of wet deposition measurements is often limited. Therefore, the use of model calculations is essential in assessing nitrogen deposition on a national scale. Accurate model inputs such as emissions, land use characteristics and meteorology are important prerequisites for reliable deposition maps. However, the best representation of reality is obtained when the model calculations are combined with actual measurements. In the Netherlands, we have a number of monitoring networks in which the atmospheric concentrations and wet and dry deposition of various nitrogen components are measured. However, the number of measurement locations varies for the different components. This means that different techniques must be used to combine measurements and model calculations.

The wet deposition of nitrogen oxides and ammonia is measured on 8 measurement locations throughout the country. For these eight locations the measured wet deposition of NO_y and NH_x is compared with the modelled wet deposition. Based on linear

regression analysis, the modelled wet deposition is then corrected towards the observed wet deposition.
The correction of the dry deposition is much more complicated. The dry deposition is strongly land use dependent and is highly variable in space. Therefore dry deposition measurements in the Netherlands cannot directly be used to derive a generic correction of the dry deposition maps and can only be used for validation purposes.
To correct the dry deposition calculations, concentration measurements are used. For this correction we rely on the property that the dry deposition is directly dependent on the

atmospheric concentration. The modelled NH_3 concentrations are compared with the measured NH_3 concentrations on more than 300 locations in the Netherlands. The relative differences are then spatially interpolated using kriging techniques. Finally, the modelled dry NH_x deposition is corrected using the derived correction field. This technique can only be used for dry NH_x deposition as it mainly consists of NH_3, but the dry NO_y deposition consists of various gaseous nitrogen oxide components.

21st International Conference on
Harmonisation within Atmospheric Dispersion Modelling for Regulatory Purposes
27-30 September 2022, Aveiro, Portugal

Development of a new Airport Dispersion Model

Saravanan Arunachalam[1], Gavendra Pandey[1], Chowdhury Moniruzzaman[1], Brian Fredrik Naess[1] and Akula Venkatram[2]
[1]Institute for the Environment, University of North Carolina at Chapel Hill [2]University of California at Riverside

Abstract

Airports are essentially large urban areas that include all facilities and activities involved in serving thousands of passengers that enter and leave the airport. Airport-related emissions constitute more than 70% of the totals for most pollutants of concern such as fine particulate matter ($PM_{2.5}$) and NO_2 that have an impact on air quality in the airport vicinity. Aircraft sources are unique due to
the transient nature of the emissions from each source, as well as the buoyant exhaust, especially during landing and takeoff operations (LTO). It is difficult to quantify these buoyant emissions and realistically model the governing physical processes. Most of the existing dispersion models, such as AERMOD, do not consider adequate treatment for this buoyant exhaust. In light of the above, we are developing a new airport dispersion model (ADM) which includes key aspects such as improved source representation of aircraft sources during landing and take-off operations, improved meteorology, new area source treatment with advanced plume rise algorithm for the buoyant exhaust from aircraft, meander during low and variable wind conditions, and additional chemical treatments such as NO/NO_2 and aerosol chemistry. This new model ADM is being evaluated using NOx, SO_2 and several other pollutant measurements from the LAX Air Quality Source Apportionment Study (AQSAS) conducted at the Los Angeles International Airport (LAX) at four core locations such as AQ (Air Quality), CN (Community North), CS (Community South), and CE (Community East) for a 71-day period during winter (02/01/2012 to 02/29/2012) and summer (07/18/2012 to 08/28/2012) seasons of 2012. Preliminary results for SO_2 during the winter season from the ADM model are encouraging especially after adding the plume rise associated with buoyant exhaust and horizontal momentum; the high over predictions are being lowered and we can capture the diurnal observed concentration magnitude at all four core sites. In addition, the meander algorithm slightly magnifies concentrations when they are otherwise underpredicted. Model

performance, characterized with Q-Q plots, improved substantially using plume rise and meander algorithms. Key model performance measure, fractional bias (based on top 26 robust highest concentrations) (FB(RHC)) has been reduced from -1.50, -0.99, -1.70, and -1.11 to -1.04, -0.36, -1.40, and -0.80 at AQ, CN, CS, and CE sites respectively. We will discuss implications of these improvements in the context of the overall model development activities focused on the LAX airport.

21st International Conference on
Harmonisation within Atmospheric Dispersion Modelling for Regulatory Purposes
27-30 September 2022, Aveiro, Portugal

CALIBRATING MULTI-MODEL ENSEMBLE PREDICTIONS FROM THE JACK RABBIT III INTERNATIONAL MODEL INTER-COMPARISON EXERCISE

Daniel Silk, Joel Howard, Simon Gant, Rory Hetherington, Adrian Kelsey

SHORT ABSTRACT

Calibrating multi-model ensemble predictions from the Jack Rabbit III international model inter-comparison exercise

Daniel Silk and Veronica Bowman (Dstl)

dssilk@dstl.gov.uk; vbowman@dstl.gov.uk;

Joel Howard (Dstl, UK)

Simon Gant, Rory Hetherington, Adrian Kelsey (UK Health and Safety Executive)

Graham Tickle (GT Science and Software, UK)

Abstract text

Structural uncertainty describes the discrepancy between a model and reality, and may arise through computational and observational limitations, model simplification, and genuine uncertainty about reality. The Jack Rabbit III (JRIII) international model inter-comparison exercise, which aims to inform the new JRIII trial design for large-scale releases of anhydrous ammonia, presents an opportunity to study the structural uncertainty in dispersion modelling. By combining a range of dispersion modelling approaches, including computational fluid dynamics, Gaussian puff, and integral models, within an ensemble framework, the uncertainty can be quantified and its impact can be minimized for downstream analysis and decision making.

Ideally, structural uncertainty is addressed within a Bayesian framework, through model selection/averaging (if the ensemble includes a sufficiently high-fidelity description of reality), or using Bayesian model stacking (when all models are misspecified to some degree). However, these approaches can require an inhibitive number of model runs. An alternative low-burden approach is to post-process the point predictions from the individual models to form a probabilistic ensemble prediction. Typically, a mixture or regression model is constructed, with component weights optimized against historical

data to improve predictive power and help quantify the structural uncertainty. The ability of ensemble methods to improve predictive power has long been recognized in weather forecasting and climate science, and recently has even been successfully applied to combine COVID-19 projections.

Here we use selected trials data to investigate the performance of low-burden methods, such as Ensemble Model Output Statistics (EMOS), for calibration of multi-model ensemble predictions of centerline concentrations. Dependent on sufficient data, we will also investigate the utility of EMOS with spatially varying weights (estimated via strictly proper scoring rules), that capture the different strengths of the alternative modelling approaches.

Acknowledgements

The contributions of Graham Tickle and the HSE staff to this work were funded by HSE. The contents, including any opinions and/or conclusions expressed, are those of the authors alone and do not necessarily reflect HSE policy.

21st International Conference on
Harmonisation within Atmospheric Dispersion Modelling for Regulatory Purposes
27-30 September 2022, Aveiro, Portugal

Examples of 30-minutes notice for fog formation or dissipation at the airport of Burgas

Damyan Barantiev1, Ekaterina Batchvarova1 and Rosen Penchev2

1Climate, Atmosphere and Water Research Institute at Bulgarian Academy of Sciences, Sofia, Bulgaria

E-mail: dbarantiev@cawri.bas.bg; ekbatch@cawri.bas.bg

2 BULATSA – Bulgarian Air Traffic Services Authority, Sofia, Bulgaria

E-mail: rosen.penchev@bulatsa.com

Abstract. The 30-minute or even 15-minute notice for fog formation or dissipation is of extreme value for air traffic regulation at airports. A model system PARAFOG has been created by French colleagues for monitoring and prediction of radiation (RAD) and stratus lowering (STL) fog at Paris airports. The tests of the system for radiation fog were very successful. Here, the case of stratus layering fog is examined for Bulgarian Black Sea coastal site on the territory of Burgas Airport (BOJ). The main challenges in the fog forecasts are the rapidly changing microphysical processes of this phenomenon, both in time and space. The observed abrupt changes in the fog characteristics and their local impact on the visibility cannot be represented accurately by modern synergistic forecasting systems based on both standard surface and satellite observations and numerical modelling. This is due to the limited ability to represent ongoing microphysical processes in the Atmospheric Boundary Layer (ABL) on local scales with the necessary high spatial and temporal resolution. This paper presents results from a preliminary test for a coastal airport of the improved version of the decision support system PARAFOG v2.1.1 (PFG2). Several episodes of fog form spring 2019 were chosen when ceilometer and surface data were available from airport weather service. The preliminary assessment of the PARAFOG decision tool as a support warning and nowcasting system for fog formation events at complex coastal terrain showed satisfactory results.

Keywords: Black Sea, Burgas Airport, coastal ABL, fog forecast, PARAFOG

TOPIC 2:

ENVIRONMENTAL IMPACT ASSESSMENT: AIR POLLUTION MANAGEMENT AND DECISION SUPPORT SYSTEMS

21st International Conference on
Harmonisation within Atmospheric Dispersion Modelling for Regulatory Purposes
27-30 September 2022, Aveiro, Portugal

DEVELOPMENT OF AN AIR POLLUTANT EMISSIONS INVENTORY AND MODELING FRAMEWORK FOR AIR QUALITY CONTROL MEASURES IN LAGOS, NIGERIA

Eva M. Eriksson[1], Fanny Velay-Lasry[1], Alex Resovsky[1], Mathieu Lachatre[1], Armand Albergel[1], Giuseppe Calori[1], Nanni, A.[1], Paula Radice[1], Olawale Abiye[2], Olusegun Fawole[2], Adebola Odu-Onikosi[2], Kolawole Mate[2], Oznur O. Kuntasal[3], Yewande A. Awe[3], Mofoluso A. Fagbeja[3], Joseph E. Akpokodje[3], Todd M. Johnson[3], Christopher Weaver[4], Francesco Forastiere[5], Joseph V. Spadaro[6]

[1]ARIA Technologies, Boulogne-Billancourt, France
[2]EnvironQuest, Lagos, Nigeria
[3]The World Bank, Washington, DC, U.S.A.,
[4]Engine, Fuel, and Emissions Engineering, Inc., Sacramento, CA, U.S.A.
[5]Department of Epidemiology, Lazio Regional Health Service, Rome, Italy
[6]Spadaro Environmental Research Consultants (SERC), U.S.A.

Abstract: A comprehensive localized emissions inventory was compiled for the State of Lagos using activity data from key contributing sectors. Estimated emissions were then spatially disaggregated over the state's administrative subdistricts to compile gridded emissions maps. These datasets were employed as part of a modeling chain consisting of numerical weather prediction and chemistry transport modeling to simulate episodes of inclement air quality in Lagos. The results from the inventory were also used in conjunction with the Greenhouse gas – Air pollution Interactions and Synergies (GAINS) model to identify cost-effective emissions reduction and pollution control measures for local authorities.

Key words: *Africa, Pollution, urban air quality, emissions accounting, emissions modeling.*

INTRODUCTION

The city of Lagos routinely experiences high levels of hazardous air pollution due to shipping, traffic congestion and resuspended road dust, unregulated industrial activity, municipal and agricultural waste burning and poor electrical grid connectivity leading to extensive portable backup generator use. As part of the World Bank's commitment to help low- and middle-income countries such as Nigeria address pollution and environmental health issues, ARIA Technologies and EnvironQuest were recruited to compile an inventory of key pollutants including particulate matter (PM), sulfur oxides (SO_x), nitrogen dioxide (NO_2), carbon dioxide (CO_2), carbon monoxide (CO), black carbon (BC) and organic carbon (OC) for the State of Lagos. The results have been validated using an atmospheric dispersion modeling approach using the Flexible Air quality Regional Model (FARM) with the spatially apportioned emissions inventory as input. The inventory is the first of its kind in Lagos and is intended to develop a data-driven air quality management plan for the state.

METHODOLOGY AND RESULTS

The emissions inventory relied on a bottom-up methodology where first-hand activity data was collected for pertinent sectors. This included reviewing recent port call registers for Lagos harbors, conducting vehicular countings on selected traffic routes, distributing digital and paper surveys to households in Lagos and consulting recent literature on residential, commercial and industrial fuel use. The activity data were then upscaled where appropriate based on, e.g., population estimates, socioeconomic indicators, sectorial growth, and road network length and vehicle fleet composition (provided as inputs to the TREFIC model).

Emissions factors conforming to international standards were then applied individually to these activity datasets and aggregated statewide. For sectors where survey data could not be collected, estimates from the Emissions Database for Global Atmospheric Research (EDGAR) were used to complement the inventory.

GIS datasets were then developed to characterize the spatial distribution of total emissions tonnage over the region. The digital maps contained roads, point emission sources (e.g. factories, power plants, abattoirs, waste dump sites), and polygons delineating the state's administrative subdistricts, known as Local Government Areas (LGAs). Emissions sectors with diffuse areal extents – including residential cooking and portable backup generator use – were allocated proportionally over each LGA based on estimated population densities. Gridded emissions maps from the EDGAR database were also incorporated where detailed spatial data were unavailable, including for the industrial sector. An initial validation of the inventory was obtained by applying EDGAR time modulation profiles to each pollutant and supplying the calculated emissions maps as input to FARM. The model was run online using boundary conditions derived from CHIMERE coupled with numerical weather simulations from WRF. The model results were extracted at the locations of measurement stations throughout the city for a comparative analysis over selected monitoring periods. In general, the model agreed well with the observations, although the results were not spatially consistent. Finally, emissions sectors in the inventory were assigned to corresponding categories of the GAINS-Nigeria model framework to conduct a cost-benefit analysis of different types of emissions control measures.

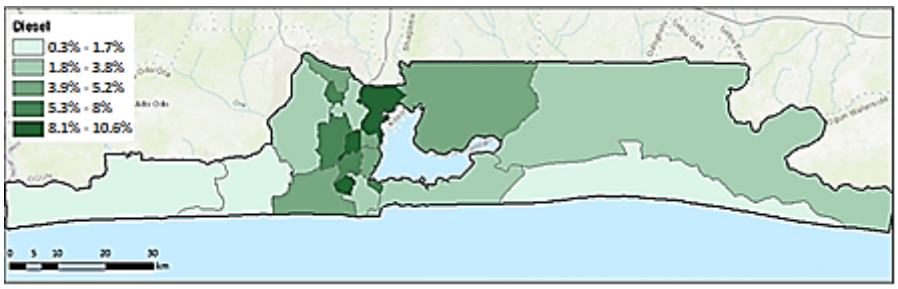

Figure 33. Distribution of emissions from diesel gensets, based on population and diesel use in each LGA.

Table 12. Final emissions inventory

	Cooking stoves	Generators	Road traffic	Trash burning	Biomass burning	Industry	Power Plants	Seaports	Waste disposal	Agriculture	Airport	TOTAL
NOx	694	21528	38388	3557	103	2915	5639	4280		722	726	78553
SOx	168	3542	6529	461	10	1662	15	3283		0	41	15711
CO	1536	1077489	236771	36272	1677	16612	2142	607		0	587	1373694
TSP	194	1021	1838	11345	279	7144	49	243	0.8	560	7	22681
PM10	185	1021	1820	11345	274	3072	49	243	0.4	166	7	18182
PM2.5	180	1010	1470	9351	159	2837	49	243	0.1	7	7	15313
BC	18	464	504	607	10	724	1	43	0	0	3	2375
NMVOC	168	27054	38275	7162	406	19955	143	197	2585	104	71	96120
CO2	1.1E+06	3.7E+06	6.0E+6	1.4E+6	3.7E+4	7.3E+5	3.0E+6	2.6E+5			1.6E+5	1.6E+7
CH4	420		1971	3521	82		53	4	66593	93	11	72748
NH3			723	1058	21	1013	0	0	16896	681	0	20392
N2O	37		209				5.0	12	0.001	2904	4	3171

CONCLUSIONS AND FUTURE WORK

Above all, this study highlighted present gaps in data availability and deficiencies in model assumptions for emission estimation in Nigeria. In particular, modeled PM concentrations are generally underestimated, especially during the dry season (October – May), perhaps due to an incomplete representation of resuspended dust from unpaved roads by the TREFIC model. PM and NO_2 underestimates may also stem from incomplete considerations of biomass burning and uncertainties regarding the spatial distribution and intensity of open trash burning. The experiences in this work could nevertheless serve to strengthen the capacity of relevant institutions to develop multi-sectoral mechanisms for collection, collation and dissemination of data relevant for achieving accurate emission estimates and instituting relevant control measures.

21st International Conference on
Harmonisation within Atmospheric Dispersion Modelling for Regulatory Purposes
27-30 September 2022, Aveiro, Portugal

COMPARISON OF CHANGES IN THE OXIDATION CAPACITY BETWEEN URBAN AND RURAL AREAS IN EUROPE

Daeun Jung[1], David de la Paz[1], Alberto Notario[2] and Rafael Borge[1]

[1] Environmental Modelling Laboratory, Department of Chemical & Environmental Engineering, Universidad Politécnica de Madrid (UPM), José Gutiérrez Abascal 2, 28006. Madrid, Spain
[2] Universidad de Castilla-La Mancha, Physical Chemistry Department, Faculty of Chemical Sceince and Technologies, Ciudad Real, Spain

Abstract: Air quality has become one of the main environmental concerns in urban areas. Many countries have been trying to reduce anthropogenic emissions, such as NO_X and VOC. However, due to the non-linear nature of atmospheric photochemistry, these reductions may result in increases in the ambient concentration of ozone, which is one of the main tropospheric oxidants, in particular, in urban areas in Europe.
Based on that, the principal aim of this study is to understand and analyse the changes in the levels of the tropospheric oxidants (O_3, OH and NO_3) which affect the oxidation capcity in the five representative cities from 2007 to 2015. We also compare the changes in urban areas with those in their surrouding areas. Then we examine the impact of these changes on secondary organic aerosols (SOA). SOA is generated by oxidation of organic species and has an influence on environmental health and climate.
This study is carried out with CMAQ with a 12 km × 12 km sptial resolution for all Europe. The temporal domain is January and July, which represent winter and summer, respectively, in the period 2007 – 2015. As a result, O_3 levels increased in winter in the five cities and also in rural areas. OH and NO_3 generally increased, but some areas responded differently. Meanwhile, O_3 concentrations were reduced in summer, except in a city and its surrounding area (The Hague), and the pattern of NO_3 variation is similar to this secondary pollutant. However, the other oxidant (OH) shows an increment in most of the studied areas except for some surrounding areas (of Milan and Valencia).

Key words: *oxidation capacity, CMAQ, air qulaity modelling, tropospheric oxidants, radiclas, ozone, OH, NO_3*

INTRODUCTION

Due to the strategies and initiatives implemented under the Air Quality Directive 2008/50/EC, anthropogenic emissions have been reduced in Europe, resulting in decreases in ambient concentrations of pollutants such as nitrogen dioxide (NO_2) and volatile organic compounds (VOCs). Despite declining levels of its main precursors, tropospheric ozone (O_3) concentration may increase due to the non-linear nature of atmospheric photochemistry. Some studies (Chang et al. 2017; Yan et al. 2018) showed that the maximum peak of ozone (O_3) decreased in Europe although the mean concentration did not as expected. Borge et al. (2019) found that daily 8-hour maximum O_3 in Spain also have increased by nearly 10 $\mu g \cdot m^{-3}$ as an average 1993-2017, in particular, in winter. Specifially, Saiz-Lopez et al. (2017) reported increases in tropospheric oxidant levels such as hydroxyl (OH) and nitrate (NO_3) radicals along with a rise of O_3 levels due to the reduction in NO_2 levels in Madrid. In other words, the reduction in NO_X emissions could cause modifications in the atmospheric oxidation capacity (AOC). A more recent study by Jung et al. (2022) confirmed that increases in the ambient levels of the atmospheric oxidants in winter but general decreases in summer in Europe. However, the AOC in urban areas seems to be modified differently because of a general increase in OH levels in summer, the opposite is true for the other areas.

AOC is the ability of the atmosphere to oxdise trace gases such as CO, CH_4 and NMVOC with oxidants thorugh phtochemical reactions involving O_3, as well as hydroxyl, and nitrate radicals (OH and NO_3). An increase in these oxidants will enhance the AOC, promoting the production of secondary pollutants, including secondary organic aerosols (SOA). SOA is the fraction of $PM_{2.5}$, formed by the oxidation of

primary organic species, in particular, VOCs by OH (Finewax et al. 2019) and NO_3 (Atkinson and Arey 2003; Brown and Stutz 2012).

The aim of this study is to analyse changes in AOC in the five representative cities in winter and summer, during the period 2007-2015. Also, the results are compared in different environments (urban and rural or suburban areas) and the impact of these changes on SOA are analysed.

METHODOLOGY

The CMAQv 5.3.2 (Community Multiscale Air Quality) (Ching and Byun 1999; Byun and Schere 2006) chemical-transport model is used to simulate air quality in January and July (representative of winter and summer conditions, respectively) of 2007 and 2015 for the whole Europe with 12 km × 12 km spatial resolution (Figure 1). Meteorological inputs are provided by WRFv 4.2.1 (Weather Research and Forecasting) (Skamarock et al. 2005; Borge, Alexandrov, et al. 2008). A constant meteorology, corresponding to the year 2015 is used both for 2007 and 2015 in order to isolate the effect of emission changes. All emission information is processed by SMOKEv 3.6.5 (Sparse Matrix Operator Kernel Emissions) (Borge et al. 2008; UNC 2015) from CAMS-REG-Apv 2.2.1 (Granier et al. 2019) derived from the TNO-MACC-II and TNO-MACC-III inventories. MEGANv 2.10 (Guenther et al. 2012) is used to process biogenic emissions. The setup of the modelling suite is identical for the two years except for the emissions used. More information about the model system is described in the study by Jung et al. (2022). The study segregated large European cities (more than 0.5 million inhabitants) in five groups regarding the trend of the AOC in the period of interest. This study focuses on representative urban areas of those five groups: Valencia, Madrid, Milan, Berlin and The Hague (Figure 1).

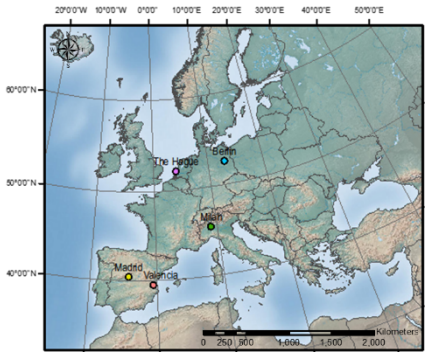

Figure 34. distribution of the five representative cities in the CMAQ modelling domain

RESULT

According to the model results, the ambient concentrations of NO_X and VOC are reduced in all studied areas. Summary of these reductions can be found in Table 1 and Table 2, for winter and for summer, respectively.

Table 13. Average concentration changes of the main O_3 precursors (NO_X and VOC) in the studied areas in winter during the period 2007-2015

Pollutant	Area	Variation	Valencia	Madrid	Milan	Berlin	The Hague
VOC	Urban	Absolute[1]	-16.0 ppb	-47.4 ppb	-63.8 ppb	-19.8 ppb	-6.5 ppb
		Relative[2]	-21 %	-28 %	-26 %	-21 %	-19 %
NO_X		Absolute[1]	-3.3 ppb	-9.4 ppb	-15.5 ppb	-4.5 ppb	-7.7 ppb
		Relative[2]	-16 %	-22 %	-21 %	-19 %	-29 %
VOC	Surrounding	Absolute[1]	-0.7 ppb	-3.4 ppb	-44.9 ppb	-11.0 ppb	-9.9 ppb
		Relative[2]	-6 %	-16 %	-24 %	-20 %	-20 %
NO_X		Absolute[1]	-0.3 ppb	-1.4 ppb	-13.0 ppb	-3.9 ppb	-12.9 ppb
		Relative[2]	-27 %	-30 %	-24 %	-24 %	-35 %

[1] Absolute (ppb) = C_{2015}-C_{2007}

[2] Relative (%) = (C_{2015}-C_{2007}) / C_{2007} × 100

Table 14. Average concentration changes of the main O_3 precursors (NO_X and VOC) in the studied areas in summer during the period 2007-2015

Pollutant	Area	Change	Valencia	Madrid	Milan	Berlin	The Hague
VOC	Urban	Absolute[1]	-8.8 ppb	-26.7 ppb	-19.1 ppb	-12.1 ppb	-6.0 ppb
		Relative[2]	-18 %	-25 %	-23 %	-19 %	-19 %
NO_X		Absolute[1]	-2.2 ppb	-5.4 ppb	-2.9 ppb	-1.4 ppb	-6.0 ppb
		Relative[2]	-21 %	-32 %	-27 %	-22 %	-30 %
VOC	Surrounding	Absolute[1]	-0.8 ppb	-2.3 ppb	-11.4 ppb	-4.8 ppb	-5.8 ppb
		Relative[2]	-2 %	-8 %	-15 %	-15 %	-18 %
NO_X		Absolute[1]	-0.4 ppb	-0.6 ppb	-1.7 ppb	-0.9 ppb	-4.1 ppb
		Relative[2]	-25 %	-30 %	-22 %	-23 %	-36 %

[1] Alsolute (ppb) = C_{2015}-C_{2007}
[2] Relative (%) = (C_{2015}-C_{2007}) / C_{2007} × 100

Table 3 shows the average concentration variation in the oxidants in the five cities and its surrounding areas in winter. OH levels generally increase consistently with O_3 rise in the cities. This seems logical since O_3 is the main source of this radical. Also, a reduction in NO_X concentration would reduce the consumption of OH through reaction 1. However, Milan and Berlin present a slight decrement (−1% and −4%, respectively), which might be due to small O_3 concentrations by low rate of photolysis. Meanwhile, this O_3 increase leads to an increment in the main nocturnal oxidant, NO_3 (thorugh reaction 2) in all cities except Berlin. The decline of NO_3 radical in Berlin might be because environmental factors affecting the kinetic rates of the reactions may be playing a stronger role.

$$NO_2 + OH \rightarrow HNO_3 \quad (1)$$

$$NO_2 + O_3 \rightarrow NO_3 + O_2 \quad (2)$$

The impact of these changes in oxidants on SOA is slightly different for each city (Table 3). Valencia and Madrid, where the levels of the oxdiants increase, present increases in SOA formation (13% and 11%, respectively), while it decreases in Berlin and Milan (−7% and −2%, respectively) with the oxidants. Lastly, the greatest reduction (−10%) in The Hague might be due to small rises in OH and low ambient VOC concentrations (less than 35 ppb during the studied period).

In surrounding areas, OH also increases generally with O_3 as it does in the cities. However, this radical in Valencia decreases by 2%, which could be because OH is reserved in other species such as HO_2 and H_2O_2. NO_3 levels in these areas generally increase with O_3, but decrease in the surrounding areas of Valencia and Madrid, where O_3 increases are small (1% and 3%, respectively). Furthermore, the other possible reason is that NO_3 might participate in chemical reactions to enhance SOA production, increasing general levels by 10% and 15%, respectively. On the other hand, the surrounding areas of Milan, Berlin and The Hague presents SOA decreases despite increases in the three oxidants, which could be related to VOC reduction.

Table 15. Average concentration variation in the main oxidants (O_3, OH and NO_3) and SOA in the five representative cities and its surrounding areas in winter during the period 2007-2015

Pollutants	Area	Valencia	Madrid	Milan	Berlin	The Hague
O_3	Urban	7 %	11 %	25 %	10 %	13 %
OH		10 %	5 %	-1 %	-4 %	1 %
NO_3		7 %	9 %	38 %	-4 %	15 %
SOA		13 %	11 %	-2 %	-7 %	-10 %
O_3	Surrounding	1 %	3 %	31 %	13 %	22 %
OH		-2 %	19 %	3 %	1 %	6 %
NO_3		-17 %	-9 %	51 %	8 %	34 %
SOA		10 %	15 %	-1 %	-8 %	-11 %

* Variation (%) = (C_{2015}-C_{2007}) / C_{2007} × 100

Table 4 shows the average variation in the three oxidants and SOA in summer in the five cities and its surrounding areas in summer. O_3 decreases in all studied cities except The Hague. However, OH is observed

to increase in all cities, which might be mainly caused by NO_2 reduction (reaction 1). It also could be because of environmental factors changing OH reaction rate constant. In The Hague, O_3 increases seem to promote OH production. On the other hand, NO_3 has lower levels in 2015 than in 2007 due to the reduction in its main precursors (reaction 2). In the case of The Hague, an increment in NO_3 (21%) is pressumably due to O_3 increases (6%). As a result of this trend, SOA decreases in all five cities (Table 4), which must be related to NO_3 drop. In The Hague, in spite of a NO_3 rise, SOA production declines, which could be firstly due to the VOC reduction. Additionally, relatively small concentrations of the radicals (OH and NO_3) could not be enough to form SOA.

O_3 changes in the vicinty to those in the cities are similar in this season. However, OH generally falls in the surrounding areas unlike the urban areas. However, Berlin and The Hague present OH declines, which might be due to relatively high O_3 levels (for Berlin) and its increase (for The Hague). This shows that O_3 is still one of the main sources of this radical. However, general O_3 drop leads to reductions in NO_3 levels in all areas except the The Hague surrounding, where NO_3 rises by 13% with an O_3 increase. As for the SOA, the production is lower in 2015 than in 2007 due to the dimmed AOC. The Hague surrounding also presents decreases in SOA formation, which should be related with VOC as mentioned before.

Table 16. Average concentration variation in the main oxidants (O_3, OH and NO_3) and SOA in the five representative cities and its surrounding areas in summer during the period 2007-2015

Pollutants	Area	Valencia	Madrid	Milan	Berlin	The Hague
O_3	Urban	-4 %	-2 %	-6 %	-5 %	6 %
OH		9 %	24 %	12 %	10 %	20 %
NO_3		-17 %	-19 %	-14 %	-23 %	21 %
SOA		-20 %	-20 %	-24 %	-23 %	-26 %
O_3	Surrounding	-8 %	-6 %	-7 %	-6 %	6 %
OH		-20 %	-17 %	-8 %	4 %	80 %
NO_3		-45 %	-39 %	-25 %	-25 %	13 %
SOA		-22 %	-20 %	-24 %	-22 %	-29 %

* Variation (%) = $(C_{2015}-C_{2007}) / C_{2007} \times 100$

CONCLUSION

In this study, the changes in the oxidation capacity of five different large European cities in the period 2007-2015 simulated with the CMAQ chemical-transport model with 12 km × 12 km spatial resolution. Furthermore, we performed a similar analysis with the results of the model in their surrounding areas. We found that O_3 commonly increases in winter but decreases in summer responding the reduction in its main precursors, NO_X and VOC. However, the tropospheric radicals, OH and NO_3 have evolved differently across the European cities. Our main preliminary finding is that the OH radical has increased more in urban areas than in rural/suburban areas both in summer and winter, which could lead to an enahnced AOC in the cities.

Regarding SOA formation, the production decreases in central European cities, while increasing in the two Spainsh cities, Valencia and Madrid. It appears to be required to more detailed study with specific VOC species such as aromatic which mainly get involved in SOA as shown in some previous studies (Majdi et al. 2019; Wu et al. 2020; Zhan et al. 2021). Furthermore, the potential role of the other relevant oxidants such as HO_2 and H_2O_2 should be analysed regarding the SOA formation.

REFERENCES

Atkinson, Roger, and Janet Arey. 2003. Gas-phase tropospheric chemistry of biogenic volatile organic compounds: A review. In *Atmospheric Environment*. https://doi.org/10.1016/S1352-2310(03)00391-1.

Borge, Rafael, Vassil Alexandrov, Juan José del Vas, Julio Lumbreras, and Encarnacion Rodríguez. 2008. A comprehensive sensitivity analysis of the WRF model for air quality applications over the Iberian Peninsula. *Atmospheric Environment* 42: 8560–8574. https://doi.org/https://doi.org/10.1016/j.atmosenv.2008.08.032.

Borge, Rafael, Julio Lumbreras, and Encarnacion Rodríguez. 2008. Development of a high-resolution emission inventory for Spain using the SMOKE modelling system: A case study for the years 2000 and 2010. *Environmental Modelling and Software* 23: 1026–1044. https://doi.org/10.1016/j.envsoft.2007.11.002.

Borge, Rafael, Weeberb J. Requia, Carlos Yagüe, Iny Jhun, and Petros Koutrakis. 2019. Impact of weather changes on air quality and related mortality in Spain over a 25 year period [1993–2017]. *Environment International* 133. Pergamon: 105272. https://doi.org/10.1016/J.ENVINT.2019.105272.

Brown, Steven S, and Jochen Stutz. 2012. Nighttime radical observations and chemistry. *Chemical Society Reviews* 41. Royal Society of Chemistry: 6405–6447.

Byun, Daewon, and Kenneth L. Schere. 2006. Review of the governing equations, computational algorithms, and other components of the models-3 Community Multiscale Air Quality (CMAQ) modeling system. *Applied Mechanics Reviews*. https://doi.org/10.1115/1.2128636.

Chang, Kai-Lan, Irina Petropavlovskikh, Owen R Cooper, Martin G Schultz, and Tao Wang. 2017. Regional trend analysis of surface ozone observations from monitoring networks in eastern North America, Europe and East Asia. Edited by Detlev Helmig and Alastair Lewis. *Elementa: Science of the Anthropocene* 5: 50. https://doi.org/10.1525/elementa.243.

Ching, J K S, and D W Byun. 1999. Chapter 1: Introduction to the Models-3 Framework and the Community Multiscale Air Quality Model. *Science Algorithms of the EPA Models-3 Community Multiscale Air Quality (CMAQ) Modeling System*.

Finewax, Zachary, Joost A de Gouw, and Paul J Ziemann. 2019. Products and Secondary Organic Aerosol Yields from the OH and NO3 Radical-Initiated Oxidation of Resorcinol. *ACS Earth and Space Chemistry* 3. American Chemical Society: 1248–1259. https://doi.org/10.1021/acsearthspacechem.9b00112.

Granier, Claire, Sabine Darras, Hugo Denier van der Gon, Doubalova Jana, Nellie Elguindi, Galle Bo, Gauss Michael, Guevara Marc, Jukka-Pekka Jalkanen, and Jeroen Kuenen. 2019. The Copernicus Atmosphere Monitoring Service global and regional emissions (April 2019 version).

Guenther, A. B., X. Jiang, C. L. Heald, T. Sakulyanontvittaya, T. Duhl, L. K. Emmons, and X. Wang. 2012. The Model of Emissions of Gases and Aerosols from Nature version 2.1 (MEGAN2.1): an extended and updated framework for modeling biogenic emissions. *Geoscientific Model Development* 5: 1471–1492. https://doi.org/10.5194/gmd-5-1471-2012.

Jung, Daeun, David de la Paz, Alberto Notario, and Rafael Borge. 2022. Analysis of emissions-driven changes in the oxidation capacity of the atmosphere in Europe. *Science of The Total Environment*: 154126. https://doi.org/https://doi.org/10.1016/j.scitotenv.2022.154126.

Majdi, Marwa, Karine Sartelet, Grazia Maria Lanzafame, Florian Couvidat, Youngseob Kim, Mounir Chrit, and Solene Turquety. 2019. Precursors and formation of secondary organic aerosols from wildfires in the Euro-Mediterranean region. *Atmospheric Chemistry and Physics* 19: 5543–5569. https://doi.org/10.5194/acp-19-5543-2019.

Saiz-Lopez, A, R Borge, A Notario, J A Adame, D de la Paz, X Querol, B Artíñano, F J Gómez-Moreno, and C A Cuevas. 2017. Unexpected increase in the oxidation capacity of the urban atmosphere of Madrid, Spain. *Scientific Reports* 7: 45956. https://doi.org/10.1038/srep45956 https://www.nature.com/articles/srep45956#supplementary-information.

Skamarock, William C, Joseph B Klemp, Jimy Dudhia, David O Gill, Dale M Barker, Wei Wang, and Jordan G Powers. 2005. *A description of the advanced research WRF version 2*.

University of North Carolina at Chapel Hill (UNC). 2015. SMOKE's v365 user's manual. Chapel Hill, NC: University of North Carolina.

Wu, Shuang, Guiqian Tang, Yinghong Wang, Yang Yang, Dan Yao, Wei Zhao, Wenkang Gao, Jie Sun, and Yuesi Wang. 2020. Vertically decreased VOC concentration and reactivity in the planetary boundary layer in winter over the North China Plain. *Atmospheric Research* 240. Elsevier: 104930. https://doi.org/10.1016/J.ATMOSRES.2020.104930.

Yan, Yingying, Andrea Pozzer, Narendra Ojha, Jintai Lin, and Jos Lelieveld. 2018. Analysis of European ozone trends in the period 1995–2014. *Atmospheric Chemistry and Physics* 18: 5589–5605. https://doi.org/10.5194/acp-18-5589-2018.

Zhan, Junlei, Zeming Feng, Pengfei Liu, Xiaowei He, Zhouming He, Tianzeng Chen, Yafei Wang, Hong He, Yujing Mu, and Yongchun Liu. 2021. Ozone and SOA formation potential based on photochemical loss of VOCs during the Beijing summer. *Environmental Pollution* 285. Elsevier: 117444. https://doi.org/10.1016/J.ENVPOL.2021.117444.

21st International Conference on
Harmonisation within Atmospheric Dispersion Modelling for Regulatory Purposes
27-30 September 2022, Aveiro, Portugal

METHODOLOGY FOR QUANTIFYING THE IMPACT OF SMART FARMING APPLICATION ON LOCAL-SCALE AIR QUALITY OF FARMS IN GREECE

Evangelia Fragkou, George Tsegas, Athanasios Karagkounis, Fotios Barmpas and Nicolas Moussiopoulos

Sustainability Engineering Laboratory, Aristotle University of Thessaloniki, Thessaloniki, Greece

Abstract:
The present work aims to enhance scientific evidence in regard to the efficiency of Smart Farming (SF) in reducing agriculture related environmental impacts, by presenting an integrated methodology for quantifying the benefits on air quality at farm-scale resulting from the GAIA Sense system application in smallholder farms in Greece. Quantitative data were collected from monitoring crop logs and questionnaires to farmers of 6 pilot areas in Greece, participating in the LIFE GAIA Sense project. Emissions and pollutant levels were calculated for two consecutive years in these pilot areas, namely 2019 (baseline year) and 2020, which is the first SF application year. The methodology for calculating realistic emissions data, following a combined Tier 1/Tier2 approach is presented. Calculated emissions were then used as input data for air quality modelling simulations, by deploying the Lagrangian air pollutant dispersion model AUSTAL, to examine the efficiency of SF in reducing local pollutant concentrations. The results show significant emissions and concentrations reductions for all pollutants and greenhouse gases studied, due to the decrease in fuel consumption and N fertilizer applied, as a result of the farmers following the SF advice.

Key words: agricultural air pollutant emissions, air pollution modelling, air pollution management

INTRODUCTION

Many agricultural activities rely on energy consumption of relevant machinery and equipment, resulting to significant emissions of Greenhouse Gases (GHGs) and air pollutants. Activities throughout the life cycle of agricultural products that rely on fossil fuel usage, e.g., energy required for routine agricultural activities (ploughing, spraying, harvesting, etc.) and for the transport/loading of the products to retailers are important emitters. All the above agricultural activities emit a significant amount of particulate matter, accounting for around 16% of PM_{10} emissions in the EU emission inventory of 2019 (EEA 2019a). Furthermore, N_2O emission from croplands as a result of biological nitrification and denitrification processes in soils is an important contributor in GHGs emissions in Europe. According to the latest EU GHG inventory, GHG emissions in the agricultural sector represent almost 10% of the total EU GHG emissions (EEA 2019b). Fertilizer application in agricultural soils is an important source of ammonia (NH_3), nitrogen oxides (NO_x) and nitrous oxide (N_2O) emissions, accounting for 93%, 8% (EEA 2019a) and 5.9% (EEA 2019b) of total EU emissions, respectively. The alkaline ammonia emissions from N fertilizer application contribute to the formation of inorganic fine airborne particulate matter ($PM_{2.5}$), with significant health and climatic effects.

In this frame, the project LIFE GAIA Sense (https://lifegaiasense.eu) targets agriculture related environmental issues through the development and application of an innovative Smart Farming (SF) system that aims at reducing the consumption of natural resources and minimising environmental impact, without sacrificing crop production. Its main purpose is to monitor crops, collect high-resolution environmental data and offer advice about irrigation, fertilisation and pesticides based on soil, weather and plant nutrition data of the specific field. The present paper presents an integrated methodology for quantifying the benefits on air quality at farm-scale resulting from the GAIA Sense SF application in smallholder farms in Greece. The first step of the methodology involves calculating the emissions of atmospheric pollutants and GHGs emitted from the agricultural activities in six GAIA Sense pilot areas in Greece, representing five different crop types. The Lagrangian air pollutant dispersion model AUSTAL is then deployed for assessing the impact of agricultural activities on the local air pollution levels.

METHODOLOGY

The proposed modelling methodology relies on the calculation of realistic emissions data following a combined Tier 1 and Tier 2 approach for emission calculation. For this purpose, detailed activity data of the SF application areas, related to agricultural activities, were acquired from the responses of participating farmers to targeted questionnaires. Quantitative activity data in questionnaire replies included the use of fertilisers (type, quantity and application frequency) and energy use (transport fuel, annual energy use for irrigation, annual consumption of machine lubricants). 17 farmers from 6 different pilot regions across Greece, representing a range of five crop types, provided usable data. Based on these data:

- Tier 1 methodology was applied to calculate emissions of PM_{10}, $PM_{2.5}$, NO, NMVOC, using the default emission factors (EFs) for NFR Source category 3.D (Crop production and agricultural soils) from Table 3.1 of the EMEPEMEP/EEA air pollutant emission inventory guidebook 2019 (EMEP/EEA, 2019). This source category includes emissions related to the application of N fertilisers (for NO), emissions from cultivated crops (for NMVOC) and farm-level agricultural operations (for particulate matter), such as ploughing, spraying, harvesting and storage/handling of agricultural product. On-site data for quantities of fertiliser (kg of fertiliser N) applied and size of the cultivated area (ha) were derived from farmers' questionnaires and logbooks. The percentage of N of each fertiliser was estimated from the fertiliser commercial name and composition.
- Tier 1 methodology was used for emissions calculation of GHGs (CH_4, CO_2, N_2O) and atmospheric pollutants (NH_3, NMVOC, NO_x, PM_{10} and $PM_{2.5}$), employing the default EFs for NFR Source category 1.A.4.c.ii-Agriculture from Table 3-1 (Tier 1 emission factors for off-road machinery) of the EMEPEMEP/EEA air pollutant emission inventory guidebook 2019 (EMEP/EEA, 2019).This source category includes exhaust emissions related to fuel consumption of off-road vehicles and other machinery used in agriculture. On-site activity data on fuel consumption were derived from farmers' questionnaires.
- Tier 1 methodology was used for calculating N_2O emissions from fertiliser application in agricultural soils, according to the default value of 1% of kg^{-1}fertiliser N applied (IPCC, 2006).
- Tier 2 methodology was applied for the calculation of NH_3 emissions resulting from soil fertilisation, taking into account the climate zone of the pilot farm, the soil pH and the amount of N applied to the soil. The EFs were selected based on the fertiliser type as recorded by the farmer and applied on each pilot farm, according to Table 3.2 EFs for NH_3 emissions from fertilisers from the EMEPEMEP/EEA 2019 air pollutant emission inventory guidebook.

The Tier 1 EFs used to calculate the total emissions are presented in Table 1. Tier 2 EFs for NH3 calculation are related to the fertiliser type applied and can be found in Table 3.2 of the EMEP/EEA 2019 air pollutant emission inventory guidebook 2019.

Table 1. Emission Factors (EFs) from NFR categories

	NFR category			
Pollutants	**Fertiliser application (NFR 3D)**	**Non-road machinery (NFR 1.A.4 cii)**	**Standing crops (NFR 3D) ($kg \cdot ha^{-1}$)**	**Agricultural operations (NFR 3D) ($kg \cdot ha^{-1}$)**
PM_{10}	-	1913 $g \cdot tonnes^{-1}$ fuel	-	1.56
$PM_{2.5}$	-	1913 $g \cdot tonnes^{-1}$ fuel	-	0.06
NO_x	-	34457 $g \cdot tonnes^{-1}$ fuel	-	-
NO	0.04 kg NO_2 kg^{-1} fertiliser N applied	-	-	-
NMVOC	-	3542 $g \cdot tonnes^{-1}$ fuel	0.86	-
NH_3	Table 3.2	8 $g \cdot tonnes^{-1}$ fuel	-	-
N_2O	0.01 kg N_2O–N $(kg\ N)^{-1}$	136 $g \cdot tonnes^{-1}$ fuel	-	-
CO_2	-	3160 $kg \cdot tonnes^{-1}$ fuel	-	-
CH_4	-	87 $g \cdot tonnes^{-1}$ fuel	-	-

The contribution of emitted pollutants on local air quality was assessed by performing dispersion calculations for a period of a year. Three pilot fields were chosen on the basis of the completeness of

activity and emission information and the availability of local meteorological measurements. These are the Elassona, Mirabello and Pella fields, located in Central, Southern and Northern parts of Greece, respectively, and in this way representing different climatic and meteorological regimes of a Mediterranean region. The Lagrangian dispersion model AUSTAL2000 (Janicke, 2002) was applied on computational domains with a total extent of 5×5 km^2 around each pilot field, and a grid resolution of 20 m. For the assessment of dispersion in the surrounding areas, yearly average fields of concentration increments for the pollutants NO_x, PM_{10}, NH_3, VOCs and N_2O were calculated, as well as deposition fields for PM_{10} and NH_3. In addition to yearly averages, additional concentration percentiles and maximum values were calculated in line with the limit values and averaging periods specified by the EU directive 2008/50/EC. These values were calculated as concentration increments due to the farming emissions, on a set of representative virtual receptor sites lying inside, near and further away from each pilot field. Given that the particular model operates under a linear assumption for concentrations, calculated concentrations represent increments attributed to the emissions under consideration. Oxidation rates of NO in AUSTAL2000 depend only on temperature and atmospheric stability class, therefore background concentrations could be set to zero for all pollutants without affecting the calculations.

Driving meteorology was obtained from hourly time series of on-site meteorological observations of wind speed, direction and temperature for the year 2020 while the atmospheric stability hourly state was determined using the Turner's method (Turner, 1970) using cloud cover information from the nearest airport. The aerodynamic roughness length was calculated using land use maps for the application areas and was set to z_0=0.1 m for all three pilot fields. The effects of local topography were taken into account by incorporating information from Digital Elevation Maps with a resolution of 90 m and the use of the diagnostic field flow model TALdia. For both studied years, a common meteorological input was used, corresponding to the 2020 conditions. Emissions from all activities were represented as polygonal area sources coinciding with the limits of each pilot field. The nominal emission height for both exhaust and suspension sources was set to 2 m above ground. As usual in the application of AUSTAL2000 over long periods, emission rates were considered constant throughout the simulation period.

RESULTS

Figure 1 presents the correlation between the total emissions of NH_3 and N_2O and NO, and the amount of fertilizer applied. Kiwi is the crop with the highest amount of N fertilizer applied in both studied years and the highest emissions, while the lowest amount of N fertilizer is applied in the case of olive production (Stylida) in 2019 (56.1 kg/ha) and walnut production (Elassona) in 2020 (47 kg/ha). In the case of Elassona, the low N fertilizer results to the lowest related emissions between the different pilot areas.

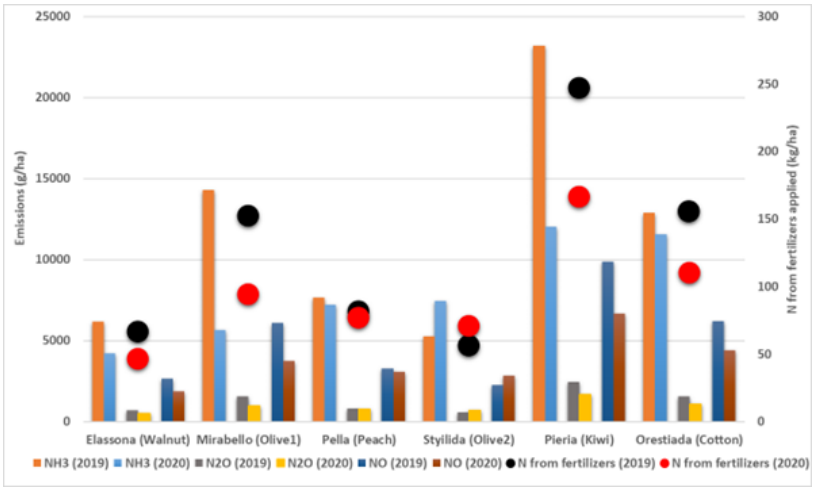

Figure 35. Calculated emissions of NH_3, N_2O and NO in the studied pilot areas, in relation to N fertilizer applied in 2019 and 2020

For evaluating the efficiency of the SF application in terms of reduction of atmospheric emissions, the differences in emissions of all pollutants for all pilot sites between the two studied years were calculated (Fig. 2). In the majority of the participating pilot fields, SF resulted in reduction of air pollutants and GHG emissions due to the lower amount of fuel consumed and N fertilizer applied. In four out of the six studied pilot areas, the quantity of N fertilizer applied was reduced by around 30%, reaching a significant 38.16% decrease in the case of Mirabello (olive crop), a 32.58% decrease in Pieria (kiwi), 29.94% in Elassona (walnut) and 29.32% in Orestiada (cotton). Mirabello pilot area demonstrates the largest NH_3 emission reduction compared to other areas, which could be attributed to the SF advice to change the fertilizer type in addition to lower fertilizer quantity. Stylida is the only pilot area in which N fertilizer applied has increased in 2020 (by 26.4%), resulting to substantial increases in emissions of NH_3 (by 41.58%), NO and N_2O (both increased by 26.4% as fuel consumption data were not available for Stylida and relevant emissions resulted solely from fertilizer application).

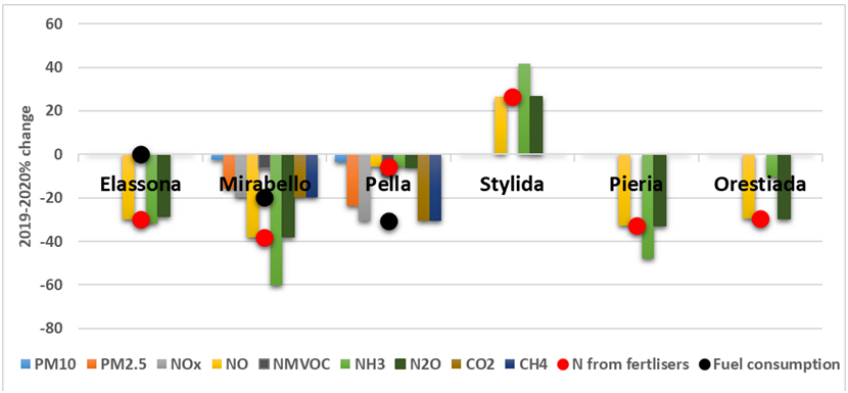

Figure 2 Percentage % change of emissions in relation to percentage change in fuel consumption and the amount of nitrogen (N) in the fertilizers applied between 2019 and 2020

In regard to the impact on the local air quality, annual average concentration increments of NO_x for the Mirabello pilot field are shown in Figure 3 (left).

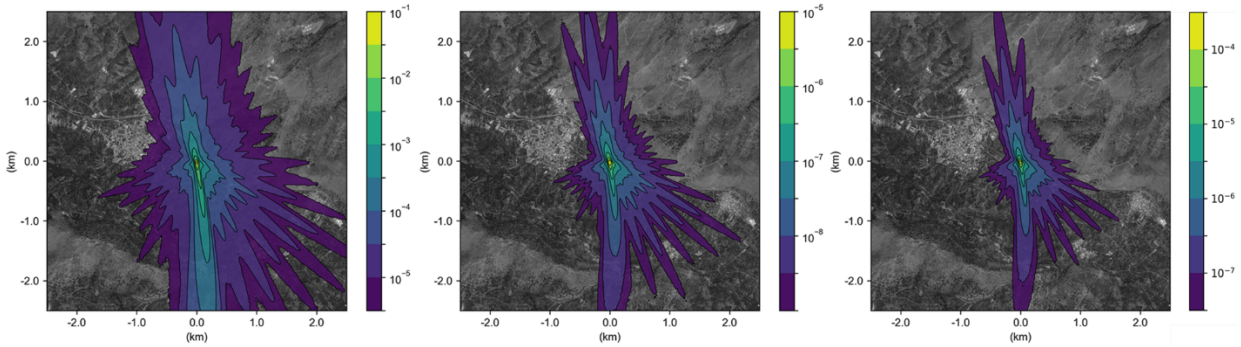

Figure 3 Annual average fields of NO_x surface concentration increment, in $\mu g/m^3$ (left), and deposition rate increments of PM_{10} (middle) and NH_3 (right), in $g/(m^2d)$, calculated around the Mirabello pilot field for 2019

The spatial maximum corresponds to less than $0.1 \mu g/m^3$ and is located near the southern boundary of the emission polygon. The plume has two prominent lobes to the N-NW to S-SE direction, while the same order-of-magnitude decrease within the first 1 km from the source is observed for NO_x as in the other two studied cases. Deposition fields for PM_{10} and NH_3 follow a very similar spatial distribution. PM_{10} deposition rates have a maximum of around $1 \cdot 10^{-5} g/(m^2d)$,while NH_3 deposition rates lie below $1.35 \cdot 10^{-4} g/(m^2d)$. For both pollutants, the bulk of the total deposition occurs within the limits of the field. Table 2 summarizes the pollution burden under the baseline (2019) and 2020 periods for the Mirabello and Pella areas (receptor inside the field). The concentration increments of gaseous pollutants are decreasing almost linearly with the corresponding reduction in emissions. Comparison of results at the three receptor locations in each field

reveals that, the near-field concentrations of PM_{10} are dominated by the smaller reduction of the coarse PM component, while in larger distances, the reduction of the $PM_{2.5}$ component becomes more significant. The decrement of PM_{10} deposition rates for 2020 is dominated by the small reduction in the coarse component emission while deposition rates for NH_3 decrease linearly with the corresponding emissions.

Table 2 Reductions of annual average concentrations in Mirabello and Pella pilot areas

Location	**Mirabello**		**Pella**	
Pollutant	**Average Annual Reduction**	**Annual Percentage Reduction (%)**	**Average Annual Reduction**	**Annual Percentage Reduction (%)**
	Concentrations (μg/m³)	**Concentrations**	**Concentrations (μg/m³)**	**Concentrations**
NO_2	$4.03 \cdot 10^{-5}$	41.66	0	0
NO_x	$4.31 \cdot 10^{-3}$	40	$6.9 \cdot 10^{-3}$	37.52
VOC	$4.43 \cdot 10^{-4}$	17.61	$7.09 \cdot 10^{-4}$	9.81
PM_{10}	$2.35 \cdot 10^{-4}$	8.25	$3.63 \cdot 10^{-4}$	4.52
NH_3	$8.15 \cdot 10^{-3}$	41.69	0	0
	Deposition g/(m²d)	**Deposition**	**Deposition g/(m²d)**	**Deposition**
PM_{10}	$1.9 \cdot 10^{-8}$	1.26	$3.3 \cdot 10^{-8}$	0.69
	Deposition g/(m²d)	**Deposition**	**Deposition g/(m²d)**	**Deposition**
NH_3	$5.4 \cdot 10^{-6}$	41.67	$2.7 \cdot 10^{-9}$	0.02

CONCLUSIONS

Atmospheric modelling is one of several components contributing to the comprehensive evaluation of the environmental impact of SF application. In the present paper, a Lagrangian dispersion model was used for atmospheric simulations to assess the efficiency of the SF GAIA Sense system in terms of local air quality improvement, which relies in a large degree on realistic atmospheric emissions data. The methodology for calculating emissions of atmospheric pollutants and GHGs related to the agricultural activities of the participating pilot farms was based on a combined Tier 1 and Tier 2 approach from the EMEP/EEA and IPCC guidebooks and on farm-level activity information from farmers' replies to targeted questionnaires, in the frame of the LIFE GAIA Sense project. The results of the present study indicate the potential benefits of SF application in the studied pilot areas in terms of improvement of local air quality, for most pollutants in direct proportion to the reduction in the corresponding emission rates.

ACKNOWLEDGEMENTS

The "LIFE GAIA Sense" Project is co-funded by the LIFE Programme of the European Union under contract number LIFE17 ENV/GR000220.

REFERENCES

EEA, 2019a: European Union emission inventory report 1990 — 2017 under the UNECE Convention on Long-range Transboundary Air Pollution (LRTAP).

EEA, 2019b: Annual European Union greenhouse gas inventory 1990–2017 and inventory report 2019EMEP/EEA, 2019 'EMEP/EEA air pollutant emission inventory guidebook – 2013', Technical report No 13/2019.

IPCC, 2006: 2006 IPCC Guidelines for National Greenhouse Gas Inventories; Volume 4: Agriculture, Forestry and Other Land Use; ''N_2O EMISSIONS FROM MANAGED SOILS, AND CO_2 EMISSIONS FROM LIME AND UREA APPLICATION''.

Janicke, L., 2002: Lagrangian dispersion modelling. *Particulate Matter in and from Agriculture*, **235**, 37-41, ISBN 3-933140-58-7.

Turner, D.B., 1970: Workbook of atmospheric dispersion estimates, Office of Air Program Pub. No. AP-26, Environmental Protection Agency, USA.

21st International Conference on
Harmonisation within Atmospheric Dispersion Modelling for Regulatory Purposes
27-30 September 2022, Aveiro, Portugal

TIME SERIES ANALYSIS OF METEOROLOGICAL PARAMETERS AND AIR POLLUTION CONCENTRATIONS IN EMILIA-ROMAGNA, ITALY, DURING COVID-19 INFECTION

Rossana Di Staso[1], Leonardo Aragão[2], Elisabetta Ronchieri[1,3], Loriano Storchi[4,5], Daniele Spiga[5], Sara Cutini[5], Davide Salomoni[3] and Pasquale Lubrano[5]

[1]Department of Statistical Sciences "Paolo Fortunati", University of Bologna, Bologna, IT
[2]Department of Physics and Astronomy "Augusto Righi", University of Bologna, Bologna, IT
[3]INFN CNAF, Bologna, IT
[4]Department of Pharmacy, D'Annunzio University of Chieti, Chieti, IT
[5]INFN Perugia, Perugia, IT

Abstract: During the pandemic, Italy experienced several phases of lockdown with different types of restrictions. Starting on February 23rd 2020, 11 municipalities in northern Italy suspended activities in schools, universities, museums, cultural venues, and all public initiatives. The ordinance announcing the national emergency was released on March 11th, stabilising the first lockdown period for the whole of Italy, which lasted until the second half of May. After a phase of cushioned restrictions during the summer, the so-called 'Second Wave' began forcing a new ordinance on October 13th with more stringent restrictions as the number of infections increased. On November 3rd, the "colour system" was introduced with three risk bands - red, orange and yellow - assigned weekly to the regions based on monitoring indicators. The main objective of the present study is to assess the impact of the meteorological and air quality conditions on COVID-19 cases in the region of Emilia-Romagna in Italy during the lockdown periods. Several pollutant time series from the Copernicus Atmosphere Monitoring Service were joined with meteorological data from the daily gridded land-only observational dataset over Europe and then compared with the total number of infections, hospitalisations and deaths. Data provided by the two monitoring systems were processed through an algorithm and organised by provinces and municipalities in Emilia-Romagna, Italy. The explorative analysis, conducted using both time series and seasonally adjusted time series, shows that pollutants most affected by lockdown phases are CO, NO_2, PM_{10}, $PM_{2.5}$ and SO_2. The findings in this study may help further studies better understand the variations 2020 and 2021 and the correlation with COVID-19 variables.

Key words: *COVID-19; Environmental Pollution; Meteorological Data; Correlation; Time Series.*

INTRODUCTION

Air pollution is one of the environmental causes of premature death in Europe. A study from the WHO (2013) suggests that the disease burden attributable to the air pollution exposition is substantial. Several researches have been conducted to assess the impact of air quality on the COVID-19 contamination. In Italy, Lolli *et al.* (2020) quantitatively assess how the meteorological and air quality parameters are correlated to the COVID-19 transmission in Milan, Florence and in Trento that are located in Italian regions, respectively Lombardy, Tuscany and Trentino-South Tyrol. Through the usage of Spearman and Kendall rank correlation tests, the authors put in evidence that temperature, dew point temperature, absolute humidity, water vapor are negatively correlated with the virus transmission. On the other hand, wind speed and atmospheric mean sea-level pressure show a certain degree of correlation, while $PM_{2.5}$ concentration positively correlates with COVID-19 transmission. These results require further investigation considering other Italian cities and regions. Another Italian territory-based study (Accarino *et al.* 2021) analyzes atmospheric pollutants concentrations (i.e., PM_{10}, $PM_{2.5}$, NO_2) and spatio-temporal distribution of COVID-19 positive cases and deaths. It evidences any potential short-term correlation between these two phenomena via Spearman's correlation index. Both studies use Spearman correlation coefficient to assess non-linear, monotonic correlations between the number of days exceeding regulatory limits for the selected pollutants and COVID-19-related parameters at territorial levels. PM_{10} and $PM_{2.5}$ show higher non-linear correlation than NO_2 with incidence, mortality and lethality rates.

This present study aims to explore the relationship between the COVID-19's spread and the meteorological and air quality conditions in the nine Emilia-Romagna (Italy) provinces (Figure 1): Piacenza, Reggio Emilia, Parma, Modena, Bologna, Ferrara, Forlì Cesena, Ravenna and Rimini. Emilia-Romagna is one of the regions that has been significantly affected by COVID-19. Starting from Piacenza province in the western part of the region, the virus spread to the central provinces in the direction of Bologna and Modena. With respect to the aforementioned studies, we have considered a larger number of air quality variables and investigated the correlations between seasonally adjusted air quality parameters and COVID-19.

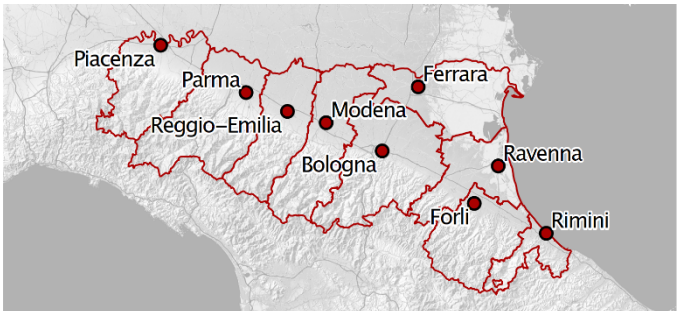

Figure 1. Distribution of the Emilia-Romagna provinces in northern Italy.

MATERIALS AND METHODS

For this study, three main steps have been pursued. Firstly, we have identified variables of interest in four categories: meteorological, COVID-19, air quality and geographical & socio-economical (Figure 2). The meteorological and air quality variables have been extracted at the municipal level of Italy and later transformed into the nine provinces of Emilia-Romagna. Then, the explorative analysis and the correlation analysis have been performed.

	Meteorological	Air quality	Covid-19	Geographical and Socio-Economical
Source	E-OBS	CAMS	CovidStat	ISTAT
Area	Italy	Italy	Emilia-Romagna	Emilia-Romagna
Period	01/01/2017 - 31/12/2020	25/12/2017 - 31/07/2021	05/03/2020 - 20/01/2022	2017-2021
Frequency	Daily	Hourly	Daily	Yearly
Variables	TG, RR, PP, QQ, HU	CO, SO_2, NMVOCs, NO, NO_2, NH_3, O_3, PANs, $PM_{2.5}$, PM_{10}	Positive Cases, Hospitalization, Deaths, Intense Care Unit cases	Population, Ages, Hospitals, Tourism, Province Areas

Figure 2. Datasets characteristics by typology.

Meteorological data are from the European Observations (E-OBS) ensemble datasets (*https://climate.copernicus.eu/*), which include daily climate measurements interpolated to provide gridded data with a spatial resolution of 10 × 10 km, approximately. The available parameters are: daily mean temperature (TG), daily minimum temperature (TN), daily maximum temperature (TX), daily precipitation sum (RR), daily mean sea level pressure (PP), daily mean relative humidity (HU) and global radiation (QQ). To reduce them to the municipality level, all grid points within the municipality area plus those up to 10 km from the border have been averaged. The four most neighbouring grid points have been employed whenever the municipality's area has been less than 100 km² (Figure 3). Consequently, we guarantee that all averages used have at least four values in their calculation, avoiding errors associated with the grid points' choice. Finally, to reduce to the provincial level, weighted averages have been assembled based on the area of each municipality within the province. Air Quality data are from the Copernicus Atmosphere Monitoring Service (CAMS, *https://atmosphere.copernicus.eu/*), implemented by the European Centre for Medium-Range meteorological Forecasts on behalf of the European Commission. We have applied the same procedure described for the meteorological data. However, as the CAMS data have an hourly frequency, it has been necessary to reduce them to daily. The highest daily concentrations have been collected at each grid point, following the analysis periods of each pollutant to proceed with the spatial

averages. For species without Air Quality Standard, the highest hourly concentration has been considered. In the end, the concentrations were available daily and at the provincial level.

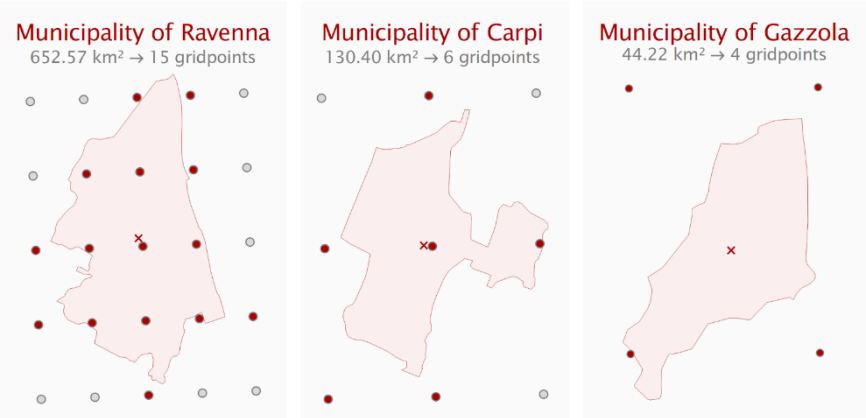

Figure 3. Examples of grid point selection for E-OBS and CAMS data extraction to municipalities with different dimensions. In both datasets the spatial resolution is approximately 10 km and marks the distance between grid points, where those highlighted in red are considered for data extraction.

COVID-19 variables have been extracted from COVIDStat (*https://covid19.infn.it/*) that reports daily information at provincial level, computed using a 7-days centered moving average. Geographical and socio-economical information are from the Italian Institute for Statistic (ISTAT, *https://www.istat.it/it/archivio/156224*). Particularly, the municipalities areas (km²) and the provincial groups have been used to reduce meteorological and air quality data to province level.

The relationship between meteorological and air quality variables versus COVID-19 related variables is analysed using different techniques, both explorative through smoothing techniques, i.e., 7-days centered moving average and seasonal adjustment with the additive decomposition of original datasets, and statistical through Spearman's correlation indexes.

RESULTS

One of the first steps of our explorative analysis consisted in understanding how meteorological and air quality variables influence each other. Correlograms (*https://r-graph-gallery.com/correlogram.html*) computed for each province show a very similar behavior.

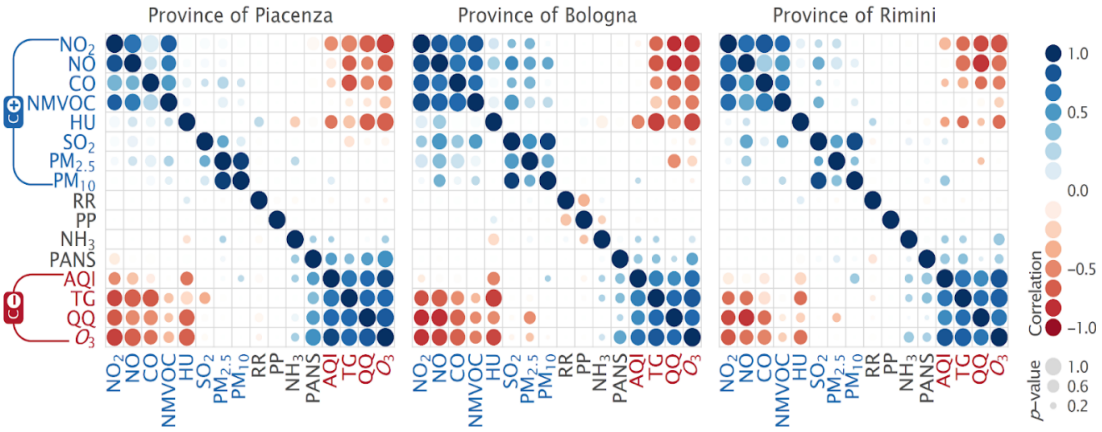

Figure 4. Correlation heatmap between and meteorological and air quality parameters for provinces of Piacenza, Bologna, and Rimini.

In Figure 4, plots relating to the provinces of Piacenza, Bologna and Rimini illustrate different areas of Emilia-Romagna, from northwest, center and southeast, respectively. Variables are sorted according to the

first principal component order. According to Figure 4, it is possible to define two groups of parameters, which tend to be negatively correlated to each other: (1) C+ that comprises NO_2, CO, NO, NMVOC, Air Relative Humidity, SO_2, $PM_{2.5}$ and PM_{10}; and (2) C- that comprises AQI, TG, QQ, and O_3. The C+ group tends to be higher in winter and autumn, and lower in the hotter periods. On the other hand, while the C- group presents parameters with opposite correlation behaviour (Figure 4). Precipitations, Sea Level Pressure, PANs, and NH_3 parameters are not considered in the analysis because they do not fit in any group since they have no strong correlations with any other parameter.

Figure 5 shows time series of meteorological and air quality parameters belonging to the C- group (i.e., O_3 and TG) and the C+ group (i.e. NO_2, SO_2 and HU). For Nitrogen Dioxide, the first lockdown period presents smoothly lower concentrations than the previous years, while the second lockdown points increased variations in concentrations that started one month before. For Sulphur Dioxide, the first lockdown highlighted higher concentrations in comparison with the same period in years preceding 2020. Timeseries of C- group parameters show entirely different behaviours. For example, O_3 concentrations rise as temperature increases, while they decrease with high precipitation, which helps clean air from particles. During both lockdown periods, O_3 concentrations were slightly above the previous year's levels, showing the impact of reducing vehicle fleet emissions of NO_2. This shows the role of seasonal cycles over air quality parameters and the importance of seasonally adjusting them. Finally, as expected, the meteorological parameters TG and HU presented no significant variations along the analysed period, remarking a small inter-annual variation that helps to fairly compare the air quality parameters.

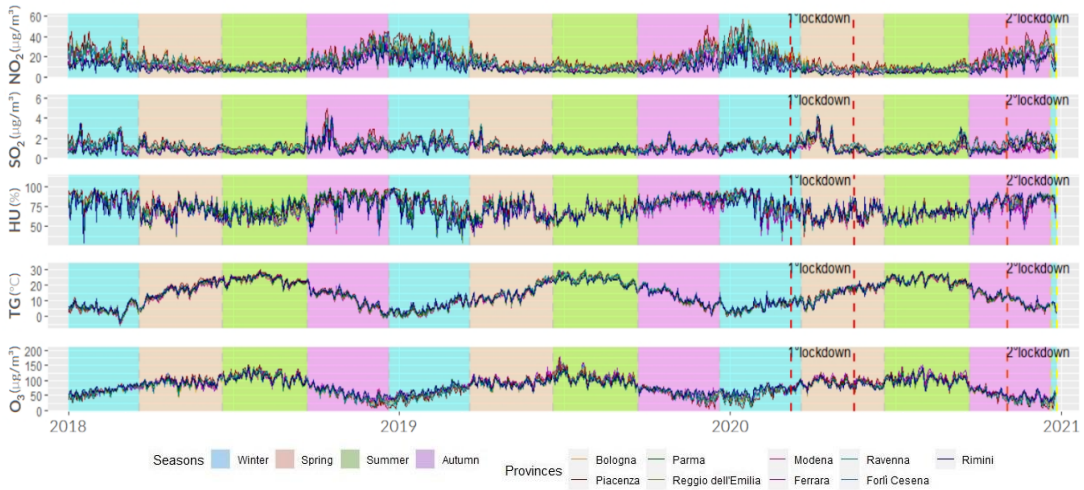

Figure 5. Time series of the analysed parameters from 01/01/2018 to 31/12/2020. Dotted lines remark the two lockdown periods in Emilia-Romagna.

After the explorative analysis, in which all the years covered by the datasets available for analysis have been considered, for the correlation analysis we have just considered the period from 05/03/2020, i.e., the date from which we have available information on the number of COVID-19 positives, deaths, hospitalizations and intensive care units, to the end of 2020. Year 2020 has been selected both because it was characterised by lockdown phases common to the whole of Italy and because at that time the vaccination campaign had not yet started, so the incidence number is not affected by the percentage of vaccinated persons.

In order to obtain seasonally adjusted air quality parameters, firstly original time series covering the complete period available have been split in their three main components (*https://www.rdocumentation.org/packages/stats/versions/3.6.2/topics/decompose*), i.e. seasonal component, trend component and reminder, through additive decomposition, then the seasonal component have been subtracted from the original data. Seasonally adjusted air quality parameters that show an interesting behaviour for the province of Bologna are shown in Figure 6, scaled with respect to their mean and standard deviation, to make them comparable on the same plot. Shaded areas represent lockdown

phases in Emilia-Romagna: Period 1 (red) correspond to the first lockdown period for the whole Italy; Periods 2 and 3 represent part of the second lockdown when the colour system was introduced with three risk bands weekly assigned to each region based on monitoring indicators. In this period, Emilia-Romagna was classified initially as High-risk zone (orange) and then as moderate-risk zone (yellow). In Figure 6, the seasonal adjusted concentrations highlight the increase of fluctuations in the first phase but especially in the last two phases of the lockdown for variables belonging to Group C+ (i.e., SO_2, PM_{10}, CO and NO_2) that tends to be flatter between June and October 2020. Both behaviors show a similarity with COVID-19 parameters (dotted lines). On the other hand, after being seasonally adjusted, O_3 (pink) and PANs (dark blue) concentrations tend to be noisier, suggesting to be unaffected by seasonality and reinforcing the results presented in Figure 5.

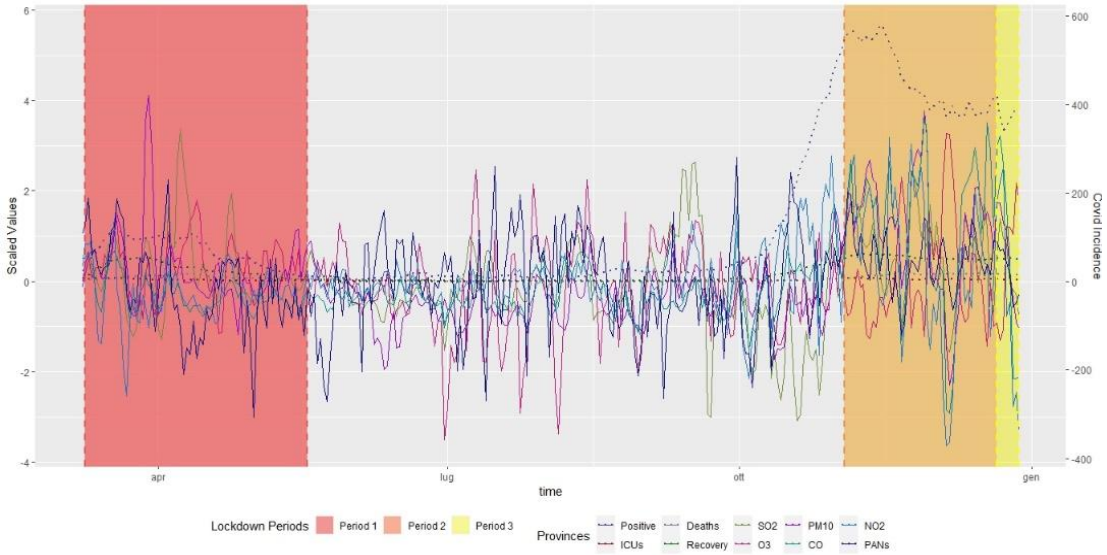

Figure 6. Scaled seasonally adjusted time series vs COVID-19 incidence with lockdown period marked in different colours in the province of Bologna from 05/03/2020 to 31/12/2020.

CONCLUSIONS

This study has explored the relationship between meteorological parameters and air quality parameters during the COVID-19 pandemic. Through time series analysis we have qualitatively shown the influence that lockdowns have had on certain air quality variables, such as SO_2, PM_{10}, CO, NO_2, NO, $PM_{2.5}$. Furthermore, the seasonal adjusted concentrations highlight a trend towards increased C+ group (i.e. SO_2, PM_{10}, CO and NO_2) fluctuations in the first phase but especially in the last two phases of the lockdown. The concentrations tend to be flatter between June and October 2020. Similar behaviours have been observed with the COVID-19 variables. Our findings show the need of considering seasonal adjusted parameters in the spread of COVID-19 pandemic. It may be useful to understand the role of seasonality during COVID-19 transmission in order to e.g., better formulate public health interventions.

ACKNOWLEDGEMENTS

This work was partially supported by the INFN CSN5 PLANET project.

REFERENCES

Accarino, G., S. Lorenzetti, and G. Aloisio, 2021: Assessing correlations between short-term exposure to atmospheric pollutants and COVID-19 spread in all Italian territorial areas. *Environ. Pollution*, **268**, 115714.

World Health Organization (WHO), 2013: Burden of disease from ambient air pollution for 2012 - summary of results. Regional Office for Europe, Copenhagen, Denmark.

Lolli, S., Y.C. Chen, and S.H. Wang, 2020: Impact of meteorological conditions and air pollution on COVID-19 pandemic transmission in Italy. *Sci Rep*, **10**, 16213.

21st International Conference on
Harmonisation within Atmospheric Dispersion Modelling for Regulatory Purposes
27-30 September 2022, Aveiro, Portugal

BOTTOM-UP INVENTORY OF RESIDENTIAL COMBUSTION EMISSIONS IN POLAND FOR NATIONAL AIR QUALITY MODELLING: CURRENT STATUS AND PERSPECTIVES

Lech Gawuc, Karol Szymankiewicz, Dorota Kawicka, Ewelina Mielczarek, Kamila Marek, Marek Soliwoda, Jadwiga Maciejewska

Institute of Environmental Protection – National Research Institute, Krucza 5/11D, 00-548 Warsaw, Poland

Abstract: : For many years, the Polish air quality modelling system was decentralized, which significantly hampered the appropriate development of methodologies, evaluation, and comparison of modelling results. The major contributor to air pollution in Poland is the residential combustion sector. The presented paper demonstrates a novel methodology for residential emission estimation utilized for national air quality modelling and assessment. Our data is compared with EMEP and CAMS inventories, and despite some inequalities in country totals, spatial patterns are similar. We discuss the shortcomings of the presented method and draw conclusions for future improvement.

Key words: *air quality; emissions; inventory; residential combustion, fuel mix.*

INTRODUCTION

One of the best sources of air quality (AQ) information is a network of atmospheric measurements sites. In order to provide comprehensive AQ assessment, data collected by such observational stations should be supplemented with AQ modelling, which can provide full spatial coverage over vast areas. AQ modelling is dependent on the emission input data, models used and methodologies applied. AQ models are frequently evaluated (Struzewska *et al.*, 2015), but some studies have identified emission inventories as one of the primary sources of uncertainty in the modelling chain (Russell and Dennis, 2000). This is connected with the fact that estimation of atmospheric pollution emissions is very challenging, primarily because of the lack of appropriate activity data. This is due to several reasons. First of all, it is common in many countries that there is no centralized database that would provide spatially resolved and consistent information about fuel sales or fuel usage on a national scale. Secondly, frequently the data is a trade secret or is incomplete and uncertain. Thirdly, many entities (e.g. cities or local governments) create their databases, which in many cases are not comparable between each other. This inevitably leads to significant discrepancies in AQ modelling results.

Pollutants emission is connected with specific human activities, and some of them are commonly observed. For example, road traffic, similarly to agricultural production, is often monitored, i.a., for economic purposes. Although the main goal of such data collection is not emission estimation, they can be easily adopted. Unfortunately, human activities connected with residential combustion are typically not monitored directly (besides population). It is hard to connect it with a distinct output such as electrical (as in the power generation sector) or goods output (as in the industrial sector). Hence it can be a source of significant uncertainties in emission inventories (Bond *et al.*, 2004). Moreover, there are various furnaces and fuels used, and it is difficult to analyze and catalogue them or formulate emission factors. Although there are examples of comprehensive emission inventories for the residential sector based on fuel consumption (Kannari et al., 2007), data access for emission estimation is problematic in many countries. For example, in Norway, there is a web-crawler utilized, which uses online estate adverts in order to collect data (Lopez-Aparicio *et al.*, 2018) in China some investigations employ indirect methods like regression models for fuel consumption estimation (Zhu *et al.*, 2020), in Vietnam (Huy *et al.*, 2021), in Lombardy (Italy) (Pastorello *et al.*, 2011) surveys were utilized as data collection method.

Poor AQ was a basis for the Court of Justice of the European Union (CJEU) sentence (from 28 February 2018) against Poland for permanent exceedances of PM10 norms (established in EU Parliament and Council Directive 2008/50/WE on 21 May 2008). Even though many activities have been undertaken to reduce emissions throughout the last two decades, nowadays, AQ in Poland is still unsatisfactory. PM10,

PM2.5 and B(a)P limit values are often exceeded in many parts of the country. The major source of those pollutants is residential fuel combustion for heating purposes.

In the year 2019, a novelization of the legal act was introduced that changed the national AQ modelling system organization. Since then, AQ modelling and preparation of emission database became the Institute of Environmental Protection—National Research (IEP-NRI) duty. Such change allowed for consequent development and enhancement of AQ modelling and emission inventory in one central institution. IEP-NRI is responsible for emission estimation from all of the existing sources (Central Emission Database – CED) from all sectors, namely: residential, transport, industry, agriculture, natural sources, other (like landfills, excavation sites, mining heaps). The inventory was created for the purpose of the national AQ modelling. It is utilized as an input for the GEM-AQ model (Kaminski *et al.*, 2008). The results of modelling serve as a supplement for AQ in-situ monitoring, which constitutes the basis of ChIEP (Chief Inspectorate for Environmental Protection) Air Quality Annual Assessments.

The main goal of this manuscript is to present the current methodology of residential emissions estimation, draw perspectives for development, and compare existing data with well-known inventories from EMEP and CAMS. There are clear advantages over those: it is a bottom-up inventory (which allows for indirect inclusion of local databases) and designed for individual buildings that allow for almost any AQ modelling spatial resolution.

The presented manuscript is an abstract of the previously published article (Gawuc *et al.*, 2021).

MATERIALS AND METHODS

The CED inventory follows a bottom-up methodology. The data presented here was prepared in late 2020 and early 2021. It is based on data from 2019, and it was utilized in the 2020 ChIEP AQ Annual Assessment ("Air Quality Assessment for the year 2020").

Residential emission estimation in CED is dependent on several inputs (Table 1). The spatial resolution is not equal for all of the data, and some datasets do not have resolution since accurate vector geometries with spatial reference represent them. For example, heating degree days (HDD) are calculated in a grid using GEM-AQ data with a resolution of 0.025 degrees for the entire country. At the same time, the fuel mix is available not in a regular grid but as table data for each "district unit" (administrative units without uniform spatial coverage – we distinguish 3592 such units covering the entire country). All of the data is assigned to buildings using their geographical location.

Table 1. Input data used for residential emission estimation.

Data	Spatial coverage (resolution, form)	Source
Buildings location, area, number of stories, function	Country (vector)	Topographic Objects Database (BDOT10k)
HDD	Country (0.025 deg, raster)	GEM-AQ
Fuel mix (gas, wood, coal, oil – expressed in unitless values 0-1)	Country (district units, table)	ChIEP, municipality offices
Gas usage for heating	4/16 Voivodships (district unit, tables)	Polish Gas Distribution Group
Buildings age (insulation factor)	Country (fixed for poviats, tables)	Main Statistics Office
Heat distribution network geometries	Poviat (vector)	Poviat Centers for Geodetic and Cartographic Documentation, heat power companies, other
Access to a heat distribution network	Local (tables or vectors)	Local Heating Plants, heat power companies

Since input data is taken from various sources, unification is a challenge. The heat distribution network and other data serve as a proxy to determine which buildings have individual heat sources (and thus emit pollution) and which do not. This is a critical step in our methodology.

ChIEP evaluates CED on a regular basis. Experts check groups or individual buildings and provide coded notes if there are some changes necessary. Several building features are considered: link to heat or gas network, fuel mix, building function, etc. Those remarks are included when emissions are processed for GEM-AQ model input.

The first step of emission processing is to combine all of the country-wide and local data for individual buildings. The second step is to calculate heat demand (HD) and to address ChIEP remarks. The last step is to calculate emissions using appropriate emission factors. For ChIEP AQ Annual Assessment, discharge of 8 pollutants is estimated (SOx, NOx, PM_{10}, $PM_{2.5}$, TSP, CO, NMVOC and B(a)P).

The CED is improved regularly. New heat distribution networks are included once they are obtained from the data providers. Fuel mixes are evaluated with the help of ChIEP and by using local emission inventories, which are systematically analyzed and included in CED. Currently, the main focus of residential sector improvement is put on aspects like fuel mixes improvement. For more information, please refer to the published full-text paper (Gawuc *et al.*, 2021).

Both CAMS and EMEP (CAMS-REG-v4) are top-down inventories and are often utilized in emission science (Clappier and Thunis, 2020; Guevara et al., 2017; Trombetti et al., 2018). EMEP data is actual for 2019 (regridded in 2021) and CAMS for 2017. There is a mismatch between the topicalities of the compared data. Moreover, each inventory is based on a different methodology and has a different spatial resolution (EMEP 0.1 deg, CAMS 0.1x0.05 deg). Since CED data has no fixed spatial resolution, it is utilized in the national AQ modelling with a homogeneous spatial resolution (0.025 deg for most of the country and 0.005 deg for the biggest cities). However, given the objective of this paper, which is a presentation of methodology used in national AQ modelling in terms of residential emission estimation, it should not hamper our analyses.

One of the possible ways to evaluate residential emission estimates included in the CED is to compare them to the existing inventories. In the next section, we present the results of the comparison between CED, EMEP and CAMS.

RESULTS

To compare CED with CAMS and EMEP inventories, we present a set of maps showing the spatial patterns of three primary pollutants: NOx, SOx and PM_{10} (Figure 1) and country totals (Table 2).

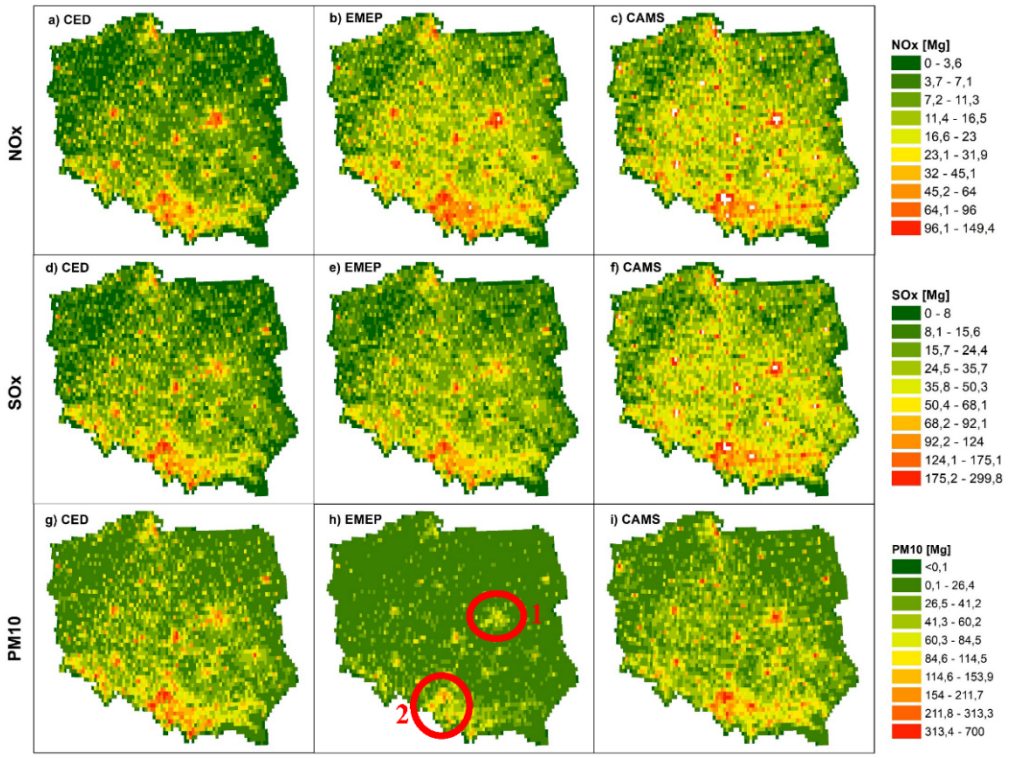

Figure 1. Annual emission discharge per cell of NOx, SOx and PM_{10} (white cells indicate values exceeding the color scale). Spatial resolution was unified (0.1 deg).

In the case of NOx CED data gives the smallest values, about twice lower than CAMS or EMEP (Table 2). Most CED NOx emissions are concentrated in the biggest cities, while the contribution of rural sites is

much lower (Figure 1 abc). When SOx emissions are compared, we notice that CED and EMEP country totals are very close, and the SOx spatial patterns are also very similar (Figure 1 de).

Table 2. Country totals for the compared inventories from the residential sector.

[Mg]	CED (2019)	EMEP (2019)	CAMS (2017)
NOx	46 222.3	73 794.5	85 722.7
SOx	109 346.3	116 409.4	170 871.0
PM_{10}	188 776.2	88 073.0	190 596.6
$PM_{2.5}$	185 236.3	58 318.0	187 384.5
B(a)P	113.5	59.7	not available
NMVOC	200 052.7	99 537.4	116 151.6
CO	1 758 858.8	1 273 909.3	1 505 800.4
TSP	204 473.8	117 225.8	not available

CAMS data gives much higher total values than CED or EMEP (Table 2), confirmed in the spatial pattern (Figure 1 f). The last pollutant discussed – PM_{10} – reveals once again a different situation (Figure 1 ghi). This time CAMS and CED country totals are very close to each other, while EMEP data gives the lowest country totals – less than half of the other inventories (Table 2). Similarly, in the case of $PM_{2.5}$ and NMVOC. Moreover, as CAMS and CED data spatial distribution is comparable, EMEP gives low PM_{10} values for the majority of Poland. Even Warsaw agglomeration (Figure 1 h1) has relatively low PM_{10} values as compared to other urbanized areas (Silesia in the southern part of the country – Figure 1 h2).

To sum up, we must comment that each emission inventory gives different results. For NOx and SOx, CED data totals are the lowest, but highest for NMVOC, TSP and CO. PM_{10} and $PM_{2.5}$ CED country totals are very close to those to CAMS and relatively close in the case of CO. EMEP is in the middle for SOx, CO and NOx, but the obtained country totals are much lower than in other inventories for the particulate matter. In general, inequalities in the presented country totals are acceptable and can be explained by different methodologies applied. Such discrepancies are not alarming since inconsistencies between emission inventories are well documented (Ferreira *et al.*, 2013; Denier van der Gon *et al.*, 2015; Guevara *et al.*, 2017; Thunis *et al.*, 2021).

SUMMARY AND PERSPECTIVES

Comparisons between different emission inventories is a challenging but necessary task. It is well established in the scientific literature that emission inventories can have serious discrepancies. Moreover, CED data is based on a bottom-up approach, which typically gives different results than top-down estimates (Guevara *et al.*, 2017). IEP-NRI is still working on the emission factors improvements.

Since CED emission inventory was created for the purpose of the national AQ modelling, the critical test of its performance is the evaluation of AQ modelling results using in-situ observations. Such evaluation is done regularly as a part of the ChIEP AQ Annual Assessment ("Air Quality Assessment for the year 2020: model evaluation").

The data that is useful for residential combustion emissions estimation is very scattered and diversified in Poland. The critical step is to identify buildings with individual furnaces from those connected to heat distribution networks. For our purposes, vector geometries of heat distribution networks were collected from Poviat Centers for Geodetic and Cartographic Documentation. To our best knowledge, IEP-NRI is the only institution in Poland that systematically gathers such data. This has been an ongoing process since the year 2018. The "non-emitting" buildings identification process is an excellent example of a novel approach to residential emission estimation in Poland.

Valuable data for residential sectors might be available in local inventories in some parts of Poland (individual cities or regions). Some of them were created, for example, for AQ improvement plans. Such inventories often contain very detailed and accurate data and since they are based on "local knowledge" they can be beneficial in the emission estimation process. Fortunately, the design of our methodology allows for the inclusion of local databases. In fact, individual buildings can have unique data.

CED is constantly under improvement. Recently, data from local databases were included for three polish cities: Bydgoszcz, Kraków and Opole. However, it is known that reciprocal links between local and national inventories are complex (Paunu *et al.*, 2021). Local data databases might introduce some underestimations since citizens could report lower fuel consumption than actual or some unreported

emissions might not be addressed accordingly. The process of including local databased will be continued in future.

We indicate other aspects that need urgent enhancement. The fuel mix database has an inconsistent spatial coverage – in some cities, it is on the district level and in some is more general. IEP-NRI, in cooperation with ChIEP, is looking for various ways to improve fuel mix data on a regular basis. Secondly, building ages are incorporated as statistical data on the poviat scale. We plan to enhance the building's age data (insulation factor) for more detail.

In future, the core of residential emission inventory will be based on CERB (Central Emission Registry from Buildings). Reporting is obligatory and includes a heat source, furnace class, number of residents, fuel type and consumption, etc. Consistent throughout the whole country, such data will be a new standard and would allow for a much better emission estimation. The CERB is planned to be fully operational in 2023.

REFERENCES

Air Quality Assessment for the year 2020: Chief Inspectorate for Environmental Protection. URL: https://powietrze.gios.gov.pl/pjp/content/show/1002921

Air Quality Assessment for the year 2020: model evaluation. Chief Inspectorate for Environmental Protection. URL: https://powietrze.gios.gov.pl/pjp/publications/card/23102

Bond TC, Streets DG, Yarber KF, Nelson SM, Woo J-H, Klimont Z. 2004. A technology-based global inventory of black and organic carbon emissions from combustion. Journal of Geophysical Research: Atmospheres, 109(D14). https://doi.org/10.1029/2003JD003697.

Denier van der Gon H a. C, Bergström R, Fountoukis C, Johansson C, Pandis SN, Simpson D, Visschedijk AJH. 2015. Particulate emissions from residential wood combustion in Europe – revised estimates and an evaluation. Atmospheric Chemistry and Physics. Copernicus GmbH, 15(11): 6503–6519. https://doi.org/10.5194/acp-15-6503-2015.

Ferreira J, Guevara M, Baldasano JM, Tchepel O, Schaap M, Miranda AI, Borrego C. 2013. A comparative analysis of two highly spatially resolved European atmospheric emission inventories. Atmospheric Environment, 75: 43–57. https://doi.org/10.1016/j.atmosenv.2013.03.052.

Gawuc L, Szymankiewicz K, Kawicka D, Mielczarek E, Marek K, Soliwoda M, Maciejewska J. 2021. Bottom–Up Inventory of Residential Combustion Emissions in Poland for National Air Quality Modelling: Current Status and Perspectives. Atmosphere. 12(11): 1460. https://doi.org/10.3390/atmos12111460.

Guevara M, Lopez-Aparicio S, Cuvelier C, Tarrason L, Clappier A, Thunis P. 2017. A benchmarking tool to screen and compare bottom-up and top-down atmospheric emission inventories. Air Quality, Atmosphere & Health, 10(5): 627–642. https://doi.org/10.1007/s11869-016-0456-6.

Huy LN, Oanh NTK, Phuc NH, Nhung CP. 2021. Survey-based inventory for atmospheric emissions from residential combustion in Vietnam. Environmental Science and Pollution Research, 28(9): 10678–10695. https://doi.org/10.1007/s11356-020-11067-6.

Kaminski JW, Neary L, Struzewska J, McConnell JC, Lupu A, Jarosz J, et al.. 2008. GEM-AQ, an on-line global multiscale chemical weather modelling system: model description and evaluation of gas phase chemistry processes. Atmospheric Chemistry and Physics. Copernicus GmbH, 8(12): 3255–3281. https://doi.org/10.5194/acp-8-3255-2008.

Lopez-Aparicio S, Grythe H, Vogt M, Pierce M, Vallejo I. 2018. Webcrawling and machine learning as a new approach for the spatial distribution of atmospheric emissions. PLOS ONE. Public Library of Science, 13(7): e0200650. https://doi.org/10.1371/journal.pone.0200650.

Pastorello C, Caserini S, Galante S, Dilara P, Galletti F. 2011. Importance of activity data for improving the residential wood combustion emission inventory at regional level. Atmospheric Environment, 45(17): 2869–2876. https://doi.org/10.1016/j.atmosenv.2011.02.070.

Paunu V-V, Karvosenoja N, Segersson D, López-Aparicio S, Nielsen O-K, et al.. 2021. Spatial distribution of residential wood combustion emissions in the Nordic countries: How well national inventories represent local emissions? Atmospheric Environment, 264: 118712. https://doi.org/10.1016/j.atmosenv.2021.118712.

Russell A, Dennis R. 2000. NARSTO critical review of photochemical models and modeling. Atmospheric Environment, 34(12): 2283–2324. https://doi.org/10.1016/S1352-2310(99)00468-9.

Struzewska J, Zdunek M, Kaminski JW, Łobocki L, Porebska M, Jefimow M, Gawuc L. 2015. Evaluation of the GEM-AQ model in the context of the AQMEII Phase 1 project. Atmos. Chem. Phys., 15(8): 3971–3990. https://doi.org/10.5194/acp-15-3971-2015.

Thunis P, Crippa M, Cuvelier C, Guizzardi D, de Meij A, Oreggioni G, Pisoni E. 2021. Sensitivity of air quality modelling to different emission inventories: A case study over Europe. Atmospheric Environment: X, 10: 100111. https://doi.org/10.1016/j.aeaoa.2021.100111.

Zhu M, Liu L, Yin S, Zhang J, Wang K, Zhang R. 2020. County-level emission inventory for rural residential combustion and emission reduction potential by technology optimization: A case study of Henan, China. Atmospheric Environment, 228: 117436. https://doi.org/10.1016/j.atmosenv.2020.117436.

21st International Conference on
Harmonisation within Atmospheric Dispersion Modelling for Regulatory Purposes
27-30 September 2022, Aveiro, Portugal

EVALUATION OF THE EFFECTS OF THE NATIONAL EMISSION REDUCTION STRATEGIES FOR YEARS 2020-2029 AND AFTER 2030 ON THE SULPHUR AND NITROGEN SURFACE CONCENTRATIONS ON THE TERRITORY OF BULGARIA

Ivelina Georgieva [1], Georgi Gadzhev[1], Kostadin Ganev[1] and Vladimir Ivanov[1]

[1] National Institute of Geophysics, Geodesy and Geography, Bulgarian Academy of Sciences

Abstract: Complying the EU Directive 2016/2284, Bulgaria developed national emission reduction strategies for years 2020-2029 and after 2030. Evaluation of the effects of these strategies on the Sulphur and Nitrogen surface concentrations on the territory of Bulgaria is the objective of the present study.
The studies are performed applying computer simulations. The simulations are performed with the US EPA Models-3 System: Meteorological model WRF; Emission model SMOKE; Atmosphere Composition Model CMAQ for the period 2008 – 2014. The provided model simulations are with horizontal resolution 9 kilometers for the region of Bulgaria. The NCEP Global Analysis Data meteorological background with 1°x1° resolution is used as a meteorological background. The models nesting capabilities were applied to downscale the simulations to 9 km resolution for Bulgaria.
Five emission scenarios are considered: 2005 emissions (reference period), 2020-2029 emissions projected with existing measures (WEM) and with additional measures (WAM), projected after 2030 WEM and WAM emissions. The comparison of the concentrations, simulated with the different scenarios makes it possible to evaluate the effect of the national emission reduction strategies.

Key words: *emission reduction, surface concentrations, computer simulations, emission scenarios.*

INTRODUCTION

The present paper presents part of the results obtained in the frame of an extensive study of the effects of different emission reduction scenarios on the air quality in Bulgaria. The set of models applied for atmospheric composition simulations is the same used in the operational Bulgarian Chemical Weather Forecast and Information System. Thus, the obtained results are fully compatible with the operational chemical weather forecast. The models are also widely used in air pollution modelling, so the obtained computer simulation results are in harmony with evaluations made for other regions. Air pollution forces many countries to take action to mitigate its adverse effects on human health and ecosystems. There is already a large amount of direct and indirect data connected to the air quality from the different surface and satellite-based observing systems. However, we need to track the various processes involved in the composition, transport, and transformation of the air pollutant species, which will help us better understand their distribution at different spatial/temporal scales. These tasks are performed by air quality modeling systems, as we use US EPA Models 3 System for modeling the air quality in our country - Bulgaria.
The main goal of this work is to make a comparison between Nitrogen (NO_2) and Sulfur (SO_2) dioxide surface concentrations, simulated with the different emission reduction scenarios (with and without measures) and the reference period (with emission for 2005), in Bulgaria.

METHODOLOGY

Based on 3D modelling tools, an extensive database was created and used for different studies of atmospheric composition. The simulations were based on the US EPA Model-3 system. - WRF v.3.2.1 (Shamarock et al. 2007), (UCAR/NCAR) - Weather Research and Forecasting Model, used as meteorological pre-processor; CMAQ v.4.6 - Community Multi-Scale Air Quality model (Byun et al., 1998), (Byun and Ching, 1999), (CMAS) the Chemical Transport Model (CTM), and SMOKE - the Sparse Matrix Operator Kernel Emissions Modelling System (CEP, 2003) the emission pre-processor of Models-3 system. This group of models is called Models-3 and is a typical example of the models created by a large number of teams in the implementation of various projects, funded mainly by the United States

Environment Agency (US EPA) - so-called “Community models”. The models in the system were adapted and validated for Bulgaria. This gave the opportunity to conduct extensive studies on a fully competitive modern level of the climate of atmospheric composition in the country. Previous results from air pollution modeling for Bulgaria are published in many papers (Gadzhev et al., 2013a, 2013b, 2013c), (Georgieva E. et al., 2017, 2019), (Georgieva I., 2014), (Syrakov et al., 2012, 2014, 2015, 2019).
The studies are performed by applying computer simulations for a 7-year period (2008 – 2014). The provided model simulations are with a horizontal resolution of 9 kilometers for the territory of Bulgaria. The large-scale (background) meteorological data used were from the ‘NCEP Global Analysis Data’ with a horizontal resolution of 1ºx1º. Using the ‘nesting’ capabilities of the models, a resolution of 9 km was achieved for the territory of Bulgaria (Fig.1). The resolution of the mother domain (Europe) is 81 km, and two other domains are nested in it and in each other – Balkan Peninsula (27 km resolution) and Bulgaria (9 km), as shown in Figure 1.
TNO inventory (Denier van der Gon et al., 2010) is exploited for the territories outside Bulgaria in the mother domain. For the Bulgarian domain, the National inventory as provided by Bulgarian Executive Environmental Agency is used.

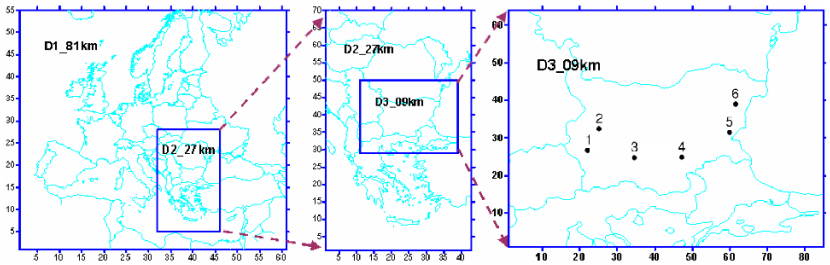

Figure 36. Model domains: Downscaling from domain Europe (81 km) to domain Bulgaria (09 km) and pointed location of some industrial zones in Bulgaria – 1 - TPP Bobovdol, 2 – Sofia city, 3 – Plovdiv city, 4 - TPP Maritsa Iztok, 5 – Burgas city, 6 - Devnya Industrial Area.

Every EU member state (According to the legislation) has to report the set of emission projections scenarios (EEA Technical report No 4/2015): projections scenario 'with existing measures' (WEM) means projections of anthropogenic Greenhouse Gas (GHG) or air pollutant emissions by sources that encompass the effects of currently implemented or adopted policies and measures; projections scenario 'with additional measures' (WAM) means projections of anthropogenic GHG or air pollutant emissions by sources that encompass the effects of policies and measures which have been adopted and implemented, as well as planned policies that are judged to have a realistic chance to be adopted and implemented in the future;
In the paper, four emission scenarios are considered for two periods, 2020-2029 and after 2030, with existing measures (WEM) and with additional measures (WAM), and the results are compared with the reference period (Ref 2005). It should be clear that only the Bulgarian emissions for 2020-2029 and 2030 have been modified according to the forecast scenarios.
The considerations and conclusions in the paper are based on simulated SO_2 and NO_2 surface concentrations on the territory of Bulgaria. Comparing the concentrations simulated with the different scenarios makes it possible to evaluate the effect of the national emission reduction strategies (EU Directive 2016/2284).

RESULTS

The Normalized Mean Bias noted as NMB (1) was used for comparison of the effect of different scenarios. The notions in these equations are i - ith value, S - the scenario output (WEM/WAM) for the selected period (2020-2029, 2030), and R - the output for the Reference period (2005). All of these scenarios are presented separately for the SO_2 and NO_2 surface concentrations and comparison with the reference period (2005) together with NMB in the following figures (Figure 2, Figure 3).

$$NMB = \frac{\sum_i S - \sum_i R}{\sum_i R} * 100[\%] \qquad (1)$$

Figure 2 presents the results from numerical experiments about NO_2 surface concentrations for different scenarios and the comparison with the results from the reference period 2005 and calculated NMB.

According to these results, we can say that not only the measures for reductions of emissions worked, but also clearly see which scenario gives better results.

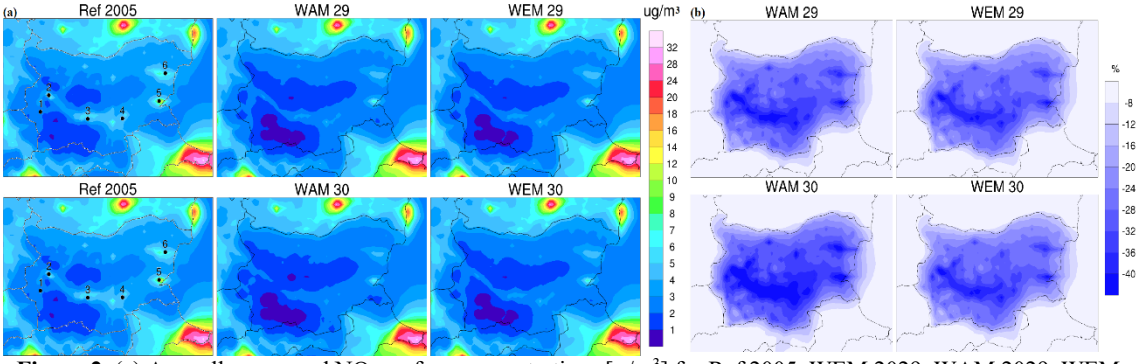

Figure 2. (a) Annually averaged NO_2 surface concentrations [μ/m^3] for Ref 2005, WEM 2029, WAM 2029, WEM 2030, WAM 2030 emissions scenarios and (b) NMB of the NO_2 surface concentrations [%] for WEM 2029, WAM 2029, WEM 2030, WAM 2030 emissions scenarios compared to the Ref 2005.

The results from all scenarios have a difference with a reduction tendency according to the reference period 2005. It is very well displayed for all plots and we can see that the values for some areas are smaller than those of Ref 2005 – 1.Sofia, 3.Plovdiv and 5.Burgas city, also 6.Devnya industrial area.
It can be stated that the scenario WAM 2030 shows significant reduction of the surface concentrations for the whole territory of the country. The NO_2 surface concentrations have a reduction for the WEM/WAM scenarios according to the Reference 2005, but on Figure 2(a) we cannot say which one of the scenarios is "working" better. All the statements are confirmed by the plots, where the NMB is calculated (b). The scale is up to 0, and all the biases are with a negative sign. That suggests that all the scenarios produce smaller concentrations compared to the reference period and emissions for 2005. All the measures show a positive effect of reduction of emissions and lead to a reduction of NO_2 surface concentrations. It can be clearly seen about 25 % reduction over the whole domain and about 40% for some areas in the southwest part of the country. The WAM scenarios show bigger reduction for both selected periods, but for WAM 2030 the effect is most strongly manifested.

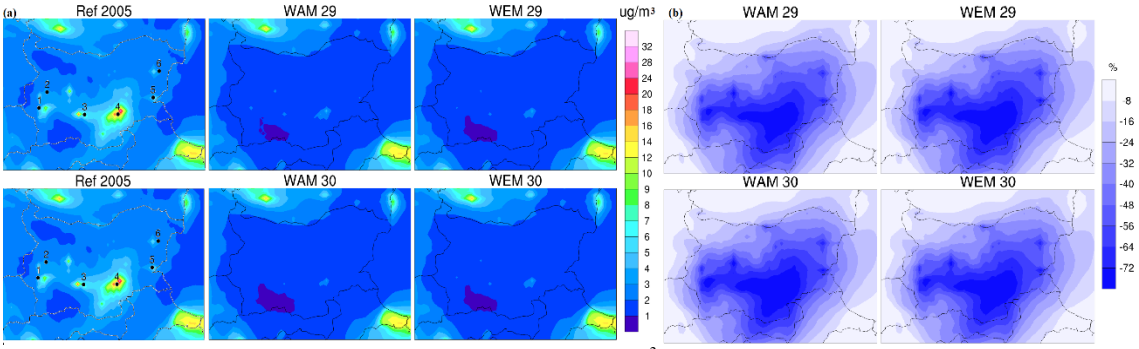

Figure 3. (a) Annually averaged SO_2 surface concentrations [μ/m^3] for Ref 2005, WEM 2029, WAM 2029, WEM 2030, WAM 2030 emissions scenarios and (b) NMB of the SO_2 surface concentrations [%] for WEM 2029, WAM 2029, WEM 2030, WAM 2030 emissions scenarios compare to the Ref 2005.

Figure 3 presents the results of the SO_2 for the different scenarios. Here, the effects of the emission reduction on SO_2 surface concentrations are very well expressed, and the differences with Ref 2005 are obvious. Again, all the scenarios show better results according to the reference period. The SO_2 plots on Figure 3(a) also shows that the scenarios of reduction of the emission lead to a decrease in the SO_2 concentrations. For all the results, we can say that more stringent measures lead to more effective results, where as in this study this is about the WAM scenario. The better results show the WAM 2030 scenario compared with the reference period and also compare with other scenarios. The results from plots on Figure 3(b) about the bias of the SO_2 concentrations, as we mention above, also have a negative sign. Here, the percentage of

reduction is very well expressed and shows very good results of taking measures. The reduction reaches 50% almost over the whole territory of the country and for all scenarios. On the plots, we can also see a reduction of 70% for some areas in the southwest part where are situated 4. TTP Maritsa Iztok and 3. Plovdiv city.

CONCLUSIONS

Complying with the EU Directive 2016/2284, Bulgaria developed national emission reduction strategies for 2020-2029 and after 2030. Evaluation of the effects of these strategies on the SO_2 and NO_2 surface concentrations on the territory of Bulgaria is demonstrated by some comparison of the concentrations, simulated with the different scenarios. This comparison makes it possible to evaluate the effect of the national emission reduction strategies: The NMB is used, and according to the results, we can conclude that the measures for reduction of emissions have good results and determine which scenario is better:
The numerical experiments about NO_2 surface concentrations for different scenarios show:
- the results from all scenarios have a difference with reduction tendency in comparison with the reference period 2005;
- the NO_2 surface concentrations are reduced for all the WEM/WAM scenarios according to the Reference 2005, but the scenario WAM 2030 shows better results for the whole territory of Bulgaria;
- all the biases are with a negative sign and show that all the scenarios have smaller concentrations compared with the reference period and emissions for 2005;
- all the measures show a positive effect of reduction of emissions and lead to a reduction of NO_2 surface concentrations;
- the reduction over the whole domain is about 25 % and about 40% for some areas in the southwest part of the country;
- the WAM scenarios show a more significant reduction for both selected periods, and also, the WAM 2030 is clearly the one with the most sound effect.

The numerical experiments about SO_2 surface concentrations for different scenarios show:
- the effects of the emission reduction on SO_2 surface concentrations are even better expressed, and the differences with Reference 2005 are obvious;
- all the scenarios show better results according to the reference period, which shows that all the scenarios of reduction of the emission lead to a decrease in the SO_2 concentrations;
- the better results are demonstrated by the WAM 2030 scenario compared with the reference period 2005 and also compared with other scenarios;
- the bias of the SO_2 concentrations also has a negative sign, and the percentage of reduction is very well expressed and shows very good results for taking measures;
- the reduction reaches 50% almost over the whole territory of the country and for all scenarios;
- a reduction of 70% is achieved for some areas in the southwest part.

For all the results, we can conclude that more stringent measures lead to more effective results, whereas this study is about the WAM scenario.

ACKNOWLEDGEMENTS

This work has been carried out in the framework of the National Science Program "Environmental Protection and Reduction of Risks of Adverse Events and Natural Disasters", approved by the Resolution of the Council of Ministers № 577/17.08.2018 and has been accomplished with the financial support by the Ministry of Education and Science (MES) of Bulgaria (Agreement № D01-279/03.12.2021) and the project" NATIONAL GEO-INFORMATION CENTER", subject of the National Road Map for Scientific Infrastructure 2017–2023, funded by Contr. No D01-161/28.08.2018.

REFERENCES

Byun, D., Young J., Gipson G., Godowitch J., Binkowski F.S., Roselle S., Benjey B., Pleim J., Ching J., Novak J., Coats C., Odman T., Hanna A., Alapaty K., Mathur R., McHenry J., Shankar U., Fine S., Xiu A., and Jang C., 1998: *Description of the Models-3 Community Multiscale Air Quality (CMAQ) Modeling System*, 10th Joint Conference on the Applications of Air Pollution Meteorology with the A&WMA, 11-16 January 1998, Phoenix, Arizona, 264-268.

Byun, D. and Ching, J., 1999: *Science Algorithms of the EPA Models-3 Community Multiscale Air Quality (CMAQ) Modeling System.* EPA Report 600/R-99/030, Washington, D.C., EPA/600/R-99/030 (NTIS PB2000-100561). https://cfpub.epa.gov/si/si_public_record_report.cfm?Lab=NERL&dirEntryId=63400

CEP, 2003: *Sparse Matrix Operator Kernel Emission (SMOKE) Modeling System*, University of Carolina, Carolina Environmental Programs, Research Triangle Park, North Carolina.

CMAS Homepage, http://www.cmaq-model.org, last accessed 2022/05/10

Denier van der Gon, H., Visschedijk, A., van de Brugh, H., Droge, R., 2010, *A high resolution European emission data base for the year 2005*, TNO-report TNO-034-UT-2010-01895 RPT-ML, Apeldoorn, The Netherlands (2010).

Directive (EU) 2016/2284 of the European Parliament and of the Council of 14 December 2016 on the reduction of national emissions of certain atmospheric pollutants, amending Directive 2003/35/EC and repealing Directive 2001/81/EC http://data.europa.eu/eli/dir/2016/2284/oj

EEA Technical report No 4/2015, *Projections in hindsight an assessment of past emission projections reported by Member States under EU air pollution and GHG legislation* https://www.eea.europa.eu/publications/projections-in-hindsight/download

Gadzhev, G., Ganev, K., Prodanova, M., Syrakov, D., Atanasov, E., Miloshev, N., 2013a, *Multi-scale Atmospheric Composition Modelling for Bulgaria*, NATO Science for Peace and Security Series C: Environmental Security, 137, 381-385.

Gadzhev, G.K., Ganev, K.G., Prodanov, M., Syrakov, D.E., Miloshev, N.G., Georgiev, G.J., 2013b, *Some numerically studies of the atmospheric composition climate of Bulgaria*, AIP Conference Proceedings, 1561, 100-111. DOI: 10.1063/1.4827219 529

Gadzhev, G., Ganev, K., Miloshev, N., Syrakov, D., Prodanova, M., 2013c, *Numerical Study of the Atmospheric Composition in Bulgaria*, Computers and Mathematics with Applications, 65, 402 – 422.

Georgieva E., Hristova E., Syrakov D., Prodanova M., Batchvarova E., 2017, *Preliminary evaluation of CMAQ modelled wet deposition of sulphur and nitrogen over Bulgaria*. HARMO 2017 – 18th International Conference on Harmonisation within Atmospheric Dispersion Modelling for Regulatory Purposes, Proceedings 2017 – October, 51 – 55.

Georgieva E., Syrakov D., Hristova E., Prodanova M., Gospodinov I., 2019, *Comparison of EMEP and WRF_CMAQ modelling results for deposition estimates in Bulgaria for 2016 and 2017*, 19th International Conference on Harmonisation within Atmospheric Dispersion Modelling for Regulatory Purposes, Harmo 2019.

Georgieva, I., 2014, *Study of the air quality index climate for Bulgaria*, Proc. of the international conference on numerical methods for scientific computations and advanced applications, May 19 – 22, 2014, Bansko, ISBN978-954-91700-7-8, 39– 42.

Shamarock, W.C., Joseph B., Dudhia J., Gill Dale M., Wang W., Jordan G., 2007: *A Description of the Advanced Research WRF Version 2*. http://www.dtic.mil/dtic/tr/fulltext/u2/a487419.pdf

Syrakov, D., Etropolska, I., Prodanova, M., Ganev, K., Miloshev, N., Slavov, K., 2012, *Operational Pollution Forecast for the Region of Bulgaria*, American Institute of Physics, Conf. Proc. 1487, 88 - 94; DOI: 10.1063/1.4758945.

Syrakov, D., Prodanova, M., Etropolska, I., Slavov, K., Ganev, K., Miloshev, N., Ljubenov T., 2014, *A multy-domain operational chemical weather forecast system*, Lecture Notes in Computer Science (including subseries Lecture Notes in Artificial Intelligence and Lecture Notes in Bioinformatics), 8353 LNCS, 413-420.

Syrakov, D., Prodanova, M., Georgieva, E., Etropolska, I., Slavov, K., 2015a, *Impact of NOx emissions on air quality simulations with the Bulgarian WRF-CMAQ modelling system*, International Journal of Environment and Pollution, 57, 3-4, 285-296.

Syrakov D., Georgieva E., Prodanova M., Hristova E., Gospodinov I., Slavov K., Veleva B., 2019, *Application of WRF-CMAQ model system for analysis of sulfur and nitrogen deposition over Bulgaria*, Lecture Notes in Computer Science (including subseries Lecture Notes in Artificial Intelligence and Lecture Notes in Bioinformatics), 11189 LNCS, 474 – 482.

UCAR/ NCAR Homepage, http://www.wrf-model.org, last accessed 2022/05/10

21st International Conference on
Harmonisation within Atmospheric Dispersion Modelling for Regulatory Purposes
27-30 September 2022, Aveiro, Portugal

EVALUATION OF THE IMPACT OF THE PROJECTED FUTURE EMISSIONS FROM ENERGY ON THE AIR QUALITY IN BULGARIA

Georgi Gadzhev[1], Kostadin Ganev[1], Ivelina Georgieva [1] and Vladimir Ivanov[1]

[1] National Institute of Geophysics, Geodesy and Geography - Bulgarian Academy of Sciences

Abstract: The strategic plans for future development of the energy production in Bulgaria will lead to a substantial change of the emissions from this source category. The evaluation of the impact of the projected future emissions from energy on the air quality in Bulgaria is the objective of the present study.
The studies are performed applying computer simulations. The simulations are performed with the US EPA Models-3 System: Meteorological model WRF; Emission model SMOKE; Atmosphere Composition Model CMAQ for the period 2008 – 2014. The provided model simulations are with horizontal resolution 9 kilometers for the region of Southeastern Europe, in particular Bulgaria. The NCEP Global Analysis Data meteorological background with 1°x 1°resolution is used as a meteorological background. The models nesting capabilities were applied to downscale the simulations to 9 km resolution.
The 2005 emissions (reference period) are taken as basic. The projected emissions (including emissions from energy production) for year 2030 are calculated for two scenarios - with existing measures (WEM) and with additional measures (WAM). Computer simulations are performed for these scenarios, as well as with the one with energy emissions reduced by a factor of 0.8. The comparison of the concentrations, simulated with the different scenarios makes it possible to evaluate the impact of different options of the future development of the energy production on the air quality in Bulgaria.

Key words: *air quality, chemical-transport models, emission scenarios, WAM, WEM.*

INTRODUCTION

The strategic plans for the future development of energy production in Bulgaria will lead to a substantial change in the emissions from this source category. The evaluation of the impact of the projected future emissions from energy on the air quality in Bulgaria is the objective of the present study.
Most countries, including Bulgaria, have developed systems for air quality forecasts (Syrakov et al., 2014, Kukkonen et al., 2012). They contain different modules for ingesting many kinds of input data and using them for simulation of the meteorological part as well as the processes of advection, diffusion, chemistry, and transformation of atmospheric pollutants. The advantage of these systems is their capability to simulate the different processes in a physically consistent way, which allows studying their influence on the atmospheric composition more thoroughly. Previous studies of the air quality adverse effects on the human body in Bulgaria (Georgieva, Ivanov, 2018) as a whole and the capital city Sofia (Georgieva, Ivanov, 2017, Georgieva 2021) have shown that their influence varies within the day, season, and the dominant pollutant. We carry out the research on the impact of projected emissions from the energy sector on the air quality in Bulgaria based on the modeling system used for forecasting the chemical weather in our country. The study takes into consideration 4 scenarios for projected emissions. The comparison of the concentrations, simulated with the different scenarios, makes it possible to evaluate the impact of different options for the future development of energy production on the air quality in Bulgaria.

METHODOLOGY

3D simulations by the US EPA Models-3 system developed by different collectives and funded mainly by the United States Environment Agency (US EPA) are made, and thus a database was created suitable for extensive research of the atmospheric composition. The system consists of three main modules. The first one is the emission preprocessor SMOKE - Sparse Matrix Operator Kernel Emissions Modelling System

(CEP, 2003). It is used for preparation of the emissions from the TNO inventory (Denier van der Gon et al., 2010) for foreign territories and the National Inventory provided by the Bulgarian Executive Environmental Agency for the territory of Bulgaria. The second module is the numerical weather prediction model - WRF version 3.4.1 (Shamarock et al. 2007, UCAR/NCAR). The initial and boundary conditions are taken from the NCEP Global Analysis Data with a horizontal resolution of 1º x 1º. The third module is the chemical-transport model CMAQ version 4.6 - Community Multi-Scale Air Quality model (Byun et al., 1998), (Byun and Ching, 1999) for simulation of the air composition based on the information from the meteorological model and emission preprocessor.
The simulations are performed for the period 2008 – 2014, and use the nesting capability of the US EPA Models-3 system (Figure 1). The meteorological data from the NCEP are used as a background for the large European domain (D1) with a resolution 81 km. The other two domains of the nesting chain are the Balkan Peninsula domain, with a spatial resolution 27 km (D2), and the Bulgaria domain (D3), with a horizontal resolution 9 km. Our study is based on the simulations from the D3.

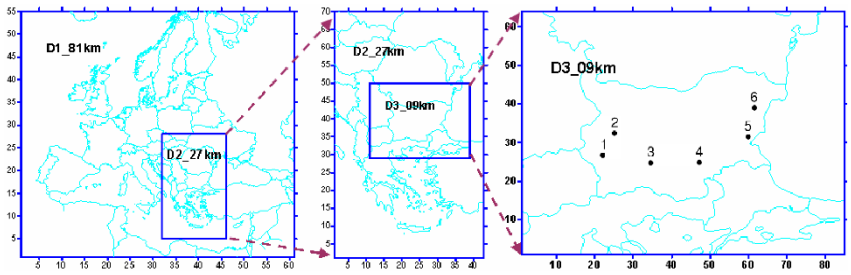

Figure 37. Model domains: Downscaling from domain Europe (81 km) to domain Bulgaria (09 km) and pointed location of some industrial zones in Bulgaria – 1 - TPP Bobovdol, 2 – Sofia city, 3 – Plovdiv city, 4 - TPP Maritsa Iztok, 5 – Burgas city, 6 - Devnya Industrial Area.

Every EU member state reports a set of emission projections scenarios (EEA Technical report No 4/2015). A projection scenario with "existing measures" (WEM) means projections of anthropogenic Greenhouse Gas (GHG) or air pollutant emissions by sources that encompass the effects of currently implemented or adopted policies and measures; projections scenario "with additional measures" (WAM) means projections of anthropogenic GHG or air pollutant emissions by sources that encompass the effects of policies and measures which have been adopted and implemented, as well as planned policies that are judged to have a realistic chance to be adopted and implemented in the future.
The forecast of air pollutant emissions according to the Bulgarian National Air Pollution Control Program 2020-2030 is given in Table 1.

Table 17. Projected air pollutant emissions for Bulgaria.

Pollutant	Emissions 2005 [kt]	Emissions 2030 WEM [kt]	Reduction factor [%]	Emissions 2030 WAM [kt]	Reduction factor [%]
SO_2	771.3	85.6	11.09	68.6	8.89
NO_X	183.2	85.4	46.61	67.8	37.01
NMVOC	80.7	55.9	69.27	47	58.24
NH_3	51.6	47	91.08	43.8	84.88
$PM_{2.5}$	30.9	18.5	59.87	8.8	28.47

Parallel calculations were carried out with 4 emission scenarios:
Scenario 1: WEM emission data for Bulgaria for 2030, with emissions from all source categories renormalized according to the ratios of the tabulated values for 2005 and projected values for 2030.
Scenario 2: WAM emission data for Bulgaria for 2030, with emissions from all source categories renormalized according to the ratios of the tabulated values for 2005 and projected values for 2030.
Scenario 3: WEM emission data for Bulgaria for 2030, with emissions from the Energy sector reduced by 20%.
Scenario 4: WAM emission data for Bulgaria for 2030, with emissions from the Energy sector reduced by 20%.
The comparison between scenarios 1 and 3 makes it possible to estimate the contribution of the sources from the Energy sector to the air quality for the whole country under the WEM scenario, and the comparison

between scenarios 2 and 4 makes it possible to estimate the contribution of the sources from the Energy sector to the air quality for the whole country under the WAM scenario.
It should be clarified here that only the Bulgarian emissions for 2030 have been modified according to the forecast scenarios (Table 1).

RESULTS

The present paper presents part of the results obtained in the frame of an extensive study of the effects of different emission scenarios on the air quality in Bulgaria. Due to volume limitations, only the impact of future emissions from the energy sector on the surface SO_2 concentrations in Bulgaria will be demonstrated. Figure 2 shows the contribution of the energy sector to the formation of surface concentrations of SO_2 for the 2030 WAM scenario. On average for the year, it would be almost entirely positive, reaching up to 10-15% in the midday and morning hours in the summer above the thermal power plant areas. Due to the more intensive transport from above and across the boundary and mixing with the layers aloft, and due to the non-linear chemical and aerosol processes and the strong emission reduction for 2030, areas with a weak negative contribution of the energy sector to the formation of ground SO_2 concentrations for this scenario are obtained.

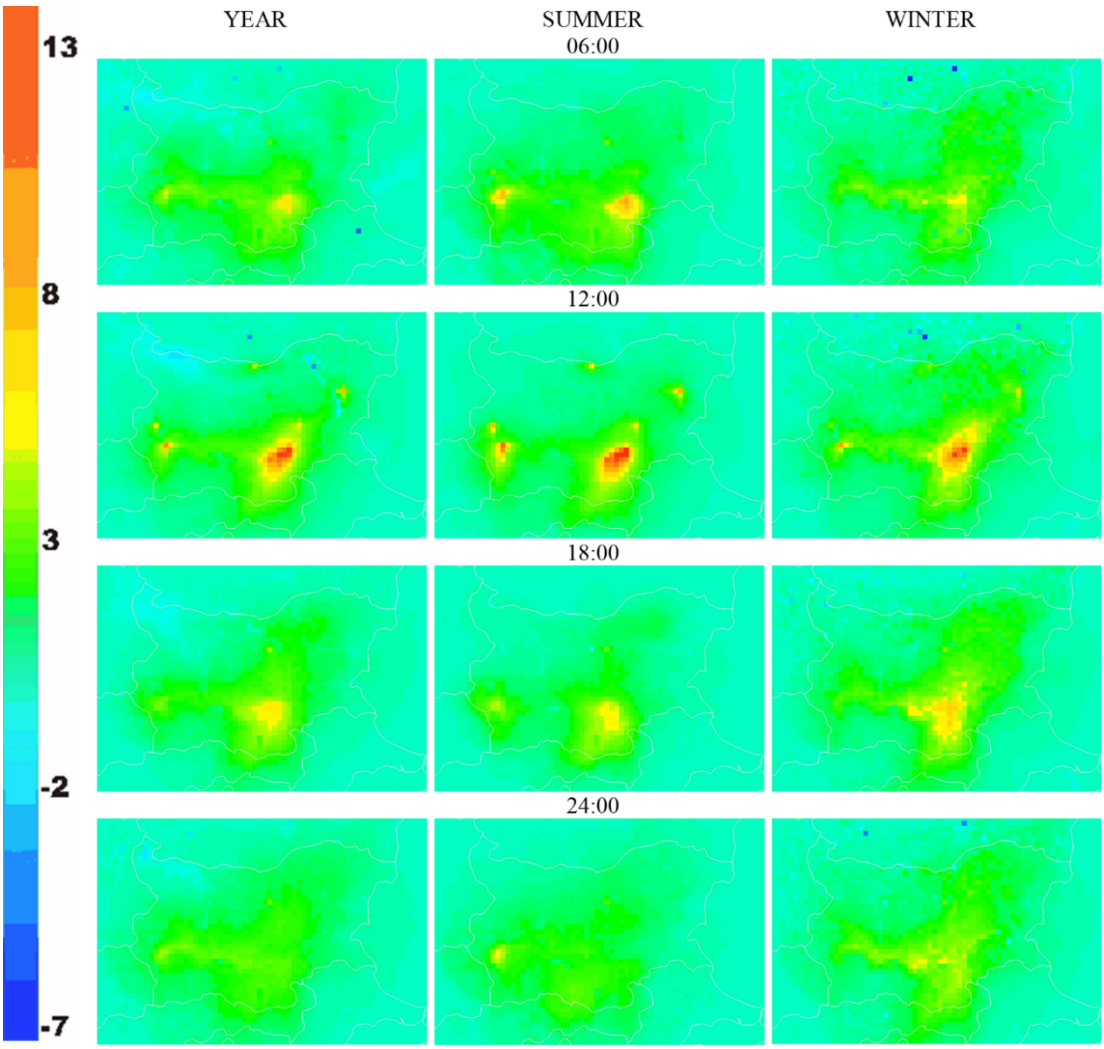

Figure 2. Maps of the relative contribution of sources from the energy sector to ground-level SO_2 concentrations obtained with 2030 WAM emissions averaged over the entire ensemble annually, for the summer and winter periods at 6, 12, 18 and 24 hours local time.

The picture for the WEM emission scenario is similar (Figure 3), with the contribution of the energy sector to the formation of SO_2 concentrations being more pronounced, especially in the winter when the energy consumption is higher.

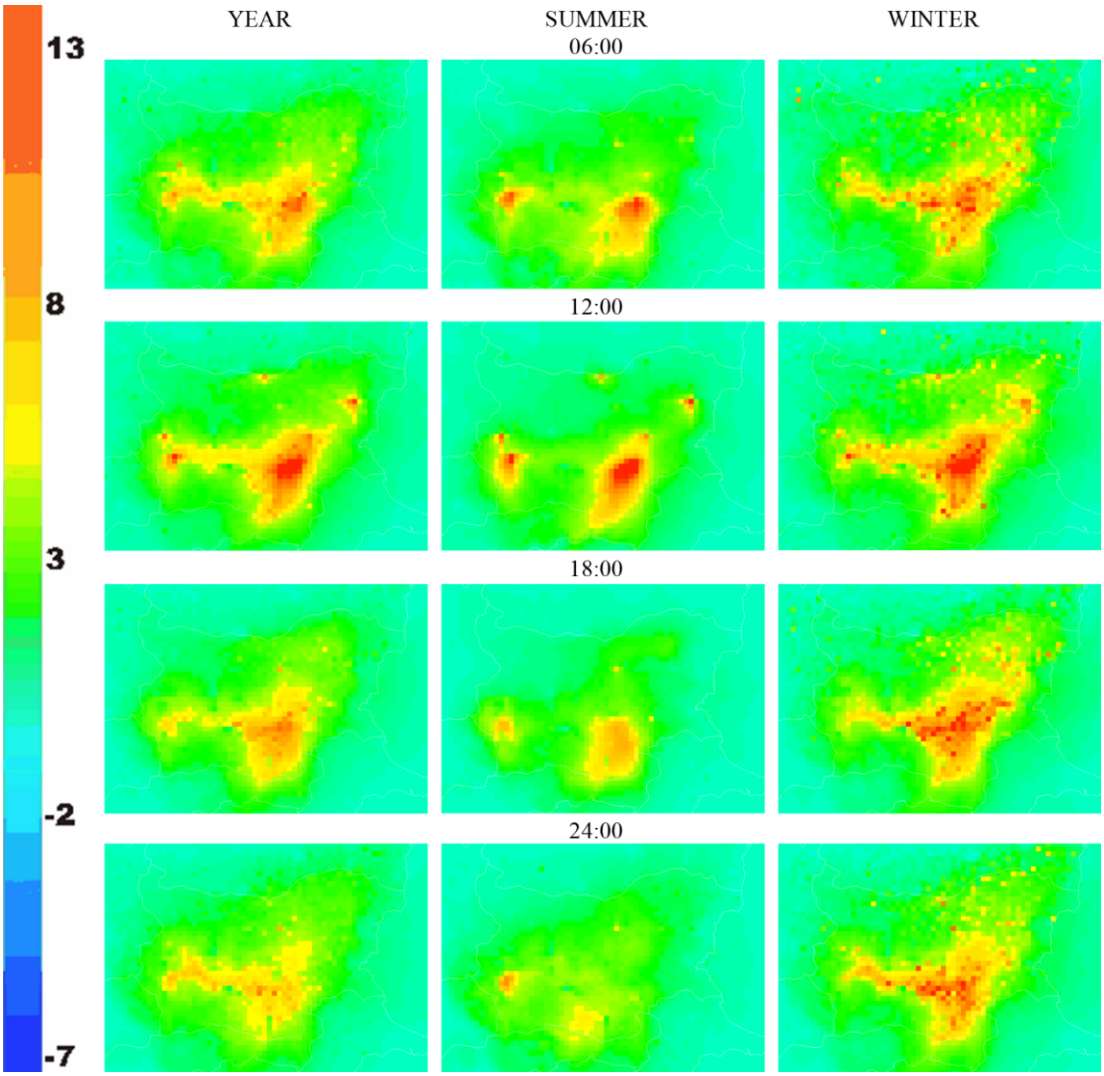

Figure 3. Maps of the relative contribution of sources from the energy sector to ground-level SO_2 concentrations obtained with 2030 WEM emissions averaged over the entire ensemble annually, for the summer and winter periods at 6, 12, 18 and 24 hours local time.

CONCLUSIONS

The differences in the estimates for the contribution of the emissions from the energy sector obtained for WAM and WEM emission scenarios are quite significant, and obviously, the 2030 WAM scenario is more favorable in terms of ambient air quality. This is well displayed for both winter and annually in the higher relative contribution and larger areas around the Thermal Power Plants in WEM scenarios (Figure 3).

ACKNOWLEDGEMENTS

This work has been carried out in the framework of the National Science Program "Environmental Protection and Reduction of Risks of Adverse Events and Natural Disasters", approved by the Resolution of the Council of Ministers № 577/17.08.2018 and has been accomplished with the financial support by the Ministry of Education and Science (MES) of Bulgaria (Agreement № D01-279/03.12.2021) and the

project" NATIONAL GEO-INFORMATION CENTER", subject of the National Road Map for Scientific Infrastructure 2017–2023, funded by Contr. No D01-161/28.08.2018.

REFERENCES

Byun, D., Young J., Gipson G., Godowitch J., Binkowski F.S., Roselle S., Benjey B., Pleim J., Ching J., Novak J., Coats C., Odman T., Hanna A., Alapaty K., Mathur R., McHenry J., Shankar U., Fine S., Xiu A., and Jang C., 1998: *Description of the Models-3 Community Multiscale Air Quality (CMAQ) Modeling System*, 10th Joint Conference on the Applications of Air Pollution Meteorology with the A&WMA, 11-16 January 1998, Phoenix, Arizona, 264-268.

Byun, D. and Ching, J., 1999: *Science Algorithms of the EPA Models-3 Community Multiscale Air Quality (CMAQ) Modeling System.* EPA Report 600/R-99/030, Washington, D.C., EPA/600/R-99/030 (NTIS PB2000-100561).

CEP, 2003: *Sparse Matrix Operator Kernel Emission (SMOKE) Modeling System*, University of Carolina, Carolina Environmental Programs, Research Triangle Park, North Carolina.

CMAS Homepage, http://www.cmaq-model.org, last accessed 2022/05/10

Denier van der Gon, H., Visschedijk, A., van de Brugh, H., Droge, R., 2010, *A high resolution European emission data base for the year 2005*, TNO-report TNO-034-UT-2010-01895 RPT-ML, Apeldoorn, The Netherlands (2010).

Directive (EU) 2016/2284 of the European Parliament and of the Council of 14 December 2016 on the reduction of national emissions of certain atmospheric pollutants, amending Directive 2003/35/EC and repealing Directive 2001/81/EC http://data.europa.eu/eli/dir/2016/2284/oj

EEA Technical report No 4/2015, *Projections in hindsight an assessment of past emission projections reported by Member States under EU air pollution and GHG legislation* https://www.eea.europa.eu/publications/projections-in-hindsight/download

Gadzhev, G. K., Ganev, K. G., Miloshev, N. G., Syrakov, D. E., & Prodanova, M. (2013). Numerical study of the atmospheric composition in bulgaria. Computers and Mathematics with Applications, 65(3), 402-422. doi:10.1016/j.camwa.2012.07.002

Georgieva, I. (2021). The assessment of air quality status in Sofia city - numerical simulations of the dominant pollutants that determines the Air Quality Index, Conference Proceedings of the SGEM Vienna Green, 21, 113-120, doi.org/10.5593/sgem2021V/4.2/s19.16

Ivanov, V., & Georgieva, I. (2017). Air quality index evaluations for sofia city. Paper presented at the 17th IEEE International Conference on Smart Technologies, EUROCON 2017 - Conference Proceedings, 920-925. doi:10.1109/EUROCON.2017.8011246

Georgieva, I., Ivanov, V. (2018). Computer simulations of the impact of air pollution on the quality of life and health risks in Bulgaria. International Journal of Environment and Pollution, 64(1-3), 35-46. doi:10.1504/IJEP.2018.099145

Kukkonen, J., Olsson, T., Schultz, D. M., Baklanov, A., Klein, T., Miranda, A. I., . . . Eben, K. (2012). A review of operational, regional-scale, chemical weather forecasting models in Europe. Atmospheric Chemistry and Physics, 12(1), 1-87, https://doi:10.5194/acp-12-1-2012

Syrakov, D., Prodanova, M., Etropolska, I., Slavov, K., Ganev, K., Miloshev, N., & Ljubenov, T. (2014). A multy-domain operational chemical weather forecast system. Lecture Notes in Computer Science (including subseries Lecture Notes in Artificial Intelligence and Lecture Notes in Bioinformatics) 8353 LNCS, 413-420 doi:10.1007/978-3-662-43880-0_47

UCAR/ NCAR Homepage, http://www.wrf-model.org, last accessed 2022/05/10

21st International Conference on
Harmonisation within Atmospheric Dispersion Modelling for Regulatory Purposes
27-30 September 2022, Aveiro, Portugal

$PM_{2.5}$ WINTERTIME SENSITIVITY TO CHANGES IN NO_X, SO_2 AND NH_3 EMISSIONS IN LOMBARDY REGION

Loris Colombo[1], Alessandro Marongiu[1] , Giuseppe Fossati[1], Giulia Malvestiti[1] and Elisabetta Angelino[1]

[1]Environmental Protection Agency of Lombardy Region (ARPA Lombardia), Air Quality Modelling and Inventory Unit, Rosellini 17, Milan 20124

Abstract: According to the results of the EU LIFE PREPAIR Project on primary emission estimates on Po-basin, the main source of primary PM_{10} is the non-industrial combustion, mainly due to biomass burning in the residential sectors. Moreover, SO_x are emitted by industrial activities and combustion, NO_x for quite a half of the total from the road transport and NH_3 from agriculture. The role of ammonia emissions is widely identified in $PM_{2.5}$ formation while the emission trend of this precursor in the last year is showing a slower slope compared to the emission estimates on NO_x and SO_2.
The aim of this work, that is part of a project required by Lombardy Region focused on the role of agricultural sector on air quality and on atmospheric ammonia emissions, is to evaluate the effects on $PM_{2.5}$ concentrations with a reduction of the emissions of NH_3, NO_x and SO_2 in the Po basin extended area. The simulation is focused on the wintertime period 1st January – 31st March 2019 based on a deeper analysis of NH_3, PM_{10}, $(NH_4)NO_3$, $(NH_4)_2SO_2$ concentrations and the daily ammonia emissions derived from slurry spreading. Based on the bulletins emitted by Regional Authority, research in scientific literature and the crops diffusion on the Lombardy Region, a reconstruction of the annual profile of slurry spreading for different crops has been improved.
The model simulations have been run by FARM-LO operational AQ model of the Environmental Agency of Lombardy Region (ARPA) over two nested domains: one including Lombardy region, the other the Po Valley and Slovenia. The model suite includes a Chemical Transport Model (FARM) and a meteorological model (WRF). Emissions have been derived for the two domains from the regional emission inventory INEMAR and from the dataset on emission inventories developed in the frame of the LIFE IP Project PREPAIR. The initial and boundary conditions are obtained by QualeAria (http://www.qualearia.it). Evaluations carried out interesting results for domain sub-areas with different dependence from NH_3 and NO_x reduction in relation to emission source types and intensities and could support AQ policy makers to better understand the impacts of precursors abatements on $PM_{2.5}$ concentration.

KEY WORDS: **EMISSION REDUCTION**, **NON-LINEARITY, WINTERTIME CHEMICAL REGIMES, PM FORMATION**

INTRODUCTION

Ammonia (NH_3) is the atmospheric pollutants that contributes significantly, together with nitrogen oxides and sulfur, to the secondary inorganic $PM_{2.5}$ formation.
This pollutant reacts in the atmosphere both with nitric acid and sulfuric acid originating ammonium nitrate and ammonium sulfate which are the inorganic ions more present in the particulate matter.
In Itay (ISPRA, 2021) and in Lombardy Region, ammonia is emitted in atmosphere mainly (94%) by the agricultural sector while the SO_X are released by the energy production and industrial sectors (90%)

(EDGAR, 2020). For NO_X, emissions are spread out from different sectors (i.e. transport, industry and agriculture). The INEMAR inventory emission (2017) has estimated that 97% of ammonia regional emission are linked both to fertilisers and zootechnical sector. The latter representes the 86% of the overall emission in atmosphere.
The aim of this work is to identify the chemical regimes where secondary inorganic PM is formed over the Po basin, which is a peculiar area where the chemical regimes distributions are the most complex, showing a non-linear processes expecially within NO_x and NH_3 (Clappier et al., 2021; Carnevale, 2020; Bessagnet, 2014). We focus the present analysis on the wintertime chemical regimes as it is the period of the year more affected by the exposure to fine particlaute matter ($PM_{2.5}$). We start describing the modelling set-up, the modelled base case concentrations and detail the indicators/statistics done to perform analysis. Then, we analyse the sensitivity of $PM_{2.5}$ concentrations to NH_3, NO_X and SO_2 emissions and finally we provide an analysis of the chemical-regimes of $PM_{2.5}$ consequently to these emissions reduction.

MATERIAL AND METHODS

Modelling set-up

The modeling study is performed by the ARIA Regional System developed by AriaNET society and used by Lombardy Environmental Agency (Arianet, 2010). The emission input consists of gridded annual (2017) emissions referred to municipalities and classified by SNAP (Selected Nomenclature for Air Pollution) codes. Meteorological input data are based on forecasts from GFS model (https://www.nco.ncep.noaa.gov/pmb/products/gfs/). The modelling domain covers the entire Po basin with an extension of 836 x 416 km^2 (Figure 1) with a grid resolution of 4 km by 4 km and includes 16 vertical levels. The initial and background concentrations are from Qualearia (http://www.qualearia.it). The base case simulations cover the entire meteorological year 2019 whereas the scenarios analyses have been focused only to wintertime.
The choice of the winter season has been derived by the analysis of ammonia emissions and their correlation with measured concentrations of PM_{10}, NH_3, $NH_4(NO_3)$ and $NH_4(SO_2)$ in 5 permanent stations.

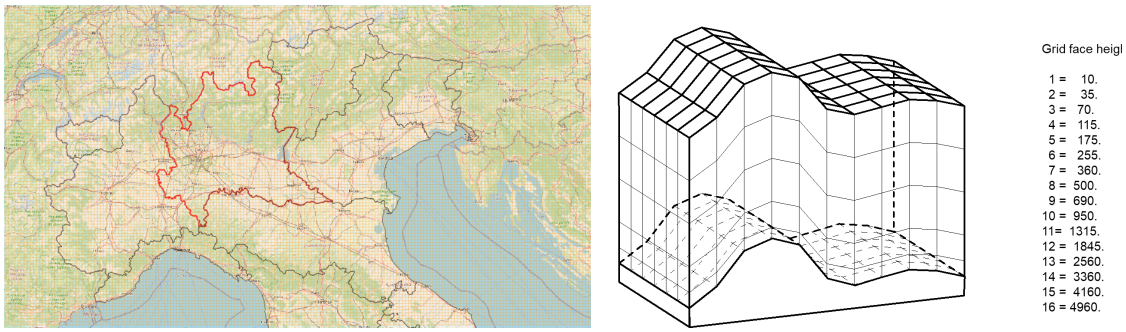

Figure 38. Horizontal and vertical discretization of the ARPA Lombardy modelling system. The grid (x,y: 210,105) has a discretization of 4 km x 4 km

In this work, we simulated a series of 16 scenarios where NO_X, NH_3 and SO_X emissions were reduced indipendently or simulaneously by 10, 25, 50, 75 % from the base case emission reference level.

Table 18. Scenarios reducing 100-α % of the emissions, one for each single precursor, for the reduction of two precursors and for the reduction of all precursors

Scenarios (name)	**NO_X (emissions 100-α)**	**NH_3 (emissions 100-α)**	**SO_X (emissions 100-α)**
Base case	100%	100%	100%

Sc_u_1a	90%	0	X
Sc_u_2a	0%	90%	X
Sc_u_1b	75%	0	X
Sc_u_2b	0	75%	X
Sc_m_1	75%	75%	X
Sc_u_1c	50%	0	X
Sc_u_2c	0	50%	X
Sc_m_2	50%	50%	X
Sc_m_2bis	25%	25%	X
Sc_u_3a	0	0	90%
Sc_u_3b	0	0	75%
Sc_m_3	75%	75%	75%
Sc_u_3c	0	0	50%
Sc_m_4	50%	50%	50%
Sc_u_f1	25%	0	x
Sc_u_f2	0	25%	x

The emission reductions were applied over the entire Po basin domain only for wintertime which covers the period from 1st January to 31st March.

The NH_3 annual emission, estimated by regional inventory INEMAR and originated by the management of nitrogen compound wastewater, have been disaggregated in space and in time to identify daily emissions on the regional territory. The contribution linked to the stabulation and warehousing is considered constant during the entire year, whereas the contribution linked to the practice of the spreading livestock manure is time-dependent following 1) Nitrate Directive 91/676/CE which regulates the distribution over different areas in Lombardy and 2) meteorological conditions (i.e. the distribution is strictly forbidden during the rainy day and over the frozen ground).

REPRESENTATION OF RESULTS AND INDICATORS

Results are presented in terms of average concentration maps of the wintertime period (1st January – 31th March. Moreover, we aggregate all the background stations located in the Po basin in order to show different behaviours in terms of response to emission changes based on different emission reductions. The impact of NO_X, NH_3 and SO_2 emission reductions on secondary organic PM2.5 has been discussed. To describe the interactions between emissions, we use the relationship proposed by Thunis and Clappier (2014). Potential impacts (P) are defined as the ratio between the concentration change and the emission reduction intensity:

$$P^{\alpha}_{NH3} = \frac{\Delta C^{\alpha}_{NH3}}{\alpha} \qquad P^{\alpha}_{NOX} = \frac{\Delta C^{\alpha}_{NOX}}{\alpha} \qquad P^{\alpha}_{SO2} = \frac{\Delta C^{\alpha}_{SO2}}{\alpha} \tag{1}$$

Where ΔC^{α}_{x} is the PM concentration change resulting from a reduction of the NH_3, NO_X and SO_2 emissions respectively; α is the emission reduction intensity that varies from 0 (no reduction and then 100% emission) to 1 (i.e. 0% emission).

RESULTS

Base Case

In Figure 2 the wintertime averaged $PM_{2.5}$ concentration fields show a diffused pollution covering the most of the Po basin, extending from the metropolitan areaof Turin till the Veneto plain. The maximum modelled values reach 53 $\mu g/m^3$ .This is due to the more stable atmospheric conditions and to the particular orographic setting that let to favour the accumulation of the particulate matter in the area. The spatial field for NO_X reflects generally the emission patterns locations resulting ”richest” in the higher urbanized area (Turin and Milan) and along the main regional and statal streets while NH_3 is more abundant in the agricultural land area between southern of Milan area and northern Emilia Romagna and in the Cuneo area. Finally, high SO_2 concentrations are located nearby big industrial sites located all over the Basin.

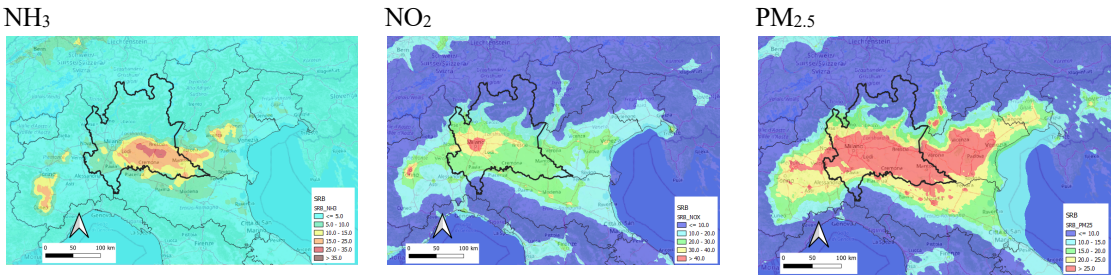

Figure 39. Spatial concentration (μg/m^3) based on the base case of the wintertime period of the NH_3, NO_2 PM precursors line and $PM_{2.5}$ concentrations

Figure 3 shows the boxplots of $PM_{2.5}$ observed values for 2019 at each monitoring station and the predicted concentration. It can be observed that the higher decreasing of precursors the higher decreasing of $PM_{2.5}$ concentrations is. Firstly, it is worth noting that the reduction is more consistent with coupled precursors rather than a singular reduction: this advantage increases more and more in function of emission reduction (but in principle with no linearity).

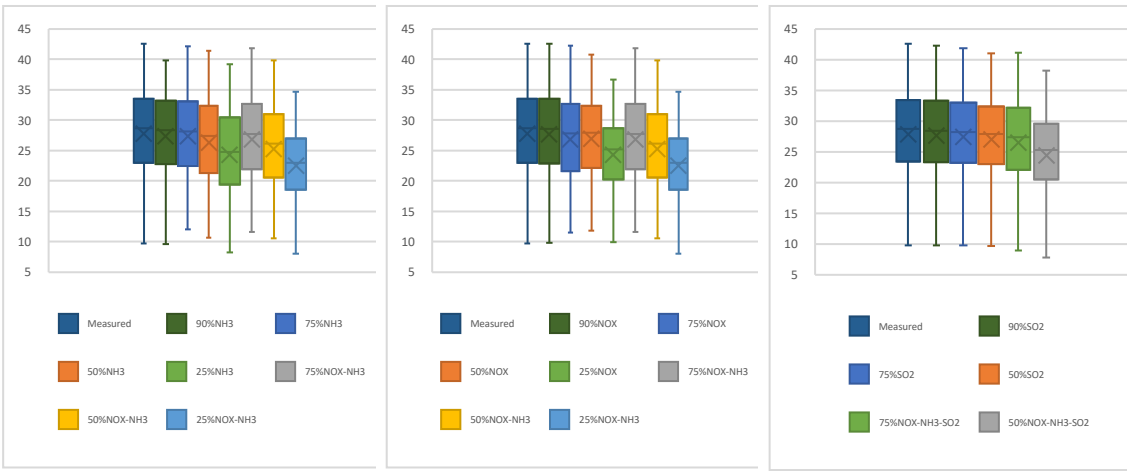

Figure 40. $PM_{2.5}$ wintertime averages concentrations (μg/m^3): boxplots of observed and predicted concentration at each monitoring point station in all scenarios, divided for the sinukar reduction of NH_3, NO_X and SO_2.

We provided the chemical regime maps for only the NO_X-NH_3 reduction also because during wintertime, the NH_3-sensitive regime area are more important with respect to SO_X (Clappier et al., 2021). By using (1) it is possible to detect the areas where a $PM_{2.5}$ stronger reduction is obtained with an identique emission reduction of precursors. By using a difference between P^{α}_{NH3} and P^{α}_{NO2} a chemical regime can be defined: if the difference will be positive a reduction of NH_3 is more effective whereas on the contrary the zones will be named NO_X- sensitive (negative difference).

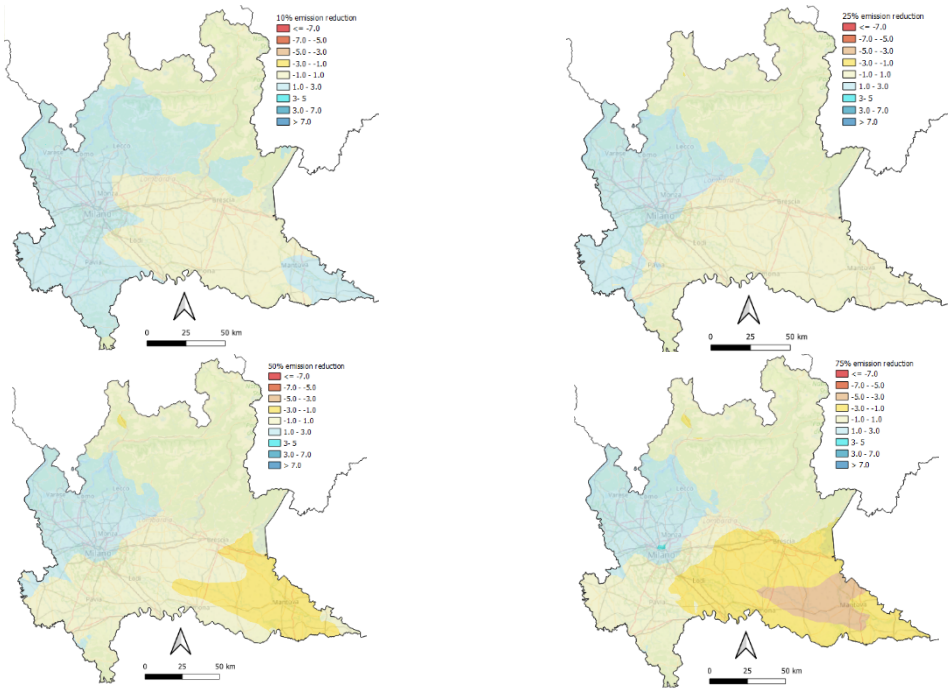

Figure 41. Wintertime chemical-regimes obtained at a reduction level of 10-25-50-75%. The maps represent the $P^{\alpha}_{NH3} - P^{\alpha}_{NO2}$ in μg/m^3 indicator that shows the NO_X- sensitive (from yellow to red) and NH_3- sensitive (from light to dark blue) areas. The light yellow represents areas sensitive to both precursors reduction.

DISCUSSION AND CONCLUSIONS

In this study we analysed the $PM_{2.5}$ sensitivities to NH_3, NO_X and SO_2 emission reductions. It can be observed that the decreasing of precursors favours a diminishing of $PM_{2.5}$ concentrations. Moreover, it is worth noting that the reduction is more consistent with coupled precursors rather than a singular reduction: this advantage increases more and more in function of emission reduction (but in principle with no linearity). It can be assessed that areas NH3-sensitive don't correspond to those where the ammonium release is higher (as presented in Figure 2 where the higher concentrations of NH_3 are in the border of Lombardy and Emilia Region). Furthermore, it can be noticed that the reduction of NH_3 is as important as of NO_X in the $PM_{2.5}$ concentration control. The chemical regimes have shown that for higher reduction of the precursors (i.e from 25% to 75%) there are as many areas NO_X-sensitive as NH_3-sensitive, but it is important to reduce coupling NO_X-NH_3. The latter behaviour is also evident in Baojing Gu et al., 2021.
The study confirms the results obtained with different hypothesis (i.e. different emission inventories, different chemical transport model, different meterological year, different boundary conditions in comparison to previous work of Clappier et al., 2021; Thunis et al., 2021) and leads robustness to the previous results present in literature; the results show that a combined reduction of the NO_X-NH_3 precursors are very large to be effective on PM abatement. An important finding which has an implication on air quality strategies is that in wintertime in urbanized areas the NH_3-sensitive areas are predominant with respect to the NO_X ones. The results obtained in this study will be used in the frame of the EU LIFE PREPAIR in order to compare with different chemical trasport models and to have the possibility to consider uncertainty in the results (for example by using ensemble method with different model).

REFERENCES

Arianet 2010: Aria Suites Tools – Reference Guide . Release 2.0 R2010.07, Milano, Italy

Bessagnet, B., Beauchamp, M., Guerreiro, C. et al. 2014: Can further mitigation of ammonia emissions reduce exceedances of particulate matter air quality standards? Environmental Science & Policy*, 44, 149‑163. DOI:10.1016/j.envsci.2014.07.011*

Carnevale, C., Pisoni, E., & Volta, M. 2010: A non-linear analysis to detect the origin of PM10 concentrations in Northern Italy. Science of the Total Environment*,* 409*(1), 182-191.*

CEC Commission of the European Communities, 1997: Report of the Commission to the Council and European Parliament: the Implementation of Council Directive 91676EEC Concerning the Protection of Waters against Pollution Caused by Nitrates from Agricultural

Clappier, A., Thunis, P., Beekmann, M., Putaud, J. P., & de Meij, A. 2021: Impact of SOx, NOx and NH3 emission reductions on PM2. 5 concentrations across Europe: Hints for future measure development. Environment International*,* 156*, 106699.*

EDGAR2020, Emission Database for Global Atmospheric research, https://edgar.jrc.ec.europa.eu/

Gu, B., Zhang, L., Van Dingenen, R., Vieno, M., Van Grinsven, H. J., Zhang, X., ... & Sutton, M. A. 2021: Abating ammonia is more cost-effective than nitrogen oxides for mitigating PM2. 5 air pollution. Science*,* 374*(6568), 758-762.*

INEMAR - ARPA Lombardia, 2021: INEMAR, Inventario Emissioni in Atmosfera: emissioni in regione Lombardia nell'anno 2017 – versione finale. ARPA Lombardia Settore Monitoraggi Ambientali.

ISPRA, 2021: Inventario nazionale delle emissioni in atmosfera 1990-2019. Informative Inventory Report 2021.

Thunis P. and A. Clappier, 2014: Indicators to support the dynamic evaluation of air quality models, Atmospheric Environment*, 98, 402-409.*

Thunis, P., Clappier, A., Beekmann, M., Putaud, J. P., Cuvelier, C., Madrazo, J., & de Meij, A. 2021: Non-linear response of PM 2.5 to changes in NO x and NH 3 emissions in the Po basin (Italy): consequences for air quality plans. Atmospheric Chemistry and Physics*,* 21*(12), 9309-9327.*

21st International Conference on
Harmonisation within Atmospheric Dispersion Modelling for Regulatory Purposes
27-30 September 2022, Aveiro, Portugal

ASSESSING THE IMPACT OF PORT EMISSIONS ON AIR POLLUTION IN GENOA

A. Bisignano[1], M. Beggiato[1], M. C. Bove[1], F. Cassola[1], R. Cresta[1], D. Sacchetti[1], P. Brotto[2], A. Mazzino[3] and P. Prati[4]

[1] Ligurian Regional Agency for Environmental Protection (ARPAL), Genoa, Italy
[2]PM_TEN srl, Genoa, Italy
[3] Department of Civil, Chemical and Environmental Engineering, University of Genoa, Genoa, Italy
[4] Department of Physics and INFN, University of Genoa, Genoa, Italy

Abstract. Maritime transport is of major importance for trade and economic development in the Mediterranean region. On the other hand, many areas of docklands are subjected to strong environmental pressure, thus requiring mitigation measures to reduce the ports impact on environment and people's health. The Interreg Maritime Project AER NOSTRUM participates to the challenge of reducing pollutants emission from port activities and, in particular, from ships. The overall goal is to contribute to the improvement of the air quality in areas overlooking the ports of the cooperation region (Italy-France), while promoting sustainable growth in compliance with the environmental standards prescribed by European laws. As a part of the project, we present some preliminary results of the air quality monitoring and simulations in progress on the port of Genoa.

KEYWORDS: **SHIP EMISSIONS, NEAR-PORT AIR QUALITY, SMART SENSORS, PM COMPOSITIONAL ANALYSIS, CALPUFF SIMULATIONS.**

INTRODUCTION

Ports play a crucial role as hubs for Mediterranean trade. At the same time, they are sources of air pollution from both the maritime traffic and the related logistic activities. Achieving environmental sustainability in ports is therefore essential for the economy and the air quality in the nearby areas, which are often highly populated. Within the framework of the INTERREG Maritime Italy-France program, the AER NOSTRUM project (http://interreg-maritime.eu/web/aer-nostrum) targets a twofold objective: firstly, to achieve a shared platform for monitoring and simulation data of air pollution; secondly, to assess the benefits of potential emission mitigation strategies. The study area includes several key economic ports of France and Italy; here the focus is on the port of Genoa, one of the busiest European seaport in terms of movements of goods and people.

Monitoring and modelling approaches are combined to assess how the port of Genoa affects the air quality. A low-cost sensor network was implemented to extend the current operational monitoring managed by the regional environmental agency. Despite the intrinsic uncertainty of these sensors, higher spatial density measurements aim to capture the dispersion patterns of pollutants in complex environments (see e.g. Popoola et al., 2019; Karagulian et al., 2019). In addition, two monthly campaigns were designed to estimate particulate matter concentration and sources through filter-based sampling and compositional analyses to feed a positive matrix factorization receptor model (Paatero and Tapper, 1994). An air quality modelling system was used to perform high resolution simulations over the port area. The simulations are ongoing and the results will be evaluated by comparison with observed data and used to investigate mitigation scenarios, such as the impact of the cold ironing on the pollutant levels. For the simulations, a high resolution emission inventory was compiled based on a detailed study of maritime traffic in the port.

MONITORING AIR QUALITY: NEAR-PORT experimental campaign.

Within the AER NOSTRUM project, the air quality monitoring in the port of Genoa is conducted through the use of both traditional and smart, low-cost instruments. The city lies on a narrow and long coastal area, enclosed between the Ligurian Sea and the Apennine Mountains and crossed by few torrential valleys. The infrastructures of the port area stretch all through the city, with potential hazardous health effects.
The selected study area is mainly affected by passenger traffic, being the core of the cruise and ferry sectors. The port's terminals constitute a critical element with respect to the city, in particular in terms of atmospheric emissions due to both the stationing of ships and the induced vehicular traffic. The existing traditional instrumentation has been enhanced and integrated to collect PM_{10} samples used for source apportionment studies. Regarding low cost instrumentation, the network is equipped with different technologies for real-time monitoring of PM and NO_2 in the air and gravimetric samplers. New sites were identified in very densely urbanized contexts, where it is usually not possible to measure pollutants concentrations using the conventional instrumentation. The smart sensors locations were also chosen according to the extension of urban area in relation to the port, the orography, the local meteorology and the critical receptors present in the area (Figure 1).

Figure 42. Monitoring network around the port of Genoa (Google Earth Pro V 7.3.4.8642)

Before installation in the proper location, the smart sensors performances require to be tested against reference air quality stations, paying particular attention to the sensitivity to environmental conditions such as temperature, humidity and concentration levels (see e.g. Spinelle et al. 2015, Bisignano et al. 2022). The calibration was carried out at an operational air quality station, under conditions similar to those of port area. An example of the comparison between official and low cost instrumentation data is shown in Figure 2, which refers to a low cost sensor equipped with the thick-film metal oxide semiconductor sensor Sens-IT (Unitec) for NO_2 and with the optical particle counter SPS30 (Sensirion) for PM.

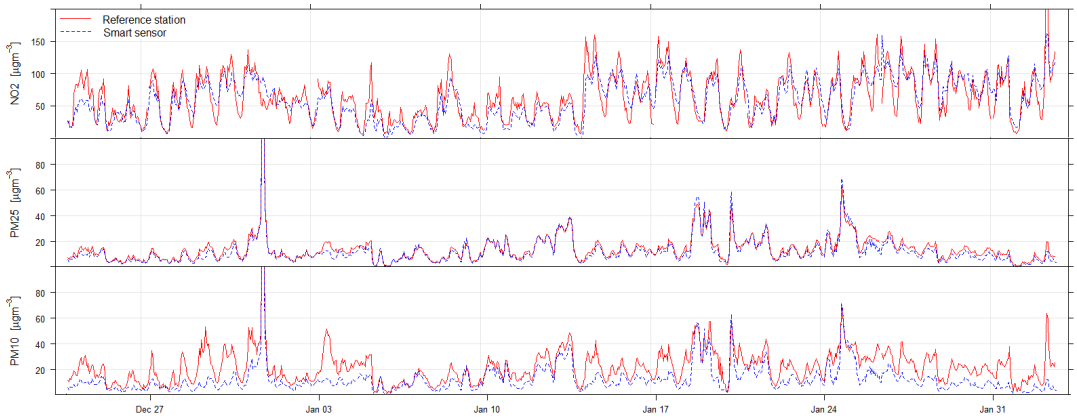

Figure 43. NO_2, $PM_{2.5}$ and PM_{10} time plots from one smart sensor against the reference station data throughout a six weeks' test.

While the smart sensor is able to reproduce reasonably well the NO_2 and $PM_{2.5}$ measurements of the reference station, the PM_{10} levels are underestimated. In order to further analyse performance for PM, Figure 3 shows the scatterplot of the reference measurements against the hourly concentrations collected by the low-cost sensor.

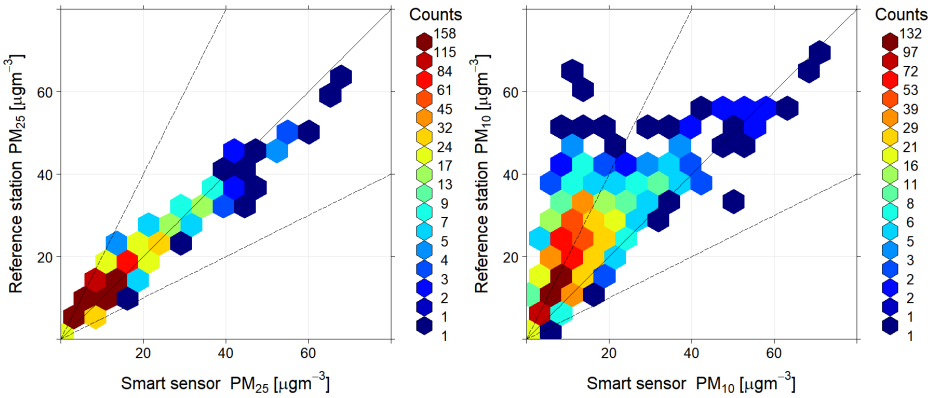

Figure 44. Scatterplots of reference against low-cost sensors data.

The overall performance for $PM_{2.5}$ is satisfactory as almost all the points are within the factor two curves, **although** the correlation slightly decreases at the lowest values, most *likely due to the low accuracy of the sensor*. PM_{10} correlation appears to be far less accurate than $PM_{2.5}$ one, highlighting an underestimation by about a factor two with respect to the reference for the majority of the measures. This behaviour is possibly due to the working principle of SPS30. It is able to capture a small fraction of the aerosol particles, upon which statistics are extrapolated. Given the low PM_{10} fraction of typical aerosol, it cannot be measured directly, but it estimated from finer particulates (Sensirion AG, 2020).

The identification of PM emission sources is still a challenging issue and it is a crucial step to design effective mitigation strategies. Within Aer Nostrum project, PM_{10} samples were collected by low-volume samplers (Skypost, TRC TECORA and Digitel DPA14 SEQ LV) designed in conformity with CEN standard. The two sampling sites was located not far from the harbour area, in a residential area close to a road with moderate traffic flow. The instrument was operated on a daily basis during two experimental campaigns: the first from August to September 2021 and the second from April to May 2022, collecting about 160 PM samples on quartz fibre filter membranes (diameter = 47 mm, pore size = 2 µm). The compositional analyses performed by different analytical methods (Bove et al., 2018) allowed a reconstruction of most of the PM mass and a first rough estimation of the mean PM origin (Figure 4) according to Perrino et al. (2009).

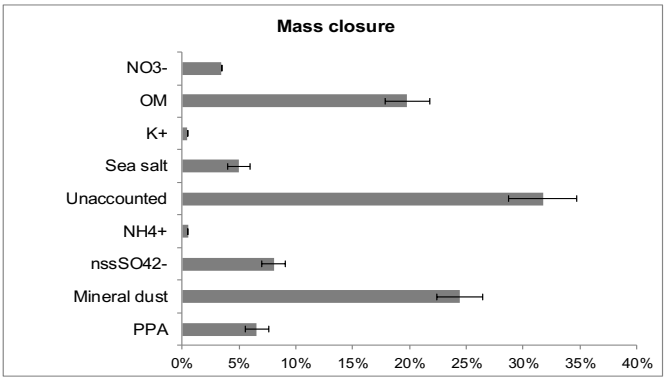

Figure 45. PM_{10} mass closure based on compositional analyses

The sea salt contribution was computed using the sea water composition (Bove et al., 2016): the average was 5 ± 1% of PM_{10}, close to typical values observed in other coastal areas of the Mediterranean basin. Not sea-salt sulphate represented about 94% of total sulphate: they can be summed to nitrate and ammonium to obtain the secondary inorganic aerosol, SIA, which turned out to be 12 ± 1%. The crustal term was calculated by summing the concentration of elements generally associated with mineral dust. Primary anthropogenic aerosol (PPA) was constituted by elemental carbon, which originates directly from combustion emission, plus primary organic carbon; this amount includes organic compounds that condense from the exhausts gases and coat the surface of elemental carbon particles. The contribution of PPA was about 7 ± 1%. Organic aerosol (OM), mostly of secondary origin, was estimated by multiplying the not-primary organic carbon by a conversion factor which estimates the average organic molecular weight per unitary carbon of the atmospheric aerosol. This factor depends on the aerosol composition and thus on the location of the sampling site. Here we used a factor equal to 1.8, since the sampling site is labelled as urban background station (Perrino et al., 2009). The average contribution of organic aerosol (OM) to PM_{10} was 20 ± 2 %.

emission and dispersion modelling: preliminary results

An air quality modelling system is used to perform high resolution simulations over the port area. Pollutant emission estimates of maritime traffic were calculated in compliance with the EMEP/EEA air pollutant emission inventory guidebook (2019). The ships categories included in the inventory are container, passenger and RoRo cargo. The ships are regarded as point sources while hotelling and as area sources while manoeuvring; in this second case, we identified a standard course between port entrance and docking and the associated emissions were distributed homogeneously over the entire area on the basis of purely geometric considerations. Emission data are used to feed CALMET/CALPUFF (Scire at al., 2000) puff-Gaussian model, which is one of the reference model commonly used in impact assessments. The flow fields required for CALMET initialization are generated by the WRF model (Skamarock and Klemp, 2008) with a resolution of 3.3 km. CALMET/CALPUFF simulations are run with a resolution of 90 m over a 6.3 × 7.2 km^2 domain. Simulations cover *the two months'* PM_{10} sampling campaign period and they are still ongoing. Examples of CALPUFF results are shown in Figure 5, where PM_{10} and NO_x near-ground hourly concentration are displayed, respectively, in the top and bottom panels. The dispersion patterns highlight how the port emissions may have a large impact on the air quality of the city, depending on the meteorological conditions.

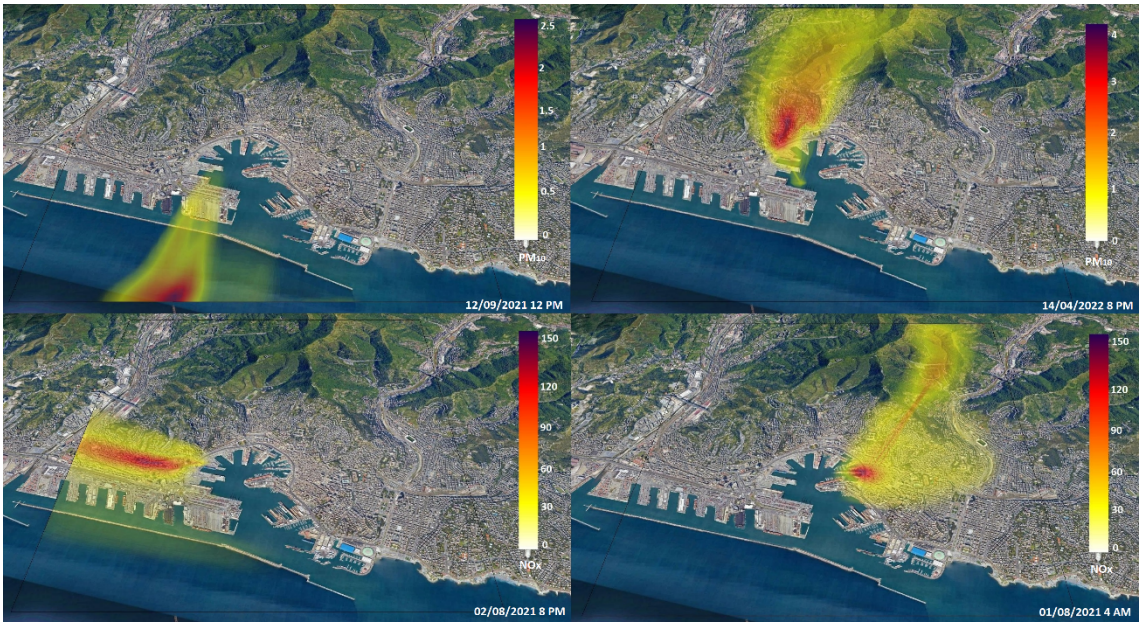

Figure 46. Examples of ground level hourly concentrations calculated by CALPUFF simulations at different times.

FUTURE WORK

The large database collected during the experimental campaign will be used to feed a receptor model through positive matrix factorisation (see e.g. Bove et al 2014).

Concerning modelling, once CALPUFF simulations are done, the first phase will be to verify the modelled PM_{10} and NO_2 concentration fields by comparing simulated and observed values at three reference station. With this aim, background concentrations are substantial source of error. Here we refer to the background as the ambient level of pollution that is not affected by port sources. At the three monitoring sites, background is estimated by means of comparison with data from other air quality stations with the same characteristics, but located outside the port airshed and thus not affected by ships emission.

The second phase will be to assess the benefits of possible emission mitigation strategies, such as the impact of the cold ironing and the use of liquefied natural gas, on the pollutant levels nearby the port. In this stage the background concentrations will be calculated using CHIMERE chemistry-transport model (Menut et al., 2021), online coupled with the WRF model and ran without port emissions.

CONCLUSIONS

The project is aimed at establishing a shared cross-border platform for experimental and modelling data of air pollution in proximity to port areas. This tool is not only intended to gather data from different seaports, but also to establish common methodologies for site surveillance and monitoring, model evaluation and mitigation strategies assessment, based on shared standards and procedures. The final objective is the definition of guidelines for planning the most suitable strategies to mitigate the impact of port emissions on the air quality.

REFERENCES

Bisignano A., F. Carotenuto, A. Zaldei and L. Giovannini, 2022: Field calibration of a low-cost sensors network to assess traffic-related air pollution along the Brenner highway. Atmos. Environ.*,* ***275****.*

Bove M.C., P. Brotto, G. Calzolai, F. Cassola, F. Cavalli, P. Fermo, J. Hjorth, D. Massabò, S. Nava, A. Piazzalunga, C. Schembari and P. Prati, 2016: PM10 source apportionment applying PMF and chemical tracer analysis to ship-borne measurements in the Western Mediterranean. Atmos. Environ.*,* ***125****, 140-151.*

Bove M.C., P. Brotto, F. Cassola, E. Cuccia, D. Massabò, A. Mazzino, A. Piazzalunga and P. Prati, 2014: An integrated PM2.5 source apportionment study: Positive Matrix Factorisation vs the Chemical Transport Model CAMx. Atmos. Environ*., **94**, 274-286.*

Bove M.C., D. Massabò and P. Prati, 2018: PMF5.0 vs CMB8.2: An inter-comparison study based on the new European SPECIEUROPE database. Atmos*, **201**, 181-188.*

European Environment Agency, EMEP/EEA air pollutant emission inventory guidebook 2019: technical guidance to prepare national emission inventories, Publications Office.

Karagulian, F.; M. Barbiere, A. Kotsev, L. Spinelle, M. Gerboles, F. Lagler, N. Redon, S. Crunaire and A. Borowiak, 2019: Review of the Performance of Low-Cost Sensors for Air Quality Monitoring. Atmosphere*,* **10***, 506.*

Menut L., B. Bessagnet, R. Briant, A. Cholakian, F. Couvidat, S. Mailler, R. Pennel, G. Siour, P. Tuccella, S. Turquety, and M. Valari, 2021: The CHIMERE v2020r1 online chemistry-transport model, Geosci. Model Dev.*, **14**, 6781-6811.*

Paatero P. and U. Tapper, 1994: Positive matrix factorization: a non-negative factor model with optimal utilization of error estimates of data values. Environmetrics ***5**, 111–126.*

Perrino C., S. Canepari, M. Catrambone, S. Della Torre, E. Rantica, and T. Sargolini, 2009: Influence of natural events on the concentration and composition of atmospheric particulate. Atmos. Environ.*, **43**, 4766-4779.*

Popoola O.A.M, D. Carruthers, C. Lad, V. Bright, M. Mead, M. Stettler, J. Saffell and R. Jones, 2009: Use of networks of low cost air quality sensors to quantify air quality in urban settings, Atmos. Environ.*, **194**, 58-70.*

Scire, J., D. Strimaitis, R. Yamartino 2000: A User's Guide for the CALPUFF Dispersion Model. Tech. rep., Earth Tech, Inc, Concord, MA.

Sensirion, 2000: Sensor Specification Statement. Retrieved from www.sensirion.com.

Skamarock W. and J. Klemp, 2008: A time-split nonhydrostatic atmospheric model for weather research and forecasting applications. J. Comput. Phys.*, **227**, 3465–3485.*

Spinelle L., M. Gerboles, M.G. Villani, M. Aleixandre and F. Bonavitacola, 2015: Field calibration of a cluster of low-cost available sensors for air quality monitoring. Part a: ozone and nitrogen dioxide. Sensor. Actuator. B Chem*., **215**, 249-257.*

21st International Conference on
Harmonisation within Atmospheric Dispersion Modelling for Regulatory Purposes
27-30 September 2022, Aveiro, Portugal

THE EFFECT ON AIR QUALITY OF INCREASED RENEWABLE ENERGY USE IN THE SPANISH ROAD TRANSPORT SECTOR

Marta G. Vivanco[1], Mark R. Theobald[1], Victoria Gil[1], Juan Luis Garrido[1], Ana R. Gamarra[2], Yolanda Lechón[2], José Luis Santiago[1], Fernando Martín[1], Alejandro Rodríguez-Sánchez[1], Carmen Lago[2] and Eugenio Sánchez[3]

[1]Atmospheric Modelling Unit, Environment Department, CIEMAT, Madrid, Spain
[2]Energy Systems Analysis Unit, Energy Department, CIEMAT, Madrid, Spain
[3]Application & Computer Systems Development Unit, Technology Department, CIEMAT, Madrid, Spain

Abstract: Atmospheric dispersion modelling is a useful tool for estimating the potential improvements in air quality from the implementation of emission reduction measures. In this study we have used the chemical transport model CHIMERE to estimate the improvements in air quality for various emission reduction scenarios related to the road transport sector in Spain. The scenarios analysed consist of two emission reduction measures related to an increased use of biofuels (increased bioethanol use and increased use of both bioethanol and biodiesel) and two scenarios with a full penetration of the electric car. The scenarios with the increased electric car use were simulated with and without emissions from the additional electricity demand taking into account the changes in the future energy mix projected for 2030. The electric car scenarios reduce concentrations of NO_2, PM and O_3 more than the biofuel scenarios due to the larger emission reductions with respect to the 2017 baseline scenario. In fact, the increased bioethanol scenario actually increases PM concentrations in some areas despite having practically the same PM emissions as the baseline due to the increase in ammonia emissions leading to an increase in secondary particle formation. Although NO_2 concentration reductions for the two electric car scenarios are similar for most of the domain, there are larger reductions in the scenario that includes changes in the energy mix in the northwest of Spain where two of the largest coal-fired power stations are located that are not included in the energy mix for 2030. For $PM_{2.5}$, the scenario taking into account changes in the energy mix reduces the concentrations the most, despite an increase in PM emissions with respect to the baseline. This is due to the large reduction in SOx emissions through the elimination of coal-fired power stations, which in turn leads to less formation of secondary particles and hence lower $PM_{2.5}$ concentrations. The health impact benefits of these effects on air quality have been estimated by Gamarra et al. (presented at this conference).

KEY WORDS: **AIR POLLUTION MODELLING; AIR QUALITY; RENEWABLE MOBILITY; BIOFUELS; ELECTRIC VEHICLES**

INTRODUCTION

As well as contributing more than a sixth of the GHG emissions emitted in the European Union (EEA, 2021), road transport is one of the main contributors to emissions of various air pollutants and their precursors. In addition, a substantial part of these emissions occur in urban areas, increasing the likelihood of impacts to health. At a national level, Spain has developed proposals to reduce emissions from the road transport sector, including Zero Emission Areas, park and ride schemes and changes to the vehicle fleet. Air quality modelling is a key tool in assessing the potential effect of these proposals on air quality as well as impacts to human health and vegetation. The objective of this study was to estimate the

effect on air quality of selected measures aimed at reducing road transport emissions (increased use of biofuels and electric vehicles) in Spain for the year 2030, using the chemical transport model CHIMERE.

Materials and methods

Description of measures and scenarios

Four scenarios were modelled, two scenarios containing measures related to increased biofuel use and two scenarios with penetration of electric vehicles. The biofuel scenarios considered an increase in the use of bioethanol in petrol vehicles (BioEt) and an increase in both bioethanol use in petrol vehicles and biodiesel in diesel vehicles (Biof).

In the BioEt scenario the current petrol fleet (cars and motorcycles) are substituted by flexible-fuel vehicles (using 85% bioethanol / 15% petrol mixture) and for other petrol vehicles the bioethanol content is increased from 5% to 10%. In the Biof scenario, fuel containing 20% biodiesel is used in all diesel vehicles (except motor cycles), in addition to the measures included in the BioEt scenario. The electric vehicle scenarios considered the full substitution of the current fleet of passenger cars (except hybrids) without considering the emissions from the additional electricity generation (EC) and with considering these emissions and taking into account the expected change in the energy mix in Spain for 2030 (EC-E). Since the energy mix for 2030 is expected to include a larger proportion of renewables, SOx and NOx emissions are expected to decrease substantially in this scenario, despite the increased electricity demand. Particulate emissions are expected to increase, however. Table 1 shows the changes in the emissions of the main species for the source sectors SNAP1 (Combustion in the production and transformation of energy) and SNAP7 (Road transport), as well as for the total anthropogenic emissions, with respect to the baseline, for each scenario. All these measures are included in the current Spanish National Energy and Climate Plan (MITERD, 2020), albeit applied to a lesser extent than in this study.

Table 19. Changes with respect to the baseline in the Spanish annual pollutant emissions for the emission sectors SNAP 1 and SNAP 7 and the total anthropogenic emissions (sum of SNAP 1 to SNAP 10) used in the air quality simulations.

	Scenario	**NH_3**	**NMVOC**	**NOx**	**$PM_{2.5}$**	**PM_{10}**	**SOx**
SNAP 1 (Combustion in the production and transformation of energy)	EC-E	--	-12%	-67%	+131%	+95%	-93%
SNAP 7 (Road transport)	BioEt	+209%	-45%	-2%	-1%	-1%	+14%
	Biof	+209%	-49%	--	-12%	-12%	+13%
	EC and EC-E	-72%	-47%	-31%	-33%	-33%	-52%
Total anthropogenic emissions	BioEt	+1%	-2%	-1%	-0.1%	-0.1%	+0.03%
	Biof	+1%	-2%	--	-0.9%	-0.9%	+0.02%
	EC	--	-2%	-10%	-3%	-3%	-0.09%
	EC-E	--	-2%	-20%	+3%	+1%	-38%

Air quality modelling

The CHIMERE chemistry transport model was used to estimate atmospheric concentrations of NO_2, O_3, PM_{10}, $PM_{2.5}$ and SO_2 for each scenario as well as the baseline (2017 emissions). The CHIMERE model has been extensively used and evaluated in Europe (Menut et al., 2013) and, in particular, in Spain (Vivanco et al, 2008; 2009a; 2009b). Model performance for estimating atmospheric concentrations has been shown to be comparable to that of other air quality models applied in Europe (Bessagnet et al, 2021). The modelling domain covered the Iberian Peninsula at a spatial resolution of 0.1° × 0.1° nested within a European domain at 0.15° × 0.15°. For the baseline emissions, the national official emission inventory for 2017 was used, to which the emission reductions for each scenario were applied. Meteorological data from the Integrated Forecasting System (IFS) of the European Centre for Medium-

Range Weather Forecasts, ECMWF (www.ecmwf.int) for 2017 were used for all scenarios. These data were obtained from the MARS archive at ECMWF through the access provided for research projects by the Spanish State Meteorological Agency (AEMET). To assess the effect of the scenarios on air quality in Spain, changes in annual mean concentrations of SO_2, NO_2, PM_{10} and $PM_{2.5}$ as well as the O_3 indicator SOMO35 (Sum of Ozone Means Over 35 ppb) with respect to the baseline were calculated. Model bias was reduced through model-measurement fusion methods, assuming that the biases (calculated for the 2017 baseline) are proportional to the atmospheric concentrations (Vivanco et al., 2021).

RESULTS AND DISCUSSION

Figure 2 shows the relative changes in the indicators calculated with respect to the baseline. The two biofuel scenarios have a very small impact on air quality with respect to those of the electric car scenarios as a result of the relatively small reductions in total emissions. The electric car scenarios substantially improve the indicators for all four pollutants, including PM concentrations in the scenario that takes into account the increased electricity demand (EC-E). This is surprising since PM emissions are expected to increase for this scenario (although total anthropogenic emissions of $PM_{2.5}$ and PM_{10} increase by only 3% and 1%, respectively). The explanation for this improvement is that the reduction in SOx emissions leads to reduced formation of secondary particles (mostly ammonium sulphate) and hence lower PM concentrations with respect to the baseline. Another notable effect of the scenarios is the increase in PM concentrations in the centre of the domain for the BioEt scenario despite a small decrease in PM emissions with respect to the baseline. This is due to an increase in NH_3 emissions leading to an increase in secondary particle formation (mostly ammonium nitrate). A more detailed analysis of the associated improvement in health impacts and cost savings as well as the co-benefits of these scenarios is provided by Gamarra et al. (2021).

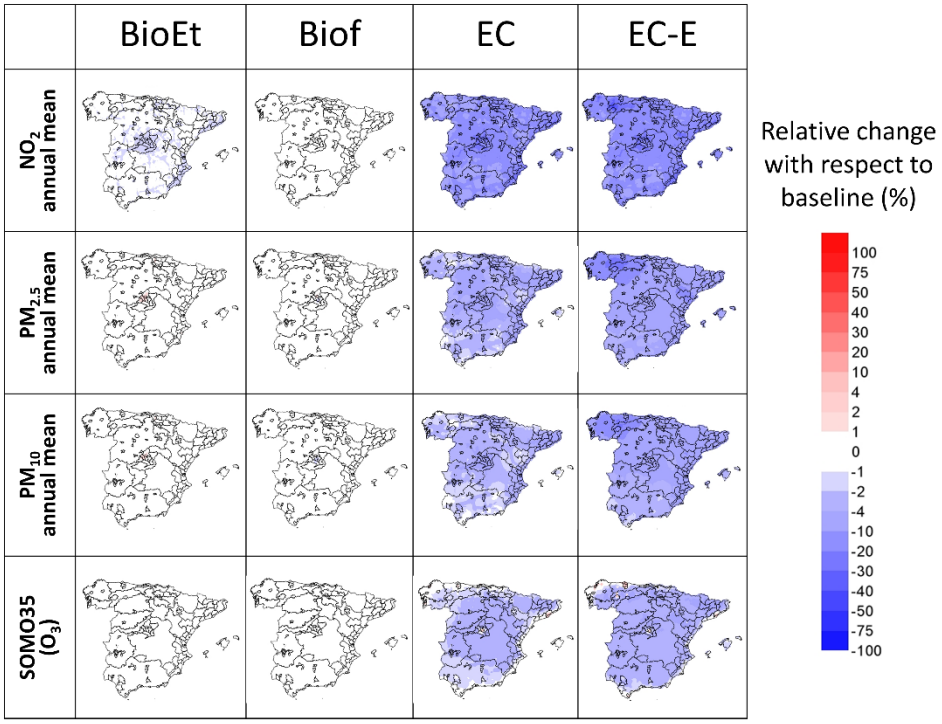

Figure 2. Change in air quality indicators in Spain with respect to the baseline values (2017) for each scenario: BioEt (increased bioethanol use), Biof (increased bioethanol and biodiesel use), EC (100% penetration of electric cars) and EC-E (same as EC but including the emissions from the additional electricity demand). Maps show the air quality assessment zones for the Spanish territory of the Iberian Peninsula, Balearic Islands, Ceuta and Melilla.

CONCLUSIONS

Based on the simulations by the CHIMERE chemistry transport model, the results of this study show that the two biofuel scenarios are not expected to have a large impact on air quality in Spain, although these scenarios should also be considered taking into account the co-benefits of the measures (e.g. the corresponding reductions in greenhouse gas emissions). The electric car scenarios do estimate a substantial benefit in terms of air quality improvements (and consequently reduced health impacts) although they do represent a maximum impact scenario (100% penetration of the electric car), representing a best case scenario to show the potential of the measures. The results also show that the influence of atmospheric chemistry on pollutant concentrations should be taken into account when assessing emission reduction scenarios. Examples of this are the reduced particle formation in the electric car scenario that takes into account the future energy mix in Spain (lower SOx emissions) and the increased particle formation in the bioethanol scenario due to increased NH_3 emissions.

ACKNOWLEDGEMENTS

This study is part of the Retos-AIRE project (Air pollution mitigation actions for environmental policy support. Air quality multiscale modelling and evaluation of health and vegetation impacts) (Grant: RTI2018-099138-B-I00) funded by MCIN/AEI/10.13039/501100011033 and by ERDF A way of making Europe. The modelling that provides data for this study is based on data provided through collaborations with other public organizations. In this regard, we thank Tragsatec for their collaboration in estimating the emission reductions for the measures in the NAPCP and to the Ministry for the Ecological Transition and Demographic Challenge for providing data from air quality stations and information on emission reductions. We are also grateful for the services offered by the European Center for Medium-Range Weather Forecasts (ECMWF), including the provision of meteorological modelling data with thanks also to AEMET for managing access to this information. Finally, we thank the Ministry of Science and Innovation for financial support through the project Retos-AIRE (RTI2018-099138-B-100).

REFERENCES

Bessagnet, B., Pirovano, G., Mircea, M., Cuvelier, C., Aulinger, A., Calori, G., Ciarelli, G., Manders, A., Stern, R., Tsyro, S., et al. Presentation of the EURODELTA III intercomparison exercise – evaluation of the chemistry transport models' performance on criteria pollutants and joint analysis with meteorology. Atmos. Chem. Phys. 2016, 16, 12667–12701, doi:10.5194/acp-16-12667-2016.

EEA (European Environment Agency), 2021. Available online: https://www.eea.europa.eu/ims/greenhouse-gas-emissions-from-transport (accessed on July 13th, 2022)

Gamarra, A.R., Lechón, Y., Vivanco, M.G., Theobald, M.R., Lago, C., Sánchez, E., Santiago, J.L., Garrido,J.L., Martín, F., Gil, V., et al. Avoided Mortality Associated with Improved Air Quality from an Increase in Renewable Energy in the Spanish Transport Sector: Use of Biofuels and the Adoption of the Electric Car. Atmosphere 2021, 12, 1603. https://doi.org/10.3390/atmos12121603

Menut, L.; Bessagnet, B.; Khvorostyanov, D.; Beekmann, M.; Blond, N.; Colette, A.; Coll, I.; Curci, G.; Foret, G.; Hodzic, A.; et al. CHIMERE 2013: a model for regional atmospheric composition modelling. Geosci. Model Dev. 2013, 6, 981–1028, doi:10.5194/gmd-6-981-2013.

MITERD, 2020. Spanish National Energy and Climate Plan 2021–2030. Available online: https://www.miteco.gob.es/images/es/pnieccompleto_tcm30-508410.pdf (accessed on 27 July 2022).

Vivanco, M.G.; Correa, M.; Azula, O.; Palomino, I.; Martín, F. Influence of model resolution on ozone predictions over Madrid Area (Spain). In Proceedings of the Lecture Notes in Computer Science (including subseries Lecture Notes in Artificial Intelligence and Lecture Notes in Bioinformatics); Springer, Berlin, Heidelberg, 2008; Vol. 5072 LNCS, pp. 165–178.

Vivanco, M.G.; Palomino, I.; Vautard, R.; Bessagnet, B.; Martín, F.; Menut, L.; Jiménez, S. Multi-year assessment of photochemical air quality simulation over Spain. Environ. Model. Softw. 2009a, 24, 63–73, doi:10.1016/j.envsoft.2008.05.004.

Vivanco, M.G.; Palomino, I.; Martín, F.; Palacios, M.; Jorba, O.; Jiménez, P.; Baldasano, J.M.; Azula, O. An evaluation of the performance of the CHIMERE model over Spain using meteorology from MM5 and WRF models. In Proceedings of the Lecture Notes in Computer Science (including subseries Lecture Notes in Artificial Intelligence and Lecture Notes in Bioinformatics); Springer, Berlin, Heidelberg, 2009b; Vol. 5592 LNCS, pp. 107–117.

Vivanco, M.G., Garrido, J.L., Martín, F., Theobald, M.R., Gil, V., Santiago, J.-L., Lechón, Y., Gamarra, A.R., Sánchez, E., Alberto, A., et al. Assessment of the effects of the Spanish national air pollution control programme on air quality. Atmosphere, 2021, 12, 158.

21st International Conference on
Harmonisation within Atmospheric Dispersion Modelling for Regulatory Purposes
27-30 September 2022, Aveiro, Portugal

A COUPLING BETWEEN RANS CFD AND STOCHASTIC LAGRANGIAN MODELLING FOR LONG TERM IMPACT ASSESSMENT ON AN INDUSTRIAL SITE

Guillevic Lamaison[1], Perrine Charvolin[1], Chi Vuong Nguyen[1], Kim Vermare[2], Aurélie Guth[2] and Lionel Soulhac[3]

[1] Univ Lyon, Ecole Centrale de Lyon, CNRS, Univ Claude Bernard Lyon 1, INSA Lyon, LMFA, UMR5509, 69130, Ecully, France
[2] EDF/DIPDE, Lyon, France
[3] Univ Lyon, INSA Lyon, CNRS, Ecole Centrale de Lyon, Univ Claude Bernard Lyon 1, LMFA, UMR5509, 69621, Villeurbanne France

Abstract: Industrial and consulting companies performed impact assessment studies of atmospheric pollutant dispersion to ensure that the concentrations around each industrial release are below the regulatory thresholds. Industrial sources are located inside a site of complex geometry with topography and various obstacles so that simple modelling approaches based on Gaussian models or using a flat rough terrain assumption are not relevant. Therefore, CFD approaches, with RANS or LES turbulence modelling, are now commonly used to simulate flow and dispersion in complex industrial or urban areas. However, for long term impact assessment, the direct application of the CFD approach is still computationally prohibitive using the typical IT resources of consulting offices or environment and safety departments.
In order to address this issue, a specific simulation approach has been developed, based on the coupling between a CFD pre-calculated wind field database and a stochastic Lagrangian dispersion model (SLAM – Safety Lagrangian Atmospheric Model). The wind field database is calculated for an ensemble of triplets of parameters representing the variety of meteorological conditions. Considering the probability of occurrence of each situation in the meteorological time series, it is possible to simulate the PDF of the concentration values and to calculate all the statistics (mean, percentiles, probability of exceedance) on a real complex site.
This modelling methodology has been applied to evaluate long term dispersion around nuclear power plants. To validate the approach, specific measurements on a realistic reduced scale model of a nuclear site have been performed in the atmospheric wind tunnel of the Ecole Centrale de Lyon. The comparison between the model and the experiment highlights the performance and capability of the model and the differences are discussed and analysed to suggest further developments and improvements of the approach..

Key words: *chronic pollution impact, CFD, Lagrangian dispersion.*

INTRODUCTION

In this short presentation we will give an overview of a methodology developped by Laboratoire de Mécanique des Fluides et d'Acoustique (LMFA) throught the last years and currently used by industrial company for long term impact assesment on their site. Until recently, impacts of chronical releases were eveluated by the mean of Gaussian models. The short time response of such models allows users to compute the impact of each hour sample taken from long time sequence of hourly meteorology, which means more than 40000 simulations for a five years range, in less than a few hours.
However, main weakness of Gaussian approaches are their bad capacities to correctly take into account real complex obstacles and realistic topography. Nuclear power plants sites are caracterised by numerous obstacles and buildinds, and sometimes complex orography as well. It's therefore quite logical to consider more perfected simulations tools, built on 3D detailed flow representation, to better represent dispersion phenomena. CFD approaches, with RANS or LES turbulence modelling, are now commonly used to simulate flow and dispersion over industrial aeras giving a response in a few hours for a particular wind condition. However, the compuation cost is still prohibitive for engineering purposes because long term impact requires hundreds of thousand CPU hours to be computed. The aim of our methodology is to drastically reduce compution time by the means of two innovations: on one side the storage of a CFD database to evaluate a full realistic 3D windfield used as an Eulerian input in a Lagrangian particles dispersion model and on the other side the reduction of the number of simulations by a meteorological classification approach. The next section globally describes these methodology called AST&Risk

(Atmospheric Simulation of Transport & Risk). Then we shortly introduce principles and validation of each part of the methodology before showing an exampe of application on a idealized nuclear site.

AST&RISK METHODOLOGY

The methodology has been implemented in the AST&Risk software platform presented in **Figure 47**. The main steps of the calculation methodology are the following:

• Meteorological preprocessing and classification: from a time series of sequential meteorological data, a meteorological preprocessing module is applied to determine the parameters. The classes are then formed and the frequencies of occurrence of the meteorological conditions of each class are determined.

• Running SLAM simulations: based on the N meteorological classes and the release parameters, the platform runs N dispersion simulations with the SLAM software, by optimizing the use of the processors allocated to the calculation.

• Statistical post-processing of the results: using the frequencies of occurrence associated with each of the classes, the concentration fields are statistically aggregated in order to obtain the average and the concentration percentiles at each point of the domain.

• 3D visualization and export of results: the graphical user interface of the AST&Risk software allows a 3D representation of the results (iso-contours of concentration, isosurface) on a cartographic background (map, aerial photo).

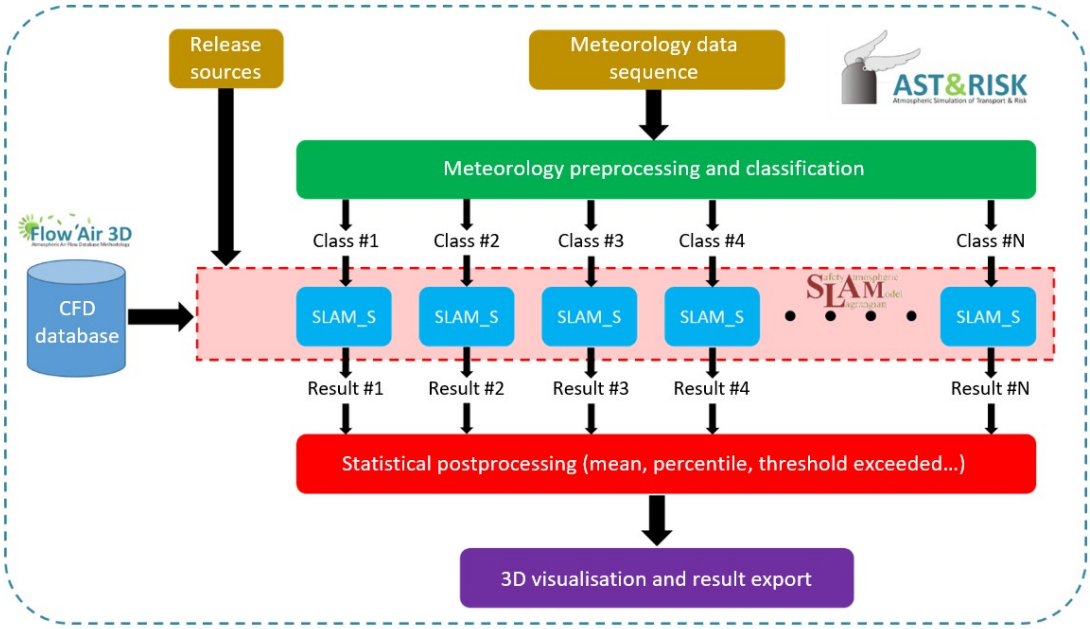

Figure 47. Overall diagram of AST&Risk methodology.

RANS CFD SIMULATIONS OF ATMOSPHERIC BOUNDARY LAYER AND LAGRANGIAN DISPERSION

The Safety Lagrangian Atmospheric Model (SLAM) is a stochastic particle dispersion model, based on the tracking of Lagrangian trajectories of individual particles. The temporal evolution of the Lagrangian velocity of each particle is given by two contributions:

$$U_i(t) = \overline{U_i}(t) + U_i'(t) \text{ with } U_i'(t+dt) = U_i'(t) + dU_i'$$

The first one is the mean velocity of the flow obtained from the CFD velocity field. The evolution of second, the fluctuating velocity, is determined by the stochastic differential equation (Thomson, 1987):

$$dU_i' = a_i(X, U', t)dt + \sum_j b_j(X, U', t)d\xi_j$$

in which the terms a_i and b_j are expressed in terms of standard deviations of velocity fluctuations σ_{u_i} and of the Lagrangian times T_{L_i} calculated from the k-ε turbulence model:

$$\sigma_u = \sqrt{\frac{2}{3}k} \text{ and } T_L = \frac{2\sigma_u^2}{C_0\varepsilon}$$

SLAM model has been validated on several configurations (Vendel et al., 2011) and required reliable CFD fields that are obtained by the simulation of the surface boundary layer in neutral, stable or unstable stratification conditions (Vendel et al., 2010b).

DATABASE OF WIND FIELD

In a simulation of the flow and dispersion with a CFD model, an important part of the computing time is devoted to modelling the flow and turbulence field. The principle of our approach, illustrated on **Figure 48**, is to prepare in advance a database of wind fields on the considered industrial site. In this way, only the dispersion is modelled in operational situations and time savings are considerable. The parameters that constitute the database are the wind direction and the inverse of the Monin-Obukhov length. As it was shown by Vendel et al. (2010a), it is possible to overcome the wind speed by normalizing the velocity and turbulence fields by the friction velocity u_* (and the same kind of assumption is made for the temperature field normalized by using the potential temperature at ground level).

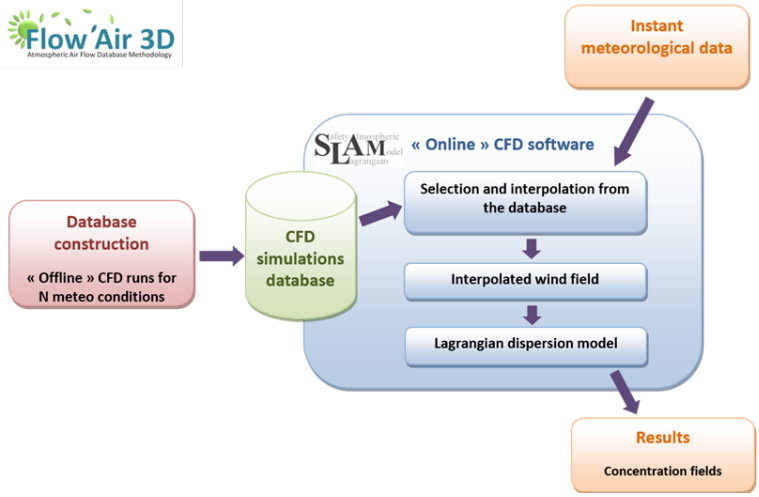

Figure 48. General desciption of Flow'Air 3D methodology.

Vendel et al. (2010a) have also shown that a discretization of the database in 18 wind directions (step of 20°) and 7 values of $1/L_{MO}$ can limit the interpolation error in the database to a few percents (**Figure 49**). Once the database is ready, it is used as input for the Lagrangian model SLAM. In operational situations, a point meteorological data (measurement or forecast) is used in a meteorological preprocessor to estimate the wind direction, the inverse of the Monin-Obukhov length and the friction velocity u_*. These parameters are interpolated in the database to obtain wind, temperature and turbulence fields corresponding to the real atmospheric conditions. These fields are then used to model the dispersion with the SLAM Lagrangian model.

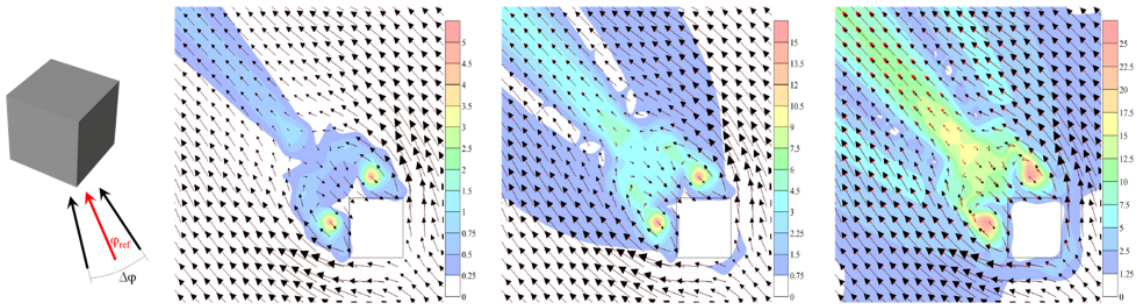

Figure 49. Validation of direction discretisation of the database approach. Comparison of velocity field between direct RANS calcultation and 3 interpolations with step angle of 5°, 10° and 20° from left to right. Colours show error levels.

METEOROLOGICAL CLASSIFICATION

In our methodology, building a CFD database of RANS simulations requires at the inlet boundary 1D horizontally homogeneous description of the ABL given by analytical profiles from Monin-Obukhov theory. We usually used profiles from Gryning et al (2007) and Truchot (2015) whose parameters are wind direction φ, friction velocity u_*, Monin-Obukhov L_{MO}, ground temperature T_0 and ABL height h_{ABL}. Those variables have to be deducted from measurements providing classically wind speed and direction, pressure, temperature and cloud cover. This is done by a meteorological preprocessing described by Soulhac et al (2011) and issuing from Fischer et al (1998). To reduce the number of parameters, choice is made to keep T_0 and h_{ABL} constant and equals to their average value on the long term sequence. A analysis of a few real meteorology data sequence in different places has given us a procedure to disctretize in class the parameters by comparison of pdf in a $(u_*, 1/L_{MO})$ coordinate system. We then validate this approach by comparison of average concentration from different sources at many distances obtain on one side by the classical sequential approach and on the other side by the classification method. Sensitivity studies have been done on the discretisation of each of the three parameters $(\varphi, u_*, 1/L_{MO})$ and a example is given on **Figure 50**.

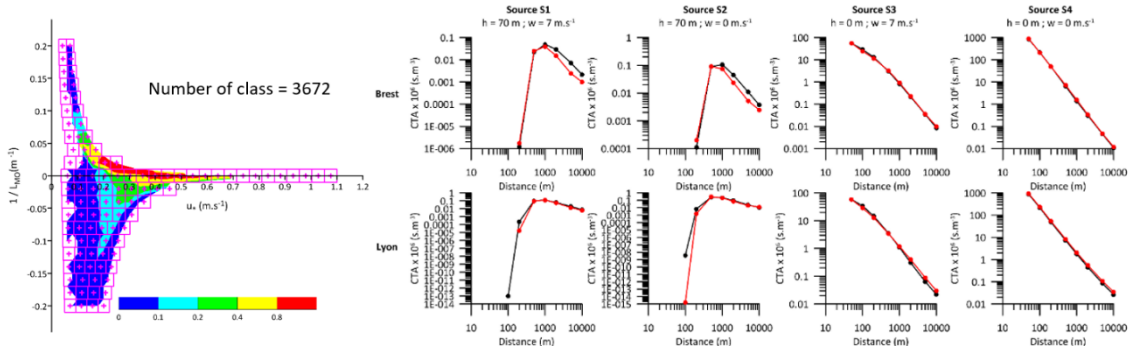

Figure 50. Validation of the classification approach. Left: illustration of class. Right: Comparison of concentration between sequential (black) and classification (red) for 4 differents sources in 2 different sets of 5 years meteorology.

APPLICATION

In order to illustrate the potentiality of the methodology without revealing confidential content, a simplified domain containing typical power plant buildings is created and meshed before a CFD database of 126 wind conditions (18 wind direction times 7 Monin-Obukhov lenght) is computed and stored. **Figure 51** shows the cylinder shaped domain of diameter 2.5 km by 500 m height, and a zoom on buildings mapped with their surface mesh (1.1 millions cells in the volume). Then, in a second step, a fictive chimney source is placed closed to the reactor building (green cylinder with red arrow at top in center of **Figure 51**) with arbitrary emission of 10 $g.s^{-1}$ of CO (carbon monoxyde) and a five years long hourly meteorological data sequence is given to the tool (see the windrose obtained by analysis of these data on the right of **Figure 51**).

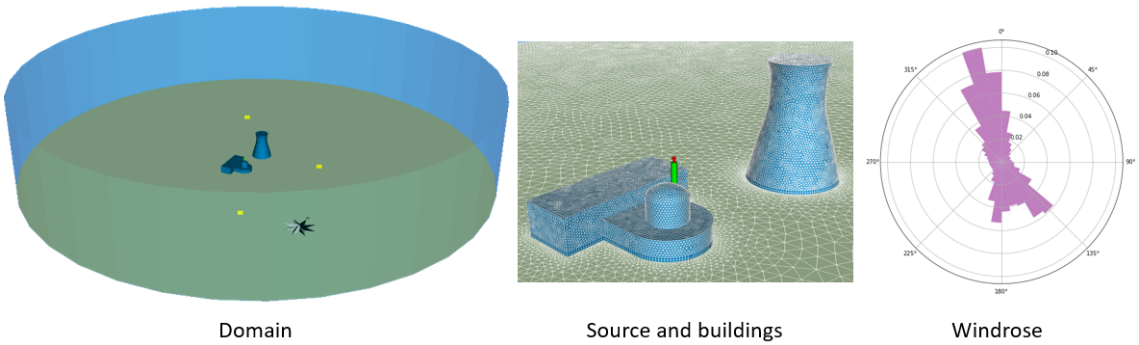

Figure 51. Configuration of the application case. Left: view of the computation domain. Center: zoom on buildings and the source. Right: Wind direction frequency occurence.

Classification methodology reduces the description of the meteorology variability to only 1620 classes and the corresponding Lagrangian simulations are runned on a laptop with a single Intel Core i9 processor and 64.0 GB of RAM. Frequency occurences of each class is then used to computed concentration mean and

percentiles fields. The whole dispersion process is achieved in less than 2.5 hours and some results are illustrated on **Figure 52** which shows isocontours of percentile 95 on ground and buildings. At three locations points, percentile repartition between 0.8 and 1 is also shown.

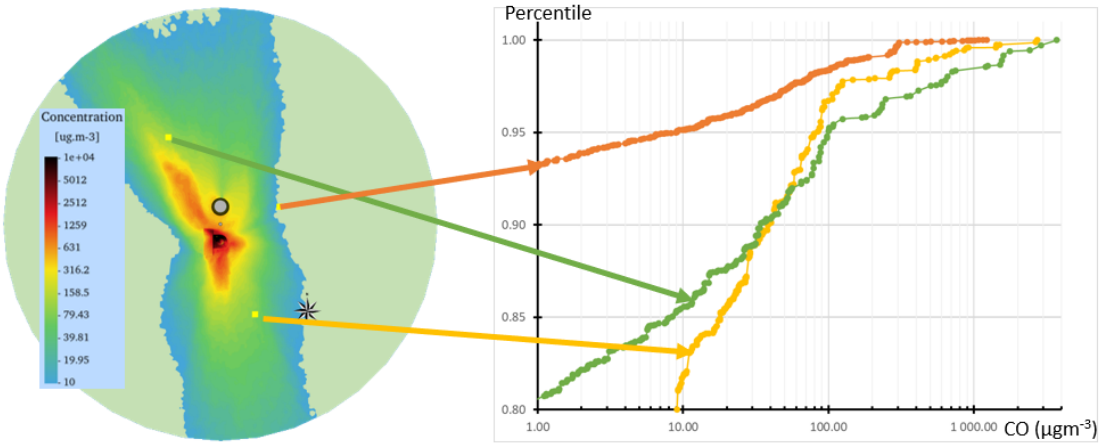

Figure 52. Cartography of percentile 95 and percentile repartition curve at three locations.

CONCLUSION

This presentation is a quick overview of a methodology developped during the last years by LMFA in collaoration with EDF-DIPDE. Improvements are regularly made on both software features and scientific content. Assumptions made by this method at each step (CFD computation, database interpolation, meteorological preprocessing and classification, Lagrangian simulations) leads to some limitations but remains also challenging as each step is perfectible to continue to improve the response quality without degrading the response time.

REFERENCES

Fisher, B. E. A., J. J. Erbrink, S. Finardi, P. P. Jeannet, S. Joffre, M. G. Morselli, U. Pechinger, P. Seibert, and D. J. Thomson, eds. 1998. *Harmonisation of the Pre-Processing of Meteorological Data for Atmospheric Dispersion Models. COST Action 710 – Final Report*. European Commission.

Gryning, Sven-Erik, Ekaterina Batchvarova, Burghard Brümmer, Hans Jørgensen, and Søren Larsen. 2007. "On the Extension of the Wind Profile over Homogeneous Terrain beyond the Surface Boundary Layer." *Boundary-Layer Meteorology* **124** (2): 251–68.

Soulhac, Lionel, Pietro Salizzoni, François-Xavier Cierco, and Richard J. Perkins. 2011. "The Model SIRANE for Atmospheric Urban Pollutant Dispersion; Part I, Presentation of the Model." *Atmospheric Environment* **45** (39): 7379–95.

Thomson, D.J., 1987: Criteria for the selection of stochastic models of particle trajectories lagrangian dispersion model in turbulent flows. *Journal of Fluid Mechanics*, **180**, 529-556.

Truchot, Benjamin. 2015. "*Guide de Bonnes Pratiques Pour La Réalisation de Modélisations 3D Pour Des Scénarios de Dispersion Atmosphérique En Situation Accidentelle. Rapport de Synthèse Des Travaux Du Groupe de Travail National*." Ministère en charge de l'écologie.

Vendel, F., G. Lamaison, L. Soulhac, L. Donnat, O. Duclaux and C. Puel, 2010a: A new operational modelling approach for atmospheric dispersion in industrial complex area. *13th Int. Conf. on Harmo. within Atmos. Disp. Modell. for Regul.Purposes, Paris, France*

Vendel, F., Lamaison, G., Soulhac, L., Volta, P., Donnat, L., Duclaux, O., et Puel, C., 2010b. Modeling diabatic atmospheric boundary layer using a RANS CFD code with k- epsilon or Reynolds-stress turbulence closure, *13th Int. Conf. on Harmo. within Atmos. Disp. Modell. for Regul. Purposes, Paris France*

Vendel, F., Soulhac, L., Mejean, P., Donnat, L., Duclaux; O., 2011 : Validation of the Safety Lagrangian Atmospheric Model (SLAM) against a wind tunnel experiment over an industrial complex area. *14th Int. Conf. on Harmo, within Atmos. Disp. Modell. for Regul. Purposes, Kos, Greece.*

21st International Conference on
Harmonisation within Atmospheric Dispersion Modelling for Regulatory Purposes
27-30 September 2022, Aveiro, Portugal

A COUPLING BETWEEN RANS CFD AND STOCHASTIC LAGRANGIAN MODELLING FOR LONG TERM IMPACT ASSESSMENT ON AN INDUSTRIAL SITE

Guillevic Lamaison[1], Perrine Charvolin[1], Chi Vuong Nguyen[1], Kim Vermare[2], Aurélie Guth[2] and Lionel Soulhac[3]

[1] Univ Lyon, Ecole Centrale de Lyon, CNRS, Univ Claude Bernard Lyon 1, INSA Lyon, LMFA, UMR5509, 69130, Ecully, France
[2] EDF/DIPDE, Lyon, France
[3] Univ Lyon, INSA Lyon, CNRS, Ecole Centrale de Lyon, Univ Claude Bernard Lyon 1, LMFA, UMR5509, 69621, Villeurbanne France

Abstract: Industrial and consulting companies performed impact assessment studies of atmospheric pollutant dispersion to ensure that the concentrations around each industrial release are below the regulatory thresholds. Industrial sources are located inside a site of complex geometry with topography and various obstacles so that simple modelling approaches based on Gaussian models or using a flat rough terrain assumption are not relevant. Therefore, CFD approaches, with RANS or LES turbulence modelling, are now commonly used to simulate flow and dispersion in complex industrial or urban areas. However, for long term impact assessment, the direct application of the CFD approach is still computationally prohibitive using the typical IT resources of consulting offices or environment and safety departments.
In order to address this issue, a specific simulation approach has been developed, based on the coupling between a CFD pre-calculated wind field database and a stochastic Lagrangian dispersion model (SLAM – Safety Lagrangian Atmospheric Model). The wind field database is calculated for an ensemble of triplets of parameters representing the variety of meteorological conditions. Considering the probability of occurrence of each situation in the meteorological time series, it is possible to simulate the PDF of the concentration values and to calculate all the statistics (mean, percentiles, probability of exceedance) on a real complex site.
This modelling methodology has been applied to evaluate long term dispersion around nuclear power plants. To validate the approach, specific measurements on a realistic reduced scale model of a nuclear site have been performed in the atmospheric wind tunnel of the Ecole Centrale de Lyon. The comparison between the model and the experiment highlights the performance and capability of the model and the differences are discussed and analysed to suggest further developments and improvements of the approach..

Key words: *chronic pollution impact, CFD, Lagrangian dispersion.*

INTRODUCTION

In this short presentation we will give an overview of a methodology developped by Laboratoire de Mécanique des Fluides et d'Acoustique (LMFA) throught the last years and currently used by industrial company for long term impact assesment on their site. Until recently, impacts of chronical releases were eveluated by the mean of Gaussian models. The short time response of such models allows users to compute the impact of each hour sample taken from long time sequence of hourly meteorology, which means more than 40000 simulations for a five years range, in less than a few hours.
However, main weakness of Gaussian approaches are their bad capacities to correctly take into account real complex obstacles and realistic topography. Nuclear power plants sites are caracterised by numerous obstacles and buildinds, and sometimes complex orography as well. It's therefore quite logical to consider more perfected simulations tools, built on 3D detailed flow representation, to better represent dispersion phenomena. CFD approaches, with RANS or LES turbulence modelling, are now commonly used to simulate flow and dispersion over industrial aeras giving a response in a few hours for a particular wind condition. However, the compuation cost is still prohibitive for engineering purposes because long term impact requires hundreds of thousand CPU hours to be computed. The aim of our methodology is to drastically reduce compution time by the means of two innovations: on one side the storage of a CFD database to evaluate a full realistic 3D windfield used as an Eulerian input in a Lagrangian particles dispersion model and on the other side the reduction of the number of simulations by a meteorological

classification approach. The next section globally describes these methodology called AST&Risk (Atmospheric Simulation of Transport & Risk). Then we shortly introduce principles and validation of each part of the methodology before showing an exampe of application on a idealized nuclear site.

AST&RISK METHODOLOGY

The methodology has been implemented in the AST&Risk software platform presented in **Figure 47**. The main steps of the calculation methodology are the following:

• Meteorological preprocessing and classification: from a time series of sequential meteorological data, a meteorological preprocessing module is applied to determine the parameters. The classes are then formed and the frequencies of occurrence of the meteorological conditions of each class are determined.

• Running SLAM simulations: based on the N meteorological classes and the release parameters, the platform runs N dispersion simulations with the SLAM software, by optimizing the use of the processors allocated to the calculation.

• Statistical post-processing of the results: using the frequencies of occurrence associated with each of the classes, the concentration fields are statistically aggregated in order to obtain the average and the concentration percentiles at each point of the domain.

• 3D visualization and export of results: the graphical user interface of the AST&Risk software allows a 3D representation of the results (iso-contours of concentration, isosurface) on a cartographic background (map, aerial photo).

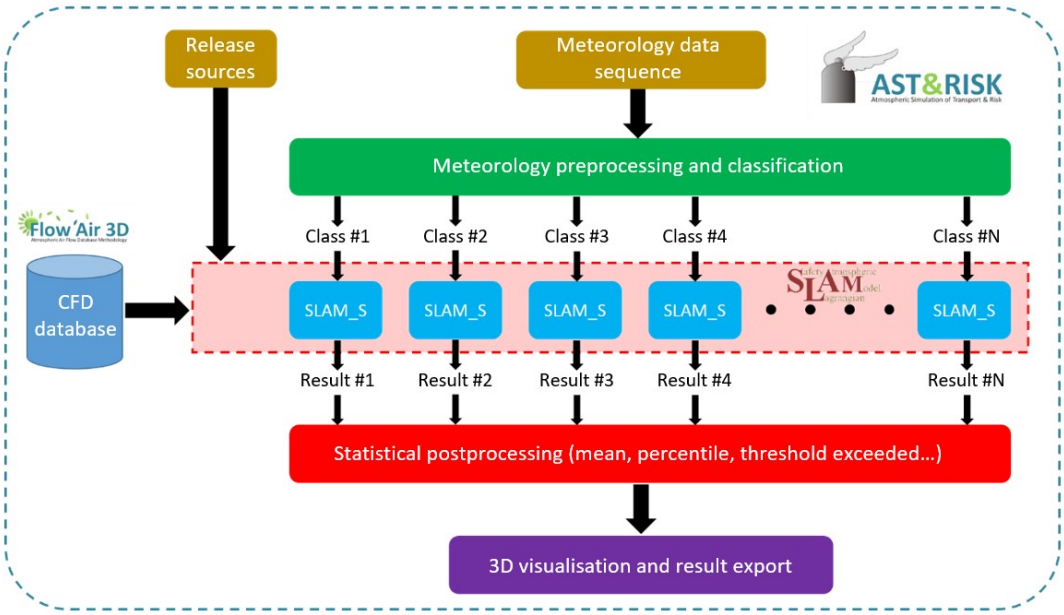

Figure 53. Overall diagram of AST&Risk methodology.

RANS CFD SIMULATIONS OF ATMOSPHERIC BOUNDARY LAYER AND LAGRANGIAN DISPERSION

The Safety Lagrangian Atmospheric Model (SLAM) is a stochastic particle dispersion model, based on the tracking of Lagrangian trajectories of individual particles. The temporal evolution of the Lagrangian velocity of each particle is given by two contributions:

$$U_i(t) = \overline{U_i}(t) + U_i'(t) \text{ with } U_i'(t+dt) = U_i'(t) + dU_i'$$

The first one is the mean velocity of the flow obtained from the CFD velocity field. The evolution of second, the fluctuating velocity, is determined by the stochastic differential equation (Thomson, 1987):

$$dU_i' = a_i(X, U', t)dt + \sum_j b_j(X, U', t)d\xi_j$$

in which the terms a_i and b_j are expressed in terms of standard deviations of velocity fluctuations σ_{u_i} and of the Lagrangian times T_{L_i} calculated from the k-ε turbulence model:

$$\sigma_u = \sqrt{\frac{2}{3}k} \text{ and } T_L = \frac{2\sigma_u^2}{C_0\varepsilon}$$

SLAM model has been validated on several configurations (Vendel et al., 2011) and required reliable CFD fields that are obtained by the simulation of the surface boundary layer in neutral, stable or unstable stratification conditions (Vendel et al., 2010b).

DATABASE OF WIND FIELD

In a simulation of the flow and dispersion with a CFD model, an important part of the computing time is devoted to modelling the flow and turbulence field. The principle of our approach, illustrated on **Figure 48**, is to prepare in advance a database of wind fields on the considered industrial site. In this way, only the dispersion is modelled in operational situations and time savings are considerable. The parameters that constitute the database are the wind direction and the inverse of the Monin-Obukhov length. As it was shown by Vendel et al. (2010a), it is possible to overcome the wind speed by normalizing the velocity and turbulence fields by the friction velocity u_* (and the same kind of assumption is made for the temperature field normalized by using the potential temperature at ground level).

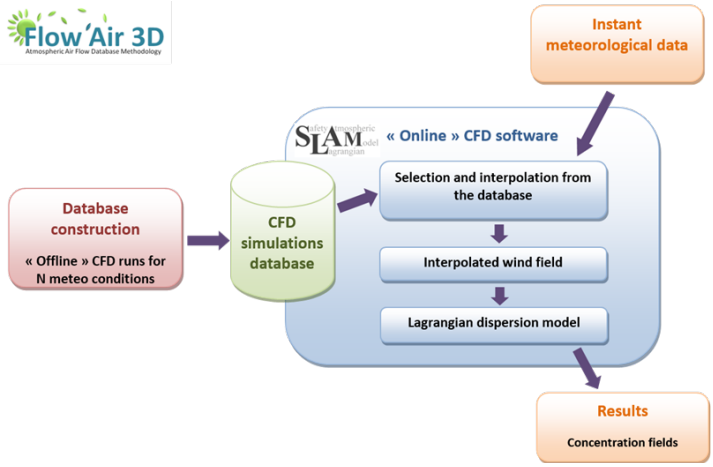

Figure 54. General desciption of Flow'Air 3D methodology.

Vendel et al. (2010a) have also shown that a discretization of the database in 18 wind directions (step of 20°) and 7 values of $1/L_{MO}$ can limit the interpolation error in the database to a few percents (**Figure 49**). Once the database is ready, it is used as input for the Lagrangian model SLAM. In operational situations, a point meteorological data (measurement or forecast) is used in a meteorological preprocessor to estimate the wind direction, the inverse of the Monin-Obukhov length and the friction velocity u_*. These parameters are interpolated in the database to obtain wind, temperature and turbulence fields corresponding to the real atmospheric conditions. These fields are then used to model the dispersion with the SLAM Lagrangian model.

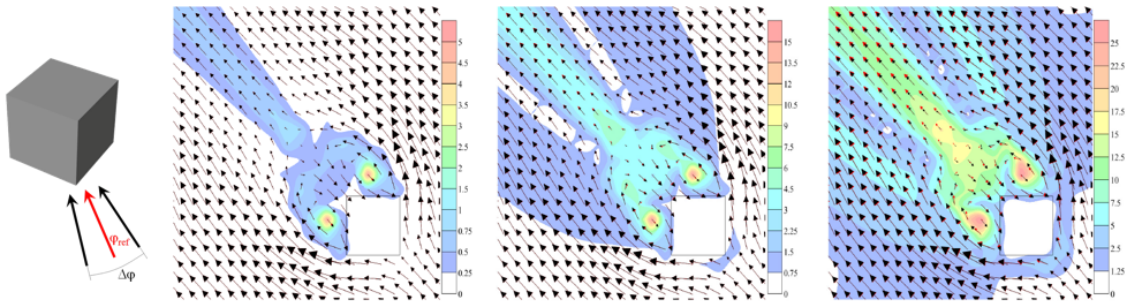

Figure 55. Validation of direction discretisation of the database approach. Comparison of velocity field between direct RANS calcultation and 3 interpolations with step angle of 5°, 10° and 20° from left to right. Colours show error levels.

METEOROLOGICAL CLASSIFICATION

In our methodology, building a CFD database of RANS simulations requires at the inlet boundary 1D horizontally homogeneous description of the ABL given by analytical profiles from Monin-Obukhov theory. We usually used profiles from Gryning et al (2007) and Truchot (2015) whose parameters are wind direction φ, friction velocity u_*, Monin-Obukhov L_{MO}, ground temperature T_0 and ABL height h_{ABL}. Those variables have to be deducted from measurements providing classically wind speed and direction, pressure, temperature and cloud cover. This is done by a meteorological preprocessing described by Soulhac et al (2011) and issuing from Fischer et al (1998). To reduce the number of parameters, choice is made to keep T_0 and h_{ABL} constant and equals to their average value on the long term sequence. A analysis of a few real meteorology data sequence in different places has given us a procedure to disctretize in class the parameters by comparison of pdf in a $(u_*, 1/L_{MO})$ coordinate system. We then validate this approach by comparison of average concentration from different sources at many distances obtain on one side by the classical sequential approach and on the other side by the classification method. Sensitivity studies have been done on the discretisation of each of the three parameters $(\varphi, u_*, 1/L_{MO})$ and a example is given on **Figure 50**.

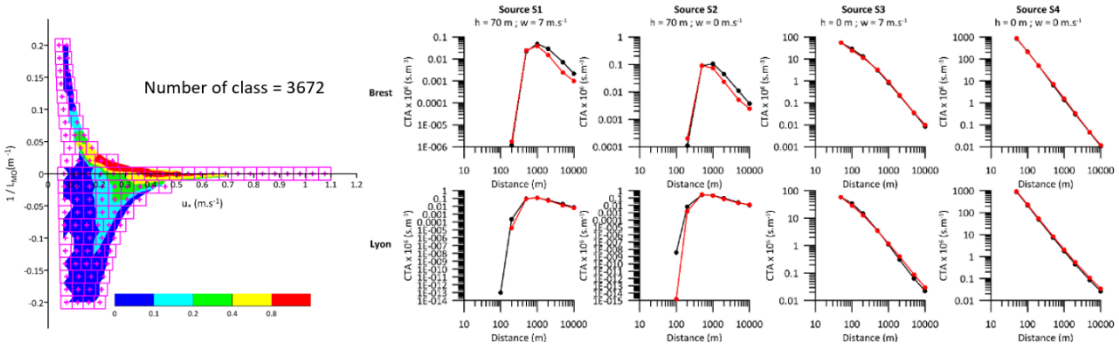

Figure 56. Validation of the classification approach. Left: illustration of class. Right: Comparison of concentration between sequential (black) and classification (red) for 4 differents sources in 2 different sets of 5 years meteorology.

APPLICATION

In order to illustrate the potentiality of the methodology without revealing confidential content, a simplified domain containing typical power plant buildings is created and meshed before a CFD database of 126 wind conditions (18 wind direction times 7 Monin-Obukhov lenght) is computed and stored. **Figure 51** shows the cylinder shaped domain of diameter 2.5 km by 500 m height, and a zoom on buildings mapped with their surface mesh (1.1 millions cells in the volume). Then, in a second step, a fictive chimney source is placed closed to the reactor building (green cylinder with red arrow at top in center of **Figure 51**) with arbitrary emission of 10 g.s^{-1} of CO (carbon monoxyde) and a five years long hourly meteorological data sequence is given to the tool (see the windrose obtained by analysis of these data on the right of **Figure 51**).

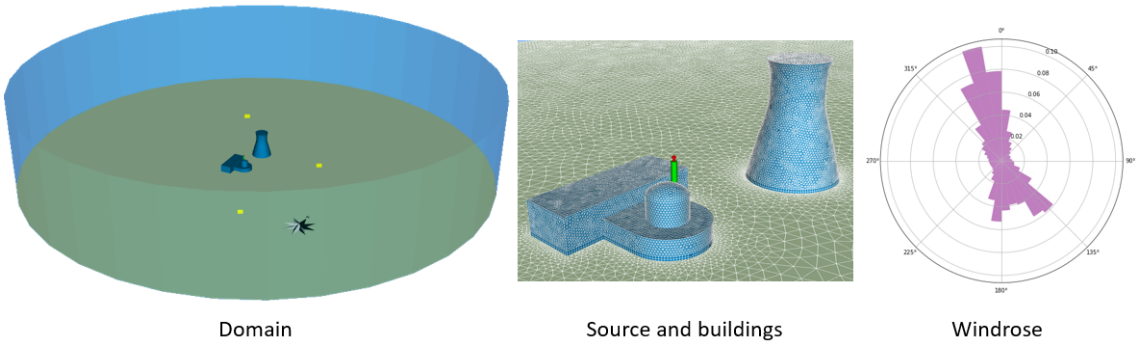

Figure 57. Configuration of the application case. Left: view of the computation domain. Center: zoom on buildings and the source. Right: Wind direction frequency occurence.

Classification methodology reduces the description of the meteorology variability to only 1620 classes and the corresponding Lagrangian simulations are runned on a laptop with a single Intel Core i9 processor and 64.0 GB of RAM. Frequency occurences of each class is then used to computed concentration mean and percentiles fields. The whole dispersion process is achieved in less than 2.5 hours and some results are

illustrated on **Figure 52** which shows isocontours of percentile 95 on ground and buildings. At three locations points, percentile repartition between 0.8 and 1 is also shown.

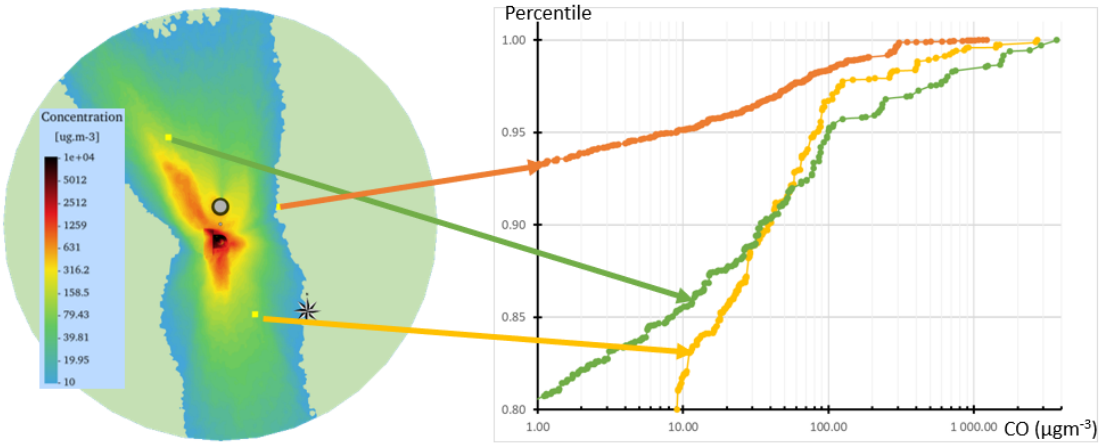

Figure 58. Cartography of percentile 95 and percentile repartition curve at three locations.

CONCLUSION

This presentation is a quick overview of a methodology developped during the last years by LMFA in collaoration with EDF-DIPDE. Improvements are regularly made on both software features and scientific content. Assumptions made by this method at each step (CFD computation, database interpolation, meteorological preprocessing and classification, Lagrangian simulations) leads to some limitations but remains also challenging as each step is perfectible to continue to improve the response quality without degrading the response time.

REFERENCES

Fisher, B. E. A., J. J. Erbrink, S. Finardi, P. P. Jeannet, S. Joffre, M. G. Morselli, U. Pechinger, P. Seibert, and D. J. Thomson, eds. 1998. *Harmonisation of the Pre-Processing of Meteorological Data for Atmospheric Dispersion Models. COST Action 710 – Final Report*. European Commission.

Gryning, Sven-Erik, Ekaterina Batchvarova, Burghard Brümmer, Hans Jørgensen, and Søren Larsen. 2007. "On the Extension of the Wind Profile over Homogeneous Terrain beyond the Surface Boundary Layer." *Boundary-Layer Meteorology* **124** (2): 251–68.

Soulhac, Lionel, Pietro Salizzoni, François-Xavier Cierco, and Richard J. Perkins. 2011. "The Model SIRANE for Atmospheric Urban Pollutant Dispersion; Part I, Presentation of the Model." *Atmospheric Environment* **45** (39): 7379–95.

Thomson, D.J., 1987: Criteria for the selection of stochastic models of particle trajectories lagrangian dispersion model in turbulent flows. *Journal of Fluid Mechanics*, **180**, 529-556.

Truchot, Benjamin. 2015. "*Guide de Bonnes Pratiques Pour La Réalisation de Modélisations 3D Pour Des Scénarios de Dispersion Atmosphérique En Situation Accidentelle. Rapport de Synthèse Des Travaux Du Groupe de Travail National*." Ministère en charge de l'écologie.

Vendel, F., G. Lamaison, L. Soulhac, L. Donnat, O. Duclaux and C. Puel, 2010a: A new operational modelling approach for atmospheric dispersion in industrial complex area. *13th Int. Conf. on Harmo. within Atmos. Disp. Modell. for Regul.Purposes, Paris, France*

Vendel, F., Lamaison, G., Soulhac, L., Volta, P., Donnat, L., Duclaux, O., et Puel, C., 2010b. Modeling diabatic atmospheric boundary layer using a RANS CFD code with k- epsilon or Reynolds-stress turbulence closure, *13th Int. Conf. on Harmo. within Atmos. Disp. Modell. for Regul. Purposes, Paris France*

Vendel, F., Soulhac, L., Mejean, P., Donnat, L., Duclaux; O., 2011 : Validation of the Safety Lagrangian Atmospheric Model (SLAM) against a wind tunnel experiment over an industrial complex area. *14th Int. Conf. on Harmo, within Atmos. Disp. Modell. for Regul. Purposes, Kos, Greece.*

21st International Conference on
Harmonisation within Atmospheric Dispersion Modelling for Regulatory Purposes
27-30 September 2022, Aveiro, Portugal

AERNOSTRUM: MONITORING OF AIR POLLUTION IN THE PORT OF LIVORNO AND OF PORTOFERRAIO ON THE ISLAND OF ELBA AND DETAILED ESTIMATE OF EMISSIONS IN THE PORTS

C.Collaveri[1], B.P.Andreini [1],E.Bini[1] , F.Dini[1] , S.Fortunato[1] , M.Rosato[1] , G.Licitra [1]*

[1] Department Regional Environmental Protection Agency of Tuscany (ARPAT)-Italy
*c.collaveri@arpat.toscana.it

Abstract:The European project AER NOSTRUM is dedicated to the evaluation of air quality monitoring in the urban areas near and inside the ports in the five regions of the Italy-France Maritime Cooperation Program 2014-2020: Tuscany, Liguria, Sardinia, Corsica and PACA. One of the specific objectives of the project is to harmonize and implement methods for monitoring and assessing air quality applying shared standards (Sulfur Oxides, Nitrogen Oxides, Volatile Organic Compounds, PM10 and PM 2.5 Dusts, PM1). The objective includes the comparison of different systems for monitoring pollutants with high or very high spatial and temporal resolution and the use of these data to validate the air quality model. This work shows some of the results of monitoring in the ports of Livorno and Portoferraio and early conclusions related to air quality in the ports and port-city interface.

Key words: *PM10, NO_2, Port Emissions, Air quality, nanoparticles, passive sampler, air quality model.*

INTRODUCTION

The activities carried out by ARPAT inside the AER NOSTRUM project are mainly related to air monitoring of pollutants at different spatial and temporal resolution. Analysis of monitoring results is performed to validate the air quality model developed by the Port Network Authority and for the construction of a detailed database of emissions from the port of Livorno. In Tuscany two ports were investigated: Livorno which is a large industrial, commercial and tourist port and Portoferraio on the island of Elba, the main island of the Tuscan archipelago. The monitoring was carried out at different temporal and spatial resolution and chemical (metals and PAH) and particle size (nano and micro particles in classes from 10 nm to 30 µm) studies were carried out on the PM. This work focuses on the first results of two campaigns: the monitoring with passive samplers of nitrogen oxides on a 10-point lattice for the study of the port-city interface and first results of the campaign on PM in the industrial site of the port of Livorno (nano and microparticle details) and Portoferraio (microparticle details).

Methods

The campaigns for the size distribution of the particles were carried out with an Optical particle counter (OPC) GRIMM mod 1108 capable of reading the counts of the size classes from 0.25 µm to 32 µm. A Nanoscan TSI SMPS mod 3910 (13 channels from 10 nm to 350 nm) was used for the nanoparticles. For both nano and microparticles the data were acquired with a time resolution of one minute. For sampling with passive samplers, the UNI EN 16339-2013 method with radiello samplers was used. Duration and distribution over the year of the campaigns comply the requisites of D.Lgs 155/2010. All the data are available in: http://www.arpat.toscana.it/temi-ambientali/aria/qualita-aria/rete_monitoraggio/struttura/autolaboratori/

Results

Study of NO_2 at the port-city interface

Monitoring of NO_2 was performed in 13 locations using passive samplers and/or chemiluminescent method. Passive samplers were used in 10 locations. Two of the 10 radiello stations coincide with the fixed stations (one of which is that of the port) and served as a control of the quality of the passive sampler data. Four campaigns were carried out to cover the different seasons in relation to the different traffic within the

port and the presence or absence of the heating source in the urban emissions. Sampling periods were as follows: summer (03/08/2021-24/08/2021 and 24/08/2021-07/09/2021), autumn (30/11/2021-14/12/2021), winter (03/03/2022-17/03/2022) and spring (17/03/2022-01/04/2022).
The different locations represent the northern area of Livorno including the contribution of the port and the industrial area of the city, the central southern area which most represents the urban component and finally there are 3 locations significantly influenced by traffic (see fig 1). One of the latter is the LI-Carducci urban traffic station which is located along a very busy 4-lane avenue.

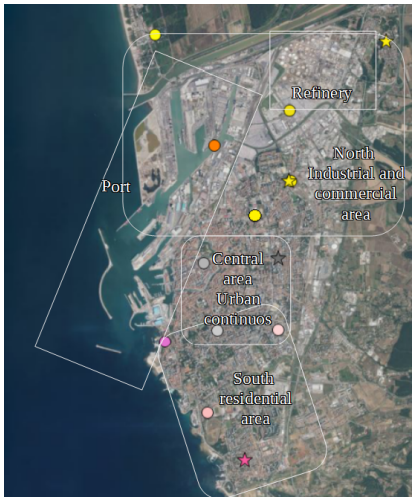

Figure 1. NO_2 monitoring positions. Dots: passive samplers, Stars: air quality monitoring stations- chemiluminescent method. Colors: Yellow- North area background, Pink- south area background, Gray- Traffic, Orange dot: passive sampler + autolaboratory port site

Results show a seasonal dependency with significantly lower summer values in all sites excluding the urban traffic station and the port location.
By attributing to the results, excluding the traffic station, a circular representativeness with a radius of 1 km, the following cartographic distribution is obtained for the measured levels. The level of the traffic station is then attributed to all the streets of the municipality with similar traffic flow (fig 2).

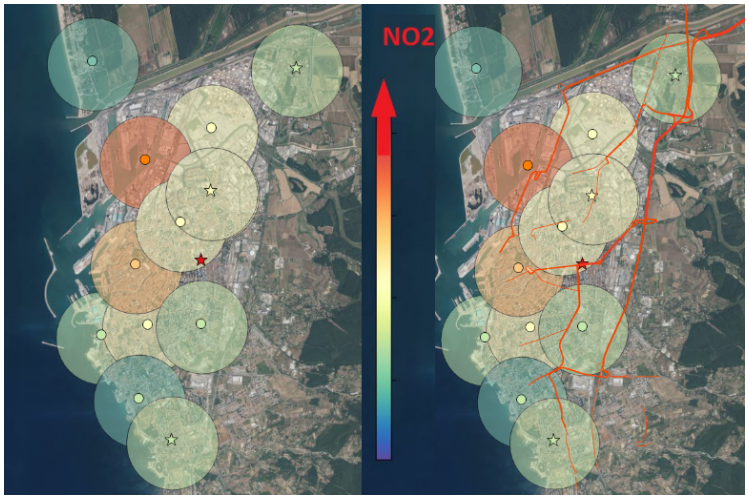

Figure 2. On the left NO_2 background levels on a buffer basis of 1 km radius. On the right the same map with NO_2 traffic levels attributed to the main roads of the town.

The contribution of the urban background, the additional contribution of the port and the contribution of traffic are clearly distinguished. Apart from the traffic site which is attributed only to the road, the highest background levels of NO_2 were measured at the port location and, secondly, in the central urban area. The

urban contribution is more relevant in the center which is more densely populated, and where the NO_2 levels are higher than those of the northern industrial area. The southern area, residential and with low population density, is the area of the city with the lowest NO_2 levels. A strong seasonal dependency, with lower values in summer, is evident for all urban stations. Also in the traffic site values are slightly lower in summer, while the port site as expected doesn't show any seasonal dependency. The port authority, through the Arianet company, has developed an air quality model over the city of Livorno based on the regional emissions inventory IRSE 2010 integrated with detailed input data on ship passages for port emissions estimation. The results of the model output for NO_2 show a similar spatial distribution with respect to data measured (fig 3) with a port and urban area interested by the higher levels. The update of the model with data from the new inventory emissions (IRSE 2017) is currently underway by Arianet. The results of the new output will be compared with the measured data by interpolating the latter with proper geostatistical techniques.

Table 1 monitoring results

Site n.	Middle levels 2021-2022
1	7
2	15
3	16
4	30
5	18
6	16
7	22
8	41
9	13
10	19
11	13
12	11
13	15

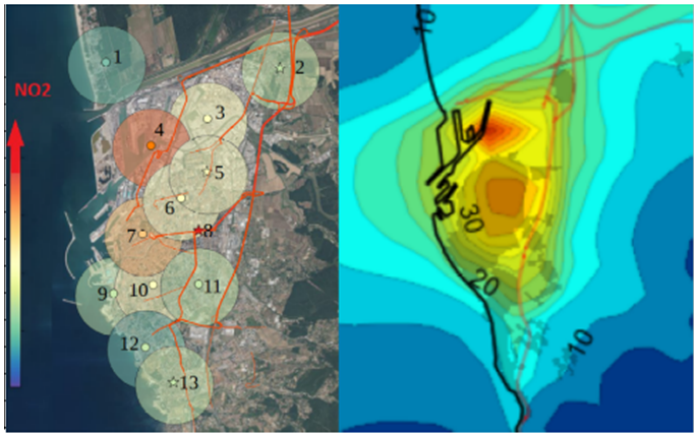

Figure 3. Measured and modelled (Arianet, R2018.17) spatial distribution values of NO_2

Study of various fractions of the particulate matter in the ports of Livorno and Portoferraio

The granulometric distribution of atmospheric dust in the port of Livorno and Portoferraio was performed. As regards the island of Elba (Portoferraio), the mobile laboratory was positioned directly on a boarding pier overlooking the gulf where the port is located (fig 4). Ship traffic consists almost exclusively of ferries and Ro-Ro cargo. The polar plots carried out with gas and particulate data per minute (fig 5) help to identify the sources that have the greatest impact on air quality data in maritime traffic and in traffic relating to vehicles boarding operations.

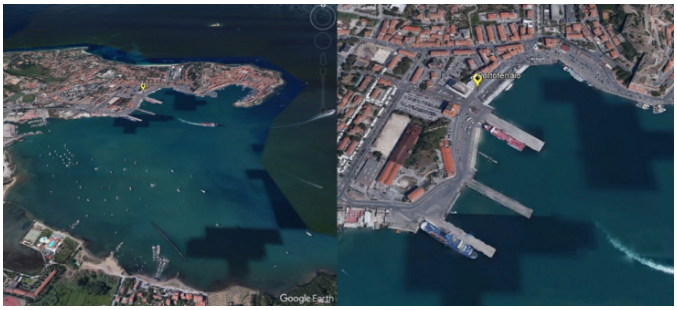

Figure 4. Site of sampling in Portoferraio

For NO_2 and SO_2 the direction with higher mean values points towards the pier and the sea, while for PM there is also a NE/SW direction corresponding to the transit of vehicles to and from the pier. This axis is slightly visible also in NO_2 graph. Finally, for PM it is evident also a NE important source that produces a localized contribution for PM1 and PM2,5 and a more diffuse contribution for PM10.

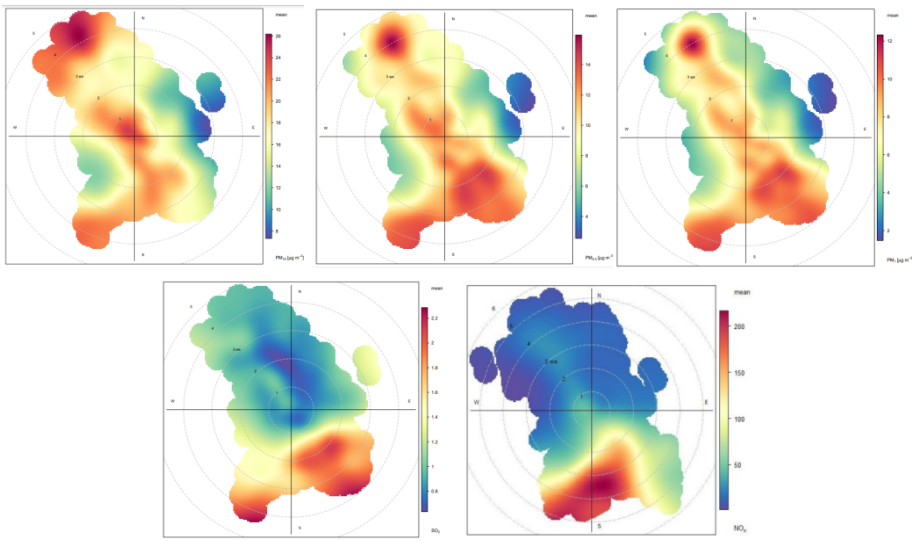

Figure 5. Polarplot PM10, PM2.5, PM1, SO_2, NO_2 Portoferraio July-September 2021

The nanoparticles were monitored for the first time at the port of Livorno. Compared to the values indicated by the WHO (World Health Organization. 2021), the values recorded throughout the first campaign were lower than the reference values for urban areas (fig 6).

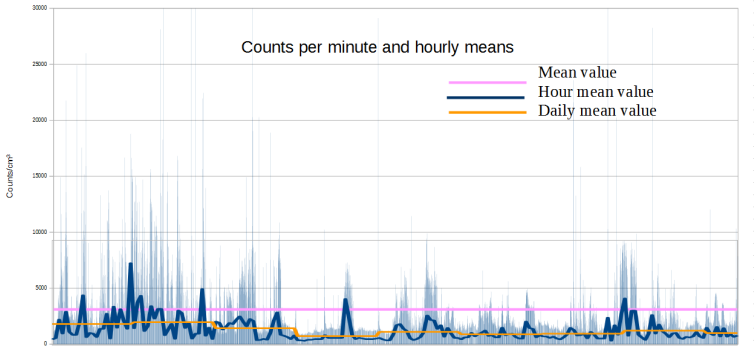

Figure 6. Nanoparticles total counts, Livorno 7-15 October 2021.Comparison with WHO reference values

Combining OPC and Nanoscan data, the percentages of particles in the 3 modes of nucleation, Aitken and accumulation were estimated (fig 7).

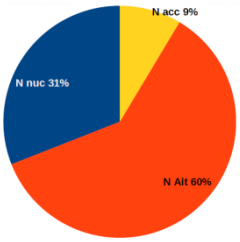

Figure 7. Percent of nucleation, Aitken and accumulation particles

In fig 8 (image provided by the port authority of Livorno together with the data on ships passages) all the docks in the area of the monitoring site (red dot in the picture) are indicated. The graphs in fig 9 show the data per minute of the total counts of the two instruments, OPC and nanoscan. The green background

indicates the periods of transit (Departure, Arrival or Maneuver) of one or more ships from or towards one of the docks of figure 8.

Figure 8. Docks near monitoring site in the industrial area of the port

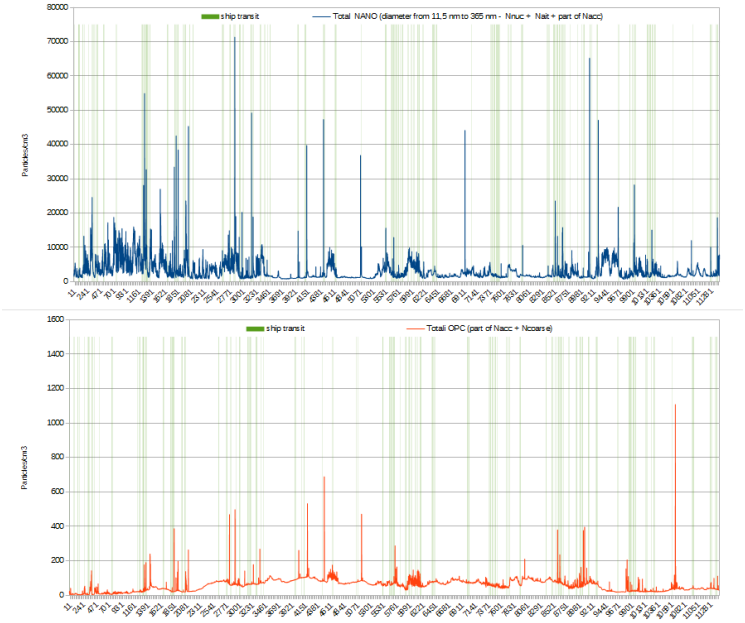

Figure 9. Total counts OPC and Nanoscan and ship transit. Livorno 7-15 October 2021

It can be observed that:

- both the nanoscan and the opc counts almost always show peak values at the passage ships, even if the peaks of coarse particles are often "delayed" than those of finer particles;
- the peaks are frequent but of short duration;
- in some moments there are peaks that do not correspond to ship passages in the area considered.

The granulometric detail at high temporal resolution, together with meteorological analysis, will be the basis for the study of sources of PM in the city focusing in particular on port emission contribution.

REFERENCES

Arianet, Sviluppo ed implementazione di un sistema integrato per la valutazione degli impatti sulla qualità dell'aria, per la gestione degli interventi previsti nel PR del Porto di Livorno, Novembre 2019 https://cloud.ldpgis.it/sites/livornosit/files/ps/all6_12_arianet_sitema_integrato_valutazioni_impatti_aria.pdf

World Health Organization. (2021). WHO global air quality guidelines: particulate matter (PM2.5 and PM10), ozone, nitrogen dioxide, sulfur dioxide and carbon monoxide. World Health Organization. https://apps.who.int/iris/handle/10665/345329

21st International Conference on
Harmonisation within Atmospheric Dispersion Modelling for Regulatory Purposes
27-30 September 2022, Aveiro, Portugal

SPECIFICATION OF ZERO-IMPACT VEHICLE EXHAUST EMISSIONS FROM THE AMBIENT AIR QUALITY PERSPECTIVE AND DEMONSTRATION OF ZERO IMPACT

Ulrich Uhrner[1], Nicola Toenges-Schuller[2], Silvia Jost[1], Raphael Reifeltshammer[1] , Werner Stadlhofer[1] and Stefan Hausberger[1]

[1] Institute of Thermodynamics & Sustainable Propulsion Systems, Graz University of Technology, AT
[2]AVISO GmbH, D

Abstract: In a novel approach, aspects of ambient air quality, atmospheric processes, road traffic and air quality guidelines have been combined to specify emission levels of vehicles that "do not affect" air quality at kerbside. Zero impact air quality targets were specified to 1.2 µg/m³ for NO_2, 0.5 µg/m³ for PM2.5 and 650 #/cm³ for particle number (PN 20-800 nm). Based on these targets zero impact vehicle exhaust emissions were inferred. A Lagrangian particle model was used to simulate the dispersion of NO_x, PM2.5 and particle number concentration (PN) in selected urban case studies for base cases (validation) and scenarios. For PM2.5 and NO_2 the base case validation was straightforward and it was demonstrated that a hypothetical 100% Zero-Impact Vehicles (ZIV) fleet fulfills above mentioned air quality targets at kerbside. For PN, the comparison of simulated versus monitored particles resulted in a large mismatch indicating an abundance of small so-called delayed aerosol particles. A correction of simulated PN vehicle emissions by a factor of ≈4 seems an appropriate correction for two base cases. For solid particles the specified limit of 650 #/cm³ can be already fulfilled with latest Euro-6 emission standards and even more with a hypothetical 100% ZIV fleet if solid particle emissions are of concern. Multiplying the ZIV scenario results by a factor of 4 would result in zero impact. However, this simple correction is difficult to justify for a future scenario.

Key words: Zero-Impact Vehicle Emissions, NO2, PM2.5, Solid and Volatile Particle Number.

INTRODUCTION

The aim of the project was to analyse the requirements of road traffic "zero impact emission levels" from an air quality perspective. First, three possible definitions of "zero impact on air quality" were developed and thereafter analysed in detail:

1) The road traffic contribution to air quality concentration levels is smaller than monitored at clean rural background and untraceable related with state-of-the-art monitoring
2) The road traffic contribution at kerbside locations shall be irrelevant according to air quality directives, i.e. shall be < 3% of air quality limits (3% irrelevance criterion")
3) Concentration at the vehicle's tailpipe < the workplace limit (960 µg/m³ for NO_2)

Table 20 summarises the results for option 1) and 2). Option 3) leads to similar emission targets as option 2) but gives different thresholds for stoichiometric and lean combustion concepts and was thus as therefore not pursued further. In the end, our zero-impact definition was "the road traffic contribution to air pollutants near roads shall be irrelevant compared to the WHO 2006 air quality guidelines, i.e. lower than 3% of these ambitious air quality (AQ) limits". For PN no air quality limit is defined or recommended in any regulations. Therefore, the ZIV PN 20-800 nm size range criteria of 650 #/cm³ was derived based on conclusion by analogy using the NO_2 zero impact target related to the NO_2 clean background target (1.2 µg/m³ : 3.6 µg/m³) and PN 20-800 nm of 2000 #cm^{-3} monitored at clean background sites.

Table 20. Comparison of the zero impact targets for the maximum traffic contribution to the ambient air concentrations near roads

Station	NO2 (µg/m³)	PM10 (m)	PM2.5 (µg/m³)	PN 20-800 (#/cm³)	eBC (µg/m³)
Clean background ≥ 900m a.s.l.	3.6	8.4	6.5	2000	0.3
3-% criterion for WHO 2005 AQ limits	1.2	0.6	0.3	650	0.1

Current contributions of road transport exhaust gas emissions to the air quality near roads in Europe were analysed to identify the relation between road vehicles emissions and pollutant concentrations measured next to the road. From the worst-case situation, identified at "Stuttgart Neckartor" in the year 2016, we assessed the necessary traffic emission reduction rates to meet the zero impact pollutant concentrations next to the road. With these reduction rates and with the corresponding fleet average emissions, the maximum emissions per kilometre for "Zero Impact Vehicles, (ZIV)" for NO_x and PM were calculated as a first assessment. For PN, source specific i.e. traffic related contributions to air quality at kerbside in Europe is rarely available. Therefore, the PM target was used and average monitored particulate numbers per emission mass were used to assess PN targets. The resulting ZIV emission targets based on the driving situation at Stuttgart, Neckartor in 2016 are shown in **Table 21**.

Table 21. Emission targets for the ZIV fleet in traffic situation according to Stuttgart, Neckartor in 2016 for the 3% irrelevance criterion.

Vehicle type	unit (activity)	EF NOx (mg/unit)	EF PM2.5 (mg/unit)	EF PN20-800 (10^{11} #/unit)
PC	km	6.7	0.4	1.2
LCV	km	7.9	0.5	1.5
HDV	kWh	28.1	1.6	4.8

DISPERSION MODELLING APPROACH

The worst-case monitoring location may not coincide with the location of poorest air quality and uncertainties and assumptions in the data analysis may lead to an underestimation of ZIV emission factors. Therefore, a detailed validation of the EFs presented in **Table 21** was performed. A sensitivity analysis for different emission and traffic conditions, air quality simulations with a Box model (chemistry/aerosols) and a Lagrangian dispersion model for different hot spots and for entire municipal areas were performed. Subsequently, some results of the dispersion modelling efforts and related challenges with focus on PN will be presented here. In addition, the air quality impact of a 100 % Euro-6d/VI fleet was evaluated as well.

The GRAMM/GRAL modelling system (Uhrner et al., 2014, Öttl 2015, Öttl 2019) was used to model detailed flow and air pollutant dispersion. Highly resolved source specific emission data have been processed for the simulations, the main set-up features are shown in **Table 22**. The flow around buildings impacting upon dispersion was accounted, except in the Vienna study. After validation of the base cases, the traffic exhaust related NO_2, PM and PN concentrations was assessed for the base case, Euro-6 scenario and ZIV emission scenario (see **Table 21**). NO_x to NO_2 conversion was computed using a simple Romberg type empirical conversion formula (Romberg et al., 1996) for the Stuttgart, Vienna and Augsburg case studies. For the Graz study a pseudo-steady state approximation approach (Seinfeld and Pandis, 1998) was used.

Table 22. Main set-up features of the the case studies, $\Delta x,y$ is the counting grid resolution

Case study	Domain size	$\Delta x,y$	Air pollutant focus	# Monitoring
Stuttgart-Neckartor	1.4 km x 1.7 km	2 m	NO_x/NO_2	2 AQ stations hotspot & bg
Vienna	30 km x 24 km	10 m	NO_x/NO_2, PM2.5	17 AQ stations
Augsburg CAZ	4 km x 6.2 km	4 m	NO_x/NO_2, PM10, PN	4 AQ stations, 2 SMPS
Graz Plüddemanngasse	1.1 km x 0.8 km	2 m	NO_x/NO_2, PN	NO_x, PN4nm, PN23nm, CO_2

In Augsburg, the focus was laid on the central activity zone (CAZ). There, SMPS measurements from the GUAN network (Sun et al., 2019) were used to monitor the urban background; SMPS measurements were undertaken by TUG in the city centre at Königsplatz (KP) next to a busy road from 16.10.2020 till 12.01.2021. PN deposition was accounted, however the impact was negligible. Coagulation was neglected as a sink process. In Graz, NO, NO_2, PN and CO_2 were measured at 1 m, 3 m and 5 m distance at a busy road. The monitoring interval was 10 minutes each location and the measurements were undertaken over 7 hours, on 20.10.2021. PN measurements were switched all 10 minutes to distinguish between total particle number (TPN) and solid particle number (SPN). However, the SPN measurement results are highly questionable and were not used. Detailed accompanying traffic monitoring was performed as well. Emissions were computed using the software PHEM (Passenger car and Heavy-duty Emission Model) from TU Graz. Meteorological data for the flow field model forcing and air quality data were only available at

30-min resolution, therefore the accompanying NO_x and PN simulations were performed as 30-min means around the Plüddemanngasse street. NO_x urban background measurements were used from the air quality station "Graz-Ost" as well as O_3 and radiation measurements from Graz-Nord, all operated by the provincial government of Styria. Due to the sampling strategy, available NO_x and CO_2 is a factor of two higher than PN. The CO_2 measurements were performed in order to monitor dilution for box model studies. Here, these measurements were used together with the NO_x measurements to evaluate the plausibility of the (10 min) PN measurements. Therefore, at first, NO_x simulations were performed and compared with 10 minutes NO_x monitored values. Thereafter, PN simulations were performed and compared with selected PN monitoring. The GRAL model was run in transient mode.

RESULTS DISPERSION SIMULATIONS - DEMONSTRATION ZERO IMPACT

Augsburg CAZ Case Study

The focus in this paper will be laid on Augsburg and Graz NOx and PN studies. In **Figure 59** the simulated annual mean (AM) NO_2 and validation of the base case is shown. High NO_2 concentrations were computed near the monitoing station Karlsstraße (KS) located in a street canyon and near the main arterial road B17 (ADTV 84 000 vehicles), located in the SW sector of **Figure 59**. In **Figure 60** the road traffic related NO_2 burden is shown for the base case (left) and the ZIV scenario (right). In the left figure, concentration values larger than the ZIV target of 1.2 µg/m³ for the AM NO_2 prevail, whereas with the ZIV scenario (right) the ZIV target of 1.2 µg/m³ is tightly fulfilled at kerbside.

In **Figure 61** total simulated mean PN concentrations are shown for base case (left). There, at "FH" monitored PN concentrations were used as urban background. The simulated increment is dominated by residential heating emissions from solid fuels. Simulated PN concentrations next to roads appear unrealistically low. Multiplying traffic related simulated exhaust particles by a factor of 3.6 yields a better match with the two monitoring stations and the resulting PN concentrations look more realistic, see **Figure 61** on the right. The target value of 650 #cm^{-3} is fulfilled at kerbside (**Figure 62**).

Figure 59. Augsburg CAZ simulated AM NO_2 2020/21, location of AQ stations and validation base case

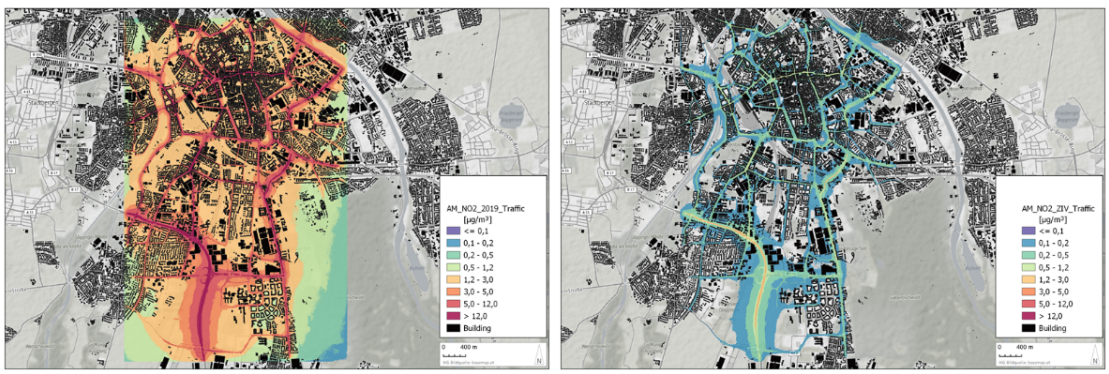

Figure 60. Augsburg CAZ simulated traffic related AM NO_2 for the base case (left) and the ZIV scenario (right)

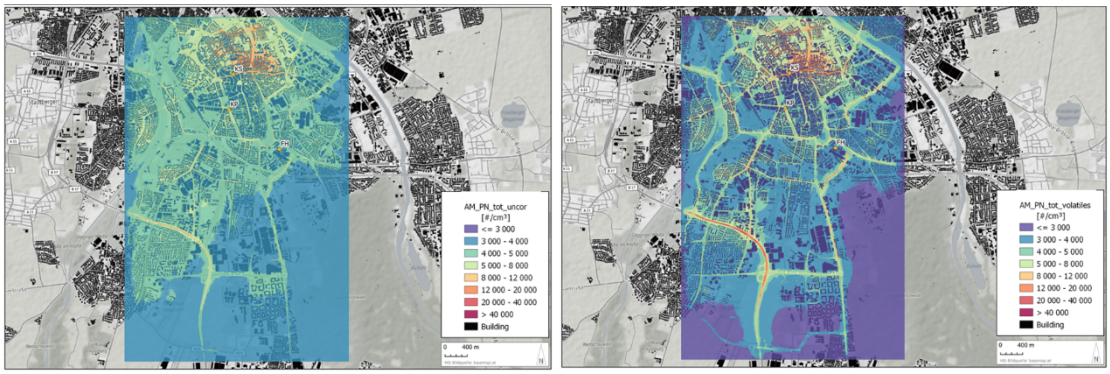

Figure 61. Augsburg CAZ simulated total mean PN (16.10.2020 till 12.01.2021) for the base case without correction for volatiles (left) and with correction for volatiles (right)

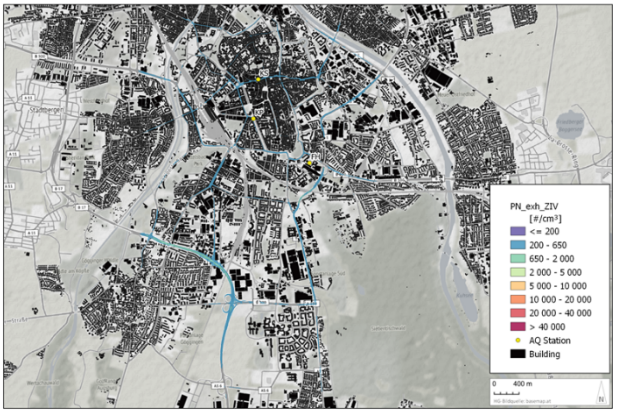

Figure 62. Augsburg CAZ simulated traffic related PN for the ZIV scenario

Graz Plüddemanngasse Case Study

In **Figure 63** simulated 30-min mean NO_x concentrations are compared versus monitored 10-min NO_x concentrations at 1 m, 3 m and 5 m distance from the road. At 1 m and 3 m a good relation is discernable. In **Figure 64** simulated 30-min mean traffic related solid PN > 23 nm (SPN23) is compared versus monitored 10 min mean total PN concentration (TPN23). The simulated spatial distribution is shown in **Figure 65**. The scatter plot of **Figure 64** indicates a good relation between these two different measures. The slope of 3.89 indicates that kerbside TPN may be composed of a large fraction of delayed aerosols mostlikely due to nucleating and rapidly growing (condensing) VOCs. Moreover, the intercept of approximately 4000 #cm^{-3} indicates the urban background and contributions from atmospheric new particle formation.

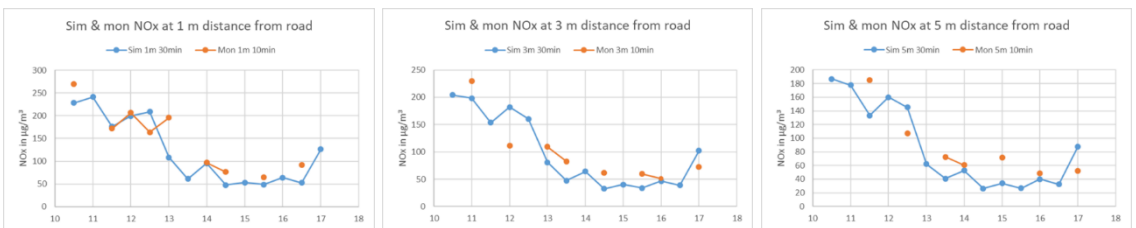

Figure 63. Base case, Graz Plüddemanngasse, simulated 30-min NOx versus monitored 10-min NOx at 1 m, 3 m and 5 m distance to road (x-axis show the hours of the day)

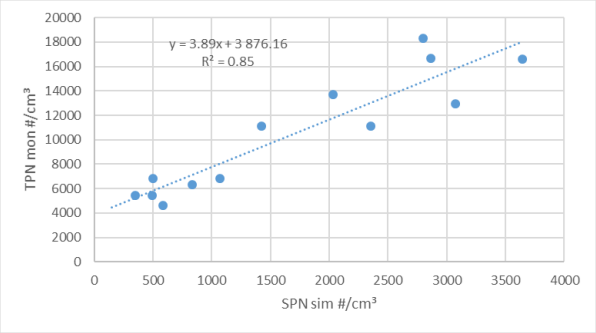

Figure 64. Simulated base case PN23 (30 min) vs monitored PN23 (10 min), questionable measurements were removed

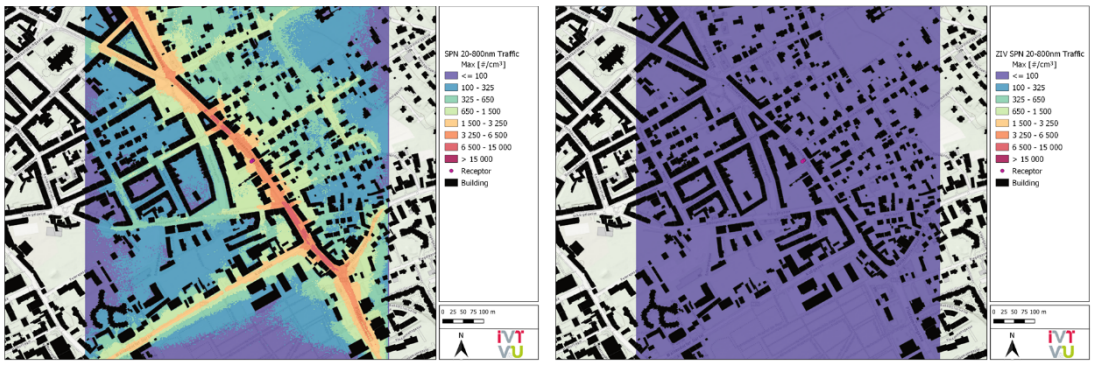

Figure 65. Graz Plüddemanngasse simulated max traffic related SPN23 base case (left), ZIV scenario (right)

CONCLUSIONS

Limits for future zero-impact vehicle exhaust emissions were analysed from the air quality perspective. Technically, to meet the 1.2 µg/m³ for NO_2 at kerbside at hot spots or under extreme driving conditions seems to be most demanding. PM and PN limits for solid particles can be already fulfilled with latest Euro-6 exhaust technologies, however the use cases indicated a dominating role of delayed aerosol most likely/probably of volatile origin. Accounting for the impact of volatiles in future scenarios bears large uncertainties. However, the commonly applied NO-to-NO_2 conversions as well.

REFERENCES

Öttl, D., 2019: Documentation of the prognostic mesoscale model GRAMM (Graz Mesoscale Model) Vs. 17.1', Amt d. Stmk. Landesregierung, Department 15, Air Quality Control.

Öttl, D. 2015: Evaluation of the revised Lagrangian particle model GRAL against wind-tunnel and field experiments in the presence of obstacles, Boundary-Layer Meteorol., No 155, pp.271-287.

Romberg, E., R. Bösinger, A. Lohmeyer, R. Runke, E. Röth, 1996: NO-NO2 - Um-wandlungsmodell für die Anwendung bei Immissionsprognosen für Kfz-Abgase. Gefahr-stoffe - Reinhaltung der Luft 56 Nr. 6, S. 215-218, (1996)

Seinfeld, J.H. and S.N. Pandis, 1998: „ From Air Pollution to Climate Change ".

Sun J., W. Birmili, M. Herrmann, T. Tuch, K. Weinhold, G. Spindler, et al., 2019: Variability of black carbon mass concentrations, sub-micrometer particle number concentrations and size distributions: results of the German Ultrafine Aerosol Network ranging from city street to High Alpine locations, Atmos. Environ. 202, 2019.

Uhrner, U., B.C. Lackner, R. Reifeltshammer, M. Steiner, R. Forkel and P.J. Sturm, 2014: Inter-Regional Air Quality Assessment, - Bridging the Gap between Regional and Kerbside PM Pollution, Results of the PMinter Project, VKM-THD Mitteilungen, Volume 98, Verlag der Technischen Universität Graz, ISBN: 978-3-85125-364-1.

WHO: Air Quality Guidelines; Global Update 2004; ISBN 92 890 2192 6; WHO, 2006

21st International Conference on Harmonisation within Atmospheric Dispersion Modelling for Regulatory Purposes
27-30 September 2022, Aveiro, Portugal

DETECTION OF LOW LEVEL CONCENTRATIONS OF HAZARDOUS MATERIALS IN THE AIR USING SEQUENTIAL MULTIVARIATE DETECTION METHODS

Victor Watson[1,2], François Septier[1], Patrick Armand[2] and Christophe Duchenne[2]

[1]Univ Bretagne Sud, CNRS UMR 6205, LMBA, F-56000 Vannes, France
[2]CEA, DAM, DIF, F-91297 Arpajon, France

Abstract: Detecting weak signals in a noisy environment is a very important matter in many application cases relating to atmospheric dispersion or radiation exposure. Let us mention the detection of abnormal chemical concentrations in the air (due for instance to a leakage in a pipe network) or the detection of abnormal levels of radioactivity or concentrations of radionuclides in the air. When the environment is noisy, it is very difficult to monitor a variation in the measurement of a quantity (concentration, radiation…) corresponding to a threat before the potential hazard materialises. However, by accumulating the data over time and space using several sensors, it is possible to say if what is measured is likely to be noise or not. Being able to detect small variations early may be a way to react before the hazard occurs. Here we propose a new method especially designed to detect weak events characterised by surreptitious releases into the air transported and dispersed by the wind over a field equipped with sensors. We use the CUSUM (Cumulative Sum) as a base for our method and we extend it to multivariate cases and asynchronous monitoring. The extension to multivariate cases is not straightforward. Indeed, if some sensors only measure noise, they will decrease the overall signal to noise ratio and thus lower the probability of detection. We propose a way to prevent this by selecting the sensors that are most likely monitoring the signal. The non-synchronicity of the monitoring between the sensors using online statistical detection methods has never been addressed before our own work. The main assumption in the literature is that when a sensor starts monitoring an event, it will continue until detection. However, for releases spreading in the field, it is very possible that a sensor stops monitoring before some others do. Our method tackles the non-synchronicity issue while keeping the required computational power low enough for online detection. This method has been validated using academic data. Now, it will be tested in a realistic twin experiment consisting in the fictitious release of a low amount of radionuclides in an urban district where sensors are supposedly set up. Both the dispersion in the complex built-up environment and the radionuclides variously affecting the sensors make this configuration of particular interest as will be described in the paper.

Key words: *Detection, CUSUM, multivariate, Low-SNR.*

INTRODUCTION

Detection of weak signals in noisy data streams is a challenge in our societies' current effort to prevent pollution risks of any type. The releases of hazardous compound into the air can have dramatic effects if an appropriate response comes too late. In this work, we present a solution to detect weak signals in noisy time series. Based on the Cumulative Sum (CUSUM) technique (Page, 1954) and its adaptation to multivariate cases (Mei et al. 2010) and (Watson et al. 2022), we propose to use the developed test statistics on a twin experimental release of a hazardous compound in an urban area. In the second section, we describe the principle of sequential detection, the CUSUM and its extension to multivariate cases. More precisely, we discuss on how we can adapt the method to deal with space-sparsity (only some sensors are monitoring the signal) and time-sparsity (sensors do not monitor the signal at the same time). In the third section, we present the experimental release that generated the data we use to test the detection techniques in the fourth section.

SEQUENTIAL DETECTION

In order to detect signal in a low signal to noise ratio case, it is sometimes impossible to tell the signal contribution based on one measurement. Sequential detection gathers the information about the signal contribution along time and make it possible to be detected. The CUSUM is a technique where a likelihood

ratio is recursively computed with each measurement so that when a change occurs in the noise distribution, this likelihood ratio rises sample after sample and reaches a threshold that cannot be reached (ideally) if the measurements only contain noise.

Let us consider a sensor which monitors a data stream x only withholding noise (following a distribution $f_0(x_k, \theta_0)$) until the change-point $k = \nu$ and then, after this change point, a signal added to the noise so the distribution becomes $f_1(x_k, \theta_1)$, then the likelihood ratio to determine if a change has likely occurred at time ν is:

$$\Lambda_\nu^n = \prod_{k=\nu+1}^{n} \frac{f_1(x_k,\theta_1)}{f_0(x_k,\theta_0)} \quad (1)$$

Because ν is unknown, it is necessary to generalize the likelihood ratio:

$$V_n = \max_{0\leq\nu<n} (\Lambda_\nu^n) = \max_{0\leq\nu<n} \prod_{k=\nu+1}^{n} L_k \quad (2)$$

Testing V_n with an adapted threshold allows determining whether there is a signal in presence. It is possible to compute the generalized likelihood ratio sequentially (Tartakovsky et al., 2014):

$$V_n = max(1, V_{n-1})L_n, n \geqslant 1, V_0 = 1 \quad (3)$$

Univariate detection

The CUSUM is obtained by using the log-likelihood instead of the likelihood in (3). This eases the computation especially for distributions from the exponential family.

$$W_n = Log(V_n) = max(0, W_{n-1}) + log(L_n), n \geqslant 1, W_0 = 0 \quad (4)$$

The CUSUM can be used to detect any kind of change in the distribution of a data-stream but it is often a change in the mean or in the standard deviation that one seeks to find. In our application case, a change in the concentration of a radionuclide in the air is consistent with an increase in the monitored mean value. **Figure 1** shows an example of how the CUSUM works on univariate data.

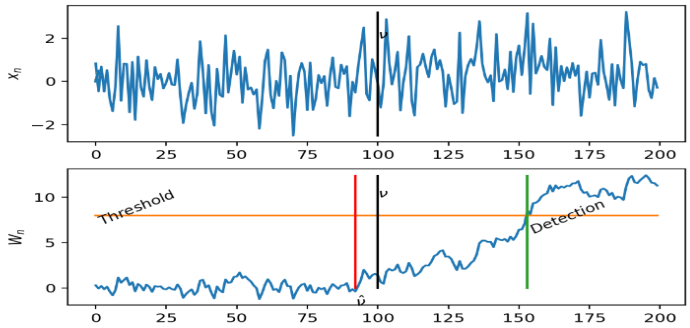

Figure 1. Detection with CUSUM of a change in the signal mean with a low signal to noise ratio (SNR). The change in the mean occurs at the time marked ν. On top, the evolution of the monitored variable x does not allow to detect directly the change in the mean. The CUSUM variable however changes its behaviour as the change-point has been passed and increases until it reaches the detection threshold. It is also possible to estimate the change-point $\hat{\nu}$ from the last time W_n crosses 0.

Multivariate detection

In the application we consider, many sensors are monitoring the area. The easiest way to associate the sensors is to construct the global test variable as the sum of all the local test variables. This technique is called SumCUSUM (Mei et al. 2010). Because the signal can be spatially sparse (only a few of the sensors

monitor the signal), Mei et al. (2010) propose a censoring technique based on a rough knowledge of the signal energy establishing local thresholds. This would only sum the local variables where a signal is most likely present and increases the performances of the methods. Watson et al. (2022) propose a relative threshold technique so that the prior knowledge of the signal energy is no longer necessary. The global variable of this censored-SumCUSUM is defined as:

$$T_{cSC}(n) = \frac{1}{\sum_{l=1}^{L} 1_{W_{n,l} \geqslant c_n}} \sum_{l=1}^{L} W_{n,l} \geqslant c_n, \tag{5}$$

With:

$$c_n = \alpha \max_{l \in [1,\dots,L]} \left(W_{n,l}\right) \tag{6}$$

The case of a time sparse problem has been considered in Watson et al (2022). Indeed, in the case of an event passing over a field of sensors, it is possible that the monitoring between the sensors is not synchronized. Bringing together these time limited exposures is possible while keeping online computation using the test variable presented hereafter:

$$T_{TESC}(n) = \frac{1}{L} \sum_{l=1}^{L} \max_{[\nu_l, N_l]} \sum_{k=\nu_l}^{N_l \leq n} log \frac{f_{1,l}(X_{k,l}, \theta_{1,l})}{f_{0,l}(X_{k,l}, \theta_{0,l})} \tag{7}$$

Watson et al. (2022) show that it is equivalent to rewrite local variables such that G_n acts as the memory of the last highest value of W_n:

$$G_n = max(G_{n-1}, W_n) = \max_{0<k\leqslant n} W_k \tag{8}$$

Thus, it is possible to simplify (7) so that:

$$T_{TESC}(n) = \frac{1}{L} \sum_{l=1}^{L} G_{n,l} \tag{9}$$

These techniques can be combined in order to be used in both time and space-sparse problems:

$$T_{CTESC}(n) = \frac{1}{\sum_{l=1}^{L} 1_{G_{n,l} \geqslant c_n}} \sum_{l=1}^{L} G_{n,l} \geqslant c_n, \tag{10}$$

TWIN EXPERIMENT OF AN INSIDIOUS RELEASE

Having available data is of considerable importance if we want to test our method of finding signals with low signal-to-noise ratios. In our application, these data are the volumetric concentrations on sensors after the transport and dispersion of a release from a point source. One can naturally think of two types of data. The first type would correspond to the real situation of a release whose source goes unnoticed and which leads to sparse detections in space and time. Although this situation certainly exists, we do not have such data. The second type could be data acquired under full-scale experimental conditions or in a wind tunnel. Nevertheless, these data would be complicated and expensive to obtain because of the need to find an available site, devices to release the tracer and measure the signals, the workforce, etc. In the absence of a real dispersion situation available, we had the idea of considering a twin experiment, i.e. to generate synthetic signals from CFD computations.

The Parallel Micro-SWIFT-SPRAY (PMSS) modelling system has been used to carry out the simulations. It is the parallel version of Micro-SWIFT-SPRAY (MSS) (Tinarelli et al. 2013) which was developed to provide a CFD solution of the flow and dispersion in the atmospheric environment in a limited amount of time. MSS is composed of the high-resolution local scale versions of the SWIFT and SPRAY models:

- SWIFT is a 3D diagnostic mass-consistent model using a terrain-following coordinate. Large scale meteorological data, local meteorological measurements, and analytical results in building-modified flow areas are interpolated and adjusted to generate 3D wind fields. Other meteorological data such as temperature or humidity are also interpolated. Eventually, the turbulent flow parameters are computed by SWIFT to be used by SPRAY.
- SPRAY is a Lagrangian particle dispersion model (LPDM) able to take into account the presence of obstacles. The dispersion of the release is simulated by following the trajectories of a large number of fictitious particles. Trajectories are obtained by integrating in time the particle velocity, which is the sum of a transport component defined by the local averaged wind generally provided by SWIFT, and a stochastic component, representing the dispersion due to atmospheric turbulence.

Both SWIFT and SPRAY can handle complex terrains and changing meteorological conditions, as well as specific release features, such as heavy gases. More recently, SWIFT and SPRAY were parallelized across time, space, and numerical particles, resulting in the PMSS system (Oldrini et al. 2017). The parallelism was shown to be very efficient, both on a multi-core laptop and on clusters of several hundreds or thousands of cores in the case of a high-performance computing centre (Oldrini et al. 2019) (Armand et al. 2021). PMSS was systematically validated over numerous experimental wind tunnel and field campaigns for both short and long releases (Trini Castelli et al. 2018). In all configurations, the PMSS results comply with the statistical acceptance criteria defined by Hanna and Chang (2012) used for validating dispersion models in built-up environments.

In the twin experiment, we used meteorological data produced by the AROME model of Météo France at a resolution of 0.025° (around 2.5 km at mid-latitude). Meso-scale weather predictions were downscaled with the PMSS modelling system in order to zoom in the central urban district south of Republic Square, in Paris (France). More precisely, the AROME meteorological profiles were extracted at the four closest points to PMSS simulation domain to nudge the flow simulations, also explicitly accounting for the whole buildings of the urban district. The 3D urban domain has dimensions of 1,100 m x 1,100 m x 1,600 m and 551 x 551 x 34 grid nodes. The horizontal mesh size is 2 m. The vertical mesh size is 2 m up to 22 m and becomes looser going up to the top of the domain. **Figure 2** shows the horizontal cross-section of the urban domain near the ground and the buildings. During the time sequence of the twin experiment, meteorological conditions varied, notably the wind speed and wind direction as indicated in **Table 1**, The fictitious source is denoted by the red dot in **Figure 2**. It was supposed to release an amount of 10^9 Bq of a radioactive tracer (gas or fine particles) at a height of 2 m for 20 minutes. Virtual sensors were also supposed to be set up at the same height as the source in the urban district. They are shown as blue dots in **Figure 2**. Dispersion simulations were carried out for 45 minutes. The results of these simulations are volumetric concentrations averaged over 1 minute and output each minute. They are used to test the detection techniques discussed in this paper.

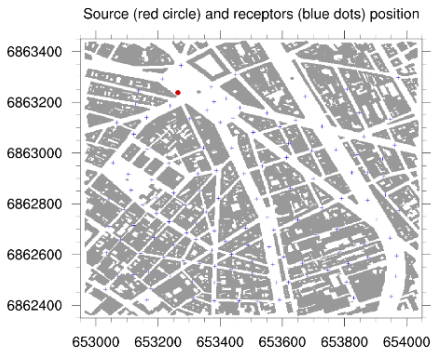

Figure 2. Horizontal cross section
of the simulation domain showing the buildings
of the urban district south of the Republic Square
in Paris (France) and the positons of the fictitious source (red dot) and virtual sensors (blue dots).

Table 1. Evolution of the wind speed and wind direction at 10 m (AROME results not considering the effect of the buildings) during the time sequence considered for the PMSS simulation (t_0 designates the instant of the fictitious release).

Time	Wind speed	Wind direction
t_0	2.6	287
t_0 + 9 min	0.95	327
t_0 + 18 min	1.05	5
t_0 + 27 min	1.8	17
t_0 + 36 min	1.0	28
t_0 + 45 min	1.9	25

SEQUENTIAL DETECTION ON EXPERIMENTAL RELEASE

In order to test the different detection techniques, we will consider a system with 25 sensors. Among these 25 sensors the main proportion only holds noise where 0 to 10 data streams hold a signal. These signals have been randomly picked out of 12 different signals extracted from the twin experiment. In the following results, all the methods are tuned to have a probability of false alarm of 1 to 1,000 during the experiment. The noise on each data-stream is Gaussian and follows the rule $N(0,1)$. Every detection rate value is evaluated with 10,000 runs with random noise generation and random sensors selection for each run.

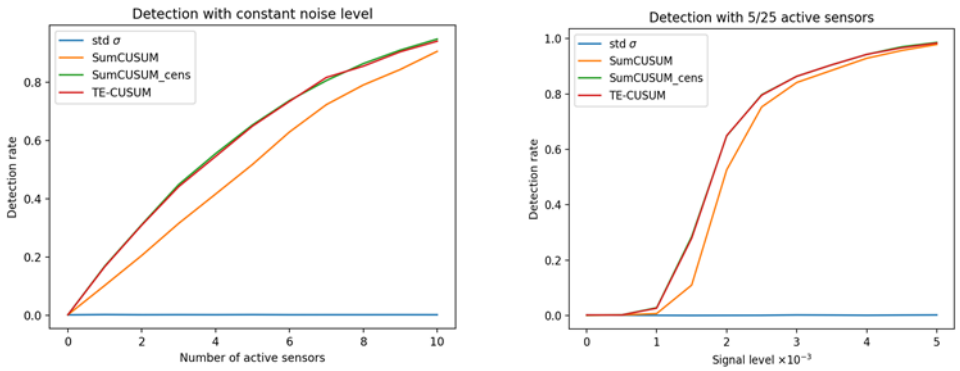

Figure 3. Detection rate depending on the number of affected sensors (left) and depending on the signal to noise ratio (right). The lower line in blue shows the results using a simple threshold solution on the data, the orange one the detection rate of the standard SumCUSUM, the green one the results taking into account the space sparsity, and the red one the results when both time and space sparsity are considered.

Figure 3 (left) shows the detection rate of each method (except for the standard threshold method) with a constant signal to noise ratio and a variable proportion of affected sensors. The probability of detecting a signal computed empirically over the 10,000 runs increases with the number of sensors monitoring a signal. It is also notable that the consideration of space sparsity improves the results over the simple SumCUSUM. Of course, this improvement reduces if the number of sensors affected by the signal is close to the total number of sensors, but such a case is unlikely in the considered application. The consideration of both space and time sparsity gives the same results than considering only space sparsity because in this experiment, there is a lot of overlapping in the exposed sensors.

Figure 3 (right) shows the detection rate of each method (except for the standard threshold method) with a constant number of impacted sensors and a variable signal to noise ratio. When the signal gain decreases, the consideration of the space sparsity shows a lesser degradation of the detection rate than the simple SumCUSUM. Again, the addition of the time sparse consideration changes quite nothing because of the data structure.

When all signals are synchronized, the test variable considering time sparsity does not decrease the detection rate. This indicates that adding the sensitivity to time differential events does not conflict with the censoring technique. An experiment where sensors monitoring is not overlapping will be necessary to show this last technique interest. This could be the case for a more time-localized event traveling quicker in space.

CONCLUSION

In this work, we have shown the interest of using sequential detection technique to quickly identify the variation of a signal characterized by a low signal-to-noise ratio. This signal could be the concentration of a hazardous compound transported and dispersed into the air. Because these techniques can detect weak signals, they can be used as powerful prevention tools. We presented various techniques considering sparsity in space when not all the sensors monitor the signal but also sparsity in time when the sensors do not monitor the signal at the same time. The results on the experimental data presented here show how powerful these techniques are even though time sparsity was not present in the experiment we used. This time sparse technique has shown good results on simple synthetic data in Watson et al. (2022). It will need a different experimental data set to be proven worthy. Besides using these techniques on more complex data set, our future work will show its efficiency on different noise distributions such as Poisson, which is more realistic for some of the detectors used in the targeted applications.

REFERENCES

Armand, P., O. Oldrini, C. Duchenne and S. Perdriel, 2021: Topical 3D modelling and simulation of air dispersion hazards as a new paradigm to support emergency preparedness and response, *Environmental Modelling & Software*, 143, 105129.

Hanna, S. and J. Chang, 2012: Acceptance criteria for urban dispersion model evaluation. *Meteorological Atmospheric Physics*, 116, 133–146.

Mei, Y., 2010: Efficient scalable schemes for monitoring a large number of data streams. *Biometrika*, 97 (2), 419–433.

Oldrini, O., P. Armand, C. Duchenne, C. Olry, J. Moussafir and G. Tinarelli, 2017: Description and preliminary validation of the PMSS fast response parallel atmospheric flow and dispersion solver in complex built-up areas, *Environmental Fluid Mechanics*, 17 (5), 997–1014.

Oldrini, O., P. Armand, C. Duchenne and S. Perdriel, 2019: Parallelization performances of PMSS flow and dispersion modelling system over a huge urban area, *Atmosphere*, 10 (7), 404.

Page, E.S., 1954: Continuous inspection schemes. *Biometrika*, 41 (1-2), 100–115.

Tinarelli, G., L. Mortarini, S. Trini Castelli, G. Carlino, J. Moussafir, C. Olry, P. Armand and D. Anfossi, 2013: Description and preliminary validation of the PMSS fast response parallel atmospheric flow and dispersion solver in complex built-up areas. American Geophysical Union (AGU) 200 (A), 311–327.

Skamarock, W.C. et al., 2008: A description of the Advanced Research WRF Version 3. No. NCAR/TN-475+STR, University Corporation for Atmospheric Research, Boulder, CO, USA, p. 113.

Tartakovsky, A., I. Nikiforov and M. Basseville, 2014: Sequential analysis: Hypothesis testing and change point detection, p. 111.

Trini Castelli, S., P. Armand, G. Tinarelli, C. Duchenne and M. Nibart, 2018: Validation of a Lagrangian particle dispersion model with wind tunnel and field experiments in urban environment, *Atmospheric environment*, 193, 273–289.

Watson, V., F. Septier, P. Armand and C. Duchenne, 2022: Sequential detection of a temporary change in multivariate time series. *Digital Signal Processing*, 127, 103545.

EU MARITIME TRANSPORT AND AIR QUALITY: IMPACTS IN CURRENT AND FUTURE CLIMATE CHANGE SCENARIOS

Michael Russo, David Carvalho, Alexandra Monteiro, Jalkanen Jukka-Pekka

SHORT ABSTRACT

Abstract title: EU maritime transport and air quality: impacts in current and future climate change scenarios

Name and Affiliation of the First Author:

Michael Russo, Department of Environment and Planning, University of Aveiro, Portugal

Email of first author: michaelarusso@ua.pt

Names and Affiliations of the Co-authors:

David Carvalho, Department of Physics, University of Aveiro, Portugal;

Alexandra Monteiro, Department of Environment and Planning, University of Aveiro, Portugal;

Jalkanen Jukka-Pekka, Finnish Meteorological Institute, Helsinki, Finland.

Abstract text *(maximum 350 words.)*

Ship engine combustion emits several atmospheric pollutants, such as Particulate Matter (PM), SOx, and NOx, which can have adverse health effects and be significant contributors to decreased air quality. Due to the distribution of maritime transport activity routes in the EU, a large portion of the population is exposed to shipping emissions throughout the European domain. Therefore, in light of the European Commission long-term objective of "zero-waste, zero-emission" for the maritime transport industry, the focus of this study is to quantify the impact of shipping emissions for the entire European domain using the WRF-CHIMERE modelling system. Both a present scenario and two climate change scenarios will be assessed and compared to study the current impact of shipping emissions and how relevant they will be in climate change scenarios. To obtain current and future contributions of maritime transport to total pollutant concentrations, simulations were divided into a present and two climate change scenarios for 2050 (RCP 4.5 and RCP 8.5). For the present scenario, simulations were made with and without shipping emissions, creating our base year for comparison. For the future scenarios, 4 simulations were run, two of which only include the effect of climate change, while the other pair include climate change and shipping emission projections. The results for the base year indicate a 20-30% (SOx), 15% (NOx), 5% (PM2.5) and 3% (O3) contribution of shipping emissions to total pollutant concentrations up to 10-20 km inland, with lower

values in the Baltic Sea due to fuel restrictions. Only accounting for the effects of climate change yields a noticeable difference in O3 and PM. Due to the increased temperature, O3 concentrations are slightly higher in some regions, while PM2.5 concentrations also increase because of the decreased precipitation. In terms of air quality with shipping projections, a slight

decrease of pollutant concentrations is expected, resulting from the fuel changes and overall decreased shipping emissions.

21st International Conference on Harmonisation within Atmospheric Dispersion Modelling for Regulatory Purposes
27-30 September 2022, Aveiro, Portugal

IMPLEMENTATION OF A DECISION SUPPORT SYSTEM FOR NUCLEAR EMERGENCIES

Cyrill von Arx

SHORT ABSTRACT

Abstract title: Implementation of a decision support system for nuclear emergencies

Name and Affiliation of the First Author: Cyrill von Arx, Swiss Federal Nuclear Safety Inspectorate ENSI, Industriestrasse 19, CH-5201 Brugg, Switzerland

Email of first author: cyrill.vonarx@ensi.ch

Names and Affiliations of the Co-authors: -

Preferred way of presentation (oral or poster): oral

Preferred topic: 2 "Environmental impact assessment: Air pollution management and decision support systems."

Abstract text *(maximum 350 words.)*

We present the development and implementation of a decision support system (DSS) for ENSI's emergency response organisation (ERO) to be used for emergencies in nuclear installations in Switzerland. In a first step detailed here, a tool for the assessment of reactor safety and radiation protection was created; in a second step, a DSS for ENSI's entire ERO shall be established.

Objectives

In case of an emergency, an efficient synthesis of available information is crucial for ENSI's ERO to ensure a timely and situation specific response, including a recommendation on emergency protective measures for the public (EPM). From the perspective of our emergency preparedness partners, the layout and presentation of ENSI's assessment and recommendations is of considerable importance. To address these two objectives, we developed and implemented a DSS for ENSI's ERO reactor safety and radiation protection groups.

Main findings

Our new DSS for the reactor safety assessment is based on IAEA IEC's Reactor Assessment Tool with questionnaire and simplified plant graphic, but accounts for Swiss specifics. At the end of each assessment cycle, a concise situation report is generated to be uploaded to the national electronic situation overview accessible to all ERO partners.

Regarding radiation protection, until recently, all products of ENSI's ERO containing results from Atmospheric Dispersion Model simulations had to be created manually; with the DSS presented here, all of them can be created in a standardised format at the push of a button. Furthermore, ERO personnel responsible for suggesting EPM now have the possibility to create an easily understandable graphic visualisation of the areas affected and measures recommended therein.

First applications of this new DSS in the context of exercises have confirmed its positive effects and demonstrated the need for even more extensive automation, semi-automation and standardisation. These aspects will be considered in the second step, the development of the DSS for the entire ERO.

Acknowledgements

-

21st International Conference on Harmonisation within Atmospheric Dispersion Modelling for Regulatory Purposes
27-30 September 2022, Aveiro, Portugal

UNDERSTANDING THE IMPACT OF CRUISE SHIPS EMISSION IN URBAN HARBOUR USING CFD MODELLING IN CAPNAVIR PROJECT

Amita Tripathi, Chen Liying, Souprayen Claude

SHORT ABSTRACT

Abstract title: Understanding the impact of cruise ships emission in urban harbour using CFD modelling in CAPNAVIR project

LE GUELLEC Malo, FLUIDYN France

Email of first author: malo.leguellec@fluidyn.com

Names and Affiliations of the Co-authors:

CHEN Liying, FLUIDYN France

SOUPRAYEN Claude, FLUIDYN France

Abstract text *(maximum 350 words.)*

The CAPNAVIR project (CAractérisation des Particules fines issues de la NAVIgation fluviale ou maRitime) is a project funded by ADEME and aimed at characterizing the sources of fine particle emissions (PM2.5 and PM1) emitted by maritime traffic in a context of urban harbours. This project brings together CEREMA, the Grand Port Maritime de Bordeaux, the CNRS aerology laboratory in Toulouse, Particle Vision in conjunction with the University of Fribourg (Switzerland) and Fluidyn.
The objective of the CAPNAVIR project is to provide in-depth knowledge of the chemical nature of emissions from cruise ships and river vessels in real navigation conditions, as well as the corresponding concentration levels of fine particles. This subject is fundamental to evaluate the means of reducing this pollution. These results will be linked to various factors that can influence emissions: technical parameters (fuel, engine load, etc.) and operating parameters (phase of activity, etc.).
The experimental site chosen is the port of Bordeaux Center which includes on the left bank both a quay for river transport and a quay for maritime passenger transport, in a fairly restricted area.
In September 2021, during a measurement campaign led by CEREMA, particle sensors were used, supplemented by sulfur dioxide measurements, as well as mini weather stations.
Modeling of the dispersion of pollutants from ships was then carried out using the 3D-CFD software, fluidyn-PANACHE, according to two emission configurations:

1. Modeling of a stationary state for liners at berth during a stopover of several hours;
2. Modeling of transient states for ocean liners and river boats navigating in the study area.

These models will make it possible to understand the impact of these different configurations and to position the sensor network in a relevant way for recording the concentrations generated by maritime traffic during a stopover (emissions lasting several hours with specific engine speeds) but also during the approach and departure navigation phases (emissions of a few tens of minutes with specific engine speeds). A comparison with the experimental data is also carried out.

21st International Conference on Harmonisation within Atmospheric Dispersion Modelling for Regulatory Purposes
27-30 September 2022, Aveiro, Portugal

YEAR TO YEAR CHANGES IN PM2.5 POPULATION EXPOSURE – A CASE STUDY FOR POLAND

Maciej Kryza, Małgorzata Werner, Krzysztof Skotak, Mike Holland, Helen ApSimon

SHORT ABSTRACT

Abstract title: Year to year changes in PM2.5 population exposure – a case study for Poland *Name and Affiliation of the First Author*: Maciej Kryza, University of Wrocław
Email of first author: maciej.kryza@uwr.edu.pl
Names and Affiliations of the Co-authors:

Małgorzata Werner, University of Wrocław

Krzysztof Skotak, Institute of Environmental Protection–National Research Institute Mike Holland, EMRC, UK
Helen ApSimon, Imperial College London

Abstract text *(maximum 350 words.)*

Population of Poland suffers from low air quality. High concentrations of harmful PM2.5 are related with large residential combustion and emission. This leads to severe health effects. Number of premature deaths due to high PM2.5 concentrations in Poland was estimated at 46300 in year 2018.
In this work we have used WRF-Chem modelled PM2.5 concentrations to answer the question how many deaths could be avoided (for adults over 30 years old) if the PM2.5 concentrations are reduced to new WHO recommended value of 5.0 $\propto$g m^{-3} (annual mean PM2.5 concentrations)? We have combined gridded WRF-Chem PM2.5 concentrations (4km x 4km grid cell) with gridded population and incidence data in communes, using WHO AirQ+ tool. We have used two WRF-Chem simulations for year 2017 and 2018. The simulations differ only in meteorology, as we have kept the same emission data for each year.
The results show that the reduction of the annual mean concentrations to WHO recommended threshold could avoid 25654 premature deaths (99 per 100000 population at risk) in year 2017 and 29280 in 2018 (113 per 100000 population at risk). These values are likely underestimated, as for both years considered the modelled PM2.5 concentrations are below those measured at air quality stations, especially during the heating season. Over 14% difference in number of premature deaths suggests that the meteorology plays important role in estimating population exposure.

21st International Conference on Harmonisation within Atmospheric Dispersion Modelling for Regulatory Purposes
27-30 September 2022, Aveiro, Portugal

IMPACT ASSESSMENT ON AIR QUALITY OF A WASTE-TO-ENERGY PLANT IN TURIN

Roberta De Maria, Stefano Bande, Francesca Bissardella, Cinzia Cascone, Stefania Ghigo, Marilena Maringo

SHORT ABSTRACT

Abstract title: Impact assessment on air quality of a waste-to-energy plant in Turin *Name and Affiliation of the First Author*: *Roberta De Maria, Arpa Piemonte*
Email of first author: *r.demaria@arpa.piemonte.it*
Names and Affiliations of the Co-authors: *Stefano Bande, Francesca Bissardella, Cinzia Cascone, Stefania Ghigo, Marilena Maringo (Arpa Piemonte)*

Abstract text *(maximum 350 words.)*

Waste treatment plants usually rise great concern in the population living in the neighbourhood about their impact on environment and health. For this reason, a Sanitary Surveillance Plan was foreseen to keep a close watch on the possible state of health changes of population living near the Turin waste-to-energy plant: SPOTT (Surveillance on POpulation health around the Turin waste-of-energy plant) project, started in 2013 and involving a group of public institutions working on sanitary and environmental topics.

Modelling simulations, using data from the Continuous Emission Monitoring System (CEMS) and, for micropollutants and metals, from discontinuous measures, will estimate the plant contribution to air quality levels and soil deposition over an area of 45 km x 48 km, including Turin and the neighbouring municipalities. Air concentrations and soil depositions of not reactive pollutants will be assessed with a lagrangian particle model (SPRAY) over three different years, to describe the plant impact during different meteorological and emissive years. Moreover, simulations will be carried out with a Chemical Transport Model (FARM) to assess the plant contribution on primary and secondary pollutant concentrations. Modelling results will give a complete description of the plant impact on air quality and support the epidemiological studies in the SPOTT project.

Results obtained with SPRAY dispersion model over 2019 have been compared to air quality national limit values and concentrations measured at monitoring sites. All the pollutant concentrations produced by the plant, both in air and in depositions, show a rather moderate contribution to measured concentrations, frequently more than one order of magnitude lower to measured values. Only for mercury, annual mean concentrations in soil depositions are comparable to those measured at Beinasco site, confirming the importance of the waste-to-energy process as source of this

pollutant. Further search will be carried out with the results of the modelling simulation over year 2016, being characterized by mercury emission levels higher than in 2019. Year 2019 is being investigated also running the CTM FARM; the results will be compared to and will integrate the information obtained with the SPRAY model.

21st International Conference on Harmonisation within Atmospheric Dispersion Modelling for Regulatory Purposes
27-30 September 2022, Aveiro, Portugal

IMPACT OF POLICY ABATEMENTS ON AIR QUALITY IN CENTRAL EUROPE

Małgorzata Werner, Anetta Drzeniecka-Osiadacz, Lech Gawuc, Maciej Kryza, Tymoteusz Sawiński, Krzysztof Skotak, Massimo Vieno

SHORT ABSTRACT

Abstract title: **Impact of policy abatements on air quality in Central Europe**

Name and Affiliation of the First Author: Małgorzata Werner, Faculty of Earth Sciences and Environmental Management, University of Wrocław, Poland

Email of first author: malgorzata.werner@uwr.edu.pl

Names and Affiliations of the Co-authors:
Anetta Drzeniecka-Osiadacz, Faculty of Earth Sciences and Environmental Management, University of Wrocław, Poland
Lech Gawuc, National Centre for Emissions Management, Institute of Environmental Protection - National Research Institute, Warsaw, Poland
Maciej Kryza, Faculty of Earth Sciences and Environmental Management, University of Wrocław, Poland
Tymoteusz Sawiński, Faculty of Earth Sciences and Environmental Management, University of Wrocław, Poland
Krzysztof Skotak, Institute of Environmental Protection – National Research Institute, Warsaw, Poland
Massimo Vieno, UK Centre for Ecology and Hydrology, Edinburgh, United Kingdom

Abstract text *(maximum 350 words.)*

Air quality in Central Europe, is still poor due to high usage of coal and wood with an associated high emissions of particulate matter (PM) from the residential sector in winter. Poor air quality is a key concern for Poland, where very high concentrations of PM_{10} and $PM_{2.5}$ are observed every winter and routinely exceeding the European air quality standards. Anti-smog policy has been introduced in most of the Polish provinces. The policies set standards for equipment used in specific regions to burn solid fuels for heating purposes as well as types and quality of such fuels.

In this work, we verify the impact and the efficacy of these policies on air quality and exceedances. We used here the EMEP MSC-W atmospheric chemistry transport model to calculate the PM concentrations. The model was run using two nested domains, a domain covering the whole Europe and the inner domain over Poland at 4 km x 4 km. We used high resolution national emission database for Poland and EMEP database outside the Polish area. The first simulation (BASE) included the actual emissions

and meteorological conditions for the year 2018. For the second run (SCENARIO), we have modified the emissions from residential heating to include changes related to the anti
smog resolutions. In general the results show a significant positive impact of the proposed policies aimed at the improvement of air quality. The largest improvement has been found during the winter where domestic generated pollution prevails.

21st International Conference on Harmonisation within Atmospheric Dispersion Modelling for Regulatory Purposes
27-30 September 2022, Aveiro, Portugal

ATMO-PLAN: AN AIR QUALITY MANAGEMENT SYSTEM FOR ENVIRONMENTAL IMPACT ASSESSMENTS AND URBAN AIR QUALITY PLANS IN EUROPE

Stijn Vranckx, Nele Smeets, Hans Hooyberghs, Wouter Lefebvre, Peter Viaene, Robin Houdmeyers, Stijn Janssen, Jorge Sousa, Alessandro D'Ausilio, Lisa Blyth, Jana Krajčovičová, Dušan Štefánik, Beňo Juraj, Zita Ferenczi, Ewa Bielas, Włodzimierz Zaleski

Short abstract

ATMO-Plan: an air quality management system for environmental impact assessments and urban air quality plans in Europe

Name and Affiliation of the First Author: Stijn Vranckx (VITO, BE)

Email of first author: stijn.vranckx@vito.be

Names and Affiliations of the Co-authors: Nele Smeets, Hans Hooyberghs, Wouter Lefebvre, Peter Viaene, Robin Houdmeyers, Stijn Janssen, Jorge Sousa, Alessandro D'Ausilio, Lisa Blyth (VITO, BE), Jana Krajčovičová, Dušan Štefánik, Beňo Juraj (SHMU, SK), Zita Ferenczi (OSMZ, HU), Ewa Bielas, Włodzimierz Zaleski (City of Krakow, PL)

Abstract text

ATMO-Plan is a user-friendly web based decision support system, designed to facilitate the assessment of the impact of emission changes on air quality on an urban scale at a high spatial resolution. The system can be configured to harmonize air quality modelling at a national level for environmental impact assessments (EIAs) and urban air quality plans. The system is operational for EIAs in Slovakia and urban air quality plans in Hungary and Krakow (Poland). The use of the tool is being explored for both Belgium and Ireland.

The web-tool applies an operational modelling chain starting from regional background concentrations, meteorology, fleet data, the road network with traffic intensities and optionally residential emissions.
Regional background concentrations for the country of interest have been modelled using a detrended kriging interpolation scheme starting from hourly pollutant concentrations. Output from any other regional model could replace these data. A road traffic emission model, FASTRACE, is applied, relying on the COPERT methodology and starting from local traffic data and national fleet data. This integration enables traffic scenarios configured for changing traffic intensities or traffic fleets (such as low emission zones).

Besides traffic data, residential emissions can be added as input data. Residential emission scenarios can be configured by defining zones with emission restrictions and rescaling of the affected emissions.

In the operational chain, these emissions are used in the bi-gaussian dispersion model IFDM model. IFDM combines these contributions from local emissions with the hourly background concentrations considering a method to avoid double counting. The model output is presented as annual average concentration maps, exceedance indicators and timeseries for NO_2, PM_{10} and $PM_{2.5}$.

Harmonization of the use of the application is foreseen by fixing all national default input data for the baseline scenario. Users can add additional scenarios starting from a copy of this baseline and adjusting the emission input.
The quality and performance of the model chain is illustrated by validation against passive sampler campaigns and observations of the national monitoring networks.

Figure 1: ATMO-Plan example showing NO_2 concentration differences for a low emission zone scenario in Bratislava, Slovakia, units: µg/m³.

21st International Conference on
Harmonisation within Atmospheric Dispersion Modelling for Regulatory Purposes
27-30 September 2022, Aveiro, Portugal

IMPLEMENTATION OF AN AIR QUALITY MODELLING AND PREDICTION SYSTEM FOR THE CITY OF GUADALAJARA INCLUDING THE INSTALLATION OF FIXED AND MOBILE MICRO-SENSORS ON VEHICLES

Mathieu Lachatre, Fanny Velay Lasry, Germain Therre, Marc Chiappero, Eva-Marie Eriksson, Claude Derognati, Gwendoline Lacressonniere, Mathieu Lachatre, Alisson Godart, Maxime Nibart, Bruno Ribstein, Larissa Zanutto, Samya Pinheiro, Pierre Castaneri, Marcia Otalora, Viet Tran, Daniel Loeb, Estefany Lopez Murillo, Elizabeth Duran Chavez, Adan Espejo, Natalia Ortiz

Implementation of an air quality modelling and prediction system for the city of Guadalajara including the installation of fixed and mobile micro-sensors on vehicles

Fanny VELAY LASRY[1], Germain THERRE[1], Marc CHIAPPERO[1], Eva-Marie ERIKSSON[1], Claude DEROGNAT[1], Gwendoline LACRESSONNIERE[1], Mathieu LACHATRE[1], Alisson GODART[1], Maxime NIBART[1], Bruno RIBSTEIN[1], Larissa ZANUTTO[2], Samya PINHEIRO[2], Pierre CASTANIER[1], Marcia
OTALORA[1], Viet TRAN[1], Daniel LOEB[1], Estefany LOPEZ MURILLO[3], Elizabeth DURAN CHAVEZ[3], Adan ESPEJO[3], and Natalia ORTIZ[3]

[1]ARIA Technologies, 8-10 rue de la Ferme, 92100 Boulogne-Billancourt, France.
[2]ARIA Do Brasil, Ladeira da Gl´oria, 26 – Gl´oria - Edif´ıcio Nex Rio - Est´udio 213, Rio de Janeiro, Brasil. [3]SEMADET, Av. Circunvalaci´on Agust´ın Y´a˜nez 2343, Moderna, 44190 Guadalajara, Jal., Mexique.

January 21, 2022

Contact: fvelay@aria.fr; mathieu.lachatre@suez.com.

abstract

The project aims to establish an air quality analysis, modeling and forecasting system platform for air pollutants for the city of Guadalajara, in the state of Jalisco, Mexico. This platform, including the implementation of innovative measurement tools (fixed and mobile micro-sensors on vehicles), already tested in France and in particular in Paris, constitutes both an operational tool for the state of Jalisco and a showcase of French technologies in the field of the “Sustainable City”.
The project, named AIRED, integrates modeling of air pollution from a regional scale (0.25° of resolution) to a few meters in the urban environment (with the SPRAY Lagrangian model). A set of six models has been assembled to combine each model strengths and domain of applicability. Two meteorological models are used (WRF and SWIFT), two eulerian CTM (CHIMERE and

FARM), the SIRANE model for atmospheric urban pollutant dispersion and the SPRAY lagrangian model. The system is running 24/7 and a results visualization platform has been deployed to allow the Secretar´ıa del Medio Ambiente y del Desarrollo Territorial (SEMADET) to communicate to the citizens on the of air quality. It includes concentration maps of pollutant, but also the Mexican Air Quality Index and a dedicated health impact index. The platform also allows the realization of scenario simulations to test regulatory measures. A local emission inventory has been elaborated for industrial, aera and traffic sources based on Mexican data. Global databases (EDGAR 2015) and air quality forecast (CAMS) are also used to feed the large scale domains. A specific module has also been implemented in order to treat the pollution coming from forest fires which are particularly active during the springtime. The combination of models with different scales of application enable the possibility to create a synergy between the modeling work and monitoring coming from satellite based instruments to street micro captors. In addition to the information generated locally by 10 monitoring stations, this project includes the installation and integration of data from 30 mobile sensors and 10 fixed sensors, in the industrial zone of Miravalle and in the central Centro of Guadalajara area. The whole system is being integrated in an information platform hosted at the University of Guadalajara.

TOPIC 3:

USE OF MODELLING IN SUPPORT OF EU AIR QUALITY DIRECTIVES, INCLUDING FAIRMODE ACTIVITIES

21st International Conference on
Harmonisation within Atmospheric Dispersion Modelling for Regulatory Purposes
27-30 September 2022, Aveiro, Portugal

HOURLY ROADSIDE TRAFFIC EMISSIONS FROM BOTTOM-UP INVENTORY FOR THE CITY OF BERLIN

E.C. Chan[1], J. Leitão[1], S.A. Schmitz[1], T.M. Butler[1] and A. Kerschbaumer[2]

[1]Institute for Advanced Sustainability Studies (IASS), Potsdam, Germany
[2]Senatsverwaltung für Umwelt, Mobilität, Verbraucher- und Klimaschutz, Berlin, Germany

Abstract: Emissions of nitrogen oxides (NO_x) and particulate matter (PM) from traffic sources are modelled for the City of Berlin with a bottom-up approach using HBEFA emission factors. Road network topology, vehicle fleet distribution, traffic activities, as well as meteorological conditions are used in tandem for generating hourly emissions at road segment resolutions. Aggregated annual daily mean emissions are presented and have been shown to be consistent with officially reported inventory values. Meanwhile, street level hourly emission data for different day types (i.e., workdays, Fridays, Saturdays, and Sundays/Holidays) are generated to coincide with local conditions representing recent observational campaigns using low-cost sensors (LCSs). These locations reflect different road types, where corresponding influences of traffic volume and traffic flow state on the emission output are evident. The results from this exercise provide high-resolution boundary conditions for future meso- and urban scale model evaluation studies, or further as a starting point for exposure assessment to traffic pollutants under different traffic activity scenarios.

KEY WORDS: **EMISSIONS, TRAFFIC, EXPOSURE, MODELLING, HBEFA, LOW-COST SENSORS (LCS)**.

INTRODUCTION

In urban areas, the local population is in close proximity with airborne pollutant sources, such as nitrogen oxides (NO_x) and particulate matter (PM) from traffic emissions. As constituents of these pollutants are well-established health risk factors even at concentrations below WHO recommended levels (DeVries et al, 2016; Corso et al, 2020), accurate quantification of traffic emission sources is important in establishing relevance and trustworthiness of air quality measurements and model results (Thunis et al, 2016). However, vehicles release pollutants in motion and at rest at irregular intervals, and their output are influenced by a number of meteorological, technological, and behavioral factors (Davison et al, 2021), thus presenting a key challenge in the construction of emission inventories from vehicle traffic at the required resolutions.

In the so-called “bottom-up” approach, traffic emissions are calculated using traffic activity at a given road segment and existing emission factors databases at a vehicle level, typically on an hourly basis. Current methodologies – such as VEIN (Ibarra-Espinosa et al, 2018) and HERMES (Guevara et al, 2020) – are derived from COPERT emission factors (Ntziachristos et al, 2009). On the other hand, Yeti (Chan et al, 2022), is a generalized, scalable framework, based on HBEFA emission factors (Keller et al, 2017), which has been shown to produce results compatible with the aggregated emission inventory for Germany in 2015 (Diegmann et al, 2020) procured using official inventory standards (VDI, 2020).

In the meantime, to further expand the understanding of micro-scale dispersion of airborne pollutants in urban environments, field-calibrated low-cost sensors (LCS; Peltier et al, 2020) have become a popular emerging technology, complimentary to traditional reference-grade instrumentation, as their accuracy and applicability continually improve (Malings et al, 2019; Zimmerman et al, 2019). These are exemplified by

the Zephyr® air quality monitors (Peterson et al, 2017), containing metal oxide sensors (MOSs) for O_3, NO, and NO_2, as well as micro-optical PM sensors. The versatility and affordability of LCSs enable deployment at high spatial resolution to capture real-time transport of pollutants (Schmitz et al, 2021).

This study presents the emission data from Yeti for the city of Berlin, with emphasis placed on nitrogen oxides (NO_x) and particulate matter (PM). Annual aggregate emissions are compared with officially reported figures (Diegmann et al, 2020), followed by the examination of hourly roadside emissions for different day types to demonstrate Yeti as a standalone tool for investigating emission source attribution, or as part of a scale air quality modelling tool chain (Kuik et al, 2018; Chan and Butler, 2021). These roadside emissions are representative of the location and meteorological conditions of measurement campaigns conducted by Schmitz et al (2021, 2022) and can serve as traffic emission boundary conditions for meso- and urban scale model evaluation exercises and pollutant exposure assessment studies.

DESCRIPTION OF INPUT DATA

Yeti requires input data for traffic flow, meteorology, and HBEFA emission factors. Table 1 shows the source data that are used to generate traffic input for Yeti, which include fleet distribution, road topology and properties, vehicle count and level of service (LOS) distributions. A generalized representation of traffic activity and emission data affords a high degree of scalability and flexibility in the use and execution of Yeti, while accommodating a wide range of details on topological, traffic, and meteorological data. The resulting hourly traffic emission data are calculated at road level resolution.

Table 23. Source data for Berlin for generating Yeti traffic emissions

Data type	Resolution	Year
Vehicle fleet distribution	Annual city mean	2020
Road network topology and properties	Per road link	2016
Vehicle category distribution (morning, evening, night)	Per road link, hourly	2014
Total vehicle count	Per road link, hourly	2015
Level of service (LOS) distributions for all day types	Per road link, hourly	2015
HBEFA emission factors (version 4.1)	Per vehicle	2019

Two different sets of meteorological data are used in this study, as they influence contributions from cold excess emissions. First, the default seasonal diurnal temperature profiles for Germany from HBEFA are used to generate the annual aggregate emissions, as presented in Figure 66. Second, roadside emissions are obtained from measurement campaigns conducted on two different streets: Frankfurter Allee in August 2018 (Schmitz et al, 2022), and Kottbusser Damm in February, 2020 (Schmitz et al, 2021). The mean diurnal temperature profile for the corresponding observation period is taken from the German Weather Service station in Berlin Tempelhof (Figure 67).

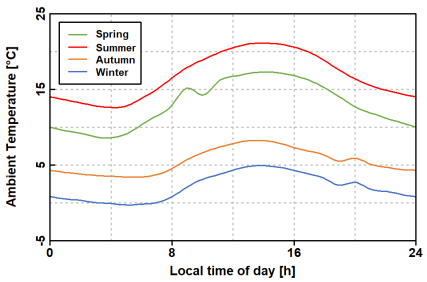

Figure 66. Mean seasonal diurnal temperature profiles in Germany from HBEFA.

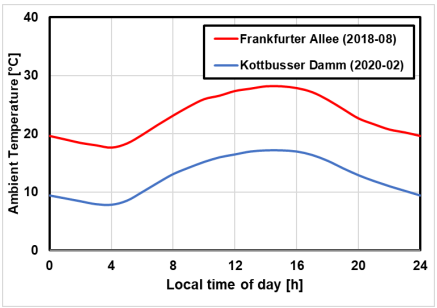

Figure 67. Mean diurnal ambient temperature profiles on-site from the air quality campaigns conducted on (Red) Frankfurter Allee in August 2018 and (Blue) Kottbusser Damm in February 2022.

ANNUAL AGGREGATE EMISSIONS

Figure 68 shows the spatial distribution of annual daily mean emissions of NO_x over the road network in Berlin. In general, higher NO_x emissions are observed along trunk roads, where overall vehicle counts are higher. Meanwhile, Table 24 shows the annual aggregate NO_x and PM emissions for Berlin calculated in Yeti in conjunction HBEFA 4.1 emission factors, accompanied by figures obtained from officially reported emission inventory in 2015 (Diegmann, 2020). While both sets of data are of comparable magnitude, the reduction of aggregate NO_x emissions in Yeti can be attributed to the displacement of vehicles belonging to Euro class III or lower with those of improved exhaust treatment technologies (Chan et al, 2022).

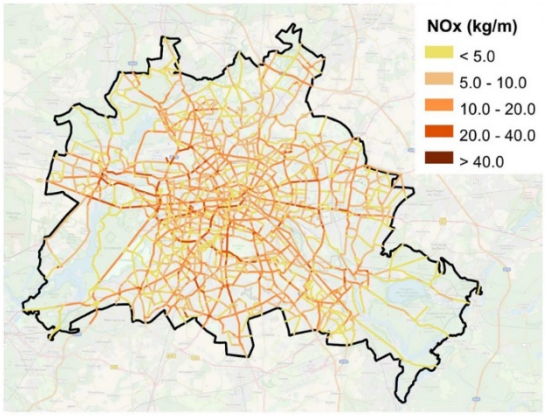

Figure 68. Spatial distribution of annual daily mean NO_x emissions from Yeti. Adopted from Chan et al (2022).

Table 24. Comparison between Yeti and reported annual aggregate NOx and PM emissions

Annual Aggregate Emissions [tonnes/day]	**NO_x**	**PM**
Yeti (HBEFA 4.1; 2020 fleet composition)	9.57	1.53
Official inventory 2015 (Diegmann et al, 2020)	15.94	1.50

Further, a breakdown of vehicle emission contributions is presented in Table 25. As expected, vehicle NO_x emissions are dominated by hot run emissions. On the other hand, the majority of PM emissions originate from non-exhaust sources, such as abrasion and resuspension. Evaporative emissions (i.e., hot soak, diurnal, and running losses) apply only to unburnt hydrocarbon emissions and are not presented here.

Table 25. Yeti emissions broken down by contributions

Contributions [tonnes/day]	**NO_x**	**PM**
Hot run	8.93	0.11
Cold excess	0.64	0.01
Non-exhaust PM	- -	1.40

Yeti is then applied at specific road segments and during periods coinciding with air quality measurement campaigns in Berlin that took place on Frankfurter Allee in August 2018 (Schmitz et al, 2022, in preparation) and Kottbusser Damm in February 2020 (Schmitz et al, 2021). The diurnal traffic activities profiles for the two measurement locations are shown in Figure 69 provided by the Berlin City Senate. Diurnal profiles for weekday (Mondays to Thursdays) and Sundays / holidays are provided as the corresponding traffic patterns display different volume and characteristics. The state of traffic flow is categorized using the level of service (LOS) definition under HBEFA, ranging from free flow (LOS 1), heavy (LOS 2), saturated (LOS 3), and stop-and-go (LOS 4). These are shown as fractions of the corresponding traffic flow in Figure 69 on an hourly basis. An additional LOS has been introduced in HBEFA 4.1 to represent heavy stop-and-go traffic (LOS 5). Figures for traffic activities in this state are not available, however, and the emission calculation proceeded with LOS 1 to LOS 4.

The diurnal hourly profiles for NO_x and PM emissions over both sites are illustrated in Figure 70. The disparity in traffic volume between the two sites can be attributed to each road type. Frankfurter Allee is a trunk (primary) road, while Kottbusser Damm serves as a distributor (secondary) road, and they are reflected by the volume of traffic and the corresponding emission levels. The diurnal peaks in emissions match the periods for peak traffic volume. Further, the level of service has also a strong influence on the emissions. This can be seen in a decrease in emissions on Frankfurter Allee on weekdays during between 10h and 14h due to a corresponding decrease in stop-and-go traffic (LOS 4). On the other hand, weekday emissions on Kotbusser Damm maintained more or less at peak levels throughout daytime period due to a consistently high level of stop-and-go traffic, representing 27% to 53% of total hourly traffic flow.

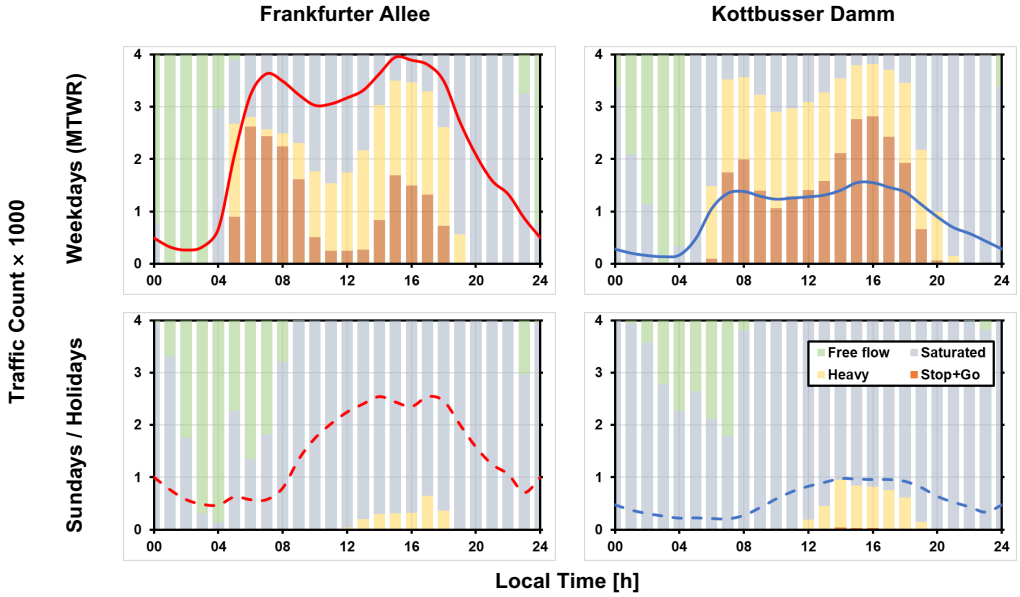

Figure 69. Mean traffic activity profiles (lines) used for calculating emissions on Frankfurter Allee and Kottbusser Damm on typical weekdays and Sundays/holidays. Colors indicate percentages of LOS.

Frankfurter Allee (2018-08) **Kottbusser Damm (2022-02)**

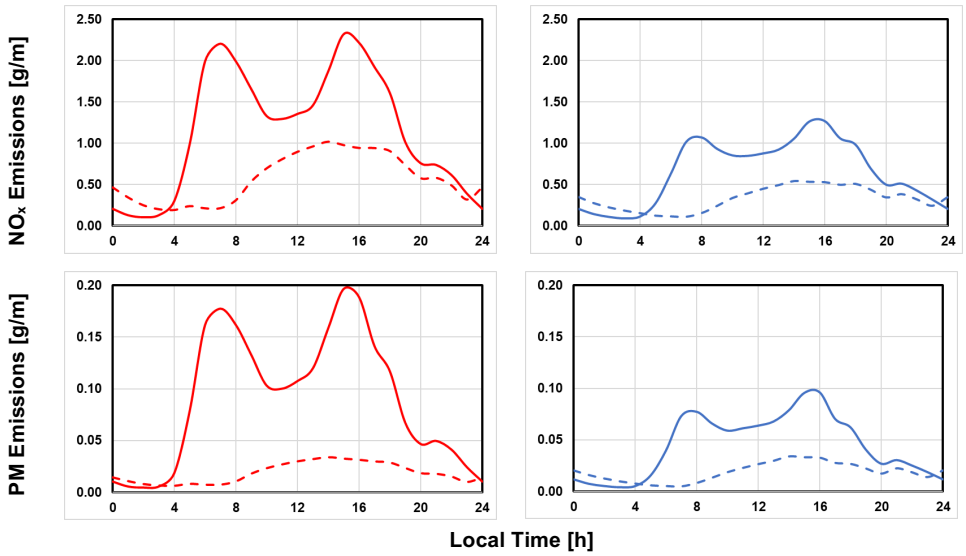

Figure 70. Hourly emissions for traffic NOx and PM on Frankfurter Allee and Kottbusser Damm over the respective observational periods. Solid lines and dashed lines represent workdays and Sundays/holidays respectively.

CONCLUSIONS AND FUTURE WORK

Using Berlin as the focal point, traffic emissions inventories are produced using Yeti for NO_x and PM with exhaust and non-exhaust contributions. The computed results are found to be consistent with officially reported emission inventory figures. The methodology is further applied to produce roadside emissions under meteorological conditions representative of specific measurement campaigns conducted on Frankfurter Allee and Kottbusser Damm. The calculated emissions reflect the traffic volume passing through the road, as well as the distribution of the traffic flow state (i.e., LOS) due to, in part, their corresponding functions as primary and secondary roads.

The results of this work can be applied as part of a meso- or urban scale modelling framework, where the prescribed emission profiles, in combination with local meteorological and background concentrations, can generate a concentration map that can be evaluated with observational data collected at the respective measurement campaigns. The diurnal profiles of emissions are found to match the diurnal patterns in NO_2 and O_3 pollution at each experimental site, highlighting the ability of LCS to complement and validate modelling studies. Further, a demographic based approach can be further developed on this framework for acute human pollutant exposure assessment by quantifying diurnal population movements between different microenvironments. In addition, impacts in local pollutant dispersion and transformation resulting from abrupt or continuous changes local traffic activities, can be quantified accordingly.

REFERENCES

Chan EC, Butler TM (2021) Geosci Model Dev 14:4555-4572.

Chan EC, Leitão J, Kerschbaumer A, Butler TM (2022) Geosci Model Dev Discuss.

Corso M, Blanchard M, Medina S, Wagner V (2020) Atmos, 11:1198.

Davison J, Rose RA, Farren NJ, et al (2021) Environ Sci Tech 55(8) 4452-4461, 2021.

DeVries R, Kriebel D, Sama S (2016) Environ Health 15:98.

Diegmann V, Mahlau A, Breitenbach Y, Tautz F (2020) "Modellrechnungen zur Zweiten Fortschreibung des Berliner Luftreinhalteplans" SenUVK Berlin.

Guevarra M, Tena C, Porquet M, et al (2020) Geosci Model Dev 13:973-903.

Ibarra-Espinosa S, Ynoue R, O'Sullivan S, et al (2018) Geosci Model Dev 11:2209-2229.

Keller M, Hausberger S, Matzer C, et al (2017) "HBEFA 3.3 Hintergrundbericht". INFRAS.

Kuik F, Kerschbaumer A, Lauer A, et al (2018) Atmos Chem Phys 18:8203-8225.

Mailings C, Tanzer R, Hauryliuk A, et al (2019) Atmos Meas Tech 12(2):903-920.

Ntziachristos L, Gkatzoflias D, Kouridis C, Samaras Z (2009) Information Technologies in Environmental Engineering, Springer, 491-504.

Peltier RE, Castell N, Clements AL et al (2020) "An Update on Low-cost Sensors for the Measurement of Atmospheric Composition" WMO 1215.

Peterson P, Aujla A, Grant K, et al (2017) Sens 17:1653.

Schmitz SA, Caseiro A, Kerschbaumer A and von Schneidemesser E (2021) Environ Res Lett 16(8):084031.

Schmitz SA, Villena G, Caseiro A, et al (2022) In Preparation.

Thunis P, Degraeuwe B, Cuvelier K, et al (2016) Air Qual Atmos Health 9:325-333.

VDI (2020) VDI 3782 Blatt 7, 2020.

Zimmerman N, Presto AA, Kumar SPN, et al (2018) Atmos Meas Tech 11(1):291-313.

21st International Conference on
Harmonisation within Atmospheric Dispersion Modelling for Regulatory Purposes
27-30 September 2022, Aveiro, Portugal

COMPARISON OF SOURCE APPORTIONMENT METHODS USING THE CMAQ MODEL

Tereza Šedivá[1,2], Dušan Štefánik[2]

[1]Comenius University, Šafárikovo námestie 6, 814 99, Bratislava, Slovakia
[2]Slovak Hydrometeorological Institute, Jeséniova 17, 833 15, Bratislava, Slovakia

Abstract: Source apportionment using the CMAQ model with 2 km resolution for January 2021 was done for air-quality monitoring stations in Slovakia. Two Brute Force Method approaches – the 100% emission reduction and bottom-up – were performed to analyze the differences in the resulting impacts of emission sectors on NO_2 and $PM_{2.5}$ concentrations. CMAQ-ISAM module was used to compute the contributions of the sectors to gain additional information about the interactions of the sectors. This work was created for the purpose of the FAIRMODE CT1 activity, which analyses the differences and fitness for purpose of the individual source apportionment methods and their use in practice.

Key words: *Source apportionment, air quality modelling, Brute Force Method, tagging method, CMAQ-ISAM.*

INTRODUCTION

Source apportionment is a method in which the origin of the concentrations in the air is determined. This is done by attributing concentrations to specific emission sources, emission sectors or areas for a given area and time period (P. Thunis et al., 2021). Understanding the origin of concentrations at a specific place can be valuable for determination of effectiveness of various emission scenarios or emission reduction measures.

The emissions in the atmosphere are exposed to atmospheric flow and they undergo chemical transformation, which is why most source apportionment methods are only feasible with chemical transport models (CTMs). CTMs account for the physical and chemical processes of the pollutants in the air and produce concentration fields based on modelled area and meteorology.

There are different source apportionment methods, which serve different purposes and might require different functionalities of the model. They can be classified into three categories that provide different results: The Emission Reduction Impact methods (ERI), which provide potential impacts; Mass-Transfer methods (MT), which provide contributions; and Incremental methods (IC), which provide increments. More details about the approaches can be found in papers by P. Thunis et al. (2019, 2021). The focus of this work is on the first 2 categories.

The Brute Force Method

The most straightforward method within the ERI category is the Brute Force Method (BMF), which requires at least two simulations – the reference simulation with full emissions and a second one with reduced emissions from one of the sources (or sectors, or areas; hereafter together as 'sources'). The potential impact of a source corresponds to the pollutant mass difference between the full and reduced simulation, divided by the emission reduction factor which ranges from 0 to 1 (Thunis et al., 2021). For species involved in complex chemical interactions, larger reductions of emissions do not generally lead to linear reduction in concentrations. Often simulations with 100% emission reduction are performed, where one of the sources is turned off completely. The impact of the emission source obtained by a simulation with a 100% emission reduction $I_{source}^{100\%\,red.}$ can be expressed as

$$I_{source}^{100\%\,red.} = C_{ref} - C_{100\%\,red.of\ source}, \tag{1}$$

where C_{ref} is the concentration of the reference run and $C_{100\%\,red.of\ source}$ is the concentration of the simulation with the 100% emission reduction of the selected source. An alternative approach to the

described BFM is running the simulation solely with the emissions from one emission source. Obviously, such simulation is going to miss concentrations created in the interactions of the pollutants with emissions from other sources. We will call this approach the bottom-up BFM. The impact of the emission source computed this way is equal to the computed concentrations:

$$I_{source}^{buttom-up} \equiv C_{source}^{buttom-up}. \quad (2)$$

The $I_{source}^{100\%\,red.} \neq I_{source}^{buttom-up}$ and the difference between them is caused by chemical reactions between the given source and all other sources – the interaction term $I_{int.}^{source}$. The interaction term of the full run can be computed as

$$I_{int.}^{ref} = C_{ref} - \sum_{source} C_{source}^{buttom-up}. \quad (3)$$

The interaction term can be positive or negative for different species and areas.

The tagging method

The other widely used source apportionment method is the tagging method, which provides the contributions of emission sources. The contributions correspond to the mass of a pollutant transferred from the emission sources to the ambient concentrations (Thunis et al., 2021). One way of computing the contributions is to use a model with a tagging algorithm. The tagging algorithm tracks the origin of each pollutant through the model simulation (Thunis et al., 2019). As an example we can take pollutant A, which reacts with pollutant B to create pollutant AB. Within the tagging method the pollutants are followed through their chemical reactions so that we can assign the total mass contribution of source of A and of source of B on total mass of AB.

The tagging method is implemented within the CMAQ-ISAM (Integrated Source Apportionment Module). The module is implemented by default in the current CMAQ model version – 5.3.3.

Simulation specification

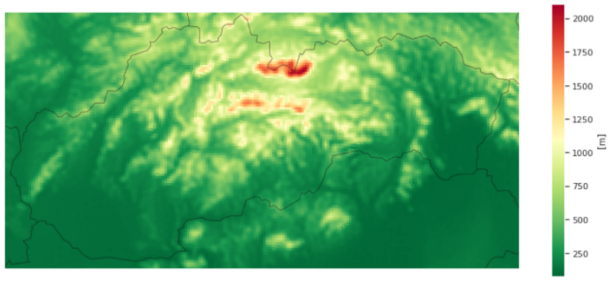

Figure 71. Model domain altitude in [m]

In this work two BF methods – the 100% emission reduction and bottom-up - are compared. CMAQ-ISAM run is also analyzed for source contributions. We ran a total of 15 simulations for the region of Slovakia and its close vicinity (Figure 1.), for January 2021 period. We used CMAQ model version 5.3.3 with 2 km resolution. The meteorology was computed in model ALADIN, the boundary conditions were taken from the global model CAMS. The first simulation – the full run with all emission streams, was ran with the ISAM module. 7 simulations were ran for the bottom-up BFM with each of the emission streams separately and 7 simulations were ran for the 100% emission reduction BMF, always omitting one of the emission streams. For Slovakia, the emission streams included agriculture, traffic, residential heating, and industry (stack sources) from the NEIS emission inventory. For surrounding countries the emissions from TNO MAC-III 2015 database (Kuenen et al., 2014) were used – the area sources of all emission sectors were aggregated into one emission stream, the stack sources from industry made a separate stream. Boundary conditions were considered as a separate emission stream. The bottom-up simulations of the individual

streams had to be run with boundary conditions of O_3, since otherwise there would be no background O_3 in the simulations. Other boundary conditions were not used for the bottom-up one stream simulations. The first 2 days of the simulations were omitted in the analysis due to influence of the initial conditions on the concentrations.

RESULTS

Comparison of 2 Brute Force methods

Comparison of 100% emission reduction BFM and bottom-up BFM was performed for NO_2 and $PM_{2.5}$ and is shown in Figures Figure **72** and **Error! Reference source not found.**. The results are displayed for the grid cells in which the National air quality monitoring stations of Slovakia (and a few stations operated by private industries U.S. Steel Košice and Slovnaft) are situated. We divided the stations into rural background (RB), suburban background (SB), urban background (UB), traffic (T) and industrial (I) for the purpose of comparison of the source apportionment at different station types. The results for each station are displayed as the impacts of the individual emission sectors from the bottom-up BFM (Eq. 2) and 100% emission reduction BFM (Eq. 1) The impacts are stacked upon each other to display a theoretical full concentration of the pollutant in each station grid cell. For comparison, the full run concentrations are displayed.

The potential impacts are often displayed as percentages but due to lack of space here the results are only displayed in $\mu g \cdot m^{-3}$ to show the differences between the concentrations at different stations and station types, as well as differences between the two BF methods – the interaction terms. However, the values should be taken with caution since the concentrations in the model heavily depend on distribution of the emission sources and resolution of the model. In the follow-up work we will also analyze percentual impacts at station grid cells.

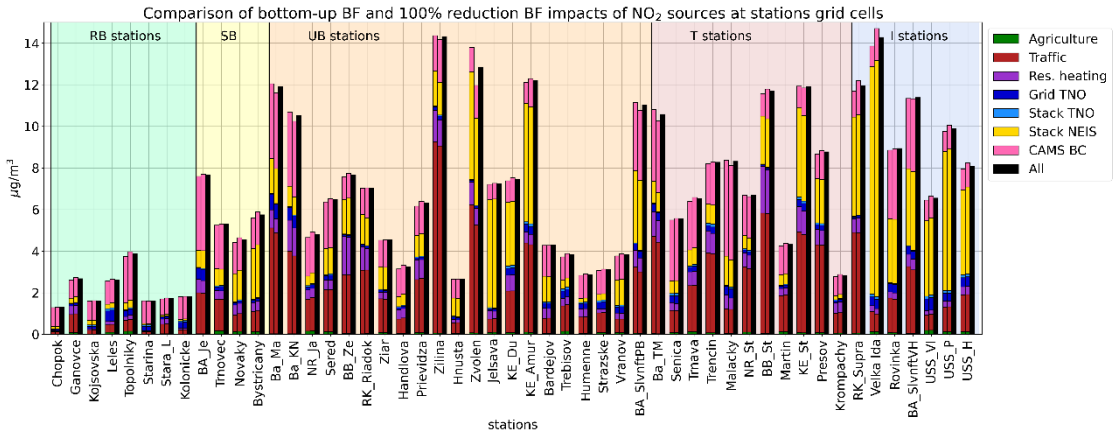

Figure 72. Comparison of bottom-up (1st column for each station) and 100% emission reduction (2nd column for each station) BFM mean impacts of NO_2 sources at station grid cells. The impacts are stacked above each other to make theoretical full concentrations from all sources combined. The black columns (3rd column for each station) show the full concentrations of NO_2 in the full run. The stations are sorted into RB – rural background, SB – suburban background, UB – urban background, T – traffic and I – industrial.

NO_2

Looking at Figure 2, we can see that for most stations the traffic and industry account for the largest impacts, and domestic emission sectors overall account for majority of concentrations (see also Figure 4) for both BF methods. This is expected due to short (2-8 hours) average lifetime of NO_2 in the air (Liu, 2016; Valin, 2013).

Further, we can see that for all station types the differences between the bottom-up BFM impacts and the 100% emission reduction impacts of emission sectors are minor for most of the stations. This result suggests that although NO_2 is a pollutant which can act non-linearly in the atmosphere, during this period for most

areas it acts almost linearly. We expect this result to be explained by the photochemistry of NO_2 in the atmosphere, which is more significant during the summer season compared to winter.

The largest absolute difference between the two BF methods was reached at the Zvolen station grid cell – almost 2 $\mu g \cdot m^{-3}$. In case of this station, the bottom-up method led to concentrations larger than the reference run, while for the 100% emission reduction method the concentrations were smaller than for the reference run. This effect can be seen at multiple stations, as well as the opposite effect where the 100% emission reduction concentrations are higher than both bottom-up and the reference concentrations (most likely due non-linear behavior of the 100% emission reduction simulations).

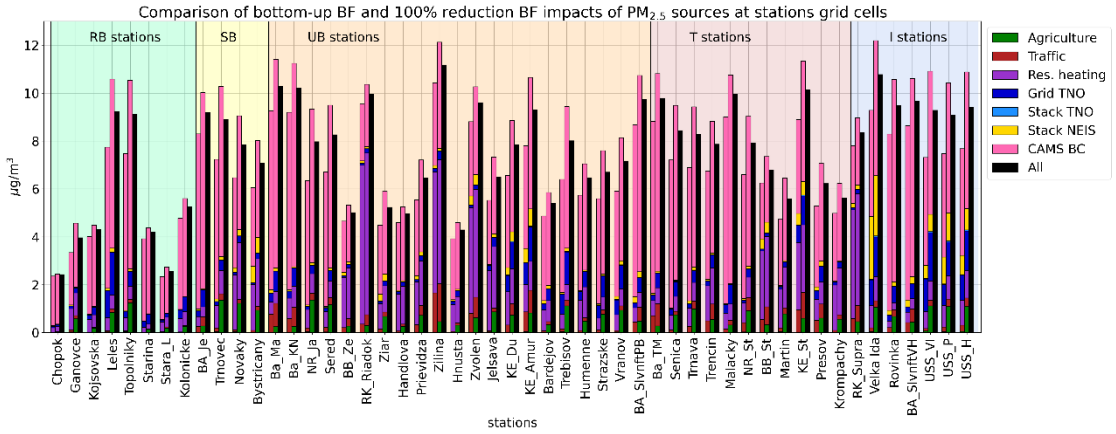

Figure 73. Same as Figure 2. but for $PM_{2.5}$.

$PM_{2.5}$

Looking at Figure 3, we can see that for majority of stations, the boundary conditions have by far the largest impact of all sectors for both BF methods. From domestic sectors, the residential heating impacts are the most significant (see also Figure 4).

We can see that for $PM_{2.5}$, the differences between the two BF methods on most stations are quite significant (around 1.85 $\mu g \cdot m^{-3}$ on average, up to more than 3.5 $\mu g \cdot m^{-3}$ for the U.S. Steel Veľká Ida station grid cell). The stacked bottom-up impacts lead to lower than full run concentrations at all stations, while the 100% emission reduction BF theoretical full concentrations are higher than the full run concentrations. This effect probably occurs because the 100% emission reduction of the emission sources can lead to very non-linear behavior; the sectors might interact differently, creating different pollutants at different rates in varying concentrations of pollutants in specific areas.

We can demonstrate this behavior on an example of the agriculture. For the bottom-up BMF, the impact of the agriculture is negligible for all stations (see also Figure 4) which means there are almost no emissions of primary $PM_{2.5}$ from the agriculture and without the interaction with other sectors, almost no $PM_{2.5}$ is created chemically. For the 100% emission reduction BMF the impact of agriculture is significant. We can conclude that here the impacts are caused almost solely by the secondary products created by interaction of agriculture with other emission sectors. Since the 100% emission reduction simulations can lead to non-linear behavior, the interaction terms for the specific emission sectors here likely cause the stacked impacts of the 100% emission reduction BFM to exceed the full run concentrations.

The CMAQ-ISAM tagging method

Lastly, we look at the source contributions from the CMAQ-ISAM module, which are displayed in Figure 4 in the third columns, alongside the bottom-up BFM, 100% emission reduction BFM and full run concentrations in columns one, two, and four, respectively. It is important to note that the source impacts and contributions serve different purposes and are computed differently so they cannot be directly compared. However, looking at the results of both approaches provides additional information. Alongside the emission sectors used for the BFM simulations, the CMAQ-ISAM also provides tagging of the initial conditions (ICON) and Other sources.

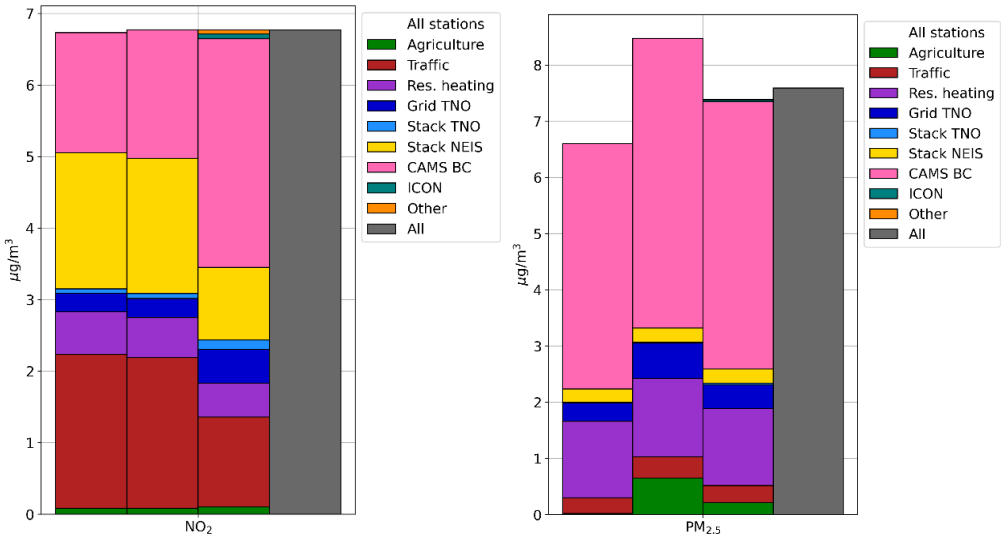

Figure 74. For NO_2 (left) and $PM_{2.5}$ (right), the results of the source apportionment methods are displayed as stacked mean impacts or contributions for all stations combined. Bottom-up BFM impacts, 100% emission reduction BFM impacts, CMAQ-ISAM contributions and full run concentrations are displayed in columns in respective order.

Looking at the NO_2 contributions (Figure 4, left), we can see that the contributions of the traffic, residential heating, and domestic industry (Stack NEIS) are smaller in comparison to the corresponding impacts while the contributions of boundary conditions and emissions of surrounding countries (Stack TNO and Grid TNO) increased. From these results we can see how the model assigns the concentrations to different emission sectors. We know that NO_2 is largely produced in the atmosphere by reaction of NO with O_3. The NO is mostly produced by traffic and industrial processes, while the O_3 is provided to the model in the form of boundary conditions. The BF methods look at the final results of the simulations of the specific streams and attribute the resulting concentrations to the stream. However, with the contributions we see, that the NO_2 was indeed produced by traffic and industry in combination with boundary conditions.

The CMAQ-ISAM module does not tag the coarse fraction of $PM_{2.5}$ which is why the stacked contributions are lower than the full run (this was not the case with NO_2, where the contributions are equal to the full run concentrations). Here the differences between the two BFM are significant. Following the analysis of the agriculture sector, here we can see how the impact of agriculture with the 100% emission reduction BFM is created by chemical reactions of pollutants from agriculture and other sectors (comparing the impacts with contributions).

REFERENCES

Kuenen, J.J.P. et al. (2014). TNOMACC_II emission inventory; a multi-year (2003-2009) consistent high-resolution European emission inventory for air quality modelling. Atmos. Chem. Phys. 14, 10963–10976. https://doi.org/10.5194/acp-14-10963-2014.

Liu F. et al. (2016). NOx lifetimes and emissions of cities and power plants in polluted background estimated by satellite observations. Atmospheric Chemistry and Physics. 16. 5283-5298. 10.5194/acp-16-5283-2016.

Thunis, P. et al. (2019). Source apportionment to support air quality planning: Strengths and weaknesses of existing approaches. Environment International. 130. 104825. 10.1016/j.envint.2019.05.019.

Thunis, P. et al. (2021). Source apportionment to support air quality management practices A fitness-for-purpose guide (V 3.1).

Valin, L. et al. (2013). Variations of OH radical in an urban plume inferred from NO2 column measurements. Geophysical Research Letters. 40. 1856-1860. 10.1002/grl.50267.

21st International Conference on
Harmonisation within Atmospheric Dispersion Modelling for Regulatory Purposes
27-30 September 2022, Aveiro, Portugal

QUALITY CONTROL INDICATORS FOR THE VALIDATION OF AIR QUALITY FORECAST APPLICATIONS IN THE FRAMEWORK OF FAIRMODE ACTIVITIES

Antonio Piersanti[1], Cornelis Cuvelier[2], Stijn Janssen[3], Alexandra Monteiro[4], Paweł Durka[5], Philippe Thunis[2] and Lina Vitali[1]

[1]National Agency for New Technologies, Energy and Sustainable Economic Development (ENEA), Bologna, Italy
[2]European Commission - Joint Research Centre (JRC), Ispra, Italy
[3]Flemish Institute for Technological Research (VITO), Mol, Belgium
[4]CESAM, Department of Environment, University of Aveiro, Aveiro, Portugal
[5]Institute of Environmental Protection (IEP) - National Research Institute, Warsaw, Poland

Abstract: In the framework of FAIRMODE activities concerning the harmonization of model validation methodologies, a specific task was dedicated to the development of a common standardized template to facilitate the screening and comparison of air quality forecast results. The proposed approach assesses the forecast model performances using, as a benchmark, the so called "persistence model", which uses measurements of the previous day as an estimate for the full forecast prediction. Consistently with the FAIRMODE approach, the proposed formulation includes measurement uncertainty and relies on the definition of specific Model Quality Objective and Criteria. The main features of the methodology are described here, together with an example of its application to evaluate the quality of one year-long model data set produced by the Italian air quality forecast system FORAIR-IT.

Key words: *air quality forecast, regulatory model applications, model benchmarking, harmonized validation methodologies, model quality objective, measurement uncertainty.*

INTRODUCTION

One of the main activities of FAIRMODE (Forum for Air Quality Modelling in Europe, http://fairmode.jrc.ec.europa.eu/) has been the development of harmonized procedures for the validation and the benchmarking of air quality model applications, especially under the implementation of the Ambient Air Quality Directive 2008/50/EC (AAQD). The main goal was the definition of common standardized Model Quality Objectives (*MQO*) and Model Performance Criteria (*MPC*) to be fulfilled in order to ensure a sufficient level of quality of a given model application. The methodology (Thunis et al., 2013; Pernigotti et al., 2013; Janssen and Thunis, 2022), consolidated in the DELTA Tool software (https://aqm.jrc.ec.europa.eu/index.aspx), has reached a good level of maturity and has been widely used and tested by model developers and users (Monteiro et al., 2018).

The approach was initially focused on applications related to air quality assessment, but was recently expanded to address additional issues typical of other model applications, such as forecasting. More in detail, the FAIRMODE working plan for the period 2020-2022 included a specific task (CT3, https://fairmode.jrc.ec.europa.eu/Activity/CT3) dedicated to the development and the testing of additional quality control indicators to be checked when evaluating a forecast application. The proposed methodology was tested in different national and geographical contexts and first outcomes sound promising, pointing out to the usefulness of the approach in highlighting shortcomings and strengths of forecasting applications. Here we present the main features of the methodology and an application for a case study (Italy).

METHODOLOGY AND APPLICATION EXAMPLE

The proposed methodology for forecast evaluation comes on top of FAIRMODE's approach applied for the validation of assessment modelling applications. Therefore, it is recommended that forecast models fulfil the standard assessment MQO, as defined in Janssen and Thunis (2022), as well as the additional forecast objectives and criteria as described here. More in detail, the specific forecast indicators investigate the capability to detect sudden changes of concentrations levels, to predict threshold exceedances and to reproduce air quality indices. The methodology, as currently implemented in the DELTA Tool software

(version 7.0), supports the following pollutants and time averages: NO_2 daily maximum and annual mean, O_3 daily maximum of 8-hour average, PM10 and PM2.5 daily and annual mean.

Comparison with the "persistence model"

When evaluating a forecast model, it is of main interest to verify its ability to accurately reproduce sudden changes in the pollutant's concentration levels. To account for this, the proposed approach assesses the forecast model performances using, as a benchmark, the so called "persistence model", which uses the measurements of the previous day as an estimate for the full forecast horizon and is by default not able to capture changes in the concentration levels (e.g. Mittermaier, 2008). More in detail, the forecast Model Quality Indicator (MQI_f) is defined as the ratio between the Root Mean Square Errors (RMSE) computed for both the forecast and the persistence models, i.e.

$$MQI_f = \sqrt{\frac{\frac{1}{N}\sum_{i=1}^{N}(M_i - O_i)^2}{\frac{1}{N}\sum_{i=1}^{N}(P_i - O_i)^2}} \quad (1)$$

where M_i, P_i, O_i represents respectively the forecast, the persistence and the measured values for day i, and N is the number of days included in the time series. Since the persistence model uses the available observations from the day before as an estimate for all forecast days, it is related to the forecast horizon (FH) as following, where, consistently with the FAIRMODE approach, measurement uncertainty (Janssen and Thunis, 2022) is also taken into accout:

$$P_i = O_{i-1-FH} \pm U(O_{i-1-FH}) \quad (2)$$

The forecast Modelling Quality Objective (MQO_f) is fulfilled when MQI_f is less or equal to 1, indicating better capabilities of the forecast model than the persistence one for a specific application.

Modelling Quality Indicator values are provided by means of the Forecast Target Plots (Figure 1), where MQI_f is the distance between the origin and a given point (representing each monitoring station). The green area identifies the fulfilment of the MQO_f. The MQI_f associated to the 90th percentile worst station is reported in the upper left corner (Janssen and Thunis, 2022 for details).

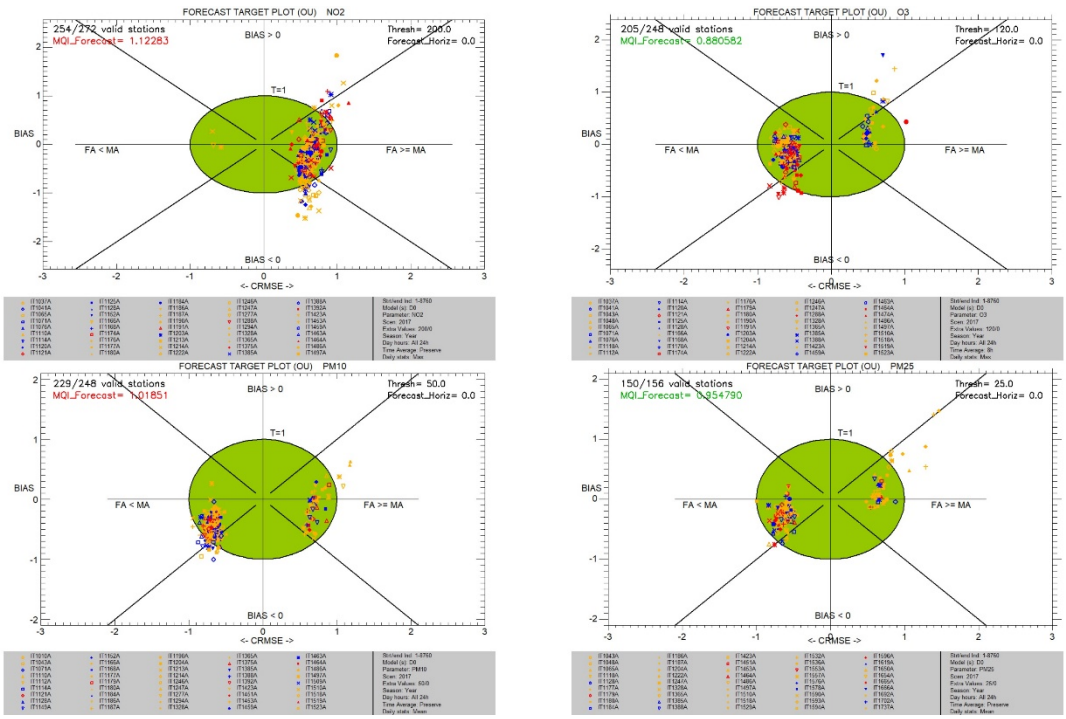

Figure 75. FORAIR-IT skills in forecasting 2017 year: Forecast Target Plots for NO_2 daily maximum (upper left), O_3 daily maximum of 8-hour average (upper right), PM10 daily mean (lower left) and PM2.5 daily mean (lower right) concentrations

As an example, Figure 1 shows, for all pollutans included within the methodology, the outcomes of the evaluation of one year-long model data set produced by the Italian air quality forecast system FORAIR-IT (Adani et al., 2022; https://impatti.sostenibilita.enea.it/en/research/activity/5479) against observations from background stations, the number of which is reported above the 90th percentile MQI_f. Results indicate a good level of quality of FORAIT-IT in simulating O_3 and PM2.5, and some room for improvement concerning NO_2 and PM10 (90th percentile MQI_f slightly higher than 1).
Additional Modelling Performance Indicators (*MPIs*) are defined based on the Mean Fractional Error (*MFE*), a normalized statistical indicator widely used in litterature (e.g. Boylan and Russell, 2006). Two different *MPIs* are defined as follows: 1) comparing the forecast model performances with the persistence model ones ($MPI_1 = MFE_f/MFE_p$); 2) evaluating forecast skills regardless of persistence aspects, using an acceptability threshold based on measurement uncertainty ($MPI_2 = MFE_f/MF_U$), where MF_U is the Mean Fractional Uncertainty, defined as follow

$$MF_U = \frac{1}{N}\sum_{i=1}^{N}\frac{2U(O_i)}{O_i} \quad (3)$$

For both *MPIs*, Modelling Performance Criteria (*MPC*) are defined, being fulfilled when *MPIs* are less or equal to 1.
MPIs based on *MFE* help in interpreting the outcomes. First of all, being *MFE* a normalized error, it does not depend on the magnitude of the absolute concentration values. Moreover, MPI_2 is formulated regardless of persistence aspects, providing, as an added value, an evaluation of the model performances quality itself.
As an example, Figure 2 shows how FORAIR-IT performances in simulating O_3 vary along with the forecast horizon. According to Forecast Target Plot outcomes (above), modelling performances get better from D0 (today forecast) to D2 (the day after tomorrow). MPI Plots (below) help to clarify that this unrealistic improvement is actually due to persistence model performances degradation. Indeed, forecast model performances get better along Y axis, where they are normalized to persistence model skills, but they slighty deteriorate along X axis, where they are considered regardless of persistence aspects. The green (orange) area indicates the fulfillment of MPC for both (one out of the two) MPIs.

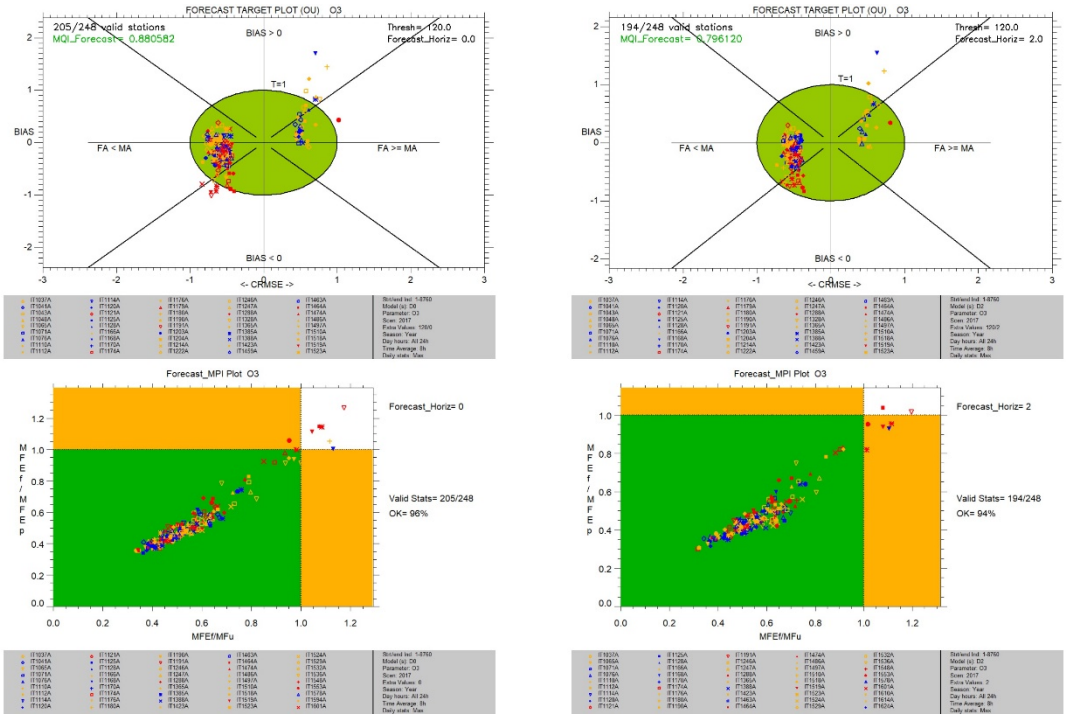

Figure 2. FORAIR-IT performances in forecasting O_3 along with the forecast horizon: skills variation from D0 (left plots) to D2 (right plots), according to Forecast Target Plot (upper plots) and Forecast MPI Plot (lower plots)

Assessment of model capability in predicting Threshold Exceedances

In addition to accurately reproducing sudden concentration changes, exceedances of specific thresholds levels (like limit values for daily concentrations) should be correctly estimated by a forecast model in order to support short-term action plans. Some commonly used threshold indicators (as defined in the right side of Figure 3) are included in the proposed validation approach, based on the 2x2 contingency table (Figure 3, left) representing the joint distribution of categorical events (below or above the threshold value) predicted by the model and observed by measurements.

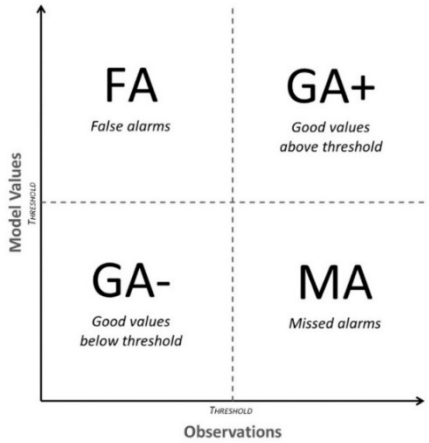

Indicator	Acronym
Accuracy = (GA_+ + GA_-) / Total	ACC
Success Ratio = GA_+ / (FA + GA_+)	SR
Probability of Detection = GA_+ /(MA + GA_+)	PD
FBias score = (GA_+ + FA) / (MA + GA_+)	FB
Threat Score = GA_+ / (MA + FA + GA_+)	TS
Gilbert Skill Score= (GA_+ - H) / (MA + FA + GA_+ - H) with H = (GA_+ + MA)(GA_+ + FA) / Total	GSS

Figure 3. Left: contingency table and definition of the threshold exceedance quantities GA_+, GA_-, FA and MA. Right: Threshold exceedances indicators (definitions and acronyms)

The statistical distribution of all the quantities and indicators defined in Figure 3 are summarized in the Forecast Summary Report. Figure 4 shows an example of FORAIR-IT skills in predicting O_3 daily maximum of 8-hour average and PM10 daily mean, for which a daily limit value is set by AAQD.
A good performance level is reached for the Accuracy, i.e. the indicator measuring the global skills in predicting good categorical answers (below or above). Few False Alarms are predicted, conversely more Missed Alarms are observed consistently with the overall model underestimation (Figure 1).

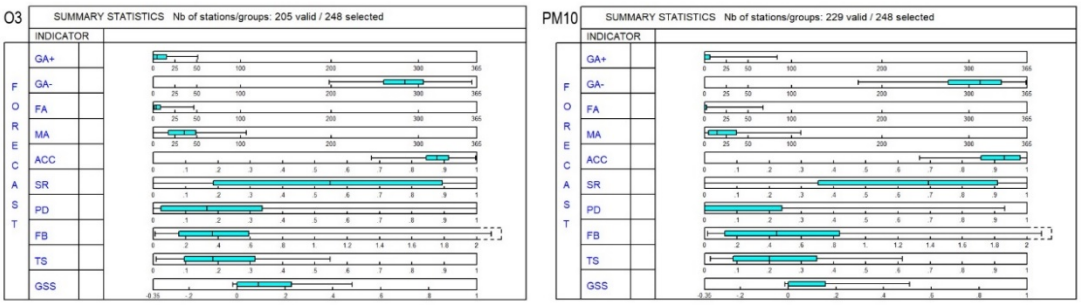

Figure 4. FORAIR-IT Forecast Summary Report for O_3 daily maximum of 8-hour average (left) and PM10 daily mean (right) concentrations

Assessment of modelling capability in predicting Air Quality Indices

The indicators presented in Figure 3 are based on a single threshold value. A simple multiple thresholds assessment is included in the proposed approach, based on Air Quality Indices, i.e a classification of concentrations levels into air quality categories commonly used for air quality forecasting purposes. More in detail, the number of days predicted by the forecast model in each category is compared with the corresponding number of measured ones. Figure 5 shows an example of the evaluation of FORAIR-IT, based on the EEA Air Quality Index table (https://www.eea.europa.eu/themes/air/air-quality-index/index). NO_2 and PM2.5 outcomes are presented at six monitoring stations, located in different geografical area and emission environments (i.e. rural, suburban, urban areas). In the context of a prevalent good agreement, a

general underestimation is observed, i.e. model values populate higher level categories to a lesser extent than the measured ones.

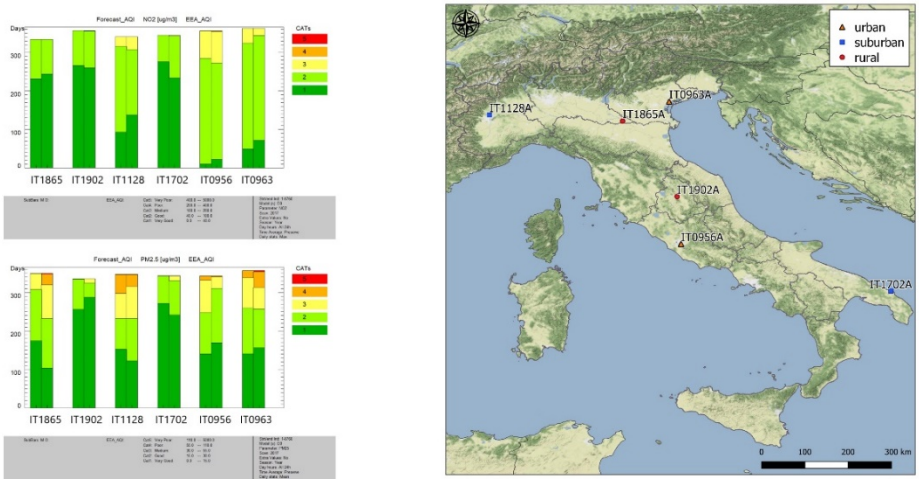

Figure 5. FORAIR-IT Forecast Air Quality Index Diagrams at six monitoring stations (right) for NO_2 daily maximum (upper left) and PM2.5 daily mean (lower left) concentrations

CONCLUSIONS

The FAIRMODE methodology for evaluating short-term forecasts of air quality, implemented in the DELTA Tool software, allows to detect 3 major capabilities which must be shown by a reliable forecast modelling system for a given application. One capability is to detect sudden changes of concentrations from day to day, which indicates that the model description is adequate to follow sharp changes of atmospheric variables. Another capability is to detect concentration threshold exceedances, which is the typical trigger of emergency measures applied by air quality managers for limiting emissions. The last capability is to reproduce multi-polluntant air quality indices, which are an effective way of presenting air quality to citizens. Both the methodology and the software are publicly available for testing and application, especially targeting European Member States and air quality forecasting services, like the Copernicus Atmospheric Monitoring Service.

REFERENCES

Adani, M., D'Isidoro, M., Mircea, M., Guarnieri, G., Vitali, L., D'Elia, I., Ciancarella, L., Gualtieri, M., Briganti, G., Cappelletti, A., Piersanti, A., Stracquadanio, M., Righini, G., Russo, F., Cremona, G., Villani, M.G., Zanini, G., 2022: Evaluation of air quality forecasting system FORAIR-IT over Europe and Italy at high resolution for year 2017. *Atmospheric Pollution Research*, **13**, 101456.

Boylan, J.W., Russel, A.G., 2006: PM and light extinction model performance metrics, goals, and criteria for three-dimensional air quality models. *Atmospheric Environment*, **40**, 4946-4959.

Janssen, S., Thunis, P., FAIRMODE Guidance Document on Modelling Quality Objectives and Benchmarking (version 3.3), EUR 31068 EN, Publications Office of the European Union, Luxembourg, 2022, ISBN 978-92-76-52425-0, doi:10.2760/41988, JRC129254.

Mittermaier, M. P., 2008: The Potential Impact of Using Persistence as a Reference Forecast on Perceived Forecast Skill. *Weather and Forecasting*, **23**, 1022-1031.

Monteiro, A., Durka, P., Flandorfer, C., Georgieva, E., Guerreiro, C., Kushta, J., Malherbe, L., Maiheu, B., Miranda, A.I., Santos, G., Stocker, J., Trimpeneers, E., Tognet, F., Stortini, M., Wesseling, J., Janssen, S., Thunis, P., 2018: Strengths and weaknesses of the FAIRMODE benchmarking methodology for the evaluation of air quality models. *Air Quality, Atmosphere & Health*, **11**, 373–383.

Pernigotti, D., Gerboles, M., Belis, C., Thunis, P., 2013: Model quality objectives based on measurement uncertainty. Part II: NO2 and PM10. *Atmospheric Environment*, **79**, 869-878.

Thunis, P., Pernigotti, D., Gerboles, M., 2013: Model quality objectives based on measurement uncertainty. Part I: Ozone. *Atmospheric Environment*, **79**, 861-868.

21st International Conference on
Harmonisation within Atmospheric Dispersion Modelling for Regulatory Purposes
27-30 September 2022, Aveiro, Portugal

AIR QUALITY (PM_{10}) SCENARIOS RESULTING FROM THE EXPANSION OF HYDROGEN FUEL CELL ELECTRIC VEHICLE IN EMILIA-ROMAGNA (NORTHERN ITALY)

Sara Fabbi[1], Giorgio Veratti[1,2] Alessandro Bigi[1] and Grazia Ghermandi[1]

[1] Dept. of Engineering "Enzo Ferrari", University of Modena and Reggio Emilia, Modena, Italy
[2] ARPAE-SIMC Servizio IdroMeteoClima, Bologna, Italy

Abstract: PM_{10} is a critical pollutant for the air quality in Emilia Romagna, a Northern Italy region that includes a large part of the Po Valley. The atmospheric levels of PM_{10} is strongly affected by vehicular traffic emissions, due to fuel exhaust and also to tires, brake and road surface wear, and to road dust resuspension (non-exhaust emissions). This study presents atmospheric PM_{10} scenarios deriving from vehicular traffic emissions in Emilia Romagna as resulting in 2030 from the growth of the Fuel Cell Electric Vehicle (FCEV) fleet in the region. Both exhaust and non-exhaust vehicular emissions are considered, evaluated according to the most up-to-date regional bottom-up emission inventory, which attributes about 60% of total primary PM_{10} traffic emissions to wear processes. PM_{10} concentration maps for actual (2019) and 2030 scenarios are obtained by both Eulerian and Lagrangian dispersion model (CHIMERE and PMSS). Preliminary results highlight the future impact on atmospheric PM_{10} from tires, brake and road surface wear produced by battery electric vehicles, due to their larger mass compared to FCEVs, which have smaller batteries and mass. These emissions will partially offset the lack of PM_{10} exhaust emissions for electric vehicles. Finally, the daily primary PM_{10} levels by traffic emissions simulated by PMSS and CHIMERE models were compared at specific sites relevant for the studied domain, i.e. the regulatory air quality monitoring stations.

Key words: PM_{10}, exhaust and non-exhaust traffic emissions, air quality, FCEV, electric vehicles

INTRODUCTION

According to the European Commission, cars are responsible for 12% of the continent's greenhouse gas emissions, making the switch to electric vehicles a key step in the EU strategy towards climate neutrality by 2050. The Commission, within its recently adopted "Fit for 55" package, planned a reduction in greenhouse gas emissions from cars by 55% by 2030 and to reach zero emissions from new cars by 2035. If only the exhaust emissions by a vehicle are considered, there is a clear local benefit in battery electric in terms of NO_x and PM_{10} and greenhouse gas emissions. However, vehicles emit also pollutants not related to the exhausts, e.g. particles due to the wear of tires, brakes and road surfaces, and these are becoming the most relevant emission of primary PM_{10} for gasoline-fuelled vehicles (Padoan et al., 2018). With the expected increase of electric vehicles in vehicular fleets, it is necessary to estimate the impact by their non-exhaust emissions on PM_{10} ambient levels.
Po valley is a large air pollution hotspot for Europe (EEA, 2020), where several impacts on public health and life expectancy by atmospheric pollutant were recorded (e.g. Vinceti, 2018; Khomenko et al., 2021). This study investigates primary PM_{10} scenarios due to the growth in hydrogen Fuel Cell Electric Vehicle (FCEV), in the Emilia-Romagna region (Northern Italy), which includes a large part of the Po Valley. The scenarios of the FCEV vehicle fleet used in the study are based on reports drafted at both the European and Italian level. A future scenario (referring to 2030) was compared with the current situation (referred to 2019). The impact of traffic emissions was simulated by the Parallel Micro SWIFT SPRAY modelling suite (PMSS, Arianet, Milan and Aria Technologies, Paris), mainly comprising a 3D a diagnostic weather model and a stochastic Lagrangian particle model. PMSS results were compared to reference simulations by the Eulerian photochemical model CHIMERE.

MATERIAL AND METHODS

Methodology to evaluate emission factors for abrasion and the total annual emission at 2030

The latest regional emissions inventory, referring to 2017 and providing the annual PM_{10} atmospheric emissions by traffic, was used in input of the dispersion models: these include both exhaust emissions (EE) and those from tire, break and road surface wear (hereafter non-exhaust emissions, NEE). For the 2019

scenario, a top-down spatial and temporal disaggregation procedure was applied to the emissions: the PM_{10} traffic emissions, originally assigned to each municipality, were attributed only to the grid cells on the main roads in that area. For the 2030 emission scenario, a bottom-up methodology was used, based on the vehicle fleet composition expected in 2030: the 2030 fleet was obtained by modifying the current fleet (i.e. 2019) according to the expected renewal rate and the entry of battery electric vehicles (BEVs), hybrid electric vehicles (HEVs) and FCEV vehicles. The total number of vehicles was left unchanged between 2019 and 2030, but different shares were applied for each category. For passenger cars (PC), the predicted share of BEV, HEV and FCEV in 2030, based on European and National studies, resulted in a 10%, 2.3% and 0.7% respectively, out of the 2 918 129 PC in the region. The same procedure was applied to heavy duty vehicles (HDV), road tractors (RT) and BUSes. In the region the share of electric and hydrogen-fuelled RT increased from 0.01% and 0.00% in 2019 to 9.8% and 0.9% in 2030. Electric and hydrogen-fuelled buses in 2019 were 0.2% and 0.0% respectively, and are expected to be 4.2% and 3.4% in 2030. In the following, with HDV+BUS we will refer to HDV, BUS and RT as well.
In drafting the annual PM_{10} emissions inventory updated to 2030, two different methodologies were followed, one for the EE and one for the NEE. For the EE, the class-dependent exhaust emission factor for PM_{10} (FE_{EE}) derived by COPERT 5 was applied to the expected fleet in 2030, based on its class composition, assuming an average annual distance of 14,000 km for the PC and about 40,000 for HDV+BUS. For NEE a non-linear relationship between the FE and the vehicle mass was assumed, based on Beddows et al. (2021), leading to the non-exhaust PM_{10} emission per unit mass. Mass for FCEV and BEV PC was assumed of 1.4 Mg and 1.8 Mg respectively (Timmers et al., 2016). While for hydrogen-powered RT a mass of 17 Mg was used, 21 Mg for electric RT, 16 Mg for hydrogen-powered BUS and 20 Mg electric BUS. For vehicles with internal combustion engine (ICE) the mass corresponding to the relevant subclasses (i.e. mini, small, medium and large) was used. For battery–equipped PCs the regenerative braking system (RBS) was also taken into account: this system allows the recharge the battery by recovering energy during deceleration and braking, reducing the wear of the brakes compared to traditional systems. Finally a specific FE_{NEE} was obtained for PC and HDV+BUS, allowing the calculation of the total annual NEE of PM_{10} for the Emilia Romagna region.

Modelling suites and model set-up
The impact of vehicular traffic emissions was assessed by the means of the Parallel Micro SWIFT SPRAY modelling suite (PMSS, Arianet, Milan and Aria Technologies, Paris, Trini Castelli et al., 2018). A modulation of both hourly and daily (weekdays, Saturdays and Sundays) emissions of the examined sources was applied. The simulation period covers the whole month of February 2019. For the calculation of the 3D wind and temperature fields, 20 vertical wind and temperature profiles obtained from the WRF-ARW meteorological model (Skamarock et al., 2008) were used, and also ground-based meteorological data collected from 12 stations of the ARPAE monitoring network. The simulation domain covers the entire Emilia Romagna region and part of the neighbouring regions and seas, for a total area of approximately 285 x 150 km^2, with a resolution of 500 x 500 m^2. The road network considered includes urban and extra-urban roads and motorways in Emilia Romagna.

RESULTS AND DISCUSSION

Emissions factors for abrasion and total annual emissions at 2030
The first results concern the FE_{NEE} of PM_{10} (FE_{NEE}) for the analysed vehicle types (PC, HDV, BUS and RT). Considering the average mass values of the various PC types representative of the 2030 vehicle fleet, the following average FE_{NEE} were obtained: 25.5 mg km^{-1} $vehic^{-1}$ for ICE, 24.4 mg km^{-1} $vehic^{-1}$ for BEV, 22.8 mg km^{-1} $vehic^{-1}$ for HEV and 21.7 mg km^{-1} $vehic^{-1}$ for FCEV. Regarding RT the FE_{NEE} values resulted: 120.0 mg km^{-1} $vehic^{-1}$ for ICE, 135.2 mg km^{-1} $vehic^{-1}$ for BEV and 118.6 mg km^{-1} $vehic^{-1}$ for FCEV. In the BUS category, the FE_{NEE} are 112.3 mg km^{-1} $vehic^{-1}$ for ICE, 128.4 mg km^{-1} $vehic^{-1}$ for BEV and 112.6 mg km^{-1} $vehic^{-1}$ for FCEV.
The total annual emissions of PM_{10} for the years 2019 and 2030 due to vehicular traffic were then compared, examining the emission due to exhaust and those due to abrasion for the considered vehicle categories. Total annual PM_{10} emission due to exhaust decreased in 2030 respect to 2019 of 52.4% for PC, from 347 to 178 Mg yr^{-1}, in line with the introduction of a large number of BEV and FCEV. A smaller decrease (26.6%, from 357 to 262 Mg yr^{-1}) was estimated for HDV+BUS, where the electric penetration is expected to be smaller.

Total annual PM_{10} NEE in 2030 results 1003 Mg yr^{-1}, assuming a 40% efficiency of the RBS. NEE in 2030, amounting to 1009 Mg yr^{-1}, are similar to 2019, as the introduction of electric and hydrogen vehicles will lead to a significant increase in the mass of the vehicle fleet. Similar results were obtained for HDV+BUS, for which a slight increase in total PM_{10} emissions was estimate, equal to 0.6%, from 349 in 2019 to 351 Mg yr^{-1} in 2030. Overall, the EE and NEE PM_{10} traffic emissions are expected to decrease of about 13%, from 2062 Mg vr^{-1} (2019) to 1794 Mg vr^{-1} (2030).

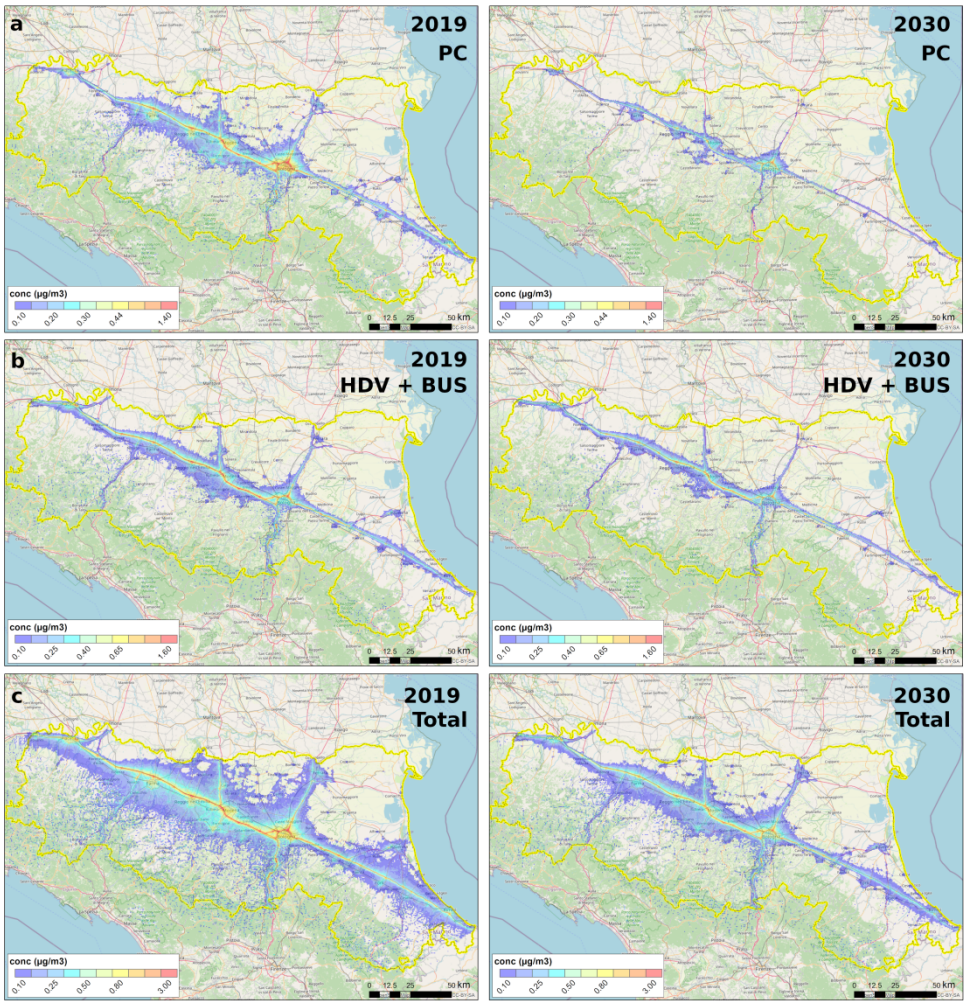

Figure 1. Concentration of primary PM_{10} at ground level (i.e. the first 4 m from the ground) due to traffic exhaust emissions of Passenger Cars (PC), Heavy Duty Vehicles, bus and road tractors (HDV+BUS), and their total, on February 15. The current scenario (2019) is on the left, the future scenario (2030) on the right.

PM_{10} concentration maps

Simulation maps of atmospheric concentration of primary PM_{10} at the ground level (i.e. within 4 metres from ground) due to EE for the current and the 2030 scenarios are presented in Figure 1, for PC and HDV+BUS. The results in Figure 1 refer to February 15, 2019, a day on which ARPAE observed high concentrations of atmospheric PM_{10} (mean level across urban and rural background sites: 67 ± 8 µg m^{-3}). These maps highlight a large decrease in PM_{10} concentration in the future scenario, particularly along the main motorway, the major roads and main urban areas.

The qualitative comparison between the concentration maps of Figure 1a (referring to PC) clearly shows the benefit on air quality of the renewal of the PC fleet. A decrease in concentration occurred, albeit minor, also for HDV+BUS (Fig. 1b), contributing to the overall improvement of air quality (Fig. 1c). Contrarily to EE, the variation in PM_{10} levels due to changes in NEE between the two scenarios is negligible, if compared to EE, for both PC and HDV+BUS.

Evaluation of the model simulations performance

At the location of the 51 air quality regulatory stations, we extracted the hourly time series of primary PM_{10} due to traffic (EE and NEE) simulated by PMSS for the lowest model layer (4 m from the ground). These hourly data were averaged to daily PM_{10}, since regulatory limits refer to this time interval and ARPAE at those 51 sites provides observations of daily PM_{10} levels (Directive EC 50/2008). These simulated PM_{10} levels by PMSS were compared with daily average values provided by a simulation run on the same domain by CHIMERE (Mailler et al., 2017), which was fed by COSMO meteorological fields and used the same emission inventory of PMSS. CHIMERE, contrarily to PMSS, provides estimates of atmospheric PM_{10} due to all the emission sources within the regional domain (e.g. traffic, industrial and non-industrial combustion, Saharan dust, etc...) and also estimates the formation of secondary PM_{10}. In order to compare the performance of the two models, the primary PM_{10} due to traffic emissions was extracted from the primary anthropogenic PM_{10}, which is directly provided in output by CHIMERE. To this end, based on the latest regional emission inventory, we computed the mean share of PM_{10} emissions by traffic (EE and NEE) over all PM_{10} anthropogenic emissions for urban polluted sites and suburban polluted sites, resulting 21% and 15%, and for rural (including some clean suburban sites) and remote sites, resulting 10.5% and 6% respectively. It was assumed that these percentages represent the fraction of primary PM_{10} due to traffic emissions respect the total primary anthropogenic PM_{10} simulated by CHIMERE in urban, rural and remote areas, respectively: this allowed the estimate of the daily primary PM_{10} by traffic from the CHIMERE output.

Table 1. Pearson's correlation coefficient (*r*) between PMSS and CHIMERE primary PM_{10} due to traffic emissions (exhaust and non exhaust) at ARPAE station sites. Type "urb" and "sub" indicate urban and suburban; "rur" indicates rural and clean suburban sites, "rem" indicates remote sites.

Station name	Type	*r*	*r*	Station name	Type	*r*	*r*
		1 – 28 Feb	9 – 24 Feb			1 – 28 Feb	9 – 24 Feb
Bogolese	urb	0.39	0.74	Timavo	urb	0.44	0.75
Cabina Mainsite	urb	0.15	0.39	Via Chiarini	urb	0.38	0.75
Caorle	urb	0.67	0.75	Villa Fulvia	urb	0.62	0.75
Ceno	urb	0.22	0.51	Zalamella	urb	0.74	0.80
Cittadella	urb	0.42	0.78	Castellarano	sub	0.62	0.76
De Amicis	urb	0.62	0.79	Cento	sub	0.74	0.82
Flaminia	urb	0.81	0.78	Remesina	sub	0.76	0.85
Franchini-Angeloni	urb	0.80	0.80	Badia	rur	0.61	0.79
Gerbido	urb	0.39	0.58	Besenzone	rur	0.44	0.34
Giardini	urb	0.73	0.87	Cabina Molinella	rur	0.70	0.73
Giardini Margherita	urb	0.11	0.37	Delta Cervia	rur	0.70	0.61
Giordani-Farnese	urb	0.48	0.73	Gavello	rur	0.50	0.51
Isonzo	urb	0.75	0.84	Gherardi	rur	0.59	0.56
Marecchia	urb	0.75	0.68	Lugagnano	rur	0.45	0.60
Montebello	urb	0.32	0.75	Malcantone	rur	0.58	0.61
Paradigna	urb	0.20	0.71	S. Rocco	rur	0.68	0.75
Parco Bertozzi	urb	0.68	0.82	San Pietro Capof.	rur	0.69	0.74
Parco Edilcarani	urb	0.56	0.82	Saragat	rur	0.41	0.55
Parco Ferrari	urb	0.78	0.87	Savignano	rur	0.82	0.77
Parco Montecucco	urb	0.51	0.65	Verucchio	rur	0.71	0.72
Parco Resistenza	urb	0.29	0.74	Castelluccio	rem	0.48	0.73
Porta San Felice	urb	0.36	0.61	Corte Brugnatella	rem	0.40	0.55
Roma	urb	0.40	0.71	Febbio	rem	0.41	0.68
S. Lazzaro	urb	0.46	0.82	San Leo	rem	0.71	0.71
San Francesco	urb	0.43	0.81	Savignano di Rigo	rem	0.51	0.67
San Lazzaro	urb	0.14	0.66				

Table 1 shows the linear correlations (estimated by the *r* Pearson's index) between the PMSS and CHIMERE simulated PM_{10} series derived as described above, for the entire month of February 2019 and for the central part of the month, 9 – 24 February 2019. In fact during the first week of February precipitations occurred in the region at several ARPAE air quality sites: since wet deposition processes were not considered in PMSS runs, during that period an overestimation of the concentrations by PMSS was observed. Linear correlation between PMSS and CHIMERE at the air quality sites is quite large, particularly over the period Feb 9 – 24: at 28 sites out of 51, *r* is larger or equal than 0.50, and the number

of sites increases to 48 if the central period of the simulation is considered. The correlation is largest at rural sites, likely due to the inability of CHIMERE in reproducing traffic peaks in urban areas.
Simulation performance was estimated according to the Root Mean Square Error (RMSE), the Mean Absolute Error (MAE) and the Normalised Mean Bias (NMB) computed on daily PMSS and CHIMERE simulations, using the latter model as a reference. Results show that the difference in RMSE and MAE increases from rural (median RMSE = 0.17 μg m^{-3}, median MAE = 0.13 μg m^{-3}) to urban sites (median RMSE = 0.63 μg m^{-3}, median MAE = 0.49 μg m^{-3}), highlighting the potential ability of PMSS in simulating the dispersion of primary pollutants over urban areas. NMB indicates larger PM_{10} estimates by PMSS at most urban sites (median NMB = 0.56 μg m^{-3}), while PMSS exhibited larger estimates than CHIMERE only at half of the rural sites, providing contrasting results for this site type, resulting in a median NMB and a mean NMB of –0.24 μg m^{-3} and 0.14 μg m^{-3}, respectively, partly due to the higher spatial resolution of PMSS.

CONCLUSIONS

In this work, a future emissive scenario (2030), in which the introduction of a large number of BEVs and FCEVs in the vehicle fleet is expected, is compared with the current one, referring to 2019. The renewal of the fleet brings a clear benefit to air quality, due to the reduction of exhaust emissions. Regarding non-exhaust emissions, no substantial differences are observed between the two scenarios, however the lower mass (by ~20%) of FCEVs compared to BEVs results in lower non-exhaust PM_{10} emission factors. The average daily concentrations of primary PM_{10} from traffic emissions (exhaust and non-exhaust) calculated by PMSS were compared with those calculated by CHIMERE over a focus period (February 2019) at regulatory air quality monitoring sites. The models show good agreement in the temporal behaviour of the concentrations, showing the effectiveness of the simulation obtained from PMSS.

ACKNOWLEDGEMENTS

The simulation with CHIMERE was performed within the PREPAIR project "LIFE15 IPE IT013" by the ARPAE-SIMC Servizio IdroMeteoClima. This study is supported by Regione Emilia Romagna and Landi Renzo spa by the project funded within the call 2019 of the programme "*Aiuti a favore della ricerca e sviluppo, art. 6 LR 14 /2014*".

REFERENCES

Beddows, D.C.S. and R.M. Harrison, 2021: PM_{10} and $PM_{2.5}$ emission factors for non-exhaust particles from road vehicles: Dependence upon vehicle mass and implications for battery electric vehicles. *Atmos. Environ.*, **244**, 117886.

EEA, 2020: Air quality in Europe — 2020 report. *EEA Report* 09/2020

Khomenko, S., M. Cirach, E. Pereira-Barboza, N. Mueller, J. Barrera-Gómez, D. Rojas-Rueda, and M. Nieuwenhuijsen, 2021: Premature mortality due to air pollution in European cities: a health impact assessment. *Lancet Planet. Health*, **5**, e121–e134.

Mailler, S., L. Menut, D. Khvorostyanov, M. Valari, F. Couvidat, G. Siour, S. Turquety, R. Briant, P. Tuccella, B. Bessagnet, A. Colette, L. Létinois, K. Markakis, and F. Meleux, 2017: CHIMERE-2017: from urban to hemispheric chemistry-transport modeling, *Geosci. Mod. Devel.*, **10**, 2397–2423

Padoan, E. and F. Amato, 2018: Vehicle Non-Exhaust Emissions: Impact on Air Quality, in *Non-Exhaust Emissions*, F. Amato editor, Academic Press, 21 – 65.

Skamarock, W., J. Klemp, J. Dudhia, D. Gill, D. Barker, M. Duda, X-Y. Huang, W. Wang, and J. Powers, 2008: A Description of the Advanced Research WRF V.3, NCAR Technical Note/TN-475+STR.

Timmers, V.R.J.H. and P.A.J. Achten, 2016: Non-exhaust PM emissions from electric vehicles, *Atmos. Environ.*, **134**, 10 – 17.

Trini Castelli S., P. Armand, G. Tinarelli, C. Duchenne and M. Nibart, 2018: Validation of a Lagrangian particle dispersion model with wind tunnel and field experiments in urban environment, *Atmos. Environ.*, **193,** 273 – 289.

Vinceti M., M. M.Werler, T. Filippini, G. De Girolamo, G. Ghermandi, S. Fabbi, G. Astolfi and S. Teggi, 2018: Adverse pregnancy outcomes in women with changing patterns of exposure to the emissions of a municipal waste incinerator. *Environ. Res*., **164,** 444 – 451.

21st International Conference on
Harmonisation within Atmospheric Dispersion Modelling for Regulatory Purposes
27-30 September 2022, Aveiro, Portugal

MODELLING BASED METHOD FOR ASSESSING THE REPRESENTATIVENESS OF AIR QUALITY MONITORING STATIONS

Jeleniewicz G., Strużewska J., Kamiński J.W., Jagiełło P., Gienibor A., Kawka M., Norowski A.

Institute of Environmental Protection – National Research Institute, Warsaw, Poland

Abstract:
The representativeness of a station is not precisely defined. The concept is not standardised in national legislation, or in practice applied by other European Union countries.
In Poland, the area of representativeness for each monitoring site is determined using the modelling and additional proxies:
1. The area of analysis was limited to a radius range depending on the type of station and air pollutant,
2. The cross-correlation field of modelled concentrations at each computational grid with modelled concentrations at measurement sites was calculated based on 1-hour data,
3. A ventilation index limits the area of representativeness based on the relative height difference not exceeding 50 m,
4. The total pollutant emissions are between 10^{-1} and 10^{1} values of the total emission flux in the grid square corresponding to the station location. If the total emission flux was zero at the station location, an area was used where the total emission value did not exceed the percentile value of 25 of the emissions within the assumed radius for the station,
5. The area of spatial representativeness is limited due to the land use category assigned to the station type. Land use categories are established based on CORINE Land Cover and the national spatial database of topography.
The common part of the areas mentioned above defines the zone of representativeness of the site.
The representativeness of a station is not precisely defined.

Keywords: *Spatial representativeness, Poland, air quality modelling, monitoring stations*

INTRODUCTION

Air monitoring networks are essential in air quality management spatial representativeness (SR) of monitoring stations is the basis of configuring monitoring networks. The evaluation of the SR of monitoring stations is essential where monitoring networks are used to estimate the number of people and extent of ecosystems exposed to the air pollution measured by a monitoring station. Therefore, to estimate the health and ecosystem impact of air pollution.
The requirement of establishing SR areas is due to the Ambient Air Quality Directive 2008/50/EC (AAQD). There is no specific methodology for SR areas in AAQD; thus, each member state uses their approach.
In Poland, the Institute of Environmental Protection National Research Institute has been responsible for a methodology of SR areas and its implementation since 2018. Our method is based on air quality modelling extended with additional spatial criteria.
Air quality modelling results are used to obtain a correlation between concentrations in site spots with other concentrations. The correlation field is calculated for each monitoring station and each pollution separately based on 1 hour modelling values.
Additional spatial criteria limiting the SR area take into account: radius range depending on the station and air pollutant type, a ventilation index, the total pollutant emissions and the land use category assigned to the station.

DATA SOURCES AND TOOLS

The air quality model GEM-AQ (Kaminski et al., 2008) was used to calculate the concentrations of pollutants at the surface from which the correlation field was obtained. Calculations with the GEM-AQ model were performed on a variable resolution grid, with approximately 2.5 km resolution over Poland.

The 2020 meteorological fields were used for all model simulations for this analysis. Local emission inventory was used over the area of Poland (CBE-Central Base of Emissions) inventory developed for 2019 by the National Balancing and Emissions Management Centre of IEP-NRI. With regard to anthropogenic emissions, data reported by member countries under the LRTAP Convention, at a resolution of 0.1° x 0.1° (approx. 10 km) for the year 2018, were used for the European area outside Poland. Outside Europe, ECLIPSE emissions prepared by IIASA were used.

All spatial analyses were performed using GIS tools. The following data sources were used for the criteria: Corine Land Cover

- BDOT10k (https://www.geoportal.gov.pl/dane/baza-danych-obiektow-topograficznych-bdot)
- Location of monitoring stations (https://powietrze.gios.gov.pl/pjp/maps/measuringstation)
- DEM for Poland (https://www.geoportal.gov.pl/dane/numeryczny-model-terenu)
- Local emission inventory for Poland (IEP-NRI)

METHODOLOGY

SR area of monitoring stations can be interpreted as the actual variability of pollutants sufficient to estimate the level of air pollution in a given zone. Thus our methodology is based on five spatial criteria. Figure 1. shows an example of all criteria for a monitoring station in a town in western Poland – Swiebozdin. Each of the criteria is described below

The area of analysis was limited to a radius range depending on the type of station and air pollutant

This criterion assumes that for each station the area the analysis is limited to the radius resulting from the surface area for which the station should be representative according to Annex 3 of the Regulation of the Minister of Climate and Environment of 11 December 2020 on the assessment of the levels of substances in the air. A summary of the information is given in Table 1. The area size for which the conditions of representativeness are expected to be met was estimated, and the radius was then calculated, assuming a circular shape of the area. The minimum radius of representativeness thus estimated was increased by a factor of 2 to 3, assuming that part of the area within the minimum representativeness circle may not be representative due to land use and emission distribution. Further enlargement of the radius of representativeness is not advisable. As a result, it may include areas where chemical ageing processes of the air mass begin to dominate.

Table 3. Maximum range of representativeness assessed under the Regulation of the Minister of Climate and Environment of 11 December 2020 on the assessment of levels of substances in the air and expert assessment

Pollution	Station type	Area	Range - radius [m]	factor	Radius [m]
C6H6, NO2, SO2, Pb, As, Cd, Ni, B(a)P, PM10, PM2.5, CO	Health protection – urban background	few km2	1 800	3	5 400
C6H6, NO2, SO2, Pb, As, Cd, Ni, B(a)P, PM10, PM2.5, CO	Health protection – rural	less than 5 km from agglomerations or industrial installations	5 000	2	10 000
NOx, SO2	Plant protection	at least 1 000 km2	17 800	2	35 600
C6H6, NO2, SO2, Pb, As, Cd, Ni, B(a)P, PM10, PM2.5, CO	Traffic	at least 200 m2	1000 (maximum impact area based on expert judgment)	1	1 000
C6H6, NO2, SO2, Pb, As, Cd, Ni, B(a)P, PM10, PM2.5, CO	Industrial urban	250 m × 250 m	1 800 (same as background stations)	3	5 400

C6H6, NO2, SO2, Pb, As, Cd, Ni, B(a)P, PM10, PM2.5, CO	Industrial suburban	250 m × 250 m	5 000 (same as background stations)	2	10 000
O3	Health protection – urban	Ara of few km2	1 800	3	5 400
O3	Health protection Plant protection - suburban	an area of dozens of km2	5 600	2	11 200
O3	Health protection Plant protection - rural	an area of several hundred km2	17 800	2	35 600
O3	Health protection Plant protection – regional background	Area from 1 000 to 10 000 km2	56 400	2	112 800

The cross-correlation field of modelled concentrations at each computational grid with modelled concentrations at measurement sites was calculated based on 1-hour data

In Poland, air quality modelling of transport and transformation of pollution in the air is a part of the support of the national system under the POŚ Act, a key aspect of the methodology is the consideration of modelling results. The modelling results for the station representativeness were used to determine the correlation field. The correlation field of modelled concentrations with modelled concentrations at gauging stations was calculated separately for each station and each pollutant based on modelled 1-hour values according to the formula:

$$AF(i,j) = \frac{\sum_{t=1}^{H}\left[C_{st}(t)\cdot C_{i,j}(t) - \overline{C_{st}}\cdot\overline{C_{i,j}}\right]}{\sqrt{\sum_{t=1}^{H}\left(C_{st}(t) - \overline{C_{st,}}\right)^2 \cdot \sum_{t=1}^{H}\left(C_{i,j}(t) - \overline{C_{i,j}}\right)^2}} \quad (1)$$

Where:
$C_{st}(t) =$ the concentration value in the grid cell at corresponding *st* station location in *i* time step
$\overline{C_{st}} =$ annual average concentration in the grid cell corresponding to the st station location
$C_{i,j}(t) =$ the concentration value in the grid cell of coordinates *i,j* at time *t*
$\overline{C_{i,j}} =$ annual average concentration in the grid cell of coordinates i,j
$H =$ number of time steps (1h time step, for the whole year)

A ventilation index limits the area of representativeness based on the relative height difference not exceeding 50 m

Due to the great importance of topography for the processing conditions, a criterion was introduced for the relative height difference in the area of influence according to the formula.

Z < Z station location + 50m, where:
Z – relative height of the terrain
Zstation – absolute height of a station

Emissions criterium

Due to the important influence of emissions on the actual variability of air pollutant concentrations, a criterion based on emission data of the pollutant under consideration or its precursors in the case of ozone and benzene has also been introduced. This criterion limits the area of representativeness using emission limit values calculated based on the pollutant's emission values at the site. The criterion results in an area where the total emission of the pollutant is between 10-1 and 101 of the total emission flux values in the grid square corresponding to the site location. Where the total emission flux was zero at the site location, an area was used where the total emission value did not exceed a percentile value of 25 from the emissions within the assumed radius for the site.

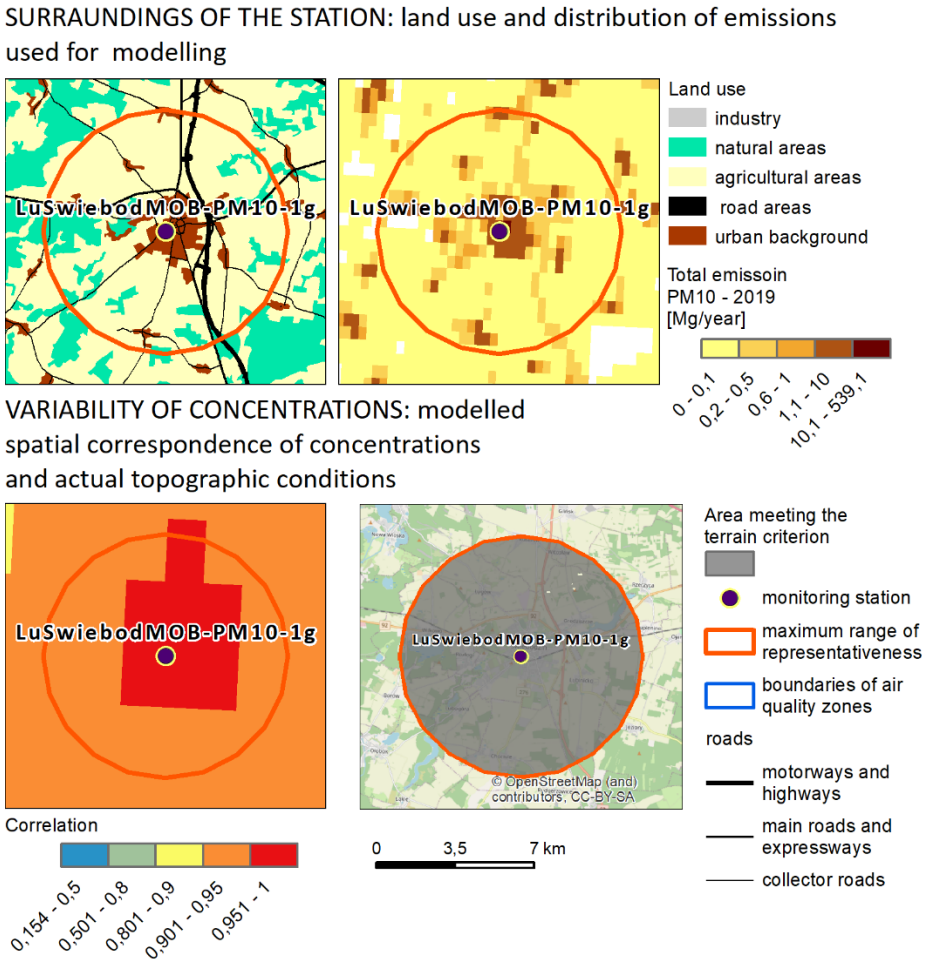

Figure 1. Characteristics of the surroundings monitoring site: surface use, distribution of PM10 emissions, the spatial distribution of correlations of modelled concentrations with concentrations modelled at the PM10 measurement site, actual topographic

Land use criterium

The area of spatial representativeness is limited due to the land use category assigned to the station type. Land use categories are established based on CORINE Land Cover and the Database of Topographic Objects (BDOT10k). Based on Corine LandCover 2018 (CLC2018), classes were created:

- urban development (Corine Land Cover codes: 1.1, 1.4, 1.2.3, 1.2.4);
- agricultural land (Corine Land Cover codes: 2);
- natural areas (including forests and water bodies) (Corine Land Cover codes: 3,4,5).
- industrial sites (Corine Land Cover codes:1.2.1, 1.3);

A spatial layer of roads was used from the Database of Topographic Objects (BDOT10k), based on which areas with a width of 500 m were created, limiting the range of representativeness in the case of traffic stations.

It was necessary to extend the area for stations located in spa/resort areas because if only urban development were selected (which implies a health exposure), the stations would be located outside the representativeness area.

RESULTS

There are almost 300 measurement stations in Poland. Each year the area of representativeness is determined for a different set of monitoring stations. The SR area is the common part of the areas resulting from the criteria presented above.

As regards the modelling results, the methodology assumed the use of a correlation function between the modelled values of one-hour concentrations in the grid square corresponding to the station location and the grid squares in the surrounding area. The area of representativeness presented for two thresholds of such spatial correspondence measure - 0.95 and 0.90.

The area satisfying the condition of correlation of modelled concentrations with concentrations modelled at the measurement stations was then limited by taking into account the surface use conditions corresponding to the station type and topographic conditions potentially affecting ventilation. In addition, emission data were taken into account, based on which the area in which the total emission of a pollutant is contained in the range from 10^{-1} to 10^{1} of the value of the total emission flux in the grid square corresponding to the location of the station was determined. In the case where the total emission flux was zero at the site location, an area was used in which the total emission value did not exceed the percentile value of 25 of the emissions within the assumed radius for the site.

The methodology allows us to map the specifics of individual pollutants and station types.

Figure 2 shows the differentiation of the representativeness areas for one station (in Swiebodzin in western Poland) but with different pollutants.

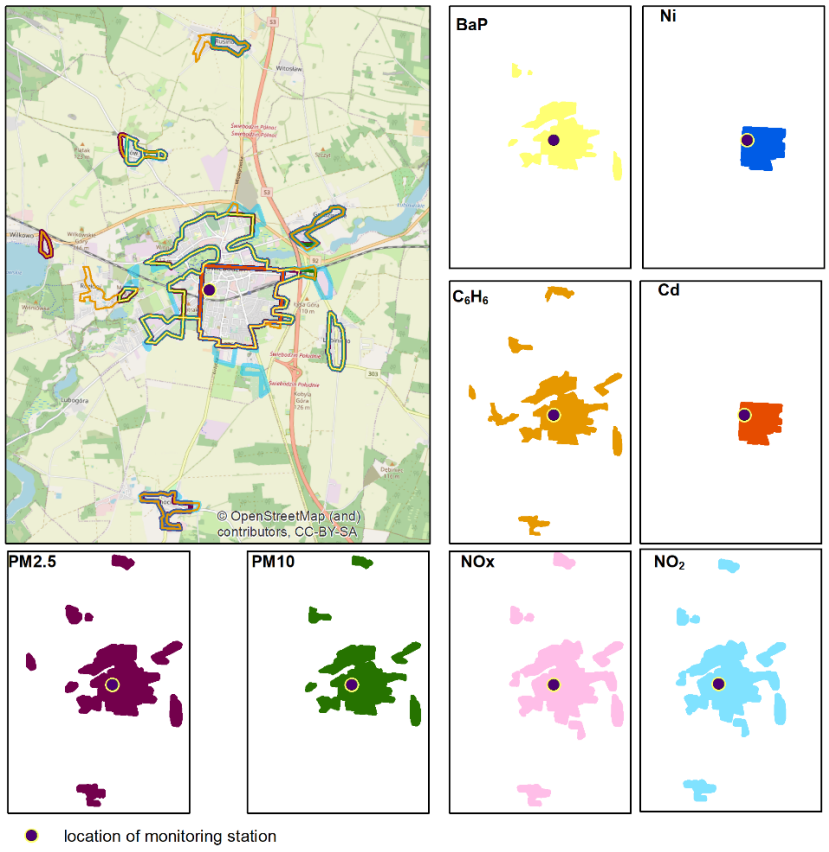

Figure 2. Variability of the SR area for a monitoring station depending on the pollutant

REFERENCES

Kaminski, J. W., Neary, L., Struzewska, J., McConnell, J. C., Lupu, A., Jarosz, J., Toyota, K., Gong, S. L., Côté, J., Liu, X., Chance, K., and Richter, A., 2008: GEM-AQ, an on-line global multiscale chemical weather modelling system: model description and evaluation of gas phase chemistry processes, *Atmos. Chem. Phys.*, **8**, 3255-3281, https://doi.org/10.5194/acp-8-3255-2008.

21st International Conference on
Harmonisation within Atmospheric Dispersion Modelling for Regulatory Purposes
27-30 September 2022, Aveiro, Portugal

FAIRMODE CT8 EXERCISE ON ASSESSMENT OF SPATIAL REPRESENTATIVENESS OF MONITORING STATIONS

Stijn Janssen, Giovanni Bonafè, Antonio Piersanti, Lina Vitali, Kristina Eneroth, Jutta Geiger, Sabine Wurzler, Roberta Amorati, Michele Stortini, Leonor Tarrason, Philippe Thunis

SHORT ABSTRACT

Abstract title: FAIRMODE CT8 exercise on assessment of Spatial Representativeness of monitoring stations

Name and Affiliation of the First Author: Stijn Janssen, VITO, Boeretang 200, 2400 Mol, Belgium

Email of first author: stijn.janssen@vito.be

Names and Affiliations of the Co-authors: Giovanni Bonafè, (ARPA-FVG, IT), Antonio Piersanti, Lina Vitali (ENEA, IT), Kristina Eneroth, (Stockholm, SE), Jutta Geiger, Sabine Wurzler, (North Rhine-Westphalia, DE), Roberta Amorati, Michele Stortini (ARPAE, IT), Leonor Tarrason (NILU, NO), Philippe Thunis (JRC, EU) on behalf of the FAIRMODE-CT8 community

Abstract

The assessment of the spatial representativeness (SR) of monitoring stations has been discussed within the air quality community for a long time. FAIRMODE has been involved in this discussion since the early days, given the potential role of modelling in this assessment process and the relevance of SR in any process where observations from monitoring stations are combined with modelling (validation, data fusion or data assimilation…).

Over the last years progress has been made within the FAIRMODE community to more clearly identify the various application fields of SR (population exposure, exceedance situations, monitoring network design, model validation,…) and the concept of a SR area was put forward which serves many purposes of these application domains. Eventually a definition was proposed to practically delineate SR areas of monitoring stations. The proposed methodology is based on (fit-for-purpose) modelling results and follows a discontiguous approach to allocate an SR area within the boundaries of the air quality zones defined under the EU Ambient Air Quality Directive (AAQD). The simple and robust assessment method relies on annual averaged concentration fields within a given margin of tolerance to identify the SR area.

Various modelling teams of the FAIRMODE CT8 community have evaluated and tested the methodology for various monitoring stations in Europe, covering the whole spectrum of rural, urban background and traffic sites. Based on the findings of the CT8 exercise, the proposed methodology was further refined and is now being proposed as the approach to be used under the revised AAQD. In addition extensions of the methodology are proposed which will be further evaluated by the CT8 group on its scientific value and practical implementation in the context of the AAQD.

21st International Conference on
Harmonisation within Atmospheric Dispersion Modelling for Regulatory Purposes
27-30 September 2022, Aveiro, Portugal

BENCHMARK ON METHODOLOGIES TO INTEGRATE LOW-COST SENSOR NETWORKS WITH OFFICIAL MEASUREMENTS TO IMPROVE (MODELLED) AIR QUALITY MAPS

Joost Wesseling, Alicia Gressent, Anil Namdeo, Assa Camara, David Roet, Fabian Lenartz, Jorge Sousa, Pascal Joassin, Philipp Schneider, Philippe Thunis, Sjoerd van Ratingen, Stig Hellebust, Stijn Janssen, Stijn Vrankx, Vera Rodrigues, Wouter Hendricx

SHORT ABSTRACT

Benchmark on methodologies to integrate low-cost sensor networks with official measurements to improve (modelled) air quality maps

Name and Affiliation of the First Author: Joost Wesseling (RIVM, NL)

Email of first author: joost.wesseling@rivm.nl

Names and Affiliations of the Co-authors: Alicia Gressent (INERIS, FR), Anil Namdeo (U. Northumbria, UK), Assa Camara (SHMU, SK), David Roet (VMM, BE), Fabian Lenartz (ISSeP, BE), Jorge Sousa (VITO, BE), Pascal Joassin (ISSeP, BE), Philipp Schneider (NILU, NO), Philippe Thunis (JRC, EU), Sjoerd van Ratingen (RIVM, NL), Stig Hellebust (UC. Cork, IE), Stijn Janssen (VITO, BE), Stijn Vrankx, (VITO, BE), Vera Rodrigues (U. Aveiro, PT), Wouter Hendricx (RIVM, NL)

Abstract text

Low-cost air quality sensors are becoming very relevant for the air quality community because of the unique spatial and temporal measurement coverage they offer. In particular, methodologies to integrate results of sensor networks with modelled data and official measurements are of great interest.

In the European Forum for Air quality Modeling (FAIRMODE), a benchmarking exercise has been organized to discuss and understand the strengths and weaknesses of the different ways low-cost sensors can be used. Present experiences suggest important roles for data fusion and assimilation approaches, and possibly other techniques with similar scopes. The focus points for this benchmark are to 1) Exchange potential concepts and best practices about the integration of sensor network data in air quality mapping methods and 2) Explore how air quality modelling can contribute to the exploitation and validation of an air quality sensor network.

Since end of 2020, groups from several European countries are working on the benchmarking exercise using data from some 1500 stationary PM2.5 sensors. The first

steps are data validity and calibration. After that, focus is on different approaches to combine the calibrated sensor data with official measurements and models. In order to objectively compare results from different calibration schemes, synthetic sensor data is created using the behaviour of real-world sensors. The first results of the benchmark will be presented and discussed.

21st International Conference on
Harmonisation within Atmospheric Dispersion Modelling for Regulatory Purposes
27-30 September 2022, Aveiro, Portugal

UNSTEADY URBAN MICROSCALE SIMULATIONS OF AIR POLLUTION FOR A FULL YEAR AND ITS PLATFORM FOR HARMONISATION

Zoltán Horváth, László Környei, Mátyás Constans, Bence Liszkai, Ákos Kovács, Tamás Budai, and Csaba Tóth

SHORT ABSTRACT

Abstract title: Unsteady urban microscale simulations of air pollution for a full year and its platform for harmonisation

Name and Affiliation of the First Author: Zoltán Horváth, Széchenyi István University, Győr, Hungary

Email of first author: horvathz@math.sze.hu

Names and Affiliations of the Co-authors: László Környei, Mátyás Constans, Bence Liszkai, Ákos Kovács, Tamás Budai, and Csaba Tóth, Széchenyi István University, Győr, Hungary

Abstract text *(maximum 350 words.)*

In this paper two approaches will be presented for the unsteady microscale simulations that assess compliance with AAQD requirements for NO2. Both methods compute the 3D unsteady Navier-Stokes (one the incompressible and the other the compressible) equations for the wind velocity field for the urban domain and then solve the dispersion equations with time dependent vertical diffusion coefficients. The method for the incompressible fluids is implemented in OpenFOAM and runs on clusters or even real HPC machines, while the other one with the in-house Fluid-Solver that runs on multicore CPU and GPU. The latter solver has a reduced order mode for the wind-field computations, too, which uses proper orthogonal decomposition of the flow state variables and can be interpreted as a machine learning method applied to the Navier-Stokes equations. Both algorithms and codes were optimized mainly in the HiDALGO-project.

The implementation and the used hardware enable us to get one day air pollution time-series and maps within half an hour with the OpenFOAM version for a 1 meter resolution computational mesh and within 5 minutes with the Fluid-Solver for a 5 meter resolution map on the standard domain of Antwerp used in the FAIRMODE Intercomparison Exercise. We ran both solvers for the full year of 2016 for Antwerp and the full 2021 for Győr, demonstration city in the HiDALGO-project. In the paper we shall provide details of the simulations and discuss the results.

In the paper we shall present an open framework as well to set up the main parameters of the physical model, the configuration of the solvers, and the computational domain. This framework has a web-based user interface, which supports the full AAQD assessment as well. Also, the framework seems suitable to compare different simulation methodologies for the same air pollution task. We shall demonstrate this feature by running and evaluating two scenarios arising from different physical modelling methodologies of the literature for the dispersion with OpenFOAM.
Finally, we shall show results to some cities from Austria, Germany, Hungary, and the Netherlands (data sources: geometry: OpenStreetMap, boundary wind: ECMWF, emission data: open inventories, or synthetic).

21st International Conference on
Harmonisation within Atmospheric Dispersion Modelling for Regulatory Purposes
27-30 September 2022, Aveiro, Portugal

THE SENSITIVITY TO FOUR DIFFERENT EMISSION INVENTORIES ON AIR QUALITY INDICES IN EUROPE

Alexander de Meij, Kees Cuvelier, Enrico Pisoni, P. Thunis, Bertrand Bessagnet

SHORT ABSTRACT

The sensitivity to four different emission inventories on air quality indices in Europe.

Alexander de Meij; MetClim, Varese, Italy

Alexander.de-meij@ext.ec.europa.eu

Kees Cuvelier; Enrico Pisoni, P. Thunis, Bertrand Bessagnet, European Commission, Joint Research Centre (JRC), Ispra, Italy*

**Retired with Active Senior agreement*

Abstract

The sensitivity to different emission inventories on particulate matter (PM) and ozone is evaluated using the EMEP model for 2015 over Europe. We run the model with Edgar_v5.0, CAMS2.2.1, CAMSV4.2 and EMEP-GNFR emission inventories, all for the year 2015. The model domain stretches from -15.05° W to 36.95° E longitude and 30.05° N to 71.45° N latitude with a horizontal resolution of 0.1° x 0.1°. The EMEP model uses meteorological initial conditions and lateral boundary conditions from the European Centre for Medium Range Weather Forecasting (ECMWF-IFS).

We reduced the emissions of NOx, PPM, VOCs, NH3 and SOx by 25% and 50% for each species separately for seven cities (Brussels, Madrid, Rome, Bucharest, Athens, Berlin and Stockholm) and two regions (Malapolska, Poland and Po Valley, Italy) to study the impact on particulate matter (PM) formation. Similar, we reduced NOx and VOCs by 25% and 50% separately to study the impact of these reductions on O3 formation.

It is important to understand the uncertainties in air quality modelling of using different emission inventories in modelling exercises, such as the Forum of Air Quality Modelling in Europe (FAIRMODE). Since often it is difficult to identify the superiority of a specific emission inventory.

21st International Conference on
Harmonisation within Atmospheric Dispersion Modelling for Regulatory Purposes
27-30 September 2022, Aveiro, Portugal

HOW DO THE REDUCTION EMISSION MEASURES OF THE SPANISH NATIONAL AIR POLLUTION CONTROL PROGRAMME IMPACT ON STREET-LEVEL AIR QUALITY IN THREE NEIGHBOURHOODS OF MADRID (SPAIN)?

Jose-Luis Santiago, Esther Rivas, Beatriz Sanchez, Marta G. Vivanco, Mark R. Theobald, Juan Luis Garrido, Victoria Gil, Alberto Martilli, Alejandro Rodríguez-Sánchez, Riccardo Buccolieri, Ana R. Gamarra, Yolanda Lechón, Eugenio Sánchez, Fernando Martín

SHORT ABSTRACT

Abstract title: How do the reduction emission measures of the Spanish National Air Pollution Control Programme impact on street-level air quality in three neighbourhoods of Madrid (Spain)?

Name and Affiliation of the First Author: Jose-Luis Santiago[1]

[1]Atmospheric Modelling Unit, CIEMAT, Av. Complutense, 40, 28040 Madrid, Spain

Email of first author: jl.santiago@ciemat.es

Names and Affiliations of the Co-authors: Esther Rivas[1], Beatriz Sanchez[2], Marta G. Vivanco[1], Mark R. Theobald[1], Juan Luis Garrido[1], Victoria Gil[1], Alberto Martilli[1], Alejandro Rodríguez-Sánchez[1], Riccardo Buccolieri[3], Ana R. Gamarra[4], Yolanda Lechón[4], Eugenio Sánchez[5], Fernando Martín[1]

[1] Atmospheric Modelling Unit, CIEMAT, Av. Complutense, 40, 28040 Madrid, Spain.
[2] Department of Geography, National University of Singapore, Singapore.
[3] Dipartimento di Scienze e Tecnologie Biologiche ed Ambientali, University of Salento, Lecce, Italy.
[4] Energy Systems Analysis Unit, Energy Department, CIEMAT, Av. Complutense, 40, 28040 Madrid, Spain.
[5] Application and Computer Systems Development Unit, Department of Technology, CIEMAT, Av. Complutense, 40, 28040 Madrid, Spain

Abstract text *(maximum 350 words.)*

European countries are committed to reduce annual pollutant emissions to meet the EU limit values regulated under the Air Quality Directive and each country has developed a national programme that includes a set of planned measures. In Spain, the 1st National Air Pollution Control Programme (NAPCP) establishes a set of existing and additional measures of emission reductions related to different sectors (electricity generation, road and off-road transport, agriculture, etc.). In this context, the objective of the present study is to assess the impact of different measures on air quality at the street scale in three highly polluted neighborhoods in Madrid. Several emission scenarios are evaluated, including

the projections for 2030 in the 1st Spanish NAPCP with existing and additional measures, as well as individual measures related to the road transport sector (an increased use of biofuels and a full penetration of the electric car). A numerical methodology based on computational fluid dynamics (CFD) simulations driven by mesoscale meteorological and air quality simulations is used to compute annual average pollutant concentrations at high spatial resolution for the various emission scenarios. The effects of the measures on air quality are computed as the differences in pollutant concentrations between emission-reduction scenarios and the base case (current emissions) under the same meteorological conditions. In addition, the health impact benefits of these measures are estimated based on these results. It is observed that the spatially-averaged annual mean NO_2 concentrations over the entire neighborhoods (similar to the mean concentration at coarse spatial resolution) exceeds the EU limit value for the base case, but these exceedances disappear for the scenario with additional measures projected to 2030. This is in agreement with the mesoscale results. However, despite the spatially-averaged annual mean concentration not being exceeded for the latter scenario, there are still areas within two neighborhoods where the annual average concentrations are above the limit value. This issue highlights the importance of assessing the impacts of emission reduction measures on air quality at high spatial resolution using CFD modelling.

21st International Conference on
Harmonisation within Atmospheric Dispersion Modelling for Regulatory Purposes
27-30 September 2022, Aveiro, Portugal

NO2 RESPONSE TO EMISSION REDUCTION SCENARIOS - COMPARING BRUTE FORCE AND TAGGING SOURCE APPORTIONMENT METHODS

Joana Ferreira, Sílvia Coelho, Diogo Lopes, Guido Pirovano

SHORT ABSTRACT

Abstract title: NO_2 response to emission reduction scenarios - comparing brute force and tagging source apportionment methods

Name and Affiliation of the First Author: Joana Ferreira, CESAM & Department of Environment and Planning, University of Aveiro, Portugal

Email of first author: jferreira@ua.pt

Names and Affiliations of the Co-authors: Sílvia Coelho[1], Diogo Lopes[1], Guido Pirovano[2] [1] CESAM & Department of Environment and Planning, University of Aveiro, Portugal

[2] Sustainable Development and Energy Sources Modelling and Air Quality UnitRicerca sul Sistema Energetico - RSE S.p.A, Milan, Italy

Abstract text *(maximum 350 words.)*

In the scope of FAIRMODE source-apportionment crosscutting activity, a modelling exercise has been performed to investigate the behaviour of the different source apportionment (SA) methods regarding NO_2, namely by analysing the NO_2 response for different scenarios and different modelling frameworks. This work presents a contribution to the referred exercise, by the application of CAMx air quality model to the Aveiro region in Portugal, at 1 km^2 spatial resolution. A winter period (22 days in December 2017), with high NO_2 concentrations registered in the air quality monitoring stations of the area, was selected, and the two main activity sectors contributing to NOx emissions were considered – industry and road transport. According to the FAIRMODE exercise guidelines, a set of 24 scenarios were run, as a Brute Force (BF) SA method, considering 25, 50, 75 and 100% (4 strengths) emission reductions of NOx and all pollutants (2 types of reduction), for the two sectors separately and combined (3 options). Additionally, the CAMx Ozone Source Apportionment Technology (OSAT) was applied, as a SA tagging method, to allow a comparison of both approaches for NO_2 concentrations. The results were analysed in three locations corresponding to the air quality measurement sites existing in the region (a traffic, an industrial and a suburban background station)

BF outputs showed a consistency of NO_2 response to the range of emission reductions (0- 100%) and an additivity regarding impacts of the two sources. The preliminary comparative analysis reveals differences between the two applied SA methods. The tagging approach shows a higher contribution of industry and a lower contribution of road transport than the BF impact on NO_2 concentrations. When the emission reduction is applied in both sectors simultaneously, the BF method leads to a higher impact on NO_2

levels. This exercise highlights the need for a better understanding of the usefulness and limitations of SA, for an adequate applicability of those methods for air quality management support.

21st International Conference on
Harmonisation within Atmospheric Dispersion Modelling for Regulatory Purposes
27-30 September 2022, Aveiro, Portugal

THE FAIRMODE CT4: INTERCOMPARISON EXERCISE OF URBAN MICROSCALE MODELS AND METHODOLOGIES FOR DERIVING ANNUAL POLLUTANT CONCENTRATIONS DISTRIBUTION WITH VERY HIGH SPATIAL RESOLUTION

Fernando Martin , Kees Cuvelier; Philippe Thunis, José Luis Santiago, Esther Rivas, Jenny Stocker, Rose Jackson, Felicita Russo, Maria Gabriella Villani, Gianni Luigi Tinarelli, Daniela Barbero, Roberto San Jose, Juan Luis Pérez-Camanyo, Gabriela Sousa Santos, John G. Bartzis, Ioannis A. Sakellaris, Nicola Masey, Scott Hamilton, Zoltán Horváth, László Környei, Bence Liszkai, Ákos Kovács

SHORT ABSTRACT

The FAIRMODE CT4: Intercomparison Exercise of Urban Microscale Models and Methodologies for deriving annual pollutant concentrations distribution with very high spatial resolution

Fernando Martín; CIEMAT, Research Center for Energy, Environment and Technology, Avenida Complutense 40, 28040 Madrid, Spain,

E-mail: fernando.martin@ciemat.es

Stijn Janssen, Jorge Sousa; VITO NV, Flemish Institute for Research and Technology. Boeretang 200, 2400 Mol, Belgium

Kees Cuvelier; Philippe Thunis, European Commission, Joint Research Centre (JRC), Ispra, Italy*

José Luis Santiago, Esther Rivas; CIEMAT, Avenida. Complutense 40, 28040 Madrid, Spain, Jenny Stocker, Rose Jackson; Cambridge Environmental Research Consultants (CERC), UK
Felicita Russo, Maria Gabriella Villani; ENEA, Italian National Agency for New Technologies, Energy and Sustainable Economic Development, 40129, Bologna, Italy.

Gianni Luigi Tinarelli, Daniela Barbero; ARIANET S.r.l., via Crespi 57 20159 Milano, Italy

Roberto San Jose, Juan Luis Pérez-Camanyo; Computer Science School, Technical University of Madrid (UPM, Campus de Montegancedo, s/n,28660 Madrid, Spain

Gabriela Sousa Santos: NILU, Norwegian Institute for Air Research, Norway.

John G. Bartzis, Ioannis A. Sakellaris; University of Western Macedonia (UOWM), Dept. of Mechanical Engineering, Sialvera & Bakola Str., 50132, Kozani, Greece.

Nicola Masey, Scott Hamilton; Ricardo Energy & Environment, 18 Blythswood Square, Glasgow, G2 4BG, UK

Zoltán Horváth, László Környei, Bence Liszkai, Ákos Kovács; Széchenyi István University, Győr, Hungary

Abstract

FAIRMODE is the Forum for Air Quality Modelling in Europe created in 2007 for exchanging experience and results from air quality modelling in the context of the Air Quality Directives (AQD) and for promoting the use of modelling for air quality assessment and management in a harmonized manner between Member States. Several working groups or cross-cutting tasks (CT) have been created to tackle several aspects of the air quality modelling in Europe. One of them is CT4 on Microscale Modelling. It refers to air quality modelling at very high spatial resolution in urban environments, where local hot-spots occur. Hence, this kind of obstacle resolving models is being required more and more in an AQD policy context. However, some techniques such as CFD require large computational resources to perform simulations over a period of one year, which makes this type of models difficult to use. In this context, one of the main aims of FAIRMODE CT4 is to determine how to derive annual averaged concentrations (and other AQD statistics such as percentiles) with a micro-scale model as a first step to discuss how to use micro-scale models for air quality assessment or planning in the framework of AQ Directives. An Intercomparison Exercise has been launched where 9 European groups have applied their urban micro-scale models and methodologies to an urban district of Antwerp (Belgium) to compute NO_2 concentrations. Three steps were designed to provide input for the intercomparison exercise: hourly NO_2 concentrations for one particular day, monthly NO_2 concentrations maps, and annual maps, respectively. The results were compared with observations from two air quality stations, and from 73 passive samplers deployed during one month in the district. The model results were also intercompared. CFD, Lagrangian, Urban Gaussian models and parameterized street canyon models were used. Additionally, different methodologies were applied for deriving long-term NO_2 averaged concentrations based on a number of steady state simulation of specific meteorological and emission conditions. In this presentation, this CT4 Intercomparison Exercise will be presented showing the main findings and possible recommendations for a good use of the microscale modelling for microscale urban air quality assessment.

TOPIC 4:

PARAMETRIZATION OF PHYSICAL PROCESSES AND MATHEMATICAL PROBLEMS IN METEOROLOGY AND AIR QUALITY MODELLING

21st International Conference on
Harmonisation within Atmospheric Dispersion Modelling for Regulatory Purposes
27-30 September 2022, Aveiro, Portugal

SENSITIVITIES IN WET DEPOSITION MODELLING APPLIED TO THE FUKUSHIMA NUCLEAR ACCIDENT

Stijn Van Leuven[1,2,3], Pieter De Meutter[1,3], Johan Camps[1], Andy Delcloo[2,3] and Piet Termonia[2,3]

[1]SCK CEN, Belgian Nuclear Research Centre, Mol, Belgium
[2]Department of Physics & Astronomy, Ghent University, Ghent, Belgium
[3]Royal Meteorological Institute of Belgium, Brussels, Belgium

Abstract: Atmospheric transport and dispersion modelling can provide crucial information to evaluate the impact of regular or accidental releases of radionuclides. One of the processes that depletes radionuclides from the atmosphere is deposition, which causes ground contamination thereby potentially impacting the food chain. Wet deposition in particular plays an often dominant role in the total deposition of radioactive material following a release of radioactive particulates in the atmosphere. In this work, the sensitivities of wet deposition contributions will be quantified with atmospheric dispersion model FLEXPART. The transport and deposition of ^{137}Cs as a result of the Fukushima Daiichi Nuclear power plant accident is used as a test case for this sensitivity study. A novel method is developed which extracts the individual scavenging contributions from the FLEXPART simulations and optimises them by comparing to measurements.

Key words: *ATM, wet deposition, sensitivity study*

INTRODUCTION

The simulation of wet deposition in atmospheric transport modelling (ATM) remains difficult in large part due to uncertainties in the parameterisation schemes used in simulations (Draxler et al., 2015, Solazzo and Galmarini, 2015, Quérel et al., 2021, Fang et al., 2022). In general, the wet scavenging coefficients range between 10^{-5} and 10^{-2} s^{-1} (Baklanov and Sørensen, 2001, Sportisse, 2007). This variation is mostly caused by the dependence of wet scavenging on the particle size distribution and rain intensity. The values of scavenging coefficients and their dependencies are difficult to measure, leading to large uncertainties in their implementation in ATM's. With the atmospheric dispersion model FLEXPART (Stohl et al., 1998, Stohl and Thomson, 1999, Stohl et al., 2005), the user is able provide a scaling factor for the wet scavenging coefficients as an input to the simulations. A revised wet deposition scheme was introduced in FLEXPART with its latest version v10.4, introducing four parameters that need to be specified for wet deposition of aerosols (Grythe et al., 2017, Pisso et al., 2019). The appropriate model parameter values are to be chosen by the user, and may differ from case to case (Grythe et al., 2017).

It is however not straightforward to find the optimal parameter values, and any such method can be computationally expensive. Here we explore a new method to optimise the scavenging coefficients which should allow for more efficient prescribing of the wet deposition parameters in FLEXPART. This is demonstrated by applying the proposed methodology to the transport and deposition of ^{137}Cs following the Fukushima Daiichi Nuclear power plant (FDNPP) accident.

METHODOLOGY

The wet deposition scheme of FLEXPART v10.4 contains up to four different scavenging processes for a given particle species, each with a corresponding scavenging coefficient Λ. The scavenging processes depend on the physical conditions of the atmosphere where the particle is located. A distinction between gases and aerosol particles is made (see Table 1).

Table 26. Model parameters for the scavenging coefficients used in FLEXPART 10.4 wet deposition scheme.

	Gases	**Particles**	
		$T < 0°C$	$T > 0°C$
In-cloud	A', B'	IN	CCN
Below-cloud	A, B	C_{snow}	C_{rain}

This new scheme was developed to better take into account the scavenging efficiencies in different conditions (Grythe et al. 2017). For gases the common parameterisation $\Lambda = AI^B$ is used (I being the rain intensity). The parameterisation of aerosol particles is more elaborate. It consists of in-cloud scavenging (nucleation) and below-cloud scavenging (impaction). The nucleation occurs by activated particles forming either cloud droplet condensation nuclei or ice nuclei, and is parameterised by the column cloud water and surface rain intensity. The overall strength of nucleation can be manually scaled by CCN and IN respectively. Below-cloud scavenging is driven by rain or snow, and is parameterised by the precipitation intensity and aerosol size. It can be manually scaled by C_{rain} and C_{snow}.

To improve the process of selecting the appropriate parameter values in ATM's, we develop a method which consists of two steps: 1) quantify individual scavenging contributions and 2) rescale the obtained contributions in an optimal way. These steps are described in more detail below.

1. Quantifying scavenging contributions

The airborne concentration at a given receptor is reduced by the scavenging that has taken place in the plume during its trajectory from the source to the receptor. The idea is to quantify how much the concentration has been reduced due to the individual scavenging processes in Table 1. Extracting these from the simulations is however not as straightforward as simply disabling some scavenging contributions, as this method will introduce certain 'compensation effects': decreasing one scavenging process causes the contribution of the other processes to simultaneously increase since there is now more concentration available to deplete. To avoid this effect, the individual scavenging contributions are directly extracted from the FLEXPART simulations.

2. Optimisation scheme

The concentration c that remains after scavenging is given by

$$c = c_0 - \sum_i \Delta c_i \,, \tag{1}$$

where c_0 is the concentration if there were no scavenging, and Δc_i are the scavenging contributions for each process. The goal is to scale the Δc_i's to find an optimal fit of c to the observations. However, directly scaling the different contributions Δc_i can quickly lead to negative concentrations. Therefore a more involved scaling scheme is proposed. With every scavenging process i, a scavenging factor A_i will be associated which acts on the concentration field through $\Delta c_i = A_i\left(c_0 - \sum_{j\neq i} \Delta c_j\right)$. In other words, the scavenging factor A_i acts on the part of the concentration field that is not affected by the other scavenging processes. From this definition, it can be shown that the individual Δc_i's scale as follows:

$$\Delta c_i = c_0 \frac{A_i}{1 - A_i} \left(1 + \sum_j \frac{A_j}{1 - A_j} \right)^{-1} . \tag{2}$$

This formulation prevents the concentrations from becoming negative and also reproduces the physical compensation effect when altering the strength of one of the scavenging processes. New Δc_i's are then generated by scaling the A_i's, so that an optimised fit can be obtained between the remaining concentrations c and the observations.

The above methodology is applied to ^{137}Cs transport and deposition following the FDNPP accident. For the FLEXPART simulations, we use meteorological data from European Centre for Medium-Range Weather

Forecasts (ECMWF) and the FDNPP source term of Terada et al., 2020. The ^{137}Cs observations are provided by the Comprehensive Nuclear Test-Ban-Treaty Organisation, which were made using the radionuclide stations from the International Monitoring System (IMS).

RESULTS

The different scavenging contributions as obtained by FLEXPART for IMS station RN71 (as an example) are shown in Figure 1. The left panel shows the contributions for the default FLEPXART scavenging parameters. These contributions are scaled by c_0 so that the sum $c/c_0 + \sum_i \Delta c_i/c_0$ is equal to 1, in accordance with Equation (1). Overall the impaction by snow (C_{snow}) has the greatest contribution for this station. Optimising the Δc_i's gives the results on the right panel. By fitting the scaling to the observations, impaction by rain (C_{rain}) and scavenging by cloud condensation nucleation (CCN) substantially increase.

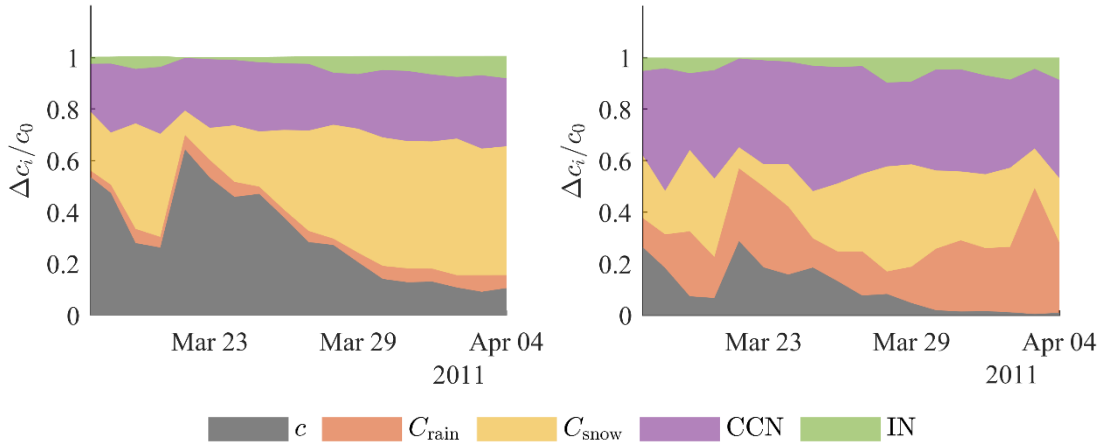

Figure 76. Scavenging contributions to simulated ^{137}Cs concentration at IMS station 71. Left: default FLEXPART deposition, Right: optimised scavenging contributions.

The distributions of the observational and model concentrations are shown on Figure 2 and Figure 3. Figure 2 shows the result for default FLEXPART parameters, while Figure 3 shows the concentrations as a result of optimising the scavenging contributions as seen above. For both Figures the distributions are shown in histogram form (left panels) and on a scatter plot (right panels). The default FLEXPART parameter values lead to an overestimation of the concentrations by around one to two orders of magnitude in this case, i.e. there is too little deposition (Figure 2). The optimisation scheme reduces this bias significantly by increasing the scavenging (Figure 3).

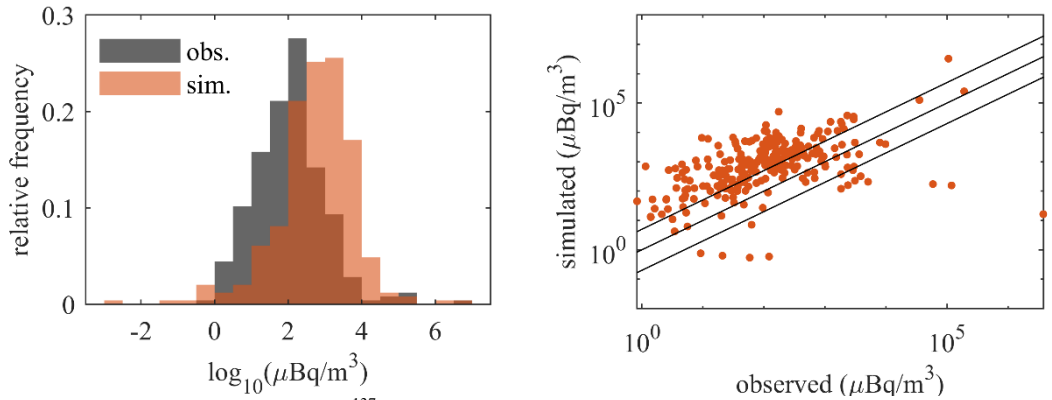

Figure 2. Concentrations with default ^{137}Cs deposition parameters compared with observational data. Black lines on the left panel show an offset of factors (1/5, 1, 5).

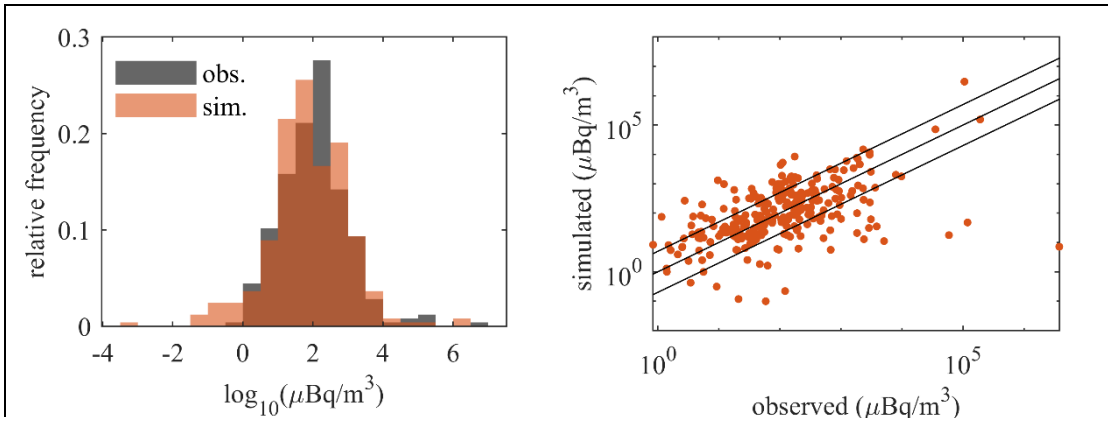

Figure 3. Optimised concentrations compared with observational data. Black lines on the left panel show an offset of factors (1/5, 1, 5).

CONCLUSIONS

Modelling of wet deposition is a crucial aspect of atmospheric transport modelling, yet large uncertainties remain in its parameterisations due to limited measurements of some scavenging processes. Sensitivity experiments could be conducted with ATM's which involve perturbing the scavenging coefficients and running the model thousands of times. Here, we have introduced a new method to scale and fit the deposition to concentration measurements using FLEXPART v10. The scaling is fitted to IMS observations, which shows a drastic improvement over the default FLEXPART deposition parameters. In principle this method only requires a single simulation, thereby greatly increasing the efficiency of prescribing the appropriate deposition parameters in FLEXPART. In the future, we intend to include the contribution of dry deposition as well.

REFERENCES

Baklanov, A. and Sørensen, J. H., 2001: Parameterisation of radionuclide deposition in atmospheric long-range transport modelling: *Physics and Chemistry of the Earth Part B-Hydrology Oceans and Atmosphere*, **26**(10), 787-799.

Draxler, R., Arnold, D., Chino, M., Galmarini, S., Hort, M., Jones, A., Leadbetter, S., Malo, A., Maurer, C., Rolph, G., Saito, K., Servranckx, R., Shimbori, T., Solazzo, E. and Wotawa, G., 2015: World Meteorological Organization's model simulations of the radionuclide dispersion and deposition from the Fukushima Daiichi nuclear power plant accident: *Journal of Environmental Radioactivity*, **139**, 172-184.

Fang, S., Zhuang, S. H., Goto, D., Hu, X. F., Li, S. and Huang, S. X., 2022: Coupled modeling of in- and below-cloud wet deposition for atmospheric 137Cs transport following the Fukushima Daiichi accident using WRF-Chem: A self-consistent evaluation of 25 scheme combinations: *Environment International*, **158**.

Grythe, H., Kristiansen, N. I., Groot Zwaaftink, C. D., Eckhardt, S., Ström, J., Tunved, P., Krejci, R., and Stohl, A., 2017: A new aerosol wet removal scheme for the Lagrangian particle model FLEXPART v10. *Geosci. Model Dev.*: **10**(4), 1447-1466.

Pisso, I., Sollum, E., Grythe, H., Kristiansen, N. I., Cassiani, M., Eckhardt, S., Arnold, D., Morton, D., Thompson, R. L., Groot Zwaaftink, C. D., Evangeliou, N., Sodemann, H., Haimberger, L., Henne, S., Brunner, D., Burkhart, J. F., Fouilloux, A., Brioude, J., Philipp, A. and Stohl, A., 2019: The Lagrangian particle dispersion model FLEXPART version 10.4: *Geosci. Model Dev.*, **12**(12), 4955-4997.

Quérel, A., Quélo, D., Roustan, Y. and Mathieu, A., 2021: Sensitivity study to select the wet deposition scheme in an operational atmospheric transport model: *Journal of Environmental Radioactivity*, **237**.

Solazzo, E. and Galmarini, S., 2015: The Fukushima-Cs-137 deposition case study: properties of the multi-model ensemble: *Journal of Environmental Radioactivity*, **139**, 226-233.

Sportisse, B., 2007: A review of parameterizations for modelling dry deposition and scavenging of radionuclides: *Atmospheric Environment*, **41**(13), 2683-2698.

Stohl, A., Forster, C., Frank, A., Seibert, P. and Wotawa, G., 2005: Technical note: The Lagrangian particle dispersion model FLEXPART version 6.2: *Atmos. Chem. Phys.*, **5**(9), 2461-2474.

Stohl, A., Hittenberger, M. and Wotawa, G., 1998: Validation of the Lagrangian particle dispersion model FLEXPART against large-scale tracer experiment data: *Atmospheric Environment*, **32**(24), 4245-4264.

Stohl, A. and Thomson, D. J., 1999: A density correction for Lagrangian particle dispersion models: *Boundary-Layer Meteorology*, **90**(1), 155-167.

Terada, H., Nagai, H., Tsuduki, K., Furuno, A., Kadowaki, M. and Kakefuda, T., 2020: Refinement of source term and atmospheric dispersion simulations of radionuclides during the Fukushima Daiichi Nuclear Power Station accident: *Journal of Environmental Radioactivity*, **213**.

21st International Conference on
Harmonisation within Atmospheric Dispersion Modelling for Regulatory Purposes
27-30 September 2022, Aveiro, Portugal

STUDY OF SPATIAL AND TEMPORAL VARIABILITY OF PRODUCTION RATES AND COMPOSITION OF NO_X SOURCES USING IN-SITU MEASUREMENTS COMBINED TO A DYNAMIC MODEL OF NO_X-O3 SYSTEM.

P. Joassin[1,2], F. Lenartz[2] and M. Dury[2]

[1]Corresponding author, p.joassin@issep.be
[2]ISSeP : Institut Scientifique de Service Public, Wallonie, Belgique

Abstract: hourly measurements of NO, NO_2 and O_3 from outdoor stations covering a full year period have been used to highlight spatial and temporal (seasons and week days) variability of NOx-O_3 system characterics, i.e. the NO_x production/dissipation rate and the equilibrium state reached by the global equation $NO + O_3 \leftrightarrow NO_2 + O_2$. A dynamic model of the NOx-O_3 system has been used to derive the fraction of NO_2 composing the NO_x sources and the efficiency of NO oxidation due to VOCs.

Key words: *NO_x , NO_2 , O_3 , VOCs , dynamic model , spatial variability , temporal variability , ozone pollution*

INTRODUCTION

Human activities sustain a strong impact on the NO_x-O_3 system, leading to local noxious concentrations of polluting substances such as ozone (De Villers Juliette, Squilbin Marianne, Vanderstraeten Peter, 2016). Anthropic emissions of NO_x, especially linked to urban traffic, residential heating and industrial activities, alter the natural cycle of tropospheric ozone (ASPA, 2004 ; RECORD, 2004). The fraction of NO_2 prevailing in the anthropic emissions of NO_x may vary regarding the nature of the NO_x sources and thus modify the potentiality of the emitting environment to produce ozone (Carslaw C. David, Beevers D. Sean, 2005). In parallel to NO_x, the implication of VOCs (volatile organic compounds) as NO oxidants, being produced by vegetation as well as industrial activities, makes more complex the prediction and prevention of ozone pollution (Grange Dorothée, Host Sabine, 2007 ; Wardle D.I., McElroy J.B. Kerr. C.T. and Francis D.R., 1997). Studies and environment surveys are therefore invited to focus on the main parameters that trigger the ozone formation, being as well the NO_x anthropic sources rates or the enhancing effects of natural/industrial VOCs. The monitoring of the chemical variables composing the NO_x-O_3 system may be based on usual time series of measurements, notwithstanding the fact that the concerned chemical species are involved in complex equilibrium dynamics (Benjamin Pajot, 2011). When the dynamics of the chemical equilibria show a characteristic frequency similar to that of the observations made by the monitoring network, a precise knowledge of the NO_x sources composition or the ozone production rate may not be acquired by a simple difference between successive measurements. The knowledge of these aspects of the NO_x-O_3 system thus requires the combination of observations time series and the modelling of the processes involving the concerned chemical species. In this study, the representation of the chemical reactions between NO_2 – NO – O_3 in a dynamic model allowed to take into account the local values of the environmental parameters acting on the equilibrium dynamics of these chemical species, of which mainly the solar U.V. irradiance and the temperature (Ayachi M., 1998). The numerical resolution made possible the determination of the NO_2 fraction in total NO_x species, highlighting the link between NO_x emissions and typical human activities. In parallel, the modelling approach allowed to compare the efficiency of the NO oxidation due to VOCs regarding the season and the urban/rural/industrial situation of the station.

MATERIAL AND METHOD

Outdoor concentrations of chemical variables nitrogen oxide (NO), nitrogen dioxide (NO_2) and ozone (O_3) have been measured using HORIBA devices (APOA-370 and APNA-370) deployed in 5 stations (Table 1) of the Wallonia telemetric monitoring network. These are situated in various environments, each one characterized by typical conditions impacting the dynamics of NO_x-O_3 system. Hourly (day and night) measurements have been continuously collected from all stations during a full year period and aggregated into four time periods corresponding to natural seasons (Table 2) and two categories of week days. A first

category gathers the working days i.e. Monday, Tuesday, Thursday and Friday (exception made for Wednesday due to unusual traffic dynamics linked to half school day). A second category consists only in the Sundays. Additional collocated and concomitant data have been collected, directly for air temperature using stations sensors or indirectly for solar U.V. irradiance and sky nebulosity using yearly climatology.

The NO_x-O_3 system dynamics have been represented using a three equations model (Equations 1-2-3) where concentrations [NO], [NO_2], [O_3] are state variables. Driven parameters of the model equations are the emission/dissipation rate ($mol.m^{-3}.s^{-1}$) of total NO_x (src_{NOx}), the fraction of NO_2 in total NO_x ($NO2_{NOx}$), the kinetic frequency (s^{-1}) of the NO_2 photo-dissociation due to solar U.V. (J_{NO2}), the kinetic coefficient ($m^3.mol^{-1}.s^{-1}$) of the NO oxidation due to ozone ($K_{NO.O3}$), and the kinetic frequency (s^{-1}) of the NO oxidation due to VOCs (F_{NO}). That last parameter synthetizes the products of the prevailing VOCs concentrations involved in NO oxidation and the proper kinetic coefficients of each of these VOCs species. Parameters J_{NO2} and $K_{NO.O3}$ are hourly calculated regarding the environmental conditions (local air temperature, solar U.V. irradiance and sky nebulosity) (Delmas R., Mégie G., Peuch V.H., 2005 ; Aumont B., 2006). Parameter src_{NOx} is derived directly from hourly measurements of chemical variables. Parameters $NO2_{NOx}$ and F_{NO} are obtained by a modelling approach, through best adjustments of default values and optimization of the NO_x-O_3 system dynamics, modelled over periods of two hours from initial to final values of the three chemical variables. Time steps of the model is fixed to 36 seconds. Optimal values of $NO2_{NOx}$ and F_{NO} are selected through the minimisation of a least squares cost function.

RESULTS

Results focus on the issues of the modelled approach, i.e. parameters F_{NO} (Figure 1) and $NO2_{NOx}$ (Figure 3) in addition with the hourly evolutions of src_{NOx} (Figure 2). Furthermore, the evolution of ratio R between the real time quotient Qr of the synthetic reaction NO + O_3 ←→ NO_2 + O_2 and its theoretical equilibrium constant Keq (Equations 4) is also displayed (Figure 4). In each figure, left assemblage of four graphs concerns evolutions for working days among the four seasons; right assemblage does the same for the Sundays.

A clear distinction appears between stations installed in environments impacted by human activities (n. 1-2-3-4) and in the only station (n. 5) free from anthropic emissions of NO_x. Temporal variability over the daily hours, as well as the opposition between working days and Sundays, is indeed strongly enhanced in stations 1-2-3-4 concerning the emission/dissipation rate of NO_x which is characterized by a two-peaks dynamics. That bimodal profile is significantly more marked during winter and fall, while slighter during summer and spring. During winter working days, NO_x emissions reach their first maxima around 7 a.m. with highest value of 100.10^{-12} $mol.m^{-3}.s^{-1}$ in stations 3 and 4 while second maxima is reached around 6 p.m. with highest value of $40\sim50.10^{-12}$ $mol.m^{-3}.s^{-1}$ in the same stations. For Sundays, the temporal variability during the day is largely smoothed. However, a difference is still prevailing between the spring/summer and the fall/winter seasons. During these last, a peak of NO_x emissions remains visible in the morning and the evening hours, especially in urban stations. The station 5, installed in a forested environment, shows flat NO_x emissions dynamics without impact of the moment within the day nor the category of the days, unlike all other stations. The seasonal variability is also quasi absent making that the emission/dissipation rate of NO_x oscillates between $\pm5.10^{-12}$ $mol.m^{-3}.s^{-1}$ in station 5. However, a clear temporal variability within a daytime scale characterises the profile of NO oxidation frequency due to VOCs observed in a forested environment. Indeed, station 5 shows a strong peak for NO oxidation frequency around 10 a.m., which is especially marked during the spring/summer seasons with values of 1000.10^{-6} s^{-1}, and the half during the fall/winter seasons. These peaks of NO oxidation frequency are similarly observed in station 5 during working days and Sundays. It must be noted that the full urban stations, namely n. 3 and 4, sustain the least levels for the NO oxidation frequency due to VOCs. The ratio R between the quotient of the NO + O_3 ←→ NO_2 + O_2 reaction and its theoretical equilibrium constant is globally characterized by a decreasing profile along the day course, remaining below 1, which significates that the reaction promotes the production of NO_2. Nevertheless, R value becomes higher than 1 in stations n. 1 and 5, during spring/summer seasons. A very strong peak of R value is indeed visible in station 5 during spring time, from the middle of the morning till the middle of the afternoon. That peak may be seen in correlation with the high dynamics of NO oxidation due to VOCs, and thus the accumulation of NO_2 leading to a relative promotion of ozone production under spring and summer sunshine.

Figures

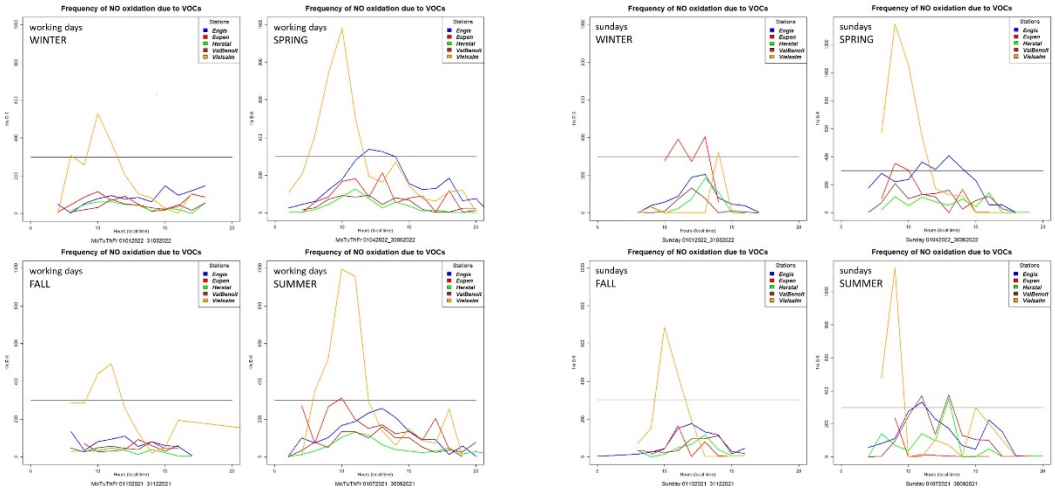

Figure 77 (working days - Sundays). Frequency of NO oxidation into NO_2 due to reaction withVOCs.

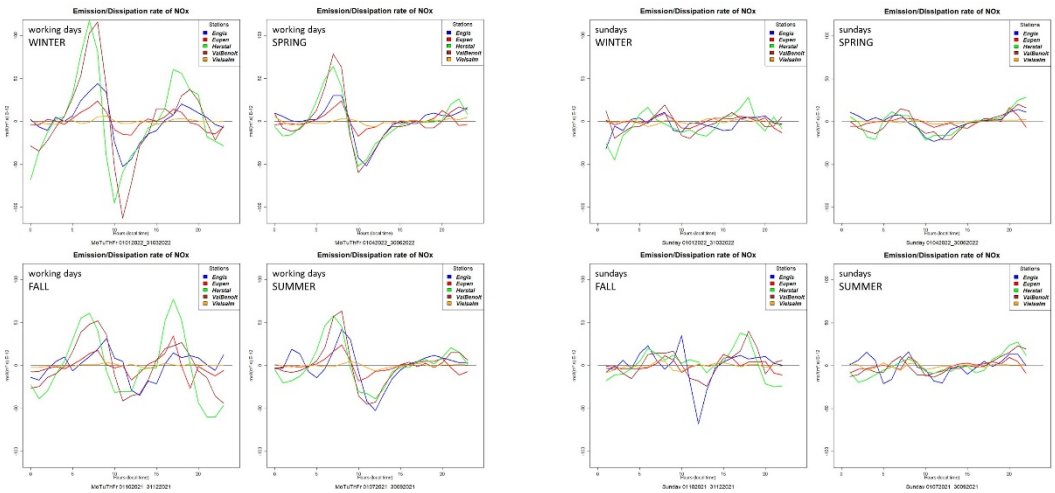

Figure 2 (working days - Sundays). Emission / Dissipation rate of NO_x.

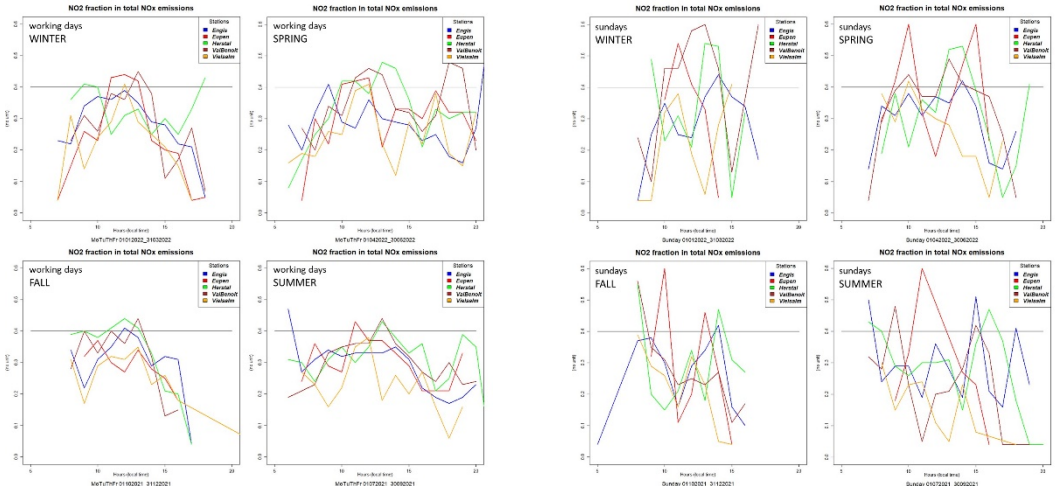

Figure 3 (working days - Sundays). NO_2 fraction in total NO_x emissions.

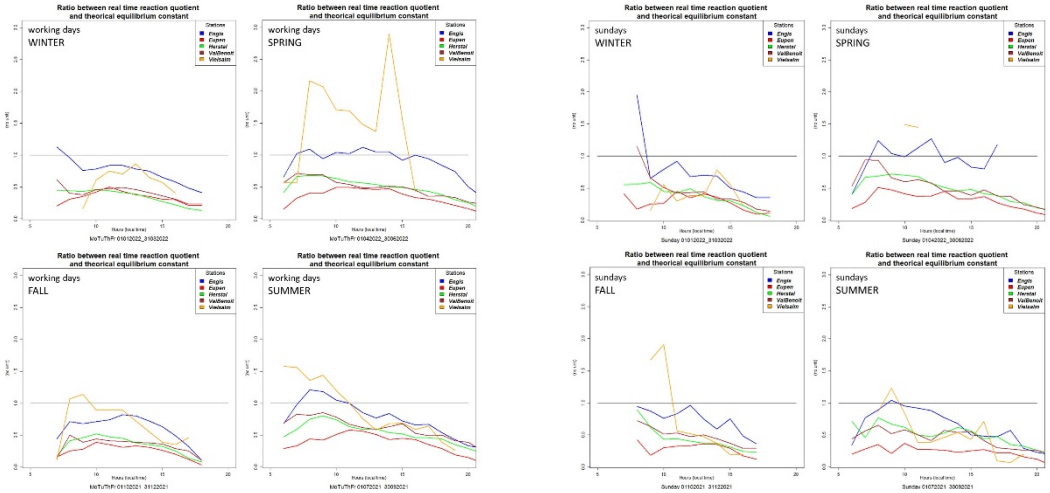

Figure 4 (working days - Sundays). Ratio between real time quotient reaction and theoretical equilibrium constant.

Tables

Table 27. List and description of telemetric stations providing NO – NO_2 – O_3 measurements

Station number	Colour in graphs	Lat. (°)	Lon. (°)	Alt. (m)	Name	Environment typology
1	Blue	50,5832	5,3974	135	Engis	Residential/near industry
2	Red	50,6288	6,0027	292	Eupen	Rural
3	Green	50,6584	5,6278	56	Herstal	Urban/near traffic ways
4	Brown	50,6134	5,5702	71	Val-Benoît	Urban
5	Yellow	50,3031	6,0017	492	Vielsalm	Forest

Table 2. Seasonal intervals used for temporal aggregation of NO – NO_2 – O_3 measurements

Season	from	to
Winter	01-01-2022	31-03-2022
Spring	01-04-2022	30-06-2022
Summer	01-07-2021	30-09-2021
Fall	01-10-2021	31-12-2021

Equations

$$\frac{dNO2}{dt} = src_{NOx} \,.\, NO2_{NOx} + [NO] \,.\, F_{NO} - [NO2] \,.\, J_{NO2} + K_{NO.O3} \,.\, [NO] \,.\, [O3] \quad (1)$$

$$\frac{dNO}{dt} = src_{NOx} \,.\, (1 - NO2_{NOx}) - [NO] \,.\, F_{NO} + [NO2] \,.\, J_{NO2} - K_{NO.O3} \,.\, [NO] \,.\, [O3] \quad (2)$$

$$\frac{dO3}{dt} = [NO2] \,.\, J_{NO2} - K_{NO.O3} \,.\, [NO] \,.\, [O3] \quad (3)$$

$$Keq = \frac{K_{NO.O3}}{J_{NO2}} \qquad Qr = \frac{[NO2]}{[NO] \,.\, [O3]} \qquad R = \frac{Qr}{Keq} \quad (4)$$

REFERENCES

ASPA, 2004: Analyse de 31 COVNM précurseurs d'ozone mesurés en continu en Alsace en 2004. *Source d'information ASPA 05121902-ID*.

Aumont B., 2006: Chimie de l'atmosphère. *Laboratoire interuniversitaire des systèmes atmosphériques (LISA)*, *université Paris Est Créteil*.

Ayachi M., 1998: Les effets du rayonnement solaire ultraviolet sur les constituants minoritaires de l'atmosphère moyenne. *Bulletin de l'Union des physiciens*, vol. 92, juin 1998, 55-86

Benjamin Pajot, 2011: Analyse et prévision de l'ozone issues d'une assimilation de données satellitaires à haute résolution. Océan, Atmosphère. Université Paul Sabatier - Toulouse III, 2011.

Carslaw C. David, Beevers D. Sean, 2005: Estimations of road vehicle primary NO2 exhaust emission fractions using monitoring data in London. *Atmospheric Environment*, vol. 39, 167–177

Delmas R., Mégie G., Peuch V.H., 2005: Physique et chimie de l'atmosphère. *Belin*, 2005, 640 p.

De Villers Juliette, Squilbin Marianne, Vanderstraeten Peter, 2016: Ozone troposphérique. *Bruxelles Environnement – IBGE – Collection fiches documentées,* fiche 10, février 2016, 9 p.

Grange Dorothée, Host Sabine, 2007: Les composés organiques volatils (COV) - Etat des lieux : définition, sources d'émissions, exposition, effets sur la santé. *Etude de l'Observatoire régional de santé d'Ile-de-France (ORS)*, décembre 2007.

RECORD, 2004: Détermination des Potentiels de formation d'ozone (PCOP) pour différentes espèces gazeuses à l'échelle de l'Europe de l'Ouest. Amélioration de l'indicateur de pollution photo-oxydante dans les Analyses de Cycle de Vie (ACV), 2004, 130 p., n°01-1007/1A.

Wardle D.I., McElroy J.B. Kerr. C.T. and Francis D.R., 1997: La science de l'ozone : perspective canadienne sur la couche d'ozone. *Environnement Canada*, 1997, chapitre 3, 17 pp.

21st International Conference on
Harmonisation within Atmospheric Dispersion Modelling for Regulatory Purposes
27-30 September 2022, Aveiro, Portugal

PROPOSAL FOR MODELLING THE DRY DEPOSITION OF SOLID PARTICLE AND GAS USING A 3D STOCHASTIC LAGRANGIAN DISPERSION MODEL

Ribstein Bruno[1], Cohen Elsa[1], Nibart Maxime[1] and Tinarelli Gianni[2]

[1] ARIA Technologies, 8, rue de la Ferme, F-92100 Boulogne-Billancourt, France
[2] ARIANET S.r.l., via Gilino 9, I-20128 Milano, Italy

Abstract: The deposit represents a flow of pollutants to the ground and depletes the plume. Dry deposition velocity models the soil's ability to retain the pollutant. ARIA/ARIANET in collaboration with CEA has developed the PSPRAY model, a Lagrangian 3D model of stochastic dispersion of pollutants in the atmosphere. A particle removal mechanism, linked to the stochastic equation solved by the model, is implemented to ensure that the dry deposition flux is proportional to the concentration at ground level. It is based on the calculation of a probability $P(h, \Delta t)$ that an amount of pollutants located at a certain height is absorbed during a certain time interval. The probability tends rapidly to zero when moving away from the ground level.

In this work we revise the implementation of this mechanism in the PSPRAY dispersion model. At each emission time step, the model emits virtual particles each carrying part of the emitted mass of pollutants. These virtual particles represent a set of solid particles or a certain volume of gas. In the presented work, an amount equal to $P(h, \Delta t) \cdot m_{par}$ is removed from the mass m_{par} carried by the particle. The proposed mechanism allows an identical treatment of the gas and solid particle cases. Thus, as the diameter of the solid particles tends towards zero, the deposition field approaches the one of a gaseous species.

Key words: *solid particles, dry deposition, lagrangian, modelling, PSPRAY, buildings.*

INTRODUCTION

In the urban environment, exposure to air pollution is a major environmental problem. Pollutants are emitted from various sources and then dispersed (advection and diffusion) over a wide range of horizontal length scales. Microscale dispersion refers to processes acting on horizontal length scales smaller than about 5 km. Public health risk assessment requires modeling of pollutant dispersion in the atmosphere. This is not always sufficient, and it is sometimes necessary to model the deposition of pollutants on the ground, or on the facades of buildings. The deposition represents a flow of pollutants to the ground that depletes the plume. The dry deposition represents the capacity of the soil to retain pollutants, the wet deposition models the washout of the plume by raindrops.

ARIA/ARIANET in collaboration with CEA has developed the PSWIFT model in the Parallel-Micro-SWIFT-SPRAY (PMSS) system. The PSWIFT model is a mass-conserving diagnostic atmospheric model. PSPRAY is a (stochastic) 3D Lagrangian Particle Dispersion Model able to account for the presence of obstacles. They have been developed with the aim to provide a simplified, but rigorous solution of the flow and dispersion in industrial or urban environments in a short amount of time (Tinarelli et al., 1994, 2012).

The dry deposition model in Pspray was historically developed in 2 parts: for solid particles and then for (dense) gases. The 2 mechanisms are different, and the results obtained are possibly also different. We review the two mechanisms and present a unified mechanism for dry deposition for any type of pollutant. After this introduction, the dispersion modeling is presented, followed by the existing and proposed mechanism of dry deposition in Pspray. The numerical experiments are described and the results are analyzed. Finally, a summary reminds the important results obtained in this work.

DISPERSION MODELLING

There are three main families of deterministic atmospheric dispersion models: the Eulerian model, the Gaussian model and the Lagrangian model. An in-depth description of the models can be found in (Hanna et al., 1982) and Rodean (1996).

- Gaussian models are used to simulate the atmospheric dispersion of non-reactive pollutants near the source. They assume a Gaussian distribution around the center of the plume. The wind and the temperature are assumed to be stationary and uniform. Mass conservation is imposed in the plane transverse to the plume axis.
- Both Eulerian and Lagrangian models solve the advection-diffusion equation. The Eulerian viewpoint considers the evolution at a fixed point, i.e., at (x, y, z) constant. In each cell, the concentration evolution is given by the incoming and outgoing mass fluxes. The Lagrangian viewpoint follows a parcel of fluid in its displacement. The position is therefore not fixed, but the material volume always gathers the same set of fluid molecules over time.

In PSPRAY, the dispersion of an airborne contaminant is simulated by following the trajectories of a large number of numerical particles, each carrying a part of the emitted mass of pollutant. The trajectories are obtained by integrating in time the velocity of each numerical particle. The velocity of each particle is the sum of a component for the transport (average wind speed from PSWIFT), another one for the turbulence (stochastic contribution via the resolution of a Langevin equation) and of eventual parameterization taken into account (for example the gravitational settling).

Each numerical particle represents a set of molecules. For a pollutant flux Q in kg/h and N_{par} numerical particles emitted every dt_{min}, each particle will carry $m_{par} = Q \cdot dt_{min}/N_{par}$. Increasing the number of numerical particles improves the accuracy of the results, since each particle carries a smaller mass. The computation time depends linearly on the number of numerical particles and the average wind. Increasing the number of numerical particles therefore also results in an increase in computation time.

DRY DEPOSITION MODELING IN PSPRAY

The deposit represents a flow of pollutants to the ground and depletes the plume. In addition to the gravitational settling, the dry deposition velocity models the soil's ability to retain the pollutant. Dry deposition is modeled in a Lagrangian manner in PSPRAY, by computing the deposition probability of each numerical particle near the ground. Monin (1959) found a solution of the 1d advection-diffusion equation with the addition of a boundary condition reflecting the interaction with the surface and considering the gravitational settling. The solution $c_{unit}(z, t; h)$ is for an instantaneous point source of unit intensity at the height h. Let a parcel of pollutant initially at $z = h$ in $t = 0$. The probability $P(h, \Delta t)$ that this parcel is absorbed during the period Δt equals exactly the fraction of pollutant no longer in the air.

$$P(h, \Delta t) = 1 - \int_0^\infty c_{unit}(z, \Delta t; h) dz$$

Deposition in PSPRAY today handles a gas differently from a solid particle.

- For a gas, a mass equal to $m_{dep} = P(h, \Delta t) \cdot m_{par}$ is removed from the mass carried by the numerical particle and is deposited on the ground. The mass carried by the numerical particle is then $(1 - P(h, \Delta t)) \cdot m_{par}$.
- For solid particles, a random number Y is extracted from a uniform distribution. If the number is $Y < P(h, \Delta t)$ then the numerical particle is entirely retained by the soil. The deposited mass equals $m_{dep} = m_{par}$ and the numerical particle is no longer transported. If the number is $Y > P(h, \Delta t)$ the numerical particle acts as if no deposition is taking place, eventually reflecting off the ground. This is the mechanism initially presented in Boughton et al. (1987).

At periodic intervals, the mass in each mesh defining the computational domain is calculated. The concentration fields in $mass/m^3$ and deposition in $mass/m^2$ are thus estimated.

LIMIT AND MODIFICATION OF THE PSPRAY DEPOSITION MODEL

We have just explained the dispersion and deposition in the PSPRAY model. We now detail the limitations to the current deposition model. For solid particles, each numerical particle carries a mass $m_{par} = Q \cdot dt_{min}/N_{par}$. With numerical resolution $dx = dy = ds$, the deposited mass will never be less than that of a numerical particle, i.e. m_{par}/ds^2. Obviously, the higher N_{par} is, the lower this deposition threshold is. Gases do not have this threshold since the mass carried by a numerical particle is depleted by deposition.

Gravitational settling is taken into account for solid particles. Gravitational settling follows a Stockes law with a Cunningham correction factor. This velocity is proportional to d^2 with d the diameter of a solid particle. The velocity is of the order of $10^{-4}\, m/s$ for $d = 1\mu m$. Because the contribution of gravitational settling is negligible for solid particles of diameter $1\mu m$, the deposition should be equivalent to that of a gas emitted in the same quantities. Figure 1 illustrates the threshold effect and shows that this is currently not the case in PSPRAY. There are 2 pollutants considered, a gas and fine particles of diameter $1\mu m$.

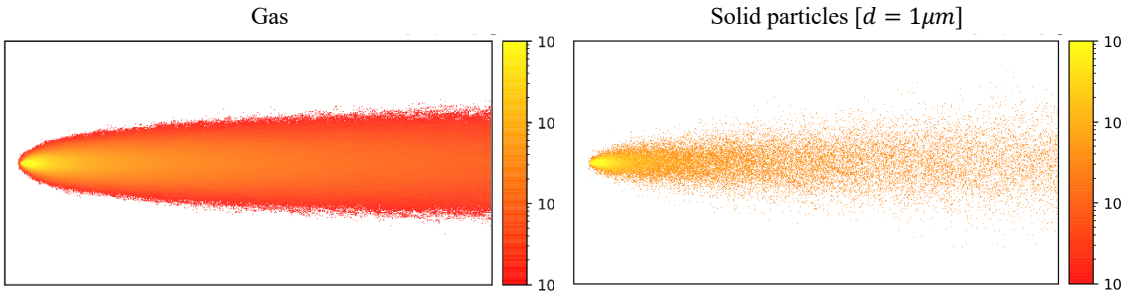

Figure 78: Dry deposition for a gas and solid particles with d=1µm (old mechanism)

Figure 2 shows the deposition along the plume axis by changing the number of digital particles emitted. It illustrates the threshold effect as the threshold decreases by increasing N_{par}. In the case $N_{par} = 100$, the computation time is 19s on 10 processors, but it increases to 160s with $N_{par} = 1000$.

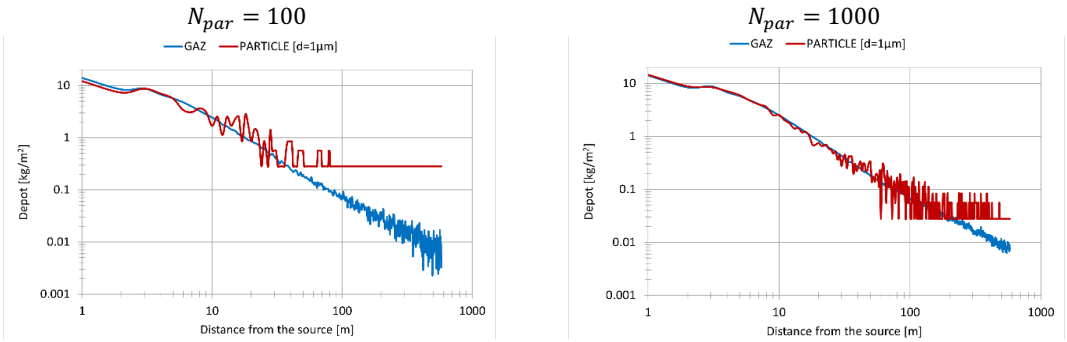

Figure 79: Dry deposition along the plume for a gas and solid particles with d=1µm (old mechanism)

The deposition probability already takes into account the gravitationnal settling and the deposition velocity. The proposed deposition mechanism is to use the one currently in place for gas.

DESCRIPTION OF THE NUMERICAL EXPERIENCES

The proposed deposition mechanism is verified in an idealized setting, and where a comparison to a Gaussian model is possible. This is the method also used by Boughton et al. (1987), and we use the same Gaussian model, namely Ermak (1977).

- The modeled domain does not include any obstacle and it covers an area of $600m \times 300m$, at the resolution of $dx = dy = 1m$.
- The weather conditions are slightly unstable. The temperature gradient is $-1.8\,°C/m$ and the wind profile follows a $u(z) = u_0(z/z_2)^{\alpha}$ law, with $z_2 = 10m$, $u_0 = 4\,m/s$ and $\alpha = 0.15$.
- A source emits a continuous flow of pollutant $Q = 10^4 kg/h$ from a height $h = 1m$. The emitted species are a gas and solid particles of diameter $1\mu m$, both have a deposition velocity $v_d = 0.1\,m/s$. $N_{par} = 1000$ numerical particles are emitted every $dt_{min} = 10s$.

Wind is uniform in the Gaussian model used, which is not the case in PSPRAY. For the Gaussian model, we choose $\sigma_z(x) = \sigma_y(x) = 0.36(x)^{0.86}$, equivalent to a B1 case of the Brookhaven National Laboratory classification. The wind chosen is $u_0 = 4\,m/s$.

RESULTS

Figure 3 shows the concentration along the plume. The concentrations in PSPRAY are estimated in a layer $dz = 2m$. With the Gaussian model, the concentration is calculated at $z = 1m$. The concentration for gas and small particles are similar, and they remain within a factor of 2 of the Gaussian model from a distance of $20m$ from the source. The concentration is obtained by PSPRAY by counting N_{snap} times the mass contained in each cell. The smallest modeled concentration equals m_{par}/N_{snap}, i.e. when a numerical particle is counted only once. This corresponds to the fluctuations shown in Figure 3.

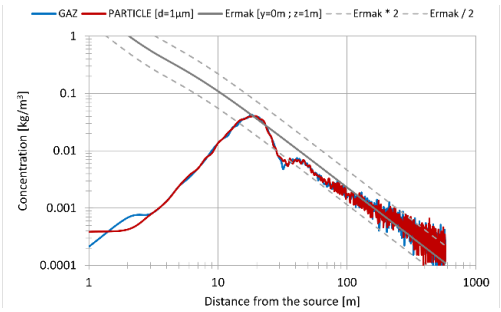

Figure 80: Concentration along the plume for PSPRAY and the Ermak (1977) Gaussian model

Figure 4 shows the deposition field along the plume, and also along the transverse axis for 2 distances from the source: $x = 100m$ and : $x = 200m$. With the proposed deposition mechanism, the deposition fields for gas and solid particles of diameter $1\mu m$ are now similar. The deposition along the plume remain within a factor of 2 from a distance of $10m$ from the source. The deposition given by the Gaussian model is increasingly smaller compared to that modeled PSPRAY. The transverse spread of the plume in the Gaussian model is increasingly larger compared to that in PSPRAY. These two observations suggest that the PSPRAY model appears to be slightly less dispersive than the Gaussian model. The weather conditions and the turbulence estimation are different in the 2 models. The study was not an inter-comparison of the 2 models, and we did not investigate this further.

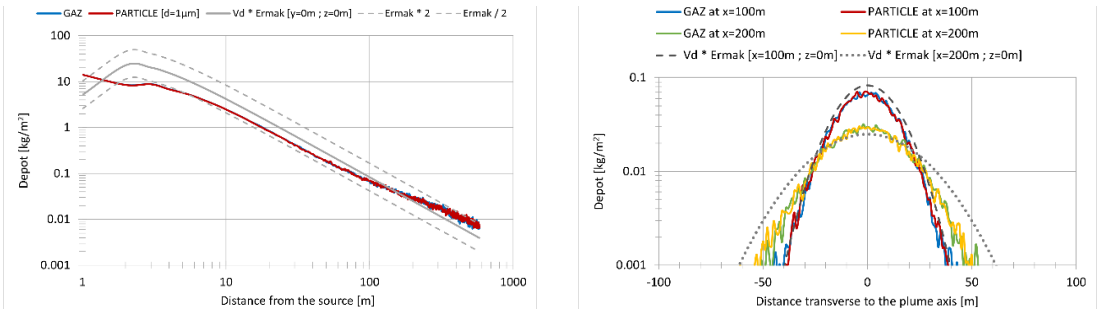

Figure 81: Dry deposition along the plume and along the transverse axis for a gas and solid particles with d=1µm for PSPRAY (new mechanism) and the Ermak (1977) Gaussian model

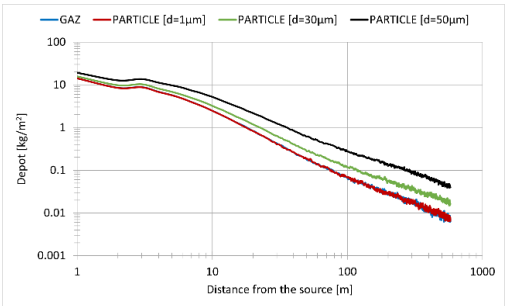

Figure 82: Dry deposition along the plume for a gas and solid particles with different diameters (new mechanism).

Finally, the figure 5 shows the evolution of the deposition for the gas and for solid particles of different diameters $d = 1\mu m$, $30\mu m$ et $50\mu m$. The gravitational settling evolves as d^2, and is approximately $10^{-4}\, m/s$ for $d = 1\mu m$. It remains negligible for $10\mu m$, but then begins to become significant.

ILLUSTRATION OF THE IMPACT OF A BUILDING

The PSPRAY model has been developed to take into account the presence of possible obstacles. With meteorological conditions similar to the previous case, the figure 6 illustrates that the presence of obstacles does not change the previous conclusions. The concentration and deposition fields for a gas and solid particles of diameter 1µm remain similar.

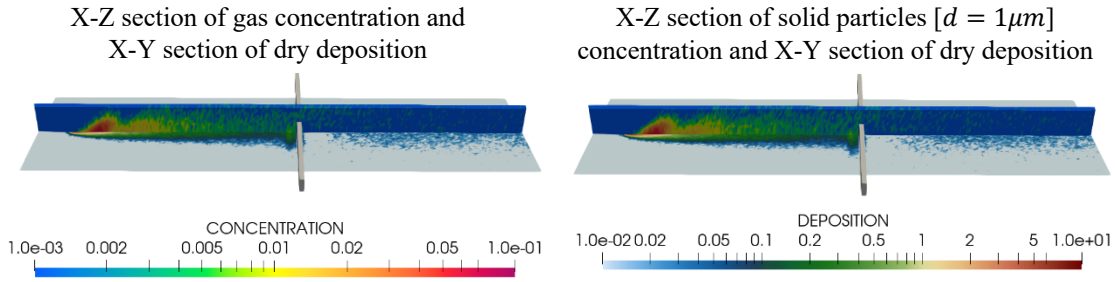

Figure 83: illustration of the impact of a building on concentration and deposition

CONCLUSION

The PSPRAY dry deposition mechanism was different for fine particles and gases. A unique dry deposition mechanism is proposed and tested on an academic configuration, and comparisons performed against a rectilinear Gaussian model. An illustration shows that the new deposition mechanism is compatible with obstacles.

In an urban environment, deposition on facades can also be significant. Although this can be modeled by the PSPRAY model, this depletion has not been analyzed. The deposition mechanism of the PSPRAY model is compared to that of a more idealized model. In order to validate the deposition model, it will be interesting to compare it to a measurement campaign, and to a more complex model than PSPRAY.

REFERENCES

Tinarelli G., Anfossi D., Brusasca G., Ferrero E., Giostra U., Morselli M.G., Moussafir J., Tampieri F., Trombetti F., 1994. Lagrangian particle simulation of tracer dispersion in the lee of a schematic two-dimensional hill. *J. Appl. Meteorol*. 33 (N. 6), 744–756.

Tinarelli G., Mortarini L., Trini Castelli S., Carlino G., Moussafir J., Olry C., Armand P., Anfossi D., 2012. Review and validation of Micro-Spray, a Lagrangian particle model of turbulent dispersion. In: Lin, J., Brunner, D., Gerbig, C., Stohl, A., Luhar, A., Webley, P. (Eds.), Lagrangian Modeling of the Atmosphere. vol 200. *Geophysical Monograph, American Geophysical Union*, Washington DC, pp. 311–327

Hanna, S.R., Briggs, G.A., Hosker, R.P., 1982. Handbook on Atmospheric Diffusion. DOE/TIC-11223. *Department of Energy*, pp. 102.

Rodean, H.C., 1996. Stochastic Lagrangian Models of Turbulent Diffusion, vol 45 American Meteorological Society, Boston, USA.

Monin, A. S., 1959: On the Boundary Condition on the Earth Surface for Diffusing Pollution, *Adv. Geophys*. 6,435-436.

Boughton B.A., Delaurentis J.M., Dunn W.E. [1987]. A Stochastic model of particle dispersion in the atmosphere. *Boundary-Layer Meteorology* 40, 147-163.

Ermak, D. L.,1977: An Analytical Model for Air Pollutant Transport and Deposition from a Point Source, *Atmospheric Environment*, 11, 231-237.

21st International Conference on
Harmonisation within Atmospheric Dispersion Modelling for Regulatory Purposes
27-30 September 2022, Aveiro, Portugal

STATE OF THE ART ON DEPOSITION BY FOG AND ITS DIFFERENCE WITH RESPECT TO DRY AND WET DEPOSITION (WASH-OUT) FOR A BETTER REPRESENTATION IN IMPACT STUDIES

Ariele Défossez[1], Rayna Charlatchka[1]

[1]Fluid Mechanics, Energy and Environment Department, EDF R&D, Chatou, France
& CEREA, joint laboratory Ecole des Ponts ParisTech / EDF-R&D, France

Abstract: Fog deposition is difficult to model. In-depth knowledge of the phenomenon becomes important when we see its impact in areas such as the efficiency of photovoltaic panels, dispersion of pollutants, etc. Various studies have recently been carried out on the subject with supporting experimental data (for example Parisfog) (Zhang X. , 2010) for model validation. The goal of this work is to achieve a state of the art on the current knowledge on the fog deposition in order to integrate it into a CFD 3D model. The calculation code, open source called «code_saturne » is developed by EDF R&D. After presenting the different dry and wet depositions, we focus on the fog deposition.

Key words: *wet deposition, dry deposition, fog water deposition, CFD, environment*

INTRODUCTION

The atmospheric dispersion models mostly take into account dry deposition. However, other phenomena such as fog can generate important deposits. Fog deposition model is not very well known. The aim of this work is to give a state-of-the-art fog deposition model after having looked at the differences with the other deposits. The result of this study will allow to choose a fog deposition model to increment it in the 3D CFD (Computation Fluid Dynamics) EDF opensource home tool called Code Saturne (https://www.code-saturne.org/cms/web). This document will give different deposition processes and their differences:

- Dry deposition
- Wet deposition: wet deposition (wash-out), wet deposition (rain out)

Wet deposition and fog model are already implemented in the code_saturne tool. This work will focus on the wet deposition during a fog.

DIFFERENT DEPOSITIONS

A dry deposition is a deposit of atmospheric species (gas or particles) at a surface of the Earth (soil, vegetation, sea...) during a weather without precipitation. A wet deposition is the deposit of atmospheric species (gas or particles) due to precipitations (rain, snow, hail...). There are several types of wet deposition (see Figure 1).

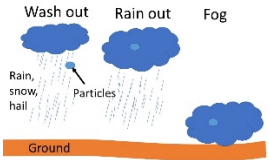

Figure 1: several types of wet deposition

Wet deposition by wash-out is the deposition of species (particulates and gaseous species) by precipitation scavenging between the bottom of the cloud and the surfaces (below-cloud capture). Gaseous species scavenging are water-soluble species. Particulate species are in collision with water droplets.
Wet deposition by rain-out is the deposition of species that were inside the clouds. It is the in-cloud capture of species. Many aerosol particles could act as cloud condensation nuclei (CCN) which lead to creation of liquid water droplets. The nucleated cloud particles are very small, but they grow. Particles can also be captured by aerosol already activated in liquid water droplets. Gaseous species are captured by liquid water

droplet (gaseous dissolution in a droplet). Wet deposition during a fog is a deposition by rain-out with fog touching the ground.

DEPOSITION MODEL

The fog deposition model in the CFD code_saturne tool is a loss term added to the species transport equation. The loss term is a deposition flux. The deposit will create a loss of water in the atmosphere, and we need to quantify the removal of fog droplets (for example by vegetation) from the atmosphere.

MECHANISMES FOR DEPOSITION

The mechanisms are different if the species is a gas or a particle. It exists several models of dry and wet deposition. The usual model assumes that sequential transfers between the atmosphere and the surface are considered resistances.

- The first transfer is between the atmospheric air and the surface. It is the atmospherically transport by turbulence for gas and particles. It is represented by an aerodynamic resistance Ra.
- The second transfer is near the surface. This quasi-laminar diffusion is represented by a quasi-laminar boundary layer resistance Rb. Brownian diffusion, inertial impact or impact by interception are the phenomena at stake for particles whereas molecularly diffusion is the phenomena for gaseous species. Other phenomena not taken into account in this model are not negligeable as thermophoresis and electrostatic forces (Wang, Zhang, & Moran, 2010). Thermophoresis should be taken into account for urban surfaces heated by the sun (Roupsard, 2013).
- The third transfer is on the surface, represented by a surface resistance Rc. There is no surface resistance for particle which is deposited directly on the surface unless the particle bounces. Several phenomena can happen for gaseous species as adsorption on surface, absorption by the surface (dissolution...), chemical reactions or several of them for dry deposition or gaseous dissolution droplet or adsorption on snow or hail for wet deposition.

Figure 2 shows a summary of the phenomena near the water droplet for wet deposition for gaseous species or particles.

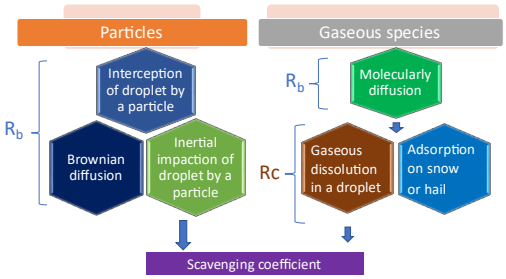

Figure 2: collision mechanisms near the surface for wet deposition for particles or for gaseous species.

Moreover, there is the sedimentation transfer. Because of Earth's gravity on particles and the air resistance, there is a gravitational particle sedimentation for wet deposition.

FACTORS INFLUENCING FOG WATER DEPOSITION

Particles/ water droplets diameter

Microphysical characteristics of several dense fogs show particles/raindrop diameters have diameters between 1 and 60 microns (Liu & Wu, 2020). Droplet sizes are around 10 µm similar to clouds and most clouds droplets have diameter over 5 µm (Seinfield & Pandis, 2016) (Gallagher, Choularton, & Fowler, 1988). Table 1 shows the main mechanism (collision and sedimentation) in function of the water droplet diameter for wet deposition (Thouron, 2017) (Wang, Zhang, & Moran, 2010). Particles with diameter with a size between 0.1 µ and 1 µ (Greenfield gap) give a weak wet deposition. As fog particles/droplets diameters are greater than 1µ, fog has mainly inertial impaction and sedimentation processes.

Table 1: main mechanism in function of water droplet diameter

Diameter (µm)	**<0.1**	**0.1 < D < 1**	**>1**	
Main mechanisms	Brownian diffusion	Greenfield gap	1.	Inertial impaction of a water droplet by particle
			2.	Sedimentation
			3.	Interception of a droplet by particle (not efficiency)

Liquid water content

Liquid Water Content LWC for fog is usually between 0.1 10^{-3} and 0.2 10^{-3} kg m^{-3} (Seinfield & Pandis, 2016). For example, two very different advection fogs deposition during several days of fog was monitored in The Netherlands (Vermeulen, et al., 1997) (Von Glasow & Bott, 1998). The characteristics of these two fogs are in the following table. The difference between the two fogs is explained by different wind speeds and droplet spectra.

Table 2:characteristics of fog deposition

	Unity	**Fog 1**	**Fog 2**
LWC	kg m^{-3}	$0.15.10^{-3}$- $0.3.10^{-3}$	$0.075.10^{-3}$- $0.125.10^{-3}$
Mean turbulent deposition flux	kg m^{-2} s^{-1}	1.46 10^{-6}	1.76 10^{-6}
Mean sedimentation flux	kg m^{-2} s^{-1}	1.96 10^{-6}	0.02 10^{-6}
Fog and cloud deposition	kg m^{-2} s^{-1}	3.4 10^{-3}	2 10^{-3}

Quantification of the species in the droplet

To measure the fog deposition, we quantify the droplets but we need to know the quantity of the species inside the droplet. Fog deposition formula should be different for gaseous species or for particles as the phenomena are not the same.

Wind Speed

For one year experiment in the Vosges (France), the paper from (Herckes, Mirabel, & Wortham, 2002) shows that the total deposition increases with the increasing wind speed (due to the impaction processes). Sedimentation and inertial impaction are the main fog deposition mechanisms (Table 1). Cloud droplet impaction is the major droplet removal process. Sedimentation can be important at low wind speed < 2 ms^{-1} (in particularly for fog). Sedimentation is the dominant process for deposition at low wind speeds (e.g.: radiation fog) while interception prevails at higher wind speeds (Von Glasow & Bott, 1998). The main mechanism for removing cloud droplets for flat terrain at low speeds is gravitational settling (Seinfield & Pandis, 2016).

Atmospheric cooling rate and aerosol properties and surface properties

The atmospheric cooling rate, the aerosol number concentration, size distribution and chemical composition have a role on CCN activation.

Fog water deposition is also sensitive to stability profile of the atmosphere and the surface roughness for complex terrain.

QUANTIFICATION OF DEPOSITION IN MODELS

A scavenging coefficient, Λ (s-1), can be used to quantify the proportion of the species removed from the atmosphere per unit of time. There are several definitions of the scavenging coefficient in the literature. The scavenging coefficient depends on gaseous species solubility, density, size of the particles, intensity of precipitation and granulometry of water droplets.

Sedimentation velocity Vs

The sedimentation velocity Vs (ms^{-1}) of water droplets is described in the Table 3 where ρ_p is the density of the particle ($kg.m^{-3}$), d_p is the diameter of the particle (m), g the gravitational acceleration (ms^{-2}), C_c is the Cunningham factor and μ_{air} is the cinematic viscosity of air ($m^2\ s^{-1}$), The factor of Cunningham is equal à 1 for particles diameter superior to one µm. It is the case for fog particles.

This sedimentation velocity comes from Stokes' law with an approximation as particle density is far bigger than air density. This formula is already incremented in code_saturne (Zhang X. , 2010).

Table 3: sedimentation velocity Vs for a spherical particle/droplet for different depositions

Wet deposition (droplets)	Fog deposition (fog droplets)
$\frac{\rho_p d_p^2 g\, c_c}{18\ \mu_{air}}$	$\frac{\rho_p d_p^2 g}{18\ \mu_{air}}$

Deposition velocity Vd, scavenging coefficient and deposition flux

To consider the deposition in our CFD model, we need to know the deposition flux. Table 4 gives examples of fog water parametrizations (deposition velocity, scavenging coefficient) to calculate the deposition flux.

Table 4: several deposition velocity Vd, scavenging coefficient and deposition flux

	Fog deposition examples	Selected fog deposition (Katata, 2014)
Deposition velocity (ms^{-1}) or scavenging coefficient (s^{-1})	$\Lambda = \frac{0.014\ L^{1.67} + 0.014\ L^{1.08d0}}{L * H_{fog}}$ $Vd = 0.195 u_*^2$ (Coniferous forest)	$Vd = Ri\ (0.095\ LAI^3 - 0.05 LAI^2 + 0.082)\ U$
Deposition flux F ($g\ m^{-2}\ s^{-1}$)	$F = C_g\ \Lambda\ h$	F = Vd *LWC

With LAI= Leaf Area Index; Ri= removal efficiency of fog droplets by different vegetation
U= lateral wind speed above the canopies (ms^{-1})

Fog water deposition model

1) The formula in the "selected fog deposition" column in the Table 4 give parametrization for fog water deposition for different surfaces (Katata, 2014). In this case, Ri represents the removal efficiency of fog droplets by vegetation. Table 5 gives the value of Ri for different vegetations.

Table 5: Value of the removal efficiency of fog droplets by different vegetation

Vegetation	Ri
Coniferous forest	1
Broad-leaved forests	0.826
Grass land	0.217

For relatively smooth surfaces such as bare soil and water, the mechanism of gravitational settling is assumed to be dominant, so the deposition velocity is the sedimentation velocity (Katata, 2014).

2) Another fog water model is described in (Zhang X. , 2010). It is based on the resistances' theory: Ra, Rb and on formulations from (Zhang L. G., 2001).

DIFFERENCE BETWEEN DEPOSITION

Wet deposition of pollutants is more efficient through fog than rain due to the larger droplet surface area and the longer residence time near the surface (Waersted, 2018). There is a significant contribution from fog water deposition to total deposition fluxes of water and pollutants (Katata, 2014). The concentrations of species as SO_4^{2-} or NH_4^+ in cloud water are five or ten times greater than in precipitation at the same sites in the United States (Seinfield & Pandis, 2016).

During the 15 months experiment in Nantes (France) where two radionuclides (beryllium ^{7}Be and lead $^{210}P_b$) were followed, dry period represents 97% of the experiment time (Laguionie, Roupsard, Maro, Solier, & Rozet, 2014). During the 15 months of experimental monitoring, deposition by rainout was the predominant mechanism. The paper from (Herckes, Mirabel, & Wortham, 2002) shows that the deposition fluxes of cloud water represent 10–28% of the total wet deposition (rain and cloud deposition) for major ions and 50% or higher for trace elements. The results are different depending on campaign conditions.

Table 6: Percentage of monthly total deposition for 15 months experiment

Particles	dry	Wet (rainout or fog)	Wet (washout)
^{7}Be	21%	67%	12%
^{210}Pb	28%	55%	17%

EXISTING MEASUREMENTS RELATED TO FOGWATER DEPOSITION

The paper from (Katata, 2014) gives a list of 26 existing measurements related to fog water deposition and their reference with different methods to measure fog water deposition. The paper gives information about uncertainties in fog water measurement methods. The deposition velocity in these studies is summarized in the following tables with a horizontal wind speed < 10 ms-1. The mean droplet diameter is between 5 and 25 micrometers.

Table 7: Minimum and maximum of the measured fog water deposition velocity from 26 campaigns

Measured deposition velocity	**Min ($m\ s^{-1}$)**	**Max ($m\ s^{-1}$)**
Short vegetation	$2.1.10^{-2}$	8.10^{-2}
Forest	$7.7\ .10^{-2}$	92.10^{-2}

CONCLUSION

To conclude, the deposition flux model is not easy to find because it exists in the bibliography various wet deposition models described in (Katata, 2014) . For radiation fog (windspeed < 2m/s) or for smooth surfaces (bare soil and water), the mechanism of gravitational settling is assumed to be dominant. As the magnitude of fog water deposition depends strongly on the vegetation, the fog water deposition model proposed by (Katata, 2014) seems to be accurate.

REFERENCES

Gallagher, M., Choularton, T. M., & Fowler, D. (1988). Measurements of the size dependence of cloud droplet deposition at a hill site. *Meteorol. Soc.*, 114, 1291–1303. https://doi.org/10.1002/qj.49711448307.

Herckes, P., Mirabel, P., & Wortham, H. (2002). Cloud water deposition at a high-elevation site in the Vosges Mountains (France). *The science of the total environment*, 296, 59–75, doi:http://dx.doi.org/10.1016/S0048-9697(02)00037-2.

Katata, G. (2014). Fogwater deposition modeling for terrestrial ecosystems: A review of developments and measurements. *Journal of Geophysical Research: Atmospheres, Atmospheres, 119(13), https://doi.org/10.1002/2014JD021669*.

Laguionie, P., Roupsard, P., Maro, D., Solier, L., & Rozet, M. (2014). Simultaneous quantification of the contributions of dry, washout and rainout deposition to the total deposition of particle-bound 7Be and 210Pb on an urban catchment area on a monthly scale. *Journal of Aerosol Science, 77, 67-84.*

Liu, Q., & Wu, B. (2020). Fog Droplet Size Distribution and the Interaction between Fog Droplets and Fine Particles during Droplets and Fine Particles during Dense Fog in Tianjin, .

Roupsard, P. (2013). Etude phénoménologique du dépôt sec d'aérosols en milieu urbain : Influence des propriétés des surfaces, de la turbulence et des conditions météorologiques.

Seinfield, J., & Pandis, S. (2016). *Atmospheric chemistry and physics : from air pollution to climate change.* Hoboken.: John Wiley & Sons_Third edition.

Thouron, L. (2017). *Modélisation dynamique multi-échelle de la pollution atmosphérique en milieu urbain.* Thèse de doctorat: université Paris Est.

Vermeulen, A. T., Wyers, G. P., Römer, F. G., Van Leeuwen, N. F., Draaijers, G. P., & Erisman, J. W. (1997). Fog deposition on a coniferous forest in The Netherlands. *Atmospheric Environment, Volume 31, Issue 3, doi:http://dx.doi.org/10.1016/S1352-2310(96)00056-8*, 375-386.

Von Glasow, R., & Bott, A. (1998). Interaction of radiation fog with tall vegetation. *Atmospheric environment*.

Waersted, E. (2018). *Description of physical processes driving the life cycle of radiationfog and fog–stratus transitions based on conceptual models.*

Wang, X., Zhang, L., & Moran, D. (2010). Uncertainty assessment of current size-resolved parameterizations. *Atmospheric chemistry and physics*.

Zhang, L. G. (2001). A size-segregated particle dry deposition scheme for an atmospheric aerosol module. Atmospheric Environment.

Zhang, X. (2010). *Modélisation du brouillard durant la campagne ParisFog : approche prédictive et étude de l'effet des hétérogénéités spatiales.* Thèse de Doctorat de l'Ecole Nationale des Ponts et Chaussées, 175 pp. .

21st International Conference on
Harmonisation within Atmospheric Dispersion Modelling for Regulatory Purposes
27-30 September 2022, Aveiro, Portugal

MODELLING FREE TROPOSPHERIC TURBULENCE IN AN ATMOSPHERIC DISPERSION MODEL

Andrew Mirza, Helen F. Dacre

SHORT ABSTRACT

Abstract title: Modelling free tropospheric turbulence in an atmospheric dispersion model.

Name and Affiliation of the First Author:

Andrew K. Mirza,

Department of Meteorology, University of Reading, Reading, United Kingdom

Email of the first author:

andrew.mirza@reading.ac.uk

Names and Affiliations of the Co-authors:

Helen F. Dacre,

Department of Meteorology, University of Reading, Reading, United Kingdom

Abstract text *(maximum 350 words.)*

Recent studies suggest that the representation of turbulent mixing above the boundary layer (hereafter referred to as the free-troposphere) may be a significant source of uncertainty in the Met Office's Numerical Atmospheric dispersion ModEl (NAME) and other similar models. Observations suggest that there is significant temporal and spatial variability in the magnitude of free-tropospheric turbulent mixing. But in NAME, the representation of this turbulence is usually assumed to have a fixed value, which may result in over- or under-estimation of mixing. We implemented in NAME a simple parameterization to represent space and time-varying turbulence in the free troposphere. The parameterization uses vertical and horizontal wind speed gradients to estimate turbulent energy dissipation. We use an empirical relationship to convert the turbulent energy dissipation into vertical velocity variance, for a fixed value of the Lagrangian

timescale. We compared the two turbulence schemes for case study periods over the United Kingdom, Ireland and surrounding water.

For the space and time-varying scheme, we found that there exists a systematic enhancement of the vertical velocity variance just above the boundary layer height around the mainland coastal regions. This enhancement begins during the early afternoon, reaches a peak during the transition from late afternoon to the early evening before decaying overnight. The synoptic conditions that may lead to the enhanced vertical velocity variance are associated with the formation of low-level jets. The mechanisms generating these jets are currently being investigated.

To evaluate the impact of the new parameterization, we use the radon tracer method and a semi-idealised radon emissions model. Our analysis suggests that the enhanced vertical velocity variance just above the boundary layer leads to enhanced ventilation of near-surface radon around coastal regions. This may have implications for source inversion modelling used to identify the probable sources of atmospheric pollutants, e.g., industrial emissions, accidental chemical releases or greenhouse gases.

Words: 305.

21st International Conference on
Harmonisation within Atmospheric Dispersion Modelling for Regulatory Purposes
27-30 September 2022, Aveiro, Portugal

NON-CO2 FORCERS AND THEIR CLIMATE, WEATHER, AIR QUALITY AND HEALTH IMPACTS – NEW PROJECT FOCI

Tomas Halenka, Ranjeet S. Sokhi

SHORT ABSTRACT

Abstract title: NON-CO2 FORCERS AND THEIR CLIMATE, WEATHER, AIR QUALITY AND HEALTH IMPACTS – NEW PROJECT FOCI

Name and Affiliation of the First Author: Tomas Halenka, Charles University, Dept. of Atmospheric Physics, Prague, Czech Republic

Email of first author: tomas.halenka@mff.cuni.cz

Names and Affiliations of the Co-authors: Ranjeet S. Sokhi, Department of Physics, Astronomy and Mathematics; School of Physics, Engineering and Computer Science; University of Hertfordshire, Hartfield, United Kingdom

And FOCI team

Abstract text *(maximum 350 words.)*

While overall the global warming with the causes and global processes connected to well mixed greenhouse gases (GHGs), especially CO2, and their impacts on global to continental scales are well understood with a high level of confidence, there are knowledge gaps concerning the impact of many non-CO2 radiative forcers leading to low confidence in the conclusions. This relates mainly to specific anthropogenic and natural precursor emissions of short-lived GHGs and aerosols and their precursors. These gaps and uncertainties also exist in their subsequent effects on atmospheric chemistry and climate, through direct emissions dependent on changes in e.g., agriculture production and technologies based on scenarios for future development as well as feedbacks of global warming on emissions, e.g., permafrost thaw. In addition to the atmospheric radiative forcing (gaseous or aerosols), albedo changes connected to land-use and land-cover can play a role, depending on the adaptation or mitigation measures included in different scenarios.

Thus, the main goal of the new EC Horizon Europe project FOCI (accepted within the call HORIZON-CL5-2021-D1-01-0 Improved understanding of greenhouse gas fluxes and radiative forcers, including carbon dioxide removal technologies), which will be presented, is to assess the impact of key radiative forcers, where and how they arise, the processes of their impact on the climate system, to find and test an efficient implementation of these processes into global Earth System Models and into Regional

Climate Models, eventually coupled with CTMs, and finally to use the tools developed to investigate mitigation and/or adaptation policies incorporated in selected scenarios of future development targeted at Europe and other regions of the world. We will develop new regionally tuned scenarios based on improved emissions to assess the effects of non-CO2 forcers. Mutual interactions of the results and climate services producers and other end-users will provide feedbacks for the specific scenarios preparation and potential application to support the decision making, including climate policy.

21st International Conference on
Harmonisation within Atmospheric Dispersion Modelling for Regulatory Purposes
27-30 September 2022, Aveiro, Portugal

TOMOGRAPHIC 3D RECONSTRUCTIONS OF ARTIFICIAL RELEASES OF SO2 IN THE ATMOSPHERIC BOUNDARY LAYER

Ignacio Pisso, Massimo Cassiani, Anna Solvejg Dinger,Hamidreza Ardeshiri, Soon-Young Park, Kerstin Stebel, Arve Kylling, Norbert Schmidbauer, Andreas Stohl

SHORT ABSTRACT

Abstract title: Tomographic 3D reconstructions of artificial releases of SO2 in the atmospheric boundary layer

Name and Affiliation of the First Author: Ignacio Pisso

Email of first author: ip@nilu.no

Names and Affiliations of the Co-authors: Massimo Cassiani[1], Anna Solvejg Dinger[1], Hamidreza Ardeshiri[1], Soon-Young Park[2], Kerstin Stebel[1], Arve Kylling[1], Norbert Schmidbauer[1] and Andreas Stohl[3]

[1]Norwegian Institute for Air Research (NILU), Kjeller, Norway
[2]GIST Gwangju Institute of science and technology, Gwangju, South Korea

[3]University of Vienna, Vienna, Austria

Abstract text *(maximum 350 words.)*

Turbulence in the planetary boundary layer controls the dispersion of air pollutants and exchange fluxes of passive and active tracers between the Earth's surface and the atmosphere. In air quality, climate and meteorological models, such effects of turbulence need to be parameterized, ultimately based on experimental data. A modeling/experimental approach was developed within the COMTESSA project to study turbulence statistics at high resolution. Using controlled tracer releases, high-resolution camera images and estimates of the background radiation, different tomographic algorithms were applied to obtain time series of 3D representations of the scalar dispersion. We used initially synthetic data to investigate different reconstruction algorithms with emphasis on algebraic iterative methods, studying the dependence of the reconstruction quality on the discretization resolution and the geometry of the experimental device in both 2D and 3D cases. For the iterative methods we assessed the computational aspects of the iterative algorithms focusing of the phenomenon of semi-convergence applying a variety of stopping rules. We also investigated the use of L^1 minimization-regularization algorithms such as LASSO and assessed the connection with compressed sensing. Based on the results and experience developed with synthetic data, we developed and applied tomographic 3D reconstructions to a field experiment in Norway, where artificial SO2 puffs were released and tracked using multiple UV

camera measurements. Here, in addition to the synthetic studies, we present actual tomographic 3D reconstructions of artificial SO2 puffs using multiple camera measurements from the experimental campaigns in Norway. We show preliminary analysis demonstrating that the 3D tomographic reconstruction can be a viable method for an improved understanding of turbulent dispersion processes and ultimately formulation of parametrizations in the atmospheric boundary layer.

21st International Conference on
Harmonisation within Atmospheric Dispersion Modelling for Regulatory Purposes
27-30 September 2022, Aveiro, Portugal

AVIATION ENVIRONMENTAL IMPACTS
Amela Jeričević, Goran Gašparac

SHORT ABSTRACT

Aviation environmental impacts:

Amela Jeričević, *Croatia Control Ltd., Velika Gorica, Croatia*

amela.jericevic@crocontrol.hr

Goran Gašparac, Croatia Control Ltd., Velika Gorica, Croatia:

Abstract text *(maximum 350 words.)*

In this research, we focused on understanding the influence of aircraft emissions on local air quality using air quality measurements and modeling results. One year of air quality data obtained at Zagreb Airport has been analyzed to assess the level of air pollution due to air traffic. Air transportation growth has rapidly increased over the years and notable influences of aviation emissions on local and regional air quality as well as on climate are identified. The environmental impacts of atmospheric emissions from aircraft have been addressed in two separate ways; aircraft pollutant emissions occurring during the landing and take-off (LTO) phase (local pollutant emissions), and the non-LTO phase (global/regional pollutant emissions). Aircraft pollutant emissions are an important source of pollution and directly or indirectly harmfully affect human health and ecosystems. The AIRMODE model was applied in order to calculate local concentrations of CO, PM10 and NO2 around the Zagreb airport in Croatia. Furhter on the WRF-Chem model was used to estimate the contributions of aviation emissions with several different emission scenarios.

21st International Conference on
Harmonisation within Atmospheric Dispersion Modelling for Regulatory Purposes
27-30 September 2022, Aveiro, Portugal

APPLICATION OF STOCHASTIC WALL BOUNDED TURBULENT FLOW MODEL TO RESUSPENSION

David Ben Shlomo, Eyal Fattal, Ronen Berkovich

SHORT ABSTRACT

Abstract title: **Application of Stochastic Wall Bounded Turbulent Flow Model to Resuspension**

Name and Affiliation of the First Author: David Ben Shlomo, Israel Ministry of Defense and Ben-Gurion University of the Negev

Email of first author: benshlod@post.bgu.ac.il

Names and Affiliations of the Co-authors: Ronen Berkovich, Ben-Gurion University of the Negev and Eyal Fattal, Israel Institute for Biological Research

Abstract text *(maximum 350 words.)*

Resuspension describes a phenomenon, which is related to the separation of particles from a surface on which they are deposited. This process plays an important role in understanding and treating the dispersion of hazardous particles from surfaces, and with respect to various environmental as well as industrial applications such as reactors performance and maintenance, ventilation, and semi-conductor fabrication. Here we introduce an up-to-date quantitative theoretical model of particle resuspension from rough surfaces under the influence of the turbulent flow. To this end, we have employed a modelling scheme that utilizes a probabilistic approach based on the stochastic Lagrangian theory to describe particle resuspension. Our model, based on the approach suggested by Fu et al. (J. Fluids Eng., 2013) incorporates the hydrodynamic forces that are exerted on a deposited particle on a rough surface with contact mechanics, including turbulent statistics associated with sweep-burst cycle. The model is in relatively good agreement with experimental data, where some deviation in high friction velocities is observed. In order to describe the resuspension process more realistically, we have

expanded the sub-model of the flow acting on the particle, so it would be based on the Generalized Langevin Equation (GLE) with a memory kernel.

21st International Conference on
Harmonisation within Atmospheric Dispersion Modelling for Regulatory Purposes
27-30 September 2022, Aveiro, Portugal

EFFECT OF BUILDING SHAPES ON FLOW FIELD AROUND A HIGH-RISE BUILDING

Keyi Chen, Ziwei Mo

SHORT ABSTRACT

Abstract title: Effect of building shapes on flow field around a high-rise building

Name and Affiliation of the First Author: Keyi Chen, School of Atmospheric Sciences, Sun Yat-sen University, Zhuhai, China

Email of first author: chenky68@mail2.sysu.edu.cn

Names and Affiliations of the Co-authors: Ziwei Mo, School of Atmospheric Sciences, Sun Yat-sen University, Zhuhai, China

Abstract text *(maximum 350 words.)*

With rapid development of urbanization, the urban population and the density of buildings are increasing significantly in urban areas of China. As high-rise buildings block the air flow and alter the wind environment, the ventilation, pollutant dispersion and outdoor human comfort are highly affected in the urban canopy layer (UCL). However, the geometries and shapes of the high-rise building complicate the wind and turbulence, which attract wide attention but need more investigation. In this study, we use computational fluid dynamic (CFD) modeling to examine the effect of building shapes on the flow field and pedestrian-level wind environment around a high-rise building. Firstly, with validation of wind tunnel data, we examine the flow fields around a high-rise building with a 1:1:2 shape. Then, ten types of typical building shapes are considered, including square, rectangle, triangle, circle, cross-shaped, T-shaped, L-shaped, #-shaped, H-shaped and Y-shaped. The mean flow and turbulence characteristics around different types of building shapes will be reported in details in the conference. Our findings can provide suggestions on improving wind comfort and pollutant dispersion in the urban areas.

21st International Conference on
Harmonisation within Atmospheric Dispersion Modelling for Regulatory Purposes
27-30 September 2022, Aveiro, Portugal

TILT CORRECTION METHOD FOR THE ESTIMATION OF SCALING VARIABLES OF MONIN-OBUKHOV SIMILARITY THEORY IN URBAN AREAS

Armando Pelliccioni, Livia Grandoni, Annalisa Di Bernardino, Paolo Monti

SHORT ABSTRACT

Abstract title: Tilt correction method for the estimation of scaling variables of Monin Obukhov Similarity Theory in urban areas

Name and Affiliation of the First Author: Armando Pelliccioni [1]

Email of first author: a.pelliccioni@inail.it

Names and Affiliations of the Co-authors: Livia Grandoni[1, 2, 3], Annalisa Di Bernardino [4], Paolo Monti [2]

[1] Compensation Authority (INAIL), Monte Porzio Catone, 00078 Rome, Italy

[2] Department of Civil, Constructional and Environmental Engineering, Sapienza University, 00185 Rome, Italy

[3] Laboratoire de Mécanique des Fluides et d'Acoustique, UMR CNRS 5509, Université de Lyon, École Centrale deLyon, INSA Lyon, Université Claude Bernard Lyon I, 69134 Écully, France

[4] Physics Department, Sapienza University, 00185 Rome, Italy

Abstract text

The Monin-Obukhov Similarity Theory (MOST) is a useful tool to study pollutant dispersion in the atmospheric boundary layer. It provides parametrizations that link the profiles of the main meteorological variables – such as temperature, wind velocity and its variance – to some scaling variables. However, the estimation of these scaling quantities is not an easy task, especially if urban areas are considered. Here the airflow becomes very complex due to the presence of the buildings. Below the constant flux layer (CFL) the so-called roughness sublayer (RSL) forms, where the airflow is three
dimensional and non-homogeneous. Several works tackled the problem of applying the MOST in urban areas. Some of them suggested the extension of the MOST also in the CFL by using local scaling variables, varying with the height. In order to estimate the scaling variables – namely the friction velocity and the Obukhov length – and apply the local MOST in urban areas, measures of turbulent fluxes at different heights are required. Alternatively, to apply the MOST only in the CFL, measures at very high altitude (beyond the RSL) should be carried out.
In the present work a method to estimate friction velocity and Obukhov length from measures of turbulent fluxes at one height within the RSL is proposed. The

measured fluxes are corrected considering the distortion of the airflow and, thus, applying a rotation to wind data.
The data used for testing the method have been acquired during a measuring campaign lasted for two years, from December 2017 to December 2019. The turbulent fluxes are measured by means of a sonic anemometer located above a building in the urban area of Rome. A sonic detection and ranging (SODAR) provides mean wind velocity and standard deviation of vertical wind velocity (σ_w) which have been used for validation.

In an already published work the improvement of the performance of the MOST for σ_w using the corrected turbulent fluxes with respect to the raw ones is shown. In the present work the database has been extended and the method tested also for mean wind velocity profiles.

21st International Conference on
Harmonisation within Atmospheric Dispersion Modelling for Regulatory Purposes
27-30 September 2022, Aveiro, Portugal

RELATIONSHIP BETWEEN ULTRAFINE PARTICLE CONCENTRATIONS AND TURBULENT PARAMETERS IN AN INDOOR WORKPLACE

Armando Pelliccioni, Monica Gherardi, Paolo Monti, Agnese Pini, Giovanni Leuzzi

SHORT ABSTRACT

Relationship between ultrafine particle concentrations and turbulent parameters in an indoor workplace

Name and Affiliation of the First Author: Armando Pelliccioni, Compensation Authority (INAIL), Monte Porzio Catone, 00078 Rome, Italy

Email of first author: a.pelliccioni@inail.it

Names and Affiliations of the Co-authors: Monica Gherardi [1], Paolo Monti [2], Agnese Pini [2], Giovanni Leuzzi [2]

[1] Compensation Authority (INAIL), Monte Porzio Catone, 00078 Rome, Italy

[2] Department of Civil, Constructional and Environmental Engineering, Sapienza University, 00185 Rome, Italy

Abstract text

In the framework of the VIEPI project (Integrated Evaluation of Indoor Particulate Exposure), an intense field campaign has been conducted in the Giacomini lecture hall at the Department of Environmental Biology of Sapienza University of Rome. The field campaign included high frequency (1 Hz) measurements of ultrafine particles (UFP) concentrations as well as air velocity and temperature measured by three ultrasonic anemometer (10 Hz) located within the room. The field campaign started on 12 October 2021 and lasted for one month.

The UFPs have been collected using a fast mobility particle size (FMPS), which is able to measure particle size distributions from 5.6 nm to 560 nm in diameter. From these data, one-minute averages of particle number concentrations (PNC, #/cm^3) and median diameters were calculated for all the campaign duration. Similarly, one minute averages of air temperature, air velocity, turbulence kinetic energy (TKE) and mean kinetic energy (MKE) have been calculated from the anemometers. Two time slots were considered for the analysis: the first one concerned nighttime hours (from 7pm to 7am), while the second one regarded daytime hours (from 7am to 7 pm). The results show that the average daily PNC are always higher than the nighttime ones during the working days (6808 #/cm^{3}and 6527 #/cm^{3}respectively), while the opposite occurs for the weekends (5283 #/cm^{3}and 7312 #/cm^3, respectively). To what concerns the median diameter, the average values are quite similar for the nights of working days and

weekends (52.7 nm and 56.6 nm, respectively), while considerable differences occurs when daytime hours are considered (38.8nm and 51.4, respectively).

These results indicate that during non-working hours the indoor can be considered as a 'reaction room isolated by the outside conditions'.
On average, both the nighttime TKE and MKE are always low (about 10^{-4} m^2/s^2), while the values during daily slots are higher (0.09 m^2/s^2 for TKE and 0.13 m^2/s^2 for MKE). The results show that the dynamics of pollutants and that of the turbulence variables are different during working hours and non-working hours and that higher UFP values are observed with low ventilation regimes, in connection with the TKE.

TOPIC 5:

URBAN SCALE AND STREET CANYON MODELLING: METEOROLOGY, AIR QUALITY AND PASSIVE CONTROL SYSTEMS

21st International Conference on
Harmonisation within Atmospheric Dispersion Modelling for Regulatory Purposes
27-30 September 2022, Aveiro, Portugal

EFFECT OF UPSTREAM BUILDING ON THE POLLUTANT DISPERSION IN URBAN CANOPY WITH CHANGES THERMAL STABILITY

Mohamed F. Yassin, Marium Malak and Musaed Shalsh

Environment & Life Sciences Center, Kuwait Institute for Research and Science, Kuwiat

Abstract: Upstream building and atmospheric stability are critical parameters in dispersing and transporting pollutants in an urban canopy. These parameters' effect can be seen locally in each building's vicinity and the pollutants' transport from one region of the urban environment to another further away. Near-field pollutant dispersion is a cause of concern for most health physicists and regulatory agencies. Therefore, the main goal of this study was to investigate and evaluate the influence of the upstream building on wind flow and near-field pollutant dispersion in the urban canopy under different atmospheric thermal stabilities. The diffusion flow and dispersal of gaseous pollutants were modeled using a computational fluid dynamics model (CFD). The CFD models were incorporated with three-dimensional standard and RNG k-ε turbulence models and were solved using Reynolds-averaged Navier–Stokes equations. The modeled results were validated against the wind tunnel experimental data. The results showed that the streamwise and spanwise velocities are significantly lower inside the building arrays than outside. The strong wind shear was observed near the building height at the center of the building arrays. The increases in the turbulent kinetic energy converged inside the building arrays. The pollutant concentration levels close to the ground level were higher under stable conditions than unstable and neutral conditions. Pollutant concentration inside the building arrays increased with stable conditions and decreased with unstable conditions.

Key words: *Atmospheric stability; Pollutant dispersion; CFD models;Wind tunnel; Upstream building.*

INTRODUCTION

The wind flow and near-field pollutant dispersion in the urban canopy are influenced by the geometrical features of buildings, which affect the dispersion of pollutants within and above the building arrays. This effect can be seen locally in each building's vicinity and the pollutants' transport from one region of the urban environment to another further away. Near-field pollutant dispersion is a cause of concern for most health physicists and regulatory agencies. Pollutants emitted from the point source within the recirculation region may re-enter the building from which they are emitted and affect an adjacent building in the vicinity. Previous studies have considered the effect of the different roof shapes on the building configurations in the urban area (e.g., Yassin et al., 2005, 2008a, b; Yassin, 2009, 2010, 2011; Kellnerova et al., 2012; Yassin and ohab, 2012a,b, 2013a,b,c,d; Yassin and Kassem, 2014; Hang et al., 2015; Wen and Malki-Epshtein, 2016; Llaguno-Munitxa et al., 2017; Ntinas et al., 2018, Yassin et al., 2021). Recently, Zhang et al. (2021) investigated the impact of the change in triangular roof angles on the diffusion of gaseous pollutants and particulate matter by the Euler–Lagrangian method. Results indicate that the lowest concentration of pollutants is when a single vortex exists. Klukova et al. (2021) discussed the effects of the roof shape and its height with the location of the source on the pollutant dispersion in the urban arrays by using CFD models. The results show that roof height, roof shape, and the source location have an essential effect on the advective and pollutant distribution and transport between the studied street canyons and urban arrays. The main aim of this study is to compute the dispersion of vehicle emissions in and out urban canopy. In particular, the investigation is made into the effect of the upstream buildings on the pollutant dispersion.

METHODOLOGY

Computational Models

The computational simulation used in the study is CFD models were based on using Reynolds-averaged Navier–Stokes equations with k-ε turbulence models. The computational model was conducted using ANSYS FLUENT software, Version 2020 R1 (ANSYS, 2020), which is a widely used model that

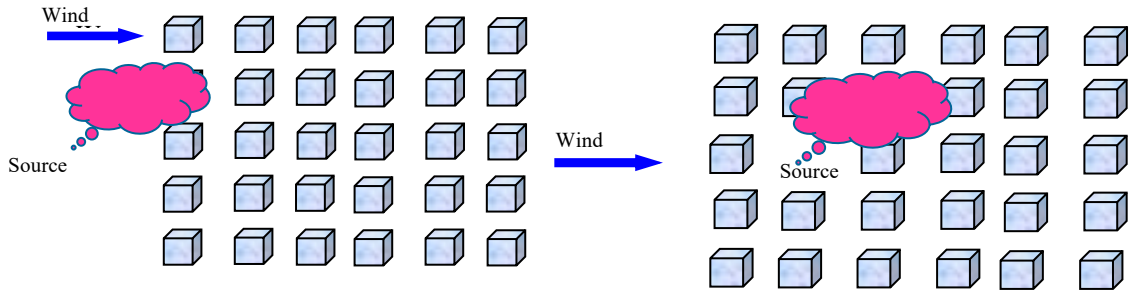

Fig. 1 building array models and point sources at the upstream distance and building

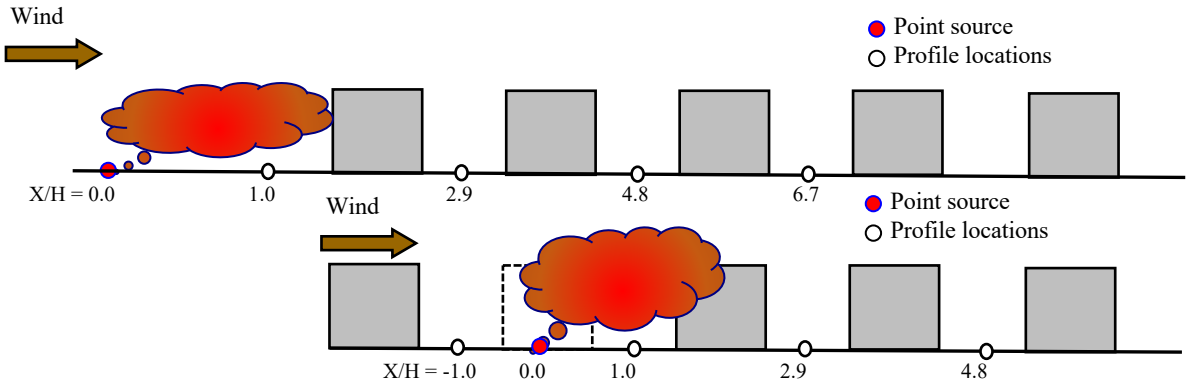

Fig. 2. Profile locations and point source outside and inside building's array.

incorporates several turbulence models. ANSYS FLUENT software for the computational is based on a finite volume approach for solving the flow and pollutant dispersion equations. The flow's computational description is based on the pseudo-steady-state incompressible RANS equations equipped with two turbulence models: the standard κ-ε turbulence model (Launder, 1974) and the RNG turbulence model (Yakhot, 1992). The equations were solved on a staggered grid using a finite volume following the semi-implicit method for the pressure-linked equations (SIMPLE) described by Patankar (1980).

Building models Configurations

Figure 1 displays building array models and point sources at the upstream distance and building. The equivalent height of the building model (H) was 100 mm. During this study, 30 three-dimensional cubical building models (0.75 H × 0.75H × 0.75H) with 6-row and 1-column buildings under approaching wind flow perpendicular to the row buildings were used, where x, y, and z denote the horizontal, lateral, and vertical axes. The distance gap between the buildings was H. The gas pollutant is emitted from a point source with a diameter of 0.067 H. The pollutant source location outside and inside the building arrays was as follows: (a) Hs = 0.0 at X/H=-1.5 distance upstream of the first array of the buildings, (b) Hs = 0.0 at X/H=0.0 inside the building's array. Fig. 2 shows the profile locations and point sources outside and inside the building's array.

Computational Domain

The computational domain of the building arrays' configurations was built using hexahedral elements with a finer resolution within the entire building area. The expansion rate between two consecutive cells was below 1.2. The grid in the simulation domain consisted of 2382693 cells, 5176261 faces, and 701640 nodes. The domain was discretized into 231.33 x 129.33x 106.67 cells. The distance of the simulation boundaries from the inlet, outlet, lateral, and upper domain was 6.67 H, 13.33 H, 16 H, and 14 H, respectively.

RESULTS AND DISCUSSIONS

Computational Simulation Validation

The computational simulation data in the study was validated using the experimental data used in the study

was obtained from then the thermal diffusion wind tunnel experiments by Yassin (2013a, b). The dimensionless concentration was provided as $K = C^*U_H H2/Q$, where C* measured the actual concentration. U_H is the free streamwise velocity at building height H. Q is the source volume flow rate. The computed and measured dimensionless concentration K out and in the building's array are shown in Fig.3. It can be observed clearly that the CFD models match reasonably well with the experimental data. Therefore, the K-ε turbulent model is applicable for the computational simulation of the pollutant dispersion in and out building's array. However, the standard κ-ε turbulence model results are in the best agreement with the experimental flow data.

Dispersion Simulation

The pollutant concentration contours in the urban canopy in the vertical plane at Y/H=0.5 and the horizontal plane at the human level are presented in Figures 4-5. It can be shown that concentrations were expected to decrease with distance from the source. Compared to the effect of the atmospheric thermal stability on the pollutant concentration, the flow suppresses' vertical motion, and the lateral movement of the flow increases under stable conditions. Consequently, the vertical spreading of pollutant plume reduces, and the lateral spread of the plume rises. The concentration levels close to the ground level were higher under stable conditions than under unstable and neutral conditions due to the lateral flow transferring the contaminant away from the building. Pollutant concentration inside the building arrays increased with stable conditions. It decreased with unstable conditions due to the air change inside the building arrays is affected mainly by the turbulence mixing between the inside arrays and the free stream and affected by the intensity of the recirculation vortex, which changed significantly in stable conditions. The pollutant concentration is higher under the neutral condition than in the unstable one and lower than the stable one. Compared to the upstream building's effect on the pollutant concentration, the upstream building's pollutant concentration levels were lower than those without the upstream building inside and outside the building arrays. This is because the movement of the large recirculation vortex in the upstream building zone was weak. The minimum value of the pollutant concentration was inside the building arrays. In the case without the upstream building, more pollutants move at the upwind building's side facet; whereas, with the upstream building, more pollutants move to the leeward wall when the source is emitted from the ground level Hs/H=0.0 and move to the windward wall when the source is emitted from the source height Hs/H=1.0. The variation in pollutant concentration in the source zone outside and inside the building arrays was lesser under stable, neutral, and unstable conditions than the concentration inside the building arrays. On the other hand, at the human level, the pollutant dispersion under the stable conditions is distributed quite symmetrically to that under the neutral and unstable conditions. The lateral dispersion of the pollutant concentration along with the downstream direction increased far away from the source.

REFERENCES

ANSYS Inc. ANSYS FLUENT software 2020, . http://www.ansys.com/

Kellnerova, R., Kukacka, L., Jurcakova, K., Uruba, V., Janour, Z., 2012. PIV Measurement of Turbulent Flow Within a Street Canyon: Detection of Coherent Motion. J Wind Eng Ind Aerodyn 104-106, 302-313.

Kluková, Z., Nosek, Š., Fuka, V., Jaňour, Z., Chaloupecká, H. and Ďoubalová, J., 2021. The combining effect of the roof shape, roof-height non-uniformity and source position on the pollutant transport between a street canyon and 3D urban array. J. of Wind Engineering and Industrial Aerodynamics, *208*, p.104468.

Launder B.E., Spalding D.E. The numerical computation of turbulent flows. Comp. Meth. Appl. Mech. Eng. 1974, *3*, 269-289.

Llaguno-Munitxa, M., Bou-Zeid, E. and Hultmark, M., 2017. The influence of building geometry on street canyon air flow: validation of large eddy simulations against wind tunnel experiments. Journal of Wind Engineering and Industrial Aerodynamics, 165, pp.115-130.

Ntinas, G.K., Shen, X., Wang, Y. and Zhang, G., 2018, February. Evaluation of CFD turbulence models for simulating external airflow around varied building roof with wind tunnel experiment. In Building Simulation (Vol. 11, No. 1, pp. 115-123). Springer Berlin Heidelberg.

Patankar S.V. Numerical heat transfer and fluid flow. McGraw-hill. 1980

Wen, H. and Malki-Epshtein, L., 2016: A Parametric Study of the Impacts of Pitched Roofs on Flow and Pollution Dispersion in Street Canyons. International Building Performance Simulation Association.

Yakhot V., Orszag S.A., Thangam S., Gatski T.B., and Speziale C.G., 1992: Development of turbulence models for shear flows by a double expansion technique, Phys. Fluids A , 4 (7): 1510-1520.

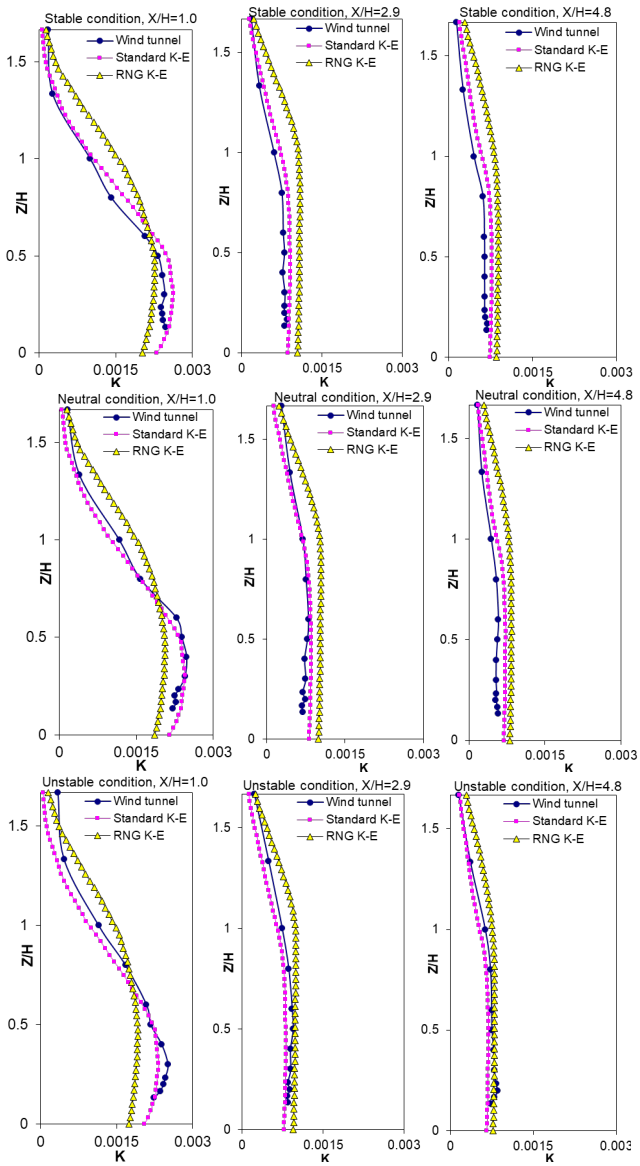

Fig. 3. The simulated and wind tunnel data of the dimensionless pollutant concentration

Yassin M.F., Kato S., Ooka R., Takahashi T. and Kouno R. (2005) "Field and Wind Tunnel study of the pollutant diffusion in built-up area under variable meteorological Conditions" Journal of Wind Engineering and Industrial Aerodynamics, 93(5), 361-382

Yassin M.F., Ohba M., and Tanaka H. (2008a) "Experimental Study on Gaseous Diffusion behind an isolated building" Environmental Monitoring and Assessment. 147 (1-3), 149-158.

Yassin M.F., Kellnerov *R.* and Janour Z. (2008b) "Impact of Street Intersections on Air Quality in an Urban Environment" Atmospheric Environment. Vol. 42/20, 4948-4963

Yassin M. F. (2009) "Numerical Study of Flow and Gas Diffusion in the Wake behind an Isolated Building" Advances in Atmospheric Sciences, 26(6), 1241-1252.

Yassin M.F. (2010) " Study on Pollutant Dispersion Within Urban Area: Under Changes of Atmospheric Stability and Wind Direction." VDM Publishing House Ltd, ISBN 978-3-639-27279-6

Yassin, M.F., 2011. Impact of height and shape of building roof on air quality in urban street canyons. Atmospheric Environment, 45(29), pp.5220-5229.

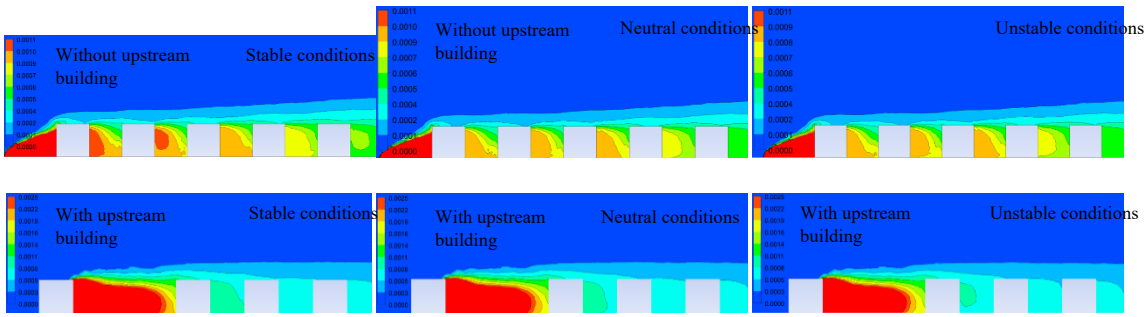

Fig.4. Dimensionless pollutant concentration under changing atmospheric thermal stability in the *x-z* at Y/H=0.5.

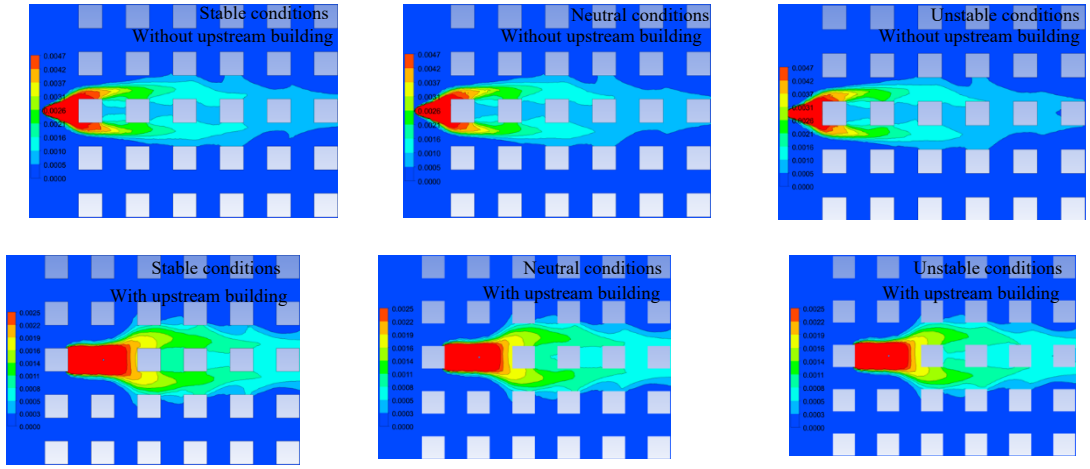

Fig. 5. Dimensionless pollutant concentration under changing atmospheric thermal stability in the *x-y* at the human level.

Yassin M.F., Ohba M. (2012a) "Experimental Simulation of Air Quality in Street Canyon under Changes of Building Orientation and Aspect Ratio" J. of Exposure Science and Envir. Epidemiology; 22(5) 502-515
Yassin M.F. and Ohba M. (2012b) "Experimental Study of the Impact of Structural Geometry and Wind Direction on Vehicle Emissions in Urban Environment" Transp. Res. P.t D: Transp. & Envir., 17, 181-189
Yassin M.F (2013a) "A wind tunnel study on the effect of thermal stability on flow and dispersion of rooftop stack emissions in the near wake of a building" Atmospheric Environment, 65, 89-100.
Yassin M.F. 2013b: Experimental Study on Contamination of Building Exhaust Emissions in Urban Environment under Changes of Stack Locations and Atmospheric Stability. Energy and Build., 62, 68-77.
Yassin M.F. (2013c) Numerical simulation of the impact of street geometry on vehicle emissions in the urban area, Int. J. of Environment and Pollution, 53(1/2), 46-63
Yassin M.F (2013d) "Numerical Modeling on Air Quality in an Urban Environment with changes of the Aspect Ratio and Wind Direction" Environmental Science and Pollution Research, 20, 3975-3988
Yassin M.F., Ohba M. (2013) "Effect of Street Geometrical Layout on Dispersion emissions of Traffic Exhaust: Experimental Simulation" Clean Technologies and Environmental Policy, 15(1) 167-177.
Yassin M.F., Kassem M. A. (2014) Effect of Building Orientations on Gaseous Dispersion in Street Canyon: a Numerical Study, Environmental Modeling & Assessment, 19(4), 335-344.
Yassin, M.F. , Alhajeri N.S., Elmi A. A., Malek M. J., Shalash M., (2021). Numerical simulation of gas dispersion from rooftop stacks on buildings in urban environments under changes in atmospheric thermal stability. *Environ Monit Assess*, **193,** 22. https://doi.org/10.1007/s10661-020-08798-x
Zhang, X., Wang, C., Liu, X., Zhou, T., Tao, C. and Shi, Q., 2021. Effect of triangular roof angle on dispersion of gaseous pollutants and particulate matter. *Environmental Science and Pollution Research*, *28*(12), pp.15537-15550.

21st International Conference on
Harmonisation within Atmospheric Dispersion Modelling for Regulatory Purposes
27-30 September 2022, Aveiro, Portugal

STUDY OF ATMOSPHERIC DISPERSION UNDER LOW WIND CONDITIONS IN AN URBAN ENVIRONMENT, FIRST RESULTS

1,2h. Bounouas, 1p. Roupsard, 2e. Dupont, 2y. Roustan, 1j. Chardeur, 1o. Connan, 1d. Hebert, 1p. Laguionie, 1d. Maro, 1h. Renard, 1m. Rozet, 2t. Regi, 2b. Carissimo, 2a. Faucheux, 2y. Lefranc

[1]Institute of Radioprotection and Nuclear Safety, Cherbourg, France
[2]CEREA, Ecole des Ponts, EDF-R&D, Ile de France, France

Abstract All atmospheric conditions must be considered in the impact calculation of industrial facilities. In low wind conditions (wind speed below 2m.s^{-1}), the meandering (low frequency horizontal wind oscillation) becomes one of the predominant physical processes which drive atmospheric dispersion of pollutants. Experimentally, it can be identified by analyzing the autocorrelation function of the horizontal wind speed components. However, modeling these situations is more complicated, and most models are unable to correctly reproduce the turbulent flow structure and the resulting plume dispersion. The CFD models could overcome these limits by adapting the existing modeling approaches to low wind speed situations. In this study, we present the first analyses of datasets from an experimental campaign that has been performed at SIRTA in the south of Paris in 2020 as well as first simulation results obtained with a CFD model using two different modelling approaches: stationary and pseudo stationary conditions. The analysis of wind data acquired during one selected time period of the campaign allowed to identify the presence of meandering and to estimate its period. Compared to concentration measurements, the first modelling approach seems to lower lateral dispersion while the second approach seems to give closer results.
Keywords *Low wind speed, built-environment, meandering, atmospheric dispersion, CFD*

INTRODUCTION

Atmospheric dispersion in low wind speed conditions (hereafter LWS) is a critical situation which is not well understood. There are several places in the world where the LWS situations are common, it can occur up to 70 % of the time in certain sites (Anfossi et al., 2005). Studies suggested that low wind is defined by its mean horizontal speed lower than 2 m.s^{-1}. In these conditions, dispersion mechanisms and turbulence properties are modified leading to the stagnation of pollutants around the source and high concentration in the atmosphere. So, it turns necessary to consider these situations when it comes to calculate the impact.

In LWS conditions, the dispersion is partially driven by the phenomenon called meandering. It is a low frequency horizontal wind oscillation. The standard deviation of wind direction increases when the wind speed decreases, therefore it becomes difficult to define a mean plume direction. The meandering disperses the plume over a rather wide angular range. Consequently, the modeling of dispersion in these situations is hampered. The existing dispersion models are unreliable in such conditions specially when the wind speed approaches zero.

Turbulence and dispersion measurements in LWS conditions are hardly available at international level, particularly in built environment. In this context, IRSN and EDF-R&D have launched a study in order to acquire experimental data and improve modeling. The objectives of this presentation are to present and analyze experimental data of dispersion of a tracer gas (Helium) under LWS conditions in urban area and to compare these results to the first simulations obtained from a CFD model.

SITE AND METHODOLOGY

Site

The experimental site is located at SIRTA (Site Instrumental de Recherche par Télédétection Atmosphérique) (Figure 1) near Paris in a peri-urban area. It includes areas of buildings and vegetation.

The height of the buildings is in the range of 5 to 30 m. LWS frequency is 20 % over 20 months at a height of 30 m.

Experimental method

Two measurement campaigns have already been carried out in 2020 (in July and September). Each campaign includes 7 experiments, which means 14 experiments in total. The acquisition of data on the dispersion of a plume is based on the use of a gas tracer (Helium). Emission and measurement points locations were decided based on weather forecasts and wind measurements. Helium concentrations were measured, using mass spectrometers, with air samples as well as in real time, in the near field of the emission point (<300m). Wind and turbulence conditions are measured by ultrasonic anemometers positioned on a 30 m mast at three heights (5m, 10m, and 30 m) and at several locations inside the buildings canopy layer. The experiments allow to determine atmospheric transfer coefficients (hereafter ATC, in $s.m^{-3}$, equal to the ratio between the concentration of helium in the air and its emission rate) which quantify the dispersion of the plume between the point of release and measurement or sampling points.

The sonic anemometers datasets were divided into subsets of two hours since the meandering period can exceed 1h in some cases (Mortarini et al., 2013). The wind components were rotated in the mean wind coordinate system before proceeding with the analysis which aims at characterizing the physical processes occurring during LWS. The meandering is characterized by an oscillating behavior of the Eulerian autocorrelation function with a negative loop for the horizontal components U and V. Regarding the vertical component W, it exhibits a classical exponential behavior (Anfossi et al., 2005).
The Eulerian autocorrelation function R of horizontal velocity components can be fitted by equation (1) (Frenkiel, 1953):

$$R(\tau) = \exp(-p\tau)\cos(q\tau) \quad (1)$$

With:

- p is a parameter associated to the turbulence time scale (small scall motions)
- q is linked to the oscillation time scale (large scale motions)
- τ is the difference time between two instants
- The meandering period (Mortarini et al., 2016) is given by equation (2) :

$$T = \frac{2\pi}{q} \quad (2)$$

- The ratio between q and p (equation (3)) define the loop parameter m which is a decisive parameter to define the meandering:

$$m = \frac{q}{p} \quad (3)$$

Following (Mortarini et al., 2016), we have defined the situations with meandering using the condition: $m_{u,v} > 1$. When $m \geq 1$ for one of the horizontal wind components the corresponding time step is classified as “almost meandering”. When $m > 1$ for both components, it is classified as meandering.

Modelling method

The simulations rely on the CFD model Code_Saturne, an open-source code developed by EDF-R&D. The mesh used in this study includes 13 million cells for an area of dimensions 2400 m x 1600 m x 300 m. Inlet profiles of wind, temperature, and turbulence, are built according to the Monin-Obukhov theory. The roughness length is specified for each grid cell through a fine land use cover map. Two calculations have been performed for a chosen release of the measurement campaign. The first consists in a unique stationary simulation with constant boundary conditions. The second uses a combination of several stationary

simulations performed with different inlet conditions representative of the temporal variation of the meteorological conditions during the release.

RESULTS

Experimental data analysis

We present here the data of the experiment 14 which took place on 11 September 2020 between 05:35 and 06:05 UTC. In this period, the mean wind speed is about 1.4 m/s at a height of 30 m. Figure 1 shows the Helium plume dispersion based on ATC distribution. Due to the predominant northern wind, ATC are higher south of the emission point.

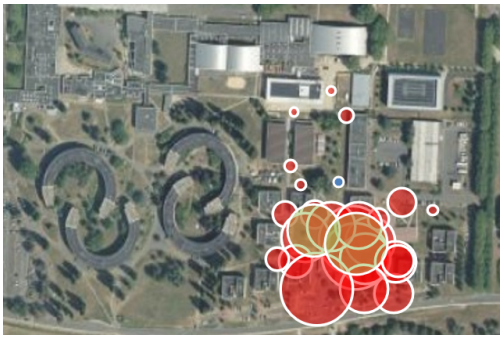

Figure 1. Helium measurements on 11 September 2020 between 5:35 and 06:05 UTC at SIRTA. Emission point in blue, ATC at sampling in red point, and ATC at real time spectrometer in green point. The bubbles size is proportional to the ATC.

The time series of wind speed components u and v and of the wind direction measured at 30 m over a selected period of 2 hours are shown in Figure 2. We can observe the meandering phenomenon, the wind direction oscillates clearly between 05:25 and 06:10. So, to verify and prove the existence this physical process, we also plotted the autocorrelation function of wind speed components in figure 3.

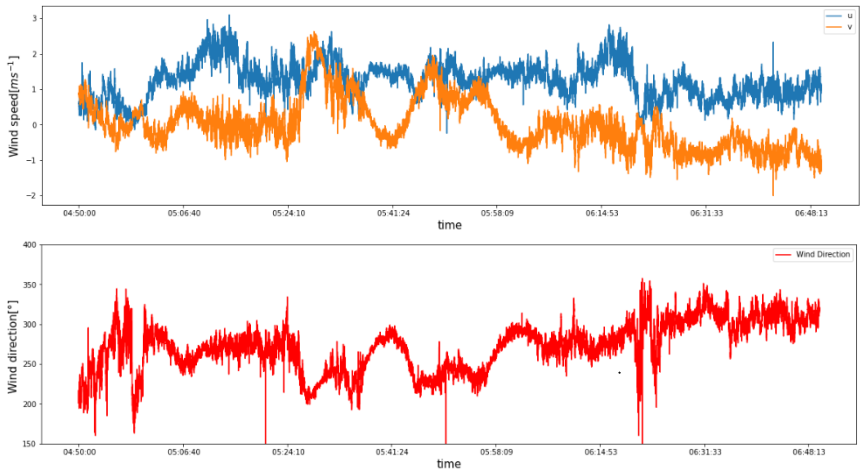

Figure 2. Horizontal wind-velocity components u and v *(top),*Wind direction *(bottom)* on 11 September 2020.

The left of Figure 3 shows the autocorrelation function for the the horizontal wind velocity component u. the negative loop appears between 500 s and 1000 s. The meandering period is 33 minutes and it is not well as marked as for the component v on the right of Figure 3. This last has a period of 21 minutes and a higher value of the parameter m. Thus the meandering appears to be stronger on the v component than the u component in this case.

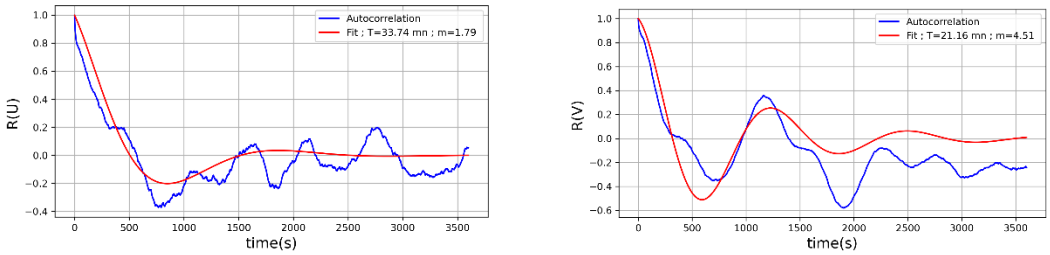

Figure 3. Autocorrelation function for the horizontal wind-velocity components u (on the left) and v (on the right) of data between 05:25 and 06:10 on 11 September 2020. Red line represents the theorical behavior proposed by (Frenkiel, 1953)

First modelling results

The results of the two calculations that have been performed for the last reject in 2020 are given in Figure 4. The first (on the left of Figure 4), that represents a unique stationary simulation underestimates the lateral dispersion. The second (on the right of Figure 4), that uses a combination of several stationary simulations better models the horizontal dispersion compared to the measurements.

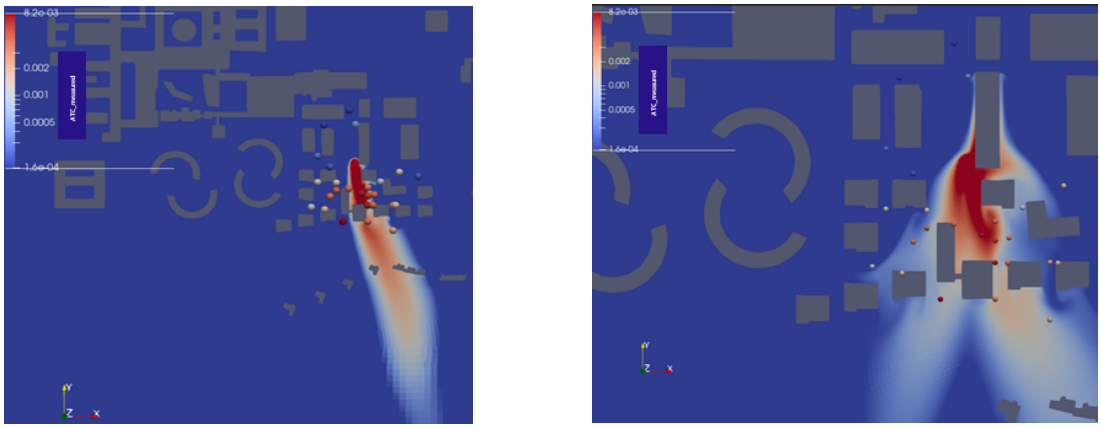

Figure 4. Two simulations of the plume dispersion for the release of 11 September 2020 Stationary case (on the left) and combination of several stationary simulations (on the right).

CONCLUSION AND OUTLOOK

To conclude, this study aims to characterize dispersion atmospheric in LWS conditions, where a specific physical process called meandering appears. The methodology used consists in experimental analyses and modelling.

The first part is based on the autocorrelation function to estimate the meandering period. We present results for a 2 hour period which includes one of the tracer releases that were performed during a measurements campaign in September 2020. By analyzing the autocorrelation functions, we show that meandering is visible on both horizontal wind components, but more in the transverse component than the longitudinal component in this case. The estimated period is around 20 minutes (for the transverse component) to 30 minutes (for the longitudinal component).

The second part is a test of two methods to model the plume dispersion of the gas tracer (Helium) used in our measurement campaigns. The model used is the CFD code code_saturne developed by EDF-R&D. The first method, which consists in a unique stationary simulation, lowers the lateral dispersion compared to the experimental results. In contrast, the model shows closer results in the case of combination of several stationary simulations, as it models more representatively this lateral dispersion.

In further studies, we will continue defining meandering for more cases of measurement campaign 2020 and studying the impact of different parameters on this process such as wind and direction speed, or the atmospheric stability. Besides, we will realize a third and a fourth experiment in 2022 to enrich and

consolidate our database. A next challenge will also be to run more simulations to better model these situations notably by adapting the Monin-Obukhov theory to LWS.

REFERENCES

Anfossi, D., Oettl, D., Degrazia, G., Goulart, A., 2005. An Analysis of Sonic Anemometer Observations In Low Wind Speed Conditions. Bound.-Layer Meteorol. 114, 179–203. https://doi.org/10.1007/s10546-004-1984-4

Frenkiel, F.N., 1953. Turbulent DifFusion: Mean Concentration Distribution in a Flow Field of Homogeneous Turbulence**This work was done under Contract NOrd 7386 with the U.S. Navy Bureau of Ordnance., in: Von Mises, R., Von Kármán, T. (Eds.), Advances in Applied Mechanics. Elsevier, pp. 61–107. https://doi.org/10.1016/S0065-2156(08)70208-4

Mortarini, L., Ferrero, E., Falabino, S., Trini Castelli, S., Richiardone, R., Anfossi, D., 2013. Low-frequency processes and turbulence structure in a perturbed boundary layer. Q. J. R. Meteorol. Soc. 139, 1059–1072. https://doi.org/10.1002/qj.2015

Mortarini, L., Stefanello, M., Degrazia, G., Roberti, D., Trini Castelli, S., Anfossi, D., 2016. Characterization of Wind Meandering in Low-Wind-Speed Conditions. Bound.-Layer Meteorol. 161, 165–182. https://doi.org/10.1007/s10546-016-0165-6

21st International Conference on
Harmonisation within Atmospheric Dispersion Modelling for Regulatory Purposes
27-30 September 2022, Aveiro, Portugal

IMPACT OF GREEN INFRASTRUCTURE ON TRAFFIC-RELATED POLLUTANT CONCENTRATION IN HIGH-RISE URBAN AREAS

Jose-Luis Santiago[1], Esther Rivas[1], Beatriz Sanchez[2], Riccardo Buccolieri[3], Oliver S. Carlo[3], Alberto Martilli[1], Marta G. Vivanco[2], Fernando Martin[1]

[1]Atmospheric Modelling Unit, CIEMAT, Av. Complutense, 40, 28040 Madrid, Spain
[2]Department of Geography, National University of Singapore, Singapore
[3]Dipartimento di Scienze e Tecnologie Biologiche ed Ambientali, University of Salento, Lecce, Italy

Abstract: Air quality is an important problem in many cities, especially in urban canyons, mainly due to high traffic emissions and the reduced ventilation of streets. Green infrastructure (GI) is being explored as a measure to control urban air pollution. However, the optimum GI design is still unclear. The objective of this study is to quantify the effects of different combinations of GI on traffic-related pollutant concentrations at the street level. Different combinations of street trees and hedgerows, as well as, green roofs and green walls are investigated. Computational Fluid Dynamics (CFD) modelling is used to simulate pollutant dispersion in an idealized urban environment. The aerodynamic effects produce an increase in pollutant concentrations. The results show that trees on the median strip reduce the street ventilation, particularly for streets parallel to the wind, and consequently, increase the pollutant concentrations at street level. On the other hand, trees in the sidewalks act as a barrier, particularly for 45º wind direction, for pollutants emitted outside. The aerodynamic effects of hedgerows are negligible, but deposition effects induce a decrease in pollutant concentrations. The effects of green walls and roofs on spatially-averaged concentrations at pedestrian levels are found to be limited to areas around the building where are implanted.

Key words: *air pollution; Computational Fluid Dynamics (CFD) model; Green Infrastructure (GI); street trees; hedgerows; green walls; green roofs; traffic-related pollution; urban environment.*

INTRODUCTION

Urban air pollution is one of the most important environmental problems for human health. Different local mitigation measures are being explored to control urban air pollution. One of the most popular measures is the use of Green Infrastructures GI, however, its optimum design is still unclear (Tomson et al., 2021). GI provides different ecosystem services/disservices such as microclimate regulation, variation of pollutant dispersion, absorption and deposition of atmospheric pollutants, emissions of biogenic volatile compounds and pollen, and noise attenuation (Abhijith et al., 2017; Buccolieri et al., 2018; Santiago and Rivas, 2021). The main effects on air quality are:

- Aerodynamic effects: trees modify the wind flow within street canyons, in most cases reducing the ventilation potential of the street.
- Deposition effects: a fraction of pollutants are removed from the air by means of deposition to tree leaves.
- Biogenic emissions.

In general, the aerodynamics effects of street trees tend to reduce street ventilation and increase traffic-related pollutant concentrations (Abhijith et al., 2017). However, on the other hand, deposition effects, which depends on the type of pollutant and vegetation specie, always improves air quality. Previous studies show that the net impact of GI may increase or decrease pollutant concentrations at the pedestrian level depending on several factors (e.g., the configuration of green infrastructure, urban morphology, location of pollutant emissions, etc) (Tomson et al., 2021). Most studies found that aerodynamic effects are more important than deposition in street environments (Vranckx et al., 2015; Santiago et al., 2017a; Santiago et al., 2019), however, both effects can induce major impacts depending on the conditions (e.g., Jeanjean et al., 2017; Santiago et al., 2017b). This issue has not been well studied and few investigations have analyzed the relative contribution of each effect toward the net impact of the GI (Buccolieri et al., 2018).

In this context, this study aims to investigate the effect of GI within an urban area on traffic-related pollutant concentration at the pedestrian level. For this purpose, Computational Fluid Dynamics (CFD) modelling is used to simulate pollutant dispersion in an idealized urban environment. Different combinations of street trees and hedgerows, as well as, green roofs and green walls are investigated and the effects of each vegetation element on the net effect of GI is analyzed. In addition, the relative contribution of deposition and aerodynamic effects of each GI element on pollutant concentrations depending on pollutant deposition velocity is studied. Three deposition velocities are simulated (V_{dep} = 0, 0.01 and 0.05 m/s). Moreover, not only the area with GI was simulated, but also the surrounding streets.

URBAN ENVIRONMENT AND GI SCENARIOS

The urban environment is composed of 7 x 7 buildings, and the height of buildings and the width of streets are 35 m (Figure 1). GI is implanted in the central area of the array of buildings (called the neighbourhood hereafter) and two configurations of trees deployment are studied (Table 1). In addition, the effects of green walls and green roofs implanted in the building located in the centre of the array are analyzed. Leaf area densities (LAD) of 0.5 m^2m^{-3} and 4 m^2m^{-3} were considered for trees and hedgerows, respectively. A more extensive comparison between different combinations of GI can be found in Santiago et al. (2022).

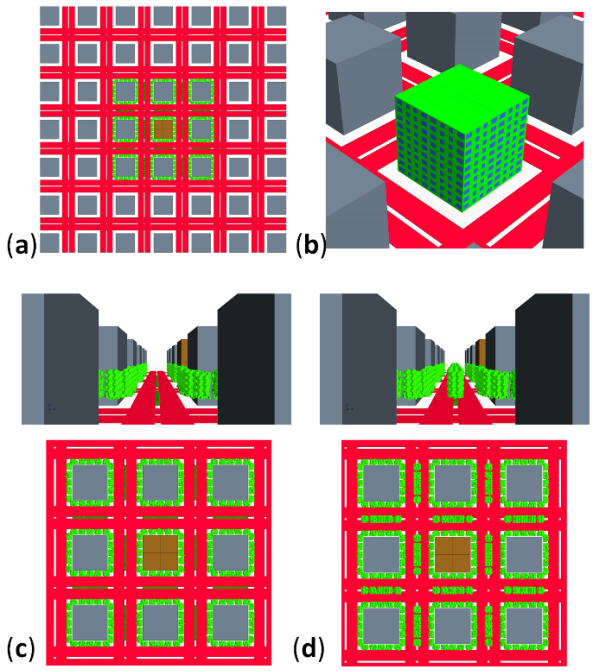

Figur Figure 84. (**a**) Array of buildings. (**b**) Green walls and green roofs locations. (**c**) VEG scenario. (**d**) VEG_TreeMedian scenario. Vegetation are in gree and traffic emission sources are in red.

Table 28. GI scenarios

Scenario	Sidewalk GI	Median strip GI	Green roofs and green walls
BASE	NO	NO	NO
BASE_GRGW	NO	NO	YES
VEG	15 m height trees	hedgerows	NO
VEG_GRGW	15 m height trees	hedgerows	YES
VEG_TreesMedian	15 m height trees	15 m height trees + hedgerows	NO
VEG_TreesMedian_GRGW	15 m height trees	15 m height trees + hedgerows	YES

CFD MODELLING SET-UP

CFD simulations are based on Reynolds-averaged Navier-Stokes (RANS) equations with a realizable *k-ε* turbulence closure. Vegetation is modelled including a sink term in the momentum equations and

sink/sources terms in the turbulence equations for k (turbulent kinetic energy) and ε (dissipation rate of turbulent kinetic energy) (Buccolieri et al., 2018). This modelled was successfully applied in several studies (Santiago et al., 2017a; Santiago et al., 2017b). The numerical domain is discretized using polyhedral and hexahedral cells with a spatial resolution of around 2.5 m with refinements of about 0.5 m close to the surfaces and emissions sources. The mesh was verified by means of tests of the grid-independence of the result (Santiago et al., 2022b). Neutral profiles of wind speed, turbulent kinetic energy and ε were imposed at inlet boundaries and two wind directions (0º and 45º) were simulated. The pollutant is considered non-reactive, and it is modelled using a transport equation. Only traffic emissions are considered. They are homogeneously distributed along the streets where two roads with 3 lanes are modelled (in red in Figure 1).

RESULTS

The modelled concentrations are normalized (equation (1)) to provide the results in a more generalizable way.

$$C_{norm}(x,y,z) = \frac{C(x,y,z)u_*}{Q} \quad (1)$$

where u_* is the friction velocity and Q is the source emission rate of traffic-related pollutant in kg m^{-2} s^{-1}.

Modelled concentrations for the VEG and VEG_TreeMedian cases and for both wind directions were spatially-averaged over the whole area where GI was implanted (*Neighbourhood*). Figure 2 shows the variation of the spatially-averaged of Cnorm respect to the BASE scenario for both wind directions and different deposition velocities.

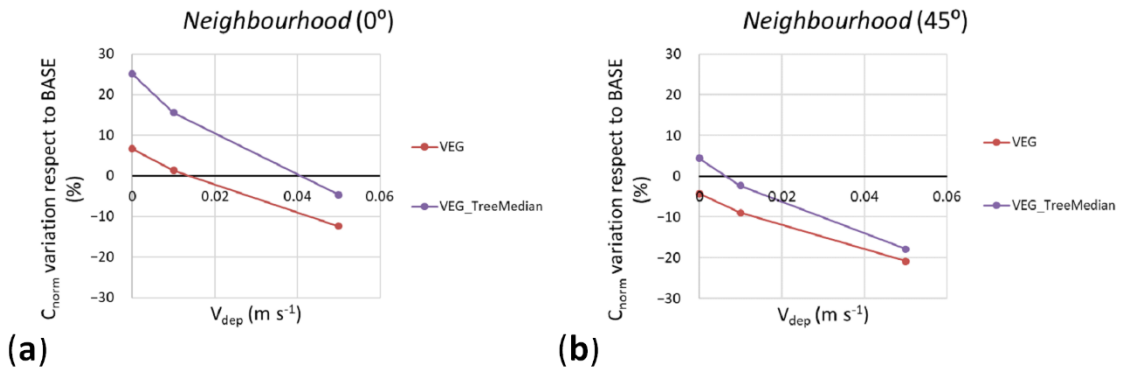

Figure 2. Variation of the spatially-averaged over the neigbourhood of Cnorm respect to the BASE case for: (a) 0º wind direction; (b) 45º wind direction for different deposition velocities

For all situations, the spatially-averaged concentrations are lower for VEG scenario than for VEG_TreeMedian scenario. This fact indicates that adding trees in the median strip produces a reduction in street ventilation respect to VEG scenario. In Figure 3, we can observe that these trees produce an increase in the spatially averaged concentrations, particularly for the 0° wind direction. In these cases, the larger increases in concentrations are found in streets parallel to the wind, due to a drastic reduction in ventilation there produced by trees in the median strip, and as a consequence, traffic-related pollutants are retained in that area. In general, the aerodynamic effects (scenarios without deposition) produce an increase in concentrations. However, for 45º VEG scenario, even without deposition, produce a reduction of concentrations. This is mainly due to sidewalks trees for this wind direction acts as a barrier for the pollutant emitted outside and without reducing the street ventilation significantly.

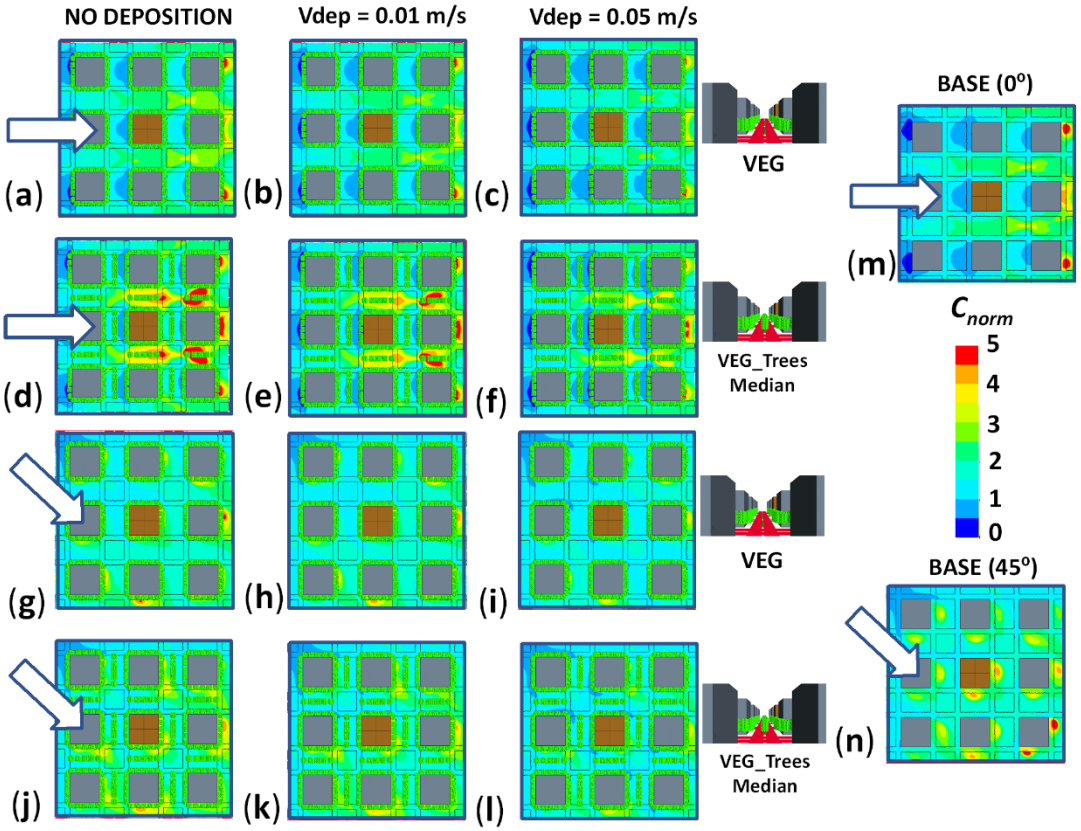

Figure 3. Maps of C_{norm} at 3 m height for both GI scenarios for both wind directions. (**a**) VEG without considering deposition for 0º wind direction; (**b**) VEG with a Vdep = 0.01 m/s for 0º wind direction; (**c**) VEG with a Vdep = 0.05 m/s for 0º wind direction; (**d**) Same as (**a**) but for VEG_TreesMedian; (**e**) Same as (**b**) but for VEG_TreesMedian; (**f**) Same as (**c**) but for VEG_TreesMedian; (**g**) Same as (**a**) but for 45º wind direction; (**h**) Same as (**b**) but for 45º wind direction; (**i**) Same as (**c**) but for 45º wind direction; (**j**) Same as (**d**) but for 45º wind direction; (**k**) Same as (**e**) but for 45º wind direction; (**l**) Same as (**f**) but for 45º wind direction; (**m**) BASE for 0º wind direction; (**n**) BASE for 45º wind direction.

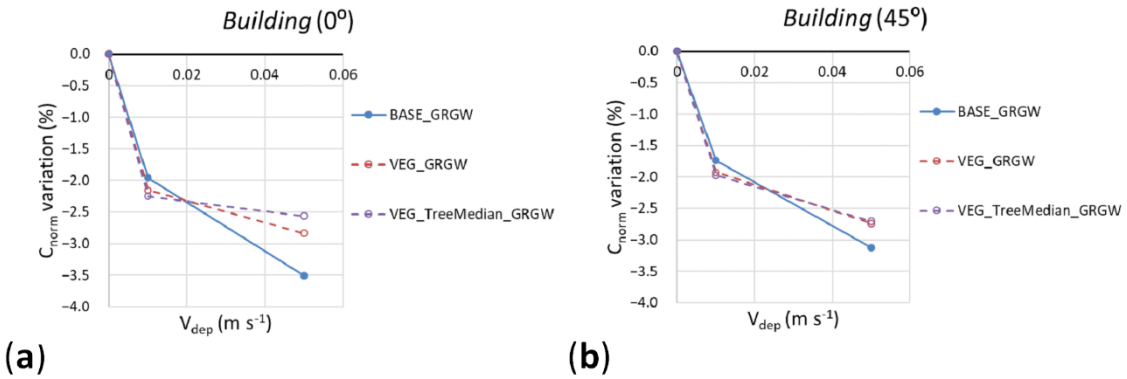

Figure 4. Variation of spatially averaged C_{norm} for GI with green roofs and green walls in the central building with respect to the same scenario without green roofs and green walls for: (a) *Building* and the 0° wind direction; (b) *Building* and the 45° wind direction.

Regarding the green roofs and green walls, it is observed that their effects are found limited to areas around the building where both measures are implemented. Figure 4 shows the variation of spatially averaged concentrations for GI with green roofs and green walls in the central building with respect to the same scenario without green roofs and green walls. The maximum reduction found is around 3.5 %.

CONCLUSIONS

The results of this study indicate that using GI alone seems to be ineffective as a general air quality mitigation measure. However, by selecting appropriate layouts of GI elements, GI could also help to reduce population exposure to air pollution even in a scenario with high buildings such as the study area investigated here. The combination of using GI with other measures such as Low Emission Zones could be more effective (Santiago et al. H21-051 presented in this conference).

ACKNOWLEDGEMENTS

This study is part of the RETOS-AIRE project (Grant: RTI2018-099138-B-I00) funded by MCIN/AEI/10.13039/501100011033 and by ERDF A way of making Europe. This study was also supported by AIRTEC-CM (S2018/EMT-4329) research project funded by Regional Government of Madrid. This work was partially supported by the computing facilities of Extremadura Research Centre for Advanced Technologies (CETA-CIEMAT), funded by the European Regional Development Fund (ERDF). CETA-CIEMAT belongs to CIEMAT and the Government of Spain.

REFERENCES

Abhijith, K.V., Kumar, P., Gallagher, J., McNabola, A., Baldauf, R., Pilla, F., Broderick, B., Di Sabatino, S., Pulvirenti, B., 2017. Air pollution abatement performances of green infrastructure in open road and built-up street canyon environments—A review. *Atmos. Environ.*, **162**, 71-86.

Buccolieri, R., Santiago, J.L., Rivas, E., Sanchez, B., 2018. Review on urban tree modelling in CFD simulations: Aerodynamic, deposition and thermal effects. *Urban For. Urban Green.*, **31**, 212-220.

Jeanjean, A. P., Buccolieri, R., Eddy, J., Monks, P. S., Leigh, R. J., 2017. Air quality affected by trees in real street canyons: The case of Marylebone neighbourhood in central London. *Urban For. Urban Green.*, **22**, 41–53.

Santiago, J. L., Buccolieri, R., Rivas, E., Sanchez, B., Martilli, A., Gatto, E., Martín, F., 2019. On the impact of trees on ventilation in a real street in Pamplona, Spain. *Atmosphere*, **10**, 697.

Santiago, J. L., Martilli, A., Martin, F., 2017b. On dry deposition modelling of atmospheric pollutants on vegetation at the mi-croscale: Application to the impact of street vegetation on air quality. *Bound. Layer Meteorol*, **162**, 451–474.

Santiago, J. L., Rivas, E., 2021. Advances on the Influence of Vegetation and Forest on Urban Air Quality and Thermal Comfort. *Forests*, **12**, 1133.

Santiago, J.L.; Rivas, E.; Buccolieri, R.; Martilli, A.; Vivanco, M.G.; Borge, R.; Carlo, O.S.; Martín, F. Indoor-outdoor pollutant concentration modelling: A comprehensive urban air quality and exposure assessment. *Air Qual. Atmos. Health* 2022, *in press*. https://doi.org/10.1007/s11869-022-01204-0

Santiago, J. L., Rivas, E., Sanchez, B., Buccolieri, R., Esposito, A., Martilli, A., Vivanco, M. G., Martin, F., 2022a. Impact of Different Combinations of Green Infrastructure Elements on Traffic-Related Pollutant Concentrations in Urban Areas. *Forests*, **13**(8), 1195.

Santiago, J. L., Rivas, E., Sanchez, B., Buccolieri, R., Martin, F., 2017a. The impact of planting trees on NOx concentrations: The case of the Plaza de la Cruz neighborhood in Pamplona (Spain). *Atmosphere*, **8**, 131.

Tomson, M., Kumar, P., Barwise, Y., Perez, P., Forehead, H., French, K., Morawska, L., Watts, J.F., 2021. Green infrastructure for air quality improvement in street canyons. *Environ. Int.*, **146**, 106288.

Vranckx, S., Vos, P., Maiheu, B., Janssen, S., 2015. Impact of trees on pollutant dispersion in street canyons: A numerical study of the annual average effects in Antwerp, Belgium. *Sci. Total Environ.*, **532**, 474–483.

21st International Conference on
Harmonisation within Atmospheric Dispersion Modelling for Regulatory Purposes
27-30 September 2022, Aveiro, Portugal

A NEW APPROACH TO COUPLING FLOW AND DISPERSION CFD SIMULATIONS IN A LARGE URBAN AREA AND BUILDINGS OF INTEREST

Xiasu Yang[1], Bruno Ribstein[1], Maxime Nibart[1], Patrick Armand[2] and Christophe Duchenne[2]

[1]ARIA Technologies, France
[2]CEA, DAM, DIF, F-91297 Arpajon, France

Abstract: In a built environment, exposure to air pollution is a major environmental problem. Near-field dispersion of pollutants involves the interaction of plumes with the flow disturbed by buildings. The phenomenon involves both meteorological and aerodynamic aspects of buildings. ARIA/ARIANET in collaboration with CEA has developed the PSWIFT & PSPRAY models in the Parallel-Micro-SWIFT-SPRAY (PMSS) system. The PSWIFT model is a mass-conserving diagnostic atmospheric model. The PSPRAY model is a 3D stochastic Lagrangian dispersion model of pollutants in the atmosphere. They are optimized for use on an urban scale, and allow simulations on large domains, such as the city of Paris, with computation times acceptable for an operational application. To obtain acceptable computation times, only mass conservation is imposed, and the influence of buildings is described geometrically in the PSWIFT model. A RANS model such as Code_Saturne allows to overcome these limitations. Indeed, the flow inside and outside buildings as exchanges at the interfaces are computed explicitly. In order to keep the computation time acceptable for the modeling of an urban area, the RANS model is not used for the whole study area. The approach proposed here consists in using PMSS for the modeling at the scale of the district and Code_Saturne on a nested domain and focused on a building of interest. While a first coupling was implemented between the two models, a new approach and first results are presented here. The flow in the nested domain encompassing the building of interest is computed by Code_Saturne on an unstructured mesh. The flow in the whole urban domain is then computed by PSWIFT on a regular mesh accounting for Code_Saturne output. The question arises of choosing the right interpolation method when moving from one mesh (unstructured for Code_Saturne) to another (structured for PSWIFT). The paper deals with this issue by comparing and discussing the flow and turbulence characteristics interpolated by PSWIFT and simulated by Code_Saturne for a choice of meteorological conditions around a railway station in Paris city (France). Then, dispersion computations are carried out with PSPRAY using PSWIFT flow both in the urban environment and in the building of interest, for fictitious releases outside and inside the station.

Key words: *indoor-outdoor transfer, 3D Lagrangian dispersion model, 3D mass-consistent model, micro-scale, Code_Saturne, Micro-SWIFT-SPRAY, urban environment*

INTRODUCTION

Industrial accidents as well as malevolent actions could result in atmospheric releases of noxious species, especially radionuclides or toxic chemicals. There is an increasing demand for modelling and decision-support systems dedicated to emergency preparedness and response. The challenge is to provide the most precise and reliable evaluation of the spatial and temporal distribution of the gases and/or airborne particles, in computation times consistent with a crisis management situation. The Parallel Micro-SWIFT-SPRAY (PMSS) modelling system developed by ARIA Technologies, ARIANET, and the CEA is an intermediate quick response capability to simulate the micro-scale processes.

Infiltration of pollutants inside buildings is a key process to estimate health effects risks due to hazardous releases, especially in urban areas. Outdoor dispersion models like PMSS (Armand *et al.*, 2010) or the emergency response code ALOHA from US-EPA, compute the infiltration inside buildings with macroscopic methods, deriving analytical indoor concentrations from the outdoor concentrations. These methods are mainly based on an infiltration / exfiltration time scale that can be, in practice, complex to estimate. This time scale is linked with the building's air exchange rate which is the number of times per hour that the volume of air within the building is completely replaced by fresh air when doors and windows are closed. Moreover, in many accidental situations (e.g. fires) or terrorist actions, hazardous releases can occur indoor, in large semi-enclosed buildings, such as industrial facilities or public places (as railway

stations or institutional buildings) which are typically the kind of buildings with an infiltration time scale that is difficult to estimate and even could not be relevant because of large openings.

To predict in detail the atmospheric dispersion and the sanitary consequences inside and outside, CFD models appear to be a possible solution. They are often used for both outdoor and indoor dispersion modelling. But the large calculation time of CFD is a significant disadvantage for operational application. The system proposed previously by Nibart et al. (2011) limits the use of CFD to the indoor flow modeling. The indoor and outdoor dispersion is done by the short response model PMSS. A coupling method has been developed between PMSS and the CFD model Code_Saturne. This paper firstly sums up the previous coupling algorithm and presents its limitations. Then improvements of the method that were partially possible thanks to PMSS and Code_Saturne are detailed. Lastly, an application on a realistic case in a dense urban area is presented.

PREVIOUS WORK

The previous coupling strategy was based on a nesting approach: an outer domain includes an inner domain discretized at a better spatial resolution. CFD model was used only for the flow in the inner domain that contains both the main target building in which indoor flow is computed and the very near outdoor environment of this building. This 3D flow, meaning wind, temperature, and turbulence fields, was stored in the same format as PSWIFT. The outer domain flow was computed with PSWIFT. The dispersion was simulated by PSPRAY in both the inner and outer domains, considering the best spatial resolution fields according to each Lagrangian particle position.

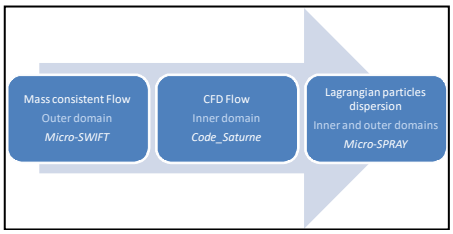

Figure 85: Indoor/outdoor coupling: workflow.

To perform this coupling, dedicated features had been developed. The standard output format of Code_Saturne is Ensight format which is not compatible with PSPRAY. This incompatibility is not only a matter of format but also of basic structure: Code_Saturne is based on a regular unstructured grid solver whereas PSPRAY requires structured wind fields as input. To deal with this issue:

- The mesh used by Code_Saturne was structured and obtained thanks to a translator tool, especially developed, that converts PSWIFT mesh (potentially topography and buildings aware) into IDEAS "unv" format which is one of the available input formats of Code_Saturne.
- A specific writer, based on PSWIFT source code, has been implemented into Code_Saturne to write the 3D field in the same format as PSWIFT.

These elements have been used successfully but lead to the three following limitations. Using regular structured grids for Code_Saturne is a significant decline. It implies a projection of obstacles (buildings) on the grid instead of cells relying on exact obstacles geometry and it makes difficult to increase spatial resolution in specific zones. The second limitation is the use of a specific version of Code_Saturne and not a standard one because of the writers. This increases the amount of work to manage the maintenance and update of the whole chain and decreases the portability of the solution. The last limitation concerns the flow itself. Code_Saturne modeling on the inner domain is initialized with data from the outer domain of PSWIFT. There is no feedback from the inner domain to the outer domain and the impact of buildings on the flow (recirculation zone, wake zone, etc) may be discontinuous around the two domains.

The nesting capability of PSPRAY was initially developed for the coupling. It was limited to two nesting levels and only one domain per level. The very first version of this feature is now generalized in PSPRAY. It is possible to consider several levels and several domains per level. Spatial parallelization is also compatible with this generalized nesting but limited to the deeper level. It has been notably successfully

used, sometimes with Code_Saturne flow coupling, in downscaling system (Oldrini et al. (2016)) or for Jack Rabit II validation that implied multiple length scale (Gomez et al., 2021).

PRELIMINARY DESCRIPTION OF THE COUPLING

We present our new approach to the coupling between Code_Saturne and PMSS. For the example, the building of interest is the "Gare du Nord" in Paris (France). The weather is stationary although a succession of stationary states could have been considered. The buildings seen by Code_Saturne and PMSS are identical. A simplified 3D geometric model for the neighborhood of Gare du Nord is created using ArcGIS and then SALOME pre-processor for Code_Saturne. This geometry is discretized with a 3D unstructured grid shown in Figure 86 (left panel), which consists of 441,953 tetrahedral elements with a maximum mesh size of $25m$. The mesh size is $10m$ for elements touching the ground and further refined to $5m$ for elements on the exterior wall of Gare du Nord and $2.5m$ for elements on the interior. Elements near the 6 entrances on the facade have a small mesh size of $0.5m$ to accurately capture the air flow into the station.

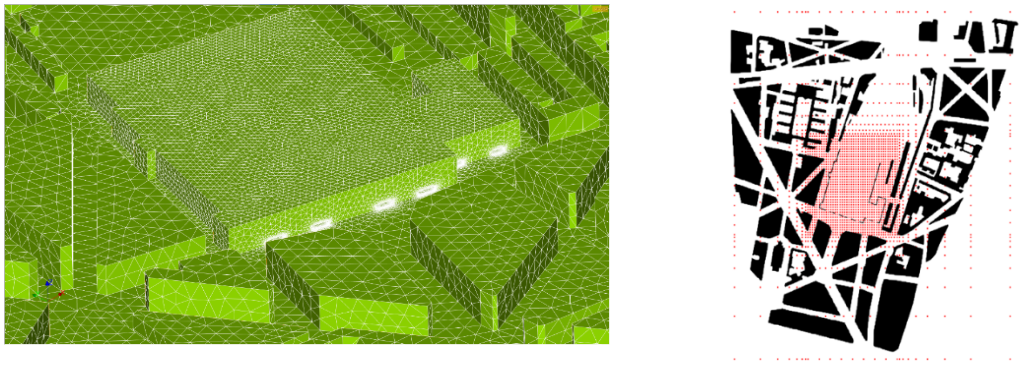

Figure 86: Simplified 3D geometry around Gare du Nord and 3D unstructured mesh generated with SALOME (left). Horizontal locations of vertical profiles extracted from the Code_Saturne simulation (right).

A steady-state 3D CFD simulation is performed on this grid using Code_Saturne, an open-source, general-purpose, finite-volume-based, unstructured CFD solver which solves the Navier-Stokes equations coupled with turbulence models. The standard 2-equation $k-\varepsilon$ turbulence model (Launder and Spalding, 1974) is used for this study with a 2-scale log law wall function. The incoming wind is at 240° south-west with a magnitude of $3.485m/s$ at $z = 10m$. An inlet boundary condition is assigned to the south, west and roof boundary faces with prescribed vertical profiles of velocity, temperature, turbulent kinetic energy (TKE) and turbulent kinetic energy dissipation rate (ε) that correspond to a neutral meteorological condition of Pasquill stability class D. Advective zero-gradient outlet boundary condition is assigned to the north and east boundary faces, and the ground (including all buildings) is modeled as rough walls with a characteristic roughness of $0.1m$. Gravity and Coriolis force are both neglected.

There are two points to emphasize here about the coupling. Once a steady-state solution is obtained in Code_Saturne, flow variables are extracted in the form of vertical profiles which are then used as initialization data for the mass-conserving PSWIFT solver. In order not to degrade the flow calculated by Code_Saturne, we avoid the creation of analytical zones around the buildings for the creation of recirculation zones, wakes or street canyons. This is an important difference with the standard way of using PSWIFT and is possible because the flow is forced by Code_Saturne. For this new coupling, PSWIFT interpolates the turbulence estimated by Code_Saturne. This also avoids double counting of turbulence. In this study, 40×40 vertical profiles are extracted within a $300m \times 300m$ square region surrounding Gare du Nord to recover detailed flow features near the station. As we move further away from Gare du Nord, the distance between two profiles becomes larger with an expansion ratio of 1.5. A total of 2435 vertical profiles are extracted. Figure 86 (right panel) shows the locations on the X-Y plane of all extracted profiles marked by red dots.

PSWIFT RESULTS

A nested PSWIFT approach is tested in the current study in order to allow enhanced grid resolution in the region of interest (RoI). The inner domain in the current study is defined by a $300m \times 300m$ square

surrounding Gare du Nord with a grid resolution of $1m \times 1m$ instead of $2m \times 2m$ which corresponds to the grid resolution outside the RoI. In the context of nested PSWIFT approach, the outer domain is denoted by Nest 1 and the RoI by Nest 2 (Nest 2 $\subseteq$ Nest 1).

In Figure 87, we compare the velocity field around Gare du Nord computed by PSWIFT in Nest 1 with the original Code_Saturne solution. This comparison shows that, by initializing PSWIFT with vertical profiles extracted from the CFD solution, the mass-conserving PSWIFT manages to recover satisfactorily the original velocity field from the CFD simulation. Flow features such as convective acceleration, flow separations, vortices, etc. are observed in the PSWIFT simulation which are impossible to capture without solving the momentum equations. We observe that the solution in Nest 2 remains globally consistent with the solution in Nest 1 with slight improvement in regions where strong velocity gradients are present (e.g., immediately in front of Gare du Nord) when compared with the Code_Saturne solution. The similarity between the two grid resolutions is important since it implies that the numerical methods in PSWIFT is consistent and that we can expect a minimal level of discontinuity across nest boundaries when using this velocity field for dispersion modeling in PSPRAY.

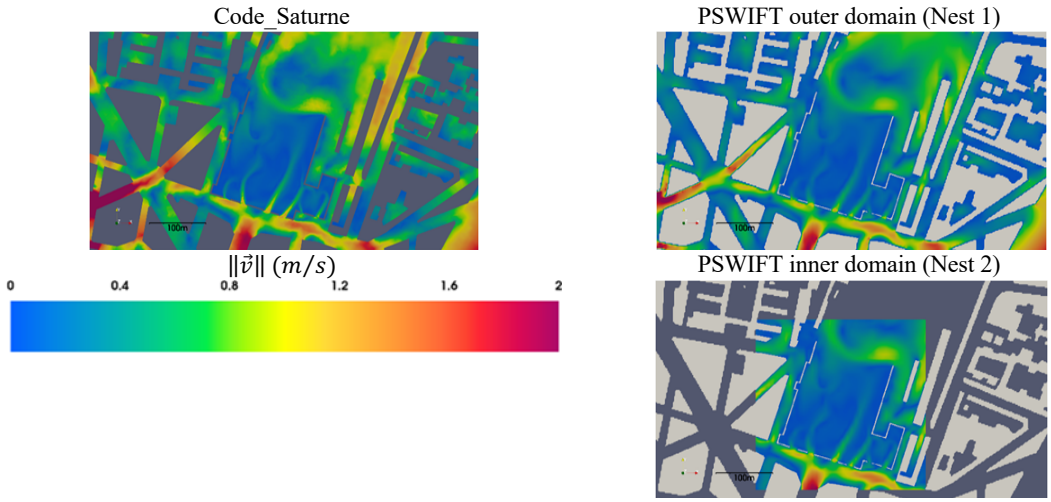

Figure 87: Velocity field comparison between Code_Saturne and PSWIFT at 2m above ground.

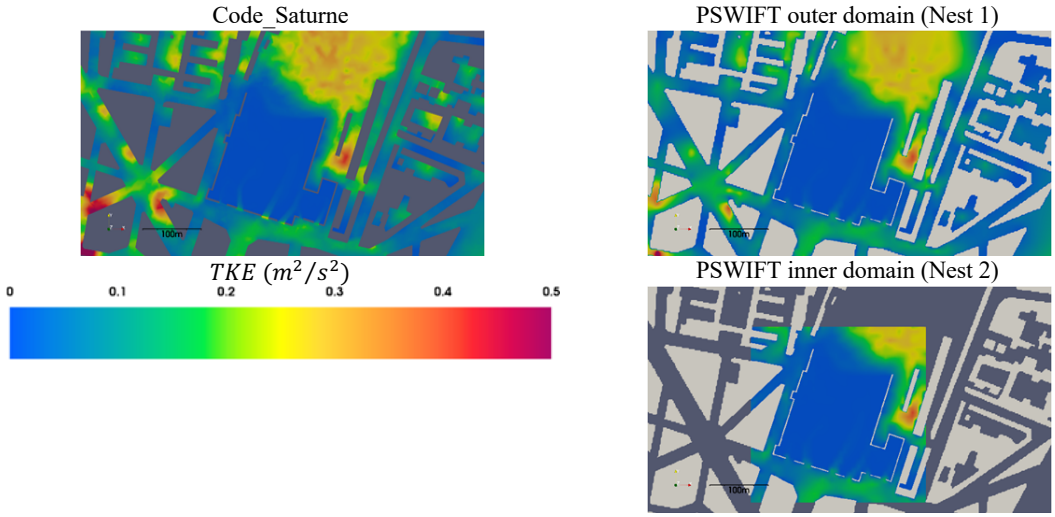

Figure 88: TKE field comparison between Code_Saturne and PSWIFT at 2m above ground.

The same analysis is also performed on the turbulence kinetic energy (TKE) field. As shown in Figure 88, PSWIFT recovers the TKE field from Code_Saturne which is obtained by solving the two-equation $k - \varepsilon$

turbulence model. In the presence of Gare du Nord, the PSWIFT simulation in Nest 1 reproduced the increase in TKE due to air inflow from the southern façade, as well as the highly turbulent wake region in the north. This level of detail is only made possible for PSWIFT by coupling with a Navier-Stokes solver with turbulence modeling capabilities. The TKE field remains consistent from Nest 1 to Nest 2.

PSPRAY RESULTS

The flows obtained in the two nests with the PSWIFT model forced by Code_Saturne are then used by the Lagrangian particles dispersion model PSPRAY. Two stationary releases of a neutral gas are considered. The first release P1 is placed outside Gare du Nord in front of the southern facade, the release P2 is placed within Gare du Nord and both sources are at $1m$ above ground. The concentration near the ground is shown in Figure 89. The numerical particles emitted from P1 enter and fill Gare du Nord by the 6 entrances in the facade following the main flow pattern. The concentration of P2 particles is at its highest level within Gare du Nord and their propagation is bounded by the solid walls. In both cases, the particles exit Gare du Nord via the northern opening and quickly dissipate into the highly turbulent wake region then propagate further downstream. The two concentration fields remain consistent from Nest 1 to Nest 2, which is the result of the grid consistency demonstrated by the PSWIFT solver as we mentioned in the previous section.

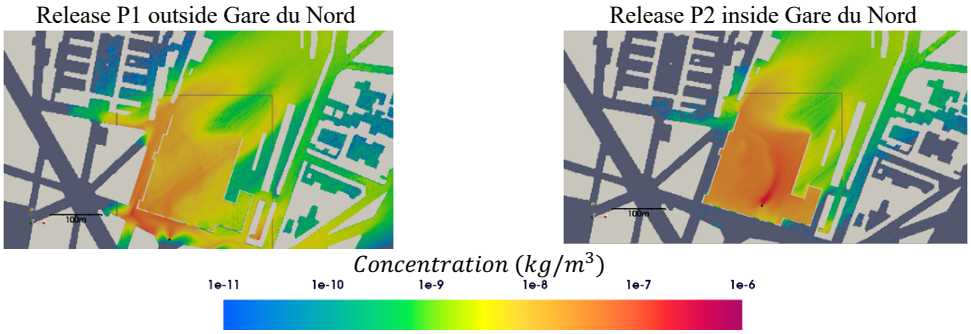

Figure 89: Dispersion modeling of releases P1 and P2 in a nested PSPRAY simulation. Positions P1 and P2 are marked by the black dot.

CONCLUSION

A coupling between PMSS and Code_Saturne had been developed to model indoor and outdoor dispersion in the surrounding neighborhoods of a building of interest. In this work, we have detailed the limitations to the historical implementation of the coupling and an update is suggested. This one benefits from the standard versions of PMSS as well as Code_Saturne. It requires no development other than an extraction of vertical wind and turbulence profiles from Code_Saturne. Note that the impact of buildings on the flow is not analytically described in PSWIFT, since it is already considered by Code_Saturne. The turbulence in the two nested domains is an interpolation of the one calculated by Code_Saturne. This new coupling shows no discontinuity at the interface between the inner domain, historically modeled by Code_Saturne, and the outer domain modeled by PSWIFT. The dispersion with PSPRAY finally shows that a plume can easily enter and leave a train station without having to estimate the building's air exchange rate.

REFERENCES

Armand P., C. Olry, J. Moussafir, A. Albergel and O. Oldrini, 2010 : Recent physical modelling developments in a lagrangian modelling system for emergency response purposes, *Proc. 13th Int. Conf. on Harmonisation within Atmospheric Dispersion Modelling for Regulatory Purposes*

Gomez, F., Ribstein B., Makké L., P. Armand, J. Moussafir and M. Nibart, 2021: Simulation of a dense gas chlorine release with a Lagrangian particle dispersion model (LPDM). *Atmospheric Environment, Volume 244,2021,117791,ISSN1352-2310,https://doi.org/10.1016/j.atmosenv.2020.117791.*

Nibart, M., P. Armand, C. Olry, C. Duchenne and A. Albergel, 2011: The indoor / outdoor pollutant transfer of a hazardous release: application to a parisian railway station. *Proc. 14th Int. Conf. on Harmonisation within Atmospheric Dispersion Modelling for Regulatory Purposes*

Oldrini O., S. Perdriel, M. Nibart, Armand P., C. Duchenne, and J. Moussafir, 2016 : EMERGENCIES - A modeling and decision-support project for the Great Paris in case of an accidental or malicious CBRN-E dispersion, *Proc. 17th Int. Conf. on Harmonisation within Atmospheric Dispersion Modelling for Regulatory Purposes*

21st International Conference on Harmonisation within Atmospheric Dispersion Modelling for Regulatory Purposes
27-30 September 2022, Aveiro, Portugal

PROPOSAL FOR MODELLING THE INFLUENCE OF ROOF SLOPE ON URBAN FLOW WITH A DIAGNOSTIC MODEL

Bruno Ribstein[1], Maxime NIBART[1], Daniel Loeb[1], Patrick Armand[2] and Christophe Duchenne[2]

[1]ARIA Technologies, France
[2]CEA, DAM, DIF, F-91297 Arpajon, France

Abstract: The dispersion of pollutants in the urban environment involves the interaction of plumes with the flow disturbed by buildings. The phenomenon includes both the meteorological conditions and the aerodynamic effects of the buildings. ARIA/ARIANET in collaboration with CEA has developed the PSWIFT model in the Parallel-Micro-SWIFT-SPRAY (PMSS) system. The PSWIFT model is a mass-conserving diagnostic atmospheric model.

The buildings are described geometrically so as not to lose resolution when projecting onto the mesh. Each building is cut into several straight triangular-based prisms from polygons stored in ESRI shapefile GIS format. In the PSWIFT model, the influence of buildings on flow is established analytically from prisms and depends on the dimensions of the building projected according to the direction of the prevailing wind.

The building cutting preprocessor was initially limited to converting flat-roofed buildings (2D polygon shapefile format and vertical extrusion using the height attribute). We here present the improvement of the preprocessor in order to treat the slope of roofs or buildings with a more complex level of detail. Simulations with the PSWIFT model were carried out using the obstacle files generated by this new version preprocessor.

The impact of the slope of roofs on the flow is studied. An isolated obstacle is considered in the presented work. The isolated obstacle allows the study of all the zones of influence of obstacles on the flow. PSWIFT results are compared against measurements in wind tunnels and/or reference numerical results of CFD models in the same configurations. The influence of buildings with slanted rools on the flow zones (cavity, displacement, skimming, wake zones) are characterized using the results of the simulations and compared with the effect of flat-roofed buildings of similar dimensions. The height of the flat-roofed buildings equals the lower, or higher, part of the sloped roofs. In the paper, it is shown that the dimensions of the zones around the buildings with sloped roofs are intermediate between those of the flat-roofed buildings considered.

Key words: *aerodynamic effects of buildings in a mass-conserving diagnostic atmospheric model.*

INTRODUCTION

In the urban environment, exposure to air pollution is a major environmental problem. Pollutants are emitted from various sources and dispersed (advection and diffusion) over a wide range of horizontal length scales. Microscale dispersion refers to processes acting on horizontal length scales smaller than about 5 km. These dispersion processes are referred to as near-field pollutant dispersion, which has different properties from far-field dispersion. Since near-field pollutant dispersion involves the interaction of plumes with the flow disturbed by buildings, the phenomenon has both meteorological and building aerodynamics aspects.

Despite the diversity of existing CFD (Computational Fluid Dynamics) approaches, these models often remain long, expensive, and difficult to implement in a suitable time frame. PMSS (Tinarelli et al., 2007) is a flow and dispersion modelling system constituted by the microscale versions of SWIFT and SPRAY (Tinarelli et al., 1994, 2012) models. It has been developed with the aim to provide a simplified, but rigorous solution of the flow and dispersion in industrial or urban environments in a short amount of time. The semi-empirical model PSWIFT is used to diagnose the flow between buildings and to evaluate the aerodynamic influence of buildings. In this work, we are interested in the impact of architectural details on the flow, and in the consideration of non-flat roof shapes. For an isolated building, the impact of a pyramid-roofed building is evaluated by comparison to a flat-roofed building of similar dimensions. After this introduction,

the numerical setup is presented, followed by a sensitivity study. The method used to model the aerodynamic effects of buildings is presented, followed by the results for the isolated building. A summary of the obtained results completes the paper.

DESCRIPTION OF THE NUMERICAL EXPERIENCES

This section presents the numerical setup. The PSWIFT model is compared to Tominaga *et al* (2015) experimental and numerical work. These authors consider pyramid-roofed buildings with three different slopes (3:10, 5:10 and 7.5:10). The results of the wind tunnel modelling (mean velocity and turbulent kinetic energy) are compared to RANS modelling and four types of turbulent closures. In our study, the flow is analyzed around a pyramid-roofed building with a roof slope of 7.5:10, the one with the greatest difference with a flat-roofed building. The building has a square base with side W=1.1He. The flow around this building is compared to flat-roofed buildings of similar dimensions. The height of the flat-roofed buildings equals the lower (He), or higher ($\mathrm{He} + \mathrm{W}/2 \cdot \tan(\theta)$ with $\tan(\theta) = 7.5/10$), part of the sloped roofs. A total of three buildings are considered during our study, listed in Table 1.

Table 29: Modelled buildings

Building	**b1**	**b2**	**b3**
Roof configuration	Flat	Flat	Pyramid
Maximum height	He	He + Wx7.5/20	He + Wx7.5/20

The direction of the wind is perpendicular to the edge of the roof. The wind profile follows a power law $u(z) = U_{He} \cdot (z/He)^{\alpha}$ with α=0.25. For the wind tunnel experiement, the reference speed equals $U_{He} = 2.6\, m/s$, the Reynolds number approximately 3500 and the roughness 10^{-4}m. The quantities are represented in PSWIFT on a scale of 1:1 (He=6m). The horizontal extent of the domain is 15He = 90m in the wind axis (X axis) by 9He = 54m in the transverse axis (Y axis). The vertical extent of the domain is 10He = 60m. The buildings are centered along the transverse axis and placed at the first third of the leeward extent.

SENSITIVITY ANALYSIS

The influence of the resolution of the flow is analyzed by comparing three different meshes: low (151x91x32), medium (226x136x43) and high resolution (451x271x78). The horizontal resolution is, respectively, 0.6m, 0.4m and 0.2m. According to Rafailidis (1997), the vertical influence of the shape of the building is limited to a thickness of 3He, where PSWIFT vertical grid is refined gradually. The following vertical grid is chosen:

[0, 0.25, 0.50, ... dz = He/K ... , 3He, 20, 25, 30, 40, 60]

with respectively dz=He/8=0.75m (32 points), dz=He/12=0.5m (43 points) and dz=He/24=0.25m (78 points). The first three levels are identical to guarantee an identical estimate of surface turbulence.

- If the wind field is best described with a high-resolution mesh, its amplitude changes little. The projected velocities U, V, W increase with the vertical grid resolution because they reach extrema values on edges of the isolated building whose representation in the PSWIFT model depends on the resolution of the mesh.
- Turbulent velocities (U* and W*) and Monin-Obukhov length (L) characterize the flow turbulence apart from the obstacle, and do not change with the grid resolution. Obstacle turbulence is essentially located at the interface between the open-air flow and the zones of influence of the obstacle. By its dependence on the vertical gradient of the projected velocities, the turbulence related to the obstacle increases with the resolution.
- Once non-dimensionalized, the flow in calm wind (with U_{He} = 0.09m/s) shows identical results for wind amplitude and turbulent kinetic energy to those obtained with U_{He} = 1m/s. This is shown in **Figure 1**. Thus, in this flow regimethe aerodynamic influence of the building does not depend on the inlet wind profile.

Wind amplitude for the low resolution simulation (U_{He} = 1m/s)

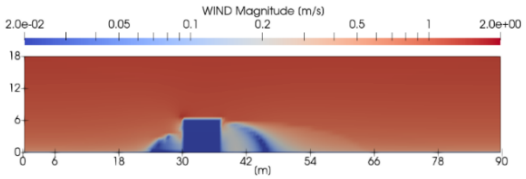

Wind amplitude for the high resolution simulation (U_{He} = 1m/s)

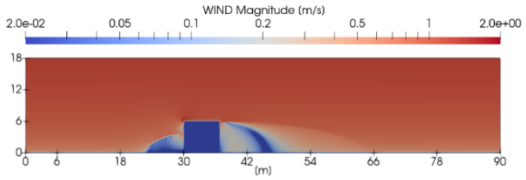

Nondimensionalized wind amplitude for the high resolution simulation (U_{He} = 0.09m/s)

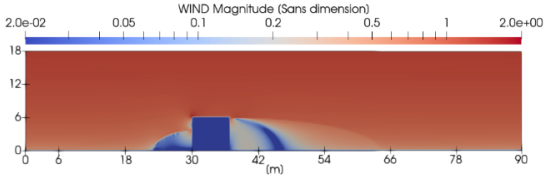

Figure 90: Sensitivity analysis on the wind amplitude

INFLUENCE OF THE BUILDING ON THE FLOW

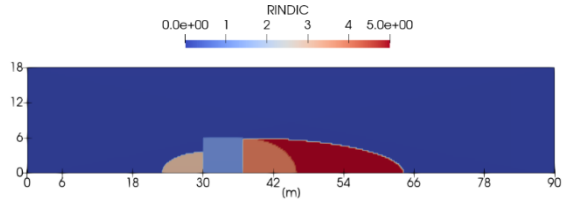

Open-air	0
Building	1
Canyon cavity	2
Displacement zone	3
Cavity area	4
Wake	5

Figure 91: Possible influences of buildings on flow (left) and its legend (right)

The PSWIFT model is a diagnostic and mass consistent model. By principle, the flow zones under the influence of buildings are taken into account owing to analytical formulae. **Figure 2** shows the RINDIC field, which characterizes the type of each zone: open-air, building, canyon zone, displacement zone, cavity zone, and wake zone. The length L_d of the displacement zone, the length L_r of the cavity zone and the length of the wake L_s are evaluated according to the wind and the dimensions of the building. **Figure 3** illustrates the method implemented in PSWIFT to account for the influence of a building on the flow.

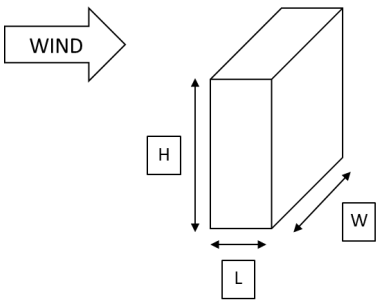

$$L_d = \frac{2W}{1 + 0.8\frac{W}{H}}$$

$$L_r = \frac{1.8W}{\left(\frac{L}{H}\right)^{0.3}\left(1 + 0.24\frac{W}{H}\right)}$$

$$L_s = 3L_d$$

Figure 92: Sketch of the dimensions of a building (left) and definition of the characteristic lengths of influence of the building on the flow (right)

Some buildings are decomposed into several triangular prism to describe their complexity. The implementation of the previous formulation in the PSWIFT model is completed by the following points.

- Sloped roofs are broken down into stripes to represent the slopes by a series of flat steps, like a pyramid or staircase. The pyramid-roofed building is described by juxtaposing the "steps" one behind the other, not by stacking or nesting the "steps" on top of each other.
- Each building is described by a set of triangular prisms. The zones of influence of a building on the flow are described from this set to overcome the specific influence of each individual prism.

- The cavity and wake zones start from the highest and most leeward point of all the prisms describing a building. The displacement zone starts from $0.6H$, which is an empirical approximation of the point of stagnation on the façade.
- For the displacement zone, the bell curve in **Figure 2** is given by the following law in $z(x)$, with x_{FACADE} being the position of the façade:

$$z(x) = 0.6H\left(1 - \sqrt{\left|\frac{x - x_{FACADE}}{L_d}\right|}\right)$$

- The curves delimiting the cavity zone and the wake zone are determined in a similar way.
- **Figure 4** illustrates the importance of setting priorities to resolve ambiguities between different areas of influence.

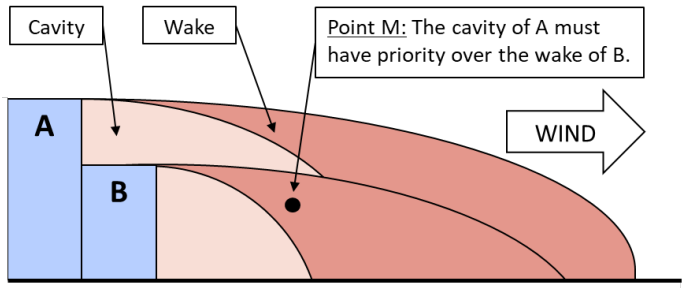

Figure 93: Diagram illustrating a practical priority problem between cavity and wake zones

RESULTS

In Y. Tominaga *et al* (2015), the roof slope appears to have little influence on the cavity length. For the three buildings described in **Table 1**, **Figure 5** shows the RINDIC field that indicates the aerodynamic effects of the buildings.

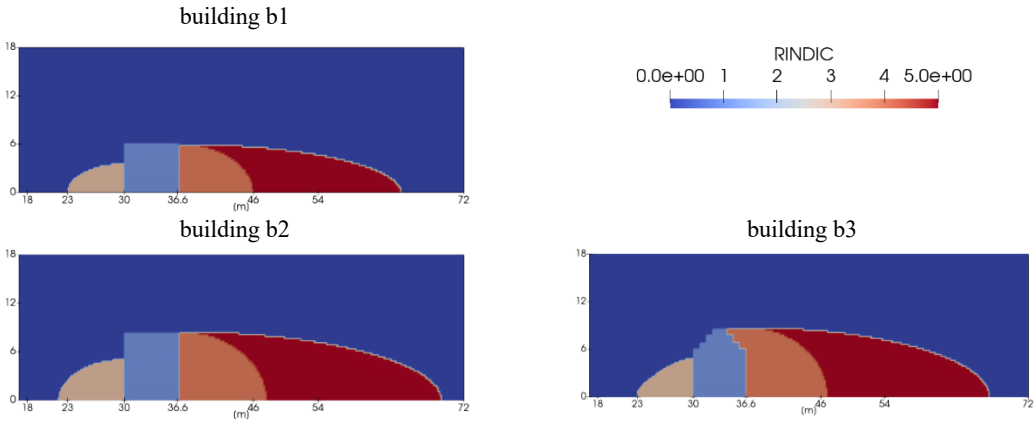

Figure 94: Possible influences of buildings on flow (RINDIC) for different buildings

The building b1 (respectively b2) has dimensions L=W=1.1He and H=He (respectively H = He $(1 + 1.1 \cdot 7.5/20)$). The numerical application of the previous formulae indicates $L_d \approx 1.17H_e$ and $L_r \approx 1.52H_e$ for building b1 and $L_d \approx 1.36H_e$ and $L_r \approx 1.80H_e$ for building b2. The figure below shows that the displacement and cavity lengths are compatible with the previous formulae.

For the pyramid-roofed building b3, the cavity and wake zones start from the highest and leeward point. The cavity length is in between those of the two flat-roofed configurations. The displacement length equals that of building b1, i.e. characteristic of the upwind façade. The stagnation point is however higher than for building b1, and corresponds to that of building b2.

Figure 6 is an application for the same pyramid-roofed building, but for a different wind direction. The wind has an angle of 45° angle with respect to the roof edge. Horizontal and vertical sections illustrate that the recirculation and wake zones orient themselves according to the wind direction. The dimensions of these characteristic zones are those of the building projected in the wind direction. They are therefore longer than in the case of wind perpendicular to the roof edge.

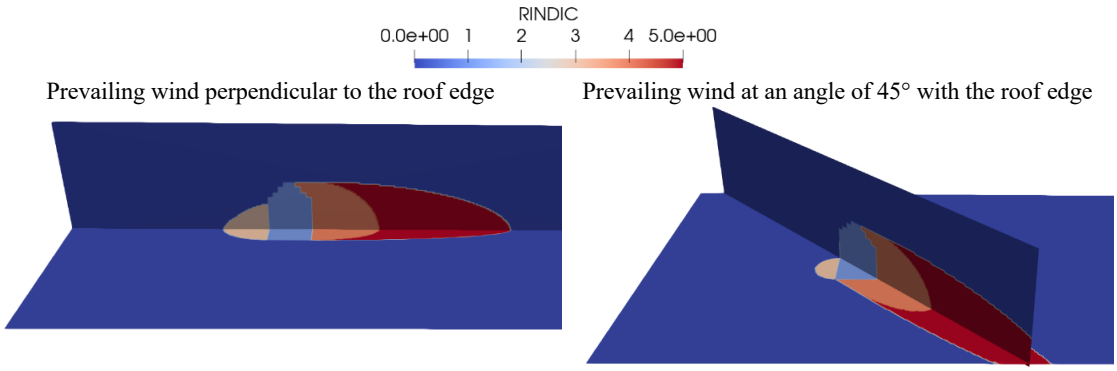

Figure 95: Zones flow characteristics (RINDIC) for the pyramid-roofed building b3

CONCLUSION

PSWIFT's pre-processor allows for a numerical description of buildings with a more complex level of detail than a flat roof representation. Buildings with sloped roofs are sliced to describe roofs with staircase steps. The work presents numerical experiments to verify the consistency of the flow for a pyramid-roofed building compared to flat-roofed buildings of similar dimensions.

In the present work, the impact of an isolated building with sloped roof is studied, and so without having to take into account the street canyons. They are likely to play an important role in a dense urban environment. Wind tunnel modelling (Rafailidis, 1997), 2D RANS simulations (Huang et al, 2009 and Takano et al, 2013), and LES simulations (Kluková et al, 2021) all suggest that street canyons and pyramidal roofs play an important role on the flow.

REFERENCES

Tinarelli G., Anfossi D., Brusasca G., Ferrero E., Giostra U., Morselli M.G., Moussafir J., Tampieri F., Trombetti F., 1994. Lagrangian particle simulation of tracer dispersion in the lee of a schematic two-dimensional hill. *J. Appl. Meteorol*. 33 (N. 6), 744–756.

Tinarelli G., Brusasca G., Oldrini O., Anfossi D., Trini Castelli S., Moussafir J., 2007. Micro-SWIFT-SPRAY (MSS): a new modelling system for the simulation of dispersion at microscale. General description and validation. In: *Air Pollution Modeling and its Application XVII. Springer International Publishing*, pp. 449-458.

Tinarelli G., Mortarini L., Trini Castelli S., Carlino G., Moussafir J., Olry C., Armand P., Anfossi D., 2012. Review and validation of Micro-Spray, a Lagrangian particle model of turbulent dispersion. In: Lin, J., Brunner, D., Gerbig, C., Stohl, A., Luhar, A., Webley, P. (Eds.), Lagrangian Modeling of the Atmosphere. vol 200. *Geophysical Monograph, American Geophysical Union*, Washington DC, pp. 311–327

Tominaga Y., Akabayashi S.-I., Kitahara T., Arinami Y., Air flow around isolated gable-roof buildings with different roof pitches: Wind tunnel experiments and CFD simulations, *Building and Environment*, Volume 84, 2015, Pages 204-213, https://doi.org/10.1016/j.buildenv.2014.11.012

Rafailidis S. Influence of Building Areal Density and Roof Shape on the Wind Characteristics Above a Town. *Boundary-Layer Meteorology* 85, 255–271 (1997). https://doi.org/10.1023/A:1000426316328

Y. Huang, X. Hu, N. Zeng, Impact of wedge-shaped roofs on airflow and pollutant dispersion inside urban street canyons, *Building and Environment*, Volume 44, Issue 12, 2009, Pages 2335-2347, https://doi.org/10.1016/j.buildenv.2009.03.024

Y. Takano, P. Moonen, On the influence of roof shape on flow and dispersion in an urban street canyon, *Journal of Wind Engineering and Industrial Aerodynamics*, Volume 123A, 2013, Pages 107-120, https://doi.org/10.1016/j.jweia.2013.10.006

Z. Kluková, Š. Nosek, V. Fuka, Z. Jaňour, H. Chaloupecká, J. Ďoubalová, The combining effect of the roof shape, roof-height non-uniformity and source position on the pollutant transport between a street canyon and 3D urban array, *Journal of Wind Engineering and Industrial Aerodynamics*, Volume 208, 2021, 104468, https://doi.org/10.1016/j.jweia.2020.104468

21st International Conference on
Harmonisation within Atmospheric Dispersion Modelling for Regulatory Purposes
27-30 September 2022, Aveiro, Portugal

MODELLING AND ASSESSMENT OF THE EFFECTS OF OBSTACLES IN URBAN CANYONS

*Oliver S Carlo [1] Riccardo Buccolieri [1], Esther Rivas [2], Jose L. Santiago [2], Pietro Salizzoni [3], Antonio Esposito [1], M. Salman Siddiqui [4], *Fernando Martin [2],*

[1] Dipartimento di Scienze e Tecnologie Biologiche ed Ambientali, University of Salento, 73100 Lecce, Italy
[2] Atmospheric Pollution Division, Environmental Department, CIEMAT, Spain
[3] Univ Lyon, Ecole Centrale de Lyon, CNRS, Univ Claude Bernard Lyon 1, INSA Lyon, LMFA, UMR5509, 69130, Ecully, France
[4] Faculty of Science and Technology, Norwegian University of Life Sciences, Ås, Norway
** Presenting author: Fernando Martin*

Abstract: Air pollution in cities, especially in the urban canyon, due to vehicular traffic emissions and reduced ventilation, is viewed as a serious human health hazard. Obstacles in the form of low boundary walls (LBWs), parked cars, trees, hedges, etc, are being explored as strategies to reduce pedestrians and nearby residents' exposure to pollutant concentrations. This study investigates a few combinations of low boundary walls and parked cars on the exposure of pollutant concentrations for pedestrians along the sidewalk, using Computation Fluid Dynamic (CFD) simulations. The results show that, for wind flowing perpendicular to the street canyon and gaseous pollutants, the effects of tightly parked cars can have a positive effect for pedestrians on the sidewalk, while LBWs have a minimal impact. More studies investigating a different combination of obstacles and their geometry, type of pollutants, and other urban and meteorological parameters are in progress and are expected to lead to more conclusive results.

Key words: *Air pollution; Computational Fluid Dynamics (CFD); parked cars; low boundary walls; traffic-related pollution; urban environment*

INTRODUCTION

Local wind flow within urban canyons plays a decisive role in the dispersion of traffic-related pollutants and mitigation of its associated risks for human health. To this end, many recent studies (Li *et al.*, 2021; Buccolieri *et al.*, 2022) point towards the potential of passive local strategies such as barriers/obstacles (e.g., trees, hedges, parked cars, low boundary walls, roadside barriers, etc.).

Studies about obstacles suggest the potential to alter source-receptor pathways, between pollutants generated on the road and the pedestrians on sidewalks; it also suggests higher potential for pollutant dilution within the street canyon itself (and even lateral entrainment) (Li *et al.*, 2021). This potential is usually studied through Computational Fluid Dynamics (CFD) models, validated with field and wind tunnel experiments. Yet very few CFD studies have been done to understand the full potential of obstacles such as low boundary walls (LBWs), parked cars and hedges (Buccolieri *et al.*, 2022), and even fewer studies have been done to test the effect of a combination of barriers (e.g., parked cars with LBWs) (e.g. (Jeanjean *et al.*, 2017; Ranasinghe *et al.*, 2019) on the net effect of pollutant dispersion within the canyon.

In this context, this study aims to investigate the effect of obstacles (LBWs and parked cars) on traffic-related pollutant concentrations. For this, CFD modelling is used to simulate pollutant dispersion in a scaled-down urban canyon. Four different scenarios are investigated for this study:

- Case A. Reference case urban canyon
- Case B. Tightly packed LBWs along the pedestrian walkway area
- Case C. Tightly packed parked cars along the pedestrian walkway area
- Case D. Tightly packed LBWs and parked cars along the pedestrian walkway area

The effect of each scenario is then analysed for pedestrian comfort in terms of pollutant concentration exposure.

DESCRIPTION OF THE STUDY AREA

The modelled parameters have been taken from the experimental study conducted during the PhD thesis work by Fellini (2021). The experiment was done to replicate an idealized urban district, where the entire wind tunnel test section was overlaid with an array of square blocks (Figure 96). The blocks were 50 cm wide and 10 cm high. The spacing between the blocks was 10 cm in the spanwise direction and 20 cm in the lengthwise direction; in a 1:200 scale, the reference street canyon matched fairly well a typical tree-lined boulevard, 40 m wide and flanked by 30 m high buildings, as in typical European city centres (e.g., Barcelona, Turin) , and perpendicular to the free-stream wind flow to account for a worst case condition (Buccolieri *et al.*, 2022). An ethane tracer was emitted by a linear source located in a slot cut in the tunnel floor, in the centre of a reference street canyon. The free stream velocity at the top of the boundary layer *(u_∞)* was kept constant at 5.5 m/s. The reference street canyon had a length *(L)*, width *(W)* and height *(H)* measuring 50 cm, 20 cm, and 10 cm, respectively. Normalizing these values with respect to the building height *H*, the length *(L)* and width *(W)* of the street are *5H* and *2H* respectively.
The experiment measured various parameters, some of which included:

1. Vertical profiles of mean velocity (m/s) along X and Z directions, along with its standard deviation components.
2. Vertical profiles of Reynolds shear stress (m^2/s^2).
3. Two-dimensional field of mean (in time) tracer concentration (ppm), along 4 sections of the reference street canyon

These were the primary parameters used to validate against the reference case of the CFD model.

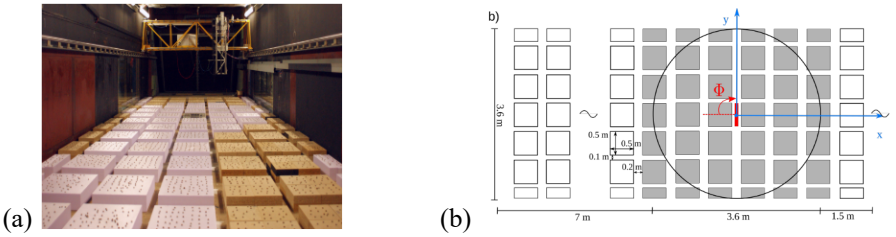

Figure 96 (a) Wind Tunnel setup; (b) Sketch of the urban canopy in the test section of the tunnel, showing the reference area (in red) considered for concentration measurements (Fellini, 2021)

CFD MODELLING SETUP

CFD simulations are based on Reynolds-averaged Navier-Stokes (RANS) equations, with a standard *k-ε* turbulence closure using the opensource simulation software OpenFOAM *(https://www.openfoam.com/)* The modelling design was adopted from Santiago *et al.*, (2007) as the simulation design was a compromise between reduced computational cost and accuracy of results – in this case a single row of 7 building blocks in the streamwise *X* direction and a cyclical boundary in the spanwise *Y* direction generated results that were validated with the experiment; smaller number of blocks led to underdeveloped results of velocity, turbulent shear stress profiles, etc., while larger number of blocks led to similar results but at a higher computation cost. The cyclical plane enforced a parallel flow; which was equivalent to simulating an infinite array of cubes in the spanwise direction, while maintain sufficient accuracy of results. All other modelling criteria was considered as per Cost Action 732 Best Practice Guidelines (Franke *et al.*, 2007)
In this model design, the numerical domain is discretized using a 676x79x49 cartesian grid. An irregular mesh was observed in the span leading up to the buildings from all directions, while in the region with buildings and obstacles a unity cell ratio was observed. The mesh was verified by several grid-independence tests, and it was found that a minimum cell size of 7.5 mm (H/13) produced sufficiently good results. The meshing of the obstacles and the pedestrian walkway zone (the region of interest for analysing pollutant concentration levels) was made smaller in size, with mesh refinement up to many levels by cell division done automatically in OpenFOAM; hence the total cell count was about $5.6x10^6$
Pedestrian walkway width was considered at 20 mm from both the windward and leeward walls of the blocks, which in a 1:200 scale would match a pedestrian walkway about 4 m in width. LBW and parked car height was measured to represent an approximate real-world height of 0.5 m (*0.025H*) and 1.5 m (*0.075H*) respectively, which when using the using the 1:200 scale was calculated as 2.5 mm and 7.5 mm respectively.

The obstacles and building blocks were modelled in software program SolidWorks *(https://www.solidworks.com/)* and imported and automatically meshed in OpenFOAM. Images of the modelled scenarios for each case can be seen from the figures shown in the 'Results' section (Figure 97, Figure 98 and Figure 99)

RESULTS

It is observed that the air flow creates a single primary vortex within the canyon, with the velocity vectors pointing towards the leeward wall at the pedestrian level (Figure 97). However there also appears a secondary vortex created at the leeward wall, also observed in other studies (Allegrini, Dorer and Carmeliet, 2013).

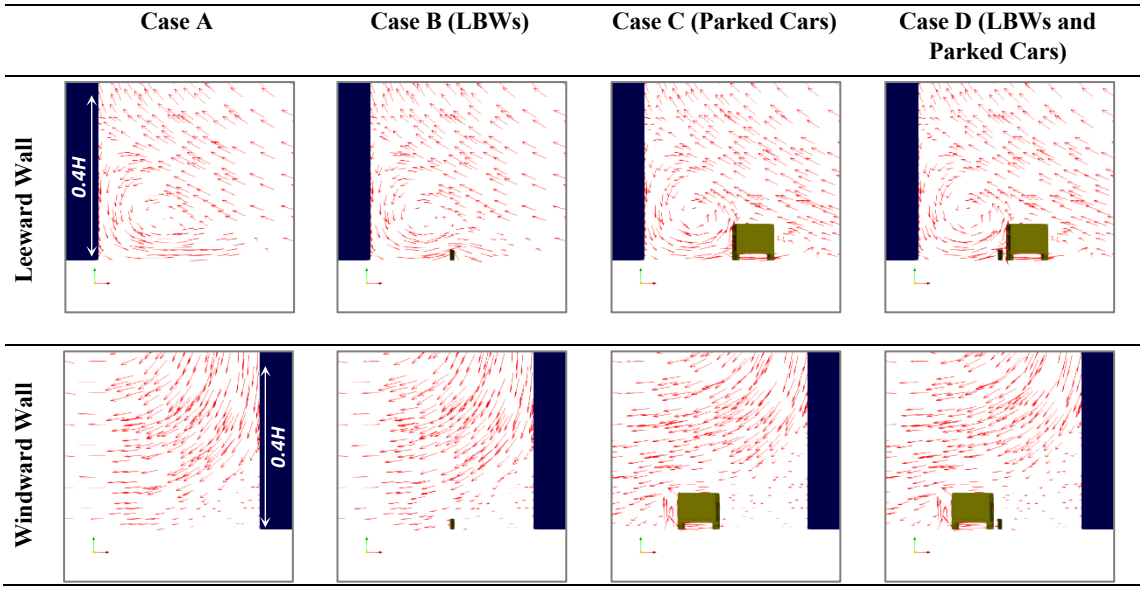

Figure 97 Velocity vector diagrams for each of the four cases taken in the X-Z plane, at both windward and leeward walls

The concentration levels for each walkway were analysed using both vertical and horizonal profiles taken at the centre of each pedestrian walkway; horizontal profile was taken at a height of *0.005H* from the ground (scaled as 1m from the ground as the approximate breathing zone). The positioning of the recorded lines is shown in Figure 98.

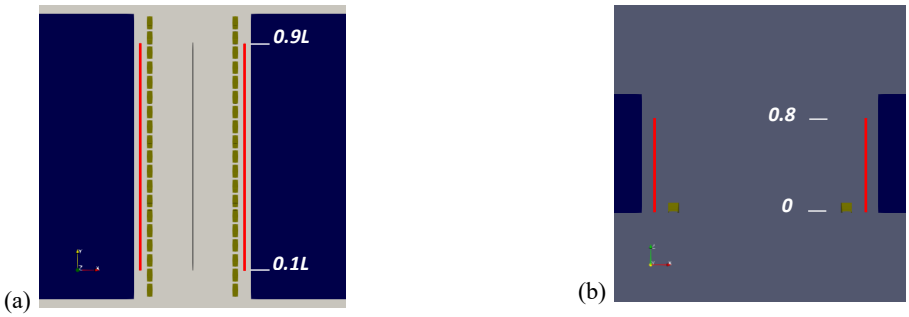

Figure 98 (a) Top view showing the horizontal and (b) side view showing the vertical profile lines (in red) considered for pollutant concentration measurements.

A greater accumulation of pollutant concentrations along the leeward wall is found (Figure 4). This was also observed from the pollutant concentration levels *(C_{norm})* on the pedestrian walkway areas, along the windward and leeward wall, for all four cases (Figure 99). The modelled concentrations being normalized (equation (1)) to provide the results in a more generalizable way

$$C_{norm}(x,y,z) = \frac{C(x,y,z) \times u_{\infty}}{Q} \quad (1)$$

where u_{∞} is the free stream velocity in ms^{-1}, $C(x,y,z)$ is the pollutant concentration in kgm^{-3}, and Q is the source emission rate of traffic pollutant in $kgm^{-2}s^{-1}$.

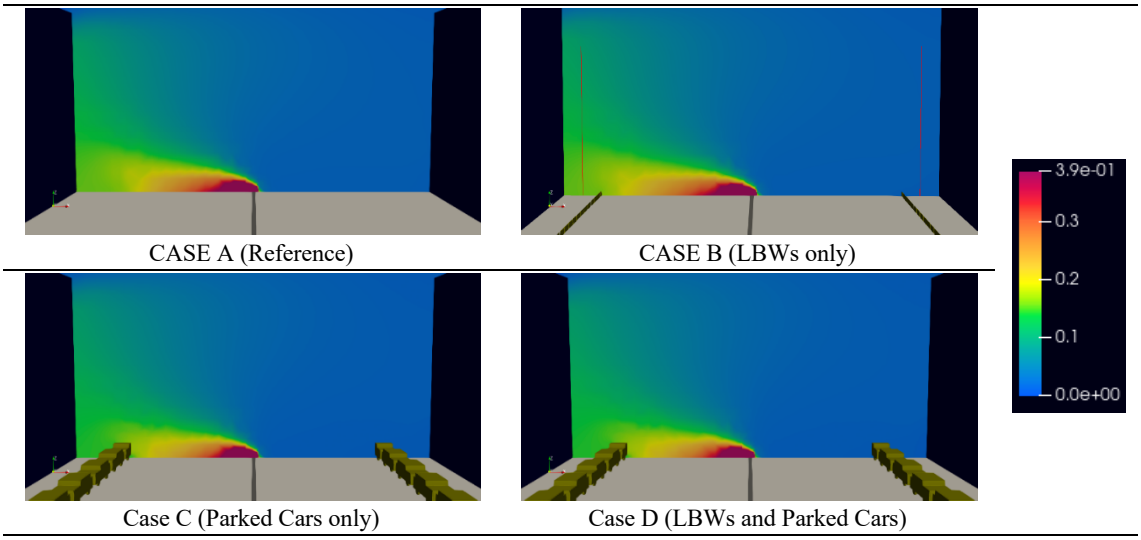

Figure 99 Pollutant concentration *(C_{norm})* contour along leeward walls for all four cases.

Obtaining the pollutant concentration (C_{norm}) values for each of the profile lines given in Figure 98, the plotted values are shown in Figure 100.

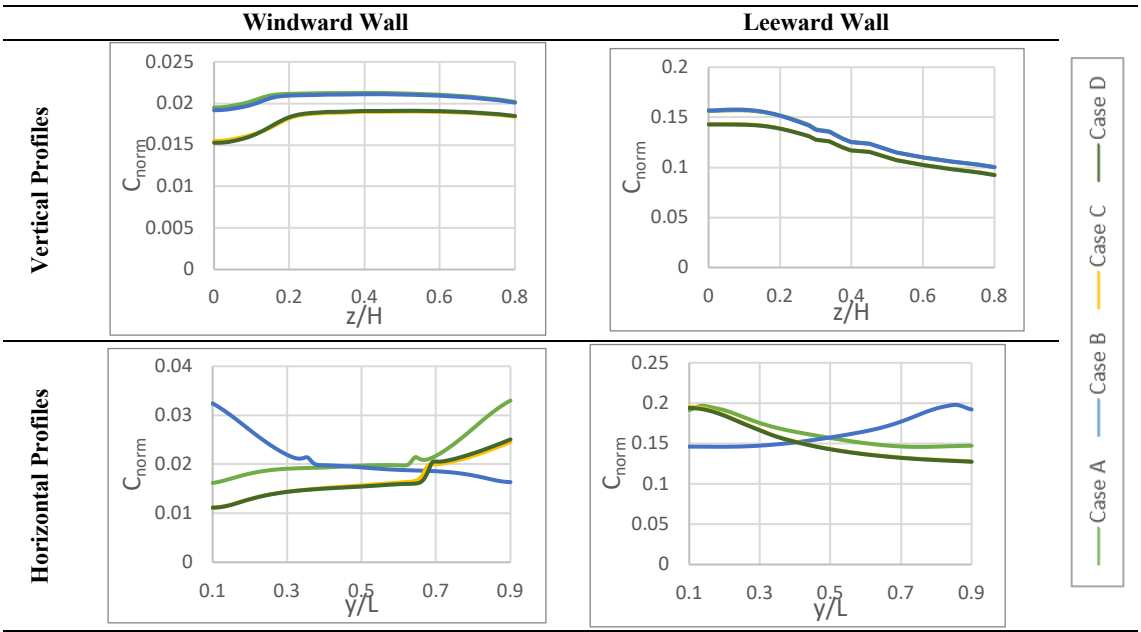

Figure 100 Vertical and horizontal profiles of pollutant concentrations for all four cases, along windward and leeward walls

From the cases it can be observed that obstacles play a significant role in concentration reductions. LBWs seem to have a very small effect overall, but parked cars show a more positive effect.
Averaging the pollutant concentration 'C_{norm}' over the horizontal profile line (taken along the pedestrian walkway) and comparing it to the base case scenario (Case A), the percentage reduction observed for each case and along both the walls are shown in Table 30.

From Table 30, it is observed that Case C and Case D shows best reduction in pollutant concentrations. Case B shows some reductions along the windward wall, while a net negative effect along the leeward wall.

	Case B (LBWs)	Case C (Parked Cars)	Case D (LBWs and Parked Cars)
Windward Wall	1.3%	21.5%	21.6%
Leeward Wall	-0.6%	7.2%	7.5%

Table 30 Percentage reduction in average pollutant concentration compared to reference case (Case A) scenario, using the horizontal profiles lines along the pedestrian walkway

The differences in concentration reductions between the windward and leeward wall for all cases may be correlated to the formation of the secondary vortex created in the leeward wall zone. But it can be observed the effect of LBWs may be negligible in this case as it was very small compared to the building height, while parked cars, being taller than LBWs, could lead to better concentration reductions. However since the effect of LBWs alone is negligible in this scenario, combining the obstacles did not produce significantly different results.

CONCLUSIONS

The height of obstacles appears to have greater effect on concentration reductions behind the obstacle, which has also been observed in other studies (Huertas *et al.*, 2021). Overall, this study suggests that obstacles (parked cars in this scenario), can be effective in reducing pollutant concentrations for pedestrians. But it should be noted that the results have been simulated for gaseous pollutants, and does not account for particulate matter pollutants – which is heavier and possesses a deposition/settling effect due to gravity (Gallagher *et al.*, 2015) . More studies would be needed to account for the effect of such obstacles on particulate matter pollutants, with changes in other urban and meteorological parameters as well.

Acknowledgements

O S C. acknowledges the Ph.D. financial support within the "Dipartimento di Eccellenza fundings" – Ph.D. course in "Scienze e Tecnologie Biologiche ed Ambientali" - XXXVI cycle - University of Salento. A.E. acknowledges the PhD financial support of the Italian Ministry of University and Research (MUR) by the PON "Ricerca e Innovazione 2014-2020-Asse IV" - PhD course in "Scienze e Tecnologie Biologiche ed Ambientali" - XXXVII cycle - University of Salento. E.R. and J.L.S acknowledges the financial support of the RETOS-AIRE (RTI2018-099138-B-I00) research project funded by Spanish Ministry of Science and Innovation MCIN/AEI/10.13039/501100011033 and by ERDF A way of making Europe.

References:

Allegrini, J., Dorer, V. and Carmeliet, J. 2013. 'Wind tunnel measurements of buoyant flows in street canyons', Building and Environment, 59, 315–326.

Buccolieri, R. et al. 2022. 'Obstacles influence on existing urban canyon ventilation and air pollutant concentration: A review of potential measures', Building and Environment, 214(February), 108905.

Fellini, S. 2021. Modelling pollutant dispersion at the city and street scales: From wind tunnel experiments to complex network theory (Doctoral Thesis). Politecnico di Torino; École Centrale de Lyon.

Franke, J. et al. 2007. Cost Action 732 Best practice guideline for the CFD simulation of flows in the urban environment, COST action.

Gallagher, J. et al. 2015. 'Passive methods for improving air quality in the built environment: A review of porous and solid barriers', Atmospheric Environment, 120, 61–70.

Huertas, J.I. et al. 2021. 'Design of road-side barriers to mitigate air pollution near roads', Applied Sciences (Switzerland), 11(5), 1–20.

Jeanjean, A. et al. 2017. 'Air quality affected by trees in real street canyons : The case of Marylebone neighbourhood in central London', Urban Forestry & Urban Greening, 22, 41–53.

Li, Z. et al. 2021. 'Review on pollutant dispersion in urban areas-part B: Local mitigation strategies, optimization framework, and evaluation theory', Building and Environment, 198(February), 107890.

Ranasinghe, D. et al. 2019. 'Effectiveness of vegetation and sound wall-vegetation combination barriers on pollution dispersion from freeways under early morning conditions', Science of the Total Environment, 658, 1549–1558.

21st International Conference on
Harmonisation within Atmospheric Dispersion Modelling for Regulatory Purposes
27-30 September 2022, Aveiro, Portugal

SIMULATIONS OF STREET-CANYON AIR-QUALITY USING FLUID DYNAMICS AND AEROSOL MODELLING

Yunyi Wang[1], Cédric Flageul[2], Chao Lin[3], Ryozo Ooka[3], Hideki Kikumoto[3], Youngseob Kim[1] and Karine Sartelet[3]

[1] CEREA, École des Ponts ParisTech, EDF R&D, 77 455 Marne la Vallée, France
[2] PPRIME Institute, Curiosity Group, Université de Poitiers, CNRS, ISAE-ENSMA, France
[3] Graduate School of Engineering, The University of Tokyo, 4-6-1 Komaba, Meguro-ku, Tokyo 153-8505, Japan

Abstract: High concentrations of nitrogen dioxide and particulate matter are often observed locally in streets. Because of the spatial resolution limit, regional-scale chemical transport models cannot reproduce these high concentrations. Traditional local-scale methods such as computational fluid dynamics (CFD) often neglect chemical reactions and aerosol dynamics, which leads to inaccuracy in the simulation of local air quality. In this study, 2D CFD simulations performed by Code_Saturne and OpenFOAM and coupled with the chemical aerosol module SSH-Aerosol are used to model pollutant dispersion, chemical reactions and aerosol dynamics during a period of 12 hours (from 4 a.m. to 4 p.m., local time, GMT+2h) in a street of Greater Paris. For both CFD codes, the setup is validated by comparing the simulated NO_2 and PM_{10} concentrations with measurements. The impact of turbulence model and coupling strategy on reactive and non-reactive pollutant concentrations is assessed by comparing the concentrations simulated by two codes. This comparison of the CFD tools provides a qualitative estimation of the uncertainty associated with the modelling of the atmospheric flow and of the coupling between dispersion, chemistry and aerosol dynamics.
In order to understand the impact of chemical processes on aerosol formation, sensitivity tests concerning gas chemistry and aerosol dynamics are conducted. A non-neglectable under-estimation of some pollutant concentrations is observed when gas chemistry and aerosol dynamics are not taken into account. Gas chemistry significantly increases NO_2 concentrations in the street, which is underestimated by 41% on average when gas chemistry is not considered. Although the impact of gas chemistry on inorganic and organic condensables is limited, inorganic and organic aerosol concentrations in the street are largely impacted by aerosol dynamics. For inorganic aerosols the concentrations increase because of the formation of ammonium nitrate, partly due to the ammonia emission by traffic and partly due to the lack of thermodynamic equilibrium between gas and aerosols in the background regional concentration with high concentrations of nitric acid. For organic aerosols, the concentrations are strongly influenced by the increase of inorganic aerosols.

Key words: *CFD, Street canyon, secondary aerosols.*

INTRODUCTION

High concentrations of nitrogen dioxide (NO_2) and particulate matter (PM) are often observed in urban street canyons, becoming a global sanitary problem. In order to model these concentrations, it is necessary to model the dispersion and transportation of several species. Computational fluid dynamics (CFD) modeling is powerful in estimating the local-scale flow and air quality because of the high resolution. However, due to the high computational cost linked to the modelling of the flow, most CFD models treat pollutants as passive scalars and they do not take into account chemical reactions between different species (Zhang et al, 2020). Neglecting chemistry may lead an underestimation of some species, for example, nitrogen dioxide and organic condensables (Lugon et al, 2020), which are important to represent PM formation. Although chemical models are increasingly coupled with CFD models (Kikumoto et al, 2012; Zhong et al, 2014), most of these chemical models neglect the formation of condensables, because they were originally designed to simulate ozone formation (Kim and Ooka, 2011) and not PM. In this study, a chemical aerosol module taking into account the formation of condensables, SSH-Aerosol (Sartelet et al, 2020), is coupled to two CFD tools: Code_Saturne (Archambeau et al, 2004) and OpenFoam (OpenFoam, 2020). Atmospheric dispersion, gas chemistry and aerosol dynamics are simulated and analysed in the

following sections. To understand the role of chemistry and aerosol dynamics, passive simulations (passive case) as well as simulations with both chemistry and aerosol dynamics (chemistry case) are analysed.

MODEL PRESENTATION

The CFD tools used are Code_Saturne v6.2 and OpenFoam v2012. Different turbulence schemes are used in the two models. In Code_Saturne, k-ε linear production is used to solve the turbulence while in OpenFoam, RNG k-ε model is employed. The 0-dimensional aerosol box model SSH-Aerosol is coupled to both CFD models. The modified version of the chemistry mechanism Carbon Bond Version 5 (CB05) (Yarwood et al, 2005) included in SSH-Aerosol is used for gas-phase chemistry. The coupling between SSH-Aerosol and the CFD models is realized through the application program interface (API).

MODEL SETUP

The street "Boulevard Alsace-Lorraine" in Greater Paris is simulated by a 2-dimensional setup. Figure 1 shows the domain of the simulations. The building height (H) on both sides of the street is 8.5 m and the width (W) of the street is 27.5 m. This corresponds to an "intermediate" aspect ratio (0.31) (Lugon et al, 2020). Traffic is considered as a street emission source and is simulated as a surface source which is placed in the middle of the street. The inlet is set at the left and the top of the domain and the outlet is set at the right of the domain.

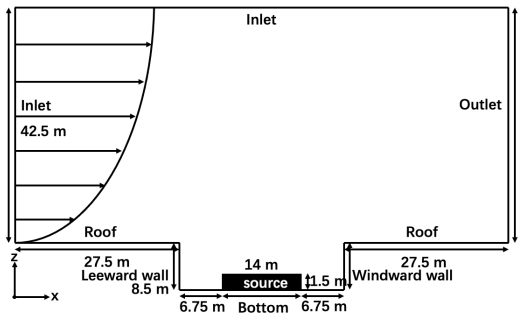

Figure 101. Street canyon domain of the model.

The simulation lasts 12.5h from 4h30 to 17h on the 30th April, 2014 in local time of Paris (GMT+2), with a constant time step Δt of 0.5 s . The first 30 minutes is the model spin-up time. Meteorological boundary conditions including hourly-varying temperature (T), humidity (H) and friction velocity (u) are obtained from Weather Research and Forecasting (WRF) simulations (Sartelet et al, 2018). Wind direction is set perpendicular to the length of the street. Hourly-varying background concentration of simulation species is acquired from regional-scale simulations (Sartelet et al, 2018) and the hourly-varying traffic emission is calculated from the COPERT (COmputer Program to calculate Emissions from Road Transport, version 2019, EMEP/EEA, 2019) methodology (Kim et al, 2022). These boundary conditions are interpolated linearly in time. As detailed in Lin et al. (2022), the simulated concentrations of NO_2 and PM_{10} compare well with observations.

COMPARISON OF CODE_SATURNE AND OPENFOAM SIMULATIONS

As discussed in Lin et al (2022), the simulations conducted with Code_Saturne and OpenFoam lead to slight differences in NO_2 (67.6 $\mu g.m^{-3}$ in OpenFoam and 70.0 $\mu g.m^{-3}$ in Code_Saturne) and PM_{10} (22.3 $\mu g.m^{-3}$ in OpenFoam and 23.4 $\mu g.m^{-3}$ in Code_Saturne) concentrations. In this section, simulations conducted by the two CFD tools are presented and a detailed comparison between the different compounds of particles is computed and analyzed.

Figure 2 compares the time-averaged air flow field and the time-averaged concentration field of inert particle components in the street canyon. As shown in Figure 2 (a), the differences in turbulent scheme result in a larger turbulent viscosity at the top of the street in OpenFoam than in Code_Saturne. The horizontal and vertical wind velocity fields are also higher at the top of the street and lower at the bottom, as shown in Figure 2 (b) and Figure 2 (c). In OpenFoam, the vortex simulated in the street is also slightly larger, with larger wind speed in the vortex. These differences in the flow field results in differences in the

concentration field. Figure 2 (d) shows the comparison of time-averaged inert particle (dust, black carbon) concentrations in the street. Inert particles are not chemically reactive. Although their spatial distribution is similar in two models, the inert concentration averaged over the canyon is slightly lower in OpenFoam (9.0 $\mu g.m^{-3}$) than in Code_Saturne (10.0 $\mu g.m^{-3}$); as the turbulent viscosity is higher in OpenFoam, emitted pollutants are more dispersed out of the canyon. In addition, because of the longer vortex in the x direction in OpenFoam, the concentrations are higher in the leeward side compared to Code_Saturne.

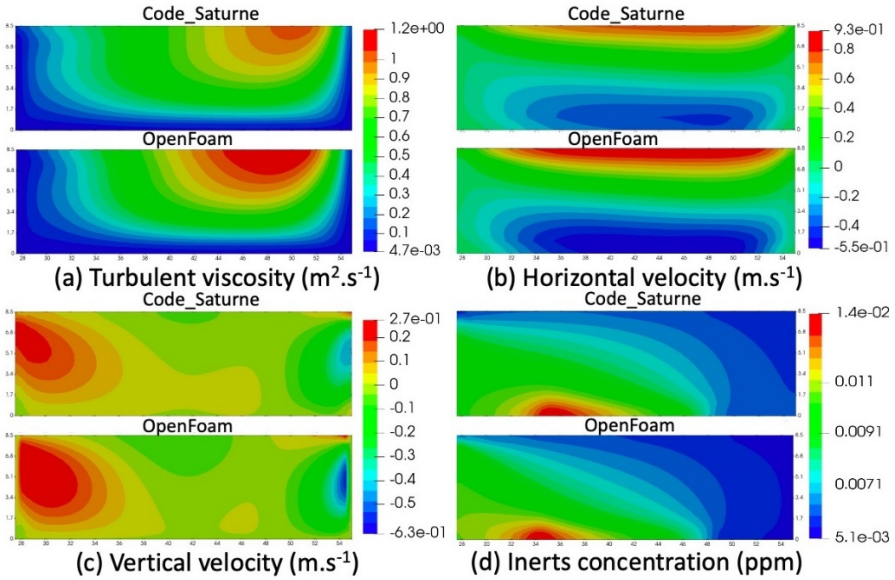

Figure 2. Time-average flow field and inert concentration field in Code_Saturne and OpenFoam.

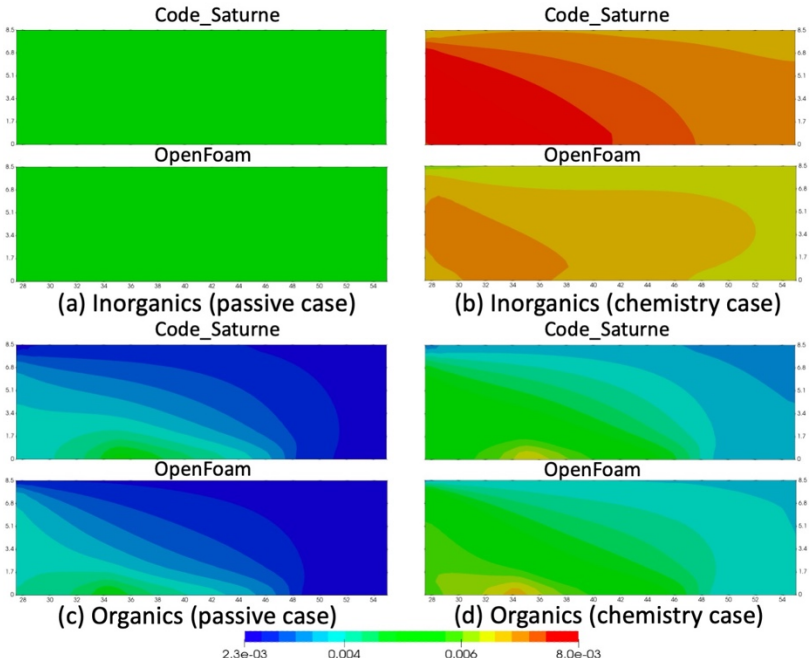

Figure 3. Time-averaged inorganic and organic concentrations in Code_Saturne and OpenFoam, the unit is ppm.

Considering the reactive compounds of particles, Figure 3 compares the time-average inorganic and organic aerosol concentrations in the passive and chemistry cases. For inorganic aerosols in Figure 3 (a) and (b), the average concentration in Code_Saturne is slightly larger than in OpenFoam both in the passive and the chemistry cases: in the passive case, the street-average inorganic concentration is 5.8 $\mu g.m^{-3}$ in OpenFoam and 6.1 $\mu g.m^{-3}$ in Code_Saturne; In the chemistry case, the street-average inorganic concentration is 7.9

$\mu g.m^{-3}$ in OpenFoam and 8.2 $\mu g.m^{-3}$ in Code_Saturne. This can be explained by the different turbulent models, which result in slightly different exchanges between the street and the background concentrations above the street. A large fraction of inorganics comes from the background concentrations (boundary conditions) as shown by the uniformity of concentrations in Figure 3(a). For organic aerosols, in the passive case, the spatial distribution difference is similar to inert matter in Figure 2 (c), as there are strong emissions in the street. The average organics concentration in OpenFoam (3.5 $\mu g.m^{-3}$) is lower than in Code_Saturne (3.9 $\mu g.m^{-3}$), which is caused by the different turbulence scheme. In the chemistry case, organic aerosol concentrations near the ground at the leeward side in OpenFoam (5.4 $\mu g.m^{-3}$ on average) is however slightly larger than in Code_Saturne (5.3 $\mu g.m^{-3}$ on average). This may be caused by the different velocities in the two models.

IMPACT OF CHEMISTRY ON THE FORMATION OF GAS AND AEROSOLS

Impact of chemistry on NO_2

The gas chemistry has a large impact on reactive gaseous species, which influences the formation of some secondary pollutants. Figure 4 presents the time-average NO_2 concentration in the street. Gas chemistry promotes its formation in the street, leading to an average increase of 40.5% in Code_Saturne and 46.7% in OpenFoam. The impact of gas chemistry is more significant in OpenFoam than in Code_Saturne, especially the flow differences between the two models lead to slightly more accumulation of emitted pollutants, such as NO, on the leeward side of the street. NO forms NO_2, as it accumulates to the leeward side.

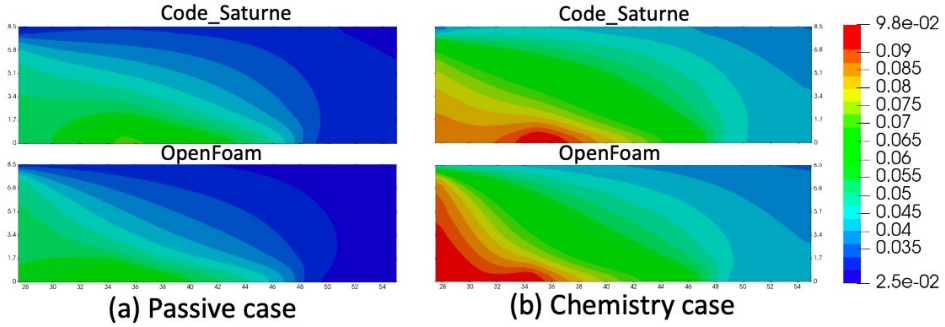

Figure 4. Time-average NO_2 concentration field in Code_Saturne and OpenFoam, the unit is ppm.

Impact of chemistry on inorganic and organic aerosols

Gas chemistry and aerosol dynamics lead to a significant increase of the average concentration of PM_{10} in the street. For the inorganic components of PM_{10}, the increase mainly comes from the increase of ammonium nitrate. In Code_Saturne and in OpenFoam, the increase of ammonium nitrate concentration is comparable (+1.9 $\mu g.m^{-3}$ on average in both OpenFoam and and Code_Saturne). Ammonium nitrate is not directly emitted from the traffic, but is formed from the condensation of ammonia (NH_3) and nitric acid (HNO_3). NH_3 is emitted from the traffic, and HNO_3 is formed from the oxidation of NO_2. As the formation of HNO_3 from NO_2 is too slow to be formed efficiently in the street, the increase of ammonium nitrate is mostly due to aerosol dynamics, and not gas chemistry.

For organic aerosols, as is shown in Figure 5 (a), the fraction of biogenic organic compounds in the chemistry case is significantly larger than in the passive case. Figure 5 (b) shows the concentration of biogenic and anthropogenic compounds on average in the passive and chemistry cases, when chemistry is activated, more than 70% of the organic aerosols increase comes from the increase of biogenic compounds. As biogenic organic aerosols are assumed to be hydrophilic in the model while most anthropogenic organic aerosols are hydrophobic, the increase of ammonium nitrate enhances the condensation of hydrophilic species, and hence biogenic organic aerosols.

CONCLUSIONS

The formation of gaseous and particle concentrations in a street of Greater Paris was simulated with two different CFD tools coupled with the same chemical model. Different turbulent schemes and pollutant dispersion only slightly impact the airflow and the concentrations. The gas and aerosol chemistry

significantly impacts the formation of secondary gaseous concentrations, such as NO_2, and to a lesser extent the formation of inorganic and organic aerosols. Inorganics increase because of ammonia emission. The increase of organics is partly due to the increase of hydrophilic compounds (biogenics) enhanced by the increase of inorganic concentrations.

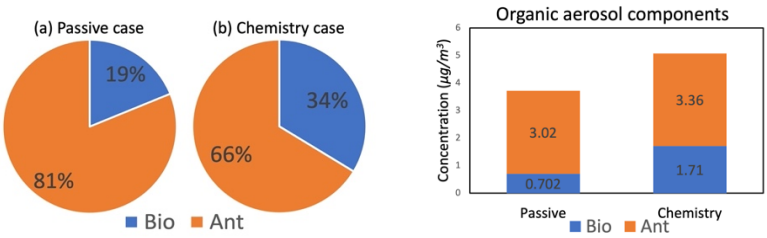

(a) Concentration fraction (b) Concentration

Figure 5. Time-average anthropogenic and biogenic concentration fraction in passive case and chemistry cases. Bio represents biogenic compounds; Ant represents anthropogenic compounds.

REFERENCES

Archambeau, F., N. Méchitoua and M. Sakiz, 2004: Code_saturne: a finite volume code for the computation of turbulent incompressible flows. *International Journal on Finite Volumes*. URL: https://hal.archives-ouvertes.fr/hal-01115371/document.

Kikumoto, H. and R. Ooka, 2012: A numerical study of air pollutant dispersion with bimolecular chemical reactions in an urban street canyon using large-eddy simulation. *Atmos. Environ*., **54**, 456–464. doi:10.1016/j.atmosenv.2012.02.039.

Kim, Y., K. Sartelet and C. Seigneur, 2011: Formation of secondary aerosols: impact of the gas-phase chemical mechanism. *Atmos. Chem. Phys*., **11**, 583–598. doi:10.5194/acp-11-583-2011.

Kim, Y., L. Lugon, A. Maison, T. Sarica, Y. Roustan, M. Valari, Y. Zhang, M. André and K. Sartelet, 2022: MUNICH v2.0: a street-network model coupled with SSH-aerosol (v1.2) for multi-pollutant modelling. Geosci. Model Dev. in review. doi: 10.5194/gmd-2022-26.

Lin, C., Y. Wang, R. Ooka, C. Flageul, Y. Kim, H. Kikumoto, Z. Wang and K. Sartelet, 2022: Modelling of street-scale pollutant dispersion by coupled simulation of chemical reaction, aerosol dynamics, and CFD. *Atmos. Chem. Phys. Discuss.*, in review. doi: 10.5194/acp-2022-365.

Lugon, L., K. Sartelet, Y. Kim, J. Vigneron and O. Chrétien, 2020: Non-stationary modeling of NO_2, NO and NOx in Paris using the Street-in-Grid model: coupling local and regional scales with a two-way dynamic approach. *Atmos. Chem. Phys*., **20**, 7717–7740. doi:10.5194/acp-20-7717-2020.

OpenFOAM: OpenFOAM user guide, [online] Available from: https://www.openfoam.com/, 2020.

Sartelet, K., F. Couvidat, Z. Wang, C. Flageul and Y. Kim, 2020: SSH-Aerosol v1. 1: a modular box model to simulate the evolution of primary and secondary aerosols. *Atmosphere*., **11**, 525. doi:10.3390/atmos11050525, 2020.

Sartelet, K., S. Zhu, S. Moukhtar, M. André, J. André, V. Gros, O. Favez, A. Brasseur and M. Redaelli, 2018: Emission of intermediate, semi and low volatile organic compounds from traffic and their impact on secondary organic aerosol concentrations over Greater Paris. *Atmos. Environ*., **180**, 126–137. doi:10.1016/j.atmosenv.2018.02.031, 2018.

Strang, G., 1968: On the Construction and Comparison of Difference Schemes, SIAM J. *Numer. Anal.*, **5(3)**, 506–517. doi:10.1137/0705041, 1968.

Yarwood, G., S. Rao, M. Yocke and G. Whitten, 2005: Updates to the carbon bond chemical mechanism: Cb05. rep. rt-0400675.

Zhang, K., G. Chen, Y. Zhang, S. Liu, X. Wang, B. Wang and J. Hang, 2020: Integrated impacts of turbulent mixing and NOX-O3 photochemistry on reactive pollutant dispersion and intake fraction in shallow and deep street canyons. *Sci. Total Environ*., **712**, 135553. doi:10.1016/j.scitotenv.2019.135553.

Zhong, J., X. Cai and W. Bloss, 2014. Modelling segregation effects of hetero-geneous emissions on ozone levels in idealised urban street canyons: Using photochemical box models. *Environ Pollut*., **188**, 132–143. doi:10.1016/j.envpol.2014.02.001.

21st International Conference on
Harmonisation within Atmospheric Dispersion Modelling for Regulatory Purposes
27-30 September 2022, Aveiro, Portugal

SENSITIVITY OF LES SIMULATIONS TO RESOLUTION, SUBGRID MODELS AND BOUNDARY CONDITIONS

Vladimir Fuka[1], Jelena Radović[1] and Štěpán Nosek[2]

[1]Department of Atmospheric Physics, Faculty of Mathematics and Physics, Charles University, Prague, Czech Republic
[2]Institute of Thermomechanics, Czech University of Sciences, Prague, Czech Republic

Abstract: Sensitivity of large eddy simulations of flow and passive scalar dispersion in idealized urban canopy. The main variable followed are the boundary conditions and the domain size. The effect on convergence to homogeneous time-averaged solution and temporal spectra is investigated.

Key words: *large eddy simulation, sensitivity, convergence, boundary conditions*

INTRODUCTION

It is common to investigate the flow in certain types of urban canopy using large eddy simulation (LES) in idealized conditions. Often, periodic boundary conditions are used to simulate a fully developed flow over an "infinite" canopy (e.g., Castro et al., 2017). Another option are turbulent inflow boundary conditions (Sessa et al., 2018). The scalar boundary conditions are typically non-periodic in either case. This work examines the effect of the periodic boundary conditions on the simulated flow and the resulting scalar dispersion in an idealized urban canopy.

The selected configuration of building of canopy with closed courtyards follows (Kluková et al., 2020) and was previously measured in wind-tunnel experiments. Only the case with uniform roof height and pitched roofs was considered for simplicity. This particular case showed the biggest discrepancy in the mean flow from the wind tunnel experiments in earlier simulations and deserves further investigation

NUMERICAL CODE, SIMULATION SETUP

Numerical model

The ELMM in-house code (Fuka, 2015) was used. ELMM solves the incompressible Navier-Stokes equations on a uniform Cartesian grid with the immersed boundary method used for solid bodies. The equations are discretized using the finite volume method with second order central spatial differences. For temporal discretization, a third-order Runge-Kutta method and the projection method are used. The mixed-time-scale (MTS) model by Inagaki et al. (2005) is used for subgrid stresses. Synthetic turbulent inflow boundary conditions are generated using the method of Xie and Castro (2008).

Setup of the simulations

The default domain originates from (Kluková et al., 2020) and comprises 4 x 4 blocks with courtyards. Each block has dimensions 2.4 H x 4.8 H (streamwise x spanwise), where H is the building height. The total dimensions of the domain are 12.8 H x 22.4 H. The default domain is visualized in Figure 1 a). The grid resolution was 18.75 cells / H in the streamwise directions and 20 cells / H in the vertical direction.

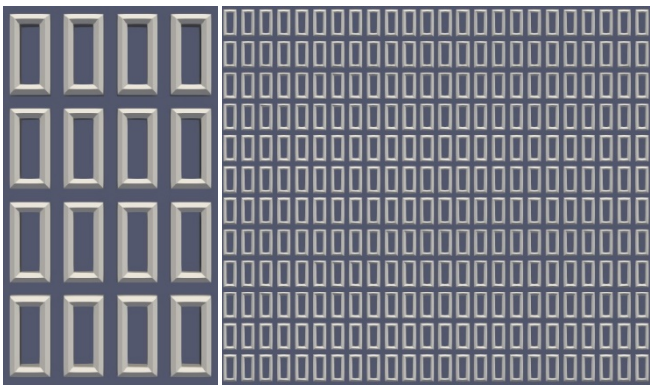

a)

b)

Figure 102**.** The default (a) and the largest (b) computational domain and the layout of the blocks of buildings around the courtyards.

Larger domains were tested. The extended domain was extended 2x in the streamwise direction, extended domain 2 was extended 4x in the streamwise direction, the very large domain 6x in the streamwise direction and 3x in the spanwise direction. The largest domain is shown in Figure 1 b). For this largest domain the grid resolution had to be reduced.

A different domain was used for simulations with turbulent inflow boundary conditions. It corresponds to the default domain extended 2x in the streamwise direction with short empty sections appended at the inflow and the outflow.

RESULTS AND DISCUSSION

The first comparison considers instantaneous and time-averaged velocity fields in domains of varying size. The periodic boundary conditions prohibit structures longer than the streamwise domain size and wider than the spanwise domain width. Moreover, a certain structure, e.g., a region of higher or slower wind speed, can cycle in a certain spanwise location many times and hence generate a negative or positive bias of wind speed. For turbulent inflow boundary conditions, the situation is different because the structures are generated with the same mean value across the span and the timescale is dictated by the generating algorithm. However, close to the inflow plane the turbulent fields are affected by the synthetic generation and need some travel time to adjust.

Instantaneous structures of the streamwise velocity component in the four configurations at z = 1.2 H are depicted in Figure 2. One can notice that even for the largest domain the structures are very long.

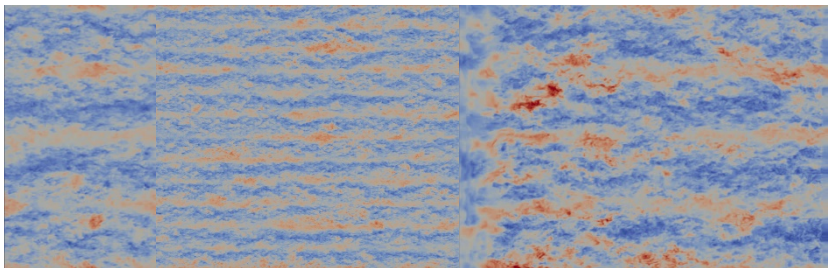

Figure 2. Instantaneous snapshots of spanwise wind velocity at height z = 1.2H for a) the default domain with periodic boundary conditions, b) the largest domain with periodic boundary conditions, c) the domain with inflow boundary conditions.

The time-averaged streamwise velocity field at the same height are shown in Figure 3 and the effect on time-averaged streamwise velocity inside the canopy (z = 0.4 H) are shown in Figure 4. The averaging time was equal in all cases to 320 H/u_*. One can clearly identify streets that are faster and streets that are slower. That also leads to asymmetric dispersion patterns (not shown here) from scalar sources located between the

streets with different windspeed. For inflow boundary conditions the wind speed is equal across the span but it changes in the streamwise direction as the flow develops.

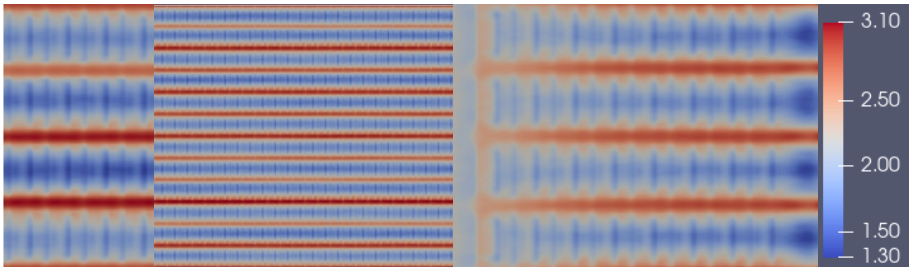

Figure 3. Time-averaged fields of spanwise wind velocity at height z = 1.2 H for a) the default domain with periodic boundary conditions, b) the largest domain with periodic boundary conditions, c) the domain with inflow boundary conditions.

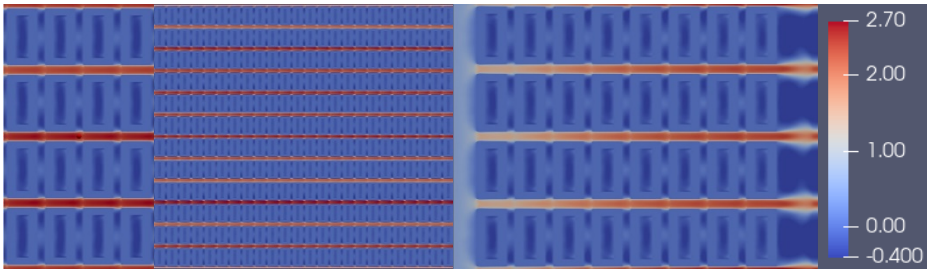

Figure 4. Time-averaged fields of spanwise wind velocity at height z = 0.4 H for a) the default domain with periodic boundary conditions, b) the largest domain with periodic boundary conditions, c) the domain with inflow boundary conditions.

We also investigated the temporal spectra of the streamwise velocity component at a fixed point above the canopy, namely at point above the central intersection at the height of 2 H in Figure 5. The results are compared to wind-tunnel measurements at the height of 1.6 H. For the largest domain the variance is lower due to lower grid resolution because the results are scaled by the variance of the resolved velocity component. One can see that the peak dictated by the domain size moves to lower frequencies but remains present even for the largest domain, which is much longer than the size of the area modelled in the wind tunnel experiment. Figure 6 compares the streamwise velocity spectra for two settings of the integral timescale for the synthetic turbulence generator. The spectra do not show such distinct peak but clearly contain much fewer low-frequency structures compared to the wind tunnel.

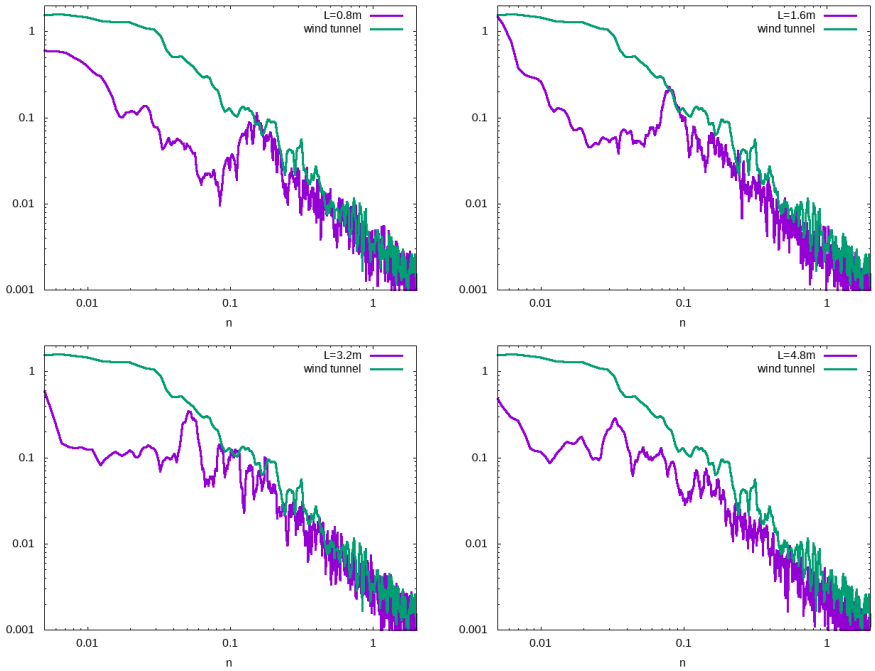

Figure 5. Dimensionless spectra of the streamwise velocity component at z = 2 H compared to wind-tunnel measurements at z = 1.6 H for different domain sizes with peridic boundary conditions. Domain length indicated in meters, H = 6.25 cm.

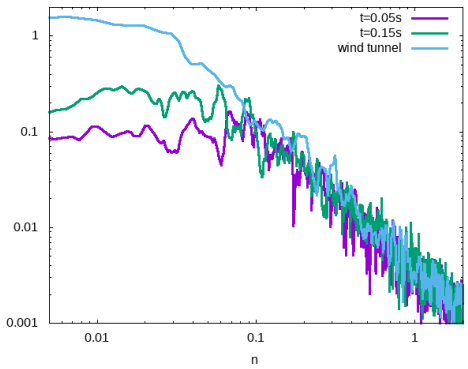

Figure 6. Dimensionless spectra of the streamwise velocity component at z = 2 H compared to wind-tunnel measurements at z = 1.6 H for two different integral time scale settings of the synthetic turbulence generator.

CONCLUSION

A subset of sensitivity tests performed for the flow in an idealized periodic urban canopy with uniform building heights is presented. The results show the effect of periodic and turbulent inflow boundary conditions on instantaneous and time-averaged flow fields. The periodic boundary conditions affect the convergence to homogeneous averaged solution by promoting structures of higher and lower wind speed to remain locked in a certain spanwise location and being recycled over the same location several times. The turbulent inflow conditions do not exhibit this problem but the flow develops in the streamwise direction and the synthetic turbulent flow needs a certain time to develop to a more natural flow. The velocity spectra are also affected and show the large importance of the structures corresponding to the streamwise domain length. Increasing the domain size did not result in improved convergence to a solution homogeneous across the span.

Other tests were performed but cannot be shown in this short contribution. They include test of grid convergence in a small domain comprising a single building block. The contribution of subgrid modelling

was also tested in different grid resolution by using different subgrid models and also by performing DNS in lower Reynolds number by increasing the value of air viscosity and scalar diffusivity. These tests also included scalar dispersion and will be a topic of future publications.

ACKNOWLEDGMENT

This work was supported by the Grant Agency of the Czech Republic grant no. 22-14608S.

REFERENCES

Castro, I.P., Z.-T. Xie, V. Fuka, A.G. Robins, M. Carpentieri, P. Hayden, D. Hertwig and O. Coceal, 2017: Measurements and Computations of Flow in an Urban Street System, *Boundary-Layer Meteorol.*, **162**, 207-230.

Fuka, V, 2015: PoisFFT – A free parallel fast Poisson solver, *Applied Mathematics and Computation*, **267**, 356-364.

Inagaki, M., T. Kondoh and Y. Nagano, 2005: A Mixed-Time-Scale SGS Model With Fixed Model-Parameters for Practical LES, *J. of Fluids Eng.*, **127**.

Kluková, Z., Š. Nosek, V. Fuka, Z. Jaňour, H. Chaloupecká and J. Ďoubalová, 2021: The combining effect of the roof shape, roof-height non-uniformity and source position on the pollutant transport between a street canyon and 3D urban array, *J. of Wind Eng. & Industrial Aerodyn.*, **208**.

Sessa, V., Z.-T. Xie and S. Herring, 2018: Turbulence and dispersion below and above the interface of the internal and the external boundary layers, *J. of Wind Eng. & Industrial Aerodyn.*, **182**, 189-201.

Xie Z.-T. and I.P. Castro, 2008: Efficient Generation of Inflow Conditions for Large Eddy Simulation of Street-Scale Flows, *Flow Turbulence Combust.*, **81**, 449–470.

21st International Conference on
Harmonisation within Atmospheric Dispersion Modelling for Regulatory Purposes
27-30 September 2022, Aveiro, Portugal

ASSESSMENT OF THE DISPERSIVE CAPACITY OF NEIGHBOURHOODS BASED ON LOCAL CLIMATE ZONES CLASSIFICATION

Andrés Simón-Moral[1], Alberto Martilli[2], Ales Padró[1], Lexuri Yurrebaso[1]*

[1]TECNALIA, Basque Research and Technology Alliance (BRTA), Derio, Spain
[2]Research Center for Energy, Environment and Technology, CIEMAT, Madrid, Spain

Abstract: NO_x dispersion simulations of a winter period were performed with the Weather Research and Forecasting model (WRF) coupled with an urban canopy scheme (BEP-BEM) in Vitoria-Gasteiz, a small size city in the north of the Iberian peninsula. Road traffic and residential heating were considered as emission sources and NO_x was treated as an inert gas, with no deposition. Comparison with observations across three urban air quality stations shows that the model is able to reproduce time and space variability. NO_x is normalized by the emission in each grid cell in order to represent the dispersion capacity of the urban canyons and results are analysed based on the Local Climate Zone (LCZ) classification. The dispersive capacity is found to be influenced by urban morphology. LCZs show different dispersion capacity, with LCZ 2 and 3 showing higher normalized concentration values than the rest. On the other hand, horizontal transport of NO_x is found to hinder the analysis and further understanding of urban winds is needed. This study shows the potential of the LCZ classification for air quality management, providing a fast screening method for cities, in order to prioritize the areas to be improved from the air pollution perspective.

Key words: *Urban air quality, mesoscale model, BEP-BEM, dispersion capacity, Local Climate Zones.*

INTRODUCTION

Air quality represents a problem for human health, being especially important in urban areas, where most of the population live. Pollutant concentration in urban street canyons mainly depends on two factors, i.e. pollutants emission and their dispersion within the canyon. Emission is mostly associated here with traffic and residential sector (e.g. boilers, cooking), which is specific for each street and can only be controlled through technological improvement (i.e. cleaner motor vehicles) or policy restrictions (i.e. low emission zones). On the other hand, dispersion depends on meteorological factors (i.e. atmospheric stability, wind speed) and the morphology or structure of the canyon, which affects wind speed and turbulence and shapes the exchange of air with higher atmospheric levels. The latter is also specific for each street canyon and could be ideally modified or smartly designed in the construction stage.

Local Climate Zones (LCZ) classification was introduced by Stewart and Oke (2012) to characterize neighbourhoods in terms of their interaction with the atmosphere, based on their fabric, land cover, structure, and metabolism. This classification has been widely used in urban climate, primarily as model input (Brousse et al. 2016), but also as a useful guidance for climate impact assessment or the need of design interventions analysis.

On the other hand, urban canyon structure is directly related with its dispersion capacity and hence LCZ classification could theoretically be used to identify potentially polluted neighbourhoods, if high emissions occur. However, this connection hasn't been documented yet.

In this work we investigate the capacity of the LCZ classification to characterize the dispersion capacity of different neighbourhoods. This is the capacity to disperse the pollutants released. For this task, a high pollution episode is simulated with the Weather and Forecasting Model (WRF, Skamarok et al. 2008), where city morphology is characterized based on the LCZ classification.

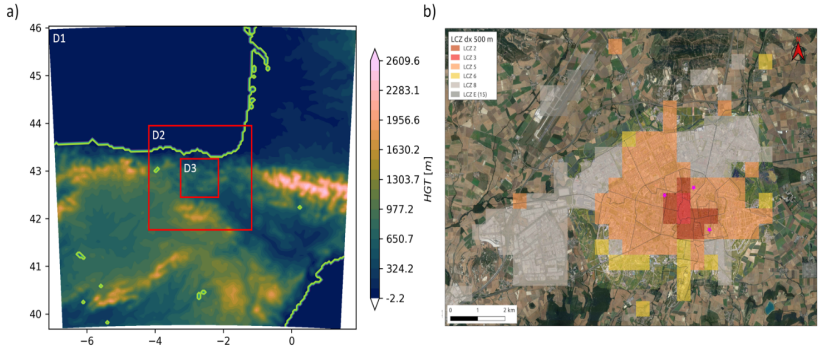

Figure1: a) Configuration of the three domains used for the simulations with 4.5 km (D1), 1.5 km (D2) and 500 m (D3) resolution, respectively. b) LCZ map for Vitoria-Gasteiz (VG) used in the simulations. The pink stars represent the measurement stations: Av. Gasteiz (West), 3 de Marzo (North) and Judimendi (South).

METHODOLOGY

In this study, the WRF model, coupled with the urban canopy parameterization BEP-BEM (Martilli et al. 2002; Salamanca et al. 2010), is used to simulate a high pollution episode in Vitoria-Gasteiz (VG), a small size city located in the north of the Iberian Peninsula (42°50′48″N 2°40′23″O). BEP-BEM is used here to account for the impact of the urban morphology on the pollutant emission and dispersion.

Three nested domains with 4.5 km, 1.5 km and 500 m resolution, respectively, are used in this study, with the smaller domain covering the city of VG (Figure 1a). The period simulated corresponds with the first week (1^{st} – 6^{th}) of January 2017, with the first day considered as spin – up. High pollution levels where registered between the 3^{rd} and 5^{th} days, making this period an interesting case study.

The LCZ map of VG was created with the *LCZ-Generator* tool (Demuzere et al. 2021), based on the WUDAPT methodology for Level 0 data (www.wudapt.org), followed by manual correction (Figure 1b). The LCZ classification is used here to assess its ability to characterize the dispersion capacity of different neighbourhoods. Next, urban morphology is characterized by calculating the average street and building width and building height for each LCZ. These parameters are required by BEP-BEM to parameterize the impact of the urban canopy on the atmosphere, and hence on pollutant dispersion.

Finally, the *wudapt-to-wrf* tool (Demuzere et al. *In preparation*) is used to convert the LCZ map into the input binary file readable by WRF. In this process, the original LCZ map with a resolution of ~50 m is averaged into the 500 m resolution grid used by WRF. Hence, due to the heterogeneity of the city, the final urban morphology parameters in each grid cell are the result of such average, being mostly a combination of different LCZs.

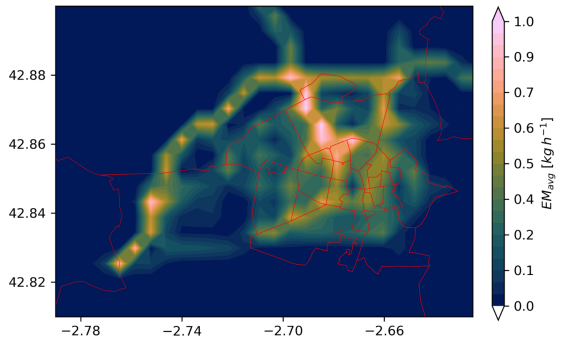

Figure 2: Mean hourly emission in kg h^{-1}.

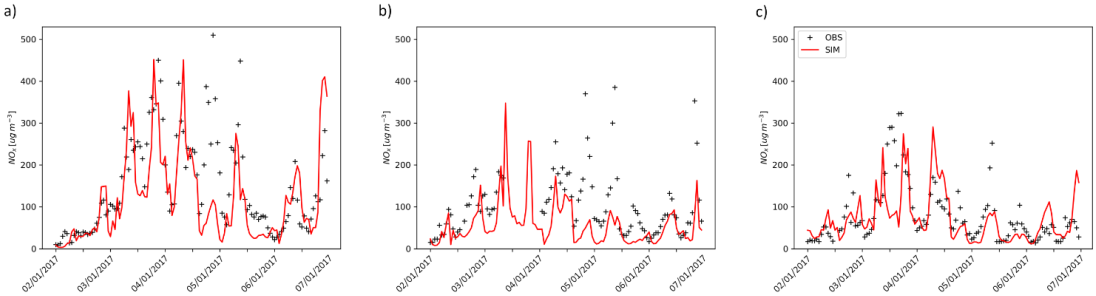

Figure 3: Observed (black crosses) and simulated (red line) hourly NO_x in the three air quality stations: a) Av. Gasteiz, b) 3 de Marzo and c) Judimendi.

NO_x dispersion is considered by activating the passive tracer variable already defined in WRF. Hence, NO_x dynamics are represented with the same diffusion coefficients than other scalars, being the ones from Bougeault and Lacarrere (1989) (Martilli et al. 2022).

Only traffic and residential emissions are considered, as they are the main contributors within the city area. This information, taken from the Air Quality Action Plan of the municipality of VG, is summed in each grid cell and introduced in the model (Figure 2), considering its diurnal variability.

The main difficulty when characterizing the dispersion capacity of a specific LCZ (or grid cell) is the advection of pollution between neighbour canyons. More pollution than what is emitted can therefore be found in an urban canyon, making difficult to assess its real dispersion capacity. To minimize this problem, two approximations are considered. First, the analysis is focused on the first vertical layer, considering emission sources and inmission levels in the first model level only. Second, to maximize the local impact on pollutant dispersion, only low wind conditions are considered. Hence, hourly situations with spatially averaged wind speed above the 50th percentile are neglected. The area used for the spatial averages extends from -2.76º to -2.63º and from 42.8º to 42.9º in longitude and latitude, respectively.

Normalized *NOx*

Pollution sources are highly heterogeneous in urban areas. Hence, to fairly evaluate the dispersion capacity of each LCZ, NO_x concentrations are normalized by the emission in each grid cell as:

$$NOx|_{NORM} = \frac{[NO_x]}{EM_{NO_x}} \quad (1)$$

where $NO_x|_{NORM}$ is the normalized NO_x concentration and $[NO_x]$ end EM_{NOx} are NOx concentration and emission, respectively, in kg h^{-1}.

This parameter represents the amount of NO_x remaining in the canyon, respect to what is emitted, and hence we define it as the inverse of the dispersion capacity.

RESULTS

Results are compared with measurements from 3 stations managed by the Basque Government (Figure 3). The model is able to qualitatively represent the increase of NO_x values observed between the 3rd and 5th of January, although it fails to reproduce the second peak observed on the 4th in Av. Gasteiz and 3 de Marzo. In addition, it captures the qualitative differences observed between the three stations, with higher values found in Av. Gasteiz, followed by 3 de Marzo and Judimendi.

Hourly averaged wind field and $NO_x|_{NORM}$, calculated as the grid cell average between all the hourly situations with spatially averaged wind speed below the 50th percentile are shown in Figure 4. Maximum values are not located where emission is higher, probably due to the different capacity to disperse pollutants in each area and the action of the wind, which shows convergence towards the area where $NOx|_{NORM}$ is maximum.

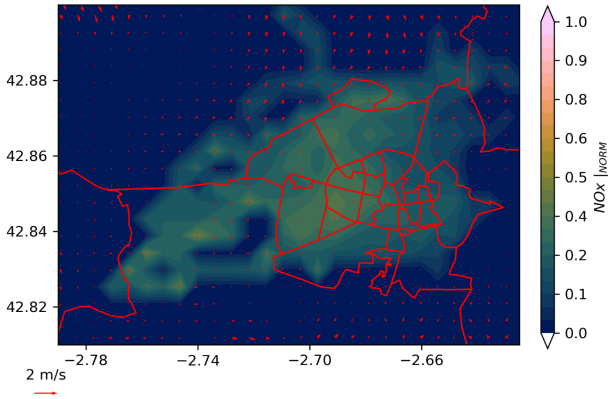

Figure 4: Mean hourly $NO_x|_{NORM}$ and wind vectors (red arrows), calculated as the average hourly $NO_x|_{NORM}$ and wind, respectively, with spatially averaged wind speed below the 50th percentile situations. The area with longitudes between -2.76º and -2.63º and latitudes between 42.8º and 42.9º is considered for the spatial average.

Box plots of $NO_X|_{NORM}$ for each LCZ are used to further study the dispersive capacity (Figure 5). Each box consists of the time median in each grid cell belonging to the correspondent LCZ. Even though averaging in time reduces the sample, it also helps minimizing inmission variability, mostly related to horizontal transport. As seen, the highest median and lower dispersion capacity is found in LCZ 3, followed by LCZ 2, LCZ 5, LCZ 8 and LCZ 6, however the differences are not big. It is important to note the high spread of the results, pointing out the complexity of avoiding non local effects and the fact that due to model resolution, morphological parameters differ between cells with the same LCZ.

Finally, the diurnal cycle of the median of $NO_X|_{NORM}$ for each LCZ is shown in Figure 6. LCZ 3 shows lower dispersion capacity during daytime (hence higher $NO_x|_{NORM}$), when the highest emission occurs, although higher during night-time. LCZ 2, with higher dispersion capacity than LCZ 3, but lower than the others, shows higher night-time $NO_x|_{NORM}$ values. This is also observed for LCZ 5. This can be especially important during high pollution episodes, where pollution remains high during the night, despite the lower emission.

The shape of the curves in Figure 6 reminds such of the emission, again pointing out the difficulty to isolate the impact of advection. In addition, the decrease seen between 0900 and 1800 UTC could be a consequence of the higher wind speed during this time period.

CONCLUSIONS

The dispersive capacity of different neighbourhoods is studied by simulating NO_x dispersion in a small sized town. A normalized NO_x is defined for each grid point, previously classified by its morphology following the LCZ classification.

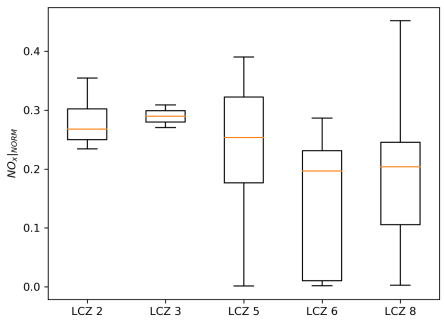

Figure 5: Box plots of $NO_x|_{NORM}$ for each LCZ. Values per box are the time mean in each point belonging to a specific LCZ. The box defines the region between 25 to 75 percentile, horizontal red lines represent the median, and the whiskers are extended to the minimum and maximum values.

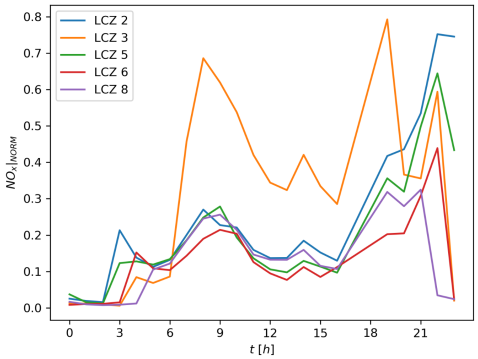

Figure 6: Diurnal cycle of the median of $NO_x|_{NORM}$ for each LCZ.

Results show that LCZ 2, 3 and 5 have the lowest dispersion capacities, tending to accumulate pollutants. In the case of Vitoria – Gasteiz, LCZ 3 has almost no traffic, making the emission, and inmission, relatively low. On the other hand, higher emissions are normally found in LCZ 2 and 5, making the accumulation of pollutants a problem, exacerbated by the fact that these LCZs are where most of the people live.

This study shows that LCZs disperse pollutants differently, making LCZ a useful classification for dispersion capacity characterization. This work points out the difficulties to avoid horizontal transport of pollutants, which could worsen the air quality in a specific area, despite its emission. The impact of such transport would also depend on the dispersive capacity of both the source and receptor of pollution.

A potential impact of wind convergence has also been hypothesized in this study. More research on pollutants dynamics and its dependency on urban morphology or urban heat island circulation would be needed. Understanding the dynamics inside urban areas and the capacity to disperse of different neighbourhoods would help optimizing traffic and hence designing cities as healthier places.

REFERENCES

Bougeault, P. and Lacarrere, P.: 1989, 'Parameterisation of Orography-Induced Turbulence in a Mesobeta-Scale Model', Mon. Wea. Rev. 117, 1872–1890.

Brousse, O., Martilli, A., Foley, M., Mills, G., & Bechtel, B. (2016). WUDAPT, an efficient land use producing data tool for mesoscale models? Integration of urban LCZ in WRF over Madrid. *Urban Climate*, *17*, 116–134. https://doi.org/10.1016/j.uclim.2016.04.00

Demuzere, M., Kittner, J., Bechtel, B. (2021). LCZ Generator: a web application to create Local Climate Zone maps. *Frontiers in Environmental Science* 9:637455. https://doi.org/10.3389/fenvs.2021.637455

Demuzere, M., Argüeso, D., Zonato, A., Kittner, J. W2W: A Python package that injects WUDAPT's Local Climate Zone information in WRF. *In preparation.*

Martilli, A., Clappier, A., Rotach, M.W., 2002. An urban surface exchange parameterization for mesoscale models. *Bound.-Layer Meteorol.* 104 (2), 261–304

Martilli, A., Sánchez, B., Santiago, JL., Rasilla, D., Pappaccogli, G., Allende, F., Martín, F., Roman-Cascón, C., Yagüe, C., Fernández, F. (2022) Simulating the pollutant dispersion during persistent Wintertime thermal Inversions over urban areas. The case of Madrid, Atmospheric Research, 270: 106058, ISSN 0169-8095, https://doi.org/10.1016/j.atmosres.2022.106058.

Salamanca, F., Krpo, A., Martilli, A., Clappier, A., 2010. A new building energy model coupled with an urban canopy parameterization for urban climate simulations—part I. Formulation, verification, and sensitivity analysis of the model. *Theor. Appl. Climatol.* 99 (3), 331–344

Skamarock, W.C., Klemp, J.B., Dudhia, J., Gill, D.O., Barker, D.M., Wang, W., Powers, J. G., 2008. A Description of the Advanced Research WRF Version 3. NCAR Technical note-475+ STR.

Stewart, I. D., and Oke, T. R. (2012). Local Climate Zones for Urban Temperature Studies. *Bulletin of the American Meteorol. Society* 93, 12, 1879-1900,https://doi.org/10.1175/BAMS-D-11-00019.1>

21st International Conference on
Harmonisation within Atmospheric Dispersion Modelling for Regulatory Purposes
27-30 September 2022, Aveiro, Portugal

ACCELERATION OF SIMULATIONS BY APPLICATION OF A KERNEL METHOD IN A HIGH-RESOLUTION LAGRANGIAN PARTICLE DISPERSION MODEL

Daniela Barbero[1,2], Bruno Ribstein[3], Maxime Nibart[3] and Gianni Luigi Tinarelli[1]

[1]ARIANET S.R.L., 20159 Milan, Italy
[2]Department of DICA, Politecnico di Milano, 20133 Milan, Italy
[3] ARIA Technologies, 92100 Boulogne-Billancourt, France

Abstract: The role of microscale atmospheric dispersion modelling is becoming increasingly important in air quality assessment, especially in residential areas, for regulatory purposes and to project pollution control strategies. Consequently, the use of these models in long-term studies and forecasting systems is growing. However, this modelling can be challenging because of the amount of time and CPU required for the simulations, especially if the computational domain has a significant extension.
This article describes the application of a concentration calculation methodology to reduce the computational time needed by microscale Lagrangian Particle Dispersion Models (LPDMs). These models normally estimate the concentration with the box counting method: a 3D mesh is set, and the density is computed counting particles in each box. An alternative method based on the use of the statistical technique of kernel density estimation is proposed to determine the concentration from the particles' position. The kernel method allows for a reduction of computational particles emitted during the simulation, guaranteeing a similar accuracy to that of box counting method. It enables therefore to optimize the overall simulation time and the required CPUs in order to improve time and cost, enhancing the efficiency of models and widening their application fields.
The use of the kernel method to perform high-resolution simulations took the first steps with an application inside the LPDM of PMSS (Parallel-Micro-SWIFT-SPRAY) system to evaluate road traffic gases emissions in urban areas, enabling an 80% simulation time reduction. In this article, additional features of this method are developed within the Micro-SPRAY model and validated against two new test cases. The test cases consider microscale simulations of industrial sources emitting gases and particles, evaluated both inside a domain divided in tiles and inside a nested domains configuration. The existing kernel method is enhanced in order to estimate the pollutant concentrations of point sources and to compute also the corresponding deposition at building-resolving scale and in nested domains with different horizontal resolution.

Key words: *kernel method, microscale simulation, lagrangian particle dispersion model, PSPRAY*

INTRODUCTION

Obtaining a correct and punctual assessment of air quality is increasingly requested to provide a better prevention of the population exposure and to define effective abatement strategies in advance. In this context, microscale atmospheric models can play a fundamental role, because they could assess, and moreover predict, air pollution levels at very high resolution. However, models that work at microscale generally have significant computational costs, in term of both CPU and time demanded for the simulations; especially for forecasting systems, which have the constrain of time, these costs can become limiting. Consequently, it is still crucial to reduce the amount of time needed for a simulation keeping the same computational resources.

Inside the microscale Lagrangian Particle Dispersion Model (LPDM) PSPRAY of the model suite PMSS (Parallel-Micro-SWIFT-SPRAY, Oldrini et al., 2011, 2017) an alternative method to compute concentrations to improve the computational time of a long-term simulation over a large urban area (Barbero et al., 2021) was already added. In addition to the box-counting method, originally applied in PSPRAY to calculate concentrations, a new algorithm called "kernel method" has been implemented, which allows to reduce the number of computational particles used for a simulation and therefore to optimize the time cost. In fact, PSPRAY is the parallel version of the LPDM SPRAY and it is based on a 3D form of the Langevin equation for the random velocity (Thomson, 1987); it simulates the dispersion of a pollutant following the trajectories of virtual particles, producing 3D concentrations fields and 2D dry

and wet depositions fields. Furthermore, PSPRAY can exploit MPI instructions to run in parallel mode, using several processors to split particles and/or to split the domain in several tiles or to use a nested configuration. The use of the kernel method has appeared promising for urban microscale simulations; therefore, some new numerical experiments have been performed considering industrial sources to test the method with point sources emitting gas and particles.

MATERIALS AND METHODS

The most common method used in LPDMs to calculate concentrations is the box-counting method, that consists in imposing a 3D mesh and computing the concentration field as the total mass of the particles falling inside a cell of the mesh divided by the cell volume. This method intrinsically requires emitting a large number of computational particles during the simulation, to avoid relatively large statistical errors.
The number of particles used in a simulation strongly influences the overall computational time, therefore an alternative method that allows to produce more regular fields with fewer particles could be useful, as in the case of the kernel method (Lorimer, 1986). This latter is based on kernel density estimation, which is a set of techniques for the nonparametric estimation of functions, and each particle is considered as the centre of a probabilistic distribution of its pollutant mass. Therefore, the concentration at a given time *t* and in a certain location in the domain defined by *x, y, z* could be computed as:

$$C(x,y,z;t) = \sum_{\mathrm{p}=1}^{Ntot} \frac{m_p}{h_x h_y h_z} K\left(\frac{x_p - x}{h_x}\right) K\left(\frac{y_p - y}{h_y}\right) K\left(\frac{z_p - z}{h_z}\right) \quad (1)$$

where N_{tot} is the total number of particles in the domain, x_p, y_p, z_p and m_p are the position and the mass of the p^{th} particle, K is a generic kernel function, which must be greater than 0 and its integral over the domain must be equal to 1, and h_i are the so-called bandwidths. K defines the shape of kernel, while the bandwidths adjust its width in the three directions of space, defining the so-called volume of influence of a particle. To obtain a field equivalent to that of the box-counting, the concentration is computed in the centres of the 3D mesh cells. The kernel method has been integrated in LPDMs at local scale since the late 1980s (Lorimer, 1986), but the inclusion in PSPRAY (Barbero et al., 2021) is the first application at microscale. The next paragraph summarizes the main specifications chosen for the kernel method, whose implementation has been adapted to the microscale.

Kernel method specifications

Kernel function and bandwidths definition

As shown in Equation (1), the kernel method in PSPRAY uses the 3D product kernel (de Haan, 1999), which is the product of independent one-dimensional kernels, defined for PSPRAY with the bi-weight kernel function in all the three space directions:

$$K(x) = \begin{cases} \frac{15}{16} * \left[1 - \left(\frac{x_p - x}{h_x}\right)^2\right]^2 & for \left|\frac{x_p - x}{h_x}\right| \le 1 \\ 0 & for \left|\frac{x_p - x}{h_x}\right| > 1 \end{cases} \quad (2)$$

However, the shape of the kernel function does not have a crucial influence on the results, but the role of bandwidths is of great importance (de Haan, 1999). The three bandwidths are computed as constants, directly proportional to PSPRAY 3D mesh sizes (Uliasz, 1994):

$$\begin{aligned} h_x &= 3.5 * \Delta x \\ h_y &= 3.5 * \Delta y \\ h_z &= 1.2 * h_0 \qquad (\mathrm{h_0 = height\ of\ ground\ level\ concentration}) \end{aligned} \quad (3)$$

The concentration is obtained by PSPRAY by counting N_{snap} times the mass contained in each cell. With the box-counting method, the smallest modeled concentration equals $\mathrm{m_p/N_{snap}}$, i.e. when a numerical particle is counted only once inside a cell. With the kernel method, the smallest modeled concentration is smaller, depending on the chosen bandwidths. In PSPRAY, with the same number of emitted particles, the smallest modeled concentration is about $K(x_p + 3.5 * \Delta x)K(y_p + 3.5 * \Delta y)K(z_p + 1.2 * \Delta z) \approx 4\%$ of the previous value. This is one of the reasons that explains why the number of emitted particles can be reduced.

Impermeable boundaries

A special treatment of the particles that are close to the ground or to obstacles is applied to prevent a mass lost due to the cut of the kernel function.

For all particles whose distance from the ground is less than its vertical bandwidth, a reflection term is introduced, which modifies the kernel function in the z direction as follows:

$$K(z) = K\left(\frac{z_p - z}{h_z}\right) + K\left(\frac{z_p + z}{h_z}\right) \quad (4)$$

This is based on the idea of considering, for each *x,y,z* point, a contribution of a virtual particle that is actually the original release reflected over the boundary, in addition to the normal contribution of the particle. Therefore, what actually goes over the boundary due to the kernel function is taken back by means of a reflected particle, whose quantity is the same as the quantity previously lost below the ground.

A different handling is necessary for particles that are close to an obstacle because it must be considered that the mass related to a particle must not contribute to the concentration both within a building and also in all the points behind the obstacle with respect to the particle itself. Therefore, the volume of influence of each particle is modified at each timestep based on the obstacles surrounding it, and its mass is distributed inside this new volume.

Deposition
In addition to the computation of concentration fields, it has been integrated also the calculation of dry and wet deposition 2D fields. The deposition fields are computed using a 2D product kernel, defined using the same kernel function of Equation (2) and the same bandwidths in horizontal directions of Equation (3).

Tiled and nested configuration
The existing kernel method has been applied also in nested configuration, as well as in tiled configuration. In these two configurations, each particle contributes only inside the domain in which it is located and the borders of adjacent tiles or nested domains are treated as impermeable boundaries. This is an approximation, but it allows to avoid an increase of time of MPI communications.

Test cases specifications
In order to perform a comparison of the methods, two different test cases have been considered, both with point sources, hereinafter referred to as “TEST CASE 1” and “TEST CASE 2”.

The TEST CASE 1 is simpler, considering one point source located at 1.5 meters from the ground and emitting a gaseous pollutant. The simulation is run with a tiled configuration, using 6 rectangular tiles, with a horizontal resolution of 1 meter. It allowed to firstly verify the same kernel method already applied with linear sources, but considering point sources.

The TEST CASE 2 was used to test the newer features of the kernel method. This test case considers a point source that emits both gases and particles, computing also the deposition. The simulation is run with a nested configuration, with two domains: the inner one with a horizontal resolution of 1 meter, and the external one with a horizontal resolution of 2 meters.

Both the test cases consider the presence of buildings in the domain and consider an averaging time for concentrations and depositions of 1 hour.

RESULTS AND DISCUSSIONS
For both the test cases, the hourly concentration and deposition fields were computed firstly using the box-counting method and then applying the kernel method using 1/5 of particles; for both methods the same number of CPU were used.

Figure 103 and **Figure 104** show the comparison between the hourly concentration fields of the gaseous pollutant at the ground level computed with the box-counting method and the kernel method respectively in TEST CASE 1 and TEST CASE 2. The obtained concentration fields of the particulate pollutants and the corresponding deposition fields in TEST CASE 2 closely resemble the ones shown. From the figures it

can be seen that the kernel method is able to provide qualitatively similar fields, emitting 1/5 of the particles that the box-counting method needs to provide a reliable statistical result. The fields produced with the kernel method appear smoothed enough and of the same shape as that of the box-counting method.

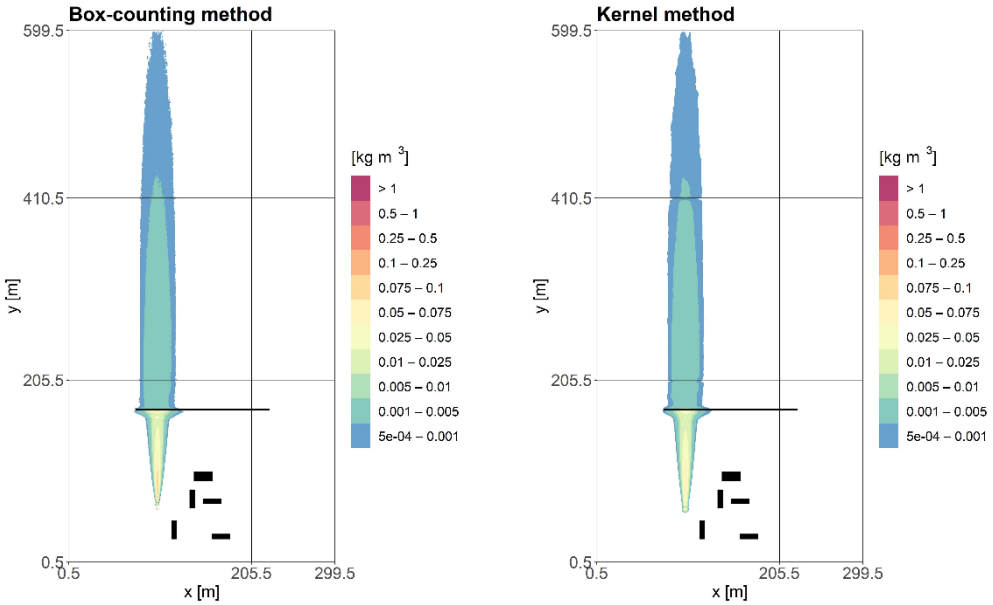

Figure 103. Hourly ground concentration fields of a gaseous pollutant computed with box-counting method (left) and kernel method (right), TEST CASE 1. The internal lines indicate the tiles of the domain, while the black rectangular shapes are the obstacles.

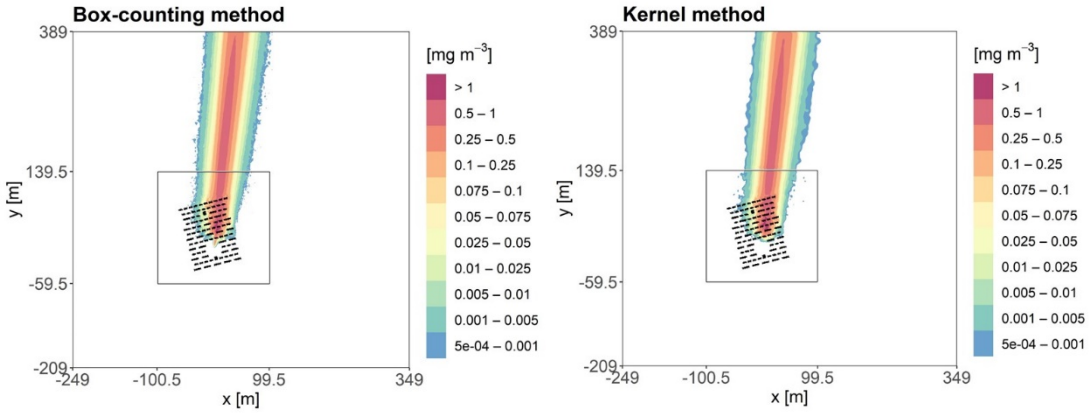

Figure 104. Hourly ground concentration fields of a gaseous pollutant computed with box-counting method (left) and kernel method (right), TEST CASE 2. The internal lines indicate the nested domain, while the black rectangular shapes are the obstacles.

The concentration fields are compared using as statistical indexes the fraction of predicted values within a factor of two of observations (FAC2), the Pearson correlation coefficient (r) and the Index of Agreement (IA) by Willmott (1981). The indexes are calculated by considering the concentration (and deposition) values at each point in the domain grid. However, all points where both resulting fields are 0 or lower than a threshold value set at 1/100 of the maximum value in the domain have been excluded, in order to avoid a non-significant bias in the statistics. Finally, it is also verified the overall reduction of time for the simulation obtained using the kernel method compared to the box-counting method, computed as:

$$Time\ reduction\ [\%] = \frac{time_{box-counting} - time_{kernel}}{time_{box-counting}} * 100 \quad (5)$$

The **Table 31** shows the statistical indexes and the reduction of time obtained in both the test cases. For TEST CASE 2 three separate analysis were carried out, for the concentration fields of gaseous pollutant and particulate pollutant and for the deposition field of the particulate pollutant.

Table 31. Statistical indexes of hourly concentration and deposition fields for comparison of box-counting method and kernel method results and obtained time reduction with kernel method

	TEST CASE 1	**TEST CASE 2**		
		Gas Concentration	**Particulate Concentration**	**Particulate Deposition**
Particles reduction [%]	80%		80%	
Time reduction [%]	68%		80%	
FAC2	0.95	0.98	0.98	0.95
Correlation	0.94	0.94	0.95	0.90
Index of agreement	0.96	0.97	0.97	0.95

The statistical analysis confirms the qualitative analysis of the figures, the concentration and deposition fields computed with the kernel method are statistically similar to those computed with the box-counting method, for both gaseous and particulate pollutants. All the statistical indexes are greater than 0.9 and close to their ideal value of 1. Regarding the reduction of time, for TEST CASE 2 the use of the kernel method allows for a reduction equal to the reduction of the particles emitted during the simulation: with a particles reduction of 80% we obtain an almost identical percent of computational time reduction. Considering the same reduction of emitted particles, the time saved is lower for TEST CASE 1. This is a result of the tiled configuration that requests more MPI communications than the nested configuration of TEST CASE 2; in that case, even if PSPRAY manages the nested domains as the tiled ones, we have only two sub-domains instead of six. The MPI communication load is independent from the calculation of concentration and constitutes a fixed part of the overall computational time. Even if this is still significant compared to the total amount of time, the advantage of using the kernel is less visible.

CONCLUSIONS

This work presents the use of kernel method as alternative to the common box-counting method to compute concentration inside the microscale Lagrangian Particle Dispersion Model PSPRAY. The method is tested to compute hourly ground concentration and deposition fields of gaseous and particulate pollutants emitted by point sources. The obtained results, although still preliminary, are promising and in line with those already obtained for linear sources, both in term of reduction of the overall computational time requested by the simulation and the statistical comparison to the box-counting method results.

REFERENCES

Barbero, D., Tinarelli, G., Silibello, C., Nanni, A., Gariazzo, C., Stafoggia, M., Viegi, G., 2021: A microscale hybrid modelling system to assess the air quality over a large portion of a large European city. *Atmospheric Environment*, **264**, 118656.

de Haan, P., 1999: On the use of density kernels for concentration estimations within particle and puff dispersion model. *Atmospheric Environment*, **33**, 2007-2021.

Lorimer, G. S., 1986: The kernel method for air quality modelling – mathematical foundation. *Atmospheric Environment*, **20**, 1447-1452.

Oldrini, O., Olry, C., Moussafir, J., Armand, P., Duchenne, C., 2011: Development of PMSS, the parallel version of Micro – SWIFT – SPRAY, paper presented at the 14th International Conference on *Harmonisation Within Atmospheric Dispersion Modelling for Regulatory Purposes*, Kos, Greece.

Oldrini O., Armand P., Duchenne C., Olry, C., Moussafir J., Tinarelli G., 2017: Description and preliminary validation of the PMSS fast response parallel atmospheric flow and dispersion solver in complex built-up areas. *Environmental Fluid Mechanics*, **17**, 997-1014.

Thomson D., 1987: Criteria for the selection of stochastic models of particle trajectories in turbulent flows. *Journal of Fluid Mechanics*, **180**, 529–556.

Uliasz, M., 1994: Lagrangian particle dispersion modeling in mesoscale applications. *Environmental Modeling*, **11**.

Willmott CJ., 1981: On the validation of models. *Physical Geography*, **2**, 184 19

21st International Conference on
Harmonisation within Atmospheric Dispersion Modelling for Regulatory Purposes
27-30 September 2022, Aveiro, Portugal

DISPERSION MODELLING OF MAJOR TRAFFIC SOURCES IN SOFIA CITY

Margret Velizarova [1], Reneta Dimitrova [1], Angel Burov [2] and Danail Brezov [3]

[1] Department of Meteorology and Geophysics, Faculty of Physics, Sofia University "St. K. Ohridski", Sofia, Bulgaria
[2] Department of Urban Planning, Faculty of Architecture, University of Architecture Civil Engineering and Geodesy, Sofia, Bulgaria
[3] Department Mathematics, Faculty of Transportation Engineering, University of Architecture Civil Engineering and Geodesy, Sofia, Bulgaria

Abstract: Many studies show the significance of transport-related air pollution in urban areas and its impact on human health. The emission inventories, including for Sofia, are often calculated on the basis of indirect arguments, using a linear first-line method with emission factors providing averaged emissions for the year. We developed a new methodology for a traffic emission inventory in Sofia city, applying more sophisticated methods and tools. The methods include a wide array of data gathering and processing as well as alternative traffic mapping and modelling steps and techniques. The traffic distribution model takes into account diverse characteristics of the street network and the spatial development of Sofia. The utilized traffic data from various sources is scarse and has poor integrity. This invoked the necessity of combination of processing, analysis and modelling techniques, among them interpolation and machine learning in order to obtain a relatively good estimate of the average annual daily traffic for the entire city street and road network.The numerical simulations with high resolution (100 m) were conducted by the Air Quality Management & Assessment System ADMS-Urban. The urban morphology and surface modelling were provided using the Street Canyon Tool implemented in ArcMap environment as well as the UMEP plugin and other native tools in QGIS. The specific emission scenarios are calculated through Comprehensive Emissions Inventory Toolkit and rely on both fleet composition changes and urban plan provisions. Meteorological conditions were provided by the Weather Research and Forecasting Model downscaling to the ADMS-Urban grid. The new applied methodology shows significant improvement for dispersion modelling of major traffic sources in Sofia city.

Key words: *Traffic, Emissions Inventory and scenarios, Dispersion modelling, Urban planning.*

INTRODUCTION

The inhabitants of the big Bulgarian cities, including the capital Sofia, are unfortunately still exposed to high levels of particulate matter (PM) despite a lot of efforts made by the government and municipality during the last decades. According to the European Environmental Agency (EEA, 2021) air pollution continued to drive a significant burden of premature death and disease in the EU member states in 2019, and the main pollutants driving this burden were particulate matter $PM_{2.5}$ (PM with diameter less than 2.5µm), nitrogen dioxide (NO_2) and ground level ozone (O_3). Road traffic is a significant contributor of NO_2 and PM emissions.

Despite some deficits of the local Gaussian type models for air quality studies, the potential of describing emissions and physical environment with fine resolution makes them very useful tool. The spatial depiction of regional air quality models due to the restriction of their spatial resolution, underestimate pollution (Georgieva et al., 2014; 2015), as they are unable to capture the high concentration gradients nearby roads with heavy traffic, and from other sources near the surface. Due to the described reason, the local models are more capable for elaboration of scenarios for the fleet in the context of implementation of measures and spatial development, as well as estimations of the exposure on the basis of model of activities and human presence. Depending on the methods, data and spatial scope applied, various modeling (Dimitrova and Velizarova, 2021) and apportionment measurement (Almeida et al., 2020) studies have shown different results for the contribution from the domestic heating, transportation and other sources in Sofia city. A

previous study for the area of Sofia city (Dimitrova and Velisarova, 2021) shows significant contrubution of transport to the concentration of PM, but some uncertainties were pointed mainly related to the emision inventory and meteorological conditions afected by lack of data and measurments of key variables esential for the model input.

Several generations of official dispersion modelling efforts for Sofia were based on first tier inventories of the traffic emissions. They are not based on actual transport model and rely on very rough estimates (EAZZ, 2019). Thus, bias is unavoidable when there are many data and knowledge gaps and lack of cross validation or shared baselines used to check the different modeling instances. The mixture of air pollution sources in Sofia leads to high seasonal concentration and numerous exceedances of the limits throughout the last decade. After the closure of the major industrial polluters, debates were provoced on which sources of pollution continued to contribute to exceedances, where to start in terms of regulation and investment in order to comply, hopefully after considering the results of more reliable and focused research.

The main goal of the present work is to apply newly developed emision inventory for high resolution dispersion modelling of major traffic sources for Sofia city. Numerical experiments were conducted using the local scale Air Quality Management & Assessment System: ADMS-Urban (CERC, 2020), coupled with a regional Weather Research and Forecasting: WRF model (Skamarock et al., 2008). This study presents a step towards a more comprehensive investigation of pollution patterns and impacts in the city of Sofia. It is linked to several experiments and future steps in development, which are expected to provide better insights at the cross point between air pollution modeling, epidemiology and urban planning scenarios.

METHODS AND INPUT DATA

The methodology used in this study includes high resolution air quality dispersion modelling (with 100 m resolution) for the area of Sofia city. The specific emission scenarios for the road transportation are calculated through the Comprehensive Emissions Inventory Toolkit (EMIT) developed by the Cambridge Environmental Research Consultants (CERC). EMIT relies on both fleet composition changes and urban plan provisions. Meteorological conditions are provided by the regional WRF model.

Transport emissions inventory and scenarios

The emission inventories, including for Sofia, are often calculated on the basis of indirect arguments, using a linear first-line method with emission factors providing averaged emissions for the year. We developed a new methodology for a traffic emission inventory in Sofia city, applying more sophisticated methods and tools. The methods include a wide array of data gathering and processing as well as alternative traffic mapping and modelling steps and techniques. The traffic distribution model takes into account diverse characteristics of the street network and the spatial development of Sofia. The utilized traffic data from various sources is scarse and has poor integrity. This invoked the necessity of a combination of processing, analysis and modelling techniques, among them interpolation and machine learning in order to obtain a relatively good estimate of the average annual daily traffic for the entire city street and road network.

One of the biggest challenges at the base is the quality of the underlying traffic and fleet data. It comes from various sources with poor access to the more complete sets, no integrity and many methodological mismatches in the data gathering approaches. There are rich data sets made available through the open data access from a municipal enterprise (Sofiaplan, 2022). With the help of own data mining and gathering to fill the gaps, and also various processing steps for matching of diverse geometry, attribute data and methods, the research tries to bridge the available resources.

As key input for traffic modeling we use data for major boulevards and junctions, various types of streets in Sofia from several sources at our disposal: measurements provided by the municipality and its planning enterprise from single days in 2017 and 2018 for almost 40 junctions, car count geolocation sample along the street network for the entire 2018 and 2019 (part of the street network) (TT TS, 2020, 2021); previous and next traffic count campaigns from consultancies (SO, 2022) covering sets of primary or secondary streets; and the Open Transport Model (OTM, 2022). For the visualization and analysis of the available data we use both QGIS tools and Python modules. Due to the low resolution of reliable data, we use machine learning algorithms, namely Random Forest and Extreme Gradient Boost (XGBoost) regressors, which

have proven well suited for such tasks (Joharestani et al, 2019). In order to avoid overfitting, we divide the city traffic network into clusters and uptate the parameters used in our models for each consecutive phase of data imputation, thus improving greatly the accuracy of predictions.

The results from the search of factors and algorithms that can support a reliable rapid traffic modeling with the use of available data with poor integrity have led to many experiments and intermediate results. Up to this point for the case of Sofia we have reached a satisfactory solution which seems to be promising for answering similar tasks elsewhere when trying to overcome data related obstacles.

The ratio of motorcycles, light and heavy vehicles is estimated by point data from historical counts and is interpolated class by class which is especially relevant for the heavy traffic on the primary transit roads and boulevards versus the minor roads. The additional input data for the elevation, width, canyon height, surface and gradient needed for EMIT is produced in QGIS thanks to available attributes, layers from publicly accessible open or free data and own processing and editing. The calculations in EMIT are returned to QGIS via shp and dbf files. One examle is shown for the $PM_{2.5}$ (a) and PM_{10} (b) emissions (Fig. 1).

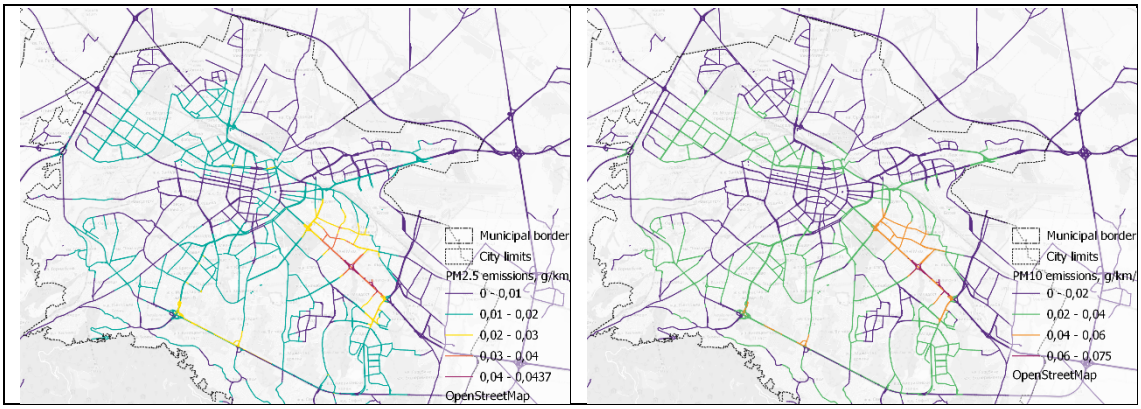

Figure 105. Amount of $PM_{2.5}$ (a) and PM_{10} (b) emissions along the primary network (g/km/s)

The fleet baseline inventory steps on one dimensional fleet stratification available as input data, distributed by general vehicle typology, type of fuel, engine size, EURO category, year of production and availability of filters (SO, 2017; MI, 2017). This available data is then juxtaposed through an Analytical Hierarchical Process to the EMIT most complete and differentiated database with the help of Excel for intermediate calculations. Thus the matching is performed with minimum expected deviation due to the association and uncertain distribution for some sub-categories. The NAEI2014 Urban 2014 version 2 is used as the closest possible database to the emission performance of the fleet in Sofia and Bulgaria at the baseline year of 2018. The rich subdivision of the fleet types allows for detailed elaboration of various scenarios for the years 2022, 2026 and 2030. The predefined general assumptions are reflected into the fleet composition changes, especially the shifts in the ratio of EURO standard and cleaning technology types.

Meteorological input

The Advanced Research version of the regional modeling system ARW-WRFv. 3.9.1 provids the nesasary metorological conditions. Three nested domains based on a Lambert projection were used with resolution of 9, 3 and 1 km. The model was implemented with 50 pressure-based terrain-following vertical levels from the surface to 50 hPa. The initial and boundary conditions were derived from the fifth generation ECMWF reanalysis for the global climate ERA5 datasets (https://cds.climate.copernicus.eu) available every 1 hour. Meteorological data for the entaire baseline year (2018) were used for the dispersion modelling. WRF can provide sufficient information for meteorological conditions at the exact location, where in-situ measurements are missing. The model output delivers additional meteorological parameters like planetary boundary layer height, sensible surface heat flux, solar radiation and precipitation. These additional variables significantly improve the description of the meteorological conditions, ensuring better air quality results. Special tool WRF to Met utility (CERC 2016) derived the meteorological conditions in the required format from the grid cells corresponding to the local area for ADMS-Urban model.

DISPERSION MODELING

The numerical simulations with high resolution (100 m) were conducted by the ADMS-Urban system supported by CERC. The urban morphology and surface modelling were provided using the Street Canyon Tool implemented in ArcMap environment as well as the UMEP plugin and other native tools in QGIS. In order to describe the road sources more accurately, the Advanced Street Canyon module option was used in network mode. This module can calculate the channeling of flow along a street, can represent asymmetric canyons and the effect of pavements within the canyon, and can model the effect of a street canyon on the surrounding area. Additional input data for building height, distance from the road centerline to the canyon wall and length of buildings adjacent to the road for each side of it were procesed and implemented.

The complex terrain was taken into account by 3D flow and turbulence field which modifies the plume trajectory and its dispersion, in order to account for the disturbances in the air flow, originating from the topography of the area (CERC, 2020). The USGS/NASA Shuttle Radar Topography Mission (SRTM; http://srtm.csi.cgiar.org) elevation data was used. The missing data was filled in, by the interpolation methods described in Reuter et al. (2007). Due to lack of data, the surface roughness length is considered as a constant number – 1.5 m, which is based on land use (large urban areas). Dry and wet deposition are also applied. The dry deposition velocity is calculated, using two components – diffusive part, due to turbulent processes and terminal velocity of a particle, due to gravitational settling in the plume (CERC, 2020).

The model results were validated at different points using measurements on montly base. Greenpeace volunteers, with help from the organization Deutsche Umwelthilfe, have installed and assembled small diffusion tubes containing a chemical substance (triethanolamine), which is absorbing the measuring component (NO_2). After measuring 30-31 days, the tubes were sent to the Passam AG Laboratory in Switzerland to provide results. The efect of low emission zones (LEZ) for 2026 and 2030 years were investigated using four specific cases representing restriction on entry into this zone for vehicles of different categories:

- Case 2026 with unaffected traffic (the same as for baseline 2018 scenario)
- Case 2026 with reduced traffic of 20%
- Case 2030 with unaffected traffic (the same as for baseline 2018 scenario)
- Case 2030 with reduced traffic of 20%.

More details on the specific methods and tools that have been applied to the development of the transport emission inventory scenarios can be find in paper of Burov and Brezov (2022). One example of the effect of LEZ using different scenarios on the pollution patern is shown (Table 1). The measured monthly mean concentration was 57.50 μg/m³ at the site G. S. Rakovski str. №193 for January 2018.

Table 32. Monthly mean NO_2 concentration at the measurement site G. S. Rakovski str. №193 (at 2.5 m height) compared for differant scenarious

Scenario	NO_2 μg/m³
Case 2018 Baseline	61.52
Case 2026 - unaffected traffic	56.99
Case 2026 - 20% reduced traffic	53.39
Case 2030 - unaffected traffic	47.49
Case 2030 – 20%reduced traffic	44.49

CONCLUSIONS

The attempt to construct and develop an integrative air pollution methodology is a challenging endeavor and the experience from the undertaken steps in this research points to the need for more supportive policies – scientific, environmental, health and urban related. Nevertheless, the approach provides first fruitful results which can be improved in many ways for the sake of truth and utmost possible proximity to real life flows and impacts from transport emissions. The rapid traffic modelling and emission inventory can become more and more precise through classical four-step transport modeling combined with activity based, machine learning, artificial intelligence, real-time, agent based, etc. approaches developed by the

public sector and academic, business and civic partners. The access to data and information is a constraint at the doorstep. Data warehouses, fleet censuses, and free spatial extents query above the confidential or personal information minimums can be truly beneficial for acceleration of the experiments and policy tests. Improvement in dispersion modelling of major traffic sources will support the management and planning of a healthy urban environment and lifestyle in Sofia city. The new applied methodology shows significant improvement for dispersion modelling of major traffic sources in Sofia city.

AKNOWLEDGMENTS

This work has been carried out in the framework of the grant № КП-06-Н54-2/15.11.2021 supported by the Research Fund at the Bulgarian Ministry of Education and Science. We acknowledge the provided access to the e-infrastructure of the NCDSC - part of the Bulgarian National Roadmap on RIs, with the financial support by the Grant № D01-221/03.12.2018.

REFERENCES

Almeida, S.M., M. Manousakas, E. Diapouli, Z. Kertesz at al., 2020: Ambient particulate matter source apportionment using receptor modelling in European and Central Asia urban areas, *Environmental Pollution*, **266** (3), 115199.

Burov, A. and D. Brezov, 2022: Transport Emissions from Sofia's Streets - Inventory, Scenarios, and Exposure Setting, *Studies in Systems, Decision and Control* – under review.

CERC, 2015: Atmospheric EMissions Inventory Toolkit user guide version 3.4.

CERC, 2016: WRF to Met utility, Version 1.4.

CERC, 2020: Urban Air Quality Management System Version 5.0.

Council of Ministers of the Republic of Bulgaria (CMRB), 2019: National Programme for Atmospheric Air Quality Improvement, (in Bugarian), https://www.moew.government.bg/static/media/ups/tiny/Air_new/Natzionalna_programa_podobriavane_KAV_2018-2024.pdf.

Dimitrova R. and M. Velizarova, 2021: Assessment of the Contribution of Different Particulate Matter Sources on Pollution in Sofia City, *Atmosphere*, **12**(4), 423, doi:10.3390/atmos12040423.

Environmental Association Za Zemyata (EAZZ), 2019: Transportation and Air Pollution in Sofia (in Bulgarian). https://www.zazemiata.org/wp-content/uploads/2019/03/Transport.pdf.

European Comission Joint Research Center (ECJRC), 2022: FAIRMODE, https://fairmode.jrc.ec.europa.eu/.

European Environmental Agency, 2021: Report N°15/2021, Air quality in Europe 2021, doi: 10.2800/549289.

Georgieva, E., D. Syrakov, M.Prodanova, I. Etropolska, K. Slavov, 2014: Evaluating the performance of WRF-CMAQ models in Bulgaria by means of the delta tool. *In Proceedings of the HARMO16*, Varna, Bulgaria, 8–11 September 2014, 304–308.

Georgieva, E., D. Syrakov, M.Prodanova, I. Etropolska, K. Slavov, 2015: Evaluating the performance of WRF-CMAQ air quality modelling system in Bulgaria by means of the DELTA tool, *Int. J. Environ. Pollut*., **57**.

Ministry of Interior (MI), 2017: 328600-72587 from 01.12.2017 (in Bulgarian). Unpublished dataset.

OTM, 2022: Open Transport Map, https://opentransportmap.info/.

Skamarock, W.C., J.B. Klemp, J. Dudhia, D.O. Gill, D.M. Barker, M.G Duda, X.-Y. Huang, W.Wang, and J. G. Powers, 2008: A Description of the Advanced Research WRF Version 3. NCAR Tech. Note NCAR/TN-475+STR, 113 pp.

Sofiaplan, 2022: Open Data (in Bulgarian), https://sofiaplan.bg/api/.

Stolichna Obshtina (SO), 2017: COA17-BK66-4393 from 28.06.2017 (in Bulgarian), Unpublished dataset.

Stolichna Obshtina (SO), 2022: Factor Noise (in Bulgarian), https://www.sofia.bg/components-environment-noise.

TomTom Traffic Stats (TT TS), 2020: Traffic Density. Ranges: Sofia. Calendar period from 2019-01-01 to 2019-12-31.

TomTom Traffic Stats (TT TS), 2021: Traffic Density. Ranges: Sofia. Calendar period from 2018-01-01 to 2018-12-31.

Joharestani, Z. M., C. Cao, X. Ni, B. Bashir, and S. Talebiesfandarani, 2019: PM2.5 Prediction Based on Random Forest, XGBoost, and Deep Learning Using Multisource Remote Sensing Data, *Atmosphere*, **10**(7), 373, doi:10.3390/atmos10070373.

21st International Conference on
Harmonisation within Atmospheric Dispersion Modelling for Regulatory Purposes
27-30 September 2022, Aveiro, Portugal

TRACER GAS EXPERIMENT OF URBAN POLLUTANT TRANSPORT: URBAN CANYONS AND INDOOR-OUTDOOR TRANSPORT

Michael D. Sohn[1], Marion L. Russell[1], William W. Delp[1], David M. Lorenzetti[1], and Richard N. Fry2

[1]Lawrence Berkeley National Laboratory, Berkeley, California, USA
[2]Defense Threat Reduction Agency, Fort Belvoir, Virginia, USA

Abstract: There is growing concern that a pollutant release in a building could cause adverse health effects, both to indoor occupants, and later to people outdoors as the pollutant leaves the building. Unfortunately, few tracer experiments exist that examine such a scenario, making it difficult to assess the suitability of transport and dispersion models for first-response decision making. We present results of an environmental tracer study consisting of five inert tracers released simultaneously on a university campus in Singapore in March 2022. Tracers were released to simulate the transport of an urban pollutant between buildings, into buildings, and from indoors to outdoors. We also measured meteorological conditions throughout the five-day, five-release, trial, using a combination of Lidar and other sensors. We deployed forty bag samplers and four Miran real-time analyzers to measure tracer concentrations in three buildings and throughout the campus. Most campus buildings were concentrated together and more than seven floors in height. In this presentation, we describe the study, model-to-measurement predictions, and collaboration opportunities to study the experimental data. Preliminary model predictions, both Gaussian-puff and CFD, show promising results. We also show that pollutants entering buildings through HVAC systems can later exhaust at appreciable concentrations. We discuss the implications of such results for first responders.

Key words: *Verification, validation, infiltration, buildings, CONTAM, CFD.*

Figure 1. Illustration of the site. Five field trials were conducted. Each trial released five tracer gases simultaneously, three outdoors and two indoors (colored buildings). Concentration over time was recorded at 40 locations, 15 indoors and 25 outdoors. Local and regional meteorological conditions were recorded throughout the trials.

Assessment of the dispersive capacity of neighbourhoods based on Local Climate Zones classification

Andrés Simón-Moral[1*], Alberto Martilli[2], Ales Padró[1], Lexuri Yurrebaso[1]

TECNALIA, Basque Research and Technology Alliance (BRTA), Derio, Spain
Research Center for Energy, Environment and Technology, CIEMAT, Madrid, Spain

NO_x dispersion simulations of summer and winter periods were performed with the Weather Research and Forecasting model (WRF) coupled with an urban canopy scheme (BEP) in Vitoria-Gasteiz, a small size city in the north of the Iberian peninsula. Road traffic, residential heating and industries registered under the European Pollutant Release and Transfer Register (E-PRTR) regulation were considered as emission sources and NO_x was treated as an inert gas, with no deposition. Comparison with observations across three urban air quality stations shows that the model is able to reproduce time and space variability, showing no trend in the deviations. NO_x is normalized by the emission in each grid cell in order to represent the dispersion capacity of the urban canyons and results are analysed for different season and wind speed, based on the Local Climate Zone classification (LCZ). The dispersive capacity is found to be influenced by meteorological conditions and urban morphology. First, more NO_x is trapped within the urban canyon in stable conditions (winter) and under calm winds. Second, LCZs are found to disperse differently, with LCZ 2 and 3 showing higher normalized concentration values than the rest. While relative differences among LCZs are coherent between seasons and wind conditions, absolute values differ. This study shows the potential of the LCZ classification for air quality management, providing a fast screening method for cities, in order to prioritize the areas to be improved from the air pollution perspective.

21st International Conference on
Harmonisation within Atmospheric Dispersion Modelling for Regulatory Purposes
27-30 September 2022, Aveiro, Portugal

URBAN ENVIRONMENTS AND REGIONAL CLIMATE CHANGE - CORDEX FLAGSHIP PILOT STUDY URB-RCC

Tomas Halenka, Gaby Langendijk

SHORT ABSTRACT

Abstract title: URBAN ENVIRONMENTS AND REGIONAL CLIMATE CHANGE - CORDEX FLAGSHIP PILOT STUDY URB-RCC

Name and Affiliation of the First Author: Tomas Halenka, Charles University, Dept. of Atmospheric Physics, Prague, Czech Republic

Email of first author: tomas.halenka@mff.cuni.cz

Names and Affiliations of the Co-authors: Gaby Langendijk, German Climate Service Center, The Helmholtz-Zentrum Hereon, Hamburg, Germany

Abstract text *(maximum 350 words.)*

Cities play a fundamental role on climate at local to regional scales through modification of heat and moisture fluxes, as well as affecting local atmospheric chemistry and composition, alongside air-pollution dispersion. Vice versa, regional climate change impacts urban areas and is expected to increasingly affect cities and their citizens in the upcoming decades. Simultaneously, the share of the population living in urban areas is growing, and is projected to reach about 70 % of the world population up to 2050. This is especially critical in connection to extreme events, for instance heat waves with extremely high temperatures exacerbated by the urban heat island effect, in particular during night-time, with significant consequences for human health. Additionally, from the perspective of recent regional climate model developments with increasing resolution down to the city scale, proper parameterization of urban processes is starting to play an important role to understand local/regional climate change. This is valid for coupled atmospheric chemistry as well, thus even air pollution modelling has to consider the urban environment. The inclusion of the individual urban processes affecting energy balance and transport (i.e. heat, humidity, momentum fluxes, emissions) via special urban land-surface interaction parameterization of distinct local processes becomes vital to simulate the urban effects properly. This will enable improved assessment of climate change impacts in the cities and inform adaptation and/or mitigation options by urban decision-makers, as well as adequately prepare for climate related risks (e.g. heat waves, smog conditions etc.). Cities are becoming one of the most vulnerable environments under

climate change. In 2013, the CORDEX community identified cities to be a prime scientific challenge. Therefore, we proposed this topic to become an activity at CORDEX platform, within the framework of so-called flagship pilot studies, which was accepted and the FPS URB-RCC activity was started in May 2021. Main aims and planning of this activity will be presented together with a call for potential participation in some experiments following adopted coordinated simulations protocol.

21st International Conference on
Harmonisation within Atmospheric Dispersion Modelling for Regulatory Purposes
27-30 September 2022, Aveiro, Portugal

POST-PROCESSING TOOLS FOR CORRECTING URBAN AIR QUALITY FORECAST MAPS

Jan Mateu Armengol, A.Criado, H. Petetin, M. Olid, J. Benavides, D.Rodriguez-Rey, M. Guevara, C. Pérez García-Pando, A. Soret, O. Jorba

SHORT ABSTRACT

Post-processing tools for correcting urban air quality forecast maps

Jan Mateu Armengol

Barcelona Supercomputing Center

jan.mateu@bsc.es

Names and Affiliations of the Co-authors: A.Criado[1], H. Petetin[1], M. Olid[1], J. Benavides[2], D. Rodriguez-Rey[1], M. Guevara[1], C. Pérez García-Pando[1,3], A. Soret[1] O. Jorba[1],

[1]Barcelona Supercomputing Center, BSC-CNS, Barcelona 08034, Spain

[2]Catalan Institution for Research and Advanced Studies, ICREA, Barcelona 08010, Spain

[3]Department of Environmental Health Sciences, Columbia University, NY 10032, USA.

Abstract

Forecasts of air quality at the street scale are extremely challenging due to both the scarceness of near-real-time observations at these scales and the strong uncertainties affecting urban models. We present a flexible post-processing methodology, that can be applied to any urban air quality model, to systematically bias adjust hourly forecast maps. Thus, correcting forecasts at monitoring stations, where large historical observational data are available, and extending such corrections to the rest of the map taking into account high-resolution spatial distributions based on experimental dosimeter campaigns. We use Universal Kriging to optimally combine hourly results of the Kalman Filter correction method applied independently at each monitoring site with a non-linear land use regression model. The capabilities of this novel methodology are assessed by cross-validating NO2 forecasts during 2019, 2020 and 2021 over the city of Barcelona, Spain, using the dispersion model CALIOPE-Urban. The sensitivity to the lead time is studied comparing 24h and 48h forecasts in 2021. The importance of this methodology is highlighted by the inter-annual variably of NO2 patterns due to the COVID-19 pandemic. We show how post-processing techniques, including machine learning and geostatistical models, are a key component of the modelling chain to obtain reliable air quality forecast maps at the street scale.

21st International Conference on
Harmonisation within Atmospheric Dispersion Modelling for Regulatory Purposes
27-30 September 2022, Aveiro, Portugal

MODELLING OF THE HORIZONTAL AIR POLLUTION GRADIENTS INSIDE A STREET CANYON USING NEW FEATURES IN THE OSPM MODEL

Matthias Ketzel, Ahmet Mustafa Tepe

SHORT ABSTRACT

Abstract title: Modelling of the horizontal air pollution gradients inside a street canyon using new features in the OSPM model.

Name and Affiliation of the First Author: Matthias Ketzel (1,2)

Email of first author: mke@envs.au.dk

Names and Affiliations of the Co-authors: Ahmet Mustafa Tepe (3,1)

(1) Aarhus University, Department of Environmental Science, Roskilde, Denmark
(2) Global Centre for Clean Air Research (GCARE), University of Surrey, Guildford, U. K.
(3) Akdeniz University, Department of Environmental Engineering, Antalya, Turkey.

Abstract text

This study investigates in details the pollution situation near one of Denmark's NO2 hot-spots, the monitoring station at H.C. Andersens Boulevard (HCAB) in Copenhagen. The investigations cover various elements as detailed traffic counts in each of the 7 traffic lanes; wind speed measurements both at a nearby roof station and inside the street canyon and measurements at different locations in the street additional to the main monitoring station.

A further development is presented for the Operational Street Pollution Model (OSPM) that allows handling the inhomogeneous distribution of the emissions over the various lanes and the positioning of the receptor location further away from the buildings. Model results are compared to long-term measurements at HCAB where the layout of the traffic lanes and the position of the monitoring station have been variable. The updated and extended OSPM is showing improved agreement compared to the standard version.

The presentation will give an overview of the study and show the main results and conclusions derived from this comprehensive project.~

21st International Conference on
Harmonisation within Atmospheric Dispersion Modelling for Regulatory Purposes
27-30 September 2022, Aveiro, Portugal

RANKING OF VARIOUS SINGLE AND COMBINATIONS OF LOCAL AIR POLLUTION MITIGATION MEASURES IN AN URBAN ENVIRONMENT

Jose-Luis Santiago, Esther Rivas, Beatriz Sanchez, Riccardo Buccolieri, Alberto Martilli, Marta G. Vivanco, Antonio Esposito, Fernando Martín

SHORT ABSTRACT

Abstract title: Ranking of various single and combinations of local air pollution mitigation measures in an urban environment

Name and Affiliation of the First Author: Jose-Luis Santiago[1]

[1]Atmospheric Modelling Unit, CIEMAT, Av. Complutense, 40, 28040 Madrid, Spain

Email of first author: jl.santiago@ciemat.es

Names and Affiliations of the Co-authors: Esther Rivas[1], Beatriz Sanchez[2], Riccardo Buccolieri[3], Alberto Martilli[1], Marta G. Vivanco[1], Antonio Esposito[3], Fernando Martín[1]

[1] Atmospheric Modelling Unit, CIEMAT, Av. Complutense, 40, 28040 Madrid, Spain.

[2] Department of Geography, National University of Singapore, Singapore.

[3] Dipartimento di Scienze e Tecnologie Biologiche ed Ambientali, University of Salento, Lecce, Italy.

Abstract text *(maximum 350 words.)*

Nowadays, urban air quality is considered one of the most important environmental challenges and different local mitigation strategies have been developed for improving urban air quality. These strategies are usually based on measures of pollutant emission reduction (e.g., traffic low emission zones-LEZ) and on passive mitigation measures (e.g., green infrastructure-GI, photocatalytic materials). Usually, the effectiveness of these strategies is studied for each measure independently and in different urban environments. In this context, the objective of the present study is the assessment of the impact of different measures on pollutant concentrations in the same urban environment, and combining LEZ with GI to improve the effectiveness of the measures. The urban environment is composed by an array of 7 x 7 buildings, and the height of buildings and the width of the streets are 35 m. The strategies investigated are:

- LEZ; a LEZ in the central area of the domain is studied. Traffic is reduced in some streets allowing circulation of vehicles only in certain streets around this zone. Three emission scenarios are considered with an emission reduction of 80% in the interior of LEZ and possible increases of traffic in the streets that surround the LEZ;

- street vegetation; different types of GI composed by different combinations of street trees and hedgerows in the sidewalks and central-reservations are implemented in the central area of the neighborhood;
- photocatalytic materials; these materials are a sink of NOx in presence of solar radiation, and are applied to sidewalks and building walls in the central area of the domain;
- combination of LEZ and GI in the street.

All scenarios have been simulated for different wind directions using CFD modelling. Results show that the larger improvement of urban air quality with individual measures is obtained by LEZ. However, unintended effects leading to an increase of concentration in the streets around LEZ can appear when a large part of traffic is diverted by those areas. In addition, the combination of LEZ and GI increases the effectiveness of the individual measures due to the greening reduces the entrance of pollutants emitted outside of LEZ to the central area of the domain.

21st International Conference on
Harmonisation within Atmospheric Dispersion Modelling for Regulatory Purposes
27-30 September 2022, Aveiro, Portugal

IMPACT OF GREEN INFRASTRUCTURE ON TRAFFIC-RELATED POLLUTANT CONCENTRATION IN HIGH-RISE URBAN AREAS

Jose-Luis Santiago, Esther Rivas, Beatriz Sanchez, Riccardo Buccolieri, Oliver S. Carlo, Alberto Martilli, Marta G. Vivanco, Fernando Martín

SHORT ABSTRACT

Abstract title: Impact of green infrastructure on traffic-related pollutant concentration in high-rise urban areas

Name and Affiliation of the First Author: Jose-Luis Santiago[1]

[1]Atmospheric Modelling Unit, CIEMAT, Av. Complutense, 40, 28040 Madrid, Spain

Email of first author: jl.santiago@ciemat.es

Names and Affiliations of the Co-authors: Esther Rivas[1], Beatriz Sanchez[2], Riccardo Buccolieri[3], Oliver S. Carlo[3], Alberto Martilli[1], Marta G. Vivanco[1], Fernando Martín[1]

[1] Atmospheric Modelling Unit, CIEMAT, Av. Complutense, 40, 28040 Madrid, Spain.
[2] Department of Geography, National University of Singapore, Singapore.
[3] Dipartimento di Scienze e Tecnologie Biologiche ed Ambientali, University of Salento, Lecce, Italy.

Abstract text *(maximum 350 words.)*

Air quality is an important problem in many cities, especially in urban canyons, mainly due to high traffic emissions and the reduced ventilation of streets. Green infrastructure (GI) is being explored as measure to control urban air pollution. Urban greening (and in particular trees) affects air quality in two ways:

- Aerodynamic effects: wind flow within streets is modified by trees, reducing in most of cases the ventilation of the street.
- Deposition effects: a fraction of pollutants is removed from air by means of deposition to tree leaves

Previous studies show the net impact of GI may increase or decrease pollutant concentrations at pedestrian level depending on several factors (e.g., configuration of green infrastructure, urban morphology, location of pollutant emissions, etc). In this context, the present study aims to investigate the effect of GI within an urban area on traffic-related pollutant concentration. The urban environment is composed by an array of 7 x 7 buildings, and the height of buildings and the width of the streets are 35 m. Traffic emission are considered in the entire neighborhood and different types of GI composed by different combinations of street trees and hedgerows in the sidewalks and central-

reservations are implemented in the central area of the neighborhood and simulated by means of RANS CFD modelling for different wind directions. Pollutant dispersion emitted by traffic obtained for this wide set of vegetation scenarios allow to determine:

- the optimal configuration of GI to improve the air quality in the streets;
- the contribution of each element (location of trees and hedgerows and tree height) to the net effect of GI;
- the relative contribution of deposition and aerodynamic effects on pollutant concentrations depending on pollutant deposition velocity.

These results are useful for the design of GI in order to be an effective measure for air pollution mitigation.

21st International Conference on
Harmonisation within Atmospheric Dispersion Modelling for Regulatory Purposes
27-30 September 2022, Aveiro, Portugal

MODELLING AND ASSESSMENT OF THE EFFECTS OF OBSTACLES IN URBAN CANYONS

Oliver Savio Carlo, Riccardo Buccolieri, Esther Rivas, Jose L. Santiago, Pietro Salizzoni, Antonio Esposito, M. Salman Siddiqui

SHORT ABSTRACT

Abstract title: ***Modelling and assessment of the effects of obstacles in urban canyons*** *Name and Affiliation of the First Author:* ***Oliver S. Carlo*** [1]
Email of first author: ***oliver.carlo@unisalento.it***

Names and Affiliations of the Co-authors: ***Riccardo Buccolieri*** [1]***, Esther Rivas*** [2]***, Jose L. Santiago*** [2]***, Pietro Salizzoni*** [3]***, Antonio Esposito*** [1]***, M. Salman Siddiqui*** [4]

1. Dipartimento di Scienze e Tecnologie Biologiche ed Ambientali, University of Salento, 73100 Lecce, Italy 2. Atmospheric Pollution Division, Environmental Department, CIEMAT, Spain
3. Univ Lyon, Ecole Centrale de Lyon, CNRS, Univ Claude Bernard Lyon 1, INSA Lyon, LMFA, UMR5509, 69130, Ecully, France
4. Faculty of Science and Technology, Norwegian University of Life Sciences, Ås, Norway Corresponding author: O.S. Carlo

Abstract text *(maximum 350 words.)*

Local wind flow within urban canyons plays a decisive role in the dispersion of traffic related pollutants and mitigation of its associated risks for human health. To this end, many recent studies(Gallagher *et al.*, 2015; Li, Ming, *et al.*, 2021; Buccolieri *et al.*, 2022) point towards the potential of passive local strategies such as barriers/obstacles (e.g., trees, hedges, parked cars, low boundary walls, roadside barriers, etc.). Studiesregarding obstacles suggest the potential to alter source-receptor pathways between pollutants generated on the road and the pedestrians on sidewalks, and also higher potential for pollutant dilution within the street canyon itself (and even lateral entrainment) (Li, Ming, *et al.*, 2021; Li, Zhang, *et al.*, 2021). This potential is usually studied through Computational Fluid Dynamics (CFD) models, validated with field and wind tunnel experiments.

Yet many gaps remain; very few CFD studies have been done for obstacles such as Low Boundary Walls (LBWs), parked cars and hedges (Buccolieri *et al.*, 2022), and even fewer studies have been done to test the effect of a combination of barriers (e.g., parked cars with LBWs) on the net effect of pollutant dispersion within the canyon. Accurately modelling the effects of each type of obstacle (or a combination) on air pollutant concentration patterns is important to determine hotspots within the urban

canyon (Lauriks *et al.*, 2021) and reduce pedestrian exposure to atmospheric pollutants. The present work investigates the effects of urban obstacles on pollutant dispersion in streets. A novel CFD model will be developed to conduct a parametric study that can allow to explore flow behavior in urban street canyon in presence of LBWs, parked cars and trees. The work shall further explore how well the CFD model capture pollutant dispersion and make comparisons against the experimental data.

References

Buccolieri, R. *et al.* 2022. 'Obstacles influence on existing urban canyon ventilation and air pollutant concentration: A review of potential measures', Building and Environment, 214(February), 108905.

Gallagher, J. *et al.* 2015. 'Passive methods for improving air quality in the built environment: A review of porous and solid barriers', Atmospheric Environment, 120, 61–70.

Lauriks, T. *et al.* 2021. 'Application of Improved CFD Modeling for Prediction and Mitigation of Traffic-Related Air Pollution Hotspots in a Realistic Urban Street', Atmospheric Environment, 246, 118127.

Li, Z., Ming, T., *et al.* 2021. 'Review on pollutant dispersion in urban areas-part B: Local mitigation strategies, optimization framework, and evaluation theory', Building and Environment, 198(February), 107890.

Li, Z., Zhang, H., *et al.* 2021. 'The effects of lateral entrainment on pollutant dispersion inside a street canyon and the corresponding optimal urban design strategies', Building and Environment, 195(February), 107740.

21st International Conference on
Harmonisation within Atmospheric Dispersion Modelling for Regulatory Purposes
27-30 September 2022, Aveiro, Portugal

DEVELOPMENT OF A NEW LAGRANGIAN AIR POLLUTION MODEL FOR DENMARK

Christopher Andersen, Matthias Ketzel, Ole Hertel, Jesper H. Christensen, and Jørgen Brandt

SHORT ABSTRACT

Abstract title: Development of a New Lagrangian Air Pollution Model for Denmark *Name and Affiliation of the First Author*: Christopher Andersen (1)
Email of first author: chan@envs.au.dk

Names and Affiliations of the Co-authors: Matthias Ketzel (1), Ole Hertel (2), Jesper H. Chris tensen (1), and Jørgen Brandt (1)

(1) Aarhus University, Department of Environmental Science, Roskilde, Denmark (2) Aarhus University, Department of Ecoscience, Roskilde, Denmark

Abstract text *(maximum 350 words.)*

The *Urban Background Model Lagrange* (UBML) is a 3D air pollution model being developed at the Department of Environmental Science, Aarhus University, to more accurately predict the local scale concentration of air pollutants in Denmark. We presuppose that UBML will perform better than its predecessor *Urban Background Model* (UBM, www.au.dk/UBM) when validated against measurements from the Danish monitoring network since it applies much more compre
hensive and realistic descriptions of the atmosphere.

The Lagrangian nature of UBML makes it possible to more accurately describe atmospheric transport and dispersion close to emission sources. The transport and dispersion are modelled by computing particle trajectories, governed by the local mean wind and a random motion, mimick ing dispersion, described by *Lagrangian stochastic* (LS) schemes. These particles (representing ensembles of fluid particles) are released from point, line, and area emission sources. Since the particle trajectories are computed independently, the model is in principle ideal to parallelize. Based on a larger literature review, a set of LS schemes has been implemented in UBML along side various parameterizations of the *planetary boundary layer* (PBL); most importantly the tur bulent velocity variance, the local decorrelation timescale, and the PBL height. For the input data, existing UBM modules have been extended for loading and transforming 3D meteorology data from the *Weather Research and Forecasting* (WRF) model and 3D chemical boundary conditions from the *Danish Eulerian Hemisphere Model* (DEHM).

Numerical tests have been conducted to test and verify the implementation of the different mod ules of UBML. Further, the model has been validated against measurementsfor different chemical species (including NO_x, CO, $PM_{2.5}$, and PM_{10}) to investigate the performance of the model when applying different combinations of LS schemes and PBL parameterizations. Preliminary results show that the model performs well with respect to measurements, and also

performs as well or even better than UBM. Additional work will have to be carried out, including the development of deposition and chemistry schemes, to improve the performance of the model further. Expectantly, UBML can be integrated into the DEHM/UBM/AirGIS modelling system (www.au.dk/AirGIS) to significantly improve human air pollution exposure modelling to further advance health impact assessments.

21st International Conference on
Harmonisation within Atmospheric Dispersion Modelling for Regulatory Purposes
27-30 September 2022, Aveiro, Portugal

INFILTRATION OF BLACK CARBON PARTICLES FROM ROAD TRAFFIC INTO BUILDINGS BY NATURAL VENTILATION: A CASE STUDY

Esther Rivas, José Luís Santiago, Alberto Martilli, Fernando Martin, Elías Díaz, Francisco Javier Gómez, Begoña Artiñano, Carlos Román-Cascón, Carlos Yagüe, David de la Paz, Rafael Borge

SHORT ABSTRACT

Abstract title: **Infiltration of black carbon particles from road traffic into buildings by natural ventilation: a case study**

Name and Affiliation of the First Author: Esther Rivas-Ramos

Environmental Department, CIEMAT – Avenida Complutense 40, 28040, Madrid, Spain *Email of first author*: esther.rivas@ciemat.es
Names and Affiliations of the Co-authors: José Luís Santiago[1], Alberto Martilli[1], Fernando Martin[1], Elías Díaz[1], Francisco Javier Gómez[1], Begoña Artiñano[1], Carlos Román-Cascón[2], Carlos Yagüe[2], David de la Paz[3], Rafael Borge[3]

[1]Environmental Department, CIEMAT – Avenida Complutense 40, 28040, Madrid, Spain

[2]Departamento de Física de la Tierra y Astrofísica, UCM – Plaza Ciencias 1, 28040 Madrid, Spain

[3]Department of Chemical and Environmental Engineering, ETSII-UPM – Calle José Gutiérrez Abascal 2, 28006, Madrid, Spain

Abstract

Road traffic has been identified as one of the major sources of particulate matter in many cities and a significant threat to human health. It is expected that the main exposure occurs outdoor in wintertime under stable atmospheric conditions. However, people spend most of their time indoors and the questions about when, how much and how particulate matter from traffic affect indoor air quality remain open. This is related to the essential role of ventilation in buildings, for example, to reduce the spreading of airborne-transmitted diseases.

In this context, this work aims to simulate the transfer of pollutants from outside into a building room and vice versa by applying a CFD model considering a numerical domain covering not only the interior of a room but also the nearby urban environment (buildings and traffic emission sources). In addition, the modelled results are assessed using measured data from experimental campaigns developed in the framework of the AIRTEC-CM project in Madrid (Spain) that intends to improve our understanding of urban air quality dynamics and the exposure of citizens to air pollution.

As first step, the capability of the CFD model to accurately reproduce the time evolution of Black Carbon (BC) concentrations as tracer of traffic emissions, both inside and outside a hospital located in an air pollution hotspot in Madrid has been evaluated for a selected winter day. Then, the influence of meteorological conditions on the infiltration of BC particles from road traffic into buildings by natural ventilation has been investigated. It should be noted that the CFD model considers both the emissions from engine exhaust, as well as non-exhaust emissions including brakes and tyres wear as well as dust resuspension.

TOPIC 6:

USE OF MODELLING IN HEALTH AND EXPOSURE ASSESSMENTS

21st International Conference on
Harmonisation within Atmospheric Dispersion Modelling for Regulatory Purposes
27-30 September 2022, Aveiro, Portugal

PERSONAL EXPOSURE ASSESSMENT THROUGH MEASUREMENT AND MODELLING

Marie Dury[1], Florent Hozay[1] and Fabian Lenartz[1]

[1]Institut Scientifique de Service Public (ISSeP), Liège, Belgium

Abstract: Modelling is commonly used to evaluate population exposure to atmospheric pollution. It allows one to assess how many people reside in a zone where pollution levels are above a certain threshold but, to the extent of our knowledge, it does not take the indoor contribution into account. In this study, we propose to compare the cumulated personal exposure as measured by about 60 different persons in the city of Liège (Belgium) during one-week experiments in the years 2018-2020, and various modelling approaches. The measurements were carried out by the citizens with a set of portable devices including the Antilope sensor system developed at the Institut Scientifique de Service Public (ISSeP). The most complex modelling system used here consists of a three-component outdoor model, working at a hourly rate and a spatial resolution of about 10 m. It is combined to an infiltration model that aims at estimating the indoor concentrations based on the outdoor concentrations, some meteorological parameters and the building ventilation properties.

KEY WORDS: **POLLUTANT EXPOSURE, OUTDOOR/INDOOR CONCENTRATIONS, LOW-COST SENSOR, MODELLING, BLACK CARBON, $PM_{2.5}$**

INTRODUCTION

Because of their important population and pollutant emission sources, it is essential to monitor accurately pollutant concentrations and their evolution over time in urban environments and to develop reliable models of personal pollutant exposure. Yet, exposure to pollutants is usually evaluated using atmospheric pollutant concentrations with a low spatio-temporal frequency on the one hand, and, on the other hand, population density maps typically generated on the basis of residency information which do not reflect population movement over time. Intersecting such information to estimate population exposure implicitly makes the assumption that everybody lives outdoors, in front of one's door, whereas we spend in general more than 80% of our time indoors (Dons, 2013). In order to achieve more accurate and consistent estimates of exposure, it is therefore essential to develop high-frequency measurements (at 1-minute rate or faster) and to assess procedures that account for population dynamics and allow one to discriminate between indoor and outdoor exposure. In this context, a low-cost versatile air monitoring device, suitable for fixed and itinerant measurements, both indoor and outdoor, named Antilope, has been developed at the Institut Scientifique de Service Public (Lenartz *et al*., 2021; 2022). In the framework of OIE (Outdoor and Indoor Exposure) project, we aimed to improve the assessment of personal exposure combining real time itinerant measurements and outdoor/indoor modelling.

MATERIALS AND METHODS

Exposure measurement campaigns

For the mobile personal exposure campaign (2018-2020), subjects were provided with a set of portable devices (set at a 1-minute rate) for seven days: an Antilope low-cost sensor system with an optical sensor for the measurement of $PM_{2.5}$ and electrochemical sensors for the indication of nitrogen oxides (NO and NO_2) and ozone (O_3) approximate levels (Figure 1), a portable AethLabs AE51 aethalometer for the measurement of black carbon (BC) and a GlobalSat DG200 GPS to track the subject location. All the measurement equipment was placed in a backpack to easily shadow the subjects in their daily activities.

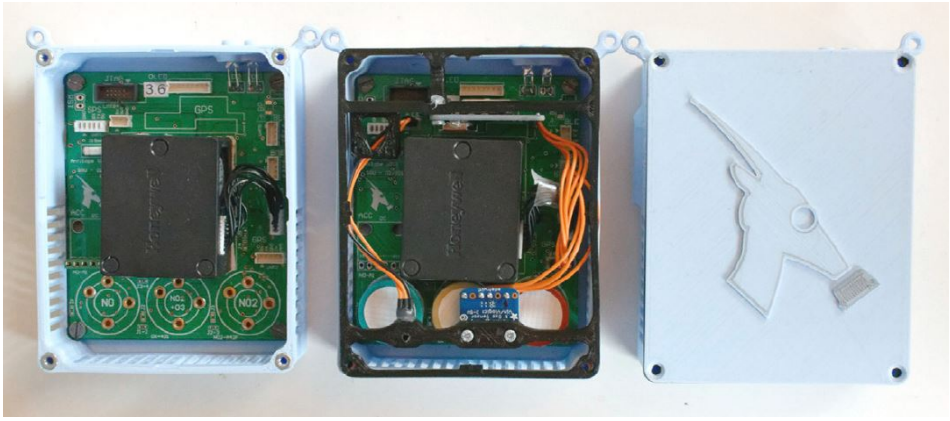

Figure 106. Enclosure of the Antilope (Lenartz *et al*., 2021).

At the beginning of their week campaign, subjects had to answer some questions about their profile (age, gender, professional status, *etc*.) and their health in general (allergy or asthma, frequency of physical activities, smoking exposure, *etc*.). They also had to describe their everyday environment through questions about their housing (heating type, ventilation, kitchen and floor equipment, *etc*.) and habits (most occupied rooms, vacuum frequency, *etc*.) as well as their place of work if relevant.

Every day during the week, participants had to fill in a journey logbook with all their activities. Each activity had to be characterized by a start time, an end time, a type (work, shopping, staying at home, cooking, sport, leisure, *etc*.) and an environment (indoor or outdoor). Travels are considered as an activity with an indoor/outdoor type according to the mode of transport (car, bus, train, walk, *etc*.). Every day, subjects also had to report any respiratory discomfort or crisis. Such information is very useful to evaluate exposure to air pollution according to activities and modes of transport as well as to corroborate some of the measurements such as the location provided by the GPS or the lack thereof.

Two measurement campaigns were also carried out in order to validate the indoor model. The first one took place in August and September 2017 in two different stores in Liège and the second in April and May 2021 in an apartment in Liège as well (Hozay, 2021).

Outdoor model

ATMO-Street (Lefebvre *et al*., 2013) simulates the dispersion of pollutants (PM_{10}, $PM_{2.5}$, BC and NO_2) from their main emission sources, *i.e*. large industries and the road network, taking meteorological conditions (temperature, wind direction/speed and solar radiation) into account. ATMO-Street was created by coupling the IFDM bi-gaussian dispersal model (Immission Frequency Distribution Model) with the OSPM (Operational Street Pollution Model). The pollutant concentrations are calculated at different receptor points of the studied territory and then interpolated to the whole area.

Regarding industry, only the most polluting industrial sources within the municipal perimeter are considered by the IFDM model, the impact of the industrial fabric as a whole being taken into account in the background concentrations. For the road network, polluting emissions are assigned to each road segment on the basis of the measured traffic. Each vehicle is assigned a COPERT emission factor

depending on its category (light or heavy vehicle, engine, Euro standard) and driving mode (urban, rural or motorway).

The model also takes the configuration of the streets into account. In the case of urban canyons, which are narrow streets with a high building height, the IFDM is replaced by the OSPM. The OSPM distinguishes between the direct contribution of traffic emissions and the contribution due to recirculation caused by the presence of vortices. Within these streets, poor dispersion and therefore local accumulation of pollutants is generally observed.

Model simulations were performed on the same period as the personal exposure campaign (2018-2020) at a hourly rate and a spatial resolution of about 10 m. As background concentrations, we used the concentrations measured at the Herstal station in the suburban area of Liège (Wallonair, 2022). We used the vehicle fleet in 2019 and estimated the traffic from the HERE floating car data for 2018.

Indoor model

The model used to assess the outdoor-indoor transfer of pollutants has been developed by Cenaero (Aeronautics Research Center). The tool « OpenModelica », which is an open-source modelling and simulation environment, was chosen to develop this model. Three different models have been developed to assess indoor black carbon (BC) concentrations respectively in a building, a car and a bus. Only the model dedicated to the building environment is used here.

The building model is a two-zone model, allowing to represent the BC concentrations in two adjacent rooms with only one of them in direct contact with the outside environment. It takes several driving forces (indoor-outdoor temperature difference and mechanical ventilation) as well as different building factors (leakage, natural ventilation, *etc*.) into account. A simplified scheme of this model and its parameters is shown in Figure 2. For the simulations, we made several assumptions (Hozay, 2021): a ventilation flow of 1 volume hour^{-1} in the stores only (absence of ventilation in the appartment), a ventilation filtration rate of 50 % (in the stores only), an air infiltration surface of 0.01 m², *etc*.

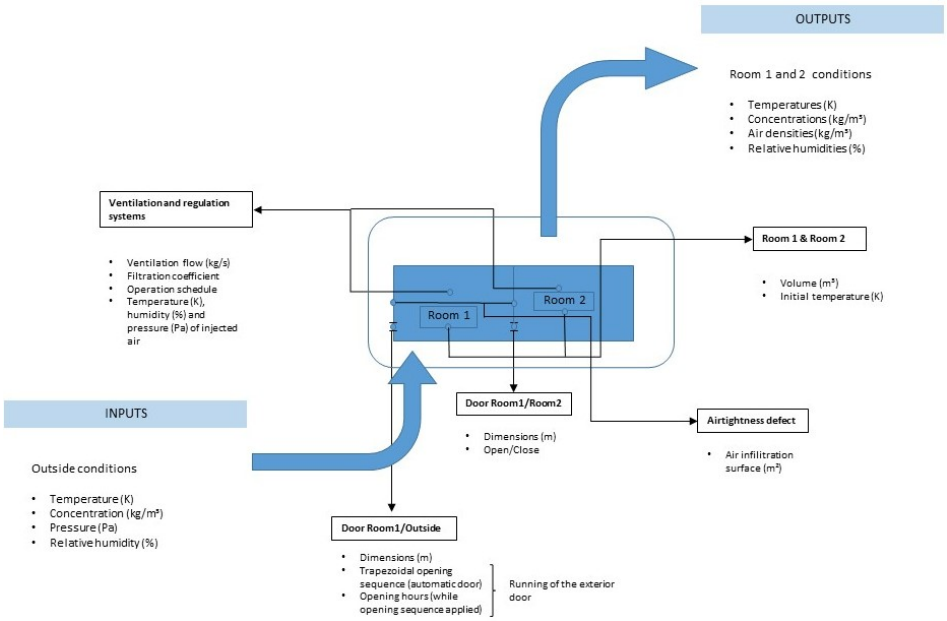

Figure 107. Simplified scheme of outdoor - indoor air pollution transfer model.

RESULTS AND VALIDATION

Mobile personal exposure campaign

Not surprisingly, the participants spent most of their time inside, at home or at work, and in daily travels, with mean exposures to $PM_{2.5}$ of 7, 4 and 6 μgm^{-3} respectively. The highest average exposures are measured during activities indoors: cooking (8 μgm^{-3}) and indoor leisure such as sport (9 μgm^{-3}). It is also during these activities that the highest concentrations were recorded with 64 μgm^{-3} for cooking, 58 μgm^{-3} for indoor leisure and 53 μgm^{-3} when being simply at home. Regarding the means of transport, the time spent travelling by car or walking was the highest in the population sample, followed by train, bus and bike. On average, pedestrians and bus commuters were exposed to 9 μgm^{-3} while car drivers, train commuters and cyclists were exposed to 5 μgm^{-3}. The lowest and highest maximum concentrations were respectively recorded for train (14 μgm^{-3}) and for bus (63 μgm^{-3}).

Although not the subject of an European directive, nor a World Health Organization (WHO) recommendation, measuring black carbon (BC), which is the product of incomplete combustion of fossil fuels or biomass, is a good indicator of traffic and heating intensity. The mobile campaign in Liège highlights the high exposure to BC when leaving and picking up children from school (1.0 μgm^{-3} on average and a maximum of 6.7 μgm^{-3}), ahead of travelling (0.9 μgm^{-3} and 4.4 μgm^{-3}), shopping in a mall (0.8 μgm^{-3} and 3.1 μgm^{-3}) and cooking/making a fire (0.7 μgm^{-3} and 4.7 μgm^{-3}). People also seem to be the most exposed to BC during bus trips (1.6 μgm^{-3}, maximum of 7.8 μgm^{-3}), but, unlike for $PM_{2.5}$, the bus is followed by the train (1.4 μgm^{-3}, max of 3.4 μgm^{-3}) and the bike (1.0 μgm^{-3}, max of 5.3 μgm^{-3}).

Outdoor model validation

The hourly pollutant concentrations simulated by ATMO-Street were compared to the concentrations measured by the citizens during their outdoor activities and travels. For this purpose, the 1-minute measurements were first aggregated at a hourly resolution and a 10 m spatial resolution. Figure 3 shows the comparison between the black carbon modelled and measured concentrations corresponding only to citizen travels in 2019 ($[BC]_{travel\_median\_meas}$ = 0.84 μgm^{-3}, $[BC]_{travel\_median\_mod}$ = 0.72 μgm^{-3}, $[BC]_{travel\_standev\_meas}$ = 4.16 μgm^{-3}, $[BC]_{travel\_standev\_mod}$ = 0.73 μgm^{-3}, RMSE = 4.2 μgm^{-3}). Some well-known traffic hotspots or pedestrian zones in the city (Place Saint-Lambert, Boulevard d'Avroy, le Carré) are identified both by the measurements and the model. If we refine the analysis depending on the travel mode, both measurements and model indicate that pollutant exposure is more important for car drivers ($[BC]_{median\_meas}$ = 0.92 μgm^{-3} and $[BC]_{median\_mod}$ = 0.80 μgm^{-3}) than for pedestrians ($[BC]_{median\_meas}$ = 0.65 μgm^{-3} and $[BC]_{median\_mod}$ = 0.54 μgm^{-3}) and cyclists ($[BC]_{median\_meas}$ = 0.60 μgm^{-3} and $[BC]_{median\_mod}$ = 0.69 μgm^{-3}). In ATMO-Street, it means that pedestrians and cyclists take itineraries with surely less traffic density.

Figure 108. Black carbon outdoor concentrations measured during multimodal travels (small circles) and modelled by ATMO-Street (large circles) in May-December 2019.

Indoor model validation

BC measurements were carried out inside and outside a clothing shop in Liège on 24-25 August 2017 ($[BC]_{outdoor\_median\_meas}$ = 1.52 µgm^{-3}, $[BC]_{Room1\_median\_meas}$ = 1.12 µgm^{-3} and $[BC]_{Room2\_median\_meas}$ = 0.65 µgm^{-3}). The more frequent variations in the indoor concentrations during day time suggest that there is a greater influence of the outside concentration during the opening hours (Figure 4). Outside this period, indoor concentrations are more stable, although an overall increase in outdoor concentration (between 7 pm and midnight) leads to a delayed increase in indoor concentrations. The opening of the doors that occurs only during the opening hours seems thus to have a short-term effect on the indoor concentrations while the ventilation (working day and night) would have a more delayed impact. The simulated concentrations for Room 1 (the room with the opening doors) are quite close to the measurements ($[BC]_{Room1_median_mod}$ = 0.92 µgm^{-3}) even if the model tends to amplify the concentration variations during the night. For Room 2, the results are not so good; the modelled concentrations are overestimated ($[BC]_{Room2_median_mod}$ = 0.87 µgm^{-3}). If, during the opening hours, the simulated concentrations for the two rooms are different and follow rather well the trend of the measured concentrations, after the store closing, the simulated concentrations for the two rooms converge which is not the case for the measurements.

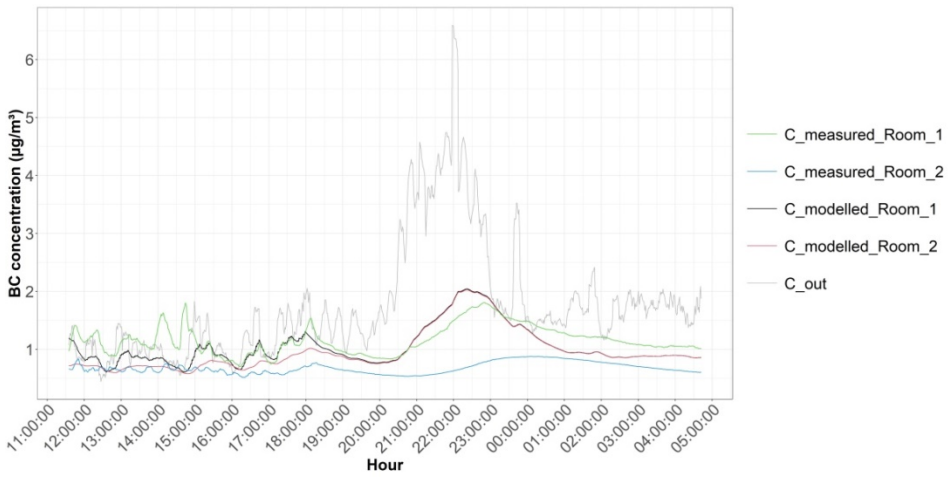

Figure 109. Measured and modelled black carbon concentrations outside and inside a store (24-25 August 2017).

The model presents better results for the store campaign than for the campaign led in the appartment. First, the modelled indoor concentrations in the apartment are less influenced by the outside concentration variations than the measured concentrations, even if we note the influence of opening the outside door on Room 1 concentrations. This suggests that, in absence of mechanical ventilation in the appartment, the model tends to underestimate the influence of the natural ventilation and infiltration. Even if, in reality, we can consider the airtightness defect insignificant compared to the mechanical ventilation, it should still influence the results. Secondly, the indoor BC sources (cooking, candles, *etc*.) more important in the appartment than in the shop are not considered in the model. Further improvements should thus include indoor sources but also deposition and atmospheric chemistry. It would also be interesting to see if the model response would be better with larger particulate matter.

REFERENCES

Dons, E., 2013: Air pollution exposure assessment through personal monitoring and activity-based modelling. PhD thesis.

Hozay, F., 2021: Analyse du transfert de black carbon (BC) d'un environnement extérieur vers un environnement intérieur - Étude de cas et modèle. Master thesis, 143 p.

Lefebvre, W., M. Van Poppel, B. Maiheu, S. Janssen, E. Dons, 2013: Evaluation of the RIO-IFDM-street canyon model chain. Atmos. Environ.*, **77**, 325–337.*

Lenartz, F., M. Dury, B. Bergmans, V. Hutsemékers, V. Broun, C. Brose and S. Guichaux, 2021: Antilope, A Portable Low-Cost Sensor System for the Assessment of Indoor and Outdoor Air Pollution Exposure. Frontiers in Sensors*, **2**, 679908.*

Lenartz, F. and M. Dury, 2022: Antilope, a low-cost portable sensor system for air quality monitoring. Research Outreach*, 131, in press.*

Wallonair, 2022: L'Air Que Vous Respirez en Wallonie. www.wallonair.be/fr/

21st International Conference on
Harmonisation within Atmospheric Dispersion Modelling for Regulatory Purposes
27-30 September 2022, Aveiro, Portugal

RELATING OUTDOOR CONTAMINANT CONCENTRATION VARIANCE TO INDOOR VARIANCE TO IMPROVE HEALTH AND EXPOSURE IMPACTS

Paul Bieringer, Scott Runyon, David Lorenzetti, Michael Sohn

Abstract title: Relating Outdoor Contaminant Concentration Variance to Indoor Variance to Improve Health and Exposure Impacts

Name and Affiliation of the First Author: Paul E. Bieringer. – Aeris, LLC

Email of first author: paulb@aerisllc.com

Names and Affiliations of the Co-authors: Scott Runyon – Aeris
David Lorenzetti – Lawrence Berkeley National Laboratory
Michael Sohn – Lawrence Berkeley National Laboratory

Preferred way of presentation (oral or poster): Oral

Abstract text *(maximum 350 words.)*

Conducting assessments for human exposure to airborne hazardous material releases within urban areas requires special treatment for several reasons. First, high population densities complicate the accurate assessment of consequences, and the presence of buildings and other structures affects wind fields and the corresponding outdoor contaminant transport and dispersion. Second, it is also possible that the release locations occur inside a building, and thus are sources for outdoor plumes. Conversely buildings can provide significant protection, both passively (e.g., because they act as low-pass filters that can reduce concentration peaks compared to an outdoor plume) and actively (e.g., through control systems and purpose-provided filters). Finally, the uncertainty associated with these natural and engineered processes can complicate the overall hazard estimate.

Unfortunately, due to the complexity of urban environments, and the limited data available, many of the operational tools currently used to produce emergency response guidance for urban scenarios have not been extensively evaluated. In this presentation we will describe a coupled urban and indoor dispersion model that can calculate mass conserving contaminant transport between outdoor urban and indoor spaces that can be used to support urban and indoor contaminant exposure assessments. This modeling system consists of a building-aware Large Eddy Simulation (LES) atmospheric and coupled outdoor urban dispersion model implemented on a Graphics Processing Unit

(GPU) computer that has been linked to a single zone building interior air exchange model. This presentation describes the use of this modeling system to develop synthetic urban and indoor contaminant dispersion scenarios, and the use of these high-fidelity data sets to support the assessment of the operational tools described above. We will show results from an effort where this tool was used to assess the accuracy of human health and exposure calculations made for coupled outdoor and indoor spaces. It is used to illustrate how indoor spaces act to reduce the concentration variance and its associated impact on human exposure calculations. These results are then used in the development of scaling relationships designed to improve indoor human exposure estimates by translating outdoor concentration variance into a more accurate corresponding indoor variance.

21st International Conference on
Harmonisation within Atmospheric Dispersion Modelling for Regulatory Purposes
27-30 September 2022, Aveiro, Portugal

ASSESSING THE IMPACT OF THE COVID-19 LOCKDOWNS: RESULTS AND IMPLICATIONS FROM A MODELLING APPLICATION IN TWO MEDITERRANEAN CITIES

Nicolas Moussiopoulos, George Tsegas

Abstract title: Assessing the impact of a traffic low emission zone on pollutant concentrations at street level through a combination of microscopic traffic simulations and air quality modelling at multiscale

Name and Affiliation of the First Author: Alejandro Rodríguez-Sánchez[1]

[1]Atmospheric Modelling Unit, CIEMAT, Av. Complutense, 40, 28040 Madrid, Spain

Email of first author: alejandro.rodriguez@ciemat.es

Names and Affiliations of the Co-authors: Jose-Luis Santiago[1], Marta G. Vivanco[1], Beatriz Sanchez[2], Esther Rivas[1], Fernando Martín[1], Mark R. Theobald[1], Juan Luis Garrido[1], Victoria Gil[1], Alberto Martilli[1]

[1] Atmospheric Modelling Unit, CIEMAT, Av. Complutense, 40, 28040 Madrid, Spain.
[2] Department of Geography, National University of Singapore, Singapore.

ABSTRACT TEXT (MAXIMUM 350 WORDS.)

Pollutants emitted by road traffic represent a major contributor to the population exposure in urban areas, becoming an important problem in urban areas. Local mitigation measures are being developed in different cities with the objective of minimizing the population exposure to traffic-related air pollution. One of the measures most usually applied is the reduction of traffic emissions in some urban areas through traffic restrictions established in various streets or avenues. In this context, this work aims at evaluating the impact on air quality of these traffic low emission zones (LEZ) and developing strategies that improve this impact. To achieve this objective, microscopic traffic simulations are performed in an urban area at a very high spatial resolution in order to simulate road traffic-related emissions in different scenarios. These emission scenarios are used by Computational Fluid Dynamics (CFD) simulations driven by meteorological and air quality mesoscale modelling to identify the impact of the different emissions on air pollutant concentrations at street level.

21st International Conference on
Harmonisation within Atmospheric Dispersion Modelling for Regulatory Purposes
27-30 September 2022, Aveiro, Portugal

POPULATION DYNAMICS AND ITS CONSEQUENCES ON HEALTH RISK MODELING FOLLOWING INHALATION EXPOSURE

Oscar Björnham[1], Daniel Elfverson[1] and Leif Persson[1]

[1]Swedish Defence Research Agency, Umeå, Sweden

Abstract:
A crucial part of risk assessment following airborne spread of toxic chemicals is the translation from concentration field to injury probabilities. The impact of population movement remains an understudied and poorly understood factor in such an enterprise. A basic level initiative to target this knowledge gap, with emphasis on a mathematical method to calculate exposure probability distributions, is presented here. Finally, qualitative results from an investigation are presented, which reveal phenomena that are present but hidden in consequence analyses when population movement is ignored.

KEYWORDS: TOXICOLOGY, DYNAMIC POPULATION, HEALTH RISK, EXPOSURE MODELING

INTRODUCTION

The most common method for estimating health risks following an airborne release of toxic chemicals is to apply tabulated values from exposure guidelines, such as AEGL or TEEL amongst many others. These tables present concentration limits for a certain set of chosen exposure times and are compiled by experts using primarily data from animal testing. Even though the tables are very useful, they are burdened by important simplifications that need to be addressed for improved health risk estimations. One evident limitation is that the guidelines are restricted to constant concentration levels, which exclusively is the case in controlled laboratory experiments. For any real life exposure, concentration varies significantly and it is therefore advisable to enhance the exposure modeling to include temporal variance. Improvement may be found by using the well-known probit model, which allows for time variance by its more general construction. Temporal variability of the exposure depends on the dynamics of both the plume itself and the motion of the population. Much effort is today focused on atmospheric dispersion modeling which improves our understanding of the plume dynamics, while modeling of the movement of the population has largely been overlooked and its impact remains to a high degree unresolved.

The intuitive Haber's rule, $k_{s,e}=cT$, to describe which exposure time, T, and concentrations, c, that are required to obtain a certain medical end point e for the substance s, has frequently been used in toxicological studies and risk estimations, as discussed by Miller et al. (Miller et al., 2000). Already in the 1930s, Bliss found that Haber's rule did not fit his experimental data with insecticides, and proposed a toxic load approach (Bliss, 1940). Toxic load, T_L, is a generalization of Haber's rule by introducing the exponent n over the concentration, which leads to the toxic load expression $T_L=c^nT$. Over the years, many more studies have contradicted Haber's rule and indicated that toxic load provides better agreement to experimental data (Atherley, 1985; Bunce & Remillard, 2003; Gardner et al., 1979; Miller et al., 2000; Ten Berge et al., 1986). Indeed, Haber's rule is only one specific case of the toxic load formulation with $n=1$. Probit analysis, i.e. regression using binomial response variables, was suggested by Bliss in 1934 (Bliss, 1934) and has become a popular method. Finney continued on Bliss analysis and established the probit analyses rigorously (Finney & Tattersfield, 1952). Toxicological parameters are typically calculated from controlled conditions where concentrations are held constant. This method allows for characterization of parameters of different

substances, which can successfully be applied in risk area estimations. However, in a real-life situation, concentration varies and the expression $c^n T$ is only applicable for time independent concentrations. Czech et al. discusses different methods to calculate toxic load from time variant concentration field (Czech et al., 2011). The integrated concentration toxic load model

$$T_L = \int_0^T c^n(t)\,dt \tag{1}$$

is clearly the most consistent method given access to the time-dependent concentration. Equipped with models able to handle nonlinear toxicology and time variant concentration field, we now approach the difficult subject of population dynamics. This is an often-overlooked or ignored aspect in consequence analysis. Indeed, the population is often treated as static (Namboothiri & Soman, 2018; Pontiggia et al., 2010). In contrast, a dynamic population is applied in some hypothetical case studies that thereby catch the combination of concentration plume and a moving population (Georgiadou et al., 2007; Lovreglio et al., 2016; Mocellin & Vianello, 2022; Wang et al., 2020).

To our knowledge, no thorough study has been conducted on the topic of population dynamics coupled to inhalation toxicology. Our ambition is to improve consequence analyses by unraveling the main properties of the interaction between a toxic plume and population dynamics. The initial approach is to identify and investigate the most fundamental and relevant features derived from population dynamics within the framework of probit analysis. To do so, we apply an integrated toxic load model on a population that are allowed to move within a domain containing a concentration field. A static population is considered a special case where the movement speed is reduced to zero. The population is assumed to be unaware of the exposure and do therefore not react in any way to the concentration field. The population dynamics is modeled as a Wiener process using the Itô diffusion framework on a 2D domain without obstacles. This is not a realistic movement of a population but it provides distinct mathematical properties that allow for a wider generalization than a specific case setup would. Even under this simplification, it is reasonable to expect that interesting features can be identified. Provided by knowledge from such a study, realism may later be improved to approach a real-life situation.

In this paper, the emphasis is particularly placed on the methodology to calculate the exposure distributions. Itô diffusion show great compatibility with the Feynman-Kac formula that enables, in a beautiful way, the problem to be cast in the form of partial differential equations (PDE). This transformation allows us to bypass time-consuming Monte Carlo simulations and directly acquire the probability distribution of the exposure with high accuracy and precision by solving the deterministic PDE.

Theory

Individuals of the population are modelled to follow random paths $X(t)$ modelled by Itô diffusions, moving in a given concentration field $c(t,x)$. As a consequence of the concentration field and the random path, an individual will be exposed to a random *logarithmic toxic load,* which is referred to as the *exposure,*

$$\Theta = \log \int_0^T c(t, X(t))^n\,dt \tag{2}$$

during the time interval $[0,T]$. A quantal toxicological response (e.g., *light injury*, or *death*) is supposed to occur in an individual if $\alpha + \beta\Theta$ exceeds an individual *random tolerance* Ψ *(Ashford & Sowden, 1970)* which is supposed to be a standard normal random variable. Here α and β are real numbers, the *probit parameters* for the quantal response in question. At the population level, the probability for the quantal response, referred to as *population injury*, is

$$Q_r = P(\alpha + \beta\Theta \geq \Psi) = \int_{-\infty}^{\infty} P(\alpha + \beta\Theta \geq \Psi \mid \Psi = \psi) P(\Psi = \psi)\,d\psi = \int_{-\infty}^{\infty} S_\Theta\left(\frac{\psi - \alpha}{\beta}\right)\frac{e^{-\psi^2/2}}{\sqrt{2\pi}}\,d\psi \tag{3}$$

where $S_\Theta = 1 - F_\Theta$ denotes the survival function of Θ and F_Θ is the cumulative distribution function (CDF). The population CDF is obtained by the law of total probability

$$F_{\Theta}(\theta) = \iint F_{\Theta|X(0)}(\theta|\ x)\,p(x)dx \tag{4}$$

where $F_{\Theta|X(0)}(\theta|\ x) = P(\Theta \le \theta|\ X(0) = x)$ is a conditional CDF and $p(x)$ is the population probability density at $t = 0$. The conditional CDF can be obtained from the conditional *moment generating function* (MGF) of $d = \exp(\Theta)$, defined by

$$M_{\mathrm{d}|X(0)}(t|\ x) = E[exp(td)|\ X(0) = x], \quad t < 0 \tag{5}$$

by deconvolution according to Rossberg (Rossberg, 2008)

$$K * F_{\Theta|X(0)}(y|\ x) = M_{\mathrm{d}|X(0)}(-exp(-y)|\ x) \tag{6}$$

Here the convolution kernel is given by

$$K(y) = \exp(-y - \exp(-y)) \tag{7}$$

By the Feynman-Kac formula (Milstein & Tretyakov, 2004)

$$M_{\mathrm{d}|X(0)}(-\omega|\ x) = u_{\omega}(0,x) \tag{8}$$

where $\omega > 0$ and $u_{\omega}(s,x)$ is solution to the terminal value problem

$$\begin{aligned} &\partial_s u_{\omega}(s,x) + L^0 u_{\omega}(s,x) - \omega c^n(s,x) = 0, \quad 0 \le s < T, x \in \mathbf{R}^2 \text{ ^ '} \\ &u_{\omega}(T,x) = 1, \quad x \in \mathbf{R}^2 \end{aligned} \tag{9}$$

Here

$$L^0 = \sum_{i=1}^{2} b_i(s,x)\partial_{x_i} + \frac{1}{2}\sum_{i,j=1}^{2} \sigma_{ik}(s,x)\sigma_{jk}(s,x)\partial^2_{x_i x_j} \tag{10}$$

is the generator of the Itô diffusion

$$dX_i(t) = b_i(t, X(t))dt + \sum_{k=1}^{2} \sigma_{ik}(t, X(t))dW_k(t), \quad i = 1,2 \tag{11}$$

defining the random trajectories of the population. In the method above, $\mathbf{R}^2$ can be replaced by a bounded domain Ω, provided that T is replaced by $T \wedge \tau$, where τ is the first exit time of the Itô diffusion, the boundary condition

$$u_{\omega}(s,x) = 1, \quad 0 \le s \le T, x \in \partial\Omega \tag{12}$$

is added in (9), and absorbing boundary conditions are applied in (11), i.e., the right hand side of (11) is multiplied by $1_{\{\tau > t\}}$.

Numerical solution

To numerically solve the deconvolution equation, eq. (6), to obtain the conditional CDF needed to compute the quantal response, it is reformulated as a minimization problem subject to some extra constraints. It has proven beneficial set up the problem using the PDF instead of the CDF, which is defined by the linear transform

$$L(f_{\Theta|X(0)}(y\,|\,x)) = \int_{-\infty}^{\theta} f_{\Theta|X(0)}(y\,|\,x)dy = F_{\Theta|X(0)}(y\,|\,x) \tag{13}$$

The proposed minimization problem reads:

$$\begin{aligned} &\min_{f_{\Theta|X(0)}} \| K * L(f_{\Theta|X(0)}(y\,|\,x)) - M_{d|X(0)}(-\exp(-y)\,|\,x) \|^2 + \lambda \| \nabla f_{\Theta|X(0)}(y\,|\,x) \|^2 \\ &\text{subject to } f_{\Theta|X(0)}(y\,|\,x) \ge 0 \text{ for all y} \in \tilde{} \\ &\int_{-\infty}^{\infty} f_{\Theta|X(0)}(y\,|\,x) = 1 \end{aligned} \tag{14}$$

where the first term is convolution equation and the second term is a penalty which stabilizes the problem by adding additional smoothness, given some penalty parameter λ. The constraints on the PDF directly translates to correct constraints on the CDF, i.e., monotonicity and boundedness in $[0,1]$. With a slight abuse of notation the discrete version of equation (14) reads:

$$\min_f \| \mathbf{K}(\mathbf{Lf}) - \mathbf{M} \|^2 + \lambda \| \nabla \mathbf{f} \|^2$$
$$\text{subject to } \mathbf{f}_i \geq 0 \text{ for all } i = 1, \ldots, N$$
$$\sum_{i=1}^{N} \mathbf{f}_i = 1 \tag{15}$$

where $\mathbf{f}$ is a pointwise approximation of the PDE, $\mathbf{K}_{j,k} = K(y_j - z_k)(z_{k+1} - z_{k-1})/2$ $\mathbf{M}_j = M_{d|X(0)}(-\exp(-y_i) \mid x)$, and $\mathbf{L}$ is a lower triangular matrix defined by equation (13). For each vector entrée

$$\mathbf{M}_j = M_{d|X(0)}(-\exp(-y_i) \mid x) = u_{-exp(-y_i)}(0, x) \tag{16}$$

a finite element solver is used to approximate the solution of the terminal value partial differential equation given by the Feynman-Kac formula. The solution to the minimization problem (15) can be obtained using a sequential least squares programming solver.

RESULTS AND DISCUSSION

A comprising quantitative study of the impact of motion is not within the scope of this work. However, an investigation using the prerequisites shown in Figure 110 provides interesting qualitative results. The domain is circular and restricted by a border that terminates all paths that extends beyond it. A symmetric two-dimensional Gaussian concentration field is located at the centre of the domain, causing exposure of the uniformly distributed population. The probability distribution for the exposure of an individual depends on its starting position, with highest exposures in the middle of the domain and lowest exposures close to the domain border. The aggregated population injury, Q_r, as a whole is the main quantity of interest. Now, since both the domain and the concentration field are rotational symmetric with regards to the centre of the domain, the exposures for different positions depend only on the radial distance from origin.

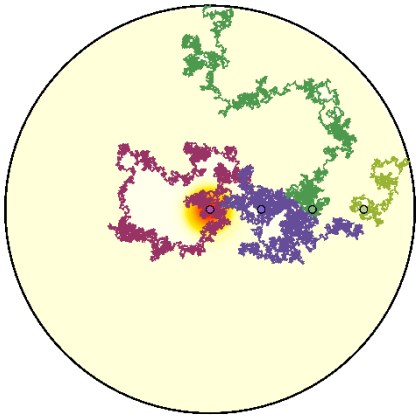

Figure 110. A circular domain with a centrally located Gaussian concentration field illustrated with a heat map. Four example paths are drawn together with their different starting positions, marked with circles. Paths are interrupted if they hit the border of the domain, as is the case for two of the paths in this example.

A probability distribution function can be found following the method described above. First, it is worth noticing that the calculated probability for injury may be considerable different using only the expectation value of Θ in comparison to using the complete distribution thereof. For low exposures, the injury risk is underestimated when using the expectation value, while the opposite is true for high exposures. This finding is related to the so-called *impact region* shown in the left panel of Figure 111. The position and width of the impact region are determined by the substance-dependent probit values α and β. Probability mass to the left of this region will give rise to negligible injury risk, while on the right side it will almost

certainly cause injury. This is a strongly nonlinear relation which means that the distribution should be used, not only the expectation value.

As long as there are people left in the domain, the probability mass flows towards higher Θ-values as time proceeds. The population injury, Q_r, increases as it enters the impact region with a maximum rate in the middle of the region.

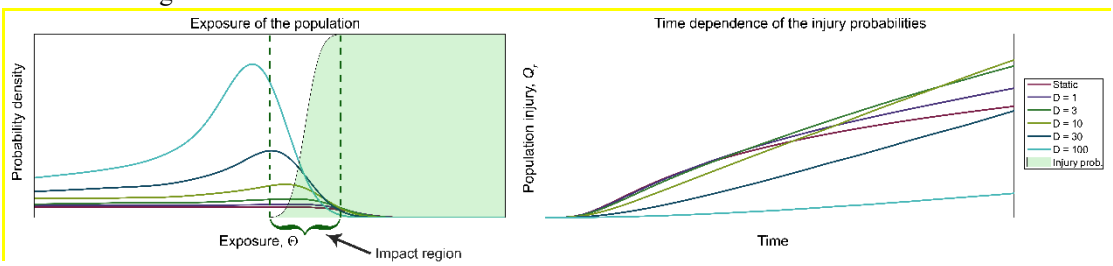

Figure 111. Left panel, the aggregated probability density distribution of Θ for the entire population at the end time of the interval displayed in the right panel. Right panel, the injury outcome given the distribution of Θ for different diffusion coefficients D. Note that "Static" actually corresponds to an almost static population; a very slow movement is actually used to obtain a non-discrete distribution. However, this slow movement does not interfere with the interpretation of the results.

As the right panel shows, slow movements (i.e., low diffusion coefficient D) give rise to the earliest population injuries. The reason is that the persons initially exposed to high concentration remain there for a long time and therefore enters the impact region first. As time progresses things change, faster movements cause far more people to visit the region with high concentration and even though the probability for each person remains low, Q_r increases relatively fast.

It was found that the movement speed that maximize Q_r changes with time, illustrated in the right panel of Figure 111. This phenomenon might be non-intuitive at first, and it underlines the complexity of this field. Its direct implication is that there is no constant factor available to translate the population injury between different movement speeds. Instead, this finding motivates further and more thorough studies on the subject.

REFERENCES

Ashford, J., & Sowden, R. (1970). Multi-variate probit analysis. *Biometrics*, 535-546.

Atherley, G. (1985). A critical review of time-weighted average as an index of exposure and dose, and of its key elements. *American Industrial Hygiene Association Journal*, *46*(9), 481-487.

Bliss, C. (1940). The relation between exposure time, concentration and toxicity in experiments on insecticides. *Annals of the Entomological Society of America*, *33*(4), 721-766.

Bliss, C. I. (1934). THE METHOD OF PROBITS. *Science*, *79*(2037), 38-39. *https://doi.org/10.1126/science.79.2037.38*

Bunce, N. J., & Remillard, R. B. (2003). Haber's Rule: the search for quantitative relationships in toxicology. *Human and Ecological Risk Assessment*, *9*(4), 973-985.

Czech, C., Platt, N., Urban, J., Bieringer, P., Bieberbach, G., Wyszogrodzki, A., & Weil, J. (2011). A comparison of hazard area predictions based on the ensemble-mean plume versus individual plume realizations using different toxic load models. 91st Annual American Meteorological Society Meeting, Seattle, Washington.

Finney, D. J., & Tattersfield, F. (1952). *Probit analysis*. Cambridge University Press; Cambridge.

Gardner, D., Miller, F., Blommer, E., & Coffin, D. (1979). Influence of exposure mode on the toxicity of NO2. *Environmental Health Perspectives*, *30*, 23-29.

Georgiadou, P. S., Papazoglou, I. A., Kiranoudis, C. T., & Markatos, N. C. (2007). Modeling emergency evacuation for major hazard industrial sites. *Reliability Engineering & System Safety*, *92*(10), 1388-1402.

Lovreglio, R., Ronchi, E., Maragkos, G., Beji, T., & Merci, B. (2016). A dynamic approach for the impact of a toxic gas dispersion hazard considering human behaviour and dispersion modelling. *Journal of Hazardous Materials*, *318*, 758-771.

Miller, F. J., Schlosser, P. M., & Janszen, D. B. (2000). Haber's rule: a special case in a family of curves relating concentration and duration of exposure to a fixed level of response for a given endpoint. *Toxicology*, *149*(1), 21-34. *https://doi.org/https://doi.org/10.1016/S0300-483X(00)00229-8*

Milstein, G. N., & Tretyakov, M. V. (2004). *Stochastic numerics for mathematical physics* (Vol. 456). Springer.

Mocellin, P., & Vianello, C. (2022). A numerical study of effects of an industrial hazardous release on people egress. *Chemical Engineering Transactions*, *90*, 445-450.

Namboothiri, N. V., & Soman, A. (2018). Consequence assessment of anhydrous ammonia release using CFD-probit analysis. *Process safety progress*, *37*(4), 525-534.

Pontiggia, M., Derudi, M., Alba, M., Scaioni, M., & Rota, R. (2010). Hazardous gas releases in urban areas: Assessment of consequences through CFD modelling. *Journal of Hazardous Materials*, *176*(1-3), 589-596.

Rossberg, A. (2008). Laplace transforms of probability distributions and their inversions are easy on logarithmic scales. *Journal of applied probability*, *45*(2), 531-541.

Ten Berge, W., Zwart, A., & Appelman, L. (1986). Concentration—time mortality response relationship of irritant and systemically acting vapours and gases. *Journal of Hazardous Materials*, *13*(3), 301-309.

Wang, J., Yu, X., & Zong, R. (2020). A dynamic approach for evaluating the consequences of toxic gas dispersion in the chemical plants using CFD and evacuation modelling. *Journal of Loss Prevention in the Process Industries*, *65*, 104156.

21st International Conference on
Harmonisation within Atmospheric Dispersion Modelling for Regulatory Purposes
27-30 September 2022, Aveiro, Portugal

ESTIMATING REGIONAL BACKGROUND CONCENTRATIONS OF $PM_{2.5}$ AND VERIFYING LOCAL SOURCE CONTRIBUTIONS IN A DATA POOR ENVIRONMENT

Eve L. Draper[1], J. Duncan Whyatt[2], Richard Taylor[3] and Sarah E. Metcalfe[1]

[1]School of Geography, University of Nottingham, University Park, Nottingham, NG7 2RD, UK
[2]Lancaster Environment Centre, Lancaster University, Bailrigg, Lancaster, LA1 4YQ, UK
[3]Nottingham City Council, Loxley House, Station St., Nottingham, NG2 3NG, UK

Abstract: Long- and short-term exposure to $PM_{2.5}$ is linked to adverse health impacts. Compared to other pollutants, $PM_{2.5}$ is monitored at far fewer stations across the UK's Automatic Urban Rural Network (AURN) hence models are widely used to simulate concentrations. A significant proportion of local $PM_{2.5}$ may be attributed to regional sources, so an accurate estimation of that component is necessary to ensure that the model gets the 'right results for the right reasons'. This study explores alternative methods of deriving background $PM_{2.5}$ concentrations in Nottingham, UK, to represent the regional component in an atmospheric dispersion model (ADMS-Urban). A model variation employing hourly background concentrations from AURN stations located up to 200km upwind of the city performed best when verified against $PM_{2.5}$ concentrations for two monitoring locations in the city. This study also uses alternative verification datasets to assess model performance in a data poor environment. This gives us confidence to apply ADMS-Urban more widely across the city to assess associations between $PM_{2.5}$ and human health.

KEY WORDS: **$PM_{2.5}$, ADMS, BACKGROUND SOURCES, HYPERLOCAL SOURCES.**

INTRODUCTION

Particulate matter with an aerodynamic diameter of ≤2.5μm ($PM_{2.5}$) is associated with many health conditions including cardiovascular diseases, respiratory diseases and reduced cognitive function (Southerland *et al*., 2022). In spite of this, in the UK, $PM_{2.5}$ is only measured at 79 of the 171 Automatic Urban and Rural Network (AURN) monitoring sites, which is far fewer than for other pollutants e.g. NO_2, measured at 145 (Defra, 2022). The association between short-term peaks in $PM_{2.5}$ and adverse health effects has been recognised, hence in the past there has been a focus on monitoring in 'hot-spot' areas, e.g. busy roads (Harrison *et al*., 2012). Research has also demonstrated the risks of long-term exposure to fine particles on human health, but monitoring has not increased based on this understanding (Southerland *et al.*, 2022). This means there is heavy reliance on air quality models to predict $PM_{2.5}$ concentrations over a city-wide scale for the purposes of decision making and human health assessments (Ortiz and Freidrich, 2013).

$PM_{2.5}$ can be a primary pollutant, from exhaust emissions, tyre and brake wear, or emissions from industrial and household combustion. However, some studies have identified that a significant amount (41% - 72%) of $PM_{2.5}$ in the UK is secondary, which is caused by chemical reactions in the atmosphere (Harrison *et al*., 2012; Yin *et al.*, 2010). $PM_{2.5}$ can travel long distances in air masses, meaning long-range transport, particularly from mainland Europe, also contributes to the $PM_{2.5}$ load in the UK (Graham *et al.*, 2020). Rural AURNs provide an indication of transboundary $PM_{2.5}$ contributions whilst urban AURNs reflect additional local contributions. It is essential to get the background and local proportions accurate in local-scale air quality modelling so that local sources can be targeted for management accordingly (Ortiz and Friedrich, 2013).

This study explores methods for determining background concentrations of $PM_{2.5}$ for use in an atmospheric dispersion model (ADMS-Urban 5.0) for local-scale $PM_{2.5}$ modelling in Nottingham, using wind direction as a predictor for background concentration. Methods for overcoming hyperlocal source contributions for the purposes of model verification are also presented.

Nottingham, UK

In Nottingham, there is one urban background AURN station that measures both $PM_{2.5}$ and PM_{10} (city centre), and one roadside station that measures PM_{10} only (Western Boulevard) (Figure 1a). In line with the objectives of the AURN, these were established to assess compliance with the Ambient Air Quality Directives and measure reduction of pollutants over time. Nottingham has an annual mean $PM_{2.5}$ of 12 $\mu g/m^3$ of which 8 $\mu g/m^3$ (67%) may be attributed to background sources (Nottingham City Council, 2018).

METHODOLOGY

Determining a suitable background dataset for model input

Four different approaches to estimating background concentrations of $PM_{2.5}$ were developed, based on data from one rural and several urban background AURN sites (Figure 1b). The year 2019 was used as this is the most recent year that was not affected by emission reductions due to the COVID-19 pandemic national lockdowns:

1. Model 1: Used hourly background data from a rural AURN, Chilbolton Observatory (southern England). This site was chosen as it was the closest rural AURN site to Nottingham that measures hourly $PM_{2.5}$ concentrations.
2. Model 2: The Chilbolton AURN values were scaled using average annual background values in rural areas outside of the Nottingham conurbation generated by the Pollution Climate Mapping (PCM) model (Defra, 2019). A single annual value was applied to uplift all hourly values from the Chilbolton AURN so they were more reflective of the $PM_{2.5}$ background climate in Nottingham (Zhong *et al.*, 2021).
3. Model 3: Hourly background data were taken from other urban background AURNs within 200km of Nottingham using wind direction as a predictor for background concentrations. Model 3 selected stations based on 8 x 45° sectors upwind of Nottingham.

4. Model 4: Takes the same approach as Model 3 but selects stations based on 12 x 30° sectors upwind of Nottingham.

Figure 1a: Nottingham AURN sites. **Figure 1b:** Background AURN locations used in models.

Model verification

Both AURN sites in Nottingham were used to verify $PM_{2.5}$ models (Figure 1a). Analysis of the city centre site prior to verification revealed a hyperlocal source of $PM_{2.5}$, which was a mobile hot food stall not representative of the wider $PM_{2.5}$ climate in Nottingham. Correspondence with the Local Authority revealed that the food outlet started operating in 2015. The lunchtime peaks present a very different temporal signature from expected local sources, such as nearby roads, that typically follow a diurnal pattern of the morning and evening rush-hours (Kendrick *et al.*, 2015) (Figure 2). For the purposes of model verification, data during periods whilst the hot food stall was operating were removed from the verification dataset.

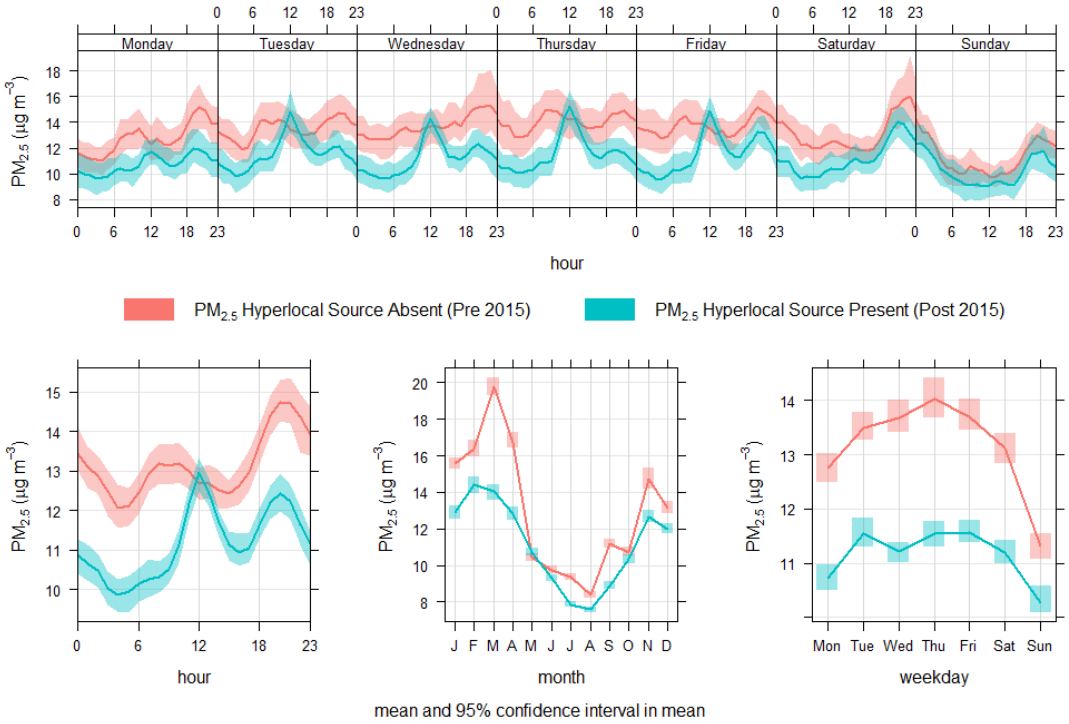

Figure 2: Time variation of $PM_{2.5}$ at the city centre AURN, pre (2008-2014) and post operation (2015-2019) of the hot food stall.

$PM_{2.5}$ was estimated at Western Boulevard (Figure 1a) by applying a $PM_{2.5}$:PM_{10} ratio from the city centre site once the influence of the hot food stall was removed from the dataset. This ratio was calculated for hourly concentrations of PM_{10} and $PM_{2.5}$ and averaged for the year, giving a value of 0.58. Hourly concentrations of the model outputs were verified against recorded hourly $PM_{2.5}$ concentrations at city centre, and hourly estimated $PM_{2.5}$ concentrations at Western Boulevard.

Model performance for $PM_{2.5}$ was tested using fraction of predictions within a factor of two (FAC2), mean bias (MB), mean gross error (MGE), normalised mean bias (NMB), correlation coefficient (r), and index of agreement (IOA).

RESULTS

Model 3 performed best for FAC2, MGE, r and IOA at both the city centre and Western Boulevard sites (Table 1). The city centre site has fewer data points for $PM_{2.5}$ than Western Boulevard due to the removal of hours influenced by the hot food stall.

Table 1: Model statistics of model performance for $PM_{2.5}$ at city centre and Western Boulevard AURN sites (hourly data). n is the number of hourly data points tested in the analysis.

Model	n	FAC2	MB	MGE	NMB	r	IOA
City Centre							
Model 1	6676	0.77	0.46	4.70	0.04	0.70	0.65
Model 2	6676	0.70	3.43	5.97	0.32	0.70	0.56
Model 3	6676	0.81	2.05	4.24	0.19	0.80	0.68
Model 4	6676	0.60	5.62	7.28	0.53	0.69	0.46

Western Boulevard							
Model 1	8481	0.81	-0.54	4.60	-0.05	0.63	0.61
Model 2	8481	0.78	2.35	5.72	0.20	0.62	0.51
Model 3	8481	0.86	1.03	4.27	0.09	0.72	0.64
Model 4	8481	0.72	4.74	6.60	0.41	0.64	0.44

DISCUSSION AND CONCLUSIONS

This study used four different datasets to represent background $PM_{2.5}$ concentrations in ADMS-Urban. Model 3, applying urban background AURNs in eight 45° wind sectors using wind direction as a predictor for $PM_{2.5}$ concentration performed most strongly across a range of test statistics at the two verification sites in the city, including FAC2 - a model is considered as acceptable when more than half of the model predictions lie within a factor of two (Derwent *et al.*, 2010). MB and MGE provide useful measures of model over- and under-estimation. Model 1 performed best for MB. Over-estimation in Model 3 may be attributed to local contributions from other urban AURN sites included within the background data input for Nottingham (Derwent *et al.*, 2010). Model 3 performed best for MGE at both sites. NMB is a measure of relative difference between modelled and observed concentrations. Model 1 performs best in this metric, however Model 3 is within the accepted range of -0.2 and +0.2 for both sites, whilst Models 2 and 4 are not (Derwent *et al.*, 2010). There is good overall agreement for modelled and observed concentrations ($r = 0.80$, city centre and $r = 0.72$, Western Boulevard) for Model 3, which performed the best in this metric out of the four models. Model performance is slightly poorer at the Western Boulevard site than the city centre. There could be two explanations for this: First, modelled concentrations at Western Boulevard are compared to concentrations based on a predicted $PM_{2.5}$: PM_{10} ratio; second, there are fewer observations at the city centre site, meaning that r may appear stronger due to a smaller number of pairings (Derwent *et al.*, 2010). Lastly, IOA is a good indicator for overall model performance, Model 3 performed the best out of the four models in this metric for both sites, giving confidence to apply this model across the city to assess relationships with health outcomes (Willmott *et al.*, 2012).

Annual mean modelled concentrations are typically used to assess relationships between health and air pollution across city scales (Huang *et al.*, 2017). However, models can also be used to simulate air pollution episodes, which are known to link to acute adverse health impacts (Bell *et al.*, 2013). These typically occur at regional scales, dominated by background $PM_{2.5}$ from mainland Europe and other conurbations in the UK, with local emissions 'topping-up' concentrations, resulting in higher-than-average $PM_{2.5}$ concentrations and more extreme exceedances of air quality thresholds (Graham *et al.,* 2020). The method used to generate background datasets for Models 1 and 2 supports the prediction of annual mean concentrations, but not episodes. In contrast, the method used to generate background datasets for Model 3 can be used to predict both annual mean and episode-specific concentrations so can be used in assessments of chronic and acute health impacts.

Verifying model performance is challenging in Nottingham. There is one site in the city centre that measures $PM_{2.5}$ which is unlikely to be representative for a population of >300,000 residents. The city centre site is also influenced by a hyperlocal source, not reflective of general conditions across Nottingham, limiting the observations available for model verification. From a wider policy perspective, the influence of hyperlocal sources on monitoring stations may affect the reporting required in accordance with Air Quality Directives. Hyperlocal sources may obscure general reductions in $PM_{2.5}$ due to national and local emission reduction interventions (Figure 2). This confirms the need to carry out rigorous assessment of monitoring data prior to use in model verification. Provision of robust statutory guidance for requirements of siting potential sources, for example, mobile hot food outlets, near to air quality monitoring stations is needed to prevent this issue.

It is difficult to assess the impacts of air pollution from monitoring alone, hence the importance of using a modelling approach to achieve better spatial representation (Conti *et al.*, 2017). Through careful scrutiny of pollutant measurements and assessment of background concentrations it is possible to generate modelled $PM_{2.5}$ concentrations at spatial and temporal scales consistent with available health outcome data to make a more rigorous assessment of associations between air pollution and human health.

ACKNOWLEDGEMENTS

This research was funded by Natural Environment Research Council (NERC), ENVISION Doctoral Training Partnership, Grant Number: NE/S007423/1.

REFERENCES

Bell, M., Zanobetti, A., Dominici, F. (2013). Evidence on the Vulnerability and Susceptibility to Health Risks Associated With Short-Term Exposure to Particulate Matter: A Systematic Review and Meta-Analysis. *Am. J. Epidemiol.,* 178(6): 865-876.

Conti, G., Heibati, B., Kloog, I., Fiore, M., Ferrante, M., 2017: A review of AirQ Models and their applications for forecasting the air pollution health outcomes. *Environ. Sci. Pollut. Res.,* 24: 6426-6445.

Defra, 2019: *Modelled background pollution data.* [Online: https://uk-air.defra.gov.uk/data/pcm-data]

Defra, 2022: *Interactive monitoring networks map.* [Online: https://uk-air.defra.gov.uk/interactive-map?network=aurn]

Derwent, D., Fraser, A., Abbott, J., Willis, P., Murrells, T., 2010: *Evaluating the performance of air quality models (No. Issue 3).* Department for Environment and Rural Affairs. [Online: https://ukair.defra.gov.uk/assets/documents/reports/cat05/1006241607_100608_MIP_Final_Version.pdf]

Graham, A., Pringle, K., Arnold, S., Pope, R., Vieno, M., Butt, E., Conibear, L., Stirling, E., McQuaid, J. (2020). Impact of weather types on UK particulate matter concentrations. *Atmos. Environ*., 5: 100061.

Harrison, R., Laxen, D., Moorrot, S., Laxen, K., 2012: Processes affecting concentrations of fine particulate matter in the UK atmosphere. *Atmos. Environ.*, 46: 115-124.

Huang, G., Lee, D., Scott, E.M., 2017: Multivariate space-time modelling of multiple air pollutants and their effects on health. *Stat. Med.*, 34: 1134-1148.

Kendrick, C., Koonce, P., George, L., 2015: Diurnal and seasonal variations of NO, NO_x and $PM_{2.5}$ mass as a function of traffic volumes alongside an urban arterial. *Atmos. Environ.,* 122: 133-141.

Nottingham City Council, 2018: *Annual Status Report 2018.* [Online https://www.nottinghaminsight.org.uk/Document-Library/Document-Library/63682]

Ortiz, S. and Friedrich, R., 2013: A modelling approach for estimating background pollutant concentrations in urban areas. *Atmos. Pollut. Res.,* 4: 147-156.

Southerland, V., Brauer, M., Mohegh, A., Hammer, M., van Donkelaar, A., Martin, R., Aptel, J., Ananberg, S., 2022; Global urban temporal trends in fine particulate matter ($PM_{2.5}$) and attributable health burdens: estimates from global datasets. *Lancet Planet. Health,* 6: E139-E146.

Willmott, C.J., Robeson S.M., Matsuura, K., 2012: A refined index of model performance. *Int. J. Climatol,* 32: 2088-2094.

Yin, J., Harrison, R., Chen, Q., Rutter, A., Schauer, J.J., 2010: Source apportionment of fine particles at urban background and rural sites in the UK atmosphere. *Atmos. Environ.*, 44: 841-851.

Zhong, J., Hood, C., Johnson, K., Stocker, J., Handley, J., Wolstencroft, M., Mazzeo, A., Cai, X., Bloss, W.J., 2021: Using Task Farming to Optimise a Street-Scale Resolution Air Quality Model of the West Midlands (UK). *Atmosphere,* 12: 983-995.

21st International Conference on
Harmonisation within Atmospheric Dispersion Modelling for Regulatory Purposes
27-30 September 2022, Aveiro, Portugal

NEW REGULATION FOR DOSE ASSESSMENT OF RADIOACTIVE RELEASES IN GERMANY

Margit Pattantyús-Ábrahám[1]

[1]German Federal Office for Radiation Protection, Oberschleissheim, Germany

Abstract:
The radiation exposure to the public originated from planned airborne releases has to be assessed each year and reported to the parliament. This assessment is two-fold, first the atmospheric dispersion of the radioactive substances is simulated, afterwards the transport and uptake of those substances by the environment, food is modelled and the radiation dose to the public is assessed. For these assessments a very conservative approach, the so-called "reference person" was used. The atmospheric dispersion modelling was done with a Gaussian plume model. The new Radiation Protection Ordinance of Germany describe a more realistic assessment approach in line with the Directive 2000/473/EURATOM affecting the followings: 1) A Lagrangian Particle dispersion model has to applied for the atmospheric dispersion modelling of the emitted radioactive substances; 2) The concept "representative person" is used for the dose assessment since 2020.
In this study we highlight the differences between the old and the new dose assessment approach. For the atmospheric dispersion simulations, the Atmospheric Radionuclide Transport Modell (ARTM) was used. For the transport and for the doses assessment the Dose-Model for ARTM (DARTM) were applied. The DARTM Version 5.2 is based on the conservative reference person approach in accordance with the old regulations. In the new DARTM 6.0 version the more realistic model "representative person" was implemented according to the new regulation. A detailed analysis of the effects of the changes on the dispersion as well as on the dose assessment results are to be presented.

KEY WORDS: **RADIOACTIVE RELEASES, DOSE ASSESSMENT, ARTM, OPERATIONAL USE, ATMOSPHERIC DISPERSION OF RADIONUCLIDSES. DARTM**

INTRODUCTION

The exposures to the public originated from airborne radioactive releases of normal operating power plants has to be reported on annual basis in Germany. The amount of the discharged radionuclides are usually so small, that for the reporting purpose the environmental transport and uptake of the radionuclides have to be assessed and thus modelled. The following paths has to be considered during the assesment of airborne discharges:

I) External exposure
   a. cloud-shine (exposure to beta and gamma radiation),
   b. ground-shine
II) Internal exposure:
   a. Inhalation of airborne material in an atmospheric plume (gases, vapours, aerosols)
   b. Ingestion including
      i. Diary products,
      ii. Meet products,
      iii. Greens,

iv. Vegetables and fruits,
v. brest milk.

The dose assessment of the radiological impact on public of airborne discharges has two main steps:

I) Simulating the atmospheric dispersion of radionuclides;
II) Simulating the uptake of the dispersed radionuclides by plants, livestock and humans by a radioecological modell.

In Germany the framework for the dose assessment is described by administrative regulations. In 2018 a new Radioation Protection Ordinance became effective prescribing to use a Lagrangian particle model instead of the previously used Gaussian plume modell for the atmospheric dispersion simultions. In addition the very conservative concept of reference person was exchanged with the more relaistic concept of the representative person. Both changes took places in order to provide a less conservative and more realistic dose assessment in line with the 2004/473/EURATOM Directive. This implied also the amendment of the administrative regulation describing the assessment framework (AVV Tätigkeiten, 2020). In Germany the dose assessment for nuclear power plants is a duty of the Federal Office for Radiation Protection (Bundesamt für Strahlenschutz, BfS).

In this work a short overview of the major changes in the regulations, their implementation in the assessment methods as well as changes in the reporting practice are presented.

Modelling the atmospheric dispersion of radionuclides

The former ordinance did not explicitely stipulated which kind of atmospheric dispersion modells should be used for the dose assessment. The corresponding administrative regulation instructed how a Gaussian plume modell has to be applied and how the gamma-cloud shine had to be estimated (AVV zu §47 StrlSchV, 2012). BfS used an in-hose developed Gaussian plume modell using annual 4D weather statistics (precipitation rate, diffusion category, wind direction and speed), constant effective source height and modified diffusion in case of orography or buildings according to the former administrative regulation. However, for special cases with considerably effects of orography and buildings on the wind field a Lagrangian particle modell was used instead of the Gaussian plume model.

The new Radiation Protection Ordinance specifies the usage of a Lagrangian particle modell for simualting the atmospheric dispersion of radionuclides. A diagnostic wind field model can be used for most of the cases. The Lagrangian particle modell ARTM was developed on behalf of BfS in order to fulfill the reporting purpose. The main differences in the atmospheric dispersion modelling between the previous and actual regulation as well as reporting pracices are shown in Table 1.

Table 33. Differences in the atmospheric dispersion modelling

	Previous regulation (2012)	**Actual regulation (2020)**
Atmospheric dispersion model	Gaussian plume	Lagrangian particle
Weather data	Annual statistic	Time series if possible
Weather data origin	Measured	Measured, Obukhov-length and mixing layer hight can be also used
Plume rise	Constant	Can be weather dependent
Buildings	Modified diffusion	Effect on wind field and diffusion
Orography	Model applies under 5° slope, modified diffusion	Effect on wind field and diffusion
Radioactive decay in the air	May included	Included
Dry deposition	Not size dependent	Size dependent
Wet deposition	Not size dependent	Size dependent
Gamma cloud shine	Estimated according to a table	Calculated according the shape of the cloud
Distribution of radionuclides	Only radial shape	Not necesserily radial

ARTM models the atmopheric dispersion in the following steps: 1) According to the wind and atmospheric stability data as well as the actual topography it calculates the three dimensional wind and turbulence filed. 2) The discharged radionuclides are simulated by numeric particles moving pursuant to these pre-calculated fields and undergo radioctive decay, as well as dry and wet deposition (if applies). These effects are explicitly taken into account during their path. The annual means of the particle positions define the calculated results (activity concentration, wet and dry deposition) and from the three dimensional plume the annual cloud-shine (gamma-radiation) is calculated. Radionuclides in liquide form or bounded to aerosols are subject to dry and wet deposition which is dependent on the aerodynamic diameter of the particle. In case of aerosols ARTM also distinguishes between activity concentrations relevant for inhalations (large particles, > 10 µm, do not reach the lung, since they are captured by the upper respiratory organs) and activity concentrations relevant for cloud-shine (beta and gamma radiation). An overall description of ARTM is given in Hanfland et al (2022), however wind field modell used in version 3.0 and in this study is described in VDI Technical Rule 3783 Blatt 8.

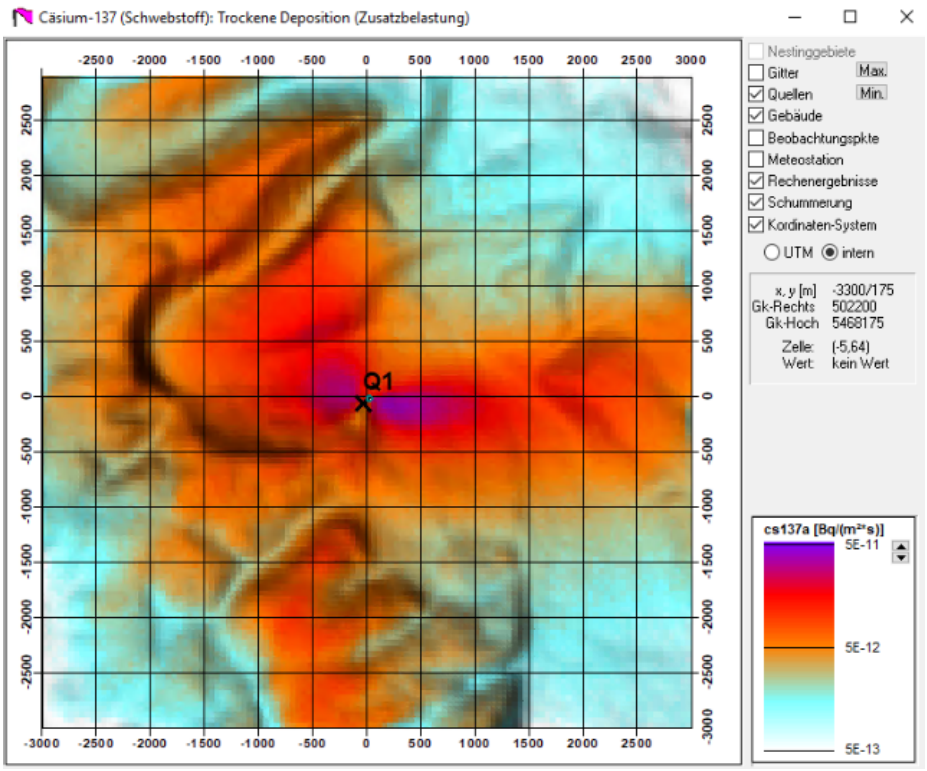

Figure 112. Dry deposition rates [Bq m^{-2} s^{-1}] of Cs-137 aerosols, computed with ARTM

The reason of the differences in the patterns of the results between simulations obtained by the Gaussian plum modes and ARTM are the usage of time dependent weather data and/or the present of considerable orography. Figure 1 shows an example where orography plays a major role in the dispersion: Aerosol particles accumulate predominantly in valley and less in ridges. Such inhomogenity caused by the orography cannot be seen in Gaussian results.

Modelling the exposition to the public

Not only the modelling of the atmospheric diseprsion but the radioecological model became in the actual administrative regulation more realistic and more complex, too. In the case of the former regulation, very conservative concept of the reference person the following assumptions were taken:
The food consumption was extreamly high (the value at 95 percentil of the distribution of food consumption of the public) in every ingestion paths: It was assumed, that the reference person eats as much vegetable products as he would follow a vegan diet but in the same time he eats as much meat products as he would hardly eat anything else. The reference person concept also used a simple approach to allocate the position of this person during the year: The highest annual value of the sum of inhalation and external doses determined the single location were the reference person stayed during the year continously. This place turned out to be very close to the fence of the nuclear facility. BfS had developed a software solution implementing the reference person for the results of the Gaussian-plume model as well as for the ARTM results. The latter software is called Dose programm for ARTM (DARTM) with version numbers until 5.2.

The concept of the reference person fullfilled the important aspect of radiological safety: it never underestimates the exposure to the public and in addition it is very simple to use. However, the chosen assumptions that are far from realistic. The concept of the representative person became more realistic, however in case of any uncertainty in the circumstantes the more conservative event has to be assumed to happen. The food consumption is presumed as the median value of the national food consumtion except one ingestion path, contributing with the highest dose, which is taken with 95 percentil value of the national food consumption distribution. The location of the stay is not necesseriliy in one place. It is may divided between work place with higher exposure, outdoor leisture and home. Also the majority of the year is spent indoor with reduced exposure to gamma radiation. By assessing the radiation exposure the model has to tackle with the possible stay locations as well as how long is it reasonable to stay in a certain place, as well as to find the maximum exposure according to the restrictions.

Table 34. Differences in the radioecological modelling

	Previous regulation (2012)	**Actual regulation (2020)**
Concept	Reference person	Representative person
Assumptions	Conservative	More realistic
Food consumption amounts	95 percentil in all paths	95 percentil in one path, the rest median
Food production	No restriction	According to local circumstances
Staying inside	Never	Part of the year, reduced exposure (γ-radiation)
Stay	One place	Can be divided according to local circumstances
Organ doses	Doses for 25 organs, separately	Only effective dosis
Breast milk path	Only transfer factors	For some radionuclides also dose coefficients

Table 2. contains the main differences between the former and actual radioecological model for the public exposure assumptions of airborne discharges. Since the differences in the assessment method imply significant changes n the computing algorithm, the developement of a complete new software was necessary. DARTM 6.0 (and versions above) fulfills the requirements of the representative person and allows the categorization of pre-selected regions according to real food production informations (exclusion some ingestion pathes) or to long term stay possibilites. Also the information on land use can be used for the identification of possible ingestion paths on the given locations.

RESULTS

The exposure of the public of a German nuclear power plan are presented, which were assessed using the former and the actual administrative regulations. The emitted radionuclides were (H-3 as H_20, C-14 as

CO_2, and the aerosols Co-60 and Cs-137). The same time period and emission term was used (1 year) for both assessment.

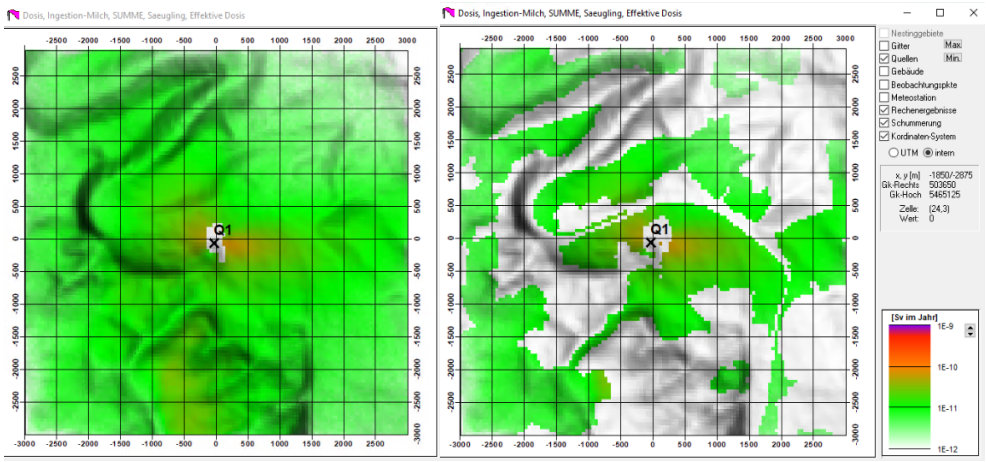

Figure 113. Annual effective dosis of the ingestion path diary products [Sv] for infants (<1 year old) assessed with DARTM version 6.01. Left: not concerning land use and actual possibilities of milk production; right: concerning actual land use.

Figure 2 shows the effective dose result for the ingestion path of infants assessed by DARTM 6.01. On the left side the effective dose results are showed on the whole computational region except the facility premises where access to the public is not allowed. The dose distribution shows influeces of the orography similar to the results showed on Figure 1. On the right side effective doses are only shown in places, where according the land use cataster milk production was likely: River beds, woods are excluded. The concept of the representative person allows such restrictions; if relialable and sufficient information about land use is present, the computed dose results can be excluded from the final dose assessment on regions were the existence of an exposition path is not likely.

Table 3 shows the effective dose results assessed by the concept of reference person and, using Gaussian plume modell as well as of the representative person using ARTM, and DARTM version 6.01 by taking or not taking the actual land use information in the assessment into account.

Table 35. Annual effective dose results [Sv] for childern (1-2 yrs) and adults

Model person	**Reference**	**Represent.**	**Represent.**	**Reference**	**Represent.**	**Represent.**
Dispersion model	**Gaussian plume**	**ARTM**	**ARTM**	**Gaussian plume**	**ARTM**	**ARTM**
Land use	**no**	**no**	**yes**	**No**	**no**	**yes**
Age class	**1-2 yrs**	**1-2 yrs**	**1-2 yr**	**>17 yrs**	**>17 yrs**	**>17 yr**
Overall dose	7.82e-8	9.66e-10	9.16e-10	3.63e-8	7.76e-10	7.34e-10
Ingestion Vegetables	5.13e-9	3.95e-10	3,73e-10	5,78e-9	5.10e-10	4.79e-10

In the given case significant differences are present between the results of the Gaussian model & reference person and Lagrangian modell & representative person. As expected the effective dose results are much higher in the case of the more conservative approach Gaussian plum model & refeence person. There was relatively small difference between the cases if land use was taken into account or not. Probably because the maxima are around the facility premises and only a part of this area was sorted out.

REFERENCES

*Allgemeine Verwaltungsvorschrift zur Ermittlung der Exposition von Einzelpersonen der Bevölkerung durch genehmigungs- oder anzeigebedürftige Tätigkeiten (**AVV Tätigkeiten**) 2020.*
Bundesrat Drucksache 644/19.
http://www.verwaltungsvorschriften-im-internet.de/bsvwvbund_08062020_SII51148301.htm In German.

Allgemeine Verwaltungsvorschrift zu § 47 Strahlenschutzverordnung: Ermittlung der Strahlenexposition durch die Ableitung radioaktiver Stoffe aus kerntechnischen Anlagen oder Einrichtungen 2012. Bundesrat Drucksache 88/12
https://dserver.bundestag.de/brd/2012/0088-12.pdf In German.

Hanfland, R., M. Pattantyús-Ábrahám, C. Richter, C. D. Brunner, C. Voigt. The Lagrangian Atmospheric Radionuclide Transport Model (ARTM) — development, description and sensitivity analysis. Air Qual Atmos Health *(2022).* https://doi.org/10.1007/s11869-022-01188-x

Environmental meteorology: Turbulence parameters for dispersion models supported by measurement data 2017, Beuth Verlag Berlin, VDI Technical Rule VDI 3783 Blatt 8.

21st International Conference on
Harmonisation within Atmospheric Dispersion Modelling for Regulatory Purposes
27-30 September 2022, Aveiro, Portugal

AIR QUALITY IMPACTS ON HUMAN HEALTH, UNDER A CLIMATE CHANGE SCENARIO: THE AVEIRO REGION CASE STUDY

Sílvia Coelho[1], Joana Ferreira[1], David Carvalho[2], Ana Isabel Miranda[1] and Myriam Lopes[1]

[1] CESAM & Department of Environment and Planning, University of Aveiro, Portugal
[2] CESAM & Department of Physics, University of Aveiro, Portugal

Abstract: Nowadays, air pollution is the biggest environmental risk factor, with many urban areas across the world facing air quality problems. Since air pollutants dispersion is highly driven by climate-related events, it is expected that climate change will affect future air quality patterns. The full understanding of the links between air pollution and climate change in urban areas, and how they affect human health, are nowadays research challenges. In this scope, air quality impacts on health were evaluated by the application of WRF-CAMx modelling system to an urban domain over the Aveiro Region, recognized as one of the regions affected by poor air quality in Portugal. The WRF-CAMx was applied for the medium-term future climate (considering the SSP2-4.5 scenario) and for the recent-past (considered as reference). Following the recommendations of the World Health Organization, concentration-response functions for different mortality health indicators were used to estimate health impacts of long-term exposures. Results indicate that, despite the climate change impacts and the general improvements in future air quality in Aveiro Region, some concerns regarding PM2.5 and O_3 concentrations will remain. Near the coastline, where most people live, premature deaths attributable to PM2.5 long-term exposure will continue to occur, regardless the different methodologies for the relative risk estimation used in the health impact assessment. The applied approach constitutes an added value in this research field, being crucial to anticipate the effects of climate change on air quality and evaluate their impacts on human health.

KEY WORDS: **AIR QUALITY; CLIMATE CHANGE; NUMERICAL MODELLING; HEALTH IMPACT ASSESSMENT; URBAN AREAS**

INTRODUCTION

Nowadays, air pollution is the biggest environmental risk factor, since exposure to air pollutants has contributed to a broad range of negative health outcomes, leading to increased mortality and morbidity (WHO 2022a). Many urban areas, particularly densely populated cities, are facing air quality problems, and it is estimated that 99% of the world's population lives in places where air quality exceeds World Health Organization (WHO) guidelines (WHO 2022a). The WHO estimates that every year ambient air pollution kills 4.2 million people worldwide due to stroke, heart disease, lung cancer, lower respiratory infections and chronic obstructive pulmonary disease (WHO 2022a). In the European Union (EU), in 2019, the estimated impacts attributable to the long-term population exposure to PM, NO_2 and O_3 concentrations were around 307000, 40400 and 16800 premature deaths, respectively (EEA 2021). Since air pollutants dispersion is highly driven by climate-related events, according to the latest Intergovernmental Panel on Climate Change report (IPCC 2021), it is expected that climate change will have complex effects on chemistry, transport and deposition of local air pollutants. Future projections of air quality patterns need to consider both climate change and future emission scenarios, due to their

closely coupled impacts on air quality. The full understanding of the links between air pollution and climate change in urban areas, and how they affect human health, are nowadays research challenges.

In this scope, the aim of this study was to evaluate air quality impacts on health, through the application of a numerical modelling system to an urban domain over the Aveiro Region, recognized as one of the regions affected by poor air quality in Portugal.

METHODOLOGY

Climate and air quality modelling

A modelling system, which includes the Weather Research and Forecasting Model (WRF) (Skamarock et al. 2019) and the Comprehensive Air Quality Model with Extensions (CAMx) (ENVIRON 2020), was applied to an urban domain over the Aveiro Region (central region of Portugal), recognized as one of the regions affected by some poor air quality events in Portugal. Both models were applied using three online-nested domains, with increasing resolution, from a coarser domain of 30 km horizontal resolution to the innermost domain of 1.2 km horizontal resolution, focusing on the Aveiro Region (Figure 114).

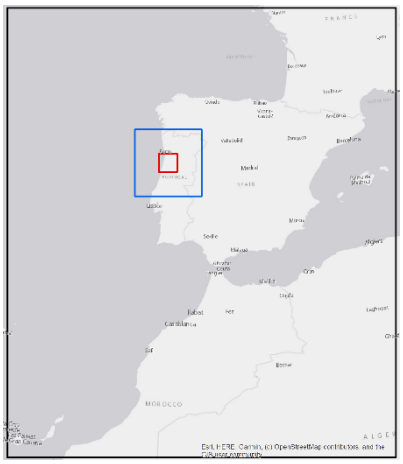

Figure 114. CAMx simulation domains: D01, with 30 km horizontal resolution (black rectangle); D02, with 6 km horizontal resolution (blue square); D03, with 1.2 km horizontal resolution (red square).

The WRF, forced by the Max Planck Institute for Meteorology Earth System Model version 1.2 (MPI-ESM1.2-HR) (Mauritsen et al. 2019), was applied for two years, one statistically representative of the recent-past (2014) and the other statistically representative of the medium-term future climate (2055). For the future climate, the new SSP2-4.5 scenario (Fricko et al. 2017) was applied, which considers a "medium pollution control" scenario, with a nominal 4.5W·m^{-2} radiative forcing level by 2100.

CAMx initial and boundary conditions were provided by the global chemical model CAM-Chem (Emmons et al. 2020). For the recent-past, anthropogenic emissions were taken from the EMEP European emission inventory (EMEP 2017), and spatially disaggregated following the Ferreira et al. (2020) approach and speciated into the CB6 chemical mechanism species considered in the CAMx simulation (Yarwood et al. 2010). In line with SSP2-4.5 scenario, future emissions were estimated according to Sá et al. (2015) approach and considering the emission projections from the Portuguese roadmap for carbon neutrality (Monjardino et al. 2019), where the average emission reduction considered was: 70% for CO; 15% for NH_3; 68% for NOx; 27% for NMVOC; 33% for PM10; 38% for PM2.5; and 35% for SOx. Note that these are average emission reduction values and that they can differ depending on the source activity considered.

Health impact assessment

According to the methodology described in Soares et al. (2019), which is usually applied by EEA in their annual assessments, long-term health impacts of PM2.5, NO_2 and O_3 exposures were estimated, considering the CAMx concentrations by grid cell and pollutant, together with population data stratified by age and sex (INE 2021). Due to the recent update of the WHO guidelines, for the relative risk (RR) estimation, two different sets of concentration-response functions (CRF) methodologies were used: (i) Jerrett et al. (2009) for O_3 and Hoek et al. (2013) for PM2.5 and NO_2, according to the recommendations of the HRAPIE (WHO 2013a) and REVIHAAP (WHO 2013b) projects; and (ii) Chen and Hoek (2020) for PM2.5 and Huangfu and Atkinson (2020) for O_3 and NO_2, according to the recommendations of WHO air quality guidelines (WHO 2021). Table 36 presents detailed information on the CRFs used.

Table 36. CRF used according to the WHO (2013a, b) and WHO (2021) recommendations.

Pollutant metric	Health outcome	RR (95% CI) per 10 µg.m^{-3}		Range of concentration		Source of health data
		WHO 2013	WHO 2021	WHO 2013	WHO 2021	
PM2.5, annual mean	Mortality, all-cause (natural), age 30+ years	1.062 [1.040; 1.083]	1.08 [1.06; 1.09]	All	> 5 µg.m^{-3}	European mortality database (WHO 2022b), ICD-10 codes A-R
NO_2, annual mean	Mortality, all-cause (natural), age 30+ years	1.055 [1.031; 1.080]	1.02 [1.01; 1.04]	> 20 µg.m^{-3}	> 10 µg.m^{-3}	European mortality database (WHO 2022b), ICD-10 codes A-R
O_3, SOMO35	Mortality, respiratory diseases, age 30+ years	1.014 [1.005; 1.024]	1.01 [1.00; 1.02]	> 70 µg.m^{-3}	> 70 µg.m^{-3}	European mortality database (WHO 2022b), ICD-10 codes J00-J99

RESULTS

Air quality characterization

The differences between the WRF-CAMx modelling results for the mid-term future climate and the reference climate, for the annual mean concentrations of PM2.5 and NO_2, and annual mean of the daily maximum 8 hours average O_3 concentrations, are shown in Figure 115.

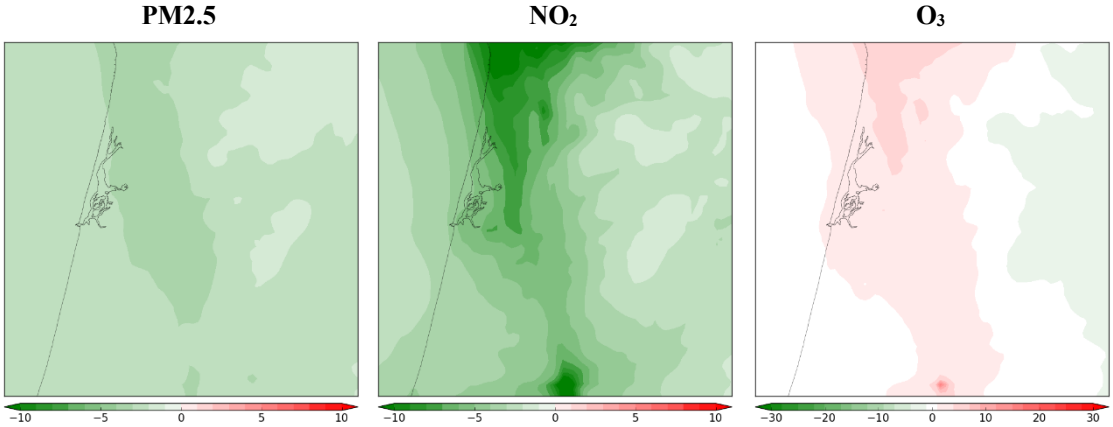

Figure 115. Differences, in µg·m^{-3}, between the mid-term future climate and the reference climate for the annual mean concentrations of PM2.5 and NO_2, and annual mean of the daily maximum 8 hours average O_3 concentrations. Note that negative (positive) values imply air quality improvement (deterioration).

Figure 115 shows a reduction in the Aveiro Region PM2.5 annual concentration values between 1 and 3 µg.m^{-3}. Although a decrease in total annual precipitation is expected in the Aveiro Region (figures not shown), which could lead to an increase in PM2.5 concentrations due to unfavourable conditions of pollutants dispersion and wet deposition, this does not happen due to the reduction of atmospheric

emissions considered for the medium-term future. Also, the 68% of emission reduction projected for NOx, mostly related with transportation and industry sectors, will lead to a reduction, up to 10 $\mu g.m^{-3}$, in the future NO_2 concentrations. In contrast, in the locations with higher NO_2 concentration reductions, an air quality deterioration (up to 3 $\mu g.m^{-3}$) due to O_3 pollution will be expected, mainly due to a temperature and short-wave downward flux increase (figures not shown), but also due to the reduction of NOx values.

The expected decrease in PM2.5 and NO_2 annual concentrations will ensure that in the future there will be no exceedances of the limit values imposed by the Air Quality Directive (EC 2008). Despite the expected increase in future O_3 concentrations, they will be below the defined target values for protection of human health. On the other hand, if the WHO air quality guidelines (WHO 2021) are considered, the future concentrations of PM2.5 and O_3 will be above the recommended air quality guideline levels.

Health impact assessment

Premature deaths, due to PM2.5, NO_2 and O_3 pollution, for the mid-term future climate, the reference climate and the difference between them, considering both WHO (2013a, b) and WHO (2021) recommendations, are shown in Table 37.

Table 37. Premature deaths, due to PM2.5, NO_2 and O_3 pollution, for the reference climate (REF), mid-term future climate (FUT) and the difference (DIFF) between future and reference climates, considering both WHO 2013 and 2021 recommendations. Premature deaths considering the 95% confidence interval are shown in brackets. Note that negative values mean avoided premature deaths.

Mortality indicator	WHO 2013			WHO 2021		
	REF	FUT	DIFF	REF	FUT	DIFF
PM2.5, all-cause (natural), age 30+ years	6945 [3864; 9767]	3359 [1858; 4867]	-3586 [-2006; -4900]	2234 [1579; 2546]	100 [62; 113]	-2134 [-1517; -2433]
NO2, all-cause (natural), age 30+ years	13 [6; 21]	0 [0; 0]	-13 [-6; -21]	241 [83; 560]	0 [0; 0]	-241 [-83; -560]
O_3, respiratory diseases, age 30+ years	0 [0; 0]	0 [0; 0]	0 [0; 0]	0 [0; 0]	0 [0; 0]	0 [0; 0]

Table 37 results point out that, due to the expected air quality improvement for the medium-term future, there will be a reduction in the number of premature deaths due to long-term exposure of PM2.5 and NO_2 concentrations, regardless of the CRF methodology used. Long-term exposure to O_3, for both CRF methodologies and periods considered, will not result in premature deaths. When considering the WHO (2013a, b) CRF methodology, PM2.5 long-term exposure led to 6945 premature deaths in the reference climate and the avoided premature deaths in the future will be around 52%. For NO_2, 13 premature deaths are estimated for the reference climate and no premature deaths are expected for the future. If the WHO (2021) CRF methodology is considered, the avoided premature deaths in the future will be around 96%, when compared with the 2234 premature deaths found in the reference, due to PM2.5 long-term exposure. For NO_2, 241 premature deaths are estimated in the reference climate and, as for the WHO (2013a, b) CRF methodology, no premature deaths are expected for the future. For both PM2.5 and NO_2, premature deaths are mostly obtained near the coastline, where the population density is higher.

CONCLUSIONS

The WRF-CAMx modelling system, followed by the health impact assessment, applied in this work constitutes an added value in this research field, allowing to anticipate the effects of climate change on air quality and evaluate their impacts on human health. Despite the climate change impacts expected for the medium-term future in Aveiro Region, with higher mean temperature and lower total precipitation,

general improvements in air quality are foreseen, mainly due to the reduction in future emissions. Nonetheless, some concerns regarding PM2.5 and O_3 concentrations remain, when the WHO air quality guideline levels are considered. In the future, premature deaths will also continue to occur due to long-term exposure of PM2.5 pollution, even if in a smaller number. With this study it is also possible to conclude that the use of different methodologies for the relative risk estimation, used in the health impact assessment, could substantially impact the number of premature deaths.

ACKNOWLEDGMENTS

Thanks are due to the financial support to the PhD grant of S. Coelho (SFRH/BD/137999/2018), the contract grants of J. Ferreira (2020.00622.CEECIND) and D. Carvalho (CEECIND/01726/2017), and to CESAM (UIDP/50017/2020+ UIDB/50017/2020+ LA/P/0094/2020), to FCT/MCTES through national funds and the co funding by the FEDER, within the PT2020 Partnership Agreement and Compete 2020.

REFERENCES

Chen J, Hoek G (2020) Long-term exposure to PM and all-cause and cause-specific mortality: A systematic review and meta-analysis. Environ Int 143:. doi: 10.1016/J.ENVINT.2020.105974

EC (2008) Directive 2008/50/EC of the European Parliament and of the Council of 21 May 2008 on ambient air quality and cleaner air for Europe. Eur Comm - Off J Eur Union L 152 (EN):

EEA (2021) Air quality in Europe 2021 - European Environmental Agency Report no 15/2021. Luxembourg

EMEP (2017) European monitoring and evaluation programme. http://www.emep.int/.

Emmons LK, Schwantes RH, Orlando JJ, et al (2020) The Chemistry Mechanism in the Community Earth System Model Version 2 (CESM2). J Adv Model Earth Syst 12:e2019MS001882. doi: 10.1029/2019MS001882

ENVIRON (2020) CAMx. User's Guide. Comprehensive air quality model with extensions. Version 7.10

Ferreira J, Lopes D, Rafael S, et al (2020) Modelling air quality levels of regulated metals: limitations and challenges. Environ Sci Pollut Res 27:33916–33928. doi: 10.1007/S11356-020-09645-9/FIGURES/10

Fricko O, Havlik P, Rogelj J, et al (2017) The marker quantification of the Shared Socioeconomic Pathway 2: A middle-of-the-road scenario for the 21st century. Glob Environ Chang 42:251–267. doi: 10.1016/J.GLOENVCHA.2016.06.004

Hoek G, Krishnan RM, Beelen R, et al (2013) Long-term air pollution exposure and cardio-respiratory mortality: A review. Environ Heal A Glob Access Sci Source 12:1–16. doi: 10.1186/1476-069X-12-43/TABLES/6

Huangfu P, Atkinson R (2020) Long-term exposure to NO2 and O3 and all-cause and respiratory mortality: A systematic review and meta-analysis. Environ Int 144:105998. doi: 10.1016/J.ENVINT.2020.105998

INE (2021) População residente (N.º) por Local de residência, Sexo e Grupo etário; Decenal - INE, Recenseamento da população e habitação - Censos 2011. In: INE - Inst. Nac. Estat. https://www.ine.pt/xportal/xmain?xpid=INE&xpgid=ine_indicadores&indOcorrCod=0011166&contexto=bd&selTab=tab2. Accessed 28 Jul 2022

IPCC (2021) Climate Change 2021: The Physical Science Basis. Contribution of Working Group I to the Sixth Assessment Report of the Intergovernmental Panel on Climate Change. Cambridge University Press (in press)

Jerrett M, Burnett RT, Pope CA, et al (2009) Long-Term Ozone Exposure and Mortality. N Engl J Med 360:1085–1095. doi: 10.1056/NEJMOA0803894/SUPPL_FILE/NEJM_JERRETT_1085SA1.PDF

Mauritsen T, Bader J, Becker T, et al (2019) Developments in the MPI-M Earth System Model version 1.2 (MPI-ESM1.2) and Its Response to Increasing CO2. J Adv Model Earth Syst 11:998–1038. doi: 10.1029/2018MS001400

Monjardino J, Dias L, Vale G, et al (2019) Relatório Setorial: Estimativa de poluentes atmosféricos. Trabalhos de base para o Roteiro para a Neutralidade Carbónica 2050. Portugal

Sá E, Ferreira J, Carvalho A, Borrego C (2015) Development of current and future pollutant emissions for Portugal. Atmos Pollut Res 6:849–857. doi: 10.5094/APR.2015.094
Skamarock WC, Klemp JB, Dudhia J, et al (2019) A Description of the Advanced Research WRF Version 4. NCAR Tech. Note NCAR/TN-556+STR. Boulder, Colorado, USA
Soares J, Horálek J, Ortiz AG, et al (2019) ETC/ATNI Report 13/2019: Health Risk Assessment of Air Pollution in Europe. Methodology description and 2017 results. Kjeller, Norway
WHO (2022a) World health statistics 2022: monitoring health for the SDGs, sustainable development goals. World Health Organization, Geneva, Switzerland
WHO (2013a) Health risks of air pollution in Europe – HRAPIE project: Recommendations for concentration–response functions for cost–benefit analysis of particulate matter, ozone and nitrogen dioxide. Copenhagen, Denmark
WHO (2013b) Review of evidence on health aspects of air pollution - REVIHAAP Project, Technical Report
WHO (2021) WHO global air quality guidelines: particulate matter (PM2.5 and PM10), ozone, nitrogen dioxide, sulfur dioxide and carbon monoxide
WHO (2022b) WHO Mortality Database. https://www.who.int/data/data-collection-tools/who-mortality-database. Accessed 28 May 2022
Yarwood G, Jung J, Whitten GZ, et al (2010) Updates to the carbon bond mechanism for version 6 (CB6). In: 9th Annual CMAS Conference. Chapel Hill, NC

21st International Conference on
Harmonisation within Atmospheric Dispersion Modelling for Regulatory Purposes
27-30 September 2022, Aveiro, Portugal

ROLE OF EMISSION INVENTORIES AND DIFFERENTIAL TOXICITY APPROACH IN MODELLING OF PM2.5 AND ASSOCIATED HEALTH IMPACTS

Paisi Niki [1], Kushta Jonilda[1], Violaris Angelos[1], Denier Van Der Gon Hugo[2], Lelieveld Jos[3]

[1]Climate and Atmosphere Research Centre (CARE-C), The Cyprus Institute, Nicosia Cyprus
[2] Netherlands Organision for Applied Scientific Research TNO, Netherlands
[3]Max Planck Institute for Chemistry, Mainz Germany

ABSTRACT

Air pollution from fine particulate matter (PM2.5) poses a major environmental health risk associated with morbidity and excess mortality. In Europe, despite efforts to minimize air pollution levels, recommended WHO safe limits for health are exceeded in many regions. Since observational data of air pollutant concentrations are spatially incomplete, regional air quality modeling is used to simulate ambient pollutant levels and associated health impacts. Use of atmospheric modelling systems is also necessary to investigate alternative scenarios and (expected) impacts of emissions reduction scenarios, air quality action plans and population development. Health impacts are calculated on the basis of annual mean PM2.5 concentrations, country level baseline mortality rates, population data and exposure – response functions. Estimates of excess mortality for air pollution related diseases (ischemic heart disease, cerebrovascular disease from ischaemic and haemorrhagic stroke, chronic obstructive pulmonary disease, lung cancer, acute lower respiratory infections and other non-communicative diseases), are typically calculated by assuming that all PM2.5 components have the same level of toxicity. In this study we access the accuracy of air quality models and the uncertainties associated with model configuration and emission inventory options with a focus on black and organic carbon aerosol over Europe. Organic aerosols are often underestimated in models related to secondary organic aerosol process parameterizations, the pathways of which are not fully known and are not all included in models. They are also reported to be more toxic than inorganic species, an approach referred to as differential toxicity, that we deploy in this study. With the utilization of the Weather Research and Forecasting model, coupled with chemistry (WRF-CHEM), we simulate the annual mean concentration of PM2.5 and the contribution of organic components over Europe. EDGARv.5 and CAMS-REGv4 emission inventories are assessed and the fraction of organic aerosols in total PM2.5 is highlighted using both similar and higher toxicity than other components. The results can contribute to more effective emission reduction strategies targeting at specific components in parallel with total fine particulate matter.

KEY WORDS: **EMISSIONS, WRF-CHEM, PM2.5, BC, OC, HEALTH IMPACTS**.

INTRODUCTION

Particulate matter with an aerodynamic diameter of less than 2.5μm (PM2.5) has been widely studied for its impacts on human health. The Global Burden of Disease study (2015) estimates that exposure to outdoor fine particulate matter is the fifth leading risk factor of death worldwide, accounting for 4.2 million deaths in 2015 (Tong, 2019, Cohen et al., 2017). Particular sub-components of PM2.5, such as organics have received great attention from the scientific community. These include Black Carbon (BC) and Organic Carbon (OC) which are mostly emitted during the incomplete combustion of organic material such as biomass and diesel fuels (Raga et al., 2018). There is growing evidence from epidemiological and toxicological studies that these particles are highly hazardous for human health, mostly due to their very small size that can not only deeply penetrate into the respiratory system, but also, carry toxic substances (e.g. PAHs, metals) that can cause oxidative stress and cell inflammation (Janssen et al., 2012). Thus it is likely that these sub-components are causing disproportional harm and monitoring and mitigating their atmospheric levels is an issue of high importance.

Chemical Transport Models are potentially powerful tools to simulate air pollution considering the complexity of the atmosphere and able to support emission reduction strategies (Thunis et al., 2022). However, there are several challenges when it comes to PM2.5 modeling. Several studies report that organic aerosols (OAs) are often underestimated by chemical transport models (Tuccella et al., 2012, Forkel et al., 2015, Berger et al., 2016). OAs are derived from multiple sources both primary (POA) (e.g. directly emitted from traffic emissions, combustion sources) and secondary (SOA) that are formed through gas-phase oxidation reactions of volatile organic compounds (VOCs) precursors (Li et al., 2021). Their complex and diverse formation pathways are not yet fully known, thus their representation in models may be incomplete. Chemical transport models are highly dependent on their input data (Thunis et al., 2021). Previous studies report that the WRF-Chem bias depends on factors such as the emission inventory, the horizontal resolution and parameterizations of the PBL turbulence (Tuccella et al., 2012). The pollutant emission fluxes are found to be a determining factor regarding the ability of a model to successfully simulate the concentrations of atmospheric constituents (Georgiou et al., 2020). These challenges can further affect air pollution studies and impact the associated socioeconomic, environmental and health impact estimations. For example, uncertainties due to emissions can account for an interval of 1.1 – 3.4 million excess deaths, deviating from their estimated 2.1 million total premature deaths per year globally (Crippa et al., 2019). In this study, we use the WRF-Chem model to simulate the atmospheric concentration of PM2.5 and their organic components over Europe. We focus on primary organic aerosols (POA) and anthropogenic secondary organic aerosols (aSOA) which are probably more important for human health outcomes than inorganic fine particles (Chowdhury et al., 2022, Daellenbach et al., 2020). Since organic aerosols are often prone to model uncertainties, we aim to find the model configuration which results in the least uncertainty in their concentration and calculate the associated excess mortality taking into account their higher toxicity.

METHODOLOGY

Model simulations are presented in Table 1. The RACM chemical option coupled with MADE-VBS aerosol scheme is used in all simulations. The RACM includes 57 chemical species and 158 gas-phase reactions (Tuccella et al., 2012). The aerosol module Modal Aerosol Dynamics Model for Europe (MADE) is for the inorganic fraction and the Volatility Basis Set (VBS) is used to calculate SOA formation. VBS acknowledges the semi-volatile nature of OA and studies suggest that is has significantly improved the model's ability to reproduce observed OA concentrations (Bergström et al., 2012, Kryza et al., 2020). A sensitivity test is performed (S_RACM_x2) where we double the anthropogenic NMVOC emissions, with the aim to increase SOA formation in the model and thus total OC concentration. We test two emission inventories EDGARv5 and CAMS-REG-AP-v4 and compare the resulting annual mean biases for PM2.5, BC and OC.

Table 38. Description of model simulations

Simulation	Simulation acronym	Group	Aim
A	S_RACM_x1	Group 1	To improve SOA formation by increasing anthropogenic NMVOC emissions.
B	S_RACM_x2		
1	S_EDGAR	Group 2	To investigate the impact of anthropogenic emissions on PM2.5 and OA concentration using also FDDA grid nudging
2	S_CAMS		

Excess mortality calculations

Based on the simulation with the least annual mean biases we obtain the annual means of PM2.5, BC, primary OC and aSOA to calculate the hazard ratios (HR) and excess mortality using the following equations.

$$HR\,(z) = exp\left(\theta \times log\left(\left(\frac{z}{a}\right)+1\right) / \left(1+exp\left(-\frac{z-\mu}{\nu}\right)\right)\right) \quad (1)$$

$$z = \max\,(0, PM2.5 - 2.4\mu g/m3)$$

where, z is the annual mean PM2.5 concentration and 2.4μg/m3 is the counterfactual concentration below which no health risk is assumed (Burnett et al., 2018). θ, a, μ, ν are the parameters of the fit for the model.

$$Premature\ Mortality_{PM2.5} = BMR \times POP \times \mathrm{HR} - 1/\mathrm{HR} \quad (2)$$

$$Premature\ Mortality_{PM2.5\ without\ POA+aSOA} = BMR \times POP \times \mathrm{HR}' - \frac{1}{\mathrm{HR}'} \quad (3)$$

$$Premature\ Mortality_{POA+aSOA} = Premature\ Mortality_{PM2.5} - Premature\ Mortality_{PM2.5\ without\ POA+aSOA} \quad (4)$$

We estimate excess mortality by firstly using total PM2.5 concentration in equation 2. Based on the same equation, we also calculate the excess mortality by using PM2.5 concentration after excluding POA+aSOA in HR'. The modified version of the initial equation is referred here as equation 3. The difference between the two mortality estimates provides the fraction of excess mortality only due to POA+aSOA (equation 4). We then assume that POA+aSOA are twice more toxic than other inorganic PM2.5 and use two times their concentration to repeat the above equations.

RESULTS

All simulations result in underestimated OC compared to station observations. When anthropogenic NMVOCs are doubled in S_RACM_x2, the OC bias reduces from -2 μg/m^3 to -1.46 μg/m^3 and is in better agreement with observations (Figure1), suggesting that SOA formation is underestimated in the model. The difference between S_RACM_x1 and S_EDGAR is the application of four dimensional data assimilation (FDDA) grid nuding that shows an improved model performance. Both PM2.5 and OC simulation is improved, with annual mean biases of -3.9 μg/m^3 and -2.9 μg/m^3 respectively for PM2.5 and -2 μg/m^3 and -1.32 μg/m^3 respectively for OC. S_EDGAR and S_CAMS result in OC annual MB of -1.32 μg/m^3 and -2 μg/m^3 respectively, however S_CAMS results in higher concentration of BC and PM2.5 compared to observations.

Table 1. Annual mean biases of PM2.5, BC and total OC from each simulation.

		S_ RACM_X1	**S_ RACM_X2**	**S_ EDGAR**	**S_ CAMS**
PM2.5	MB (μg/m3)	-3.93	-2.36	-2.99	+3.93
BC	MB (μg/m3)	-0.12	-0.15	-0.12	+4
OC	MB (μg/m3)	-2.01	-1.46	-1.32	-2.03

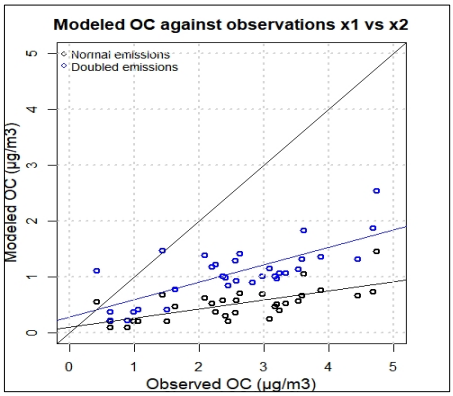

Figure 1: Comparison of modeled total OC with observations from S_EDGAR (black) and S_EDGAR_2 (blue).

We chose S_EDGAR to calculate excess mortality from PM2.5 exposure in Europe and the the EU-27. We calculate that 416×10^3 (95% Confidence Interval CI: 342×10^3 - 489×10^3) excess deaths are attributed to PM2.5 exposure in the EU-27, which is equal to 129 excess deaths per 100K persons annually. About 9% is attributed to POA+aSOA fraction assuming equal toxicity, whereas their contribution can increase up to 18% when we assume doubled toxicity. This is equal to 37×10^3 (CI: 31×10^3 - 43×10^3) and 78×10^3 (CI: 65×10^3 - 91×10^3) excess deaths annually assuming equal and doubled toxicity respectively.

Table 2. Excess Deaths (mean + 95% CI) due to PM2.5 and POA+aSOA assuming equal and doubled toxicity.

		European Region	**EU-27**
PM2.5	Absolute	683000 (561000-805000)	416000 (342000-489000)
	Normalized	127 per 100K	129 per 100K
POA + aSOA (equal toxicity)	Absolute	61000 (51000-71000) (~9%)	37000 (31000-43000) (~9%)
	Normalized	11 per 100K persons	11 per 100K persons
POA + aSOA (doubled toxicity)	Absolute	128000 (106000-150000) (~18.7%)	78000 (65000-91000) ~18%
	Normalized	23 per 100K persons	24 per 100K persons

With our differential toxicity approach, we attribute 40×10^3 additional excess deaths per year to POA+aSOA fraction in the EU-27. These numbers are masked by the unspeciated PM2.5 mass concentration when equal toxicity is assumed. Here we want to highlight that the health benefit with respect to avoidable excess deaths of an emission reduction measure can be much more than what is thought. Air pollution mitigation measures that focus on organic-rich emission sources (e.g. residential combustion and traffic sectors) can result in higher health benefit than policies that do not discriminate for different PM2.5.

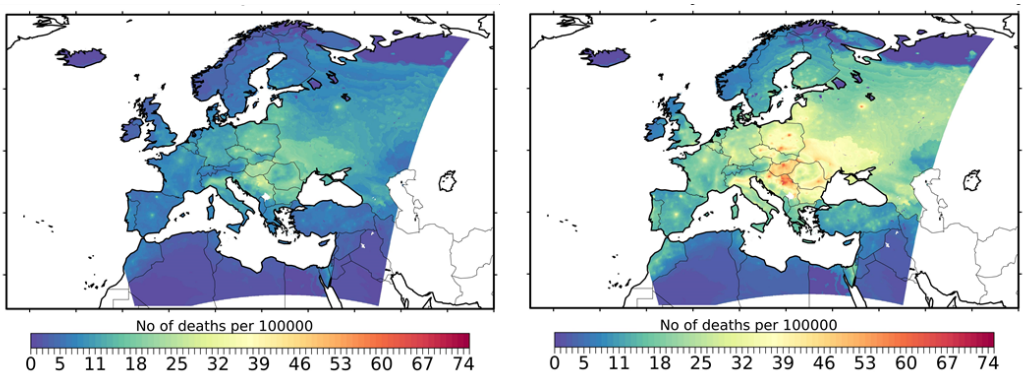

Figure 2: Excess mortality due POA+aSOA assuming equal (left panel) and doubled (right panel) toxicity.

Furthermore, south-eastern (e.g. Hungary, Romania, Croatia) and some central (e.g. Czech Republic, Poland) EU countries are facing increased health burden due to POA+aSOA exposure (Figure 2). In these countries we estimate that 35 – 50 per 100K population die prematurely from POA+aSOA per year (assuming doubled toxicity). Emissions of hazardous organic aerosols from combustion sources dominate these regions. Although toxicity is more relevant for acute health effects, it is important to mitigate their emissions with source-specific emission reduction measures to improve air quality in the surrounding regions. Finally, to better assess the model's performance, future simulations will be performed with combinations of different emission data from the two emission inventories.

REFERENCES

Berger, A., Barbet, C., Leriche, M., Deguillaume, L., Mari, C., Chaumerliac, N., Bègue, N., Tulet, P., Gazen, D., & Escobar, J., 2016: Evaluation of Meso-NH and WRF/CHEM simulated gas and aerosol chemistry over Europe based on hourly observations. *Atmospheric Research, 176–177, 43–63.*

Burnett R., Chen H., Szyszkowicz M., Fann N., Hubbell B., Pope A., Apte J., Brauer M., Cohen A., Weichenthal S., Coggins J., Di Q., Brunekreef B., Frostad J, Lim S., Walker K., Spadaro J. Thurston G. D., Hayes R. B., Lim C., Turner M., Jerret M., Krewski, S. J. V., 2018: Global estimates of mortality associated with longterm exposure to outdoor fine particulate matter. *Proceedings of the National Academy of Sciences of the United States of America, 115(38), 9592–9597.*

Cohen, A. J., Brauer, M., Burnett, R., Anderson, H. R., Frostad, J., Estep, K., Balakrishnan, K., Brunekreef, B., Dandona, L., Dandona, R., Feigin, V., Freedman, G., Hubbell, B., Jobling, A., Kan, H., Knibbs, L., Liu, Y., Martin, R., Morawska, L., Forouzanfar, M. H., 2017: Estimates and 25-year trends of the global burden of disease attributable to ambient air pollution: an analysis of data from the Global Burden of Diseases Study*, 2015: The Lancet, 389(10082), 1907–1918.*

Chowdhury, S., A. Pozzer, A. Haines, K. Klingmüller, T. Münzel, P. Paasonen, A. Sharma, C. Venkataraman and J. Lelieveld (2022) Global health burden of ambient PM2.5 and the role of anthropogenic black carbon and organic aerosols*. Environ. Int. 159, 107020.*

Crippa, M., Janssens-Maenhout, G., Guizzardi, D., Van Dingenen, R., & Dentener, F., 2019: Contribution and uncertainty of sectorial and regional emissions to regional and global PM2.5 health impacts*. Atmospheric Chemistry and Physics, 19(7), 5165–5186.*

Daellenbach, K. R., Uzu, G., Jiang, J., Cassagnes, L.-E., Leni, Z., Vlachou, A., Stefenelli, G., Canonaco, F., Weber, S., Segers, A., Kuenen, J. J. P., Schaap, M., Favez, O., Albinet, A., Aksoyoglu, S., Dommen, J., Baltensperger, U., Geiser, M., Haddad, I. El, Prévôt, A. S. H., 2020: Sources of particulate-matter air pollution and its oxidative potential in Europe. Nature, 587(7834), 414–419.

Forkel, R., Balzarini, A., Baró, R., Bianconi, R., Curci, G., Jiménez-Guerrero, P., Hirtl, M., Honzak, L., Lorenz, C., Im, U., Pérez, J. L., Pirovano, G., San José, R., Tuccella, P., Werhahn, J., & Žabkar, R., 2015: Analysis of the WRF-Chem contributions to AQMEII phase2 with respect to aerosol radiative feedbacks on meteorology and pollutant distributions*. Atmospheric Environment, 115, 630–645.*

Georgiou, G. K., Kushta, J., Christoudias, T., Proestos, Y., & Lelieveld, J., 2020: Air quality modelling over the Eastern Mediterranean: Seasonal sensitivity to anthropogenic emissions. *Atmospheric Environment.*

Janssen, N. A., Gerlofs-Nijland, M. E., Lanki, T., Salonen, R. O., Cassee, F., Hoek, G., Ischer, P., Brunekreef, B., & Krzyzanowski, M., 2012: Health effects of black carbon. *World Health Organization - Regional Office for Europe.*

Kryza, M., Werner, M., Dudek, J., & Dore, A. J., 2020: *The effect of emission inventory on modelling of seasonal exposure metrics of particulate matter and ozone with the WRF-chem model for Poland. Sustainability (Switzerland)*, 12(13), 1–16.

Lelieveld, J., Evans, J. S., Fnais, M., Giannadaki, D., & Pozzer, A., 2015. The contribution of outdoor air pollution sources to premature mortality on a global scale. *Nature, 525 (7569), 367–371.*

Li, Z., Zhou, R., Li, Y., Chen, M., Wang, Y., Huang, T., Yi, Y., Hou, Z., Meng, J., & Yan, L., 2021: Characteristics and Sources of Organic Aerosol Markers in PM2.5. *Aerosol and Air Quality Research, 21(9), 210180.*

Raga, G. B., Kuylenstierna, J., Environment Institute, S., Dore, C., Claxton, R., & Shindell, D., 2018: Addressing Black Carbon Emission Inventories. A report by the Climate And Clean Air Coalition Scientific Advisory Panel.

Thunis, P., Clappier, A., Pisoni, E., Bessagnet, B., Kuenen, J., Guevara, M., & Lopez-aparicio, S., 2022: A multi-pollutant and multi-sectorial approach to screening the consistency of emission inventories. *5271–5286. Geoscientific Model Development.*

Thunis, P., Crippa, M., Cuvelier, C., Guizzardi, D., de Meij, A., Oreggioni, G., & Pisoni, E., 2021: Sensitivity of air quality modelling to different emission inventories: A case study over Europe. *Atmospheric Environment: X, 10, 100111.*

Tong, S., 2019: Air pollution and disease burden. The Lancet Planetary Health, 3(2), e49–e50.

Tuccella, P., Curci, G., Visconti, G., Bessagnet, B., Menut, L., & Park, R. J., 2012: Modeling of gas and aerosol with WRF/Chem over Europe: Evaluation and sensitivity study. *Journal of Geophysical Research Atmospheres, 117(3).*

21st International Conference on
Harmonisation within Atmospheric Dispersion Modelling for Regulatory Purposes
27-30 September 2022, Aveiro, Portugal

HEALTH IMPACT BENEFITS OF INCREASED RENEWABLE ENERGY USE IN THE SPANISH ROAD TRANSPORT SECTOR

Ana R. Gamarra[1], Carmen Lago[1], Yolanda Lechón[1], Marta G. Vivanco[2], Mark R. Theobald[2], Victoria Gil[2], Juan Luis Garrido[2], José Luis Santiago[2], Fernando Martín[2], Alejandro Rodríguez-Sánchez[2] and Eugenio Sánchez[3]

[1]Energy Systems Analysis Unit, Energy Department, CIEMAT, Madrid, Spain
[2]Atmospheric Modelling Unit, Environment Department, CIEMAT, Madrid, Spain
[3]Application & Computer Systems Development Unit, Technology Department, CIEMAT, Madrid, Spain

Abstract: This work assesses the health impact in terms of the reduction in premature deaths associated with improvements in air quality resulting from dual-target strategies for mitigating climate change and reducing human health impacts of the road transport sector by 2030 in Spain. The impact on air quality of increased biofuel use and increased penetration of electric cars was assessed by air quality modelling (Vivanco et al. (presented at this conference)). From the estimates of population exposure to NO_2, particulate matter (PM) and O_3, the associated avoidable mortality and external costs compared to the baseline scenario without measures were calculated. The results show that electric car penetration provided the greatest benefits, even when taking into account emissions due to additional electricity demand.

KEY WORDS: **HEALTH IMPACT ASSESSMENT; AIR POLLUTION MODELLING; EXTERNAL COSTS; RENEWABLE MOBILITY; ENVIRONMENTAL CO-BENEFITS.**

INTRODUCTION

Transport remains one of the main sources of environmental impacts in Europe, accounting for more than a fifth of greenhouse gas emissions (GHG), most of which are generated by road transport (71.7%) (European Environment Agency, 2019). In addition to carbon emissions, road traffic releases other pollutants that affect human health. Road transport, and specifically internal combustion engine vehicles, emits many pollutants to the air, such as carbon dioxide (CO_2), sulfur dioxide (SO_2), oxides of nitrogen (NOx), particulate matter of various size fractions (PM_{10}, $PM_{2.5}$, and ultrafine), non-methane volatile organic compounds (NMVOCs)(Mcadam & Aubin, 2015), among many others.

The development of coherent national strategies aimed to ensure co-benefits that achieve both environmental and social well-being policies is one pathway to maximize the highest potential well-being. In Spain, the integrated National Energy and Climate Plan (NECP) (MITECO, 2019) and the 1st National Air Pollution Control Program (NAPCP) (MITERD, 2019) provide a framework for this in the horizon 2030. There are synergies between air pollution control and climate change mitigation and climate change and air pollution reduction strategies have relevant co-benefits in terms of costs (Sampedro et al., 2020) but adverse side-effects of mitigation have also been identified (Edenhofer et al., 2014).

In recent years, apart from planning and infrastructural measures (such as Zero emission areas in cities and public transport development), progress has been made in heavy duty transportation and passenger mobility by road with policies aimed to increase of use of natural gas electric vehicles (EV), and to a lesser extent in other alternative advanced fuels and bio-fuels.

The objective of this study is to assess the health impact and associated external costs (ExC) of selected measures for the decarbonization of the transport sector in Spain, namely the blending of biofuels and the use of electric vehicles, by estimating health impacts and the associated ExC. A baseline of the year 2017 and future scenarios for the year 2030 are used for the assessment of individual measures.

MATERIALS AND METHODS

Air quality modeling has been used in combination with health impact assessment (HIA) to estimate the effect on premature mortality of measures implementation for increasing renewable energy in the transport sector. Air quality modelling and results of the scenario assessment are described in Gamarra et al. (2021).

Four scenarios with a substantial transformation of road transport in Spain have been assessed for the year 2030: two for biofuels and two for electric cars. The measures have been selected among the proposed in the NAPCP. The two scenarios for biofuels assess an ambitious increase in biofuel blending in fuels for petrol vehicles only (BioEt) and all petrol and diesel vehicles (Biof), respectively. The other two scenarios consider the total substitution of the current fleet of fossil-fuel passenger cars by EV (except the baseline hybrid fleet). One scenario (EC) does not take into account the additional emissions caused by the increased electricity consumption while the other (EC-E) does. This scenario also includes more renewable electricity generation by 2030. Table 39 provides a brief description of the selected scenarios and measures.

Table 39. Summary table of scenarios and measures.

Scenario		Description of measures
Biofuels	BioEt	Renovation of petrol passenger fleet (cars and motorcycles) to flexible–fuel vehicles and the use of E85 petrol (85% bioethanol / 15% petrol mixture) by the year 2030. Other petrol vehicles: increase bioethanol content from E5 (5%) to E10 (10%).
	Biof	Increased biofuel use by two combined measures: - Increased bioethanol use in petrol vehicles (Same as Scenario BioEt) - Increased biodiesel use: Use of biodiesel (B20; 20% biodiesel) in diesel vehicles (except motorcycles).
Electric car	EC	Promotion of electromobility: Current fleet of passenger cars (except hybrids) substituted by electric cars. The scenario does not include the additional electricity generation.
	EC-E	Promotion of electromobility: Current fleet of passenger cars (except hybrids) replaced by electric cars. The scenario includes the additional electricity generation, considering the share of technologies in the power mix for 2030 (considered in NECP) and the change in the absolute production by renewables and fossil technologies.

Health impact assessment (HIA)

The impacts on mortality were estimated using the proposed concentration-response functions (CRF) for key pollutants to be included in cost-benefit analysis supporting air quality policy by the Health Risks of Air Pollution in Europe (HRAPIE) project (Holland, 2014; WHO, 2013). The mortality impact expresses the change in the number of premature deaths associated with a change in pollutant exposure with respect to the baseline (2017). The key pollutants are particulate matter (PM), nitrogen dioxide (NO_2), and ozone (O_3).

The area of study is the Spanish territory of the Iberian Peninsula and Balearic Islands. A GIS model was used for the HIA. For HIA input data, official data sources were used by age and settlements and estimated rate of growth for the population projected to 2030. Health data on baseline mortality rates by age and regional location at NUTS3 level corresponding to total non-accidental causes by age (ICD, codes A00-R99) were obtained from the Instituto Nacional de Estadística (INE) database. Finally, ExC

associated to mortality using the Value of Statistical Life (VSL)(Schucht et al., 2015). The VSL is a method of valuing risk to life which is derived from the trade-offs people are willing to make between fatality risk and wealth. We used the proposed values for OECD, adjusted according to country and time.

RESULTS AND DISCUSSION

The results of avoided mortality (Table 40) show that the scenarios that most reduce NO_2 (EC and EC-E) lead to the highest reduction in premature deaths. The difference between the avoided mortality for the EC scenarios is small, with the scenario that includes the additional power demand (EC-E) reducing deaths the most. This is mainly due to the expected decarbonization of the electricity mix in 2030, since the additional demand was added to a cleaner power system (without coal based power production, less fossil fuels and more renewables).

Interestingly, a reduction in total NOx emissions of 10.4% in the EC scenario reduces premature deaths due to exposure to NO_2 by 5070 (long-term plus acute avoided mortality) whereas the larger reduction of NOx emissions in the EC-E scenario (19.6%) only leads to additional reduction of 82 premature deaths (4839 plus 313 premature deaths). This is because the additional reduction in NOx emissions (from fossil-fuel electricity generation) is very localized in an area with a low population density, and so the population that benefits from these reductions is smaller. The reduction in mortality due to $PM_{2.5}$ exposure is also greater for the EC-E scenario. In contrast to the EC scenario, this reduction is not due to decreased $PM_{2.5}$ emissions but is the result of the large reductions in SOx emissions (less secondary particle formation), as described in (Gamarra et al., 2021) . The change in mortality due to the adoption of electric cars is a reduction of 14.4%-15.9%, with a large contribution from the reduction of NO_2 concentrations.

The impact reductions of the biofuel measure scenarios are much lower than the EC scenarios as a result of smaller emission reductions. In the BioEt scenario, the increased particle formation due to the larger NH_3 emissions increases mortality from exposure to PM; however, this increase is more than compensated for by the reduction in mortality due to exposure to NO_2 and O_3, leading to a net benefit. The Biof scenario also has a net benefit in terms of avoided premature deaths, mostly due to a reduction in exposure to PM.

Table 40. Number of avoided premature deaths. NO2ac: acute mortality; PM10inf:infant mortality.

	BioEt	**Biof**	**EC**	**EC-E**
NO_2	331	18	4,771	4,839
NO_2ac	19	1	299	313
$PM_{2.5}$	−123	110	1,387	1,931
PM_{10}inf	−0.1	0.14	1.14	1.5
O_3	5	5	8	28
Total	231	133	6,467	7,113

With regards to the spatial distribution of impacts, the change in mortality impacts with respect to the 2017 baseline is irregularly distributed throughout the domain (Figure 116).

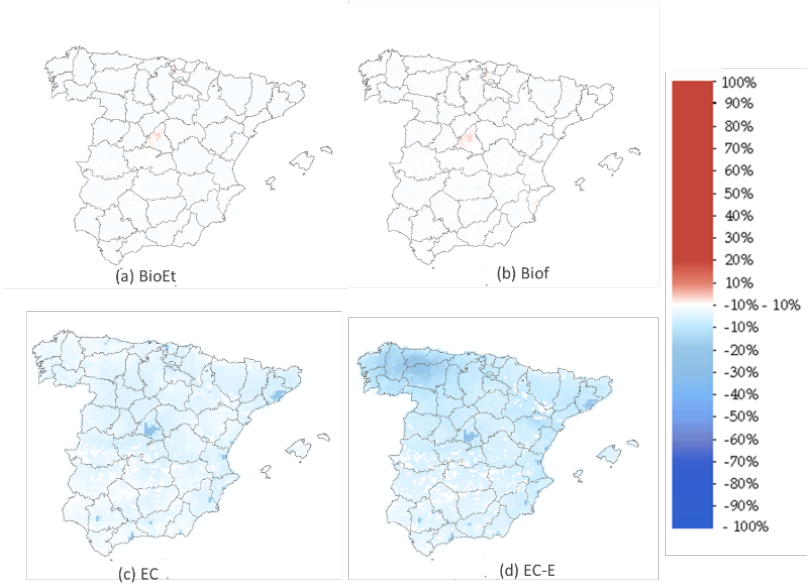

Figure 116. Spatial distribution of the relative change in mortality attributable to air pollutant emissions for the four scenarios: a) BioEt; b) Biof; c) EC and d) EC-E, with respect to the reference scenario.

Avoided external costs

The external costs of premature deaths due to the improvement (positive values) or worsening of air quality (negative values) with respect to the baseline are presented in Table 41 and Figure 2.

Table 41. Avoided ExC associated with the health impacts of air pollution with respect to the baseline (MEur2019).

	BioEt	**Biof**	**EC**	**EC-E**
NO_2	1,323	71	19,077	19,347
NO_2ac	75	2	1,197	1252
$PM_{2.5}$	−493	439	5,546	7722
PM_{10}inf	−1	1	8	10
O_3	19	20	32	113
Total	923	533	25,860	28,444

The assessed scenarios with measures for increased renewable energy for mobility are expected to offer a co-benefit for the pathway to sustainability. In order to estimate the co-benefits between ambient air impacts on health and GHG mitigation, the global warming potential as well as the ExC associated with the principal GHGs (CO_2, NO_2 and CH_4) have been estimated. Life Cycle Assessment was used to calculate the Well-to-wheel GHG emissions production of fuel (Well-to-tank, WTT), as well as the GHG emissions from the combustion stage for fuels (Tank-to-wheel, TTW). In EC-E the life cycle GHGs of the power mix in Spain for 2030 (NECP (MITECO, 2019)) were included. Finally, the ExC associated with the GHG emissions have been calculated using the damage factors developed in the CASES project. Details on sources can be found in Gamarra et al. (2021).

Figure 117 shows the avoided costs associated with air pollution (top) and GHG emissions (bottom) with respect to the baseline of the scenarios BioEt, Biof and the EC-E. In contrast to the impact on mortality due to air pollution, the benefits of both biofuel measures are positive and closer to the benefits from EC-E. In the case of biofuels, the impact of reducing GHG is positive and even compensates the ExC associated with health impacts.

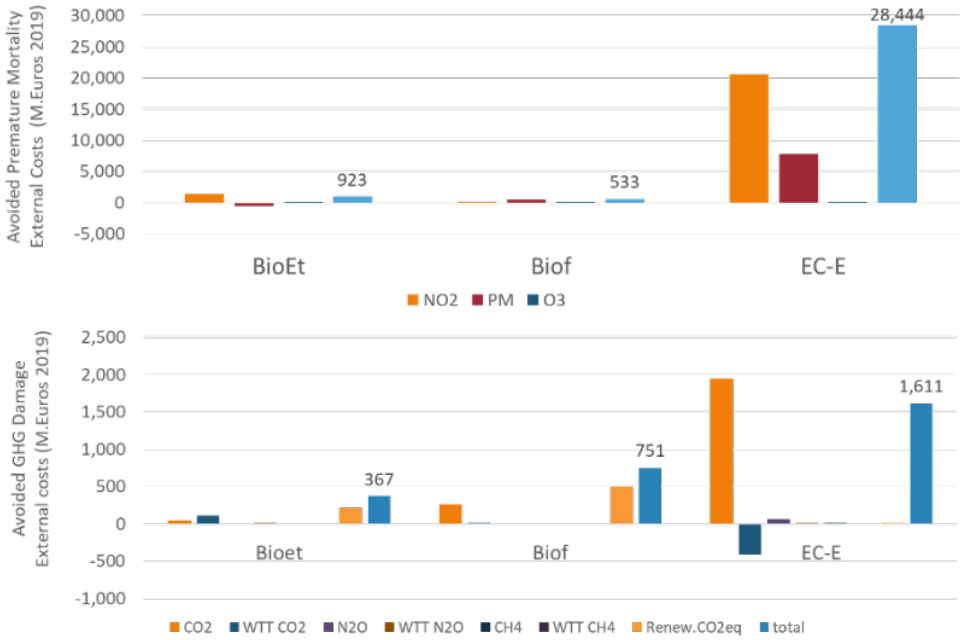

Figure 117. Avoided external costs due to changes in human exposure to air pollution (top) and due to changes in GHG emissions for the three scenarios:Bioet, Biof and EC-E (EC has been excluded since it does not consider the same scope as the other scenarios).

CONCLUSIONS

In this study we have assessed the impact on air quality and the associated avoided mortality of four policy measures to decarbonize the Spanish transport sector based on biofuel blending and the adoption of EV.

The results of the HIA show a great benefit associated with the scenario that maximizes electric car use (EC and EC-E), and an overall negative impact in the biofuel scenario (Biof). Comparing EC and EC-E, the increase in electricity production required by the operation of EC-E does not preclude the benefits of this measure. With respect to the Biofuel measures, the BioEt scenario reduces mortality (and ExC), while the Biof scenario increases mortality mainly due to higher $PM_{2.5}$ emissions with impacts expected in the most populated urban areas. However, it is the NOx emission reductions that lead to the largest reductions in premature deaths.

From the point of view co-benefits, the estimated GHG emissions and associated climate-induced damages indicate that the measures proposed in all scenarios can help to reduce externalities, even in the Biof scenario. However, the design of policies for road transport should optimize the benefits taking special care on where and how biofuels can contribute to a more sustainable road sector. It would be better to prioritize the adoption of electric vehicles in those urban areas where biofuel measures lead to the largest increase in mortality, and foster biofuel use in areas with lower population density.

ACKNOWLEDGEMENTS

This study is part of the Retos-AIRE project (Grant: RTI2018-099138-B-I00) funded by MCIN/AEI/10.13039/501100011033 and by ERDF A way of making Europe.

REFERENCES

Edenhofer, O., Sokona, Y., Minx, J. C., Farahani, E., Kadner, S., Seyboth, K., Adler, A., Baum, I., Brunner, S., Kriemann, B., Savolainen Web Manager Steffen Schlömer, J., von Stechow, C., & Zwickel Senior Scientist, T., 2014: IPCC. Mitigation of Climate Change. Working Group III Contribution to the Fifth

Assessment Report of the Intergovernmental Panel on Climate Change. www.cambridge.org
European Environment Agency, 2019: Transport. EEA. https://www.eea.europa.eu/themes/transport/
Gamarra, A. R., Lechón, Y., Vivanco, M. G., Theobald, M. R., Lago, C., Sánchez, E., Santiago, J. L., Garrido, J. L., Martín, F., Gil, V., & Rodríguez-Sánchez, A. , 2021: . Avoided Mortality Associated with Improved Air Quality from an Increase in Renewable Energy in the Spanish Transport Sector: Use of Biofuels and the Adoption of the Electric Car. Atmosphere 2021, Vol. 12, Page 1603, 12, (12), 1603. https://doi.org/10.3390/ATMOS12121603
Holland, M. , 2014:. Implementation of the HRAPIE Recommendations for European Air Pollution CBA work. http://ec.europa.eu/environment/air/pdf/CBA HRAPIE implement.pdf
Mcadam, K., & Aubin, P. L. , 2015:. Effective Interventions to Mitigate Adverse Human Health Effects from Transportation-Related Air and Noise Pollution A Rapid Review.
MITECO. , 2019:. Plan Nacional Integrado de Energía y Clima 2021-2030- Ministerio para la Transición Ecológica. https://www.miteco.gob.es/images/es/pnieccompleto_tcm30-508410.pdf
MITERD. , 2019:. I Programa Nacional de Control de la Contaminación Atmosférica. Ministerio para la Transición Ecológica. Dirección General de Biodiversidad y Calidad Ambiental. Subdirección General de Calidad del Aire y Medio Ambiente Industrial.
OECD. , 2016:. The Economic Consequences of Outdoor Air Pollution. In The Economic Consequences of Outdoor Air Pollution. OECD. https://doi.org/10.1787/9789264257474-en
Sampedro, J., Smith, S. J., Arto, I., González-Eguino, M., Markandya, A., Mulvaney, K. M., Pizarro-Irizar, C., & Van Dingenen, R. , 2020: Health co-benefits and mitigation costs as per the Paris Agreement under different technological pathways for energy supply. Environment International, 136, 105513. https://doi.org/10.1016/J.ENVINT.2020.105513
Schucht, S., Colette, A., Rao, S., Holland, M., Schöpp, W., Kolp, P., Klimont, Z., Bessagnet, B., Szopa, S., Vautard, R., Brignon, J. M., & Rouïl, L. , 2015: Moving towards ambitious climate policies: Monetised health benefits from improved air quality could offset mitigation costs in Europe. Environmental Science and Policy, 50, 252–269. https://doi.org/10.1016/j.envsci.2015.03.001
WHO, 2013: Health risks of air pollution in Europe – HRAPIE project, Recommendations for concentration–response functions for cost–benefit analysis of particulate matter, ozone and nitrogen dioxide. http://www.euro.who.int/pubrequest

21st International Conference on
Harmonisation within Atmospheric Dispersion Modelling for Regulatory Purposes
27-30 September 2022, Aveiro, Portugal

NUMERICAL DISPERSION MODELLING OF THE DROPLETS EXPIRED BY HUMANS

Livia Grandoni[1,2,3], Agnese Pini[1], Armando Pelliccioni[2], Pietro Salizzoni[3], Loic Méès[4], Giovanni Leuzzi[1], Paolo Monti[1]

[1] Department of Civil, Constructional and Environmental Engineering, Sapienza University, 00185 Rome, Italy
[2] Italian Workers' Compensation Authority (INAIL), Department of Occupational and Environmental Medicine, Epidemiology and Hygiene, Monte Porzio Catone (Rome), Italy
[3]Laboratoire de M´ecanique des Fluides et Acoustique, University of Lyon, CNRS UMR 5509 Ecole Centrale de Lyon, INSA Lyon, Universit´e Claude Bernard, 36 Avenue Guy de Collongue, Ecully, ´ 69134, France.
[4]Univ Lyon, CNRS, Ecole Centrale de Lyon, INSA Lyon, Univ Claude Bernard Lyon 1, LMFA, UMR5509, Ecully, 69130, France.

Abstract: Owing to the COVID-19 pandemic, in the last two years the attention of the scientific community has focused on the study of the dispersion of small droplets ejected by humans during different respiratory activities. The properties of the droplets usedas input data in numerical simulations and models that forecast the dispersion of the expired particle-laden air cloud are of major importance in order to obtain reliable results. Recent numerical simulations highlighted that a lack of knowledge concerning droplet size and velocity distributions still exists. In fact, only a few works faced this problem since it is particularly difficult to measure droplet sizes over a large range and to measure sizes and velocities simultaneously. Consequently, the droplet velocity is generally assumed to be either zero or equal to the air velocity. In this work numerical simulations have been conducted using as inputs experimental data collected by the authors, taking advantage of the innovative information of particle velocity related to their size. Two measurement campaigns have been carried out involving 20 volunteers, who spoke and coughed following a precise protocol. The size and the 3 velocity components of the ejected droplets have been measured simultaneously for particles down to 2 μm, using an extended version of the Interferometric Laser Imaging Droplet Sizing technique.

KEY WORDS: **DROPLET DISPERSION, DROPLET VELOCITY, DROPLET SIZE, AIRBORNE DISEASE**.

INTRODUCTION

The airborne disease transmission is strictly linked to the dispersion of the droplet loaden air cloud emitted by humans during different respiratory activities. The dispersion process of the ejected cloud and the distances traveled by the droplets have been assessed by means of experiments, numerical simulations and simplified models (Bourouiba et al, 2014; Abkarian et al, 2020; Bahl et al, 2021; De Padova and Mossa, 2021; Dbouk and Drikakis, 2020; Busco et al, 2020; Li et al, 2022; Xie et al, 2007). Realistic input data (air velocity and droplets size and velocity at the emission point) must be provided to models and numerical simulations to obtain reliable results to be used in guidelines, as occurred during COVID-19 pandemic. Therefore, the experimental characterization of the source is of major importance. Even though several works exist in the literature concerning the source characterization (Asadi et al, 2019; Johnson et al, 2011; Chao et al, 2009; Duguid, 1946; Gupta et al, 2010; Kwon et al, 2012) the knowledge is still lacking (Rosti et al, 2020; Seminara et al, 2020). Particularly, a discrepancy among the measured droplet size distributions

emerges from he literature (Bourouiba, 2021; Johnson et al, 2011; Seminara et al, 2020). Besides, several works measured the velocity (or the airflow) of the ejected air (Kwon et al, 2012; Chao et al, 2009; Abkarian et al, 2020; Gupta et al, 2010), but only few detected the droplet velocity (Bahl et al, 2020; Nishimura et al, 2013; de Silva et al, 2021; Bahl et al, 2021). The simultaneous measurement of droplet size and velocity could also provide interesting information, as the velocity of the droplets at the source could depend on their size. This kind of measurement is very rare due to its complexity. The simultaneous measurement of droplet size and velocity has been carried out in two very recent works for the respiratory activity of coughing (de Silva et al, 2021; Bahl et al, 2021), even if limited to droplets larger than 30 μm and to two of the three velocity components. Note that most of the studies focused on extreme respiratory events such as sneezing and coughing, while less works concerned the activity of speaking, despite its importance in airborne pre-symptomatic or asymptomatic transmission. In this work we carried out detailed measurement to characterize the droplet emission during the respiratory activity of speaking. Namely, simultaneous measurements of the size and the three velocity components of the droplets have been performed, for particles down to 2 μm. The experimental data have been, then, used as input in numerical simulations.

MATERIALS AND METHODS

Measurement campaign

The measurement campaign has been carried out in the Laboratoire de Mécanique des Fluides et d'Acoustique of the Ecole Centrale de Lyon. It has been asked to 20 volunteers to count from "one" to "one hundred" in order to simulate the respiratory activity of speaking. The size and the three velocity components of the ejected droplets have been measured simultaneously by means of the technique Interferometric Laser Imaging for Droples Sizing (ILIDS). In the ILIDS the droplets are illuminated by a laser light sheet and out-of-focus images of them are taken by means of system of lenses and a camera. The light scattered by the liquid spherical droplets is characterized by regular interference fringes, from whose spacing the droplet size can be deduced. The velocity of each of the detected droplets is obtained by measuring their displacement in consecutive images, known the time lag. More details about the ILIDS can be found in the work by Mees et al (2011). The ILIDS setup and the related image treatment have been improved with respect to the classical application of the technique to measure droplet sizes down to 2 μm - absolute limit of the ILIDS - and the three velocity components.

Numerical simulation setup

Ansys Fluent has been employed to simulate the dispersion of the droplets ejected during the respiratory activity of speaking. The simulation domain is a regular box 3 m high, 2 m wide and 2 m long, representing a portion of an indoor environment. Although the process of speaking is highly unsteady due to the variety of phonemes, it can be modelled as a continuous turbulent jet (Abkarian et al (2020), considering mean quantities to characterize it. Therefore, a stationary emission of the particle-laden air cloud is assumed in the simulations. The emission of air and droplets occurs from a surface of 0.013 m x 0.013 m representing the mouth, which is located on the left side of the domain at 1.6 m from the floor (the average height of the human mouth). The air is continuously ejected from the mouth at a speed of 0.5 m/s (*velocity inlet* boundary condition). The latter value is taken from the work by Abkarian et al (2020). Note that the value is lower than the one reported by Gupta et al (2010), who measured a mean airflow of 0.8 l/s, which corresponds to a velocity of ~ 4 m/s, considering a mouth opening of ~ 1.8 cm^2. Kwon et al (2012) and Chao et al (2009) refers to ~ 4 m/s as a maximum expiration air velocity instead. The other boundary conditions used are the following: *wall* at the floor, at the ceiling and at the side faces; *pressure outlet* at the face opposite to the mouth; *velocity inlet* with a velocity of 0.01 m/s at the face all around the mouth. The temperature of the air ejected at the mouth is set to 306.15 K (Xie et al, 2007), higher than the ambient temperature (~ 293.5 K). The temperature of the ambient air is maintained by imposing at the side walls and around the mouth a fixed temperature of 293.5 K, while the floor and the ceiling are adiabatic. The mesh consists of ~ $7 \cdot 10^6$ hexahedral cells, whose maximum size is of 0.013 m; the cell size reduces getting closer to the mouth.

1024 particle streams (i.e groups of droplets with the same features), for a total of 10240 droplets, are injected in the domain from the surface simulating the mouth. The droplets are modelled as inert spherical water particles; therefore, evaporation is not taken into account. The droplet size and velocity distribution given as input to the simulations are obtained from the measurement campaign.

A standard k-ε turbulence model has been used to solve the air motion, considering the buoyancy effect only on turbulence production. For the particle motion the Lagrangian dispersion model implemented in Ansys Fluent (Discrete Phase Model with Discrete Random Walk activated) has been employed. The simulations have been stopped once all the residuals were lower than 10^{-6}.

RESULTS AND DISCUSSION

Size distributions and injections

In Figure 1a the droplet size distribution obtained from the experimental data is shown. Most of the droplets lie in the range 2-4 μm; the number of droplets rapidly decreases until a relative maximum occurs between 25 and 30 μm. From the experiments the velocity distribution of the droplets appears to vary with their size, mostly the longitudinal component (x), i.e the component parallel to the mean airflow ejected from the volunteers' mouth. The five size distributions obtained for five different droplet size classes are depicted in Figure 1b. In Figure 1c the considered droplet injection is shown. Droplets of different sizes are randomly distributed within the mouth surface; the velocity is assigned to the droplets so that different droplet size classes are characterized by different velocity distribution.

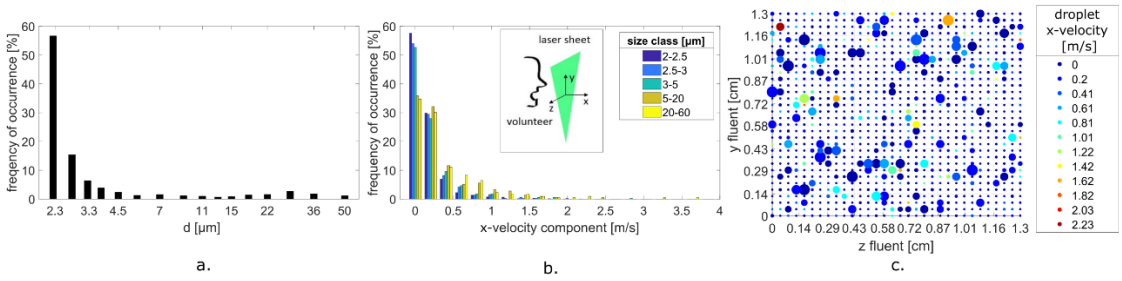

Figure 118. a. Droplet size distribution and b. x-component velocity distributions for five different droplet size classes obtained from the experimental data. c. Injection considered as input for numerical simulations; the area of the graph coincides with the area of the mouth surface from which the injection takes place; each circle corresponds to an injected droplet; the size of the circle is proportional to the size of the droplet, while the color is related to droplet velocity (only the longitudinal velocity component is represented for the sake of brevity)

Simulation results

The air exiting the mouth forms a jet, which is initially horizontal. Moving away from the mouth the jet velocity decreases until its buoyancy – due to the temperature difference between ejected and ambient air – prevails and the jet starts rising. Because of the low ejection velocity, the air jet moves horizontally only for a short distance. Once the air has reached the ceiling, it expands and exits the domain. Given the set boundary conditions, the air exits mainly through the *pressure outlet* face (right side).

As expected, larger – and, thus, heavier – droplets quickly fallout from the air jet and start settling. Droplets of sizes ~ 28 - 50, ~ 22 and ~ 18 μm start falling out from the air jet at 5, 15 and 25 cm from the mouth, respectively. On the contrary, smaller droplets are transported by the air towards the ceiling. In general, only droplets of size d > 16 μm settle within 2 m from the mouth (Figure 3a). The mean, minimum and maximum distances traveled by the droplets before settling is represented in Figure 3b. The distance decreases with droplet size; droplets of size d ~ 50 μm are removed from the air within 50 cm from the mouth, droplets of size d ~ 36 μm within 1 m, the others settle at a distance x ≥ 2m. Droplets smaller than 16 μm rise with the gaseous phase; however, only the smallest remain close to the ceiling, larger droplets tend then to move downwards. In fact, the sizes of the droplets exiting the domain from the lower and the

upper part of the *pressure outlet* face and from the ceiling vary (Figure 3c). Namely, the prevailing size of the droplets exiting the domain from the ceiling is d ~ 2 μm, while the prevailing sizes are d ~ 5 μm e d ~ 18 μm for the upper and the lower part of the *pressure outlet* face, respectively.

Figure 4 depicts droplet number concentration fields on sections transversal to the mean airflow (i.e. parallel to the mouth surface) at 5, 25 and 40 cm from the mouth. Droplet concentration decreases (along with potential risk of infection) moving away from the mouth; however, the area contaminated by the droplet obviously becomes wider due to the spread of the particle loaden air cloud. Far from the mouth the droplets are approximatively completely mixed in the air; this situation corresponds to a concentration within a transversal section of ~ 0.17 #/cm^2. The dark blue line in Figure 4 indicates the concentration of 0.17 #/cm^2. Closer to the mouth the risk is, thus, higher due to zones of higher droplet concentrations. The high droplet concentration area moves upwards due to buoyancy effects, so that at about 40 cm from the mouth its height is greater than the zone where a common person breath (> 2 m). Droplet concentration at mouth height (~ 1.6 m) decreases from ~ 400 #/cm^2 to ~ 0.3 #/cm^2 and to ~ 0 #/cm^2 at 1 mm, 25 cm and 40 cm from the mouth, respectively. The presence of droplets below the mouth height is due to settling droplets. Note that in the concentration fields in Figure 4 no distinction among different droplet sizes is considered; however, the concentration fields vary with droplet size.

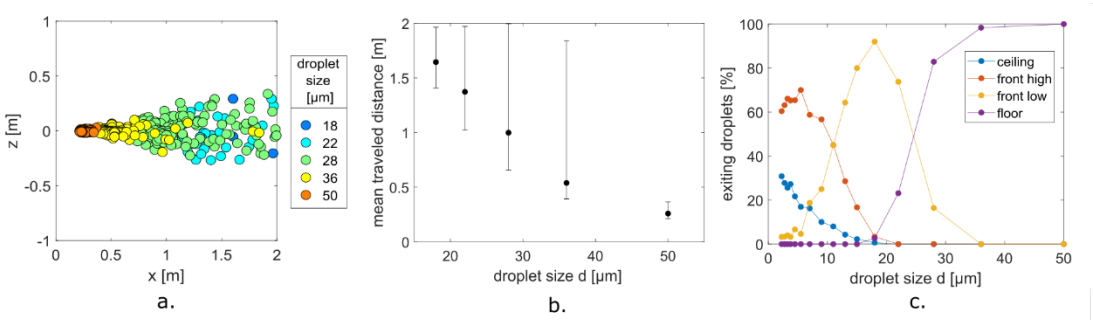

Figure 3. a. Settled droplets; each circle corresponds to a droplet, circle color is related to droplet size, b. mean, maximum and minimum traveled distances before settling and c. percentage of particles of each size class exiting through different domain zones

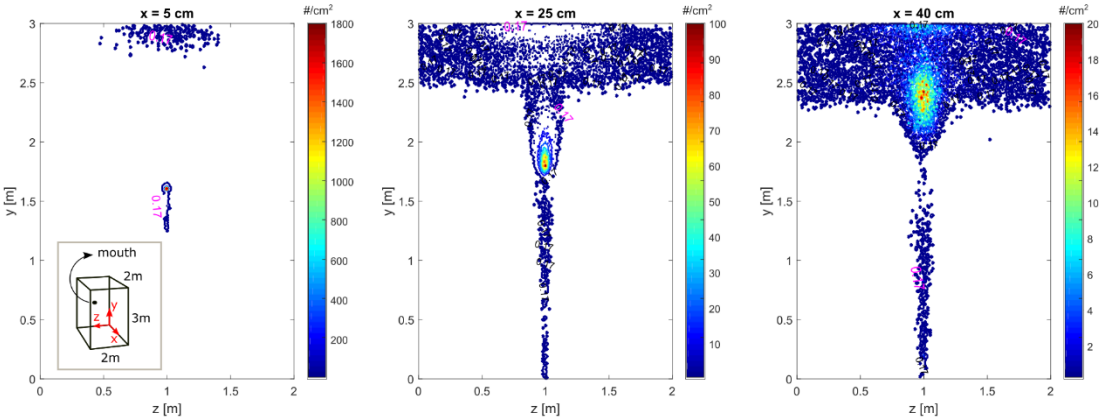

Figure 4. Droplet number concentration fields on transversal sections at 5, 25 and 40 cm from the mouth

CONCLUSIONS

Numerical simulations have been carried out to model the dispersion process of droplets ejected by humans while speaking. Detailed input data consisting in droplet velocity and size distributions have been obtained from a measurement campaign involving 20 volunteers. The ejected particleladen air cloud moves

horizontally for a short distance, then it starts to rise due to buoyancy effects. Larger heavier droplets soon fallout from the cloud and start settling, while smaller lighter particles are transported by the air towards the ceiling. Only droplets larger than 16 μm settle on the floor; droplets of size d ~ 50 μm and 36 μm are removed from the air within 50 cm and 1 m from the mouth, respectively, the others can travel longer distances or remain suspended. Droplet concentration reduces moving away from the mouth due settling and to the cloud spread. Closer to the mouth the infection risk is higher than far from the ejection, where droplets are almost uniformly distributed in the ambient air; concentrations higher than the completely mixed condition are found within 30-40 cm from the mouth. Note that the considered ambient air temperature is typical of a winter condition; Other simulations are worth to be carried out to assess a summer condition, where the buoyancy effect is weaker. Besides, other simulations are needed to test the sensibility of the results to the detail of the provided input data.

REFERENCES

Abkarian, M., Mendez, S., Xue, N., Yang, F. and Stone, H. A., 2020: Speech can produce jet-like transport relevant to asymptomatic spreading of virus. Proc. Natl. Acad. Sci.*, **117 (41)**, 25237-25245.*

Asadi, S., Wexler, A. S., Cappa, C. D., Barreda, S., Bouvier, N. M. and Ristenpart, W. D., 2019: Aerosol emission and superemission during human speech increase with voice loudness. Sci. Rep. ***9(1)**,2348.*

Bahl, P., De Silva, C. M., Chughtai, A. A., MacIntyre, C. R. and Doolan, C., 2020: An experimental framework to capture the flow dynamics of droplets expelled by a sneeze. Exp. Fluids., ***61**,176.*

Bahl, P., De Silva, C., Raina MacIntyre, C. R., Bhattacharjee, S., Chughtai, A. A. and Doolan, C., 2021: Flow dynamics of droplets expelled during sneezing. Phys. Fluids., ***33(11)**, 111.*

Bourouiba, L., 2021: The fluid dynamics of disease transmission. Annu. Rev. Fluid. Mech., ***53(1)**, 473–508.*

Bourouiba, L., Dehandschoewercker, E. and Bush, J. W. M., 2014: Violent expiratory events: on coughing and sneezing. J. Fluid. Mech., ***745**, 537–563.*

Busco, G., Yang, S. R., Seo, J. and Hassan, Y. A., 2020: Sneezing and asymptomatic virus transmission. Phys. Fluids, ***32(7)**, 073,309.*

Chao, C. Y. H., Wan, M. P., Morawska, L., Johnson, G. R., Ristovski, Z. D., Hargreaves, M., Mengersen, K., Corbett, S., Li, Y., Xie, X. and Katoshevski, D., 2009: Characterization of expiration air jets and droplet size distributions immediately at the mouth opening. J. Aerosol Sci., ***40(2)**, 122–133.*

Dbouk, T. and Drikakis, D., 2020: On coughing and airborne droplet transmission to humans. Phys. Fluids, ***32(5)**, 053,310.*

De Padova, D. and Mossa, M., 2021: Multi-phase simulation of infected respiratory cloud transmission in air. AIP Advances*, **11(3)**, 035,035.*

De Silva, C. M., Bahl, P., Doolan, C. and Raina MacIntyre, C., 2021: Bespoke flow experiments to capture the dynamics of coughs and sneezes. Meas. Sci. and Technol., ***32(12)**, 125,302.*

Duguid, J. P., 1946: The size and the duration of air-carriage of respiratory droplets and droplet-nuclei. J. Hyg., ***44(6),** 471–479.*

Gupta, J. K., Lin, C. H. and Chen, Q., 2010: Characterizing exhaled airflow from breathing and talking. Indoor Air, ***20(1)**, 31–39.*

Johnson, G. R.,, Morawska, L., Ristovski, R. D., Hargreaves, M., Mengersen, K., Chao, C. Y. H., Wan, M. P., Li, Y., Xie, X., Katoshevski, D. and Corbett, S., 2011: Modality of human expired aerosol size distributions. J. Aerosol Sci., ***42(12)**, 839–851.*

Kwon, S. B., Park, J., Jang, J., Cho, Y., Park, D. S., Kim, C., Bae, G. N. and Jang, A., 2012: Study on the initial velocity distribution of exhaled air from coughing and speaking. Chemosphere*, **87(11)**, 1260-4.*

Li, M., Chong, K. L., Ng, C. S., Bahl, P., De Silva, C. M., Verzicco, R., Doolan, C., Raina MacIntyre, C. and Lohse, D., 2022: Towards realistic simulations of human cough: Effect of droplet emission duration and spread angle. Int. J. Multiph. Flow*, **147,** 103,883.*

Mees, L., Lebrun, D., Fréchou, D. and Boucheron, R., 2011: Interferometric laser imaging technique applied to nuclei size measurements in cavitation tunnel. Paper presented at the 2nd International Conference on Advanced Model Measurement Technology for EU Maritime Industry (AMT'11), Apr 2011, Newcastel upon Tyne, United Kingdom.

Nishimura, H., Sakata, S. and Kaga, A., 2013: A new methodology for studying dynamics of aerosol particles in sneeze and cough using a digital high-vision, high-speed video system and vector analyses. PLoS One*, **8(11)**, e80,244.*

Rosti, M. E., Olivieri, S., Cavaiola, M., Seminara, A. and Mazzino, A., 2020: Fluid dynamics of covid19 airborne infection suggests urgent data for a scientific design of social distancing. Sci. Rep.*, **10**, 22,426.*

Seminara, G., Carli, B., Forni, G., Fuzzi, S., Mazzino, A. and Rinaldo, A., 2020: Biological fluid dynamics of airborne COVID-19 infection. Rend. Fis. Acc. Lincei*, **31(3)**, 505–537.*

Xie, X., Li, Y., Chwang, A. T., Ho, P. L. and Seto, W. H., 2007: How far droplets can move in indoor environments–revisiting the wells evaporation-falling curve. Indoor Air*, **17(3)**, 211–225.*

21st International Conference on
Harmonisation within Atmospheric Dispersion Modelling for Regulatory Purposes
27-30 September 2022, Aveiro, Portugal

ASSESSING THE IMPACT OF THE COVID-19 LOCKDOWNS: RESULTS AND IMPLICATIONS FROM A MODELLING APPLICATION IN TWO MEDITERRANEAN CITIES

Nicolas Moussiopoulos, George Tsegas and Eleftherios Chourdakis

Sustainability Engineering Laboratory, Aristotle University of Thessaloniki, Thessaloniki, Greece

Abstract:
Activity restrictions implemented to control the spread of the COVID-19 virus imposed a significant effect on the air quality of cities across the world. The initiative of the World Meteorological Organisation / Global Atmospheric Watch for studying effects of the 2020 COVID-19 lockdowns on air quality has produced two sets of analysis results for cities across the world, based on observational data and modelling, respectively. The modelling study aims to evaluate the modelling tools in a regime involving significant changes of activity, and at the same provide insights on the effect of selectively reduced emissions on the chemistry and composition of urban pollutants. For most of the cities, a reduction on NO_x average concentrations between 11% and 70% was calculated for the lockdown period, while PM_{10} was reduced by 8% up to 35% in a good agreement with measured reductions observed during the 2020 lockdown period compared to the corresponding period of 2019. Taking advantage of an operational Air Quality Modelling System, which is in continuous application in the cities of Thessaloniki and Nicosia, the contribution of sectoral emissions and the role of meteorology over the observed concentration reductions was assessed. The study reveals that in both cities, observed reductions of urban $PM_{2.5}$, PM_{10} and NO_x concentration patterns can be mainly attributed to the corresponding emissions reductions in the transport and heating sectors, while O_3 is strongly affected by titration near the city centre. At the same time, meteorological patterns appear to strongly influence and even mask these effects in terms of daily averages, while the impact of imposed large-scale boundary conditions on the modelling results can also be significant.

KEY WORDS: AIR QUALITY, URBAN AIR QUALITY, EMISSIONS, LOCKDOWN, COVID-19

INTRODUCTION

Activity restrictions related to lockdowns are causing an unprecedented effect regarding air quality, particularly in urban areas. Modelling tools are instrumental in assessing the magnitude of the effects, as well as apportion contributions of individual activity sectors, particularly where no observations are present. As a result, the lockdown periods provided a unique opportunity for testing and validating simulation models in activity levels and regimes hard to observe under normal conditions. The present study presents preliminary results from a modelling study coordinated by the World Meteorological Organisation / Global Atmospheric Watch (WMO/GAW) aiming to assess effects of the 2020 COVID-19 lockdowns on air quality. Detailed results are further presented for the cities of Thessaloniki, Greece and Nicosia, Cyprus where an Operational Air Quality Management System (AQMS) was in continuous application throughout 2019 and 2020.

METHODOLOGY

In the frame of the WMO/GAW coordinated study regarding the effects of the 2020 COVID-19 lockdowns on air quality, two sets of analysis results have been produced based on data originating from measurements and from modelling results, respectively. The main goal of the modelling study lies in evaluating the modelling tools in a regime involving substantial changes of activity, as well as to provide

a detailed understanding of the effect of selectively reduced emissions on the chemistry and composition of urban pollutants.

Most of the 16 groups participating in this study applied process-based chemical dispersion models under two different emission scenarios for the year 2020: a counterfactual "business as usual" (baseline or BAU) scenario, under the working assumption that normal level activities occurred without any lockdown effects, as well as a "lockdown" scenario (COVID-19) taking into account the activity reductions during the lockdown periods applied in each individual city. For the European study areas, the emissions reduction scenario (COVID-19) was based on a set of sectoral activity emissions quantified as reduction factors provided by the CAMS consortium and calculated at the BSC (Guevara et al., 2021). In order to isolate effects of meteorology, a common set of meteorological driver fields was used for both scenarios. A harmonized approach was used for the comparative performance evaluation of models and analysis of results in terms of several pollutants, with emphasis on secondary substances including O_3, NO_x, O_x and SOA, as well as BC, OC and inorganic aerosol components. A detailed presentation of the analysis is under preparation.

The AQMS developed by the Laboratory of Heat Transfer and Environmental Engineering of the Aristotle University of Thessaloniki (LHTEE/AUTh) (Moussiopoulos et al., 2010; Moussiopoulos et al., 2012) was utilized for the assessment of different activity and emissions scenarios in Greece and Cyprus, based on quantified activity restriction data in economic sectors and activities that have been affected by the lockdown measures. Local gridded emissions for both study areas are based on national inventories developed and maintained by the AUTh group and provide separate contributions for the main activity sectors.

The simulations cover the period of March to mid-April 2020, consisting of three distinct phases, namely the pre-lockdown phase (1/3 - 8/3), the partial lockdown phase (9/3 - 22/3) and the full lockdown phase (23/3 – 12/4). During the pre-lockdown phase, slight decreases in the emissions of specific sectors such as aviation and road transport can already be noticed. Within the partial lockdown phase, these reductions gradually increase, while during the full lockdown phase the emissions of the main sectors remain constantly at notably low levels, especially for the case of NO_x. Figure 1 depicts the activity reduction factor (per sector) compared to a baseline situation for both cities under investigation.

MEMO was initialized with vertical profiles originating from the Global Forecast System (GFS; ULR1). Initial and boundary conditions for pollutant concentration fields were derived from the CAMS-ensemble operational output (URL2). Topography and land use data were obtained from the high-resolution satellite elevation datasets of NASA's Shuttle Radar Topography Mission - SRTM/90 m database (URL3) and the Corine Land Cover 2006 (URL4) database, respectively.

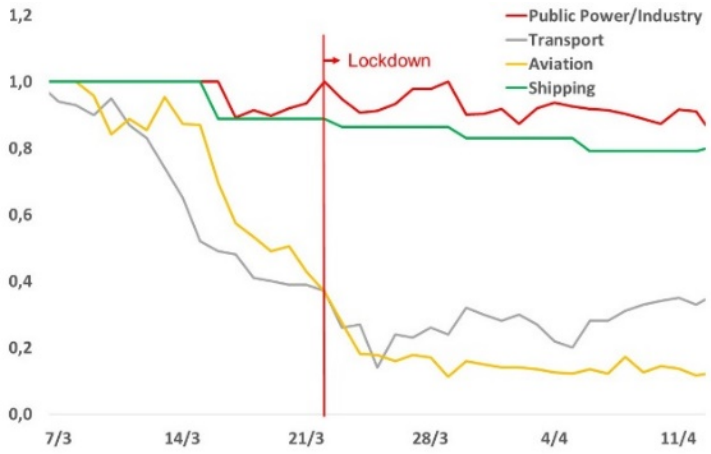

Figure 119. Sectoral activity reductions provided by CAMS/BSC, compared to the baseline situation as used for Thessaloniki and Nicosia (shipping activities relevant only regarding the Cyprus simulations)

RESULTS

Figures 2 and 3 depict a set of preliminary results from the WMO/GAW modelling study regarding NO_x and PM_{10}. In these figures, a comparison of average concentrations under the baseline and the lockdown scenario is presented for the set of 19 cities under investigation. For most of the cities, a reduction on NO_x average concentrations between 11% and 70% was calculated for the lockdown period, while PM_{10} was reduced by 8% up to 35% in a good agreement with measured reductions observed during the 2020 lockdown period compared to the corresponding period of 2019. The magnitude of reductions attributed to activity patterns is similar to the day-by-day influence of meteorology, however a clear reduction trend for the lockdown period is reproduced.

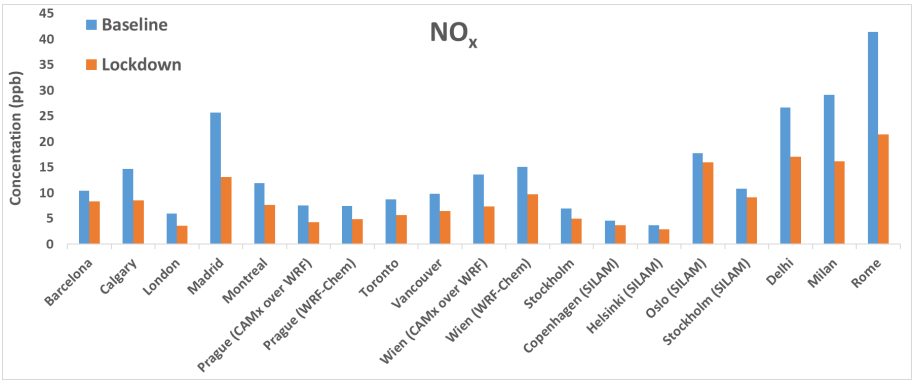

Figure 2. Comparison of modelling results regarding the baseline and lockdown scenarios for the 19 cities of the WMO/GAW study analysis as regards NO

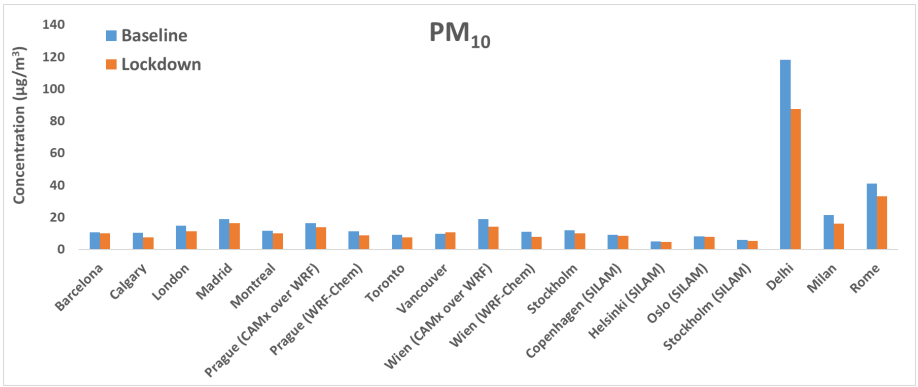

Figure 3. Comparison of modelling results regarding the baseline and lockdown scenarios for the 19 cities of the WMO/GAW study analysis as regards PM_{10}

In Figures 4 to 7, the results of MARS-aero simulations for the baseline and the COVID-19 lockdown scenarios are presented and compared with observational data for selected locations in the areas under investigation. In the case of Nicosia, the model accurately reproduces the observed concentration reductions in urban hotspot for the case of NO_2. The magnitude of reductions attributed to activity patterns is similar to the day-by-day influence of meteorology, however a clear reduction trend for the lockdown period is reproduced. As regards Thessaloniki, the model also reproduces the observed reduction in downtown traffic locations, with less accuracy though.

The model is also capable of reproducing the observed increases in suburban sites for O_3, which can be attributed to the corresponding decreases in NO_2 in titration-dominated regions. In the case of the Panorama residential station, a clear increasing trend is observed during the lockdown period (see Figure 5). More specifically, throughout the partial lockdown phase, the average calculated concentrations for the COVID-19 scenario are increased by 6.5%, while during the full lockdown phase this elevation reaches 11.4%.

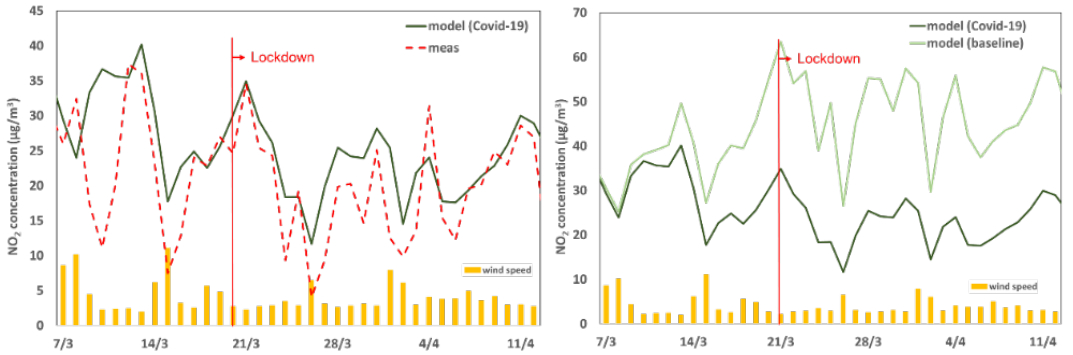

Figure 4. MARS-aero simulations for NO_2 for an urban hot spot of Thessaloniki (Ag. Sofias)

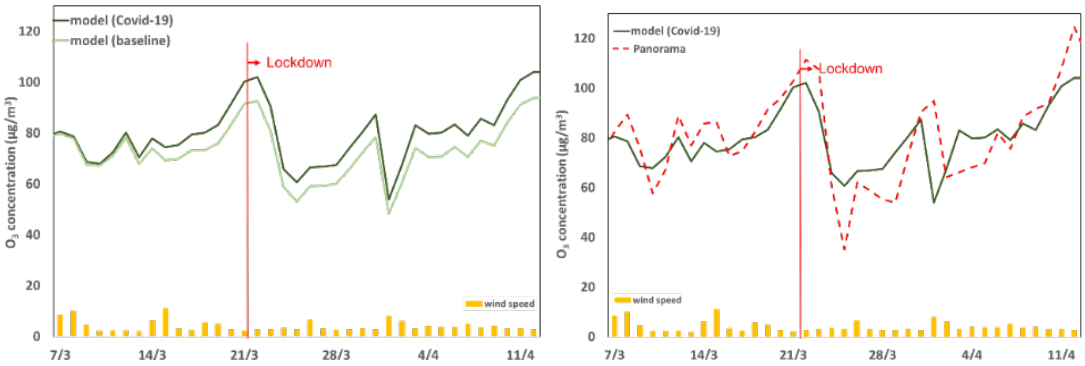

Figure 5. MARS-aero simulations for O_3 for a suburban location of Thessaloniki (Panorama)

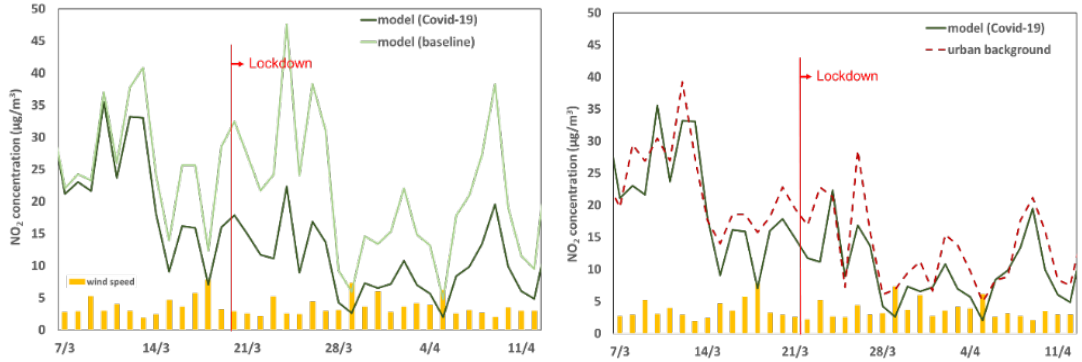

Figure 6. MARS-aero simulations for NO_2 for a residential location of Nicosia

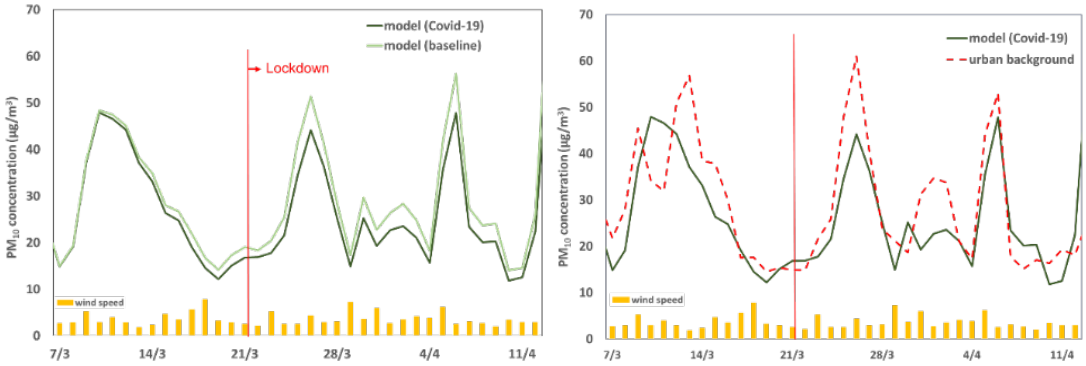

Figure 7. MARS-aero simulations for PM_{10} for a residential location of Nicosia

As indicated from the performance statistics over the application period (Table 1), the model exhibits a fairly good agreement with the observed values regarding NO_2 for urban hotspots in both cities under investigation. This is also the case for O_3 with respect to the suburban location of Panorama. On the other hand, the calculated results for PM_{10} reproduce the observed values with less accuracy, particularly in the timing and magnitude of strong episodic peaks. These shortcomings can be directly attributed to limited accuracy of the boundary conditions.

Table 42. Statistics regarding the accuracy of the model in the frame of the present case studies

	CC	**BIAS (μg/m^3)**	**NMSE**	**IoA**
Thessaloniki centre – NO_2	0.73	5.98	0.15	0.71
Thessaloniki centre – PM_{10}	0.53	-7.34	0.31	0.64
Thessaloniki suburban – O_3	0.85	-1.10	0.03	0.84
Nicosia residential – NO_2	0.76	-1.60	0.08	0.82
Nicosia residential – PM_{10}	0.67	-2.10	0.12	0.69
Nicosia residential – O_3	0.84	3.29	0.04	0.82

CONCLUSIONS

Modelling simulations of air quality under the 2020 COVID-19 lockdowns in several cities all over the world are coordinated in the framework of an WMO/GAW initiative. Preliminary results show a consistent reduction of urban NO_2 concentrations between 11% and 70%, while PM_{10} was reduced by 8% up to 35% compared to a BAU scenario. These results are in a good general agreement with reductions observed in monitoring data between 2020 and the corresponding period of 2019. Detailed calculations for two Eastern-Mediterranean cities confirm the significant decrease in urban NO_2 concentrations during the COVID-19 lockdown, which can be directly attributed to the corresponding reductions in NO_x emissions, particularly on the transport sector, while O_3, as a secondary pollutant, displayed a more complicated response. In the case of PM, calculated concentrations indicate a slight decrease in the COVID-19 scenario during the lockdown phase. However, since seasonal PM patterns were BCs-dominated, reflecting a strong influence of large-scale effects such as Saharan dust episodes, regional-scale scenarios should be utilized in order to more accurately simulate the total lockdown effects on PM levels. Uncertainties, in particular in diurnal PM patterns, could be further reduced by improving the representation of heating emissions, especially for the case of Thessaloniki. It is also evident that imposed BCs largely dominate both O_3 and coarse PM_{10} (due to dust transport) and can partly mask the local emissions signal even for NO_x, less so for $PM_{2.5}$. These effects indicate that the multiscale approach, also favoured in the frame of the ongoing WMO/GAW initiative, will be necessary to minimise such uncertainties and provide reliable sectoral attribution.

REFERENCES

Moussiopoulos, N., G. Tsegas, I. Douros, E. Chourdakis and K. Nikolaou, 2011: Development of an air quality management system for Thessaloniki, Proceedings of the 16th International Symposium on Environmental Pollution and its Impact on Life in the Mediterranean Region (MESAEP2011), Ioannina, Greece, 24-27 September.

Moussiopoulos, N., I. Douros, G. Tsegas, S. Kleanthous and E. Chourdakis, 2012: An air quality management system for policy support in Cyprus. Hindawi Publishing Corporation, Advances in Meteorology, doi:10.1155/2012/959280.

Moussiopoulos, N., I. Douros, G. Tsegas, S. Kleanthous and E. Chourdakis, 2010: An air quality management system for Cyprus. Global Nest Journal, 12:92-98.

*Guevara, M., O. Jorba,, A. Soret, H. Petetin, D. Bowdalo, K. Serradell, C. Tena, H. Denier van der Gon, J. Kuenen, V.-H. Peuch and C. Pérez García-Pando, 2020: Time-resolved emission reductions for atmospheric chemistry modelling in Europe during the COVID-19 lockdowns. Atmos. Chem. Phys., **21**, 773–797, https://doi.org/10.5194/acp-21-773-2021, 2021.*

URL1: https://www.ncdc.noaa.gov/data-access/model-data/model-datasets/global-forcast-system-gfs

URL2: https://atmosphere.copernicus.eu/about-cams

URL3: http://www2.jpl.nasa.gov/srtm/

URL4: http://www.eea.europa.eu/data-and-maps/data/corine-land-cover

.

21st International Conference on
Harmonisation within Atmospheric Dispersion Modelling for Regulatory Purposes
27-30 September 2022, Aveiro, Portugal

AN INTEGRATED TOOL TO ASSESS THE CLIMATE AND HEALTH BENEFITS OF URBAN STRATEGIES AND MEASURES

Niko Karvosenoja[1], Ismo Hämäläinen[1], Santtu Karhinen[1], Mikko Savolahti[1], Ville-Veikko Paunu[1], Janne Pesu[1], Jaakko Kukkonen[2], Timo Lanki[3,4]

[1] Finnish Environment Institute (SYKE), Helsinki, Finland
[2] Finnish Meteorological Institute, Helsinki, Finland
[3] Finnish Institute for Health and Welfare (THL), Kuopio, Finland
[4] University of Eastern Finland, Kuopio, Finland

Abstract: Climate change mitigation experts and policy makers need tools to quantify the impacts of climate measures on air pollution, human health and costs to the society. We have developed a harmonized tool ALasSken-ihQ (Impact Assessment Tool for Climate Measures in Cities), that enables the assessment of climate measures' effect on GHG emissions and PM2.5 induced health impacts and costs in an integrated manner. We will present the main features and demonstrate the use of the tool.

KEY WORDS: **GREENHOUSE GASES, CLIMATE, FINE PARTICLES, EMISSIONS, HUMAN HEALTH, COSTS**

INTRODUCTION

Climate change mitigation actions are needed at all levels of society. Decisions are made at cities concerning many major greenhouse gas (GHG) emission sources, e.g. urban transport and residential heating. Often such local emission sources cause, in addition to GHGs, emissions of air pollution harmful to human health, such as fine particles (PM2.5).

Experts and policy makers who prepare city level strategies call for tools to assess the efficiency of climate mitigation measures in terms of potential to reduce GHG emissions. In addition, they wish to obtain information about the side-effects of the climate measures to the society, especially impacts on human health. To match the needs for the capabilities to assess the health externalities caused by various local air pollution emission sources, a health damage cost tool for city experts (ihQ) was developed in an earlier project (Karvosenoja et al., 2021).

However, the ihQ tool provides only limited information about the efficiency of actual climate or air pollution measures to reduce emissions. According to the interviews of city experts on the use of the ihQ tool, the main limitation of the use of the tool is, how to estimate air pollution emission changes due to different climate or air pollution measures. Therefore, we have now integrated the ihQ tool within the city level ALasSken scenario tool that allows users to interactively study the implementation of individual climate measures on-line.

In this text, we will present a harmonized tool, ALasSken-ihQ (Impact Assessment Tool for Climate Measures in Cities), that enables the assessment of climate measures' effect on GHG emissions and

PM2.5 induced health impacts and costs in an integrated manner. We will demonstrate the architecture and functionalities of the tool user interface.

METHODOLOGY

The ALasSken-ihQ tool combines the functionalities of the regional GHG emission scenario calculation ALasSken and municipality health damage cost tool ihQ. The following chapters present the main features of both.

Alassken

The ALasSken tool has been developed to support the planning of municipal climate roadmaps that identify measures to reduce regional GHG emissions. As a starting point for each individual municipality, the tool includes a Baseline scenario with existing measures that depicts exogenous GHG reductions resulting from national roadmaps, strategies, and subsidy mechanisms. Thereafter, user of the tool can define additional measures in each emission sector (see e.g., Karhinen et al., 2021) to examine a set of action sets, by which one can achieve the regional emission reduction targets. The action set can include, for example, reduction in oil heating, changing the fuel mix in district heat generation, and improving the accessibility of different services within the municipality.

ihQ

The ihQ tool assesses the effect of changes in air pollution emissions originating from different emission source sectors on human health impacts attributed to the $PM_{2.5}$ concentrations for selected municipalities. The modelling covers both primary $PM_{2.5}$ and secondary formation from main inorganic PM precursor gases. The health impacts are expressed as monetary values, i.e. health damage costs, based on Nordic Value of Statistical Life (VSL) estimates. The modelling set-up and the use of the IhQ tool have been reported in detail in Karvosenoja et al. (2021) and Kukkonen et al. (2020).

Integrated ALasSken-ihQ

The harmonized open-access ALasSken-ihQ tool will present on-line GHG emissions as well as $PM_{2.5}$ emissions and their health impact induced damage costs of the studied measures. First, the tool was developed for measures in the road transport sector to examine, e.g., how improvements in service accessibility, public transportation and light traffic network would decrease passenger car driving distances, and thus, reduce the GHG and exhaust and non-exhaust primary $PM_{2.5}$ emissions. The first version of the ALasSken-ihQ tool does not include the calculation of secondary PM.

User interface and baseline scenario

ALasSken-ihQ is to be developed for an on-line open-access tool. As for autumn 2022, the development is still partly in progress. An english demo-version with functionalities for health damage cost calculation only in the road traffic sector can be found in *https://ihq-demo-harmo.netlify.app/*. The final version will be launched at the end of 2022. The following will present the main features and the use of the ALasSken-ihQ tool.

The user of ALasSken-ihQ first selects the city in question from the list of 310 Finnish municipalities. The tool opens a Baseline scenario for the city in 2030 that includes already decided climate actions. This stage is depicted for Helsinki as an example in Figure 1. For Helsinki the Baseline scenario includes, e.g., phase-out of coal in district heat production, promotion of energy renovations in public buildings and measures to promote public transport (e.g. City of Helsinki, 2018).

The user view shows GHG emission reductions in the Baseline scenario in 2030 compared to the reference year 2007 (-55.1% in case of Helsinki), and the gap still remaining to reach the goal which is 80% GHG emission reduction (876.3 kilotons of CO2 equivalents). User can also change the assumption of emission reduction target using the respective slider.

The lower part of Figure 1 shows the different activity sectors where it is possible to vary the extent of how different climate measures are used. The view shows also how much GHG emissions are reduced in the Baseline scenario 2030 compared to 2007 in each of the sectors (i.e. 61.0% in Buildings: Energy use, 41.1% in Road Traffic and 44.0% in Other sectors). The following chapter describes the way these climate measures in Road Traffic sector can be studied and the results as impacts on GHG emissions, PM2.5 emissions and health damage costs.

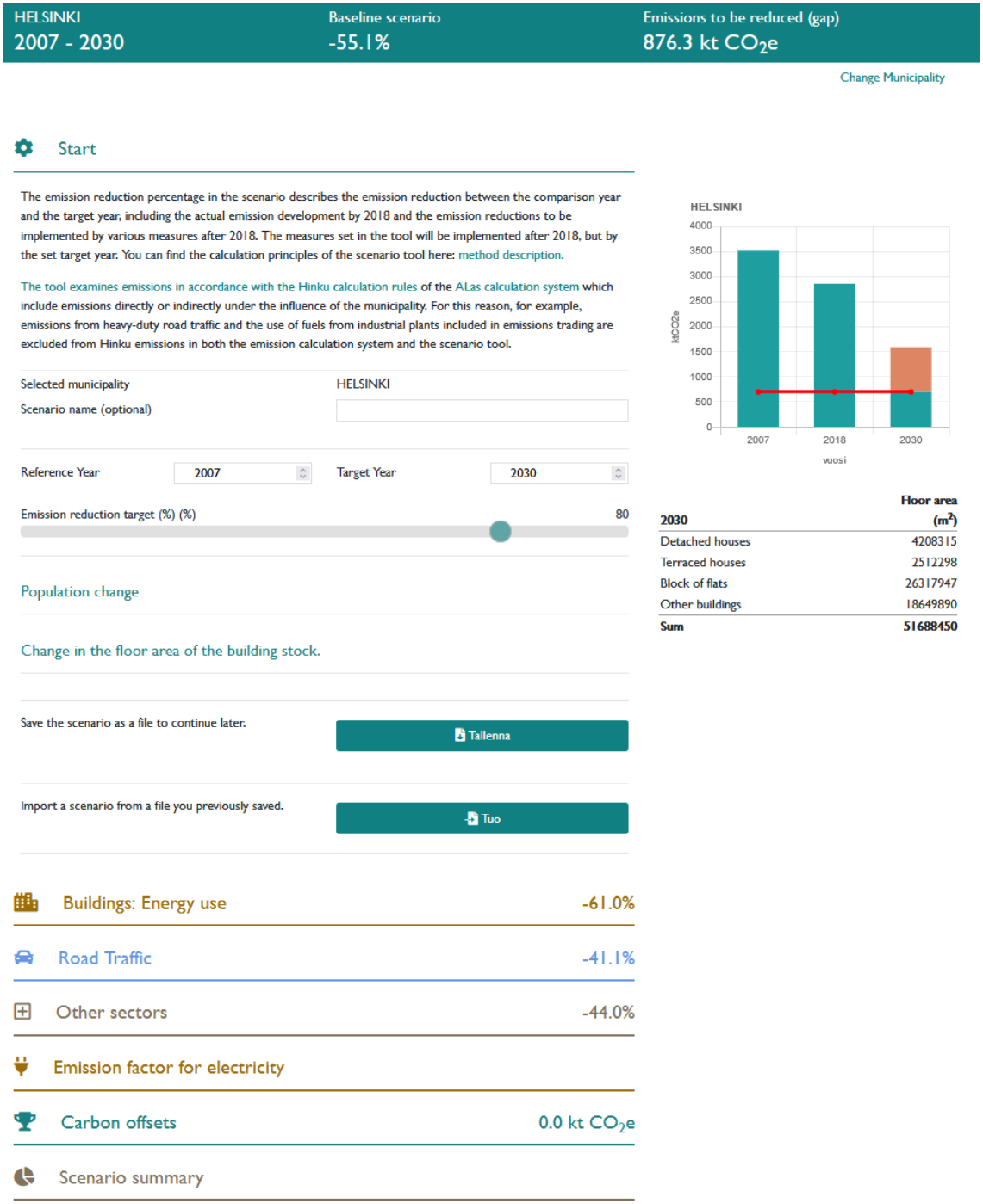

Figure 120. User interface of ALasSken-ihQ with the Baseline scenario for Helsinki

Additional climate measures and health damage costs caused by $PM_{2.5}$

The basic idea of the ALasSken-ihQ tool is to enable user to study the introduction or the rate of the use of individual climate measures. By clicking the sectors, the tool will open the selection of sub-sectors, and further the selection of measures. Figure 2 shows as an example the selection of varying the rate of different fuel types of passenger cars in the Road Traffic sector. In addition to fuel types of different types of vehicles, other measures in the Road Traffic sector include mainly measures related to vehicle mileage (e.g. accessibility of grocery stores, schools, public transport etc., congestion outside the city, shares of public transport and other transport modes, improvements of cycling infrastructure etc.).

In Figure 2, the user has changed the share of fully electric passenger vehicles to 20% (instead of 6% in the Baseline scenario), which increases the total GHG emission reduction in Helsinki by 1%-unit compared to the Baseline scenario, to 56.1% from 2007. Respectively, GHG emission reduction in the Road Traffic sector increases from 41.1% to 46.0%.

The detailed results as vehicle mileage, GHG emissions, PM2.5 emissions and health damage costs due to PM2.5 are shown on the right-hand side of the user view. In addition, the bar figure below the tables shows the relative change compared to Baseline scenario. As the user applies the sliders, the numbers and bars changes simultaneously, which makes quick, screening-type studying of the measures practical.

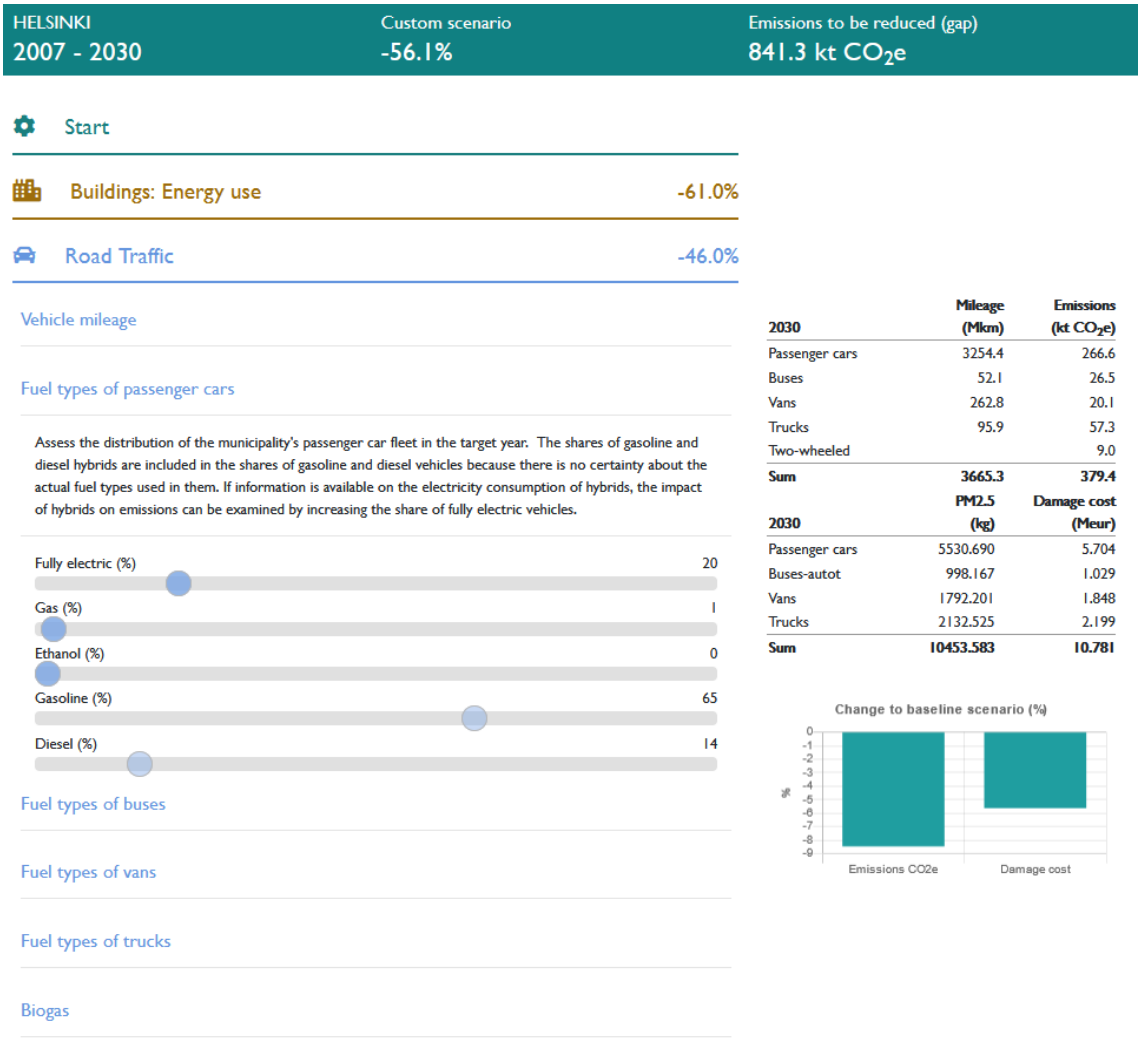

Figure 2. User interface of ALasSken-ihQ with one additional measure on road traffic (higher percentage of fully electric passenger cars) on top of the Baseline scenario for Helsinki

CONCLUSIONS AND NEXT STEPS

The ALasSken-ihQ is an open-access, user-friendly web-based assessment tool. It provides opportunities for municipality and city level experts to quickly evaluate the impacts of various climate measures on both (i) GHG emissions and (ii) the health impacts and costs attributed to the $PM_{2.5}$ pollution.

In the first phase the tool was developed to include only measures in the road transport sector. In the future, it will be extended to cover other sectors relevant to urban air pollution, especially residential heating and machinery. In addition, the modelling framework will be further developed to include investments and other costs of climate measures, as well as macro-economic effects to the society, in order to enable performing more complete cost-benefit analysis. The tool could be extended to function also for other countries, if the underlying emission and dispersion computations would be available for the region.

REFERENCES

City of Helsinki: The Carbon-neutral Helsinki 2035 Action Plan. Publications of the Central Administration of the City of Helsinki 2018:4.

Karhinen S., Peltomaa J., Riekkinen V., Saikku L. 2021. Impact of a climate network: The role of intermediaries in local level climate action. Global Environmental Change 67(9):102225

Karvosenoja N, Savolahti M, Paunu V-V, Munther J., Hämäläinen I., Kukkonen J., Lanki T. 2021. Operational health damage cost model for municipality policy assessments. 20th International Conference on Harmonisation within Atmospheric Dispersion Modelling for Regulatory Purposes 14-18 June 2020, Tartu, Estonia. Extended abstract, 5 pp.

Kukkonen, J., Savolahti, M., Palamarchuk, Y., Lanki, T., Nurmi, V., Paunu, V.-V., Kangas, L., Sofiev, M., Karppinen, A., Maragkidou, A., Tiittanen, P., and Karvosenoja, N.: Modelling of the public health costs of fine particulate matter and results for Finland in 2015, Atmos. Chem. Phys., 20, 9371–9391. https://doi.org/10.5194/acp-20-9371-2020*, 2020.*

21st International Conference on
Harmonisation within Atmospheric Dispersion Modelling for Regulatory Purposes
27-30 September 2022, Aveiro, Portugal

AN INTEGRATED APPROACH TO ESTIMATE AND PREDICT DYNAMIC INFILTRATION FACTORS OF FINE PARTICLES IN LONDON HOMES

Tuan Vu, Gregor B. Stewart, Nutthida Kitwiroon, Hanbin Zhang, Benjamin Barratt, Sean D. Beevers

SHORT ABSTRACT

Abstract title: **An integrated approach to estimate and predict dynamic infiltration factors of fine particles in London homes**

Name and Affiliation of the First Author: Tuan Vu, MRC Centre for Environment and Health, Environmental Research Group, Imperial College London, UK

Email of first author: *tuan.vu@imperial.ac.uk*

Names and Affiliations of the Co-authors: Gregor B. Stewart[1], Nutthida Kitwiroon[1], Hanbin Zhang[1], Benjamin Barratt[1,2,] and Sean D. Beevers[1,2]

[1]MRC Centre for Environment and Health, Environmental Research Group, Imperial College London, UK;[2]NIHR HPRU in Environmental Exposures and Health, Imperial College London, UK

ABSTRACT TEXT (MAXIMUM 350 WORDS.)

Whilst at home indoors, people are exposed to either outdoor particles that enter indoors or particles emitted from indoor activities. Apportionment of the contribution of outdoor-originated aerosols or indoor source-generated aerosols to home air quality is needed when estimating their exposure to indoor air pollution. This study aims to develop a new integrated approach for estimating and predicting dynamic infiltration factors (F_{in})- a key parameter which represents the equilibrium fraction of outdoor particles that penetrates indoors and remains suspended.

Fine particles were measured in indoor environments of 130 London homes during a period of one to six months each home while a dataset of hourly concentrations of outdoor pollutants at these homes was modelled by our CMAQ-urban model (20m × 20m grid). Dynamic infiltration factors and loss rates of $PM_{2.5}$ (in six-hour moving average time resolution) were estimated by applying an enhanced mass balance model. In addition, we investigated environmental factors which affect F_{in} and loss rates of fine particles using a random forest algorithm.

As our preliminary results, averaged indoor and outdoor concentrations of $PM_{2.5}$ at London homes were 11.9 and 11.1 $\mu g.m^{-3}$ during the sampling campaign, respectively. Infiltration factors varied between homes, with a median value of 0.57 (IQR:0.26), suggesting a significant portion of indoor $PM_{2.5}$ (52%) are attributed to outdoor. Higher values of F_{in} were found during the daytime and weekend. Partial dependence plots show that infiltration factors strongly depend upon outdoor/indoor climate, particle chemical composition and home location and characteristics. Furthermore, we developed a new machine learning approach that we can predict the infiltration fraction of outdoor $PM_{2.5}$ in a house based on a limited measurement dataset.

21st International Conference on
Harmonisation within Atmospheric Dispersion Modelling for Regulatory Purposes
27-30 September 2022, Aveiro, Portugal

BENZO(A)PYRENE CONCENTRATIONS IN CENTRAL EUROPE – THE ROLE OF METEOROLOGICAL CONDITIONS AND HEALTH IMPACT ANALYSIS

Paweł Porwisiak, Maciej Kryza, Massimo Vieno, Janice Scheffler, Mike Holland, Lech Gawuc, Bruce Denby, Qing Mu, Małgorzata Werner

SHORT ABSTRACT

Abstract title: **Benzo(a)pyrene concentrations in Central Europe – the role of meteorological conditions and health impact analysis**

Name and Affiliation of the First Author: Paweł Porwisiak, University of Wrocław, Faculty of Earth Sciences and Environmental Management, Poland

Email of first author: *pawel.porwisiak@uwr.edu.pl*

Names and Affiliations of the Co-authors:

Maciej Kryza, University of Wrocław, Faculty of Earth Sciences and Environmental Management, Poland

Massimo Vieno, UK Centre for Ecology and Hydrology, Edinburg, UK

Janice Scheffler, UK Centre for Ecology and Hydrology, Edinburg, UK

Mike Holland, EMRC, UK

Lech Gawuc, National Centre for Emissions Management, Institute of Environmental Protection - National Research Institute, Warsaw, Poland

Bruce Denby, Norwegian Meteorological Institute, Oslo, Norway

Qing Mu, Norwegian Meteorological Institute, Oslo, Norway

& Małgorzata Werner, University of Wrocław, Faculty of Earth Sciences and Environmental Management, Poland

ABSTRACT TEXT (MAXIMUM 350 WORDS.)

Air pollution originating from the household is one of the most important issue especially during the winter time in countries where coal substantially contribute to energy production. One of the most hazardous component of particulate matter is benzo(a)pyrene (BaP). This study focuses on the impact of the different meteorological conditions on BaP concentrations as well as an impact on human health. For this study, we used the EMEP MSC-W atmospheric chemistry transport model with the meteorological data from Weather Research and Forecasting model to analyse the spatial and temporal distribution of BaP over Europe. The model setup has two nested domains, with the inner domain at 4x4km^2 over Poland, which is a hotspot for BaP concentrations . We carried out three experiments; 1) average meteorological conditions during the winter season for the year 2018 (BASE), 2) cold winter during the

year 2010 (COLD), and finally 3) a warm winter during year 2020 (WARM). We used high resolution national emission database for Poland and EMEP database outside the Polish area. The emission data were for the year 2018 and we kept the same emissions for all three simulations.

The modelled concentrations were used to estimate the total areas where the annual average target value (TV) of BaP concentration (1 ng/m^3) was exceeded. The ALPHA-RiskPoll model was used to analyze the health impact of BaP concentrations. For all experiments, the highest monthly average concentrations were calculated for the period from November to March with the highest values found in the center and south of Poland, especially in the medium-sized and large cities. The majority of Poland exceeds the target level of benzo(a)pyrene mainly during the cold months. The exceedance of annual mean BaP TV concentration concerned most of the area for the BASE and COLD run (85 and 92% respectively) and more than half (64%) of the area for the WARM run. The high B(a)P concentrations have a severe impact on health, such as e.g. respiratory diseases.

21st International Conference on
Harmonisation within Atmospheric Dispersion Modelling for Regulatory Purposes
27-30 September 2022, Aveiro, Portugal

PREDICTION OF THE MAXIMUM WIND SPEED IN INDOOR ENVIRONMENTS FOR EFFICIENT NATURAL VENTILATION

George C. Efthimiou, Fotios Barmpas, George Tsegas and Nicolas Moussiopoulos

Sustainability Engineering Laboratory (SEL), Aristotle University of Thessaloniki, 54124, Thessaloniki, Greece

Abstract: The efficient natural ventilation in indoor environments is extremely important especially this period with the appearance of new hazardous viruses such as COVID-19. It is well known that the maximum wind speed causes the lowest individual exposure to hazardous substances in an environment (either indoor or outdoor) and as a result its reliable prediction by a numerical model (either simple or complex) becomes of utmost importance. In this study a deterministic model, that was developed for the outdoor environment, is examined as a possible candidate to predict the maximum wind speed in indoor environments. For the needs of the study a wind tunnel experiment is simulated by the LES methodology in order to acquire the maximum wind speed at various locations in an indoor environment. Then the deterministic model, without any change in its parameters, is validated successfully with the LES maximum wind speeds. The present deterministic model can be incorporated in simple methodologies (e.g. RANS) provided that the latest are able to predict the mean speed, the turbulent intensity and a hydrodynamic time scale.

KEY WORDS: DETERMINISTIC MODEL, LES, WIND TUNNEL EXPERIMENT, NATURAL VENTILATION, MAXIMUM WIND SPEED.

INTRODUCTION

Scientific interest on indoor air pollution increases, since modern people spend most of their time within enclosed spaces (Klepeis et al., 2001). Concentration values of several pollutants may be higher indoors than outdoors, due to building construction materials, paints, furniture, equipment, smoking, cleaning products and other sources (Zhang and Smith, 2003). Furthermore, this period, it is of utmost importance to study indoor air quality due to the appearance of new hazardous viruses such as COVID-19 (Diaz-Calderon et al., 2021).

The introduction of outdoor air in an indoor environment is one important factor in promoting good air quality. Air may enter in several different ways such as through windows and doors. One method of natural ventilation is the wind induced cross-ventilation which has been utilized in traditional and modern buildings for air quality improvement (e.g. Heracleous and Michael, 2019). While there are several cross-ventilation studies that examine both the indoor and outdoor part of the flow (e.g. Ramponi and Blocken, 2012), most detailed investigations of flow and pollutant dispersion at confined spaces usually consider only the indoor part.

Furthermore, it is well known that the lowest individual exposure to hazardous substances is caused by the maximum wind speed and as a result its reliable prediction by a numerical model becomes of utmost importance. In case of complex models (e.g. LES) the prediction of the maximum value can be achieved

by the wind speed time series. However, in case of simple models (e.g. RANS) the incorporation of a deterministic model could be a possible solution. For this reason, in the present study, a deterministic model that was developed for the outdoor environment (Efthimiou et al., 2017) is tested without any change in its parameters, in order to check its suitability to be used in the indoor environment.

METHODOLOGY

In this study we use the theoretical approach proposed by Efthimiou et al. (2017) in order to approximate the maximum time-averaged wind speed in the interval $\Delta\tau$, $V_{max}(\Delta\tau)$, which is modelled by:

$$V_{max}(\Delta\tau) = \bar{V}\left[1 + b\left(\frac{\Delta\tau}{T_V}\right)^{-\nu} I\right] \quad (1)$$

where $\bar{V}$ is the mean wind speed and I is the wind-speed fluctuation intensity given by:

$$I = \frac{\overline{V'^2}}{\bar{V}^2} \quad (2)$$

T_V is the wind-speed integral time scale derived from the wind-speed autocorrelation function $R_V(\tau)$ via:

$$T_V = \int_0^\infty R_V(\tau)d\tau \quad (3)$$

and $R_V(\tau)$ is defined as:

$$R_V(\tau) = \frac{\overline{V'(t)V'(t+\tau)}}{\overline{V'^2}} \quad (4)$$

It should be noted that Eq. 1 was developed initially for the estimation of maximum concentrations of airborne pollutants released from point sources. The parameters b and ν in Eq. 1 can be derived empirically and typically exhibit a wide range of values as demonstrated in previous studies. This is a result of the combination of limitations of the model, experimental errors, insufficient stationarity of the time series and the finite duration of the analyzed signal used to derive these values. Previous studies on the dispersion of airborne material in atmospheric flows suggested indicative values of b = 1.5 and ν = 0.3. For the wind speed in the Atmospheric Surface Layer (Efthimiou et al., 2017) the values for these parameters were set equal to b = 6.0 and ν = 0.3 and the same values are used also in this study for the indoor environment.

The wind tunnel experiment

The experimental measurements were conducted in the atmospheric boundary layer wind tunnel at Niigata Institute of Technology (e.g. Shirzadi et al., 2020). The target building was a cuboid with dimensions of 0.2 m × 0.2 m × 0.16 m for the building width, depth, and height, with two openings of dimensions 0.036 m × 0.092 m over the windward and leeward facades as shown in Figure 1. The target building was surrounded by eight similar buildings without openings, which were arranged in a regular configuration with a planar area ratio of 25%. According to Scopus the specific experiment has been cited 28 times until 13 March 2022.

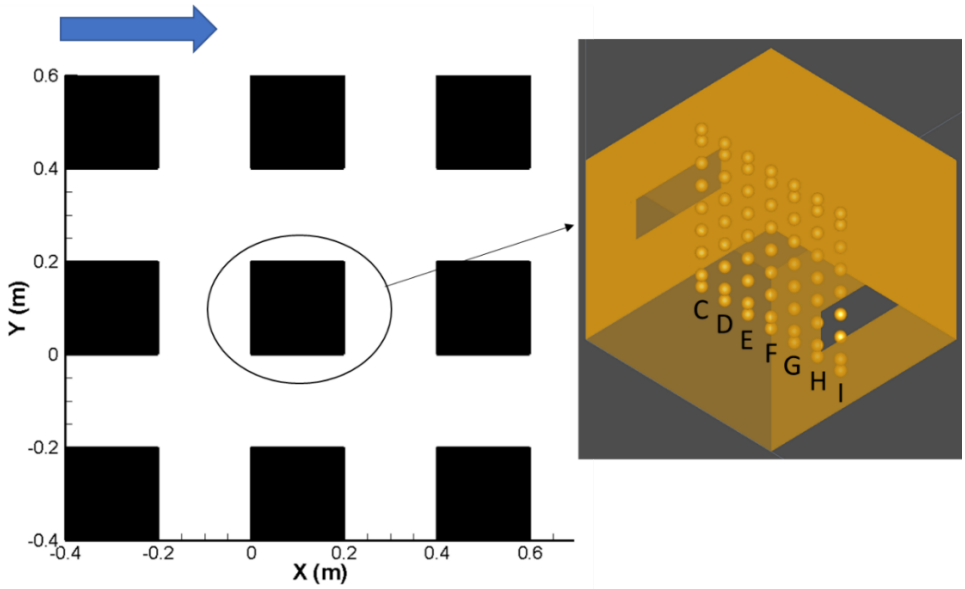

Figure 121. Urban model of idealized complexity mounted in the boundary-layer wind tunnel and close-up view of the interior of the target building. The 63 sensors inside the target building are presented also (yellow circles).

The numerical simulations

The wind flow computations were performed with the CFD code ADREA-HF (http://www2.ipta.demokritos.gr/pages/ADREA-HF.html). The Eulerian version of the model, solving the LES equations has been used in this study. The code uses finite volumes with rectangular parallelepiped cells for the discretization of the transport equations. To describe the complex geometry, the volume porosity concept is used with solid surfaces of any orientation allowed to cross the computational cells.

In the present simulation, the domain extends horizontally by 0.8 m upwind of the first and lateral buildings and by 2.4 m downwind of the last buildings. The vertical dimension of the domain is 0.96 m. The above dimensions conform to the recommendations of COST Action 732.

The grid is Cartesian. Cubic cells have been selected inside the urban area in order to decrease the discretization errors. Outside the urban area, the grid increases logarithmically by a factor of 1.1. It is well known by CFD practices for microscale modeling that the building height should be described by at least ten cells. Thus, a minimum cell size should be equal to $dx_{min} = dy_{min} = dz_{min} = 0.008$ m. The total number of cells of the present simulation is 1,464,750.

Concerning the boundary conditions, similar strategy has been folowed with Tolias et al., 2018 using the values of the present experiment.

RESULTS AND DISCUSSION

Estimation of the b parameter

Initially the estimation of the b parameter is performed. The autocorrelation time T_V is calculated from the autocorrelation function $R_V(\tau)$ (Eq. 3) on the interval from 1.0 to zero. The wind-speed time series are considered to be characterized by a sufficiently high temporal resolution. At each sensor location, a numerical peak $V_{max}(\Delta\tau)$ is identified and a b value is estimated from Eq. 1 using $V_{max}(\Delta\tau)$; the values of b range from 1.9 to 9.1 (Fig. 2). The value of 6, is exceeded five times out of 63 (i.e. 7.9%) and seems to point more to 'outlier' behaviour. This dataset clearly indicates that a value of b = 6.0 is appropriate for

this flow scenario. This is an important finding as the value of 6.0 was estimated also in Efthimiou et al., 2017 for the outdoor environment.

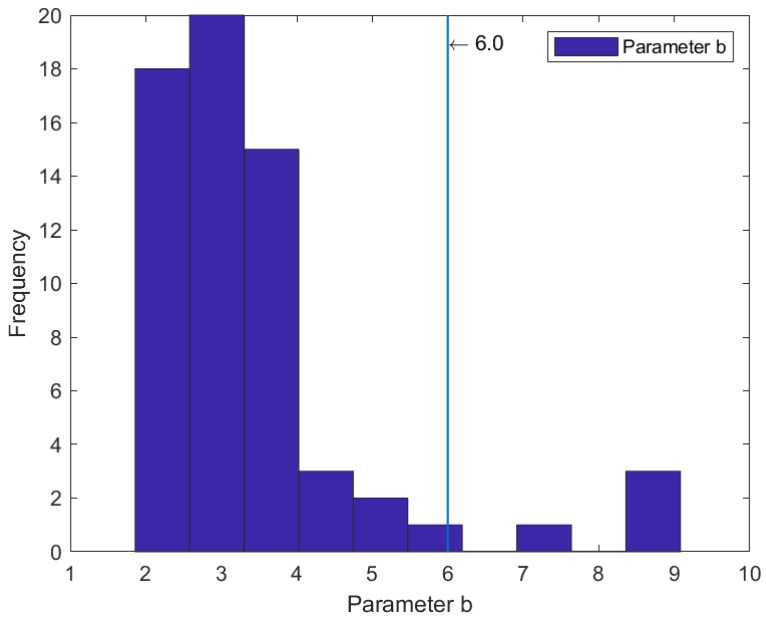

Figure 2. Histogram of the parameter b.

Performance of the deterministic model

Fig. 3 shows a scatter plot comparing $V_{max}(\Delta\tau)$ as obtained from the deterministic model (Eq. 1) fed by LES results and the equivalents predicted by the LES simulation. More specifically, horizontal axis x is the maximum wind speeds predicted from the LES wind speed time series. The deterministic model provides a success rate of 92.1% (only five values are below the 1:1 line), which supports the hypothesis that, similar to the outdoor environment, the proposed theoretical $V_{max}(\Delta\tau)$ serves as an upper bound of the corresponding predicted $V_{max}(\Delta\tau)$.

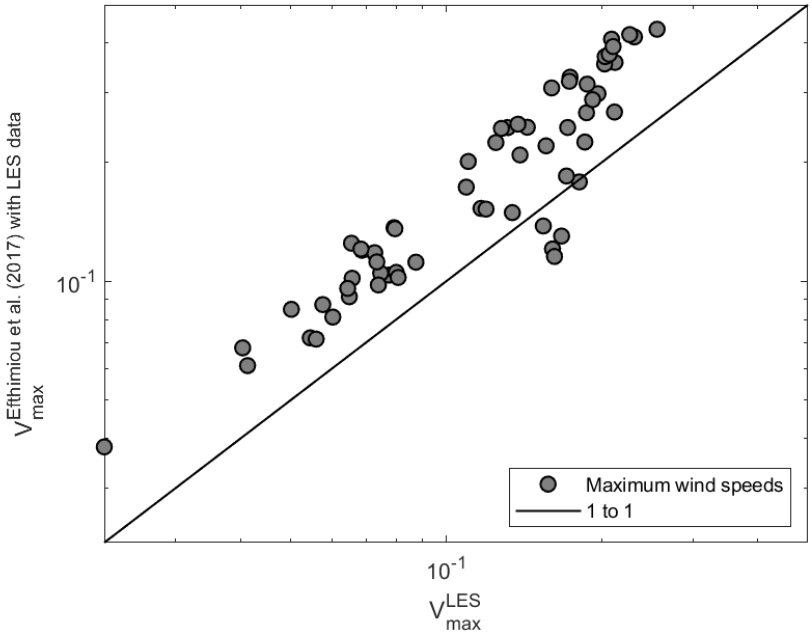

Figure 3. Performance of the deterministic model (Eq. 1).

CONCLUSIONS

By using an existing deterministic model for estimating the maximum wind speed in the Atmospheric Surface Layer based on readily available turbulence statistics (Efthimiou et al., 2017), we demonstrated that this modelling approach can be succesfully implemented also in the indoor environment without any change in its parameters.

The problem itself is quite complex and adequate validation studies require extensive experimental datasets that will include wind speed time series. Such comprehensive validation efforts exceed the scope of a single study, but the work presented here represents a significant first step towards a thorough testing of the proposed methodology.

The deterministic model broadens the capability of ensemble-averaged computational models such as Reynolds–averaged Navier Stokes–CFD models to estimate the maximum wind speed provided that reliable predictions of mean wind speeds, wind-speed fluctuations and integral time scales are available from these computations. This is a work that will be performed in the future.

REFERENCES

Diaz-Calderon, S. F., Castillo, J. A. and Huelsz, G., 2021: Indoor air quality evaluation in naturally cross-ventilated buildings for education using age of air. J. Phys.: Conf. Ser., 2069 012182.

Efthimiou, G. C., Hertwig, D., Andronopoulos, S., Bartzis, J. G. and Coceal. O., 2017: A statistical model for the prediction of wind-speed probabilities in the atmospheric surface layer. Boundary Layer Meteorology, ***163****, 179-201.*

Heracleous, C., Michael, A., 2019: Experimental assessment of the impact of natural ventilation on indoor air quality and thermal comfort conditions of educational buildings in the Eastern Mediterranean region during the heating period. Journal of Building Engineering, ***26****, 100917.*

Klepeis, N. E., Nelson, W. C., Ott, W. R., Robinson, J. P., Tsang, A. M., Switzer, P., Behar, J. V. and Engelmann, W. H., 2001: The national human activity pattern survey (NHAPS): a resource for assessing exposure to environmental pollutants. Journal of Exposure Analysis and Environmental Epidemiology, ***11****, 231–252.*

Ramponi, R. and Blocken, B., 2012: CFD simulation of cross-ventilation for a generic isolated building: Impact of computational parameters. Building and Environment, ***53****, 34–48.*

Shirzadi, M., Mirzaei, P. A. and Tominaga, Y., 2020: CFD analysis of cross-ventilation flow in a group of generic buildings: Comparison between steady RANS, LES and wind tunnel experiments. Build Simul., ***13****, 1353–1372.*

Tolias, I. C., Koutsourakis, N., Hertwig, D., Efthimiou, G. C., Venetsanos, A. G. and Bartzis, J. G., 2018: Large Eddy Simulation study on structure of turbulent flow in a complex city. Journal of Wind Engineering & Industrial Aerodynamics, ***177****, 101–116.*

Zhang, J. and Smith, K. R., 2003: Indoor air pollution: a global health concern. British Medical Bulletin, ***68****, 209–225.*

21st International Conference on
Harmonisation within Atmospheric Dispersion Modelling for Regulatory Purposes
27-30 September 2022, Aveiro, Portugal

THE CLAQC TOOL – COUNTRY LEVEL AIR QUALITY CALCULATOR. AN EMPIRICAL MODELLING APPROACH

Lara Aleluia Reis

Exposure to air pollution is one of the major health concerns worldwide. In 2019, according to HIME, 1 in 9 death worldwide were caused by fine particulate matter (PM2.5) and ozone (O3) air pollution. To that extent, it is vital to consider the air pollution health dimension in the design of policies and provide tools that can inform policy. To understand how to effectively intervene on air pollution or derive air pollution co-benefits, it is crucial to estimate the effects of national or sub-national policy interventions on emission reductions. This is especially important in integrated assessment and global policy scenario assessment.

This paper describes the CLAQC tool, CLAQC is a modeling tool that predicts monthly and annual concentration levels of two major air pollutants, ozone and fine particulate matter. It takes as input sectoral emissions at the national level. The model is written in open source languages (R and Python) and stored in an open GitHub repository to allow for transparency and community development. CLAQC builds on the recent advancements of the CAMS system and uses CAMS global gridded emissions and CAMS reanalysis pollutant concentrations. It was designed to provide insights for national and regional policy support. It is easy-to-use and fast, allowing to simulate large sets of scenarios and implementation in optimization frameworks. One of its main advantages, compared to already existing models of the same type, is that it accounts for the sectoral contributions of several pollutants. We use and compare two different empirical methodological approaches: Elastic net modeling and extreme gradient boosting regressor. Our approach provides a complementary method that relies on observed changes in concentrations given changes in emissions and meteorology. We perform out-of-sample validation and simulate a set of conceptualized policy scenarios. We show that the fuel-related sector dedicated

policies have heterogeneous reductions potentials depending on the county's characteristics. Generally, the models perform well for most countries and pollutants and can be used for policy support. Finally, we have developed an online tool where the model results are available, and a framework for method selection per country.

21st International Conference on
Harmonisation within Atmospheric Dispersion Modelling for Regulatory Purposes
27-30 September 2022, Aveiro, Portugal

QUANTIFYING HAZARDOUS AREAS TO AIRCRAFT OCCUPANTS FROM VOLCANIC SULPHUR DIOXIDE

Nina Kristiansen, Claire S. Witham

SHORT ABSTRACT

Abstract title: Quantifying hazardous areas to aircraft occupants from volcanic sulphur dioxide

Name and Affiliation of the First Author: Nina I. Kristiansen, Met Office, Exeter, UK. Email of first author: nina.kristiansen@metoffice.gov.uk
Names and Affiliations of the Co-authors:
Claire S. Witham, Met Office, Exeter, UK.
Frances M. Beckett, Met Office, Exeter, UK.

Abstract text (maximum 350 words.)

Volcanic eruptions can emit large quantities of sulphur dioxide (SO_2) into the atmosphere from explosive and effusive eruptions. Exposure to high concentrations of SO_2 can be harmful to people and the environment. Aircraft encounters with a volcanic SO_2 cloud could represent a health hazard to those onboard. Therefore, the aviation industry wishes to better understand the potential risks to their passengers and crew from volcanic SO_2. In this study we have assessed concentration levels of volcanic SO_2 in the atmosphere and demonstrate the impact of applying SO_2 concentration thresholds on the requirement to produce volcanic SO_2 forecasts for aviation.

The recommended concentration threshold for human exposure to SO_2 set by the World Health Organisation (WHO) is 500 $\mu g/m^3$ over 10 minutes. We have used dispersion model simulations to assess when and where the WHO concentration value is exceeded in the atmosphere following SO_2 rich volcanic eruptions. We have considered eight historic eruptions classified as small, moderate, or large based on the amount of SO_2 released, the release height and duration. The WHO SO_2 concentration value is exceeded for all eruptions but the time period and area over which the concentration value is exceeded vary, depending greatly on the eruption characteristics. Eruptions which release large quantities of SO_2 over a short period of time to high altitudes give the most extensive exceedance area and duration. Effusive eruptions which release SO_2 over long periods can lead to prolonged exceedances, but over small areas because emissions from this type of activity are at lower altitude where SO_2 is efficiently removed from the atmosphere.

In several cases, the SO_2 exceedance area can be considerably larger and extend for longer than the volcanic ash hazard area for the same eruption. For example, following the 2019 eruption of Raikoke, the SO_2 exceedance area reached up to 1.7 million km^2 (size of Alaska) and the WHO concentration value was exceeded for about two weeks, while volcanic ash was considered hazardous to aviation for about five days. Applying a higher SO_2 concentration threshold (WHOx6) reduces the maximum exceedance area by ~70% and the duration of exceedance by ~50%.

21st International Conference on
Harmonisation within Atmospheric Dispersion Modelling for Regulatory Purposes
27-30 September 2022, Aveiro, Portugal

UNDERESTIMATION OF POPULATION EXPOSURE ESTIMATES IN ESTABLISHED METHODS

Martin Otto Paul Ramacher, Johannes Beiser

SHORT ABSTRACT

Abstract title: Underestimation of population exposure estimates in established methods

Name and Affiliation of the First Author:

Ramacher, Martin Otto Paul, (Helmholtz-Zentrum hereon)

Email of first author: martin.ramacher@hereon.de

Names and Affiliations of the Co-authors:

Bieser, Johannes (Helmholtz-Zentrum hereon)

Abstract text *(maximum 350 words.)*

Exposure to air pollution is a global health threat. Global and regional air pollution exposure assessments are generally accounting for spatiotemporal changes in air pollutant concentrations (derived from measurements and models), but do not take into account the mobility of populations. Instead, residential addresses are used as an assumption for a never moving and thus *static* population. This static assumption for populations is known to introduce bias in exposure estimates, but still it is applied in regional and global scale exposure and health assessment studies, which are used for policy support.

However, state-of-the art approaches to air pollutant exposure modelling can consider the mobility of a population. Such *dynamic* populations in exposure estimates have been mainly applied on the urban-scale, identifying an underestimation of population exposure and therefore health effects. Thus, there is evidence that existing regional exposure estimates are underestimating the population exposure to air pollutants.

Consequently, in this study we aimed at identifying the bias arising from *static* assumptions in regional-scale exposure assessments. Therefore, we applied the time-microenvironment-activity concept to develop a method for regional exposure assessments integrating population activity. This development of a *dynamic* exposure model for the regional scale takes into account recently published information on day and night time populations for the whole of Europe, Copernicus Monitoring Service Land use information and Eurostat population statistics. The developed *dynamic* exposure model can be applied to field of air pollutant concentrations derived with any air quality model, for any European domain or period. We applied (1) the developed *dynamic* exposure model and (2) a *static* residential addresses dataset to air pollutant concentrations for

the whole of Europe (model ensemble) and compared the resulting exposure estimates.
The results of this study show substantial differences in population exposure, predominantly in urban areas and the surrounding areas especially for short-lived pollutants such as NO_2 and O_3. In general, we could show that the exposure derived with static populations is lower compared to dynamic populations for the whole of Europe. Our results indicate that the exposure and finally the adverse health effects are underestimated for the entire European population when applying *static* populations.

TOPIC 7:

INVERSE DISPERSION MODELLING AND SOURCE IDENTIFICATION

21st International Conference on
Harmonisation within Atmospheric Dispersion Modelling for Regulatory Purposes
27-30 September 2022, Aveiro, Portugal

USING ENSEMBLE NWP DATASETS TO OVERCOME METEOROLOGICAL ERRORS IN A BAYESIAN INVERSE MODELLING SYSTEM

Helen N. Webster[1,2] and David J. Thomson[1]

[1]Met Office, FitzRoy Road, Exeter, EX1 3PB, UK
[2]College of Engineering, Mathematics and Physical Sciences, University of Exeter, Exeter EX4 4QF, UK

Abstract: Source inversion techniques have been developed to constrain uncertain emission estimates and improve atmospheric dispersion model forecasts. Errors in input meteorological data can lead to discrepancies between the predicted and observed plume location and impact the performance of source inversion techniques. This study explores using ensemble meteorological datasets to account for meteorological errors in a Bayesian source inversion scheme. The source inversion scheme estimates height- and time-varying emission rates for a known source location. An ensemble of source inversion calculations is performed using the ensemble meteorological data, and a best ensemble member chosen using one of two metrics. The metrics (the evidence measure and a cost function) are easily obtained from the Bayesian framework. An iterative approach is adopted which is well suited for operational use. The method is successfully applied to the 2011 eruption of the Icelandic volcano, Grímsvötn and improvements to ash cloud forecasts are obtained using the optimal ensemble meteorological members.

KEY WORDS: EMISSION ESTIMATES, BAYESIAN SOURCE INVERSION, METEOROLOGICAL ERRORS, ENSEMBLE NWP DATA

INTRODUCTION

There are often large uncertainties in estimates of emissions, particularly during an incident when little information may be known. The resulting atmospheric dispersion model predictions are therefore subject to large uncertainties. In recent years, source inversion techniques have been developed, combining atmospheric dispersion modelling, observations and prior information, to constrain emission estimates and to improve atmospheric dispersion model forecasts.

Uncertainties also exist in the meteorological data used as input to atmospheric dispersion models. This can lead to discrepancies between modelled and observed plume locations and can impact the performance of source inversion schemes. Numerical Weather Prediction (NWP) ensembles are commonly used in meteorological communities to represent uncertainty within NWP forecasts. We explore the use of ensemble NWP data to minimise the impact of meteorological errors in a source inversion scheme.

Intem for volcanic ash

InTEM for volcanic ash is a Bayesian source inversion which can be used operationally during a volcanic eruption to obtain an optimal height- and time-varying estimate of ash emission rates (Pelley et al., 2021). It combines atmospheric dispersion modelling using NAME (Jones et al., 2007), retrievals of ash column loads from satellite observations and a first guess of ash emissions based on eruption plume height reports. Gaussian probability distributions are assumed and errors in the satellite observations and in the

prior are considered. The optimal emission estimate is identified from the peak of the posterior distribution, subject to a non-negative constraint on the emissions. During a volcanic eruption, InTEM for volcanic ash can be run in 'rolling mode' where iterations of InTEM are conducted at regular intervals, making use of additional observations and information on the volcano's behaviour since the last instance, to extend and refine the emissions estimate.

Accounting for meteorological uncertainties

Operational NWP model simulations are conducted at regular intervals (typically every few hours) and, since meteorological errors are known to increase with forecast lead time, an 'analysis' meteorological dataset is used as input with InTEM, constructed by concatenating short-term forecasts from consecutive NWP model runs. This provides a continuous historical dataset, enabling long-lasting eruptions to be studied. Meteorological data from the global version of the Met Office's NWP model, the Unified Model (Walters et al., 2019) are typically used as input to InTEM and currently InTEM does not account for uncertainties in the input meteorology. An ensemble of source inversion calculations can, however, be conducted using ensemble NWP datasets, with each ensemble member yielding an optimal ash emission estimate.

From within the ensemble, a best solution can be selected using a chosen metric. Given N ensemble members from each NWP model run and the fact that ensemble members are uncorrelated between consecutive NWP model runs, the number of 'analysis' meteorological datasets which can be constructed from the ensemble NWP data grows rapidly as N^p, where p is the number of NWP model runs. We therefore choose to employ an iterative method, which selects a best ensemble member from each NWP model run in turn. This approach fits well with the 'rolling mode' used operationally.

Selection metrics

For choosing the best ensemble member, two selection metrics are considered, both of which are easily obtained from the Bayesian framework. For each NWP ensemble member k, the posterior probability distribution, $P(\boldsymbol{e}, k|\boldsymbol{o})$, is given by

$$P(\boldsymbol{e}, k|\boldsymbol{o}) = \frac{P(\boldsymbol{o}|\boldsymbol{e}, k)P(\boldsymbol{e}|k)}{P(\boldsymbol{o}|k)}, \quad (1)$$

where $\boldsymbol{o}$ is the set of observations and $\boldsymbol{e}$ is the height- and time-varying ash emission estimate. In the absence of any preference for the ensemble members, $k = 1,\ldots,N$, they are assumed to be equally likely, $P(k) = 1/N$.

The evidence measure

At the second level of inference, the most plausible ensemble member k, given the observations dataset $\boldsymbol{o}$, is given by,

$$P(k|\boldsymbol{o}) \propto P(\boldsymbol{o}|k)P(k). \quad (2)$$

The evidence value $P(\boldsymbol{o}|k)$ in equation (1) can therefore be used to select the best NWP member from within the ensemble.

The cost function measure

Assuming the that the ensemble member k and the emission vector $\boldsymbol{e}$ are independent in the prior distribution, the posterior probability distribution for the emissions and the ensemble member satisfies

$$P(\boldsymbol{e}, k|\boldsymbol{o}) \propto P(\boldsymbol{o}|\boldsymbol{e}, k)P(\boldsymbol{e}). \quad (3)$$

With the assumed Gaussian probability distributions, the best (emissions, ensemble member) pair is found from the minimum of a quadratic cost function, subject to a non-negative emissions constraint.

Case study: Grímsvötn 2011

The Icelandic volcano Grímsvötn (64.42° N, 17.33° W) erupted at 19:13 UTC on 21st May 2011, with maximum plume heights reported up to 20 km above sea level (asl). The eruption lasted until 02:30 UTC on 25th May 2011 and hourly satellite retrievals of ash column loads are obtained from SEVIRI data, using the approach of Francis et al. (2012).

Figure 1 compares satellite observations, at 23:00 UTC on 23rd May 2011, to the model predicted ash cloud obtained using meteorological data from the global version of the Unified Model. Figure 1(a) shows the modelled ash cloud using the prior estimate of ash emissions and in Figure 1(b), the posterior estimate of emissions obtained by InTEM is used. The pink-shaded regions denote satellite observed ash-free locations. The modelled ash cloud using the prior mean estimate of ash emissions covers a large geographical region and includes a branch of the ash cloud located north of Iceland which is not observed by the satellite, and which contradicts the ash-free observations in this region. Using the posterior estimate of emissions obtained by InTEM leads to a significant improvement in the modelling of the Grímsvötn ash cloud, which is now predicted to affect a much smaller region and removes the ash cloud branch to the north of Iceland. There are still, however, some errors in the size and location of the forecast ash cloud which are likely caused by errors in the input NWP data.

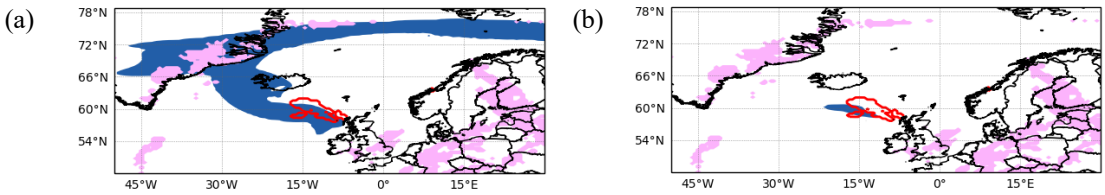

Figure 122. The modelled (blue filled contour) and observed (red open contour) ash clouds, with column loads greater than 0.5 g m^{-2}, at 23:00 UTC on 23rd May 2011. Observed clear sky regions are shaded pink. The modelled plume uses the (a) mean prior and (b) posterior estimate of ash emissions.

Alongside deterministic NWP data from the global version of the Unified Model, we use ensemble meteorological data from the ECMWF Integrated Forecast System (IFS). The input meteorological fields from all datasets are three-hourly and the spatial resolution of the global Unified Model data is 0.3515625° by 0.234375° (~25 km in mid-latitudes) and the ECMWF data is on a 0.5° by 0.5° latitude-longitude grid. The 'analysis' global Unified Model dataset is constructed from data from four NWP model runs a day (i.e., using data out to T+6 hours), whereas the 'analysis' ECMWF datasets are constructed from data from two NWP model runs a day (i.e., using data out to T+12 hours). Two iterative best meteorological datasets are constructed from the ensemble NWP data by selecting the best ensemble member from each 12 hour ensemble NWP model run in turn, using either the evidence or cost function measures.

RESULTS

Figure 2 shows the selected ensemble member from within the 21 ensemble members at each NWP run using either the evidence or cost function measures. The iteration here is over the NWP model runs, with the number of observations and the time period considered increasing with each iteration. The estimate of ash emissions is extended in time and refined at each iteration. Note that the meteorological data from previous NWP model runs / iterations are fixed, using the best ensemble member identified from each NWP model run. The final iteration covers the time period until 00:00 UTC on 31st May 2011, thereby making use, in the source inversion calculation, of downwind observations of the ash cloud after the eruption had ended. In the main, the two selection measures choose different ensemble members at each iteration, although the same members are selected on more occasions than would be expected by chance.

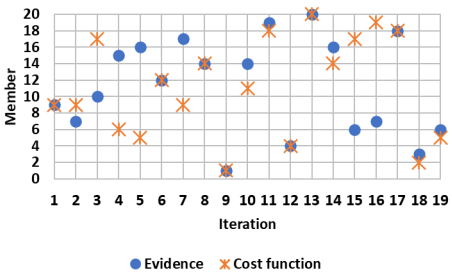

Figure 2. The selected ensemble member at each iteration (from each NWP model run) in the two iterative best meteorological datasets, chosen by the evidence and cost function measures.

Height- and time-varying emission estimates obtained from InTEM with either of the two iterative best meteorological datasets (*IBE* selected using the evidence measure and *IBCF* selected using the cost function measure) or global Unified Model data (*UMG*) are compared in Figure 3. The total fine ash emission estimates vary by about a factor of 4, with the least ash estimated to be emitted using *UMG* data (see Table 1). Retrieved ash column loads from satellite observations are compared to model predictions of ash column load obtained using the optimal emission estimate from the source inversion (shown in Figure 3) and the corresponding meteorological dataset. The normalised mean square error and the figure of merit in space (calculated with a column load threshold of 0.5 g m^{-2}) are presented in Table 1. The performance of the two iterative best meteorological datasets is similar, according to these statistics. However, both perform significantly better than the global Unified Model meteorological data. Figure 4 shows the modelled and observed ash clouds obtained using the two iterative best meteorological datasets (*IBE* and *IBCF*) at 23:00 UTC on 23rd May 2011. Compared with the modelled ash cloud obtained using global Unified Model meteorological data in Figure 1(b), we see that there is an improvement in the predicted location of the ash cloud using the two iterative best meteorological datasets. The modelled ash cloud obtained using the *IBE* dataset is larger in size than that predicted using the *IBCF* dataset. This is a consequence of the greater ash emission quantities estimated using the *IBE* meteorological dataset.

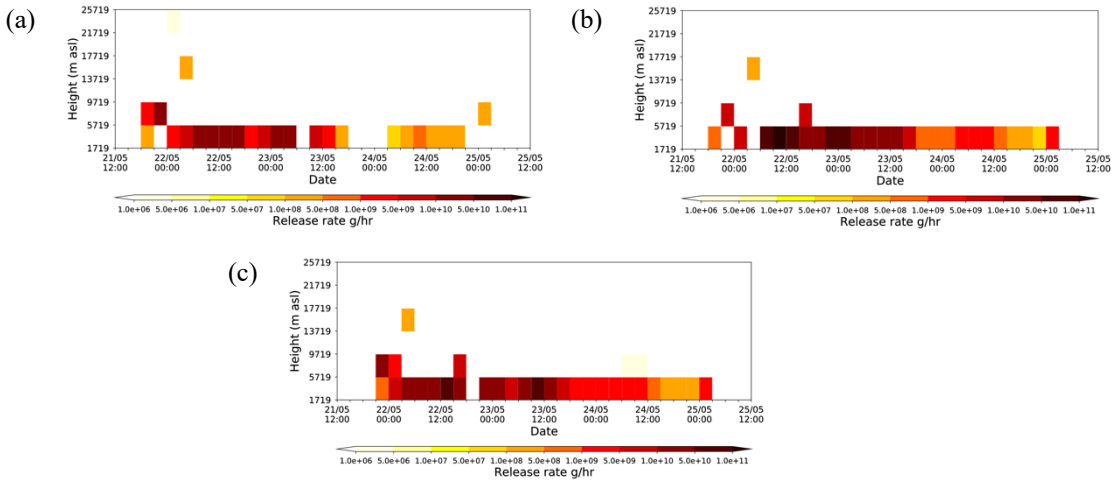

Figure 3. The InTEM-derived height-time profile of ash emissions obtained using (a) global Unified Model (*UMG*) meteorological data, (b) the iterative best evidence (*IBE*) meteorological dataset, and (c) the iterative best cost function (*IBCF*) meteorological dataset.

Table 43. The estimated total fine ash emissions, and the normalised mean square error and figure of merit in space (calculated with a column load threshold of 0.5 g m^{-2}) comparing observations to model predictions using the *UMG*, *IBE* and *IBCF* meteorological datasets

Meteorological dataset	Total fine ash emission estimates (Tg)	Normalised mean square error	Figure of merit in space

UMG	0.4	116.1	0.262
IBE	1.8	51.6	0.456
IBCF	1.1	51.5	0.462

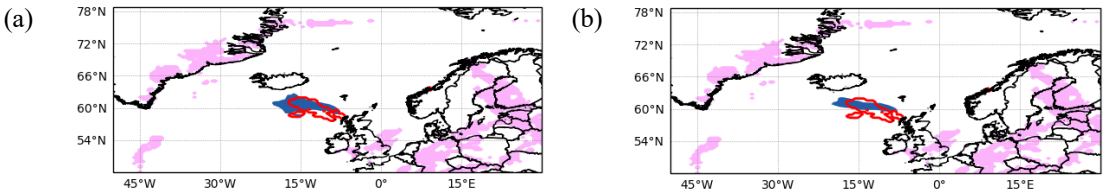

Figure 4. The modelled (blue filled contour) and observed (red open contour) ash clouds, with column loads greater than 0.5 g m^{-2}, at 23:00 UTC on 23rd May 2011. Observed clear sky regions are shaded pink. The modelled plume uses ash emission estimates, obtained by InTEM using meteorological data from the two iterative best meteorological datasets (a) *IBE* and (b) *IBCF*, together with the corresponding meteorological dataset.

DISCUSSION AND CONCLUSIONS

An iterative method, well suited for operational use, has been developed for identifying good-performing meteorological datasets and overcoming limitations due to errors in input NWP data in a source inversion technique for estimating emissions. The method is successfully applied to the Grímsvötn 2011 eruption, leading to improvements in modelling the volcanic ash cloud. At each iteration a fixed number of source inversion calculations are required, and the method is therefore viable for long-lasting incidents. Furthermore, the calculations are independent and hence the method is efficient since calculations can be conducted in parallel.

At each iteration only one ensemble member is chosen from the considered ensemble NWP model run. This best selection is then fixed, even though later observations could provide useful information on earlier meteorology. The iterative best meteorological datasets may not be the same as the analysis datasets with the highest evidence / lowest cost function values from within the full N^p possible combinations. That said, in the 2011 Grímsvötn eruption case study, the iterative best meteorological datasets were found to give good ash cloud predictions and improvements over using the deterministic meteorological dataset.

The selection of a best ensemble member at each iteration needs to be robust and supported by sufficient observations. Insufficient observations will lead to similar metric values and an inability to select the good ensemble members from the pack. In these cases, one could consider postponing selection decisions until further supporting evidence is available, although this adds to the computational resource required. In the first instance, the user needs to be confident that selection decisions are robust and supported by sufficient observations, for example, by considering the variation in the selection measures within the ensemble.

The iterative method has been seen to perform well for a case study when significant meteorological errors were present in the deterministic NWP data. There is, however, more scope for further testing and analysis. In particular, there would be interest in exploring other case studies with limited observations or with an accurate deterministic NWP dataset.

REFERENCES

Francis, P. N., M. C. Cooke and R. W. Saunders, 2012: Retrieval of physical properties of volcanic ash using Meteosat: A case study from the 2010 Eyjafjallajökull eruption. Journal of Geophysical Research: Atmospheres, ***117*** *(D20). doi: 10.1029/2011JD016788*

Jones, A. R., D. J. Thomson, M. Hort and B. Devenish, 2007: The U.K. Met Office's next-generation atmospheric dispersion model, NAME III. In C. Borrego & A.-L. Norman (Eds.), Air Pollution Modeling and its Application XVII (p. 580-589), Springer.

*Pelley, R. E., D. J. Thomson, H. N. Webster, M. C. Cooke, A. J. Manning, C. S. Witham and M. C. Hort, 2021: A near-real-time method for estimating volcanic ash emissions using satellite retrievals. Atmosphere, **12**. doi: 10.3390/atmos12121573*

*Walters, D., A. J. Baran, I. Boutle, M. Brooks, P. Earnshaw, J. Edwards, ... and M. Zerroukat, 2019: The Met Office Unified Model Global Atmosphere 7.0/7.1 and JULES Global Land 7.0 configurations. Geoscientific Model Development, **12**, 1909–1963. doi: 10.5194/gmd-12-1909-2019*

21st International Conference on
Harmonisation within Atmospheric Dispersion Modelling for Regulatory Purposes
27-30 September 2022, Aveiro, Portugal

VALIDATION STUDY OF WINDTRAX BACKWARD LAGRANGIAN MODEL

Francesca Tagliaferri[1], Marzio Invernizzi[1] and Selena Sironi[1]

[1]Department of Chemistry, Materials and Chemical Engineering, Politecnico di Milano, Milano, Italy

Abstract: In last years, atmospheric dispersion models have reached considerable popularity in environmental research field. In this regard, given the difficulties associated to the estimation of emission rate for some kind of sources, and due to the importance of this parameter for the reliability of the results, backward dispersion models may represent very promising tools. This paper discusses a critical validation of the Windtrax backward Lagrangian model: the investigation does not only deal with the strict reliability of the model but also assesses under which conditions (i.e. stability class, number, and location of the sensors) the model shows the greatest accuracy. For this purpose, Windtrax results have been compared to observed values obtained from available experimental datasets. From this study, it turns out a general tendency of the model to predict the observed values with a good level of accuracy, especially under neutral atmospheric conditions. In addition, it seems that Windtrax underestimates the emission during unstable stratification and overestimates during stable conditions. Finally, by the definition of scenarios in which only a portion of the concentration sensors was considered, Windtrax performance appears better than acceptable even with a small number of sensors, as long as the positioning is not in the strict vicinity of the source.

KEY WORDS: DISPERSION MODELLING, BACKWARD STOCHASTIC MODEL, INVERSE MODELLING, VALIDATION STUDY

INTRODUCTION

In last years, urbanization and industrialization have been major contributing factors to the poor air quality. Having information on atmospheric pollution and its environmental impact on citizens is the starting point for improving air quality (Wang et al., 2008). Therefore, the evaluation of the extent of exposure to chemicals becomes a key issue. In this regard, dispersion modelling represents a useful tool for reproducing spatio-temporal distribution of contaminants emitted by a specific source thereby quantifying the areas of population exposure as well as the ground level concentrations of contaminants (Mangia et al., 2014). However, the characterization of the emission source, which is a fundamental step in the implementation of atmospheric dispersion models, is not trivial (Invernizzi et al., 2018). In particular, it is necessary to define the emissive flux released by the source whose estimation, in case of complex sources (e.g. floating roof tanks, tanks topped by grates), may be critical (Invernizzi et al., 2018). To this end, it would be extremely useful to apply an inverse dispersion model: so, by knowing a concentration value in space, to quantify the emission rate of the source.

The Windtrax software (Crenna, 2006) is a backward Lagrangian stochastic model, based on the principles of Monin-Obukhov Similarity Theory (MOST) (Flesch and Wilson, 2005, 1995), that computes an ensemble of random paths backward in time from the detectors to the sources thus quantifying the unknown emission rates from measured downind concentrations. The studies available in literature regarding the application of the Wintrax model are generally focused on the evaluation of how well it predicts the emission of pollutants from area sources, which is typically the way in which agricultural sources are treated. On the contrary, the present study focuses on the application of Windrax for a different type of source. In fact, before tackling datasets with complex sources, it was decided to

initially test the model by considering sources, such as stacks, never discussed in literature in similar studies. Also, when dealing with sources of this kind, being easy to characterize, the observed emission rate to compare with the model output is more reliable and consequently the model validation is more robust. Precisely, two experimental campaigns with a point source (i.e. stack) will be considered. In this study, a validation of the model was carried out not limiting to this, but also trying to understand under which conditions (i.e. stability class, number and location of the sensors) it provides a greater accuracy. The aim of this work is to validate the Windtrax model by comparing the model results with observed values taken from datasets of real experimental fields available in literature.

METHODS

Uttenweiler and Round Hill campaigns

The Uttenweiler campaign was conducted in a pre-existing pig farm in 12 and 13 December 2000 and 31 October 2001. The farm is situated outside the small village Uttenweiler, 20 km west of the city of Bielberach (5331621 N, 548508 E) in Germany. The surrounding area is mostly flat. This farm consists of the pig barn and the feed processing room. The gas tracer, sulphur hexafluoride (SF6) was continuously emitted by a single point source located on a building. It was at 8.5 m above the ground level, and it was connected to the internal ventilation system.

The second campaign is the Round Hill experiment (Cramer et al., 1958). The site area, with a flat terrain, is close to the Round Hill Field Station of the Massachusetts Institute of Technology (338022 E, 4600793 N). The site roughness was around 7-30 cm and the vertical emission consisted of a stack at 30 cm from the ground releasing SO2. A large number of experiments were conducted, some of them have been considered in the present study. The data set was obtained by means of the website http://www.harmo.org/jsirwin.

Model Validation

The first objective of this work was to estimate the performance of the Windtrax model in predicting the experimental data thereby performing a model validation. For this purpose, some statistical indicators were used (Chang and Hanna, 2004; Gustafson and Yu, 2012): Mean Bias (MB), Normalized Mean Bias (NMB), Root Mean Squared Error (RMSE), Normalized Mean Squared Error (NMSE), Index of Agreement (IOA) and FAC2. The equations of each indicator are reported by Invernizzi et al. (2021).

RESULTS AND DISCUSSION

Uttenweiler campaign

As first test, all the possible concentration sensors (12 measurement points) of the Uttenweiler campaign were entered as input data. In Table 44 the statistical indicators computed by considering all the 14 experiments are reported.

Table 44. Statistical indicators computed by considering all the experiments

MB	NMB	RMSE	NMSE	IOA
46.3	0.3	94.1	0.21	0.7

Focusing on the statistical indicators NMB, NMSE and IOA, the values predicted by the Windtrax model (Crenna, 2006) appear quite good. To confirm this, it is emphasized that the totality of the values obtained belong to the FAC 2 range.

Given that 12 concentration sensors are rarely available, it was decided to evaluate the quality of the model progressively reducing the number of concentration sensors up to a single measurement point. The Uttenweiler campaign is characterized by a particular positioning of the concentration sensors: it develops in one or two transects (depending on the specific experiment) placed approximately perpendicular to the direction in which the wind was blowing. In experiments with two transects, these are placed parallel to each other and downwind of the emission source: so, one closer to the source and one further away. To show the results of this test, i.e. validation of the model when reducing the number of measurement points a table with the percentage errors between the modelled and the observed value and the standard deviation

of the modelled result for each experimental trial (identified by a letter B-O) is reported (Table 45). The different configurations implemented into the model are:

0) The entire concentration sensors,
1) The entire transect of concentration sensors closest to the source,
2) The entire transect of concentration sensors farthest from the source,
3) Two downwind sensors on the transect closest to the source,
4) Two downwind sensors on the transect farthest from the source,
5) One downwind sensor on the transect closest to the source,
6) One downwind sensor on the transect farthest from the source,

Table 45. Percentage Error of the modelled value with respect to the observed value and standard deviation of the model result, for different spatial configurations of the concentration sensors (0-6)

	0		**1**		**2**		**3**		**4**		**5**		**6**	
	ER%	**SD**	**ER%**	**SD**	**ER%**	**SD**	**ER%**	**SD**	**ER%**	**SD**	**ER%**	**SD**	**ER%**	**SD**
B (N/S)*	-13.6	14.1	-3.4	30.9	-2.9	18.5	-10.3	21.6	-2.3	19.6	-40.8	17.0	-9.9	26.0
C (N/S)*	-14.4	12.7	-13.2	29.3	-29.8	15.9	-22.5	16.1	-29.0	10.4	-26.0	17.1	-24.6	28.3
D (S)*	6.8	32.5	10.3	47.4	-30.0	35.0	1.9	28.0	-6.2	102.8	0.6	28.9	-31.7	39.6
E (N/S)*	26.1	44.4	24.6	28.3	7.3	20.1	-3.7	31.1	29.8	24.5	-17.4	21.7	35.0	37.3
F (N/S)*	54.7	15.2	72.8	56.8	8.8	18.4	43.3	53.1	-17.0	19.3	46.4	48.7	-5.9	45.3
G (N/S)*	28.3	23.5	77.2	34.6	-6.1	16.7	39.1	27.4	-27.5	42.0	32.8	36.9	-29.0	19.5
H (S)*	25.4	28.9	100.3	29.8	-27.3	13.8	151.3	95.8	-25.4	14.0	130.8	101.2	-30.6	22.1
M (S)*	34.2	45.2	125.3	83.1	-24.1	29.2	94.9	101.3	-19.8	24.4	93.7	77.6	11.1	67.7
N (S)*	-5.6	27.0	27.0	88.0	-22.3	46.6	27.1	56.5	-33.3	35.2	192.4	219.0	-40.4	20.6
O (VS)*	-16.8	41.0	192.3	197.5	-35.3	32.4	169.1	114.2	-38.6	18.4	304.5	396.6	-39.3	25.7

* N/S = neutral/stable; S = stable; VS = very stable

For the sake of clarity, a conditional formatting is used to have an easy-to-use overview of the model response: the percentage errors are shaded in yellow with increasing intensity as further away from zero (ideal value), the standard deviations in blue.
From Table 45, it is possible to observe that the highest values of percent error and standard deviation occur when considering experiments with stable and very stable conditions, particularly in situations where the concentration sensor was positioned on the transect closest to the source. This may be related to the fact that the plume emitted from the source under stable conditions is poorly dispersed in both the vertical and horizontal directions, so it is less likely having the plume to pass through the concentration sensors and this effect is more pronounced in the vicinity of the emission source where the pollutant is less diluted and

dispersed. The average percentage error computed by considering the absolute values of the percentage errors of the single experiments is about 41%, while considering only experiments in neutral/stable condition the average error decreases up to 24%. However, for the experiment D, performed in stable conditions, low percentage errors are detected, even on receptors positioned close to the source. This may be attributed to the fact that the location of the concentration sensors in all the configurations developed for this experiment and the wind direction are such that the plume always crosses only one sensor. Therefore, since this sensor is the only one which contributes to the quantification of the emission rate and it has been maintained in all the configurations, the removal of the other receptors does not affect the results.
Concerning the influence of the number of receptors, it seems that the reduction of the number of sensors does not necessarily improve the model performance. Thus, it can be inferred that the correct downwind placement of the sensor is much more significant than the number of sensors.
To conclude, this dataset highlights good performance of the model in predicting the emission rate under neutral condition. Under stable conditions great care must be taken with the location of the sensor due to the fact that the plume is poorly dispersed. In this sense, a possible solution might be to move the sensor away from the source.

Round Hill campaign

The Round Hill campaign is characterized by sensors positioned along arcs at different distances from the source (i.e 50 m, 100 m and 200 m). In particular, eight experiments characterized by different stability classes, were chosen to be tested: three of them are conducted under Moderately Unstable (MU) conditions, two in Neutral (NN) conditions, two in Moderately Stable (MS) conditions and only one in Extremely Stable (ES) conditions. In this way, it was possible to test the performance of the model under different stability conditions. In addition, for each experiment, different configurations of receptors were considered: in conf. (1) one arc of six downwind receptors at 50 m from the source (blue in Figure 2), in conf. (2) one downwind receptor at 50 m from the source (brown); in conf. (3) one downwind receptor at 100 m from the source (green) and in conf. (4) one downwind concentration at 200 m from the source (yellow).
In Figure 123, % errors obtained for the different configurations of receptors (1- 4) for the eight experiments are reported. It should be noted that in configuration 4, the first and third columns are missing, due to the failure to obtain a model result for the specific experiments.

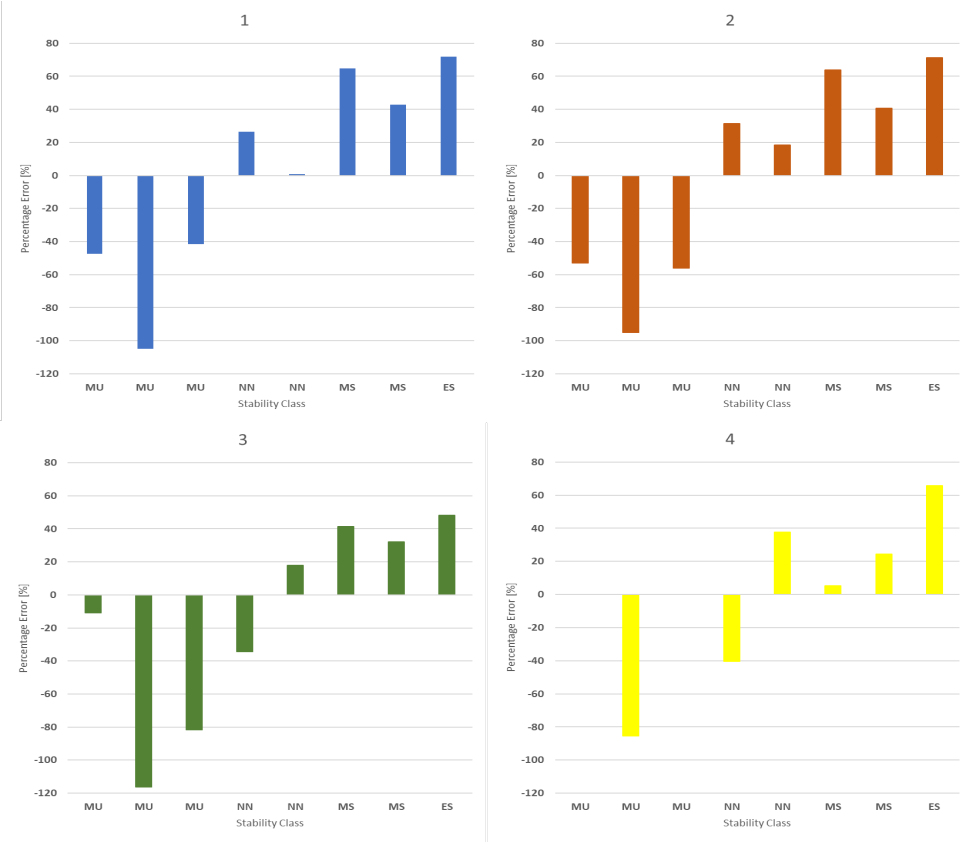

Figure 123. Percentage Error for the eight experiments with different stability class, in four different spatial configuration of concentration sensors (1-4).

From Figure 123, a general tendency of the model to overestimate in stable atmospheric conditions and to underestimate in unstable conditions is observed. In addition, higher accuracy of the model in predicting the experimental data under neutral condition in shown. The percentage errors for neutral stability class are always good, with an average absolute value of 10 %. Conversely, the mean % error for experiments in unstable conditions is about -60%; in stable conditions is about 50%. Although absolute values of percentage errors obtained under stable and unstable conditions are comparable, it seems that the unstable conditions have a much more fluctuating error pattern (i.e. very low errors in some experiments, very high in others and eventually no results). This is probably attributable to the high level of turbulence in unstable condition.
By reducing the number of sensors, it seems that the model still responds well, as for Uttenweiler campaign.
In Table 46, the statistical indicators discussed are computed distinguishing between the experiments conducted in neutral, stable and unstable conditions. Overall, it seems that the model predicts the experimental data with a quite high level of accuracy, with the best values obtained in neutral conditions.

Table 46. Statistical indicators for all the considered experiments

MB			**NMB**			**RMSE**		
Unstable	**Neutral**	**Stable**	**Unstable**	**Neutral**	**Stable**	**Unstable**	**Neutral**	**Stable**
6.3	-0.6	-3.1	0.5	-0.1	-0.5	7.3	1.7	3.3
NMSE			**IOA**			**FAC2**		
Unstable	**Neutral**	**Stable**	**Unstable**	**Neutral**	**Stable**	**Unstable**	**Neutral**	**Stable**

0.3	0.1	0.5	0.005	0.1	0.4	81 %	100 %	50 %

CONCLUSIONS

The present study aims to test the performance of the backward Lagrangian model Windtrax, to evaluate the model reliability in predicting the observed emission rate. In addition, it also tries to understand under which conditions the performance of the model are expected to be higher.

From the results of this study, it turns out a general tendency of the model to predict the observed values with a good level of accuracy. In particular, for the Uttenweiler campaign, acceptable values of the performance indicators are obtained. For the Round Hill dataset, the model results are even better: in this case, an average percentage error of about 40% over all the experiments is estimated. In addition, this study highlights the importance of a correct positioning of the concentration sensor to make the model result reliable. Also, from this evaluation, the performance of the model in different stability conditions were investigated. In this regard, it appears that the model is more reliable for neutral conditions, where a good agreement between the experimental data and the simulated values are observed.

In conclusion, Windtrax seems very promising for the estimation of the emission rates. However, it is worth highlighting that it is not a trivial tool, and therefore, to obtain reliable results, it requires a deep preliminary study, regarding the position of the concentration sensor and the optimal meteorological conditions.

REFERENCES

Chang, J.C., Hanna, S.R., 2004: Air quality model performance evaluation. Meteorol. Atmos. Phys. https://doi.org/10.1007/s00703-003-0070-7

Cramer, H.E., Record, F.A., Vaughan, H.C., 1958: The study of the diffusion of gases or aerosols in the lower atmosphere 19, 1–185.

Crenna, B., 2021: Thunderbeachscientific [WWW Document]. URL http://www.thunderbeachscientific.com/

Crenna, B., 2006: An introduction to WindTrax 19.

Flesch, T.K., Wilson, J.D., 2005: Estimating Tracer Emissions with a Backward Lagrangian Stochastic Technique 513–531. https://doi.org/10.2134/agronmonogr47.c22

Flesch, T.K., Wilson, J.D., 1995: Backward-Time Lagrangian Stochastic Dispersion Models and Their Application to Estimate Gaseous Emissions 1–27.

Gustafson, W.I., Yu, S., 2012: Generalized approach for using unbiased symmetric metrics with negative values: Normalized mean bias factor and normalized mean absolute error factor. Atmos. Sci. Lett. 13, 262–267. https://doi.org/10.1002/asl.393

Invernizzi, M., Ilare, J., Capelli, L., Sironi, S., 2018: Proposal of a method for evaluating odour emissions from refinery storage tanks. Chem. Eng. Trans. 68, 49–54. https://doi.org/10.3303/CET1868009

Invernizzi, M., Capra, F., Sozzi, R., Capelli, L., Sironi, S., 2021: Development and Evaluation of a Fluctuating Plume Model for Odor Impact Assessment. Applied Science.

Mangia, C., Cervino, M., Gianicolo, E.A.L., 2014: Dispersion models and air quality data for population exposure assessment to air pollution. Int. J. Environ. Pollut. 54, 119–127.

Wang, G., Bosch, F.H.M. Van Den, Kuffer, M., 2008: Modelling urban traffic air pollution dispersion. Int. Arch. Photogramm. Remote Sens. Spat. Inf. Sci. 37, 153–158

21st International Conference on
Harmonisation within Atmospheric Dispersion Modelling for Regulatory Purposes
27-30 September 2022, Aveiro, Portugal

^{137}CS SOURCE RECONSTRUCTION OF UNPRECEDENTED WILDFIRES IN THE CHERNOBYL EXCLUSION ZONE IN APRIL 2020

Olivier Saunier[1] and Olivier Masson[1]

[1]Institut de Radioprotection et de Sûreté Nucléaire (IRSN), Fontenay-aux-Roses, France

Abstract: In April 2020, fires of unprecedented proportions took place in Ukraine in the territories of the Chernobyl Exclusion Zone. These fires led to the re-suspension of ^{137}Cs, which was then dispersed across Europe. Inverse modelling techniques incorporating the multiplicity and mobility of the fires were applied to estimate the total amounts of ^{137}Cs emitted into the atmosphere. The calculations indicate that the estimated ^{137}Cs source term for the whole fire period is around 1,000 GBq. The atmospheric dispersion simulations performed using this source term are consistent with the observations. Indeed, the proportion of measurements for which the observed and modelled concentrations agree within a factor of 2 (FAC2) is about 50% and the FAC5 scores are above 75%. Furthermore, the modelling proved to be very useful and robust in predicting concentration levels in France and Europe. It was possible to accurately determine the arrival times of the plume at the impacted stations and thus confirm whether the measured ^{137}Cs levels were related to a contribution from forest fires or only to the usual resuspension of ^{137}Cs from the Chernobyl accident and nuclear weapons testing.

KEY WORDS: INVERSE MODELLING, MULTI-SOURCES, WILDFIRES, ATMOSPHERIC TRANSPORT MODELLING.

INTRODUCTION

During April 2020, wildfires with unprecedented proportions occurred in the contaminated territories following the Chernobyl accident of 1986. For about 4 weeks, the fires spread around and within the Chernobyl exclusion zone and came within a few kilometres of the power plant and radioactive waste storage facilities. Throughout this period, the fires promoted the re-suspension of ^{137}Cs into the air, which was then dispersed across Europe. Although the ^{137}Cs concentration levels were too low to have any impact on human health and the environment, IRSN activated its crisis centre to monitor and analyse the event. One of the objectives was to use modelling tools to predict the dispersion of the ^{137}Cs plume over Europe and to anticipate a possible arrival of contaminated air masses in France.

One of the key challenges was to estimate the time-dependent quantity of ^{137}Cs re-emitted into the atmosphere. The Ukrainian Hydrometeorological Institute (UHMI) performed source term assessment based on environmental parameters such as satellite observations of burned areas, biomass density, and contamination density maps (Protsak et al. 2020). According to the UHMI, 870 km^2 burnt and the total ^{137}Cs source term was around 700 GBq. Another way to assess radionuclide amounts emitted from the burnt areas is to apply inverse modelling techniques which combine rigorously observed and modelled air concentrations. In Masson et al. (2021), such methodology was implemented assuming that the source emission was a point source. However, regarding spreading and moving fires and the occurrence of several fire outbreaks at the same time, considering the source emission as a unique point represents an approximation.

In this study, an adaptation of the inverse modelling approach is therefore proposed to deal with multi-sources emission, and it is applied to retrieve the total ^{137}Cs emissions. Using this source term, atmospheric transport modelling is then carried out to evaluate the ^{137}Cs air concentrations levels expected at European

scale and to identify the geographical areas which could be impacted by the passage of the plume. The main results obtained are discussed and validated by performing model-to-data comparison.

Observations

Measurement data have been shared within the Ring-of-Five (ro5) European monitoring network whose main objective is to strengthen international collaboration between radioprotection organizations on rapid monitoring information sharing. In total, about 1100 results were gathered throughout Europe. Maximum concentration values were measured in Ukraine near the Chernobyl nuclear power plant (180 mBq/m^3 on April 13th). As described in Masson et al (2021), these concentrations do not lead to any health or environmental issues. Outside Ukraine, the highest values were measured in Belarus (several hundred µBq/m^3 on April 12th), in the Russian Federation and in Greece (several tens of µBq/m^3). In Poland, Czech Republic and Austria, the maximum of measured concentrations was much lower, generally between 2 and 4 µBq/m^3. In France, the maximum reported concentration is 1.2 µBq/m^3, higher values, up to 5 µBq/m^3, were measured in Belgium and northern Germany. These values are not exclusively related to the wildfires of 2020. Indeed, there is a residual background of ^{137}Cs in Europe, linked to the Chernobyl accident of 1986 and the nuclear weapon tests of the 1960s. This background varies significantly from one country to another and can also be affected by meteorological conditions. In the territories located in the Chernobyl exclusion zone, the average background level is around 3.5 mBq/m^3. In contrast, it is much lower in the Kiev region, averaging a few µBq/m^3. The analysis of the measurement data in Ukraine nevertheless shows that the wildfires caused a very significant increase in airborne ^{137}Cs levels, by a factor of 100 to 1000 compared with the values usually recorded in these territories. Outside Ukraine, the ^{137}Cs background is generally around a few µBq/m^3 or much lower in Western Europe, below 1 µBq/m^3 in France. Consequently, the identification of the origin of the measured ^{137}Cs air concentration can be made very tough when the measured levels are close to the background. The air sampling periods, which are generally weekly, do not allow the accurate identification of the passage of a plume that has passed over a station during shorter period. Atmospheric transport modelling is therefore very suitable in discriminating the origin of the ^{137}Cs measured. For this purpose, the first step is to estimate ^{137}Cs emissions into the atmosphere by inverse modelling.

Source term assessment methodology

In Masson et al. 2021, a first estimate of the ^{137}Cs emissions was performed by inverse modelling assuming that the source emission was a point source. This assumption represents an approximation with regard to spreading and moving fires and the occurrence of several fire outbreaks at the same time. Therefore, in this study, we propose a more realistic assessment taking into account the multiplicity and mobility of the fires. For this purpose, we first based ourselves on the results published in the UHMI report, which identify 6 main fires areas located in the Chernobyl contaminated territories. We then estimated the releases over time for each fire by inverse modelling, considering each fire as a point source and imposing the release periods of each fire by exploiting satellite observations of the burnt areas. The analysis of the satellite images shows that never more than two outbreaks burned simultaneously, which reduces the number of degrees of freedom associated with the inverse problem. The source term assessment methodology is based on a variational approach (Masson et al. 2021) and consists in combining air concentration measurements and results from the atmospheric dispersion model. This method is based on a source-receptor relationship which links the source term x to be estimated to airborne concentration measurements y:

$$y = \sum_{i=1}^{6} H_i x_i + \epsilon \quad (1)$$

H_i is the source-receptor matrix associated to the fire i. Its elements correspond to the response of the dispersion model for a ^{137}Cs unit release emitted from the fire i, at different measurement points. The dispersion model used is the Eulerian ldx model which is a part of the IRSN's C3X emergency response operational platform. The meteorological fields are provided by the ARPEGE model developed by Météo-

France. The spatial resolution is 0.1° x 0.1° with a 1-hour time resolution. The dry deposition is modelled using a simple schema with a constant deposition velocity: $v_d = 2.10^{-3}$ m·s^{-1}. For wet deposition, two different settings are used (Querel et al. 2021) depending on whether aerosol scavenging takes place below or within the cloud. The vector ϵ represents a combined model-representation-instrumental error. The resolution of the inverse problem (1) consists in determining the components of the source term x such that ϵ is minimal. The following cost function J(x) is therefore introduced and minimized by using iterative quasi-Newton gradient methods:

$$J(x) = \sum_{i=1}^{6} \sum_{j=1}^{d} \left(\ln(y_j + \theta) - \ln(H_i x_i + \theta)_j\right)^2 \quad \text{Subject to } x \geq 0 \qquad (2)$$

Where d is the number of measurements. To assign a relatively similar weight to each concentration, the logarithm of the concentrations is considered in the cost function. A threshold θ was established in order to take into account measurement values lower than detection limits. In this study, θ = 1 µBq·m^{-3}.

RESULTS AND DISCUSSION

Source term

Twenty-two different daily releases were estimated by inverse modelling between April 2nd and 24th 2020. Although satellite images after April 24 indicate a persistent residual fire, releases were assumed insignificant after that date. The estimated ^{137}Cs source term for the entire fire period lies around 1,000 GBq. This estimate is consistent with recently published assessments using different approaches (De Meutter et al. 2021). In particular, the evaluated quantities are compatible with those obtained in Masson et al. (2021) by assuming the release point as fixed and using meteorological fields at a coarser spatial resolution (0.25° x 0.25°). The temporal evolution of the release rates is shown in Figure 124. Firstly, it can be seen that releases occurred almost every day with a maximum reached on 16 and 20 April with respectively 160 GBq and 148 GBq released into the atmosphere. Figure 124 shows the number of observations exploited to estimate each daily release during the inverse modelling process. In particular, we notice that this number varies very significantly with time. For example, a high number of observations is available for the reconstruction of the releases between April 3 and 6, which allows a higher confidence in the estimation of the source term during this period. On the other hand, for the most significant releases on 15 and 16 April, the number of observations used is limited, less than 10, which makes the estimation of these releases relatively uncertain. After 20 April, the number of observations is also too low to be able to provide a realistic estimate of the releases.

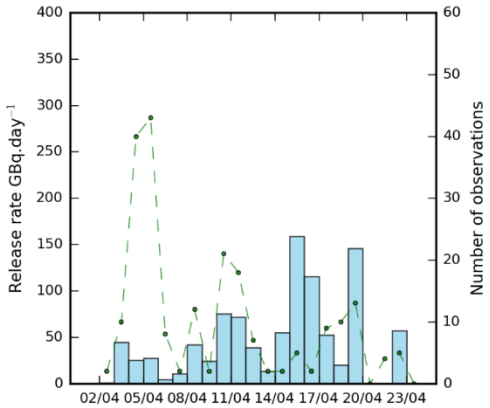

Figure 124: April 2nd to April 24th 2022 ^{137}Cs daily release rates reconstructed by inverse modelling (blue rectangles). The green dashed line represents the number of observations used for each daily release rate.

Plume dispersion analysis

From the source term estimated by inverse modelling, the simulation of the dispersion of the ^{137}Cs plume was carried out using ldX. Figure 125 shows the simulation of the ^{137}Cs plume dispersion at different times. According to the simulation, the plume first moved towards the Russian Federation on 3 April. From 5 April onwards, the plume started to impact the countries located further south (Romania) and west (Hungary, Austria and Poland). The observed values in these countries effectively show an increase in ^{137}Cs concentration levels which is consistent with the modelling. From 8 April onwards, the plume reached Germany, the south-east of France and the north of Italy. However, the simulated concentration levels are very low, barely above 1 µBq/m^3 and therefore very close to the detection limits. This explains why several stations located in Germany or Switzerland did not report any concentration above the detection limits. Between 10 and 20 April, the plume mainly concerned the Russian Federation, Belarus and Romania. On 14 April, the plume moved far north and reached the extreme north of Norway. The maximum simulated concentrations exceeded 30 µBq/m^3 but the plume passed through this region relatively quickly, in about a few hours. This explains why the weekly sampling carried out in northern Norway showed little variation compared to weekly averages with a concentration of only 0.5 µBq/m^3. From 20 April onwards, the plume again moved towards Greece and then affected all the countries bordering the Mediterranean Sea as far as south-eastern France.

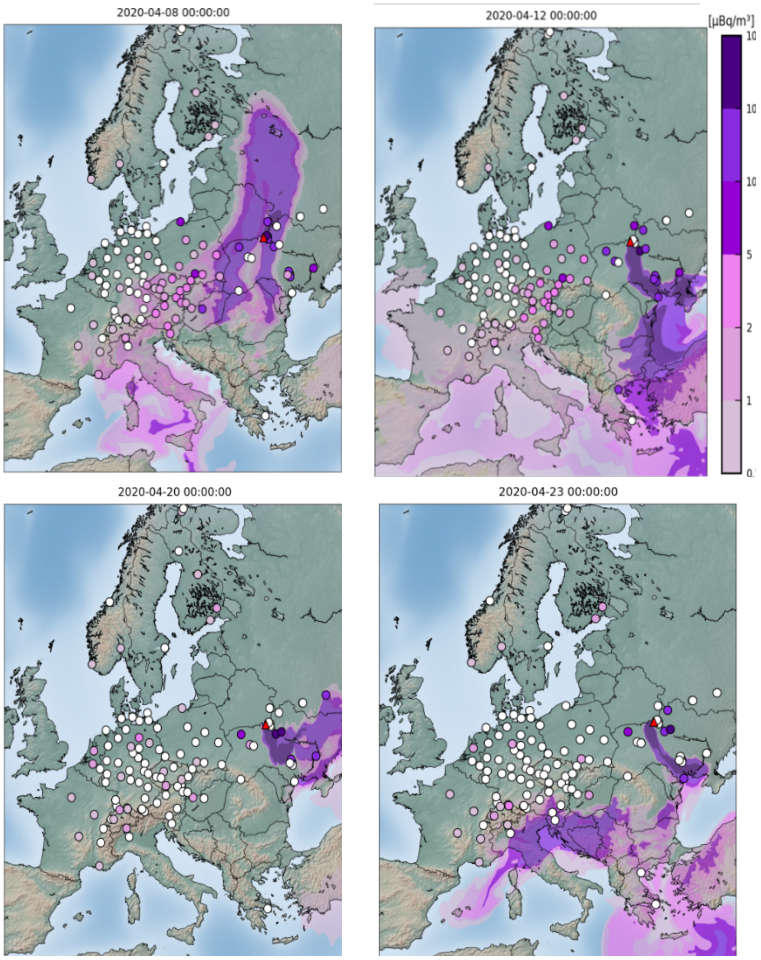

Figure 125: Instantaneous modelled ^{137}Cs concentration fields shown together with time-averaged measurements. The dots represent the observed concentrations. Measurements under detection limit are represented by white dots.

Figure 3 shows the simulated and observed time-integrated ^{137}Cs concentration between 2 and 24 April. The maximum time-integrated concentrations are logically located in the vicinity of the fire area.

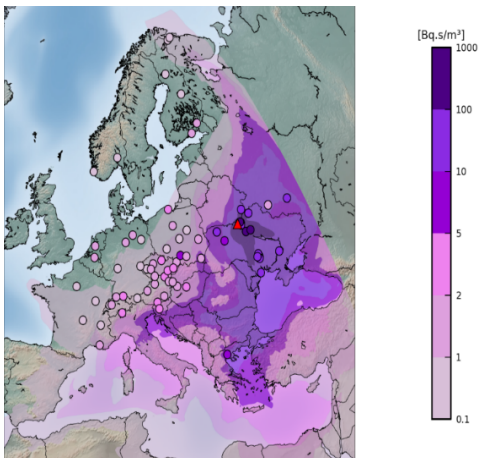

Figure 126: Time-integrated modelled ^{137}Cs air concentration in the period 2 April 2020 to 24 April 2020. Dots represent observed time-integrated air concentrations.

It can be seen that the modelled time-integrated concentrations are in very good agreement with the observations, especially in Ukraine and Greece, where the concentration values are well above the background values. Moreover, around 50% of the simulated ^{137}Cs concentrations were within a factor of 2 compared to the observed concentrations. This score provides significant validation of the reconstructed source term. In Western Europe, modelled time-integrated concentrations highlight that wildfires had a very limited impact, even though at some stations they may have led to a slight increase in concentration levels (south-east France, Poland, Czech Republic). The simulations confirm that the plume reached the extreme north of Norway in a very attenuated way. On the other hand, the increase in concentration levels observed in Belgium, the Netherlands and northern Germany cannot be explained by the fires. A contribution from only to the local re-suspension of ^{137}Cs from the Chernobyl accident may be a possible hypothesis.

CONCLUSION

The forest fires that occurred in April 2020 in the Chernobyl exclusion zone were the largest in terms of area burned, with 870 km^2. These wildfires led to re-suspension of historically deposited ^{137}Cs into the atmosphere. Measurements of ^{137}Cs concentrations in the air showed a significant increase in concentration levels in the areas closest to the fires, notably in Ukraine and Belarus, but without this posing a threat to health. In Central and Western Europe, the increase in concentrations was more modest, often close to the usual values, making the interpretation of the measurements more complex. Atmospheric transport modelling has proven to be very useful in quantifying the impact of fires on a European scale. In a first step, inverse modelling have been applied to retrieve the total ^{137}Cs amounts emitted into the atmosphere over 3 weeks. The estimated source term is of the order of 1,000 GBq, consistent with other published assessments. This source term was then used to simulate the dispersion of the ^{137}Cs plume on a continental scale. The proportion of simulated and observed concentrations that is within a factor of 2 reaches 50%, which shows the relevance of the reconstructed source term. The modelling of the plume dispersion highlights that many European countries were at some time impacted by the passage of the plume. The highest simulated concentration levels were logically concentrated in Ukraine and the Russian Federation. Further west, the simulated concentration levels are very low, close to the values usually recorded in this season. However, the modelling made it possible to dissociate a slight increase in concentrations linked to a local re-suspension from that directly linked to a contribution from Chernobyl wildfires.

REFERENCES

De Meutter, P, Gueibe, C, Tomas, J, Apituley, A, Bruggeman, M, Camps, J, den Outer, P, Delcloo, A, Knetsch, G-J, Roobol, L & Verheyen, L, 2021: The assessment of the April 2020 chernobyl wildfires and their impact on Cs-137

levels in Belgium and The Netherlands, Journal of environmental radioactivity, vol. 237, 106688, pp. 1-11. https://doi.org/10.1016/j.jenvrad.2021.106688

Masson, O., Romanenko, O., Saunier, O., Kirieiev, S., Protsak, V. et al.. Europe-wide atmospheric radionuclide dispersion by unprecedented wildfires in the Chernobyl Exclusion Zone, April 2020. Environmental Science and Technology, American Chemical Society, 2021, 55 (20), pp.13834-13848.

Protsak, V. P., Wojciechowicz, O. V., Laptev, G. V. Estimation of radioactive source term dynamics for atmospheric transport during wildfires in Chernobyl Zone in Spring 2020. https://uhmi.org.ua/msg/fire2020/analytical.pdf

Quérel, A., Quélo, D., Roustan, Y., Mathieu, A.: 2021: Sensitivity study to select the wet deposition scheme in an operational atmospheric transport model, Journal of Environmental Radioactivity, vol. 237, 106772, https://doi.org/10.1016/j.jenvrad.2021.106712

21st International Conference on
Harmonisation within Atmospheric Dispersion Modelling for Regulatory Purposes
27-30 September 2022, Aveiro, Portugal

SIMULATING THE DISPERSION OF MICROPLASTICS IN THE ATMOSPHERE TOWARDS A REMOTE SITE

Massimo Martina[1], Silvia Ferrarese[1] and Silvia Trini Castelli[2]

[1] Department of Physics, University of Torino, Torino, Italy
[2] Institute of Atmospheric Sciences and Climate, CNR, Torino, Italy

Abstract: The study of the dispersion of microplastics in the atmosphere represents a pioneering field of research, a very few works on this subject can be found in literature. In this work, the potential long-range dispersion of microplastics in the atmosphere is investigated using the Lagrangian stochastic particle model MILORD. The rationale is to apply MILORD model in the backward mode, in order to identify possible emission sources that may determine the microplastics pollution in sites or areas of interest. The sensitivity to the resolution of the meteorological input, to the diffusion parameters and the effect of the settling velocity values have been primarily investigated. A case study has been chosen for reference, concerning the observations of atmospheric microplastics deposition in a remote and pristine site in French Pyrenees, for which the long-range dispersion may play a main role. Preliminary results of simulations for different periods and different model configurations are presented and discussed.

KEY WORDS: ATMOSPHERIC MICROPLASTICS; BACKWARD DISPERSION; LONG-RANGE; MILORD MODEL; NUMERICAL SIMULATION.

INTRODUCTION

In 2015 for the first time the microplastics total atmospheric fallout, mostly composed by fibres, was highlighted in Greater Paris (Dris et al., 2015), some years later González-Pleiter et al. (2021) presented the first direct evidence of the microplastics presence above the planetary boundary layer. In the meantime, several studies sampled and reported the atmospheric microplastics deposition in different places: many cities, such as London (Wright et al., 2020), Hamburg (Klein et al., 2019), Dongguan (Cai et al., 2017), some remote and pristine area, as the French Pyreenes (Allen et al., 2019) and the Tibetan Plateau (Zhang et al., 2021), and in the ocean too (Liu et al., 2019; Trainic et al., 2020). The unequivocal presence of microplastics, hereafter MPs, in the atmosphere highlighted the importance to thoroughly investigate all the possible transport pathways in order to properly address the problem, using advanced tools like numerical models. Modelling MPs dispersion in the atmosphere is still a pioneering research field, so there is not an established reference framework yet. Hence, with the aim to contribute building a useful framework, in this work the long-range atmospheric dispersion model MILORD is applied to investigate the effects on microplastic transport of some key parameters, such as the settling velocity, at the same time assessing the model sensitivity to the resolution of the meteorological input and to the value of the diffusion coefficients. The case here under study refers to the work of Allen et al. (2019), where the deposition of MPs in the remote site of Bernadouze in the French Pyreenes and their possible atmospheric pathways were investigated.

Sensitivity on resolution and diffusion parameters

MILORD simulates the transport, diffusion, removal and deposition of tracers on the long-range, that is at the planetary scale. MILORD is grid-free, being a Lagrangian model, and the dependency on the grid resolution regards only the meteorological datasets used in input. In previous studies a resolution of 0.5° × 0.5° of the ECMWF analyses was used for the input files to address long-range dispersion (Boetti, 2015; Greco, 2018), a grid spacing that is still characteristic of large scale simulations. Clearly, this horizontal resolution can be too coarse to properly resolve the orography, in particular in complex terrain. For example, in the considered case study (Allen et al., 2019), the altitude of the Bernadouze meteorological station is 1425 m whereas the height obtained by the ECMWF files, interpolating the values over the 0.5° × 0.5° resolution, is only about 640 m in the surrounding of the site.

Focusing on the orography, its altitude is determined for each particle location and at every timestep, hence an interpolation method is necessary to extrapolate the orography out of the values at the grid-points of the ECMWF input files. In MILORD, a bilinear function is used to assign the height of the orography at the particle location, interpolating the values available at the four grid-points of the grid-cell to which the particle coordinates belong. Clearly a coarse horizontal spatial resolution leads to a smoothing of the orography that can affect the representativeness of the real altitudes and it may influence the particle trajectories computation. The meteorological variables are also input at the same resolution; therefore, smaller scale circulations may be difficult to be captured. For these reasons, to assess the sensitivity of the model to the resolution of the input fields, ECMWF meteorological fields at the finer horizontal scale of 0.25° × 0.25° were used for the first time in the model MILORD, in addition to the original 0.5° × 0.5° set; for each resolution 11 pressure levels were considered from the ECMWF analysis files: 1000, 925, 850, 700, 500, 400, 300, 250, 200, 150, 100 hPa.

As regards the diffusivity, in previous works (Desiato, 1998; Boetti, 2015) it was proven that the tracer dispersion in MILORD simulations is well-captured using large values of the diffusion coefficients, Kx = Ky = 15000 and Kz = 150 m^2/s (Set I). Here, the efficacy of those values was tested also for the case where a finer resolution of the input meteo fields is used. Furthermore, for both resolutions of the ECMWF input, the model sensitivity was evaluated using a second set of value for the diffusion coefficients, Kx = Ky = 1500 and Kz = 50 m^2/s (Set II), largely varying their magnitude, so to appreciate potential differences in the spread of the plume of particles. The simulations were run in backward mode for a 13-days period in November 2017, the retro-emission starting on 28/11 at 00:00 and ending on 16/11 at 00:00. Assuming that MPs particles in the French Pyrenees site arrived continuously through the atmosphere, the retro-emission was continuous and for each timestep one particle was retro-emitted so to easily track single trajectories.

A first interesting achievement was the improvement in the reliability of the orography values using the 0.25° × 0.25° resolution: the corresponding height interpolated at Bernadouze site was about 1450 m instead of 640 m. Since here particles arriving at the receptor are traced, the height of the emission is assigned at the surface, referring to the height of the orography and corresponding to pressure values of 960 hPa and 855 hPa, respectively. The 3D plots in Figures 1 and 2 represent the plume of particles moving in the domain in the 13-days simulation period, for the two resolutions 0.5° × 0.5° and 0.25° × 0.25 °, respectively. By the comparison between the 3D-plot, outlining the particles height distribution, it is possible to observe some difference in using Set I instead of Set II for the diffusion coefficient values. As expected the lowest diffusion coefficients leads to a lesser vertical diffusion. The lower diffusivity has an effect also on the horizontal, allowing particles from larger distances to travel further and reach the receptor. The 3D-plot reported in Figure 2, which used the 0.25° × 0.25° resolution, show a similar behaviour and analogous differences when varying the diffusion coefficients. Even using diffusion coefficient values orders of magnitude lower than the usually adopted do not affect significantly the particle dispersion since the main distribution path remains. The evidence reported by Desiato (1998) and Boetti (2015), assessing that the high values of diffusivities are more representative at these large scales,

remains confirmed also when using the finer resolution of 0.25° × 0.25°; thus, the Set I is maintained to model the diffusion of MPs in the long-range dispersion.

A large variation appears comparing the 3D-plot obtained with the different resolutions, comparing Figure 1 and Figure 2: with the finer one, 0.25° × 0.25°, more MPs are found to reach higher altitudes and the shape of the area covered by the particles in the 13-days simulation shows some difference, yet overall, compared to the coarse one, the particles well depict the core of the dispersion region; these differences can be ascribed to the differences in the ECMWF wind fields at the two resolutions.

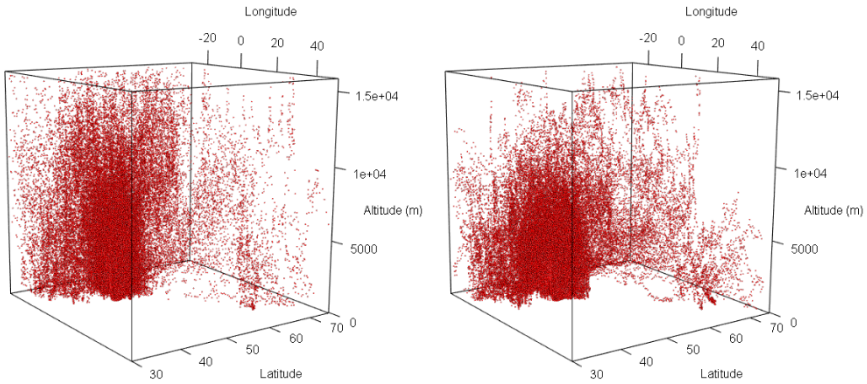

Figure 1. The 3D-plots illustrate the particles height distribution referring to the November period using horizontal resolution of 0.5° × 0.5°; considering SET I (left) and Set II (right) diffusion coefficients.

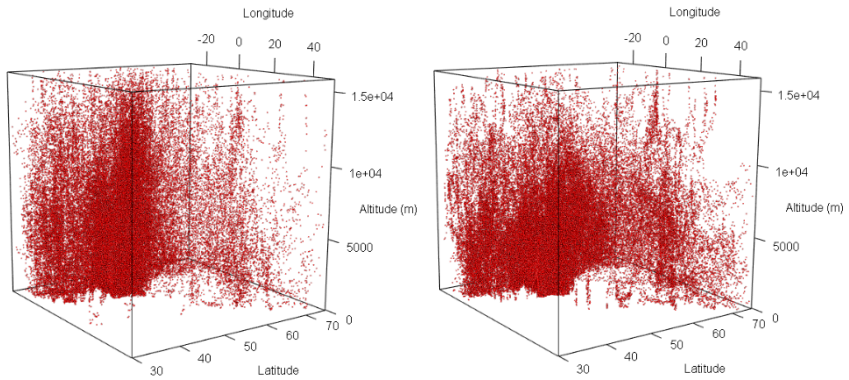

Figure 2. As in Figure 1 but for the horizontal resolution 0.25° × 0.25° for the meteorological input field

Influence of the settling velocity on dry deposition

A first study on the influence of different settling velocities on the dry deposition was conducted. Four different runs were performed using four different deposition velocity values, based on the literature (Table 1), for three different periods of the year (November 2017, January and March 2018), and for each resolution, to assess the possible influence of the velocity on MPs dry deposition.

Table 47. Settling velocity values reported in the literature until 2020

Reference	Settling Velocity (ms^{-1})
Allen et al. (2019)	0.1
Wright et al. (2020)	0.06 (fibrous MPs)
Trainic et al. (2020)	0.32 (non-fibrous MPs)
Allen et al. (2019)	0.001

The computation of the dry deposition in MILORD is done by a subroutine that calculates it at each time step if the particles is inside the Planetary Boundary Layer, hereafter PBL, based on the following formula:

$$D_{dry} = N_0\left(1 - e^{-\lambda_d \Delta t}\right) \quad (1)$$

where N_0 is the initial pollutant amount and λ_d is the dry deposition coefficient defines as:

$$\lambda_d = \frac{v_d}{H(x,y,t)} \quad (2)$$

with v_d representing the deposition velocity and H(x,y,t) the particle height.

The calculation in the backward mode has been modified so that the reverse modelling reconstructs the amount of pollutant that the particle would have lost due to the depletion processes, before reaching the sampled site (receptor). For this investigation, the simulations considered a period of one day in which the back-trajectory of one particle was followed and only the settling velocity value was modified from one simulation to another. The analysis here presented refers, as example, to the November case study: the single particle is retro-emitted on 26/11/2017 at 00:00 and the simulation of the backward trajectory lasts one day, starting at 00:00 on 26/11/2017 and ending at 00:00 on 25/11/2017.

For each resolution, two graphs were elaborated and compared:

1. The trajectory map; here the colour scale represents the amount of MPs carried by the particle in base-10 logarithmic scale. (Figures 3).
2. The amount of MPs transported by the particle as a function of the distance it covers; here the line-graphs outline the influence of the settling velocity on the dry deposition: the vertical axis shows the amount of MPs carried by the particle, whereas the horizontal axis represents the distance travelled by the particle (Figures 4).

By the comparison of the trajectory maps (Figure 3) a variation emerges in the path followed by the particle considering the two resolutions. This is reasonable since, with the finer resolution, the interpolated wind field manage to better capture smaller circulation structures. Furthermore, for the case of November, a remarkable difference in the amount of MPs transported appears comparing the simulations with different resolutions: with the finer one the particle spends less time inside the PBL, hence it “acquires” a lesser amount of MPs due to the dry deposition. Moreover, Figure 4 shows that when considering the highest settling velocity of 0.32 ms^{-1}, a particle should carry a much greater amount of MPs arriving from distance greater than 250 km, making this velocity a less probable value for the long-range transport compared to the others.

In this single-particle case, the difference in the MPs amount is due to the fact that when travelling close to the PBL height, even small differences in the value of the wind field and turbulence, determining the displacement of the particle, and in the PBL height daily development, may let the particle move out/in the PBL layer. Only when inside the PBL, the particle gains back the ‘dry-deposited’ amount in the backward mode, thus leading to potential differences in the particle MPs mass. Concerning the trajectories, it is important to notice that in these simulations only one particle was considered and back-tracked, while in the Lagrangian modelling approach a great number of particles must be released and traced in order to statistically describe the actual path of the plume. In this sense on average the paths followed by the particles are in good agreement for the simulations corresponding to the two resolutions of the input fields.

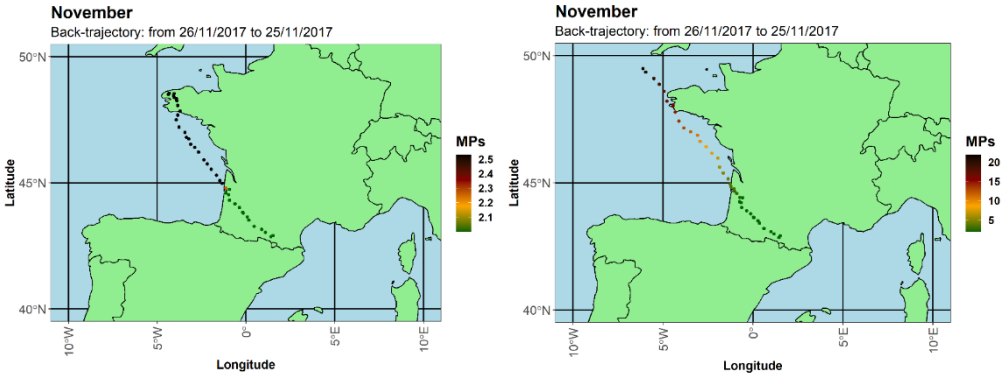

Figure 3. November case. One particle retro-emitted the 26/11/2017 and the followed daily back-trajectory, using the meteorological input fields with 0.5° × 0.5° (left) and 0.25° × 0.25° (right) grid resolution.

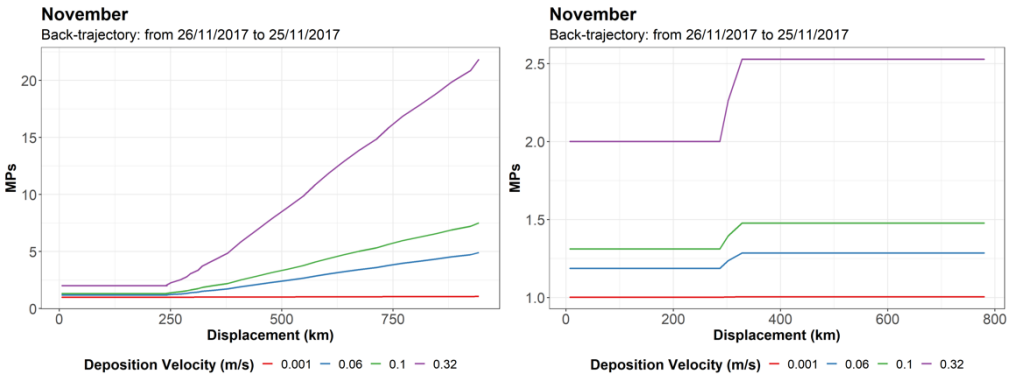

Figure 4. November case. Amount of MPs carried by the particle as function of the travelled distance from the receptor site, using the meteorological input fields with 0.5° × 0.5° (left) and 0.25° × 0.25° (right) grid resolution.

CONCLUSIONS

Even in the difficulty to obtain quantitative results, an important first study was conducted comparing four different settling velocities, based on the reviewed literature, to assess their influence on the dry deposition in the long-range transport. The less likely value for the settling velocity characterizing the long-range transport was found to be 0.32 ms^{-1}, reported by Wright et al. (2020) to describe non-fibrous microplastic.

Moreover, the influence of settling velocities was also evaluated using the two different resolutions of the meteorological fields, 0.5° × 0.5° and 0.25° × 0.25°. The investigation delineates a remarkable changing, comparing the two resolutions, in the amount of MPs transported by the particle in order to arrive at the receptor; further investigations will be necessary regarding the finer resolution in order to understand if some changes in the parameterization of the physical processes will be required.

REFERENCES

Allen S., Allen D., Phoenix V. R., et al., 2019: Atmospheric transport and deposition of microplastics in a remote mountain catchment, Nat. Geosci., 12, 339-344

Boetti M., 2015: Modelling the pollutant dispersion of the Fukushima nuclear plant release, Master thesis

Cai L., Wang J., Peng, J. et al., 2017: Characteristic of microplastics in the atmospheric fallout from Dongguan city, China: preliminary research and first evidence, Environ. Sci. Pollut. R., 24, 24928–24935

Dris R, Gasperi J, Rocher V, Sead M., et al., 2015: Microplastic contamination in an urban area: a case study in Greater Paris, Env. Chem., 12 (5), 592-599

Evangeliou N., Grythe H., Klimont Z., et al., 2020: Atmospheric transport is a major pathway of microplastics to remote regions, Nat. Commun., 11, 3381

González-Pleiter M., Edo C., Aguilera Á., et al., 2021: Occurrence and transport of microplastics sampled within and above the planetary boundary layer, Sci. Total. Environ., 761, article 143213

Greco S., 2018: Study of CO2 high concentration events at Plateau Rosa station with atmospheric trajectories and Lagrangian dispersion models, Master thesis

Klein M, Fisher E., 2019: Microplastic abundance in atmospheric deposition within the metropolitan area of Hamburg, Germany, Sci. Total Environ., 685, 96-103

Liu K., Wu T., Wang X., et al., 2019: Consistent transport of terrestrial microplastics to the ocean through atmosphere, Environ. Sci. Technol., 53, 10612–10619

Obbard R. W., 2018: Microplastics in polar regions: the role of long-range transport, Curr. Opin. J. Environ. Sci. Health, 1, 24-29

Trainic, M., Flores, J.M., Pinkas I., et al., 2020: Airborne microplastic particles detected in the remote marine atmosphere, Commun. Earth Environ., 1, 64

Wright S.L., Ulke J., Font A., et al., 2020: Atmospheric microplastic deposition in an urban environment and an evaluation of transport, Environ. Int., 136, article 105411

Zhang Y., Gao T., Kang S., et al., 2021: Microplastics in glaciers of the Tibetan Plateau: evidence for the long-range transport of microplastics, Sci. Total Environ., 758, 143634

21st International Conference on
Harmonisation within Atmospheric Dispersion Modelling for Regulatory Purposes
27-30 September 2022, Aveiro, Portugal

QUANTIFYING THE IMPACT OF COVID-19 RESTRICTIONS ON EMISSIONS USING INVERSE MODELLING AND MEASUREMENTS

Amy Stidworthy[1], David Carruthers[1], Molly Oades[1], Rod Jones[2], Olalekan Popoola[2], Jim Mills[3] and Felicity Sharp[4]

[1]CERC, 3 King's Parade, Cambridge, CB2 1SJ, UK
[2]Yusuf Hamied Department of Chemistry, University of Cambridge, Lensfield Road, Cambridge, CB2 1EW, UK
[3]Scotswolds, UK
[4]ACOEM, UK

Abstract: An inversion system that uses a Bayesian approach to combine measurements and ADMS-Urban modelled data by adjusting individual source emissions, subject to estimated uncertainty in the measurements and emissions, has previously been applied to optimising road traffic emissions in Cambridge. In this study the system has been applied specifically to the impact of interventions, in particular the impact of COVID-19 lockdowns on NO_X emissions from road traffic and other sources in London.

The ADMS-Urban model was used to calculate *a priori* hourly NO_X concentrations at 195 receptors in London representing 115 reference monitors and 80 Breathe London Network AQMesh sensors. Input data included hourly meteorological measurements from Heathrow Airport, hourly NO_X concentrations from 4 rural background monitoring sites and buildings road centreline data from Ordnance Survey. *A priori* emissions were obtained from the London Atmospheric Emissions Inventory (LAEI) for 35 point sources, approximately 70,000 major road sources and 2,500 1km grid cells representing minor road, heating and other sources. The analysis period was 1 January 2020 to 30 April 2021. Estimated uncertainties of 4 and 12 $\mu g/m^3$ were applied to reference and sensor measurements respectively, while emissions uncertainties of 100%, 50%, 20% were applied to road traffic, fuels and other emissions respectively. Road traffic emissions were assumed to have error covariance of 40% of their emissions uncertainty.

Measured NO_X concentrations in London reduced significantly during lockdown, with the greatest reduction (around 60%) at kerbside and roadside sites in Central London. However, poor dispersal conditions led to increased concentrations at times when restrictions were tightest. In contrast, inversion system results demonstrate that NO_X emissions from road traffic dropped by around 60% in London compared with pre-lockdown levels and that this reduction occurred when the strictest lockdown measures were in force. The results also show that NO_X road traffic emissions were still approximately 30% lower than pre-lockdown levels at the end of April 2021. This analysis demonstrates that lower cost sensors such as AQMesh can provide valuable insight into the effects of policy measures (in this case lockdown restrictions), if their increased uncertainty compared with reference monitors is accounted for.

KEY WORDS: COVID-19, ADMS-URBAN, LOCKDOWN, NO_X, INVERSION

INTRODUCTION

Dramatic changes in transport patterns occurred in London during March 2020 caused by movement restrictions (known as "lockdowns") imposed by the UK Government to limit the spread of the COVID-19 virus (DfT, 2021). These changes caused unprecedented changes in road traffic emissions compared with standard emissions inventories. Emissions inventories based on road traffic activity data take time to collate, but estimates of lockdown-induced emissions changes were needed on shorter timescales, for example for air quality forecasting. This presents a unique and valuable opportunity to analyse and understand the effects on emissions and air quality of a massive step-change in transport activity.

Background

The first lockdown restrictions in London were implemented on 17 March 2020: people were asked to socially distance from others and avoid unnecessary travel. The first full lockdown came into force on 24 March: people were only allowed to leave their homes for limited reasons and schools were closed except for the children of keyworkers. From 10 May, people were allowed outside for unlimited exercise. From 15 June all shops were allowed to open, but restrictions on social gatherings remained. On 17 October additional measures were implemented in London: different households were not allowed to mix indoors. On 5 November a second national lockdown was enforced: people were asked to stay at home wherever possible but schools remained open. That lockdown ended on 6 December 2020, but on 6 January 2021 England entered its third full lockdown, with schools again closed for most children. Schools re-opened on 8 March 2021 and restrictions gradually eased through the spring and summer of 2021.

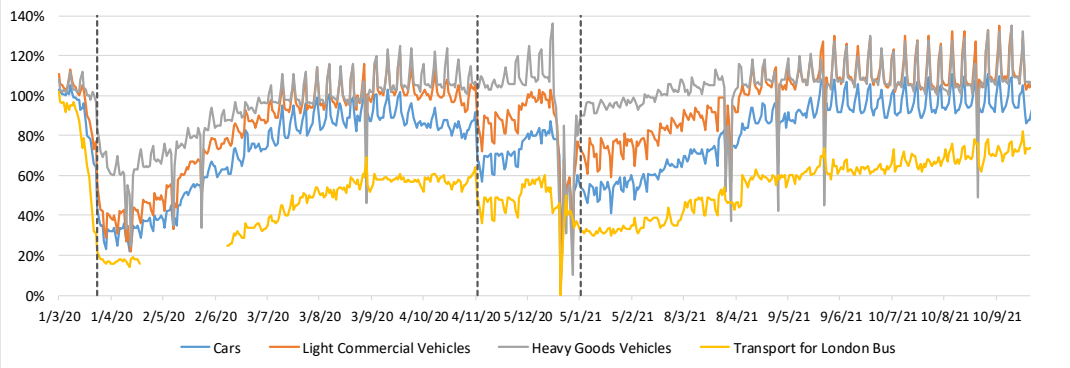

Figure 127. UK Government data (DfT, 2021) on the use of different transport modes in England, Scotland and Wales, as a percentage change compared with the equivalent day in the first week of February 2020. Transport for London (TfL) bus data is London-specific and compared with the equivalent day in 2019. Large discontinuities in HGV activity are due to bank holidays, smaller discontinuities are weekday/weekend differences. TfL bus data from April to June 2020 is missing because no payment was required; no payment means no data.

Government data on the use of different transport modes (Figure 127) shows some reduction across all modes in advance of the March lockdown; a dramatic reduction on 24 March; gradual increases to near-normal levels for HGVs and LGVs by mid-July 2020; and car use did not reach pre-pandemic levels until June 2021. Car use was less than 40% of pre-lockdown levels in lockdown 1, 70% in lockdown 2 and 50% in lockdown 3. TfL bus trips were still at 70% of pre-pandemic levels at the end of September 2021.

(a)

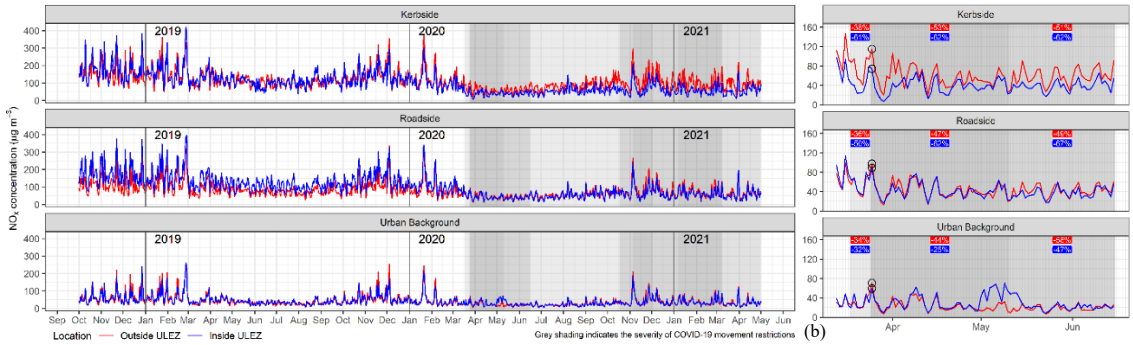

Figure 128. Mean daily mean NO_X concentration over 151 reference monitors, by site type and location with respect to the central London Ultra Low Emissions Zone (ULEZ). The darkness of the grey shading indicates the severity of the lockdown restrictions. (a) 1 October 2018 to 30 April 2021; (b) 12 March to 15 June 2020. The labels give the mean concentration for that period as a percentage change from the mean concentration for 1 January to 16 March 2020.

Measured NO_X concentrations in London reduced significantly during lockdown, with the greatest reduction (around 60%) at kerbside / roadside sites in Central London (Figure 128). However, poor dispersal conditions led to increased concentrations at times when restrictions were tightest. At roadside and urban background sites during lockdown 1 (Figure 128b), measured concentrations were highest on 25 March. For these sites, the reduction in concentration was greater *after* the restrictions began to be lifted from 10 May than when London was under the most severe restrictions (24 March to 9 May).

METHODOLOGY

CERC have developed a data assimilation scheme that applies a Bayesian inversion technique to a high resolution (street-level) atmospheric dispersion model to modify pollution emission rates based on local measurements (Carruthers *et al.*, 2020). This scheme has been applied to investigate changes in NO_X emissions from traffic in London during the period from 1 January 2020 to 30 April 2021, as part of the Breathe London Pilot Project. This project installed 100 AQMesh sensors at sites across London to measure NO_X, NO_2, $PM_{2.5}$ and CO_2; two Google cars collected reference-standard mobile measurements at 1-second resolution for one year; and CERC carried out high resolution dispersion modelling and source apportionment modelling using the ADMS-Urban model (Stocker *et. al.*, 2012). The 2-year pilot project concluded in November 2020; the static sensors were maintained until the end of April 2021 to capture what was expected to be the 'COVID-19recovery period'.

ADMS-Urban is a comprehensive system (Stocker *et. al.*, 2012) that is widely used for modelling air quality in large urban areas, cities and towns. It is a practical urban air quality model which explicitly represents the full range of source types occurring in an urban area, takes account of complex urban morphology including street canyons, and provides output of short and long term average pollutant concentrations from street-scale to urban-scale. ADMS-Urban was used to calculate *a priori* hourly NO_X concentrations at 195 receptors in London representing 115 reference monitors and 80 Breathe London Network AQMesh sensors. Input data included hourly meteorological measurements from Heathrow Airport, hourly NO_X concentrations from 4 rural background monitoring sites and buildings road centreline data from Ordnance Survey. *A priori* emissions were obtained from the 2013 edition of the London Atmospheric Emissions Inventory (LAEI) (published in 2016) interpolated to 2019 and road traffic emissions calculated using emission factors for 2019 from EFT version 8.0, including adjustments for real-world conditions (Carslaw and Rhys-Tyler, 2013). Modelled sources include 35 point sources, approximately 70,000 major road sources and 2,500 1km grid cells representing minor road, heating and other sources.

The CERC Inversion System (Figure 129) optimises modelled concentrations in relation to monitored data by adjusting the emissions data that are used to calculate the modelled concentrations, taking into account the known (or estimated) uncertainty in both the *a priori* emissions data and the monitored data. The results are adjusted modelled concentrations for every modelled receptor and associated adjusted emissions for every source, for every hour modelled. Estimated uncertainties of 4 and 12 µg/m^3 were applied to reference and sensor measurements respectively, while emissions uncertainties of 100%, 50%, 20% were applied to road traffic, fuels and other emissions respectively. Road traffic emissions were assumed to have error covariance of 40% of their emissions uncertainty related, for example, to common emission factors.

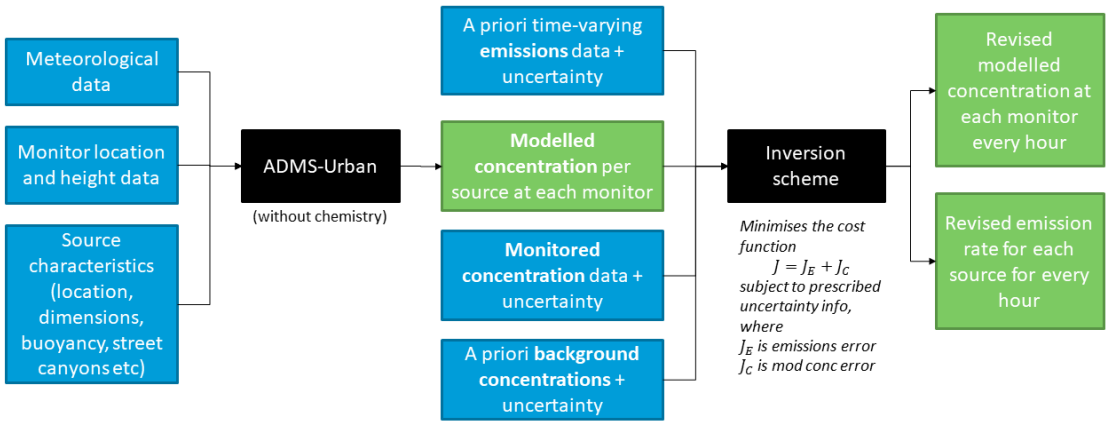

Figure 129. Schematic of the CERC Inversion System. Blue represents a non-calculated dataset, green represents a calculated dataset and black represents a process.

RESULTS

Figure 130 compares modelled and observed NO_X concentration results from January 2020 to April 2021. The *a posteriori* modelled values and observed values for reference sites are almost indistinguishable, confirming that the Inversion System is working as expected; it has, to a large extent, corrected the *a priori* model error. Higher measurement uncertainty was attributed to AQMesh measurements, so, as expected, there are greater differences between *a posteriori* modelled values and observed values at AQMesh sites. On 24 March the impact of the lockdown is clear: until 24 March, the *a priori* modelled values agreed well with measured values; a few days before 24 March the *a priori* modelled values began to diverge from the observed and *a posteriori* modelled values, meaning that emissions were beginning to diverge from the emissions inventory; and the peak on 25 March can be seen in both the *a priori* and *a posteriori* modelled values, suggesting that this was caused by poor dispersal conditions. The gap between *a priori* modelled values and observed values is greatest on 24 March, it reduces towards the end of the analysis period, but remains significant even in April 2021.

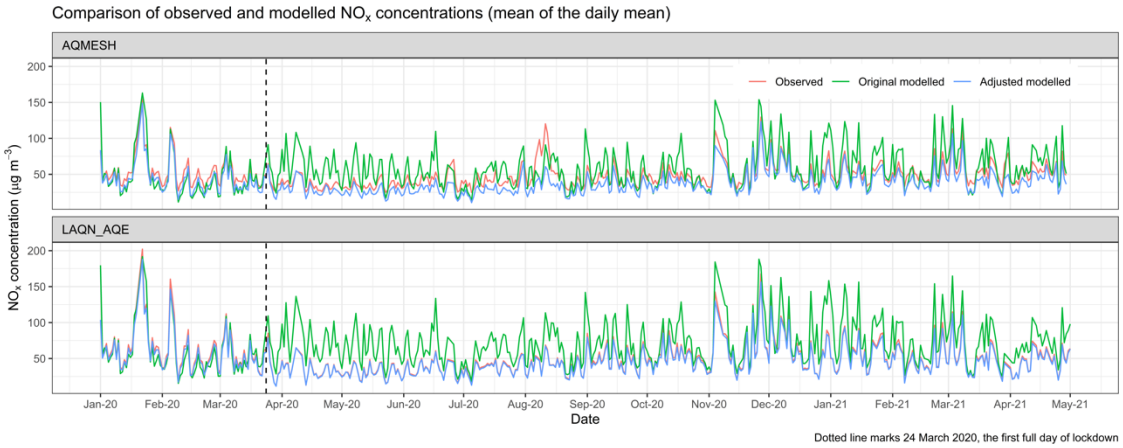

Figure 130. Comparison of observed and modelled NOX concentrations, averaged over all stations and showsn as the mean of the daily mean values. Observed values are shown in orange; *a priori* ('original') modelled values in green; and *a posteriori* ('adjusted') modelled values in blue. The vertical dotted line marks 24 March 2020, the first full day of COVID-19 lockdown in London. The upper panel shows the results for AQMesh locations; the lower panel shows the results for reference-standard monitoring sites.

The Inversion System results (Figure 131) show that emissions changed more dramatically than concentrations on 24 March 2020, with approximately 60% emissions reduction in the first lockdown phase compared with pre-lockdown levels. Emissions gradually increased during summer and early autumn 2020 as restrictions were relaxed but by the end of April 2021 had not yet returned to normal. During the second full lockdown in November 2020 emissions were 30% lower than pre-lockdown levels, and in the third full lockdown in early 2021 emissions were around 38% lower than normal, according to these estimates.

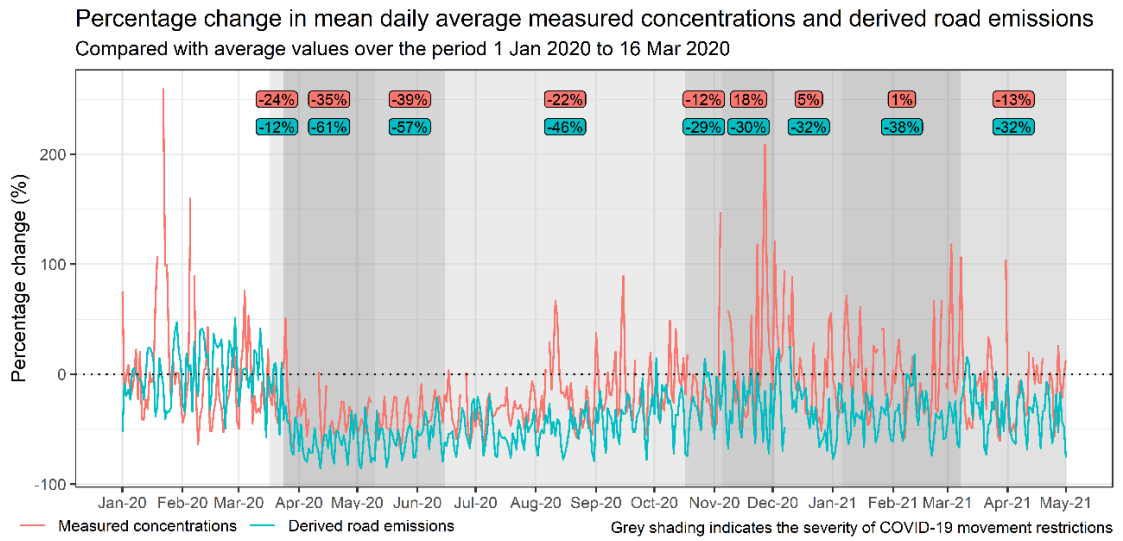

Figure 131. Comparison of the percentage change in emissions (blue) with the percentage change in measured concentrations, both in relation to pre-lockdown levels. The darkness of the grey shading indicates the severity of the lockdown restrictions. The labels give the average value over the relevant lockdown phase.

CONCLUSIONS

Bayesian-based inversion techniques combining high resolution modelling with measurements from reference-grade monitors and lower cost sensors suggest that London road traffic NO_X emissions reduced by around 60% compared with pre-lockdown levels immediately following the imposition of the COVID-19 lockdown on 24 March. The same analysis suggests that road traffic NO_X emissions remained around 30% lower than pre-lockdown levels at the end of the analysis period (30 April 2021). This demonstrates that lower cost sensors such as AQMesh can provide valuable insight into the effects of policy measures (in this case lockdown restrictions), if their increased uncertainty compared with reference monitors is accounted for.

ACKNOWLEDGMENTS

The Breathe London pilot project was delivered by a consortium led by Environmental Defense Fund Europe and funded by the Children's Investment Fund Foundation, with continued funding from Clean Air Fund and additional funding support provided by Valhalla Charitable Foundation. The project was convened by C40 Cities and the Greater London Authority. The project consortium included ACOEM Air Monitors, Cambridge Environmental Research Consultants, Google Earth Outreach, the National Physical Laboratory and the University of Cambridge. The pilot phase ran from July 2018 to November 2020. The extension of monitoring and analysis to April 2021 was funded by a UKRI COVID-19 grant.

REFERENCES

Carruthers D., Stidworthy A., Clarke D., Dicks J., Jones R., Leslie I., Popoola O. A. M. and Seaton M., 2019: Urban emission inventory optimisation using sensor data, an urban air quality model and inversion techniques. International Journal of Environment and Pollution, ***66****, issue 4, 252-266.*

Carslaw, D. and Rhys-Tyler, G., 2013: New insights from comprehensive on-road measurements of NOx, NO2 and NH3 from vehicle emission remote sensing in London, UK. Atmos. Env., ***81****, 339–347.*

Stocker J., Hood C., Carruthers D. and McHugh C., 2012: ADMS-Urban: developments in modelling dispersion from the city scale to the local scale. International Journal of Environment and Pollution, ***50****, 308-316.*

UK Government Department for Transport, 2021. Transport use during the coronavirus pandemic.
https://www.gov.uk/government/statistics/transport-use-during-the-coronavirus-COVID-19-pandemic

21st International Conference on
Harmonisation within Atmospheric Dispersion Modelling for Regulatory Purposes
27-30 September 2022, Aveiro, Portugal

TESTING A MACHINE LEARNING MODEL FOR THE SOURCE TERM ESTIMATION

Stefano Alessandrini[1], Scott Meech[1], Will Cheng[1], Christopher Rozoff[1] and Rajesh Kumar[1]
[1]Reseach Applied Laboratory (RAL), National Center for Atmospheric Research (NCAR), Boulder, Colorado, United States

Abstract: Mathematical models are considered an important tool to quantitively assess the impact on the environment and the population deriving from the release of hazardous materials. The source parameters are often unknown and, consequently, based on rudimentary assumptions. This is particularly true of accidental and intentional releases associated with terrorist incidents. A common approach in the literature for source term estimation (STE) is to have a backward plume originating from each available sensor measuring the tracer concentration. The area exhibiting the maximum overlap of all the backward plumes represents a first guess for the most likely release location. We have followed a different approach based on machine learning in this work. A simple setup with sensors' displacement along a straight line downwind the release is considered. A considerable amount (~400) of forward plumes is then simulated, released from random locations, and with random meteorologies to build a dataset, which includes some meteorological variables and concentrations at the sensors. The dataset is then split into a training and a testing section. A feed-forward neural network (NN) is then trained on the training dataset using the concentrations at the sensors and the meteorological variables as input variables, and the source location coordinates as output variables. The verification is then carried out over the testing dataset, comparing the location predictions from the NN with the real ones. The advantage of the NN-based system is to provide a much quicker STE estimate (within a fraction of seconds on a standard laptop) which is of paramount importance in case of accidental releases. In fact, the computationally expensive task of building the training dataset and training the NN can be done offline in any area where an accidental release is expected.

KEY WORDS: SOURCE TERM ESTIMATION, GAUSSIAN PLUME MODEL, INVERSE MODELING, NEURAL NETWORKS

INTRODUCTION

Mathematical models are considered an important tool to quantitively assess the impact on the environment and the population deriving from the release of hazardous materials. The source parameters are often unknown and, consequently, based on rudimentary assumptions. This is particularly true of accidental and intentional releases associated with terrorist incidents. In the literature, source term estimation (STE) techniques are considered an inverse atmospheric dispersion problem that uses downwind concentrations measured by an array of sensors together with meteorological parameters and plume modeling to estimate the source location, mass emission rate and duration. One approach for STE is to have a backward plume driven by reversed wind originating from each available sensor measuring the tracer concentration (Stohl, 1998, Jaffe et al., 1999). The area exhibiting the maximum overlap of all the backward plumes represents a first guess for the most likely release location. A forward plume model can then be used to determine the emission rate. A cost function, such as the mean squared error between simulated and measured concentrations, can be minimized by varying the emission rate. A more refined approach includes the source and concentrations error covariance matrices in the cost function computation and variational methods for its minimization (Bieringer et al., 2015).

In this work, we followed a different STE approach based on machine learning (ML) techniques. To our knowledge, ML has already been applied to STE problems in very few works. Fanfarillo (2019), for instance, explored the use of Artificial Neural Networks (ANNs) in a deep learning tensor flow environment to reconstruct the heat source location on a 2D metal plate on which four temperature sensors were displaced. Qiu et al. (2018) proposed a fast dispersion prediction and source estimation method based on artificial neural network (ANN), particle swarm optimization (PSO), and expectation maximization (EM). Their strategy used many predetermined scenarios to train the ANN for dispersion prediction. PSO and EM were applied to estimate the source parameters and accelerate the convergence process. Like Qiu et al. (2018), the approach proposed here aims to generate a considerable amount of emission scenarios from a point source. The release is considered in one setup with a typical sensors' displacement along a straight line downwind. A considerable amount (~400) of forward Gaussian plumes is then simulated, released from random locations, and with random meteorologies to build a dataset, which includes some meteorological variables and concentrations simulated at the sensors. The dataset is then split into a training and a testing section. A feed-forward neural network (NN) is then trained on the testing dataset using the concentrations at the sensors and the meteorological variables as input variables and the source location coordinates as output variables. The verification is then carried out over the testing dataset, comparing the NN location predictions from the NN with the real ones.

Models

a) Gaussian plume model

To build the synthetic dataset used to train the NN, we have used the simple Gaussian plume as in Sutton (1953), which describes the spatial distribution at the ground level of an inert gaseous pollutant downwind of a point source. It is based on the equation:

$$C(x,y) = \frac{Q}{\pi\sigma_z\sigma_y u} exp\left(-\frac{y^2}{2\sigma_y^2}\right) exp\left(-\frac{h^2}{2\sigma_z^2}\right), \quad (1)$$

where C is the steady state concentration, σ_z and σ_y are the vertical and cross-wind standard deviations of the pollutant distribution, u the wind speed, Q the source strength, and h the effective source height.
The reference frame has the x-axis parallel to the wind, with the origin matching the source location. To obtain σ_z and σ_y as a function of the downwind distance x and the Pasquill-Turner stability category (Pasquill, 1979), we used the Pasquill-Gifford analytical relationships (Pasquill, 1979).

The range of applications of eq.1 is limited to cases with homogeneous and stationary turbulence and on flat terrain. Despite these limitations, we decided to use this model as we needed a fast way to run a large number of experiments. Also, we wanted to focus our attention on exploring the effectiveness and potential issues of using machine learning for STE rather than having a more refined plume model.

b) Neural Networks (NN)

As previously mentioned, our approach is based on using ANNs to determine the source characteristics from information coming from measured downwind concentrations and meteorological conditions. For this purpose, we used a feed-forward NN with hidden layers and backpropagation for training. It is applied using the "Neuralnet" package (Fritsch et al., 2019) from R (R core team, 2020).
This NN has a simple structure that connects some input variables with a response variable, passing by one or more hidden layers of neurons, which process the information. More information about input and output variables will be provided in the next section.

Dataset

We have used a computational domain of 10 km x 10 km to run the Gaussian plume model and build the dataset on which the NN is applied. Ten sensors are located on the East side of the domain, and the sources are displaced over a regular grid made of 18 columns x 21 rows (378 sources) as in Fig.1. From each source, a plume is originated, and the resulting simulated concentrations at the sensors are considered as if they were measured in a real experiment. In the first experiment, only one plume from each source is generated using a constant wind u=5 ms^{-1}, v=0 m/s with a constant Pasquill-Turner stability class equal to "D." The resulting dataset is then made by 378 rows (one for each source) and 12 columns that correspond to ten simulated (measured) concentration values at the sensors plus the x, y coordinates of the source. In a second experiment, each source still originates only one plume. The intensity of the u component of the wind and the stability class are randomly selected in the range respectively between 0.5 m/s and 10 m/s and from "A" to "F ." In this second case, the resulting dataset is the same as in the first experiment plus two additional columns, including the values of the wind intensity and the stability class.

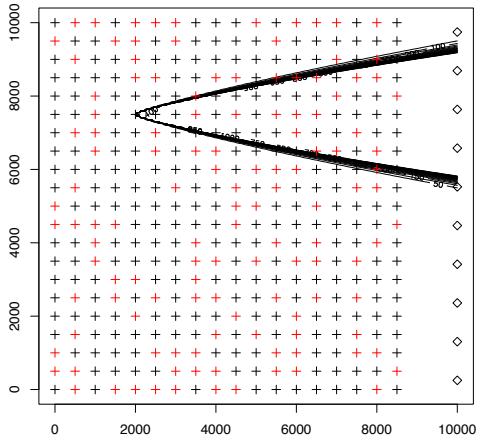

Figure 132. The setup used to build the synthetic dataset of concentrations recorded (simulated) by ten sensors (diamonds). The sources from which a Gaussian plume is released are indicated by crosses. Simulated concentrations at the sensor locations are used in the dataset as they were measured in a real experiment. Red (black) crosses indicate those sources for which the coordinates are used for verification (training).

RESULTS

The dataset is then split into a training and a testing section. For both experiments, ~1/3 (128 rows) of the dataset are used for verification, while the remaining for training the NN. For experiment one, a feed-forward neural network (NN) is trained on the training dataset using as input variables the concentrations at the sensors. As output variables, the source location coordinates x and y. In the second experiment, the input variables also include wind speed and stability class. Once the training is completed, in the testing phase, only the input variables are provided to the NN, which returns, as output, the estimated source coordinates. The verification is then carried out by comparing the NN's predicted coordinates with the real ones.

To have an overall evaluation of the model's performance, we have used the mean absolute error (MAE) and the mean distance error (MDE) that are obtained as:

$$MAE = \sum_{1}^{N} \frac{|c_p - c_o|}{N}$$

and

$$MDE = \sum_{1}^{N} \frac{d_{p,o}}{N}$$

where N is the number of cases (128 rows) in the testing dataset, c_p, c_o are the x or y coordinates respectivley of the predicted and observed source location, and $d_{p,o}$ is the Euclidean distance between the predicted and observed source locations.

A few attempts (not shown) have been made for both experiments changing the number of neurons in the hidden layers of the NN in order to optimize the NN STE's performance in terms MAE and MDE. In both experiments, the best results (smallest MAE and MDE) are obtained with more than one hidden layer and more than ten neurons in the first layer. Figures 2 and 3 show a summary of the verification results for both experiments with the optimal NN configuration defined in these attempts. Scatter diagrams comparing the predicted against observed x and y source coordinates are compiled in the first two panels. In the right panel, the origin and tip of the arrows indicate the observed and the predicted source location, respectively.

In both experiments, the NN-based STE exhibits a better accuracy in predicting the y coordinate of the source with an MAE for y smaller than for x. The sensor's displacement along a straight line perpendicular to the wind direction allows a better prediction of the source location along the y direction. Comparing the two experiments, adding the variability derived from different stability classes and wind speed in the second experiment degrades the overall performances with a higher MDE (981 m in exp.1 against 368 m in exp.2)

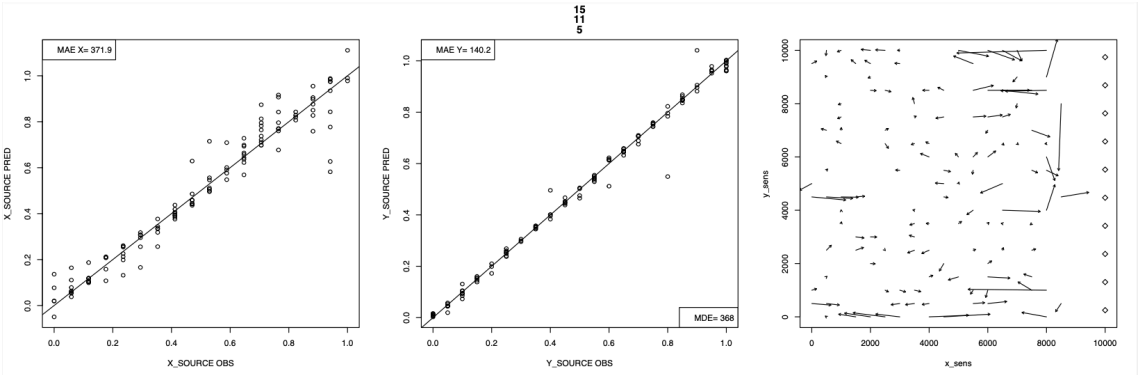

Figure 2. Experiment num.1; Scatter diagrams comparing the predicted against observed x and y source coordinates are compiled in the first two panels. In the right panel, the origin and tip of the arrows indicate the observed and the predicted source location, respectively. MAE values for x and y coordinates and MDE values are also reported.

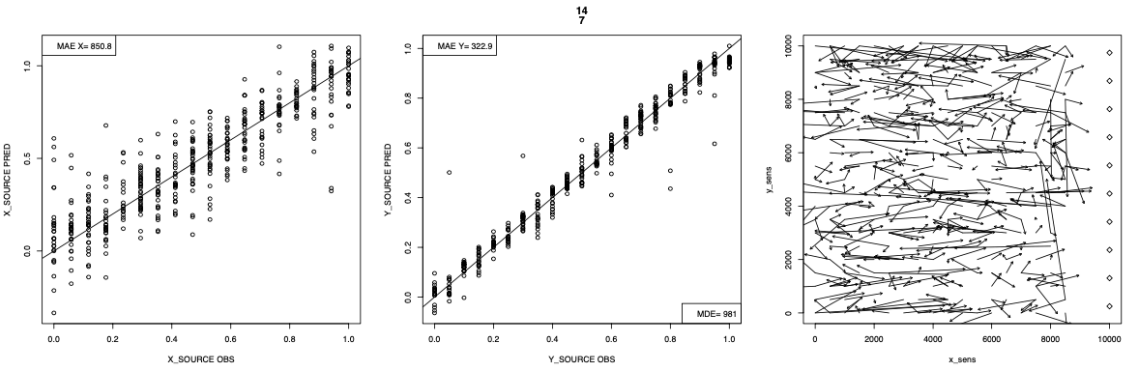

Figure 3. As Figure 2, but for experiment num.2

CONCLUSIONS

A source term estimation (STE) system based on machine learning technique has been applied to a synthetic dataset built with a simple setup. Simulated concentrations from a Gaussian plume are used as if they were measured from ten sensors located along a straight line perpendicular to the wind direction. One plume is generated from each of the 368 sources located upwind of the sensors. Two experiments are carried out. The wind speed and stability class are kept constant in the first experiment. In the second experiment, they are randomly assigned to each of the 368 plumes. NN-based STE performances are evaluated in terms of mean absolute error (MAE) and mean distance error (MDE), comparing only the predicted and actual source location. In the first experiment, the accuracy in estimating the source location is excellent, with an MDE of 368m. The performances are degraded in the second experiment with an MDE of 981m. Also, this experiment's set up allows better accuracy in predicting the y coordinate rather than the x coordinate of the source. These results look promising, but further investigations in real conditions are needed, including a comparison with a traditional STE approach.

REFERENCES

P.E. Bieringer , L.M. Rodriguez , F. Vandenberghe , J.G. Hurst , G. Bieberbach , I. Sykes , J.R. Hannan , J. Zaragoza , R.N. Fry ,Automated source term and wind parameter estimation for atmospheric transport and dispersion applications, Atmos. Environ. 122 (2015) 206.

Fanfarillo, A., 2019, November. Quantifying Uncertainty in Source Term Estimation with Tensorflow Probability. In 2019 IEEE/ACM HPC for Urgent Decision Making (UrgentHPC) (pp. 1-6). IEEE.

Stefan Fritsch, Frauke Guenther and Marvin N. Wright (2019). neuralnet: Training of Neural Networks. R package version 1.44.2. https://CRAN.R-project.org/package=neuralnet

Jaffe, D., Anderson, T., Covert, D., Kotchenruther, R., Barbara, B., Danielson, J.,Simpson, W., Bernsten, T., Karlsdottir, S., Blake, D., Harris, J., Carmichael, G., Uno, I., 1999. Transport of Asian air pollution to North America. Geophys. Res. Lett. 26, 711e714.

Pasquill, F., 1979. Atmospheric dispersion modeling. Journal of the Air Pollution Control Association, 29(2), pp.117-119.

R Core Team (2020). R: A language and environment for statistical computing. R Foundation for Statistical Computing, Vienna, Austria. URL https://www.R-project.org/.

Stohl, A., 1998. Computation, accuracy and applications of trajectories: a review and bibliography. Atmos. Environ. 32, 947e966.

Sutton, G., 1964. Micrometeorology. Scientific American, 211(4), pp.62-77.

Qiu, S., Chen, B., Wang, R., Zhu, Z., Wang, Y. and Qiu, X., 2018. Atmospheric dispersion prediction and source estimation of hazardous gas using artificial neural network, particle swarm optimization and expectation maximization. Atmospheric environment, 178, pp.158-163.

21st International Conference on
Harmonisation withinAtmospheric Dispersion Modelling for Regulatory Purposes
27-30 September 2022, Aveiro, Portugal

COMPARISON OF THE ACCURACY OF K-EPSILON AND K-OMEGA SST TURBULENCE MODELS IN AN UNKNOWN SOURCE PARAMETERS ESTIMATION APPLICATION

Panagiotis Gkirmpas, Nicolas Moussiopoulos, Lenidas Ntziachristos

Sustainability Engineering Laboratory, Department of Mechanical Engineering, Aristotle University of Thessaloniki, 54124 Thessaloniki, Greece

Abstract:
The present work aims to identify the source location and the release rate of an unknown air pollutant source in an urban-like domain by implementing two different turbulence models for the calculation of the meteorological parameters via CFD simulations. The MUST wind tunnel experiment is selected for the methodology's application. The k-epsilon and the k-omega SST turbulence models have been utilized separately in a forward RANS steady-state simulation for wind field and turbulence parameters calculation purposes. The estimated meteorological parameters are used in the backward CFD simulations to resolve the adjoint equations and to calculate the adjoint concentrations. The simulations are performed using the OpenFOAM open-source CFD suite. The source location is predicted using a cost function that correlates the modelled and observed concentrations, while the release rate is estimated using a quadratic cost function. The results indicate good agreement between the estimated source parameters of the two cases and the corresponding values of the true source. Very high accuracy is achieved in source location identification in the k-omega SST case. The performance of the k-epsilon case is lower in regard to the source location estimation, but a better solution is achieved for the release rate calculation compared with the k-omega case.

KEYWORDS: INVERSE DISPERSION MODELLING, SOURCE TERM ESTIMATION, COMPUTATIONAL FLUID DYNAMICS, K-EPSILON TECHNIQUE, K-OMEGA SST TECHNIQUE, POINT SOURCE IDENTIFICATION

INTRODUCTION

Releases of airborne gases or agents can lead to negative impacts on the environment and on the population's health. In the case of toxic releases, the so-called Hazardous Material (HazMat) threats, either industrial accidents or malevolent actions can be the underlying cause. In many cases, the characteristics of the source of this pollutant are unknown. Such an event must be addressed immediately based on accurate information provided to the decision makers and the relevant authorities. Especially in high densely urban areas, the estimation of the unknown source parameters is crucial for the protection of the population. The characterization of the parameters of the unknown source is called Source Term Estimation (STE) and combines Atmospheric Transport and Dispersion Models (ATDM), inverse modelling techniques, and data from the sensors of a measurement network. An STE problem can be solved by applying both forward and backward approaches. In the forward approach the ATDM calculates the concentration field for specific source parameters (location, release rate) and compares this concentration to the observed concentrations of the sensors. The ATDM runs by using different values of source parameters until a good agreement between the estimated modelled concentrations and the observed concentrations is achieved. In the backward approach, the ATDM is solved once in the reverse direction from each sensor to estimate the source parameters by means of Source Receptors Functions (SRF) which describe the sensitivity of sensors concentration to the source parameters. A literature review of STE techniques is given in Hutchinson et al. (2017). In complex geometry of urban or industrial areas, the Computational Fluid Dynamics (CFD) models are used to simulate the meteorological parameters that are affected by the turbulence phenomena as a result of interaction between the wind flow and the geometry surfaces. CFD models utilize different approaches to calculate a consistent wind field, such as the Reynolds Averaged Navier Stokes (RANS) and the Large Eddy Simulation (LES). A variety of methods have been proposed in the RANS approach for the estimation of turbulence parameters. Two widely used turbulence models are the k-epsilon model that resolves the

turbulence kinetic energy, k, and the turbulent kinetic energy dissipation rate, epsilon, and the k-omega SST that solves the turbulence kinetic energy, k, and the turbulence specific dissipation rate, omega.

In the presented study, the RANS approach is combined with the k-epsilon, and the k-omega SST turbulence models to resolve the airflow in an urban-like domain. Each case is utilized in an STE sensitivity application. The geometry of the Mock Urban Setting Test (MUST) wind tunnel experiment and the corresponding datasets are used for evaluating the methodology. For the STE problem, a backward approach is investigated, where the SRF are stored based on the values of the adjoint concentrations. The methodology follows the two-step approach (Efthimiou et al., 2017) to estimate the source parameters. Firstly, the source location is estimated using a correlation-based cost function. Then, the release rate is calculated in the determined source location by a quadratic cost function. The results for each turbulence model case are compared to each other. Also, the contribution of each turbulence model in the source parameters estimation is investigated. The open-source CFD model suite OpenFOAM is utilized in this investigation. The methodology has a wide range of applications, including support of rapid response to accidental or malicious substance releases and determination of emission factors of spatially ambiguous sources. In addition, the methodology will enable detection and quantification of transient emissions from shipping sources in harbour areas near dense urban fabric. To this end, a developed high-resolution modelling toolbox will support control and enforcement of shipping emission limits in harbour areas.

METHODOLOGY

Overall, the methodology for the estimation of the unknown source parameters is summarized in the following computational steps:

1. A forward steady-state CFD simulation runs to calculate the wind field.
2. The above wind field is used "reversed" in backward steady-state CFD simulations. The adjoint advection-diffusion equations are solved by considering every sensor as a source.
3. The SRFs are stored based on the values of adjoint concentrations.
4. The correlation-based cost function is calculated in every cell of the computational domain. The cell with the minimum value indicates the location of the source.
5. The quadratic cost function is solved for the estimated source location to calculate the release rate.

The methodology is applied in two cases, using two turbulence techniques to calculate the wind field during the forward simulation. Each turbulence model is combined with the RANS steady-state approach. In the first case, the two-equation turbulence k-epsilon model is applied. The turbulent quantities that k-epsilon solves are the turbulence kinetic energy k (m^2s^{-2}) and the turbulent kinetic energy dissipation rate epsilon (m^2s^{-3}). In the second case, the turbulence effect is estimated using the two-equation model k-omega SST, which solves the turbulence kinetic energy k (m^2s^{-2}), and the turbulence-specific dissipation rate omega (s^{-1}).

The solution of the wind field is used (inversed) for resolving the adjoint advection-diffusion equation (Marchuk, 1982; 1996). The adjoint equation is solved for every sensor of the measurement network to calculate the adjoint concentrations based on the relation:

$$-\frac{\partial c_n^*}{\partial t} - u_i \frac{\partial c_n^*}{\partial x_i} - \frac{\partial}{\partial x_i}\left(Dc + \frac{v_t}{Sc_t}\right)\frac{\partial c_n^*}{\partial x_i} = p_n \quad (1)$$

where u_i are the three velocity components in the Cartesian coordinate system ($i = (x, y, z)$), c_n^* is the adjoint concentration at measurement point n, Dc is the diffusion coefficient, v_t is the turbulent viscosity, Sc_t is the turbulent Schmidt number, and p_n is the scalar product that describes the source term in each sensor's location. Note that the term $-\partial c_n^*/\partial t$ is defined in transient conditions and is neglected for the steady-state solution.

The SRF can be stored based on the values of the adjoint concentrations c_n^*. The SRF expresses the sensitivity of sensors concentrations to the source parameters and can estimate the calculated concentration of the forward dispersion solution at the sensors based on the adjoint concentration via the relationship (Kovalets et al., 2011):

$$c_n^c = q_s c_n^* \quad (2)$$

where q_s is the source release rate. The total number of SRF is equal to the number of sensors. The location can be estimated by solving the correlation-based cost function from the relationship:

$$J = -\frac{\langle (c^c - \langle c^c \rangle)(c^o - \langle c^o \rangle) \rangle}{\sqrt{\langle (c^c - \langle c^c \rangle)^2 \rangle} \sqrt{\langle (c^o - \langle c^o \rangle)^2 \rangle}} \quad (3)$$

where c^o is the observed concentration measured in the n sensor and c^c is calculated by equation (2) for an arbitrary release rate q_s. As shown in Efthimiou et al. (2017) study, the value of the cost function J does not depend on the value of the release rate q_s. Note that the angled brackets indicate the average values over all sensors. The cost function J is calculated in every cell of the computational domain, and the source location is estimated to the coordinates of the cell center with the minimum value of J. The release rate is calculated, for the estimated location, by the following relationship:

$$q_s = \frac{\sum_{n=1}^{K} c_{n,k}^* c_n^o}{\sum_{n=1}^{K} \left(c_{n,k}^*\right)^2} \quad (4)$$

where k is the cell of the estimated source location.

The methodology is applied using MUST wind tunnel experiment test case. The wind tunnel experiment took place in the WOTAN wind tunnel at the Hamburg university to simulate the corresponding field experiment in a scale of 1:75. The field and wind tunnel experiments provide datasets for the study of the airflow and the dispersion in a simplified urban-like area. The geometry of the MUST field experiment consisted of 120 shipping containers placed in 12 rows of 10 containers. Each container has a 2.42 m length, 12.2 m width, and 2.54 m height. The concentrations in the wind tunnel experiment were measured from 256 sensors placed between containers at 1.275 m height.

In this work, the geometry of the MUST experiment is used to configure the computational domain (Figure 1). The shipping container arrangement is rotated at 45 degrees to the inlet of air flow to simulate a -45 degrees approaching wind flow. The computational domain dimensions are 340 m at the x-axis, 300 m at the y–axis, and 21 m at the z-axis. An unstructured tetrahedral computational mesh was constructed using the Ansys Fluent tool. The total number of computational cells is 1024119. Furthermore, 248 pollutant concentration receptor points are used to extract the appropriate data for the STE application.

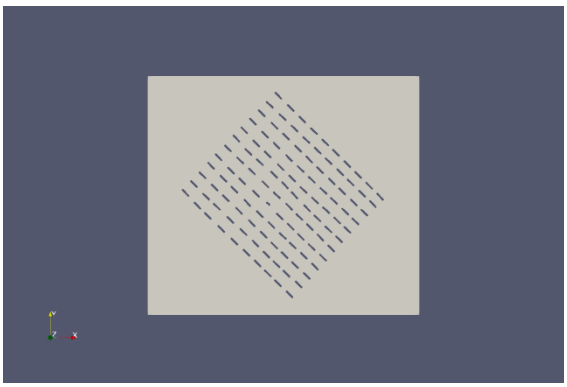

Figure 133. The structure of computational domain in x-y level

The forward simulation is implemented for the steady-state using the SimpleFoam solver. To determine the Atmospheric Boundary Layer (ABL) conditions for the velocity and the turbulence quantities at the inlet boundary, the equations of OpenFOAM class atmBoundaryLayer are used. The reference velocity is u_{ref} = 5 ms^{-1} at a height of z_{ref} = 7.29 m. The other two velocity components are kept equal to zero. Each forward simulation runs for 4000 seconds with a timestep equal to 1 second.

For the backward simulations, the solver ScalarTransportFoam was modified to accommodate the steady-state condition. The total number of simulations for each case is equal to the number of receptor points (248). Every backward simulation runs for 2000 sec with a timestep of 1 sec. The value of Schmidt number

was selected equal to 0.7. The wind speed and turbulent viscosity fields were exported by the final timestep of the forward simulations.

RESULTS

Figure 1 presents the vertical profile of the three velocity (u/u_{ref}, v/v_{ref}, w/w_{ref}) components at x = -109.95 m and y = 0.825 m for two turbulence models (k-epsilon and k-omega SST). The specific point is located in the shipping containers area. The simulated velocities are compared to the corresponding wind tunnel measurements. Note that observations are available only for the two velocity components (u, w). The results show that the profiles of the two simulations are similar for the u and v velocity components, while there is a divergence below 5 m height in the w component. In the v component, both model profiles follow the distribution of the corresponding measurements. This agreement between modeled and measured velocities is apparent very near the ground surface and lower than the shipping container's height. On the other hand, a high bias is evident for the w velocity below the 5 m height. In this case, the k-omega SST models reduce the variance between modeled and measured w velocity. The explanation of this bias has to take into account the height of the shipping containers (2.54 m). As a result, the existence of obstacles appears to affect the model's accuracy.

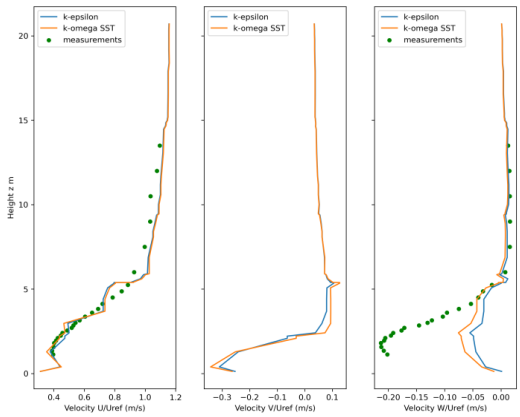

Figure 134. Comparison between modeled and measured velocity components profile (u/u_{ref}, v/v_{ref}, w/w_{ref}) at x = -109.95 m and y = 0.825 m

Table 1 presents the results of source parameters estimation (source location and release rate) in the two investigated cases, k-epsilon and k-omega SST. In the k-omega SST case, the distance between the cell of the estimated location and the true location is negligible. Specifically, the distance between the point that is located in the true source and the corresponding predicted point is 1.28 m in the k-omega SST case, while for k-epsilon it is 7.91 m. On the other hand, the k-epsilon implementation provides better results in the release rate estimation. The divergence between the estimated and the corresponding true release rate is $0.41 \cdot 10^{-5}$ kg s^{-1} in the k-epsilon, and $0.63 \cdot 10^{-5}$ kg s^{-1} in the k-omega SST case.

Table 48. Source parameters estimation results

Case	**Location – Domain coordinates**			**Release rate**
	***X* (m)**	***Y* (m)**	***Z* (m)**	***q* (kg/s)**
True source	-102,48	-7.06	0.00	$1.35 \cdot 10^{-5}$
Estimated source k-epsilon	-97.22	-12.03	3.20	$0.94 \cdot 10^{-5}$
Estimated source k-omega SST	-102.28	-7.39	1.22	$0.72 \cdot 10^{-5}$
Divergence true - estimated (k-epsilon)	5.26	4.97	3.20	$0.41 \cdot 10^{-5}$
Divergence true - estimated (k-omega SST)	0.20	0.33	1.22	$0.63 \cdot 10^{-5}$

To quantify the quality of the solution, the quantities $R_H = \sqrt{(x_e - x_t)^2 + (y_e - y_t)^2}$ for the horizontal and $R_V = |z_e - z_t|$ for the vertical distance are calculated. Respectively, for the release rate ratio, $\Delta q = \max[(q_e/q_t), (q_t/q_e)]$, is used as a bias estimator, where (x_e, y_e, z_e, q_e) are the estimated source parameters and (x_t, y_t, z_t, q_t) are the true source parameters. The estimated source parameters results are evaluated based using the criteria of Kovalets et al. (2011), where a good solution is considered to be achieved for $R_H \leq 15$ m, $R_V \leq 1.5$ m and $\Delta_q \leq 4$. Table 2 presents the results for the horizontal and vertical distances and the release rate ratio. The low bias in horizontal and vertical distances indicates a good solution for the source location estimation in the k-omega SST implementation. On the other hand, in the k-epsilon case, the vertical criteria are not met. In both cases, good results are provided for the release rate calculation.

Table 49. Horizontal and vertical distances and release rate ratio results

Case	R_H (m)	R_V (m)	Δq (-)
k-epsilon	7.24	3.20	1.44
k-omega SST	0.39	1.22	1.88

CONCLUSIONS

The CFD models can accurately estimate the meteorological parameters and the pollutant dispersion over complex geometry such as a dense urban area, taking into account the small-scale turbulence effects. The STE methods can successfully use CFD models to estimate the parameters of an unknown source. In this work, two turbulence models (k-epsilon and k-omega SST) are investigated in an STE application using the computational domain and measurement set of the MUST wind tunnel experiment. The methodology solves a correlation-based cost function to estimate the source location. The release rate is calculated for the predicted source location by solving a quadratic cost function. Results indicate very high accuracy in the location estimation by the k-omega SST case. The horizontal uncertainty of the location estimation is insignificant, while the vertical one is very low. In the k-epsilon case, a higher bias is found at both horizontal and vertical levels. On the other hand, a better solution is achieved regarding the release rate calculation using k-epsilon implementation. Both cases provide good results in release rate prediction. The foreseen applications of the methodology include support of rapid response to accidental or malicious substance releases as well as detection and quantification of transient emissions from shipping sources in harbour areas in support of control and enforcement of emission limits.

ACKNOWLEDGEMENTS

P. Gkirmpas acknowledges the Helmholtz Association of German Research Centers for funding the doctoral dissertation through the European program Helmholtz European Partnership for Technological Advancement (HEPTA). Also, he acknowledges the Graduate School of the Centre for Climate and Environment (GRACE) at the Karlsruhe Institute of Technology (KIT) for financial support.
The authors would like to acknowledge the SCIPPER Project (project that has received funding from the European Union's Horizon 2020 research and innovation programme under grant agreement No 814893) for financial support.

REFERENCES

Efthimiou G. C, I. V. Kovalets, A. Venetsanos, S. Andronopoulos, C. D. Argyropoulos and K. Kakosimos, 2017: An optimized inverse modelling method for determining the location and strength of a point source releasing airborne material in urban environment, Atmospheric Environment, ***170****, 118-129.*

Hutchinson, M, H. Oh and W.-H. Chen, 2017: A review of source term estimation methods for atmospheric dispersion events using static or mobile sensors, Information Fusion, ***36****, 130-148.*

Kovalets, I. V, S. Andronopoulos, A. G. Venetsanos, J. G. Bartzis, 2011: Identification of strength and location of stationary point source of atmospheric pollutant in urban conditions using computational fluid dynamics model, Mathematics and Computers in Simulation, ***82****, 244-257.*

Marchuk, G, 1982: Mathematical Modelling in the Environmental Problems, Nauka, Moscow.

Marchuk, G, 1996: Adjoint Equations and Analysis of Complex Systems, Kluwer Academic Publishers, Dordrecht, Netherlands

21st International Conference on
Harmonisation within Atmospheric Dispersion Modelling for Regulatory Purposes
27-30 September 2022, Aveiro, Portugal

EMISSIONS CALIBRATION IN A EMISSIONS CALIBRATION IN A COUNTRY SCALE HIGH RESOLUTION AIR QUALITY MODEL

Andrew Beddows, Nutthida Kirwiroon, Nosha Assareh, Gregor Stewart, Sean Beevers

SHORT ABSTRACT

Abstract title: **Emissions calibration in a country scale high resolution air quality model**

Name and Affiliation of the First Author: Andrew Beddows, Imperial College London

Email of first author: a.beddows@imperial.ac.uk

Names and Affiliations of the Co-authors: Nutthida Kirwiroon, Nosha Assareh, Gregor Stewart, Sean Beevers, Imperial College London

ABSTRACT TEXT (MAXIMUM 350 WORDS.)

We present the results of an emissions calibration process of unprecedented scale – improving traffic emissions estimates in a model which includes every road in the UK, down to residential street level. The CMAQ-urban model is a one-way coupling of the CMAQ CTM with a kernel modelling technique based on the ADMS roads model. The contribution from each road source is represented as a series of links 10 m long and summed onto a fixed 20 m x 20 m grid. The road classification includes open (e.g. motorways), typical (average urban roads surrounded by low rise buildings) and street canyons classified by orientation. This model has been in use for several years and has provided high resolution exposure data with UK wide coverage for a number of health studies. However, a significant limitation has been a lack of road traffic emissions data leading to some roads not being included in previous model outputs. Here we address the lack of detailed traffic counts and emissions by utilising ~12,000 diffusion tube and local sensor measurements, with a road traffic emissions optimisation method (EOM), combined with existing traffic datasets, to provide hyperlocal model predictions every 20m, close to ~400,000 km of UK roads.

The EOM uses model sensitivity coefficients in Taylor series expansions of the models' response to varying emissions, allowing Monte Carlo emissions calibration to be performed at every monitoring location. This has allowed the creation of previously unavailable road emissions estimates, and the calibration of emissions on those roads that were already in the model.

The model performance compares favourably with out of sample measurements and addresses the uncertainty in NO_X, NO_2 and PM emissions from road transport, which for the former have been underpredicted and for the latter are uncertain, due to the difficulty in predicting non-exhaust emissions. This approach is ideally suited to the use of the ever increasing low cost sensor networks globally, turning a detailed network of measurements in a powerful hyperlocal model of human exposure, where none existed previously, able to provide data for policy development, health research and reporting city and country scale emissions.

21st International Conference on
Harmonisation within Atmospheric Dispersion Modelling for Regulatory Purposes
27-30September 2022, Aveiro, Portugal

SOURCES AND DISPERSION OF BTX EMISSIONS IN A PORT AREA IN GREECE

Fameli Kyriaki - Maria,Vasiliki D. Assimakopoulos, Theodore M. Giannaros and Vasiliki Kotroni

Institute for Environmental Research and Sustainable Development, National Observatory of Athens,V.Pavlou and I. Metaxa str., 152 36 Athens, Greece

Abstract: Port cities usually face serious environmental problems due to the multiply anthropogenic activities that take place there. In the present study the port of Piraeus, which is located at the southern suburbs of the Greater Athens Area, Greece was chosen for the examination of the local sources and pollutants dispersion. The area of interest is well-known for the record of ozone exceedances during summer and particulate pollution episodes during winter. However the role of the anthropogenic Non-Methane Volatile Organic Chemicals (NMVOCs) to the local air quality has been limited examined. NMVOCs at an urban environment originate mainly from road transport, industrial activities and biomass burning. More specifically, NMVOCs include a group of aromatic compounds known as BTX (Benzene, Toluene and Xylene), the monitoring of which provides significant information of the VOCs levels. The purpose of this study is to focus on the local sources of NMVOCs emissions and the dispersion of the BTX species at the Piraeus where the main commercial and passenger port of Greece is located. For this reason a detailed emission inventory was developed covering all the anthropogenic sources (traffic, residential heating, navigation, non-road and industrial activities) at a spatial scale of 1 x 1 km^2. Moreover, the Comprehensive Air quality Model with eXtensions (CAMx) was applied for two periods in autumn (16th September 2021) and winter (1st February 2022) in order to study the impact of different meteorological conditions on the dispersion of BTX species. During both periods low wind speeds prevailed in the area while the wind direction and temperature profiles were different. All the necessary meteorological parameters for the numerical application with CAMx were provided by the meteorological model WRF. Model results revealed that in autumn BTX concentrations ranged from 0.12 ppb to 1.4 ppb while the peak value was observed at night. The plume that was created within the day remained in the area close to the port affecting the local suburbs. However, in winter part of pollutants emitted at the port area due to activities related to navigation were transferred north leading to higher BTX concentrations at the urban center of Athens..

KEY WORDS: NMVOCS, BTX EMISSIONS, AIR QUALITY MODELLING, PORT,GREECE.

INTRODUCTION

According to the European Environment Agency (https://www.eea.europa.eu/data-and-maps/indicators/eea-32-non-methane-volatile-1) Non-Methane Volatile Organic Compounds (NMVOCs), are a group of organic compounds that differ widely in their chemical composition but exhibit similar behavior in the atmosphere. NMVOCs are emitted into the atmosphere from a large number of sources, including combustion activities, solvent use and power generation processes. Some species included in NMVOCs are dangerous to human health, especially in case of exposure for a long time to very high concentrations. More specifically, NMVOCs includes a group of aromatic compounds known as BTEX from the initials of Benzene, Toluene, Ethylbenzene and Xylene, the monitoring and calculation of which can provide an important picture of the VOCs levels in an area. According to the international literature,

the main sources of aromatic volatile organic compounds and especially benzene are the chemical industry, oil refineries, oil storage tanks and Industrial Areas (Wallace, 1989) while in the densely populated areas the input from vehicles, especially under heavy traffic conditions, is significant (Liu et al. 2008, Caselli et al. 2010). Biomass burning for residential heating is another source of BTEX especially in the winter (Duan and Li, 2017). BTEX concentrations in the atmosphere of cities worldwide are quite high (Sekar et al. 2019, Montero-Montoya et al. 2018). Indicatively, the average annual benzene concentration in Verona, Italy in 2012 was 1.81 μg/m^3 (Schiavon et al. 2015) while 8-h measurements at a port in northern France in July 2009 revealed values of 4.9 ± 0.3 μg/m^3 (Roukos et al. 2011). At the study of Marć et al. (2014) conducted in Polish cities (Gdansk, Gdynia, and Sopot) in 2012, the recorded benzene levels were 0.72 ± 0.11, 0.66 ± 0.51, and 0.63 ± 0.55 μg/m^3, respectively.

Regarding Athens, Chatzis et al. (2005) showed that the mean annual benzene concentration is 20.4 μg/m^3 and the proximity to a busy road significantly affects benzene levels both outdoors and indoors. The daily profile of aromatic VOCs (toluene and benzene) in Athens, according to measurements conducted by Kaltsonoudis et al. (2016), is highly related with vehicles traffic especially in summer (average value 0.22 ppb = 0.70 μg/m^3). In winter, the biomass burning increases benzene levels in the atmosphere significantly; the average value is 1.00 ppb = 3.19 μg/m^3 while with the inclusion of biomass burning the average value is almost three times higher (3.18 ppb = 10.14 μg/m^3). In the present study the port of Piraeus, which is located at the southern suburbs of the Greater Athens Area, Greece was chosen for the examination of the local sources of NMVOCs emissions and pollutants dispersion with the photochemical model CAMx. The area of interest is well-known for the record of ozone exceedances during summer and particulate pollution episodes during winter. However the role of the anthropogenic NMVOCs to the local air quality has been limited examined.

METHODOLOGY

Study area description

The Greater Athens Area (GAA) is the most populated area in Greece; almost half of the greek population lives and works there.Concequently, pollution episodes continue to occur due to the complex topography and meteorology of the area coupled to the local emissions sources as well as the transport of particles and ozone precursors from remote areas (Pateraki et al. 2013). In the present study the area close to the port of Piraeus, which is located at the southern suburbs of the GAA, was chosen for the examination of the local sources and pollutants dispersion (Fig.1). It is the biggest commercial and passenger port in Greece. With about 18.6 million passengers it was the busiest passenger port in Europe in 2014 and according to Eurostat database for top container ports in 2019 Piraeus ranked 4th in Europe (20th in 2010). Concequently, multiple anthropogenic activities are concentrated around the port (local market, hotels, dense road network and public transport, medium and small size industries) and the population density in the area ranges from 10.000 to 23.000 people/km^2 (Eurostat, JRC-GEOSTAT 2018). Moreoner, ferry boats operate frequently at a local ferry line that connects Attica with the nearby Salamis Island.

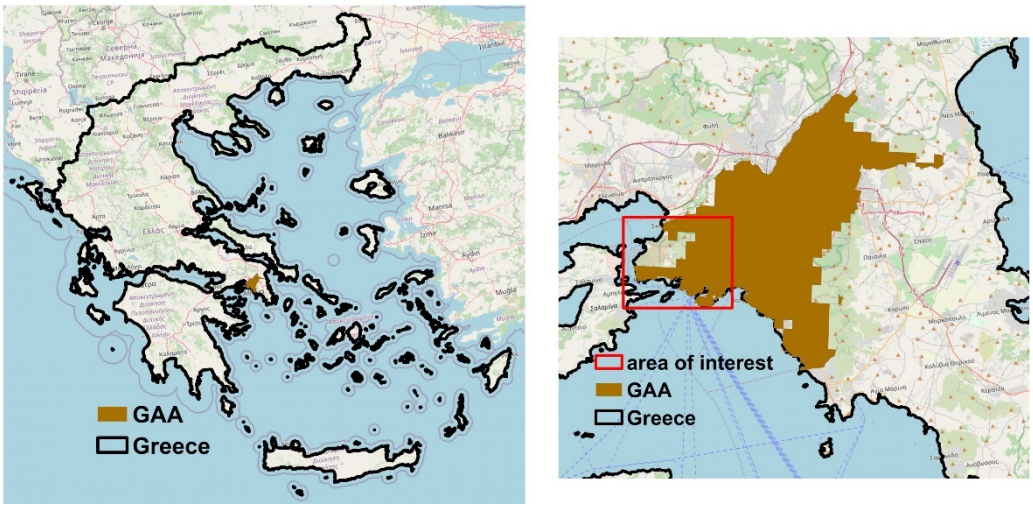

Figure 1. Map of Greece (left), the GAA and the area of interest (right).

Emissions inventory

For the purposes of this study the FEI-GREGAA Emissions Inventory (E.I.) developed by Fameli and Assimakopoulos (2016) was updated in order to improve the spatial resolution (from 2x2 km^2 to 1x1 km^2) and the period (reference year: 2018). According to the land use map, provided by the European program COPERNICUS, the study area is characterized by 14 different land use categories (CorineLandCover - CLCcodes) including urban areas, areas of anthropogenic activities such as the industrial zones of Keramos, Neo Faliro, Agios Ioannis Rentis, other small scale industries, the Shipyards of Skaramaga and Perama, the sewage treatment plant installed on Psyttalia Island, the port of Piraeus, while the western part of the area is covered by low vegetation and coniferous forest. It is obvious that they determine the emission levels and the measured concentrations of pollutants and particulates. Five (out of the eight) different emission sources of FEIGREGAA E.I. are included in the area of interest (road transport, residential heating, navigation, non road mobile & machinery and industry). Industrial NMVOCs emissions are not included in this study since they have not been submitted to the European Pollutant Release and Transfer Register (E-PRTR). However, it should be mentioned that the annual emissions of NMVOCs from the nearby refineries in Aspropyrgos and Elefsina were 1770 tonnes and 812 tonnes (reference year: 2017), respectively while benzene emissions were 29.8 tonnes and 11.8 tonnes, respectively.

Air quality modelling

It should be noted that under suitable prevailing meteorological conditions, the above pollutants are often transported within the GAA, affecting the air quality of the neighboring urban areas. For this reason, the Comprehensive Air quality Model with eXtensions (CAMx, www.camx.com) was applied for two periods in autumn (16th September 2021) and winter (1st February 2022) in order to study the impact of different meteorological conditions on the dispersion of BTX species. The necessary meterorological parameters for the air quality applications were provided by the WRF model while the updated FEI-GREGAA E.I. was used as input (including the BTX aromatic compounds). The chemical mechanism CB6 was selected in order to simulate the photochemical activities that take place in the atmosphere.

RESULTS

Sources of nmvocs emissions

Concerning NMVOCs emissions, the sectors that contribute mostly to the annual total value are road transport (76%; 1605.45 tonnes) and residential heating (19%; 403.27 tonnes) while navigation and non road mobile & machinery follow having 4% (81.53 tonnes) and 1% (29.89 tonnes) contribution respectively. It should be noted that the 9.5% of NMVOCs emissions from road transport corresponds to

BTX species and more specifically 2.0% accounts to Benzene, 4.4% to Toluene and 3.1% to m/p - Xylene.The annual gridded NMVOCs emissions from road transport and navigation are presented in Fig.2. The maximum value per cell is 77.92 tonnes/km^2 for road transport and it is located at the centre of Piraeus where the majority of vehicles (passenger cars, public transport and trucks) commute. However, a great part of NMVOCs are emitted at the sourounding area of the port due to traffic problems. It is found that driving under low speed conditions affects the pollutants emitted negatively (Fameli ans Assimakopoulos 2015). Almost 4.4 times lower (17.42 tonnes/km^2) is the highest emission value from navigation which as expected appears at the the passenger port of Piraeus while remarkable values are attributed at the ferry line Perama - Salamis Island (13.41 tonnes/km^2) as well as at the Piraeus Container Terminal Single Member S.A. (PCT; 5.3 tonnes/km^2).

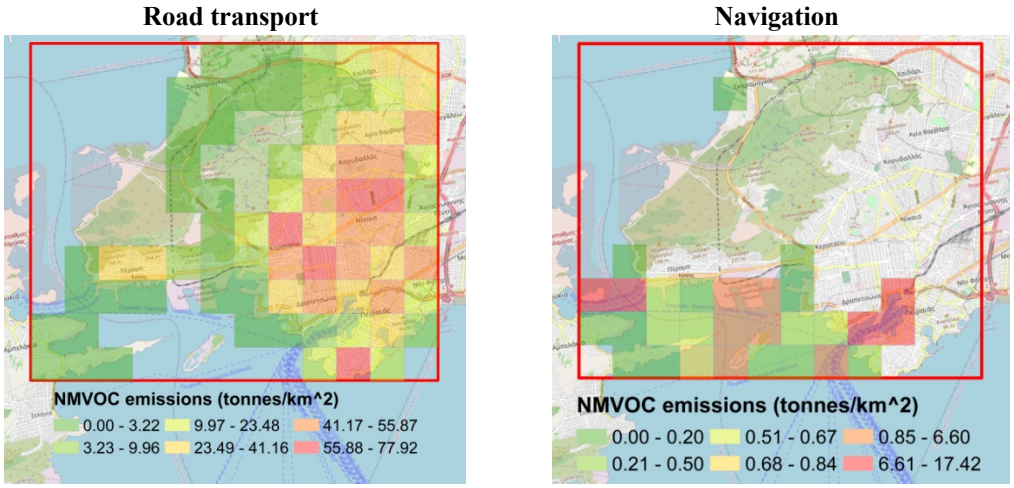

Figure 2. Gridded annual emissions from road transport (left) and navigation (right).

Air quality - case studies analysis

During the first case study (16th September 2021) the mild synoptic conditions that prevailed, due to the existence of a high barometric pressure system above Greece, favored the development of a local circulation system and the predominance of low wind speeds. Consequently, the calm wind conditions produced unfavorable ventilation conditions that led to increased pollutants concentrations over the area of interest. As shown in Fig.3 a plume of high BTX concentrations was developed at the surrounding area of the port of Piraeus in the morning and remained there till late in the evening. In general concentrations ranged from 0.12 ppb to 1.4 ppb (below the limit value). The first peak appeared at 09:00 LT (1.4 ppb) at the port of Piraeus while a nighttime high value was also observed slightly east to the morning one. This diurnal variation is consistent with the anthropogenic activities. During daytime, traffic is more intense in the morning and evening following the working hours as well as the operation of the local market. Moreover, the majority of passenger ships depart from Piraeus early in the morning. In September the outdoor temperature is quite high so there is no need for residential heating in Athens. Thus, pollutants concentrations are not affected by this source.

The second case study refers to a winter day on 1st February 2022. South-Southwest low-intensity winds formed the meteorological field and much lower temperatures were recorded in comparison to the first case study. Local circulation systems prevailed, mainly affected by the topography. As a result pollutants emitted by the anthropogenic activities at the urban area remained within the urban center. During the winter the scheduled vessels routes are limited since the tourist season has ended and they cover mainly local needs. As presented in Fig.4, the group of BTX showed a maximum in the morning hours (0.33 ppb) at the urban center and for the rest of the day values remained rather low (below 0.27 ppb). It should be noted that the concentrations of benzene and other NMVOCs measured in the area by a nearby air quality station were also very low. Comparing winter and autumn simulated concentrations, the differences in the spatial dispersion of BTX are obvious. Under the prevalence of low wind speeds, southern suburbs are

mainly affected in September because of the local emissions sources (road transport and in particular navigation) while in winter BTX fields are concentrated in the urban center.

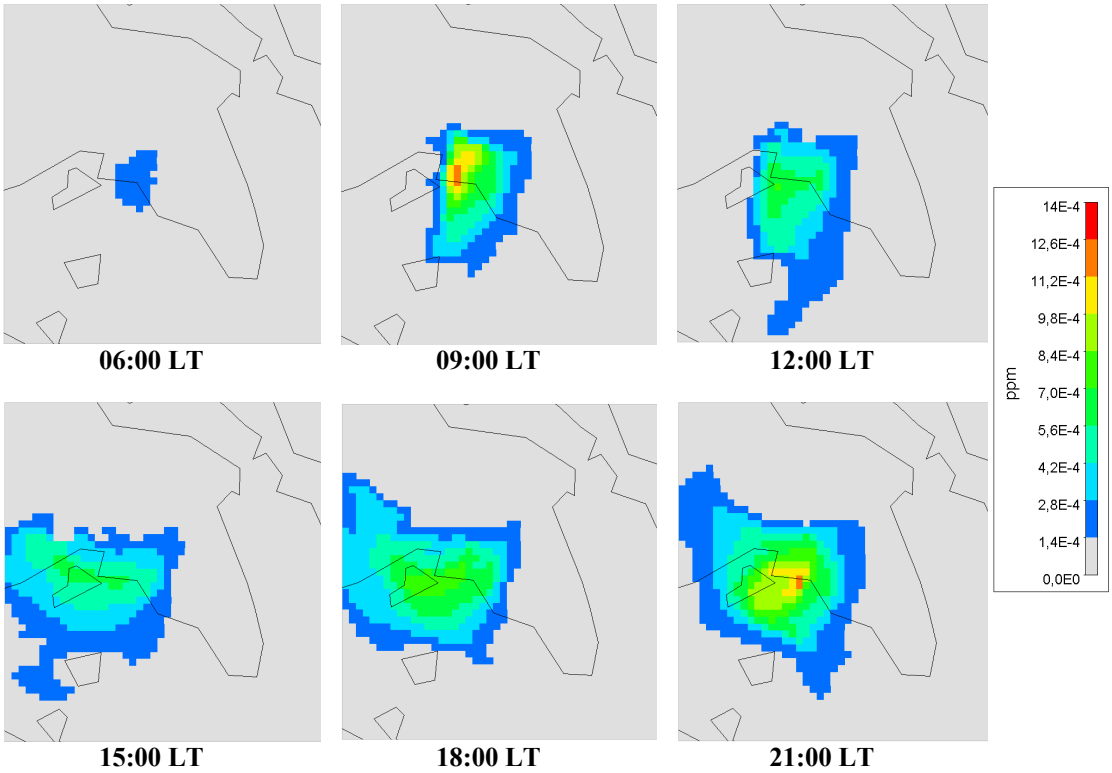

Figure 3. Dispersion of BTX model concentrations over the area of interest on 16th September 2021.

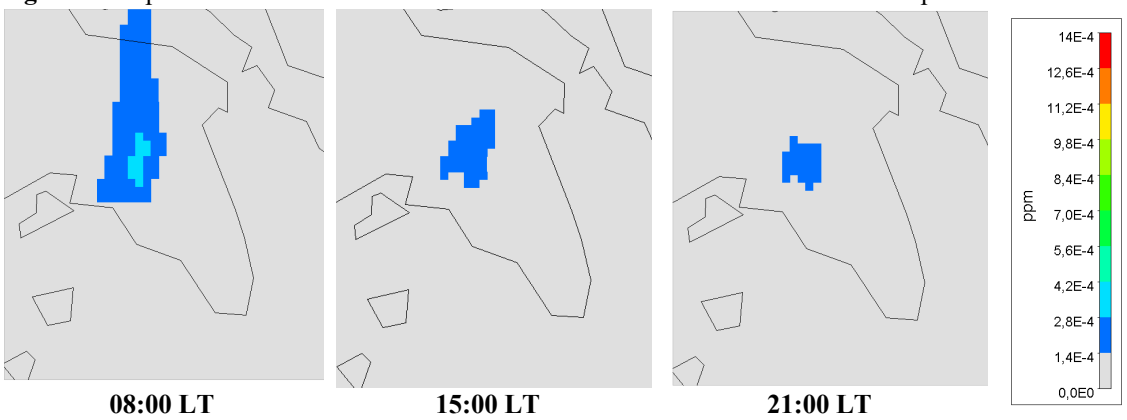

Figure 4. Dispersion of BTX model concentrations over the area of interest on 1st February 2022.

REFERENCES

Wallace, LA., 1989: Major sources of benzene exposure. *Environ Health Perspect*, **82**,165–169.

Liu, Y., M. Shao, L. Fu et al., 2008: Source profiles of volatile organic compounds (VOCs) measured in China: Part I[J]. *Atmospheric Environment*, **42**, 6247-6260.

Caselli, M., G. de Gennaro, A. Marzocca et al, 2010: Assessment of the impact of the vehicular traffic on BTEX concentration in ring roads in urban areas of Bari (Italy). *Chemosphere*, **81**, 306-311.

Duan, X., Y. Li, 2017: Sources and Fates of BTEX in the General Environment and Its Distribution in Coastal Cities of China. *J. Environ. Sci. Public Heal.,* **01**, 86–106.

Sekar, A, G.K. Varghese, M.K. Ravi-Varma, 2019: Analysis of benzene air quality standards, monitoring methods and concentrations in indoor and outdoor environment. *Heliyon,* 5, e02918.

Montero-Montoya, R., R. López-Vargas, O. Arellano-Aguilar, 2018: Volatile organic compounds in air: sources, distribution, exposure and associated illnesses in children. *Ann Glob Health,* **84**, 225–238.

Schiavon, M., M. Redivo, G. Antonacci, E.C. Rada, M. Ragazzi, D. Zardi, L. Giovannini, 2015: Assessing the air quality impact of nitro- gen oxides and benzene from road traffic and domestic heating and the associated cancer risk in an urban area of Verona (Italy). *Atmos Environ*, **120**, 234–243.

Roukos, J., N. Locoge, P. Sacco, H. Plaisance, 2011: Radial diffusive samplers for determination of 8-h concentration of BTEX, ace- tone, ethanol and ozone in ambient air during a sea breeze event. *Atmos Environ*, **45**,755–763.

Marć, M., J. Namieśnik, B. Zabiegała, 2014: BTEX concentration levels in urban air in the area of the Tri-City agglomeration (Gdansk, Gdynia, Sopot), Poland. *Air Qual Atmos Health,* **7**, 489–504.

Chatzis, C., E.C. Alexopoulos, A. Linos, 2005: Indoor and outdoor personal exposure to benzene in Athens, Greece. *Sci. Total Environ.,* **349**, 72–80.

Kaltsonoudis, C., E. Kostenidou, K. Florou, M. Psichoudaki, S.N. Pandis, 2016: Temporal variability and sources of VOCs in urban areas of the eastern Mediterranean. *Atmos. Chem. Phys*, **16**, 14825– 14842.

Pateraki, S., V.D.Assimakopoulos, T. Maggos, K.M. Fameli, V. Kotroni, C. Vasilakos, 2013: Particulate matter pollution over a Mediterranean urban area. *Sci Total Environ*, **463–464**, 508 - 524.

Fameli, K.-M., V.D. Assimakopoulos, 2016: The new open Flexible Emission Inventory for Greece and the Greater Athens Area (FEI-GREGAA): Account of pollutant sources and their importance from 2006 to 2012. *Atmos. Environ*, **137**, 17 - 37.

Fameli, K.M., V.D. Assimakopoulos, 2015: Development of a road transport emission inventory for Greece and the Greater Athens Area: Effects of important parameters. *Sci. Total Environ*, **505**, 770 - 786.

AKNOWLEDGEMENTS

Part of this work was funded by the Hellenic Environmental Center S.A.

21st International Conference on
Harmonisation within Atmospheric Dispersion Modelling for Regulatory Purposes
27-30 September 2022, Aveiro, Portugal

A BAYESIAN INFERENCE TECHNIQUE COMBINED WITH A STOCHASTIC WIND MODELING TO IMPROVE MULTIPLE SOURCE PARAMETERS ESTIMATION IN THE ATMOSPHERE

Roseane Albani[1], Vinícius Albani[2], Luiz Eduardo da Silva[3], Hélio Migon[1,3] and Antônio da Silva Neto[1]

[1] Polytechnic Institute, Rio de Janeiro State University, Nova Friburgo (RJ), Brazil
[2] Dept of Mathematics, Federal University of Santa Catarina, Florianopolis (SC), Brazil
[3] Institute of Mathematics, Federal University of Rio de Janeiro, Rio de Janeiro (RJ), Brazil

Abstract: We present a new methodology to estimate multiple source parameters in the framework of Bayesian Inference. In the Bayesian inference technique, the estimation problem is modeled as the determination of the full conditional probability density of the unknown parameters. In turn, the full conditionals are the product of the likelihood function, which relates observed and model-predicted concentrations and a prior density for the unknowns. The full conditionals for the unknown source parameters are not usually easily sampled. Thus, the estimation technique presented in this work combines a Metropolis-Hastings step for those unknowns that cannot be sampled directly with a Gibbs step for those sampled directly from its full conditionals. The proposed algorithm estimates the cartesian source coordinates, the source strength, the number of emissions, the precision of the observational data, and the constant in the Lasso prior distribution. In addition, we proposed a Bayesian dynamic linear model (DLM) to obtain high-frequency average wind data. In this model, we obtain the joint modeling of the wind intensity and direction. We evaluate the algorithm with the multiple tracer releases field experiment FFT07.

Key words: *Source Identification Modelling , Atmospheric Dispersion, Bayesian Inference, MCMC, Finite Element Method, Wind Forecast, Bayesian Dynamic Linear Models.*

INTRODUCTION

Atmospheric pollution is a considerable environmental concern since it strongly affects the population's quality of health and influences the ongoing climate change. In many situations, it is necessary to investigate the geographical localization and magnitude of atmospheric pollutants emissions to decide, possibly based on simulations of a dispersion model, which regions will be affected by their damaging effects, allowing the establishment of emergency measurements.

The methodologies to identify the source parameters via inverse problem modelling require a systematic procedure, which involves some coupled steps, such as the definition of a forward problem or dispersion model, usually an advection-diffusion partial differential equation (PDE). The dispersion model incorporates all the relevant physical processes involved in the case under investigation. The closer the forward problem is in describing such a situation, the better the results of the inverse problem will become. Also, the methodology to solve the forward problem strongly impacts the solution of the dispersion model and, consequently, the accuracy of the source parameters estimation.

In this work, we present a contribution to improving the forward model, more precisely in the pollutant transport by the wind, using a Bayesian Dynamic Linear Model (DLM) to obtain time-dependent wind intensity and direction. Such a model allows us to introduce the local wind changes in the dispersion model, potentially improving their accuracy. A customary procedure in source identification modelling is to substitute the advection-diffusion PDE with its adjoint one. It allows the forward model to be solved only

once for all the iterations of the inverse problem. This strategy considerably reduces the computations of the source identification algorithm, enabling faster responses. The adjoint state dispersion model is solved using the finite element formulation from (Do Carmo and Galeão, 1991) suitable to solve transient advection-diffusion PDEs. Finally, the source parameters are estimated using a Metropolis in Gibbs Monte Carlo Markov chain (MCMC) algorithm to obtain simultaneously the source parameters, the uncertainty in the data, and the parameters in the prior distributions.
In comparison with the previous work, Albani et al. (2021), there are considerable improvements. The dispersion model is now transient and considered a more realistic wind field. The proposed inversion technique is more robust since it appropriately addresses the weight of the prior densities in the estimation.

Description of the case of study

The proposed methodology to estimate simultaneously the source parameters and the number of sources is simulated and evaluated against the case 55 of the multiple emission tracer experiment FUSION Field Trial 2007 (FFT-07) (Storwald, 2007). During Trial 55, the tracer gas polypropylene (C3H6) was released continuously for 10 minutes at a constant emission rate from four-point sources and then sampled over an array of 100 sensors. The sensors were arranged considering a distance of 50 m from each other, over a sampling grid of 450 x 475 m and 2 m above the ground level. The C3H6 concentrations were sampled over about 15 minutes. High frequency 10Hz three-dimensional sonic anemometers were displayed on three 32-m lattice towers. In this work, we used the meteorological datasets measured in the centre of the grid of sensors.
The towers were equipped with five three-dimensional sonic anemometers at levels 2, 4, 8, 16, and 32 m. The sonic anemometer measured the three wind speed components u,v, w, in m/s, and the air temperature, in K. Although the meteorological dataset's time-series length is 50 minutes, just 14 minutes were applied to consider the concentration sampling period. As the concentration gas sampler units were arranged at 2 m above the ground level, we used only the zonal and meridional wind components data records measured at this same height. The arrangements of the concentration sampling units and emission sources are depicted in Fig. 1.

METHODOLOGY

The proposed methodology to identify multiple atmospheric releases is based on three main steps: the development of a Bayesian dynamic linear model (DLM) to forecast high frequency average wind data, considering Trial 55 of the FFT07 experiment. This model simultaneously takes into account the wind intensity and direction through the joint modelling of the zonal (u) and meridional (y) wind components.This model is partially based on in García et al. (2020). This wind field is one of the input data to the dispersion model. Considering the flat terrain topography, the turbulent diffusion coefficient in the vertical direction is described according to the Monin-Obukhov similarity theory. An usual procedure to solve source estimation problems is to change the advection-diffusion PDE by its adjoint one. Such a strategy considerably reduces the simulation's burden to solve the inverse problem, since in this case, the adjoint PDE needs to be solve only once, for all the iterations of the inverse problem. We avoid a detailed description of the forward problem modelling procedure for the sake of space, but it can be found, e.g. in a forthcome work and in Albani and Albani. (2019). The resulting adjoint-state PDE for the dispersion model was numerically solved using the finite element formulation proposed by Do Carmo and Galeão (1991).
We briefly describe the technique used to estimate the source parameters. Let $\mathbf{C}^{\text{obs}}$ denote the vector containing *n* values of observed concentrations of C3H6 at different sensors and time instants. The pollutant was emitted from a set of unknown sources. We aim to find the sources locations and their respectives emission rates. Assume, for simplicity, that the number *S* is fixed. Then, the vector containing the location (x_s, y_s, z_s) and strength (Q_s) of the *s*th source, for $s = 1, \cdots, S$, is defined as $\mathbf{w}_s = [x_s, y_s, z_s, Q_s]$. We can parameterize all the sources with respect to a given one. Thus, for $s = 2, \cdots, S$, we can write $\mathbf{w}_s = \mathbf{w}_1 + \mathbf{v}_s$. The aim is to reduce the set where the unknowns are defined, simplifying the inverse problem solution. More precisely, we let the entries of $\mathbf{w}_1$ to vary in the whole computational domain, whereas $\mathbf{v}_s$ varies in a much more restricted set. In other words, we are assuming that all the sources are close to each other.

The estimation is made by a Bayesian technique (Gamerman and Lopes, 2006). Thus, we setup prior densities for the unknowns and likelihood functions linking unknown to observed concentrations to build full conditional probability densities. As we shall see, some of such full conditionals will be sampled by the Metropolis in Gibbs Markov chain Monte Carlo algorithm (MCMC) (Albani et al., 2021). It combines a Metropolis-Hastings step for those unknowns that cannot be directly sampled with a Gibbs step for those that are sampled directly from its full conditional.

The first source has a uniform prior, i.e., $\mathbf{w}_1$ has uniform distribution in the set

$$A_\eta = [x_{min}, x_{max}] \times [y_{min}, y_{max}] \times [z_{min}, z_{max}] \times [Q_{min}, Q_{max}].$$

The xy-part of this set is defined based on the wind mean direction during the data collection and the concentration distribution in the domain given by the isopleth in Figure 2. The zQ-part of the set is the same used to solve the dispersion problem numerically.

For $s = 2, \cdots, S$, $\mathbf{v}_s$ has a Lasso prior truncated in the computational domain, with

$$P(\mathbf{v}_s|\alpha) \propto \exp\left(-\alpha\|\mathbf{v}_s\|_{\ell_1}\right).$$

For simplicity, we use the same α for all $s = 2, \cdots, S$. The scalar α is also unknown and has the prior distribution $\mathrm{Gamma}(1/3,1/3)$. As the concentration observation is uncertain, we assume a log-normal distribution for the noise, which means that, the relationship between observed and numerically calulated concentrations are given as follows, for $i = 1, \ldots, n$,

$$\boldsymbol{C}_i^{obs} = C_i(\mathbf{w}_1, \mathbf{v}_2 \cdots, \mathbf{v}_S)\exp(\varepsilon),$$

where ε is the noise and have Gaussian distribution with mean zero and variance $1/p$, with p called precision. Therefore, the likelihood function of $\mathbf{w}_1, \cdots, \mathbf{w}_S$ is the following

$$P\left(\mathbf{C}^{\mathrm{obs}}\middle|p, \mathbf{w}_1, \mathbf{v}_2 \cdots, \mathbf{v}_S\right) \propto p^{\frac{n}{2}}\exp\left(-p\left\|\log\left(\mathbf{C}^{\mathrm{obs}}\right) - \log(C(\mathbf{w}_1, \mathbf{v}_2 \cdots, \mathbf{v}_S))\right\|_{\ell_2}^2\right).$$

The quantity p is unknown and have the prior distribution $\mathrm{Gamma}(1/3,1/3)$.

The full conditionals are the following,

$$P(\mathbf{w}_1, \mathbf{v}_2 \cdots, \mathbf{v}_S|p, \alpha, \mathbf{C}^{\mathrm{obs}}) \propto P\left(\mathbf{C}^{\mathrm{obs}}\middle|p, \mathbf{w}_1, \mathbf{v}_2 \cdots, \mathbf{v}_S\right)P(\mathbf{w}_1)P(\mathbf{v}_2|\alpha) \cdots P(\mathbf{v}_S|\alpha),$$

$$P(p|\mathbf{w}_1, \mathbf{v}_2 \cdots, \mathbf{v}_S, \mathbf{C}^{\mathrm{obs}}) \propto P\left(\mathbf{C}^{\mathrm{obs}}\middle|p, \mathbf{w}_1, \mathbf{v}_2 \cdots, \mathbf{v}_S\right)P(p),$$

$$P(\alpha|\mathbf{v}_2, \cdots, \mathbf{v}_S) \propto P(\mathbf{v}_2|\alpha) \cdots P(\mathbf{v}_S|\alpha)P(\alpha),$$

Where $P(\mathbf{w}_1)$, $P(p)$, and $P(\alpha)$ denote the prior densities for the unknowns $\mathbf{w}_1$, p, and α.

The full conditional for p and α can be approximated, as mentioned above by the distributions $\mathrm{Gamma}(a, b)$ and $\mathrm{Gamma}(c, d)$, respectively, where

$$a = \frac{1}{2} + \frac{n}{3}, \qquad b = \frac{1}{3} + \left\|\log\left(\mathbf{C}^{\mathrm{obs}}\right) - \log(C(\mathbf{w}_1, \mathbf{v}_2 \cdots, \mathbf{v}_S))\right\|_{\ell_2}^2,$$

$$c = \frac{1}{3} + (S - 4), \qquad d = \frac{1}{3} + \sum_{s=1}^{S}\|\mathbf{v}_s\|_{\ell_1}.$$

In the MCMC algorithm, the sampling of p and α can be performed directly from the full conditionals, leading to Gibbs steps. Samples for $\mathbf{w}_1, \mathbf{v}_2 \cdots, \mathbf{v}_S$ will be approximated by a Metropolis-Hastings step.

Numerical results

In this section, we present numerical experiments using the Metropolis in Gibbs algorithm applied to the FFT07 dataset. The xy-components of the set A_η are defined based on the 15 minutes average concentration distribution in the xy-plane provided by the isopleth in Fig. 1 (right), the distribution of the sensors in the xy-plane in Fig. 1 (left), and the 15 minutes average wind direction, also in the xy-plane indicated by the arrow in Fig. 1 (left). The resulting region in xy-plane is indicated by the rectangle in Fig. 1 (left). The zQ-components are the same used to solve the forward problem. Thus, the prior density of η is the uniform distribution defined in the set

$$A_\eta = [-100,100] \times [50,600] \times [0,50] \times [0,30],$$

with the spatial parameters defined in meters and the source strengths defined in g/s. Notice that, the actual locations of the sources are inside A_η, as the crosses in the left panel of Fig. 1 show.

The Markov Chain generated by the MCMC algorithm in Algorithm 1 has 100 thousand states, with a burn-in set of 20 thousand states. From the remaining 80 thousand states, we select 4000 using a step-size of 20 states. Table 1 compares the true source parameters with the summary statistics of the chains generated by the MCMC algorithm. For comparison, we included the parameters estimated in Albani et al. (2020). It also presents the relative error of the estimations obtained by the MCMC algorithm and in Albani et al. (2020). In Albani et al. (2020), the source parameters were estimated from the same set of experimental data using Tikhonov-type regularization, where the objective functional was minimized using different techniques, including the combination of the genetic algorithm with a gradient descent method (GA+GD) and a combination of particle swarm optimization with GD (PSO+GD). The convergence of the chains was tested using the Gelman Rubin test (Gelman and Rubin, 1992), where the value 1.00 indicates that the chains converged. The relative error is evaluated as follows,

$$RELATIVE\ ERROR = 100\frac{|TRUE\ VALUE - ESTIMATED\ VALUE|}{TRUE\ VALUE},$$

representing a percentage of the true value of the parameter of interest. The minimum and maximum relative errors for the samples on each chain were evaluated and also presented in Table 1. The average relative error for the estimated values using the MCMC algorithm and the techniques from Albani et al. (2020) were also presented. Table 1 also presents the summary statistics for the precision p, and the parameter of the Lasso prior α.

By comparing relative errors and their average values it follows that the results obtained by the MCMC algorithm were slightly more accurate than those from Albani et al. (2020). The computational time to generate the Markov chains was similar to the time to perform the estimation procedure in Albani et al. (2020). Moreover, the estimations using the MCMC algorithm were obtained from 100 concentration values from 10 different sensors, whereas the estimation in Albani et al. (2020) considered the average of the concentration values from 50 sensors. This means that the proposed inversion tool used the available data more efficiently by considering a transient dispersion model. In addition, the present technique estimates the uncertainty in the data and sets appropriately the weight of the prior distributions simultaneously to the estimation of the source parameters, which improves its accuracy and performance in comparison to the techniques presented in Albani et al. (2020). There, a Morozov-type discrepancy principle (Albani and De Cezaro, 2019) was used to appropriately find the regularization parameter.

The potential stabilization of the Markov chains is illustrated by the histograms in Fig. 3 and values equal to 1.00 in the Gelman-Rubin test presented in Tab. 1. It is worth mentioning that, although the overall accuracy of the estimations was slightly better than in previous works, in some cases, the regions defined by the Markov chains failed to contain the true values of source parameters. Since the problem under consideration is highly ill-posed and the data is rather noisy, such behavior can be expected.

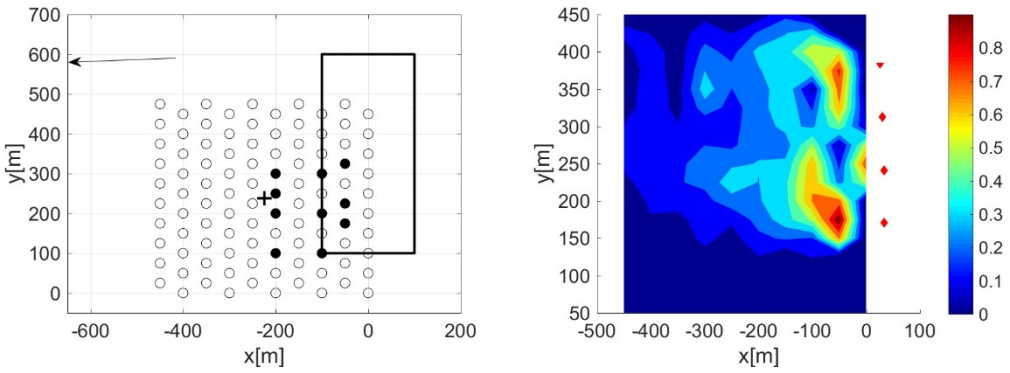

Figure 1: Left: Distribution of the sensors in the *xy*-plane of the computational domain. The arrow indicates the wind direction. The cross represents the position of the tower used to measure the wind speed and direction. The sensors

used in the simulations are the filled circles. The rectangle is the xy-part of the set A_η defining the uniform prior of η. Right: Isopleth showing the average concentration distribution for the trial 55 of the FFT07 in the computational domain. The diamonds represent the actual locations of the sources.

MCMC Summary Results									Results from Albani et al. (2020)			
Param.	True	Min.	Q1	Median	Q3	Max.	GR Test	Error (Min-Max)	GA+GD	Error	PSO+GD	Error
x_1 [m]	33,0	-12.1	-7.47	-6.80	-6.11	-1.53	1.00	121 (105–137)	33.6	1.73	28.7	13.1
y_1 [m]	171	216	225	228	232	249	1.00	33.3 (26.2–45.5)	171	0.26	172	0.59
z_1 [m]	2,00	0.50	0.84	1.02	1.18	2.28	1.00	49.2 (0.00–75.1)	2.32	16.0	0.01	100
Q_1 [g/s]	11,4	8.60	9.33	9.44	9.55	10.1	1.00	17.1 (11.1–24.5)	10.8	5.18	7.46	34.5
x_2 [m]	33,8	-5.07	-0.67	-0.01	0.65	4.70	1.00	100 (86.1–115)	8.51	74.8	28.3	16.3
y_2 [m]	241	287	298	300	302	313	1.00	24.6 (19.1–30.1)	245	1.87	240	0.36
z_2 [m]	2.00	0.01	0.32	0.50	0.66	1.77	1.00	75.2 (11.3–99.4)	1.69	15.5	2.04	2.00
Q_2 [g/s]	11.4	9.26	9.90	10.0	10.1	10.6	1.00	12.2 (7.18–18.7)	3.65	68.0	4.44	61.0
x_3 [m]	30,0	-28.9	-24.4	-23.7	-23.0	-18.6	1.00	179 (162–196)	64.0	113	200	567
y_3 [m]	313	95.5	105	108	112	129	1.00	65.4 (58.9–69.5)	305	2.66	124	60.4
z_3 [m]	2.00	1.14	1.48	1.66	1.82	2.92	1.00	17.2 (0.00–46.0)	8.69	335	1.46	27.0
Q_3 [g/s]	4.65	4.89	5.54	5.65	5.75	6.33	1.00	21.4 (5.15–36.1)	10.1	116	0.01	100
x_4 [m]	26,0	-1.89	2.68	3.34	4.03	7.65	1.00	87.1 (70.6–107)	57.5	121	-5.27	120
y_4 [m]	384	407	424	428	431	438	1.00	113 (5.77–14.1)	360	6.24	372	3.17
z_4 [m]	2.00	0.52	0.87	1.05	1.22	2.31	1.00	47.5 (0–74.0)	11.3	465	6.51	226
Q_4 [g/s]	11.4	8.95	9.64	9.75	9.85	10.4	1.00	14.4 (8.75–21.4)	24.5	115	11.6	2.19
Average								55 (36–69)		91		83
p	-	0.06	0.10	0.11	0.12	910	1.00					
α	-	188	893	1213	1594	4506	1.00					

Table 1: Comparison between the True source parameter values (True), the summary of the MCMC results, and the parameters estimated in Albani et al. (2020). For the MCMC results, we have the minimum value (Min.), the first

quartile (Q1), the median value (Median), the third quartile (Q3), the maximum value (Max.) and the value of the Gelman-Rubin convergence test (GR Test). The percentage error is the relative error multiplied by 100. It is evaluated with respect to the median value and the maximum and minimum possible error values considered in the samples (Min-Max). The relative error for the parameters estimated in Albani et al. (2020). GA+GD stands for the combination of the genetic algorithm with gradient descent (GD) and PSO+GD the combination of particle swarm optimization with GD. The row average presents the average of the relative errors.

CONCLUSION

The proposed methodology presented median values that were at least as accurate as previous approaches that used sofisticated inverse modeling techniques. This means that the presente estimation procedure that uses a more accurate dispersion model can present a better performence. However, in many cases, the credibility regions provided by the Markov chains failed include the true source parameters. This issue shall be addressed in future research by improving the MCMC algorithm and by including additional concentration data from other sensors in the computational domain.

ACKNOWLEDGEMENTS

RA thanks Fundação Carlos Chagas Filho de Amparo à Pesquisa do Estado do Rio de Janeiro (FAPERJ) for the financial support through the grants E-26/202.932/2019 and E-26/202.933/2019. AJSN acknowledges the financial support provided by the Coordenação de Aperfeiçoamento de Pessoal de Nível Superior (CAPES) through the grants 88887.311757/2018-00 and 88887.194804/2018-00, the Conselho Nacional de Desenvolvimento Científico e Tecnológico (CNPq) through the grant 308958/2019-5, and the Fundação Carlos Chagas Filho de Amparo à Pesquisa do Estado do Rio de Janeiro (FAPERJ) through the grant E-26/202.878/2017. HM thanks PAPD/Rio de Janeiro State University for the financial support through the grant E-26/007/10667/2019.

REFERENCES

Albani, R. and V. Albani 2019: Tikhonov-Type Regularization and the Finite Element Method Applied to Point Source Estimation in the Atmosphere. *Atmos. Environ.*, **211**, 69–78.

Albani, R., V. Albani, and A. Silva Neto 2020: Source characterization of airborne pollutant emissions by hybrid metaheuristic/gradient-based optimization techniques. *Environ Pollut.*, **267**, 115618.

Albani, R., V. Albani, H. Migon, and A. Silva Neto 2021: Uncertainty quantification and atmospheric source estimation with a discrepancy-based and a state-dependent adaptative MCMC. *Environ Pollut.*, **290,** 118039.

Albani, V. and A. De Cezaro 2019: A Connection Between Uniqueness of Minimizers and Morozov-like Discrepancy Principles in Tikhonov-type Regularization. *Inverse Probl. Imaging*, **13,** 211–229.

Do Carmo E. and A. Galeão 1991: Feedback Petrov-Galerkin methods for convection-dominated problems. *Comput Methods Appl Mech Eng*, **88,** 1–16.

Gamerman, D. and H. F. Lopes 2006: *Markov chain Monte Carlo: stochastic simulation for Bayesian inference*. CRC Press.

García, I., S. Huo, R. Prado, and L. Bravo 2020: Dynamic bayesian temporal modeling and forecasting of short-term wind measurements. *Renewable Energy*, **161,** 55–64.

Gelman, A. and D. B. Rubin 1992: Inference from iterative simulation using multiple sequences. *Statist. Sci.*, **7**, 457–472.

Storwold, D 2007: Detailed test plan for the fusing sensor information from observing networks (fusion) field trial 2007 (fft-07). *US Army Dugway Proving Ground West Desert Test Center Doc. WDTC-TP-07-078*, **46**.

21st International Conference on
Harmonisation within Atmospheric Dispersion Modelling for Regulatory Purposes
27-30 September 2022, Aveiro, Portugal

MCMC METROPOLIS-HASTING ALGORITHM IN THE SOURCE INVERSION PROBLEMS OF AIR POLLUTANTS IN URBAN CFD MODELLING

Martin Ferrand, Konstantin Kuznetsov, Bertrand Carissimo, Marc Bocquet

SHORT ABSTRACT

Abstract title: MCMC Metropolis-Hasting algorithm in the source inversion problems of air pollutants in urban CFD modelling

Name and Affiliation of the First Author: Martin Ferrand, CEREA, École des Ponts, EDF R&D, Ile de France, France

Email of first author: *martin.ferrand@edf.fr*

Names and Affiliations of the Co-authors: Konstantin Kuznetsov, Bertrand Carissimo, Marc Bocquet, CEREA, École des Ponts, EDF R&D, Île-de-France, France

ABSTRACT TEXT (MAXIMUM 350 WORDS.)

Beyond estimating the quantity of emitted pollutant and its evolution over time, there is a greater challenge in locating the source of the emission. This work presents a method for assessing the position and volume of a source of urban air pollution based on a limited number of measurements of pollutant concentrations. Using a Markov Chain Monte Carlo (MCMC) method with Metropolis-Hasting sampling, we create a map of probabilities and locate the most probable place of leakage and its emission rate.

Since buildings geometry has a big impact on the turbulent air flow, computational fluid dynamics (CFD) simulations with first-order and second-order moment turbulent closures are used for accurate predictions, which are computationally expansive compared to simpler Gaussian dispersion models. To efficiently compute the Jacobian matrix of the corresponding transport problem, the adjoint-solution approach is used. This allows us to combine two computationally costly methods, MCMC and CFD, and provide a map of possible pollutant sources within a reasonable timeframe.

To account for the unstructured mesh required by the building aware CFD, a new discrete proposal distribution for the Metropolis-Hasting sampler meant to sample locations of possible sources is proposed. This method is implemented in code_saturne benefiting from domain parallelism, which allows to use complex adaptive meshes, distributed on cluster memory. The new proposal samples cells instead of coordinates. Because only fluid cells are drawn, this sampler naturally addresses complex geometries and heterogeneous mesh refinements.

Finally, the method is illustrated and validated on the Mock Urban Setting Test experiment.

21st International Conference on
Harmonisation within Atmospheric Dispersion Modelling for Regulatory Purposes
27-30 September 2022, Aveiro, Portugal

CO2 PLUME DETECTION AND INVERSION USING CONVOLUTIONAL NEURAL NETWORKS: APPLICATION TO SYNTHETIC IMAGES OF XCO2 FIELDS OVER URBAN AREAS

Joffrey Dumont Le Brazidec, Pierre Vanderbecken, Alban Farchi, Yelva Roustan, Marc Bocquet, Jinghui Lian, Grégoire Broquet, Thomas Lauvaux, Alexandre Danjou

SHORT ABSTRACT

Abstract title: CO2 plume detection using deep neural networks: application to synthetic images of the XCO2 field over the Paris area

Name and Affiliation of the First Author:

Joffrey Dumont Le Brazidec.
CEREA, École des Ponts and EDF R&D, Île-de-France, France

Email of first author:

joffrey.dumont@enpc.fr

Names and Affiliations of the Co-authors:

Pierre Vanderbecken.
CEREA, École des Ponts and EDF R&D, Île-de-France, France

Alban Farchi.
CEREA, École des Ponts and EDF R&D, Île-de-France, France

Yelva Roustan.
CEREA, École des Ponts and EDF R&D, Île-de-France, France

Marc Bocquet.
CEREA, École des Ponts and EDF R&D, Île-de-France, France

Jinghui Lian.
LSCE, Laboratoire des sciences du climat et de l'environnement, Île-de-France, France
& Origins.S.A.S, Suez Group, Île-de-France, France

Grégoire Broquet.
Laboratoire des Sciences du Climat et de l'Environnement, LSCE/IPSL, CEA-CNRS-UVSQ, Université Paris-Saclay, 91198 Gif-sur-Yvette, France

Thomas Lauvaux.
LSCE, Laboratoire des sciences du climat et de l'environnement, Île-de-France, France

Alexandre Danjou.
Laboratoire des Sciences du Climat et de l'Environnement, LSCE/IPSL, CEA-CNRS-UVSQ, Université Paris-Saclay, 91198 Gif-sur-Yvette, France

ABSTRACT TEXT (MAXIMUM 350 WORDS.)

Carbon dioxide emissions, accounting for more than 70% of global anthropogenic greenhouse gas releases, are the main driver of climate change. Current emissions estimates, which are needed to guide reduction policies, rely on statistical data of energy consumption including self-reporting from emitters and are subject to important uncertainties.
In order to assess these emissions in an independent, timely and accurate manner, the Copernicus CoCO2 project aims to build a prototype system for a CO2 emission monitoring service exploiting atmospheric CO2 measurements. As part of this project, our goal is to build a modelling inverse system to improve the quantification of CO2 sources of large magnitude at urban scale based on the spaceborne imagery of the CO2 atmospheric plumes from these sources.
The reconstruction of such sources depends on the detection of the associated plumes in the satellite images of the CO2 average column concentrations (XCO2), which represents a significant challenge. Indeed, the signal of CO2 plumes induced by cities emissions is intrinsically difficult to detect since it rarely exceeds values of a few ppm and is perturbed by variable regional CO2 background signals.

To tackle the problem of CO2 plume detection, we investigate the potential of deep learning methods and especially neural networks. Our models are trained on hourly simulated XCO2 fields in the region of Paris, tracing the plume from Paris and other biogenic and anthropogenic fluxes and are applied on two problems.
In a first step, convolutional neural networks are trained to predict the presence of the CO2 plume from Paris in an image. The impact of using additional input information such as meteorological conditions or temporal variations is studied and the performance of the network is evaluated. We show that full-day plumes (between 11 am and 6 pm) are detected with an accuracy superior to 80%, some of them being missed due to day meteorological conditions. On the other hand, plumes at other times are always detected by the neural network.
In a second step, we examine the possibilities of using neural networks specialised in object detection or semantic segmentation to the more ambitious problem of defining the plume contour.

21st International Conference on
Harmonisation within Atmospheric Dispersion Modelling for Regulatory Purposes
27-30 September 2022, Aveiro, Portugal

BAYESIAN TRANSDIMENSIONAL INVERSE RECONSTRUCTION OF THE 137CS FUKUSHIMA-DAIICHI RELEASE

Joffrey Dumont Le Brazidec, Marc Bocquet, Olivier Saunier, Yelva Roustan

SHORT ABSTRACT

Abstract title: Bayesian transdimensional inverse reconstruction of the 137Cs Fukushima-Daiichi release

Name and Affiliation of the First Author:

Joffrey Dumont Le Brazidec.
IRSN, PSE-SANTE, SESUC, BMCA, Fontenay-aux-Roses, France
& CEREA, École des Ponts and EDF R&D, Île-de-France, France

Email of first author:

joffrey.dumont@enpc.fr

Names and Affiliations of the Co-authors:

Marc Bocquet.
CEREA, École des Ponts and EDF R&D, Île-de-France, France

Olivier Saunier.
IRSN, PSE-SANTE, SESUC, BMCA, Fontenay-aux-Roses, France

Yelva Roustan.
CEREA, École des Ponts and EDF R&D, Île-de-France, France

ABSTRACT TEXT (MAXIMUM 350 WORDS.)

The Fukushima-Daiichi accident involved massive and complex releases of radionuclides in the atmosphere. The releases assessment is a key issue and can be achieved by advanced inverse modelling techniques combined with a relevant dataset of measurements. A Bayesian inversion is particularly suitable to deal with this case. Indeed, it allows for rigorous statistical modelling and enables easy incorporation of information of different natures into the reconstruction of the source and the associated uncertainties.

We propose several methods to better quantify the Fukushima-Daiichi ^{137}Cs source term and the associated uncertainties. Firstly, we implement the Reversible-Jump MCMC algorithm, a sampling technique able to reconstruct the distributions of the ^{137}Cs source magnitude together with its temporal discretisation. Secondly, we develop methods to (i) mix both air concentration and deposition

measurements, and to (ii) take into account the spatial and temporal information from the air concentration measurements in the assessment of the error covariance matrix.

Using these methods, we obtain distributions of non uniform in time ^{137}Cs release rates between March, 11 and 24 and assess the performance of our techniques by carrying out a model-to-data comparison. The total released reconstructed activity is estimated to be between 10 and 25 Pbq, and the reconstruction of the source term temporal discretisation yields a highly variable profile between March 14 and 15, and between March 19 and March 21.

21st International Conference on
Harmonisation within Atmospheric Dispersion Modelling for Regulatory Purposes
27-30 September 2022, Aveiro, Portugal

SOURCE CHARACTERISATION OF LARGE-SCALE URBAN FIRES BY INVERSE MODELLING

Emilie Launay, Virginie Hergault, Marc Bocquet, Joffrey Dumont Le Brazidec, Yelva Roustan

SHORT ABSTRACT

Abstract title: Source characterisation of large-scale urban fires by inverse modelling

Name and Affiliation of the First Author:

Émilie LAUNAY, Laboratoire Central de la Préfecture de Police, Paris, France & CEREA, École des Ponts, EDF R&D, Île-de-France, France.

Email of first author: emilie.launay@interieur.gouv.fr

Names and Affiliations of the Co-authors:

Virginie HERGAULT, Laboratoire Central de la Préfecture de Police, Paris,

France. Marc BOCQUET, CEREA, École des Ponts, EDF R&D, Île-de-France,

France.

Joffrey DUMONT LE BRAZIDEC, CEREA, École des Ponts, EDF R&D, Île-de-France, France.

Yelva ROUSTAN, CEREA, École des Ponts, EDF R&D, Île-de-France, France.

Abstract text

Large-scale fires such as warehouse fires that have occurred in recent years or dramatic accidents like the Paris Notre-Dame Cathedral fire in 2019 have highlighted the need to develop means of assessing the toxicity risks for the population and the environment of plumes smoke. One of the challenges is to quickly provide the authorities with information on the areas impacted by the plume and the pollutant concentration levels

to which the populations are likely to be or have been exposed. The Laboratoire Central de la Préfecture de Police (LCPP) aims to deploy a number of devices for measuring pollutants and tracers of smoke combustion during a fire. Subsequently, the application of an atmospheric dispersion model within the framework of a data assimilation approach should provide a source characterisation and a finer estimate of the concentration levels at points of interest.

Several inverse methods using a data assimilation approach have been implemented. Semi-Bayesian methods and a Markov Chain Monte Carlo (MCMC) Bayesian method are considered for the characterisation of the source, noticeably the emission height linked to plume rise. We use the Lagrangian Parallel Micro Swift Spray (PMSS) model developed by AriaTechnologies, fed with meteorological fields provided by Météo France, to represent the atmospheric dispersion.
These inverse methods are applied within a synthetic framework corresponding to the Notre-Dame Cathedral fire, with a source term based on the study of the Institut National de l'Environnement Industriel et des Risques (INERIS). Due to the lack of measurements during the fire, arbitrary observations are generated approximating the real conditions to which the investigation teams would have been subjected. The sensitivity of the reconstructed source term to the use of the forecasted meteorological data versus the analysed ones is investigated. Finally, a large warehouse fire that occurred in Aubervilliers near Paris in 2021 is studied using real observations. They were collected by the LCPP and AirParif and are used to reconstruct the source defined by an emission height and a temporal intensity release, with quantification of uncertainties and sensitivity analysis of model error.

21st International Conference on
Harmonisation within Atmospheric Dispersion Modelling for Regulatory Purposes
27-30 September 2022, Aveiro, Portugal

BAYESIAN INFERENCE OF EMISSION SOURCES BASED ON A DISPERSION MODEL AND SENSOR NETWORKS.

J. Sousa, H. Hooyberghs, W. Lefebvre, S. Vranckx and S. Janssen*

VITO, Boeretang 200, 2400 Mol, Belgium

* jorge.sousa@vito.be

In this talk we will discuss the use of a Bayesian inference methodology combined with a the ATMO-Street atmospheric dispersion model. The methodology uses data from low cost and densely distributed sensors to correct on an hourly basis the concentration maps and the emission values. The data assimilation procedure starts by considering an emission inventory with a given uncertainty. Subsequently the uncertainty in the input is translated via an ensemble of model runs into a concentration field with the respective uncertainties. The methodology uses as a backbone the ensemble Kalman filter with an augmented state for inverse problems. The weights given to the observations or the model output are dependent on the corresponding observational and numerical uncertainties. By applying this methodology,
it was demonstrated that an updated air quality map can be produced considering local sensor data, in the same time providing updated information about the underlying temporal and spatial emission pattern. Figure 1 gives an example of the application of the Bayesian data assimilation technique for $PM_{2.5}$ concentration in a Chinese town based on 12 low cost PM sensors. The ATMO-Street model cannot reproduce the high PM concentration episode, because of a local spatial and temporal high emission event. However, by assimilating these observations, the high PM concentration episodes can be captured providing a better match in all the sensors. Finally, after the updated emission step, a localized zone with increased emissions can be observed which better explains the observations.

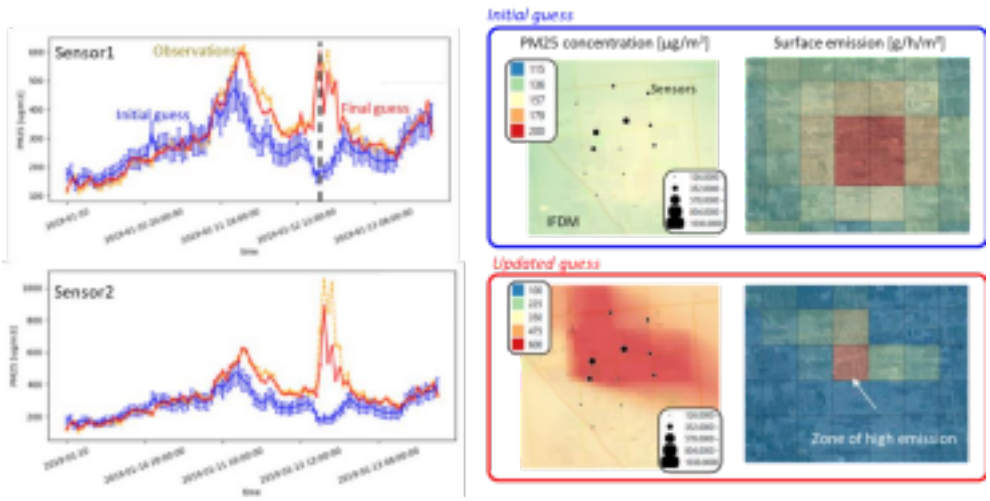

Figure 1 Evaluation of the data assimilation methodology under the situation where a PM25 episode is cause by localized emissions. Left - the time series of 2 sensors showing the difficulty to model the peak. After assimilation the peak is captured. Right - Concentration and emissions map before (top) and after (bottom) assimilation.

21st International Conference on
Harmonisation within Atmospheric Dispersion Modelling for Regulatory Purposes
27-30 September 2022, Aveiro, Portugal

QUANTIFICATION OF TEMPERATURE DEPENDENCE OF NOX EMISSIONS FROM ROAD TRAFFIC IN NORWAY USING AIR QUALITY MODELLING AND MONITORING DATA

Eivind Wærsted

SHORT ABSTRACT

Quantification of temperature dependence of NOx emissions from road traffic in Norway using air quality modelling and monitoring data

Eivind G. Wærsted; Norwegian Meteorological Institute, Henrik Mohns plass 1, 0313 Oslo, Norway

eivindgw@met.no

Ingrid Sundvor; Norwegian Institute of Transport Economics, Gaustadalléen 21, 0349 Oslo, Norway

Bruce R. Denby; Norwegian Meteorological Institute, Henrik Mohns plass 1, 0313 Oslo, Norway

Qing Mu; Norwegian Meteorological Institute, Henrik Mohns plass 1, 0313 Oslo, Norway

ABSTRACT

Emissions of nitrogen oxides (NOx) from road traffic are dependent on a range of factors including vehicle type, speed, driving patterns and engine temperature. Recently a number of studies have indicated that ambient air temperature plays an important role in vehicle NOx emissions, mainly due to various technical challenges of diesel vehicles that occur at low ambient temperatures. This study aims to derive a correction formula to account for this temperature dependence when calculating emissions from road traffic in Norway. Measured NOx concentrations in the period 2016–2019 at 46 sites dominated by road traffic sources are compared to the NOx concentrations calculated with the chemistry-transport modelling system EMEP/uEMEP at the same sites. The model has good road traffic volume input data, but no temperature dependence in the emission factors. A clear temperature dependence in the observed-to-modelled ratio of NOx concentration is found. The ratio increases from 1.09 at high temperatures to 2.9 at low temperatures. The increase occurs gradually in the temperature range from -13 °C to +14 °C. Assuming this temperature dependence in the bias is due to the road traffic emissions, a correction formula for these emissions is derived. The correction factor is 1 at high temperatures and 3.28 at low temperatures, with a linear increase in the range from +12.4 °C to -12.9 °C. Thus, our results suggest that road traffic emissions should be 3.3 times higher at temperatures below -13 °C than at high temperatures, and 2.7 times higher at -7 °C. The temperature range and magnitude of this temperature dependence are consistent with the existing literature on emission measurement experiments performed on various models of diesel vehicles. The derived temperature dependence can be used to correct road traffic emissions. However, the parameter values in the correction are dependent on the vehicle fleet composition and are applicable only for the current Norwegian vehicle fleet.

21st International Conference on
Harmonisation within Atmospheric Dispersion Modelling for Regulatory Purposes
27-30 September 2022, Aveiro, Portugal

COMBINING SENTINEL OBSERVATIONS WITH PLUME BACKTRACKINGS FROM A DISPERSION MODEL TO IMPROVE WILDFIRE DETECTION

Marie Mulder

Titel: Combining sentinel observations with plume backtrackings from a dispersion model to improve wildfire detection

During the last decades, there has been an increase in wildfires around the globe. Climate change with higher temperatures and lower humidity, due to changing precipitation patterns, is the main factor raising the fire risk. Using earth observations is an important method to detect wildfires. Especially in areas far from populated regions, satellites support the identification of wildfires and allow issuing warnings in case of a developing event. False detections of fires by satellites are a common problem. The main goal of this work is to improve the detection of wildfires by using state-of-the-art earth observation data, specifically data from Sentinel missions, together with modelling approaches in a combined new methodology. Most of the current methods to detect wildfires by earth observations mainly use a single satellite-based data source to retrieve surface information. The benefit to existing methods is that surface- and atmospheric observations from Sentinels-3 and -5P will be combined, with the aim to reduce the number of false alarms. Sentinel-3 and Sentinel-5P can be used as independent data sources, one (S-3) able to detect thermal anomalies in the surface, and the other (S-5P) capable of detecting direct fire emissions such as CO and HCHO in the atmosphere, to improve the capability to distinguish real fires from false alarms. The combined use with the Lagrangian particle dispersion model FLEXPART will allow the backtracking of fire emissions plus the aerosol mid height from Sentinel-5P to better identify wildfires sources. For this purpose, so called ‘source-receptor sensitivities’, SRS are calculated, that provide information on the times and areas potentially contributing to the observed plume. Finally, identified wildfires can be validated using Sentinel-2 images. The innovation of our approach is to combine sentinel observations with atmospheric smoke plume simulations, by applying a dispersion model in backward mode to backtrack the possible source region of the smoke plume.

21st International Conference on
Harmonisation within Atmospheric Dispersion Modelling for Regulatory Purposes
27-30 September 2022, Aveiro, Portugal

INVERSE TRANSPORT AND DISPERSION MODELLING FOR ANTHROPOGENIC GREENHOUSE GAS EMISSIONS ASSESSMENT: CO2 FROM THE OSLO URBAN AREA AND FUGITIVE CH4 FROM OIL FACILITIES IN THE NORWEGIAN SEA

Ignacio Pisso, Susana Lopez-Aparicio, Dam Vo Tanh, Franck Delauge, Terje Krognes, Magadalena Pühl, Alina Fiehn, Amy Foulds, Grant Allen

SHORT ABSTRACT

Abstract title: Inverse transport and dispersion modelling for anthropogenic greenhouse gas emissions assessment: CO2 from the Oslo urban area and fugitive CH4 from oil facilities in the Norwegian sea

Name and Affiliation of the First Author: Ignacio Pisso, NILU

Email of first author: ip@nilu.no

Names and Affiliations of the Co-authors: Susana Lopez-Aparicio[1], Dam Vo Tanh[1], Franck Delauge[1], Terje Krognes[1], Magadalena Pühl[2], Alina Fiehn[2], Amy Foulds[3], Grant Allen[3]
[1]Norwegian Institute for Air Research (NILU), Kjeller, Norway

[2] Deutsches Zentrum für Luft- und Raumfahrt (DLR), Institut für Physik der Atmosphäre, Oberpfaffenhofen, Germany

[3]School of Earth, Atmospheric and Environmental Sciences, University of Manchester, Manchester, UK

ABSTRACT TEXT (MAXIMUM 350 WORDS.)

Cities account for more than 70% of global fossil-fuel CO2 emissions, and urban areas are set to increase. The Oil&Gas sector has been shown to be a significant source of CH4 with fugitive emissions from infrastructure installations such as offshore oil platforms. Norway has set the target of cutting greenhouse gas (GHG) emissions by at least 40% compared to 1990 levels by 2030. This goal will require the implementation of policy measures aiming at strong reductions of GHGs emissions, requiring control and verification for success. The URGE (URban Greenhouse gases Emissions) and ORME (Oil Rigs Methane Emissions) projects aimed at assessing the GHGs emission flux methodologies including comprehensive uncertainty estimates based on inverse transport modelling techniques and optimized use of measurements. URGE aimed at establishing a consistent CO2 urban emission inventory and ORME to contribute to the assessment of CH4 emissions from the Oil&Gas sector. For the URGE project we present a summary of the final results: two urban CO2 emission inventories to support reduction of urban emissions; measurements with small sensors based on off-the-shelf open components and open-source software and the assessment of associated uncertainties; alternative distributed databases models for data storage and distribution; optimization of emission estimates and their uncertainties based on inverse modelling with source-receptor relationships and observing system simulation experiments (including sensitivity studies of the relationship of spatio-temporal scales of input and output of the dispersion model; and optimal measurement locations based on Lagrangian transport (FLEXPART) modelling using complementary atmospheric measurements of CO, APO and 14CO2. For ORME we report on the Lagrangian modelling activity of used to support the flux assessment. Source identification with backward modelling helped to

interpret in situ observations carried by DLR and FAAM aircraft. In addition, forward transport modelling of the emissions in high resolution constrained the plume height for mass balance assessment. We discuss the dependency of the uncertainty of the flux estimates on the choice of the meteorology and the model parameters. We address the data exchange formats, the algorithms and data structures that could be used for inter-comparisons exercises with similar activities.

TOPIC 8:

MODELLING AIR DISPERSION AND EXPOSURE TO ACCIDENTAL RELEASES

21st International Conference on
Harmonisation within Atmospheric Dispersion Modelling for Regulatory Purposes
27-30 September 2022, Aveiro, Portugal

SOFTWARETOOLS FOR SIMULATING DISPERSION OF HAZARDOUS MATERIALS IN INDUSTRIAL ENVIRONMENTS

Bernd Leitl, S. Michel, S Schalau, H. Plischka, J. Turnow, B. Schalau, F. Harms

HARMO2022 short abstract

S. Michel, S Schalau, H. Plischka, J. Turnow, B. Schalau, F. Harms, B. Leitl

Softwaretools for simulating dispersion of hazardous materials in industrial environments

Licensing and operation of industrial facilities carrying hazardous materials requires the assessment of consequences resulting from potential releases of such substances. Typically, estimating safe distances and evaluation of threats is based on atmospheric dispersion modeling near the release. The simulation tools applied in this context are often based on Gaussian dispersion models or empirical models which might not be called 'state-of-the-art' anymore for this kind of application. Local flow and dispersion patterns are usually influenced by complex obstacles such as buildings or facilities and/or gravity driven transport phenomena. More advanced simulation tools such as Lagrangian dispersion models are promoted and expected to provide more reliable predictions even for transient dispersion phenomena such as accidental releases. However, a reliable Lagrangian transport modeling requires the corresponding flow field to be known with sufficient accuracy and detail even in complex industrial structures. Computational Fluid Dynamics is anticipated to provide means for qualified Eulerian flow and dispersion modeling capabilities and open-source software packages like openFOAM are used increasingly for such tasks, even if the models often not have undergone an application-specific validation. Thus, the German Federal Ministry for Economic Affairs and Climate Action provided funding for a joint research project evaluating the potential of the openFOAM software toolbox for applied hazmat dispersion modeling. Within the scope of the project, RANS- and LES-based wind field simulators are developed. Solutions for common problems in the context of near-ground wind flow modeling are developed. For instance, for the RANS-type wind field generator an improved formulation of quasi-stationary inflow boundary conditions was developed to be consistent with the preferred turbulence model. For the LES-type wind field model, for example an artificial inflow generator was implemented to substantially reduce the necessary computational domain size and increasing the efficiency of simulations in the context practical applications. The contribution will summarize main results of the project and document results of application-specific model evaluations based on new, dedicated reference data generated in the project.

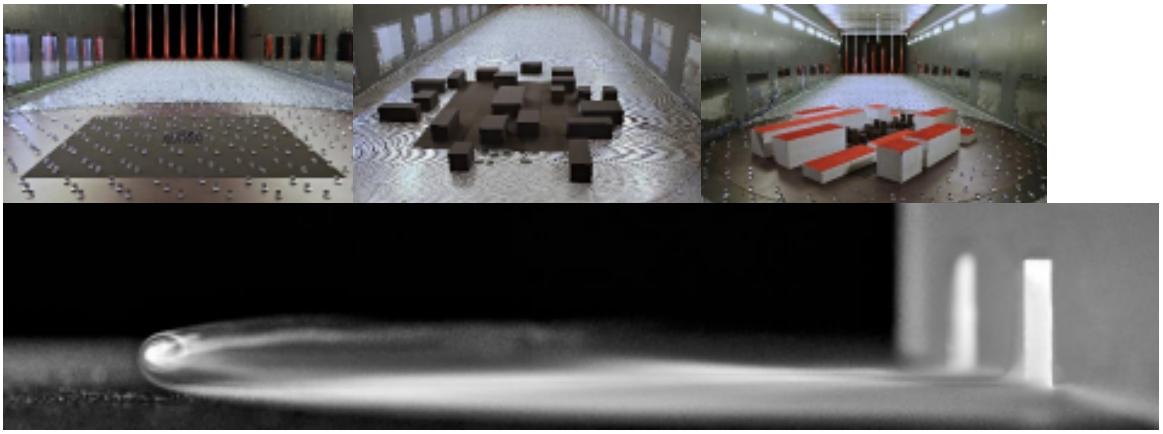

corresponding author: Bernd Leitl, University of Hamburg, Meteorological Institute, bernd.leitl@uni-hamburg.de

21st International Conference on
Harmonisation within Atmospheric Dispersion Modelling for Regulatory Purposes
27-30 September 2022, Aveiro, Portugal

MULTI-LEVEL PROBABILISTIC MODEL FOR WIND TRAJECTORIES AND POLLUTANT DISPERSION

Ziv Klausner, Jonathan Milo, Tel Aviv University; Eyal Fattal

SHORT ABSTRACT

Abstract title: Multi-level probabilistic model for wind trajectories and pollutant dispersion

Name and Affiliation of the First Author: Ziv Klausner, Israel Institute for Biological Research *Email of first author*: ziv.klausner@mail.huji.ac.il

Names and Affiliations of the Co-authors: Jonathan Milo, Tel Aviv University; Eyal Fattal, Israel Institute for Biological Research

Abstract text *(maximum 350 words.)*

Accidental release of pollutant gaseous materials into the atmosphere is associated with inherent uncertainty. A major aspect of uncertainty involves the average wind spatial field. In many applications of emergency response to accidental release, the information on this field is derived from a network of weather stations. Such networks are usually sparse, which required an interpolation process. Such process is incorporated with uncertainty. Moreover, the wind field itself exhibits variability, both spatial and temporal. As the wind field dictates the trajectory in which a pollutant plume is transported, this trajectory is influenced by the above-mentioned aspects of uncertainty. Given a wind trajectory, the area affected can be estimated by a Gaussian plume model. However, the major concern of decision makers operating in emergency response scenarios is to receive an estimate to the degree of risk the population faces, while the affected area is of lesser interest.

This study uses a multi-level probabilistic framework in order to concisely describe the uncertainty associated with wind trajectories. This framework also enables a quantification of the risk of exposure in probabilistic terms. The resultant model provides a probability map of the risk of exposure to a given critical level. It was applied to the metropolitan area of Tel-Aviv. It was found that the spatial distribution of the wind data can be very well represented by a small sample of four weather stations. Based on these sample stations, empirical Mahalanobis distance functions were calculated for each season of the year. These functions were found to fit well the logistic distribution. Based on these functions, wind trajectory realizations were generated, and for each realization a concentration field were calculated, using a Gaussian segmented plume model. As it was found that for each location, the

probability to be exposed to a given critical level follows the power-law distribution, only a small number of realizations were required. These were used to estimate the distributions' parameters. Thus, overall probability maps of exposure can be calculated based on a small number of realizations.

21st International Conference on
Harmonisation within Atmospheric Dispersion Modelling for Regulatory Purposes
27-30 September 2022, Aveiro, Portugal

WIND TUNNEL AND MATHEMATICAL MODELLING OF THE NEAR-SOURCE REGION OF JACK RABBIT II MOCK URBAN ENVIRONMENT CHLORINE RELEASES

Thomas O. Spicer[1] *and Chad T. Smith*[1]

[1]Martin Department of Chemical Engineering, University of Arkansas, Fayetteville, AR, USA

Abstract:
Led by the U.S. Department of Homeland Security Science & Technology (DHS S&T) Chemical Security Analysis Center (CSAC), the Jack Rabbit II (JR II) chlorine release trials were conducted at the U.S. Army Dugway Proving Ground in 2015 and 2016. A 50:1 scale model of the 2015 JR II Mock Urban Environment (MUE) was built in the Chemical Hazards Research Center (CHRC) ultra-low speed wind tunnel. Video records from JR II Trial 4 were used to develop a methodology to physically model the near field behavior of the chlorine cloud in the MUE by comparison with videos taken in the wind tunnel. In the wind tunnel model, the simulated source gas cloud (a mixture of carbon dioxide, sulfur hexafluoride, and air) was made visible by mixing with commercial theater fog. In the near-source region, a wall jet was formed from the vertically downward chlorine release. The wall jet was formed in the wind tunnel by placing a plate over an area gas source. The density and volumetric rate of the diluted wall jet were determined experimentally so that the physical model behavior was consistent with Trial 4 observations. The approach was validated using JR II Trial 5 conditions, and the agreement between wind tunnel and field-scale observations was very good. In separate tunnel tests, (repeated) concentration measurements were made using an NDIR gas sensor. Concentration measurements in the wind tunnel showed similar times to cloud arrival and duration of exposure as observed in the JR II near-field JAZ measurements. The wind tunnel concentrations were larger than JAZ measurements but generally within a factor of 2. Having established the near-field behavior of the field-scale releases with the developed wind tunnel methodology, a simple mathematical model was developed that predicts the development of the contaminant cloud from storage (stagnation) conditions as a saturated liquid to depressurized conditions. One benefit of such a mathematical model is that the lessons learned from JR II and the wind tunnel study can be extended to other toxic inhalation hazards (TIH) such as ammonia as planned for the Jack Rabbit III test program.

Key words: *Chlorine; Wind tunnel; Jack Rabbit II*

INTRODUCTION

The Jack Rabbit II (JR II) test program was undertaken to address critical knowledge gaps for assessment of the consequences of a large-scale release of chlorine, an important toxic inhalation hazard (TIH). Conducted at Dugway Proving Ground (DPG), test releases at roughly 10:1 scale with current transportation practices for chlorine, the JR II program was planned to address questions involving the interaction of a chlorine cloud with a mock urban environment (MUE) in the 2015 test season and in an open environment in the 2016 test season. An overview of the test program is available (Fox et al., 2022).

In this work, experiments were conducted in a wind-tunnel scale model of the field releases in the MUE. A sonic anemometry study conducted between the 2015 and 2016 JR II test seasons (JR II-S) was used to confirm that the wind tunnel model was representative of the wind field, particularly in the vicinity of the MUE. Video records from JR II Trial 4 were used to develop the wind tunnel methodology to describe the near field behavior of the chlorine cloud in the MUE. The wind tunnel methodology was verified by comparison with Trial 5. A complete summary of this work can be found in Spicer and Smith (2021).

Wind tunnel model

The Chemical Hazards Research Center (CHRC) wind tunnel is an ultra-low-speed boundary layer wind tunnel capable of producing airflows that simulate the (neutral) constant stress layer of the atmospheric boundary layer. It was designed and constructed specifically for the study of atmospheric dispersion of denser-than-air gases at low wind speeds.

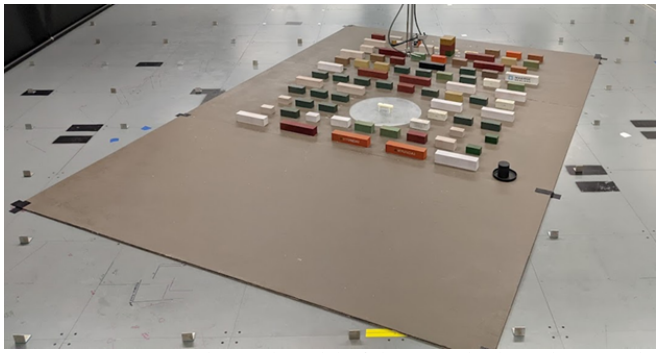

Figure 135. *Wind tunnel model of the MUE looking downwind*

As shown modeled in **Figure 135**, the JR II tests were conducted on a gravel pad built on the surrounding playa (approximately 61 cm above the playa) and aligned with the historical wind direction. Because of the change in elevation, the MUE was constructed 200 ft (61 m) downwind of the leading edge of the gravel pad. The MUE consisted of CONEX containers of various sizes numbered by row (upwind to downwind) and position (left to right), so the left most CONEX on the third row was 3.1. Inside the MUE, the release area consisted of a chlorine tank (capacity of 7.7 m^3 liquid) placed in the center of a circular concrete pad (25 m diameter). At the downwind edge of the MUE, a stack of six CONEX containers (in three levels) was built to mimic a tall urban structure (CONEX 11.4) which was the focus of the sonic anemometry study. Froude number scaling was used to set the tunnel wind speed based on observed wind speeds at DPG.

Wind tunnel model of sonic anemometry field tests

Measurements during the JR II -S were completed in March 2016, and the study is summarized by Pirhalla, et al. (2020). The MUE used in 2015 was modified during JR II-S by removing three CONEX containers from Row 12 so that additional anemometers could be placed downwind of CONEX 11.4. Wind tunnel velocity and turbulence measurements were made with a 3D LDV system (Lopes, 2023).

*Using measurements from MET Tower 3 upwind of the gravel pad, six time periods were found to have constant wind field properties (denoted A-F in Spicer and Smith, 2021). Since the overall objective was to verify the ability to model conditions in the JR II field tests, two time frames (**Table 50**) were studied because those agreed best with JR II test conditions (historical average wind direction is 165°).*

Table 50. *Sonic Anemometry Study Conditions*

Time Frame	Date and Time	Height (m)	Wind Speed (m/s)	Average Wind Direction
C	3/24/2016 11:00 am	2 4	3.35 3.79	164°
E	3/27/2016 7:00 am	2 4	4.38 4.96	166°

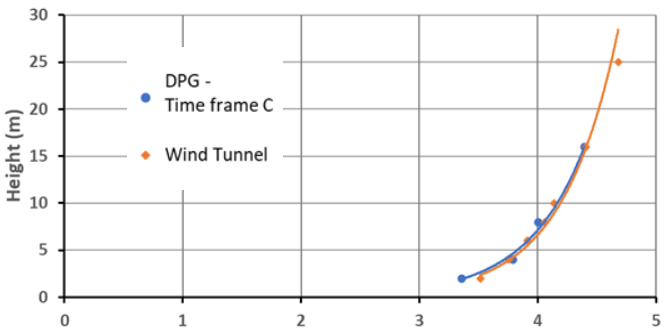

Figure 136. *Time Frame C MET Tower 3 velocity profile comparison*

Velocity measurements made at the MET Tower 3 location for Time Frame C are shown in **Figure 136** as an example. Using Froude number scaling, the wind tunnel velocity profiles agreed closely with velocity profiles from JR II-S.

Figure 137 *illustrates the comparison between measured u and w velocity vectors along the MUE centerline. Wind tunnel measurements were in good agreement with field-scale measurements. The effect of a dividing stream line can be seen. This effect can result in higher than expected gas concentrations on the roof of a tall building in an urban environment (Hanna and Chang, 2015).*

Measurements of the friction velocity ($U_* = \sqrt[4]{(u'v')^2 + (u'w')^2}$) are shown in **Table 51**. The agreement between field and tunnel scaled friction velocity is good. Tunnel measurements were also made at scaled heights of 10 and 6 m, and using wind tunnel measurements, the average (scaled) frcition velocity was

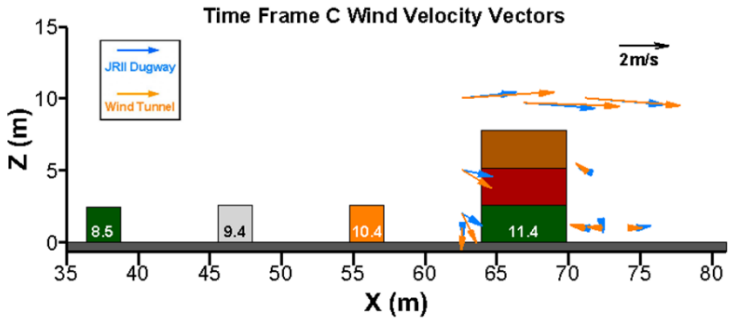

Figure 137. *Comparison of centerline u and v velocity vectors for the wind tunnel and field study for Time Frams C.*

0.177 and 0.227 m/s for Time Frames C and E, respectively. The surface roughness (z_o) was estimated to be 0.7 mm at field scale which is consistent with Hanna's recommendation of 0.5 mm (Hanna, 2020). At wind tunnel scale, the roughness Reynolds number ($Re_* = U_* z_0/\nu$ where ν is the kinematic viscosity) would be approximately 0.2. This value of Re_* is less than the criteria of 1 recommended by Snyder and Castro (2002), but exceeds the value of 0.135 for a smooth wall. (It is worth noting the the field scale flow has a $Re_* \approx 6$.) Despite this concern, the wind tunnel measurements are consistent with field measurements, and here, the turbulence of the approach flow was not as important as the momentum of the release.

Table 51. *Comparison between Field and Scaled Tunnel Friction Velocity for Time Frames C and E.*

	Time Frame C		Time Frame E	
Field Scale Height (m)	JR II-S U_* (m/s)	Scaled Tunnel U_* (m/s)	JR II-S U_* (m/s)	Scaled Tunnel U_* (m/s)
16	0.165	0.185	0.204	0.203
8	0.183	0.196	0.239	0.217
4	0.177	0.163	0.244	0.211
2	0.182	0.133	0.228	0.169

Physical model of the jr ii mue chlorine releases

The MUE chlorine releases were vertically downward from a 15.2 cm circular hole (1 m above grade) made instantaneously in the dissemination vessel bottom. The flashing-two phase flow hit the concrete pad and formed a wall jet that flowed radially outward. The mass remaining in the vessel was measured with load cells. The mass release rate was constant during most of the release, but the amount of chlorine that moved downwind was reduced by aerosol rainout on the concrete pad (Spicer and Tickle, 2021). For comparison purposes, the rate chlorine moved downwind was simplified to two alternatives: (i) a constant rate of aerosol and (ii) a lower constant rate of aerosol with susbequent release of gas from the liquid rainout that remained. In the physical model developed here, the single constant rate approximation was used.

Due to the violent nature of the flow and the corrosive behavior of chlorine, only thermocouples were deployed on (and in) the concrete pad. These measurements confirmed that a thin liquid film was deposited on the concrete surface which subsequently evaporated. The concentration, density, and velocity of the chlorine/air aerosol wall jet was unknown. Chlorine liquid rainout was found to be limited to the concrete pad, so the physcial model was built to model the outward flowing aerosol wall jet at the concrete pad edge.

In the physical model, three parameters at the concrete pad edge were unknown: the depth, velocity, and density of the wall jet. The wall jet was made by suspending a circular disk of the same (scaled) diameter

as the concrete pad over the wind tunnel floor area source (see **Figure 1**). The gas supply composition (density) and flow rate were controlled using mass flow controllers. The gap between the circular disk and the model surface controlled the veocity. The gas supply was made visible using theater fog.

Visual comparison with field scale video record

Two upwind camera locations from the field tests were selected to determine the upwind and lateral motion of the chlorine cloud. The gas cloud time of arrival at certain locations was measured. In the model, Trial 4 conditions were used to determine the wind tunnel parameters to best model the release, and Trial 5 was used for validation. For Trial 5, the average time to reach locations A-L in the wind tunnel are compared with field observations in **Figure 138.** Trial 5 cloud time of arrival for locations A-L. Overall, arrival times agree well. Comparison of video records provided a global confirmation that the model is an effective representation of the field scale tests.

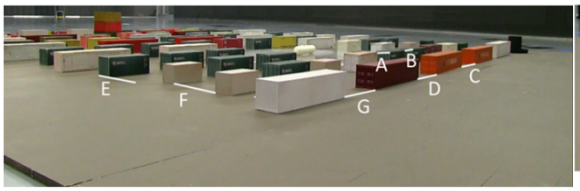

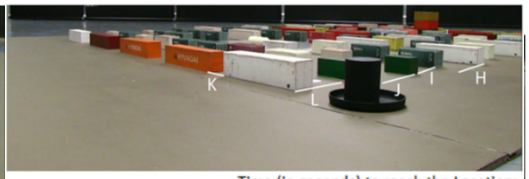

Time (in seconds) to reach the Location:

			Locations:	A	B	C	D	E	F	G
			Official JRII Trial 5 time:	2.9	3	6.8	6.2	11.2	18.1	18
Run Examples	Run 6	680 LPM 49% Cl_2		1.5	1.5	5.75	6	11.25	14.25	17
	Run 9			1.5	1.75	5.5	7	11.5	13.75	15.25
	Run 12			1.5	1.5	5.75	6.5	11.5	15.25	16.75
			15 Repeated Runs							
			Average Times	1.43	1.50	5.45	6.45	11.72	14.48	16.30
			Standard Deviation	0.148	0.164	0.302	0.343	0.452	0.658	0.819

Time (in seconds) to reach the Location:

			Locations:	H	I	J	K	L
			Official JRII Trial 5 time:	8.3	8.2	11.6	13.7	16
Run Examples	Run 5	680 LPM 49% Cl_2		7.75	8.25	10.25	13.5	18
	Run 9			7.75	7.75	10.75	12.75	17.5
	Run 12			7.75	8.25	11	13.5	19
			15 Repeated Runs					
			Average Times	7.82	8.08	10.77	12.92	18.37
			Standard Deviation	0.200	0.336	0.417	0.479	0.574

Figure 138. *Trial 5 cloud time of arrival for locations A-L*

Having found wind tunnel parameters to model the field release, a comparison video was prepared using Trial 5 conditions. In each of the comparison video frames **Figure 139**, the color of the chlorine cloud has been detected digitally and enhanced (with addition of green) at pixel level to facilitate the comparison between field and tunnel clouds. In the field releases, portions of the chlorine cloud that include aerosol are opaque, and portions of the cloud that are transparent are chlorine gas only (no aerosol present).

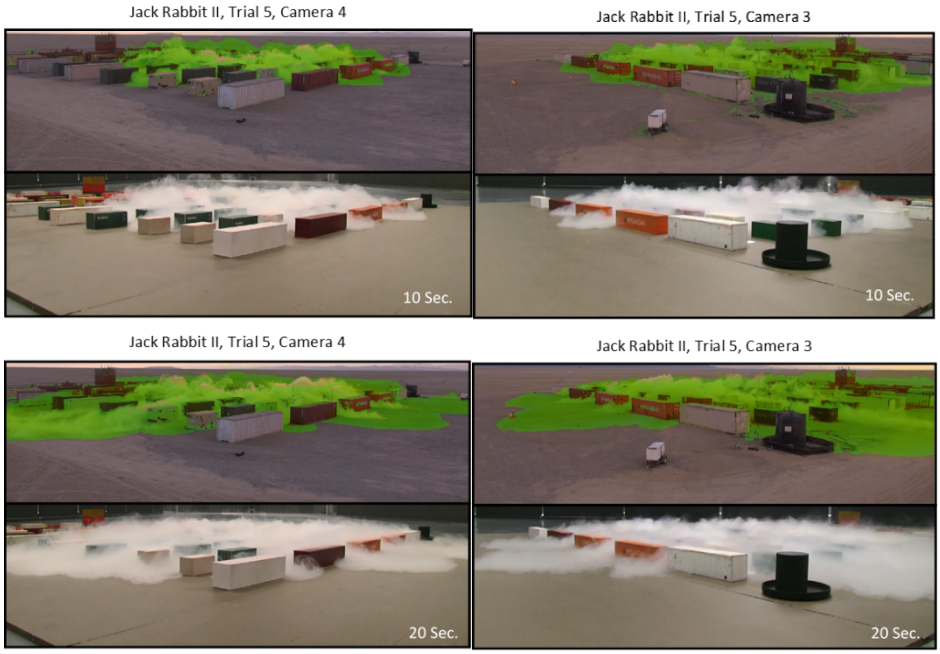

Figure 139. *Trial 5 comparison between wind tunnel and JR II video frames at selected times.*

Field and wind tunnel scale concentration measurements

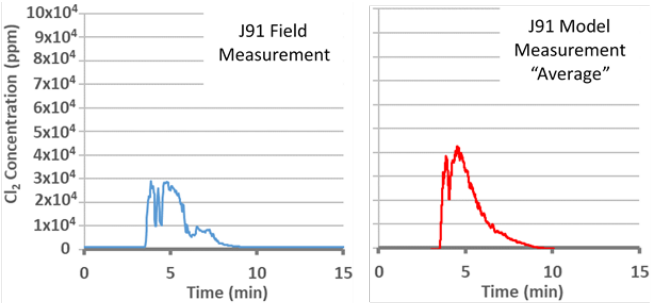

Figure 140*. J91 measurements in Trial 4, averaged model measurements, and two individual model measurements.*

During the MUE experiments, JAZ sensors were deployed to measure chlorine concentrations. In the wind tunnel, SF_6 was used as one source gas component to obtain the needed initial gas density. The Cambustion NDIR500 Fast Carbon Monoxide and Carbon Dioxide Analyzer was developed to measure CO and CO_2 in internal combustion engines using an NDIR sensor. Cambustion loaned our project an instrument for the wind tunnel tests. The source gas was composed of SF_6, CO_2, and air. The concentration of CO_2 was maximized for measurement sensitivity, and the presence of SF_6 was found to not interfere with the measurements. **Figure 140** shows examples of one comparison between the J91 field scale measured concentration and the average wind tunnel concentration from multiple releases. To complete the NDIR measurements with available mass flow controllers, the molecular weight of the source gas was reduced from 1.96 g/L to 1.79 g/L because this was the maximum density gas mixture deliverable while also containing sufficient carbon dioxide. To accommodate this change, a higher volumetric flow rate was required, but at the time of the NDIR experiments, the optimum flowrate was still undetermined, and a flowrate of 794 L/min was used (approximately 17% larger than desired). Maximum measured model concentrations were generally within a factor of 2 of field scale measurements.

CONCLUSIONS

The JR II chlorine field tests conducted in 2015 and 2016 were modeled in the CHRC wind tunnel. In the 2015 test season, a MUE was built in the field tests, and a 50:1 scale model of the MUE was built in the wind tunnel. The sonic anemometry measurements in the MUE between test seasons were used to validate the model field scale turbulence and velocity. Using the upwind MET 3 measurements, the chlorine releases were modeled as a gas wall jet at the edge of the (field scale) 25 m diameter concrete pad. Model parameters of the wall jet (depth, density, and volumetric flow rate) were experimentally determined so that cloud time of arrival between field and model scale at various locations were in good agreement using the conditions for Trial 4. Model parameters of the wall jet were validated by comparison with observations in Trial 5. Scale up of these model parameters provided an estimate of field scale flow conditions which could not be measured due to the complexity of the flow (e.g., jet density and velocity).

ACKNOWLEDGEMENTS

This project was conducted under contract HDTAT FA8075-14-D-0003 DO FA807517F1402 with the U.S. Department of Homeland Security Science & Technology (DHS S&T) Chemical Security Analysis Center (CSAC). David Cotsman at Transport Canada also provided useful guidance on the project. Cambustion, Ltd. loaned the NDIR500 Fast Carbon Monoxide and Carbon Dioxide Analyzer and provided support in making measurements with the system under novel circumstances. Several students including Mr. Samuel Gallimore and Mr. Sami Fares were critically important in the conduct, analysis of the wind tunnel work.

REFERENCES

Fox, S., S. Hanna, T. Mazzola, T. Spicer, J. Chang, and S. Gant, „Overview of the Jack Rabbit II (JR II) field experiments and summary of the methods used in the dispersion model comparisons," *Atmospheric Environment*, **269**, 118783, 2022.

Hanna, S., „Meterological data recommendations for input to dispersion models applied to Jack Rabbit II trials," *Atmospheric Environment*, **235**, 117516, 2020.

Hanna, S., and J. Chang, „Skyscraper rooftop tracer concentration observations in Manhattan and comparisons with urban dispersion models,“ *Atmospheric Environment*, **106**, 215-222, 2015.

Lopes, P.V., „Experimental and Computational Study of a Scale Model of the Jack Rabbitt II Special Sonic Anemometry Study,“ University of Arkansas Martin Department of Chemical Engineering, PhD Dissertation, 2023 (in preparation).

Pirhalla, M., D. Heist, S. Perry, S. Hanna, T. Mazzola, S. Pal Arya, and V. Aneja, “Urban wind field analysis from the Jack Rabbit II Special Sonic Anemometer Study,” *Atmospheric Environment*, **243**, paper 117871, 2020.

Snyder, W.H., and I.P. Castro, „The critical Reynolds number for rough-wall boundary layers,“ *Journal of Wind Engineering and Industrial Aerodynamics*, **90**, 41-54, 2002.

Spicer, T. and C.T. Smith, Jack Rabbit II Mock Urban Environment Trials: Wind Tunnel Model Investigation and Validation, U.S. Department of Homeland Security Science & Technology Chemical Security Analysis Report CSAC 21-005, 2021.

Spicer, T.O., and G. Tickle, „Simplified source description for atmospheric dispersion model comparison of the Jack Rabbit II chlorine field experiments,“ *Atmospheric Environment*, **244**, 117866, 2021.

21st International Conference on
Harmonisation within Atmospheric Dispersion Modelling for Regulatory Purposes
27-30 September 2022, Aveiro, Portugal

OPERATIONAL DISPERSION ENSEMBLE AT METEOSWISS

Pirmin Kaufmann[1] and Stefan Rüdisühli[2]

[1]Federal Office for Meteorology and Climatology MeteoSwiss, Zurich Airport, Switzerland
[2]Institute for Atmospheric and Climate Science, ETH Zurich, Zurich, Switzerland

Abstract: In the first hours of an accidental dispersion of airborne hazardous material, emergency response heavily relies on forecasting the expected plume with an atmospheric transport model. Such a prediction of atmospheric dispersion is, however, inherently uncertain. The two main sources of uncertainty are the source term and the meteorological prediction. In the short term, the source term is often largely unknown and the most important goal of the dispersion simulation is determining the potentially affected area. The meteorological uncertainty, which can lead to completely different affected areas depending on the meteorological evolution, should be the main concern at that stage. In numerical weather prediction, the common way to quantify the uncertainty of the meteorological evolution is by conducting ensemble simulations. At MeteoSwiss, this approach has now been extended operationally to dispersion simulations. To this end, a 21-member meteorological ensemble drives a 21-member dispersion ensemble. The probabilistic dispersion forecasts are calculated routinely for a predefined set of standardized source terms, covering the four nuclear power plant sites in Switzerland and a few in neighboring countries. These routine forecasts are updated every six hours and cover 48 hours after initialization time. On-demand calculations are also available and can be requested by the Swiss National Emergency Operations Centre (NEOC). The probabilistic results are visualized as charts that depict, in several ways, the ensemble minimum, mean and maximum, as well as quantiles and probabilities. A first preoperational set of charts have been routinely delivered to the NEOC since May 2021, and the operational production in the final setup started in December 2021.

Key words: *ensemble dispersion modeling, visualization, emergency response, nuclear emergency preparedness, atmospheric dispersion model, meteorological uncertainty, ensemble prediction*

INTRODUCTION

After an accidental release of airborne hazardous material, emergency response during the early stage relies heavily on atmospheric dispersion simulations. Until recent years, these simulations were commonly based on single deterministic runs of a meteorological model. Sørensen et al. (2020) identified two main sources of uncertainty in atmospheric dispersion simulation results: the source term and the meteorological prediction. They state that while the former may be better dealt with by using a scenario-based approach, the latter can be estimated in a straightforward fashion by using ensemble simulations. With the recent advent of ensemble models in operational numerical weather prediction (NWP), the opportunity arose to likewise run multiple instances of an atmospheric dispersion model, driven by different members of the meteorological ensemble, as a way to account for the uncertainty of the meteorological situation. Efforts toward this goal are documented, e.g., in Leadbetter et al. (2020). We present below the new operational dispersion ensemble system by the Federal Office for Meteorology and Climatology MeteoSwiss.

Operational setup at meteoswiss

From 2019 to 2021, MeteoSwiss implemented an ensemble dispersion simulation system. It is based on the COSMO NWP model (Baldauf 2011). The operational COSMO-1E and COSMO-2E setups at MeteoSwiss, with grid spacings of respectively 1.1 km and 2.2 km, are meteorological ensembles driven by boundary conditions from the global ECMWF IFS-ENS ensemble (Leutbecher et al., 2017). In Rüdisühli and Kaufmann (2020), we described a preoperational 11-member dispersion ensemble based on COSMO-1E. For rountine operations, however, we decided to switch to a 21-member ensemble based on COSMO-2E. Our main motivation was the longer forecast duration of COSMO-2E, which integrates 120 h into the future, while COSMO-1E produces only 33 hour forecasts. Experience during the preoperational phase in 2021 showed that 33 hours of simulation is often not enough for the cloud to reach the model boundary. In

addition, a dispersion ensemble based on COSMO-2E has the advantage of almost twice the number of ensemble members and of a smaller computational footprint thanks to the lower resolution (doubling the horizontal grid spacing reduces the total number of grid cells by a factor of four). The dispersion ensemble uses all 21 members of COSMO-2E to generate a dispersion ensemble with the particle dispersion model FLEXPART (Pisso et al. 2019) in a version adapted to COSMO output (Henne et al., 2016). Both COSMO-2E and the dispersion ensemble are running every six hours, providing probabilistic dispersion forecasts out to 48 hours. They are calculated routinely for a predefined set of standardized source terms, covering the four Swiss nuclear power plants and two sites in neighboring countries close to the Swiss border. On-demand calculations can be requested by the Swiss National Emergency Operations Centre (NEOC; "NAZ" in German) and are started by the bench forecaster at MeteoSwiss. The set of charts produced in the preoperational phase since May 2021 and during the second half of 2021 have been reviewed and optimized together with the NEOC and the Swiss Nuclear Safety Inspectorate (ENSI). On 7 December 2021, the dispersion ensemble was operationalized.

Operational set of probabilistic charts

The probabilistic results derived from the dispersion ensemble are visualized as charts depicting ensemble minimum, mean and maximum, as well as quantiles and probabilities, in several ways. The charts from the routine production cycle have been sent to the NEOC as test deliveries since May 2021 and operationally since 7 December 2021.

Probabilites

The probability of a property is calculated separately for each model grid cell from the number of ensemble members that exhibit it. In Figure 141, the property of interest is nonzero activity concentration, shown for four different forecast times. Probability of integrated concentration, deposition, and affected area are visualized in the same way. (The affected area is defined as the union of nonzero activity concentration in the lowermost 500 m AGL and nonzero total deposition at the surface.)

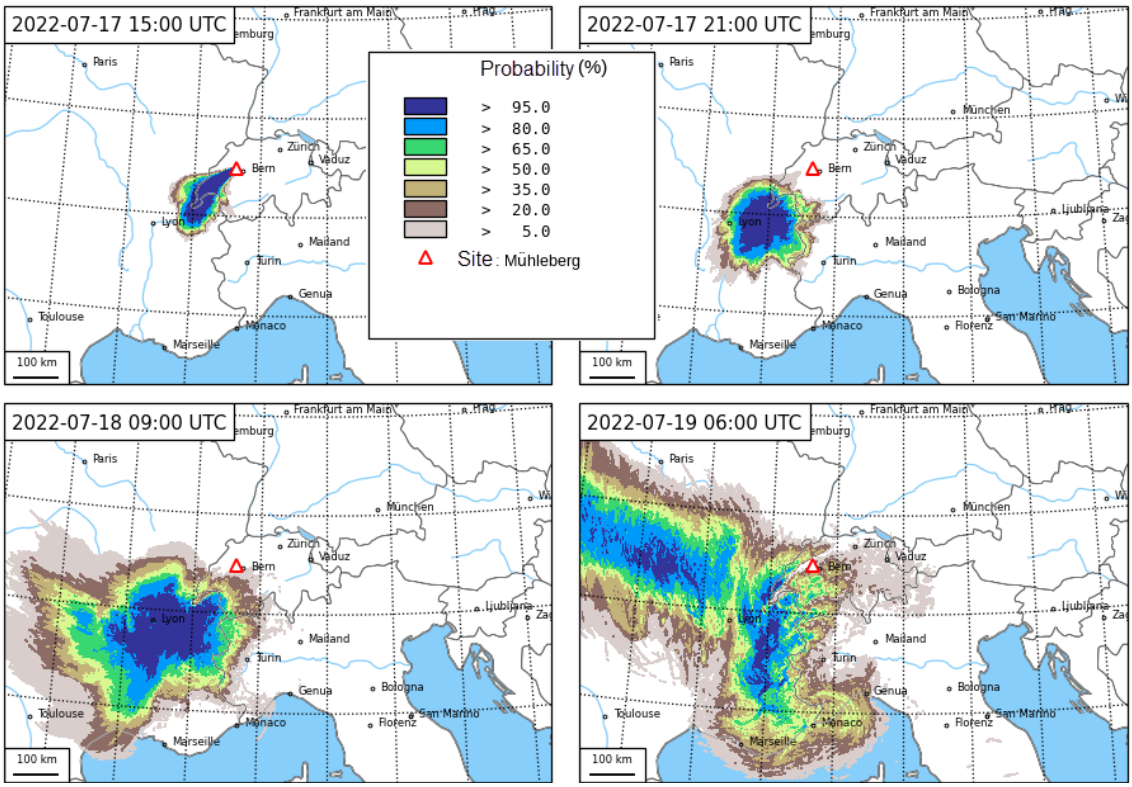

Figure 141. Probability of nonzero activity concentration in the lowest 500 m AGL, for a hypothetic release during 6 h at Mühleberg (red triangle), for 6, 12, 24, 45 h after begin of release.

Percentiles and Other Ensemble Statistics

A percentile of a quantity is calculated separately for each model grid cell from the values of that grid cell in all ensemble members. For integrated concentration (example in Rüdisühli and Kaufmann (2020) for an 11-member instead of a 21-member ensemble) and deposition (example in Figure 142), the 5th, 50th, 75th, 95th percentiles are shown as four-panel plots. The 95th percentile is drawn on separate charts for these quantities, and additionally for activity concentration and affected area.

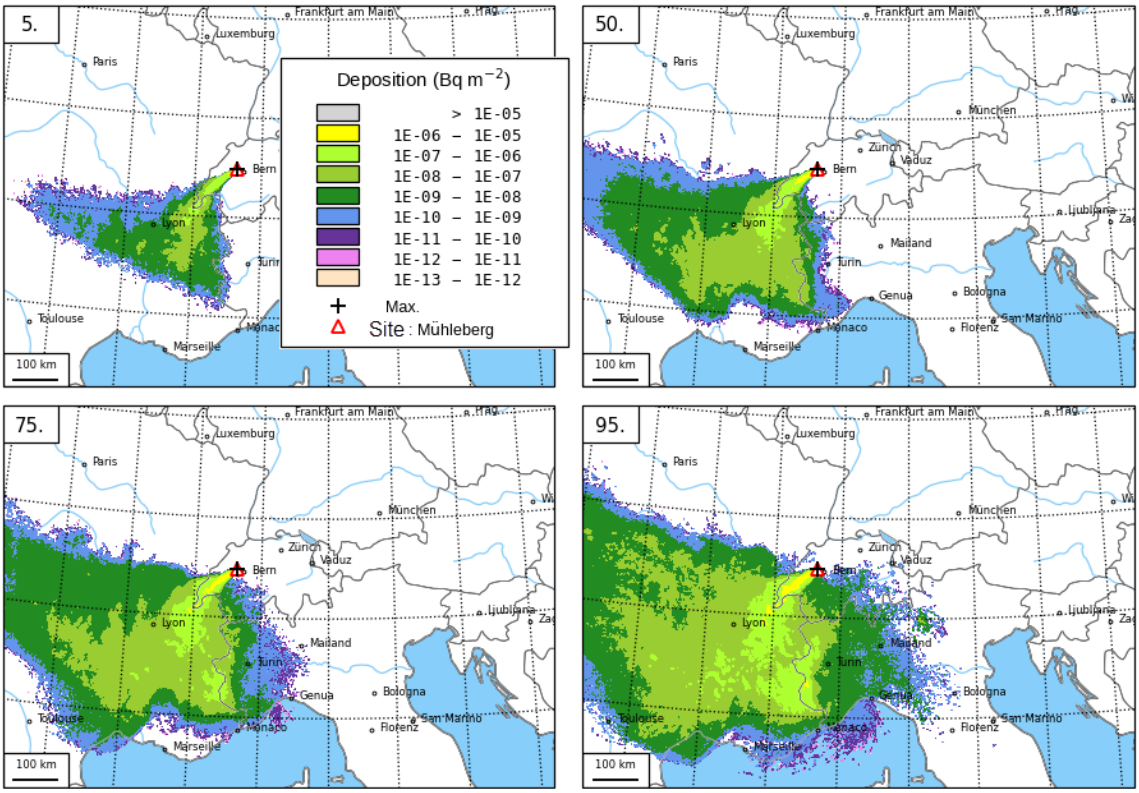

Figure 142. Percentiles of accumulated deposition, for a hypothetic release of 21.6 kBq during 6 h at Mühleberg (red triangle); 5th, 50th, 75th, 95th percentile at end of simulation (45 h after begin of release).

In addition to percentiles, other ensemble statistics are charted, namely the minimum, the mean and the maximum for all quantities.

Cloud Timing

An example of an arrival time plot is show in Figure 143. The color scale has been changed since a similar chart appeared in Figure 2 of Rüdisühli and Kaufmann (2020), in response to a request by the product user (NEOC) to increase the contrast between successive levels. An equivalent plot for departure time (not shown) is also produced. The two plots show at each model grid cell the time until the number of ensemble members with nonzero concentration increases above two for arrival time or decreases below two for departure time.

CONCLUSION AND OUTLOOK

We present a set of chars that have been routinely produced for emergency preparedness for half a year. How the uncertainty information provided by the dispersion ensemble is best integrated in the decision making process remains to be seen. Experience with the plots will grow over time, which will likely lead to further modifications in the time to come.

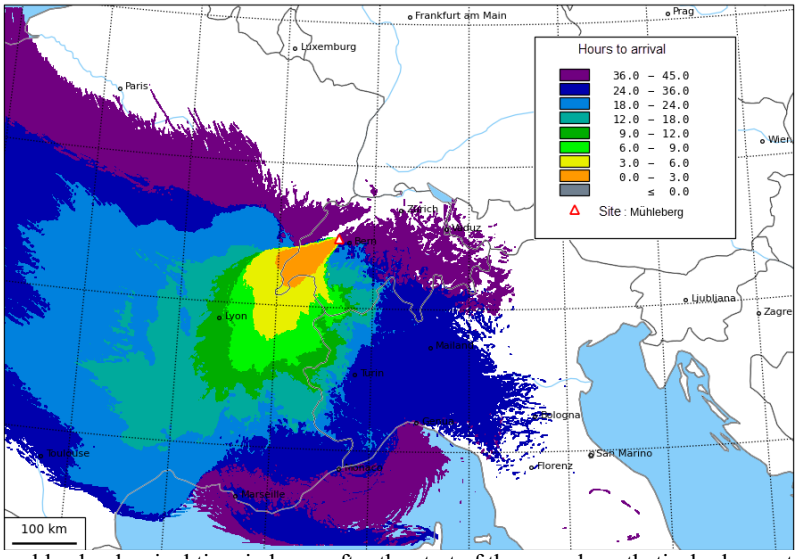

Figure 143. Ensemble cloud arrival time in hours after the start of the same hypothetical release at Mühleberg (red triangle). The arrival time is defined as the first time after the release when two or more ensemble members have nonzero concentrations, excluding only the most cloud-free member at each grid point.

REFERENCES

Baldauf, M., A. Seifert, J. Förstner, D. Majewski, M. Raschendorfer, and T. Reinhardt, 2011: Operational convective-scale numerical weather prediction with the COSMO model: Description and sensitivities. *Monthly Weather Review* 139 (12), pp 3887-3905. https://doi.org/10.1175/MWR-D-10-05013.1

Henne, S., Brunner, D., Oney, B., Leuenberger, M., Eugster, W., Bamberger, I., Meinhardt, F., Steinbacher, M., and Emmenegger, L. , 2016: Validation of the Swiss methane emission inventory by atmospheric observations and inverse modelling, Atmos. Chem. Phys., 16, 3683–3710, https://doi.org/10.5194/acp-16-3683-2016.

Leadbetter SJ, Andronopoulos S, Bedwell P, Chevalier-Jabet K, Geertsema G, Gering F, Hamburger T, Jones AR, Klein H, Korsakissok I, Mathieu A, Pázmándi T, Périllat R, Rudas Cs, Sogachev A, Szántó P, Tomas JM, Twenhöfel C, de Vries H, Wellings J., 2020: Ranking uncertainties in atmospheric dispersion modelling following the accidental release of radioactive material. *Radioprotection*, 55(HS1): S51–S55, https://doi.org/10.1051/radiopro/2020012

Leutbecher, M., Lock, S.-J., Ollinaho, P., Lang, S. T. K., Balsamo, G., Bechtold, P., Bonavita, M., Christensen, H. M., Diamantakis, M., Dutra, E., English, S., Fisher, M., Forbes, R. M., Goddard, J., Haiden, T., Hogan, R. J., Juricke, S., Lawrence, H., MacLeod, D., Magnusson, L., Malardel, S., Massart, S., Sandu, I., Smolarkiewicz, P. K., Subramanian, A., Vitart, F., Wedi, N. and Weisheimer, A., 2017. Stochastic representations of model uncertainties at ECMWF: state of the art and future vision. *Q. J. R. Meteorol. Soc.*, 143, 2315–2339, https://doi.org/10.1002/qj.3094.

Pisso, I., Sollum, E., Grythe, H., Kristiansen, N. I., Cassiani, M., Eckhardt, S., Arnold, D., Morton, D., Thompson, R. L., Groot Zwaaftink, C. D., Evangeliou, N., Sodemann, H., Haimberger, L., Henne, S., Brunner, D., Burkhart, J. F., Fouilloux, A., Brioude, J., Philipp, A., Seibert, P., and Stohl, A., 2019: The Lagrangian particle dispersion model FLEXPART version 10.4, *Geosci. Model Dev.*, 12, 4955–4997, https://doi.org/10.5194/gmd-12-4955-2019.

Rüdisühli, S., and P. Kaufmann: Visualization of ensemble dispersion simulations at MeteoSwiss. 20th International Conference on Harmonisation within Atmospheric Dispersion Modelling for Regulatory Purposes, 14-18 June 2020, Tartu, Estonia. Available from https://www.harmo.org/Conferences/Proceedings/_Tartu/publishedSections/H20-104_stefan_ruedisuehli.pdf

Sørensen, J. H., J. Bartnicki, A. M. Blixt Buhr, H. Feddersen, S. C. Hoe, C. Israelson, H. Klein, B. Lauritzen, J. Lindgren, F. Schönfeldt, and R. Sigg, 2020: Uncertainties in atmospheric dispersion modelling during nuclear accidents. *Journal of Environmental Radioactivity*, 222, https://doi.org/10.1016/j.jenvrad.2020.106356.

21st International Conference on
Harmonisation within Atmospheric Dispersion Modelling for Regulatory Purposes
27-30 September 2022, Aveiro, Portugal

PLANNING FOR JACK RABBIT III FIELD EXPERIMENT FOCUSING ON ANHYDROUS AMMONIA

Steven Hanna[1], Ronald Meris[2], Sun McMasters[3], Joseph Chang[4], Thomas Mazzola[5], Scott Bradley[5], Thomas Spicer[6], Simon Gant[7]

[1]Hanna Consultants, Kennebunkport, Maine USA
[2]US Defense Threat Reduction Agency (DTRA), Fort Belvoir, Virginia USA
[3]RUS Department of Homeland Security (DHS), Edgewood, Maryland, USA
[4]Rand Corporation, Arlington, Virginia USA
[5]Systems Planning and Analysis, Alexandria, Virginia USA
[6]University of Arkansas, Fayatteville, Arkansas USA
[7]UK Health and Safety Executive, Buxton, UK

Abstract: The series of Jack Rabbit field experiments, involving large (1 to 20 tons) releases of hazardous pressurized liquefied gasses, is continuing. Jack Rabbit III will focus on anhydrous ammonia, building on experiences with Jack Rabbit I (10 trials with 1 or 2 tons of either chlorine or anhydrous ammonia) in 2010, and Jack Rabbit II (9 trials with 4 to 20 tons of chlorine) in 2015 and 2016. This paper describes the initial planning of JR III, where laboratory studies, small-scale field studies, and full-scale field experiments will take place over the next four years. The research plan builds on knowledge gap documents presented at the HARMO20 Conference. The JR III laboratory studies have begun and are investigating uptake of ammonia by various substrates and vegetation. The full-scale studies will likely take place, as for Jack Rabbit I and II, at a remote large field site with minimal population density out to at least 50 km. But, because several knowledge gaps concern effects of terrain, substrate, and vegetation types on transport and dispersion and deposition, small-scale field studies are planned for hilly and/or vegetated sites.

Key words: *Jack Rabbit III field experiment, toxic industrial chemicals, anhydrous ammonia, dense gas dispersion, deposition*

INTRODUCTION

Releases of 1 or 2 tons of chlorine or ammonia from pressurized tanks occurred in 2010 during the Jack Rabbit I field experiment (see Hanna et al., 2012). Jack Rabbit II, which involved 4 to 20 ton releases of chlorine, took place in 2015 and 2016, and has been much more thoroughly studied and results presented in a special issue of the journal, *Atmospheric Environment*. For example, Fox et al. (2022) present an overview of JR II; Mazzola et al. (2021) present results of a 17-model comparison exercise using data from JR II trials 1, 6, and 7; and Spicer and Tickle (2021) discuss the source emissions models.

One reason for initiating the Jack Rabbit field experiments was that there was found to be a relatively large difference between several dense gas dispersion model predictions of concentrations resulting from chlorine railcar accidents (Hanna et al., 2008). It was uncertain whether there were problems with estimating the source term, the transport and dispersion, or other model components. In addition to research purposes, another reason for conducting the JR I and JR II field experiments was to provide critical information (e.g., videos and response guidance) about actual large-scale releases for use in training emergency responders.

Observations from JR I and II have led to improved models for the variation of emission rate with time from tanks containing pressurized liquefied gases (Spicer and Tickle, 2021). Spicer et al. (2019) used videos showing liquid pools under the JR II release tank to estimate the rainout (about 30 % on average). Because of the extensive in situ sampling and the videos of the initial cloud, models for the initial broad lateral cloud growth could be improved. The 17 model comparison exercise (Mazzola et al., 2021) used observed concentrations on sampling arcs at distances from 200 m to 11 km, and allowed modelers to improve their parameterizations. We discovered that one of the more useful instruments was also one of the less expensive – a drone with a video camera operated by Professor Andy Byrnes of Utah Valley University.

A limitation of JR I and II was that the field study took place over a flat desert playa with minimal vegetation. As a result, the removal of gas by deposition to the surface was minimal. In the vegetated parts of the world, there would probably be more significant deposition of chlorine or ammonia. Also, there were not significant variations in terrain elevation over the sampling domain. The boundary layer meteorologists on the team pointed out that, in the early morning (8 or 9 am LDT), the cloud was being transported and diffused in a non-steady boundary layer transitioning from stable to unstable.

Anhydrous ammonia was chosen for JR III because it is the most produced, consumed, and distributed hazardous chemical in the US. The major transportation modes of distributing large volume of liquified anhydrous ammonia are pipeline, tanker truck, railcar, and nurse tanks. It is not as hazardous as chlorine, though, with toxicity limits of AEGLs and ERGs that are a factor of about 40 to 100 greater than those for chlorine. Another difference is that, at ambient temperature, ammonia gas is lighter than air, while chlorine gas is heavier than air (both are denser than air when released from a liquefied pressurized container, due to their imbedded aerosols and their cold temperature). Anhydrous ammonia is soluble in and reacts exothermally with water (including ambient humidity), rendering aerosol and vapor that can be denser than air. Moreover, its reactivity with water is chemically reversible posing invisible toxic inhalation hazards to the emergency responders and residents in event of chemical spill or leak.

It is important to note that the critical Richardson number, Ri_c, can be used to estimate whether a cloud is behaving as a dense gas rather than a neutral (passive) gas. Ri_c is proportional to relative density difference times the acceleration of gravity (g), times the cloud dimension, divided by the square of the wind speed (or friction velocity). Thus, as the cloud becomes diluted by ambient air, and its relative density difference approaches zero, the Ri drops below its critical value and the cloud behaves like a neutral gas.

The motivation for Jack Rabbit III is that, while anhydrous ammonia is being more widely used in the world, there are several unknowns regarding its emission, transport and dispersion, deposition, and re-evaporation. The cloud density may initially be greater than that of air due to its cold temperature and due to tiny ammonia and water aerosols, as seen in the photo of the Blair Nebraska ammonia release in Figure 1. This was not a pressurized release, but closer to ambient pressure liquid that was overfilled from a barge, so as the liquid ammonia flows out, it would quickly start to cool below its boiling point due to evaporation, and break up into droplets. Air was entrained into the ammonia flow, and ambient humidity likely condensed on the ammonia droplets. But, as the cloud moves downwind and warms, the aerosol evaporates, and the cloud may become buoyant, and eventually becomes neutral (Ri drops below its critical value). In addition, the deposition of anhydrous ammonia to vegetation and the substrate, and subsequent re-evaporation, are not well-known, and will be addressed in JR III. The effects of the initial jet resulting from a leak from a pressurized container can be significant, rapidly transporting the initial plume upwards or sideways (see Figure 2, where the ammonia jet is directed upwards, and Figure 3 [Desert Tortoise Trial 2], where the ammonia jet is directed horizontally downwind). Furthermore, JR III will also address health effects of anhydrous ammonia, including applications of toxic load parameterizations.

Ongoing JR III planning

As done in JR II, many experts in the international community are included in JR III working groups (WGs), which are listed below, along with issues currently being raised in bimonthly meetings:

- Source WG – Focusing on continuous release from hole in pipeline

- Instrumentation WG – Comparing capabilities of in situ and remote (stand-off) instruments; tallying quantitative needs (e.g., numbers and range of concentrations observed)
- Human Effects WG – Reviewing existing summaries of health effects of anhydrous ammonia; considering calculation of toxic load.
- Modelers WG – Comparing model predictions for existing ammonia field studies (Desert Tortoise and FLADIS); estimating downwind cloud concentrations and dimensions for various possible source scenarios.
- Emergency Responders WG – Working with industry associations and government agencies to determine current practices and how they can be assessed with new field data.
- Deposition & Surface Chemical Reactivity WG – Providing oversight of current laboratory studies, planning deposition and chemical reactivity measurements for possible small scale field studies in vegetated areas.
- Data Quality WG – Assessing data quality procedures used in JR II and defining needs for the JR III anhydrous ammonia laboratory and field studies; estimating uncertainties in observations.

Several papers at this conference will describe results of the international model comparison exercise being carried out by the JR III Modelers WG for three Desert Tortoise trials and three FLADIS ammonia field trials. This should improve harmonization of models used for ammonia release scenarios.

A few knowledge gaps to be resolved in JR III

There are some challenges for the JR III planning, and a few are outlined below.

Composition of aerosol – There is uncertainty in assessing the visible aerosol cloud as seen in Figure 1. Do the liquid drops contain mostly condensed ambient water or ammonia? Or perhaps ammonia in solution?

Previous experience with the JR II chlorine cloud suggest that remote (standoff) detectors can ”see” only a short distance into the edge of the cloud. It would be desirable to obtain a full cross section.

Vertical profiles of concentration in the cloud were obtained during some JR II trials at a few tower locations, and only to a height of 6 m. Taller and more towers or remote sensors are needed.

Deposition and surface reactivity measurements are complicated by the fact that some of the deposited chemical desorbs after the cloud goes by. Another fraction remains at the surface as reaction products. So far, we have not devised a good way to measure these components.

It is expected that the deposition of ammonia to the surface will be much greater in vegetated areas or areas with fertile soil. However, these areas tend to be closer to populated areas or sensitive ecosystems, and it is necessary to release smaller amounts. Currently the group is searching for possible vegetated sites.

It is hoped to carry out some tests in complex terrain, where the initial dense cloud is expected to follow the slope. Unfortunately, such effects are site specific, but the goal is to design terrain experiments such that the results are of general use.

JR III work schedule

The current list of major work efforts and the timeline for their completion are given in Figure 4. It is important to state that this is tentative. Note that the large-scale field tests will not take place until 2025. In the meantime, laboratory studies and small-scale field experiments will be underway. A series of ammonia deposition experiments will take place in the Univ. Arkansas wind tunnel, following the methodologies used for chlorine by Spicer et al. (2021). In addition, the U.S. Army Combat Capabilities Development Command Chemical Biological Center in Edgewood, MD, is currently conducting chamber studies on the effects of ammonia on various materials.

Since we encourage collaborations with outside groups, please send a message to the author (stevenrogershanna@gmail.com) if you wish to participate in the planning and the subsequent field experiments.

REFERENCES

Fox, S., S. Hanna, T. Mazzola, T. Spicer, J. Chang, and S. Gant, 2021: Overview of Jack Rabbit II (JR II) field experiment and summary of the methods used in the dispersion model comparison. *Atmos. Environ.* **269** https://doi.org/10.1016/j.atmosenv.2021.118783

Hanna, S., R. Britter, E. Argenta, and J. Chang, 2012: The Jack Rabbit chlorine release experiments; dense gas removal from a depression by crosswinds. *J. Haz. Mat.* **213-214**, 406-412.

Hanna, S., S. Dharmavaram, J. Zhang, I. Sykes, H. Witlox, S. Khajehnajafi, and K. Koslan, 2008: Comparison of six widely-used dense gas dispersion models for three recent chlorine railcar accidents. *Process Safety Progress.* **27**; 248-259.

Mazzola, T., S. Hanna, J. Chang, S. Bradley, R. Meris, S. Simpson, S. Miner, S. Gant, J. Weil, M. Harper, J. Nikmo, J. Kukkonen, J.-M. Lacome, M. Nibart, O. Bjornham, S. Khajehnajafi, K. Habib, P. Armand, T. Bauer, L. Fabbri, T. Spicer, and N. Ek, 2020: Results of comparisons of the predictions of 17 dense gas dispersion models with observations from the Jack Rabbit II chlorine field experiment. *Atmos. Environ*. **244,** 117887. https://doi.org/10.1016/j. atmosenv.2020.117887

Spicer, T. and G. Tickle, 2021: Simplified source description for atmospheric dispersion model comparison of the Jack Rabbit II chlorine field experiments. *Atmos. Environ*. **246** https://doi.org/10.1016/j.atmosenv.2021.117997.

Spicer, T., A. Feuvrier and S. Fox, 2019: Transient large-scale chlorine releases in the Jack Rabbit II field tests: rainout source data analysis from video records. *J. Loss Prev. Process. Ind.* **59**, 35–43.

Spicer, T., S. Fox and B Hicks, 2021: Prelininary assessment of chlorine reactivity with environmental materials accounting for boundary layer and maximum deposition effects. *Atmos. Environ.* **256**, 118274.

Figure 1. Blair, Nebraska, ammonia accident.

Figure 2. TRANSCAER training exercise with ammonia

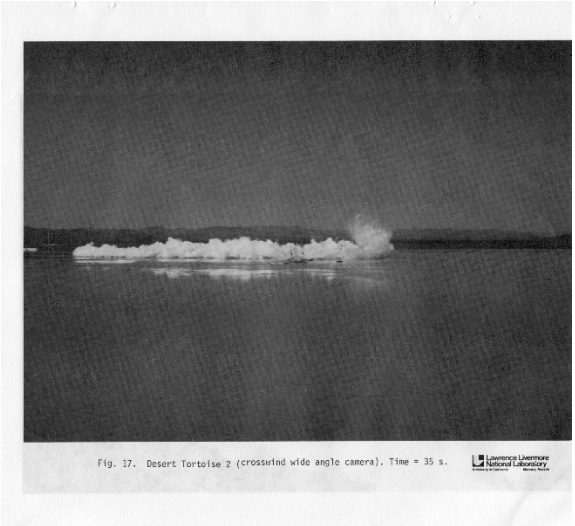

Figure 3. Desert Tortoise 2 field experiment at Nevada Test Site.

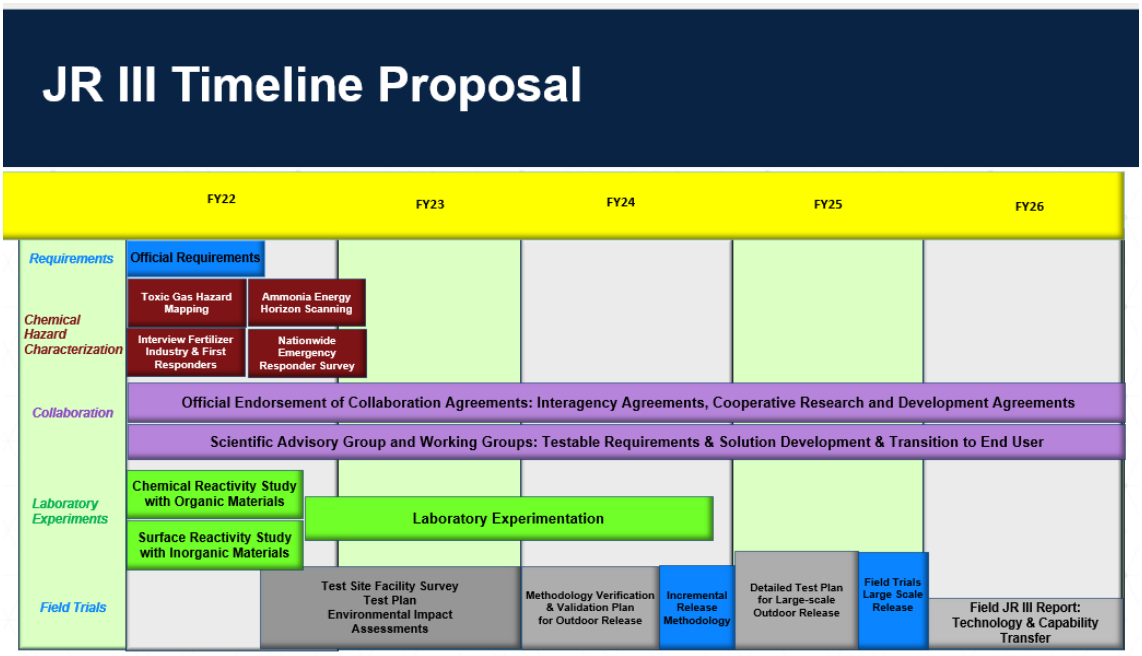

Figure 4. Proposed JR III general work tasks and timelines

21st International Conference on
Harmonisation within Atmospheric Dispersion Modelling for Regulatory Purposes
27-30 September 2022, Aveiro, Portugal

TOWARDS THE USE OF METEOROLOGICAL ENSEMBLES FOR SHORT DISTANCE DISPERSION OF RADIONUCLIDES IN CASE OF AN ACCIDENTAL RELEASE IN THE ATMOSPHERE

Youness El-Ouartassy[1,2], Irène Korsakissok[2], Matthieu Plu[1], Olivier Connan[3], Laurent Descamps[1], Laure Raynaud[1]

[1]CNRM, University of Toulouse, Météo-France, CNRS, Toulouse, France
[2]Institut de Radioprotection et de Sûreté Nucléaire (IRSN), PSE-SANTE/SESUC/BMCA, Fontenay-aux-Roses, France
[3]Institut de Radioprotection et de Sûreté Nucléaire (IRSN), PSE-ENV/SRTE/LRC, Cherbourg-En-Cotentin, France

Abstract: Numerical models of atmospheric dispersion are used for predicting the health and environmental consequences of nuclear accidents, in order to anticipate the countermeasures necessary to protect the populations. However, the simulations of these models suffer from significant uncertainties, arising in particular from input data: weather conditions and source term. To characterize weather uncertainties, it is essential to combine a well-known source term data and meteorological ensembles to generate ensemble dispersion simulations which has the potential to produce different possible scenarios of radionuclides dispersion during emergency situations. In this study, the fine-scale operational weather ensemble AROME-EPS from Météo-France is coupled to the Gaussian puff model pX developed by the French Institute for Radiation Protection and Nuclear Safety (IRSN). The source term data is provided by Orano La Hague reprocessing plant (RP) that regularly discharges ^{85}Kr during the spent nuclear fuel reprocessing process. Then, to evaluate the dispersion results, a continuous measurement campaign of ^{85}Kr air concentration was recently conducted by the Laboratory of Radioecology in Cherbourg (LRC) of IRSN, around RP in the North-Cotentin peninsula. This work investigates the meteorological uncertainties in dispersion simulations at local and medium distances (2-20km). The probabilistic performance of the dispersion ensemble simulations was evaluated using two probabilistic scores: Relative Operating Characteristic (ROC) curves and Peirce Skill Score (PSS). The results highlight the added value of ensemble forecasts compared to a single deterministic one, and their potential interest in the decision process during crisis situations.

Key words: *Ensembles, meteorological uncertainties, atmospheric dispersion model, ^{85}Kr, pX, AROME-EPS.*

INTRODUCTION

The dispersion of radionuclides released into the atmosphere depends on the physico-chemical properties of the released substances, the emission parameters (e.g. source elevation, timing and duration of the release) and meteorological conditions at the accident site (e.g. wind speed and direction). In order to forecast the dispersion of radionuclides in the early phase of nuclear accidents and to support decisions and warnings, atmospheric dispersion models (ADM) are commonly used to predict the transport of radioactive pollutants through the atmosphere as well as the quantities of radioactive material deposited on the ground. This information is essential for decision makers in order to anticipate the countermeasures necessary to protect the population against contamination.

The outputs from ADM simulations suffer from significant uncertainties that hinder their use in an operational context. Meteorological forecasts, which are an essential input data, are one of the main sources of these uncertainties. Weather information used for dispersion prediction is, frequently, provided by Numerical Weather Predictions (NWP) as 3-D or 4-D physical fields. For weather prediction, meteorological uncertainties are usually accounted for by building an ensemble of NWP instead of using a single, deterministic forecast. The objective of this work is to investigate the impact of the meteorological uncertainties on local-scale dispersion by using the operational high-resolution meteorological ensemble

AROME-EPS (Bouttier et al., 2012) of Météo-France. It is a 16-members ensemble with a resolution of 2.5 x 2.5 km and hourly forecasts. Given the objective of the study, only first 25 vertical levels [10-3000 m] are used to cover the entire Atmospheric Boundary Layer (ABL). Then, AROME-EPS ensembles are used as input of IRSN's short-range Gaussian puff model pX (Korsakissok et al., 2013) around La Hague Reprocessing Plant (RP) at local and medium scales (2-20 km) (Figure 1).

Case study

The present study focuses on the dispersion of ^{85}Kr at short and medium distances (less than 20 km), in the North-Cotentin peninsula located in the North-West of France territory (Figure 1). The potential interest of the La Hague area is that the release rate of ^{85}Kr emitted by the RP into the atmosphere is known with a good accuracy. In addition, there is a sufficient density of meteorological measurements combined with ^{85}Kr radiological air concentration measurements (Figure 1). Meteorological measurements are carried out by Météo-France on a regular basis. IRSN's LRC laboratory regularly performs meteorological and radiological measurements in the framework of measurement campaigns (Connan et al., 2014). In this work, continuous radiological measurements (every 1 minute) were conducted by LRC as part of the DISKRYNOC project (DISpersion of KRYpton in the NOrth-Cotentin). Additional meteorological and air concentration measurements, as well as release data (every 10 minutes), are carried out by Orano for the environmental monitoring of the RP. For these reasons, the La Hague experimental site is an ideal environment for the study and validation of atmospheric dispersion simulations.

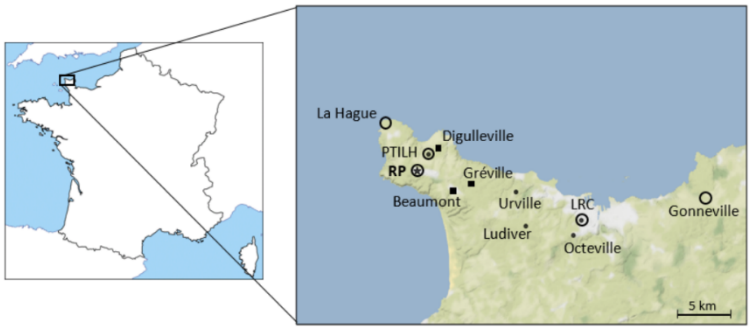

Figure 144. *Location of North-Cotentin peninsula (left panel) and map of the monitoring sites (right panel). The dots and squares indicate the locations of the ^{85}Kr measurement stations carried out by IRSN and RP, respectively, as part of the DISKRYNOC campaign. The RP facility location is marked with a star. The circles indicate the locations of the 3D-wind measurement sites (from IRSN or Météo-France).*

Coupling arome-eps ensembles to dispersion model px

Before coupling the numerical weather predictions from AROME-EPS to the pX model, it is necessary to evaluate them in order to have an exhaustive overview of their quality and to take it into account in the interpretation of atmospheric dispersion simulations. Wind speed and direction are the most influential variables on the transport of a plume through the atmosphere. The meteorological ensembles were thus evaluated by calculating comparative evaluation scores (e.g bias, spred-skill ratio, rank diagram) based on the observations of 3D-wind over a two-months period (Dec. 2020-Jan. 2021). The results of this evaluation showed that the high horizontal, vertical and temporal resolution of the AROME-EPS forecasts allow them to correctly represent the uncertainties within ABL, despite slight errors in the wind speed forecast.

Simulations set-up

Once meteorological forecasts from AROME-EPS have been qualified, they are coupled to the Gaussian dispersion model pX by running in parallel several simulations with the pX model, each using a different member of the AROME-EPS ensemble as input (Figure 2), along with the source term data provided by RP La Hague. This allows to generate an ensemble of dispersion simulations composed of 16 members. Furthermore, in order to quantify the benefit of using ensembles instead of deterministic simulations, an additional pX simulation was performed using the deterministic weather forecast from AROME as input of the model. Then, in order to ensure that the source emission does not occur above the ABL, a minimum value of 200 m is imposed to the ABL height before being applied to the pX simulations. In addition, the

effects of the complex topography (coastline, rocky terrain) and buildings on the plume dispersion may lead to downwash effects that are not explicitly taken into account by the Gaussian puff model. To compensate for this limitation, 8 effective heights have been tested: 20, 50, 100, 150 and 200 m. The most optimum simulations were obtained by using the physical stack height of 100 m.

Even though the NWP forecasts are given with an hourly frequency, the pX simulations were performed in this study with a time step of 10 minutes in order to better capture the temporal variations of the plume. Two stability diagnoses were used to perform pX simulations: Pasquill and Doury (El-Ouartassy et al., 2022).

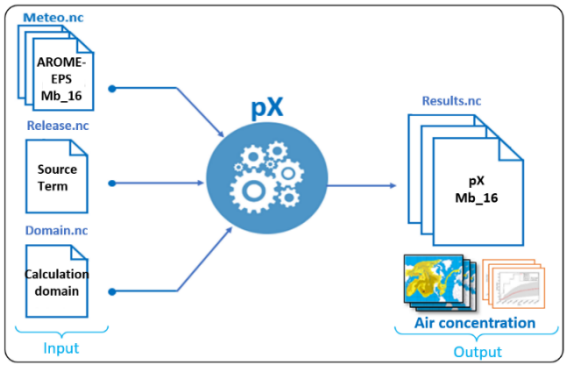

Figure 2. Coupling of AROME-EPS meteorological ensembles to the Gaussian dispersion model pX.

Statistical indicators for dispersion ensemble evaluation

It is often a desirable feature for a dispersion model to be able to correctly predict a threshold exceedance. It is particularly useful for decision-making purposes, when protective actions for the population are based on the prediction of zones where a given dose threshold could be exceeded. Evaluating the model performance for this kind of purpose is often based on contingency tables allowing to compare the series of observations and simulations by counting four features: (i) true positive (TP) when a peak is observed and well simulated, (ii) false negative (FN) when a peak is observed but not simulated, (iii) false positive (FP) when there is no observed but simulated peak and (iv) true negative (TN) when there is no observed and no simulated peak. Then, the performance of the ensemble is measured using hit rate (H) and false alarm rate (F) metrics. The hit rate is the fraction of the observed events that are successfully reproduced (Equation (1)). The false alarm rate is the fraction of the simulated peaks that are not observed (Equation (2)).

$$H = \frac{TP}{TP + FN} \tag{1}$$

$$F = \frac{FP}{FP + TN} \tag{2}$$

In the case of the AROME-EPS-pX ensemble, there are 16 possible decision thresholds (x=1,2,...,16). In order to identify the most optimal ones, the ROC (Relative Operating Characteristic) curves are commonly used as a graphical summary of the decision-making skill of an ensemble, by connecting all points [F(x), H(x)] for each decision threshold x. In addition, to better capture the internal variation of the performance of the model according to the decision thresholds, the Peirce skill score (PSS) was calculated for each x, as follows:

$$PSS(x) = H(x) - F(x) = \frac{TP \times TN - FP \times FN}{(TP + FN) \times (FP + TN)} \tag{3}$$

Note that the threshold that presents a better compromise between the probability of detection and the probability of false detection of events corresponds to the one that maximizes the PSS.

RESULTS

Simulations and observations at all stations were aggregated in order to investigate the probabilistic performance of the ensembles, using ROC curves and PSS. As shown in Figure 3, The pX-Pasquill ensembles perform better than pX-Doury, with a PSS_{MAX}=0.72 corresponding to an optimal decision thresholds of 3 and 4 members (against a PSS_{MAX}=0.63 and optimal decision thresholds of 3 members for pX-Doury ensembles). This difference in performance seems normal given that the variation in atmospheric stability conditions is better captured with the Pasquill's stability classes (six classes for Pasquill against two classes for Doury). In both cases, the ensemble performs better than the deterministic simulation in a range of seven decision thresholds, which represents almost 50% of the possible values of the decision thresholds. These results highlight the robustness of the probabilistic simulations compared to the deterministic simulation in the process of the prediction of threshold exceedances.

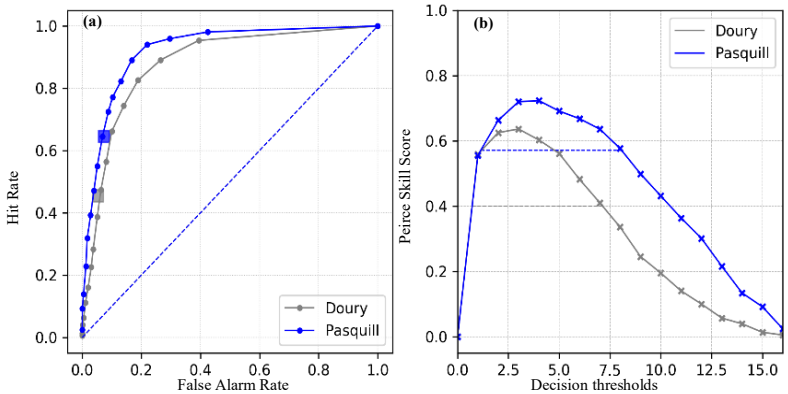

Figure 3. *ROC curves (a) and the PSS as a function of decision thresholds (b) of the pX ensemble simulations performed with Pasquill stability classes and Doury classes, by aggregating simulations and observations at all stations. The values of the scores for the deterministic pX simulation are indicated by squares in the ROC curves and by horizontal dashed lines in the PSS curves. The diagonal dashed lines are the no-skill lines (H=F).*

To go further into the analysis of the probabilistic performance of the ensembles, the effect of the distance from the source is investigated in Figure 4. In this case, the dispersion simulations were generated, with the two diffusion configurations of Pasquill and Doury, by aggregating data for two groups of stations. The first is the *-10km* group which contains stations at distances less than 10km from the source: PTILH (2km), Digulleville (2.6km), Beaumont (4.2km) and Gréville (5.2km). The second is the *+10km* group which contains stations beyond 10km: Urville (10.4km), Ludiver (12.7km), Octeville (17.7km) and LRC (18km). For both groups of stations, pX-Pasquill simulations give better scores than pX-Doury, both for deterministic and ensemble pX outputs.

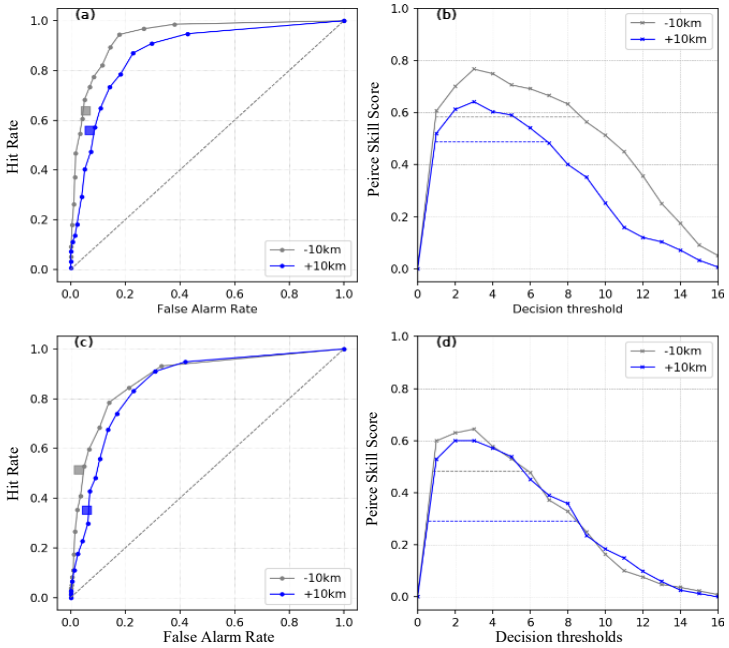

Figure 4. *ROC curves (a, c) and the PSS as a function of decision thresholds (b) of the pX ensemble simulations performed with Pasquill stability classes (a, b) and Doury classes (c, d), by aggregating data in the two groups of stations: -10km (gray) and +10km (blue).*

Taking into account both meteorological and model uncertainties would imply generating an ensemble by also perturbing model parameters (Pasquill/Doury, source elevation, stability). In this perspective, a 32-member super-ensemble was generated by combining pX-Pasquill and pX-Doury ensembles. The result (not shown here) is very similar to the pX-Pasquill ensemble.

CONCLUSIONS AND PERSPECTIVES

In this study we explored the potential value of using fine-scale spatial and temporal meteorological ensembles to represent the effect of meteorological uncertainties on ADM outputs. The high-resolution operational forecasts AROME-EPS of Météo-France have been coupled to IRSN's Gaussian puff short-range dispersion model pX to generate a 16-member dispersion ensemble which accounts for meteorological uncertainties. This study presents a strategie to evaluate the ability of a dispersion ensemble to forecast threshold exceedances, using probabilistic scores. For this purpose, we used an original data set of continuous ^{85}Kr air concentration measurements (DISKRYNOC campaign recently conducted by IRSN), along with a well-known source term (every 10 minutes, provided by Orano La Hague RP) and meteorological data (NWP from Météo-France and continuous observations from Météo-France/IRSN).

As a first step, the assessment of the quality of the AROME-EPS forecasts, in terms of wind speed and direction, in the North-Cotentin peninsula was carried out, using meteorological observations, over the two-month period of interest (Dec. 2020-Jan. 2021). The results showed that AROME-EPS performs well in the North-Cotentin area. Then, an ensemble dispersion modeling chain was implemented using the AROME-EPS forecasts as inputs to the pX model. Then, two configurations of dispersion simulations were run, with Pasquill and Doury Gaussian standard deviations. The probabilistic consistency of the two resulting dispersion ensembles was then compared by calculating two probabilistic scores: ROC curves and PSS. This evaluation process was performed in two parts. First, by comparing the overall performance of the two configurations by aggregating the data from all the measurement stations. In this case the best results were obtained with Pasquill standard deviations. Secondly, by comparing the performance of the two configurations in the near fields (stations located less than 10km from the source) and far fields (stations beyond 10km from the source). The results showed that the Pasquill simulations were still the most consistent with observations. In all cases studied, the best decision threshold is 3 members, and the ensembles performed better than the deterministic simulations. For operational purposes during emergency situations, this result would imply that in this configuration, when 3 or more members of the ensemble forecast a threshold exceedance, protective actions should be recommended.

To complement this study, it would be interesting to develop complementary indicators that evaluate the consistency of dispersion ensembles in terms of intensity between the simulated and observed peaks. Another perspective of this study is to work on the clustering of the meteorological ensembles in a perspective of reducing the number of members while keeping the consistency of the dispersion ensembles. This can significantly reduce the computational time of ADM runs, which is a crucial issue in the case of a real nuclear accident.

REFERENCES

Bouttier, F., L. Raynaud, O. Nuissier and B. Ménétrier, 2016: Sensitivity of the AROME ensemble to initial and surface perturbations during HyMeX. *Quarterly Journal of the Royal Meteorological Society.*, **142**, 390–403.

Connan, O., L. Solier, D. Hébert, D. Maro, M. Lamotte, C. Voiseux, P. Laguionie, O. Cazimajou, S. Le Cavelier and C. Godinot, 2014: Near-field krypton-85 measurements in stable meteorological

conditions around the AREVA NC La Hague reprocessing plant: estimation of atmospheric transfer coefficients. *Journal of environmental radioactivity*, **137**, 142–149.

El-Ouartassy, Y., I. Korsakissok, M. Plu, O. Connan, L. Descamps et L. Raynaud, 2022: Combining short-range dispersion simulations with fine-scale meteorological ensembles: probabilistic indicators and evaluation during a ^{85}Kr field campaign. *Atmospheric Chemistry and Physics*, in review.

Korsakissok, I., A. Mathieu, and D. Didier, 2013: Atmospheric dispersion and ground deposition induced by the Fukushima Nuclear Power Plant accident: A local-scale simulation and sensitivity study. *Atmospheric environment*, **70**, 267–279.

21st International Conference on
Harmonisation within Atmospheric Dispersion Modelling for Regulatory Purposes
27-30 September 2022, Aveiro, Portugal

ATMOSPHERIC DISPERSION CHARACTERISTICS OF RADIOACTIVE MATERIALS OBTAINED FROM WRF/HYSPLIT IN NUCLEAR POWER PLANTS

Hyun-Ha Lee[1], Chun-Ji Kim[2], Su-Bin Oh[2], Sang-Hyun Lee[3], and Chun-Sil Jin[1]

[1]Korea Institute of Nuclear Safety, Daejeon, Republic of Korea
[2]BomIn Science Consulting, Incheon, Republic of Korea
[3]Department of Atmospheric Science, Kongju National University, Gongju, Republic of Korea

Abstract: Understanding the diffusion characteristics of radioactive materials in Nuclear Power Plants (NPPs) is essential to preparing for nuclear accidents. In this study, we analyzed the diffusion characteristics of radioactive materials in NPPs using the coupling method of Weather Research and Forecasting (WRF) and Hybrid Single-Particle Lagrangian Integrated Trajectory (HYSPLIT). The Kori and Wolsong NPPs, which are the target sites of this study, are located on the southeast coast of the Korean Peninsula, adjacent to the mountains. We suggested considerations for a methodology creating high-resolution and three-dimensional local meteorological fields near the NPPs based on previous studies demonstrating the performance improvement of local meteorological field simulation over complex topography. For the multiscale dynamical downscaling, we then increased the spatial resolution by gradually reducing the size of the domain using the one-way (parasitic) nesting method. We also updated land-use and topography data to improve the model performance of local wind fields around the NPPs. We performed the HYSPLIT model using the improved meteorological fields simulated by the WRF model as input data. As a result, we obtained forward trajectory, concentration, and deposition data of Cs-137 released from NPPs sites during 2013-2017 (5 years). The surrounding topography influenced the annual dispersion characteristics of NPPs. Due to the mountainous terrain adjacent to the inland direction of the NPPs, the radioactive material had a higher concentration in the ocean direction. The seasonal characteristics showed the influence of the diffusion direction and speed related to the seasonal wind, which appeared predominantly on the Korean Peninsula.

Key words: *Atmospheric dispersion, WRF, HYSPLIT, dynamic downscaling method, nuclear power plants*

INTRODUCTION

Nuclear power takes approximately one-third of the low-carbon electricity generation worldwide, supplying energy efficiently for households and industries. However, nuclear power plants (NPPs) can affect fatal impacts on the public and the environment in case of unexpected radioactive accidents. The radioactive materials released in the atmosphere can cause severe damage near the NPP and downwind regions by short- and long-range transport. For example, the Fukushima Daiichi NPP accident, which occurred after the tsunami in Japan on 11 March 2011, caused significant ongoing radioactive contamination in the vicinity of the site and far downwind area (~80 km) through the atmospheric transport. The Japanese authorities took several emergency actions at the early stage of the accident to mitigate the radiologic health impact, including a mandatory evacuation of over 200,000 inhabitants near the NPP site and monitoring food, water, and placement of radiation limits over the downwind affected areas. In addition, the long-term health and environmental impacts are ongoing over the radioactive contamination areas. For taking timely actions to mitigate the health and environmental impacts under accidental radioactive conditions, it is essential to predict the atmospheric dispersion of radioactive materials, especially near the accidental site.

Atmospheric dispersion models are used in simulating the atmospheric dispersion of radioactive materials. Many atmospheric dispersion models have different complexities in representing atmospheric processes, such as the Hybrid Single-Particle Lagrangian Integrated Trajectory (HYSPLIT) model, the FLEXible PARTicle dispersion model (FLEXPART), and the Gaussian puff model. They were used to analyze the atmospheric dispersion of radioactive materials for the Chernobyl and Fukushima NPP accidents (Stohl et

al., 2012; Srinivas et al., 2012). In addition, the models have also been used to simulate radioactive dispersions of hypothetic accident scenarios for accidental preparedness and NPP site selection. The study emphasized the quality of meteorological input data for effective emergency response at the early accidental stage. In South Korea, NPPs are sitting on complex terrains close to coastal and mountainous areas. Due to their topographical complexity, the local meteorological fields near the NPPs form complicatedly under different synoptic weather conditions. However, many meteorological models frequently overestimate wind speeds of the atmospheric boundary layer, despite alleviation efforts, which can result in false atmospheric dispersion of radioactive materials (Lim et al., 2019).
In this study, we analyzed the diffusion characteristics of radioactive materials in Kori and Wolsong NPPs using the coupling method of Weather Research and Forecasting (WRF) and Hybrid Single-Particle Lagrangian Integrated Trajectory (HYSPLIT). We performed the HYSPLIT model using the improved meteorological fields simulated by the WRF model as input data, and then we analyzed the diffusion characteristics of each NPP.

DATA AND METHODS

The meteorological input data using dynamical downscaling method

The dynamic downscaling method is developed based on the WRF version 3.6.1 for producing high-resolution local meteorology near the Kori and Wolsong NPPs situated in a southeastern coastal region in Korea. The WRF model uses fully compressible and non-hydrostatic governing equations using the Arakawa C-grid system. In addition, it includes various physical parameterizations of atmospheric shortwave/longwave radiation transfer, land-atmosphere interaction, ABL turbulence mixing, and grid and subgrid cloud physics. The WRF model, as one of the high-fidelity regional atmospheric models, is suitable for simulating multiscale atmospheric phenomena (e.g., cyclones, typhoons, land/sea breezes). In addition, it can be easily compatible with the atmospheric dispersion models of HYSPLIT and FLEXPART-WRF through model-model coupling interfaces (Draxlet and Hess, 1997 and 1998; Brioude et al., 2013).
The one-way nesting technique is adopted using the WRF model to produce fine-scale local meteorology near the NPPs from large-scale meteorological forecasts. As shown in the Fig. 1, the coarsest domain (D01) covers a broad East Asia region, including Korea, China, and Japan, to represent synoptic meteorological phenomena on a model grid resolution of 32.4 km. Next, the meteorological fields are repeatedly downscaled to 10.8 and 3.6 km grid resolutions, focusing on northeastern Asia and the Korean Peninsula regions. Finally, the dynamic downscaling method produces high-resolution local meteorology for the NPPs with a grid resolution of 1.2 km. The finest domain (D04) covers large areas from the NPPs enough to evaluate short-range atmospheric dispersions from the Kori and Wolsong NPPs. Table 1 summarizes the grid configuration and physical schemes used in the dynamic downscaling method.

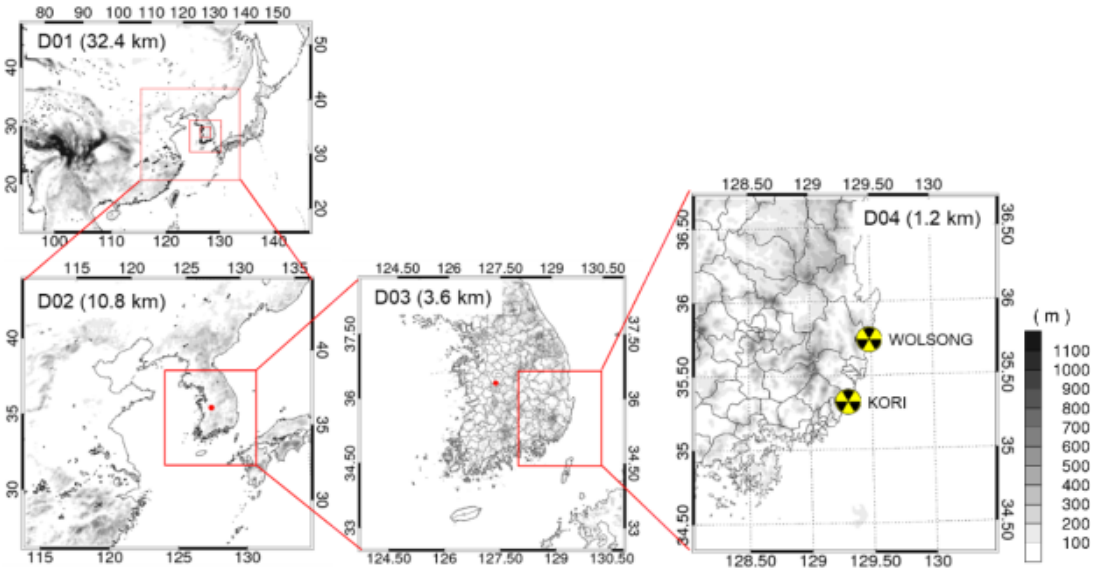

Figure 145. Domain configuration of the dynamic downscaling method for the Kori and Wolsong nuclear power plants (NPPs). Shading denotes the topographic height

Table 1. Model grid configuration and physical schemes for the dynamic downscaling method.

	D01	D02	D03	D04
Horizontal grid (grid spacing)	181×134 (32.4 km)	190×181 (10.8 km)	181×190 (3.6 km)	181×217 (1.2 km)
Vertical grid	56 levels			
Shortwave radiation	Goddard			
Longwave radiation	RRTM			
Land surface process	NOAH LSM			
Urban canopy model	VUCM			
Turbulence process	MYNN Level 2.5			
Cumulus parameterization	Grell-Devenyi			
Cloud Physics	Modified Purdue Lin			
Four-dimensional data assimilation	○	○	○	×

We added a new subgrid-scale topographic drag parameterization in the WRF model to improve the prediction skill of local wind fields near the NPPs. It accounts for the subgrid-scale topographic variation within the dynamic downscaling grid as an enhanced aerodynamic roughness length ('effective roughness length'). In order to determine the effective roughness length, we use an empirical formulation of Zhu et al. (2017). In addition, we update the model land-use and topography data.

The coupling of wrf and hysplit

We used HYSPLIT (Hybrid Single-Particle Lagrangian Integrated Trajectory), a three-dimensional atmospheric diffusion model developed by NOAA/ARL (National Ocean and Atmospheric Administration/Air Resource Laboratory). HYSPLIT is one of the most extensively used atmospheric transport and dispersion models in the atmospheric sciences community. It has been used in a variety of simulations describing the atmospheric transport, dispersion, and deposition of pollutants. HYSPLIT simulates the transport and diffusion in the atmosphere based on the Lagrangian method, so it is possible to trace the concentration of pollutants and the forward and backward trajectories. For more details, see the publication written by Stein et al. (2015).

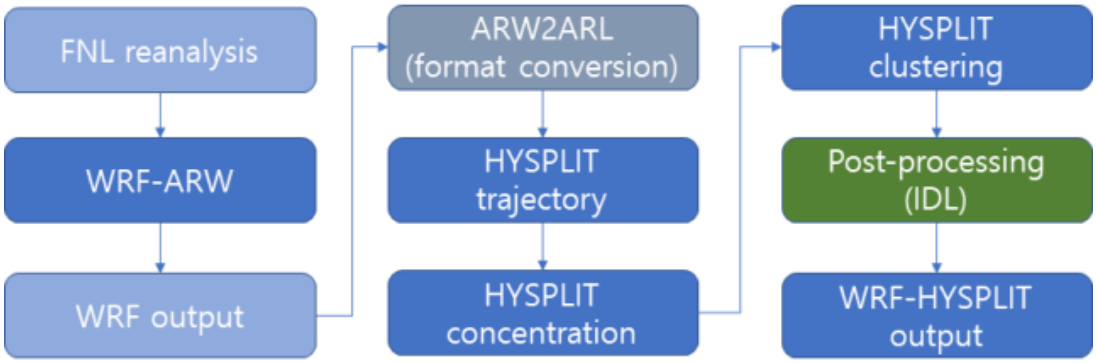

Figure 2. Coupling diagram of meteorological model (WRF) and diffusion model (HYSPLIT).

We constructed a combined system of a meteorological model and a diffusion model that uses the high-resolution three-dimensional meteorological information obtained through the developed dynamic local

detailed meteorological field modeling technique as input data for HYSPLIT. The radioactive material discharge points of HYSPLIT were set at the locations of the Kori and Hanul nuclear power plants. The diffusion modeling area was composed of the area including the 100 km area around the nuclear power plant in consideration of the diffusion impact range. For the meteorological input data of HYSPLIT, data such as temperature, wind (u, v component), surface pressure, boundary layer altitude, and mixing ratio calculated from the meteorological model are used. Figure 2 shows the coupling diagram of the WRF and HYSPLIT models.

RESULTS

We simulated high-resolution local meteorological field and dispersion modeling using WRF/HYSPLIT for the Kori and Wolsong NPPs from 2013 to 2017 (5 years). The vertically averaged (0~100 m) concentration, deposition, and forward trajectory of Cs-137 emitted from the Kori and Wolsong NPPs were simulated. The radioactive material was released from each NPPs at noon every day and dispersion was simulated for up to 48 hours. In this simulation, the trajectory was simulated assuming that it was emitted at an altitude of about 1500 m (850 hPa), a height representing the typical movement of a synoptic meteorological system.

We analyzed seasonal and 5-year averaged concentration and deposition distributions to understand the general dispersion characteristics in the Kori and Wolsong NPPs. A wind rose diagram was plotted using the 10 m wind direction and speed data observed from the meteorological tower located within each NPP site for reference data to explain the dispersion characteristics of the area around the NPP. The wind rose is a graphical tool used to show wind speed and wind direction for a particular location over a specified period. The wind rose is divided into several spokes which represent the frequency of winds blowing from a particular direction. Here, the Beaufort wind force scale was used as the wind speed scale frequency.

The concentration and deposition distributions near the Kori and Wolsong NPPs showed a seasonal difference, which seems to reflect the influence of the seasonal and local winds. Seasonal winds are the winds that last for a particular season and are caused by changes in temperature. Local winds are caused by the uneven heating of land and water. The local winds are classified into four types – sea breeze, land breeze, valley breeze, and mountain breeze. Seasonal winds tend to be more constant, while local winds are more variable and can change direction quickly. The difference in seasonal dispersion characteristics in each NPP area can be explained by the occurrence characteristics of these seasonal and local winds.

The 5-years averaged concentration distribution near Kori and Wolsong NPPs showed that dispersion was mainly in the ocean direction rather than the inland direction in all seasons and annuals. The averaged concentration and deposition spread along the coast, and the values were inversely proportional to the distance from the NPPs. According to the seasonal distribution of radioactive material dispersed from the Kori and Wolsong NPPs, it was dispersed in the south-east direction during winter, in the north-north-east direction during spring and summer, and in the north-east direction during autumn. This seems to be the effect of the mountainous terrain adjacent to the inland direction of NPPs. As such, the high-resolution dispersion modeling developed in this study reflected the detailed dispersion characteristics that did not appear at low resolution due to the effect of topography.

In addition, the similarity of the averaged concentration patterns for each from 2013 to 2017 means that the 5-year averaged data effectively explains the concentration characteristics near the NPPs. Therefore, the dispersion impact assessment map produced using the 5-year averaged data will also help understand the general dispersion characteristics in the NPP area and can be used as a meaningful reference in case of an accident.

CONCLUSION

In this study, we analyzed the diffusion characteristics of radioactive materials in Kori and Wolsong NPPs using the coupling method of Weather Research and Forecasting (WRF) and Hybrid Single-Particle Lagrangian Integrated Trajectory (HYSPLIT). We suggested considerations for a methodology creating high-resolution and three-dimensional local meteorological fields near the NPPs based on previous studies demonstrating the performance improvement of local meteorological field simulation over complex topography. For the multiscale dynamical downscaling, we then increased the spatial resolution by gradually reducing the size of the domain using the one-way (parasitic) nesting method. We also updated land-use and topography data to improve the model performance of local wind fields around the NPPs. We performed the HYSPLIT model using the improved meteorological fields simulated by the WRF model as input data. The surrounding topography influenced the annual dispersion characteristics of NPPs. Due to the mountainous terrain adjacent to the inland direction of the NPPs, the radioactive material had a higher concentration in the ocean direction. The seasonal characteristics showed the influence of the diffusion direction and speed related to the seasonal wind, which appeared predominantly on the Korean Peninsula.

In the future study, we will analyze the predominant diffusion characteristics in the nuclear power plant area by performing cluster analysis using dispersion modeling results.

REFERENCES

Brioude J, D. Arnold, A. Stohl, M. Cassiani, D. Morton, P. Seibert, et al., 2013: The Lagrangian particle dispersion model FLEXPART-WRF version 3.1. *Geosci Model Dev*., **6(6)**, 1889-1904.

Draxler R. R. and G. D. Hess, 1997: Description of the HYSPLIT_4 modelling system. NOAA technical memorandum ERL ARL-224. Silver Spring, MD, pp. 24.

Draxler R. R. and G. D. Hess, 1998: An overview of the HYSPLIT_4 modelling system for trajectories, dispersion, and deposition. *Aust. Meteor. Mag*., **47**, 295-308.

Lim K.-S. S., J.-M. Lim, H. H. Shin, J. Hong, Y.-Y. Ji and W. Lee, 2019: Impacts of subgrid-scale orography parameterization on simulated atmospheric fields over Korea using a high-resolution atmospheric forecast model. *Meteorol. Atmos. Phys.*, **131(4)**, 975-985.

Srinivas C. V., R. Venkatesan, R. Baskaran, V. Rajagopal and B. Venkatraman, 2012: Regional scale atmospheric dispersion simulation of accidental releases of radionuclides from Fukushima Dai-ichi reactor. *Atmos. Environ.*, **61**, 66-84.

Stein, A. F., R. R. Draxler, G. D. Rolph, B. J. B. Stunder, M. D. Cohen and F. Ngan, 2015: NOAA's HYSPLIT atmospheric transport and dispersion modeling system. *Bull. Amer. Meteor. Soc.*, **96**, 2059-2077.

Stohl A, P. Seibert, G. Wotawa, D. Arnold, J. F. Burkhart, S. Eckhardt, et al., 2012: Xenon-133 and cesium-137 releases into the atmosphere from the Fukushima Dai-ichi nuclear power plant: determination of the source term, atmospheric dispersion, and deposition. *Atmos. Chem. Phys.*. **12(5)**, 2313-2343.

Zhu X., G. V. Iungo, S. Leonardi and W. Anderson, 2017: Parametric study of urban-like topographic statistical moments relevant to a priori modelling of bulk aerodynamic parameters. *Boundary-Layer Meteorol.,* **162(2)**, 231-253.

21st International Conference on
Harmonisation within Atmospheric Dispersion Modelling for Regulatory Purposes
27-30 September 2022, Aveiro, Portugal

DEVELOPMENT OF A DYNAMIC DOWNSCALING METHOD FOR USE IN SHORT-RANGE ATMOSPHERIC DISPERSION MODELLING NEAR NUCLEAR POWER PLANTS

Sang-Hyun Lee[1], Su-Bin Oh[2], Chun-Ji Kim[2], Hyun-Ha Lee[3] and Chun-Sil Jin[3]

[1]Department of Atmospheric Science, Kongju National University, Gongju, Republic of Korea
[2]BomIn Science Consulting, Incheon, Republic of Korea
[3]Korea Institute of Nuclear Safety, Daejeon, Republic of Korea

Abstract: This study presents a new high-resolution (~1 km) meteorological downscaling method for modeling of short-range (<100 km) atmospheric dispersion of accidental NPP plumes. Six considerations from literature reviews have been suggested for a new dynamic downscaling method. The dynamic downscaling method is developed based on the Weather Research and Forecasting (WRF) model version 3.6.1, applying high-resolution land-use and topography data. In addition, a new subgrid-scale topographic drag parameterization has been implemented for a realistic representation of the atmospheric surface-layer momentum transfer. Finally, a year-long simulation for the Kori and Wolsong NPPs, located in southeastern coastal areas, has been made for 2016 and evaluated against operational surface meteorological measurements and the NPPs' on-site weather stations. The new dynamic downscaling method can represent multiscale atmospheric motions from the synoptic to the boundary-layer scales and produce 3-dimensional local meteorological fields near the NPPs with a 1.2 km grid resolution. Comparing the year-long simulation against the measurements showed a salient improvement in simulating near-surface wind fields by reducing the root mean square error of approximately 1 $m \cdot s^{-1}$. Furthermore, the improved wind field simulation led to a better agreement in the Eulerian estimate of the local atmospheric dispersion. The new subgrid-scale topographic drag parameterization was essential for the improved performance, suggesting the importance of the subgrid-scale momentum interactions in the atmospheric surface layer. A new dynamic downscaling method has been developed to produce high-resolution local meteorological fields around the Kori and Wolsong NPPs, which can be used in short-range atmospheric dispersion modeling near the NPPs.

Key words: *Atmospheric dispersion, dynamic downscaling method, subgrid-scale topographic drag, WRF*

INTRODUCTION

Nuclear power plants (NPPs) can affect fatal impacts on the public and the environment in case of unexpected radioactive accidents. The radioactive materials released in the atmosphere can cause severe damage near the NPP and downwind regions by short- and long-range transport. For taking timely actions to mitigate the health and environmental impacts under accidental radioactive conditions, it is essential to predict the atmospheric dispersion of radioactive materials, especially near the accidental site. Atmospheric dispersion models are used in simulating the atmospheric dispersion of radioactive materials. Local meteorology has a crucial influence on atmospheric dispersion in models; therefore, high-fidelity meteorological data is a prerequisite for reliable atmospheric dispersion modeling of radioactive materials. In South Korea, NPPs are sitting on complex terrains close to coastal and mountainous areas. Due to their topographical complexity, the local meteorological fields near the NPPs form complicatedly under different synoptic weather conditions (Lim *et al*., 2019). Lee *et al*. (1997) showed that local sea/land breezes played a critical role in determining the atmospheric concentrations of radioactive materials near the Wolsong NPP. In addition, the importance of wind fields, mainly low-level winds, was emphasized in the atmospheric scalar dispersion, such as radionuclides (Srinivas *et al*., 2012). However, many meteorological models frequently overestimate wind speeds of the atmospheric boundary layer (ABL), despite alleviation efforts, which can result in false atmospheric dispersion of radioactive materials. In this study, we aim to develop a new high-resolution (~1 km) dynamic downscaling method for modeling of short-range (<100 km) atmospheric dispersion of accidental NPP plumes.

MATERIALS AND METHODS

Considerations for a new dynamic downscaling method

This study targets the Kori and Wolsong NPPs sites for a new dynamic downscaling method located on the southeast coast of the Korean Peninsula. Based on literature reviews, we suggest six considerations for a dynamic downscaling method for modeling short-range (<100 km) atmospheric dispersion from the NPP sites as follows: First, the meteorological data should be three-dimensional for use in atmospheric dispersion models and have a high spatial resolution to represent complex local circulations near the NPPs. Dynamic downscaling methods based on regional atmospheric models are frequently used for three-dimensional, high-resolution local meteorological fields. They are accomplished by direct numerical integration of a regional atmospheric model using the initial and boundary conditions obtained from the global climate model (GCM). They can give high-resolution meteorological data by resolving local circulations. Second, the dynamic downscaling method should sufficiently represent multiscale atmospheric interaction processes from the synoptic scale (~1000 km) to the ABL scale (~1 km). The Kori and Wolsong NPPs are situated in complex terrain areas, they are likely to be affected by local circulations and the ABL under different synoptic weather conditions. Third, the dynamic downscaling domain should be large enough to cover the area of approximately 100 km from the NPPs so that short-range atmospheric dispersion modeling sufficiently resolves the hypothetical radioactive influences. Forth, a realistic representation of the land use and topography of the dynamic downscaling domain is essential for better simulation of local meteorology. However, the default land-use and topography data in the WRF model are based on somewhat old data; thus, static data updates will be necessary. Fifth, the subgrid-scale surface drag should be adequately represented so that the dynamic downscaling method can represent the fine-scale terrain effects that are not resolved by the model grid cells. The turbulent momentum transfer is essential in determining wind fields in the ABL, especially over complex terrain areas. It has been shown that subgrid-scale topographic drag parameterization is an efficient way to simulate better near-surface wind fields in regional atmospheric models. Sixth, long-term local meteorological data, including meteorological variabilities of annual, seasonal, and hourly timescales, will be needed to estimate reliable short-range (<100 km) atmospheric dispersions near NPPs. In doing so, the dynamic downscaling method should be fed reliable initial and boundary meteorological conditions from high-fidelity large-scale meteorological forecasts.

Development of a dynamical downscaling method for the southeastern coastal npps in korea

The one-way nesting technique is adopted using the WRF model to produce fine-scale local meteorology near the NPPs from large-scale meteorological forecasts. It is a dynamic technique that downscales coarse meteorological data to fine resolution, and it may be beneficial compared to the two-way (interactive) nesting technique, reducing associated numerical errors. Fig. 1 shows the configuration of four nested grid domains for the Kori and Wolsong NPPs. First, the coarsest domain (D01) covers a broad East Asia region, including Korea, China, and Japan, to represent synoptic meteorological phenomena on a model grid resolution of 32.4 km. Next, the meteorological fields are repeatedly downscaled to 10.8 and 3.6 km grid resolutions, focusing on northeastern Asia and the Korean Peninsula regions. Finally, the dynamic downscaling method produces high-resolution local meteorology for the NPPs with a grid resolution of 1.2 km. The finest domain (D04) covers large areas from the NPPs enough to evaluate short-range atmospheric dispersions from the Kori and Wolsong NPPs.

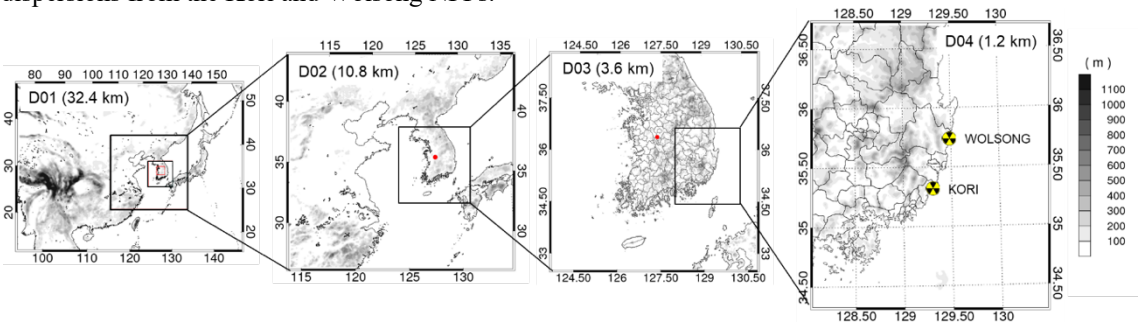

Figure 146. Domain configuration of the dynamic downscaling method for the Kori and Wolsong nuclear power plants (NPPs). Shading denotes the topographic height

This study added a new subgrid-scale topographic drag parameterization in the WRF model to improve the prediction skill of local wind fields near the NPPs. It accounts for the subgrid-scale topographic variation within the dynamic downscaling grid as an enhanced aerodynamic roughness length ('effective roughness length'). In order to determine the effective roughness length, we use an empirical formulation of Zhu *et al*. (2017), obtained from a series of large-eddy simulations under various hypothetical surface heterogeneities, as follows:

$$\frac{z_0}{\sigma_h} = \alpha(1 + \beta s_h) \quad (1)$$

where z_0 is the aerodynamic roughness length, and σ_h and s_h are the standard deviation and skewness of subgrid topographic heights, and α and β are the fitting constants. Here, we use α = 0.1 and β = 0.2 for the non-uniform roughness case.

Along with the new subgrid-scale topographic drag parameterization, local land use and topography of the dynamic downscaling domain are updated with high-resolution national datasets. First, we update the model land-use data using the 1:25,000 land cover dataset of the Korea Ministry of Environment (KME). The dataset is made from satellite imagery, aerial photograph, and field survey of the Korean Peninsula, classifying 22 land-use classes. The converted data were gridded for the WRF Preprocessing System (WPS) database. The forest regions and the urbanized areas near the NPPs are distinctive from the updated land-use distribution. Meanwhile, we update the model topographic height data using the high-resolution Shuttle Radar Topography Mission (SRTM) topography data with a spatial resolution of a 3-arc second (~90 m).

Experimental setup and evaluation method

Long-term simulations of local meteorology have been conducted to evaluate the new dynamic downscaling method for the Kori and Wolsong NPPs. In particular, two simulations of the year 2016 were conducted with and without the subgrid-scale topographic drag parameterization, and they were compared against the surface measurements obtained from the Automatic Synoptic Observing System (ASOS) stations of the Korea Meteorological Administration (KMA) and the on-site meteorological stations of the NPPs. The analysis focused on investigating the effects of the new ingredient in simulating local winds and local dispersion characteristics around the NPPs. The EXP1 is the simulation without the subgrid-scale topographic drag parameterization, whereas the EXP2 is the simulation with the subgrid-scale topographic drag parameterization.

We used the recirculation factor (*RF*) by Allwine and Whiteman (1994) to evaluate the model performance in simulating local dispersion characteristics. The *RF* is defined using the total distance traveled during a fixed period (S) and the resultant transport distance during the period (L) as follows:

$$RF = 1 - \frac{L}{S} \quad (2)$$

The *RF* is a time-integral quantity calculated from wind data collected at fixed time intervals at single meteorological stations. This study estimated the *RF* quantities every day using hourly simulated and measured near-surface wind fields at every measurement station, and the quantity ranges from 0 to 1. As *RF* is close to 1, the endpoint of an air parcel returns to the starting point (high recirculation). In contrast, when *RF* is close to 0, the air parcel transports with little recirculation. The local flows with daily *RF* >0.6 indicate that recirculation dominates, whereas local flows with daily *RF*<0.2 indicate that ventilation dominates.

RESULTS

Evaluation of local winds

Figure 2 shows statistical evaluation results of the simulated near-surface wind speeds against the 22 ASOS measurements. The simulated values at the nearest grid point of the measurement stations were used for the model-measurement comparison, and the MBE and RMSE were calculated for the two experiments with or without the new subgrid-scale topographic drag parameterization. The comparison was made for all-day, daytime (0900~1500 LST), and nighttime (2100~next day 0300 LST) periods. The simulation without the subgrid-scale topographic drag parameterization ('EXP1') overestimated the measured wind speeds for

most stations by approximately 1 $m \cdot s^{-1}$ on average. The wind speed overestimation was more significant in wintertime than in summertime. The RMSE values range from 1.6 $m \cdot s^{-1}$ in June to 2.2 $m \cdot s^{-1}$ in January. In addition, the model overestimated wind speeds in the daytime than in the nighttime. This result is consistent with previous studies that reported overestimated near-surface wind speed in the WRF model. Meanwhile, the simulation with the subgrid-scale topographic drag parameterization ('EXP2') reduced the model's high wind speed biases significantly, ranging the MBE values within ±0.3 $m \cdot s^{-1}$ on average. The RMSE values range from 1.1 m·s-1 in November to 1.4 $m \cdot s^{-1}$ in April. In addition, the improvement of the model performance in simulating local winds was apparent in both the daytime and nighttime.

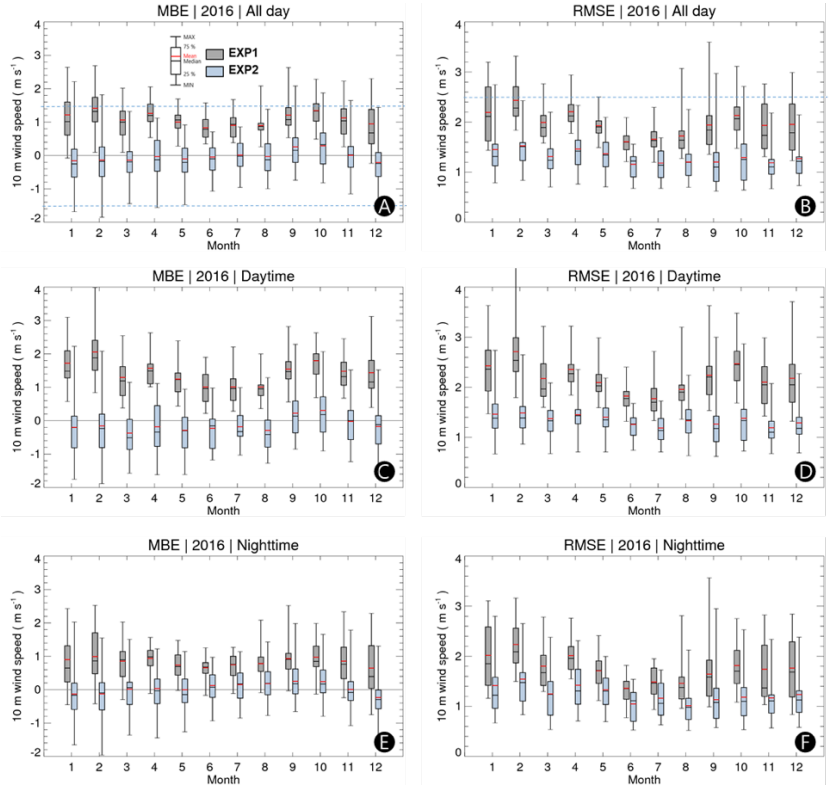

Figure 2. Statistical evaluation results of near-surface wind speeds simulated with and without the subgrid-scale topographic drag parameterization in terms of mean bias error (*MBE*) (left panels) and root mean square error (*RMSE*) (right panels). The daytime period is 0900~1500 LST, and the nighttime is 2100~ 0300 LST.

We further evaluated the model performance in simulating local winds by comparing it against the on-site measurements at the Kori and Wolsong NPPs. Figure 3 shows the RMSE values for the near-surface winds of 2016 simulated with and without the subgrid-scale topographic drag parameterization. The simulation EXP2 significantly improved the poor wintertime model performance of the EXP1, reducing the RMSE from 4.3 $m \cdot s^{-1}$ to 1.4 $m \cdot s^{-1}$ at the Wolsong site in January. These results confirm that the subgrid-scale topographic drag process improves the model performance in simulating local winds near the NPP sites, showing the potential of the new dynamic downscale model for local wind simulations.

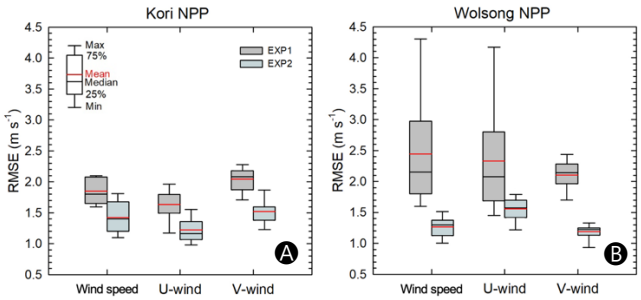

Figure 3. Statistical evaluation results of 10 m wind speed of wind speed of all-component, u-wind, and v-wind in RMSE using meteorological measurement station of (A) Kori and (B) Wolsong NPPs.

Evaluation of local atmospheric dispersion characteristics

The daily RF quantities were calculated for 2016 using hourly simulated and measured near-surface wind fields at the surface measurement stations. Figure 4 compares spatial distributions of the annual mean RF measured and simulated with and without the subgrid-scale topographic drag parameterization. The RF values calculated from the surface measurements ranged from 0.3 to 0.6 over the Kori and Wolsong NPPs domain. The coastal areas near the Kori and Wolsong NPPs had relatively low RF values of approximately 0.2, while recirculation dominates inland mountainous areas. In simulation EXP1, the RF values were lower than 0.3 for most domain areas and less than 0.2 at the Kori and Wolsong NPP sites. Meanwhile, the RF values in the simulation EXP2 increased up to 0.3-0.6 over inland mountainous areas, reducing the model-measurement discrepancy in the EXP1.

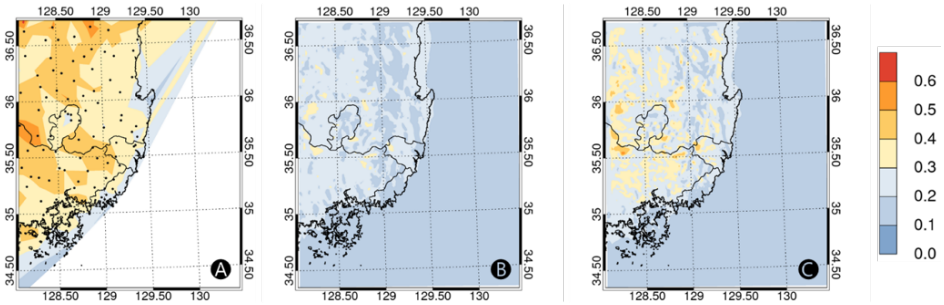

Figure 4. Spatial distributions of the annual mean recirculation factor (*RF*) values estimated from (A) the surface measurements, (B) the simulation EXP1, and (C) the simulation EXP2.

CONCLUSION

The model validation results showed that the new dynamic downscaling method could produce reliable local winds and atmospheric dispersion characteristics near the Kori and Wolsong NPPs mainly by applying the new subgrid-scale topographic drag parameterization. Meteorological models frequently overestimate near-surface wind speeds over complex terrain areas. This study found that updating land-use and topography data, as in many previous studies, has a limitation in reducing common model errors over complex terrain without considering the subgrid-scale topographic drag parameterization. It suggests that subgrid-scale turbulent momentum interaction is essential in modeling high-resolution local winds over complex terrain areas. Because of the good meteorological performance of the dynamic downscaling method, the model reasonably reproduced the atmospheric dispersion characteristics estimated from the near-surface wind measurements over the domain. Overall, the new dynamic downscaling method showed the potential to produce high-resolution local meteorological fields over the Kori and Wolsong NPPs domain. Furthermore, it can generally apply to produce high-fidelity meteorological data over complex terrain areas for atmospheric dispersion modeling purposes. The short-range (<100 km) atmospheric dispersion characteristics of radioactive materials from the Kori and Wolsong NPPs will be investigated using atmospheric dispersion models (e.g, HYSPLIT, Flexpart).

REFERENCES

Allwine K. J. and C. D. Whiteman, 1994: Single-station integral measures of atmospheric stagnation, recirculation and ventilation. *Atmos. Environ.,* **28(4)**,713-721.

Lee G. B., M. C. Lee and Y. I. Song, 1997: A study on mesoscale atmospheric dispersion of radioactive particles released from nuclear power plants. *J. Radiat. Prot*., **22(4)**, 273-288.

Lim K.-S. S., J.-M. Lim, H. H. Shin, J. Hong, Y.-Y. Ji and W. Lee, 2019: Impacts of subgrid-scale orography parameterization on simulated atmospheric fields over Korea using a high-resolution atmospheric forecast model. *Meteorol. Atmos. Phys.*, **131(4)**, 975-985.

Srinivas C. V., R. Venkatesan, R. Baskaran, V. Rajagopal and B. Venkatraman, 2012: Regional scale atmospheric dispersion simulation of accidental releases of radionuclides from Fukushima Dai-ichi reactor. *Atmos. Environ.*, **61**, 66-84.

Zhu X., G. V. Iungo, S. Leonardi and W. Anderson, 2017: Parametric study of urban-like topographic statistical moments relevant to a priori modelling of bulk aerodynamic parameters. *Boundary-Layer Meteorol.,* **162(2)**, 231-253.

21st International Conference on
Harmonisation within Atmospheric Dispersion Modelling for Regulatory Purposes
27-30 September 2022, Aveiro, Portugal

UPDATED ATMOSPHERIC DISPERSION SIMULATIONS AND SOURCE TERM RECONSTRUCTION OF THE FUKUSHIMA ACCIDENT AT LOCAL SCALE

Valentin Jacques[1], Irène Korsakissok[1], Olivier Saunier[1]

[1]IRSN, Fontenay-aux-Roses, France

Abstract: In the event of an accidental release of radionuclides into the atmosphere, IRSN uses atmospheric dispersion models to assess the health and environmental consequences and recommend actions to protect the population. IRSN's operational crisis platform C3X embeds the Gaussian puff model pX used at local scale (~1-50 km) and Eulerian model ldX for regional and continental scale (~50-10000 km). Evaluating these models by comparison with radiological measurements in the environment is a crucial element to estimate the reliability and limitations of their forecasts. Their inputs are meteorological fields and source term (time-varying quantities released into the atmosphere for several radionuclides). To compensate for the lack of key information on the state of the reactor inherent to emergency situations, IRSN has developed inverse modelling methods to improve the source term assessment by simultaneously using measurements in the environment and dispersion models. These methods were applied to the Fukushima accident by using gamma dose rate measurements at Japan scale with the ldX model, but not with the pX model so far.
In the past years, the model pX has been improved to better deal with intermediate spatial scale (up to 50-100 km) and to optimize computational time. In this study, the new version of the model was used to simulate the atmospheric dispersion from the Fukushima accident within 80 km around the plant, using several meteorological fields with different spatial resolutions and several published source terms. The quality of the simulations was then assessed by comparison with different types of measurements. The analysis of statistical indicators showed that using the new version of pX improves the realism of the simulations.
In a second step, inverse modelling techniques were used to estimate source terms based on the new version of the pX model. This set of source terms is obtained by considering several meteorological fields and by varying the input parameters related to the inverse modelling process such as the number of measurements used and the choice of the minimized cost function. The results were then compared with recently published source terms.

Key words: *Fukushima, Gaussian puff model, model-to-data comparisons, inverse modelling, sensitivity study.*

INTRODUCTION

This study presents updated atmospheric dispersion simulations of the Fukushima accident, using IRSN's Gaussian puff model pX within 80 kilometers of the Fukushima Nuclear Power Plant (NPP). In Korsakissok et al., 2013, such model-to-data comparisons were presented, using gamma dose rate observations. The present paper aims to compare these previous results with those obtained with an updated pX model modified to better account for heterogeneous and unstationary meteorological data. In addition, high-resolution meteorological data provided by the Japanese Meteorological Research Institute (MRI) have been used, along with the fields from European Center of Medium-range Weather Forecast (ECMWF), and three source terms from the literature are compared. The objective of these "direct simulations" (by opposition to inverse modelling simulations) is (a) to validate the modifications made in pX's physical schemes in a real, complex case study using statistical and graphical indicators and (b) to quantify the sensitivity to such a model change, compared to that of input data (meteorology and source term). In the second part of this study, an inverse modelling method is used with the pX model to obtain new source terms. The sensitivity to the various configurations is assessed, including specific parameters to inverse modelling. Then, a model-to-data comparison is carried out with these new source terms.

MODEL AND DATA DESCRIPTION

Model description

The Gaussian puff model pX represents physical processes that drive the transport and deposition of pollutants in the atmosphere. It includes advection, diffusion, radioactive decay and filiation, wet scavenging and dry deposition. It was validated both on classical atmospheric dispersion experiments and

compared to environmental measurements within 80 kilometers of the Fukushima NPP (Korsakissok et al., 2013). Atmospheric dispersion simulation of radionuclides emitted during the Fukushima accident was the first use of the pX model at such a long range and highlighted the need for improvements of the physical models embedded within pX in order to better represent heterogeneous meteorological data and interactions between the plume and the unstationary Atmospheric Boundary Layer (ABL). In particular, the following modifications have been implemented since 2013.

1. **The height of the puff centreline is recomputed at each time step, so that the meteorological parameters driving the puff's transport and diffusion are interpolated at a realistic height, representative of the elevation of the plume material as the vertical spread progressively extends.**
2. **The interaction between the plume and the unstationary boundary layer height (BLH) has been improved. In unstable situations, the capping inversion is modelled as a reflecting plane, the number of plume reflections being adapted (between 1 and 4 reflections) to keep the computational error for both concentration and puff centreline below 1%. In stable situations, no reflection on the BLH is considered. To avoid unrealistic re-concentration of the pollutants when the BLH decreases during night times, we keep reflections on a residual height equal to the maximum height that has been "seen" by the puff during its travel.**

In the following results, the pX version used in (Korsakissok et al., 2013) will be named "pX v1, while the version containing the improvements described above will be called pX v2. The standard deviation laws presented here are those of Pasquill, similarly as in (Korsakissok et al., 2013).

Inverse modelling methodology

The method is based on a variational approach consisting in minimizing a cost function which measures the differences between the model predictions $H\sigma$ and the real measurements μ (gamma dose rate measurements), where σ is the source term to estimate and H the Jacobian matrix computed as described in (Winiarek et al., 2012). Each column of H represents the dispersion model's response to a unitary release emitted for one hour, for one radionuclide whose release rate is to be estimated.

The method for inverse modelling using gamma dose rate observations is described in detail in Saunier et al. (2013). The gamma dose rate assessment for each element of H matrix is computed from the activity concentrations and surface activities simulated by the dispersion model (ldX in Saunier et al. (2013), pX in this study). Gamma dose rate measurements sum the direct contribution of the plume (plume radiation) and the gamma radiation emitted by radionuclides that fell to the ground (deposited radiation) through dry and wet deposition processes. To reduce the number of unknown parameters, two steps are defined:

1. Periods during which releases may have occurred are identified. It is assumed that the release is composed of a single radionuclide which acts like a passive tracer. Only the plume component of the dose rate signal is considered at this stage. An automatic algorithm is used to analyse the slope in the dose rate signal and the peaks corresponding to the passage of the plume are extracted.
2. It is then assumed that most of the dose rate signal is due to 8 radionuclides. Some isotopic ratios are fixed (from secular equilibrium or deduced from environmental measurements):

$$\frac{\sigma_{^{137m}Ba}}{\sigma_{^{137}Cs}} = 0.946;\ \frac{\sigma_{^{132}Te}}{\sigma_{^{132}I}} = 1.03;\ \frac{\sigma_{^{137}Cs}}{\sigma_{^{134}Cs}} = 0.94$$

In addition, flexible constraints are added by imposing that the radionuclides be released in realistic proportions. The bounded of the isotopic ratios are assessed by analysing the environmental observations and the knowledge of the core inventory of the FD-NPP:

$$1.67 < \frac{\sigma_{^{132}Te}}{\sigma_{^{134}Cs}} < 16;\ 2 < \frac{\sigma_{^{131}I}}{\sigma_{^{134}Cs}} < 100;\ 0.1 < \frac{\sigma_{^{133}Xe}}{\sigma_{^{134}Cs}} < 10000;\ 0.1 < \frac{\sigma_{^{136}Cs}}{\sigma_{^{134}Cs}} < 0.5 \quad (1)$$

Then, release rates are estimated for each radionuclide by minimizing a cost function that represents the model-to-observations discrepancy:

$$J(\sigma) = \|\mu - H\sigma\|^2 + \lambda^2\|\sigma\|^2 + \sum_{j=1}^{4} r_j(\sigma) \quad (2)$$

With $r_j(\sigma) = \exp\left(\frac{\sigma_j}{\sigma_{134_{Cs}}} - a_j\right) + \exp\left(\frac{\sigma_{134_{Cs}}}{\sigma_j} - b_j\right)$ and a_j and $b_j$are the nuclide ratios defined in (1). In the cost function (2), a regularization term $\lambda^2\|\sigma\|^2$ is added to guarantee stability, existence, and unicity of the solution.

The cost function (2) is obtained assuming that observations errors are Gaussian that led to give more weight to large gamma dose rate values. An alternative is to use Log-Normal observations errors implying the following cost function:

$$[\ln(\|\mu + s\|) - \ln(\|H\sigma + s\|)]^2 + \lambda^2\|\sigma\|^2 + \sum_{j=1}^{4} r_j(\sigma)$$

With a threshold s on measurements and simulations to avoid zero values.

Meteorological datasets

Two sources of 3-D meteorological data are used in this study. The first dataset comprises the fields from the ECMWF at 0.125° spatial resolution and 3-hours time step, already used in previous studies (Korsakissok et al., 2013; Saunier et al., 2013). The second dataset was provided by the MRI at 3-km resolution and 1-hour time step (Sekiyama et al., 2013). More precisely, one member of the ensemble of simulations was used (member 8), following (Quérel et al., 2021).

Concerning the ECMWF data, two different sets of meteorological fields were generated. In Korsakissok et al., 2013, these fields were modified by using wind observations at Fukushima NPP on March 15th, 2011 from 18:00 to 24:00 Japanese standard time. This episode is particularly tricky to simulate, due a conjunction of complex orography (seashore, mountains and valleys), turning wind, and local precipitation. Thus, due to difficulties to accurately reproduce wind observations at the release point, it was decided in Korsakissok et al., 2013 to use homogeneous wind data for this episode instead of the modelled wind fields. In addition, radar rain fields replaced the ECMWF rain forecasts and a constant BLH of 1000 meters was assumed, as the pX version used at this time was not able to correctly model unstationary BLH. In the present study, we use two ECMWF-based datasets, both with radar rain:

- The “corrected” ECMWF dataset, with the modifications carried out for Korsakissok et al., 2013 study (wind observations on March 15th between 18:00 and 24:00 JST, constant BLH of 1000m),
- The “original” ECMWF dataset (with heterogeneous wind and BLH) from 12 to 26 March.

Source terms

Eleven years after the catastrophe, the atmospheric releases due to the Fukushima accident are still uncertain. Here, we use three source terms from the literature: those from (Katata et al., 2015; Mathieu et al., 2012; Saunier et al., 2013). The source term from (Saunier et al., 2013) was determined from gamma dose rate measurements, using the same inverse modelling technique as in this study, but at the Japanese scale with the Eulerian model ldX. (Katata et al., 2015) only reconstructed the release rates of ^{137}Cs, ^{131}I and ^{132}I but not noble gases. Table 52 shows the total emitted quantities for the three selected source terms. While kinetics differ, the total quantities of Caesium and Iodine are of the same order of magnitude.

Table 52. *Total emitted quantities of radionuclides (in Bq) given by (Katata et al., 2015; Mathieu et al., 2012; Saunier et al., 2013), from 12 to 26 March, 2011.*

Bq	Mathieu et al	Saunier et al	Katata et al
Noble gases	6,54e+18	1,21e+19	0,00e+0
Caesium	5,82e+16	3,57e+16	2,89e+16
Iodine	4,09e+17	1,42e+17	1,50e+17
Total	7,18e+18	1,24e+19	2,66e+17

Observations and model-to-data scores

Gamma dose rate observations within 100 kilometers from Fukushima NPP are used for model-to-data comparisons and/or inverse modelling. These are the same as used in Korsakissok et al., 2013 with some

additional stations that were available in the following years. In total, 27 stations were judged to have sufficiently complete and reliable data in this perimeter.
Gamma dose rates at these stations were compared with pX simulation results, using classical statistical scores: Fac2 (resp. Fac5) is the proportion of simulated values within a factor 2 (resp.5) of the observations; Mean Normalized Bias Error (MNBE) and Normalised Mean Error (NME) are also computed, along with the Pearson Correlation Coefficient (PCC), the Figure of Merit in Time (FMT) and the Integrated Fractional Bias Error (IFBE). Most of these scores were used in previous studies (Korsakissok et al., 2013; Saunier et al., 2013). A global score was based on these seven indicators. This "global score" has a mean value of seven, and a lower score indicates a better model-to-data agreement. A "perfect" score obtained by a simulation that would have the best possible values for all indicators would be 1.55. This global score is perfectible and used in conjunction with separate statistical scores and graphical, qualitative analysis.

Results for forward simulations

Forward simulations were carried out with the pX model and 18 configurations: 3 meteorological fields and 3 source terms, both for pX v1 and pX v2. The statistical and qualitative analysis of these results showed that the best results, all configurations considered, were obtained with the new version of pX model, using ECMWF data with radar rain and the source term from Saunier et al, 2013. The global score obtained was 4 (to be compared to 1.55 for a "perfect" model). On average, the global score obtained by all simulations with the new pX version (for the different input datasets) was 6, while the global score of pX v1 was almost 8. The sensitivity of the global score to a change of meteorological fields of source term is of the same order of magnitude as the difference obtained by upgrading the pX model (Figure 147). In other words, model uncertainties are not negligible compared to input data uncertainties. Finally, it is interesting to note that the "corrected" ECMWF fields are not useful anymore with the new version of the pX model. Indeed, the wind fields correction was introduced because of errors in the wind direction in the lower ABL, typically at 10-20 meters height. When recalculating the plume centreline as a function of time, the driving wind direction is then taken at higher levels, which are more reliable.

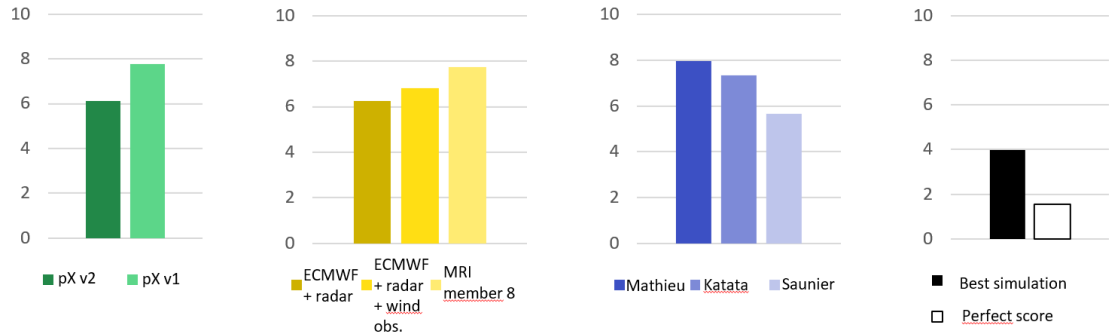

Figure 147: Global score for the different pX simulations on gamma dose rate stations : sensitivity to change in (a) model, (b) meteorological data, (c) source term, and (d) score of the "best" simulation (pX v2, ECMWF+radar, source term from Saunier et al).

Results for inverse modelling

In addition to the various configurations used for direct simulations, parameters specific to the inverse modelling technique were also perturbed: the number of stations used for inversion (10 vs. 27 stations) and the cost function minimized by the algorithm (Gaussian Uniform vs. Log Normal). Thus, 24 configurations were tested, producing 24 source terms that were then used for pX simulations and compared with observations. We showed that in that case, the sensitivity of global indicators to these new parameters was higher than the sensitivity to model version or meteorological data. As in the direct simulations, pX v1 gave better results than pX v2, and ECMWF original fields with radar rain gave the best results. The best results were obtained using 10 stations for inverse modelling and the Log Normal cost function. The total activity for this source term is 4.17 10^{18} Bq, about half that of Saunier et al, 2013.

The source term derived in this study, used with pX in forward mode, has a better global score than all previous configurations. In detail, it significantly improves all statistical indicators compared to the "best simulation" among the direct simulations (Table 53). A graphical comparison of gamma dose rate time series on stations also shows that, in almost all cases, this source term allows to better reproduce the observations compared to all configurations tested in the forward simulations (Figure 148).

***Table 53**: Statistical model-to-data scores obtained on the gamma dose rate stations for pX simulations using ECMWF meteorological data (unmodified) and (a) inverse source term from (Saunier et al., 2013), (b) inverse source term computed in this study. The scores are compared with those of a "perfect" model.*

	PCC	FAC2	FAC5	FMT	MNBE	NME	IFBE	Global
(a) ECMWF / Saunier 2013	0.44	0.42	0.72	0.57	-0.16	0.63	0.24	3.98
(b) ECMWF / This study	0.78	0.79	0.93	0.74	0.03	0.3	0.01	2.14
Perfect score	1	1	1	1	0	0	0	1.55

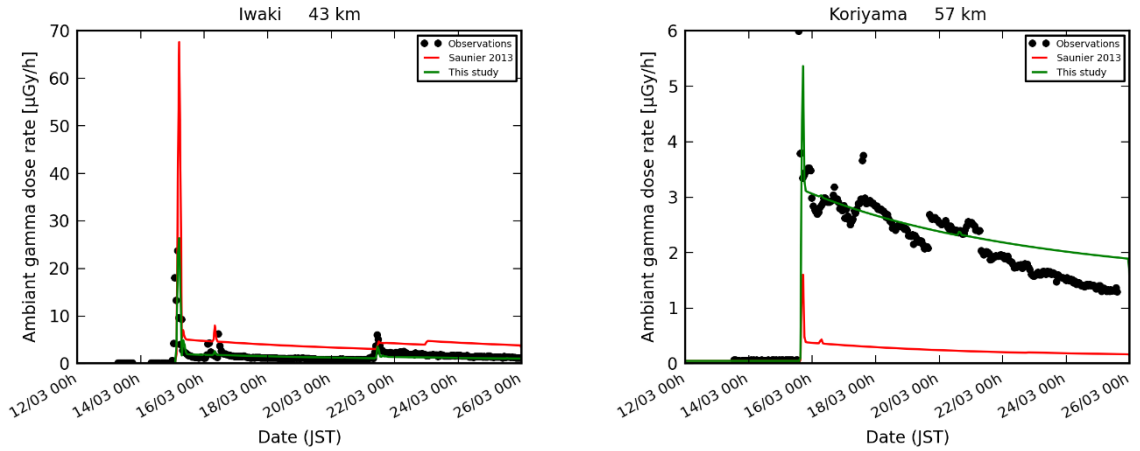

Figure 148: Gamma dose rate as a function of time at two stations: Iwaki, located 43 km south of NPP and Koriyama, 57 km west of NPP, in Abukuma valley. Observations (black dots) are compared with simulations using inverse source term from (Saunier et al., 2013), and inverse source term computed in this study.

CONCLUSION

IRSN's operational Gaussian puff model has been adapted to better represent unstationnary and heterogeneous meteorological data at intermediate scale and was evaluated against gamma dose rate observations on the Fukushima case, up to 80 km of the plant. This model-to-data comparison showed that the physical improvements in the model were able to increase the model's performance. The sensitivity to such a change in the model was shown to be comparable, in order of magnitude, to that of a change in meteorological data or source term. An inverse modelling method was also applied to derive a source term from the gamma dose rate observations. The sensitivity to various parameters, including number of stations and cost function used, was assessed. The best result was obtained by using a subset of 10 stations out of 27 and a Log Normal cost function. The source term constructed with this method was able to significantly improve model-to-data scores. Future work could include using this source term with IRSN's long distance model ldX and continue model-to-data comparisons with other observation data (air activity concentrations and deposition). Using radar rain data with high-resolution MRI meteorological model and/or the whole meteorological ensemble may also bring further improvement.

REFERENCES

Katata, G., Chino, M., Kobayashi, T., Terada, H., Ota, M., Nagai, H., Kajino, M., Draxler, R., Hort, M.C., Malo, A., Torii, T., Sanada, Y., 2015. Detailed source term estimation of the atmospheric release for the Fukushima Daiichi Nuclear Power Station accident by coupling simulations of an atmospheric dispersion model with an improved deposition scheme and oceanic dispersion model. Atmos. Chem. Phys. 15, 1029–1070. https://doi.org/10.5194/acp-15-1029-2015

Korsakissok, I., Mathieu, A., Didier, D., 2013. Atmospheric dispersion and ground deposition induced by the Fukushima Nuclear power plant accident : a local-scale simulation and sensitivity study. Atmospheric Environment 70, 267–279. https://doi.org/10.1016/j.atmosenv.2013.01.002
Mathieu, A., Korsakissok, I., Quélo, D., Groëll, J., Tombette, M., Didier, D., Quentric, E., Saunier, O., Benoit, J.-P., Isnard, O., 2012. Atmospheric dispersion and deposition of radionuclides from the Fukushima Daiichi nuclear power plant accident. Elements 8, 195–200.
Quérel, A., Quélo, D., Roustan, Y., Mathieu, A., 2021. Sensitivity study to select the wet deposition scheme in an operational atmospheric transport model. Journal of Environmental Radioactivity 237, 106712. https://doi.org/10.1016/j.jenvrad.2021.106712
Saunier, O., Mathieu, A., Didier, D., Tombette, M., Quélo, D., Winiarek, V., Bocquet, M., 2013. An inverse modeling method to assess the source term of the Fukushima Nuclear Power Plant accident using gamma dose rate observations. Atmos. Chem. Phys. 13, 11403–11421. https://doi.org/10.5194/acp-13-11403-2013
Sekiyama, T., Kajino, M., Kunii, M., 2013. Ensemble simulation of the atmospheric radionuclides discharged by the Fukushima nuclear accident. Presented at the EGU General Assembly C1 - Vienne, pp. EGU2013-1695.
Winiarek, V., Bocquet, M., Saunier, O., Mathieu, A., 2012. Estimation of errors in the inverse modeling of accidental release of atmospheric pollutant: Application to the reconstruction of the cesium-137 and iodine-131 source terms from the Fukushima Daiichi power plant. J. Geophys. Res. 117, D05122. https://doi.org/10.1029/2011jd016932

21st International Conference on
Harmonisation within Atmospheric Dispersion Modelling for Regulatory Purposes
27-30 September 2022, Aveiro, Portugal

A PROBABILISTIC APPROACH FOR DETERMINING POTENTIALLY AFFECTED AREAS FOR ACCIDENTAL RELEASES

Astrid Kloosterman[1],Chris Twenhöfe1[1], Teun van Dillen[1], and Jasper Tomas[1]

[1] National Institute for Public Health and the Environment (RIVM), Bilthoven, The Netherlands

Abstract: Protective measures such as evacuation, sheltering, and iodine thyroid blocking can avoid or reduce health effects due to exposure to released radioactivity in the air during a nuclear accident. Preparation of these protective measures demands insight into the potentially affected areas. For this, a probabilistic approach is applied to calculate effects of potential releases and some characteristics of the resulting affected areas are studied. This contributes to the development of a robust method for identifying planning zones and provides insight into the relevant indicators for assessing the planning areas.

Key words: *radioactivity, atmospheric dispersion, emergency respons & preparedness, probabilistic calculations*

INTRODUCTION

An accident in a nuclear power plant can result in a release of radioactive materials into the atmosphere. This may lead to radiation exposure away from the release location due to dispersion of the radioactive material. When the radioactive cloud passes, external radiation from the cloud and inhalation of radioactive material in the air will result in a radiation dose. In addition, deposited radioactive material can further increase the dose after cloud passage by exposure to external radiation from the ground. Protective measures such as evacuation, sheltering, or iodine thyroid blocking can avoid or reduce health effects resulting from the radiation dose. The projected dose, received by the population can be compared to predetermined dose criteria and forms a basis for decisions on protective measures. Preparations for this are carried out in so called planning areas which requires a detailed knowledge of the potential affected areas.

Since meteorological conditions strongly influences the potential affected area, a wide range of realistic meteorological conditions need to be considered to identify these areas. For this purpose, probabilistic modelling is particularly well suited and involves the simulation of multiple releases of radioactive material under varying meteorological conditions, covering also the seasonal and day-to-night variations.

In this study, we applied probabilistic modelling using a range of atmospheric releases conditions. We studied some geometrical characteristics of the affected area and its dependance on the duration of the release and on the release height.

METHODS

Model chain

For all scenarios in this study we performed atmospheric dispersion model calculations of approximately 1000 model runs using varying meteorological conditions taken from a database covering three years of meteorological data. Releases were simulated with the dispersion model NPK-PUFF (Tomas *et al.*, 2017, 2019, 2021, De Meutter *et al.*, 2021*)* for every 26th hour between 2015 and 2017 using meteorological data

from the numerical weather prediction model HARMONIE (Bengtsson *et al.*, 2017). This approach provides a representative picture of meteorological conditions including influences of the different seasons as well as day-to-night variations.

Each dispersion calculation is used to evaluate the resulting radiation doses in the effect area in the absence of any protective measures. These doses are then compared with established dose criteria for evacuation, sheltering, and iodine thyroid blocking. Areas above one of these three dose criteria are identified and characterized by its surface area and the maximum distance of its boundary to the release location. This results in a distribution of approximately 1000 distances and areas for each dose criterion for which 50th, 70th, 80th, 90th, and 95th percentiles are calculated. This methodology to determine and characterize the distances is visualized in Figure 1.

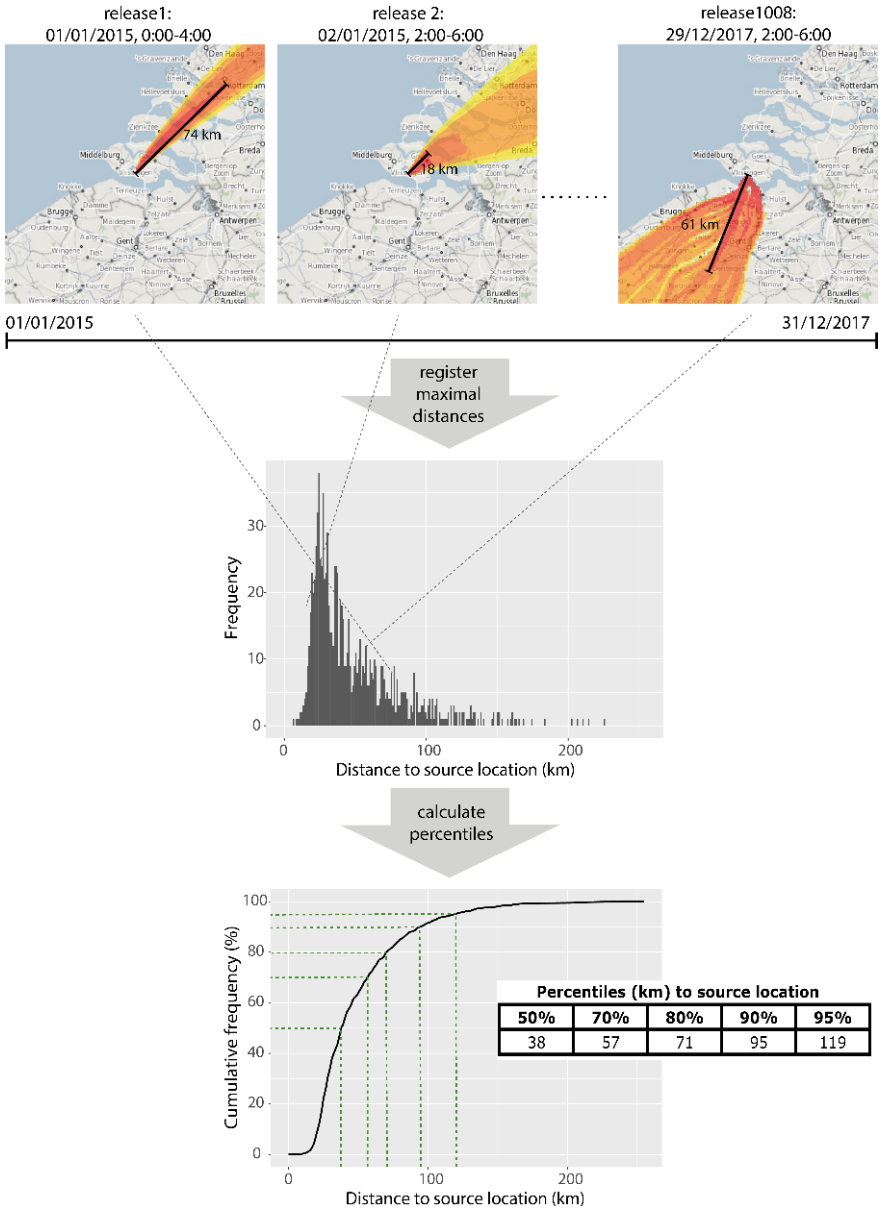

***Figure 149**. A release of radioactive material to the atmosphere is simulated for every 26th hour between 2015 and 2017. We determined the maximum distances (shown in this figure) and surface areas (not shown in this figure) where the calculated dose exceeds the criterionrelated to a certain protective measure. This results in a distribution of maximum distances for which several percentiles are tabulated.*

Release scenarios (source terms)

We considered four scenarios for the release of the radioactive material. Two scenarios represent a large core meltdown accident and are used to study the effect of varying release durations of 4 hour (scenario 1a) and 96 hours (scenario 2b). To study the effect of release height, two scenarios are included having a release height of 25 m (scenario 2a) and 60 m (scenario 2b). More details on these scenarios can be found in ref. Tomas *et al.*, 2021.

Dispersion and dose model npk-puff

We used NKP-PUFF (Gaussian puff methodology) for modelling the atmospheric dispersion of the released radioactivity and calculating the resulting dosimetric endpoints, which enables the subsequent comparison with dose criteria for the protective measures. These endpoints are the effective dose in the first seven days after start of release (evacuation, sheltering) and the thyroid dose for children due to inhalation of iodine radioisotopes in the first seven days after start of release (iodine tablets). The endpoints are calculated on three nested, square grids centered around the release location. The inner (smallest) grid measures 150x150 km with a resolution of 1x1 km, the second grid measures 300x300 km with a resolution of 2x2 km and the largest outer grid measures 600x600 km with a resolution of 4x4 km. This results in a high resolution of output close of to the release location and in lower resolutions further away, limiting calculation times. Due to the domain of the meteorological data, the distances where exceedance of the criteria may occur are limited to 250 km from the source location.

Meteorological data

We used meteorological data from the numerical weather prediction (NWP) model HARMONIE from the Royal Netherlands Meteorological Institute (KNMI) (Bengtsson et al., 2017). The domain covers the Netherlands. These data have a spatial resolution of 2.5 km in the horizontal directions and are available on five vertical levels: 10, 50, 100, 200, and 300 m measured from ground-level.

RESULTS & CONCLUSION

Tables 1-4 list percentiles of the distribution of maximum distances and the distribution of areas where exceeding of dose criteria occurs for the four release scenarios. The distance percentiles can be used as a measure for the distances of the planning areas. The area percentiles provide additional insight into the size of the affected regions. To study the relation between maximum distance and area in more detail, scatter plots of these quantities are shown in Figures 2 and 3.

***Table 54**. Percentiles of maximum distance and surface area for exceeding dose criteria in scenario 1a.*

Measure	**Percentiles (km) distance**					**Percentiles (km^2) surface area**				
Dose criterion	**50%**	**75%**	**80%**	**90%**	**95%**	**50%**	**75%**	**80 %**	**90%**	**95%**
Evacuation (adults) *100 mSv effective dose*	4	6	8	11	14	3	5	7	12	18
Sheltering (adults) *10 mSv effective dose*	16	24	30	42	55	29	56	89	207	592
Iodine tablets (1-year-old) *50 mSv thyroid dose*	38	57	71	95	119	161	310	456	707	1007

***Table 2**. Percentiles of maximum distance and surface area for exceeding dose criteria in scenario 1b.*

Measure	**Percentiles (km) distance**					**Percentiles (km^2) surface area**				
Dose criterion	**50%**	**75%**	**80%**	**90%**	**95%**	**50%**	**75%**	**80 %**	**90%**	**95%**
Evacuation (adults) *100 mSv effective dose*	2	2	3	3	3	2	3	3	4	5

Sheltering (adults) *10 mSv effective dose*	11	14	16	18	21	43	56	65	80	97
Iodine tablets (1-year-old) *50 mSv thyroid dose*	30	37	41	47	55	282	380	449	551	693

***Table 3**. Percentiles of maximum distance and surface area for exceeding dose criteria in scenario 2a.*

Measure	**Percentiles (km) distance**					**Percentiles (km^2) surface area**				
Dose criterion	**50%**	**75%**	**80%**	**90%**	**95%**	**50%**	**75%**	**80 %**	**90%**	**95%**
Evacuation (adults) *100 mSv effective dose*	-	-	1	2	3	-	-	1	1	1
Sheltering (adults) *10 mSv effective dose*	6	8	10	13	17	5	9	13	19	29
Iodine tablets (1-year-old) *50 mSv thyroid dose*	11	16	19	26	33	15	28	44	74	103

***Table 4**. Percentiles of maximum distance and surface area for exceeding dose criteria in scenario 2b.*

Measure	**Percentiles (km) distance**					**Percentiles (km^2) surface area**				
Dose criterion	**50%**	**75%**	**80%**	**90%**	**95%**	**50%**	**75%**	**80 %**	**90%**	**95%**
Evacuation (adults) *100 mSv effective dose*	-	-	-	-	-	-	-	-	-	-
Sheltering (adults) *10 mSv effective dose*	5	7	9	12	15	4	5	7	12	16
Iodine tablets (1-year-old) *50 mSv thyroid dose*	11	16	19	26	33	14	24	37	67	91

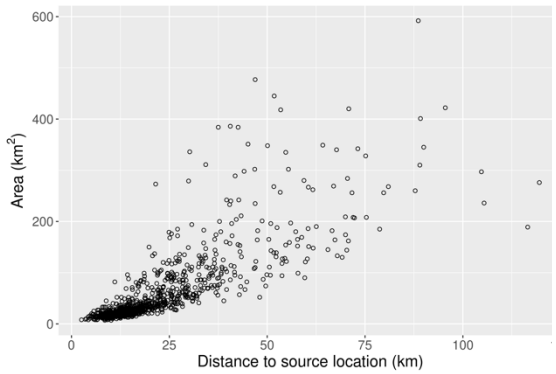

***Figure 150.** Scatter plot of the maximum distance and area for exceeding dose criterion for sheltering for scenario 1a (4 hours release time).*

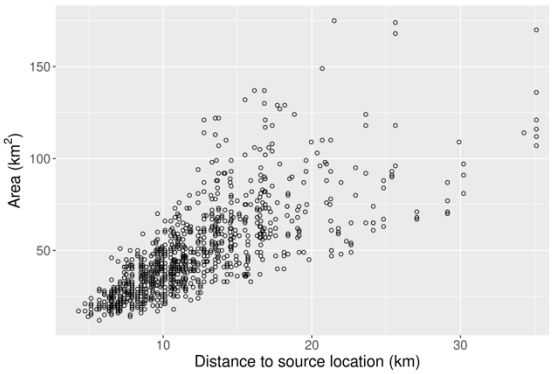

***Figure 151.** Scatter plot of the maximum distance and area for exceeding dose criterion for sheltering for scenario 1b (96 hours release time).*

Release duration

Comparing the results of scenarios 1a and 1b shows that scenario 1a, with a shorter release duration for the same amount of radioactivity, has larger maximum distances and areas. This is a natural consequence of the variability in the meteorological conditions during the 96 hours interval as compared to the 4 hour interval. Also, the difference between the 50th percentiles and the 95th percentiles are relatively larger for scenario 1a. This holds for all dose criteria and for both maximum distances as well as for surface areas. This implies that a potentially affected area has more variations and uncertainties in size and distance for shorter release durations.

Release height

When the release height is increased, the concentration of radioactivity at ground level close to the source will be less. The corresponding dosimetric effect leads to maximum distances that are slightly lower for

heigher release for effective doses. This effect is less pronounces for the maximum distances for the thyroid doses.

CONCLUDING REMARKS

This study presents a methodology for identifying characteristics of planning zones for nuclear accidents. It gives results for two specific scenarios but it also provides insight into indicators that can be applied in deriving planning areas. Furthermore, the methodology can be applied to a wide range of cases where the current meteorological conditions are for example unknown or rapidly changing.

REFERENCES

Bengtsson, L., et al. 2017: The HARMONIE–AROME Model Configuration in the ALADIN–HIRLAM NWP System. Monthly Weather Review **145**(5): 1919-1935.

Tomas, J, A. van Dijk, C. J. W. Twenhöfel, 2017: Modelling atmospheric dispersion of radioactivity with NPK-PUFF using meteorological data from HIRLAM and Harmonie-AROME. 18th Harmonisation within Atmospheric Dispersion Modelling for Regulatory Purposes. Bologna, Italy, 2017:877-81.

Tomas, J. and C. J. W. Twenhöfel, 2019: The effects of uncertainties on the radiological assessment in the (pre-) release phase of a nuclear accident. 19th International Conference on Harmonisation within Atmospheric Dispersion Modelling for Regulatory Purposes, June 2019, Bruges, Belgium.

Tomas, J., V. Peereboom, A. Kloosterman, A. Van Dijk, 2021: Detection of radioactivity of unknown origin: Protective actions based on inverse modelling. Journal of Environmental Radioactivity, 235-236.

Tomas, J, A. Kloosterman, C. J. W. Twenhöfel, T.van Dillen, 2021: Radiologische gevolgen van mogelijke ongevalsscenario's voor Kerncentrale Borssele. RIVM report 2021-0047.

De Meutter, P, C. Gueibe, J. Tomas, P. den Outer, A. Apituley, M. Bruggeman, J. Camps, A. Delcloo, GJ. Knetsch, L. Roobol and L. Verheyen, 2021. The assessment of the April 2020 Chernobyl wildfires and their impact on Cs-137 levels in Belgium and The Netherlands. Journal of Environmental Radioactivity, 237.

21st International Conference on
Harmonisation within Atmospheric Dispersion Modelling for Regulatory Purposes
27-30 September 2022, Aveiro, Portugal

NEW DEVELOPMENTS AND VALIDATIONS OF THE BUILD OPERATIONAL DISPERSION MODEL FOR ACCIDENTAL OR DELIBERATE RELEASES IN COMPLEX AREA

Lionel Soulhac[1], Guillevic Lamaison[2], Perrine Charvolin[2], Chi Vuong Nguyen[2], Mehdi Slimani[3], and Patrick Armand[3]

[1] Univ Lyon, INSA Lyon, CNRS, Ecole Centrale de Lyon, Univ Claude Bernard Lyon 1, LMFA, UMR5509, 69621, Villeurbanne France
[2] Univ Lyon, Ecole Centrale de Lyon, CNRS, Univ Claude Bernard Lyon 1, INSA Lyon, LMFA, UMR5509, 69130, Ecully, France
[3] CEA, DAM, DIF, F-91297 Arpajon, France

Abstract: The accidental or deliberate release of CBRN (Chemical, Biological, Radiological and Nuclear) material into the atmosphere is an important issue for the safety of people and the protection of the infrastructures. In this context, first responders, public authorities and industrial companies need operational simulation tools to take decisions and support actions in emergency situations. Because urban and industrial areas concentrate human population and activities, atmospheric dispersion of CBRN events over complex built-up terrain is the most probable and the most critical situation and the associated physical processes of flow and dispersion have to be described with a specific attention. To reach these objectives, Laboratoire de Mécanique des Fluides et d'Acoustique (LMFA) and Commissariat à l'Energie Atomique et aux Energies Renouvelables (CEA) develop an operational dispersion model, called BUILD (Building Urban and Industrial Lagrangian Dispersion model), which is dedicated to simulate the transport of CBRN pollutants in complex built area. The BUILD model is based on a "SIRANE like" improved parametrization for the dense part of an urban area (Soulhac et al., 2011, 2012, 2017) associated with an obstacle-wake parametrization to describe the flow upwind and downwind of buildings. A stochastic Lagrangian particles approach is coupled with the simplified flow defined above to simulate the transport and dispersion of pollutants in the domain. Different kind of sources can be considered and specific processes like plume rise, deposition and radioactive decay are considered. The BUILD model has been optimized, with parallelization and domain splitting, in order to simulate the dispersion in a complex buildings arrangement in a computational time less than one minute on a laptop. The present paper describes the new developments and physical parameterizations of the model, added to represent the complex features of the flow around an isolated building or around a group of buildings of any organisation. These developments have been validated against wind tunnel data and CFD RANS and LES simulations on different idealized configurations geometries.

Key words: *Atmospheric dispersion modelling, emergency response, Lagrangian model.*

INTRODUCTION

The accidental or deliberate release of CBRN (Chemical, Biological, Radiological and Nuclear) material into the atmosphere is an important issue for the safety of people and the protection of the infrastructures. In this context, first responders, public authorities and industrial companies need operational simulation tools to take decisions and support actions in emergency situations, more specifically in the case of accidental or deliberate release within an urban or industrial complex-built area where human population and activities are concentrated. To reach these objectives, LMFA and CEA develop an operational dispersion model, called BUILD (Building Urban and Industrial Lagrangian Dispersion model), which aims to simulate the transport of CBRN pollutants in complex built area. The BUILD model is based on a "SIRANE like" improved parametrization for the dense part of an urban area (Soulhac et al., 2011, 2012, 2017) associated with an obstacle-wake parametrization to describe the flow upwind and downwind of buildings. A stochastic Lagrangian particles approach is coupled with the simplified flow defined above to simulate the transport and dispersion of pollutants in the domain. Specific processes like plume rise, deposition and radioactive decay are considered. The BUILD model has been optimized, with

parallelization and domain splitting, in order to simulate the dispersion in a complex buildings arrangement in a computational time less than one minute on a laptop.
The next section describes the URBAN (Universal Recognition of Buildings Area & Network) geometrical preprocessor. Then we introduce the parameterization of the flow inside the canopy and around an obstacle. Afterwards, the Lagrangian dispersion model is described. Finally, the last section presents two case studies used to validate BUILD: isolated obstacle (Gamel, 2015) and idealized street network (Garbero, 2010).

Urban geometrical preprocessor

BUILD relies on a simplified description of the geometry of the site considered. The area is divided into 1 km x 1 km tiles. Each tile is described with a resolution of 1 meter. Several image processing algorithms are then applied in order to simplify the geometry of the buildings and to identify the topology and characteristics of the site (**Figure 152**). Recent developements have been done in order to estimate the boundary of the roughness sublayer and to evaluate the geometry of the recirculation zone upwind obstacles (**Figure 153**).

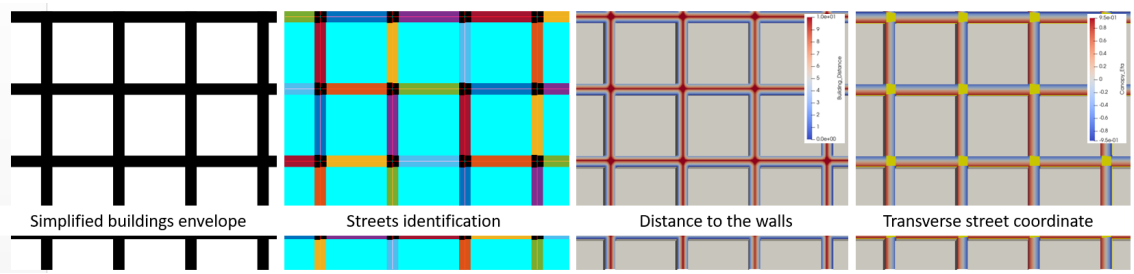

***Figure 152**. Steps of the URBAN geometrical preprocessor on an idealized street network.*

a) Boundary of the roughness sublayer (orange lines) above an isolated obstacle (grey square)

b) Recirculation zones (grey zones) of industrial buildings (white shapes)

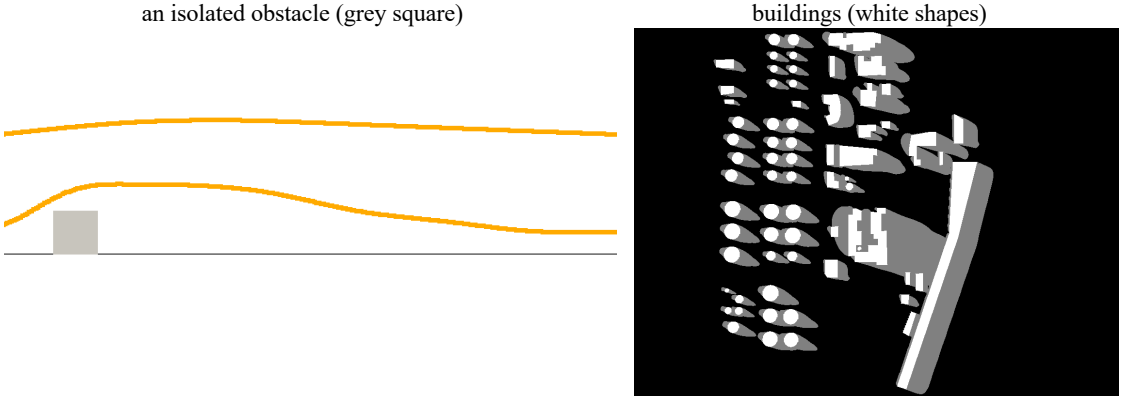

***Figure 153**. Boundary of the roughness sublayer above an isolated obstacle (a) and recirculation zones around industrial buildings considering a 290° wind direction (b) estimated by the URBAN geometrical preprocessor.*

WIND FLOW AND TURBULENCE PARAMETERIZATION IN THE BUILDING CANOPY

Street network model

Thanks to the geometrical preprocessor, each pixel of the domain is located in relation to the streets. Its coordinates in the local coordinates system are determined by means of the two variables $\eta = 2y/W$ and $\zeta = 2z/H - 1$ (**Figure 154**-a). The mean longitudinal velocity in each street is assumed uniform (**Figure 154**-b) and parameterized following the approach implemented in the SIRANE model (Soulhac et al., 2008, 2011). The transverse velocity field is defined with linear profiles, in agreement with the experimental data of Salizzoni et al. (2011) (**Figure 154**-c):

$$\begin{cases} \overline{v}(\eta,\zeta) = v_{\text{street}} f_v(\eta) g_v(\zeta) \\ \overline{w}(\eta,\zeta) = w_{\text{street}} f_w(\eta) g_w(\zeta) \end{cases} \text{ with } \begin{cases} f_v(\eta) = 1-\eta^2 \\ g_v(\zeta) = \zeta \\ f_w(\eta) = \eta \\ g_w(\zeta) = 1-\zeta^2 \end{cases} \quad (1)$$

where v_{street} is calculated as proportional to the perpendicular component of the friction velocity of the overlying surface boundary layer and w_{street} deduced from the continuity equation ($w_{\text{street}} = H/W \,.\, v_{\text{street}}$). Similarly, the turbulent kinetic energy field in each street is assumed to be uniform, with a value related to the external friction velocity: $k_{\text{street}} = 0.5u_*$.

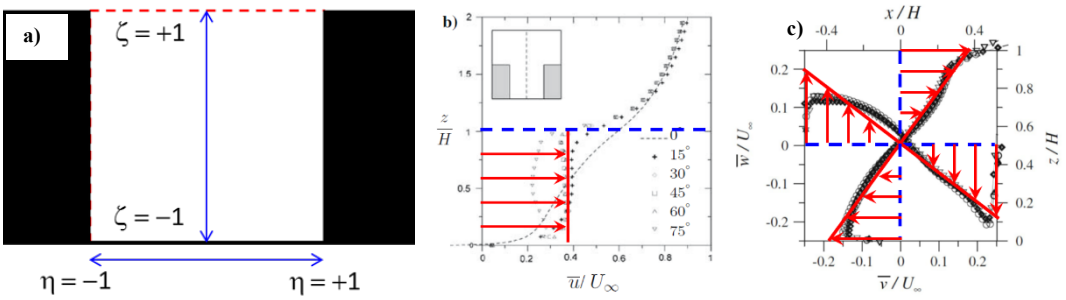

***Figure 154**. Parameterization of the flow in each street: a) local coordinate system, b) longitudinal mean velocity with numerical profiles of Soulhac et al. (2008), and c) transverse mean velocity field with experimental profiles from Salizzoni et al. (2011)*

Building wake model

In the case of low building density, the BUILD model represents the large recirculation area downwind of the obstacle (Hosker, 1985) which is the main feature of the flow around each obstacle. An advection-diffusion process of the velocity defect in the wake of the obstacle has been implemented to determine the shape of the recirculation zone. This process has been emulated by an image processing algorithm, using translation-blurring of the image of each building. The boundary of the recirculation is estimated by thresholding the grayscale velocity defect field, adjusting the threshold to get the recirculation length provided by empirical rules (Hosker, 1985). Once the geometry of the recirculation is known, similar parameterizations to equations 1 are used to evaluate the velocity field inside each recirculation (**Figure 155**).

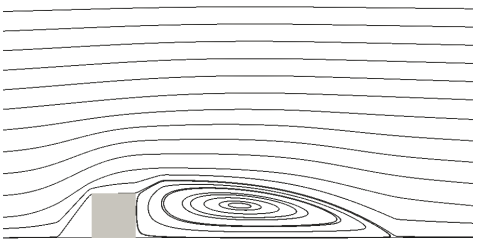

***Figure 155**. Steamlines of the velocity field around an isolated obstacle*

Lagrangian dispersion model

BUILD models the turbulent dispersion using a stochastic particle approach, based on the tracking of Lagrangian trajectories of individual particles in the velocity and turbulence field defined previously. The temporal evolution of the i^{th} component of the Lagrangian velocity of each particle is evaluated with the relation:

$$U_i(t) = \overline{U}_i(t) + U_i'(t) \text{ with } U_i'(t+dt) = U_i'(t) + dU_i' \quad (2)$$

where the mean Lagrangian velocity $\overline{U}_i$ is equal to the local Eulerian velocity $\overline{u}_i$. The evolution of the fluctuating velocity U_i' is determined by the stochastic differential equation (Thomson, 1987):

$$dU_i' = a_i(\boldsymbol{X}, \boldsymbol{U}', t)dt + \sum_j b_j(\boldsymbol{X}, \boldsymbol{U}', t)d\xi_j \quad (3)$$

where a_i and b_j are expressed in terms of standard deviations of the velocity fluctuations σ_{u_i} and of the Lagrangian times $T_{L,i}$. Once the numerical particles have been transported using the previous equations, the concentrations are calculated dividing the sum of the mass of all the particles present in a grid cell by the volume associated to this grid cell.

VALIDATIONS OF THE BUILD MODEL

Isolated obstacle

BUILD has been validated against wind tunnel data and CFD RANS and LES simulations on two case studies. The first one deals with the flow around an isolated obstacle. This case, considering a bi-dimensional obstacle, is used to evaluate the building wake model. **Figure 156** and **Figure 157** compare vertical profiles of the wind speed and the turbulent kinetic energy estimated by BUILD in respect to wind tunnel data (PIV) and CFD RANS and LES simulations. The results show a good agreement of BUILD estimates with experimental and RANS data downwind the obstacle. However, the results show higher discrepancies between BUILD estimates and the others data concerning the vertical profile above the obstacle, at $x/H = 0$ (H is the obstacle height). Indeed, BUILD fails to model the turbulent kinetic energy increase and the negative wind speed just above the obstacle, indicating the presence of a recirculation zone. It is due to the fact that the building wake model implemented into BUILD focuses on the recirculation zone downwind buildings.

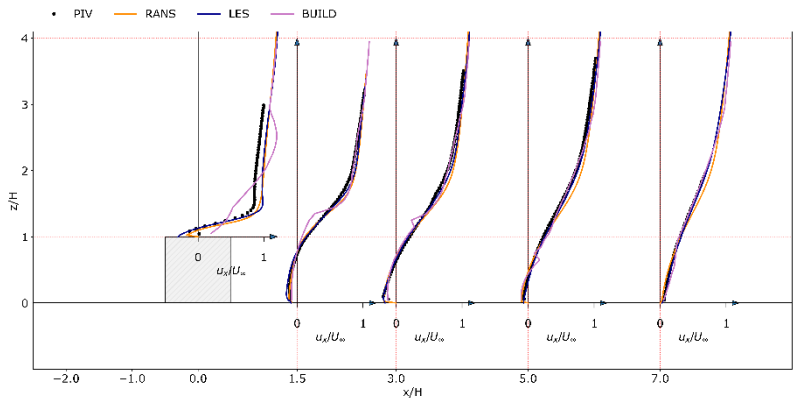

***Figure 156**. Vertical profiles of the dimensionless wind speed, u_x/U_∞, in the case of isolated obstacle (grey square). u_x, U_∞, and H denote the x component of the wind speed, the norm of the wind speed at the top of the boundary layer, and the obstacle height.*

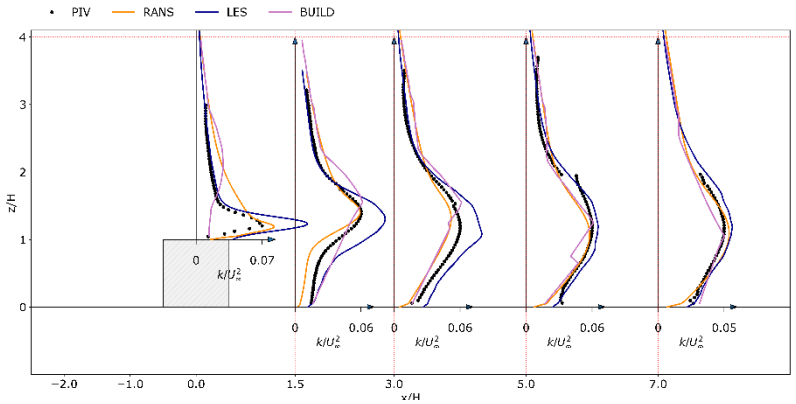

***Figure 157**. Vertical profiles of the dimensionless turbulent kinetic energy, k/U_{∞}^2, in the case of isolated obstacle (grey square). k, U_{∞}, and H denote the turbulent kinetic energy, the norm of the wind speed at the top of the boundary layer, and the obstacle height.*

Idealized street network

The second case study deals with the flow and the dispersion within and above an idealized street network. This case is used to evaluate the street network and the Lagrangian dispersion models implemented in BUILD. **Figure 158** compares horizontal profiles at $z = 0.5H$ and $z = 2H$ of the concentration estimated by BUILD in respect to wind tunnel data (FID) and a RANS simulation with a wind direction of 30 °. The results indicate that BUILD models correctly the horizontal variability of the concentration within the street network and above the urban canopy. Moreover, BUILD estimates are in the same order of magnitude as the FID data, with nevertheless higher discrepancies for the farthest profiles.

a) $z = 0.5H$ b) $z = 2H$

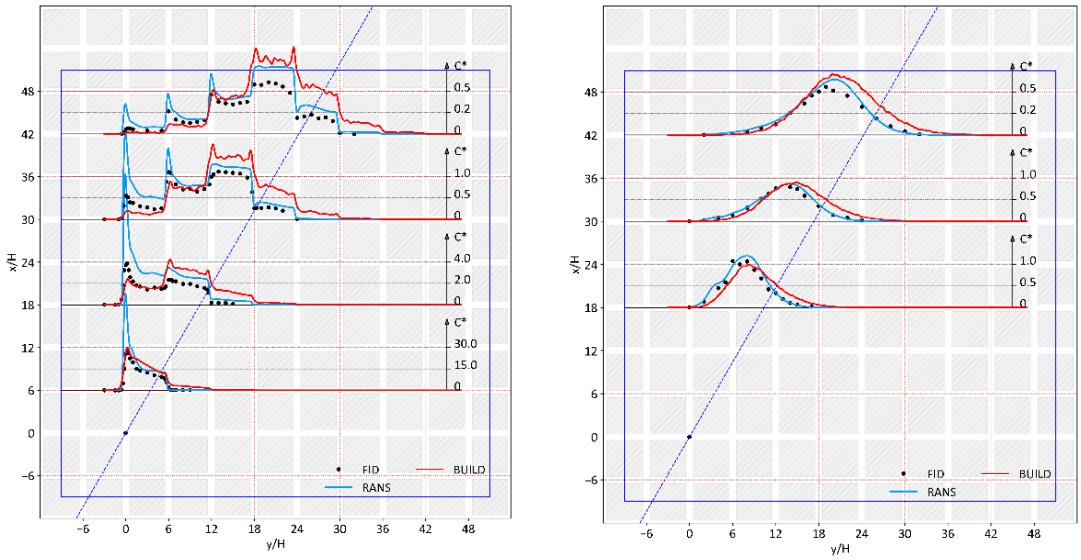

***Figure 158**. Horizontal profiles at $z = 0.5H$ (a) and $z = 2H$ (b) of the dimensionless concentration, $C^* = CU_{\delta}\delta^2/Q$, in the case of street network with a wind direction of 30 ° (in respect to the x-axis). The grey squares represent the buildings, the blue square shows the domain considered with the CFD RANS simulation, the blue dash line indicates the wind direction axis, and the blue point indicate the source position (located within an intersection at $z = 0.5H$). C, U_{δ}, Q and H denote the concentration, the wind speed at $\delta = 4H$, the source rate, and the buildings height, respectively.*

CONCLUSION

This article presents the main features of the BUILD model for the simulation of atmospheric dispersion at the local scale, based on simplified parameterizations of the influence of buildings and obstacles, especially

in urban or industrial environments. The comparison on two case studies of BUILD estimates with experimental data and CFD simulations shows that BUILD success to model the main features of the flow downwind an obstacle and the dispersion of pollutants within and above a street network.

REFERENCES

Gamel, H. (2015). Caractérisation expérimentale de l'écoulement et de la dispersion autour d'un obstacle bidimensionnel (Doctoral dissertation, Ecully, Ecole centrale de Lyon).

Garbero, V., Salizzoni, P., & Soulhac, L. (2010). Experimental study of pollutant dispersion within a network of streets. *Boundary-layer meteorology*, **136(3)**, 457-487.

Hosker, R. P., 1985. Flow around isolated structure and building clusters: a review. In ASHRAE Transactions.

Salizzoni, P., Marro, M., Soulhac, L., Grosjean, N. & Perkins, R.J., 2011. Turbulent Transfer Between Street Canyons and the Overlying Atmospheric Boundary Layer. *Boundary-Layer Meteorology*, **141(3)**, 393 414.

Soulhac, L., Perkins, R. J., & Salizzoni, P. (2008). Flow in a street canyon for any external wind direction. *Boundary-Layer Meteorology*, **126(3)**, 365-388.

Soulhac, L., Salizzoni, P., Cierco, F. X., & Perkins, R. (2011). The model SIRANE for atmospheric urban pollutant dispersion; part I, presentation of the model. *Atmospheric environment*, **45(39)**, 7379-7395.

Soulhac, L., Salizzoni, P., Mejean, P., Didier, D., & Rios, I. (2012). The model SIRANE for atmospheric urban pollutant dispersion; PART II, validation of the model on a real case study. *Atmospheric environment*, **49**, 320-337.

Soulhac, L., Nguyen, C. V., Volta, P., & Salizzoni, P. (2017). The model SIRANE for atmospheric urban pollutant dispersion. PART III: Validation against NO2 yearly concentration measurements in a large urban agglomeration. *Atmospheric environment*, **167**, 377-388.

Thomson, D. J., 1987. Criteria for the selection of stochastic models of particle trajectories in turbulent flows. *Journal of Fluid Mechanics*, 180, 529 56.

21st International Conference on
Harmonisation within Atmospheric Dispersion Modelling for Regulatory Purposes
27-30 September 2022, Aveiro, Portugal

STUDY OF THE UNCERTAINTIES FOR CONCENTRATION IN THE REALISTIC BUILT-UP AREA OF PARIS, THE SURE PROJECT

Olivier Oldrini[1], Patrick Armand[2], Sylvie Perdriel[3] and Christophe Duchenne[2]

[1]MOKILI, Paris, France
[2]CEA DAM DIF, Arpajon, France
[3]AmpliSIM, Paris, France

Abstract: Usage of more complex, 3D-meshed, atmospheric dispersion models (ADMs) for decision-making is increasing due to integration of parallel algorithm in models and to the availability of parallel computing power. Such models are usually deployed for calculation in urban domains. Such areas lead to complex flow and dispersion patterns with high variability according to the incoming wind and the source location. In this paper, the variance of concentration for a typical accidental or malevolent release in a realistic urban setup was investigated. The project, named SURE (Simulate UnceRtainties in case of Emergencies), investigated the variances due to an ensemble of 21 meteorological members and 27 possible source locations. A preliminary analysis was performed and demonstrated its interest in helping understand the probable variability of the plume and anticipate specific behaviors of the plume in support of crisis management.

Key words: *emergencies, crisis management, uncertainties, parallel computing, PMSS, built-up area, urban setting, the SURE project, high resolution*

INTRODUCTION

Usage of more complex, 3D-meshed, atmospheric dispersion models (ADMs) for decision-making (see for instance Armand et al. 2021) is increasing due to integration of parallel algorithm in models and to the availability of parallel computing power. Such models are usually deployed for calculation in urban domains that require very fine grid steps and where flow and dispersion are complex. Complex flow patterns are exemplified by wind deflection causing updrafts or downdrafts, channeling between the buildings, acceleration between the obstacles or deceleration behind them. In the vicinity of obstacles, horizontal or vertical rotating-eddies are taking place. These flow effects combine together to transport airborne species, flushing them from relatively high-speed areas while trapping them in low speed areas. These complex flows can therefor lead to very different concentration patterns depending on the source location and the flow conditions.

In this paper, we try to estimate the variance of concentration for a typical accidental or malevolent release in a realistic urban setup. We rely on the setup of the EMERGENCIES project, using a very large urban setup of 40 x 40 km over the Greater Paris area. The domain is using a horizontal grid with at 3 m resolution, and the release is occurring in the vicinity of the Grand and the Petit Palais museum right in the center of Paris. This project, named SURE (Simulate UnceRtainties in case of Emergencies), is dedicated to estimate the variances of concentration due to uncertainties both for the source location and the meteorological forecast. After describing the simulation setup relying on 27 locations for the release term, combined with 21 individual realizations for the meteorological forecast, we will briefly describe the wind flow ensemble before discussing some interesting features of the preliminary results obtained regarding the concentration ensemble.

SIMULATION SETUP

The SURE project uses the calculation domain taken from the EMERGENCIES project (Oldrini et al. 2021) and covering the Greater Paris Area (Figure 1). The domain dimensions are 38.4 x 40.8km, with a horizontal mesh size of 3m, and consists of 12 668 x 13 335 grid points. The vertical mesh has 39 grids points up to 1 000m, the first level above ground being at 1.5m. The domain is decomposed in 1 088 subdomains of 401 x 401 points, which are computed in parallel. The model used is the Parallel Micro SWIFT SPRAY (PMSS) model (Oldrini et al. 2017 and 2019), combining a parallel urbanized diagnostic model with a parallel Lagrangian particle model.

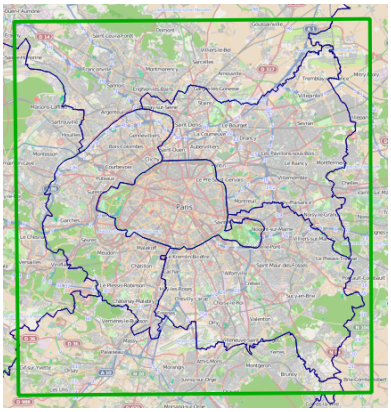

Figure 159. *Domain covering the Greater Paris area*

The meteorological ensemble relies on the mesoscale inputs from the German ICON-D2 model (Reinert et al. 2020), with a horizontal grid resolution of around 2.1km. The German Meteorological Office produces a deterministic simulation, referenced as det0, plus 20 perturbations, pert1 through pert20. The day used for the simulation was the 12th of July 2021, and the 21 SWIFT meteorological calculations were performed between 6am and 12am.

The dispersion scenario consists of a release of 1kg of a passive fictious specie with a duration of 10min and starting at 7am. The dispersion simulation is run for 5hrs between 7am and 12am. 40 000 particles are emitted by the model every 10s, hence 4.8 millions of Lagrangian particles are emitted during the 10min release. The source is located in the vicinity of the Grand Palais and the Petit Palais Museum, in the center of Paris. To take into account the uncertainty regarding the source location, 27 geographic locations have been taken into account. These locations are a combination of 9 horizontal locations (see Figure 2) and 3 vertical heights, 2, 20 and 40m above the ground. The release locations are numbered from 0 to 26: the releases are numbered from west to east, then from north to south, then from ground to upper air. The horizontal spread of the releases is around 100m from west to east and from north to south.

Figure 160. *9 ground locations of the release between the Grand Palais (left side building) and the Petit Palais (right side building) as red dots.*

The calculations were performed on the Topaze supercomputer of the Centre Commun Recherche et Technologie (CCRT) at the CEA. The supercomputer has 864 computing nodes, each node consisting of 2 AMD EPYC Milan processors at 2.45GHz. Each node has 128 computing cores and 256GB of RAM.

The calculation for the 21 meteorological scenarios were performed first and produced around 2.4TB of data for each member. They used 1089 computing cores each and lasted around 50min. The calculations for the dispersion consist of 567 dispersion scenarios, because of the 27 possible locations combined with the 21 meteorological members. Each dispersion simulation required 500 computing cores and lasted around 1h30 The storage of the 27 dispersion members associated with one meteorological member required between 3 and 5TB.

PRELIMINARY WIND FLOW ANALYSIS

In order to get an overview of the variability of the wind flow, statistics have been derived regarding the profile closest to the location of the release near the museum. **Table 55** and **Table 56** present the average and the standard deviation regarding the wind at three heights above ground in this location. The average wind speed close to the ground is around 2.5m/s, and the wind is mainly from the south east, with a small rotation of the wind from 140 to 170° during the time frame. The standard deviation of the wind close to the ground is more intense for the east west component, ranging from 0.64m/s up to 1.44m/s, than the north

south one, ranging from 0.37m/s up to 0.87m/s. The wind direction standard deviation is mainly between 10 and 20°.

Table 55. *Average over the meteorological ensemble of the wind profile closest to the source*

Hour	wind speed (m/s)			wind direction (°)		
	10m	**37m**	**77m**	**10m**	**37m**	**77m**
6h	2.0	3.3	4.2	142	143	145
7h	2.4	3.7	4.4	134	136	138
8h	2.6	4.0	4.6	143	144	145
9h	2.7	4.2	4.8	162	163	164
10h	2.6	4.0	4.6	171	173	173
11h	2.7	4.1	4.6	166	168	169
12h	2.5	3.7	4.2	167	168	169

Table 56. *Standard deviation over the meteorological ensemble of the wind profile closest to the source*

Hour	U/V components (m/s)			wind direction (°)		
	10m	**37m**	**77m**	**10m**	**37m**	**77m**
6h	0.64 / 0.53	0.94 / 0.80	1.08 / 0.87	18	16	15
7h	0.51 / 0.37	0.78 / 0.59	0.89 / 0.71	13	12	12
8h	0.85 / 0.57	1.3 / 0.90	1.51 / 1.03	17	16	16
9h	0.52 / 0.59	0.78 / 0.98	0.90 / 1.20	11	11	11
10h	0.84 / 0.75	1.27 / 1.20	1.45 / 1.39	19	19	20
11h	0.78 / 0.60	1.16 / 0.97	1.30 / 1.14	17	17	17
12h	1.44 / 0.87	2.11 / 1.32	2.36 / 1.51	32	31	31

PRELIMINARY ANALYSIS AND DISCUSSION REGARDING THE CONCENTRATION

In order to perform a first analysis and discussion of the 567 concentration fields obtained, we performed both a statistical analysis and studied samples from specific members.

Statistical analysis

The statistical analysis has been performed using the Climate Data Operators (CDO) from the Max-Planck-Institut für Meteorologie. The statistical treatment performed have been the calculation of the mean, of the standard deviation, and also of the probability of exceeding a critical threshold. Not all the initial analysis performed will be presented here. We will try to focus on other results than the ones emphasizing the larger spread of the ensemble compared to a single deterministic scenario, and on the obvious influence of the meteorology on the direction of the plume. The **Figure 161** presents the ensemble average in the vicinity of the release locations and will be used to explain the patterns in the subsequent figures.

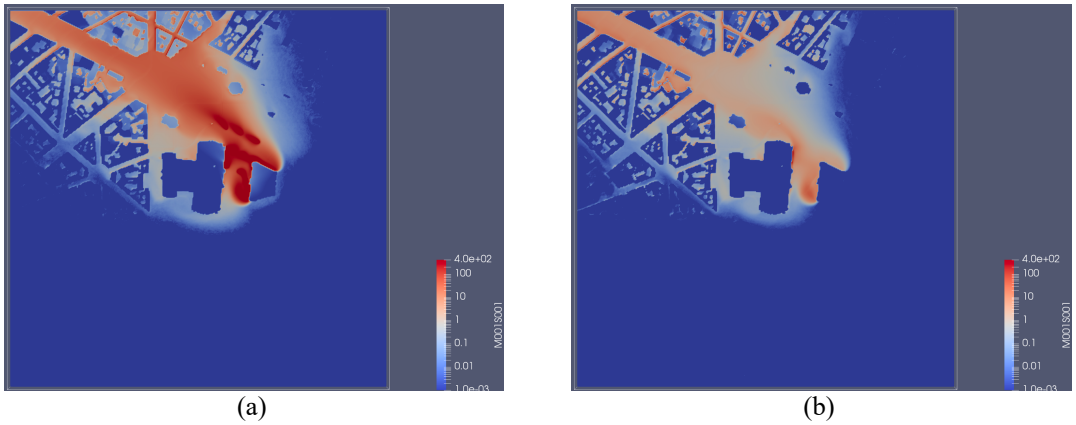

(a) (b)

Figure 161. Ensemble average over the 567 members of the concentration near the ground, at 7h10 (a), hence at the end of the release, and 7h30 (b), hence 20mn after the end of the release.

The **Figure 162** displays the ratio of the standard deviation of the concentration to the average concentration, computed using the 567 members of the concentration ensemble. Apart from the obvious impact of the boundaries of the average plume, where the concentration is very low, and where the ratio of the standard deviation to the average is large, two features are interesting: two patterns of high variance in locations with high concentration, because they are in the interior of the average plume. The first pattern is more discernable at 7h10, even if it is still visible at 7h30, and is located just north east of the release point and oriented from the north west to the south east. The second pattern can be seen between the two large buildings (Grand Palais and Petit Palais from west to east) and in the wake of the Grand Palais up to the small buildings in its wake. These two patterns of high variance in high concentration areas materialize probably the separation areas of two different behaviors of the dispersion: either the pollutant is mainly entrapped between the large buildings, with a small initial spread, and a longer time to disperse that tends to keep it inside the streets in the west. Or the pollutant is more influenced by the free flow, with an initial dispersion that leads to higher concentration to the north west of the Petit Palais and an initial transport to the narrow streets north of the museum.

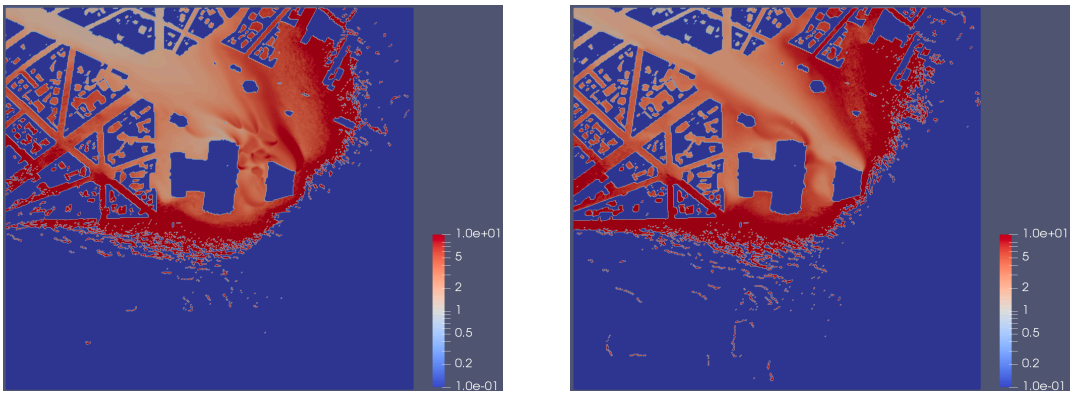

(a) (b)

Figure 162. Ratio of the standard deviation of the concentration to the average concentration, computed using the 567 members of the concentration ensemble, at 7h10 (a) and 7h30 (b).

The **Figure 163** displays the probability of exceeding a critical threshold, but with statistics limited to a part of the ensemble: the concentration members related to the source location 0, then to location 8, which are respectively the more north western, the more south eastern location. Both sources are near the ground. The elements the most noticeable, which are related to the entrapment of the pollutant between the Grand and the Petit Palais are: first the time delay of roughly 30mn for the probability to exceed the threshold to clear significantly the area, and secondly the lateral spread of the entrapment area. Regarding the entrapment of the pollutants in the enclosed courtyard in the denser build-up areas, the intensity and location of such places are quite similar in both cases, at least for the most significant ones.

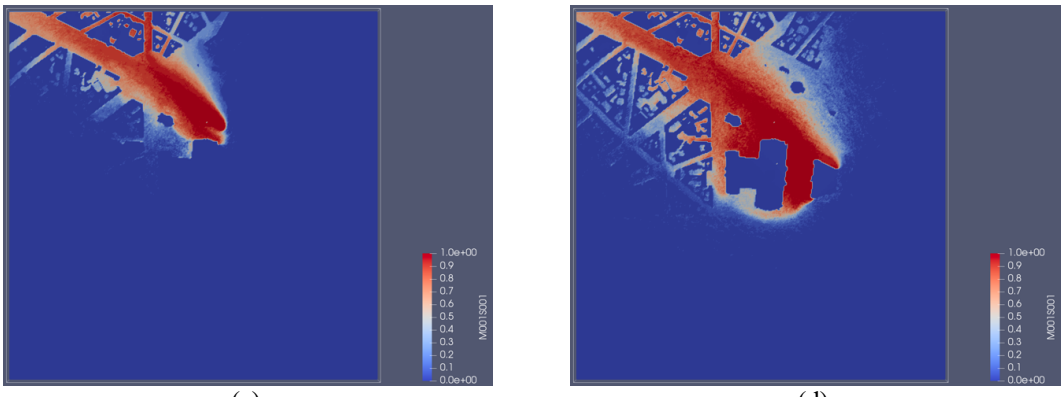

(a) (d)

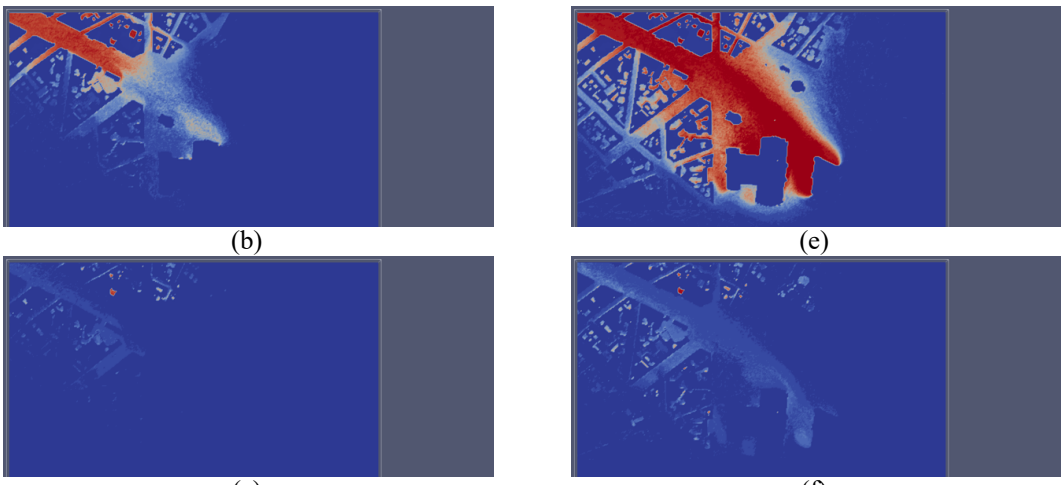

(b) (e)

(c) (f)

Figure 163. Probability of exceeding a critical threshold for the members limited to source location 0 at 7h10 (a), 7h30 (b) and 8h00 (c), and limited to source location 8 at 7h10 (d), 7h30 (e) and 8h00 (f).

This notion of entrapment will be illustrated furthermore in the following sections dedicated to the analysis of specific members.

Sample analysis

Regarding the analysis of some samples we decided to compare the influence of the vertical uncertainty regarding the source location, while keeping the same meteorological conditions. The influence of the meteorological member on the plume direction and duration of pollutant transport is obviously of the uttermost importance but do not present any novelty or surprise.

The **Figure 164** presents the evolution of the plume using the member det0 for the release location 8 and 18, which are, respectively, the most south eastern location near the ground (i.e. entrapped between the buildings) and the most north western location at the maximum height above ground. The dispersion patterns in the far field are not so dissimilar, except for a delay regarding the plume related to location 8, that suffers an obvious initial entrapment between the buildings. This leads also to a different path around the topography in the north west of the domain. Nonetheless, the more interesting feature is the persistency of a concentration plume near the source for the location with the least initial entrapment between the buildings, i.e. the source location 18. This source is high above ground, at 40m, but continues to release pollutants entrapped at 9h00, while the other source is not. After a careful examination of the results in the near field, we noticed the elevated source tends to transport more efficiently the pollutants in the enclosed courtyards several hundred of meters downwind of the initial release. These enclosed courtyards then take a longer time to release the pollutants trapped inside them. Presumably, the higher above ground release leads to high concentrations just at the building tops, where the surface exchange of the enclosed courtyard are located, while the release near the ground is not.

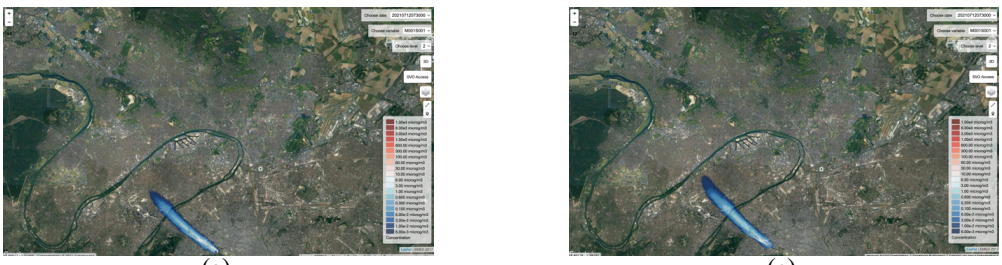

(a) (e)

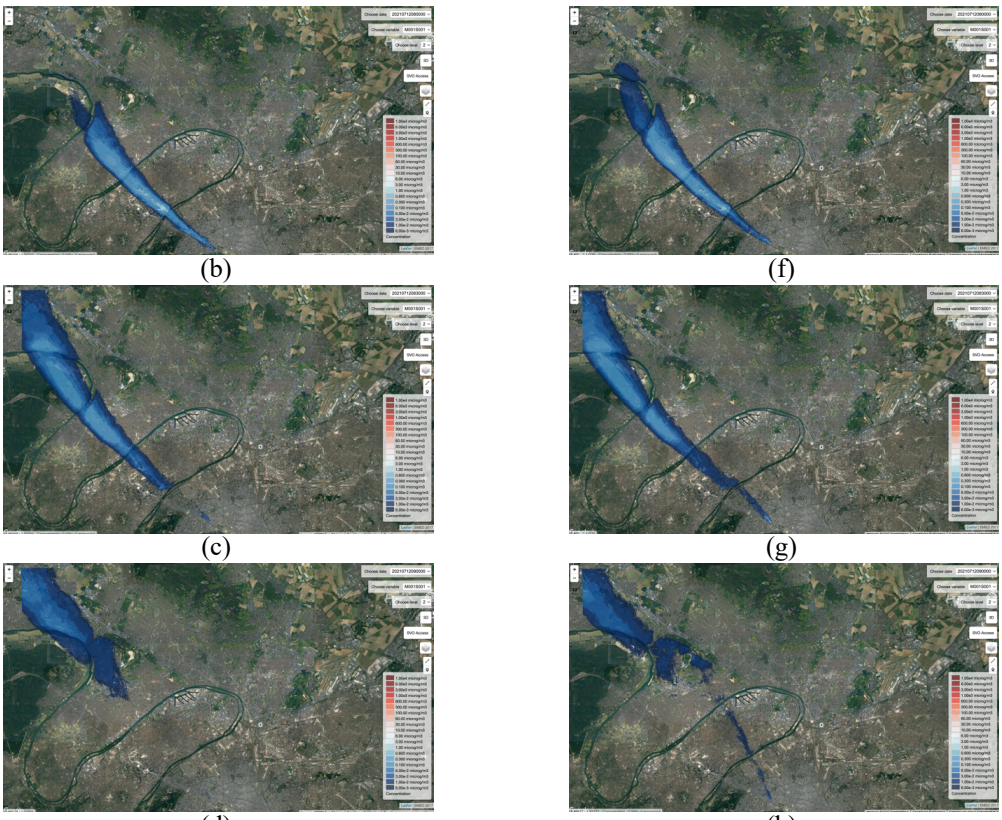

Figure 164. Dispersion plume near the ground using the meteorological member det0 for the release location 8 at 7h30 (a), 8h00 (b), 8h30 (c) and 9h00 (d), and the location 18 at 7h30 (e), 8h00 (f), 8h30 (g) and 9h00 (h).

CONCLUSION

The SURE project was aimed to estimate the variance of concentration for a typical accidental or malevolent release in a realistic urban setup, and to improve the knowledge of emergencies practitioners.

The project uses the very large and high-resolution domain of the EMERGENCIES project located in the Greater Paris area. The meteorology uses 21 members and, combined with 27 locations for the release, the dispersion uses 567 members. The project generated large amount of data and was processed on the Topaze supercomputer at the CEA. The release scenario consists of an accidental or malevolent 1kg fictious release during 10min between the Grand Palais and the Petit Palais museum, in the center of Paris.

The preliminary analysis of the meteorological members indicates a wind speed between 2 and 3m/s near the ground, with a wind mainly from the south east. The wind direction shows a limited but interesting variance for the wind direction with a standard deviation between 10 and 20°.

Due to the large amount of data to process, only a preliminary analysis of the concentration was performed using either statistical processing on the full ensemble, and on parts of it, or using specific scenario samples. We presented here some particular features detected in the preliminary analysis: for instance, high variance zones located, not on the boundaries of the ensemble plume, but within the plume. This seems related to two major dispersion patterns, either an initial entrapment or a direct transportation to the buildings downwind of the release: it allows to detect the high variability zone between the two dispersion behaviors. Interesting far-field features were also pointed out: for instance, the longer entrapment of the toxic material in case of higher above ground release, than releases near the ground and entrapped between large buildings.

We consider that such knowledge will help the emergency practitioners and the modeling expert to gain better understanding and anticipation of behaviors of the plume. Moreover, we expect this kind of calculation to be performed more routinely in the near future during the occurrence of such accidental or malevolent situations, and hence to help the modeling expert having a better anticipation of the variability of the situation. Due to the large amount of data, additional analysis is still underway and additional material will be shared with the community in the year to come.

REFERENCES

Armand, P., Oldrini, O., Duchenne, C., & Perdriel, S. (2021). Topical 3D modelling and simulation of air dispersion hazards as a new paradigm to support emergency preparedness and response. Environmental Modelling & Software, 143, 105129.

Oldrini, O., Armand, P., Duchenne, C., Olry, C., Moussafir, J., & Tinarelli, G. (2017). Description and preliminary validation of the PMSS fast response parallel atmospheric flow and dispersion solver in complex built-up areas. Environmental Fluid Mechanics, 17(5), 997-1014.

Oldrini, O., & Armand, P. (2019). Validation and sensitivity study of the PMSS modelling system for puff releases in the Joint Urban 2003 field experiment. Boundary-Layer Meteorology, 171(3), 513-535.

Oldrini, O., Armand, P., Duchenne, C., Perdriel, S., & Nibart, M. (2021). Accelerated Time and High-Resolution 3D Modeling of the Flow and Dispersion of Noxious Substances over a Gigantic Urban Area—The EMERGENCIES Project. Atmosphere, 12(5), 640.

Reinert, D., Prill, F., Frank, H., Denhard, M., Baldauf, M., Schraff, C., ... & Zängl, G. (2020). DWD database reference for the global and regional ICON and ICON-EPS forecasting system. Technical Report Version 2.1. 1.

21st International Conference on
Harmonisation within Atmospheric Dispersion Modelling for Regulatory Purposes
27-30 September 2022, Aveiro, Portugal

LAGRANGIAN PLUME-RISE DISPERSION MODELLING OF LARGE-SCALE LITHIUM-ION BATTERY FIRES IN OPEN SURROUNDING WITH APPLICATION TO THE FIRE IN MORRIS, USA, 2021

Christian Lejon[1], Daniel Vågberg[1], Fredrik Schönfeldt[2], Leif Persson[1], Jan Burman[1], Birgitta Liljedahl[1], Daniel Elfverson[1], Joakim Eriksson Rydman[1], Jan Sjöström[1], Oscar Björnham[1]

[1]CBRN Defence and Security, Swedish Defence Research Agency, Cementvägen 20, SE-901 82 Umeå, Sweden

[2]Defence Technology, Swedish Defence Research Agency, Gullfossgatan 6, SE-164 40 Kista, Sweden

Abstract: The large scale lithium-ion-battery (LIB) fire in a warehouse in Morris 2021 is reviewed. Particulate and gaseos emission factors of LIB combustion as well as heat release rates are collected, based on published literature. A Lagrangian plume rise model is utilized which introduces a vertical speed component, due to buoyant flux of the Briggs formulation, to the Langevin equation. Validation is done in discussion to plume footage and the warehouse contents. The presentation will further emphasize risk areas and plume-rise modeling in the Lagrangian framework.

Key words: *Lithium ion battery, Langevin equation, Briggs Plume Rise, Langrangian Dispersion Model, Morris*

INTRODUCTION

The ongoing paradigm shift within the energy sector from fossil to renewable sources has resulted in a spike need for batteries. Several large-scale battery facilities are already established and more are under fast development. It is estimated that the total battery demand is expected to increase about ten-fold to ~2000 GWh until year 2030 (Placek, 2021). Infrastructure to handle new and recycled batteries are on build-up where large amounts of LIBs are stored, sometimes in limited spaces.

The number of incidents and fires related to thermal runaway of LIBs has increased. Today, LIBs are estimated to cause 48% of all waste fires in UK (National Fire Chief Council, 2021). Fires in transportation sector occurs, as the Felicity Ace Burns where 4000 vehicles onboard a ship caught fire. Some examples in storage and factories are the 2021 Victoria Big Battery incident, where a fire broke out in two of the 212 Tesla Megapacks providing 450-MWh of energy storage (Andy Blum, 2022), the 2022 fire at the Salt River Project 40 MWh battery energy storage system in Arizona, USA (Hering, 2022), the 2021 explosion at the Beijing Jimei Dahongmen 25 MWh solar-storage-charging integrated station project (China Electric Power Technology Co., 2021), and the 2021 large scale battery fire in a warehouse storage in Morris, USA. Almost 3000 civilians were evacuated in the latter (Katherine Rosenberg-Douglas, 2021) in fear of particularly the highly toxic hydro fluoric gas (HF).

This article maps the fire properties of LIBs themselves to the large-scale fire in Morris 2021 where nearly 70 metric tonnes LIBs (~ 59 MWh) burned. With both public and first-responder health as primary concern, three aspects to model a large scale LIB fire successfully are identified; the emission factors of relevant toxic substances, the heat release rate, and the meteorology. The current work goes into details on these subjects and gives a state-of-the art knowledge base. To this end, the large-scale Morris fire is used as a

case study because of its relatively well-documented content, sensor measurements, progression, and plume footage for validation of the theoretical framework.

MATERIALS AND METHODS

Morris Fire: The warehouse has a footprint of $A_B = 6500\,\mathrm{m}^2$ and is surrounded by residential homes and in the wind direction during the fire predominantly industrial sites or green areas; yet 3000 people were evacuated. The estimated amount of batteries were ~68 metric tonnes of LIBs (Leonard Zintak). First-hand information from the Morris Fire Protection & Ambulance District revealed that the large amount of batteries stored in the warehouse was the main component in the fire (80%) (Tracey, 2022) and that most of it was consumed.

Emission Factors: The electrolyte is the most flammable component, however combustion products are H_20 and CO_2. Asphyxiants CO and CO_2 are more than one order of magnitude less toxic than the irritant gases (Peng et al., 2020) and therefore further neglected in this study. Emitted HF levels per kg LIB is reported to 3 - 11 mg/kg (Larsson et al., 2014). While HF is individually the most important irritant gas to comprise respiratory system, other common irritant gases are together comparable to HF (Peng et al., 2020), thus the total emission factor is here chosen $EF_{\text{irritant gases}} \approx 22$ mg/kg.

Ultrafine particles (<560nm) are present in LIB fires and PM2.5 emission factor is around 20 g/kg LIB (Premnath et al., 2022). The inhalable fraction is unfortunately not well researched neither in terms of composition nor size distribution or mass. The modelling is endowed a mono-modal log-normal size distribution with mode of 0.11 μm and a geometric standard deviation of 2.2 following data from (Hertzberg & Blomqvist, 2003).

Energy Release: The combustion heat due to the electrolyte and other combustible material of the LIB acting as fuel is the major heat source while the resistive Joule heat of internal shorts is only about 10% overall (Ribière et al., 2012). Heat release per kg LIB packs are ~10 $MJ{\cdot}kg^{-1}$ (Larsson et al., 2014; Peng et al., 2020; Ping et al., 2015). Radiative heat loss (*vis.* convective heat for plume-rise) of 5% is applied based on previous work on open fires (Hans Boot, 2020), considering here the partial enclosure of the roof.

The Morris Weather Situation: Strong daytime convection and a weak 2-4 ms^{-1} south-westerly general wind and thunderstorms in the afternoon and evening but surprisingly small gustiness of the wind concludes the weather situation (NOAA Weather Prediction Center, 2022; OGIMET, 2022; University of Wyoming, 2022). The ERA5 dataset (ECMWF, 2022) for Morris indicates the planetary (convective) boundary layer (PBL) height is at maximum 1200. During the night-time of intense fire (29th to 30th), the PBL is stably stratified and just over 100 meters deep.

Plume Rise in the Lagrangian Dispersion Model "LPELLO":

The plume rise phenomenon is modeled according the well-known Briggs formalism for stack gas dispersion (Arya, 1999; Beychok, 2005). For the transitional case of buoyancy- and momentum-controlled plume rise, the so-called one-third and two-third laws relate the plume height (z'_c) to mean wind at the stack exit ($\bar{u}$) and downwind distance (x):

$$z'_c = \left[\frac{3}{\beta_m^2} \frac{F_m x}{(\bar{u})^2} + \frac{3}{2\beta_b^2} \frac{F_b x^2}{(\bar{u})^3} \right]^{1/3}, \qquad (17)$$

where $\beta_m = 0.6$and $\beta_b = 0.6$are entrainment coefficients. In fact, the momentum flux can be omitted. The driving fluxes linked and buoyancy (F_b) is assessed by (Beychok, 2005)

$$F_b = \frac{gQ}{\pi c_{pa} T_a \rho_a} \quad (18)$$

Here ρ represents density and T temperature. Subscripts s and a indicate in-plume and the ambient environment, respectively, g is the acceleration due to gravity, and c_p the specific heat capacity of air at constant pressure. The only source attribute to determine buoyancy flux is the power emitted into convective heat flux (Q)

The atmospheric dispersion of particles and passive gases is modelled with an in-house implementation of the Langevin equation (LPello). LPello is a Lagrangian particle model based on similarity theory from Zilitinkevich et al. (Zilitinkevich et al., 1998) and (Zilitinkevich et al., 1992) to express the mean wind velocity components for the stably and unstably stratified boundary layer. The needed input to the fix-point iteration solution of the two equations in two variables to obtain the Obukhov length and friction velocity is taken from the ERA5 dataset (Arya, 1988). The valid limits of Monin-Obukhov similarity theory are respected by prescribing smaller Obukhov lengths to either -50 m or +75 m and smaller wind speeds to 2 m/s.

For plume rise, the time derivative of equation (17) adds vertical velocity to the model particles. The lateral transport in LPello is governed by the logarithmic wind profile and for the plume-rise $\bar{u}$ is defined as the average at the stack exit and the velocity at the PBL height. The final plume height is determined by among other parameters the heat release rate Q, atmospheric stability, and $\bar{u}$ (Beychok, 2005).

RESULTS AND DISCUSSION

Morris Plume Behavior: Fortunately, a passenger on a scheduled flight took aerial photos of the plume at a point of seemingly high plume-rise, see Figure 165 (left). The weather situation in the photos is interpreted as thick convective boundary layer where the top of the cumulus clouds indicate the upper limit of the PBL, which may be all the way up to 1200m as indicated in the ERA5 dataset. On the contrary, the smoke plume does not rise adiabatically like the thermals due to entrainment and reach its equilibrium at a lower level. Based on the stereographic information (second photograph not shown) and tools from projective geometry (*Geometric invariance in computer vision*, 1992) the plume height is estimated to ~600m at this point.

Figure 165 *Left: Photograph taken from a scheduled flight (Steph, 2021). The PBL height is at miximum 1200m this day and plume height is estimated to ~600m. Right: Snapshot from a video (Grundy Countys Sheriff's Office, 2021) (in*

fair use) with the smoke mixing different from that of left side, from the ground to ~100m based on eye-balling objects such as trees and building in the footage.

Videos taken by the Grundy Countys Sheriff's Office show both the inside of the building with hot spots as well as the plume. The snapshot in Figure 165 (right) indicates a much lower smoke plume, that extends from the ground to around 100m by visual comparison to objects in the frame. Likely this footage is captured later in the evening as the overall light intensity is lower. The twofold aspects of the lower plume rise are lower power output from the fire and more stable atmospheric conditions.

Source Term: The complete source term is the total battery amount present at the site in Morris multiplied by the emission factors for irritant gases (≈ 1.5 kg), particulate matter (≈ 1700 kg), and the heat release (≈$6.8 \cdot 10^5$ MJ) which divided by the reported duration of 18 hrs yields $Q_{flat} \approx 1.05$ MW. Since the final plume height is a function of Q (Beychok, 2005), the estimated height in Figure 165 (left) of ~600m can be used to determine a matching heat release rate at the source; $Q_{plume} \approx 70$ MW. This considerable difference from the flat rate is ascribed to large temporal fire intensity variations, which is supported by the low plume height observed in Figure 165 (right). Although the final plume height according to the Briggs formulae should be discussed for low wind speed, a final plume height of ~50 m is derived with corresponding settings: Pasquill class = D, $\bar{u} = 1\ ms^{-1}$, and, remarkably low, $Q_{plume} \approx 0.2$ MW.

Modelling: The simulations are validated by modeling a heat release of $Q_{plume} \approx 70$ MW to mimic the plume in Figure 165 (left). By visual comparison, in Figure 166 the plume is projected onto a patchwork of Google satellite hybrid Maps, fair agreement has been obtained. The modelled plume is bending slightly faster the the real scenario owing to modeling difficulties at low wind speed. Atmospheric stability and source strength is further elaborated on in conjunction with estabilshed exposure guideline levels for irritant gases and particulate matter in the presentation.

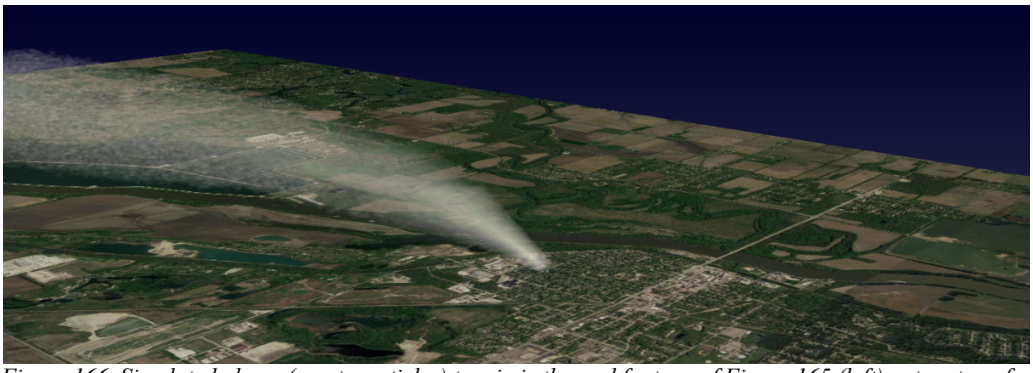

Figure 166. Simulated plume (gas + particles) to mimic the real footage of Figure 165 (left) put on top of a patchwork from Google Maps (in fair use).

CONCLUSIONS

Because of the expansive growth of energy storage in LIBs and their ability to set on fire, the combustion products of LIBs are here reviewed. The plume trajectory of a large scale fire incident in Morris, USA, year 2021 is retrofitted with fair succes with a Lagrangian particle model incorporating the empircal Briggs formula for stack gas plume rise. The advantage of this concept lies in the possibility to model both physical particles and gases in the same framework, both while in plume and afterwards when the plume has reached its equilibrium height and the added buoyancy term is diminiuated. The presentation will add risk area estimations based on modeled concentrations and exposure guideline levels.

REFERENCES

Arya, S. P. 1988: Introduction to Micrometeorology. Academic press.

Arya, S. P. 1999: Air Pollution Meteorology and Dispersion. Oxford University Press.

Beychok, M. 2005: Fundamentals of Stack Gas Dispersion (4th ed.).

Blum A., P. Rogers, C. Grant, G. Hough. 2022: Victorian Big Battery Fire: July 30, 2021: https://victorianbigbattery.com.au/wp-content/uploads/2022/01/VBB-Fire-Independent-Report-of-Technical-Findings.pdf

Boot, H. and S. R., Pérez, 2020: Modelling of the plume rise phenomenon due to warehouse or pool fires considering penetration of the mixing layer. Journal of Loss Prevention in the Process Industries, 65, 104109-104121.

China Electric Power Technology Co., 2021: Accident analysis of Beijing Jimei Dahongmen 25 MWh DC solar storage charging integrated station project. https://ctif.org/sites/default/files/2021-05/Accidental%20analysis%20%281%29.pdf

ECMWF. 2022. ECMWF Reanalysis v5 (ERA5). Retrieved March 29 from https://www.ecmwf.int/en/forecasts/dataset/ecmwf-reanalysis-v5

Geometric invariance in computer vision. 1992. MIT Press.

Grundy Countys Sheriff's Office. 2021: Retrieved 20220706 from https://www.facebook.com/GrundyCountySheriff/videos/

Hering, G., 2022: AES battery blaze in Arizona continues to burn; cause unknown. Retrieved 07-11 from https://www.spglobal.com/marketintelligence/en/news-insights/latest-news-headlines/aes-battery-blaze-in-arizona-continues-to-burn-cause-unknown-70024511

Hertzberg, T. and P. Blomqvist, 2003: Particles from fires—a screening of common materials found in buildings. Fire and Materials, 27(6), 295-314.

Larsson, F., Andersson, P., Blomqvist, P., Lorén, A., B.-E. Mellander, 2014: Characteristics of lithium-ion batteries during fire tests. Journal of Power Sources, 271, 414-420. https://doi.org/10.1016/j.jpowsour.2014.08.027

Leonard Zintak, V. S. ACTION MEMORANDUM – Request for an Exemption from the $2 Million and 12-month Statutory Limits, and for Emergency and Time-Critical funding for the Morris Lithium Battery Fire Site in Morris, Grundy County, Illinois (Site ID #C5TN). (966433).

National Fire Chief Council, 2021: Lithium-ion battery waste fires costing UK over £100m a year. Retrieved 07-11 from https://www.nationalfirechiefs.org.uk/News/lithium-ion-battery-waste-fires-costing-uk-over-100m-a-year

NOAA Weather Prediction Center. 2022: WPC Archive of the National Forecast Chart. Retrieved March 15 from http://www.wpc.ncep.noaa.gov/noaa/noaa_archive.php

OGIMET. 2022. Formulario para peticion de mensajes aeronauticos. Retrieved March 29 from https://www.ogimet.com/metars.phtml.en

Peng, Y., Yang, L., Ju, X., Liao, B., Ye, K., Li, L., Cao, B., Y Ni,. 2020: A comprehensive investigation on the thermal and toxic hazards of large format lithium-ion batteries with LiFePO4 cathode. J Hazard Mater, 381, 120916. https://doi.org/10.1016/j.jhazmat.2019.120916

Ping, P., Wang, Q., Huang, P., Li, K., Sun, J., Kong, D., C. Chen, 2015. Study of the fire behavior of high-energy lithium-ion batteries with full-scale burning test. Journal of Power Sources, 285, 80-89. https://doi.org/10.1016/j.jpowsour.2015.03.035

Placek, M., 2021: Projected global battery demand from 2020 to 2030, by application. Retrieved 07-11 from https://www.statista.com/statistics/1103218/global-battery-demand-forecast/

Premnath, V., Wang, Y., Wright, N., Khalek, I., S. Uribe, 2022: Detailed characterization of particle emissions from battery fires. Aerosol Science and Technology, 56(4), 337-354. https://doi.org/10.1080/02786826.2021.2018399

Ribière, P., Grugeon, S., Morcrette, M., Boyanov, S., Laruelle, S., G. Marlair 2012: Investigation on the fire-induced hazards of Li-ion battery cells by fire calorimetry. Energy Environ. Sci., 5(1), 5271-5280. https://doi.org/10.1039/c1ee02218k

Rosenberg-Douglas K., M. Prosser., S. Freishtat. 2021: Morris mayor says officials were unaware battery business was operating in building that's still on fire. Thousands remain evacuated. Retrieved 07-11 from https://www.chicagotribune.com/news/breaking/ct-morris-industrial-fire-update-20210630-ni5h54n76bc5fdzmi7vdnv24bm-story.html

Steph. (2021, July 29). ”Saw this #southchicago #fire from the air …“ [Tweet]. https://twitter.com/Steph77038771/status/1410006565231509508

Tracey, S., 2022: Personal communication., Deputy Chief at Morris Fire Protection & Ambulance Dist.

University of Wyoming, Department of Atmospheric Science 2022: Atmospheric Soundings. Retrieved March 29 from http://weather.uwyo.edu/upperair/sounding.html

Zilitinkevich, S., Fedorovich, E., M. Shabalova, 1992: Numerical model of a non-steady atmospheric planetary boundary layer, based on similarity theory. Boundary-Layer Meteorology, 59(4), 387-411.

Zilitinkevich, S., Johansson, P. E., Mironov, D. V., A. Baklanov 1998: A similarity-theory model for wind profile and resistance law in stably stratified planetary boundary layers. Journal of Wind Engineering and Industrial Aerodynamics, 74-6, 209-218. https://doi.org/Doi 10.1016/S0167-6105(98)00018-X

21st International Conference on
Harmonisation within Atmospheric Dispersion Modelling for Regulatory Purposes
27-30 September 2022, Aveiro, Portugal

ENHANCED AEROSOL DYNAMICS IN A LAGRANGIAN PARTICLE DISPERSION MODEL

Pontus von Schoenberg,[1,2] Peter Tunved[2], Radovan Krejci[2] and Niklas Brännström[1]

[1]Department of Environmental Science, Stockholm University, Stockholm, Sweden
[2] Swedish Defence Research Agency, FOI, Sweden

Abstract Dispersion of hazardous material in the atmosphere is often modelled using particle dispersion models. Traditionally, these particle models suffer from having only a rudimentary description of the physiochemical transformations during the transport. To overcome this limitation we have studied the feasibility of including more advanced aerosol dynamics in a Lagrangian Particle Dispersion Model (LPDM). The advanced aerosol dynamic includes condensational growth, coagulation, chemical interactions, nucleation of new aerosols as well as an advanced wet deposition scheme and dry deposition.

The motivation for this study is to improve forecasting tools a nuclear accident event. As an initial step we have chosen a simplified case where gaseous radioactive caesium is released into the atmosphere followed by an immediate condensation onto the pre-existing ambient aerosol. This setting mimics well a Fukushima-Daiichi type of nuclear power plant accident. We have used PELLO, which is a LPDM driven by a numerical weather forecast from ECMWF. The PELLO model initially release 300000 model particles and we stored the weather parameters along their trajectories. The evolution of aerosol properties along each trajectory was then simulated with the aerosol and chemical process model CALM.
The advantage of post-processing the PELLO trajectories with CALM is that the model particles are no longer inert which means that, for example, the aerosol size distribution will evolve throughout the simulation. To obtain the predicted aerosol properties at any given point in model spatial and temporal domain, the contribution of the initial released particles is summed up either using box counting or kernel density estimations.

To assess our modelling approach – and in lieu of data from a repeating nuclear power plant accident – we have used measurements of ambient aerosol size distribution from three different measurement stations. One is the upwind station describing the aerosol size distribution at the source of the fictive power plant failure and the other two stations were used as receptor points downwind. This allow us to compare the temporal development of the measured and simulated size distribution and the radioactivity distribution of the released radioactive material that reached the receptor point.

Key words: Dispersion modeling, Lagrangian Particle Dispersion model (LPDM), Aerosol dynamics, Kernel Density Estimations

21st International Conference on
Harmonisation within Atmospheric Dispersion Modelling for Regulatory Purposes
27-30 September 2022, Aveiro, Portugal

IMPROVING URBAN MODEL PREDICTIONS IN COUPLED INDOOR-OUTDOOR HAZARD ASSESSMENT

David Lorenzetti, Michael Sohn, Paul Bieringer, Peter Melling, Scott Kreyenhagen, Martyn Bull, Russell Mills

SHORT ABSTRACT

Abstract title: Improving urban model predictions in coupled indoor-outdoor hazard assessment

Name and Affiliation of the First Author: David Lorenzetti (Lawrence Berkeley National Laboratory)

Email of first author: dmlorenzetti@lbl.gov

Names and Affiliations of the Co-authors:

Michael Sohn (Lawrence Berkeley National Laboratory)

Paul Bieringer (Aeris LLC)

Peter Melling (Riskaware)

Scott Kreyenhagen (Aeris LLC)

Martyn Bull (Riskaware)

Russell Mills (Riskaware)

ABSTRACT TEXT (MAXIMUM 350 WORDS.)

To assess urban-scale consequences of human exposure to airborne contaminants, a simulation tool should predict the transport of an outdoor plume into buildings, and potentially the exfiltration of indoor air to the outdoors. This talk gives an overview of the Integrated Urban effort to update the urban models from the Hazard Prediction and Assessment Capability, within the Joint Effects Model framework. The project encompasses all aspects of urban model integration, including: streamlining the ingestion of geospatial data; accessing both single- and multi-zone building models through a unified interface; adapting the user interface to the TAK framework; incorporating new outdoor transport models; and propagating uncertainty and variability across model boundaries, for better health consequence assessments.

21st International Conference on
Harmonisation within Atmospheric Dispersion Modelling for Regulatory Purposes
27-30 September 2022, Aveiro, Portugal

PHYSICAL MODELLING OF ROUGH BOUNDARY LAYER FLOWS AND SOURCE DISPERSION IN WIND TUNNEL

Valery Babin

SHORT ABSTRACT

Abstract title: Physical modelling of rough boundary layer flows and source dispersion in Wind Tunnel

Name and Affiliation of the First Author: V. Babin

Environmental Wind Tunnel Laboratory, Department of Applied Mathematics, Division of Environmental Sciences, IIBR

Email of first author: valeryb@iibr.gov.il

Names and Affiliations of the Co-authors: C. Moryosef[1], M. Hotoveli[2]and Y. Bohbot-Raviv[1]

[1]Environmental Wind Tunnel Laboratory, Department of Applied Mathematics, Division of Environmental Sciences, IIBR

[2]Environmental Wind Tunnel Laboratory, Department of Environmental Physics, Division of Environmental Sciences, IIBR

Abstract text

Physical modelling of puff and continuous point sources in a rough boundary layer flow performed in environmental wind tunnel laboratory (EWTL) at IIBR. In the current work the wind tunnel facility is introduced and an experimental study conducted to investigate plume and puff dispersion behaviour downstream of an urban-like roughness is presented. In order to model a scaled rough boundary layer, staggered arrays of L shape elements with aspect ratio of 1 and 2 in the presence of triangular spires and dragon teeth were used. Systematic continuous and short time releases of ethane gas from ground level point source located in urban environment were performed. Pollutant concentration measurements were applied using a two-head Fast Flame Ionization Detector (FFID) system (Cambustion®) placed on a transvers system at number of locations relative to the source. The concentration measurements were accompanied by velocity flow field measurements using a two-component Laser Doppler Anemometer (LDA, Dantec, FiberFlow®). The obtained results for the flow and concentration were respectively examined based on atmospheric boundary layer flows and on common semi-empirical Gaussian models. Puff and plume dispersion parameters' dependence on experimental conditions were examined. The highly valued data sets of non dimensional dispersion parameters in urban environment are used for Lagrangian Stochastic Dispersion Model validation and help plan complex field concentration measurements

campaigns.

21st International Conference on
Harmonisation within Atmospheric Dispersion Modelling for Regulatory Purposes
27-30 September 2022, Aveiro, Portugal

INTERCOMPARISON BETWEEN OBSERVATIONS AND 3D HIGH RESOLUTION MODELS FOR POLLUTANTS DISPERSION IN THE HARBORS OF MARSEILLE AND TOULON IN 2021

Sonia Oppo[1], Eve-Agnès Fiorentino[1], Alexandre Armengaud[1], Christos Boikos[4], Leonidas Ntziachristos[4], Bruno Ribstein[2], Frédéric Mahé[2], Barbara D'Anna[3], Grazia Maria Lanzafame[3], Quentin Gunti[1,3]

[1]AtmoSud, air quality observatory in the Provence-Alpes-Côte d'Azur region France
[2]*Aria Technologies, France*
[3] Laboratoire Chimie-Environnement, Université Aix-Marseille, CNRS, Marseille, France
4 Sustainability Engineering Laboratory, Aristotle University of Thessaloniki, Greece

Abstract:
AtmoSud, the air quality observatory in the Provence-Alpes-Côte d'Azur region of France, has an operational air quality monitoring mission (forecasting, information, awareness and contribution to the improvement of knowledge). In the case of accidental situations, we use 3D Lagrangian modelling, which allows us to follow the dispersion of plumes at high resolution, thus enabling us to assess the impacted areas. The PMSS model used by AtmoSud is a Lagrangian model developed by ARIA Technologies and ARIANET allowing the advection of gases and aerosols in 3D thanks to the interpolation of wind fields taking into account buildings and topography.
Within the framework of two European projects, AtmoSud had the opportunity to use high resolution modelling to reproduce measurement campaigns:

- The SCIPPER[2] project gathering a large consortium of 17 partners from 9 European countries, aims at evaluating the contribution of ships to the pollution of cities. The objective of the modelling part is to use the Lagrangian PMSS model and FLUENT model, operated by the Aristotle University of Thessaloniki, to reproduce the concentrations of several pollutants monitored during a measurement campaign carried out in the summer of 2021 in Marseille;
- The Franco-Italian project AER NOSTRUM[3], which focuses on the pollution of several Mediterranean ports, will evaluate the performance of the PMSS model in reproducing the concentrations of a measurement campaign carried out in 2021 in the Toulon harbour;

Key words: *Lagrangian particle modelling, RANS-CFD modelling, urban dispersion modelling, high-resolution wind flow modelling, high resolution dispersion modelling, shipping emissions impact*

INTRODUCTION

Shipping represents 80% of our goods undergoing overseas transport. Emissions related to maritime traffic are an important contributor of gaseous emissions (such as SO_2, NOx, black carbon, VOCs,…) and have also an impact on climate change. Coastal areas, densely populated in France, are particularly impacted by shipping. Since 2020, regulations for emissions in Mediterranean Sea evolved until the limitation of fuel sulphur content (0.5%) and the application of Tier I-III standards for emissions. In spite of this important progress, littoral zone and people living in the port area, are still directly impacted by vessel's plumes.
In this context, AtmoSud is involved in different projects to improve its understanding of atmospheric pollution and consolidate his expertise on its territories.

[2] https://www.scipper-project.eu/
[3] https://interreg-maritime.eu/fr/web/aer-nostrum/

These projects propose an interdisciplinary approach, combining air quality measurements, shipping emissions calculated considering the automatic identification system and high resolution modelling approaches.

AIR QUALITY MODELLING

Description of PMSS

The PMSS (Parallel-Micro-SWIFT-SPRAY, Oldrini et al., 2011) modelling system is a combination of two individual PSWIFT and PSPRAY models developed and distributed by ARIA Technologies. It is dedicated to small scale and complex terrain, such as urban or industrial environments.
The PSWIFT model is a 3D wind field model which produces a mass-consistent wind field using data from a dispersed meteorological network or even observational data from measuring sites. The PSPRAY model is a parallelized 3D particle Lagrangian dispersion model that simulates the advection and diffusion of gaseous species in the atmosphere. It produces 3D concentrations and also dry and wet deposition.

Description of FLUENT model

Ansys FLUENT is a fluid simulation software that provides modelling capabilities for a wide range of fluid flow studies. In this specific work the RANS-CFD approach was implemented. In this approach, the governing fluid flow equations are resolved in a very high-resolution computational domain (0.5-2 meters), simulating 3D gas-transport. The model takes into account the local topography of the ground and buildings as well as phenomena like turbulence, mass transfer, diffusion and heat transfer (ANSYS Fluent 2022 R1, Theory Guide, 2021).

Emissions and meteorology

For each measurement campaign, a work of identification of individual plumes has been implemented. Then, thanks to the Automatic Identification System (AIS) and Ports Authorities, which allows to give the position of ship, we retraced all the ships that were present in the harbour during peak concentrations.
Finally, for each ship, the emissions of selected pollutants have been estimated thanks to the technical characteristics of each individual vessel, the load of the engine and the fuel consumption.
For the other kind of emissions, we added linear road emissions that are the second main source of emissions in these cases.
Concerning meteorological input, for both cities, we used several sites of measurement close to the port, near ground level. These meteorological data are used by PSWIFT to reconstruct wind field by interpolation and by taking into account buildings.

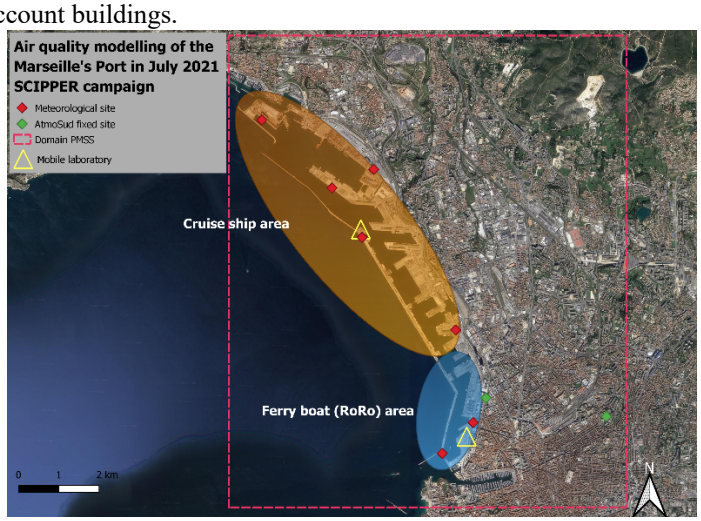

Figure 167 : Geographical situation of the SCIPPER campaign in July 2021

CAMPAIGNS

Marseille

Marseille is the second most populated city in France (870 000 people and more than 1.5 million in the urban district) and it's the most important port city in the country. Ferry and cruise ship traffic are the main activities of the port.

The impact of the port on local air quality is significant considering it was the greatest contributor to NOx emissions in 2019 (31%), followed closely by traffic emissions (30%) in the urban district of Marseille (source: https://cigale.atmosud.org/).
A measurement campaign was conducted in July 2021, in the frame of the SCIPPER project. It aims to assess the impact of shipping emissions on air quality. It was a combination of remote measurements and fixed stations allowing to capture a maximum of plumes. These plumes had been identified and will be exploited for air quality modelling. Meteorological data like temperature, wind speed and wind direction had been recorded too (see **Figure 168**).

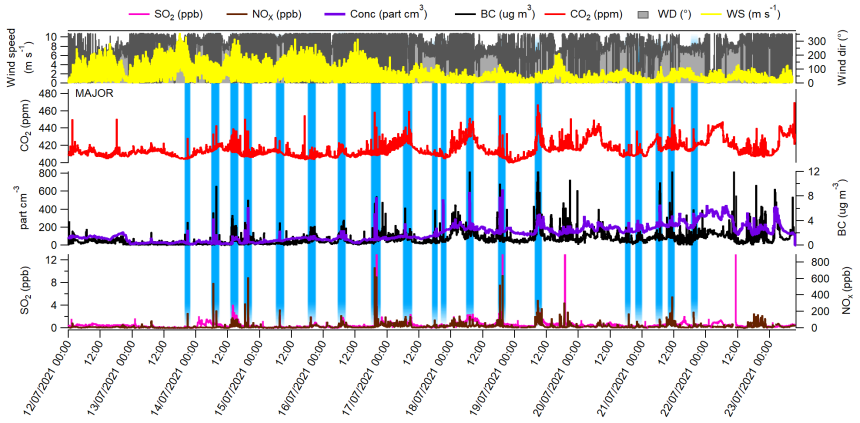

Figure 168: Temporal variations of the major pollutants and weather data observed in the "La Major" site between 12/07/2021 and23/07/2021. Car trucks and ship suspected plumes have been highlighted in light blue. Reference: Lanzafame et al., SCIPPER project D3.4, 2022

Toulon

Toulon is the third-largest French city on the Mediterranean coast after Marseille and Nice and has a population of 176 000 people.
Ferry and cruise ship traffic are the main activities of the port. The port of Toulon is the main departure for ferries to Corsica.
The impact of the port on local air quality is equal to traffic road sector for NOx emissions in 2019 (42%, source: https://cigale.atmosud.org/).
A measurement campaign was conducted in summer 2021, in the frame of the AER NOSTRUM project.
The aim was similar to SCIPPER measurement campaign: evaluate the contribution of shipping emissions in the port urban area. Fixed station and some micro-sensors had been placed in order to monitor: PM10, PM2.5, CO_2, SO_2, BC and NOx (see **Figure 169**).

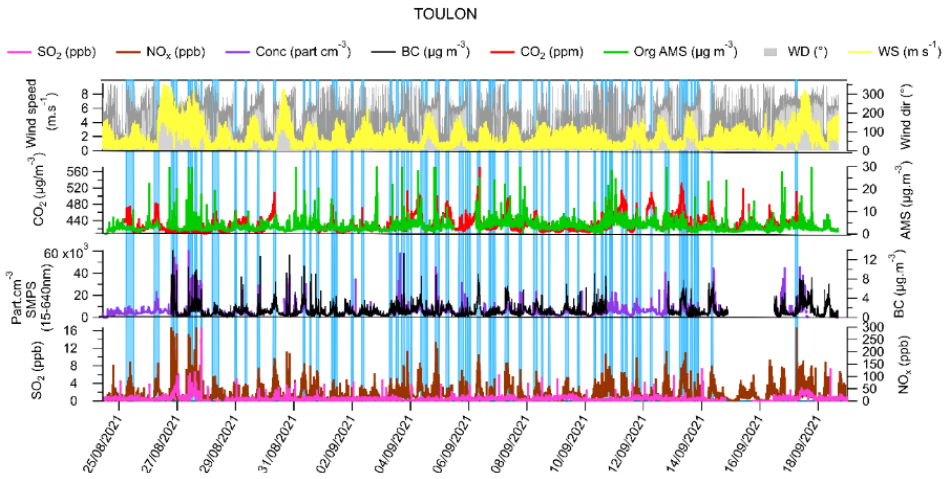

Figure 169: Temporal variations of the major pollutants and weather data observed in the mobile laboratory in Toulon between 25/08/2021 and 18/09/2021. Car trucks and ship suspected plumes have been highlighted in light blue.

VALIDATION'S METHODOLOGY

The methodology consists of running PMSS for few hours with the estimated shipping emissions in order to have the concentration all along the plume trajectory. The aim is to evaluate if the plume intersects the mobile lab (plumes has been chosen because they had been monitored) and if simulated concentrations were close to measurements (see **Figure 170** and Error! Reference source not found.). This comparison is only made for NOx and SO_2.

Each plume is investigated and gives the performance score of the each models' setup. Each study case will be function of the ship emissions, the meteorological condition, the speed of exhaust, the stack's height and diameter and the background pollution.

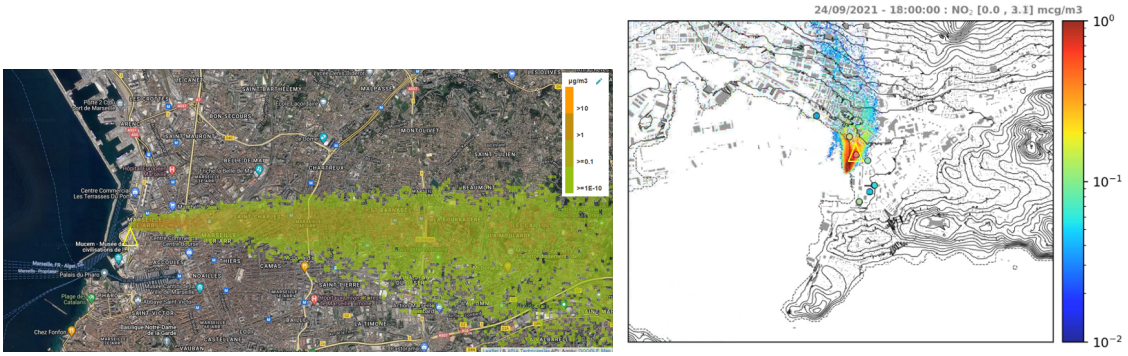

Figure 170 : Example of plume modelling with PMSS, simulated concentrations of SO_2 in Marseille (left), simulated concentrations of NO_2 in Toulon (right). Mobile laboratories sites obervations (yellow triangles, right and left). Micro-sensors (circles)

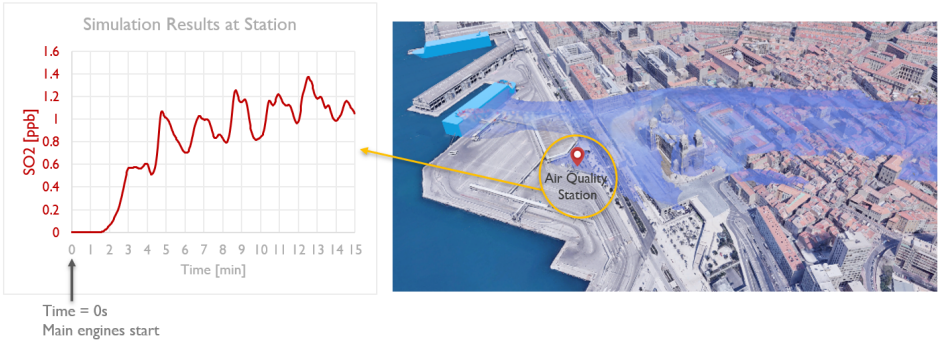

Figure 171: Time-series of SO_2 concentrations calculated with the CFD model, exported at La Major measurement site

CONCLUSIONS

We use FLUENT (RANS-CFD approach) and PMSS model (SWIFT and SPRAY codes) in order to investigate the dispersion of the exhaust gases emitted by shipping activities during air quality measurement campaigns. The intercomparison of simulation results and measurement data is particularly important for building a reliable settings of high resolution models. This study could be a first step for a future real-time dispersion system for shipping plumes in the main harbors of the region.

REFERENCES

ANSYS Fluent 2022 R1 Theory Guide, ANSYS, Inc., 275 Technology Drive Canonsburg, PA 15327, 2021

Grigoriadis A, S. Mamarikas, L. Ntziachristos, E. Majamäki, J-P Jalkanen (2021) New set of emission factors and activity information, SCIPPER project, Deliverable D4.1- https://www.scipper-project.eu/library/

Lanzafame G.M, L. Le Berre, B. Termine-Roussel, B. D'Anna, P. Simonen, M. Dal Maso, A. M. Hallquist, J. Mellqvist, (2022) Atmospherically sampled ship plume characterisation, SCIPPER project, Deliverable D3.4- https://www.scipper-project.eu/library/

Oldrini O., C. Olry, J. Moussafir, P. Armand and C. Duchenne, (2011) Development of PMSS, the Parallel Version of Micro SWIFT SPRAY. Proc. 14th Int. Conf. on Harmonisation within Atmospheric Dispersion Modelling for Regulatory Purposes, 443-447

21st International Conference on
Harmonisation within Atmospheric Dispersion Modelling for Regulatory Purposes
27-30 September 2022, Aveiro, Portugal

MULTI-MODEL ENSEMBLE DISPERSION PREDICTION SYSTEM FOR NUCLEAR EMERGENCY RESPONSE

Chun-Sil Jin, Hyun-Ha Lee, Jeong-Wan Kwon, Dong-Il Kim

SHORT ABSTRACT

Abstract title: Multi-Model Ensemble Dispersion Prediction System for Nuclear Emergency Response

Name and Affiliation of the First Author: *Chun-Sil Jin, Korea Institute of Nuclear Safety, Daejeon, Republic of Korea*

Email of first author: *csjin@kins.re.kr*

Names and Affiliations of the Co-authors: *Hyun-Ha Lee*[1], *Jeong-Wan Kwon*[1] *and Dong-Il Kim*[1]

[1] *Korea Institute of Nuclear Safety*

ABSTRACT TEXT

In case of nuclear accident in neighboring countries, a multi-model ensemble dispersion prediction technique is applied to the Accident Dose Assessment Modeling system (ADAMO) which was developed for a nuclear emergency response in Korea. Using four global meteorological forecasting models (KMA-UM, NOAA-GFS, KINS-GWRF, and CMC-GDPS) and two atmospheric dispersion models (FLEXPART and HYSPLIT), eight meteorology-dispersion combinations are constructed. The multi-model ensemble mean outperforms most of the individual models with smaller biases and higher correlation on the spatial and temporal variation of wind fields. If methods such as performance-based ensemble mean and reduced ensemble members are considered, the accuracy of the prediction can be further improved. In addition, uncertainty of the dispersion prediction and various prediction scenarios can be provided to decision makers, ultimately increasing the reliability of the system.

21st International Conference on
Harmonisation within Atmospheric Dispersion Modelling for Regulatory Purposes
27-30 September 2022, Aveiro, Portugal

EXPERIMENTAL CAMPAIGN OF CO2 MASSIVE ATMOSPHERIC RELEASES IN AN URBAN AREA

Lauris Joubert, Guillaume Leroy, Théo Claude

SHORT ABSTRACT

Abstract title: EXPERIMENTAL CAMPAIGN OF CO2 MASSIVE ATMOSPHERIC RELEASES IN AN URBAN AREA

Name and Affiliation of the First Author: Lauris Joubert[1]

[1]Ineris

Email of first author: lauris.joubert@ineris.fr

Names and Affiliations of the Co-authors: Guillaume Leroy[1], Théo Claude[1]

[1]Ineris

ABSTRACT TEXT (MAXIMUM 350 WORDS.)

Over the last decades, several campaigns were carried out to collect data regarding releases and atmospheric dispersion of dense chemical products in an open field. All these experimental data are valuable information to challenge the predictions of numerical tools (gaussian, integral-type and CFD tools) and, if needed, to improve the code itself and the way we are using it. On the other hand, little attention has been paid to atmospheric dispersion releases with massive flow rates in a complex urban environment.

To fill this gap, Ineris launched an experimental campaign intented to study atmospheric dipersion of massive CO2 releases on the Cenzub site (action training center in urban area located in Sissonne, France). Four CO2 releases were performed with mass flowrates between 8 and 10 kg/s in four different configurations: two axial street releases (one in a small sloped street and the other one in a big street) and two impacting releases (against a small and high-rise building). Several technologies of CO2 sensors were used to ensure a better measurement accuracy.

Main experimental campaign features and preliminary data analysis will be presented.

21st International Conference on
Harmonisation within Atmospheric Dispersion Modelling for Regulatory Purposes
27-30 September 2022, Aveiro, Portugal

NOVEL SIMPLIFIED METHODOLOGIES ON EXPOSURE UNCERTAINTY QUANTIFICATION FROM ACCIDENTAL AIRBORNE RELEASES

John Bartzis, Ioannis A. Sakellaris , George Efthimiou, Spyros Andronopoulos, Ilias Tolias, Alexandros Venetsanos

SHORT ABSTRACT

Abstract title: Novel simplified methodologies on exposure uncertainty quantification from accidental airborne releases

John G. Bartzis. University of Western Macedonia (UOWM), Dept. of Mechanical Engineering, Sialvera & Bakola Str., 50100, Kozani, Greece.

bartzis@uowm.gr

Ioannis A. Sakellaris[1], George Efthimiou[2], Spyros Andronopoulos[3], Ilias Tolias[3], Alexandros Venetsanos[3]

[1] University of Western Macedonia (UOWM), Dept. of Mechanical Engineering, Sialvera & Bakola Str., 50100, Kozani, Greece.
[2] Laboratory of Heat Transfer and Environmental Engineering, Aristotle University Thessaloniki, 54124, Thessaloniki, Greece.
[3] Environmental Research Laboratory, INRASTES, NCSR Demokritos, Patriarchou Grigoriou & Neapoleos Str., 15310, Aghia Paraskevi, Greece.

ABSTRACT TEXT

The exposure estimation due to an accidental or deliberate airborne release event, is a critical step for proper emergency response interventions. Any systematic and reliable approach to this problem requires the knowledge not only of the exposure itself but also its associated uncertainty. It is noted that special attention is needed for short exposure times and/or short duration releases due to the fact that the relevant times could become comparable with the ambient air turbulence time scales resulting to a more stochastic than deterministic behaviour for the respective exposures. Exposure uncertainty quantification is a rather complex problem and its direct modelling treatment would require an exceptionally large computation effort that often can be proved impractical especially for geometrically complex urban environments. The challenges here are (a) to provide simplified methods and tools attractive at the application/operation level but reliable enough to meet the user requirements and (b) to be applicable to any real release time duration or/and exposure time. A radically new approach is under development (a) by making full use of the real detailed inlet flow and release rate signals, (b) by performing a limited number of steady state only flow and dispersion simulations under reference inflow and release conditions and (c) by projection of the steady state/reference results to real atmospheric and release conditions via appropriate novel scaling approaches based on experimental evidence and theory. In this study experimental evidence is provided supporting the validity of the whole approach using the University of Hamburg Michelstadt wind tunnel experiments for continuous and puff releases. Furthermore, it is noticed the present approach opens new ways of handling exposure uncertainty on practical level.

TOPIC 9:

HIGHLIGHTS OF PAST WORK. SESSION DEVOTED TO REVIEWS AND TO PROMINENT SCIENTISTS AND ‘GOLDEN PAPERS’ OF THE PAST, WHICH HAVE STILL RELEVANCE AND SHOULD NOT BE FORGOTTEN

21st International Conference on
Harmonisation within Atmospheric Dispersion Modelling for Regulatory Purposes
27-30 September 2022, Aveiro, Portugal

WHAT WERE PASQUILL AND GIFFORD THINKING?

Steven Hanna

Hanna Consultants, Kennebunkport Maine USA

Abstract: The Pasquill-Gifford (PG) sigma curves (σ_y and σ_z) have been used to calculate dispersion in the atmosphere for about 60 years. In the early years, harmonization occurred in use of PG sigma curves in operational transport and dispersion models. Some operational models still make use of the curves. This paper provides some historical background, including justifications by Pasquill and Gifford for distributing their σ_y and σ_z nomograms. I worked with both of them in the 1970s and 1980s. First, it is important to point out that both Pasquill and Gifford were leading international experts on the basic physics of atmospheric boundary layer turbulence and diffusion, as shown by their seminal books and journal articles. Frank Pasquill always pointed out that it was best to use either observations or models of turbulence components (e.g., σ_u, σ_v, and σ_w) and Lagrangian time or distance scales in atmospheric diffusion models. But, he said, if you don't have that information, here is an alternative simple method that uses nomograms to estimate plume width and depth. Gifford later added his own interpretations, converted plume width and depth to σ_y and σ_z, and added more data. The PG curves are basically lines drawn through observations of variations of σ_y and σ_z, for five stability classes (A through E) with distance from all available field data that they could find at the time. The lines intentionally followed certain theoretically-justified slopes at asymptotes (e.g., linear at small distances). The user could, given the stability class and downwind distance, estimate σ_y and σ_z by eye.

Key words: *Pasquill-Gifford curves, dispersion modeling*

INTRODUCTION

This paper summarizes the rationale for development of simple dispersion nomograms by Frank Pasquill and Frank Gifford in the 1960s.

Frank Pasquill's early work history:

- He worked from 1937 to 1943 at the Chemical Defence Establishment of the Meteorological Office at Porton Down. He modified O.G. Sutton's equations based on these experiments and the results are now known as the Sutton-Pasquill model of evaporation.
- From 1943 to 1946, he worked in Queensland, Australia on classified work on the dispersion of toxic agents. In 1946, he returned to head a new unit of the Meteorological Office at Cambridge.
- In 1950, he was assigned to the Atomic Energy Research Establishment at Harwell. He worked with N.G. Stewart on the dispersion of radionuclides from nuclear plants and from the atomic testing.
- In 1954, he returned to Porton Down to conduct field measurements on the structure of atmospheric turbulence and the dispersion of pollutants. He developed a simple method for assessing atmospheric stability based on wind speed, solar radiation, cloud cover, and time of day. This resulted in the Pasquill stability classes A (very unstable) through F (very stable). In addition, he developed curves that are now interpreted as the vertical and horizontal dispersion coefficients
- He wrote the first edition of his book Atmospheric Diffusion in 1961, and the second edition in 1974. A subsequent issue was coauthored by F.B. Smith.
- Was Chief of the Boundary Layer Branch of the UK Met Office for several decades.

Frank Gifford's early work history

- He was a weather forecaster with the US Air Force during WWII, and contributed to the D-Day forecast.
- He received a PhD in Meteorology from Penn State, under Hans Panofsky.
- He was Director of NOAA's Atmospheric Turbulence and Diffusion Laboratory in Oak Ridge TN for about 25 years
- He initially studied local and mesoscale meteorology at Oak Ridge area. He then developed basic turbulence and dispersion theories for use by the AEC and DOE. He was on many international committees with Von Karman, Pasquill etc.
- Chief author of chapter on Turbulence and Diffusion in DOE M&AE 1968

RESEARCH INTERESTS IN 1950s AND 1960s

The atmospheric turbulence and diffusion topic was of great interest in the years following WWII, mainly because of the need to understand the spread and deposition of materials from nuclear explosions and from releases of chemical and biological agents in warfare. The top international fluid dynamicists were involved in fundamental research on the topic. Frank Pasquill and Frank Gifford were part of this set of experts. I recall Frank Gifford describing his meetings with Von Karman, Batchelor, Corrsin, Frenkiel, Inoue, Kolmogorov, Monin, Priestley and Obukhov.

Both Pasquill and Gifford developed advanced versions of Taylor's (1921) theory, which says that turbulent dispersion is the result of the effects of turbulent velocity fluctuations over the duration of travel of the pollutant cloud (see Pasquill 1974 and Gifford 1968, which contain comprehensive summaries of their rationale). For example, assume that $\sigma_y(t)$ is the standard deviation of the lateral distribution of pollutant in a cloud at a time, t, after the cloud is released from a source location. In Taylor's theory, it is assumed that σ_y depends on σ_v, T_v, and t, which are the standard deviation of the lateral turbulent speed fluctuations, the integral time scale of these fluctuations, and the time of travel from the source to the location of interest, respectively.

For continuous plumes, Pasquill converts Taylor's equation to an integral over the energy spectrum for lateral turbulence. He shows that the travel time and the sampling time act as high-pass filter (i.e., only eddies with frequencies higher less than the inverse of the travel time and/or sampling time can be "felt" by the dispersion process). For example, for a sampling time of 10 minutes, any eddies with time scales much greater than 10 minutes cannot influence the dispersion. Similarly, the averaging time (or resolution) of the turbulent speed measurements acts as a low pass filter. For example, for a sampler time resolution of 1 minute, any eddies with time scales much less than 1 minute cannot influence the observed dispersion.

Furthermore, Pasquill points out that the turbulence time scales felt by a fixed anemometer (T_E for Eulerian) are likely smaller than those felt by the cloud (T_L for Lagrangian), which is moving with the wind. The variable β is defined as T_L/T_E and is found to have a typical value of about 4.

So, the bulk of the research by Pasquill and Gifford was directed towards using observations or parameterizations of σ_y and T_v to calculate cloud dispersion. The theory was extended to handle instantaneous or time variable sources.

It is assumed that the cross-wind distributions of concentration in a plume are Gaussian. For a continuous plume, σ_y is the lateral direction and σ_z is the vertical direction. For an instantaneous release, the along wind dispersion, σ_x, is also important.

DEVELOPMENT OF P-G NOMOGRAMS

Although both Pasquill and Gifford recommended use of the above basic science concepts along with observations of turbulence fluctuations to calculate transport and dispersion, they recognized that, for

operational purposes, detailed local turbulence observations are seldom available. As a simpler alternative method, Pasquill suggested a way to estimate lateral and vertical cloud dispersion based on nomograms. These could be used quickly and with minimal knowledge of the weather conditions. It is assumed that there is flat open terrain with grass or other some other surface with similar roughness. A continuous non-buoyant point source is assumed, at an elevation within the surface boundary layer (usually a height less than 100 m).

Buckingham's pi theorem was used, which suggests that dispersion expressed as σ_y or σ_z is dependent on downwind distance, x, and a measure of stability class, which can be defined knowing time of day, wind speed U, and insolation or heat flux from surface (see Figure 1). Pasquill collected many sets of field observations of σ_y and σ_z and plotted the data versus x for each stability class. The reason why distance, x, is used rather than travel time, t, is that most available field experiments make use of a spatial network of samplers. The simple relation, x = Ut, is assumed. A line was fitted to the observations by eye and assuming certain asymptotic behavior (such as the fact that σ_y or σ_z are known to be linearly related to x at small x). The resulting σ_y and σ_z nomograms are in Figure 2, from Gifford (1976).

The appendices to reports by Pasquill include plots of the actual observations used for developing the best-fit lines. For example, there is a separate plot for σ_y for stability class D. As found for most atmospheric observations, there is significant scatter of about plus and minus a factor of about two, with occasional larger differences. We find this amount of scatter with current field studies, too.

Later, Bruce Turner (at the EPA) and Gary Briggs (at Frank Gifford's ATDL in Oak Ridge) fit simple one-line analytical formulas to the PG nomograms, for use in numerical models. Briggs' formulas conformed to known theoretical formulas at the large and small distance asymptotes. Briggs also suggested separate formulas for rural and urban land use (see Briggs (1972) and Hanna, Briggs, and Hosker (1982)). Golder (1972) suggested modifications for accommodating alternate metrics for stability such as the Obukhov length, L. Frank Pasquill's associate director of the Boundary Layer Branch, F.B. Smith, developed methods to correct the nomograms to account for a full range of surface roughnesses.

FURTHER COMMENTS

Note that the σ_z curves in Figure 2 for the most unstable stability classes (A and B) swoop upwards at large distances. For example, at the top of the figure, the σ_z curve "leaves the figure" at x = 3 km, where σ_z is approximately equal to distance travelled. As Pasquill points out, there are not adequate samplers to determine σ_z from a vertical profile, so it is calculated, in practice, from the Gaussian formula, assuming knowledge of σ_y, cloud centerline concentration C, source emission rate Q, and wind speed U:

$$\sigma_z = (Q/C)/(\pi U \sigma_y) \quad (1)$$

We now know, from convective scaling analysis and further laboratory and field studies (Weil. 1988), that, for near-surface releases, the height where maximum concentration occurs increases with distance and approaches $z_i/2$, where z_i is the mixing depth (usually about 1 or 2 km) on sunny summer days with light winds. As a result, ground level cloud centerline C is smaller (by a factor of 2 or 3) than it is at a height of $z_i/2$, and, hence, σ_z is overestimated by eq. (1). State-of-the-art modeling systems such as AERMOD (Cimorelli et al., 2004) use new convective scaling formulas for very unstable conditions.

I advise today's model developers that any new formulas had better follow the PG curves fairly closely, especially for stabilities close to neutral (classes C and D and E) since the PG curves are based on many observations, including the widely-used Prairie Grass data. This robust nature of the Gaussian plume formula applications with σ_y and σ_z from the PG curves also leads to it being relatively unbiased when included in multi-model comparison exercises involving new field observations of dispersion (e.g., Hanna et al., 2019).

REFERENCES

Briggs, G., 1972: Diffusion estimation for small emissions. ATDL Cont. File No. 79, ATDL, Oak Ridge, TN.

Cimorelli, A., S. Perry, A. Venkatram, J. Weil, R. Paine, R. Wilson, R. Lee, W. Peter and R. Brodes, 2004: AERMOD: A Dispersion Model for Industrial Source Applications. Part I: General Model Formulation and Boundary Layer Characterization. *J. Applied Meteorol*. **44**, 682-693.
Gifford, F.A., 1961: Use of routine meteorological observations for estimating atmospheric dispersion. *Nucl. Saf*., **2**(4), 47-57.
Gifford, F.A., 1968: An outline of theories of diffusion in the lower layers of the atmosphere, in Meteorology and Atomic Energy-1968 (D.H. Slade, ed.), USAEC report TID-24190, USAEC, NTIS, 66-116.
Gifford, F.A., 1976: Turbulent diffusion – typing schemes; A review. *Nucl. Saf*., **17**(1), 71.
Golder, D., 1972: Relations among stability parameters in the surface layer. *Bound.-Lay. Meteorol.* **3**, 47-58.
Hanna, S., G. Briggs and R. Hosker, 1982: Handbook on atmospheric dispersion. USDOE /TIC-11223, NTIS, 102 pp.
Hanna, S., J. Chang and T Mazzola, 2019: An analytical urban puff dispersion model compared with tracer observations in JU2003. *Bound.-Layer Meteorol.* **171**(3): 377-39.
Pasquill, F., 1962: The estimation of the dispersion of windborne material. *Meteorol. Mag*., **90**, 33.
Pasquill, F., 1971: Atmospheric dispersion of pollution. *Quart. J. Roy. Soc.* **97**, 369-395.
Pasquill, F., 1974: Atmospheric Diffusion, 2nd ed., Ellis Horwood Limited, Sussex, England, 429 pp.
Taylor, G.I., 1921: Diffusion by continuous movements. *Proc. London Math Soc*., **20**, 196.
Weil, J., 1988: Dispersion in the convective boundary layer. Lectures on Air Pollution Modeling (A. Venkatram, A. and J. C. Wyngaard, Eds.), Amer. Meteor. Soc., 167–227.

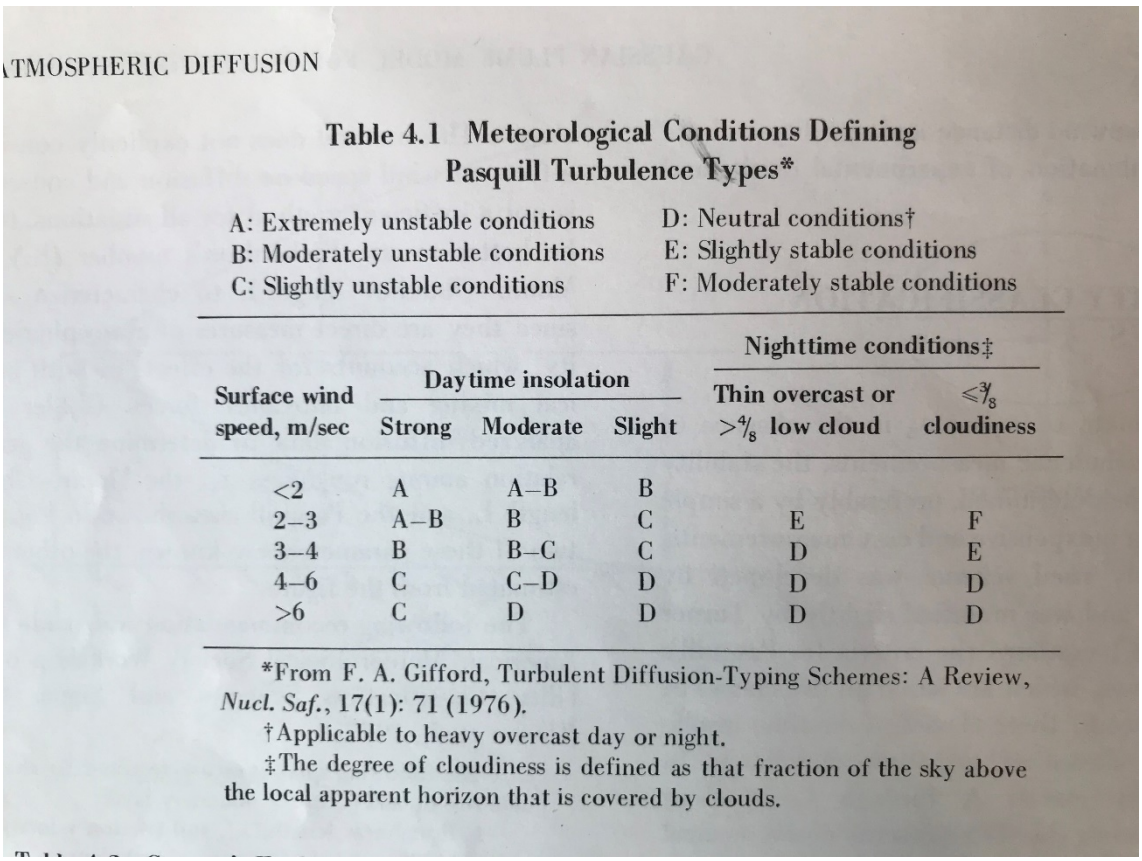

ATMOSPHERIC DIFFUSION

Table 4.1 Meteorological Conditions Defining Pasquill Turbulence Types*

A: Extremely unstable conditions
B: Moderately unstable conditions
C: Slightly unstable conditions
D: Neutral conditions†
E: Slightly stable conditions
F: Moderately stable conditions

Surface wind speed, m/sec	Daytime insolation			Nighttime conditions‡	
	Strong	Moderate	Slight	Thin overcast or >4/8 low cloud	≤3/8 cloudiness
<2	A	A–B	B		
2–3	A–B	B	C	E	F
3–4	B	B–C	C	D	E
4–6	C	C–D	D	D	D
>6	C	D	D	D	D

*From F. A. Gifford, Turbulent Diffusion-Typing Schemes: A Review, *Nucl. Saf.*, 17(1): 71 (1976).

†Applicable to heavy overcast day or night.

‡The degree of cloudiness is defined as that fraction of the sky above the local apparent horizon that is covered by clouds.

Figure 172. Pasquill method for estimating stability class (from Hanna et al. 1982 and originally published by Gifford, 1976)

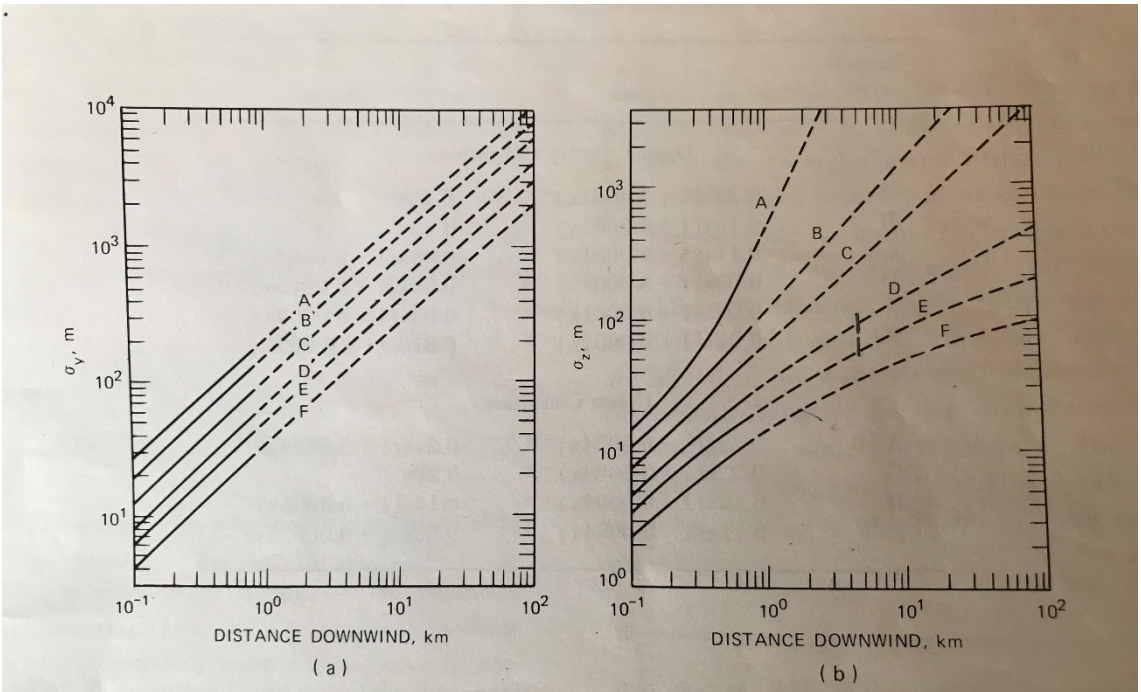

Fig. 4.4 Curves of σ_y and σ_z for turbulence types based on those reported by Pasquill (1961). [From F. A. Gifford, Turbulent Diffusion-Typing Schemes: A Review, *Nucl. Saf.*, 17(1): 71 (1976).]

Figure 2. Pasquill-Gifford nomograms for σ_y and σ_z, as a function of downwind distance and stability class (from Hanna et al. 1982 and originally published by Gifford, 1976)

TOPIC SS1:

MODELLING ODOUR DISPERSION AND EXPOSURE

21st International Conference on
Harmonisation within Atmospheric Dispersion Modelling for Regulatory Purposes
27-30 September 2022, Aveiro, Portugal

CRITICAL DISCUSSION OF THE DETERMINATION OF ANNOYANCE DUE TO ENVIRONMENTAL ODOUR EMISSION

Günther Schauberger [1] and Martin Piringer [2]

[1]WG Environmental Health, University of Veterinary Medicine, Vienna, Austria
[2]Central Institute of Meteorology and Geodynamics, Vienna, Austria

Abstract: The ambient concentrations of odorous substances from industrial and waste water treatment plants, livestock buildings, and other odour emitting units can be determined by the use of dispersion models in the same way as other air-borne pollutants. By the fact that the perception of odour and the related annoyance have to be predicted to assess the impact of an odour source, the calculated odour concentration alone does not provide reliable information. In this context we discuss the specific features of odour perception starting with the quantification of mixtures of odorous substances and the necessity of time resolved emission data. Further on weighting factors are discussed to calculate the perception-related odour emission on the basis of the ambient odour concentration. The following factors are discussed: daily and annual modification to predict the outdoor activities, hedonic tone considering the offensiveness, the reasonableness or local factor to describe the impact of the protection level for different zones, and the peak-to-mean factor to mimic the human perception of odour during one breath. This perception-related exposure improves the prediction of odour annoyance.

Key words: *environmental odour, emission, dispersion modelling, annoyance.*

INTRODUCTION

Environmental odour is the most frequent cause for complaints of residents besides noise (e.g., Yang et al., 2022). The perception of odour is based on odorous substances with a concentration above the odour concentration threshold. Environmental odour can be caused by a single substance or by a mixture of various odorous substances. In general, the dilution in the atmosphere and the related ambient concentration of odorous substances can be determined by the use of dispersion models in the same way as other air-borne pollutants like ammonia, particulate matter (PM), and nitrogen oxide are handled. In general, a dispersion model delivers the ambient concentration as hourly mean values C of a pollutant which is used to determine the exposure E. The relevant exposure depends on the dose-response relationship. In many cases, the health effect or the impact on the environment is evaluated by daily, seasonal or annual mean values of the ambient concentration.

The exposure of such pollutants is evaluated for each substance individually. In most of the cases the evaluation is performed by a limit or boundary value for the exposure which is derived by epidemiological studies. For a certain site, the evaluation by a limit value results in a dichotomic decision, if health threat can be expected by the ambient exposure.

Besides many similarities in the modelling of such pollutants, environmental odour has to be handled in a specific way, considering that an odour perception can cause annoyance and complaints.

In this paper, the exceptional position of environmental odour is critically discussed to demonstrate how odour has to be handled. Besides the quantification of odour emission, four predictors are discussed which allow to determine the perception-related exposure on the basis of the ambient odour concentration, modelled by a dispersion model.

MODELLING OF AMBIENT EXPOSURE

In the field of air quality, the goal of the procedure is the decision, if a health- or environmental-related threat can be expected by the emission of a pollutant for a certain site. In many cases also a background concentration has to be taken into account, which is caused by other sources of the same pollutant.

The calculation of the ambient concentration of a certain pollutant starts from the quantification of the emission Q, to the dilution in the atmosphere, calculated by a dispersion model, which results in the ambient concentration C at a certain site. The ambient concentration is a time series of hourly mean values. The exposure E is then calculated from this time series by mean values with different duration (day, month, of year). The time scale for the calculation of the mean (day, month, year) depends on how the exposure is defined for the dose-response function. In the end, the decision if a health or environmental threat can be expected, is based on the exceedance of limit or boundary values.
For environmental odour the principle difference is the fact, that the human perception of odorous substances is the relevant key target. In Figure 1, the schematic diagram shows the steps which are necessary to assess odour annoyance. The main discrepancies between an ordinary pollutant and odour will be discussed.

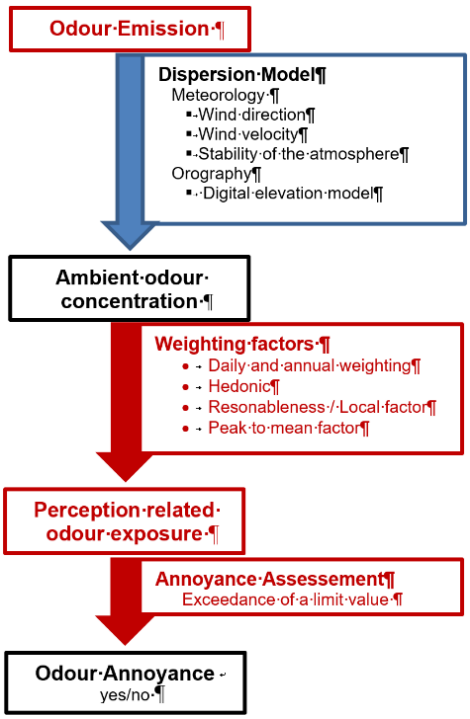

Figure 1. Schematic diagram showing the procedure from the source, described by the emission flow rate, the dilution in the atmosphere by the use of a dispersion model and the determination of the perception related odour exposure by the use of weighting factors, and the assessment if odour annoyance by the use of limit values. The odour specific steps are highlighted in red.

CRITICAL DISCUSSION OF ODOUR AS A POLLUTANT

Odour emission

In contrast to ordinary pollutants, odour emissions are characterised not by only one odorous substance but by a mixture of substances which are not known in detail. E.g. for pig odour several tens of substances are known with a wide variety of chemical and odour threshold concentrations (Liu, 2013; Qu and Feddes, 2007).In a working hypothesis the behaviour of odour substances is assumed as inert gases. For cattle it could be shown that in the near range volatile fatty acids and phenols are the key odorants, whereas in greater distances indole compounds become the key odorants (Trabue et al., 2011). The mixture of several odorous substances is difficult to predict. The translation from the chemical concentration of a single substance c_i to an odour concentration C_{OD} can be done by a rough estimation considering the odour threshold concentration $C_{S,i}$ of a certain substance by $C_{OD} = \Sigma\,(c_i / C_{S,i})$. The odour threshold concentration $C_{S,i}$ is the concentration which causes a barely perceivable perception of odour with $C_{OD} = 1$ ou/m^3. This

method is often called sum of the odour activity value *SOAV* (Capelli et al., 2013; Parker et al., 2012). More sophisticated conversion methods use not only the odour threshold concentrations of individual substances but also the slope *k* of the odour intensity - concentration relationship (Weber-Fechner law) (Kim and Park, 2008; Wu et al., 2016). The main objection against the additive behaviour of individual substances of a mixture ($C_{OD} = \Sigma (c_i / C_{S,i})$) is the uncertainty if augmentation ($C_{OD} > \Sigma (c_i / C_{S,i})$), protection ($C_{OD} < \Sigma (c_i / C_{S,i})$), or dominance by a stronger component, and synergistic effects can be expected (Kim and Kim, 2014; Moskowitz and Barbe, 1977).

By these constraints, the odour concentration is determined in general as an integral value of all substances. The measurement is then performed by an olfactometer which dilutes the odorous air in the range of 2^2 to 2^{16} with the goal to reach the limit concentration of 1 ou/m³ to detect the odour threshold by 50% of the panellists (prEN 13725, 2019). An overview of the methodology is given by Sówka et al. (2021). Due to the dilution, the odour concentration has to be at least 100 ou/m³ which means that ambient odour concentrations in the field cannot be detected by this method. This integral approach to measure all odorous substances together can cause problems, because the relationship between the odour intensity (= perception of humans) and the chemical concentration can show large differences (Guo et al., 2006; Wu et al., 2016).

In general, the odour emission rate is given as an annual mean value. This is a useful approach if the annual mean value of the ambient concentration is used as the relevant exposure value. In this case, the annual mean ambient concentration is proportional to the annual mean emission concentration. For odour a certain percentile (between 85% and 99.9%) is used to evaluate if annoyance can be expected. This means that not only the mean value but also the variability of the ambient concentration is taken into account. The range of the coefficient of variation (CV) lies between 5 and 20% for logarithmically transformed emission rates (Schauberger et al., 2016). If only the annual mean value of the emission is used, the variability is underestimated because the emission is assumed as constant. For a more realistic assessment, hourly varying odour emission rates should be available (Brancher et al., 2021; Brancher et al., 2019; Schauberger et al., 2014).

Weighting factors

The following four weighting factors should improve the explanatory power of the calculated ambient odour concentration. These predictors are used to get a more reliable measure to predict the occurrence of annoyance.

Daily and annual weighting. Regardless if odour perception occurs during a cold winter night or on an enjoyable summer evening, for the prevention of odour annoyance all hourly ambient odour concentration values account to the same extent. Due to weighting factors as predictors for the probability of staying outdoor (temperature and time of the day), the predictability can be improved. The weighting factors can be derived by complaint statistics (Blumberg and Sasson, 2001; Schauberger et al., 2006) or by an annoyance surveillance (Zhang et al., 2021). Functions for the two weighting factors, the time of the day and the day of the year, were suggested by Schauberger et al. (2009) and Piringer and Schauberger (2013).

Hedonic tone. The offensiveness of the odour perception, often measured in terms of "hedonic tone", in the pleasant–unpleasant dimension, is a powerful predictor of annoyance. It is shown that exposure-annoyance as well as exposure–symptom associations are strongly influenced by the hedonic tone. Whereas pleasant odours induce little to no annoyance, both neutral and unpleasant ones can cause high levels of annoyance (Sucker et al., 2008). In some countries (e.g. Germany, Ireland, and Belgium), the national odour impact criteria NOIC differ by the hedonic tone which means that for agricultural odour sources, the limit values depend on the kind of animals. This approach is suggested by the German odour guideline (TA Luft, 2021) not only for odour emissions caused by animal husbandry but also for all other odour sources.

Reasonableness / local factor. The protection level depends on the zoning of an area depending on the intended utilisation (pure residential areas vs rural or industrial zones) considering the expected air quality level. In many NOIC, this predictor is included in the limit values to assess the odour annoyance.

Peak-to-mean. An averaging time of one hour for the ambient odour concentration, which is the common output of dispersion models, is not representative for the perception of odour because the perception

depends on the duration of a single human breath. Besides simple parametrisations with a constant factor (Environment Protection Authority New South Wales, 2016; TA Luft, 2021), also more elaborated methods are in use, depending on the meteorological situation (Oettl and Ferrero, 2017; Piringer et al., 2015; Schauberger et al., 2013).

Annoyance assessment

The impact of environmental odour on humans is assessed by the occurrence of annoyance. The annoyance is determined by a nonlinear criterion, calculating the exceedance probability p_T of a certain threshold E_T of the perception-related exposure. By this criterion the right tail of the cumulative distribution function of the perception-related exposure is used for the annoyance assessment. The exceedance probability which is used for odour lies in the range between 20% in agriculturally dominated areas in Germany and 0.1% in Australia. The limit value of the exceedance probability depends on the selected odour concentration threshold. Two approaches are in use. In Germany and Austria, the limit value for annoyance is determined by an exceedance probability of p_T = 10% (pure residential) and p_T= 15% (rural and industrial sites) for a perception-related exposure E_T = 1 ou/m³. In many other jurisdictions the limit value for annoyance is determined by the perception related exposure E_T for a certain exceedance probability p_T in the range of $2\% < p_T < 0.1\%$ (Sommer-Quabach et al., 2014).

CONCLUSIONS

Environmental odour behaves similar compared to other air-borne pollutants. Therefore, the dilution in the atmosphere is handled in the same way by the use of dispersion models. The main discrepancy is the fact, that the impact of environmental odour on humans is caused by the perception of odour. The adaptation to the sense of smell starts by the measurement of the odour concentration with olfactometers, using panellists as sensors for the odour threshold concentration. The calculated ambient odour concentration as output of the dispersion model has to be modified to mimic the odour perception in a better way as it is done by the concentration itself. This perception-related odour exposure is determined by the time of the day and day of the year as predictors for the outdoor behaviour, the hedonic tone taking into account the offensiveness of a certain odour quality (e.g. poultry vs horse), the reasonableness (local factor) describing the protection level of certain sites (e.g. pure residential areas vs. rural or industrial sites) and the peak to mean factor taking into account, that the hourly mean value does not represent the perceived odour of individual breaths. In many jurisdictions these four factors are hidden in the established national odour impact criteria which are used to assess if odour annoyance can be expected.

REFERENCES

Blumberg, D.G., Sasson, A., 2001. Municipal hotlines and automated weather stations as a tool for monitoring bad odour dispersion: The northern Negev case. Journal of Environmental Management 63, 103-111.

Brancher, M., Hoinaski, L., Piringer, M., Prata, A.A., Schauberger, G., 2021. Dispersion modelling of environmental odours using hourly-resolved emission scenarios: Implications for impact assessments. Atmospheric Environment: X 12, 100124.

Brancher, M., Piringer, M., Schauberger, G., 2019. Fluctuation of odour emissions over time: Realising hourly emission rates for odour dispersion modelling. , 8th IWA Odour & VOC Air Emission Conference, Hangzhou, China pp. 238-247.

Capelli, L., Sironi, S., Del Rosso, R., Guillot, J.-M., 2013. Measuring odours in the environment vs. dispersion modelling: a review. Atmos. Environ. 79, 731-743.

Environment Protection Authority New South Wales, 2016. Approved Methods for the Modelling and Assessment of Air Pollutants in New South Wales, Sydney, NSW.

Guo, H., Yu, Z., Lague, C., 2006. Livestock odour dispersion modeling: A review, CSBE/SCGAB 2006 Annual Conference 2006. Canadian Society for Bioengineering, Edmonton, Alberta, p. 170.

Kim, K.-H., Kim, Y.-H., 2014. Composition of key offensive odorants released from fresh food materials. Atmos. Environ. 89, 443-452.

Kim, K.H., Park, S.Y., 2008. A comparative analysis of malodor samples between direct (olfactometry) and indirect (instrumental) methods. Atmos. Environ. 42, 5061-5070.

Liu, D., 2013. Application of PTR-MS for optimization of odour removal from intensive pig production with emphasis on biofiltration, Department of Engineering – Biological and Chemical Engineering. Aarhus University,, Aarhus.
Moskowitz, H.R., Barbe, C.D., 1977. Profiling of odor components and their mixtures. Sens. Processes 1, 212-226.
Oettl, D., Ferrero, E., 2017. A simple model to assess odour hours for regulatory purposes. Atmos. Environ. 155, 162-173.
Parker, D.B., Koziel, J.A., Cai, L., Jacobson, L.D., Akdeniz, N., Bereznicki, S.D., Lim, T.T., Caraway, E.A., Zhang, S., Hoff, S.J., Heber, A.J., Heathcote, K.Y., Hetchler, B.P., 2012. Odor and odorous chemical emissions from animal buildings: Part 6. odor activity value. Transactions of the ASABE 55, 2357-2368.
Piringer, M., Knauder, W., Petz, E., Schauberger, G., 2015. A comparison of separation distances against odour annoyance calculated with two models. Atmospheric Environment 116, 22-35.
Piringer, M., Schauberger, G., 2013. Dispersion modelling for odour exposure assessment, in: Belgiorno, V., Naddeo, V., Zarra, T. (Eds.), Odour Impact Assessment Handbook. Wiley, pp. 125-176.
prEN 13725, 2019. Stationary source emissions - Determination of odour concentration by dynamic olfactometry and odour emission rate from stationary sources. CEN, European Committee for Standardization.
Qu, G., Feddes, J.J.R., 2007. Development of a reference artificial swine odor. Transactions of the ASABE 50, 1789-1793.
Schauberger, G., Piringer, M., Heber, A.J., 2014. Odour emission scenarios for fattening pigs as input for dispersion models: A step from an annual mean value to time series. Agriculture, Ecosystems and Environment 193, 108-116.
Schauberger, G., Piringer, M., Petz, E., 2006. Odour episodes in the vicinity of livestock buildings: A qualitative comparison of odour complaint statistics with model calculations. Agriculture, Ecosystems and Environment 114, 185-194.
Schauberger, G., Piringer, M., Petz, E., 2009. Weighting of odour sensation by the time of the day and time of the year to improve the reliability of the calculated separation distance, in: Franz-Bernd, F. (Ed.), WASSER • ABWASSER • UMWELT Schriftenreihe des Fachgebietes Siedlungswasserwirtschaft der Universität Kassel. Kassel university press, Kassel.
Schauberger, G., Piringer, M., Petz, E., 2013. Assessment of seperation distances to avoid odour annoyance: interaction between odour impact criteria and peak-to- mean factors, 15th Conference on Harmonisation within Atmospheric Dispersion Modelling for Regulatory Purposes, Madrid, Spain, pp. 613-617.
Schauberger, G., Piringer, M., Petz, E., 2016. Influence of the variability of the odour emission rate on the calculation of the separation distance for various odour impact criteria. Chemical Engineering Transaction 54, 193-198.
Sommer-Quabach, E., Piringer, M., Petz, E., Schauberger, G., 2014. Comparability of separation distances between odour sources and residential areas determined by various national odour impact criteria. Atmospheric Environment 95, 20-28.
Sówka, I., Miller, U., Sobczyński, P., 2021. Dynamic olfactometry and modeling as methods for the assessment of odour impact of public utility objects. Environ. Prot. Eng. 42, 143-152.
Sucker, K., Both, R., Bischoff, M., Guski, R., Krämer, U., Winneke, G., 2008. Odor frequency and odor annoyance Part II: Dose - Response associations and their modification by hedonic tone. Int. Arch. Occup. Environ. Health 81, 683-694.
TA Luft, 2021. Neufassung der Ersten Allgemeinen Verwaltungsvorschrift zum Bundes–Immissionsschutzgesetz (Technische Anleitung zur Reinhaltung der Luft – TA Luft). Bundesministerium für Umwelt,, Naturschutz und Reaktorsicherheit, Bonn.
Trabue, S., Scoggin, K., McConnell, L., Maghirang, R., Razote, E., Hatfield, J., 2011. Identifying and tracking key odorants from cattle feedlots. Atmos. Environ. 45, 4243-4251.
Wu, C., Liu, J., Zhao, P., Piringer, M., Schauberger, G., 2016. Conversion of the chemical concentration of odorous mixtures into odour concentration and odour intensity: A comparison of methods. Atmospheric Environment 127, 283-292.

Yang, W., Li, W., Zhang, Y., Han, M., Zhai, Z., Cui, H., 2022. Exposure-response Relationship and Chemical Characteristics of Atmospheric Odor Pollution from a Cigarette Factory. Aerosol and Air Quality Research 22, 210314.
Zhang, Y., Yang, W., Schauberger, G., Wang, J., Geng, J., Wang, G., Meng, J., 2021. Determination of Dose–Response Relationship to Derive Odor Impact Criteria for a Wastewater Treatment Plant. Atmosphere 12, 371.

21st International Conference on
Harmonisation within Atmospheric Dispersion Modelling for Regulatory Purposes
27-30 September 2022, Aveiro, Portugal

DEVELOPMENT OF A SIMULATION TOOL TO EVALUATE THE APPLICABILITY OF THE GRADIENT METHOD FOR THE ESTIMATION OF ODOUR EMISSION FLUXES

Giulia Uvezzi[1], Alessandra Panzitta[1], Beatrice Julia Lotesoriere[1], Marzio Invernizzi[1], Roberto Sozzi, Laura Capelli[1]

[1] Politecnico di Milano, Department of Chemistry, Materials and Chemical Engineering "Giulio Natta" - P.za Leonardo da Vinci 32, 20133 Milano, Italy

Abstract: Micrometeorological methods are commonly used in agro-meteorology for the estimation of biogenic emissions. Despite being often mentioned, their practical application for indirect estimation of odour emission rates is extremely rare. Among the existing methods, this work focused on the Gradient Method and the main objective was to identify the technical characteristics required for analysers to be used for the estimation of odour fluxes. This evaluation was carried out through the implementation of a flexible simulation tool which, by using reference odour fluxes and real meteorological data measured during the year 2015 by an ultrasonic anemometer (Tor Vergata, Rome), made it possible to recreate the functioning of a measuring device, and thus to assess a priori the possibility of applying these methods. For this purpose, the absolute concentration and concentration difference at the measurement point were determined in order to assess the limits of detection and resolution required by the odour analyser. The results showed that for an odour flux of 1 $ou_E/m^2/s$, if 50 ou_E/m^3 is taken as the lower resolution limit for odour concentration measurements, the percent data that could hypothetically result above this limit would be 33.3% if considering two measurement heights of 0.5 m and 3.5 m, and 44.3% if considering two measurement heights of 0.5 $m - 10$ m. Similar considerations can be made based on analysis of the absolute concentration measured at the two sampling heights. Moreover, the influence of atmospheric stability on the data above the background odour has been investigated: the measurement of the concentration gradient as well as of the absolute concentration, regardless of the chosen measurement heights, is only feasible under the conditions described by categories D and F. In conclusion, the gradient method represents an attractive and potentially applicable alternative for estimating odour emissions, since the developed simulation tool has demonstrated to be suitable to evaluate the conditions of applicability of the method as a function of specific emission and meteorological conditions. However, the effective direct applicability to the odour concentration requires further study and experimental campaigns.

Key words: *Odour emissions, Micrometeorological methods, area sources*

INTRODUCTION

Several applications of micrometeorological methods for the emission rate estimation of odorous compounds such as NH_3 (Galle, et al., 2000; Kamp, et al., 2020), H_2S (Baek, et al., 2006), dimethyl sulphide (DMS) (Zemmelink, et al., 2002), and VOCs (terpenoids) (Darmais, et al., 2000) are reported in the literature. In a recent review paper, which investigates different micrometeorological methods focusing on their applicability to odours (Lotesoriere B. J., 2022), the Gradient Method (GM) is identified as the potentially most interesting method to be applied directly to odour. Based on this observation, in this work we decided to simulate the implementation of an experimental setup for the application of the GM for the estimation of odour fluxes, with the aim of investigating the technical characteristics, such as limits of detection and resolution, for analysers to be suitable for this type of purposes. Thus, the novel aspect of the work is the construction of a tool that allows to evaluate in a preliminary way the feasibility of an effective experimentation in the field and the characteristics of the required measuring instruments.

MATERIALS AND METHODS

In general, micrometeorological methods are based on the principle of measuring the concentration of a substance in order to indirectly estimate its emission flux. However, in this work, aimed at the development of a tool to recreate a numerical environment that allows identifying the technical characteristics of the measurement system for concentration assessment, it was necessary to proceed in a different way, i.e. to assume that the flux is known and, from it, to derive the concentrations to be measured.

The data used for the implementation of the tool are:

- The micrometeorological observations detected by the micrometeorological tower of ARPA Lazio inside the Experimental Campus at the Tor Vergata (Rome) site of CNR-ISAC (Institute of Atmospheric Sciences and Climate), and their main elaborations, referred to one entire solar year (2015). The territory surrounding the meteorological station can be considered as horizontally homogeneous and free of significant obstacles that could disturb the measurements, which makes it an ideal site for micrometeorological measurements
- Hypothetical odour flux values ($ou_E m^{-2} s^{-1}$) based on the database of the Olfactometric Laboratory of Politecnico of Milan, in order to compute the associated concentration value ($ou_E m^{-3}$).

The simulation tool developed in this study has the objective to assess the instrumental requirements, in terms of resolution and detectability, for odour concentration analysers to be suitable for the implementation of the GM and provide useful output data. To do this, assuming a certain value for the odour flux, we calculated the concentration gradient as well as the absolute concentration values at two different heights above the emitting surface. The choice of the two measurement heights to be used for the calculations was made based on the scientific literature, and also considering the height at which the triaxial ultrasonic anemometer is located in Tor Vergata. The height z_1 was set at 0.5 m, because it was considered an easily accessible height for the installation of the instrumentation, while for the height z_2 we decided two consider two different cases: the first is z_2=10 m, because it is the same height at which the anemometer is located, while the other is z_2=3.5 m, since in the scientific papers regarding the GM application, often a Δz of 3-4 m is considered (Baek, et al., 2006) (Todd, et al., 2005) (Galle, et al., 2000) (Kamp, et al., 2020) (Phillips, et al., 2004) (Darmais, et al., 2000) (Zemmelink, et al., 2002)**.**

Definition of the instrumental resolution: computation of the concentration gradient

The resolution is the ability of the measurement system to detect smallest changes in the characteristic of the measurement results. Thus, it can be evaluated based on the computation of the concentration gradient ΔC between the two measurement heights considered, z_1 and z_2. Indeed, the minimum measurable concentration difference can be expressed by making explicit the concentration gradient ΔC from the flux equation of the gradient method:

$$\Delta C = C(z_2) - C(z_1) = -\frac{F_c}{k u_*} \cdot \left[ln\left(\frac{z_2}{z_1}\right) - \Psi_c(\zeta_2) + \Psi_c(\zeta_1) \right] \quad (1)$$

The odour fluxes (F_c) were assumed equal to 0.1, 1 and 10 $ou_E m^{-2} s^{-1}$. The value of the friction velocity u_* was obtained from the triaxial ultrasonic anemometer considering an average of 30 minutes. As described before, the height z_1 was considered equal to 0.5 m, while z_2 was varied to 3.5 m and 10 m, respectively. The stability parameters ($\zeta_2$and ζ_2) were computed every 30 minutes from the value of the Monin-Obukhov length (L), given by the anemometer. By analysing the existing literature, and in particular the work of Högström (Högström, 1985), the Von Karman constant (k) was set equal to 0.4. The simplified form proposed by Gryanik (Gryanik, et al., 2020) was used to calculate the universal stability function (Ψ_c).

Definition of the instrumental detection limit: computation of the absolute concentration

The detection limit can be defined as the lowest quantity or concentration that can be reliably detected by the analyser. Thus, it can be evaluated by computing the absolute concentration at the measurement heights considered. The absolute concentration can be expressed according to the Monin-Obukhov Similarity theory as the vertical profile of the mean concentration:

$$C(z) = C(z_{0c}) + \frac{C_*}{k} \cdot \left[ln\left(\frac{z}{z_{0c}}\right) - \Psi_c(\zeta) \right] \quad (2)$$

The scale concentration (C_*) was evaluated as the ratio between the odour flux and the friction velocity (u_*). The roughness length z_{0c} was assumed to be equal to 10^{-3} m and three different measurement heights (0.5, 3.5 and 10 m) were considered. The stability parameter and the universal stability function are computed in the same way described for the computation of the concentration gradient. The estimation of

the average concentration near the ground of a passive scalar $C(z_{0c})$, whose emission rate F_c is known, was realised by applying an old model developed by Steven Hanna in 1971 (Hanna, 1971) with this correlation:

$$C_0 = A \cdot \frac{F_c}{U} \quad (3)$$

The coefficient A is linked to the extension of the urban portion above the measurement point and the atmospheric stability classes, and it was estimated according to the values reported in Table 57.

Table 57*. Values for coefficient A depending on the Pasquill atmospheric stability classes (Hanna, 1971).*

	A
Daytime and sunny hours (cat. A)	48
Daytime hours with partly cloudy skies (cat. B)	57
Daytime hours with cloud cover (cat. C)	100
Day/night hours with cloudy skies and/or strong winds (cat. D)	180
Night-time	545

In order to estimate the mean wind speed (U) at the height where C_0 is measured, i.e. near the ground, it was decided to use the relationship reported in Hanna's Handbook (Hanna, 1971), which allows to compute U at the required height (z) as a function of the value measured at z_m and a p-exponent depending on the Pasquill atmospheric stability classes for rough urban surfaces (Table 58):

$$U(z) = U(z_m) \cdot \left(\frac{z}{z_m}\right)^p \quad (4)$$

Table 58. *Values for p-exponent depending on atmospheric stability classes for rough urban surfaces (Hanna, 1971).*

	p
Daytime and sunny hours (cat. A-C)	0,15
Day/night hours with cloudy skies and/or strong winds (cat. D)	0,25
Night-time	0,50

PRESENTATION OF RESULTS

Equations (1) and (2) enable the calculation of the expected concentration gradients and absolute concentration values at different heights for a given odour flux. In order to gain some useful information about the practical applicability of the GM to odour emissions, i.e. based on odour concentration measurements, we decided to proceed as follows: we decided to "fix" a possible value for the instrumental resolution ($\Delta C_{min,ins}$) and lower detection limit ($C_{min,ins}$), thereby hypothesizing cutting-edge technologies for odour concentration measurements. Then, by applying equations (1) and (2) we evaluated the "measurable" number of experimental observations, in terms of concentration gradient and absolute concentration, considering the fixed instrumental technical characteristics $\Delta C_{min,ins}$ and $C_{min,ins}$. Regarding the instrumental lower detection limit, it must be considered that "background odour" of ambient air is typically estimated to be in the range between 5-60 $ou_E m^{-3}$, so the practical lower limit of dynamic olfactometry, which is the reference method for the measurement of odour concentration, is assumed to be 50 $ou_E m^{-3}$. For this reason, both the instrumental resolution and lower detection limit were set equal to 50 $ou_E m^{-3}$, meaning that the we assumed that the odour analyser is capable of measuring absolute concentrations and concentration differences above 50 $ou_E m^{-3}$ ($C>50$ $ou_E m^{-3}$ and $\Delta C>50$ $ou_E m^{-3}$).

RESULTS AND DISCUSSION

Evaluation of measurable odour concentration gradients

As expected, the concentration gradient increases with the difference between the two measurement heights, as well as with the odour flux assumed. As a consequence, it turns out that, if 50 $ou_E m^{-3}$ is taken as the lower limit for the instrument resolution, for a flux of 0.1 $ou_E m^{-2} s^{-1}$ most of the data cannot be measured. For a flux of 1 $ou_E m^{-2} s^{-1}$, the data that could hypothetically be sampled are 33.3% considering the measurement heights of 0.5m-3.5m and 44.3% for the measurement heights 0.5m-10m. Finally, for a flux of 10 $ou_E m^{-2} s^{-1}$, even more satisfactory results are achieved, as the concentration gradients that could be quantified are 99.8% and 100%, respectively. As an example, Figure 173 (left) shows the results of the evaluations regarding the concentration gradients assuming a flux (F_c) of 1 $ou_E m^{-2} s^{-1}$.

Evaluation of the measurable absolute odour concentration values

Also in this case, as expected, higher absolute concentrations are obtained for higher odour fluxes. Moreover the absolute concentration decreases with the measurement height. Considering a flux of 1 $ou_E m^{-2} s^{-1}$ and an instrumental lower detection limit of 50 $ou_E m^{-3}$, the measurable data are 58.95%, 52.8% and 49.8% for the 3 measurement heights, respectively. Conversely, if considering a flux of 10 $ou_E m^{-2} s^{-1}$ (Figure 173, right).

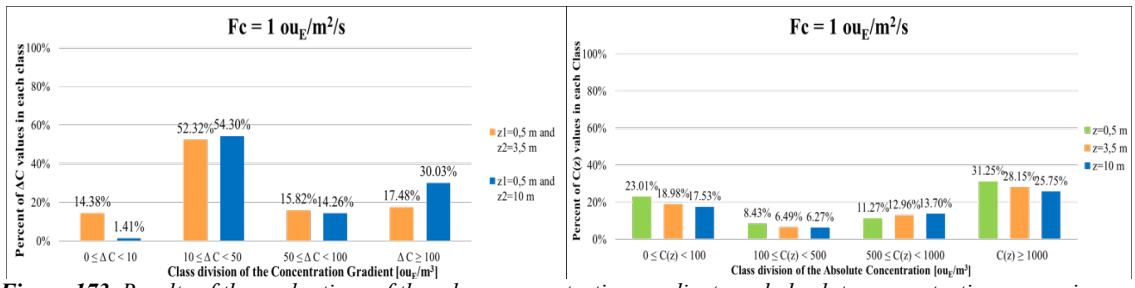

Figure 173. *Results of the evaluations of the odour concentration gradients and absolute concentrations assuming an odour flux (F_c) of 1 $ou_E m^{-2} s^{-1}$.g*

Evaluation of the influence of atmospheric stability

In the previous sections we have investigated the number of measurable data if applying the GM to the direct measurement of the odour concentration, by fixing the lower detection limit and resolution of a hypothetical analyser. Since the obtained results point out that not all experimental data would be measurable, especially if considering low odour fluxes, it could be interesting to study the influence of atmospheric stability both on the concentration gradients and on the absolute concentrations, in order to assess whether more favourable conditions exist to maximise the values of these parameters and thus increase the percent of measurable data.

Starting from the odour concentration gradients, by analysing the meteorological data from Tor Vergata, it is possible to explore which stability classes result in a higher number of measurable data, always considering a minimum instrumental resolution of 50 $ou_E m^{-3}$. As shown in Figure 174, for a flux of 0.1 and 1 $ou_E m^{-2} s^{-1}$, the measurable data mostly fall within the stability classes D and F, with no major differences for the two pairs of heights considered. This means that odour concentration gradients would be measurable in nocturnal or diurnal periods close to adiabaticity (class D) or in exclusively nocturnal and stable situations (Class F). Stability class E represents situations close to stability, with fairly high winds and slightly cloudy sky, therefore being another favourable weather condition for estimating concentration gradients. The reason why the percent of measurable data falling within this class is low, is because the occurrence of this atmospheric condition is rare.

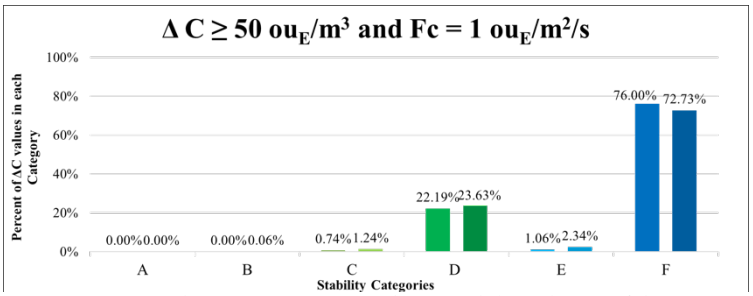

Figure 174. *Distribution among Atmospheric Stability Classes of the Concentration Gradient values above 50 ou_E/m^3, evaluated by assuming a flux (F_c) equal to 1 $ou_E/m^2/s$ for the two pairs of measurement heights considered.*

A similar analysis was carried out for the absolute concentrations, giving that for a flux of 0.1 $ou_E m^{-2} s^{-1}$ the measurement of the absolute concentration, regardless of the chosen measuring heights, is only feasible under the night conditions described by categories D and F. For higher fluxes, such as 1 $ou_E m^{-2} s^{-1}$ and 10 $ou_E m^{-2} s^{-1}$, the quantification of the absolute concentration is also practicable in the conditions described by categories D and, to a small extent, also in daytime conditions described by classes A, B, and C.

CONCLUSIONS

In this study the main objective was to implement a tool that enables to design a potential experimental campaign for applying the GM with the purpose of estimating odour emissions. The developed tool allows a preliminary assessment of the possibility of applying the method, and in particular to define the technical specifications of the instruments to be used in order to obtain an acceptable quantity of measurable data. The analysis of the obtained results showed that, especially considering the odour concentration gradients, a satisfactory amount of measurable data is only obtained for relatively high odour fluxes, i.e. > 1 $ou_E m^{-2} s^{-1}$, which are not very common for real odour sources. In conclusion, the GM represents an attractive and potentially applicable alternative for estimating odour fluxes from extended passive area sources, such as landfills, considering that the existing chamber methods are not very effective due to their intrinsic limitation linked to the impossibility of covering large surfaces (Mønster, et al., 2019). However, this study points out that great attention should be paid to carefully design the experimental campaign, in order to ensure to obtain a reasonable number of useful results. The developed simulation tool has proved to be suitable for preliminary evaluations on the applicability of the method according to specific emission and meteorological conditions. Further studies are needed in order to verify the applicability of the method on real odour sources.

REFERENCES

Baek, B., Todd, R., Cole, N. & Koziel, J., 2006. Ammonia and hydrogen sulphide flux and dry deposition velocity estimates using vertical gradient method at a commercial beef cattle feedlot.. *Int. J. Glob. Environ. Issues,* Volume 6, p. 189–203.

Darmais, S. et al., 2000. Emission fluxes of VOC by orange trees determined by both relaxed eddy accumulation and vertical gradient approaches. *Chemosph. - Glob. Chang. Sci. ,* Volume 2, p. 47–56.

Darmais, S. et al., 2000. Emission fluxes of VOC by orange trees determined by both relaxed eddy accumulation and vertical gradient approaches. *Chemosph. - Glob. Chang. Sci. ,* Volume 2, p. 47–56.

Galle, B. et al., 2000. Measurements of ammonia emissions from spreading of manure using gradient FTIR techniques. *Atmos. Environ. ,* Volume 34, p. 4907–4915.

Gryanik, V., Lüpkes, C., Grachev, A. & Sidorenko, D., 2020. New Modified and Extended Stability Functions for the Stable Boundary Layer based on SHEBA and Parametrizations of Bulk Transfer Coefficients for Climate Models. *J. Atmos. Sci. ,* Volume 77, p. 2687–2716.

Hanna, S., 1971. *Handbook on atmospheric diffusion models.*. s.l.:s.n.

Högström, U., 1985. Von Kármán's Constant in Atmospheric Boundary Layer Flow: Reevaluated. *J. Atmos. Sci. ,* Volume 42, p. 263–270.+.

Kamp, J. et al., 2020. The Aerodynamic Gradient Method: Implications of Non-Simultaneous Measurements at Alternating Heights. *Atmosphere (Basel),* Volume 11, p. 1067.

Lotesoriere B. J., I. M. P. A. U. G. S. R. S. A. a. C. L., 2022. Micrometeorological Methods for the Indirect Estimation of Odorous Emissions. *Critical Reviews in Analytical Chemistry.*

Mønster, J., Kjeldsen, P. & Scheutz, C., 2019. Methodologies for measuring fugitive methane emissions from landfills – A review. *Waste Manag. ,* 87(835–859).

Phillips, S., Arya, S. & Aneja, V., 2004. Ammonia flux and dry deposition velocity from near-surface concentration gradient measurements over a grass surface in North Carolina. *Atmos. Environ.,* Volume 38, p. 3469–3480.

Todd, R., Cole, N. & Harper, L., 2005. Ammonia and gaseous nitrogen emissions from a commercial beef cattle feedyard estimated using the flux-gradient method and N: P ratio analysis. *Sci. Anim. ,* p. 1–8.

Zemmelink, H. et al., 2002. Simultaneous use of relaxed eddy accumulation and gradient flux techniques for the measurement of sea-to-air exchange of dimethyl sulphide. *Atmos. Environ.,* Volume 36, pp. 5709-5717.

21st International Conference on
Harmonisation within Atmospheric Dispersion Modelling for Regulatory Purposes
27-30 September 2022, Aveiro, Portugal

A DYNAMIC ODOUR MAPPING SYSTEM AS A TOOL TO SUPPORT LOCAL AUTHORITIES AND WASTEWATER TREATMENT PLANTS IN ODOUR IMPACT MANAGEMENT

Iwona Rackiewicz[1], Agnieszka Bartocha[1], Tomasz Przybyła[1], Marek Rosicki[1], Piotr Michałek[1]

[1]ATMOTERM S.A. R&D Unit, Poland

Abstract: Wastewater treatment plant may be a source of nuisance for neighbouring urban areas. Complaints from residents force local authorities and wastewater treatment plants to take action to reduce odour impacts. The need for understanding and assessing the impacts is limited by the available budget. The article presents a low-cost Dynamic Odour Mapping System developed and implemented in one of the wastewater treatment plants serving the city of Bydgoszcz with a population of nearly 350,000. The system consists of four main units: low-cost sensors measuring H_2S and NH_3, an emission modelling system, an odour dispersion modelling system and an odour dispersion dynamic map. Low-cost sensors supported the identification of the main emission sources at the plant and are used for dynamic emission estimation of H_2S and NH_3. Developed algorithms for emission assessment, using sensors data, provide real-time information for the modelling system. Calpuff software is used for H_2S and NH_3 dispersion modelling and its results are presented on the map in historical and nowcasting mode. The main feature that distinguishes the Dynamic Odour Mapping System from others is its dynamic data processing and near real-time information publication. The article describes the main features of the system and discusses its innovative part, how it responds to the needs of the local community, and further directions for development.

Key words: *odour dispersion modelling, low-cost sensors air quality mapping, wastewater treatment plant.*

INTRODUCTION

Municipal wastewater treatment plants (WWTP) are one of the most common sources of odour emissions. Regardless of the modern technological solutions applied to minimise the odour nuisance associated with this type of facility, they may cause unpleasant olfactory experiences for the residents of neighbouring settlements and may even be perceived as a health hazard. The problem of odorous air pollution around WWTPs is mainly due to: processes of anaerobic decomposition of organic substances contained in wastewater, causing the formation of odorous compounds (hydrogen sulphide (H_2S), ammonia (NH_3), mercaptans, aldehydes, ketones and fatty acids), improperly conducted wastewater treatment processes at the WWTP, increasing public awareness and related expectations regarding the quality of the environment.

A lack of Polish and EU legal regulations unambiguously defining the methods of assessing the environmental impact of odour facilities, as well as the lack of a specific odour standard, cause the approach to the abovementioned assessment to vary. In practice, sensorial, instrumental, and mathematical methods are used to assess the odorous impact of industrial activities, which may potentially cause odour nuisance to the environment (Bax C., Sironi S., Capelli L, 2020).

The sensorial method (dynamic olfactometry) can be used for the determination of the odour concentration of a gaseous sample in the European odour unit per cubic metre ($ou_E m^{-3}$), following the European standard EN 13725 “Stationary source emissions - Determination of odour concentration by dynamic olfactometry and odour emission rate” (Standard EN 13725:2022). Determining the volumetric flow rate of the gas at the source enables the calculation of odour emission in odour units per second ($ou_E s^{-1}$), which can be used as input data for modelling. However, this method requires a specialised piece of equipment (olfactometer) and measurements carried out by a panel of human assessors (being the sensors), which is connected with the relatively high costs of this type of research. The sensorial method also cannot be used continuously,

which is important in the case of sources characterised by temporal variabilities, such as sewage treatment plants.

The technological advances made in recent years in constructing low-cost sensors to measure environmental parameters have created new possibilities for building measurement systems. Such measurements can be carried out continuously. However, they cannot determine the concentration of the odour mixture in $ou_E m^{-3}$. Still, it is possible to determine the concentration of selected individual chemical compounds in $\mu g m^{-3}$. Based on the literature (Baawain, M., Al-Mamun, A., Omidvarborna, H. *et al.*, 2019), it can be assumed that hydrogen sulphide is the leading substance for wastewater treatment plants. Knowing the concentration of hydrogen sulphide (in $\mu g m^{-3}$) at the odour detection threshold allows its concentration to be determined in $ou_E m^{-3}$ (according to EN 13725, the odour concentration at the detection threshold is by definition equal to 1 $ou_E m^{-3}$), as a multiple of the detection threshold.

METHODOLOGY

A data fusion concept combining dispersion modelling with sensor network data was applied to the development of a dynamic air quality map, which was a goal of ISSOP research and development project financed by the National Centre for Research and Development (NCBR) and carried out by Atmoterm in the period 2016-2020. The advantage of this solution, in comparison with the systems based only on a network of sensors, are: greater reliability of the results, lower operating costs, greater system stability, the possibility to determine concentrations at any point of the analysed area, the determination of the contribution different emission sources or their groups. The original ISSOP system was prepared to monitor and predict PM2.5, PM10, NO_2, CO, ozone and VOC concentrations. The respective LUMA sensors were developed to run the system effectively.

One of the extensions of the system is a Dynamic Odour Mapping System (DOMS) focused on H_2S and NH_3 concentrations as well as odour units. The system provides nowcasting/forecasting data and also allows analysis of historical data. In addition to the data fusion algorithm the LUMA sensors are also implemented in this case as auxiliary data sources for emission correction. The system was developed in response to enquiries received regarding a cost-effective tool for monitoring odour nuisance in residential areas adjacent to the waste water treatment plant.

Modelling system setup

The modelling system consists of the CALMET meteorological diagnostic model, the WRF prognostic model, the CALPUFF dispersion model and a dedicated set of pre/postprocessing tools. A simplified diagram of the system is shown in the figure below.

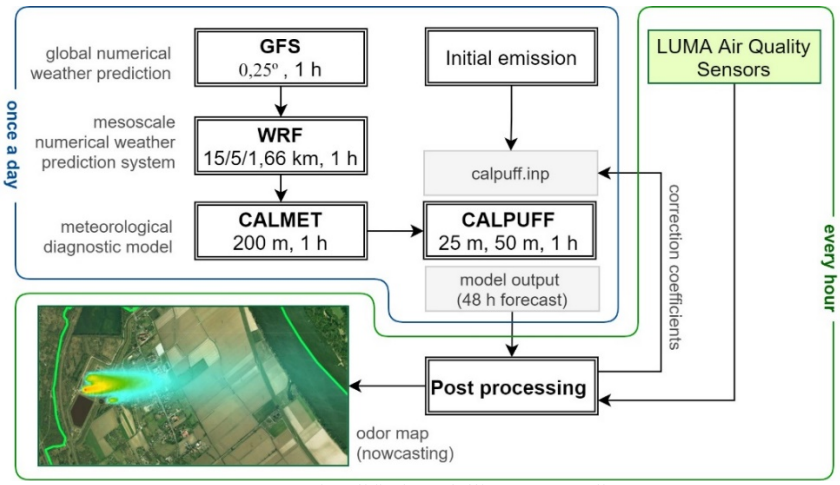

Figure 175. Simplified modelling system diagram

The meteorological data set is determined in the CALMET model in version 7. The input data for the CALMET model includes a geophysical data file and a meteorological data file. The geophysical model

was prepared on the basis of SRTM and Corine Land Cover 2018 data. The input meteorological datasets for the CALMET model are determined in the WRF forecast model version 4.2. The meteorological boundary and initial conditions for the mesoscale WRF model are obtained from the global GFS model with a spatial resolution of 0.25º × 0.25º and a time resolution of 1 hour. Calculations in the WRF model are performed once a day for 48 hours of the forecast period for 3 mutually nested domains (d01 - 15 km resolution covering Central Europe area, d02 - 5 km resolution covering the country territory and d03 - 1.66 km resolution covers the area of the city where the WWTP is located). WRF model settings include Thompson 7-class microphysics scheme, Yonsei University-Pleim-Chang (YSU) PBL scheme, Kain-Fritsch cumulus scheme (d01) and RRTMG long wave and shortwave radiation scheme.

Pollutants dispersion modelling is determined using CALPUFF model developed by Sigma Research Corporation. Emissions are introduced to the model through dedicated emission files calpuff.inp which include emitter's parameters (location, elevation, stack parameters) and emission characterisation. Each emission source is modelled independently. CALPUFF model calculations are initiated daily using the initial emissions estimated with the first approximation.

Emissions

The emissions from the WWTP are not continuous or cyclical, they are episodic (e.g. unloading or discharges of wastewater, etc.), which significantly complicates the modelling process, especially in terms of modulating emissions over time. Therefore, it was decided to use measurement data from detectors located as close as possible to the emission source. The measurement data, read hourly via the API, allows for the correction of the initial emissions estimated to the first approximation. The emissions adjustment is made at the post-processing stage. All operations on the output dataset are performed with the use of CALSUM and CALPOST postprocessors and specially developed Python scripts.

Sensors development

For H_2S measurements Alphasense H2S-B4 sensors have been implemented into LUMA device. Winsen ZE03-NH3 sensors have been applied for NH_3 measurements. The Dynamic Odour Map System uses sensors in two modes: for dynamic emission correction and for assimilation process. Sensors located close to the main emission sources support emission calculations; sensors placed at the boundary of the WWTP site are used in fusion process in modelling.

Mapping system

The open-source TerriaMap project was used to present the modelling results in the form of spatial concentration distribution maps. Data is collected on an ongoing basis via a special API from the LUMA sensors service system and from the modelling system. Data is saved and then is undergoing geoprocessing through data pasteurization. The system ensures scalability thorough application of docker services for all components of the data processing and visualization system.

Implementation of the system and results

The system has been implemented in a Wastewater Treatment Plant (WWTP) located in Bydgoszcz City in 2020. The project was initiated by the complaints of residents living close to the WWTP and financed by City budget. The implementation consisted of two steps: pilot study and full operation phase.

Pilot study

In the first step, the prototypes of low-cost sensors for H_2S and NH_3 measurement were designed, produced and calibrated. The calibration process was carried out for the detection of the leading substance H_2S in field conditions. The reference device was the Draeger PAC 6500 instrument. The field calibration process has been conducted in the Wastewater Plant and has lasted 4 days. The results showed very good agreement of designed devices (LUMA sensors) with the reference device with accuracy of 0.1 ppm. For the NH_3, factory calibration parameters provided by the sensor manufacturers were used. The final location of sensors has been selected based on measurements and information received from WWTP officers (figure below). Selected locations included the main emission sources: 1, 3.1, 3.2, 18, 5 and the boundary of the WWTP close to the nearest residential houses (no. 2 – the gate).

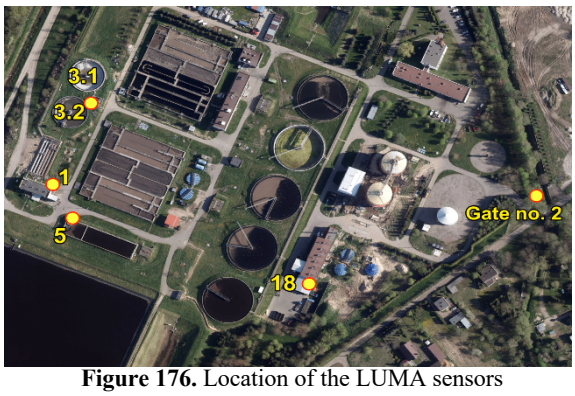

Figure 176. Location of the LUMA sensors

Operation phase

Operation phase which includes launching a modelling run and map presentation in public portal, started in the December 2021. The analysis of LUMA sensors measurements helped to design the parameters of the odour mapping portal. Scale levels for H_2S odour impact have been established. Detection threshold for H_2S was set up at 1 μgm^{-3} (AIHA, 2013). According to the British guidelines on odour management (Environment Agency: H4 Odour Management, 2011) 3 ou was applied as the comparative level for 1-hour concentrations for WWTP (moderately offensive odours). Exposure above this level may be associated with the potential for odour nuisance.

The modelling system is running with variable density grid. At WWTP site and in the surrounding area the receptor grid resolution is 25 m, at the remaining area it is 50 m. The discrete receptors corresponding to the sensor's locations were added to the grid. Initial emissions implemented in the model based on F.L. Colomer et al. (2012) and C. Zhang et al. (2017) are being corrected using the LUMA sensors measurements. The concentration values obtained from the model and the sensors at the measuring points are read. Then the normalized concentration difference for the partial results is determined, obtained from the calculations carried out for each emission source independently. In the last step, a matrix of correction factors for the initial emission is built, scaling and summation of the results is performed.

Model runs in the forecast mode and the forecast includes 48 hours ahead. Results of modelling are presented in the public portal: the Dynamic Odour Mapping System. The DOMS enables presentation of dynamic concentrations changes on an hourly basis using a time slider. The System presents results for the current day, two past days and two days ahead. Map for H_2S concentrations is available in two units: μgm^{-3} and in odour units: oum^{-3}. User can select a layer for presentation and obtain information on concentration in a selected place by clicking at the point on the map (figure 3).

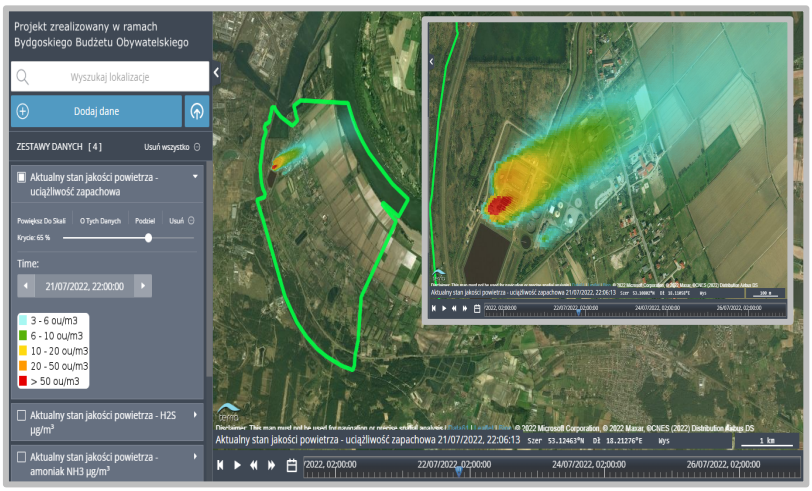

Figure 177. The Dynamic Odour Mapping System

RESULTS

The preliminary analysis was prepared after the DOMS system operation for six months. Bearing in mind the main objective of the DOMS which is to monitor odour nuisance in residential areas adjacent to the wastewater treatment plant, the analysis is focused on odour impact assessment at two neighbouring locations: the school and the district council building. The figure below presents time series modelling results of 1-hour H_2S odour concentrations at two locations and the comparative level of 3 oum^{-3}. H_2S concentrations range from 0 oum^{-3} to 36,7 oum^{-3}. Zero values are observed with wind directions towards the WWTP. H_2S concentrations are generally higher during summer than during the winter season. The comparative level is exceeded in both locations. However, the 98th-percentile will be calculated after the full year of the system operation and the conclusions will be prepared.

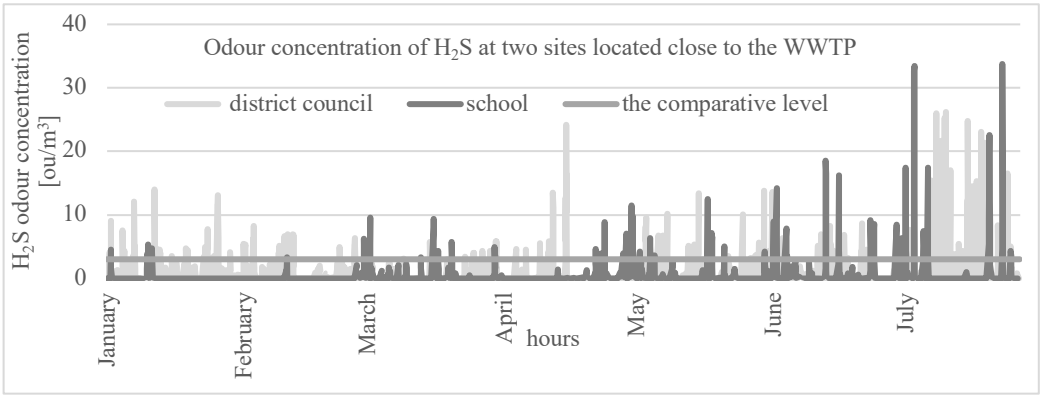

Figure 178. Time series of H_2S odour 1-hour concentration from 1.01.2022 to 26.07.2022

CONCLUSIONS AND RECOMMENDATIONS

1. **The Dynamic Odour Map System enables the identification of possible problems associated with odour nuisance episodes caused by WWTP.**
2. **The Dynamic Odour Map System is a useful tool for public information system concerning odour problems, especially with limited budget availability. The main advantages of DOMS are: the possibility to determine concentrations at any point of the analysed area, real time and forecast data delivery, lower costs than traditional measurement systems and the determination of the contribution of different emission sources or their groups.**
3. **The System may support the WWTP in emission management. It enables identification of the main emisison sources and gives information about impact of the installation on the neighbouring area.**
4. **Sensors may be implemented in the modelling system in two different ways: for dynamic emission correction calculation and in fusion process.**
5. **Further studies are planned on improvement of emission inventory from WWTP and model verification.**

REFERENCES

AIHA, 2013: Odor Thresholds for Chemicals with Established Health Standards, 2nd Edition

Bax C., Sironi S., Capelli L, 2020: How Can Odors Be Measured? *An Overview of Methods and Their Applications; Atmosphere* 2020, 11

Baawain, M., Al-Mamun, A., Omidvarborna, H. *et al.*, 2019: Measurement, control, and modeling of H_2S emissions from a sewage treatment plant. *Int. J. Environ. Sci. Technol.* 16, 2721–2732

F.L. Colomer et al, 2012.; Estimation of hydrogen sulfide emission rates at several wastewater treatment plants through experimental concentration measurements and dispersion modeling*; Journal of the Air & Waste Management Associatio*n, 62:7, 758-766

Environment Agency: H4 Odour Management. How to comply with your environmental permit; March 2011(https://assets.publishing.service.gov.uk/government/uploads/system/uploads/attachment_data/file/296737/geho0411btqm-e-e.pdf

C. Zhang et al, 2017.; Emission factor for atmospheric ammonia from a typical municipal wastewater treatment plant in South China; Environmental Pollution, 220:B, 963-970

21st International Conference on
Harmonisation within Atmospheric Dispersion Modelling for Regulatory Purposes
27-30 September 2022, Aveiro, Portugal

A NOVEL APPROACH FOR TRACING THE ORIGIN OF ODOUR NUISANCE WITH SMART METEO-DISPERSIVE MODELLING SYSTEM

Francesco Uboldi[1], Silvia Trini Castelli[2], Gianni Tinarelli[1], Piero Malguzzi[3], Oxana Drofa[3], Paolo Bonasoni[3]

[1]ARIANET Srl, Milano, Italy
[2]National Research Council, Institute of Atmospheric Sciences and Climate, Torino, Italy
[3]National Research Council, Institute of Atmospheric Sciences and Climate, Bologna, Italy

Abstract: A new methodology to trace backward the origin of odour nuisance has been developed. It is based on the modelling system SMART, where the RetroSPRAY model is interfaced with the regional atmospheric model MOLOCH. The novelty is represented by the pre- and post-processing of the input and output, respectively. For the input, the citizens' notifications of nuisance received through the NOSE Web-App are elaborated, for the output a combination of puffs released backward in time from the locations and at the time of the notifications is implemented. The approach used is briefly presented and discussed.

Key words: *odour nuisance; backward simulations; SMART modelling system; NOSE Web-App*

INTRODUCTION

Tracing the provenience and emission sources of odours is a challenging task, due to its transient characteristics, its distinctive features and the difficulty to have dedicated monitoring systems. Lagrangian particle dispersion models can be adapted and fruitfully used for this purpose. The meteo-dispersive modelling suite SMART (Spray-Moloch Atmospheric Regional Tool), recently developed (Bisignano et al., 2020; Trini Castelli et al., 2020), has been applied and further renovated in the frame of the NOSE Project (Network for Odours Sensitivity, *https://nose-cnr.arpa.sicilia.it/*) and its related web-application. NOSE has been realized by CNR-ISAC and ARPA Sicilia and it is aimed at tracking episodes of odour nuisance through a citizen-science approach.

A new and original approach has been developed for using the SMART system in the field of odour nuisance assessment, implementig in it a version of the SPRAY Lagrangian stochastic particle model that includes the backward-mode option, RetroSPRAY (Armand et al. 2013). When treating pollutant dispersion, with RetroSPRAY it is possible to trace the plausible location of an unknown source from concentration observations by identifying areas with maximum spatial and temporal consistency among backward puffs from each sensor (Tinarelli et al., 2018).

The new challenge regards using signals from citizens, i. e. qualitative and subjective information, in place of observed concentrations as input receptors for RetroSPRAY. The notifications received through the NOSE Web-App are sparse in space and time. In a first approach they have been aggregated in a regular grid and, based on thresholds and selective criteria, the grid cells representative of sensible "pseudo-receptors" for the backward releases are identified (Trini Castelli et al., 2022). Then, a second method based on a cluster analysis of the notifications and on the same selective criteria has been adopted, identifying the cluster centroids as pseudo-receptors, with the aim of making the elaboration of the input more automatic and reliable.

The simulations with RetroSPRAY are then performed by releasing, from the identified pseudo-receptor locations (either gridboxes or cluster centres), a series of retro-puffs at each time interval in which a significant number of signals are collected. As final output, the retro-concentration fields generated by the

retro-puffs are combined at all possible emission times, through a process that produces maps describing the region where possible sources can be potentially located.

The two methods for elaborating the input for the backward release in SMART modelling system for the NOSE Web-App are briefly presented and compared. The applicability of this approach is supported by the results obtained in two case studies, related respectively to an unknown release and to a source that was identified after the area was monitored as a consequence of the citizens' warnings.

THE NEW DEVELOPMENTS

A clever elaboration of the received notifications (Figure 1) is the first step to generate proper 'receptors' for the back-trajectories and determine the input to the RetroSPRAY dispersion model. Citizen notifications include a subjective evaluation of odour intensity, on a scale from 1 to 5. In our approach, only alerts with intensity 3, 4 or 5 have been used. The period of time defining the event (enabling the definition of a notification peak, usually a few hours) is divided in 30-minute intervals. Then all notifications within the same time interval are associated at the same discrete time and spatially aggregated.

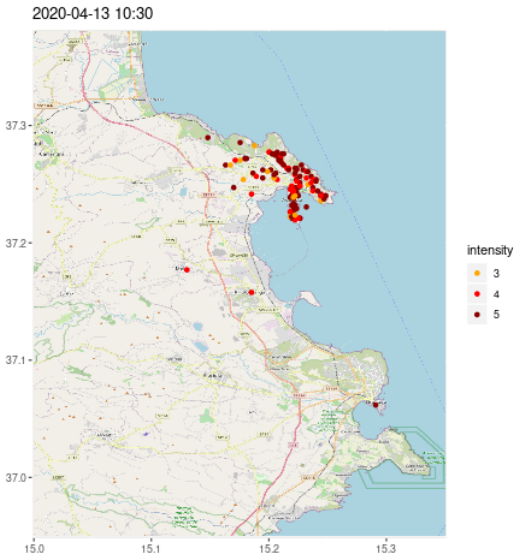

Figure 179. Example of the location of the citizens' notifications with their related 'intensity of nuisance' received in the interval 10:00-10:30 for the case study here considered.

In the first case, a 500-m-spacing grid is defined on the domain. Then alerts exceeding the (subjective) odour intensity threshold are counted within each grid cell at each time, in order to identify the cells that can be considered as sensible pseudo-receptors for the release of backward stochastic trajectories. In the second case a simple cluster analysis application based on spatial coordinates is applied at each time interval. A spatial scale of 500 m and a variable minimum number of alerts per cluster are used to choose the clustering level. The minimum alert number per cluster may vary from 3 to 10 depending on the maximum number of citizen notifications received at each time interval. The cluster centroids are identified as location of "pseudo-observations" and are used as "retro-emission" sources in a time-backward RetroSPRAY simulation.

In Figure 2 the two aggregation methods are compared, starting from the alerts shown in Figure 1. In the maps, only spatial locations of pseudo-receptors are shown. In both cases pseudo-observations are defined at some, not all, times within the event period here considered, from 08:00 to 11:00 on 2020-04-13. In the GRID case, only 5 gridboxes act as pseudo-receptors, defining a total of 14 pseudo-observations: their locations are the same at all times, so when a sufficient number of alerts falls within a gridbox an observation is defined and this may happen in the same gridbox at several times. On the contrary, the cluster centroids are recalculated at each time, then their locations differ at different times, even if they may happen

to be close to each other. As a result, 12 pseudo-observations are defined within the time period, each at a different location.

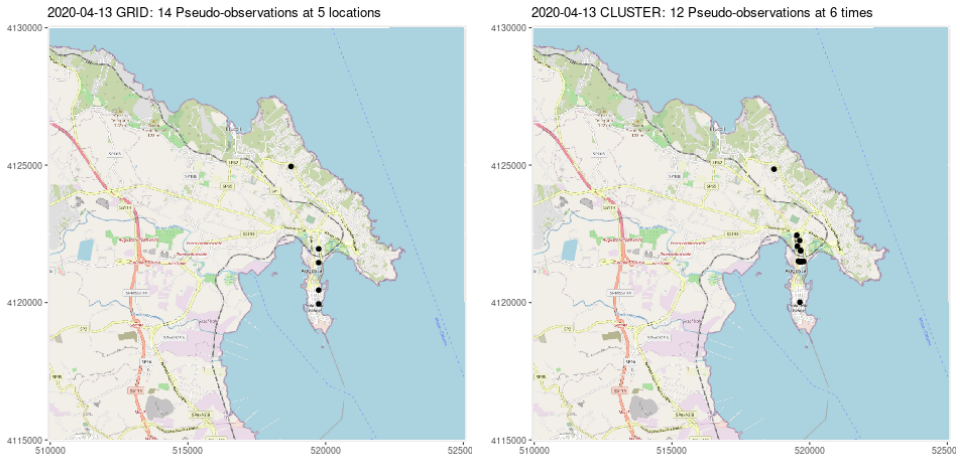

Figure 2. Aggregation of citizen alerts in pseudo-receptors, to be used as retro-sources in a RetroSPRAY backward simulation. Left: GRID aggregation; right: CLUSTER ANALYSIS aggregation. Only spatial locations are shown here: pseudo-observations (i. e. retro-emissions) are defined at some, not all, times in these locations, but, in both cases, they span the interval between 08:00 and 11:00 of 2020-04-13.

THE SIMULATIONS WITH SMART MODELLING SYSTEM

For the numerical simulations in the backward mode, to trace the potential origin of the odour nuisance, the SMART modelling system is applied. The 3D meteorological fields from MOLOCH atmospheric model, provided at 500 m horizontal grid space, are processed by the ARAMIS turbulence and boundary-layer parameterization code, preparing the proper input for the RetroSPRAY Lagrangian particle model.

The retro-emissions for RetroSPRAY are defined at the locations and at the time-intervals of the gridded or clustered notifications, which can be considered as 'pseudo-observations'. They are independent from each other and each of them generates a 'retro-concentration' field, as 'retro-puffs', moving backward, following the atmospheric flow upstream and dispersing according to the turbulence conditions. The RetroSPRAY simulations are performed by releasing, from the identified receptors, a series of retro-puffs at each time interval in which a significant number of signals are collected, here determined as a 30' time frequency. The retro-puff moving back from the location of a pseudo-observation indicates all possible positions of a source that, in a forward SPRAY integration, could determine that observation.

In the following an example of the simulated retro-puffs, originated by three of the emitting grid cells identified for the case study on 2020-04-13, is presented. Different pseudo-observations have been determined in the interval 0800-11:00 local time (LT). A total of 9 retro-puffs moving backward in time are thus traced. The numerical integration lasts for a reasonable time before the first pseudo-observations, here taken back to 06:00 LT. Thinking 'forward', this approach allows searching for a source area that could start emitting in the interval 06:00-06:30 LT. As examples, the pattern and location of the retro-puffs arriving at the three selected receptors at different notification-times during the period 08:00-11:00 LT, are plotted at different time frames, back in time: between 10:00-10:30 LT (Figure 3), 08:00-08:30 (Figure 4) and 06:00 and 06:30 (Figure 5).

The retro-concentration fields generated by the retro-puffs are then combined at all possible emission times, through a process that calculates their geometric average and their arithmetic average, in order to build final maps describing the region where possible sources can be potentially located. Further processing of this information enables associating a related probability density map, indicating the possible locations of the source in the different areas.

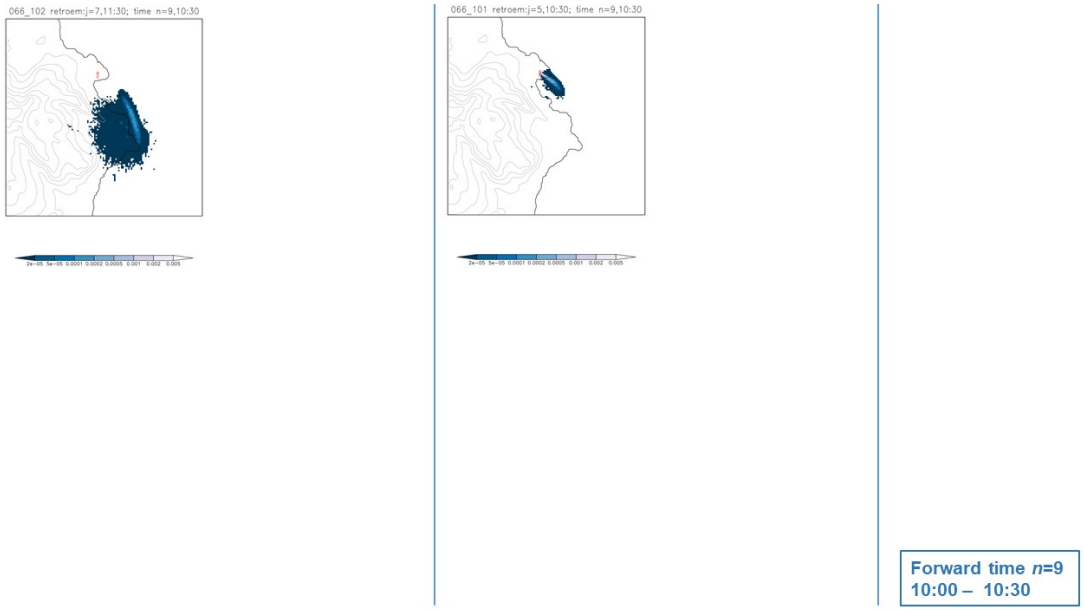

Figure 3. Pattern and location of the retro-puffs simulated by the SMART modelling system in backward mode, through the dispersion model RetroSPRAY, in the timeframe 10:00-10:30.

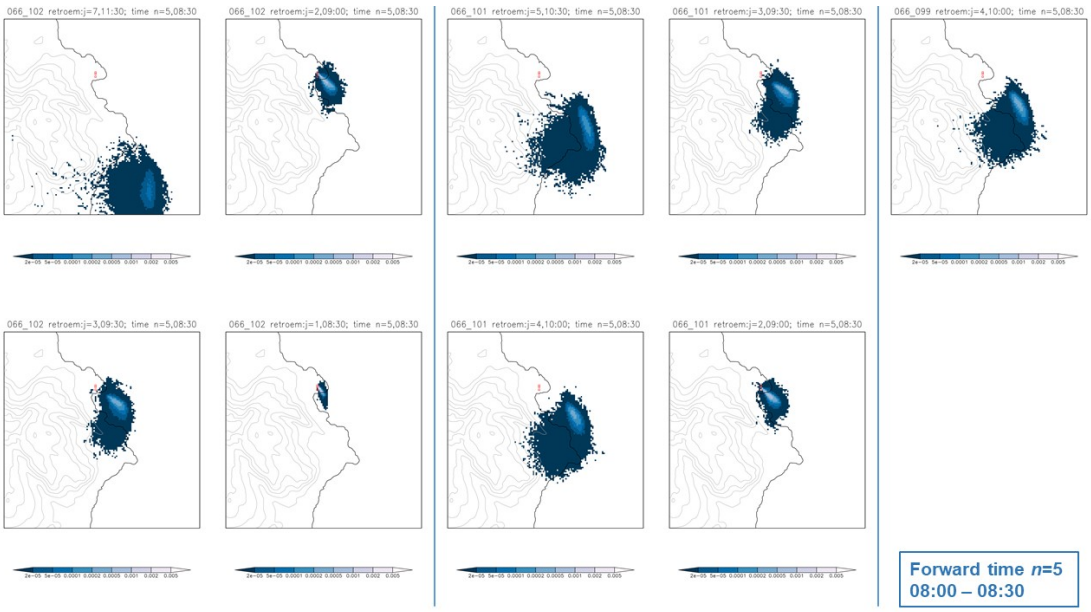

Figure 4. As in Figure 3 but for the timeframe 08:00-08:30

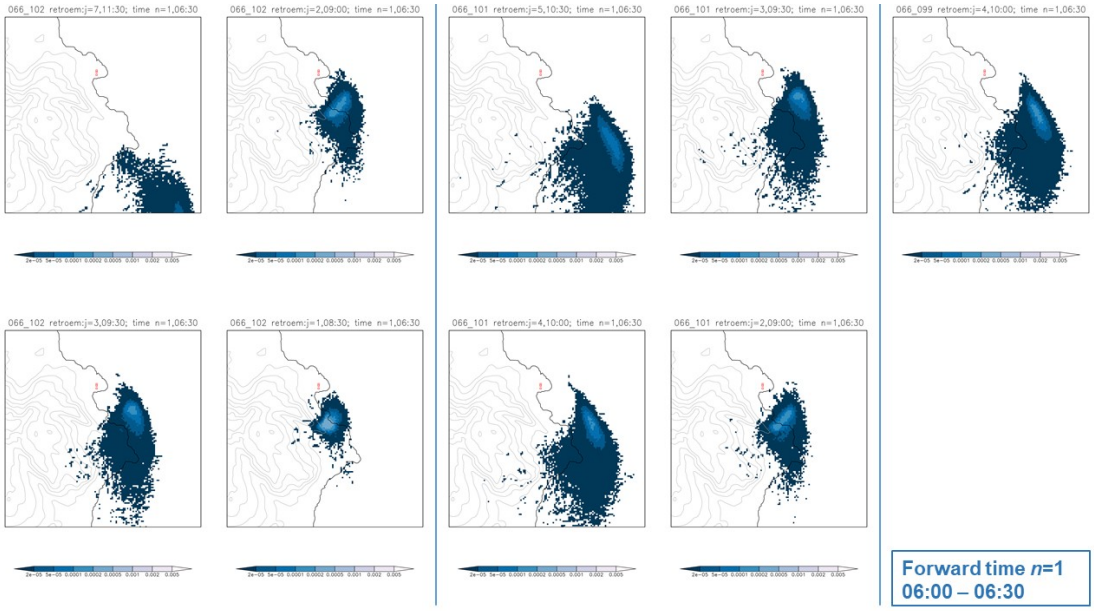

Figure 5. As in Figure 3 but for the timeframe 06:00-06:30

DISCUSSION AND CONCLUSIONS

The newly developed approach implemented to use, after appropriate processing, citizens' warnings from NOSE WEB-APP as input to RetroSPRAY model, demonstrates to be promising and applicable. The methodology has been applied to two rather different case studies, one with a high number of notifications, the other with a lower number of notifications but for which the source was then identified. In both cases, the simulations provided reliable results. In the first case, this has been confirmed by performing test simulations in forward mode, where potential releasing sources have been placed in different locations in the areas identified as more or less possible origin of odour nuisance, and also in the region outside them. It was seen that the sources placed in the 'most probable' areas were in fact affecting the receptor locations during the main hours of the recorded warnings. In the second case, the most problable area identified by the simulations and following output elaboration was in fact hosting the plant that produced the odour nuisance after an accidental release.

The new modules, elaborating the citizens' notifications and the final maps of probability density, are being integrated with the SMART modelling suite and the full package is presently going to be interfaced to NOSE alert system, with the aim of making available an operational system that can respond to a nuisance event in the timeframe of a few hours.

REFERENCES

Armand P., Olry C., Albergel A., Duchenne C. and Moussafir J., 2013: Development and application of Retro-Spray, a backward atmospheric transport and dispersion model at the regional and urban scale. Proceedings of the 15th Conference on Harmonisation within Atmospheric Dispersion Modelling for Regulatory Purposes – 6-9 May 2013, Madrid, Spain, pp. 789-893.

Bisignano A., Trini Castelli S., and Malguzzi P., 2020: Development and verification of a new meteo-dispersive modelling system for accidental releases in the Italian territory: SMART. Air Pollution Modeling and its Application XXVI, C. Mensink, W. Gong and A. Hakami (eds.) Springer Proceedings in Complexity, Springer International Publishing Switzerland, 77-81

Tinarelli, G., Uboldi F., Carlino G., 2018: Source term estimation using an adjoint model: a comparison of two different algorithms. Int. J. Environment and Pollution, Vol. 64, Nos. 1/3, 2018

Trini Castelli S., Bisignano A., Donateo A., Landi T.C., Martano P., Malguzzi P., 2020: Evaluation of the turbulence parameterisation in the MOLOCH meteorological model. Quart J Roy Meteorol Soc. 146,124-140

Trini Castelli S., Tinarelli G., Uboldi F., Malguzzi P., Bonasoni P., 2022: Developments of SPRAY Lagrangian particle dispersion model for tracing the origin of odour nuisance. Air Pollution Modeling and its Application XXVII,

C. Mensink, O. Jorba Casellas (eds.) Springer Proceedings in Complexity, Springer International Publishing witzerland, in press.

21st International Conference on
Harmonisation within Atmospheric Dispersion Modelling for Regulatory Purposes
27-30 September 2022, Aveiro, Portugal

THE INTERNATIONAL HANDBOOK ON THE ASSESSMENT OF ODOUR EXPOSURE BY USING DISPERSION MODELLING

Jennifer Barclay[1], Carlos Diaz[2], Günther Schauberger[3]

[1]ASG Atmospheric Science Globa, Pty Ltd, Auckland, New Zealand
[2]Olores.org, Spain
[3]WG Environmental Health, Unit for Physiology and Biophysics, University of Veterinary Medicine, Vienna, Austria

Names and Affiliations of TG Leaders and Co-authors: *Imelda Shanaha[4], Anne-Claude Romain[5], Gianni Tinarelli[6], Roberto Bellasio[7], Rodrigo Rosales[8], Silvia Trini Castelli[9], Giuseppe Brusasca[10], Loren Tick[11], Jean-Michel Guillot[12], Andrew Balch[13], Heike Hauschildt[14], Giusy Oliva[15], Tiziano Zarra[15,] Christelle Escoffier[16]*

[4]TMS Environment Ltd, Dublin, Ireland; [5]University of Liege, Arlon, Belgium; [6]Università degli Studi di Salerno, Salerno, Italy; [7]Enviroware srl, Italy; [8]Environmental Assessment Service, Santiago; [9]National Research Council, CNR-ISAC, Torino; [10]ARIANET srl, Milano, Italy; [11]LT Environmental LLC; [12] Ecole des Mines d'Ales France; [13]Air Environment Consulting Pty Ltd, Brisbane, Australia; [14]Olfasense, Germany; [15]Università degli Studi di Salerno, Salerno, Italy; [16]Università degli Studi di Salerno, Salerno, Italy; [17]Wood Group UK Ltd, London, UK;

Key words: Odours, Dispersion Modelling, Handbook, Meteorology.

A new development towards the first worldwide guideline on the assessment of odour exposure by using dispersion modelling has taken its first steps. Modelling odours is complex and often requires forgetting traditional dispersion modelling operating modes and focusing on exposure. Odours are perceived in seconds which is key in calculating their impact in the ambient air. Most odour incidents are generated during calm or very low wind speeds which do not facilitate the dispersion of an odour and that makes modelling extremely challenging.

Development of the first International Handbook on Odour Modelling is an initiative promoted by over 50 experts around the globe in the area of modelling odours. The group is led by Carlos Diaz (Spain), Jennifer Barclay (New Zealand) and Günther Schauberger (Austria). The first meeting took place in August 2020, with planned monthly meetings. The aim of this paper is to report on the advances being made for this initiative.

1. INTRODUCTION

Odour issues are currently one of the major causes of environmental grievances around the world, and in some countries, are routinely the cause of the most environmental complaints to regulatory authorities. There continue to be multiple reasons for the increase of odour complaints, including an unrelenting urban expansion of residential areas into land use areas once mainly agricultural. In addition, there is an increasingly higher aesthetic, environmental expectation of citizens, who are less familiar and tolerant of odours than in the past, as well as concerns over potential health risks from airborne odorous substances.
In most countries, environmental regulations cover most types of common air pollutants including NO_2 or SO_2, with the criterion being based on the occurrence of health effects following short- and/or long-term exposure to the pollutants. As such, there is little health risk variation between jurisdictions, states, and countries. However, odour regulation tends to be much more varied across a wide spectrum: from having little to no specific mention in environmental legislation to extensive and rigid requirements that include a combination of odour source testing, odour dispersion modelling, ambient odour monitoring, setback

distances, process operations, and odour control procedures. Odour legislation can be highly variable from one country to the next and it can also be highly variable from one jurisdiction to the next, within the same country (Bokowa, et al., 2021).
For regulatory purposes, much of the focus of attention in the last couple of decades has been in trying to establish odour guidelines in the hope of bringing a degree of consistency to the control and regulation of odours. With the focus on setting regulations, less effort has been spent in a variety of jurisdictions on assessing the best tools suited to compute odour impacts with respect to accurate emission rates, source characterization, and the important role of local meteorology, interpretation of modelled results, or the suitability and applicability of one dispersion model over another. The 'International Handbook on the Assessment of Odour Exposure by using Dispersion Modelling' aims to address several of these key issues central to the theme of effective management and odour regulation.

A principal aim of the proposed Handbook on odour dispersion modelling will be to provide some guidance on this complex topic in a way that will be of benefit to countries with advanced odour regulations and to those countries that are looking to create regulations surrounding odour management. The Handbook will be a collaborative work by more than 60 international odour experts from nineteen countries including; Belgium, Italy, France, Austria, Spain, United Kingdom, Germany, Israel, Ireland, Brazil, Chile, Peru, Ecuador, United States of America, Qatar, Australia, China, Japan and New Zealand.
The world's odour dispersion modelling group meet once per month via teleconference while the Special Task groups, of which there are 6 also meet every month. Each task group has between 5 and 10 members who have been responsible for writing and reviewing individual sections within each task group. Seven task groups have been identified and are detailed below.
Each task group was guided by a set of principal themes which are central to the Handbook, and are as follows:

- The resulting document will be a Handbook rather than a guideline. This is to prevent conflict with those jurisdictions\states\countries that already have guidelines and regulations.
- The Handbook is to be of benefit for jurisdictions\states\countries that have strict odour regulations and for those who are just beginning to consider odour legislation.
- Rather than focus on any individual model and country, or how they apply odour regulation, the focus of attention will be on the parameters themselves.
- Valid, workable references are a key component of the document which will include live links wherever possible.
- Individual task groups will focus on the pros and cons of key subject areas. It is not the Handbook intent to disregard any existing regulations. There are many countries with advanced odour legislation that is outdated, and it can take a long time for new guidelines to progress.

The Handbook will be forward-looking making the best use of the experts' experience as well as recognizing that changing regulations can take a long time.

2. CONTENT OF THE HANDBOOK

Each of the key sections of the handbook are briefly summarised below.

2.1 Definitions and References

The aim of Task Group 1 (TG1) is to gather a list of commonly- used odour terms and provide a detailed definition of each terms meaning. By far the majority of odour terms are common throughout the world, but there are some important exceptions, which require an explanation otherwise the term could be mis-understood. An example of two such confusing odour terms is:

- the definition of odour and its unit.
- FIDOL vs FIDOS vs FIDO.

In Australasia (New Zealand and Australia), USA, and Europe the term, 'odour unit' is the common term for the unit of measure of odour concentration. In Australasia and the USA, this term is known as 'ou', and in Europe is known as ou_E/m^3. They have the same meaning, but one is expressed as dilutions and the other as dilutions per cubic metre. The main difference between them is that when an emission rate, for an area source as an example, is calculated, ou_E/m^3 gives an emission rate of $ou_E/m^2/s$ whereas ou gives an emission rate of ou.m/s the former being a more logical way of expressing emission rates per unit area.
Critical to the guideline is the definition of an odour unit. One *odour unit* is the amount of odorant(s) that, when evaporated into one cubic metre of neutral gas at standard conditions, elicits a physiological response from a panel (detection threshold) equivalent to that elicited by one Reference Odour Mass (ROM), evaporated in 1 m^3 of neutral gas at standard conditions. The most known ROM is *the European Reference Odour Mass* (EROM) that corresponds to 123 µg of n-butanol defined in the standard EN 13725. The *odour concentration* is the number of *odour units* in a cubic metre of gas at standard conditions for Olfactometry.
A commonly used acronym used to define an *odour impact criterion (OIC)* is the term *FIDOLS*, that stands for *Frequency, Intensity, Duration, Offensiveness, Locatio*n and *Sensitivity*. Whilst the first 4 factors are well described in the literature, the one that refers to Sensitivity is not that well described, and is not recognised in some countries.
These are two examples of just a couple of the commonly used odour terms whose use and meaning can be entirely different depending on where you are located. A key aim of TG1 is to define all of the main odour terms around the world as well as ensure the Handbook is consistent in its use of terms throughout the document.

2.2 Meteorology

Task Group 2 (TG2) has identified 4 major section titles: meteorological conditions; types of meteorological data; meteorological models and how they deal with data, and; model performance assessment and reporting.
There will be discussion about processing weather station data, the use and relevance of single station observation data versus that from numerical weather prediction models, and when to use single meteorological station data versus 3D data for odour assessments. The discussion will also cover complex meteorological conditions, the length of meteorological data (how many years), and the relevance of comparing the modelled meteorological data against the long-term historic records.
Rather than discuss any one model, TG2 will focus on a number of regulatory models commonly used in odour assessments around the world including (CALMET, AERMET\AERMINUTE, ADMS, GRAL and AUSTAL) and focus on how they use critical parameters. For example, 'roughness length' is an important meteorological parameter used by all models to express the roughness of the surface. It affects the intensity of the mechanical turbulence and the fluxes of various quantities above the surface. Most models use roughness length the same way, but some models such as AERMOD are very sensitive to roughness length, while others such as CALPUFF are only moderately so.
Advice will be provided on the validity of meteorological\dispersion models according to the complexity of the study. For example, in flat terrain, sources grouped together, with no obstacles and moderate winds (steady state conditions) from a single weather station it may be appropriate to use a simple steady state Gaussian plume model. But, for complex atmospheric environments (non-steady state conditions) such as coastal zones and complex terrain it is necessary to develop the meteorological data from three-dimensional diagnostic and or prognostic numerical meteorological models.
An important section of TG2 is model evaluation and how to report the meteorology used in the dispersion modelling. Meteorology is usually the most important input component of dispersion modelling alongside the emissions data. This section will provide advice on appropriate and useful analysis and evaluation tools and will explain how to use these tools to evaluate the meteorological data.

2.3 Emissions and Source Characterization

Odour emissions depend strongly on the type of sampling method used. In the case of area sources, the most common odour source, there are two commonly used worldwide sampling methods: the dynamic wind tunnel and the static flux chamber. For both of these systems, the emission rate is calculated as the product of concentration and airflow through the device. Over the last 30 years there has been a long-standing debate about the appropriateness and accuracy of wind tunnels vs flux chambers for quantifying area source emissions as the sampling devices give quite different results compared to each other and emission theory The situation is even more confusing if the scientific literature is consulted as little guidance is provided in the selection and operation of sampling devices to obtain meaningful emission rate estimates and how these compare to odour criteria in use.
Task Group 3 (TG3) will address the complex issues surrounding odour emission quantification.

2.4 Dispersion Models and Algorithms

Dispersion models can be used to predict impacts at a location, or to calculate an emission rate based on concentrations at a location. There are four types of regulatory air pollution models used in the world for odour assessments, of which three types are more commonly used. First, there are the steady-state Gaussian plume models such as AERMOD and ADMS, then the non-steady state Lagrangian puff models such as CALPUFF and SCIPUFF, and particle models; TAPM, AUSTAL, LAPMOD, GRAL and SPRAY.
Steady-state plume models assume straight-line trajectories and steady-state meteorological conditions. They have spatially uniform meteorological fields, have no memory of the previous hour's emissions, and assume a non-zero wind speed. They are ideally suited for screening cases and near-field, flat terrain applications away from the coast, where conditions are expected to be steady-state. The second type of model, the Lagrangian approach, solves a set of equations that mathematically follows the release of pollution parcels, either as puffs or particles as the plume moves through the atmosphere. These Lagrangian models allow, in such a system, to follow curved trajectories along the plume centrelines and simulating the dispersion through gaussian puffs around them. The 3D meteorology has full spatial variability in the winds and turbulence fields. The model retains information from previous hours of emissions and is well suited for modelling stagnation, fumigation, and recirculation events typical of worst-case dispersion of odours.
Eulerian grid models such as CALGRID and CMAQ, although mentioned in the Handbook are not suited to odour modelling. These models consider a fixed 3D Cartesian grid as a frame of reference where the advection-diffusion equation is numerically solved rather than in a moving frame of reference. These models are best used for explicit chemistry computations in particular ozone, air toxics, and secondary aerosols modelling and are not commonly used for odours.
TG4 recognizes that the mechanisms of odorant dispersion in the atmosphere are the same as the dispersion of other pollutants. However, there are some special problems that must be considered when attempting to quantify a source's odour impact with dispersion modelling. Among them are determining the emission rates of the pollutant, the short time period over which odours are observed, the enhancing or masking of odours by the combinations of different odours, and the high degree of subjectivity amongst a population in the perception and intensity of odours.
TG4 considers that two key factors that should be considered in evaluating whether to use a conventional steady-state plume model such as ADMS or AERMOD, or a more sophisticated approach are, whether the steady-state assumption is valid, and, whether the technical parameterizations in the plume model adequately treat the situation to be modelled.

2.5 Dose Response

The role of Task Group 5 (TG5) is to discuss the dose response to odours, in other words, to assess the odour impact experienced by the community. The community impact of odours has been assessed over time with it generally being accepted that annoyance is linked to odour concentration, the frequency of impact

is critical, and that the impacts of odour can go beyond annoyance effects leading to potential health impacts if not correctly managed.
The acronym FIDOLS features strongly in this section (frequency, intensity, offensiveness, duration, location, and sensitivity), where each parameter is discussed in depth. Several attempts have been made in order to describe a mathematical function that addresses all of the FIDOLS factors, but there are no mathematical functions describing FIDOLS factors that are integrated within dispersion models due to the subjective nature of odours. As a consequence, the result produced by modelling an odour emission rate, unfortunately cannot be used as the only proof that an impact is not made when there is an evidence of odour complaints in area. TG5 discuss in depth, FIDOLS factors, percentiles and peak to mean ratios.

2.6 Reporting

The final chapter of the handbook will be 'Reporting' which will be prepared by Task Group 6 (TG6). The aim of this Chapter is to discuss how much and what information should be included in an odour assessment technical report. The report should clearly set out the assumptions on which the modelling has been based and should especially consider the uncertainty associated with the model inputs and the validation of monitoring data for inclusion in the study.

3. Conclusions

To date, the world odour dispersion model groups have met monthly since the idea of the 'worldwide odour dispersion model group" was conceived. Individual members of the group recognize the advantages of collaborative research and learning, which includes;

- Development of higher-level thinking, oral communication, and leadership skills.
- Exposure to and an increase in understanding of diverse perspectives.
- May provide opportunities where multiple different world-wide approaches may be applied to existing problems and lead to the development of innovative solutions.
- Discussions amongst colleagues can stimulate new ideas and increase creativity.

Acknowledgments

This project has received funding from the *Environmental International Society of Odour Managers (AMIGO for its acronym in Spanish)*. Further, the authors wish to acknowledge all of the following contributing authors: *Laura Capelli, Phyllis Diosey, Dietmar Öttl, Hélène Piet Sarnet, Luis Diaz, Andrea Rossi, Hellen Arichábala, Débora Lia Perazzoli, Rafael Geha, Kenny K M Lok, Geordie Galvin, Nick Jones, Manuel Santiago, Maurizio Grez, Andrea Peña, Catalina Pérez, Chaim Kolominskas, Valérie Nastasi, Ainhoa Antón, Emanuelle Duthier, Sarveshkumar Sharma, Eric Concepción, Oliver Olang, Rossella Prandi, Constanza Fariña, Jerome Godart, Adrien Bouzonville, Angie Wagner, Martí de Riquer, Eva Berbekar, Laura Hinderink, Roberto Sozzi, Mathias Rau, Ainhoa Antón, Helga Lauerbach, Osnat Yossef.*

21st International Conference on
Harmonisation within Atmospheric Dispersion Modelling for Regulatory Purposes
27-30 September 2022, Aveiro, Portugal

IDENTIFICATION OF ODOUR SOURCES IN THE ORE MOUNTAINS BY COSMO-MUSCAT SIMULATIONS

Ralf Wolke

Identification of odour sources in the Ore Mountains by COSMO-MUSCAT

Ralf Wolke, Roland Schrödner, Matthias Faust

Leibniz institute for Tropospheric Research (TROPOS), Leipzig, Germany

During the last years, the local authorities of the Erzgebirge region have received an increasing number of complaints about stink events in their localities. These events are mainly observed for specific weather situations with southerly wind. The origin of stink is supposed in the North Bohemian Basin. However, the stink is not smelled in near-emission areas. Therefore, it is suspected that the fetid substance is formed by chemical transformations and mixing of different air masses. The search for the stink sources using chemistry transport modelling is presented in the paper. The investigations are performed with the chemistry transport model system COSMO-MUSCAT and the Lagrangian particle model COSMO-LAPASI. Horizontal grid resolutions up to 100 m are used for an appropriate description of the mountainous topography and the exact location of the emissions. Additionally, to usual dispersion calculations, a detailed analysis of forward and backward trajectories is performed. A result of the present study is the fact of the accumulation of air masses in the North Bohemian Basin, which occurs in most cases. Thus, many potential sources of odor problems can come into question. Those can be related to a larger industrial area at its best.

TOPIC SS2:

NATURE-BASED SOLUTIONS

21st International Conference on
Harmonisation within Atmospheric Dispersion Modelling for Regulatory Purposes
27-30 September 2022, Aveiro, Portugal

DYNAMIC MODELLING OF THE COOLING POTENTIAL AND HYGROTHERMAL BEHAVIOUR OF GREEN WALLS IN BUILDINGS

Allan Alvarado

SHORT ABSTRACT

Abstract title: Dynamic modelling of the cooling potential and hygrothermal behaviour of green walls in buildings

Name and Affiliation of the First Author: Allan A. Alvarado-Alvarado[1]

[1]Sustainable Energy, Air and Water Technology (DuEL), Department of Bioscience Engineering, University of Antwerp, Groenenborgerlaan 171 2020 Antwerp, Belgium

Email of first author: Allan.AlvaradoAlvarado@uantwerpen.be

Names and Affiliations of the Co-authors: Jan Poppe[2], Bert Belmans[2], Siegfried Denys[1]

[1]Sustainable Energy, Air and Water Technology (DuEL), Department of Bioscience Engineering, University of Antwerp, Groenenborgerlaan 171 2020 Antwerp, Belgium

[2]Energy and Materials in Infrastructure and Buildings (EMIB), Department of Applied Engineering, University of Antwerp, Groenenborgerlaan 171 2020 Antwerp, Belgium

Abstract text

Urban green infrastructure (UGI) has received attention in the last decades, given its cooling potential to mitigate the urban heat island effect (UHI), particularly in buildings and street levels. Green walls (GW) are a type of UGI, and they can be classified into green facades (GF) and living wall systems (LWS). There are many phenomena involved in the cooling effect of GW like shading, insulation, and evapotranspiration (ET). The latter is considered the primary process as plants consume a large amount of solar radiation as latent heat. Besides, water evaporation also occurs in the substrate, which doubles the effect in the case of an LWS. The hygrothermal properties account for heat and moisture transport through materials as GWs are placed as an extra compartment in a building. Nevertheless, when studying the hygrothermal properties of GW in buildings, a quantitative evaluation of the ET effect remains a challenge. The latter responds that additional input is necessary to model the ET in a GW besides the building materials' properties, such as weather data, plant species, e.g., leaf area index (LAI), substrate type and water saturation and GW geometry. This study aims to model and validate the hygrothermal behaviour of GWs under different building materials configurations by

accounting for the most influential transport phenomena. The modelling study is completed in the commercial software COMSOL Multiphysics ®, and experimental results are obtained from GWs evaluated in a building facade and a climate chamber. For this purpose, heat and moisture balances coupled with additional sink terms for the latent heat of ET are considered. Stationary and transient conditions are studied, and ET vs no ET conditions are compared. As outputs, the temperature and moisture across the GW can be predicted, especially on the outer surface of the building's masonry. Finally, a sensitivity analysis is carried out by varying the input parameters, e.g. LAI, to study their

21st International Conference on
Harmonisation within Atmospheric Dispersion Modelling for Regulatory Purposes
27-30 September 2022, Aveiro, Portugal

MODELLING THE IMPACTS OF URBAN TREES ON AIR QUALITY IN STREETS

Alice Maison[1,2], Youngseob Kim[1] and Karine Sartelet[1]

[1]CEREA, École des Ponts, EDF R&D, Marne-la-Vallée, France
[2]Université Paris-Saclay, INRAE, AgroParisTech, UMR EcoSys, 78850 Thiverval-Grignon, France

Abstract: Models are commonly used to study air quality in urban areas, which are known to be areas of poor air quality. To model air pollutant concentrations at a fine scale (street) and over entire cities, fast running codes are developed such as the Model of Urban Network of Intersecting Canyons and Highways (MUNICH). They used simplified parameterizations especially for transport. Although they can not reproduce finely the street micrometeorology, they can reproduce the gradients of concentrations between the streets and the urban background. These transport parameterizations have been recently improved and the effect of the tree crown was included in MUNICH. Planting trees in cities has been widely developed nowadays mainly for their capacity to decrease temperatures and limit the urban heat island. Tree effects on air quality are various, they can have a positive impact by capturing pollutants by dry deposition. However, trees reduce air flow in the street and limit pollutant dispersion. They also emit volatile organic compounds (BVOCs) that can lead to ozone and secondary organic aerosol production. The objective of this study is to analyse and compare these three effects of trees on air quality based on simulation results from MUNICH. For the test case presented here, the tree aerodynamic effect is the main effect, it induces an increase of the concentrations (up to +10%). The decrease of concentrations due to dry deposition is very limited (less than 1%). The BVOC emission has a negligible impact on particle formation at the local scale.

Key words: *air quality modelling, street-network model, urban tree, biogenic emissions, volatile organic compounds*

INTRODUCTION

Urban areas concentrate population and human activities inducing higher pollutant emissions. The presence of high buildings and artificial impervious surfaces strongly modifies the energy and water balances and reduces air flow inside streets. These processes lead to a degradation of the air quality especially at the street level due to traffic related emissions. Models are widely used tools for understanding processes and predicting air quality. They can be of various types and resolutions depending on the system studied. At the street level, higher pollutant concentrations are often observed compared to the concentrations in the urban background and they cannot be represented using chemical-transport models that have spatial resolution of the order of kilometer. Computational Fluid Dynamics (CFD) models coupled to chemistry/aerosol models may be used to compute the pollutant concentrations over limited areas of cities, but they are too expensive to use over a whole city. Hence, simplified street-network models, such as the Model of Urban Network of Intersecting Canyons and Highways (MUNICH, http://cerea.enpc.fr/munich/), are developed. They include the main processes that influence pollutant concentrations: emissions, transport, deposition, chemistry and aerosol dynamics. However, the streets are not discretized finely, but in MUNICH concentrations are assumed to be homogeneous in each street segment. The complex street micrometeorology is simplified by considering only the vertical transfer between the street and the background and the horizontal transfer between the streets. Urban trees are usually not taken into account in simplified street-network models. However, planting trees in cities is largely promoted for all the ecosystem services vegetation can bring (improve human thermal comfort, limit water runoff, store carbon and enhance human well-being). Regarding tree effect on air quality, trees represent surfaces available for pollutant dry deposition, and hence can contribute to reduce air pollutants concentrations. However, trees also emit volatile organic compounds, which may affect air quality and the presence of trees in street canyons reduces the wind velocity in the street and limits pollutant dispersion. Recent developments were done to include these tree

effects on air quality in MUNICH. The tree aerodynamic effect, that has been largely studied with CFD models, was parameterized based on CFD simulations using the open-source code Code_Saturne (https://www.code-saturne.org/). Dry deposition of gas and aerosols on street surfaces and tree leaves are modelled using existing parametrizations based on a resistive approach. BVOC emissions are added in the street following the Guenther approach. The objective of this study is to compare the effects of urban trees on air quality.

MATERIALS & METHODS

Setup of munich simulations without tree

To model and analyse the effects of trees on air quality at street level, this study relies on a test case where simulations are performed over a Paris suburb (Kim et al., 2022). The street network is composed of 577 streets located in an eastern suburb of Paris (Kim et al., 2018). MUNICH considers homogeneous street segments with homogeneous pollutant concentrations. Several processes are modelled: emission of traffic-related pollutants, using emission factors from the COPERT methodology, advection between street segments, and vertical transfers between the street and the background (Maison et al., 2022a). These transfers depend on the meteorological conditions above the street, computed with WRF (Weather Research and Forecasting) simulations (Lugon et al., 2020) and the background concentrations, computed with Polair3D simulations (Sartelet et al., 2018; André et al., 2020). The gas-phase chemistry occurring in the street is based on the CB05 scheme (Yarwood et al., 2005), with additional reactions to represent the formation of condensables (Sartelet et al., 2020). The aerosol dynamics is simulated with the SSH-aerosol model, which is coupled to MUNICH (Lugon et al., 2021; Kim et al., 2022). Dry deposition on street walls and ground is considered using a resistive approach and the parametrizations of Zhang et al. (2002; 2003) and Hicks et al. (1987) for gaseous pollutants and the parametrizations of Zhang (2001) for aerosols. A detailed description of the reference case can be found in Kim et al. (2022).

Addition of trees in munich simulations

Simulations are performed over the entire street network but trees are added in only one street, corresponding to the boulevard Alsace Lorraine (BAL) (48°51'08.1"N 2°30'38.0"E). The total length of BAL is 1140m, and trees are added every 10 m. Trees are assumed to be *Sophora japonica*, and their characteristics are listed in Table 1.

Table 1. Street and tree characteristics simulated

Category	Symbol	Definition	Value	Unit
Average street characteristics (BAL)	H	Building height	8.6	m
	W	Street width	27.5	m
	a_r	Street aspect ratio	0.31	-
Tree characteristics	LAI	Leaf area index	9.0	$m^2.m^{-2}$
	h	Tree crown height	8.0	m
	r	Tree crown radius	2.5	m
	h_t	Tree trunk height	3.0	m

The three main tree effects on air quality are considered in MUNICH. First, the tree crown slows down air flow inside the street and limits pollutant dispersion; this aerodynamic effect was parameterized in a previous study (Maison et al., 2022b) by modifying the expression of the horizontal and vertical transports. Then, in addition to street surfaces, dry deposition of gas and aerosols on tree leaves are considered. It is also parameterized with a resistive approach assuming that the gaseous species can be deposited on the leaf cuticle or on the mesophyll by entering through the stomata following Wesely (1989); Walmsley and Wesely (1996) and that the aerosols can only be deposited on the leaf cuticle following Zhang (2001). The eventual resuspension is not considered here. Finally, BVOC emissions from trees are added inside the street. The emissions factors of isoprene and three monoterpene species (α-pinene, β-pinene and limonene)

are calculated with the empiric approach of Guenther et al. (1995), Guenther (2000) and Owen et al. (2001). The emissions factors are functions of biotic factors dependent on the tree, as the leaf biomass, and of abiotic factors, as the photosynthetically active radiation (PAR) and the leaf surface temperature. Because estimating the leaf surface temperature would require an advanced plant physiology model, most air quality models assume that the leaf temperature equals the air temperature to compute BVOC emission factors. The simulations are performed on a warm and sunny summer day (July 18, 2014), where the air temperature varies between 22.0°C at 5:00 am (UTC) and 34.8°C at 3:00 pm with a daily average value of 28.7°C. The PAR reaches 1979.4 $\mu mol.m^{-2}.s^{-2}$ at noon. These meteorological conditions lead to relatively high emissions of BVOC (maximum values of 552.5 $\mu g.s^{-1}$ per tree for isoprene and 13.7 $\mu g.s^{-1}$ per tree for monoterpenes). The wind speed above the street is between 1.6 $m.s^{-1}$ at 5:00 am and 4.8 $m.s^{-1}$ at 4:00 pm (daily average value of 3.2 $m.s^{-1}$). The angle between the wind direction and the street orientation is 20° until 2:00 a.m., then it increases to become perpendicular to the street (about 90°) between 8:00 a.m. and 7:00 p.m. and finally decreases to 45° at midnight.

In order to study these effects individually and then combined, five simulations are performed. One reference simulation without tree (ref), three simulations with each of the specific tree effects (aero: tree aerodynamic effect, dep: dry deposition on leaves and bvoc: BVOC emission) and finally, one simulation with the three tree effects combined (3eff). To go further in the analysis of the interaction between tree effect and aerosol dynamics, two additional simulations are performed by deactivating the condensation of aerosol (ref and aero without condensation).

RESULTS & DISCUSSION

The temporal evolution of the concentrations in the street, expressed in $\mu g.m^{-3}$, is compared between the simulation cases in fig. 1a for nitrogen dioxide (NO_2) and fig. 1b for particulate matter less than 10 µm in diameter (PM_{10}). To quantify the impact of trees, the relative deviation (RD) of concentrations (in %) is calculated between the simulations with and without trees, as shown in fig. 1c for NO_2 and fig. 1d for PM_{10}. The daily average and maximum concentrations and relative tree effects are also compared between the simulations for a larger number of species in Table 2.

Figure 1. Temporal evolution (a, b) and relative deviation (RD) (c, d) of NO_2 (a, c) and PM_{10} (b, d) concentrations in the street for the five simulations.

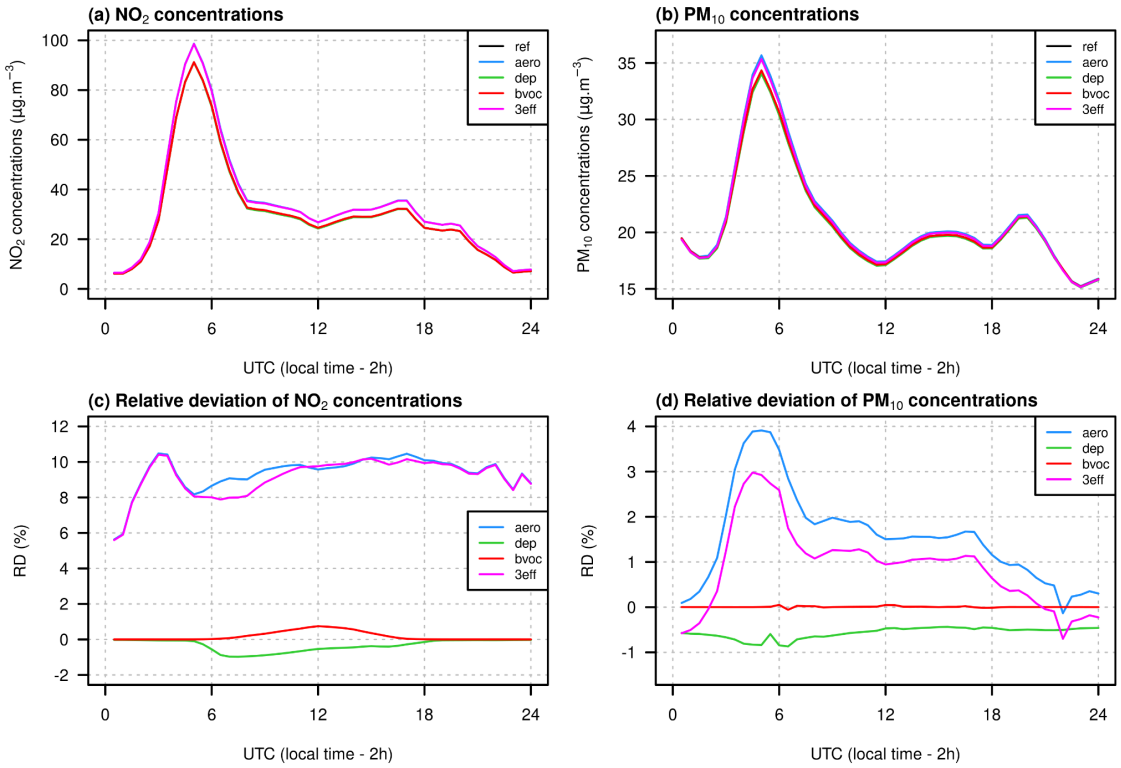

The observed concentrations in fig. 1a and 1b are higher around 5 a.m., which corresponds to the traffic peak hour, combined to a low wind situation (< 2 $m.s^{-1}$) that limits the dispersion of pollutants. The afternoon traffic peak induces a lower increase of concentrations because emissions are lower, more spread in time, and the wind speed is higher. Trees do not change the temporal variations. Figures 1c and 1d show that for all species, the tree aerodynamic effect is the main effect that leads to an increase in concentrations, which is significant for NO_2 and for particles emitted in the street by traffic such as black carbon (BC_{10} in Table 2). The dry deposition on leaves is low and leads to less than 1% decrease in concentrations. BVOC emitted by the trees induces a small increase of NO_2 during daytime (up to 0.7%). Table 2 shows that the increase in organic particles (org_{10}) due to the BCOV oxidation at the street scale is negligible, because at this scale, oxidation is not rapid enough to produce condensable compounds. This induces a non-significant increase in $PM_{2.5}$ and PM_{10} concentrations. The aerodynamic effects on inorganics ($inorg_{10}$) is mostly related to the condensation of ammonia (NH_3) emitted by traffic, which condenses with nitric acid to form ammonium nitrate. The effects on organics are linked to the condensation of emitted semi volatile organic compounds and to the increase of inorganics, leading to enhanced condensation of organic hydrophilic condensables brought from the background to the street.

Table 2. Average (avg) and maximum (max) concentrations and relative deviations (RD) for various species and for the five simulations.

Species	Concentration (µg.m^{-3})										RD (%)							
	ref		aero		dep		bcov		3eff		aero		dep		bcov		3eff	
	avg	max	avg	max	avg	max	avg	max	avg	max	avg	max	avg	max	avg	max	avg	max
NO_2	30.5	91.2	33.4	98.7	30.4	91.1	30.6	91.2	33.3	98.6	9.4	10.5	-0.3	-1.0	0.2	0.7	9.2	10.4

$PM_{2.5}$	17.2	26.8	17.5	27.7	17.1	26.6	17.2	26.8	17.4	27.5	1.3	3.7	-0.5	-0.8	0.01	0.1	0.7	2.9
PM_{10}	20.8	34.3	21.1	35.7	20.6	34	20.8	34.3	21	35.3	1.6	3.9	-0.6	-0.9	0.01	0.1	0.9	3.0
org_{10}	5.5	8.7	5.6	9.0	5.5	8.6	5.5	8.7	5.5	8.9	0.9	3.7	-0.7	-1.3	0.02	0.2	0.01	2.4
$inorg_{10}$	2.4	3.6	2.4	3.8	2.4	3.6	2.4	3.6	2.4	3.8	0.7	4.5	-0.5	-1.0	0.01	0.3	0.1	3.3
NH_3	3.3	4.2	3.3	4.2	3.3	4.2	3.3	4.2	3.3	4.2	0.4	3.6	-0.3	-0.9	0.00	0.1	0.1	3.6
BC_{10}	1.2	3.0	1.3	3.2	1.2	2.9	1.2	3.0	1.2	3.1	4.5	6.7	-0.8	-1.0	0.00	0.0	3.5	5.6

CONCLUSION

The comparison of tree effects on air quality at the street level demonstrates that the tree aerodynamic effect is predominant at the street level and leads to a significant increase in NO_2 concentration, and to pollutants emitted by traffic. This suggests that trees should not be planted in streets with high traffic emissions. Dry deposition of gas and particles on leaves is limited, therefore, we cannot rely only on this process to significantly improve air quality in streets. In the case studied here, temperature and BVOC emissions are quite high, and it shows that at the local scale the tree emissions have a limited impact on particle formation, because the residence time is too low to oxidise the emissions and produce condensables.

Note that the simulations were performed on a specific day here and that the tree effects on concentrations depend on street and tree characteristics, time of the year, and meteorological conditions.

The perspective of this work is to better estimate the BVOC emissions by using parameterizations of the leaf surface temperature instead of assuming it is equal to the air temperature, and to take into account the shadow created by buildings on the radiative budget. MUNICH will be coupled with an urban climatic model including a modelling of the tree water stress that can influence BVOC emissions. The effect at the city scale will be studied by running simulations with MUNICH coupled to a chemistry transport model over the entire city of Paris, taking into account the diversity of trees.

REFERENCES

André, M., Sartelet, K., Moukhtar, S., Andre, J. M. and Redaelli, M., 2020: Diesel, petrol or electric vehicles: What choices to improve urban air quality in the Ile-de-France region? A simulation platform and case study. Atmospheric Environment **241**, 117752.

Guenther, A., 2000: Natural emissions of non-methane volatile organic compounds, carbon monoxide, and oxides of nitrogen from North America. Atmospheric Environment **34**(12–14), 2205–2230.

Guenther, A., Hewitt, C. N., Erickson, D., Fall, R., Geron, C., Graedel, T., Harley, P., Klinger, L., Lerdau, M., Mckay, W. A., Pierce, T., Scholes, B., Steinbrecher, R., Tallamraju, R., Taylor, J. and Zimmerman, P., 1995: A global model of natural volatile organic compound emissions. Journal of Geophysical Research **100**(D5), 8873.

Hicks, B. B., Baldocchi, D. D., Meyers, T. P., Hosker, R. P. and Matt, D. R., 1987: A preliminary multiple resistance routine for deriving dry deposition velocities from measured quantities. Water, Air, and Soil Pollution **36**(3–4), 311–330.

Kim, Y., Wu, Y., Seigneur, C. and Roustan, Y., 2018: Multi-scale modeling of urban air pollution: development and application of a Street-in-Grid model (v1.0) by coupling MUNICH (v1.0) and Polair3D (v1.8.1). Geoscientific Model Development **11**(2), 611–629.

Kim, Y., Lugon, L., Maison, A., Sarica, T., Roustan, Y., Valari, M., Zhang, Y., André, M. and Sartelet, K.,

2022: MUNICH v2.0: A street-network model coupled with SSH-aerosol (v1.2) for multi-pollutant modelling. Geoscientific Model Development Discussion [preprint].

Lugon, L., Sartelet, K., Kim, Y., Vigneron, J. and Chrétien, O., 2020: Nonstationary modeling of NO2, NO and NOx in Paris using the Street-in-Grid model: coupling local and regional scales with a two-way dynamic approach. Atmospheric Chemistry and Physics **20**(13), 7717–7740.

Lugon, L., Sartelet, K., Kim, Y., Vigneron, J. and Chrétien, O., 2021: Simulation of primary and secondary particles in the streets of Paris using MUNICH. Faraday Discussion. **226**(0), 432–456.

Maison, A., Flageul, C., Carissimo, B., Tuzet, A. and Sartelet, K., 2022a: Parametrization of Horizontal and Vertical Transfers for the Street-Network Model MUNICH Using the CFD Model Code_Saturne. Atmosphere **13**(4), 527.

Maison, A., Flageul, C., Carissimo, B., Wang, Y., Tuzet, A. and Sartelet, K., 2022b: Parameterizing the aerodynamic effect of trees in street canyons for the street network model MUNICH using the CFD model Code_Saturne. Atmospheric Chemistry and Physics **22**(14), 9369–9388.

Owen, S. M., Boissard, C. and Hewitt, C. N., 2001: Volatile organic compounds (VOCs) emitted from 40 Mediterranean plant species: VOC speciation and extrapolation to habitat scale. Atmospheric Environment **35**(32), 5393–5409.

Sartelet, K., Couvidat, F., Wang, Z., Flageul, C. and Kim, Y., 2020: SSH-Aerosol v1.1: A Modular Box Model to Simulate the Evolution of Primary and Secondary Aerosols. Atmosphere **11**(5), 525.

Sartelet, K., Zhu, S., Moukhtar, S., André, M., André, J. M., Gros, V., Favez, O., Brasseur, A. and Redaelli, M., 2018: Emission of intermediate, semi and low volatile organic compounds from traffic and their impact on secondary organic aerosol concentrations over Greater Paris. Atmospheric Environment **180**, 126–137.

Walmsley, J. L. and Wesely, M. L., 1996: Modification of coded parametrizations of surface resistances to gaseous dry deposition. Atmospheric Environment **30**(7), 1181–1188.

Wesely, M. L., 1989: Parameterization of surface resistances to gaseous dry deposition in regional-scale numerical models. Atmospheric Environment **23**(6), 1293–1304.

Yarwood, G., Rao, S., Yocke, M., and Whitten, G., 2005: Updates to the carbon bond chemical mechanism: CB05. US EPA Final Report, 161 pp.

Zhang, L., 2001: A size-segregated particle dry deposition scheme for an atmospheric aerosol module. Atmospheric Environment **35**(3), 549–560.

Zhang, L., Brook, J. R. and Vet, R., 2003: A revised parameterization for gaseous dry deposition in air-quality models. Atmospheric Chemistry and Physics **3**(6), 2067–2082.

Zhang, L., Moran, M. D., Makar, P. A., Brook, J. R. and Gong, S., 2002: Modelling gaseous dry deposition in AURAMS: a unified regional air-quality modelling system. Atmospheric Environment **36**(3), 537–560.

21st International Conference on
Harmonisation within Atmospheric Dispersion Modelling for Regulatory Purposes
27-30 September 2022, Aveiro, Portugal

THE ROLE OF GREEN ROOFS ON CITIES AIR QUALITY: INDIRECT AND DIRECT IMPACTS

Sandra Rafael[1], Ana Ascenso[1], Bruno Augusto[1], Diogo Lopes[1] and Ana I. Miranda[1]

[1]CESAM & Department of Environment and Planning, University of Aveiro, Portugal

Abstract: Green roofs, as part of nature-based solutions, have been pointed out as a solution to pursue the goal of sustainable cities. This study aims to investigate the direct and indirect impacts of green roofs on air quality, focusing on particulate matter (PM10), nitrogen dioxide (NO_2) and ozone (O_3). For that, the numerical modelling system composed of the WRF-SLUCM-CHIMERE models was applied to 1-year period (2017), in the Porto urban area. First, the modelling setup was applied to assess the direct impact of green roofs on air quality-related due to changes in local meteorology. Then, the indirect impact was assessed, aimed to investigate the impacts of green roofs on air quality based on the combined effects of meteorology and atmospheric emissions (linked to buildings' energy savings). For that, the EnergyPlus model was added to the cascade of models to investigate the role of green roofs in the buildings' energy needs. The related changes in the atmospheric emissions were then used as input data in the WRF-SLUM-CHIMERE system to assess the air quality impacts. The EnergyPlus application also allows the analysis of green roof impacts in terms of environmental and economic indicators (based on the carbon emissions avoided and energy savings, respectively). The direct impact results showed that green roofs promote a temperature increase during the autumn and winter seasons, and a temperature decrease during the spring and summer seasons. Both negative (concentrations increase) and positive (concentrations decrease) impacts were obtained for the primary (PM10 and NO_2) and secondary (O_3) air pollutants, respectively, due to changes in the dynamical structure of the urban boundary layer. The indirect effects of green roofs showed their potential to enhance the energy efficiency of buildings, reducing their cooling and heating needs. The changes in energy consumption promoted a reduction in the environmental (-16004 t CO_2 per year) and economic indicators (-12549 k€·year^{-1}). Regarding air quality, the impact was negligible. The obtained results highlight the need for a multipurpose evaluation of the impacts of green roofs, with the different effects having to be traded off against each other to better support the decision-making process.

Keywords: *air quality, energy performance, green roofs, numerical modelling, urban areas*

INTRODUCTION

Cities stand as a hub of economic growth, innovation, culture and creativity; however they are facing pressures related to social, economic and environmental problems, such as overcrowding, air pollution and climate change effects (Alberti et al., 2019). To deal with these pressures, cities are increasingly embracing innovation and novel technologies (i.e., enhanced abatement technology), soft-measures (i.e., nature-based solutions) and behavioural changes (through citizen's engagement), leading the way towards local solutions to global challenges (Alberti et al., 2019).

Green roofs combine technology and nature in a single solution, which can have the potential to turn cities' challenges into opportunities. Green roofs are vegetated surfaces, consisting of plants usually grown on particular substrate material on a building rooftop (Shafique et al. 2020). They offer many benefits to buildings and their surrounding environment (Castleton et al., 2010). Several studies have been exploring green roofs' environmental benefits, but the majority of them were focused on the effects on the city microclimate. Few studies have been assessing the impacts of green on air quality, and those hardly take into account the impacts of green roofs' energy savings on air quality, the so-called indirect effect.

In this context, the main goal of this study is to assess the direct (due to changes in local climate) and indirect (combining the effects of meteorology and atmospheric emissions) impacts of green roofs on air quality during a 1-year period, having as a case study the Porto urban area. Three urban air pollutants were analysed: particulate matter with an equivalent aerodynamic diameter equal or less than 10 μm (PM10),

nitrogen dioxide (NO_2) and ozone (O_3). For that, a numerical modelling approach composed by the WRF-SLUCM-CHIMERE models was applied. The EnergyPlus model was also used to support the indirect assessment.

METHODOLOGY

A specific methodology was applied to assess the direct and indirect impacts of green roofs in the Porto urban area. Two main steps were performed: i) definition of the numerical modelling; and ii) design and characterization of scenarios. A detailed description is presented in the following sub-sections.

Case study

The Porto urban area is located in the northern region of Portugal and it is the second-largest Portuguese city, and one of the major urban areas in south-western Europe. The Porto urban area is predominantly covered by artificial surfaces, characterised by a mixed land use: commercial/industrial and residential areas. According to the Portuguese Statistics Institute (INE, 2018), with a total of 418 038 buildings, 99% of them for residential purposes, the Porto urban area concentrates the largest proportion of the housing stock in Portugal, with 34.2% of buildings and 31.6% of households, in 2017. Due to its dimension and economic activities (e.g., maritime port, airport and oil refinery), the Porto urban area has been facing air quality problems. After a reducing trend in the annual PM10 and NO_2 concentrations during the economic crisis (2007-2015) (Monteiro et al., 2018), an increase in the annual average values of air pollutants concentrations has been observed since 2017 (Rafael et al., 2020). The current and projected trends in air quality and climate (Rafael et al., 2020), together with the importance of housing stock to energy consumption, make this city an interesting and challenging case study to evaluate the potentialities of green roofs.

Numerical modelling

The modelling system composed by the WRF-SLUCM-CHIMERE models was applied to a 1-year simulation (2017). The modelling setup was applied for the study period for the baseline and "green roof" scenarios.

The Weather Research and Forecasting (WRF) model (Skamarock et al., 2008), version 3.7, coupled with the single layer urban canopy model (SLUCM) (Kusaka et al., 2001), was used. The WRF-SLUCM was set up with three domains: the coarse domain (D1), covers Europe and part of the North of Africa and has 210 × 185 horizontal grid cells with a horizontal resolution of 25 km; the nested domain (D2) includes Portugal mainland and has 131 × 176 horizontal grid cells with a horizontal resolution of 5 km; and D3 is focused on the Porto urban area and has 71 × 91 horizontal grid cells with a horizontal resolution of 1 km. The vertical grid was composed of 30 vertical layers up to the top of the computational domain (50 hPa). The two-way nesting technique was applied for the simulations (Skamarock et al., 2008). The physical parameterizations adopted can be found in Rafael et al. (2021). Information regarding the land use/land cover was taken through a combination between the Corine land cover project 2006 version (CLC2006), with a 3 arc-seconds horizontal resolution, and the Porto Urban Atlas from the European Environmental Agency, with 10 m x 10 m of horizontal resolution, in a complementary approach to better detail Porto urban features. Both land use databases were remapped to the United States Geological Survey (USGS) 33 land use categories.

The meteorological initial and boundary conditions for the coarse domain (D1) were obtained from the European Centre for Medium-Range Weather Forecasts (ECMWF) Re-Analysis Interim (ERA-Interim) model data (http://www.ecmwf.int/en/research/climate-reanalysis/era-interim) with 1°×1° spatial resolution and temporal resolution of 6-h for surface and pressure levels. For the other domains, the initial and boundary conditions came from the respective parent domain. The sea surface temperatures and the soil moisture were also initialized using the ECMWF data.

The outputs from the WRF model were used as meteorological input data for the CHIMERE model. The CHIMERE chemistry-transport model is an open access multi-scale Eulerian chemical transport model (CTM), which applies the integration of the mass continuity equation to estimate the concentrations of several chemical species in each cell of a given grid. The chemical mechanism MELCHIOR-2 was used to

simulate the concentration of 44 gaseous species from a set of 120 chemical reactions. The anthropogenic emissions were obtained from the European Monitoring and Evaluation Programme (EMEP) inventory, which was improved based on a top-down methodology. The biogenic emissions were calculated using the Model of Emissions of Gases and Aerosols from Nature (MEGAN), part of the CHIMERE model. Further details can be found in Rafael et al. (2021).

EnergyPlus version 9.1.0 (EnergyPlus, 2019) was applied to assess the impact of green roofs on building energy needs, as part of the green roof indirect scenario. EnergyPlus is a stand-alone building energy simulation model capable of modelling the hourly energy consumption of a building subject to user-specified environmental and operating conditions (Fantozzi et al., 2021). The EnergyPlus model was applied to two kinds of household buildings - typical building configuration (two storeys) and the tallest building (six storeys) - chosen due to their predominance in the study area (81% of the total building typologies), which allowed to extrapolate the obtained outcomes from an individual building to the Porto urban area. For both configurations, data related to the materials and construction configuration, energy loads and heating and cooling technology usage were kept constant. The construction elements, such as roofs, walls and floors, were obtained from the report of the most used materials in the construction sector in Portugal (OERCO2, 2017). Further details can be found in Rafael et al. (2021). For the two-building configurations two settings were assumed: i) a typical roof, considering a horizontal roof with white gravel (B1); and ii) an extensive green roof (B2).

”Green roof” scenarios

To accomplish the proposed goal, three scenarios were established and assessed:

- The Baseline scenario (BS) considers the current urban morphology;
- Scenario 1 (S1) considers that 100% of the urban areas (i.e., the simulation grid cells with USGS land use urban categories) have green roofs (covered with vegetated surfaces). This scenario implies that changes in air quality data are only related to changes in the meteorological variables, according to the linkages between meteorology and air quality, and so, S1 assesses the direct benefits of green roofs.
- Scenario 2 (S2) also considers that 100% of urban areas are covered with green roofs but aims to assess the indirect benefits of green roofs. The S2 assessment comprises three steps: 1) application of the EnergyPlus model to explore the effects of green roofs on the buildings’ energy needs; 2) analysis of green roof impacts in terms of environmental and economic indicators (based on the carbon dioxide emissions avoided and on energy savings, respectively); step 2 also includes the recalculation of the EMEP emission inventory for the Porto urban area, due to the impact of green roofs on the energy demand for heating and cooling purposes (focused on the sectors where there is a direct link between energy consumption and atmospheric emissions); 3) application of WRF-SLUCM-CHIMERE to assess local air quality.

Should be noted that the environmental and economic effects of green roofs were explored individually, for each building configuration in analysis, and extrapolated to the Porto urban area, to give an insight into the potential of green roofs at the city level. A detailed description of the proposed methodology and scenarios can be found in Rafael et al. (2021).

RESULTS AND DISCUSSION

Direct effects

To evaluate the direct effects of green roofs on air quality, their influence on meteorological variables was first investigated. The analysis of the spatial effects of green roofs on the air temperature of the Porto urban area for the year 2017 (results not shown), revealed: i) distinct seasonal behaviours, with green roofs increasing the average air temperature in the autumn and winter seasons (October to March) and decreasing it in the spring and summer seasons (April to September); ii) similar spatial patterns were obtained throughout the year, with the magnitude of the differences varying according to the month in analysis, and with higher differences (positive or negative) being obtained in more densely built-up areas (the magnitude of differences increases as more pronounced is the level of urbanization). Figure 1 shows the spatial distribution of the annual air quality concentration differences between the S1 and BS results. Three main

conclusions can be drawn from the analysis of Figure 1: i) an increase in the annual average concentrations of primary pollutants – PM10 and NO_2 – was obtained, indicating an overall negative green roof effect, while the annual O_3 concentrations – secondary pollutant – decreases, corresponding to a positive effect; ii) the air pollutants patterns differ along the year, with increases and decreases in the concentration levels; and iii) the impact of green roofs on air quality is slight, with the average monthly differences ranging between -2 $\mu g \cdot m^{-3}$ and +2 $\mu g \cdot m^{-3}$.

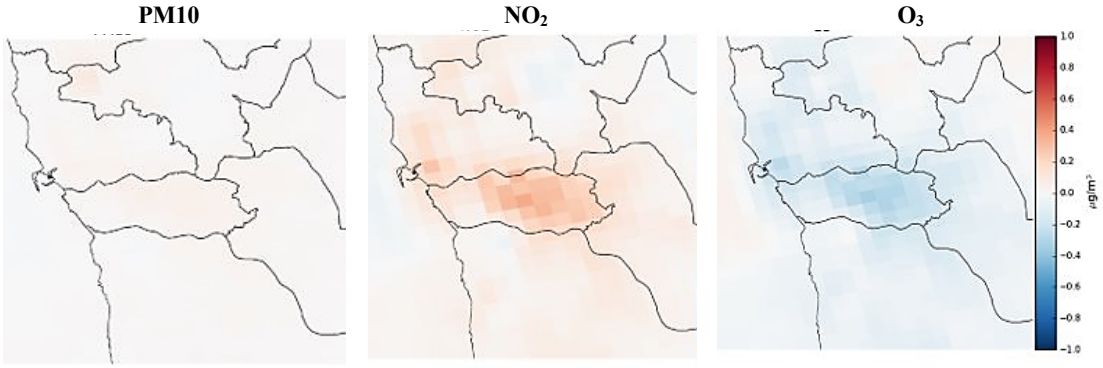

Figure 180. Spatial distribution of the absolute annual differences between the green roof scenario (S1) and the baseline scenario (BS) results for PM10, NO_2 and O_3 concentrations.

Indirect effects

To explore the indirect effects of green roofs on air quality, their influence on the different typologies of buildings was first investigated. The results (not shown) revealed a decrease in the energy needs for heating and cooling with green roofs, which is more pronounced in the warmer months (cooling needs) and in the typical two floors building. The overall improvement of the building's energy performance due to green roofs has implications for the environmental (CO_2 emissions avoided) and economic indicators of buildings and, consequently, in the Porto urban area. At the city level, the results revealed a potential reduction in the CO_2 emissions of -2332 t for cooling and -13672 t for heating, for a total of 16004 t CO_2 per year (see Figure 2). Regarding the costs, it is expected a total monetary saving of 12549 k€·$year^{-1}$, with the heating processes contributing to a saving of 11183 k€·$year^{-1}$ and the cooling processes contributing with 1366 k€·$year^{-1}$.

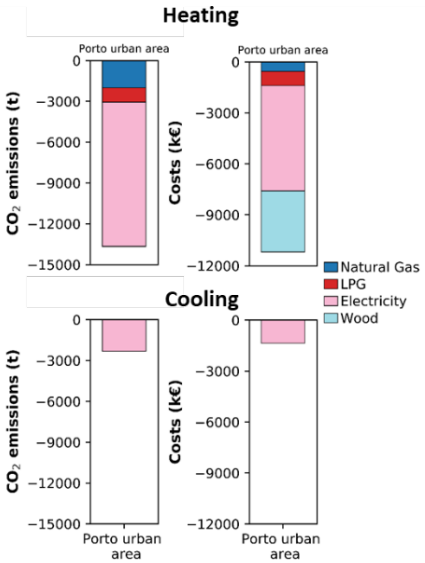

Figure 2. Environmental (CO_2 emissions) and economic indicators (costs) related to the energy savings promoted by green roofs, in the Porto urban area.

The energy savings promoted by green roofs have also implications for the magnitude and spatial distribution of atmospheric emissions. The results revealed an overall tendency of green roofs to promote reductions in PM10, PM2.5 and NOx emissions from the energy production sector and the commercial and residential combustion sectors. Despite this positive trend, the obtained reductions represent less than 5% of the total emissions of the Porto urban area. As result, the implications of the emissions changes on air quality were negligible, with the individual impact of the emissions changes in the PM10, NO_2 and O_3 concentrations, on an annual average, being around +/- 1 $\mu g \cdot m^{-3}$.

More details about the obtained results can be found in Rafael et al. (2021).

CONCLUSIONS

The current research has three main outcomes: i) the effects of green roofs on air temperature vary according to the season, highlighting the capability of this NBS to regulate the local climate; ii) both negative and positive impacts were estimated for the primary and secondary pollutants, respectively, with an overall increase of PM10 and NO_2 annual concentrations, and a decrease of O_3 level; iii) green roofs promote an increase in the buildings energy efficiency, reducing the cooling and heating needs, mainly in the warmer months; and iv) the indirect impact of green roofs on air quality was slight. This type of results shows that changes in urban structure can influence different aspects (climate, energy consumption, emissions and air quality) of the built-up environment.

ACKNOWLEDGEMENTS

This work was supported by the project GENESIS (PTDC/GES-URB/29444/2017) funded by the Portuguese Science and Technology Foundation through national funds and by the European Community Fund FEDER within the COMPETE2020 program. Thanks are also due for the financial support to the PhD grant of A. Ascenso (SFRH/BD/136875/2018) and B. Augusto (2020.06293.BD), to the contract granted of S. Rafael (2020.02543.CEECIND) and to CESAM (UIDP/50017/2020+UIDB/50017/2020+ LA/P/0094/2020).

REFERENCES

Alberti, V., M. Alonso Raposo, C. Attardo, D. Auteri, R. Ribeiro Barranco, F. Batista E Silva, P. Benczur, et al., 2019: The Future of Cities, Vandecasteele, I., Baranzelli, C., Siragusa, A. and Aurambout, J. editor(s), EUR 29752 EN, Publications Office of the European Union, Luxembourg. ISBN 978-92-76-03847-4 (online), 978-92-76-03848-1 (print).

Castleton, H.F., V. Stovin, S.B.M. Beck, J.B. Davison, 2010: Green roofs; building energy savings and the potential for retrofit. *Energy Build.,* **42**, 1582-1591.

Fantozzi, F., C. Bibbiani, C. Gargari, R. Rugani, G. Salvadori, 2021: Do green roofs really provide significant energy saving in a Mediterranean climate? Critical evaluation based on different case studies. *Front. Archit. Res.,* **10**, 447-465.

INE – Instituto Nacional de Estatística (Statistics of Portugal), 2018: Estatísticas da Construção e Habitação 2017. ISBN: 978-989-25-0444-5.

Kusaka, H., H. Kondo, Y. Kikegawa, F. Kimura, 2001: A simple single layer urban canopy model for atmospheric models: comparison with multi-layer and slab models. *Boundary Layer Meteorol.*, **101**, 329-358.

Monteiro, A., Russo M., Gama C., Lopes M., Borrego C., 2018: How economic crisis influence air quality over Portugal (Lisbon and Porto)? *Atmos. Pollut. Res.,* **9**, 439-445.

OERCO2 - Online Educational Resource for Innovative Study of Construction Materials Life Cycle, 2017: Study of most used materials in construction sector in Portugal. URL https://oerco2.eu/wp-content/uploads/2013/02/1.2.1.-Report-Construction-materials-in-Portugal_EN.pdf.

Rafael, S., B. Augusto, A. Ascenso, C. Borrego, A.I. Miranda, 2020: Re-Naturing Cities: Evaluating the effects on future air quality in the city of Porto. *Atmos. Environ*., **222.**

Rafael, S., L.P. Correia, A. Ascenso, B. Augusto, D. Lopes, A.I. Miranda, 2021: Are green roofs the path to clean air and low carbon cities?. *Sci. Total Environ.,* **798,** Article number 149313.

Shafique, M., X. Xue, X. Luo, 2020: An overview of carbon sequestration of green roofs in urban areas. *Urban For. Urban Green.,* **47**, Article number 126515.

Skamarock, W.C., J.B. Klemp, J. Dudhia, D.O. Gill, D.M. Barker, X.Y. Huang, W. Wang, J.G. Powers, 2008: A Description of the Advanced Research WRF Version 3. NCAR/TN-475+STR, pp.113.

21st International Conference on
Harmonisation within Atmospheric Dispersion Modelling for Regulatory Purposes
27-30 September 2022, Aveiro, Portugal

IMPACTS OF AN EVAPORATING WATERBODY IN URBAN FABRIC THROUGH LARGE-EDDY SIMULATIONS

Carlo Cintolesi[1], Petros Ampatzidis[2], Andrea Petronio[3] and Silvana Di Sabatino1

[1]Department of Physics and Astronomy, University of Bologna, Bologna, Italy
[2]Department of Architecture and Civil Engineering, University of Bath, Bath, UK
[3]IE-FLUIDS s.r.l, Trieste, Italy

Abstract:
The evaporation and condensation of water are crucial phenomena that drives many physical processes in urban environment both in terms of buoyancy force generated and heat sink or source introduced. This work presents and implements a general evaporation and condensation model that includes the heat exchange due to the water change of phase. Such a general approach can be applied to different simulation techniques. Two geometries paradigmatic of a city fabric are investigate under a mixed convective regime, and considering a waterbody which is warmer and colder compared to the building temperature. Globally, the water evaporation leads to an increase of convective motions that enhance the vertical transport and the turbulent mixing between urban canyons and the surrounding atmosphere. To the best of the authors knowledge, this is one of the first study directly reproducing the evaporation form a waterbody in urban context.

Key words: *Urban Canyon, Water Evaporation, Computational Fluid Dynamics, OpenFOAM.*

INTRODUCTION

Nowadays, critical issues affect the human health and the liveability in city contexts, including the Urban Heat Island and Urban Pollutant Island, which are expected to be exacerbated by the actual trend of climate change. To address such issues, there is a growing interest in Nature-Based Solutions (NBSs) as tools to develop suitable mitigation and adaptation strategies (EC, 2015). Nonetheless, there is no clear consensus on the efficacy and best practices to implement NBSs, that can exhibit benefits as well as unexpected collateral effects.

The present contribution wants to address this lack by analysing the impact of blue NBS, such as waterbody, on the thermo-fluid dynamics of two archetypal urban configurations. Overall, the water evaporation reduces the temperature within urban canyons, while the vapor increases the convection and turbulent mixing at the roof-top level; thus, enhancing the mass and momentum exchange between the canyon and surrounding atmosphere. The physical process is numerically reproduced utilising computational fluid dynamics approach: Large-Eddy Simulations (LES) particularly suitable for reproducing the turbulent flows, and Reynolds-Averaged Navier-Stokes (RANS) simulations, more suitable for studying complex geometries. The thin water film model accounts for the water change of phase and the consequent heat transfer (Cintolesi et al, 2016 & 2017). Such model is implemented in new solvers developed within the OpenFOAM (2018) toolbox. Two configurations are considered: an idealised urban canyon is studied in detail through LES, showing that a waterbody is particularly effective in improving the in-canyon circulation, turbulent kinetic energy and turbulent kinetic fluxes at the roof-top interface. A more realistic configuration reproducing an array of 7×3 square building with a waterbody in the middle is simulated and analyses through RANS.

In the following, we provide a brief overview of the implemented mathematical model with references for further details and a complete description, an outlook of the two cases under analysis with the main results, and some final comments.

MATHEMATICAL MODEL AND SIMULATION APPROACH

The mathematical model for the air dynamics and for the water evaporation, as well as the simulation approaches adopted, are here shortly reported. A complete discussion and description of the models can be found in references reported. Simulations have been performed using the open-source software OpenFOAM (2018), using a home-made solver implementing the evaporation model. All the simulations have been successfully validated against experimental and numerical datasets reported in literature.

Governing equations

The air is considered an incompressible fluid and the Boussinesq approximation is adopted for the buoyancy effects. The governing equations read:

$$\frac{\partial u_j}{\partial x_j} = 0, \tag{1}$$

$$\frac{\partial u_i}{\partial t} + u_j \frac{\partial u_i}{\partial x_j} = -\frac{\partial p}{dx_i} + \nu \frac{\partial^2 u_i}{\partial x_j \partial x_j} + b_i, \tag{2}$$

$$b_i = g_i(1 - \beta_T \Delta T - \beta_\omega \Delta\omega), \tag{3}$$

where u_i is the air velocity component, p is pressure,ν in the kinematic viscosity, and $b_i$is the buoyancy force. This last is the sum of the temperature and vapour contribution: $g_i$is the gravity acceleration vector, $\beta_{T/\omega}$is the thermal/vapour expansion coefficient, ΔT and $\Delta\omega$ are the temperature and vapour variation respect to the reference temperature and vapour. Equations for temperature and vapour concentration are:

$$\frac{\partial T}{\partial t} + u_j \frac{\partial T}{\partial x_j} = \alpha_T \frac{\partial^2 T}{\partial x_j \partial x_j} + S_\omega, \tag{4}$$

$$\frac{\partial \omega}{\partial t} + u_j \frac{\partial \omega}{\partial x_j} = \alpha_\omega \frac{\partial^2 \omega}{\partial x_j \partial x_j}, \tag{5}$$

where $\alpha_{T/\omega}$is the thermal/vapour molecular diffusivity and S_ω is the sink term due to the evaporation of water at the boundary of the air domain.

The water model is based on the thin-film assumption, i.e. the waterbody is modelled as a wet surface that can evaporate infinitely (Petronio, 2010). The velocity of evaporation U_ω essentially depends on the vapour gradient in the surface normal direction, and it is estimated with a semi-impermeable model (Welty et al., 2007), that reads:

$$U_{\omega,i} = -\frac{\alpha_\omega}{1-\omega_\Gamma}\left(\frac{d\omega}{dn_i}\|_\Gamma\right) n_i, \tag{6}$$

with n_i the normal versor to the wet surface. The subscript Γ denotes that quantity are evaluated at the surface; hence, the evaporation velocity is defined just at the wet surface. The heat sink S_ω is proportional to the divergence of the evaporation velocity as follows:

$$S_\omega = \frac{1}{\rho\, c_p}\frac{\partial}{\partial x_i}\left(\rho_\star L_h U_{\omega,i}\right), \tag{7}$$

where ρC_p are the density and specific heat of air, respectively, while $\rho_\star$ is the density of the mixture of air and water vapour, which is taken equal to air density for simplicity, and L_h is the latent heat of vaporization. The temperature sink term is numerically applied to the first cell near the wet surface in the air domain.

Additional information and a complete description of the present evaporation model can be found in Cintolesi et al. (2016, 2017).

Water channel in an idelised urban canyon

The first case study (see Figure 1) consists of an infinite array of urban canyon with unity aspect ratio, including a water channel at the street level ($0.65 < x/H < 1.35$). This case was simulated with the Large-Eddy Simulation techniques (e.g. Sagaut, 2000), using the Smagorinsky (1963) model to account for the unresolved Sub-Grid Scale (SGS) turbulent motions. The atmospheric wind leads to a Reynolds number based on the free-stream velocity U_0 is $Re = U_0 H/\nu = 2 \times 10^4$; hence, within the range if the Reynolds independence. Temperature of the buildings and domain is constant while different temperatures are imposed to water. The domain is discretised using 1,592,562 cells and the mesh is stretched near the solid and water surfaces ensuring a direct resolution of the wall-boundary layer. The numerical schemes used for solving the equations ensure an overall accuracy of the second order. The simulations are run until a steady-state statistical regime is established, and then the statistics are collected for analysis. Details on geometry, mesh and numerical settings can be found in Cintolesi et al. (2021). Three simulations are studied: the neutral case without channel (as a reference), the warmer case where the channel is hotter than buildings (Richardson number $Ri = 3.4$), and the colder case where the channel is colder than buildings ($Ri = -3.4$). The Richardson number indicates that both cases are in free convection regime; notice that the positive and negative signs are introduced to distinguish the cases with hot and cold water, respectively.

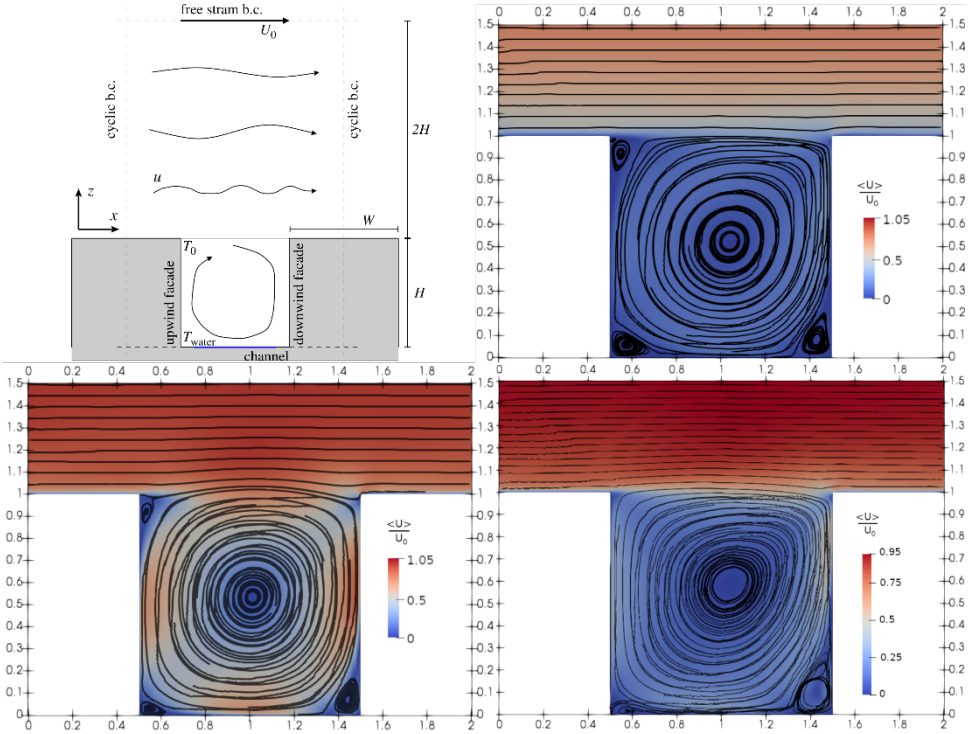

Figure 181**.** From the top-left panel in clockwise order: geometry of idealised urban canyon; streamwise dimensionless velocity distribution and streamlines for neutral case (no waterbody); the warmer waterbody; the colder waterbody.

Figure 1 shows the dimensionless streamwise velocity intensity and the streamlines in the canyon for the three cases under consideration. Compared to the neutral case (top-right panel), the warmer channel (bottom-left panel) exhibits an increased in-canyon circulation, a less extended corner-recirculation regions, and higher out-canyon velocity. The colder channel (bottom-right panel) slightly increase the in-canyon motion while increasing the out-canyon flow velocity and destroys the corner-recirculation regions at the upwind façade. This is mainly due to the vertical velocity generated at this façade by the buoyancy force triggered by the cold air advected from the channel. The increase in velocity above the canyon is probably

due to the destruction of the roof shear layer by the vertical motions generated by the buoyancy. The temperature and vapour fields (not shown) are essentially higher in a thin layer near the water channel, while they are rather homogenously distributed inside the canyon. Outside the canyon they tend to rapidly assume their reference values. In both cases, the temperature in the canyon drops due to the evaporation process, which produces an energy sink at the surface of the water. In the case of the warmer channel, this sink is counterbalanced by thermal conduction, the temperature drop is of the order of 3% inside the canyon, and imperceptible outside. In the case of the colder channel, the cooling is much more intense: between 10-20% in the canyon and about 7% outside. Second-order statistics (not here reported) show a general increase in turbulent kinetic energy: overall, with four times in the warmest case, three times in the coldest case compared to the neutral one, and especially at the roof level of buildings where turbulent exchanges with the atmosphere are most intense. Mean turbulent kinematic momentum fluxes $u'w'/u_0^2$ exhibit larger peaks at height $z/H = 1$, indicating a region of greater mixing at vertical turbulent transport.

Waterbody in a simplified urban neigborhood

The second case study (see Figure 2) consists of a simplified urban neighbourhood composed by a grid of 7×3 square buildings, where the central building has been replaced by an square with a waterbody. This case was investigated through a RANS simulation, utilizing the RNG $k-\varepsilon$ model for turbulence. A synthetic turbulent atmospheric boundary layer impacts the buildings along the x-direction giving a Reynolds number of $Re = 2.9 \times 10^4$. The computational grid is of 846,976 cells and wall functions are used to correctly reproduce the wall-boundary layer. Details validation, computational grid and settings can be found in Ampatzidis et al. (2022). Three cases are simulated: neutral (no waterbody), warmer waterbody with respect to the building constant temperature ($Ri = 1.1$), and colder waterbody ($Ri = -1.1$). Again, the flow regime is of mixed convection.

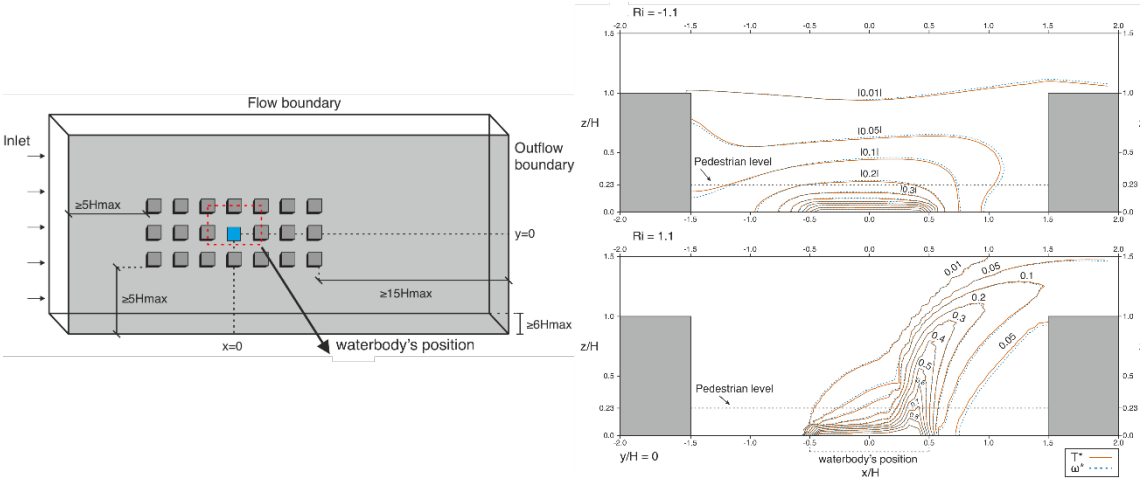

Figure 2. Vertical section along the x-direction of the waterbody square. Left panel: geometry and computational domain. Right panel: dimensionless temperature and vapour contour lines above the waterbody for colder case (top) and warmer case (bottom).

Figure 2 shows the contour line of the dimensionless temperature $T^* = (T - T_0)/\Delta T$ and vapour $\omega^* = (\omega - \omega_0)/\Delta\omega$ in the square with waterbody. Temperature and vapour present similar features and in both cases, with colder and warmer waterbody, higher concentrations are located in a thin layer above the water surface. However, the colder case exhibits an increase of thermo-vapour stratification and a moderate reduction of temperature in the square, while the warmer case develops a strong upward thermal-vapour plume which drives above the buildings the hot and humid air. The air circulation (not shown) in the square presents a large clockwise vortex, which is reduced by in extension and intensity in the colder case and is destroyed by the upward thermal plume in the warmer case. Turbulent kinetic energy peaks near the top corner of the downwind building for the neutral and colder case, while the warmer case has a spot of high turbulent energy where the upward plume is deviated by the ambient air flow (Ampatzidis et al., 2022).

Between the downwind building, the circulation is not significantly altered in the colder case and shows a regime similar to the skimming flow, where the in-building circulation is dominated by a main recirculation vortex. On the contrary, in the warmer case the recirculation region is destroyed, and the in-building flow is no longer separated from the surrounding atmospheric wind.

FINAL REMARKS

A water evaporation model that accounts for heat transfer by water change of phase has been applied for numerical simulations of two archetypal cases: an idealised urban canyon with water channel and a simplified urban neighbourhood with a waterbody in a square, and in a regime of mixed convection. The former is reproduced by a high-accurate LES, the latter by an RANS simulation. For both geometries, three scenarios are investigated: the neutral case (no waterbody) is compared with the case including a warmer and a colder waterbody (compared to the building constant temperature). In the idealised urban canyon, the warmer channel triggers a thermo-vapour buoyancy force that enhances the main clockwise vortex, at the same time the in-canyon temperature does not increase because of the cooling effect of the evaporation. The colder channel does not improve the internal vortex velocity (but a localised buoyancy force generated near the upwind buildings remove the corner recirculation regions) and reduce the temperature in the canyon. In both cases, the presence of vertical convective motions increases the turbulence intensity and turbulent kinetic fluxes at the building-roof level, leading to a larger mass and momentum exchange between the canyon and the surrounding atmospheric wind. In the simplified urban neighbourhood, in general, the presence of waterbody promotes mixing and increased the circulation in the square and downwind between buildings. The colder waterbody increases the thermo-vapour stratification in the square and slightly alter the air dynamics, while the warmer waterbody generates a strong upward convective plume that destroy the recirculation vortex in the square and the skimming flow regime in the downwind building canyons. The warmer case can represent a night-time configuration in real city, when the waterbody heated during the day can improve mixing and vertical flows (thus also the dispersion of pollutants). Overall, blue infrastructure in city context which are composed also by these positive effects should be balanced by an increase in humidity, which can decrease environmental comfort.

REFERENCES

Ampatzidis P., C. Cintolesi, A. Petronio, S. Di Sabatino, T. Kershaw, 2022: Evaporating waterbody effects in a simplified urban neighbourhood: a RANS analysis. *Accepted for publication on J. of Wind Engineering and Ind. Aerodynamics*.

Cintolesi, C, A. Petronio, V. Armenio, 2016: Large-eddy simulation of thin film evaporation and condensation from a hot plate in enclosure: First order statistics, *Int. J. of Heat and Mass Transfer*, **101**.

Cintolesi, C, A. Petronio, V. Armenio, 2017: Large-eddy simulation of thin film evaporation and condensation from a hot plate in enclosure: Second order statistics, *Int. J. of Heat and Mass Transfer*, **115**.

Cintolesi C., F. Barbano, S. Di Sabatino, 2021: Large-eddy simulation analyses of heated urban canyon facades, *Energies*, **14**.

EC - European Commission, 2015: Nature-Based Solutions and Re-Naturing Cities, Final Report of the Horizon 2020 Expert Group on Nature-Based Solutions and Re-Naturing Cities, European Union, Brussels.

OpenFOAM, 2018: The OpenFOAM Foundation, version 6.0. Available online: openfoam.org (accessed on 1 May 2019).

Petronio, A., 2010: Numerical investigation of condensation and evaporation effects inside a tub. Ph.D. thesis. School of Environmental and Industrial Fluid Mechanics, University of Trieste.

Sagaut, P., 2000: Large eddy simulation for incompressible flows: an introduction. Springer, Berlin

Smagorinsky, J., 1963: General circulation experiments with the primitive equations: I: the basic experiment. *Mon Weather Rev* 91-99

Welty, J., C. Wicks, G. Rorrer, R. Wilson, 2007: Fundamentals of Momentum, Heat and Mass Transfer. Wiley.

21st International Conference on
Harmonisation within Atmospheric Dispersion Modelling for Regulatory Purposes
27-30 September 2022, Aveiro, Portugal

LARGE-EDDY SIMULATIONS OF NATURE-BASED SOLUTIONS EFFECTIVENESS IN POLLUTANT REMOVAL FROM URBAN CANYONS

Silvana Di Sabatino[1], Carlo Cintolesi[1]

[1]Department of Physics and Astronomy, University of Bologna, Bologna, Italy

Abstract: The paradigmatic case of a periodic square urban canyon at $Re = 2 \times 10^4$, where a pollutant is released at the street level, forms the basic geometry to investigate the effectiveness of two grey and green Nature-Based Solutions (NBSs) in enhancing pollutant dispersion. First, the simulation approach is validated successfully against laboratory and numerical datasets. Second, the NBSs are virtually introduced and analysed: the grey NBS (roof obstacles) generates highly energetic turbulence motions at the rooftop level, which destroys the sharp shear layer, increases the mixing and the pollutant dispersion. Greater vertical turbulent mass fluxes near the upwind building, where pollution accumulates, are detected. The reduction in the pollution concentration within the canyon is about 34%. The green NBS (roof trees), instead, mainly acts as a sink of momentum and as a predominant effect decreasing the forced circulation within the canyon, leading to a slightly higher pollutant concentration. In this case, the shear layer is destabilised, but the atmospheric wind is less energetic throughout the area above the canyon. This generates a reduction of turbulent mixing and vertical trasport at the interface.

Key words: *Nature-Based Solutions, Urban Canyon, Rooftop trees, Large-Eddy Simulations, OpenFOAM.*

INTRODUCTION

Strategies for improving the pollution removal from urban canyons are of major importance when the control of air quality in cities is in question. In the last decade, increased attention has been paid to the use of Nature-Based Solutions (NBSs), and the European Commission itself has made them a crucial tool for structuring mitigation measures and adapting to the adverse effects of climate change (Faivre et al, 2017). In an idealized urban canyon, the removal occurs at the building-roof level. Overall, it is supported by turbulent kinematic fluxes and limited by roof shear, which creates a sharp separation between the recirculation region inside the canyon and the atmospheric wind above (Michioka et al., 2014).

In this work, the roof morphology is modified through the introduction of two NBSs of grey and green type, *i.e.* rectangular solid infrastructures and low trees, respectively. The effect of these NBSs on the general air dynamics is studied employing accurate numerical experiment, performed adopting the Large-Eddy Simulation (LES) approach. Such methodology realistically reproduces three-dimensional and time-dependent turbulent motions, directly resolving the more energetic scale of motion and modelling via a Sub-Grid Scale (SGS) model the less energetic ones. This work reports some of the first high-resolution numerical studies of NBS using LES, which, due to its ability to resolve transient and three-dimensional motion, as well as its advanced turbulent modelling, is most suitable than the wider-used Reynolds-Averaged Navier-Stokes simulations when the purpose is to analysed pollutant dispersion mechanisms in urban contexts. Such methodology is increasingly used for various practical applications but is still not widely used due to its relatively higher computational cost and lower numerical robustness, which requires special attention in numerical and computational grid settings.

SIMULATION APPROACH

Mathematical model

The air is modelled as an incompressible gas and the pollutant concentration is a passive scalar that is realised, advected and diffused in air. If trees are present, their canopy is modelled as a moment sink S_i^{tree}. The equations of motion are:

$$\frac{\partial u_j}{\partial x_j} = 0, \tag{1}$$

$$\frac{\partial u_i}{\partial t} + u_j \frac{\partial u_i}{\partial x_j} = -\frac{\partial p}{dx_i} + \nu \frac{\partial^2 u_i}{\partial x_j \partial x_j} - S_i^{tree}, \tag{2}$$

$$\frac{\partial c}{\partial t} + u_j \frac{\partial c}{\partial x_j} = \lambda \frac{\partial^2 c}{\partial x_j \partial x_j}, \tag{3}$$

where the summation on repeated index is assumed, u_i are the velocity components, p is the pressure, ν is the kinematic viscosity, c is the pollutant concentration and λ its molecular diffusivity. The sink due to the foliage reads:

$$S_i^{tree} = C_d \cdot LAD \cdot |u| \cdot u_i \tag{4}$$

whit C_d is the drag coefficient and LAD is the Leaf Area Density, which varies with respect to the distance from the trunk and depends on the type of tree under analysis. Linked to the latter, the Leaf Area Index is defined as the integral of the LAD function.

Numerical methodology

The equations of motion have been resolved adopting the LES technique (e.g. Rodi et al., 2013). The sub-grid scale model used is the dynamic Lagrangian model proposed by Menveau et al. (1996). Such a model is based on the classical Smagorisky (1963) model, but the empirical parameter is computed dynamically and estimated in each computational cell through a Lagrangian procedure. For this reason, the model is particularly suitable for reproducing anisotropic and localised turbulence, which characterised the system under analysis. The effects of turbulence on pollutant concentration are also reproduced taking advantage of the Reynolds analogy. Details on the sub-grid scale model used are not reported here for the sake of brevity; we refer to Cintolesi et al. (2021) for a detailed discussion.

Implementation and schemes

The mathematical model reported, as well as the dynamic Lagrangian SGS model, has been implemented in a home-made software, developed within the OpenFOAM (2018) toolbox. The discretization schemes ensure a global accuracy of the second order.

CASE STUDIES

The cases under investigation are based on the same idealised geometry: the reference case is a periodic array of infinite square urban canyon (Figure 1, left panel) of height H. The obstacle case is obtained by adding to the rooftop a series of rectangular blocks (Figure 1, centre panel) of height $0.1H$, depth and width $0.05H$, placed at a distance of $0.15H$ from each other. The tree case, instead, have a series of low-growing trees on the rooftop: they are composed by a solid cylindric trunk (diameter $0.02H$ and height $0.15H$) placed at a distance $0.1H$from the edge and $0.4H$ from each other. The canopy is a porous medium with a sphere shape, centred at the end of the trunk. Two radii were chosen to represent small trees (radius $0.05H$) and big trees (radius $0.1H$). Such dimensions were selected to be representative of Laurel trees, with a $C_d = 0.2$ and a Leaf Area Index of 8, while the LAD has been chosen to be higher in the external par and lower near the trunk. It can be observed that the settings of the size and distribution of the elements on the roof is somewhat subjective; this contribution is one of the first work on this topic and a sensitivity study on parameters used has not been conducted.

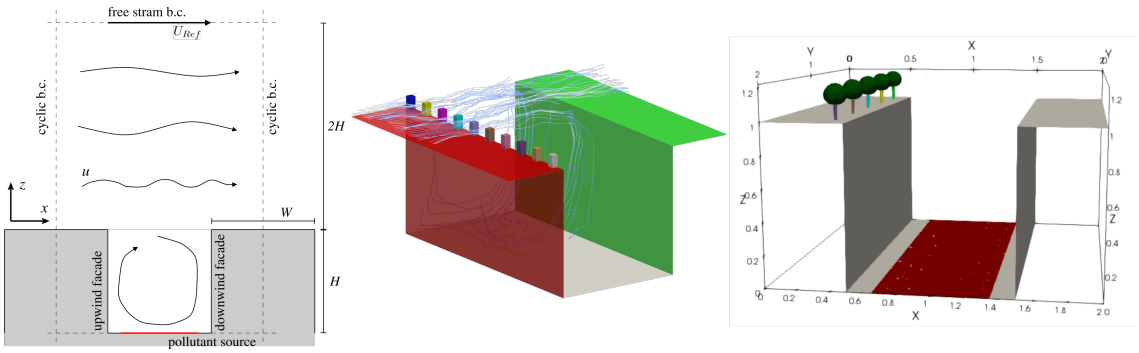

Figure 1: Sketch of case studies. Left, reference case: urban canyon with smooth roof. Centre, obstacle case: canyon with grey infrastructure on the roof. Right, tree case: canyon with trees on the roof.

In all cases the atmospheric wind is perpendicular to the canyon axis, and the Reynolds number based on the free-stream velocity is $Re = 2 \times 10^4$ (hence, in regime of Reynolds independence). The pollutant is realised with constant flux at the street level from a band of width $0.7H$, mimicking the traffic pollution from a roadway.

Computational mesh and validation

The three geometries are discretized by 1 592 562 cells, 4 087 700 cells, and 2 040 786 cells for the reference, obstacle and tree cases (respectively). The computational grid is refined near the solid surfaces ensuring the direct resolution of the wall-boundary layer, and a refinement region is created near the obstacles where turbulence is expected to be more intense. Simulations have been run till the systems reach a statistical steady state before the statistics have been computed. The simulations approach has been successfully validated by comparing the results obtained in the reference case with experimental and numerical datasets reported in literature (see Cintolesi et al., 2021).

OBSTACLE-ROOF CASE

In this case solid infrastructure have been added to destabilise the sharp shear layer that establishes at the roof level ($z/H = 1$) and that separates the in-canyon circulation to the surrounding atmospheric flow. Figure 2 shows the velocity streamlines within the canyon for the reference and the obstacle case. The general circulation is not altered but the presence of the obstacles weakens and reduces the extent of the recirculation zones at the upwind façade ($x/H = 0.5$). This is significant for the enhancement of pollutant dispersion, as the highest concentrations are found on the upwind façade where the pollutant is transported by the principal canyon vortex. In particular, the reduction of recirculation at roof level allows a higher momentum mass exchange with the atmosphere. It can be noted also that the separation line between the internal vortex and the atmospheric flow is slightly curved upwards.

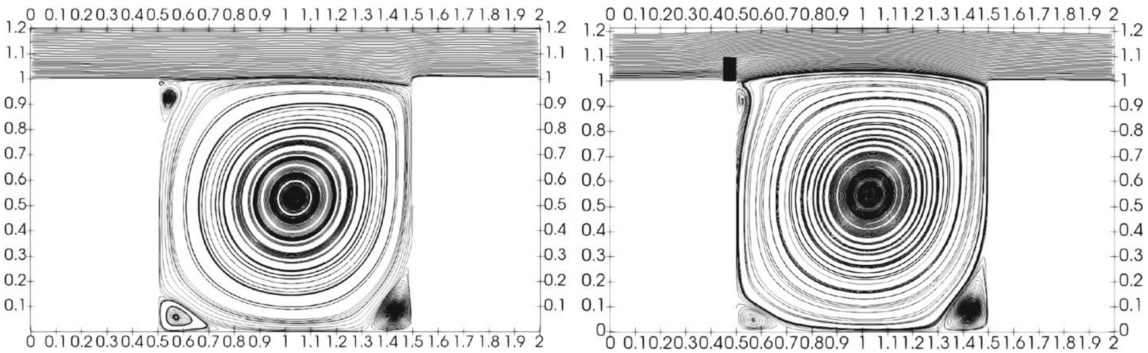

Figure 2: Streamlines of the reference case (left panel) and obstacle case (right panel).

The turbulent kinetic energy ($u_i'u_i'/2$) and the turbulent momentum kinetic fluxes ($u'w'$) - not shown – exhibits higher values at the interface when obstacles are present, along with a pick that is slightly shifted upward. Thus, the obstacles act as turbulent generators, increasing the level of turbulence at the interface between the canyon and the atmosphere, weakening the flow separation. The interface is less stable and turbulent mixing and transport of mass and momentum in the vertical direction are intensify.

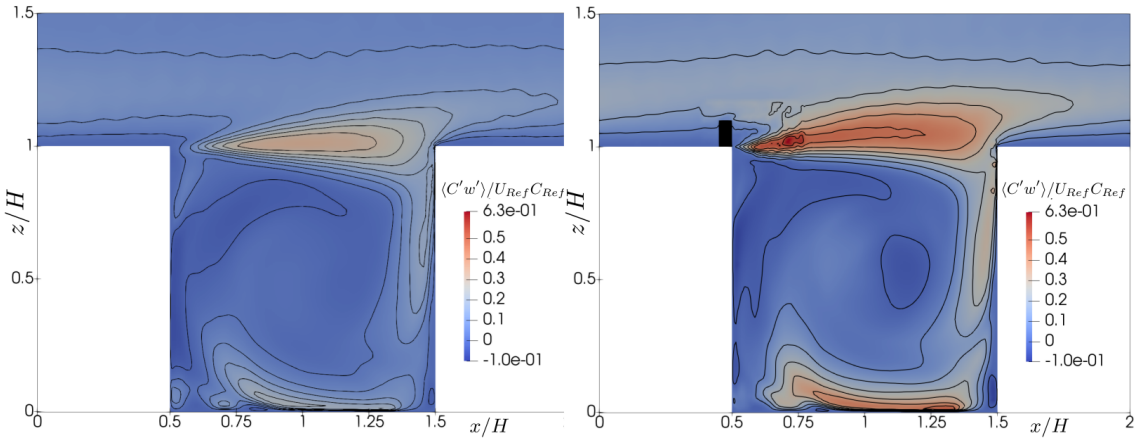

Figure 3: Dimensionless turbulent concentration fluxes in the reference (left) and obstacle case (right).

Figure 3 reports the dimensionless turbulent concentration fluxes ($c'w'$). Two main spots of high value are detectable: above the street where the pollutant is realised, and at the canyon-atmosphere interface. The turbulence generated by obstacles destabilised the roof shear layer and induce a more efficient vertical mixing at the interface. To better quantify the effectiveness of obstacles in enhance the pollution transfer through the roof interface, the convective transfer coefficient (Barlow and Belcher, 2002) was computed as the integral along the interface of the vertical concentration fluxes $cw >$, and it is 7% higher (per unit of time) in the obstacle case. Also, a direct estimation of the concentration of pollutant in the canyon reveal that the obstacle case has 34% lower concentration that the reference case with smooth roof.

TREE-ROOF CASES

The tree case wants to assess whether green infrastructure can help the dispersion of pollutants in urban canyons. The velocity streamlines do not differ substantially from the reference case; hence, the discussion is supported by variables plots over vertical lines placed at three selected locations: near the upwind façade ($x/H = 0.75$), in the canyon centre ()$x/H = 1$, near the downwind façade ($x/H = 1.25$). Figure 4 shows the dimensionless streamwise velocity (u) and the turbulent kinetic momentum fluxes ($u'w'$) along such three vertical lines. Overall, the velocity field is not substantially altered by the presence of trees within the canyon, and a decrease in velocity is detectable only at the canopy level (marked with a dotted line) as a result of the leaf-induced momentum sink. Interestingly, the velocity reduction produced is weakly correlated with canopy size, and both large and small trees produce similar profiles. Regarding turbulent fluxes, no relevant differences can be observed within the canyon, while lower peaks at the interface and the generation of a secondary peaks localised at the height of the trees can be detected. For the secondary peaks, trees with a larger crown produce more intense turbulent flows.

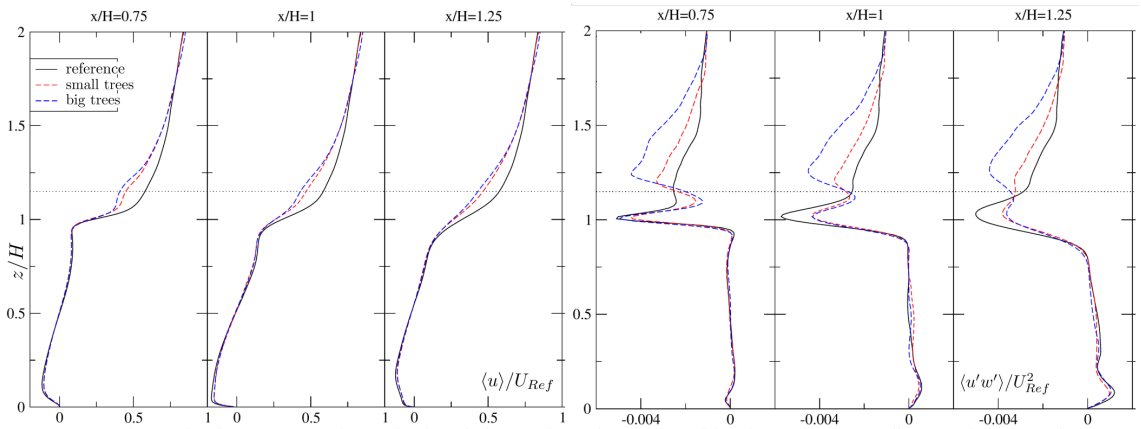

Figure 4: Dimensionless streamwise velocity (left panel) and turbulent kinetic momentum fluxes (right panel) along three selected vertical lines within the canyon.

An analysis of pollutant concentration fluxes and the average concentration – not reported - within the canyon reveals that this configuration of trees tend to slightly decrease the pollutant dispersion, and higher concentration are detected in the canyon compared to the reference case. This can be due also to the reduction of turbulence intensity highlighted at the interface ($z/H = 1$).

FINAL REMARKS

In the present study has been shown that grey infrastructures (solid obstacles) on rooftop have positive effects on the dispersion of pollutants from an urban canyon, mainly due to the turbulence generated at the canyon-atmosphere interface with enhances turbulent mixing and transport. Instead, green infrastructures (trees) are not as effective for the same purpose and even show an slightly adverse effect. This is probably due to the fact that tree canopies act by reducing atmospheric wind speed and are less effective in generating turbulence than solid obstacles. Furthermore, obstacles act at roof level by destabilising the shear layer and, thus, the interface separating the internal circulation of the canyon from atmospheric wind; whereas trees act at the canopy level, which is positioned higher up. The trees are therefore less effective in weakening the separation between in- and out-canyon flows. A different configuration of the trees, as well as the introduction of a pollutant-sink term due to canopy trees, could lead to better results in terms reduction of canyon pollution and will be the subject of future studies.

REFERENCES

Barlow J., S. Belcher, 2002: A wind tunnel model for quantifying fluxes in the urban boundary layer. *Boundary-Layer Meteorol* **104**.

Cintolesi C., B. Pulvirenti, S. Di Sabatino, 2021: Large-Eddy Simulations of Pollutant Removal Enhancement from Urban Canyons. *Boundary-Layer Meteorol.*, **180**, 79-104.

Faivre N., M. Fritz, T. Freitas, B. De Boissezon and S. Vandewoestijne, 2017: Nature-Based Solutions in the EU: Innovating with nature to address social, economic and environmental challenges. *Environmental Research*, **159**.

Michioka T., A. Sato, H. Takimoto, M. Kanda, 2011: Large-eddy simulation for the mechanism of pollutant removal from a two-dimensional street canyon. *Boundary-Layer Meteorol,* **138.**

Meneveau C., T. Lund, W. Cabot, 1996: A Lagrangian dynamic subgrid-scale model of turbulence. *J. Fluid Mech.,* 316-353.

OpenFOAM, 2018: The OpenFOAM Foundation, version 6.0. Available online: openfoam.org (accessed on 1 May 2019).

Rodi W., G. Constantinescu, T. Stoesser, 2013: Large-eddy simulation in hydraulics, 3rd edn. CRC Press, Taylor and Francis Group, Boca Raton.

Smagorinsky, J., 1963: General circulation experiments with the primitive equations: I: the basic experiment. *Mon Weather Rev,* 91-99

21st International Conference on
Harmonisation within Atmospheric Dispersion Modelling for Regulatory Purposes
27-30 September 2022, Aveiro, Portugal

NATURE-BASED SOLUTIONS FOR CLIMATE CHANGE ADAPTATION: IMPACTS ON TEMPERATURE AND AIR QUALITY IN EINDHOVEN, THE NETHERLANDS.

Ana Ascenso[1], Carla Gama[1], Peter Roebeling[1,2] and Ana I. Miranda[1]

[1]CESAM & Department of Environment and Planning, University of Aveiro, Portugal
[2]Wageningen Economic Research, Wageningen University and Research, The Netherlands

Abstract: Nature-Based Solutions (NBS) can provide answers to the challenges that urban areas are currently facing, associated with urban densification and climate change. This work aims to assess how NBS can contribute to climate change adaptation, focusing on temperature attenuation and air quality improvement in the city of Eindhoven (Netherlands). The state-of-the-art WRF-CHEM air quality modelling system was applied for the recent past (2013) and RCP4.5 medium-term future (2048) with a spatial resolution of 1 km^2. The NBS chosen for this study, green roofs industrial areas, was defined taking into consideration the municipality's aspirations and challenges. Model results show annual averaged reductions in temperature of approximately 0.5ºC and slight changes in air quality. The seasonal analysis indicates that NBS can have a stronger impact during warmer months. These results corroborate that NBS can be a contributor to climate change adaptation but their impact on air quality-related challenges needs further analysis concerning the addressed spatial and temporal resolution.

Key words: *Climate change, RCP4.5, Green Roofs, Urban areas, WRF-CHEM*

INTRODUCTION

The foreseen climate change (CC) impact on the natural and human systems is a major concern in terms of increased frequency, intensity, and/or duration of extreme weather events. Cities, in particular, are highly vulnerable to climate change effects as extreme weather events can be especially disruptive to complex urban systems due to the high level of urbanization and demographic growth. Nature-based solutions (NBS), including ecosystem-based adaptation, can reduce risks for ecosystems and benefit people, providing they are planned and implemented in the right way and place. NBS are known for their multiple benefits such as their potential to improve quality of life, and biodiversity and reduce the impact of floods, urban heating and air pollution.

This work aims to assess how NBS can contribute to climate change adaptation, focusing on temperature attenuation and air quality improvement in the city of Eindhoven (Netherlands). Few studies look at climate change and NBS on an annual basis and many don't test realistic measures. Moreover, the range of results can vary significantly between studies and methodologies. In this study, we performed high-resolution air quality simulations (1 km x 1 km) to assess the impact of local-specific NBS. With this communication, we aim to contribute to the discussion regarding the best approach to assess the urban impact of NBS and to increase the knowledge about its different effects.

METHODOLOGY

The WRF-CHEM online air quality model was applied to estimate hourly three-dimensional fields that comprise a wide range of meteorological and air pollution variables, such as temperature at 2 m (T2), nitrogen dioxide (NO_2) and ozone (O_3), the main variables assessed in this study.

WRF-CHEM is the Weather Research and Forecasting (WRF) model coupled with Chemistry (CHEM). It is a fully coupled mesoscale online model in which the air quality component is consistent with the meteorological component. Three online-nested domains with increasing resolution at a downscaling ratio of five are used – with the coarser domain of 25 km x 25 km horizontal resolution covering Europe and part of the North Atlantic Ocean, and the innermost domain of 1 km x 1 km horizontal resolution covering the area containing the case-study region (51 km × 41 km). The main WRF-CHEM parametrizations and

input data are presented in Table 1. For a more detailed description of the modelling setup and its evaluation, see Ascenso et al. (2021).

Table 59. Main physical and chemical parametrizations adopted for WRF-CHEM simulations.

Processes	Options
Microphysics	Morrison double-moment
Short-wave radiation	RRTMG scheme
Long-wave radiation	RRTMG scheme
Surface layer	MM5 Monin-Obukhov scheme
Land-surface	Unified Noah land-surface model
Urban canopy model	Single-layer, UCM
Boundary-layer	MYNN 2.5 level TKE scheme
Cumulus	Grell 3D ensemble scheme
Photolysis	Fast-J
Gas-phase mechanism	RADM2
Aerosol module	MADE/SORGAM
Aerosol-radiation feedback	Turned on
Aerosol optical properties	Volume approximation

Acronyms: MADE/SORGAM - Modal Aerosol Dynamics Model for Europe /Secondary Organic Aerosol Model; MYNN - Mellor-Yamada-Nakanishi-Niino; RADM2 - Regional Acid Deposition Model, 2nd generation; RRTMG - Rapid Radiative Transfer Model for General Circulation Models; TKE - Turbulent Kinetic Energy.

Two main sets of simulations were performed. The first used reanalysis data (ERA-INT) to define and evaluate the model setup. The second used projected data (MPI) to assess CC and NBS impacts, individually and combined. These simulations were performed for a representative year of the recent past (2013) and of the medium-term future (2048), based on the RCP4.5 scenario and EURO-CORDEX data. The simulations comprise three scenarios: i. Base scenario (2013 simulation with no land use changes); ii) Future scenario (2048 simulation with no land use changes); iii) Future scenario + NBS (2048 simulation with land use changes). Figure 1 shows a summary of the study methodology.

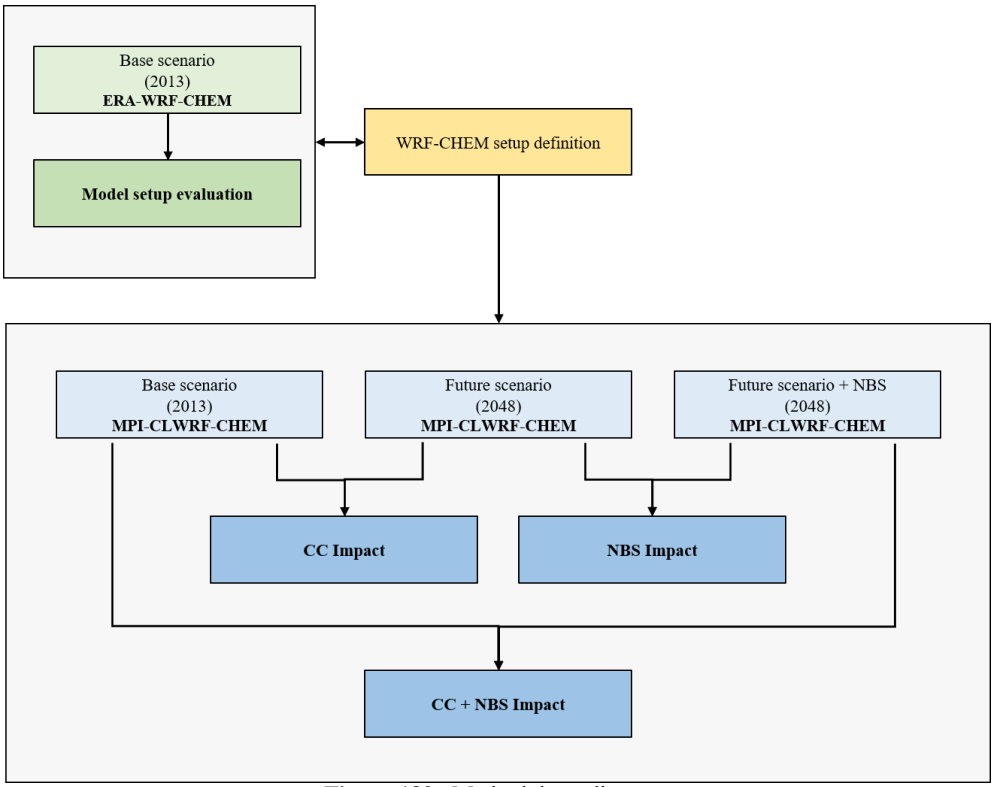

Figure 182. Methodology diagram

The NBS scenario was defined with the help of the municipalities during co-creation workshops, within the scope of the UNaLab project (https://unalab.eu/en). In this study, we assessed the impact of green roofs in industrial areas. The scenario was implemented in the model by changing land use for the grid cells that overlapped with the implementation areas. These grid cells were considered as urban land use in the USGS land used dataset for the base scenario, and were changed to grass for the NBS scenario. Related variables, such as albedo, were also changed by modifying the land use information. The area of implementation covered 5 km^2 in the model (5 model cells), which corresponds to 6% of the case-study area.

RESULTS AND DISCUSSION

To assess seasonal differences in the impact of NBS, the year was divided into cold months (November to April) and hot months (May to October). The CC impact was calculated from the difference between the Future and Base scenarios, and the NBS impact was calculated from the difference between the Future and Future + NBS scenarios. Finally, the Future NBS impact was calculated from the difference between the Future + NBS scenario and the Base scenario (see Figure 1).

Temperature

Figure 2 compiles the results for daily average temperature. The results indicate that NBS can counterbalance the increase in temperature expected in the hotter months due to CC, mainly in the areas close to the NBS implementation. Even though NBS promote a decrease in temperature throughout the year, this impact is more meaningful during the warmer months (up to -4%). These results are due to the increase in evapotranspiration and change in the surface albedo.

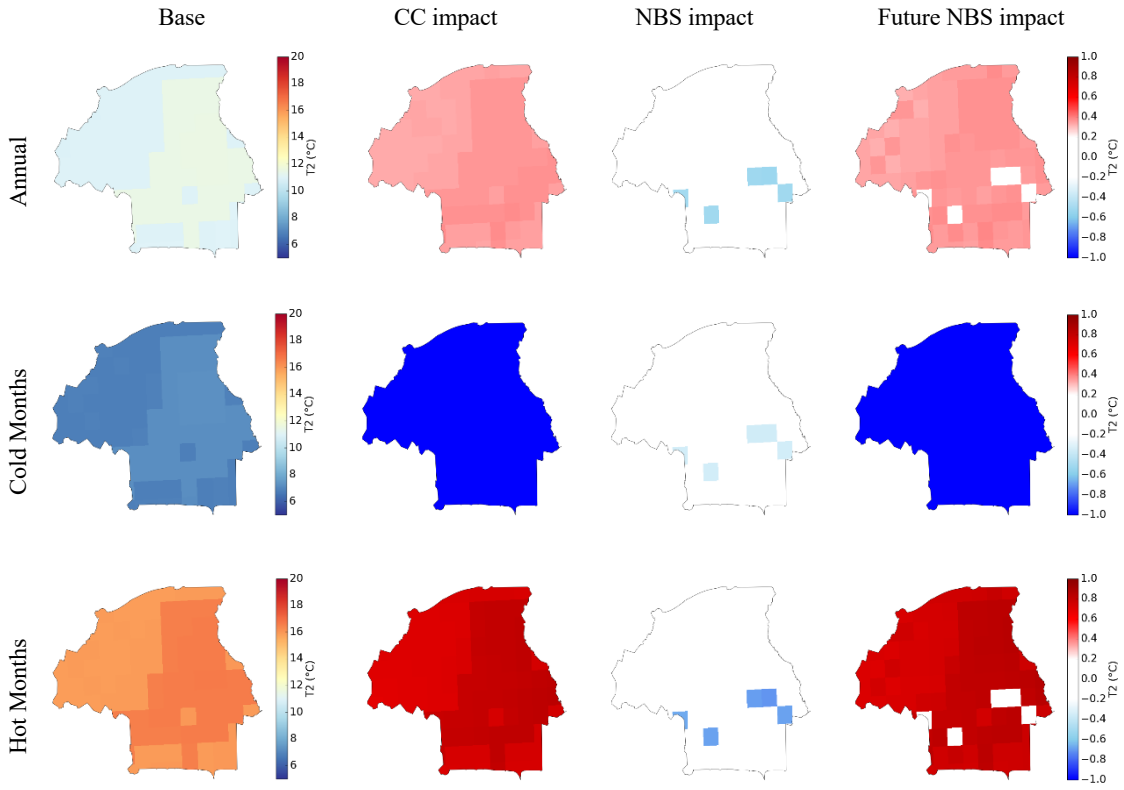

Figure 60. Impact of CC and NBS on the average daily mean temperature, for annual, cold and hot months.

Air Quality

Figure 3 compiles the results for NO_2 concentrations. The results indicate that NBS will promote a small increase in NO_2 concentrations (from +0.1 to +1.2 $\mu g/m^3$); this impact is also larger during the warmer months. These results are maybe due to the decrease in temperature and its impacts on the boundary layer

height. Simultaneously, NO_2 concentrations are estimated to increase in the future (+2%, on average), therefore, the future NBS impact will exacerbate the Base scenario concentrations by an average of + 5% (+0.7 µg/m^3) leading to an anual mean NO_2 concentraion of 17 µg/m^3. However, this change can be considered negligible.

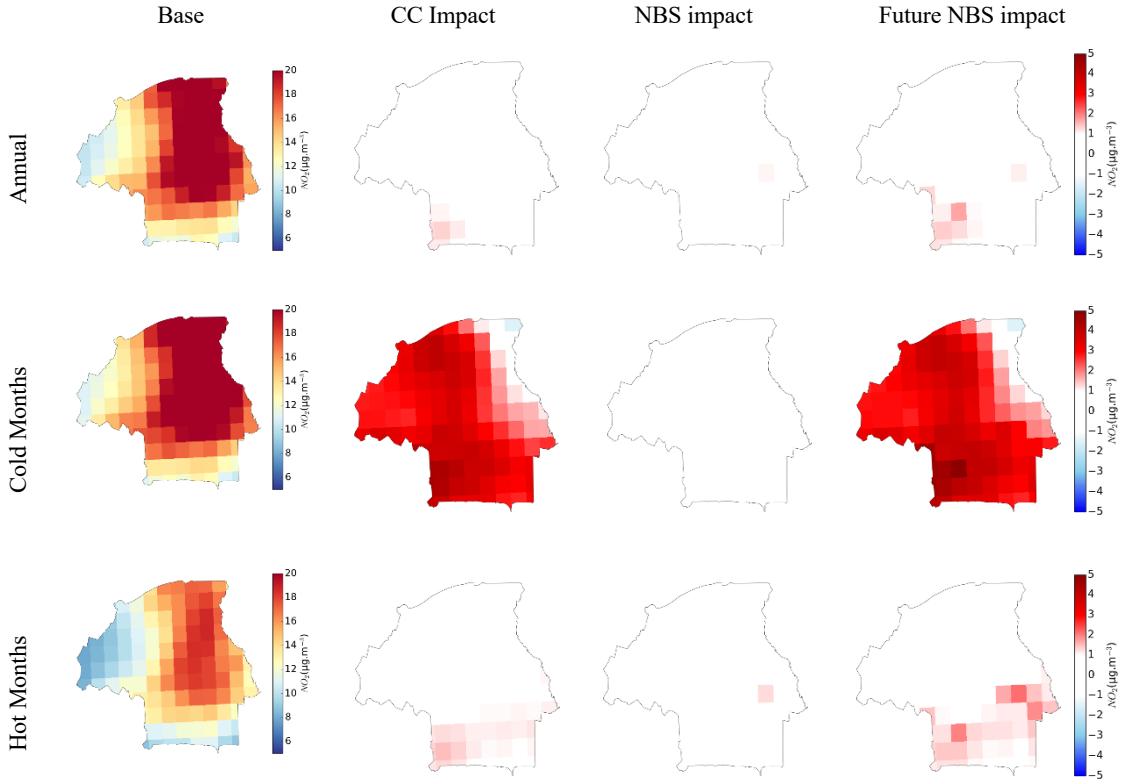

Figure 61. Impact of CC and NBS on the average daily mean NO_2 concentration, for annual, cold and hot months.

Figure 4 compiles the results for O_3 concentrations. The results indicate that NBS will promote a very small decrease in O_3 concentration (up to -0.6 µg/m^3) and the maximum impact is seen in warmer months. This may be related with the decrease in temperature and with the changes in the atmospheric nitrogen oxides. O_3 concentrations are estimated to decrease in the future (-3%, on average), therefore, the future NBS impact will promote a larger decrease in O_3 concentrations, as compared to the Base scenario by an average of - 5% (-3.4 µg/m^3), leading to an anual mean O_3 concentraion of 61 µg/m^3. However, this change can be considered negligible.

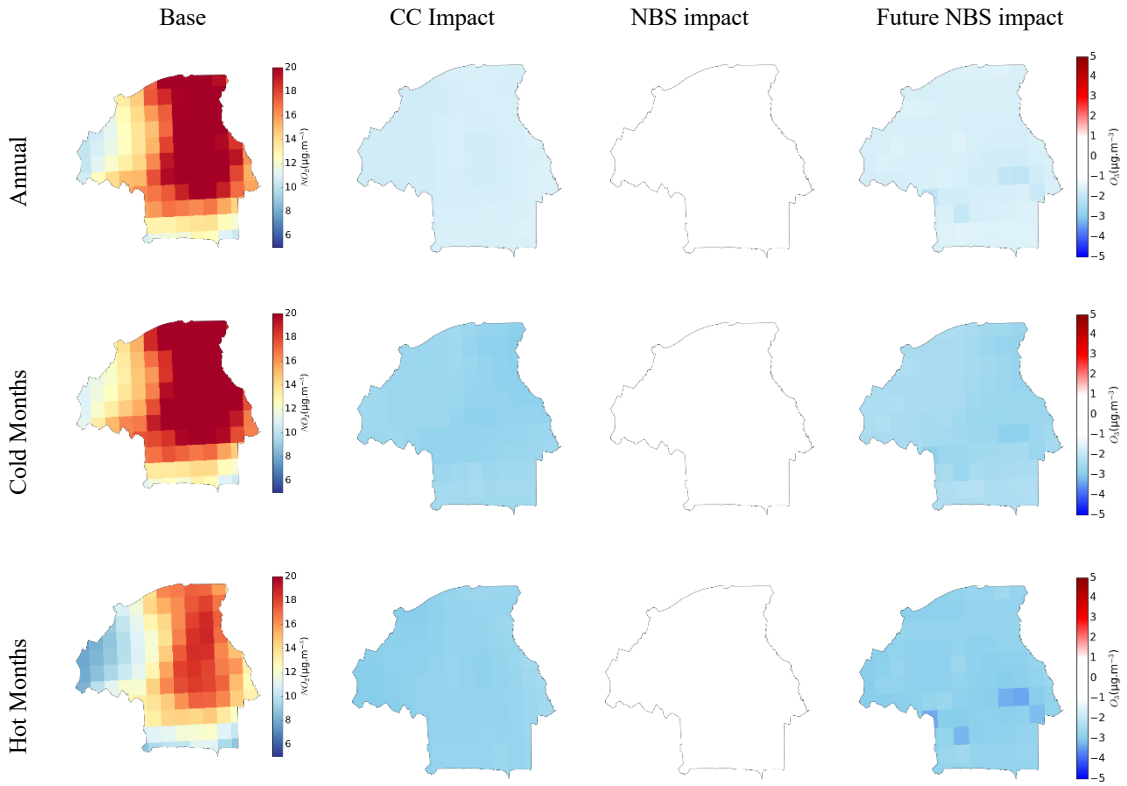

Figure 62. Impact of CC and NBS on the average daily mean O_3 concentration, for annual, cold and hot months.

CONCLUSIONS

This study assessed the impact of green roofs in a medium-term future climate scenario (2048; RCP4.5) and their ability to offset the impacts of climate change. Model results show annual averaged reductions in temperature of approximately 0.5ºC that can minimize the increase in temperature caused by climate change. However, the air quality results showed very small changes in concentrations (positive and negative, alike). The seasonal analysis shows that NBS have a stronger impact during hot months. These results corroborate that NBS could contribute to climate change adaptation but their average yearly impact, especially on air quality can be negligible; suggesting that long-term averages are not the best methodology to showcase the maximum NBS benefits or disadvantages. Further analysis concerning the addressed spatial and temporal resolution is needed.

ACKNOWLEDGEMENTS

The authors would like to thank the municipality of Eindhoven for providing information on the scenarios studied and data regarding the city's land-use characteristics. This work was supported by the UNaLab project (Grant Agreement No. 730052, Topic: SCC-2-2016-2017: Smart Cities and Communities Nature-based solutions) and the GENESIS project (PTDC/GESURB/29444/2017). Thanks are also due for the financial support to the PhD grants of A. Ascenso (SFRH/BD/136875/2018). Finally, thanks are due to FCT/MCTES for the financial support to CESAM (UIDP/50017/2020+UIDB/50017/2020), through national funds.

REFERENCES

Ascenso, A., Augusto, B., Silveira, C., Rafael, S., Coelho, S., Monteiro, A., Ferreira, J., Menezes, I., Roebeling, P., & Miranda, A. I. 2021. Impacts of nature-based solutions on the urban atmospheric environment: a case study for Eindhoven, The Netherlands. Urban Forestry & Urban Greening, 57, 126870. https://doi.org/10.1016/j.ufug.2020.126870

21st International Conference on
Harmonisation within Atmospheric Dispersion Modelling for Regulatory Purposes
27-30 September 2022, Aveiro, Portugal

PASSIVE POLLUTANT CONCENTRATION CONTROL BY ROADSIDE HEDGEROWS IN URBAN STREETS

Christof Gromke

SHORT ABSTRACT

Abstract title: Passive pollutant concentration control by roadside hedgerows in urban streets

Name and Affiliation of the First Author: Christof Gromke, Laboratory of Building and Environmental Aerodynamics, Institute for Hydromechanics, Karlsruhe Institute of Technology KIT, Karlsruhe, Germany

Email of first author: gromke@kit.edu

Names and Affiliations of the Co-authors: none

ABSTRACT TEXT (MAXIMUM 350 WORDS.)

Traffic pollutant dispersion in an urban canyon with street flanking hedgerows was investigated in an atmospheric boundary layer wind tunnel. Two types of arrangements of hedgerows were studied (i) one central hedgerow between the main traffic lanes, and (ii) two eccentric hedgerows sidewise of the main traffic lanes. Hedges of different permeability (porosity) and height were examined. Special focus was laid on the middle area of the urban street canyon and for perpendicular approach flow since pollutant concentrations are maximal here for this wind condition.

The measurement results show distinct overall improvements in air quality for street canyons with hedges in comparison to the hedge-free case. The improvements were greater for the centrally arranged hedgerows than for sidewise hedgerow arrangements. For centrally arranged hedgerows, average reductions in the middle area of the urban street canyon between 46 and 61% were observed at pedestrian head height level on the leeward side in front of the building. For arrangements of two sidewise hedgerows, corresponding average reductions between 18 and 39% were found. At the lower façade wall ($\leq$ 1/3 of canyon height) on the leeward canyon side, reductions in traffic pollutant concentrations ranging from 39 to 56% for the urban street canyon with one central hedgerow and from 1 to 20% for the canyon with two eccentric hedgerows were registered. In the lateral end areas of the street canyon, reductions in pollutant concentrations were found with central hedgerows (10 - 43%) but increases with two sidewise hedgerows (< 10%). However, since the concentrations in these areas are intrinsically low, the rather slight increases are not critical and overall, for the entire street canyon, a marked improvement in air quality prevails.

The present investigation suggests that hedgerows, in particular centrally arranged hedgerows, can effectively be employed as a passive control measure for concentrations of traffic pollutants in urban streets. Their presence results in noticeable improvements in air quality and provides a significant remedy to the pedestrians' and residents' exposure in the most severe polluted middle area of urban street canyons.

21st International Conference on
Harmonisation within Atmospheric Dispersion Modelling for Regulatory Purposes
27-30 September 2022, Aveiro, Portugal

ASSESSING THE IMPACTS OF GREEN INFRASTRUCTURES ON URBAN AIR QUALITY

Vera Rodrigues[1], Bruno Augusto[1], Kevin Oliveira[1], Sandra Rafael[1], Ana Ascenso[1], Cristina Matos Silva[2] and Ana Isabel Miranda[1]

[1]CESAM and Department of Environment and Planning, University of Aveiro, 3810-193 Aveiro, Portugal
[2]CERIS, Instituto Superior Técnico, Universidade de Lisboa, Av. Rovisco Pais, 1049-001 Lisboa, Portugal

Abstract: Nature-based solutions have been pointed as innovative solutions to deal with current and future challenges related to air pollution and climate change. Although the potential of green infrastructures, such as green walls and green roofs, to mitigate air pollution has been documented, evidence at a local scale is still limited. This work aims to increase knowledge about the potentialities of green walls and green roofs in improving local air quality, focusing on particulate matter and nitrogen dioxide pollutants.
The Computational Fluid Dynamics ENVI-met model was applied to a particular hour of a summer day over a built-up environment centered in the Avenida da República, in the city of Lisbon (Portugal). The dimensions of the computational domain are 674 m × 886 m × 200 m, and it contains 184 buildings, with the tallest building being 40 m. In addition to the baseline simulation, modelling was also done considering the application of green walls and green roofs to specific buildings located near the main avenue. Hedera helix, LAI= 1.5 and leaf angle distribution 0.5, was used for the green walls' vegetation, as they are the most common species found in direct green facades around the world.
The overall results show no disturbances exerted by green walls on the turbulent flow dynamics and on the air quality levels, when compared to the baseline scenario (without green walls). While, the integrated scenario with green roofs will lead to potential local benefits of green infrastructures on O_3 concentrations, followed by variable impacts on NO_2 concentrations.

Key words: *Green infrastructures, CFD modelling, air pollution, urban areas.*

INTRODUCTION

Urban areas are facing a continuous and unsustainable growth of population, associated with several environmental pressures. Despite the progress over the last few decades to control air pollution owing to the application of strict measures to reduce emissions, several European countries are still facing air pollution events with regular exceedances of the established legal limit values. Additionally, the increase in the percentage of people living in urban areas together with air pollution events results in growing threat for human health. The major air pollutants problems in urban areas are associated with Ozone (O_3), Nitrogen Oxides (NO_x) and particulate matter (PM).

Computational Fluid Dynamics (CFD) models usually allow taking into account the morphological specificities of the urban environment, and consequently they are able to simulate the flow dynamics perturbations caused by distinct urban obstacles and to assess the effectiveness of distinct countermeasure to control air pollution in urban areas. Nature-based solutions provide sustainable, cost-effective, multipurpose and flexible alternatives for tackling societal challenges, such as air pollution and human health protection. Innovative solutions supported by nature such as green walls and green roofs, play an important role on urban planning, leading to several benefits for the urban environment. Specifically, CFD models have been applied to assess the role of NBS in mitigating air pollution, mainly considering the effects of green infrastructures induced by mechanical drag and/or including pollutant removal by deposition and filtration mechanisms. Although the effects of green infrastructures on urban atmospheric dynamics and air quality levels have been widely studied, their impact is still not fully understood. This work aims to assess the impact of a set of green infrastructures on local flow dynamics and air quality levels in a particular area of the city of Lisbon considering two distinct green scenarios.

METHODOLOGY

To evaluate the impact of green infrastructures in the air quality of a main Avenue in Lisboa (Portugal) the CFD model ENVI-met was applied for a particular hour of a particular weekday - 4 PM, 18th June 2018. This day was selected because traffic countings were available and this hour was chosen because air quality values measured in the city centre in thise day were very high.

The ENVI-met model

ENVI-met is a three-dimensional model developed to numerically simulate surface-vegetation-air interactions in complex urban areas (Bruse and Fleer, 1998 and Huttner, 2012). The model is able to simulate the turbulent flow dynamics within the atmospheric boundary layer, numerically solving the Navier-Stokes equations applying Reynolds averages. The k-ε closure scheme is used adding two additional equations to compute the turbulent kinetic energy and the dissipation rate. ENVI-met is suited for the estimation of pollutants dispersion of gases and particles by means of the Eulerin approach, including pollutants deposition on surfaces. It also takes into account gases chemical reactions, namely the NO-NO_2-O_3 reaction cycle. The model calculations include radiation fluxes from shading, reflection and re-radiation from urban obstacles (e.g., buildings and vegetation); transpiration, evapotranspiration and sensible heat fluxes from the vegetation; water and heat exchange inside the soil system, including water uptake by vegetation.

The software is designed for microscale simulations with a typical horizontal resolution from 0.5 to 10 m and applying a time step of 1 to 5 seconds. ENVI-met has been widely applied to assess the impact of greening strategies in urban microclimates (Lee et al., 2016), although the impact of green walls using ENVI-met is still scarce. Multiple validation exercises were carried out to assess the model performance (Simon et al., 2018).

Case study description and model setup

The study area is located over the Avenida da República in the Portuguese city of Lisbon. The selected study area is in the central part of the city, being an highly urbanized area with tall buildings. This area has important traffic accesses with multiple lanes. The computational domain includes also an underground tunnel with a length of 460 meters, that passes in the middle of the main Avenue. This tunnel comprises two open areas for natural ventilation. The domain contains a total of 184 buildings, with the tallest building being 40 m. Therefore, the computational domain for this study covers a horizontal area of 674 m × 886 m with a uniform Cartesian grid and a vertical height of 200 m with variable grid setup. The horizontal grid resolution of 2 m x 2 m was kept the same all over the domain. For the vertical resolution, the lowest five grid cells have a finer resolution of 0.4 m, then a 2 m resolution was set from z = 2 m to z = 60 m, and for the remaining cells above 60 m a telescoping factor of 25% was applied. To avoid numerical problems caused by model boundary interference with internal model dynamics and guarantee a minimum spacing between the obstacles and the model boundaries, nested grids were added to each side of the computational domain, in a total of 337 x 443 x 100 grid cells.

To quantify the impact of the green scenarios, three computational domains were created: a baseline, a green walls scenario and an integrated scenario. These scenarios were co-created with local stakeholders and the location of the green infrastructures was decided based on a set of practical constraints. The green walls scenario consists of the baseline set-up with the implementation of green walls in 13 specific buildings near the main avenue (identified in green in Figure 1a)). Hedera helix, LAI= 1.5 and leaf angle distribution 0.5, was used for greening of the green walls. Green roofs on 8 selected buildings (identified in green in Figure 1b)) were also considered, and the integrated scenario (Figure 1c)) includes, in addition to the green walls, the green roofs at the 8 buildings together with a green corridor implemented in three distinct areas over the tunnel of the main Avenue.

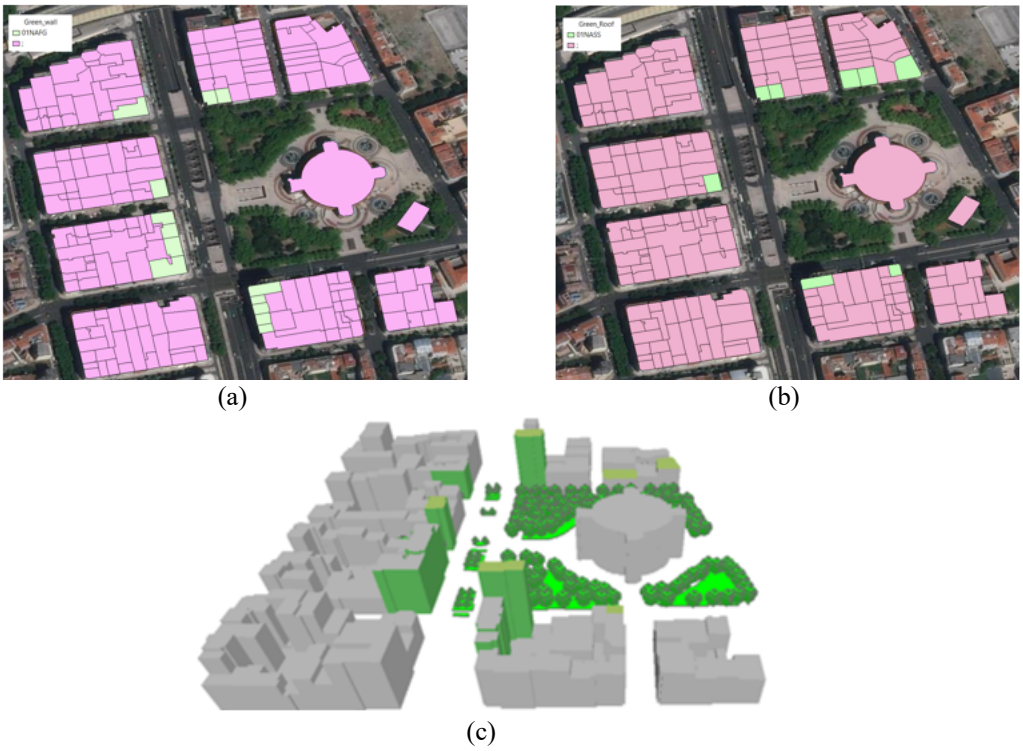

Figure 183. Computational domain: (a) Green walls scenario. (b) Green roofs, part of the integrated scenario were set in 8 selected buildings. (c) 3D view of the integrated scenario.

For the soil and surface parameters, since the area is highly urbanized, a default pavement was applied over the domain except for the main green areas with unsealed soil. Due to the lack of available data regarding vegetation, the same tree characteristics (deciduous trees, with LAD = 1.1 m^2/m^3) were used for the vegetation part of the baseline domain.

Emissions data

The case study accounts for multiple line sources and 2 area sources related to the tunnel openings. For this work, only atmospheric emissions from the transport sector were quantified. Traffic of motorcycles, light and heavy vehicles as well as buses was counted onsite for two periods in two strategically different locations. Traffic counts occurred during a weekday between 7:30 and 10:30 and between 17:00 and 20:00, in 15-minute intervals, for a total of 12 lanes. Counts were also done at the tunnel entrance during the same period and for a total of 2 lanes. All the roads on the northern side of the domain were accounted for. The traffic counts were then used to obtain the average daily traffic. Hourly distribution was then extrapolated using ENVI-Met's traffic model profiles. For the unaccounted lanes, the values were inferred based on similar lanes in the domain. In total, 22 different pollution sources were considered as linear sources, corresponding to the traffic lanes and an additional area source, corresponding to the openings of the tunnel.

Background concentrations

A background was added using data from a background monitoring station located in the city. For the simulation period, the background values were: NO=12 $\mu g.m^{-3}$; NO_2=68 $\mu g.m^{-3}$; PM10=21 $\mu g.m^{-3}$; PM2.5=14 $\mu g.m^{-3}$; O_3=87 $\mu g.m^{-3}$.

Meteorological data

A meteorological station located nearby the computational domain (2.85 km far away northeast), the "Lisboa – Gago Coutinho" station, was selected to provide the required meteorological data for the ENVI-met simulations. Meteorological data at 4 PM on the 18th June 2018 were used for the simulation, in particular a mean wind speed value of U=1.5 $m.s^{-1}$ and a north wind direction were considered. The initial

meteorological boundary conditions in the ENVI-met simple forcing option were set. The surface roughness length value was defined as 1 m, which is considered typical for a build-up area.

RESULTS

Simulation results were analyzed comparing the baseline with the green walls and the integrated scenarios estimated values for NO_2, O_3, PM10 and PM2.5 concentrations. Figure 2 shows the horizontal contour of NO_2 and O_3 concentrations at pedestrian level (z=2 m)for the baseline.

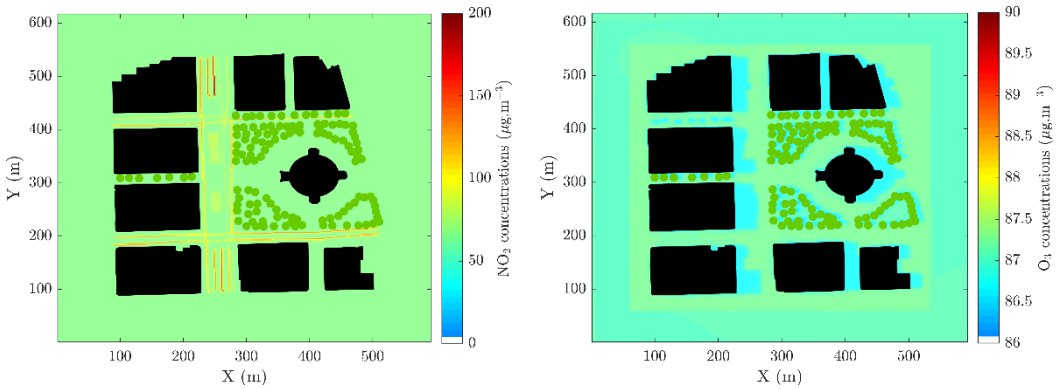

Figure 184. Horizontal iso-contour at pedestrian level for the baseline of NO_2 (a) and O_3 (b) concentrations.

The results indicate a minimum of 68 $\mu g.m^{-3}$ and a maximum of 185 $\mu g.m^{-3}$ of NO_2 concentrations, and a minimum of 86 $\mu g.m^{-3}$ and a maximum of 87 $\mu g.m^{-3}$ of O_3 concentrations. PM10 concentrations range from a minimum of 21 $\mu g.m^{-3}$and a maximum of 29 $\mu g.m^{-3}$, while PM2.5 concentrations range from 14 $\mu g.m^{-3}$ to 18 $\mu g.m^{-3}$.Overall, O_3 concentrations are lower nearby the east-side buildings façades. Hot-spots of NO_2 concentrations are found over the main roads, as expected.

When comparing results from the green walls and the baseline scenarios we found a negligible impact for all the pollutants, while the integrated scenario denotes the capability to change pollutants concentrations. Figure 3 shows the horizontal contour at pedestrian level (z=2 m) of the differences of NO_2 (Figure 3a)) and O_3 (Figure 3b)) concentrations between the baseline and the integrated scenario. increase

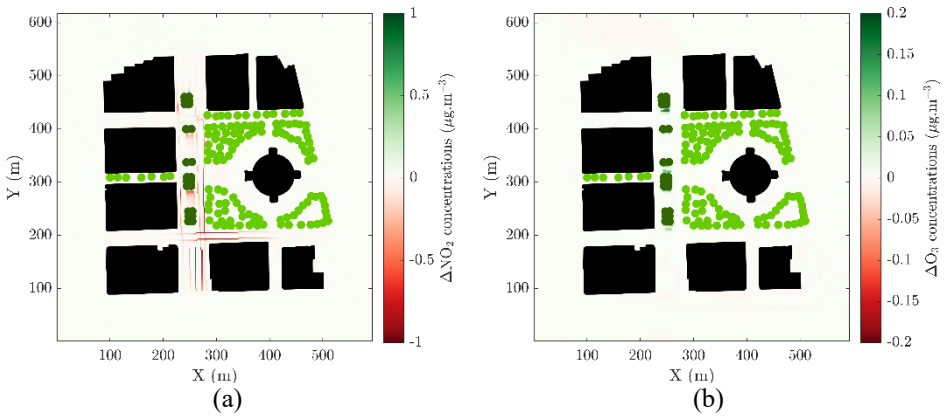

Figure 185. Horizontal iso-contour at pedestrian level for the NO_2 (a) and O_3 (b) concentrations differences between the baseline and the integrated scenario results.

The implementation of the integrated scenario will lead to a maximum increase of 2 $\mu g.m^{-3}$ of the NO_2 concentrations, at a specific grid cell, while NO_2 concentrations will decrease a maximum of 1.7 $\mu g.m^{-3}$ at another grid cell (reduction of 1.5%), compared to the baseline. The impact of the integrated scenario on O_3 concentrations is distinct compared to its influence on NO_2 concentrations, because this scenario will

lead to no increase of O_3 concentrations and a potential decrease of 0.6 $\mu g.m^{-3}$ (maximum reduction of 0.7%). Therefore, these results point out potential local benefits of green infrastructures on O_3 concentrations, followed by either positive or negative impacts on NO_2 concentrations, highlighting the relevance of further research focused on the interlinks between NO_2 and O_3 concentrations and the potential impacts of green infrastructures on the concentration of those pollutants at microscale.
Particulate matter concentrations are much less influenced by the integrated scenario green infrastrcutures. The results indicate a minor PM10 concentrations increase of 0.6% and a decrease of 0.5% at specific grid cell, while for PM2.5 concentrations these changes are even lower.
The impacts of the simulated green scenarios on pollutant concentrations are directly linked with the impacts of those scenarios on the flow dynamics. The results indicate a local (at a specific grid cell) increase of 10% and a decrease of 12% of the wind velocity, followed by an increase of 3% and a strong decrease of 35% of the turbulent kinetic energy. The impacts of the green scenarios on the temperature patterns are insignificant (lower than 0.1%).

CONCLUSIONS

This study aimed to foster urban microclimate knowledge and to assess green infrastructures impacts on air quality, evaluating the effectiveness of green urban planning strategies. No disturbances exerted by the green walls scenario on the turbulent flow dynamics and on the air quality levels were obtained, when compared to the baseline scenario. On contrary, the overall results point out potential local benefits of green infrastructures on O_3 concentrations, followed by either positive or negative impacts on NO_2 concentrations, highlighting the relevance of further research focused on the interlinks between NO_2 and O_3 concentrations and the potential impacts of green infrastructures on the concentration of those pollutants at microscale. Particulate matter concentrations are not influenced by the integrated scenario.
The results of this case study are very useful to establish a set of guidelines to be disseminated to stakeholders and decision makers for regulatory purposes, promoting important social, environmental and economic benefits.

AKNOWLEDGEMENTS

This work was supported by the project GENESIS (PTDC/GES-URB/29444/2017) funded by the Portuguese Science and Technology Foundation through national funds and by the European Community Fund FEDER within the COMPETE2020 program. Thanks are due for the financial support to the PhD grant of A. Ascenso (SFRH/BD/136875/2018), B. Augusto (2020.06293.BD), and CESAM (UIDB/50017/2020+UIDP/50017/2020), to FCT/MCTES through national funds, and the co-funding by the FEDER, within the PT2020 Partnership Agreement and Compete 2020. Thanks are also due to FCT/MCTES for the contract granted to S. Rafael (2020.02543.CEECIND).

REFERENCES

Bruse, M. and H. Fleer, 1998: Simulating surface-plant-air interactions inside urban environments with a three dimensional numerical model. Environ. Model. Softw., **13**, 373–384.

Huttner, S., 2012: Further Development and Application of the 3D Microclimate Simulation ENVI-Met. Mainz University, Germany.

Lee, H., H. Mayer, and L. Chen, 2016: Contribution of trees and grasslands to the mitigation of human heat stress in a residential district of Freiburg, Southwest Germany. Landsc. Urban Plan., **148**, 37–50.

Simon, H., J. Lindén, D. Hoffmann, P. Braun, M. Bruse, and J. Esper, 2018: Modeling transpiration and leaf temperature of urban trees – A case study evaluating the microclimate model ENVI-met against measurement data. Landsc. Urban Plan., **174**, 33–40.

21st International Conference on
Harmonisation within Atmospheric Dispersion Modelling for Regulatory Purposes
27-30 September 2022, Aveiro, Portugal

AERODYNAMIC PARAMETERISATION TO MODEL DRY DEPOSITION OF PARTICULATE MATTER ON URBAN GREEN INFRASTRUCTURE

Tess Ysebaert

SHORT ABSTRACT

Abstract title: Aerodynamic parameterisation to model dry deposition of particulate matter on urban green infrastructure

Name and Affiliation of the First Author: Tess Ysebaert[a]

[a] Sustainable Energy, Air & Water Technology (DuEL), Department of Bioscience Engineering, University of Antwerp, Belgium

Email of first author: tess.ysebaert@uantwerpen.be

Names and Affiliations of the Co-authors: Roeland Samson[b] and Siegfried Denys[a] a Sustainable Energy, Air & Water Technology (DuEL), Department of Bioscience Engineering, University of Antwerp, Belgium

b Laboratory of Environmental and Urban Ecology, Department of Bioscience Engineering, University of Antwerp, Belgium

Abstract text

Urban green infrastructure, in particular green walls, offers opportunities as a nature based solution to urban PM pollution, but the uncertainty of their effectiveness is hindering their implementation. Computational fluid dynamics (CFD) models of PM capture by green walls are useful tools to increase their applicability. In CFD models, the correct description of the vegetation-wind interaction is key and the accuracy of the modelled wind flow is highly linked to the uncertainty about the drag coefficient. To address the uncertainty of the model parameters describing the aerodynamic effect, the Wilcox revised k-ω model with adapted momentum and turbulence sink terms was parameterised by comparison with wind tunnel experiments at multiple wind speeds. All simulations were performed with the commercial software Comsol Multiphysics® (version 5.6). The optimised parameters served as input for a size-resolved dry deposition model. The transport of particles in the wind tunnel setup was modelled with a Lagrangian dispersion model, making use of the already simulated flow field. The mechanisms leading to PM deposition on vegetation were implemented and the

optimised drag coefficient was used in these equations. The model was validated with extensive wind tunnel experiments including various wind speeds, PM concentrations and PM size distributions. Moreover, real PM was used, namely elemental carbon with a diameter < 300 nm and Arizona fine test dust with a diameter of 1-10 μm. In this way, real particle dynamics could be studied. The aerodynamic modelling of green walls in the wind tunnel setup demonstrated that the optimise model parameters provided a more accurate description of the aerodynamic effect of climbers compared to conventional CFD models using a value of 0.2 for the drag coefficient. In addition, this improved the modelling of PM capture by vegetation, since these models are relying on the drag coefficient as well.

HARMO 21 Programme:
Oral Presentations

Monday, 26 September 2022 (Department of Environment and Planning)	
16:00-18:00	Registration (Department of Environment and Planning, University of Aveiro)

Tuesday, 27 September 2022 (Department of Environment and Planning)	
08:00 - 19:00	Registration (Department of Environment and Planning, University of Aveiro)
09:00 - 09:10	Welcome by the organizers, Opening (Carlos Borrego Auditorium)
09:10 - 09:50	Plenary session 1 (Carlos Borrego Auditorium, Chair: A. Miranda) **Topic 9:** Highlights of past work. Session devoted to reviews and to prominent scientists and 'golden papers' of the past, which have still relevance and should not be forgotten
09:10 - 09:50	Keynote Speaker H21-062: Steve Hanna: What were Pasquill and Gifford Thinking?
09:50 – 12:40	Plenary session 2 (Carlos Borrego Auditorium, Chair: N. Moussiopoulos) **Topic 1:** Model evaluation and quality assurance – model validation, model intercomparisons, model uncertainties and model sensitivities
09:50 – 10:10	H21-126: Eliott Lumet, Mélanie C. Rochoux, Simon Lacroix, Thomas Jaravel, Olivier Vermorel: Sensitivity analysis of microscale pollutant dispersion large-eddy simulations towards observation network design
10:10 – 10:30	H21-039: Dietmar Öttl: Recent developments in high-resolution wind field modelling in complex terrain for dispersion simulations using GRAMM-SCI
10:30 – 11:00	Coffee/Tea Break, Poster Session
11:00 – 11:20	H21-076: Rafael Borge, David de la Paz, Jose María Cordero, Golam Sarwar, Sergey Napelenok: Comparison of Source Apportionment Methods to attribute summer tropospheric O3 and NO2 levels in Madrid (Spain)
11:20 – 11:40	H21-046: David Carruthers, Jenny Stocker, Amy Stidworthy, Christina Hood, Rose Jackson, Molly Oades, Stephen Smith, Daniel Connolly, Shyn Tong, Alison Davies, Sean Beevers, Nutthida Kitwiroon, Nosha Assareh, Paul Agnew, Vivien Bright, John Stedman, Beth Conlan, Massimo Vieno, Stefan Reis: DEFRA 2021 AIR QUALITY MODEL INTER-COMPARISON EXERCISE
11:40 – 12:00	H21-003: Roy Wichink Kruit, Addo van Pul, Koen Siteur: Measurement-model fusion techniques to quantify nitrogen deposition in the Netherlands
12:00 – 12:20	H21-150: Joana Ferreira, Sílvia Coelho, Diogo Lopes, Guido Pirovano: NO2 response to emission reduction scenarios - comparing brute force and tagging source apportionment methods
12:20 – 12:40	H21-113: Raido Kiss, Marko Kaasik, Terje Tammekivi, Seffen Noe: SO2 and NOx peak concentrations, vertical profiles and model-identified origins from distant sources
12:40 – 14:00	Lunch (Crasto Restaurant, University of Aveiro)
14:00 - 15:40	Plenary session 3 (Carlos Borrego Auditorium, Chair: D. Carruthers) **Topic 6:** Use of modelling in health and exposure assessments
14:00 – 14:20	H21-163: Nicolas Moussiopoulos, Evangelia Fragkou, George Tsegas, Athanasios Karagkounis, Fotios Barmpas: METHODOLOGY FOR QUANTIFYING THE IMPACT OF SMART FARMING APPLICATION ON LOCAL-SCALE AIR QUALITY OF FARMS IN GREECE
14:20 – 14:40	H21-097: Sílvia Coelho**,** Joana Ferreira, David Carvalho, Ana Isabel Miranda, Myriam Lopes: AIR QUALITY IMPACTS ON HUMAN HEALTH, UNDER A CLIMATE CHANGE SCENARIO: THE AVEIRO REGION CASE STUDY

14:40 – 15:00	H21-033: Marie Dury, Florent Hozay, Fabian Lenartz: Personal Exposure Assessment through Measurement and Modelling
15:00 – 15:20	H21-010: Nina Kristiansen, Claire S. Witham: Quantifying hazardous areas to aircraft occupants from volcanic sulphur dioxide
15:20 – 15:40	H21-006: Martin Otto Paul Ramacher, Johannes Beiser: Underestimation of population exposure estimates in established methods

15:40 – 16:10	Poster Pitches Session 1 (Carlos Borrego Auditorium, Chair: C. Gama)

16:10 – 16:30	Coffee/Tea Break, Poster Session

16:30 - 18:30	Plenary session 4 (Carlos Borrego Auditorium, Chair: P. Thunis) **Topic 6:** Use of modelling in health and exposure assessments
16:30 – 16:50	H21-162: Nicolas Moussiopoulos, George Tsegas: ASSESSING THE IMPACT OF THE COVID-19 LOCKDOWNS: RESULTS AND IMPLICATIONS FROM A MODELLING APPLICATION IN TWO MEDITERRANEAN CITIES
16:50 – 17:10	H21-164: George Efthimiou, Fotios Barmpas, Nicolas Moussiopoulos: PREDICTION OF THE MAXIMUM WIND SPEED IN INDOOR ENVIRONMENTS FOR EFFICIENT NATURAL VENTILATION
17:10 – 17:30	H21-125: Livia Grandoni, Agnese Pini, Loic Méès, Pietro Salizzoni, Armando Pelliccioni, Giovanni Leuzzi, Paolo Monti: numerical dispersion modelling of the droplets expired by humans
17:30 – 17:50	H21-129: Tuan Vu, Gregor B. Stewart, Nutthida Kitwiroon, Hanbin Zhang, Benjamin Barratt, Sean D. Beevers, Presenter: Andrew Beddows: An integrated approach to estimate and predict dynamic infiltration factors of fine particles in London homes

18:00	Leaving University of Aveiro (by bus, Rectory Building, University of Aveiro)

19:00 – 21:00	Ice Breaker (Sétimo Bar, Barra Beach)/Return by bus

21:00	End of Day 1

Wednesday, 28 September 2022 (Department of Environment and Planning)

09:00-16:00	Registration (Department of Environment and Planning, University of Aveiro)

09:00 - 11:00	Plenary session 5 (Carlos Borrego Auditorium, Chair: F. Martin) **Topic SS2:** Nature-based Solutions
09:00 – 09:40	Keynote Speaker H21-074: Sandra Rafael, Ana Ascenso, Bruno Augusto, Diogo Lopes, Ana Isabel Miranda: THE ROLE OF GREEN ROOFS ON CITIES AIR QUALITY: INDIRECT AND DIRECT IMPACTS
09:40 – 10:00	H21-029: Alice Maison, Cédric Flageul, Karine Sartelet, Bertrand Carissimo, Andrée Tuzet, Yunyi Wang: Modelling the impacts of urban trees on air quality in streets.
10:00 – 10:20	H21-123: Vera Rodrigues, Kevin Oliveira, Bruno Augusto, Sandra Rafael, Ana Ascenso, Ana Isabel Miranda: ASSESSING THE IMPACTS OF GREEN INFRASTRUCTURES ON URBAN AIR QUALITY
10:20 – 10:40	H21-098: Carlo Cintolesi, Silvana Di Sabatino, Andrea Petronio: IMPACTS OF AN EVAPORATING WATERBODY IN URBAN FABRIC THROUGH LARGE-EDDY SIMULATIONS

10:40 – 11:00	Coffee/Tea Break, Poster Session

11:00 - 12:40	Plenary session 6 (Carlos Borrego Auditorium, Chair: P. Armand) **Topic SS2:** Nature-based Solutions

11:00 – 11:20	H21-130: Ana Ascenso, Carla Gama, Peter Roebeling, Ana Isabel Miranda: Nature-based solutions for climate change adaptation: impacts on air quality and temperature in Eindhoven, The Netherlands.
11:20 – 11:40	H21-170: Tess Ysebaert: Aerodynamic parameterisation to model dry deposition of particulate matter on urban green infrastructure
11:40 – 12:00	H21-009: Christof Gromke: Passive pollutant concentration control by roadside hedgerows in urban streets
12:00 – 12:20	H21-026: John G. Bartzis, Ioannis A. Sakellaris, George Efthimiou, Spyros Andronopoulos, Ilias Tolias, Alexandros Venetsanos: Novel simplified methodologies on exposure uncertainty quantification from accidental airborne releases
12:20 – 12:40	H21-135: Guillevic Lamaison, Perrine Charvolin, Chi Vuong Nguyen, Kim Vermare, Aurélie Guth, Lionel Soulhac: A COUPLING BETWEEN RANS CFD AND STOCHASTIC LAGRANGIAN MODELLING FOR LONG TERM IMPACT ASSESSMENT ON AN INDUSTRIAL SITE

12:40 – 14:00	Lunch (Crasto Restaurant, University of Aveiro)

14:00 - 15:40	Plenary session 7 (Carlos Borrego Auditorium, Chair: B. Leitl) **Topic 3:** Use of modelling in support of EU air quality directives, including FAIRMODE activities
14:00 – 14:20	Keynote Speaker Philippe Thunis: FAIRMODE: update on on-going harmonisation activities
14:20 – 14:40	H21-018: Bertrand Bessagnet, Kees Cuvelier, Enrico Pisoni, Philippe Thunis, Alexander de Meij, Alexandra Monteiro, Angelos Violaris, Jonilda Kushta, Bruce R. Denby, Qing Mu, Eivind G. Wærsted, Marta García Vivanco, Mark R. Theobald, Victoria Gil, Ranjeet S Sokhi, Kester Momoh, Ummugulsum Alyuz, Rajasree VPM, Saurabh Kumar, Elissavet Bossioli, Georgia Methymaki, Darijo Brzoja, Velimir Milić, Arineh Cholakian, Romain Pennel, Sylvain Mailler, Laurent Menut, Gino Briganti, Mihaela Mircea, Claudia Flandorfer, Kathrin Baumann-Stanzer, Virginie Hutsemékers, Elke Trimpeneers: The FAIRMODE CT9 platform: assessing sensitivity of model responses to emission changes towards effective emission reduction strategies
14:40 – 15:00	H21-049: Jose-Luis Santiago, Esther Rivas, Beatriz Sanchez, Marta G. Vivanco, Mark R. Theobald, Juan Luis Garrido, Victoria Gil, Alberto Martilli, Alejandro Rodríguez-Sánchez, Riccardo Buccolieri, Ana R. Gamarra, Yolanda Lechón, Eugenio Sánchez, Fernando Martín: How do the reduction emission measures of the Spanish National Air Pollution Control Programme impact on street-level air quality in three neighbourhoods of Madrid (Spain)?
15:00 – 15:20	H21-112: Stijn Janssen, Giovanni Bonafè, Antonio Piersanti, Lina Vitali, Kristina Eneroth, Jutta Geiger, Sabine Wurzler, Roberta Amorati, Michele Stortini, Leonor Tarrason, Philippe Thunis: FAIRMODE CT8 exercise on assessment of Spatial Representativeness of monitoring stations
15:20 – 15:40	H21-043: Edward Chan, Joana Leitão, Seán A. Schmitz, Timothy M. Butler, Andreas Kerschbaumer: Hourly Roadside Traffic Emissions from Bottom-up Inventory for the City of Berlin

15:40 – 16:10	Poster Pitches Session 2 (Carlos Borrego Auditorium, Chair: B. Augusto)

16:30 - 18:30	Plenary session 8 (Carlos Borrego Auditorium, Chair: C. Mensink) **Topic 3:** Use of modelling in support of EU air quality directives, including FAIRMODE activities
16:30 – 16:50	H21-011: Alexander de Meij, Kees Cuvelier, Enrico Pisoni, P. Thunis, Bertrand Bessagnet: The sensitivity to four different emission inventories on air quality indices in Europe.
16:50 – 17:10	H21-025: Tereza Šedivá, Dušan Štefánik: COMPARISON OF SOURCE APPORTIONMENT METHODS USING THE CMAQ MODEL
17:10 – 17:30	H21-066: Joost Wesseling, Alicia Gressent, Anil Namdeo, Assa Camara, David Roet, Fabian Lenartz, Jorge Sousa, Pascal Joassin, Philipp Schneider, Philippe Thunis, Sjoerd van Ratingen, Stig Hellebust, Stijn Janssen, Stijn Vrankx, Vera Rodrigues, Wouter Hendricx: Benchmark on methodologies to integrate low-cost sensor networks with official measurements to improve (modelled) air quality maps

17:30 – 17:50	H21-073: Antonio Piersanti, Cornelis Cuvelier, Stijn Janssen, Alexandra Monteiro, Durka Paweł, Philippe Thunis, Lina Vitali: QUALITY CONTROL INDICATORS FOR THE VALIDATION OF AIR QUALITY FORECAST APPLICATIONS IN THE FRAMEWORK OF FAIRMODE ACTIVITIES
17:50 - 18:10	H21-091: Zoltán Horváth, László Környei, Mátyás Constans, Bence Liszkai, Ákos Kovács, Tamás Budai, and Csaba Tóth: Unsteady urban microscale simulations of air pollution for a full year and its platform for harmonisation
18:10 – 18:30	H21-038: Fernando Martin , Kees Cuvelier; Philippe Thunis, José Luis Santiago, Esther Rivas, Jenny Stocker, Rose Jackson, Felicita Russo, Maria Gabriella Villani, Gianni Luigi Tinarelli, Daniela Barbero, Roberto San Jose, Juan Luis Pérez-Camanyo, Gabriela Sousa Santos, John G. Bartzis, Ioannis A. Sakellaris, Nicola Masey, Scott Hamilton, Zoltán Horváth, László Környei, Bence Liszkai, Ákos Kovács: The FAIRMODE CT4: Intercomparison Exercise of Urban Microscale Models and Methodologies for deriving annual pollutant concentrations distribution with very high spatial resolution

18:30	End of Day 2

Thursday, 29 September 2022 (Rectory Building, University of Aveiro)

09:00-16:00	Registration (Rectory Building, University of Aveiro)

09:00 – 10:20	Parallel session 1 (Renato Araújo Auditorium, Rectory Building, Chair: M. Ketzel) **Topic 4:** Parametrization of Physical Processes and Mathematical Problems in Meteorology and Air Quality Modelling	Parallel session 2 (Acts Room, Rectory Building, Chair: E. Batchvarova) **Topic 1:** Model evaluation and quality assurance – model validation, model intercomparisons, model uncertainties and model sensitivities
09:00 – 09:20	H21-032: Stijn Van Leuven, Pieter De Meutter, Johan Camps, Piet Termonia, Andy Delcloo: Sensitivities in wet deposition modelling applied to the Fukushima nuclear accident	Simon Gant, Joe Chang, Sun McMasters, Ron Meris, Scott Bradley, Sean Miner, Matthew King, Steven Hanna, Thomas Mazzola, Tom Spicer, Rory Hetherington, et al.: SUMMARY OF RESULTS FROM THE JACK RABBIT III INTERNATIONAL MODEL INTER-COMPARISON EXERCISE ON DESERT TORTOISE AND FLADIS
09:20 – 09:40	H21-054: Bruno Ribstein, Maxime NIBART, Gianni Tinarelli: PROPOSAL FOR MODELLING THE DRY DEPOSITION OF SOLID PARTICLE AND GAS USING A 3D STOCHASTIC LAGRANGIAN DISPERSION MODEL	H21-002: Zita Ferenczi, Emese Homolya, Krisztina Lázár, and Anita Tóth: Effect of the uncertainty in meteorology on air quality model predictions
09:40 – 10:00	H21-070: David Ben-Shlomo, Eyal Fattal, Ronen Berkovich: Application of Stochastic Wall Bounded Turbulent Flow Model to Resuspension	H21-064: Adrienn Varga-Balogh, Ádám Leelőssy, Róbert Mészáros: PM2.5 predictions for urban monitoring sites in Budapest using statistical fusion of CAMS air quality models
10:00 – 10:20	H21-117: Ignacio Pisso, Massimo Cassiani, Anna Solvejg Dinger,Hamidreza Ardeshiri, Soon-Young Park, Kerstin Stebel, Arve Kylling, Norbert Schmidbauer, Andreas Stohl: Tomographic 3D reconstructions of artificial releases of SO2 in the atmospheric boundary layer	H21-040: Daniel Silk, Joel Howard, Simon Gant, Rory Hetherington, Adrian Kelsey, Presenter: Stephanie Schaap: Calibrating multi-model ensemble predictions from the Jack Rabbit III international model inter-comparison exercise
10:20 – 10:40	H21-056: Andrew Mirza, Helen F. Dacre: Modelling free tropospheric turbulence in an atmospheric dispersion model.	H21-174: Roberto San Jose, Juan L. Pérez: Source apportionment analysis in PM and O3 concentrations during COVID-19 lockdown period in Madrid (Spain)

10:40 – 11:00	Coffee/Tea Break, Poster Session , Group Photo

11:00 – 12:40	Parallel session 3 (Renato Araújo Auditorium, Rectory Building, Chair: J. Bartzis) **Topic 7:** Inverse dispersion modelling and source identification	Parallel session 4 (Acts Room, Rectory Building, Chair: C. Borrego) **Topic 1:** Model evaluation and quality assurance – model validation, model intercomparisons, model uncertainties and model sensitivities
11:00 – 11:20	H21-131: Stefano Alessandrini, Scott Meech: TESTING A MACHINE LEARNING MODEL FOR THE SOURCE TERM ESTIMATION	H21-094: Tristan Carion, Michal Shimoni, Loic Francotte, Arthur Vandenhoeke, Andy Delcloo, Bart Janssen, Piet Termonia: Evaluation of a military CBRN-hazard prediction procedure with a Lagrangian dispersion model
11:20 – 11:40	H21-059: Joffrey Dumont Le Brazidec, Pierre Vanderbecken, Alban Farchi, Yelva Roustan, Marc Bocquet, Jinghui Lian, Grégoire Broquet, Thomas Lauvaux, Alexandre Danjou: CO2 plume detection and inversion using convolutional neural networks: application to synthetic images of XCO2 fields over urban areas	H21-161: Goran Gašparac, Amela Jeričević, Theresa Klausner, Heidi Huntrieser, Heinfried Aufmhoff, Anke Roiger: Regional modeling and assessment of SO2 concentrations in a complex environment using aviation measurements
11:40 – 12:00	H21-110: Andrew Beddows, Nutthida Kirwiroon, Nosha Assareh, Gregor Stewart, Sean Beevers: Emissions calibration in a Emissions calibration in a country scale high resolution air quality model	H21-021**:** Renske Timmermans, M. Schaap, R. Kranenburg, Pinxteren, Augustin Colette, Stephen Matthew Platt: Evaluation of modelled source attributions with observational based source attribution
12:00 – 12:20	H21-069: Martin Ferrand, Konstantin Kuznetsov, Bertrand Carissimo, Marc Bocquet: MCMC Metropolis-Hasting algorithm in the source inversion problems of air pollutants in urban CFD modelling.	H21-014: Maeva Caillat, Valentin Pibernus, Sylvain Girard, Patrick Armand, Christophe Duchenne: Innovative probabilistic modelling of risk zones in the event of accidental atmospheric releases
12:20 – 12:40	H21-027: Emilie Launay, Virginie Hergault, Marc Bocquet, Joffrey Dumont Le Brazidec, Yelva Roustan: Source characterisation of large-scale urban fires by inverse modelling	H21-087: Alison McGillivray, Mike Harper, Frank Hart, Stephen Puttick, Adeel Ibrahim, Simon Gant, Rory Hetherington: Phast modelling of the Desert Tortoise and FLADIS ammonia trials for the Jack Rabbit III model inter-comparison exercise

12:40 – 14:00	Lunch (Crasto Restaurant, University of Aveiro)

14:00 - 18:30	Parallel session 5 (Renato Araújo Auditorium, Rectory Building, Chair: B. Carissimo) **Topic 8:** Modelling air dispersion and exposure to accidental releases	Parallel session 6 (Acts Room, Rectory Building, Chair: P. Suppan) **Topic 1:** Model evaluation and quality assurance – model validation, model intercomparisons, model uncertainties and model sensitivities
14:00 – 14:20	H21-004: Thomas Spicer, Chad T. Smith: WIND TUNNEL AND MATHEMATICAL MODELLING OF THE NEAR-SOURCE REGION OF JACK RABBIT II MOCK URBAN ENVIRONMENT CHLORINE RELEASES	H21-168: Alexey Gusev, Emese Homolya, Krisztina Lázár, Anita Tóth, Presenter: Mihaela Mircea: EURODELTA-Carb exercise: Intercomparison of modelled estimates of benzo(a)pyrene (BaP) in Europe
14:20 – 14:40	H21-061: Steve Hanna, Ronald Meris, Sun McMasters, Joseph Chang, Thomas Mazzola, Thomas Spicer, Simon Gant: Planning for Jack Rabbit III Field Experiment Focusing in Anhydrous Ammonia	H21-128: Patrick Armand, Christophe Duchenne: New insight on 3D modelling of the dispersion of gases released from an industrial facility in a complex environment

14:40 – 15:00	H21-067: Youness El-Ouartassy, Matthieu Plu, Irène Korsakissok, Laurent Descamps, Laure Raynaud, Olivier Connan: Towards the use of meteorological ensembles for short distance dispersion of radionuclides in case of an accidental release in the atmosphere	H21-153: Saravanan Arunachalam, Brian Fredrik Naess, Akula Venkatram: Development of a new Airport Dispersion Model
15:00 – 15:20	H21-085: Christian Lejon, Daniel Elfversson, Daniel Vågberg, Leif Persson, Joakim Eriksson Rydman, Oscar Björnham, Birgitta Liljedahl, Jan Sjöström: LAGRANGIAN PLUME-RISE DISPERSION MODELLING OF LARGE-SCALE LITHIUM-ION BATTERY FIRES IN OPEN SURROUNDING WITH APPLICATION TO THE FIRE IN MORRIS, USA, 2021	H21-068: Daniel Loeb, Maxime Nibart, Bruno Ribstein, Anne-Sophie Saffre, Frédéric Mahe, Claude Derognat: IMPROVEMENT AND VALIDATION OF THE AIRCITY EVERYWHEREPOLLUTION STATISTICAL MODEL OVER THE AIX-MARSEILLE METROPOLIS
15:20 – 15:40	H21-093: Irène Korsakissok, Olivier Saunier, Valentin Jacques: Updated atmospheric dispersion simulations and source term reconstruction of the Fukushima accident at local scale	H21-107: Malo Le Guellec, Liying Chen, Amita Tripathi, Sophie Vecchiola, Anne Mathieu, Philippe Laguionie, Olivier Connan, Denis Maro, Luc Solier, Irène Korsakissok, Perrine Charvolin-Volta, Guillevic Lamaison, Lionel Soulhac: DISPERSION OF RADIONUCLIDES IN A URBAN ENVIRONMENT (DIFLU): COMPARISON OF NUMERICAL RESULTS WITH EXPERIMENTAL MEASUREMENTS

15:40 – 16:00	Coffee/Tea Break, Poster Session

16:00 16:30	Keynote Speaker Philippe Thunis: Air Quality: update on the revision of the EU rules

16:30 – 17:10	Poster Pitches Session 3 (Renato Araújo Auditorium, Rectory Building, Chair: J. Ferreira)

17:10 – 18:30	Parallel session 7 (Renato Araújo Auditorium, Rectory Building, Chair: S. Di Sabatino) **Topic 8:** Modelling air dispersion and exposure to accidental releases	Parallel session 8 (Acts Room, Rectory Building, Chair: Z. Ferenczi) **Topic SS1:** Modelling Odour Dispersion and Exposure
17:10 – 17:30	H21-122: Astrid Kloosterman, Chris Twenhöfel, Teun van Dillen, Jasper Tomas: A probabilistic approach for determining potentially affected areas for accidental releases	H21-060: Alessandra Panzitta, Alessandra Panzitta, Beatrice Julia Lotesoriere, Marzio Invernizzi, Roberto Sozzi, Laura Capelli: Development of a simulation tool to evaluate the applicability of the Gradient Method for the estimation of odour emission fluxes
17:30 – 17:50	H21-134: Lionel Soulhac, Guillevic Lamaison, Perrine Charvolin, Chi Vuong Nguyen, Mehdi Slimani, Patrick Armand: New developments and validations of the BUILD operational dispersion model for accidental or deliberate releases in complex area	H21-088: Silvia Trini Castelli, Francesco Uboldi, ARIANET Srl, Milano, Italy Gianni Tinarelli, Piero Malguzzi, Oxana Drofa, Paolo Bonasoni: A NOVEL APPROACH FOR TRACING THE ORIGIN OF ODOUR NUISANCE WITH SMART METEO-DISPERSIVE MODELLING SYSTEM
17:50 - 18:10	H21-141: Olivier Oldrini, Sylvie Perdriel, Patrick Armand, Christophe Duchenne: STUDY OF THE UNCERTAINTIES FOR CONCENTRATION IN THE REALISTIC BUILT-UP AREA OF PARIS, THE SURE PROJECT	H21-154: Jennifer Barclay, Carlos N. Diaz, Imelda Shanahan, Christelle Escoffie, Anne-Claude Romain, Andrew Balch, Rodrigo Rosales, Gianni Tinarelli, Giuseppe Brusasca, Giusy Oliva, Tiziano Zarra, Günther Schauberger, Silvia Trini Castelli: THE INTERNATIONAL HANDBOOK ON THE ASSESSMENT OF ODOUR EXPOSURE BY USING DISPERSION MODELLING

18:10 – 18:30	H21-079: Chun-Sil Jin, Hyun-Ha Lee, Jeong-Wan Kwon, Dong-Il Kim: Multi-Model Ensemble Dispersion Prediction System for Nuclear Emergency Response	H21-167: Damyan Barantiev, Ekaterina Batchvarova, Rosen Penchev: Examples of 30-minutes notice for fog formation or dissipation at the port of Burgas

20:00	Conference Dinner (Meliá Ria Hotel & Spa)

18:30	End of Day 3

Friday, 30 September 2022 (Rectory Building, University of Aveiro)

09:00-12:00	Registration (Rectory Building, University of Aveiro)

09:00 – 10:20	Plenary session 9 (Renato Araújo Auditorium, Rectory Building, Chair: V. Rodrigues) **Topic 5:** Urban Scale and Street Canyon Modelling: Meteorology, Air Quality and Passive Control Systems
09:00 – 09:40	Keynote Speaker H21-159: Paul Bieringer, Scott Runyon, David Lorenzetti, Michael Sohn: Relating Outdoor Contaminant Concentration Variance to Indoor Variance to Improve Health and Exposure Impacts
09:40 – 10:00	H21-047: Esther Rivas, José Luís Santiago, Alberto Martilli, Fernando Martin, Elías Díaz, Francisco Javier Gómez, Begoña Artiñano, Carlos Román-Cascón, Carlos Yagüe, David de la Paz, Rafael Borge: Infiltration of NOx from road traffic into buildings by natural ventilation: a case study
10:00 – 10:20	H21-166: Silvana Di Sabatino, Carlo Cintolesi: LARGE-EDDY SIMULATIONS OF NATURE-BASED SOLUTIONS EFFECTIVENESS IN POLLUTANT REMOVAL FROM URBAN CANYONS
10:20 – 10:40	H21-152: Matthias Ketzel, Ahmet Mustafa Tepe: Modelling of the horizontal air pollution gradients inside a street canyon using new features in the OSPM model

10:40 – 11:00	Coffee/Tea Break, Poster Session

11:00 – 12:40	Parallel session 10 (Renato Araújo Auditorium, Rectory Building, Chair: A. Jeričević) **Topic 5:** Urban Scale and Street Canyon Modelling: Meteorology, Air Quality and Passive Control Systems	Parallel session 11 (Acts Room, Rectory Building, Chair: M. Kaasik) **Topic 7:** Inverse dispersion modelling and source identification
11:00 – 11:20	H21-140: Jan Mateu Armengol, A.Criado, H. Petetin, M. Olid, J. Benavides, D.Rodriguez-Rey, M. Guevara, C. Pérez García-Pando, A. Soret, O. Jorba: Post-processing tools for correcting urban air quality forecast maps	H21-022: Jorge Sousa, H. Hooyberghs, W. Lefebvre, S. Vranckx, S. Janssen: Bayesian inference of emission sources based on a dispersion model and sensor networks
11:20 – 11:40	H21-080**:** Michael Sohn, Marion L. Russell: TRACER GAS EXPERIMENT OF URBAN POLLUTANT TRANSPORT: URBAN CANYONS AND INDOOR-OUTDOOR TRANSPORT	H21-127: Amy Stidworthy, David Carruthers, Molly Oades, Rod Jones, Olalekan Popoola, Jim Mills, Felicity Sharp: QUANTIFYING THE IMPACT OF COVID-19 RESTRICTIONS ON EMISSIONS USING INVERSE MODELLING AND MEASUREMENTS
11:40 – 12:00	H21-102: Yunyi Wang, Cédric Flageul, Chao Lin, Ryozo Ooka, Hideki Kikumoto, Youngseob Kim, Karine Sartelet: Simulations of street-canyon air-quality using fluid dynamics and aerosol modelling	H21-165: Panagiotis Gkirmpas, Fotios Barmpas, Nicolas Moussiopoulos, presenter : COMPARISON OF THE ACCURACY OF K-EPSILON AND K-OMEGA SST TURBULENCE MODELS IN AN UNKNOWN SOURCE PARAMETERS ESTIMATION APPLICATION

12:00 – 12:20	H21-096: Christopher Andersen, Matthias Mensink Ketzel, Ole Hertel, Jesper H. Christensen, and Jørgen Brandt: Development of a New Lagrangian Air Pollution Model for Denmark	H21-075: Olivier Saunier, Olivier Masson: Cs-137 source reconstruction of unprecedented wildfires in the Chernobyl exclusion zone in April 2020
12:20 – 12:40	H21-145: Tomas Halenka, Gaby Langendijk: URBAN ENVIRONMENTS AND REGIONAL CLIMATE CHANGE - CORDEX FLAGSHIP PILOT STUDY URB-RCC	H21-008: Helen Webster, David Thomson: USING ENSEMBLE NWP DATASETS TO OVERCOME METEOROLOGICAL ERRORS IN A BAYESIAN INVERSE MODELLING SYSTEM

12:40 – 14:00	Lunch (Crasto Restaurant, University of Aveiro)

14:00 - 18:30	Plenary session 12 (Renato Araújo Auditorium, Rectory Building, Chair: S. Trini Castelli) **Topic 2:** Environmental impact assessment: Air pollution management and decision support systems
14:00 – 14:20	H21-124: Daniela Barbero, Bruno Ribstein, Maxime Nibart, Gianni Luigi Tinarelli: Acceleration of simulations by application of a kernel method in a high-resolution Lagrangian Particle Dispersion Model
14:20 – 14:40	H21-157: Ulrich Uhrner, Nicola Toenges-Schuller, Raphael Reifeltshammer, Werner Stadlhofer, Silvia Jost, Stefan Hausberger: Specification of Zero-Impact vehicle exhaust emissions from the ambient air quality perspective and demonstration of Zero Impact
14:40 – 15:00	H21-144: Daeun Jung, David de la Paz, Alberto Notario, Rafael Borge: COMPARISON OF CHANGES IN THE OXIDATION CAPACITY BETWEEN URBAN AND RURAL AREAS IN EUROPE
15:00 – 15:20	H21-041: Michael Russo, David Carvalho, Alexandra Monteiro, Jalkanen Jukka-Pekka: EU maritime transport and air quality: impacts in current and future climate change scenarios
15:20 – 15:40	H21-103: Marta G. Vivanco, Mark R. Theobald, Victoria Gil, Juan Luis Garrido, Ana R. Gamarra, Yolanda Lechón, José Luis Santiago, Fernando Martín, Alejandro Rodríguez-Sánchez, Carmen Lago, Eugenio Sánchez: THE EFFECT ON AIR QUALITY OF INCREASED RENEWABLE ENERGY USE IN THE SPANISH ROAD TRANSPORT SECTOR
15:40 – 16:00	H21-089: Stijn Vranckx, Nele Smeets, Hans Hooyberghs, Wouter Lefebvre, Peter Viaene, Robin Houdmeyers, Stijn Janssen, Jorge Sousa, Alessandro D'Ausilio, Lisa Blyth, Jana Krajčovičová, Dušan Štefánik, Beňo Juraj, Zita Ferenczi, Ewa Bielas, Włodzimierz Zaleski: ATMO-Plan: an air quality management system for environmental impact assessments and urban air quality plans in Europe

16:40	Closing and Goodbye Coffee Break

16:40	End of Day 4

HARMO 21 Programme:
Poster Presentations

27 sept 15:40 – 16:10	Poster Pitches Session 1 (Carlos Borrego Auditorium)

H21-023: Jens Peter Frankemölle, Johan Camps, Pieter De Meutter, Johan Meyers: Near-range Gaussian plume modelling for gamma dose rate reconstruction
H21-092: Rory Hetherington, Graham Tickle, Veronica Bowman, Daniel Silk, Simon Gant, Adrian Kelsey, Alison McGillivray, Harvey Tucker: DRIFT MODELLING OF THE DESERT TORTOISE AND FLADIS AMMONIA TRIALS FOR THE JACK RABBIT III MODEL INTER-COMPARISON EXERCISE
H21-151: Ana R. Gamarra, Marta G. Vivanco, Mark R. Theobald, Yolanda Lechón, Carmen Lago, Victoria Gil, Juan Luis Garrido, José Luis Santiago, Fernando Martín, Alejandro Rodríguez-Sánchez, Eugenio Sánchez. Presented by Alejandro Rodriguez-Sanchez: Assessing the impact of a traffic low emission zone on pollutant concentrations at street level through a combination of microscopic traffic simulations and air quality modelling at multiscale
H21-044: Hanane Bounouas, Johann Chardeur, Olivier Connan, Didier Hebert, Philippe Laguionie, Denis Maro, Hugo Renard, Pierre Roupsard, Marianne Rozet, Eric Dupont, Thaddé Régi, Bertrand Carissimo, Aurélien Faucheux, Yannick Lefranc, Yelva Roustan: STUDY OF ATMOSPHERIC DISPERSION UNDER LOW WIND CONDITIONS IN AN URBAN ENVIRONMENT, FIRST RESULTS
H21-139: Guilhem Balvet, Martin Ferrand, Yelva Roustan, Jean-Pierre Minier, Christophe Henry, Inria Sophia Antipolis: Treatment of the near ground effect in Lagrangian stochastic methods applied to a 2-D point source dispersion after an isolated obstacle in a neutral flow
H21-063: Boulos Alam, Rayan Nkenfack Soppi, Amir Ali Feiz, Pierre Ngae, Pramod Kumar, Amer Chpoun: Numerical modelling of pollutant dispersion over an idealized urban area using different algebraic closure models
H21-045: Joffrey Dumont Le Brazidec, Marc Bocquet, Olivier Saunier, Yelva Roustan: Bayesian transdimensional inverse reconstruction of the 137Cs Fukushima-Daiichi release
H21-030: Paweł Porwisiak, Maciej Kryza, Massimo Vieno, Janice Scheffler, Mike Holland, Lech Gawuc, Bruce Denby, Qing Mu, Małgorzata Werner: Benzo(a)pyrene concentrations in Central Europe – the role of meteorological conditions and health impact analysis
H21-005: Mohamed Yassin: EFFECT OF UPSTREAM BUILDING ON THE POLLUTANT DISPERSION IN URBAN CANOPY WITH CHANGES THERMAL STABILITY.
H21-077: Iwona Rackiewicz, Agnieszka Bartocha, Tomasz Przybyła, Marek Rosicki, Piotr Michałek: A DYNAMIC ODOUR MAPPING SYSTEM AS A TOOL TO SUPPORT LOCAL AUTHORITIES AND WASTEWATER TREATMENT PLANTS IN ODOUR IMPACT MANAGEMENT: A DYNAMIC ODOUR MAPPING SYSTEM AS A TOOL TO SUPPORT LOCAL AUTHORITIES AND WASTEWATER TREATMENT PLANTS IN ODOUR IMPACT MANAGEMENT
H21-055: Bruno Ribstein, Maxime Nibart, Patrick Armand, Christophe Duchenne: A NEW APPROACH TO COUPLING FLOW AND DISPERSION CFD SIMULATIONS IN A LARGE URBAN AREA AND BUILDINGS OF INTEREST
H21-081: Bianca Tenti, Enrico Ferrero: SMOKE PLUME FROM FIRE LAGRANGIAN SIMULATION: DEPENDENCE ON DRAG COEFFICIENT AND RESOLUTION
H21-106: Marie Mulder: Combining sentinel observations with plume backtrackings from a dispersion model to improve wildfire detection
H21-082: Eve Draper, J. Duncan Whyatt, Sarah E. Metcalfe: Estimating regional background concentrations of PM2.5 and verifying local source contributions in a data poor environment
H21-012: Sofia Farina, Dino Zardi: NUMERICAL MODELING OF PASSIVE TRACER DISPERSION FROM A CONTINUOUS POINT SOURCE IN A STEADY THERMALLY DRIVEN SLOPE WIND
H21-015: Lech Gawuc, Karol Szymankiewicz, Dorota Kawicka, Ewelina Mielczarek, Kamila Marek, Marek Soliwoda, Jadwiga Maciejewska: BOTTOM-UP INVENTORY OF RESIDENTIAL COMBUSTION EMISSIONS IN POLAND FOR NATIONAL AIR QUALITY MODELLING: CURRENT STATUS AND PERSPECTIVES
H21-156: Cyrill von Arx: Implementation of a decision support system for nuclear emergencies
H21-053: Bruno Ribstein, Maxime Nibart, Daniel Loeb, Patrick Armand, Christophe Duchenne: PROPOSAL FOR MODELLING THE INFLUENCE OF ROOF SLOPE ON URBAN FLOW WITH A DIAGNOSTIC MODEL

28 Sept 15:40 – 16:10	Poster Pitches Session 2 (Carlos Borrego Auditorium)

H21-020: Arièle Defossez, Rayna Charlatchka: State of the art on deposition by fog and its difference with respect to dry and wet deposition (wash-out) for a better representation in impact studies
H21-024: Victor Watson, François Septier, Patrick Armand, Christophe Duchenne: Detection of low level concentrations of hazardous materials in the air using sequential multivariate detection methods
H21-028: Margret Velizarova, Reneta Dimitrova, Angel Burov, Danail Brezov: Dispersion modelling of major traffic sources in Sofia city
H21-031: Pirmin Kaufmann, Stefan Rüdisühli: Operational Dispersion Ensemble at MeteoSwiss
H21-037: Dušan Štefánik, Jana Krajčovičová, Tereza Šedivá: ASSESSMENT OF THE IMPACT OF THE RESIDENTIAL HEATING EMISSIONS ON CONCENTRATIONS BY LOCAL AND REGIONAL AIR-QUALITY MODELS
H21-042: Loris Colombo, Alessandro Marongiu, Giuseppe Fossati, Giulia Malvestiti, Elisabetta Angelino: PM2.5 WINTERTIME SENSITIVITY TO CHANGES IN NOX, SO2 AND NH3 EMISSIONS IN LOMBARDY REGION
H21-048: Oscar Björnham, Daniel Elfverson, Leif Persson: Population dynamics and its consequences on health risk modeling following inhalation exposure
H21-050: Jose-Luis Santiago, Esther Rivas, Beatriz Sanchez, Riccardo Buccolieri, Oliver S. Carlo, Alberto Martilli, Marta G. Vivanco, Fernando Martín: IMPACT OF GREEN INFRASTRUCTURE ON TRAFFIC RELATED POLLUTANT CONCENTRATION IN HIGH-RISE URBAN AREAS
H21-052: Francesca Tagliaferri, Marzio Invernizzi, Selena Sironi: VALIDATION STUDY OF WINDTRAX BACKWARD LAGRANGIAN MODEL
H21-017: Ivelina Georgieva, Georgi Gadzhev, Kostadin Ganev, Vladimir Ivanov: EVALUATION OF THE EFFECTS OF THE NATIONAL EMISSION REDUCTION STRATEGIES FOR YEARS 2020-2029 AND AFTER 2030 ON THE SULPHUR AND NITROGEN SURFACE CONCENTRATIONS ON THE TERRITORY OF BULGARIA
H21-071: Boris Mifka, Maja Telišman Prtenjak, Ivna Kavre Piltaver, Darko Mekterović, Josipa Kuzmić , Marijan Marcijuš, Irena Ciglenečki: The aspects of numerical simulations on desert dust outbreaks over the Adriatic Sea; influence of Asian and African deserts
H21-072: Alex Resovsky, Eriksson, E. M., Velay-Lasry, F., Resovsky, A., Lachatre, M., Albergel., A., Calori, G., Nanni, A., Radice, P., Abiye, O., Fawole, O., Adebola, O., Mate, K., Kuntasal, O. O., Awe, Y. A., Fagbeja, M. A., Akpokodje, J. E., Johnson, T., Weaver, C., Forastiere, F., Spadaro, J. V.: DEVELOPMENT OF AN AIR POLLUTANT EMISSIONS INVENTORY AND MODELING FRAMEWORK FOR AIR QUALITY CONTROL MEASURES IN LAGOS, NIGERIA
H21-078: Andrea Bisignano, M. Beggiato, M. C. Bove, R. Cresta, F. Cassola, D. Sacchetti, A. Mazzino, P. Prati: ASSESSING THE IMPACT OF PORT EMISSIONS ON AIR POLLUTION IN GENOA
H21-016: Georgi Gadzhev, Kostadin Ganev, Ivelina Georgieva, Vladimir Ivanov: Evaluation of the Impact of the Projected Future Emissions from Energy on the Air Quality in Bulgaria
H21-083: Chun-Ji Kim, Su-Bin Oh, Sang-Hyun Lee, Hyun-Ha Lee, Chun-Sil Jin: Atmospheric dispersion characteristics of radioactive materials obtained from WRF/HYSPLIT in nuclear power plants
H21-086: Margit Pattantyús-Ábrahám: NEW REGULATION FOR DOSE ASSESSMENT OF RADIOACTIVE RELEASES IN GERMANY
H21-090: Małgorzata Werner, Anetta Drzeniecka-Osiadacz, Lech Gawuc, Maciej Kryza, Tymoteusz Sawiński, Krzysztof Skotak, Massimo Vieno. Presented by Paweł Porwisiak: Impact of policy abatements on air quality in Central Europe
H21-051: Jose-Luis Santiago, Esther Rivas, Beatriz Sanchez, Riccardo Buccolieri, Alberto Martilli, Marta G. Vivanco, Antonio Esposito, Fernando Martín: Ranking of various single and combinations of local air pollution mitigation measures in an urban environment
H21-084: Sang-Hyun Lee, Su-Bin Oh, Sang-Hyun Lee, Hyun-Ha Lee, Chun-Sil Jin: DEVELOPMENT OF A DYNAMIC DOWNSCALING METHOD FOR USE IN SHORT-RANGE ATMOSPHERIC DISPERSION MODELLING NEAR NUCLEAR POWER PLANTS

29 Sept 16:30 – 17:10	Poster Pitches Session 3 (Renato Araújo Auditorium, Rectory Building)

H21-099: Niki Paisi, Jonilda Kushta, Angelos Violaris, Hugo Denier Van Der Gon, Jos Lelieveld: Role of Emission Inventories and Differential Toxicity Approach in Modelling of PM2.5 and Associated Health Impacts

H21-101: Grzegorz Jeleniewicz, Joanna Strużewska, Jacek Kamiński, Paulina Jagiełło, Aneta Gienibor, Marcin Kawka, Aleksander Norowski: MODELLING BASED METHOD FOR ASSESSING THE REPRESENTATIVENESS OF AIR QUALITY MONITORING STATIONS
H21-104: Ana R. Gamarra, Marta G. Vivanco, Mark R. Theobald, Yolanda Lechón, Carmen Lago, Victoria Gil, Juan Luis Garrido, José Luis Santiago, Fernando Martín, Alejandro Rodríguez-Sánchez, Eugenio Sánchez. Presented by Alejandro Rodriguez-Sanchez: HEALTH IMPACT BENEFITS OF INCREASED RENEWABLE ENERGY USE IN THE SPANISH ROAD TRANSPORT SECTOR
H21-105: Vladimír Fuka, Štěpán Nosek, Jelena Radović: Sensitivity of LES simulations to resolution, subgrid models and boundary conditions
H21-108: Bernd Leitl, S. Michel, S Schalau, H. Plischka, J. Turnow, B. Schalau, F. Harms: Softwaretools for simulating dispersion of hazardous materials in industrial environments
H21-114: Roberta De Maria, Stefano Bande, Francesca Bissardella, Cinzia Cascone, Stefania Ghigo, Marilena Maringo: Impact assessment on air quality of a waste-to-energy plant in Turin
H21-119: Benoît Cuilhe, Martin Ferrand, Yelva Roustan, Bertrand Carissimo: Recent developments in high-resolution wind field modelling in complex terrain for dispersion simulations using GRAMM-SCI
H21-121: Andres Simon-Moral, Alberto Martilli, Ales Padró, Lexuri Yurrebaso: Assessment of the dispersive capacity of neighbourhoods based on Local Climate Zones classification
H21-133: Roseane Albani: A BAYESIAN INFERENCE TECHNIQUE COMBINED WITH A STOCHASTIC WIND MODELING TO IMPROVE MULTIPLE SOURCE PARAMETERS ESTIMATION IN THE ATMOSPHERE
H21-136: Alexandre Armengaud, Sonia Oppo, Eve-Agnès Fiorentino, Frédéric Mahé, Barbara D'Anna: INTERCOMPARISON BETWEEN OBSERVATIONS AND 3D LAGRANGIAN MODEL SIMULATIONS FOR POLLUTANTS DISPERSION IN THE HARBORS OF MARSEILLE AND TOULON IN 2021
H21-138: Armando Pelliccioni, Livia Grandoni, Annalisa Di Bernardino, Paolo Monti: Tilt correction method for the estimation of scaling variables of Monin-Obukhov Similarity Theory in urban areas
H21-142: Elisabetta Ronchieri, Leonardo Aragão, Rossana Di Staso: TIME SERIES ANALYSIS OF METEOROLOGICAL PARAMETERS AND AIR POLLUTION CONCENTRATIONS IN EMILIA-ROMAGNA, ITALY, DURING COVID-19 INFECTION
H21-146: Tomas Halenka, Ranjeet S. Sokhi: NON-CO2 FORCERS AND THEIR CLIMATE, WEATHER, AIR QUALITY AND HEALTH IMPACTS – NEW PROJECT FOCI
H21-155: Kyriaki-Maria Fameli, Vasiliki D. Assimakopoulos, Theodore M. Giannaros: SOURCES AND DISPERSION OF BTX EMISSIONS IN A PORT AREA IN GREECE
H21-109: Silvia Trini Castelli, Massimo Martina: SIMULATING THE DISPERSION OF MICROPLASTICS IN THE ATMOSPHERE TOWARDS A REMOTE SITE
H21-158: Maciej Kryza, Małgorzata Werner, Krzysztof Skotak, Mike Holland, Helen ApSimon: Year to year changes in PM2.5 population exposure – a case study for Poland
H21-160: Amela Jeričević, Goran Gašparac: Aviation environmental impacts
H21-137: Alexandre Armengaud, Morgan Jacquinot, Romain Derain, Benjamin Rocher, Damien Piga: AZUR MODEL: A NEW SPATIAL ESTIMATION METHOD FOR DAILY MAPPING PARTICLES AND NITROGEN DIOXYDE
H21-169: Chiara Collaveri, Bianca Patrizia Andreini, Elisa Bini, Fiammetta Dini, Stefano Fortunato, Marina Rosato, Gaetano Licitra: AERNOSTRUM: Monitoring Of Air Pollution in the Port of Livorno and of Portoferraio on the Island of Elba and Detailed Estimate of Emissions in the Ports
H21-172: Niko Karvosenoja, Ismo Hämäläinen, Santtu Karhinen, Mikko Savolahti, Ville-Veikko Paunu, Janne Pesu, Jaakko Kukkonen, Timo Lanki: An integrated tool to assess the climate and health benefits of urban strategies and measures
H21-173: Pontus von Schoenberg, Peter Tunved, Niklas Brännström: Enhanced aerosol dynamics in a lagrangian particle dispersion model
H21-058: Oliver Savio Carlo, Riccardo Buccolieri, Esther Rivas, Jose L. Santiago, Pietro Salizzoni, Antonio Esposito, M. Salman Siddiqui. Presented by Fernando Martin: MODELLING AND ASSESSMENT OF THE EFFECTS OF OBSTACLES IN URBAN CANYONS
H21-007: Günther Schauberger, Martin Piringer: CRITICAL DISCUSSION OF THE DETERMINATION OF ANNOYANCE DUE TO ENVIRONMENTAL ODOUR EMISSION
H21-149: Agnese Pini, Tommaso Vigilante, Livia Grandoni, Giovanni Leuzzi, Armando Pelliccioni, Paolo Monti. ANALYSIS OF THE INFLUENCE OF GEOMETRIC AND VENTILATION FACTORS ON INDOOR POLLUTANT DISPERSION: A NUMERICAL STUDY

H21-118: Ignacio Pisso, Susana López-Aparicio, Dam Vo Tanh, Franck Delauge, Terje Krognes, Magdalena Pühl, Alina Fiehn, Amy Foulds, Grant Allen: Inverse transport and dispersion modelling of anthropogenic greenhouse gas emissions: urban CO2 and offshore oil CH4
H21-100: Alessandro Bigi, Sara Fabbi, Giorgio Veratti, Alessandro Bigi, Grazia Ghermandi: Air quality (PM_{10}) scenarios resulting from the expansion of the hydrogen fuel cell electric vehicles in Emilia Romagna (Northern Italy)
H21-036: Pascal Joassin, F. Lenartz, M. Dury: STUDY OF SPATIAL AND TEMPORAL VARIABILITY OF PRODUCTION RATES AND COMPOSITION OF NO X SOURCES USING IN-SITU MEASUREMENTS COMBINED TO A DYNAMIC MODEL OF NO X -O3 SYSTEM
H21-111: Malo Le Guellec, Liying Chen, Claude Souprayen: Understanding the impact of cruise ships emission in urban harbour using CFD modelling in CAPNAVIR project

POSTER SESSIONS

Session 1 – 27 and 28th Sept – Dept Environment and Planning
Session 2 – 29 and 30th Sept – Rectory Building

Posters should be put on the first day of the session and removed on the second day until 17:00

Session 1 – 27th and 28th Sept – Dept Environment and Planning

Ref	Title and Authors	Pitch Session
H21-005	Mohamed Yassin: EFFECT OF UPSTREAM BUILDING ON THE POLLUTANT DISPERSION IN URBAN CANOPY WITH CHANGES THERMAL STABILITY	27 set, 15:40
H21-012	Sofia Farina, Dino Zardi: NUMERICAL MODELING OF PASSIVE TRACER DISPERSION FROM A CONTINUOUS POINT SOURCE IN A STEADY THERMALLY DRIVEN SLOPE WIND	27 set, 15:40
H21-015	Lech Gawuc, Karol Szymankiewicz, Dorota Kawicka, Ewelina Mielczarek, Kamila Marek, Marek Soliwoda, Jadwiga Maciejewska: BOTTOM-UP INVENTORY OF RESIDENTIAL COMBUSTION EMISSIONS IN POLAND FOR NATIONAL AIR QUALITY MODELLING: CURRENT STATUS AND PERSPECTIVES	27 set, 15:40
H21-020	Arièle Defossez, Rayna Charlatchka: State of the art on deposition by fog and its difference with respect to dry and wet deposition (wash-out) for a better representation in impact studies	28 set, 15:40
H21-023	Jens Peter Frankemölle, Johan Camps, Pieter De Meutter, Johan Meyers: Near-range Gaussian plume modelling for gamma dose rate reconstruction	27 set, 15:40
H21-024	Victor Watson, François Septier, Patrick Armand, Christophe Duchenne: Detection of low level concentrations of hazardous materials in the air using sequential multivariate detection methods	28 set, 15:40
H21-028	Margret Velizarova, Reneta Dimitrova, Angel Burov, Danail Brezov: Dispersion modelling of major traffic sources in Sofia city	28 set, 15:40
H21-030	Paweł Porwisiak, Maciej Kryza, Massimo Vieno, Janice Scheffler, Mike Holland, Lech Gawuc, Bruce Denby, Qing Mu, Małgorzata Werner: Benzo(a)pyrene concentrations in Central Europe – the role of meteorological conditions and health impact analysis	27 set, 15:40
H21-031	Pirmin Kaufmann, Stefan Rüdisühli: Operational Dispersion Ensemble at MeteoSwiss	28 set, 15:40
H21-037	Dušan Štefánik, Jana Krajčovičová, Tereza Šedivá: ASSESSMENT OF THE IMPACT OF THE RESIDENTIAL HEATING EMISSIONS ON CONCENTRATIONS BY LOCAL AND REGIONAL AIR-QUALITY MODELS	28 set, 15:40
H21-042	Loris Colombo, Alessandro Marongiu, Giuseppe Fossati, Giulia Malvestiti, Elisabetta Angelino: PM2.5 WINTERTIME SENSITIVITY TO CHANGES IN NOX, SO2 AND NH3 EMISSIONS IN LOMBARDY REGION	28 set, 15:40
H21-044	Hanane Bounouas, Johann Chardeur, Olivier Connan, Didier Hebert, Philippe Laguionie, Denis Maro, Hugo Renard, Pierre Roupsard, Marianne Rozet, Eric Dupont, Thaddé Régi, Bertrand Carissimo, Aurélien Faucheux, Yannick Lefranc, Yelva Roustan: STUDY OF ATMOSPHERIC DISPERSION UNDER LOW WIND CONDITIONS IN AN URBAN ENVIRONMENT, FIRST RESULTS	27 set, 15:40
H21-045	Joffrey Dumont Le Brazidec, Marc Bocquet, Olivier Saunier, Yelva Roustan: Bayesian transdimensional inverse reconstruction of the 137Cs Fukushima-Daiichi release	27 set, 15:40
H21-053	Bruno Ribstein, Maxime Nibart, Daniel Loeb, Patrick Armand, Christophe Duchenne: PROPOSAL FOR MODELLING THE INFLUENCE OF ROOF SLOPE ON URBAN FLOW WITH A DIAGNOSTIC MODEL	27 set, 15:40
H21-055	Bruno Ribstein, Maxime Nibart, Patrick Armand, Christophe Duchenne: A NEW APPROACH TO COUPLING FLOW AND DISPERSION CFD SIMULATIONS IN A LARGE URBAN AREA AND BUILDINGS OF INTEREST	27 set, 15:40
H21-063	Boulos Alam, Rayan Nkenfack Soppi, Amir Ali Feiz, Pierre Ngae, Pramod Kumar, Amer Chpoun: Numerical modelling of pollutant dispersion over an idealized urban area using different algebraic closure models	27 set, 15:40
H21-077	Iwona Rackiewicz, Agnieszka Bartocha, Tomasz Przybyła, Marek Rosicki, Piotr Michałek: A DYNAMIC ODOUR MAPPING SYSTEM AS A TOOL TO SUPPORT LOCAL AUTHORITIES AND WASTEWATER TREATMENT PLANTS IN ODOUR IMPACT MANAGEMENT	27 set, 15:40

H21-081	Bianca Tenti, Enrico Ferrero: SMOKE PLUME FROM FIRE LAGRANGIAN SIMULATION: DEPENDENCE ON DRAG COEFFICIENT AND RESOLUTION	27 set, 15:40
H21-082	Eve Draper, J. Duncan Whyatt, Sarah E. Metcalfe: Estimating regional background concentrations of PM2.5 and verifying local source contributions in a data poor environment	27 set, 15:40
H21-092	Rory Hetherington, Graham Tickle, Veronica Bowman, Daniel Silk, Simon Gant, Adrian Kelsey, Alison McGillivray, Harvey Tucker: DRIFT MODELLING OF THE DESERT TORTOISE AND FLADIS AMMONIA TRIALS FOR THE JACK RABBIT III MODEL INTER-COMPARISON EXERCISE	27 set, 15:40
H21-106	Marie Mulder: Combining sentinel observations with plume backtrackings from a dispersion model to improve wildfire detection	27 set, 15:40
H21-139	Guilhem Balvet, Martin Ferrand, Yelva Roustan, Jean-Pierre Minier, Christophe Henry, Inria Sophia Antipolis: Treatment of the near ground effect in Lagrangian stochastic methods applied to a 2-D point source dispersion after an isolated obstacle in a neutral flow	27 set, 15:40
H21-149	H21-149: Agnese Pini, Tommaso Vigilante, Livia Grandoni, Giovanni Leuzzi, Armando Pelliccioni, Paolo Monti. ANALYSIS OF THE INFLUENCE OF GEOMETRIC AND VENTILATION FACTORS ON INDOOR POLLUTANT DISPERSION: A NUMERICAL STUDY	29 set 16:30
H21-151	Ana R. Gamarra, Marta G. Vivanco, Mark R. Theobald, Yolanda Lechón, Carmen Lago, Victoria Gil, Juan Luis Garrido, José Luis Santiago, Fernando Martín, Alejandro Rodríguez-Sánchez, Eugenio Sánchez. Presented by Alejandro Rodriguez-Sanchez: Assessing the impact of a traffic low emission zone on pollutant concentrations at street level through a combination of microscopic traffic simulations and air quality modelling at multiscale	27 set, 15:40
H21-156	Cyrill von Arx: Implementation of a decision support system for nuclear emergencies	27 set, 15:40

Session 2 – 29th and 30th Sept – Rectory Building

Ref	Title and Authors	Pitch Session
H21-007	Günther Schauberger, Martin Piringer: CRITICAL DISCUSSION OF THE DETERMINATION OF ANNOYANCE DUE TO ENVIRONMENTAL ODOUR EMISSION	29 set, 16:30
H21-016	Georgi Gadzhev, Kostadin Ganev, Ivelina Georgieva, Vladimir Ivanov: Evaluation of the Impact of the Projected Future Emissions from Energy on the Air Quality in Bulgaria	28 set, 15:40
H21-017	Ivelina Georgieva, Georgi Gadzhev, Kostadin Ganev, Vladimir Ivanov: EVALUATION OF THE EFFECTS OF THE NATIONAL EMISSION REDUCTION STRATEGIES FOR YEARS 2020-2029 AND AFTER 2030 ON THE SULPHUR AND NITROGEN SURFACE CONCENTRATIONS ON THE TERRITORY OF BULGARIA	28 set, 15:40
H21-036	H21-036: Pascal Joassin, F. Lenartz, M. Dury: STUDY OF SPATIAL AND TEMPORAL VARIABILITY OF PRODUCTION RATES AND COMPOSITION OF NO X SOURCES USING IN-SITU MEASUREMENTS COMBINED TO A DYNAMIC MODEL OF NO X -O3 SYSTEM	29 set, 16:30
H21-048	Oscar Björnham, Daniel Elfverson, Leif Persson: Population dynamics and its consequences on health risk modeling following inhalation exposure	28 set, 15:40
H21-050	Jose-Luis Santiago, Esther Rivas, Beatriz Sanchez, Riccardo Buccolieri, Oliver S. Carlo, Alberto Martilli, Marta G. Vivanco, Fernando Martín: IMPACT OF GREEN INFRASTRUCTURE ON TRAFFIC RELATED POLLUTANT CONCENTRATION IN HIGH-RISE URBAN AREAS	28 set, 15:40
H21-051	Jose-Luis Santiago, Esther Rivas, Beatriz Sanchez, Riccardo Buccolieri, Alberto Martilli, Marta G. Vivanco, Antonio Esposito, Fernando Martín: Ranking of various single and combinations of local air pollution mitigation measures in an urban environment	28 set, 15:40
H21-052	Francesca Tagliaferri, Marzio Invernizzi, Selena Sironi: VALIDATION STUDY OF WINDTRAX BACKWARD LAGRANGIAN MODEL	28 set, 15:40
H21-058	Oliver Savio Carlo, Riccardo Buccolieri, Esther Rivas, Jose L. Santiago, Pietro Salizzoni, Antonio Esposito, M. Salman Siddiqui. Presented by Fernando Martin: MODELLING AND ASSESSMENT OF THE EFFECTS OF OBSTACLES IN URBAN CANYONS	29 set, 16:30
H21-071	Boris Mifka, Maja Telišman Prtenjak, Ivna Kavre Piltaver, Darko Mekterović, Josipa Kuzmić , Marijan Marciju̇š, Irena Ciglenečki: The aspects of numerical simulations on desert dust outbreaks over the Adriatic Sea; influence of Asian and African deserts	28 set, 15:40
H21-072	Alex Resovsky, Eriksson, E. M., Velay-Lasry, F., Resovsky, A., Lachatre, M., Albergel., A., Calori, G., Nanni, A., Radice, P., Abiye, O., Fawole, O., Adebola, O., Mate, K., Kuntasal, O. O., Awe, Y. A., Fagbeja, M. A., Akpokodje, J. E., Johnson, T., Weaver, C., Forastiere, F., Spadaro, J. V.: DEVELOPMENT OF AN AIR POLLUTANT EMISSIONS INVENTORY AND MODELING FRAMEWORK FOR AIR QUALITY CONTROL MEASURES IN LAGOS, NIGERIA	28 set, 15:40
H21-078	Andrea Bisignano, M. Beggiato, M. C. Bove, R. Cresta, F. Cassola, D. Sacchetti, A. Mazzino, P. Prati: ASSESSING THE IMPACT OF PORT EMISSIONS ON AIR POLLUTION IN GENOA	28 set, 15:40
H21-083	Chun-Ji Kim, Su-Bin Oh, Sang-Hyun Lee, Hyun-Ha Lee, Chun-Sil Jin: Atmospheric dispersion characteristics of radioactive materials obtained from WRF/HYSPLIT in nuclear power plants	28 set, 15:40
H21-084	Sang-Hyun Lee, Su-Bin Oh, Sang-Hyun Lee, Hyun-Ha Lee, Chun-Sil Jin: DEVELOPMENT OF A DYNAMIC DOWNSCALING METHOD FOR USE IN SHORT-RANGE ATMOSPHERIC DISPERSION MODELLING NEAR NUCLEAR POWER PLANTS	28 set, 15:40
H21-086	Margit Pattantyús-Ábrahám: NEW REGULATION FOR DOSE ASSESSMENT OF RADIOACTIVE RELEASES IN GERMANY	28 set, 15:40
H21-090	Małgorzata Werner, Anetta Drzeniecka-Osiadacz, Lech Gawuc, Maciej Kryza, Tymoteusz Sawiński, Krzysztof Skotak, Massimo Vieno. Presented by Paweł Porwisiak: Impact of policy abatements on air quality in Central Europe	28 set, 15:40
H21-099	Niki Paisi, Jonilda Kushta, Angelos Violaris, Hugo Denier Van Der Gon, Jos Lelieveld: Role of Emission Inventories and Differential Toxicity Approach in Modelling of PM2.5 and Associated Health Impacts	29 set, 16:30
H21-100	Alessandro Bigi, Sara Fabbi, Giorgio Veratti, Alessandro Bigi, Grazia Ghermandi: Air quality (PM10) scenarios resulting from the expansion of the hydrogen fuel cell electric vehicles in Emilia Romagna (Northern Italy)	29 set, 16:30
H21-101	Grzegorz Jeleniewicz, Joanna Strużewska, Jacek Kamiński, Paulina Jagiełło, Aneta Gienibor, Marcin Kawka, Aleksander Norowski: MODELLING BASED METHOD FOR ASSESSING THE REPRESENTATIVENESS OF AIR QUALITY MONITORING STATIONS	29 set, 16:30
H21-104	Ana R. Gamarra, Marta G. Vivanco, Mark R. Theobald, Yolanda Lechón, Carmen Lago, Victoria Gil, Juan Luis Garrido, José Luis Santiago, Fernando Martín, Alejandro Rodríguez-Sánchez, Eugenio Sánchez. Presented by	29 set, 16:30

	Alejandro Rodriguez-Sanchez: HEALTH IMPACT BENEFITS OF INCREASED RENEWABLE ENERGY USE IN THE SPANISH ROAD TRANSPORT SECTOR	
H21-105	Vladimír Fuka, Štěpán Nosek, Jelena Radović: Sensitivity of LES simulations to resolution, subgrid models and boundary conditions	29 set, 16:30
H21-108	Bernd Leitl, S. Michel, S Schalau, H. Plischka, J. Turnow, B. Schalau, F. Harms: Softwaretools for simulating dispersion of hazardous materials in industrial environments	29 set, 16:30
H21-109	Silvia Trini Castelli, Massimo Martina: SIMULATING THE DISPERSION OF MICROPLASTICS IN THE ATMOSPHERE TOWARDS A REMOTE SITE	29 set, 16:30
H21-111	Malo Le Guellec, Liying Chen, Claude Souprayen: Understanding the impact of cruise ships emission in urban harbour using CFD modelling in CAPNAVIR project	29 set, 16:30
H21-114	Roberta De Maria, Stefano Bande, Francesca Bissardella, Cinzia Cascone, Stefania Ghigo, Marilena Maringo: Impact assessment on air quality of a waste-to-energy plant in Turin	29 set, 16:30
H21-118	Ignacio Pisso, Susana López-Aparicio, Dam Vo Tanh, Franck Delauge, Terje Krognes, Magdalena Pühl, Alina Fiehn, Amy Foulds, Grant Allen: Inverse transport and dispersion modelling of anthropogenic greenhouse gas emissions: urban CO2 and offshore oil CH4	29 set, 16:30
H21-119	Benoît Cuilhe, Martin Ferrand, Yelva Roustan, Bertrand Carissimo: Recent developments in high-resolution wind field modelling in complex terrain for dispersion simulations using GRAMM-SCI	29 set, 16:30
H21-121	Andres Simon-Moral, Alberto Martilli, Ales Padró, Lexuri Yurrebaso: Assessment of the dispersive capacity of neighbourhoods based on Local Climate Zones classification	29 set, 16:30
H21-133	Roseane Albani: A BAYESIAN INFERENCE TECHNIQUE COMBINED WITH A STOCHASTIC WIND MODELING TO IMPROVE MULTIPLE SOURCE PARAMETERS ESTIMATION IN THE ATMOSPHERE	29 set, 16:30
H21-136	Alexandre Armengaud, Sonia Oppo, Eve-Agnès Fiorentino, Frédéric Mahé, Barbara D'Anna: INTERCOMPARISON BETWEEN OBSERVATIONS AND 3D LAGRANGIAN MODEL SIMULATIONS FOR POLLUTANTS DISPERSION IN THE HARBORS OF MARSEILLE AND TOULON IN 2021	29 set, 16:30
H21-137	Alexandre Armengaud, Morgan Jacquinot, Romain Derain, Benjamin Rocher, Damien Piga: AZUR MODEL: A NEW SPATIAL ESTIMATION METHOD FOR DAILY MAPPING PARTICLES AND NITROGEN DIOXYDE	29 set, 16:30
H21-138	Armando Pelliccioni, Livia Grandoni, Annalisa Di Bernardino, Paolo Monti: Tilt correction method for the estimation of scaling variables of Monin-Obukhov Similarity Theory in urban areas	29 set, 16:30
H21-142	Elisabetta Ronchieri, Leonardo Aragão, Rossana Di Staso: TIME SERIES ANALYSIS OF METEOROLOGICAL PARAMETERS AND AIR POLLUTION CONCENTRATIONS IN EMILIA-ROMAGNA, ITALY, DURING COVID-19 INFECTION	29 set, 16:30
H21-146	Tomas Halenka, Ranjeet S. Sokhi: NON-CO2 FORCERS AND THEIR CLIMATE, WEATHER, AIR QUALITY AND HEALTH IMPACTS – NEW PROJECT FOCI	29 set, 16:30
H21-155	Kyriaki-Maria Fameli, Vasiliki D. Assimakopoulos, Theodore M. Giannaros: SOURCES AND DISPERSION OF BTX EMISSIONS IN A PORT AREA IN GREECE	29 set, 16:30
H21-158	Maciej Kryza, Małgorzata Werner, Krzysztof Skotak, Mike Holland, Helen ApSimon: Year to year changes in PM2.5 population exposure – a case study for Poland	29 set, 16:30
H21-160	Amela Jeričević, Goran Gašparac: Aviation environmental impacts	29 set, 16:30
H21-169	Chiara Collaveri, Bianca Patrizia Andreini, Elisa Bini, Fiammetta Dini, Stefano Fortunato, Marina Rosato, Gaetano Licitra: AERNOSTRUM: Monitoring Of Air Pollution in the Port of Livorno and of Portoferraio on the Island of Elba and Detailed Estimate of Emissions in the Ports	29 set, 16:30
H21-172	Niko Karvosenoja, Ismo Hämäläinen, Santtu Karhinen, Mikko Savolahti, Ville-Veikko Paunu, Janne Pesu, Jaakko Kukkonen, Timo Lanki: An integrated tool to assess the climate and health benefits of urban strategies and measures	29 set, 16:30
H21-173	Pontus von Schoenberg, Peter Tunved, Niklas Brännström: Enhanced aerosol dynamics in a lagrangian particle dispersion model	29 set, 16:30